

INMATEH -

**AGRICULTURAL
ENGINEERING**

SEPTEMBER - DECEMBER

No liability is assumed by the editorial staff for the content of scientific papers and opinions published in this volume. They represent the author's point of view

Managing Editorial Board - INMA Bucharest

Editor in Chief

Lucian-Ionel CIOCA, Professor, PhD.Eng., "Lucian Blaga" University of Sibiu

Executive Editor

Lucreția POPA
PhD.Eng, SR I

Assistant Editor

Nicolae-Valentin VLADUȚ
PhD.Eng, SR I
Mihai-Gabriel MATAȚHE
PhD.Eng, SR I

Logistic support, database

Virgil MURARU
PhD.Eng, SR I

Scientific Secretary

Cârdei Petre, math.

Official translator

RADU Daniela-Cristina, English

Editorial Board

- *QUENDLER Elisabeth – Austria, Vienna, Univ. of Natural Resources & Applied Life Sciences;*
- *Ir. HUYGHEBAERT Bruno – Belgia, Walloon Agricultural Research Center CRA-W;*
- *Van IMPE F.M. Jan – Belgia, KU Leuven University*
- *FABBRO Dal Inacio Maria - Brazil, Campinas State University;*
- *ATANASOV Atanas – Bulgaria, "Angel Kanchev" University of Rousse*
- *MOLINOS-SENANTE María – Chile, Pontificia Universidad Católica - Vicedecana, Escuela de Ingeniería UC*
- *BILANDZIJA Nikola – Croatia, Zagreb University, Faculty of Agriculture;*
- *KOSUTIC Silvio – Croatia, Zagreb University, Faculty of Agriculture;*
- *KOVACEV Igor - Croatia, Zagreb University, Faculty of Agriculture;*
- *GONZÁLEZ Omar – Republic of Cuba, Central University "Marta Abreu" de las Villas;*
- *KATHIJOTES Nicholas – Cyprus, University of Nicosia;*
- *HERAK David - Czech Republic, Czech University of Agriculture Prague;*
- *BORCHARD Nils – Finland, Natural Resources Institute Finland (Luke);*
- *SAUER Johannes – Germany, Technical University Munich;*
- *FENYVESI László – Hungary, Hungarian Institute of Agricultural Engineering Godollo;*
- *PEEYUSH Soni - India, Indian Institute of Technology, Kharagpur;*
- *MOHAMMADREZA Alizadeh – Iran, Department of Agricultural Engineering, Rice Research Institute of Iran (RRII);*
- *De WRACHIEN Daniele - Italy, State University of Milan;*
- *BIOCCA Marcello - Italy, Agricultural Research Council, Agricultural Engineering Research Unit;*
- *COLANTONI Andrea – Italy, University Viterbo;*
- *SARAUSSKIS Egidijus – Lithuania, Vytautas Magnus University, Faculty of Agricultural Engineering;*
- *KRIAUCIUNIENE Zita - Lithuania, Vytautas Magnus University;*
- *DUKE Mike – New Zealand, University of Waikato, Faculty of Science and Engineering;*
- *EWEMOJE Temitayo Abayomy – Nigeria, University of Ibadan, Faculty of Technology, Department of Agricultural and Environmental Engineering;*
- *SKIERUCHA Wojciech – Poland, Institute of Agro-physics Polish Academy of Sciences, Lublin;*
- *EKIELSKI Adam - Poland, Warsaw University of Life Sciences;*
- *KOT Sebastian - Poland, Czestochowa University of Technology*
- *SAVIN Lazar– Serbia, University of Novi Sad, Faculty of Agriculture, Department of Agricultural Engineering;*
- *SIMIKIC Mirko– Serbia, University of Novi Sad, Faculty of Agriculture, Department of Agricultural Engineering;*
- *MARTINOV Milan - Serbia, Faculty of Agriculture, Department of Agricultural Engineering,*
- *TURAN Jan – Slovakia, Technical University Kosice, Dept Elect & Multimedia Commun, Kosice;*
- *MADYIRA M. Daniel - South Africa, University of Johannesburg, Mechanical Engineering Science Department*
- *COZ FERNANDEZ Alberto – Spain, University of Cantabria, School of Nautical Studies, Department of Chemistry and Process & Resource Engineering;*
- *ERTEKIN Can - Turkey, Akdeniz University Antalia;*
- *KABAŞ Önder –Turkey, Antalia, Agricultural Scientific Research Institute of Batı Akdeniz;*
- *SELVI Kemal Çağatay - Turkey, Samsun, University of Ondokuz Mayıs, Faculty of Agriculture, Department of Machines for Agriculture;*
- *ÖTLEŞ Semih - Turkey, Ege University, Engineering Faculty, Food Engineering Department;*
- *MARUSCHAK Pavlo - Ukraine, Ternopil Ivan Pul'uj National Technical University, Department of Technical Mechanics and Agricultural Engineering;*
- *BULGAKOV Volodymyr – Ukraine, National University of Life and Environmental Sciences of Ukraine;*
- *PARASCHIV Gigel - Romania, Politehnica University of Bucharest;*
- *VOICU Gheorghe - Romania, Politehnica University of Bucharest;*
- *BIRIŞ Sorin - Romania, Politehnica University of Bucharest;*
- *MAICAN Edmond - Romania, Politehnica University of Bucharest;*
- *FILIP Nicolae - Romania, Technical University Cluj Napoca;*
- *COZAR Onuc-Romania, „Babes-Bolyai” University of Cluj-Napoca Romania, Faculty of Physics;*
- *VLASE Sorin - Romania, “Transilvania” University of Braşov;*
- *ȚENU Ioan - Romania, USAMV Iași;*
- *HERIŞANU Nicolae - Romania, Politehnica University of Timisoara;*
- *MARSAVINA Liviu - Romania, Politehnica University of Timisoara*
- *MARINCA Vasile - Romania, Politehnica University of Timisoara*
- *GERGEN Iosif - Romania, USAMVB Timișoara;*
- *BORDEAN Despina-Maria - Romania, USAMVB Timișoara;*
- *BUNGESCU Sorin - Romania, USAMVB Timișoara;*
- *VOICEA Iulian - Romania, INMA Bucharest*
- *DEAK Gyorgy - Romania, INCDPM;*
- *BELC Nastasia - Romania, IBA Bucharest;*
- *BUȚU Alina - Romania, INCDSB Bucharest;*
- *PAUN Mihaela - Romania, National Institute of Research and Development for Biological Sciences, INCDSB*

INMATEH - Agricultural Engineering journal is indexed in the next international databases:
ELSEVIER /SciVerse SCOPUS, CLARIVATE - WEB of SCIENCE- Emerging Sources Citation Index (ESCI),
ULRICHS Web: Global Serials Directory, CABI, SCPIO, Index COPERNICUS International, EBSCO Publishing,
Elektronische Zeitschriftenbibliothek

INMATEH - Agricultural Engineering
vol. 65, no. 3 / 2021

e-ISSN: 2068 – 2239; p: ISSN: 2068 – 4215

<https://inmateh.eu/>

E-mail: inmatehjournal@gmail.com

Edited by: **INMA Bucharest**

Copyright: INMA Bucharest / Romania

National Institute for Research-Development of Machines and Installations
Designed for Agriculture and Food Industry - INMA Bucharest
6, Ion Ionescu de la Brad Bvd., sector 1, Bucharest, ROMANIA

CONTENT

		Page(s)
1.	<p>RESEARCH ON SHREDDED BIOMASS DRYING IN A VIBRATING FLUIDIZED BED DRYER Pavel Ioan¹⁾; Chirita Alexandru Polifron¹⁾; Matache Gabriela¹⁾; Popescu Alina¹⁾; Pavel Kati¹⁾, Ștefan Vasilica²⁾ ¹⁾Hydraulics and Pneumatics Research Institute INOE 2000-IHP Bucharest, Romania; ²⁾ National Institute of Research – Development for Machines and Installations Designed for Agriculture and Food Industry – INMA Bucharest</p>	09
2.	<p>EXPERIMENTAL TEST AND FINITE ELEMENT ANALYSIS OF POTATO IMPACT ACCELERATION Deng Weigang, Liu Chenglong, Li Peng, Wang Yanlong, Xie Shengshi, Wang Chunguang * College of Mechanical and Electrical Engineering, Inner Mongolia Agricultural University, Hohhot, China</p>	19
3.	<p>DEVELOPMENT AND TEST OF CORN STRAW KNEADING AND CONVEYING DEVICE / Geng Aijun^{1,2)}, Gao Ang¹⁾, Zhang Ji^{*1)}, Zhang Zhilong¹⁾, Hu Xiaolong¹⁾, Li Ke¹⁾ ¹⁾ Shandong Agricultural University, College of Mechanical and Electrical Engineering/ China; ²⁾ Shandong Provincial Engineering Laboratory of Agricultural Equipment Intelligence/ China</p>	29
4.	<p>GRAIN AUGER CONVEYOR-DISTRIBUTOR Kupreenko Aleksey¹⁾; Kuznetsov Yuri^{*2)}; Bychkova Tatiana¹⁾; Kravchenko Igor³⁾; Aldoshin Nikolay³⁾; Kalashnikova Larisa⁴⁾ ¹⁾Bryansk State Agrarian University / Russia; ²⁾Orel State Agrarian University named after N.V. Parakhin / Russia; ³⁾Russian State Agrarian University, Russia; ⁴⁾Orel State University named after I.S. Turgenov / Russia</p>	39
5.	<p>LONGITUDINAL COMPRESSING AND SHEARING PROPERTIES OF SILAGE CORN STALK IN NORTH CHINA PLAIN Chen Meizhou¹⁾, Xu Guangfei¹⁾, Wei Maojian¹⁾, Song Zhicai¹⁾, Wang Wenjun¹⁾, Diao Peisong^{*1)} Teng Shaomin²⁾ ¹⁾School of Agricultural and Food Science, Shandong Univ. of Technology, Zibo/China; ²⁾Menoble Co., Ltd., Beijing / China</p>	47
6.	<p>EXPERIMENTAL STUDY ON AIR FLOW FIELD CHARACTERISTICS OF SUCTION METERING DEVICE Meng Zhang¹⁾; Zeqi Liu¹⁾; Yajun Zhuang¹⁾; Jie Han¹⁾; Xiang Yin^{1,3)}; Yulong Chen^{*1,2)} ¹⁾ School of Agricultural Engineering and Food Science, Shandong University of Technology, Zibo / China; ²⁾ Research of Institute of Ecological Unmanned Farm, Shandong University of Technology, Zibo / China; ³⁾ Shandong provincial key laboratory of dry-farming machinery and informatisation, Zibo / China</p>	57
7.	<p>STRENGTH TESTING OF STRIPPING CYLINDER'S TOOTH Buryanov Alexey, Chervyakov Ivan, Kolin'ko Alexey Federal State Budgetary Scientific Institution «Agricultural Research Centre «Donskoy» / Russia</p>	67
8.	<p>WORKSPACE ANALYSIS OF A FLAME INTRA-ROW WEEDING ROBOT IN VEGETABLE FIELD AND NUMERICAL SIMULATION OF PROPANE COMBUSTION Bing Xu¹⁾, Decong Zheng¹⁾, Jiaxin Wang²⁾, Youzhi Yang³⁾ ¹⁾ College of Agricultural Engineering, Shanxi Agricultural University, Taigu / China ²⁾ College of Mechanical and Electronic Engineering, Northwest A&F University, Yangling / China ³⁾Quick Intelligent Equipment Co., Ltd, Changzhou / China</p>	73
9.	<p>WORK MOTION STUDY OF PIVOT TYPE TRAILER OPERATION ON TWO WHEEL TRACTORS Muhammad Dhafir¹⁾, Muhammad Idkham, Safrizal, Agus Arip Munawar Agriculture Engineering Department Universitas Syiah Kuala / Indonesia</p>	82
10.	<p>DESIGN AND EXPERIMENT OF A NEW ROTARY COATING MACHINE BASED ON LabVIEW Xiwen Zhang, Zhanfeng Hou[*], Nianzu Dai Inner Mongolia Agricultural University, College of Mechanical and Electrical Engineering, Inner Mongolia, China</p>	91
11.	<p>MATHEMATICAL MODELING OF EAR GRAIN SEPARATION PROCESS DEPENDING ON THE LENGTH OF THE AXIAL FLOW THRESHING APPARATUS Cujbescu D.¹⁾, Găgeanu I.^{*1)}, Iosif A.²⁾ ¹⁾ INMA Bucharest / Romania; ²⁾ Herman Oilfield Inspection Service, Ploiești / Romania</p>	101
12.	<p>RESEARCH ON VISUAL NAVIGATION PATH DETECTION METHOD FOR DENSE PLUM GROVE XiaoDan Ren¹⁾; Haichao Wang^{*2)}; Xin Shi²⁾ ¹⁾Inner Mongolia Technical College of Mechanics and Electrics, Department of Electrical Engineering, Inner Mongolia/ China; ²⁾Inner Mongolia Agricultural University, College of Energy and Transportation Engineering, Inner Mongolia / China</p>	111
13.	<p>RESEARCH OF A LATERAL REAMER BIT FOR DIGGING PLANTING HOLE IN ROCKY ABANDONED MINE AREA Luo Haifeng[*], Chen Chaoyu Beijing Forest University, Beijing / China</p>	119
14.	<p>THEORETICAL CONSIDERATIONS ON THE OPTIMIZATION OF THE WORKING PROCESS OF VARIABLE WIDTH PLOUGHS Nuțescu C.¹⁾, Găgeanu I.^{*2)}, Cujbescu D.^{*2)} ¹⁾University Politehnica of Bucharest / Romania; ²⁾INMA Bucharest / Romania</p>	129

		Page(s)
15.	DESIGN AND TEST EVALUATION OF THE SUBSOILER EQUIPPED WITH TILLAGE DEPTH MONITORING AND CONTROL SUBSOILING ASSEMBLIES / Lou Shangyi¹⁾, He Jin^{*1)}, Li Hongwen¹⁾, Wang Qingjie¹⁾, Lu Caiyun¹⁾, Wu Yihang¹⁾, Liu Peng¹⁾, Li Hui²⁾ ¹⁾ College of Engineering, China Agricultural University, Beijing / China; ²⁾ Shandong Academy of Agricultural Machinery Sciences, Jinan / China	139
16.	EFFECT OF SEED FILLING AND RELEASING ANGLES ON THE PERFORMANCE OF COMPOUND VACUUM SEED METERING DEVICE Liu Zeqi¹⁾, Zhang Meng¹⁾, Han Jie¹⁾, Zhuang Yajun¹⁾, Yin Xiang^{1,3)}, Chen Yulong^{*1,2)} ¹⁾ School of Agricultural Engineering and Food Science, Shandong University of Technology, Zibo / China; ²⁾ Research of Institute of Ecological Unmanned Farm, Shandong University of Technology, Zibo / China; ³⁾ Shandong provincial key laboratory of dry-farming machinery and informatization, Zibo / China	153
17.	THREE DIMENSIONAL SIMULATION OF OIL FLOW CHARACTERISTICS IN LUBRICATION SYSTEM OF ROTARY TILLAGE ENGINE Junxiang Gao, Xiaoliang Gao[*], Wei Zou[*] ¹⁾ Hunan Financial and Industrial Vocational-Technical College, Heng'yang, Hunan / China	163
18.	STUDY ON PRECISE FEEDING CONTROL OF DAIRY COWS BASED ON WIRELESS COMMUNICATION TECHNOLOGY AND DAIRY COW INFORMATION MANAGEMENT TECHNOLOGY Bin Li[*], Mingjun Ma, Chaoju Yang Xinxiang Vocational and Technical College, Xinxiang, Henan / China	173
19.	DEM PARAMETERS CALIBRATION OF MIXED BIOMASS SAWDUST MODEL WITH MULTI-RESPONSE INDICATORS Gong Xun¹⁾, Bai XueWei^{*1)}, Huang HaiBo¹⁾, Zhang FengYu¹⁾, Gong YuanJuan¹⁾, Wei DeSheng²⁾ ¹⁾ Shenyang Agricultural University, College of Engineering, Shenyang / China; ²⁾ Sunbon Agricultural Machinery Manufacturing Company, Siping / China	183
20.	DESIGN AND EXPERIMENT OF CENTRIFUGAL COLLISION TEST DEVICE FOR MILLET AND SWEET BUCKWHEAT GRAIN Sun Jingxin¹⁾, Yang Liqin²⁾, Xu Baohui¹⁾, Guo Yuming^{*3)}, Cui Qingliang³⁾, Zhang Yanqing³⁾ ¹⁾ Department of Mechanical and Electrical Engineering, Yuncheng University, Yuncheng / China; ²⁾ Planning Finance Office, Yuncheng University, Yuncheng / China; ³⁾ College of Agricultural Engineering, Shanxi Agriculture University, Taigu / China	193
21.	EXHAUST NOISE ANALYSIS RESEARCH FOR A SINGLE-CYLINDER DIESEL ENGINE AND EVALUATION OF NOISE FILTRATION BY SIMULATION / Golgot Claudiu^{*1)}, Filip Nicolae¹⁾ Faculty of Road Vehicles, Mechatronics and Mechanics, Technical University of Cluj–Napoca / Romania	203
22.	DESIGN AND PARAMETER OPTIMIZATION OF LAYERED FERTILIZATION OPENER FOR WHEAT, BASED ON EDEM Zhilong Zhang^{1,2)}, Jinlong Zheng¹⁾, Aijun Geng^{1,2)}, Ji Zhang^{1,2)}, Abdalla N. O. Kheiry³⁾, Ang Gao¹⁾ ¹⁾ Shandong Agricultural University, Tai'an /China; ²⁾ Shandong Provincial Engineering Laboratory of Agricultural Equipment Intelligence, Tai'an; ³⁾ Sudan University of science and Technology, Khartoum, Sudan	213
23.	STUDY ON ACTIVE ANTI ROLLOVER CONTROL AND MODEL TEST OF TRACTOR MOMENTUM FLYWHEEL Weihong Qiao¹⁾, Qihong Wei Xinxiang vocational and technical college, Xinxiang, Henan / China	225
24.	METHOD OF THEORY OF DIMENSIONS IN EXPERIMENTAL RESEARCH OF SYSTEMS AND PROCESSES / МЕТОД ТЕОРІЇ РОЗМІРНОСТЕЙ В ЕКСПЕРИМЕНТАЛЬНИХ ДОСЛІДЖЕННЯХ СИСТЕМ І ПРОЦЕСІВ Dmytriv V.T.¹⁾, Dmytriv I.V.¹⁾, Horodetskyi I.M.²⁾, Horodniak R.V.¹⁾, Dmytriv T.V.³⁾ ¹⁾ Lviv Polytechnic National University, Institute of Mechanical Engineering and Transport, Lviv, Ukraine ²⁾ Lviv National Agrarian University, Faculty of Mechanic, Power Engineering and Information Technologies, Lviv-Dubliany, Ukraine; ³⁾ Lviv Polytechnic National Univ., Institute of Computer Technologies, Automation and Metrology, Lviv / Ukraine	233
25.	DEVELOPMENT AND TESTING OF BED FORMER IMPLEMENT POWERED BY HAND TRACTORS Mustaqimah¹⁾, Ramayanty Bulan^{*1)}, Syafrandi¹⁾, Reza Imanda¹⁾, Uzair¹⁾, Dewi Sartika T.²⁾, Agustami Sitorus³⁾ ¹⁾ Department of Agricultural Engineering, Syiah Kuala University/ Indonesia; ²⁾ Department of Civil Engineering, Nusa Putra University/ Indonesia; ³⁾ Research Centre for Appropriate Technology, Indonesian Institute of Sciences (LIPI)/ Indonesia	241
26.	OPTIMUM WORKING CONDITIONS FOR VARIABLE WIDTH PLOUGHS Cârdei P.¹⁾, Nuțescu C.^{*2)}, Matache M.¹⁾, Cristea O.¹⁾ ¹⁾ INMA Bucharest / Romania; ²⁾ U.P. Bucharest / Romania	248
27.	CALIBRATION OF BONDING MODEL PARAMETERS FOR COATED FERTILIZERS BASED ON PSO-BP NEURAL NETWORK Xin Du, Cailing Liu[*], Meng Jiang, Hao Yuan, Lei Dai, Fanglin Li, Zhanpeng Gao College of Engineering, China Agricultural University, Beijing / China	255

		Page(s)
28.	<p>RESEARCH PROGRESS OF AGRICULTURAL IMPLEMENT GUIDANCE SYSTEMS. A REVIEW Zhenguo Zhang^{1,2}, Jin He^{*1}, Hongwen Li¹, Qingjie Wang¹, Wenchao Yang¹, Quanyu Wang¹ ¹ College of Engineering, China Agricultural University, Beijing / China; ² College of Mechanical and Electrical Engineering, Xinjiang Agricultural University, Urumqi / China</p>	265
29.	<p>DEVELOPMENT OF TECHNOLOGIES FOR OBTAINING COMPOSITE MATERIALS BASED ON THE USE OF OILSEED FLAX FIBERS Gorach Olga¹, Dombrovska Olena², Tikhosova Anastasiia² ¹ Kherson State Agrarian and Economic University, Kherson / Ukr.; ² Kherson National Technical University, Kherson</p>	275
30.	<p>DEVELOPMENT AND TEST OF FREQUENCY SUBSECTION REGULATION SYSTEM FOR COMBINE HARVESTER HEADER CUTTER Li Ying¹, Guan Zhuohuai¹, Chen Yisong² ¹Nanjing Institute of Agricultural Mechanization, Ministry of Agriculture and Rural Affairs, Nanjing / China ² Mechanical Engineering, Jiangsu University, Zhenjiang / China</p>	283
31.	<p>MECHANIZATION DEVICES FOR HANDLING BRANCHES IN MODERN ORCHARDS Hui Li^{1,2}, Xin Yang¹, Aiqian Yang² ¹ College of Mechanical and Electrical Engineering, Hebei Agricultural University, Baoding / China; ² Research Institute of Mechanical and Electronic, Hengshui University, Hengshui / China</p>	293
32.	<p>EXPERIMENTAL RESEARCH AND CFD MODELING OF MODULAR POULTRY BREEDING Trokhaniak V.I.¹, Spodyniuk N.A.¹, Antypov I.O.¹, Shelimanova O.V.¹, Tarasenko S.V.¹, Mishchenko A.V.¹ ¹ National University of Life and Environmental Sciences of Ukraine / Ukraine</p>	303
33.	<p>THEORETICAL ANALYSIS OF STRENGTH RESISTANCE TO DISPLACEMENT OF IMPROVED DIGGING WORKING BODY OF POTATOE HARVESTING COMBINE Nalobina O.O.¹, Shymko A.², Bundza O.Z.¹, Holotiuik M.V.¹, Herasymchuk O.², Puts V.S.², Shovkomyd O.² ¹National University of Water and Environmental Engineering, Soborna / Ukraine; ²Lutsk National Technical University, Lutsk / Ukraina</p>	312
34.	<p>DESIGN OF DEEP-FERTILIZATION MECHANISM WITH DEFORMED GEARS AND PERFORMANCE TESTS Feng Jinlong^{1,2,3}, Yi Shujuan^{*1}, Li Qichao³ ¹ College of Engineering, Heilongjiang Bayi Agricultural University, Heilongjiang Daqing, China ² Quality Supervision and Testing Center for Agricultural Processed Products of the Ministry of Agriculture (Daqing), Heilongjiang Daqing / China; ³ College of Mechanical and Electrical Engineering, Lingnan Normal University, Zhanjiang / China</p>	321
35.	<p>DESIGN AND EXPERIMENTAL STUDY OF FLEXIBLE THRESHING UNIT FOR CHINESE CABBAGE SEEDS Shengsheng Wang^{1,2}, Pan Chen¹, Jiangtao Ji^{1,2}, Mengqing Lu¹ ¹ College of Agricultural Equipment Engineering, Henan University of Science and Technology / China; ² Collaborative Innovation Center of Machinery Equipment Advanced Manufacturing of Henan Province / China</p>	333
36.	<p>DESIGN AND TEST OF SELF-PROPELLED STRADDLE-TYPE <i>LYCIUM BARBARUM</i> L. SPRAYING MACHINE ZeNing, Gao¹; QingYu, Chen¹; GuangRui, Hu¹; Chao, Chen¹; ChuanLin, Li¹; Jun, Chen^{*1} ¹ College of Mechanical and Electronic Engineering, Northwest A&F University, Yangling / China</p>	345
37.	<p>THEORETICAL INVESTIGATION OF HEAT PRODUCTION FEASIBILITY BY MEANS OF WIND MECHANICAL PLANTS Holovko Volodimir^{1,2}, Kohanevich Volodimir¹, Shikhailov Mikola¹, Sukmaniuk Olena³, Kukharets Savelii³ ¹ Renewable Energy Institute of NAS of Ukraine / Ukraine ² National Technical University of Ukraine «Igor Sikorsky Kyiv Polytechnic Institute» / Ukraine ³ Department of Mechanical and Engineering Agroecosystems, Polissia National University / Ukraine</p>	355
38.	<p>MACHINE LEARNING TECHNIQUES IN PLANT DISEASE DETECTION AND CLASSIFICATION. A STATE OF THE ART Sreya John, Arul Leena Rose¹ Department of Computer Science, College of Science and Humanities, SRM Institute of Science and Technology, Kattankulathur, Chennai / India</p>	362
39.	<p>EVALUATION OF THE PLACES FOR CREATION OF APIARIES AND OPTIMAL DISTRIBUTION OF THE BEE COLONIES Atanasov Atanas^{*1}, Georgiev Ivan² ¹ University of Ruse, Agro-industrial Faculty / Bulgaria; ² University of Ruse, Faculty of Natural Sciences and Education, Department of Applied Mathematics and Statistics / Bulgaria</p>	373
40.	<p>NEW METHOD FOR DOSING LIQUID MIXTURE'S COMPONENTS BY MEANS OF OVERPRESSURE Cerempei Valerian¹, Molotcov Iurii², Popa Lucretia³ ¹ UASM Chişinău / Republica Moldova; ² ITA Mecagro Chişinău / Republica Moldova; ³ INMA Bucharest / Romania</p>	381

		Page(s)
41.	RESEARCHES ON THE TESTING IN LABORATORY CONDITIONS OF AN ECOLOGICAL CLIMATE SYSTEM USED FOR SELFPROPELED AGRICULTURAL MACHINES / Găgeanu Iuliana, Cujbescu Dan*, Dumitru Cristinel INMA Bucharest / Romania	391
42.	THE FUNCTIONAL CONTROLABILITY OF MILK EJECTION OF THE ADAPTIVE MILKING SYSTEM Dmytriv I.V. ¹⁾ Lviv Polytechnic National University, Institute of Engineering Mechanics and Transport, Lviv / Ukraine	399
43.	PARAMETER OPTIMIZATION AND EXPERIMENT OF SLIDER-HOLE-WHEEL SEED-METERING DEVICE BASED ON DISCRETE ELEMENT METHOD Xiaoshuang Zhang ¹⁾ , Dequan Zhu ^{*1,2)} , Kang Xue ¹⁾ , Lanlan Li ¹⁾ , Jianjun Zhu ¹⁾ , Shun Zhang ¹⁾ , Juan Liao ¹⁾ ¹⁾ School of Engineering, Anhui Agricultural University, Hefei / China; ²⁾ Anhui Province Engineering Laboratory of Intelligent Agricultural Machinery and Equipment, Hefei / China	410
44.	MATERIAL MOVEMENT WITHIN A SINGLE-SCREW EXTRUDER Dorokhov A.S. ¹⁾ , Zagoruiko M.G., Maradudin A.M., Bashmakov I.A. FSBSI "Federal Scientific Agronomic and Engineering Centre VIM"/ Moscow / Russia	421
45.	EXPERIMENTAL STUDIES OF THE INTERACTION OF TRACTOR DRIVE WHEELS WITH THE SOIL IN THE PLOWED FIELD Gennadii Golub ^{*1)} , Viacheslav Chuba ¹⁾ , Yaroslav Yarosh ²⁾ , Oleksandr Solarov ³⁾ , Nataliya Tsyvenkova ^{1,2)} ¹⁾ National University of Life and Environmental Sciences of Ukraine / Ukraine; ²⁾ Polissia National University / Ukraine; ³⁾ Sumy National Agrarian University / Ukraine	430
46.	CREEP PROPERTIES AND PREDICTION MODEL OF PADDY SOIL UNDER COMPRESSION Guoyang Liu ¹⁾ , Junfang Xia ^{1,2)} , Kan Zheng ^{*1,2)} , Jian Cheng ¹⁾ , Liu Jiang ¹⁾ , Liwei Guo ¹⁾ ¹⁾ College of Engineering, Huazhong Agricultural University, Wuhan / China ²⁾ Key Laboratory of Agricultural Equipment in Mid-lower Reaches of Yangtze River, Ministry of Agriculture and Rural Affairs, Wuhan / China	441
47.	SIMULATION OF DESIGN VARIABLES EFFECT ON PERFORMANCE OF A COMMON BEANS (<i>Phaseolus vulgaris</i> L) PORTABLE THRESHER Patrick W. Wamalwa ^{1*} , Christopher L. Kanali ²⁾ , Erick K. Ronoh ²⁾ , Gareth M. Kituu ²⁾ ¹⁾ Egerton University, Faculty of Engineering, Agricultural Engineering Department, Egerton / Kenya; ²⁾ Jomo Kenyatta University of Agriculture and Technology, Nairobi / Kenya	452
48.	A REVIEW ON THE TECHNOLOGY OF STRAW RETURNING BY MACHINING Liang Fang ^{1,2)} , Wang YuBing ¹⁾ , Deng WeiHong ¹⁾ , Yuan Shaoning ¹⁾ , Wang Zirui ¹⁾ ¹⁾ College of Engineering, Huazhong Agricultural University, Wuhan / China; ²⁾ Key Laboratory of Agricultural Equipment in Mid-lower Yangtze River, Ministry of Agriculture and Rural Affairs, Wuhan / China	465
49.	APPLICATION OF BIG DATA ANALYSIS IN PATH PLANNING OF INTELLIGENT PICKING ROBOT Hejun Zhao ^{1) 2) *} , Stoyanets Nataliya ¹⁾ , Guohou Li ³⁾ ¹⁾ Sumy National Agrarian University, Ukraine. ²⁾ Xinxiang Vocational and Technical College, Xinxiang, Henan, China. ³⁾ Henan Institute of Science and Technology, Henan, China Yao	476
50.	DEVELOPMENT AND TESTING OF SOIL IMPURITIES REMOVING APPARATUS FOR POTATO Hongguang Yang, Huanxiong Xie*, Hai Wei, Jianchun Yan, Huichang Wu, Longlong Ji, Xiaowei Xu Nanjing Institute of Agricultural Mechanization, Ministry of Agriculture and Rural Affairs, Nanjing / China	485
51.	RESEARCH ON THE DEGREE OF UNIFORMITY OF THE DISTRIBUTION OF SOLID ORGANIC FERTILIZERS Ștefan V.* ¹⁾ , Zaica A ¹⁾ , Iosif A. ²⁾ ¹⁾ National Institute of Research Development for Machines and Installations Designed to Agriculture and Food Industry – INMA Bucharest / Romania; ²⁾ Herman Oilfield Inspection Service, Ploiești / Romania	495
52.	INTEGRATED NAVIGATION METHOD OF ELECTRIC FORKLIFT BASED ON IMPROVED UKF ALGORITHM Yibo Li ^{*1)} , Shipeng Zhu ¹⁾ ¹⁾ College of Automation, Shenyang Aerospace University, Shenyang / China	505

**RESEARCH ON SHREDDED BIOMASS DRYING IN
A VIBRATING FLUIDIZED BED DRYER
/
CERCETARI PRIVIND USCAREA BIOMASEI MARUNTITE
INTR-UN USCATOR CU PAT FLUIDIZAT VIBRANT**

**Pavel Ioan^{*1)}; Chirita Alexandru Polifron¹⁾; Matache Gabriela¹⁾; Popescu Alina Iolanda¹⁾;
Pavel Kati¹⁾, Ștefan Vasilica²⁾**

¹⁾Hydraulics and Pneumatics Research Institute INOE 2000-IHP Bucharest, Romania

²⁾National Institute of Research – Development for Machines and Installations Designed
for Agriculture and Food Industry – INMA Bucharest

E-mail: pavel.ihp@fluidas.ro

DOI: <https://doi.org/10.35633/inmateh-65-01>

Keywords: biomass, dryers, vibrating fluidized bed, vibrations

ABSTRACT

The article presents aspects related to energy potential of the shredded biomass from agricultural secondary production, coming from maintenance operations to cutting trees and vines and an original solution of dryer with vibrating fluidized bed with continuous operation equipped with adjustments of the transit time of biomass in the dryer. Also, it was analysed the dynamic behaviour of the biomass tray as well as of a biomass particle for the variant of vibrating fluidized bed.

ABSTRACT

Articolul prezinta aspecte legate de potentialul energetic al biomasei maruntite din productia secundara agricola, provenita din operatiile de intretinere la taierea pomilor si vitei de vie si o solutie originala de uscator cu pat fluidizat vibrant cu functionare continuua dotat cu reglaje ale timpului de tranzit al biomasei in uscator. De asemenea s-a analizat comportamentul dinamic al cuvei cu biomasa precum si al unei particule de biomasa pentru varianta de pat fluidizat vibrant.

INTRODUCTION

The cuttings in the orchards are made in the non-vegetative period and as a result the average humidity of the cut branches is 30-35%. If a humidity of 35% of a ton of cuttings is taken into account, by drying up to an average humidity of 15%, it results in 765 kg of biomass usable for the production of thermal energy that has an energy potential of 11.856 MJ or 3.3 MWhth. From a hectare of intensive orchards annually, on average, about 3 tons of biomass are cut, which have an energy potential of 35.628 GJ/ha·year.

The biomass from the cuttings is transported to the row end where it is chopped with specialized equipment at 10..50 mm and stored in containers with perforated walls for good air circulation, for natural drying, or for immediate use and dried in specialized installations. On average, the bulk density of the wet cut is 250 kg/m³, which leads to a need of about 12 containers for one hectare of orchard. By natural drying or in dryers, the biomass reaches an average humidity of 15% and a bulk density of about 200 kg/m³.

One ton of dry biomass has an energy potential of 15.530 GJ /t.bm or 4.3 MWhth. From the published data, for Europe, results an average cost of gathering, chopping and transport for a ton of cuts of about 40 €/t. Taking into account the costs for drying and a profit of 20%, it results that a ton of biomass usable for the production of thermal energy can be sold for about 80€/t. The specific price for the primary energy of biomass is in the case studied of 5.2 €/GJ or 18.6 €/MWhth, values much lower than those for diesel of 33.22 €/GJ or for LPG of 21.52 €/GJ (Pavel et al., 2020).

The researchers showed that for drying biomass from 30% to 15%, 70% of the energy consumed is used for processing, while for the actual pelleting of pellets - only 7%. Regarding the moisture of biomass for pelleting, Li, Yadong and Liu, Henry (Yadong and Henry, 2000), stated that it should be between 6-12%, and Obernberger, I. and Thek, G (Obernberger and Thek, 2004) recommend values of 8-12%. It should be noted that the moisture content of the raw material in the initial phase can far exceed the required level. Humidity after maintenance cuttings in orchards or vines is up to 50%. For economic reasons, reducing the high humidity of the harvested biomass is recommended to be achieved under natural conditions, using solar energy or atmospheric air (Ericsson and Werner, 2014; Iftekhhar et al., 2017).

The humidity of dry biomass under natural conditions depends very much on the humidity of the ambient air. At the ambient air temperature, $t_a = 25\text{ }^\circ\text{C}$ and its humidity, $\varphi_a = 85\%$ the wood can be dried in natural conditions up to a minimum humidity of 18% (Ivanov, 1956). Therefore, in order to obtain biomass in accordance with technological requirements, it must be further dried under artificial conditions.

Experimental research, performed jointly by researchers from Canada and the US (Rezaei et al., 2016), showed that the size, shape and density of biomass particles influence transportability and fluidization, drying rate and decomposition. Also the air temperature and the drying speed influence the uniformity of the deep drying of the biomass particle (Pazyuk et al., 2018).

There is a wide variety of artificial drying methods (Gavrilencov et al., 2014) and in specialized articles scientists study different types of dryers: with active ventilation (Gaponyuk et al., 2014), with infrared radiation with vibrating trays (Bandura et al., 2019), with electromagnetic vibrations (Burdo et al., 2017), with intermittent drying (Kumar et al., 2008), with convective drying (Ahrné et al., 2007), with microwave (Apolzan et al., 2020) or a combination of a convective method of heat supply with the introduction of ozone as a drying agent (Tsurkan et al., 2013). For the study of dynamic behaviour a new solution of dryer with vibrating fluidized bed with continuous workflow is presented, a solution for which a national patent application was submitted.

MATERIALS AND METHODS

CALCULATION OF THE TECHNOLOGICAL DRYING PROCESS

Drying is the operation by which water from solid materials (in our case biomass) is removed with the help of air which has the role of bringing the heat necessary to vaporize moisture and to evacuate the resulting water vapour. The speed of the drying process is defined by the amount of moisture removed from the surface unit of the material to be dried in the unit of time.

In the technological process of artificial drying (fig.1) wet biomass and dry air enter and dry biomass and wet air come out.

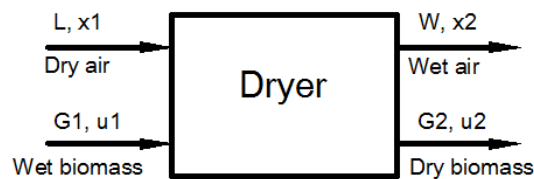


Fig. 1- Block diagram of the artificial drying process

x_1 - air humidity at the inlet [kg water / kg wet air]; x_2 - air humidity at outlet [kg water/kg wet air]; L - absolutely dry air flow [kg air/h]; G_1 - input biomass flow [kg /h]; G_2 - output biomass flow [kg /h]; u_1 - absolute humidity of the input biomass [kg water / kg wet biomass]; u_2 - absolute humidity of the output biomass [kg water/kg wet biomass]; W - the amount of water removed from the biomass [kg water/h]

The material balance of a dryer is as follows:

The general balance equation:

$$G_1 = G_2 + W \quad (1)$$

The biomass moisture balance equation:

$$G_1 \cdot u_1 = G_2 \cdot u_2 + W \quad (2)$$

The balance equation of absolutely dry biomass:

$$G_1 \cdot (1 - u_1) = G_2 \cdot (1 - u_2) \quad (3)$$

The amount of water removed from the biomass:

$$W = G_1 \times u_1 - G_2 \times u_2 = G_1 \times \left(u_1 - \frac{1 - u_1}{1 - u_2} \right) \quad (4)$$

The humidity balance equation in the dryer:

$$L \cdot x_1 + G_1 \cdot u_1 = L \cdot x_2 + G_2 \cdot u_2 \quad (5)$$

$$L \cdot (x_2 - x_1) = G_1 \cdot u_1 - G_2 \cdot u_2 = W \quad (6)$$

The air requirement:

$$L = \frac{W}{x_2 - x_1} \quad (7)$$

The specific air consumption:

$$I = \frac{L}{W} = \frac{1}{x_2 - x_1} \quad [\text{kg wet air /kg removed water}] \quad (8)$$

The speed of the drying process:

$$w = \frac{dW}{A \cdot dt} \quad (9)$$

where:

- w - speed of the drying process;
- dW - the amount of moisture removed;
- A - the unit of surface of the material subjected to drying;
- dt - unit of time.

The drying time:

When the drying speed is known, the drying time is determined by integrating the equation:

$$w = \frac{dW}{A \cdot dt} \Rightarrow t = \int \frac{dW}{A \cdot w} \quad (10)$$

The theoretically deduced equations for the drying speed are complicated and difficult to apply and the solution of the problem must be accompanied by experimental data at laboratory scale which are transposed at industrial scale.

NEW DRYER SOLUTION WITH VIBRATING FLUIDIZED BED AND CONTINUOUS OPERATION

The dryer solution shown in fig. 2 is with vibrating bed and self-feeding with biomass; it uses hot air or from atmosphere and allows adjustments for the transit time of biomass through the dryer, consequently adjustment of the biomass drying degree at the output of the dryer.

The dryer consists of an outer housing (3), inside which there is a vibrating tray (2) which rests on four springs (9) and is vibrated by the electric vibrating motor (11). The hot air enters through two pipes (15) which have three flaps (12) with which it adjusts the distribution of hot air on the six pairs of hole profiles (13) located on the bottom of the tray. The feeding flap is a common body with the vibrating tray and when their mass decreases due to the loss of water from the dry biomass, the springs (9) lift the vibrating assembly and initiate the self-feeding with biomass from the feeding tray (8).

When the weight of the tray increases due to re-feeding, it presses the springs and with it moves the feeding flap that closes the feeding orifice. The advance speed of the biomass in the dryer is made by adjusting the angle (a) of the baffles (14), by adjusting the angle (b) of the working position of the vibrating tray and by adjusting the amplitude (eccentricity against weights), frequency (electric motor rotational speed) and the direction of rotation of the vibrating motor.

The outer housing stands on four legs and consists of a biomass feeding tray (8), a humid air exhaust chimney (7) and an inspection hole (4).

The feeding of the tray with biomass is done in self-feeding regime. The feeding flap (6) is fixed to the vibrating tray and moves with it. When the biomass to be dried loses between 10-65% water by evaporation, due to weight loss, the springs (9) lift the vibrating tray and with it the feeding flap that allows the biomass to fall from the feeding tray (8) into the vibrating tray (2) for re-feeding. For example, for the conditions imposed during the simulation, when reducing the weight from 50 kg to 30 kg (approx. 65%), the vertical displacement of the vibrating tray is approx. 20 mm (fig. 11).

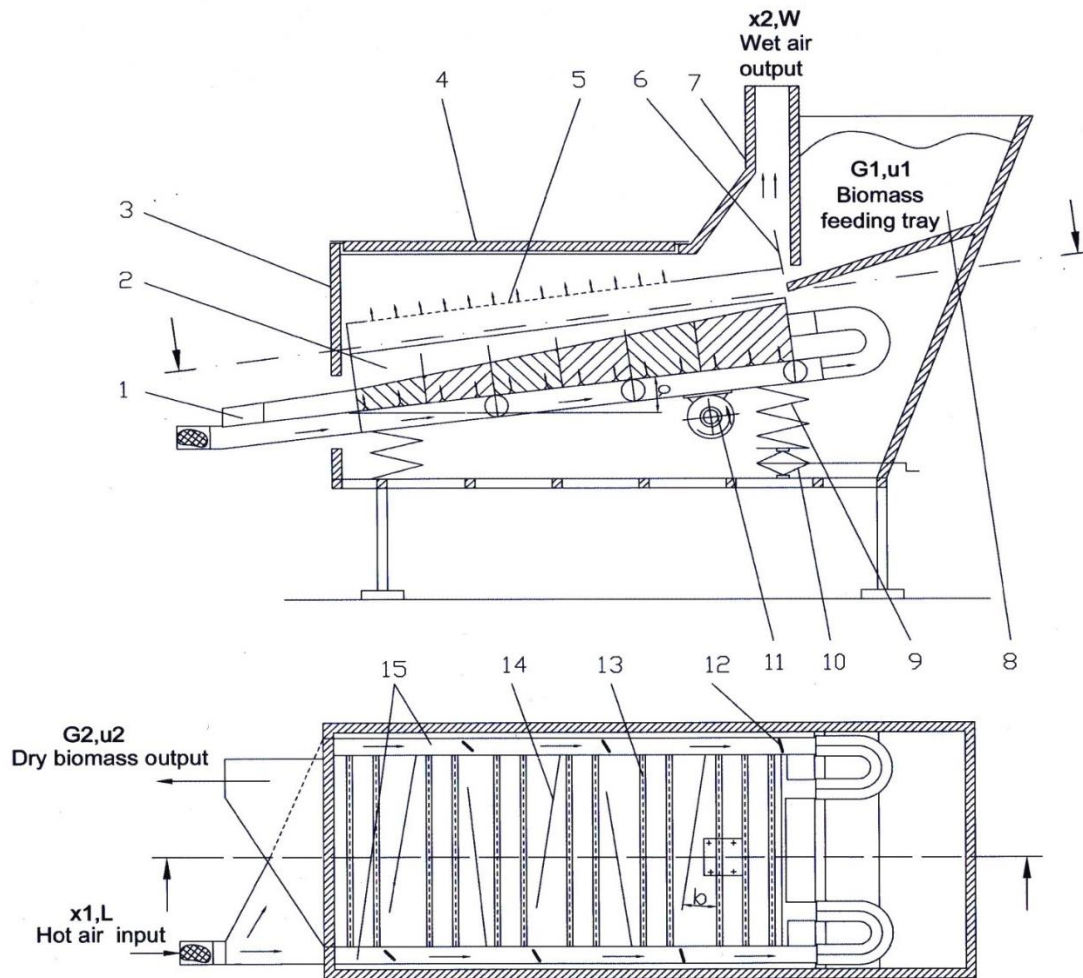


Fig. 2 - Principle drawing of the dryer with vibrating fluidized bed for shredded biomass

1- dry biomass output; 2-vibrating tray; 3- outer housing; 4-inspection hole; 5- filter; 6-feeding flap; 7- humid air exhaust chimney; 8- feeding tray with biomass; 9-spring; 10- jack for adjustment of the working angle; 11- industrial vibrator with electric motor; 12- hot air dose adjustment flaps; 13- L profile with holes; 14-baffle; 15- hot air supply pipes; x_1 - air humidity at the inlet; x_2 - air humidity at outlet; G_1 - input biomass flow; G_2 - output biomass flow; u_1 - absolute humidity of the input biomass; u_2 - absolute humidity of the output biomass; L - absolutely dry air flow; W - the amount of water removed from the biomass

Uniform distribution of air flow inside the drying tray is very important because it determines both the drying efficiency and the homogeneity of the products that are dried (Amanlou et al., 2010). Thus, on the sides of the vibrating tray are placed two hot air supply pipes (15) in which are installed three adjustment flaps (12) for dosing the hot air through the holes profiles (13) over which the biomass to be dried moves. The surplus of hot air is directed to the wettest area, to the biomass freshly introduced in the dryer.

The humidity of the biomass at the output of the dryer (1) depends on the granulation of the biomass, on the humidity of the raw material, on the flow and temperature of the hot air introduced in the pipes (15) and on the transit time of the dryer. The latter can be adjusted by changing the angle (b) of the baffles (14) or by changing the relief angle of the vibrating tray (a) using the jack (10). The arrow of the springs (9) is calculated for the weight of the vibrating tray loaded with biomass and for the size of the desired feeding orifice. Also, the amplitude, frequency (rotational speed) and direction of vibrations produced by the vibrator with electric motor influence the transit time of the biomass in the dryer. When the humidity of the biomass at the output of the dryer is the desired one if the adjustments made are maintained and the introduced biomass is approximately of the same humidity, the dryer feeds itself and works continuously.

SIMULATION

The following will present a numerical simulation performed with a proprietary 2D multibody dynamics software (Liu et al., 2016), developed in the institute, which analyses only the mechanical aspects of the dryer, the results were plotted with the help of the Amesim software facilities and the physical model was made in

AutoCAD in order to be able to enter the precise coordinates in the calculation. The role of the simulation is to validate the new dryer concept and to see the influence that certain parameters have on the process of displacement of a biomass particle on the dryer tray.

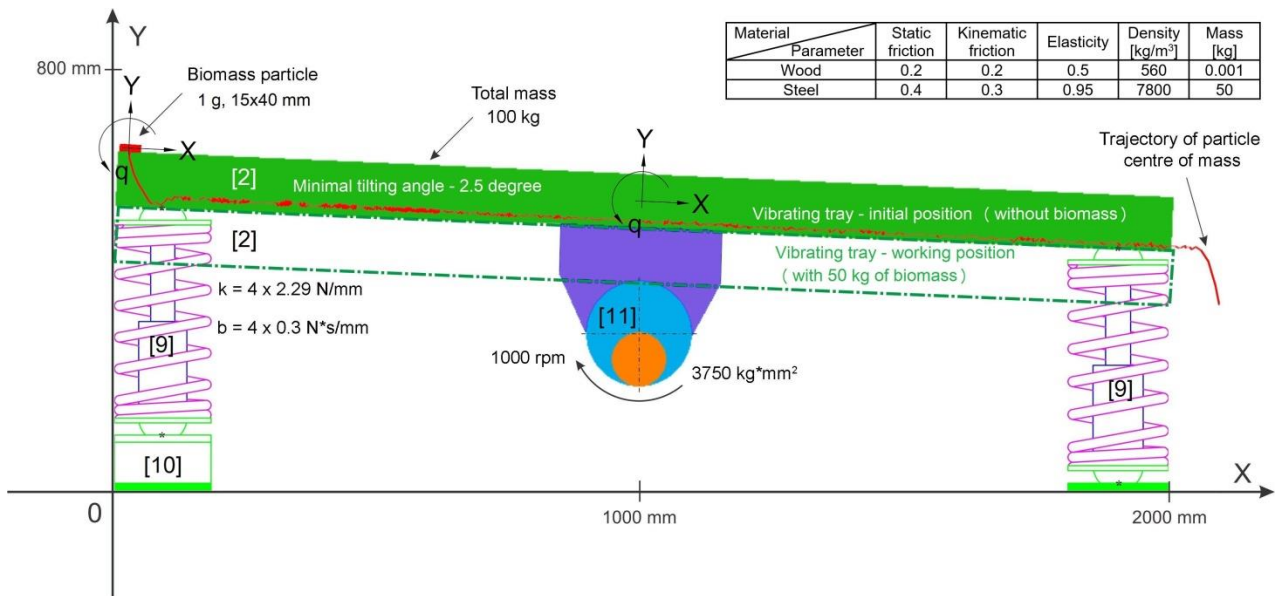


Fig. 3- Physical simulation model of the dryer

[2] - vibrating tray; [9] – springs and dampers; [10] - jack for adjustment of the working angle; [11] - industrial vibrator with electric motor

Figure 3 shows the physical model of the numerical simulation, it consists of:

- the vibrating tray [2], it has an initial mass of 50 kg, when not loaded, and when the dryer is loaded to its maximum capacity, it supports a maximum load of 50 kg of biomass, in total 100 kg ;
- the 4 springs with dampers, that have the role of stabilizing the vibrations of the tray, have the following parameters: $k = 2.29 \text{ N/mm}$ and $b = 0.3 \text{ N*s/mm}$;
- the industrial vibrator with electric motor which has a speed of 1000 rev/min and moment of inertia of the eccentric of 3750 kg*mm^2 ;
- the biomass particle with dimensions of 15x40 mm and mass of one gram (see figure 4).

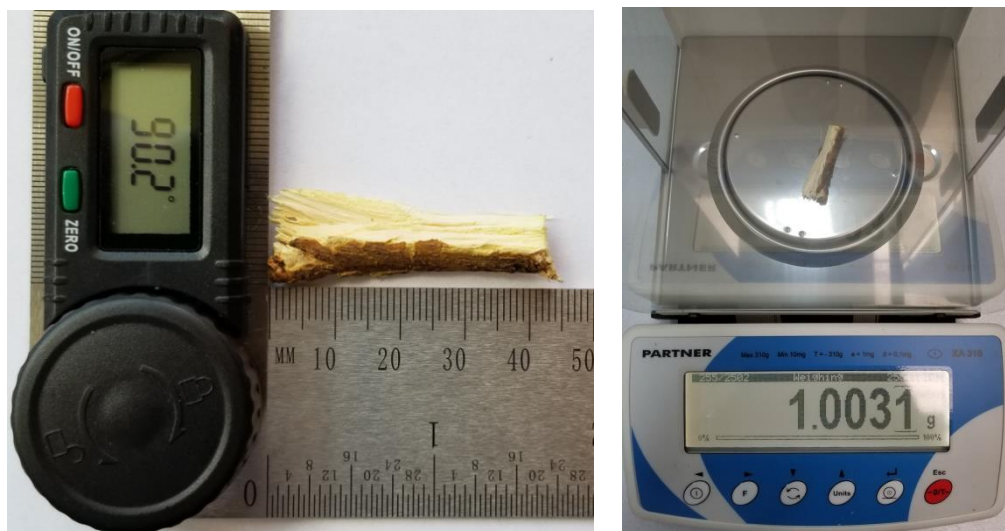


Fig. 4 - Biomass particle dimensions and mass

RESULTS

A new solution of dryer with vibrating fluidized bed, with continuous operation and multiple adjustments for the transit time of the biomass in the dryer and an algorithm for calculating the material balance, speed and drying time was presented (equations (1-10)). During the simulation, the dynamic behaviour of a 1 gram

biomass particle was analysed and its amplitude, shape and duration of displacement over a length of 2 ml were determined.

Numerical simulation results: The study performed with the help of numerical simulation presents the analysis of the dynamic behaviour of the dryer tray and the biomass particle.

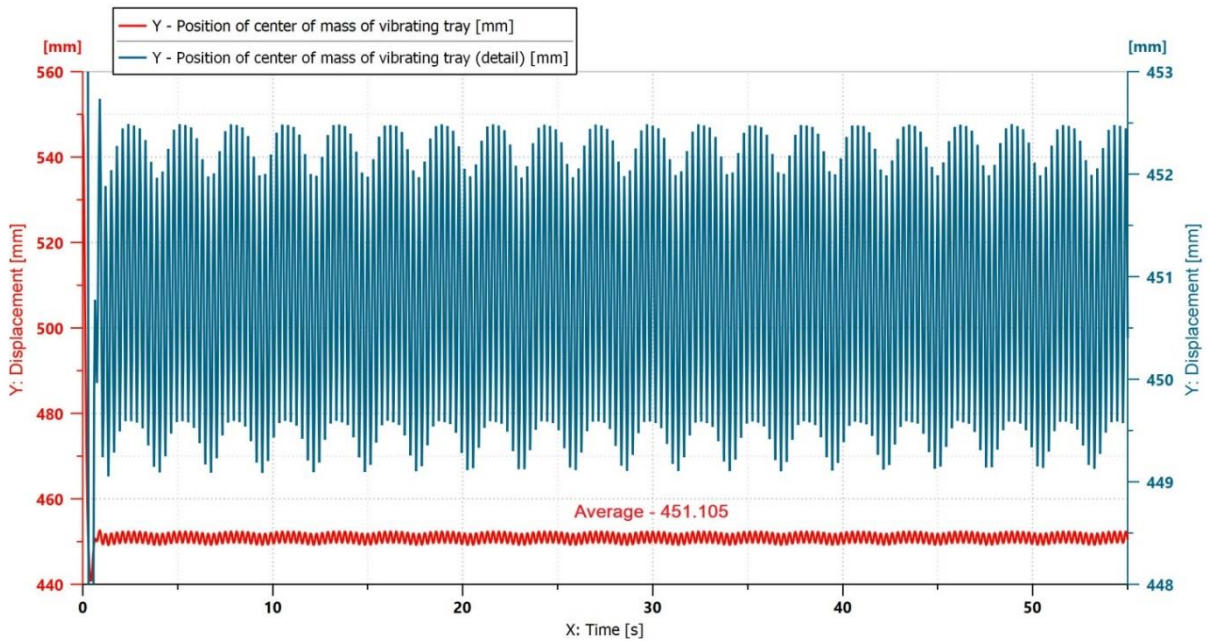


Fig. 5 - Y - Position of centre of vibrating tray mass (red) and in detail (blue)

Figure 5 shows the variation in time of the displacement on the Y-axis of the centre of gravity of the vibrating tray. In the graph, you can see how when the tray is loaded with the maximum amount of biomass, it goes down about 100 mm (550 mm to 451.1 mm); this displacement closes the biomass-feeding flap of the dryer. In the detail on the same figure, it can be seen that the amplitude of the vibration is about 3 mm.

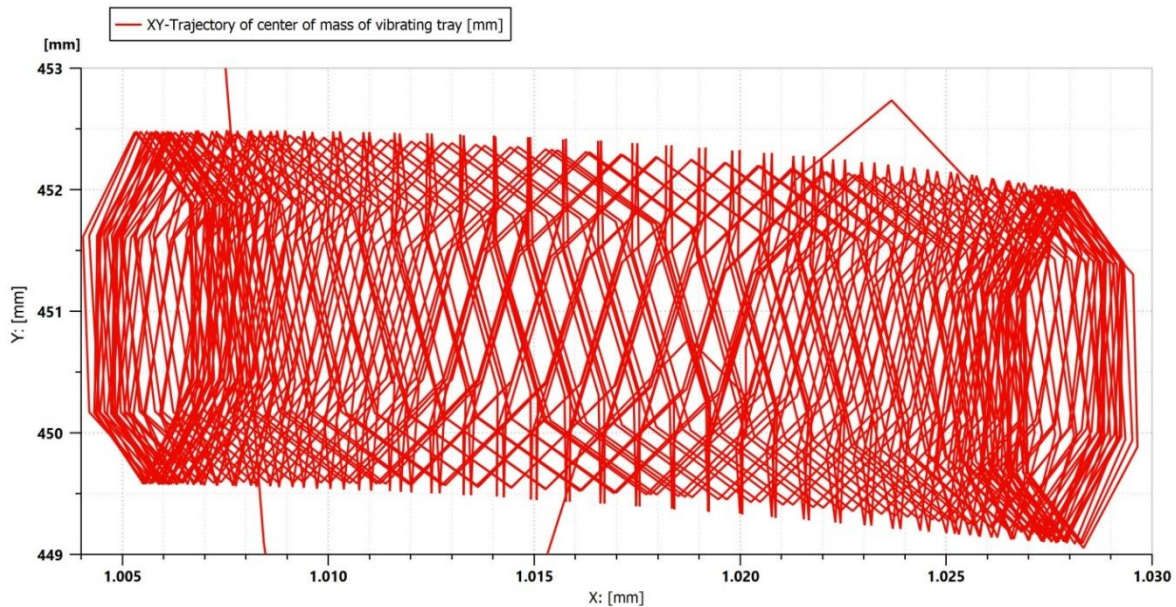


Fig. 6 - XY-Trajectory of centre of vibrating tray mass

Figure 6 shows the variation in time of the trajectory of the centre of mass of the tray; it can be observed that for a certain cycle the amplitude of the movement on the Y-axis has the value of 3 mm. On the X-axis the vibrating tray during operation moves a total of 26 mm; this movement does not affect the physical process of fluidization of particles.

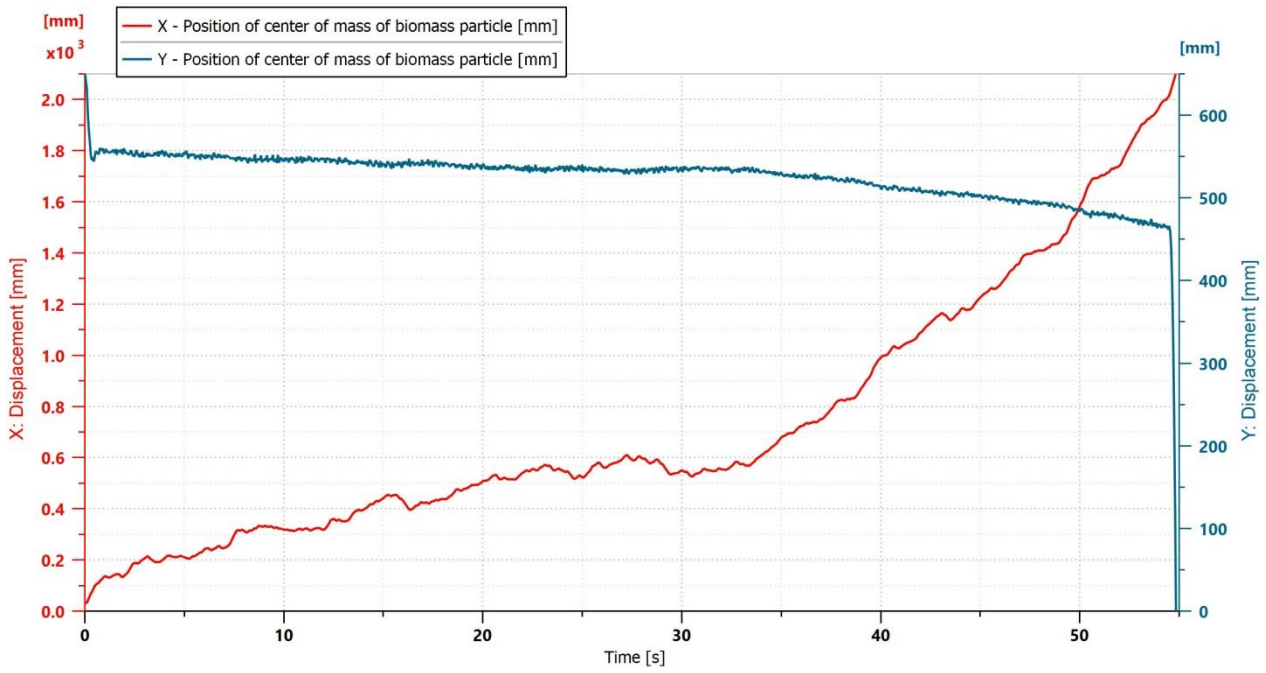


Fig. 7- Position on X&Y - axis of centre of biomass particle mass

Figure 7 shows the time variation of the displacement of the centre of gravity of the biomass particle on the X - axis with red colour and with blue colour on the Y - axis.

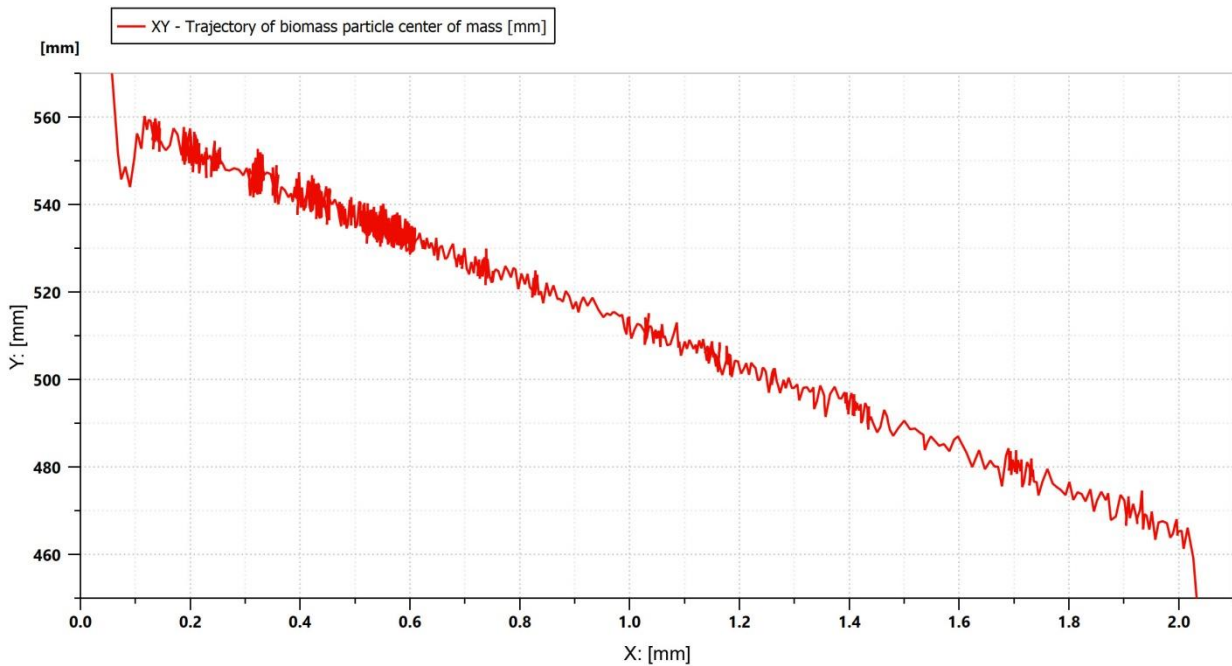


Fig. 8 - XY-Trajectory of centre of biomass particle mass

The time variation of the trajectory of centre of the biomass particle mass is shown in figure 8.

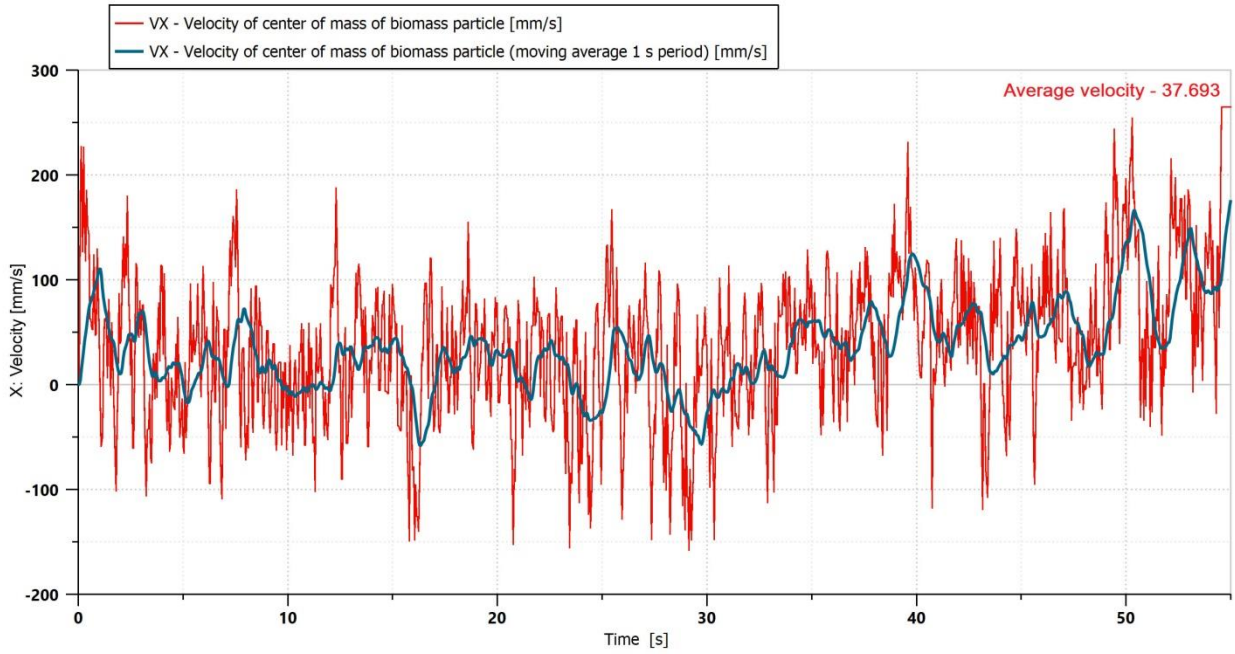


Fig. 9 - VX - Velocity of centre of biomass particle mass

The linear displacement velocity on the x-axis of the biomass particle is shown in Figure 9. It can be seen that for the angle of -2.5 degrees, the average linear velocity of the particle is about 37 mm/s. Also in the same figure, you can see the behaviour of the particle, the linear velocity of the particle is both positive and negative because the angle of inclination is small.

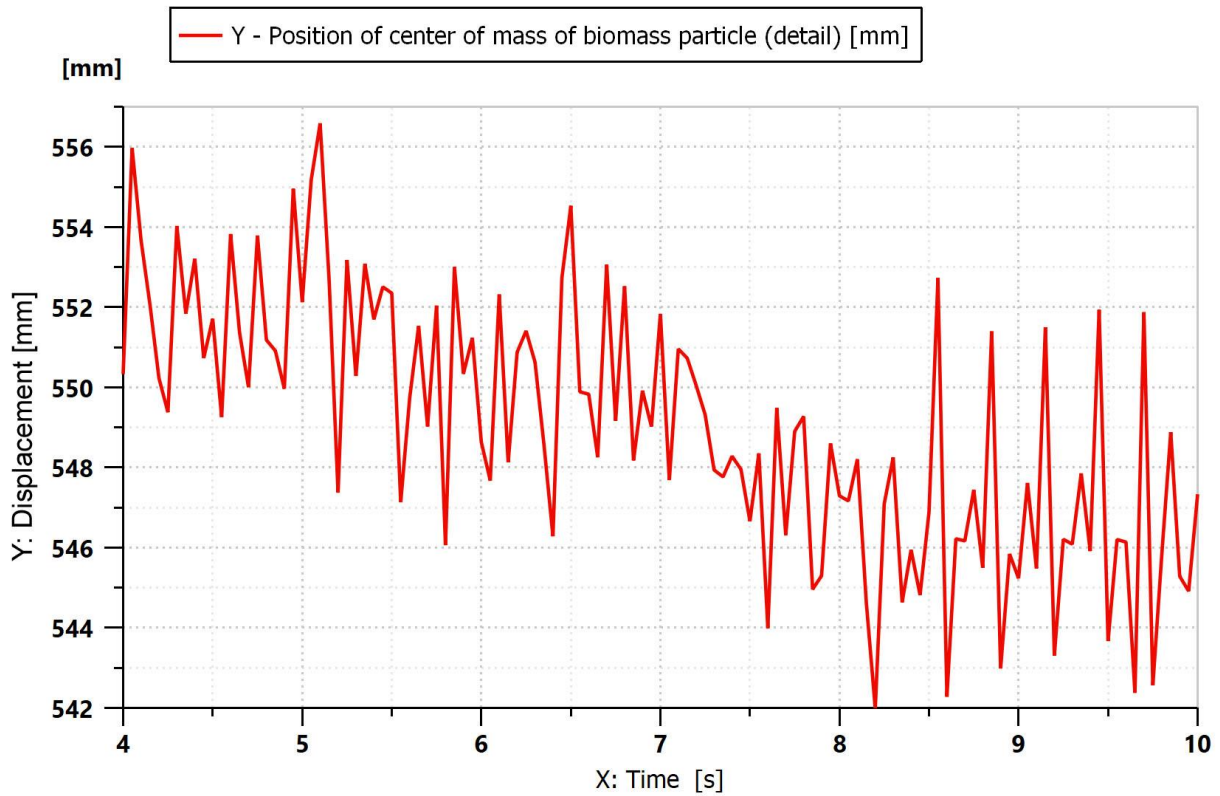


Fig. 10 - Y - Position of centre of biomass particle mass (detail)

On the detail presented in figure 10, it can be observed that the amplitude of the particle vibration varies between 2 and 11 mm. On average it has the value of 6 mm and the frequency of the particle vibrations has the average value of 8 Hz.

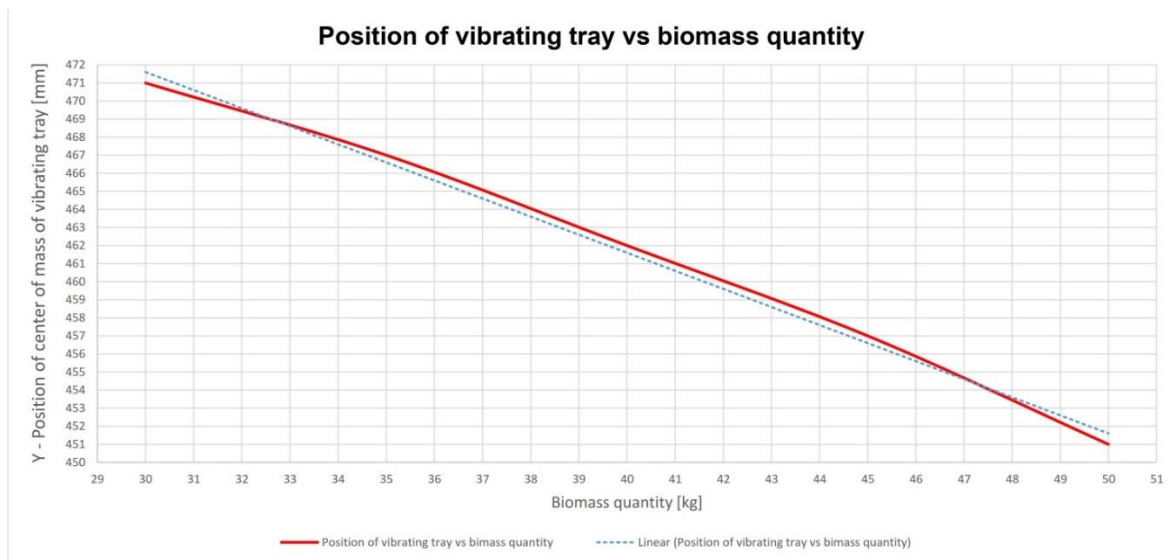


Fig.11 - Position of vibrating tray vs biomass quantity

CONCLUSIONS

The article presents a new dryer solution with vibrating fluidized bed that aerates the shredded biomass by controlled vibrations to increase the contact surface of the particles with the hot air in order to speed up the drying. The presented solution allows adjustments of frequency and amplitude, of working angle, of loading capacity at the vibrating tray obtaining a drying speed in relation to the followed humidity rate. It also allows the adjustment of the amount of hot air in different areas of the vibrating tray. The humid hot air is filtered through a sieve that self-shakes by vibration with the tray and before leaving the dryer preheats the biomass in the feed tray.

The simulation was done in order to study the motion of a biomass particle to estimate the transit time of wood chips in a dryer with vibrating tray. The study of dynamic behaviour mainly refers to the movement of a biomass particle of a rectangular shape weighing 1 gram. For the inclination angle of -2.5 degrees, the average frequency of 8 Hz and the average vibration amplitude of 6 mm, the average speed of the particle displacement was 37 mm / sec.

The implementation of the presented solution can bring energy savings because it does not impose conditions for the air temperature at the inlet, having multiple possibilities for adjusting the drying speed to achieve the humidity conditions of the biomass at the exit of the dryer. It is of simple construction, works continuously and does not require an operator for refeed. It consists of standardized elements (electric vibrating motor, springs) and a metal construction easy to make in any size for different productivity.

The presented dryer can be part of a biomass technological processing line whose final purpose is to obtain pellets, briquettes or shredded, dry biomass, for use in direct combustion in thermal boilers for hot water, electricity or hot air.

ACKNOWLEDGMENTS

This paper has been funded by the Romanian Ministry of Research and Innovation under NUCLEU Programme, Financial Agreement no. 18N/2019, Ad 13/14.04.2021, Project code PN 19-18.01.01, Theme 1, Phase "Advanced research on the development of an optimized heat generator solution, based on the TLUD principle". This paper has been developed, as part of a project co-financed by the European Union through the European Regional Development Fund, under Competitiveness Operational Programme 2014 - 2020, Priority Axis 1: Research, technological development and innovation (RD&I) to support economic competitiveness and business development, Action 1.2.3 – Partnerships for knowledge transfer, project title: Eco-innovative technologies for recovery of biomass wastes, project acronym: ECOVALDES, SMIS code: 105693-594, Financial agreement no. 129/23.09.2016.

REFERENCES

- [1] Ahmné L. M., Pereira N.R., Staack N., Floberg P., (2007), Microwave Convective Drying of Plant Foods at Constant and Variable Microwave Power, *Drying Technology*, vol. 25 (7-8), London/UK, pp. 1149-1153;
- [2] Amanlou Y., Zomorodian A., (2010), Applying CFD for designing a new fruit cabinet dryer, *Journal of Food Engineering*, vol. 101, (1), pp. 8-15;
- [3] Apolzan R, Perebiceanu A., Mateias F., (2020), Microwave Drying of Biomass, *Hidraulica Magazine*, no.3, ISSN 1453-7303, pp. 33-43;
- [4] Bandura V., Mazur V., Yaroshenko L., Rubanenko O., (2019) Research on sunflower seeds drying process in a monolayer tray vibration dryer based on infrared radiation, *INMATEH – Agricultural Engineering*, vol. 57, no.1, Bucharest/Romania, pp. 233-242;
- [5] Burdo O., Bandura V., Zykov A., Zozulyak I., Levtrinskaya J., Marenchenko E., (2017), Development of wave technologies to intensify heat and mass transfer processes, *Eastern European Journal of Advanced Technology*, vol. 4, no.11(88), Kharkiv/Ukraine, pp. 14-18;
- [6] Ericsson K., Werner S., (2014), The introduction and expansion of biomass use in Swedish district heating systems, *Biomass Bioenergy*, vol. 94, pp. 57-65;
- [7] Gaponyuk O.I., Ostapchuk M.V, Stankevich G.M., (2014), *Active ventilation and grain drying (Активне вентилявання та сушіння зерна)*, Polygrap Publishing House, Odessa/Ukraine p. 325;
- [8] Gavrilencov A.M. et al., (2014), *Methods of substantiation of the choice of drying method and type of drying units for agro-industrial complex (CAI) (Методика обоснования выбора способа сушки и типа сушильных установок для АПК)*;
- [9] Iftekhar C.M., Norton H.B., Duffy A., (2017), Technological assessment of different solar-biomass systems for hybrid power generation in Europe, *Renewable and Sustainable Energy Reviews*, vol.68, pp. 1115–1129;
- [10] Ivanov V.F., (1956), *Wooden constructions (Деревянные конструкции)*. Literature for constructions and architecture, Leningrad-Moscow / Russia, p. 254;
- [11] Kumar C., Karim M. A., & Joardder M. U. H. (2014). Intermittent drying of food products: a critical review. *Journal of Food Engineering*, vol. 121, “Elsevier” Publishing House, Amsterdam / Netherlands, ISSN: 0260-8774, pp 48-57;
- [12] Li Y., Henry L., (2000), High-pressure densification of wood residues to form an upgraded fuel, *Biomass and Bioenergy*, vol. 19, ISSN: 0961-9534, pp. 177-186;
- [13] Liu J., Ji J., Zhou J., (2016), Synchronization of networked multibody systems using fundamental equation of mechanics, *Applied Mathematics and Mechanics (English Edition)*, vol. 37 (5), Shanghai University and Springer-Verlag Berlin Heidelberg, DOI 10.1007/s10483-016-2071-8, pp. 555–572;
- [14] Obernberger I., Thek G., (2004), Physical characterization and chemical composition of densified biomass fuels with regard to their combustion behaviour, *Biomass and Bioenergy*, vol. 27, ISSN: 0961-9534, pp. 653-669;
- [15] Pavel I., Matache G., Chiriță Al. P., Popescu, A.I., Diaconu C., (2020), Biomass Processing from Agricultural Residual Production and Maintenance Operations when Cutting Trees and Vines. *Hidraulica Magazine* no. 4 ISSN 1453-7303, pp. 93-97;
- [16] Pazyuk V., Petrova Zn., Chepeliuk O., (2018), Determination of rational modes of pumpkin seeds drying. *Ukrainian Food Journal*. vol. 7, Issue 1, Kyiv/Ukraine, pp. 135-150;
- [17] Rezaei H., Lima C. J., Lau, A. et al., (2016), Size, shape and flow characterization of ground wood chip and ground wood pellet particles, *Powder Technology*, vol. 301, “Elsevier “Publishing House, pp. 737–746;
- [18] Tsurkan O.V., Necheporenko S.A., Blyznyuk M. Ya., (2013), Modern methods of drying grain materials (Сучасні способи сушіння зернових матеріалів), *Vibratsiyi v tekhnitsi ta tekhnolohiyakh*. no.1, Vinnytsia/Ukraine, pp. 130-134.

EXPERIMENTAL TEST AND FINITE ELEMENT ANALYSIS OF POTATO IMPACT ACCELERATION

马铃薯碰撞加速度试验测试与有限元分析

Deng Weigang, Liu Chenglong, Li Peng, Wang Yanlong, Xie Shengshi, Wang Chunguang *

College of Mechanical and Electrical Engineering, Inner Mongolia Agricultural University, Hohhot, China

Tel: +86 13948815406; E-mail: nndjdwcg@126.com

DOI: <https://doi.org/10.35633/inmateh-65-02>

Keywords: Impact acceleration, Collision test, Finite element analysis, Potato mass, Drop height

ABSTRACT

To analyze the maximum acceleration (a_{max}) of a potato colliding with different objects, both experimental test and finite element analysis (FEA) methods were used. Results showed that when potatoes were collided with the single rod, the steel plate and the double rods, the average discrepancies of FEA and experimental test values were 5.3%, 3.95% and 5.04%. The a_{max} increased with the increase of potato drop height, and decreased with the increase of potato mass. Under the same conditions, the a_{max} decreased in turn when the potatoes were collided with the steel plate, the single rod and the double rods. The FEA results showed that the a_{max} in collision with the steel plate was 60.78% to 96.29% higher than that with the double rods. The a_{max} in collision with the steel plate was 53.89% to 83.27% higher than that with the double rods. The a_{max} in collision with the single rod covered with soil was 37.65% and 31.54% lower than that without soil from different drop height or with different potato mass. The research methods and conclusions of this article provided a basis for the analysis of impact mechanics and damage mechanism of potatoes, and contributed to further researches related to solid-like agricultural and food products.

摘要

为了分析马铃薯与不同对象碰撞的最大加速度, 分别采用试验测试和有限元分析方法进行研究。结果表明: 马铃薯分别与单杆条, 钢板和双杆条碰撞时, 有限元分析和试验结果的差别分别为5.3%, 3.95%和5.04%。马铃薯最大碰撞加速度随碰撞高度增加而变大, 随马铃薯质量增大而减小。碰撞条件相同时, 马铃薯与钢板、单杆条和双杆条碰撞的最大加速度依次减小。马铃薯与钢板碰撞的最大加速度比与双杆条碰撞时高60.78%到96.29%, 比与单杆条碰撞时高53.89%到83.27%。马铃薯从不同高度或者以不同质量分别与单杆条碰撞时, 有土壤条件下最大碰撞加速度比无土壤条件下分别减小37.65%和31.54%。本文的研究方法和结论为马铃薯碰撞分析和损伤机理研究提供了基础, 为类似的固体农业物料和食品研究提供了参考。

INTRODUCTION

Mechanical collision in the harvesting and post-harvesting processes is among the major causes of the losses and damages of potatoes (Celik, 2017; Nikara et al., 2020). According to an American study, 70% of potato damage is caused by harvesting, 30% during transport and storage (Peters, 1996). The impact acceleration of potato not only has a positive correlation with its damage (Thomson and Lopresti, 2018; Xie, 2020a), but also is the key parameter to the study of potato impact kinematics and dynamics. Researchers have adopted experimental studies¹ to analyze the potato mechanical impact and bruising based on various instruments including pendulum collision device, free drop collision device, electronic potato, instrumented sphere and acceleration measuring unit (Canneyt et al., 2004; Dănilă, 2015; Deng et al., 2020; Geyer et al., 2009; Hyde et al., 1992; Mathew and Hyde, 1997; Nikara et al., 2018; Rady and Soliman, 2015; Strehmel et al., 2010; Xie et al., 2018; Xie et al., 2020a; Xie et al., 2020b). But in the process of mechanized harvesting, sorting and transporting, potatoes usually collide with cylindrical steel rods with different tilt angles in different directions, which is a very complicated process. There are many difficulties to be solved in the process of collision analysis through experimental test. Finite element analysis (FEA) is a successful analysis tool for developing approximate solutions to complex engineering problems and is very popular (Caglayan et al., 2018; Celik et al., 2019).

¹ Weigang Deng, As. Prof. Ph.D. Stud. Eng., Chenglong Liu, Stud.; Peng Li, Stud.; Yanlong Wang, Stud.; Shengshi Xie, Lect. Ph.D. Eng.; Chunguang Wang, Prof. Ph.D. Eng.

There have been many researches using FEA to study the collision damage of fruits and vegetables (Ahmadi *et al.*, 2016; Caglayan *et al.*, 2018; Celik, 2017; Celik *et al.*, 2019; Cerruto *et al.*, 2015; Gao *et al.*, 2018; Kabas and Vladut, 2015; Li *et al.*, 2013; Nikara *et al.*, 2020).

Various influence factors on potato impact acceleration had been studied, which mainly consisted of drop height, impact material, soil type, potato mass, size, inside temperature and modulus of elasticity (Bentini *et al.*, 2006; Cerruto *et al.*, 2015; Geyer *et al.*, 2009; Mathew and Hyde, 1997; Thomson and Lopresti, 2018; Xie *et al.*, 2020a; Xie *et al.*, 2020b). These studies were mainly based on experimental tests, and the way to obtain the impact acceleration was usually to implant an acceleration sensor into the real or instrumented potatoes. During the finite element analysis, potatoes were usually replaced by spheres, and the collision object was just steel plate (Cerruto *et al.*, 2015).

Based on the above mentioned, there are few studies on the impact acceleration of potatoes using both the experimental test and finite element method. And the study on the comparisons of the potato impact acceleration with colliders of the steel plate, the single rod and the double rods has not been found yet. In the study of potato collision, there are few studies considering the effect of soil. In this article, both the FEA and experimental testing methods were adopted to analyze the impact acceleration of potatoes colliding with different objects in the process of harvesting, sorting and transportation. This article revealed the influence of potato mass, drop height, soil and colliders with different structures on the maximum acceleration (a_{max}) of potatoes, and provided references for potato breeding, structural design, and adjustment of working parameters of potato harvesting and post harvesting equipment.

MATERIAL AND METHODS

● Raw materials for test

Potatoes were dug out manually one day before the test from the potato planting base in Wuchuan County, Hohhot City. Ellipsoidal potatoes with undamaged surfaces were selected as the experimental materials. The potatoes were sealed with the soil in black plastic bags to avoid light and stored at a room temperature of about 15°C. The variety of potato was FuRuiTe, which was widely planted in Inner Mongolia Autonomous Region. Before the test, potatoes were washed clear with cold water, and then the excess was cutted off with a knife to make the tuber mass reach the specified value.

● Potato collision test process

The potato collision tests were carried out via the potato impact test rig and acceleration acquisition system (Xie *et al.*, 2018), shown in Fig.1.

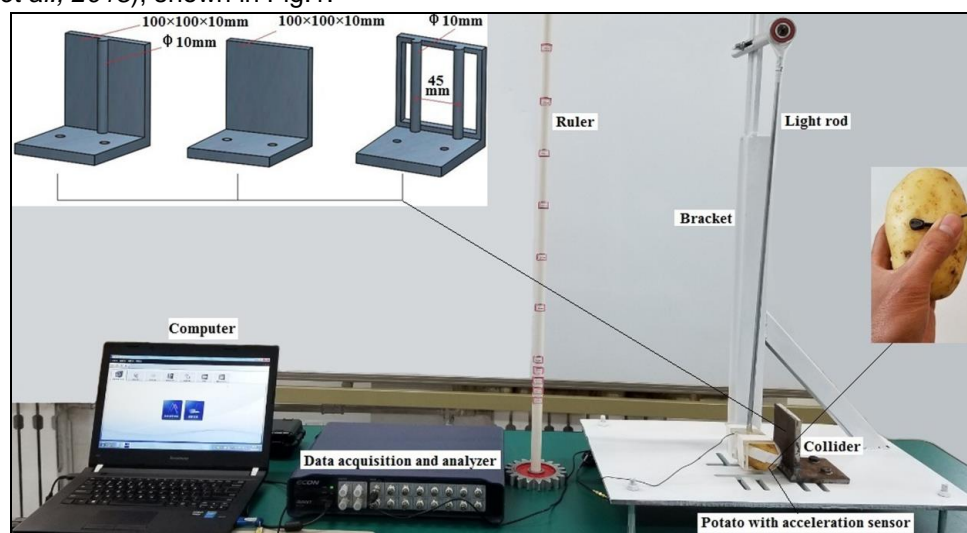


Fig. 1 - Test equipment

Both potatoes and colliders can be quickly replaced, so that the impact accelerations of potatoes under different conditions can be obtained. The acceleration acquisition system included a data acquisition and analyzer (AVANT-MI7016, Hangzhou Yiheng Technology Co., Hangzhou, China.), a 1.2 g-mass acceleration sensor with the accuracy of ± 1.048 mv/m/s² and dimensions of 13x7.2x5.3 mm (1A803E, Jiangsu Donghua Testing Technology Co. Jiangsu, China.) and a computer.

In order to simulate the collision of potatoes during the harvesting and post-harvesting processes, three types of colliders (the single rod, the steel plate and the double rods) were analyzed. All the materials of the colliders were 65Mn steel. During the test, the acceleration sensor was fixed on the surface of the potato near the collision point with soft tape. The potato was lifted to a certain height and then released to collide with the collider. The test program was shown in Table 1. To obtain the reliable results, ten replicates were performed for each collision test.

Table 1

Program of collision tests				
Test number	Drop height (mm)	Potato mass (g)	Colliders	Analysis methods
1	100	250	single rod / steel plate / double rods	experimental test / FEA
2	200			
3	300			
4	400			
5	500			
6	600			
7	300	150		
8		250		
9		350		
10		450		

● Three dimensional solid modeling of potato

The procedure of the three dimensional modeling of potato was shown in Fig.2.

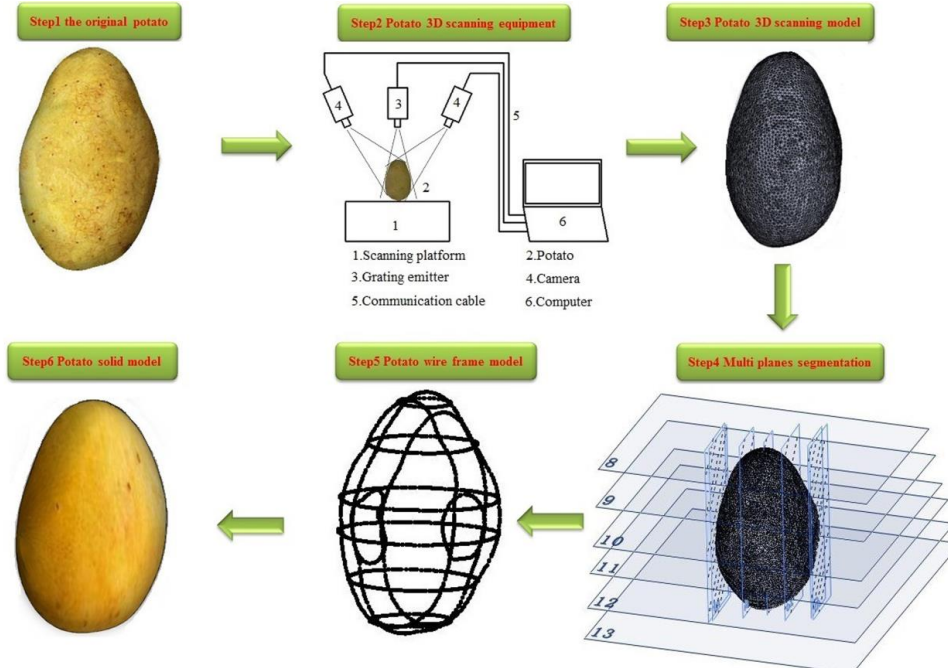


Fig. 2 - Modeling procedure of the potato three dimensional model

To obtain the irregular solid model of potato, a real ellipsoid potato with a mass of 250 g and a volume of 256 cm³ was used (Fig.2-step1). The 3D scanning method and non-contact raster photography scanning technology were applied to obtain the 3D scanning model of the real potato (Meng et al., 2015) (Fig.2-step2). The 3D scanning model was a polygonal mesh model established on the basis of point cloud data (Giammanco et al., 2017), and the size of the polygon was related to the curvature of the model surface. To facilitate the meshing and control of the model during the FEA process, the potato 3D scanning model was imported into SolidWorks in STL format to obtain the three dimensional solid model (Fig.2-step3). The multiple parallel planes along the long axis and short axis of the ellipsoid potato were established (Fig.2-step 4). A cross curve was generated at the intersection of each plane and the model, and the potato wire frame

model was constructed (Fig.2-step 5). The potato solid model was generated from the wire frame model based on the surface modeling method in SolidWorks (Fig.2-step6). The models of the three types of colliders were directly built in SolidWorks and each of the collider was formed an assembly with the potato solid model.

● FEA procedure

The FEA program was shown in Table 1. During the FEA process, potatoes were collided with different colliders at different velocities. The instantaneous impact contact velocity can be calculated according to Eq. (1).

$$v_0 = \sqrt{2gH} \quad (1)$$

where v_0 is the impact contact velocity. H is the potato drop height and g is the standard earth gravity (9.806 m/s²). The FEA process was carried out in ANSYS Workbench 19.2, and LS-DYNA was used as the analysis module due to its good capability of nonlinear analysis. Potato was regarded as a nonlinear body, and the material model was bilinear isotropic elastic-plastic. The modulus of elasticity of potato was 3.35MPa, the yield strength was 0.8776MPa and tangent modulus was 0 MPa (Deng *et al.*, 2021). The potato Poisson's ratio was 0.49 (Caglayan *et al.*, 2018; Celik *et al.*, 2019). The materials of the colliders were 65Mn, the modulus of elasticity was 206 GPa and Poisson's ratio was 0.3. The rod diameters of the colliders were 10mm. The contact types between the potato and colliders were frictionless. During the collision process, the potato was regarded as a flexible body, and the colliders were rigid with fixed constraints. The impact contact velocity was set as the initial conditions. The FEA calculation time was 15ms, and the output was set to 60 equal interval results. After pre-processing, the K file was generated and solved by LS-DYNA solver and post processed by LS-Prepost 4.5. A Lenovo desktop computer (Intel Core i5-4460 CPU @ 3.20 GHz, NVIDIA GeForce GT 750, and RAM: 4 GB) was utilized as the solving platform. The FEA collision models and mesh parameters were shown in Fig.3.

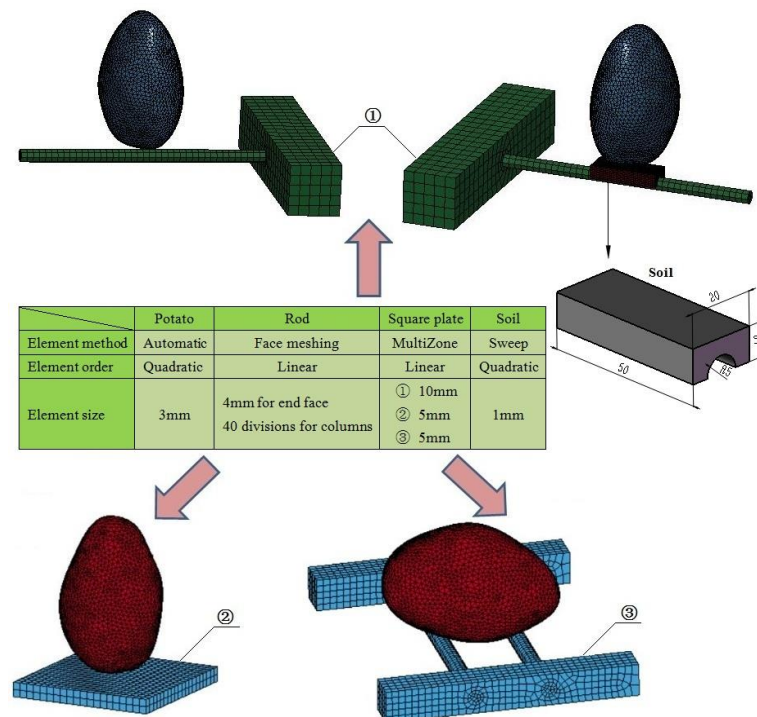


Fig. 3 - FEA collision models and mesh parameters

To analyze the effect of soil on potato impact acceleration, a rectangular soil block with a thickness of 5mm was covered on the collider of the single rod. According to the potato mass and drop heights in Table 1, the finite element analysis was carried out to compare with the collider of the single rod without the cover of soil. Due to the large deformation of soil in the collision process, the Explicit Dynamics was used as the analysis module to make the calculation process easier to converge. The soil was considered as a flexible and nonlinear body with a density of 1500 kg/m³, modulus of elastic 1.2 MPa, Poisson's ratio of 0.3 and yield stress of 0.4 MPa (Gao *et al.*, 2014; Jia *et al.*, 2011; Zhang *et al.*, 2019). The volume of the potato solid

model was 252cm^3 , and the corresponding potato mass can be obtained by setting different densities. The different drop heights were simulated by setting the corresponding impact contact velocity according to the Eq.(1).

● Potato collision kinematics analysis

The potato collision process included a compression and a recovery stage (Deng *et al.*, 2020). In the compression stage, the potato velocity gradually decreased from the initial impact contact velocity, and the acceleration gradually increased from zero. When the compressive displacement reached the maximum, the potato velocity decreased to zero and the acceleration increased to the maximum. The curves of the collision velocity and acceleration of potato were shown in Fig.4. v_0 was the initial impact contact velocity. t_m was the time of the maximum compressive displacement (Fig.4(a)), and at this time the potato impact acceleration was the maximum value a_m (Fig.4(b)).

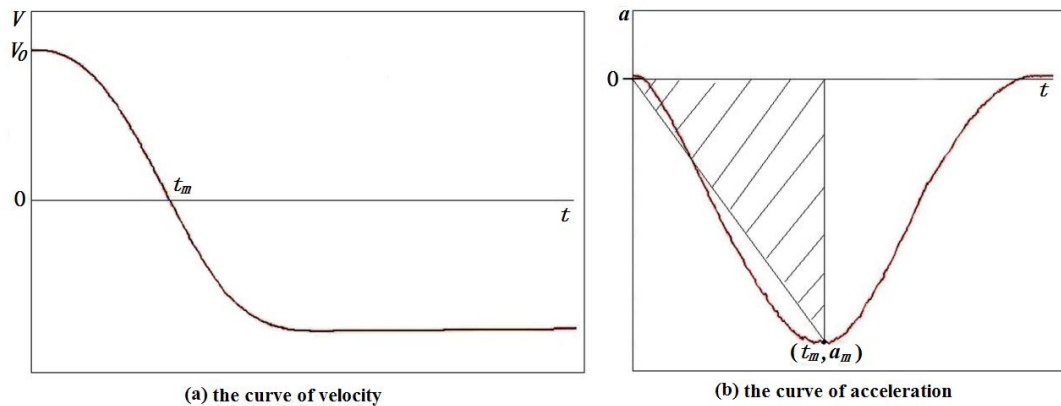


Fig. 4 - Curves of potato collision velocity and acceleration

During the compression stage, the impact velocity and acceleration of the potato satisfied the following equation.

$$\int_0^t a dt = v_0 - v_t \quad (2)$$

where: t is the impact contact time; a is the potato impact acceleration. v_0 is the initial impact contact velocity. v_t is the potato velocity at the time of t . When v_t was zero, the potato compressive displacement reached the maximum value, and the corresponding time was t_m . According to Eq. (1), Eq. (2) can be transformed into the Eq. (3).

$$\int_0^{t_m} a dt = \sqrt{2gH} \quad (3)$$

where t_m is the time of the maximum compressive displacement. H is the potato drop height and g is the standard earth gravity (9.806 m/s^2). The integral value on the left side of the Eq. (3) can be approximated by the shaded area in Fig.4(b). Therefore, Eq. (4) can be obtained.

$$\frac{1}{2} a_m t_m = \sqrt{2gH} \quad (4)$$

Where a_m is the maximum collision acceleration of potato and the following equation can be obtained.

$$a_m = \frac{2\sqrt{2gH}}{t_m} \quad (5)$$

It was shown in Eq.(5) that when the potato drop height was a constant, the maximum collision acceleration was inversely proportional to the corresponding impact contact time.

RESULTS AND DISCUSSION

● Comparison of test and FEA results

According to the program in Table 1, both the experimental test and FEA methods were used to obtain the a_{max} of the potato colliding with the three types of colliders. Under the same condition, the discrepancy of a_{max} obtained by the two methods was calculated according to Eq. (6).

$$e = \frac{|a_{max}(FEA) - a_{max}(Test)|}{a_{max}(Test)} \times 100\% \quad (6)$$

where e is the discrepancy; $a_{max}(FEA)$ is the a_{max} obtained by the FEA method; $a_{max}(Test)$ is the a_{max} obtained by the experimental test. The values and discrepancies of a_{max} were shown in Table 2.

Table 2

Values and discrepancies of a_{max} obtained by the experimental test and FEA method

Test number	a_{max} for single rod collision			a_{max} for steel plate collision			a_{max} for double rods collision		
	Test (m/s ²)	FEA (m/s ²)	e (%)	Test (m/s ²)	FEA (m/s ²)	e (%)	Test (m/s ²)	FEA (m/s ²)	e (%)
1	675.1	664.05	1.64	718.74	753.89	4.89	447.04	427.96	4.27
2	979.1	1004.9	2.64	1176.52	1132.9	3.71	628.24	648.85	3.28
3	1329.99	1273.1	4.28	1462.7	1429.9	2.24	798.1	817.85	2.47
4	1610.06	1508.7	6.30	1731.62	1676.9	3.16	919.2	966.25	5.12
5	1807.99	1721.9	4.76	1951.8	1916.1	1.83	1015.38	1099.55	8.29
6	1972.5	1909	3.22	2257.16	2135.7	5.38	1149.94	1222.3	6.29
7	1469.29	1568.9	6.78	1667.5	1766.7	5.95	1083.6	1014.1	6.41
8	1329.99	1273.1	4.28	1462.7	1429.9	2.24	798.1	817.85	2.47
9	1180.5	1112.3	5.78	1340.84	1235.5	7.86	771.13	713.4	7.49
10	1152.26	999.35	13.27	1143.34	1117.3	2.28	672.82	643.75	4.32
	Average of e		5.3	Average of e		3.95	Average of e		5.04

According to the results in Table 2, the discrepancies of a_{max} between the FEA and test results were almost within 10%. When potatoes were collided with the single rod, the steel plate and the double rods, the average discrepancies of a_{max} were 5.3%, 3.95% and 5.04%, respectively. The results in Table 2 showed that it was accurate and reliable to use the FEA method to analyze the potato impact acceleration, and it also provided a verification basis for the use of FEA to study the collision issues of potatoes during the harvesting and post-harvesting processes.

The test results of the presented research for potatoes colliding with the single rod were based on the earlier research conducted by Xie *et al.* (2020a, 2020b), which were in good agreement with the presented FEA results. When the potato was collided with the steel plate, Cerruto *et al.* (2015) reported that the a_{max} were 935 m/s² and 1437 m/s² for the drop heights of 100 mm and 200 mm with the potato mass of 250 g and modulus of elasticity of 3.5 MPa. The a_{max} showed in the presented simulation were 753.89 m/s² and 1176.52 m/s² in the same conditions of drop height, potato mass and collider. The differences could be due to the different potato shape and modulus of elasticity.

● Effect of drop height and potato mass on impact acceleration

According to the results in Table 2, the curves of the a_{max} of test with different drop heights were shown in Fig.5 when the potato mass was 250 g.

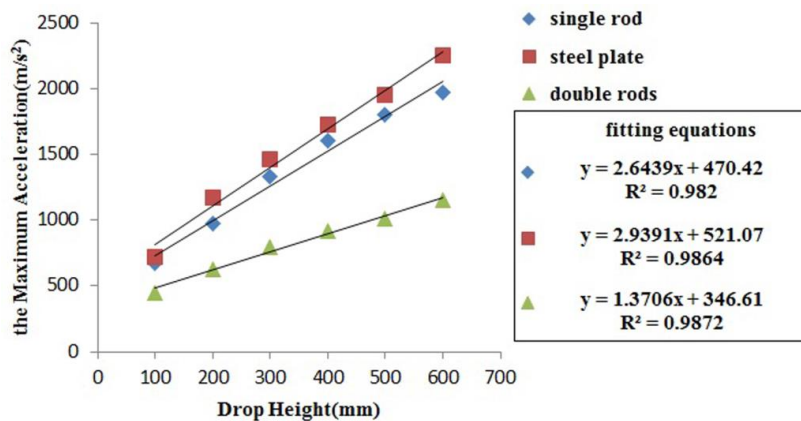


Fig. 5 - Curves of the a_{max} with the drop height

As the drop height increased, the a_{max} gradually increased. Within the range of the potato drop height in Table 1, the fluctuation amplitudes of the test a_{max} for the single rod, the steel plate and the double rods were 1297.4 m/s², 1538.42 m/s², and 702.9 m/s², respectively. The fitting equations showed that there were linear relationships between the drop height and the a_{max} for all the three types of colliders, and the minimum R² value was 0.982. When the potato mass was a constant, the higher the drop height was, the larger the collision velocity and momentum would be. The impact contact time decreased slightly with the increase of drop height (Gao *et al.*, 2018). According to the impulse theorem, the collision contact force would increase due to the larger momentum and shorter impact contact time, so that the a_{max} increased with the increase of the drop height.

The curves of the a_{max} of test with different potato masses were shown in Fig.6 when the potato drop height was 300 mm. The larger the potato mass was, the smaller the a_{max} would be. Within the range of the potato mass in Table 1, the fluctuation amplitudes of the test a_{max} for the single rod, the steel plate and the double rods were 317.03 m/s², 524.16 m/s², and 410.78 m/s², respectively. The fitting equations showed that there were linear relationships between the potato mass and the a_{max} for all the three types of colliders, and the minimum R² value was 0.8481.

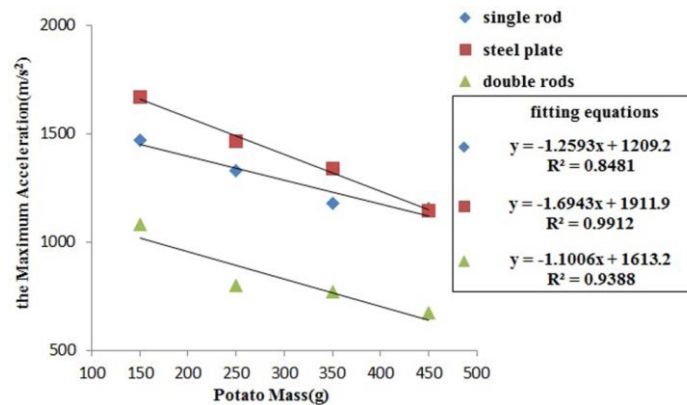


Fig. 6 - Curves of the a_{max} with the potato mass

The trends of the acceleration curves both in Fig.5 and Fig.6 were similar with the test results conducted by Xie *et al.* (2020a, 2020b) and Geyer *et al.* (2009), and consistent with the FEA results conducted by Cerruto *et al.* (2015).

According to the FEA results, the relationship between the impact contact time corresponding to the a_{max} and the potato mass can be obtained, as shown in Fig.7. The larger the potato mass was, the longer the impact contact time for the a_{max} would be. According to the Eq.(5), when the drop height was a constant, the a_{max} was negative to the impact contact time. Therefore, the a_{max} decreased with the increase of the potato mass in Fig.6.

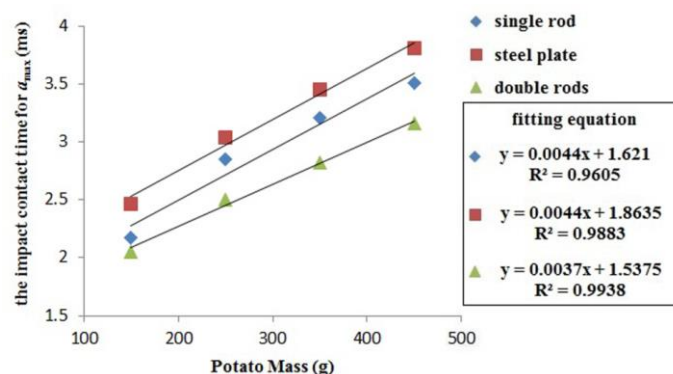


Fig. 7 - Curves of impact contact time with potato mass

Another explanation for the decreased a_{max} with the increased potato mass was that the thickness of potato tissue between the acceleration sensor and collider cushioned the increase of acceleration when the sensor was implanted into the potato (Geyer *et al.*, 2009; Xie *et al.*, 2020a).

According to the effects of potato mass and drop height on the impact acceleration of potato, selecting potato with moderate mass for breeding can reduce the impact acceleration in the process of potato

harvesting. Adjusting the working parameters of the potato harvester and controlling of the relative height between the potato conveying arm and transport vehicle reasonably to reduce the drop height between the potato and the colliders can effectively reduce the potato impact acceleration, thus reducing the potato damage rate.

● Effect of colliders on potato impact acceleration

Based on the curves in Fig.5 and Fig.6, it can be found that the a_{max} had the same trends when potatoes were collided with the single rod, the steel plate and the double rods. Under the same conditions, the a_{max} for the potato colliding with the steel plate was the largest, and that was the smallest for the double rods. It was because of that when the potato was collided with the double rods, the contact area increased, and the collision contact force became smaller, so that the a_{max} became smaller. When the potato was collided with the single rod, the normal collision direction of the potato changed during the collision process because of the cylindrical curved surface of the rod and the irregular curved surface of the potato. Therefore, the acceleration component in the normal collision direction was reduced. When the potato was collided with the steel plate, the acceleration was mainly on the normal direction of the steel plate surface. So, the a_{max} would be greater than that of the single rod collision. Based on the test results in Table 2, when the potato mass was 250 g and the drop height was from 100 to 600mm, the a_{max} in collision with the steel plate was 60.78% to 96.29% higher than that with the double rods, and 6.46% to 20.16% higher than that with the single rod. When the drop height was 300mm and the potato mass was from 150 to 450 g, the a_{max} in collision with the steel plate was 53.89% to 83.27% higher than that with the double rods, and -0.77% to 13.58% higher than that with the single rod.

● Effect of soil on potato impact acceleration

The effect of soil on potato impact acceleration was shown in Fig.8. The a_{max} in collision with the single rod covered with soil increased linearly with the increase of drop height, and decreased linearly with the increase of potato mass, which had the same trend as that without the cover of soil. When 250g potato collided with the 65Mn single rod from 100 to 600 mm drop height, the a_{max} with soil was 37.65% lower than that without soil. When the drop height was 300mm and the potato mass was from 150 to 450 g, the a_{max} with soil was 31.54% lower than that without soil. The results indicated that soil can buffer the collision between potato and rod, effectively reduce the impact acceleration of potato, and thus reduce the occurrence of potato damage.

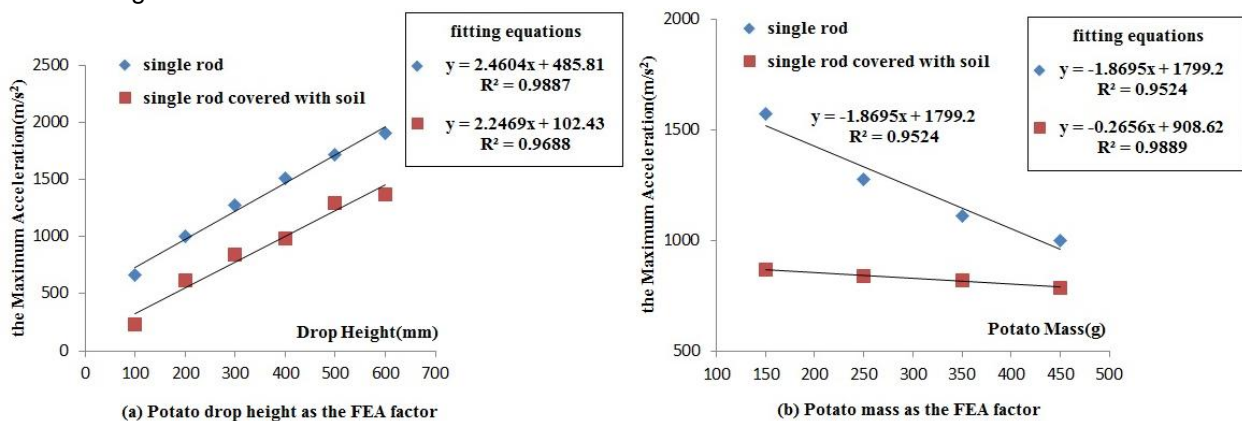


Fig. 8 - Curves of the a_{max} with or without soil

In the process of potato mechanized harvesting, the reasonable adjustment of the structural parameters of the potato-soil separation device can increase the normal acceleration of the upper separation screen appropriately, which is not only conducive to the crushing and separation of potato soil mixture, but also can reduce the occurrence of potato damage due to the buffering of soil. Because of the less soil on the lower separation screen, the normal acceleration should be reduced and the tangential acceleration should be increased. Therefore, it is beneficial to reduce the damage of potato and to make the potato move quickly to the back of the separation screen.

CONCLUSIONS

Analyzing the impact acceleration of potatoes under the impact loading is important for the research of potato impact kinematics and dynamics and can help to understand the occurrences of potato damage. In this article, both the experimental test and FEA method were used to analyze the impact acceleration of potatoes colliding with the single rod, the steel plate and the double rods. The results showed that when potatoes were collided with the single rod, the steel plate and the double rods, the average discrepancies of the a_{max} obtained by the FEA method and the experimental test were 5.3%, 3.95% and 5.04%, respectively. The trends of the a_{max} for the potato colliding with the three types of colliders were the same. And the a_{max} increased with the increase of the drop height, and decreased with the increase of the potato mass. Under the same conditions, the a_{max} decreased in turn for the potato colliding with the steel plate, the single rod and the double rods. In the range of drop height and potato mass level carried out by the FEA, the a_{max} of the collision between potato and single rod with soil condition was 37.65% and 31.54% lower than that without soil. This study had also highlighted that advanced reverse engineering, computer aided design, and simulation techniques were very useful and should be considered as important applications in the areas of agricultural and food research.

ACKNOWLEDGMENTS

This work was supported by the National Natural Science Found of China (31901409) and the Natural Science Foundation of Inner Mongolia Autonomous Region of China (2019BS05012).

REFERENCES

- [1] Ahmadi, E., Barikloo, H., Kashfi, M., (2016), Viscoelastic finite element analysis of the dynamic behavior of apple under impact loading with regard to its different layers, *Comput. Electron. Agric.*, Vol.121, pp.1-11, Elsevier, Oxford/U.K.;
- [2] ASAE S368.4 DEC2000 (R2017), (2017), *Compression test of food materials of convex shape*. St. Joseph, MI: American Society of Agricultural Engineers (ASAE) Standards, U.S.A.;
- [3] Bentini, M., Caprara, C., Martelli, R., (2006), Harvesting Damage to Potato Tubers by Analysis of Impacts recorded with an Instrumented Sphere, *Biosystems Engineering*, Vol.94, Issue 1, pp.75–85, Academic Press INC Elsevier Science, San Diego/U.S.A.;
- [4] Caglayan, N., Oral, O., Celik, H. K., et al., (2018), Determination of time dependent stress distribution on a potato tuber during drop case, *Journal of Food Process Engineering*, Vol.41, Issue 7, pp.e12869.1-12869.7, Wiley-Blackwell, Malden/ U.S.A.;
- [5] Canneyt, T.V., Tijskens, E., Ramon, H. et al., (2004), Development of a predictive tissue discoloration model based on electronic potato impacts, *Biosystems Engineering*, Vol.88, Issue 1, pp.81-93, Academic Press INC Elsevier Science, San Diego/U.S.A.;
- [6] Celik, H.K, (2017), Determination of bruise susceptibility of pears (Ankara variety) to impact load by means of FEM-based explicit dynamics simulation, *Postharvest Biology and Technology*, Vol.128, pp.83–97, Elsevier, Amsterdam/Netherland;
- [7] Celik, H.K., Cinar, R., Yilmaz, D., et al., (2019), Mechanical collision simulation of potato tubers, *Journal of Food Process Engineering*, Vol.42, Issue 5, Wiley-Blackwell, Malden/ U.S.A.;
- [8] Cerruto, E., Aglieco, C., Gottschalk, K., et al., (2015), FEM analysis of effects of mechanical impact parameters on fruit characteristics, *Agricultural Engineering International: CIGR Journal*, Vol.17, Issue 3, pp.430–440, Florida/U.S.A.;
- [9] Dănilă, D.M., (2015), Assessing the potato impact response using a pendulum controlled and designed by computer, *Bulletin of the Transilvania University of Brasov*, Vol.8, Issue 1, pp.65-70, Brasov / Romania;
- [10] Deng, W.G., Wang, C.C., Xie, S.S., (2020), Impact peak force measurement of potato, *International Journal of Food Properties*, Vol.23, Issue 1, pp.616–626, Taylor & Francis INC., Philadelphia/U.S.A.;
- [11] Deng, W.G., Wang, C.C., Xie, S.S., (2021), Collision simulation of potato on rod separator, *International Journal of Food Engineering*, Vol.17, Issue 6, pp.435–444, Berkeley/U.S.A.;
- [12] Gao, X.Y., Zhang, Q.M., et al., (2014), Experimental study on quasi-static performances of soil material (土壤准静态压缩力学性能实验研究), *Transactions of Beijing Institute of Technology*, Vol.34, Issue 8, pp.771-775, Beijing/China;

- [13] Gao, Y.W., Song, C.B., Rao, X.Q., et al., (2018), Image processing-aided fea for monitoring dynamic response of potato tubers to impact loading, *Computers and Electronics in Agriculture*, Vol.151, pp.21-30, Elsevier, Oxford/U.K.;
- [14] Geyer, M. O., Praeger, U., König, C., et al., (2009), Measuring behavior of an acceleration measuring unit implanted in potatoes, *Transactions of the ASABE*, Vol.52, Issue 4, pp.1267–1274, U.S.A.;
- [15] Giammanco, I.M., Maiden, B.R., Estes, H.E., et al., (2017), Using 3d laser scanning technology to create digital models of hailstones, *Bulletin of the American Meteorological Society*, Vol.98, Issue 7, pp.1341-1347, Boston/ U.S.A.;
- [16] Hyde, G. M., Brown, G., Timm, E., et al., (1992), Instrumented sphere evaluation of potato packing line impacts, *Transactions of the ASAE*, Vol.35, Issue 1, pp.65-69, St. Joseph / U.S.A.;
- [17] Jia, J.X., Yang, D.Q., Zhang, D.X., (2011), Finite element analysis between soil and share during potato harvesting (马铃薯收获过程中土壤与挖掘铲相互作用的有限元分析), *Journal of Agricultural Mechanization Research*, Vol.33, Issue 1, pp.28-31, Heilongjiang/China;
- [18] Kabas, O., Vladut, V., (2015), Determination of Drop-Test Behavior of a Sample Peach Using Finite Element Method, *International Journal of Food Properties*, Vol.18, Issue 11, pp.2584-2592, Taylor & Francis INC., Philadelphia/U.S.A.;
- [19] Li, Z., Li, P., Yang, H., et al., (2013), Internal mechanical damage prediction in tomato compression using multiscale finite element models, *Journal of Food Engineering*, Vol.116, Issue 3, pp. 639-647, Oxford/U.K.;
- [20] Meng, J.G., Wang, C.G., Xie, S.S., et al., (2015), Based on 3D Scanning Modeling and Motion Simulation Analysis of the Potato (基于3D扫描的马铃薯建模及运动仿真分析), *Journal of Agricultural Mechanization Research*, Issue 10, pp.64-67, Heilongjiang/China;
- [21] Mathew, R., Hyde, G.M., (1997), Potato impact damage thresholds, *Transactions of the ASAE*, Vol.40, Issue 3, pp.705-709, ST. Joseph / U.S.A.;
- [22] Nikara, S., Ahmadi, E., Nia, A. A., (2018), Scanning electron microscopy study of microstructure damage and micromechanical behavior of potato tissue by impact during storage, *Journal of Food Process Engineering*, Vol.41, Issue 6, pp.e12831, Wiley-Blackwell, Malden/ U.S.A.;
- [23] Nikara, S., Ahmadi, E., Nia, A.A., (2020), Finite element simulation of the micromechanical changes of the tissue and cells of potato response to impact test during storage by scanning electron microscopy, *Postharvest Biology and Technology*, Vol.164, Elsevier, Amsterdam/Netherlands;
- [24] Peters, R., (1996), Damage of potato tubers, a review, *Potato Research*, Vol.39, pp.479–484, Amsterdam/Netherlands;
- [25] Rady, A., Soliman, S., (2015), Evaluation of mechanical damage of Lady Rosetta potato tubers using different Methods, *International Journal of Postharvest Technology & Innovation*, Vol.5, Issue 2, Geneva / Switzerland;
- [26] Strehmel, N., Praeger, U., König, C., et al., (2010), Time course effects on primary metabolism of potato (*Solanum tuberosum*) tuber tissue after mechanical impact, *Postharvest Biology and Technology*, Vol.56, pp.109–116, Elsevier, Amsterdam/Netherlands;
- [27] Thomson, G.E., Lopresti, J.P., (2018), Size and temperature characteristics of potatoes help predict injury following impact collisions, *New Zealand Journal of Crop and Horticultural Science*, Vol.46, Issue 1, pp.1-17, Taylor & Francis, Oxford/U.K.;
- [28] Xie, S.S., Wang, C.C., Deng, W.G., (2018), Model for the prediction of potato impact damage depth, *International Journal of Food Properties*, Vol.21, Issue 1, pp.2517–2526, Taylor & Francis INC., Philadelphia/U.S.A.;
- [29] Xie, S.S., Wang, C.C., Deng, W.G., (2020a), Experimental study on collision acceleration and damage characteristics of potato, *Journal of Food Process Engineering*, pp.e13457, Wiley-Blackwell, Malden/ U.S.A.;
- [30] Xie, S.S., Wang, C.C., Deng, W.G., (2020b), Collision damage test and acceleration characteristic analysis of potato (马铃薯碰撞损伤试验与碰撞加速度特性分析), *Journal of China Agricultural University*, Vol.25, Issue 1, pp.163-169, Beijing/China;
- [31] Zhang, Sh.L., Dai, F., Zhao, W.Y., et al., (2019), Finite element analysis of the dynamic interaction between the soil-rolling device of whole film double ditch laminating machine and seedbed (全膜双垄沟覆膜机镇压装置与种床土壤动态互作有限元分析), *Journal of China Agricultural University*, Vol.24, Issue 9, pp.147-159, Beijing/China.

DEVELOPMENT AND TEST OF CORN STRAW KNEADING AND CONVEYING DEVICE

/ 玉米秸秆揉切输送装置的研制与试验

Geng Aijun^{1,2}, Gao Ang¹, Zhang Yinuo¹, Zhang Ji*¹, Zhang Zhilong¹, Hu Xiaolong¹¹ Shandong Agricultural University, College of Mechanical and Electrical Engineering/ China;² Shandong Provincial Engineering Laboratory of Agricultural Equipment Intelligence/ China

Tel: +86-0538-8242500; E-mail: sdauzhangji@163.com

DOI: <https://doi.org/10.35633/inmateh-65-03>**Keywords:** *Straw utilization; Crushing straw; Kneading and cutting straw Test;***ABSTRACT**

Aiming at the low comprehensive utilization rate of corn straw resources, a straw kneading and cutting conveyor suitable for corn harvester was designed to improve the utilization rate of corn straw resources. The workbench module of ANSYS is used to carry out modal analysis of the two blades, and it is determined that the vibration frequency will not cause damage to the blade sweeping bore. By changing the structure of the movable blade shaft, the speed of the blade shaft can be reduced while ensuring the effect of straw crushing and collecting. In order to determine the best working parameters, three-factor and three-level orthogonal test was carried out with blade arrangement, blade shaft speed and length of feed straw as test factors, and the crushing rate of straw as evaluation index. The results show that the main factors influencing the crushing rate of straw are blade shaft speed, blade arrangement and the minor factor is the length of feed straw. Finally, the optimum combination parameters, blade arrangement, blade shaft speed 400 r/min and whole plant feed with straw, were determined. The corresponding straw crushing rate was 96.39%. The research meets the requirements of straw crushing and can provide technical scheme for comprehensive utilization of corn straw.

摘要

针对玉米秸秆资源的综合利用率低的问题,设计了一种适用玉米收获机的秸秆揉切输送装置以提高玉米秸秆资源的利用率。利用 ANSYS 的 workbench 模块对两种刀片进行模态分析,确定振动频率不会导致刀片扫膛受损;通过改变刀轴的结构在保证秸秆粉碎及收集效果的同时降低刀轴转速以减少能耗。为确定最佳工作参数,以刀片排列方式、刀轴转速及喂入秸秆长度为试验因素,以秸秆粉碎率为评价性指标,进行三因素三水平正交试验,结果表明影响秸秆粉碎率的主要因素为:刀轴转速、刀片排列方式,次要因素为喂入秸秆长度。最终确定最优组合参数刀片为混合排列、刀轴转速 400r/min、喂入秸秆为整株,对应试验的秸秆粉碎率为 96.39%。该研究满足秸秆粉碎要求可为玉米秸秆综合利用提供技术方案。

INTRODUCTION

China is a big agricultural country (Du Y. et al., 2019, Liu C. et al., 2019), and corn is grown in a large area (Ding N. et al., 2021). Corn stalks are rich in nutrients, which can be used as animal feed or they can be returned to the field as plant nutrients (Liu C. et al., 2017). Although the method of returning whole corn stalks to the field avoids the waste of resources and environmental pollution, the large amount of returning to the field leads to the slow decomposing efficiency of the stalks, and a large amount of accumulation on the surface of the land affects the growth of next season crops (Shi N. et al., 2020). The results showed that the effect was the best when the amount of straw returned to the field is 30-50% (Zhao H. et al., 2003). The lower part of corn straw 60 cm accounted for one third of the weight of straw, so the lower part of corn straw is crushed and returned to the field, and the upper part of corn straw is crushed and collected to maximize the utilization of straw resources.

Researchers had conducted many studies on the cutting characteristics of crops and straw crushing devices (Wang I. et al., 2020, He J. et al., 2018, Shi Y. et al., 2019). The existing corn harvesters chop straw mainly in the drum type, the scalpel cutting type and the stalk cutting type (Zhang J. et al., 2018). Drum-type is cut by multiple moving knives and fixed knives, but the cut straw is cylindrical, which is not palatable to animals. The stalk is unsupported when cutting with a flail knife, and cutting the stalk requires a faster rotation speed and consumes more power. The stem-drawing knife extrusion-cutting type is composed of two stem-drawing rollers with opposite rotation directions. The two stem-drawing rollers must meet the same speed and the blades are on the same horizontal line, otherwise it is easy to collide (Xin S. et al., 2020).

Aiming at the problems of these three straw cutting methods, this paper designs a straw kneading and conveying device installed below the stem pulling roller device. The blades of the serrated blade and the triangular blade and the serrated blade are matched with the fixed knife to shred the straw. At the same time, the stalks are conveyed in a spiral arrangement by the cutting blades, which improves the palatability of the stalk feed for animals, reduces the speed of the knife shaft, and reduces the power demand.

MATERIALS AND METHODS

Structure and working mechanism

In the corn harvester table shown in Figure 1, the straw kneading and cutting conveyor was installed under the puller roll. During the corn harvest, corn straw was fed to the heading roll under the push and pull of the conveying chain. At the same time, the rotor milling cutter under the heading roll cuts off the straw and sends the lower part of the cut straw into the straw kneading and cutting conveyor. The straw was harvested under the pulling action of the heading roll, and the remaining corn straw was fed into the straw kneading and cutting conveyor. Under the action of moving blade and fixed blade in the straw kneading and cutting conveyor, the straw was crushed, and then centralized transported to the fan to complete the straw collection.

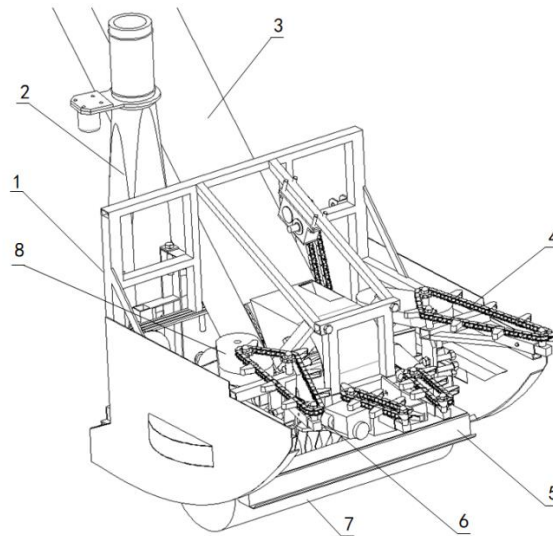


Fig. 1 - Corn harvester cutting table

1. Rack; 2. Draught fan; 3. Ear conveying device; 4. Conveying chain; 5. Rotor milling cutter; 6. Shapping roll; 7. Straw kneading and cutting conveying device

In order to verify the practicability of straw kneading and conveying device, designing the testbed of straw kneading and conveying device has been done. It was made of bottom case, rack, cutter shaft, shaft sleeve, triangular blade, jagged blade, adjustable-speed motor, drive system and so on. It is shown in fig. 2.

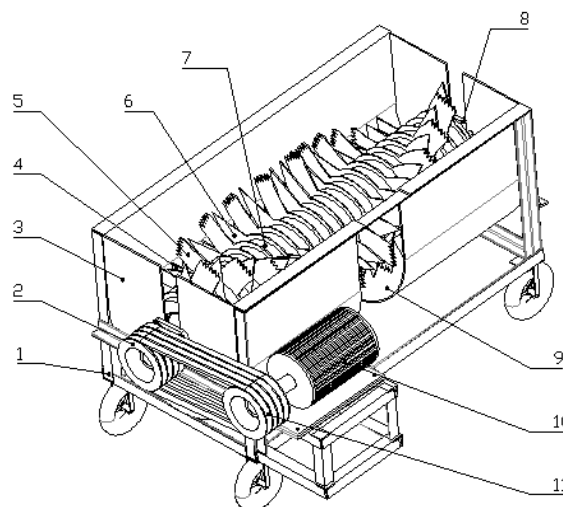


Fig.2 - Structure diagram of straw cutter

1. Rack; 2. Belt pulley; 3. Type a Belt pulley; 4. The fixed blade; 5. Triangular blade; 6. Jagged blade; 7. Type a Shaft sleeve; 8. Cutter shaft; 9. The outlet of straw delivery; 10. Motor; 11. Transmission

The straw kneading and conveying device was installed under the pull stem device of corn harvester. After the corn straw in the field was cut by the stubble cutter harvester, corn bundles were picked by pulling of double-roller stem pulling device and the straw was transported inside straw kneading and conveying device. The straw was cut with the blade of cutter shaft and the stationary knife of the bottom case. The cutting edges of the blade are arranged spirally on the tool shaft, which produce transverse thrust on the straw during the work, and transport the straw to the straw conveyor port on the bottom shell while crushing the straw.

The design of cutter shaft

While cutting the straw, the movable blade also leaves a space in the bottom shell of the straw kneading and cutting conveyor device to transport the chopped straw, and the saw tooth has a good effect of kneading and cutting the straw (Zhang Z. *et al.*, 2021). The movable blade was designed as a serrated blade with a multiple serrations on the outer circumference as shown in Figure 3. In order to avoid the blockage of corn straw caused by too small space reserved by serrated blade in the bottom shell of the device, a triangular blade with a serrated blade on the outer circumference was designed, as shown in Figure 4. As the sawtooth blade has a good kneading and cutting effect on corn straw, the triangular blade is helpful for the conveying efficiency of corn straw in the bottom shell of the device and prevents blockage. Therefore, the blades on the cutter shaft are arranged in the way of sawtooth blade and triangular blade spacing, and the cutting blades are arranged in a spiral shape, as shown in Figure 5.

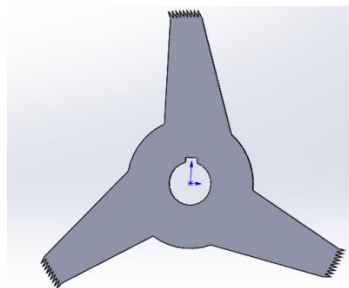


Fig. 3 - Jagged blade

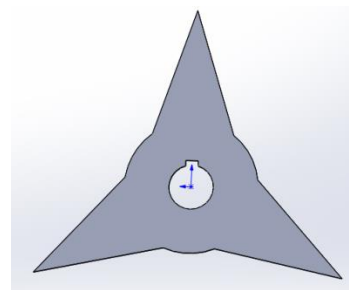


Fig. 4 - Triangular blade

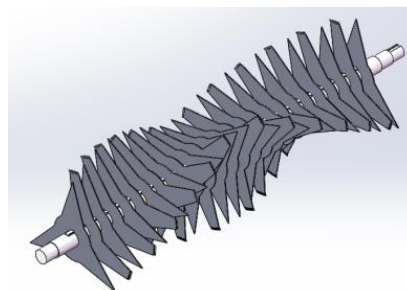


Fig. 5 - Knife shaft

The corn straw contains about 40% fibrin (Chen Z. *et al.*, 2013), which had great influence on the mechanical strength and elasticity of straw. Cutting the straw with the measures of smooth cut could effectively destroy fibrin physical property of straw (Mou X. *et al.*, 2020). The sliding cutting angle and cutting corners had great effect on cutting energy consumption when cutting, so selecting reasonable cutting angle could decrease power loss effectively and increase straw smashing quality (Liu P *et al.*, 2019). Figure 6 shows the force when the movable blade and the fixed blade clamp the straw.

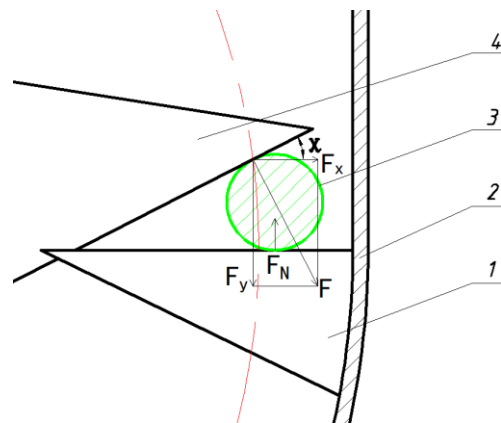


Fig. 6 - Stress analysis

1. Fixed blade; 2. Bottom shell; 3. Straw; 4. Movable blades

The moving blade exerts a shearing force F on the straw during high-speed rotation, which could be decomposed into a force F_x in the direction of leaving the clamping range of the movable knife and the fixed knife and a vertical downward pressure F_y . The fixed knife provides a vertical upward force for the straw. The supporting force F_N , the condition that the material was not pushed out was $\chi \leq \phi_1 + \phi_2$, where χ was the sliding angle of the movable knife, ϕ_1 was the friction angle of the movable knife to the straw, and ϕ_2 was the friction angle of the fixed knife to the straw. χ changes during the cutting process, so it was required that the maximum value of the pushing angle should meet the conditions of the above formula. Usually, $\phi_1=32^\circ$, $\phi_2=18^\circ$, so χ was generally less than 50° . When the sliding cut angle was in the range of $35-45^\circ$, the average cutting torque was lower and the cutting energy consumption was lower. In order to cut reliably, the sliding cut angle $\chi=30^\circ$ was used.

Design of cutter shaft

The long section of straw that was not cut when the straw was cut was easily entangled in the gap between the main shaft and the blade, which affected the normal operation of the cutter shaft. The shaft sleeve with an outer diameter of 150 was designed to be installed between adjacent blades on the cutter shaft. On the one hand, the shaft sleeve can be used to axially space and position the blades. On the other hand, the larger outer diameter can prevent the cutter shaft from tangling grass.

The distance between adjacent blades was 44 mm. That was to say, the width of the sleeve was 44 mm. The fixed blades were installed in the middle of two adjacent blades in a staggered way. A keyway was provided on the cutter shaft and the blade, and the key was matched to realize the cutter shaft to drive the blade to rotate at a high speed. In order to make the cutting edges of the blades spirally arranged, the opening positions of the key grooves on the blades are also different, and the angle between the key grooves of two adjacent blades is about 7° . It was assembled on the cutter shaft according to the principle of one sleeve and one blade. The cutter shaft was installed on the shell through two bearings, and finally connected to the speed regulating motor through the belt drive system.

Experiment design

The main working part of the straw kneading and cutting conveying device was the blade. The blade structure and rotating speed directly affect the degree of straw crushing. For the ear picking device, when the ordinary ear picking roller was used, the straw fed into the straw kneading and cutting conveying device was the whole straw, while when the stalk pulling knife roller was used as the ear picking device, the straw fed into the straw kneading and cutting conveying device was pre-cut to 7 cm or 14 cm. In order to obtain the best smashing effect, the three variable factors of the blade arrangement, the rotation speed of the knife shaft and corn stalk length of the feed straw were tested to determine the optimal combination.

Test equipment and materials

The test bench of the straw kneading and cutting conveying device was shown in Figure 7. The motor selection model was YVP132M-4 variable frequency speed regulating three-phase asynchronous motor, with a power of 7.5KW and a torque of 49.7Nm. Choose Senlan SB4037.5 frequency converter to control the motor speed.



Fig. 7 - Test bench

In the experiment, corn stalks were selected as field stalks harvested after maturity of corn. The stalks were straight, free from diseases and insect pests, and suffered no bending. The stalks above 60 cm on the ground were cut and collected, as shown in Figure 8.



Fig. 8 - Corn stover

According to the requirements of "NYT 2088-2011 corn silage harvester operation quality" standard (Lv J. et al., 2016), corn straw silage should be carried out under the condition of 65% - 70% moisture content of straw. The qualified cutting length of silage corn straw was 3cm-5cm, and the required crushing qualified rate was greater than or equal to 95%. In this paper, the qualified length of straw crushing was selected to be 5cm, and the crushed total straw and the weight of the qualified length of straw were weighed by electronic scale, as shown in Figure 9. The qualified rate of crushing was calculated as follows:

$$p = \frac{ma}{m} \times 100\% \quad (1)$$

where, p - qualified rate of straw crushing, %;

ma - mass of straw with qualified crushing length, kg;

m - total mass of crushed straw, kg.



Fig. 9 - Weighing the straw

RESULTS

Stress analysis

Modal analysis (Zahid, F.B. et al., 2020) was used to calculate the natural frequency and vibration mode of the structure (Bo H. et al., 2016). The blade rotates under the action of the blade shaft, resulting in vibration deformation. It was necessary to avoid the natural frequency of the structure when designing to prevent the blade from sweeping bore and parts from being damaged due to excessive vibration. Modal analysis of the two blades was carried out in this paper.

Import the three-dimensional models of the two blades established by SolidWorks into the Ansys workbench module, create the analysis type as "Modal", set the material of the blade to high-strength 65 manganese steel, density $\rho=7.85\text{g/cm}^3$, Young's modulus $E=196500\sim 198600\text{MPa}$, Poisson's ratio $\mu=0.288$. After loading the model, the sixth-order mode was analysed and calculated, and the resulting sixth-order modal shape diagrams were shown in Figures 10 and 11. It could be seen that the maximum deformation of the serrated blade was 0.02268mm, and the maximum deformation of the triangular blade was 0.03422mm. The deformation of the blade was small, and vibration deformation will not cause problems such as blade sweeping and damage to parts.

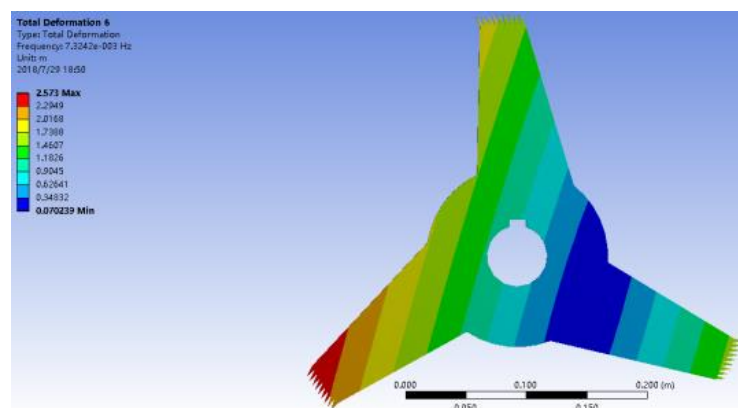


Fig. 10 - Six-order modal shape of jagged blade

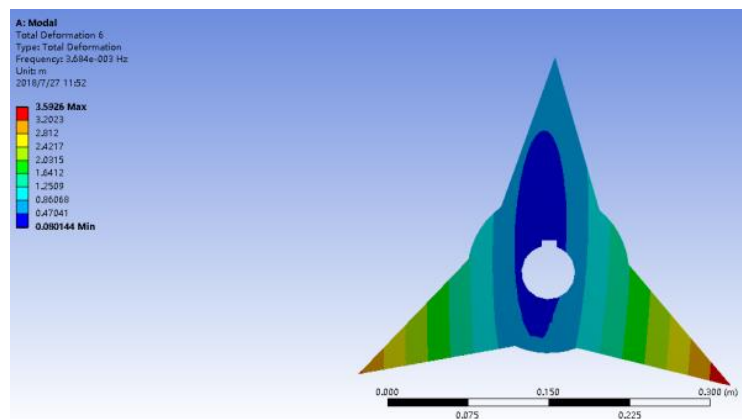


Fig. 11 - Six-order modal shape of triangular blade

Analysis of test data

In order to determine the factor level of the rotation speed of the cutter shaft, a single factor test was performed on the test bench first, and a mixed arrangement of blades was selected. The rotation speed directly affects the power loss. In order to reduce the power loss of the device, determine the minimum rotation speed that meets the shredding needs, select the rotation speed to start the test from 200r/min, and gradually increase the rotation speed. Calculated from the test data, the average pass rate of straw crushing was 65.28% when the rotating speed was 200r/min. The higher the rotating speed, the higher the pass rate of crushing. When the rotating speed was 350r/min, the average pass rate of straw crushing could reach 92.53%. The three levels of cutter shaft speed were 300r/min, 350r/min, and 400r/min.

The blade arrangement and straw feeding length were tested under these three speeds, and the data were shown in figure 12. In the figure, the broken line connected by diamond represents the arrangement of mixed blades, the broken line connected by square represents serrated blades, and the broken line connected by triangle represents triangular blades.

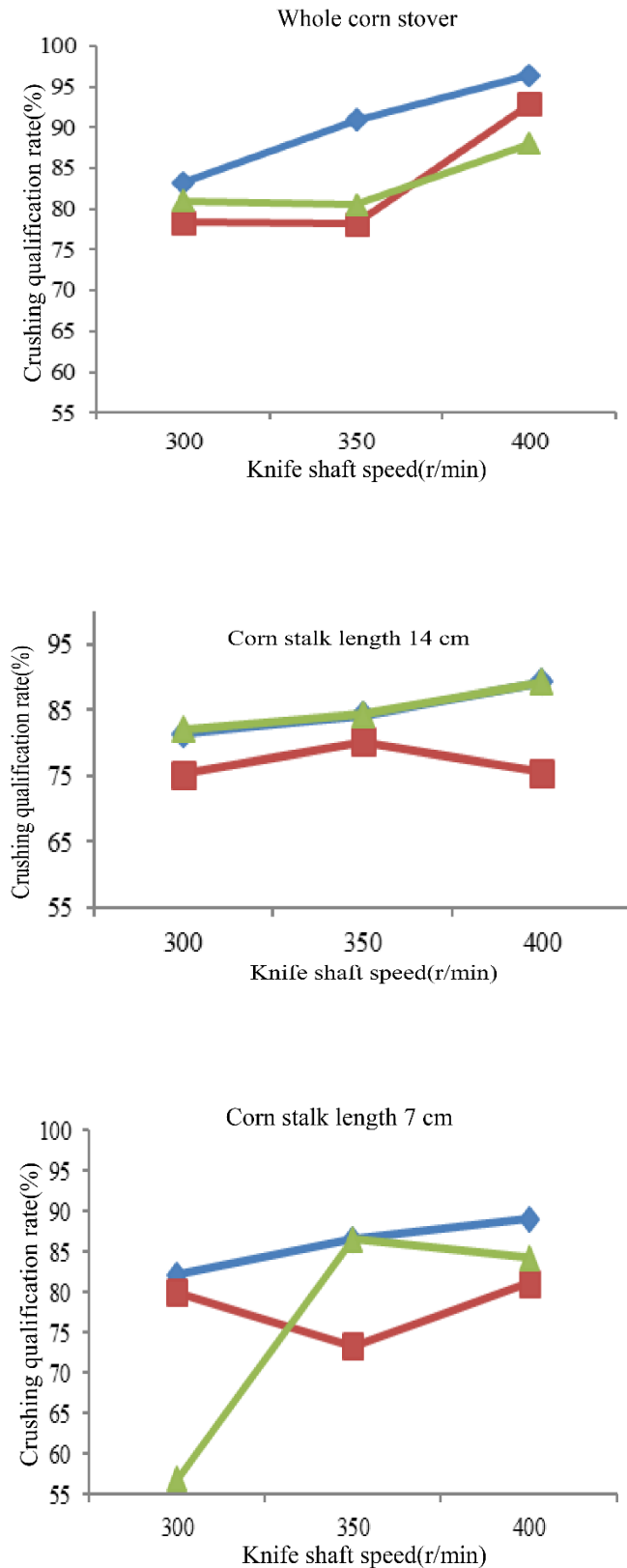


Fig.12 - Effect of different combination of factors on the grinding yield

In order to improve the qualified rate of straw crushing, three factors and three levels of orthogonal test were carried out on three variable factors: blade arrangement (A), blade shaft speed (B) and feed straw length (C). The factors and levels are shown in Table 1. The test results are shown in Table 2.

Table 1

Levels	Factors		
	Blade arrangement (A)	Blade shaft speed (B) (r/min)	Corn stalk length (C) (cm)
1	Mixed arrangement	300	7
2	Zigzag arrangement	350	14
3	Triangular arrangement	400	Whole corn stover

Table 2

Serial number	A	B	C	Average accuracy /%
1	1	1	1	82.19
2	1	2	2	84.21
3	1	3	3	96.39
4	2	1	2	80.19
5	2	2	3	78.18
6	2	3	1	81.19
7	3	1	3	80.96
8	3	2	1	86.52
9	3	3	2	89.24

Analysis of variance

The test results were imported into SPSS for variance analysis (Tanner-Smith, E.E., 2014, Guo M. et al., 2017). The results were shown in Table 3. The Sig values were all greater than 0.05, which indicated that there was no significant difference in average yield due to different levels of factors. Factor A and factor B have a significant influence on the test results, of which factor B has a greater influence on the test results, while factor C has no influence on the significance of the test results. At this time, you can select the combination of A1, B3, and C3 with the largest average number from Figure 10 to form the optimal combination of A1B3C3. The resulting optimal combination plan A1B3C3 exists in the orthogonal test table 2. Therefore, the combination of A1B3C3 was the best. The optimal combination plan was that the blades are arranged in a mixed manner, the speed of the knife shaft was 400 r/min, and the straw was fed to the whole plant.

Table 3

Source of variation	Sum of squares	Degree of freedom	Mean square	F	Sig.
A	96.771	2	48.386	1.842	0.352
B	100.345	2	50.172	1.910	0.344
C	5.473	2	2.736	0.104	0.906
Error	52.53	9	/	/	/

CONCLUSIONS

A straw kneading, cutting and conveying device installed under the rod puller was designed. The stalk was shredded by the blades of the serrated blade, the triangular blade and the serrated blades and the fixed knife. At the same time, the stalks were conveyed in a concentrated manner by the spiral arrangement of the cutting blades. While ensuring the effect of straw crushing and collecting, the rotation speed of the cutter shaft was reduced, and the power consumption was reduced.

The cutting angle of the cutting edge was calculated by analysing the cutting process, and a modal analysis of the blade was made. The blade vibration and deformation are small, which avoids problems such as blade sweep.

The influencing factors of the crushing pass rate of straw were tested by design test. Variance analysis showed that when the blades were mixed and arranged, the rotation speed of the cutter shaft was 400r/min, and the feed straw was the whole plant, the highest pass rate of straw crushing was 96.39%, which was the best combination scheme.

ACKNOWLEDGEMENT

This work was sponsored by the Shandong Provincial Key Science and Technology Innovation Engineering Project (2018CXGC0217) and China Post-Doctoral Fund Project (2017M612309).

REFERENCES

- [1] Bo, H., Lin, J. (2019). Study on the design and parameters of corn straw returning machine (玉米秸秆还田机的设计与参数研究). *Journal of Agricultural Mechanization Research*, Vol.11, pp.99-103, Beijing/China.
- [2] Ding, N., Li H., Yan, A., Li, S., Han, L., Wei W. (2021). Experiment on Multi-stage Continuous Cold Roll Forming of Straw (秸秆多级连续冷辊压成型试验研究). *Transactions of the Chinese Society for Agricultural Machinery*, Vol.52, issue 5, pp.279-285, Beijing/China.
- [3] Du, Y., Fu, S., Mao, E., Zhu, Z., Li, Z. (2019). Development Situation and Prospects of Intelligent Design for Agricultural Machinery(农业机械智能化设计技术发展现状与展望). *Transactions of the Chinese Society for Agricultural Machinery*, Vol.50, issue 9, pp.1-17, Beijing/China.
- [4] Guo, M., Feng, B., Guan, Y. (2017). Experimental Design and Software Application (实验设计与软件应用). *Beijing: Chemical Industry Press*, 7.
- [5] He, J., Li, H., Chen, H., Lu, C., Wang, Q. (2018), Research Progress of Conservation Tillage Technology and Machine (保护性耕作技术与机具研究进展). *Transactions of the Chinese Society for Agricultural Machinery*, Vol.49, issue 4, pp.1-9, Beijing/China.
- [6] Liu, C. (2017). Vigorously promote the mechanized return of corn stalks to the field (大力推进玉米秸秆机械化还田技术). *Use and Maintenance of Agricultural Machinery*, Vol.10, pp.68-73, Harbin/China.
- [7] Liu, P., He, J., Li, H., Wang, Q., Lu, C., Lou, S., Liu, W., Cheng, X. (2019), Kinematic analysis and experiment of corn spreading process. *INMATEH-Agricultural Engineering*, Vol.58, issue 2, pp.83-95, Beijing/China.
- [8] Liu, C., Lin, H., Li, Y., Gong, L., Miao, Z. (2019). Analysis on Status and Development Trend of Intelligent Control Technology for Agricultural Equipment(农业装备智能控制技术研究现状与发展趋势分析). *Transactions of the Chinese Society for Agricultural Machinery*, Vol.51, issue 1, pp.1-18, Shanghai/China.
- [9] Lv Ji., Yang Y., Shang Q., Wang, Y., Li, Z., Tong, S., Zhu, Q. (2016). Experimental study on shredding performance of corn silage harvester (玉米青贮收获机切碎性能试验研究). *Journal of Northeast Agricultural University*, Vol.47, issue 4, pp.102-108, Harbin/China.
- [10] Mou, X., Jiang, H., Sun, Y., Xu, H., Yao, Y., Geng, D. (2020). Simulation Optimization and Experiment of Disc-type Grain Crushing Device of Silage Corn Harvester (青贮玉米收获机圆盘式籽粒破碎装置仿真优化与试验). *Transactions of the Chinese Society for Agricultural Machinery*, Vol.51, issue s1, pp.218-226, Zibo/China.
- [11] Shi, N., Chen, H., Wei, Z., Hou, S., Zou, Z., Wang X. (2020). Design and experiment of stalk returning proportion adjusting device for corn original stubble (玉米原茬地秸秆还田比例调节装置设计与试验). *Transactions of the Chinese Society of Agricultural Engineering (Transactions of the CSAE)*, Vol.36, issue 21, pp.11-22, Harbin/China.
- [12] Shi, Y., Luo W., Hu Zh., Wu, F., Gu, F., Chen, Y. (2019). Design and Test of Equipment for Straw Crushing with Strip-laying and Seed-belt Classification with Cleaning under Full Straw Mulching(全量秸秆粉碎条铺与种带分型清秸装置设计与试验). *Transactions of the Chinese Society for Agricultural Machinery*, Vol.50, issue 4, pp58-67, Nanjing/China.

- [13] Tanner-Smith, E.E., Tipton, E. (2014). Robust variance estimation with dependent effect sizes: practical considerations including a software tutorial in Stata and SPSS. *Research Synthesis Methods*, Vol.5, issue 1, pp.13-30, Nashville/USA.
- [14] Wang, L., Zhang, Z., Liu, T., Wang, Y., Jia, F., Jiang, J. (2020). Design and test of chopping stalk crushing device for corn harvester cutting table (玉米收获机割台砍劈式茎秆粉碎装置设计与试验). *Transactions of the Chinese Society for Agricultural Machinery*, Vol.51, issue 7, pp.109-117, Harbin/China.
- [15] Xin S., (2020), Study on the mechanism and key technology of corn ear picking with vertical roller (立辊采摘玉米穗机理及关键技术研究). *Gansu Agricultural University*, Lanzhou/China.
- [16] Zhao, H., Ning, T., Nie, L., Wang, B., Tian, S., li, Z. (2013). Comparison of yields and nutrient compositions between different harvesting heights of maize stover (玉米原茬地秸秆还田比例调节装置设计与试验). *Scientia Agricultura Sinica*, Vol.46, issue 20, pp.4354-4361, Tai'an/China.
- [17] Zhang, J., Yu, Y., Yang, Q., Zhang, J., Zhang, Z., Geng, A. (2018), Design and Experiment of Smashed Straw Unit for High Stubble Maize Double Header (全量秸秆粉碎条铺与种带分型清秸装置设计与试验). *Transactions of the Chinese Society for Agricultural Machinery*, Vol.49, issue s1, pp.42-49, Ta'ian/China.
- [18] Zhang, F., Song, X., Zhang, X., Zhang, F., Wei, W., Dai F. (2019). Simulation and experiment on mechanical characteristics of kneading and crushing process of corn straw (玉米秸秆揉丝破碎过程力学特性仿真与试验). *Transactions of the Chinese Society of Agricultural Engineering (Transactions of the CSAE)*, Vol.35, issue 9, pp58-65, Gansu/China.
- [19] Zhang, Z., Yu, Y., Yang, Q., Geng, A., Zhang, J. (2020). Development and evaluation of the finger wheel and cutting disc combined device for stalk returning. *INMATEH-Agricultural Engineering*, Vol.64, issue 2, pp.54-64, Ta'ian/China.
- [20] Zahid, F.B., Zhi, C.O., Khoo, S.Y. (2020). A review of operational modal analysis techniques for in-service modal identification. *Journal of the Brazilian Society of Mechanical Sciences and Engineering*, Vol.42, issue 8, Kuala Lumpur/Malaysia.

GRAIN AUGER CONVEYOR-DISTRIBUTOR / ШНЕКОВЫЙ ТРАНСПОРТЕР-РАСПРЕДЕЛИТЕЛЬ ЗЕРНА

Kupreenko Aleksey ¹⁾; Kuznetsov Yury ^{*2)}; Bychkova Tatiana ¹⁾; Kravchenko Igor ³⁾;
Aldoshin Nikolay ³⁾; Kalashnikova Larisa ⁴⁾ ¹

¹⁾Bryansk State Agrarian University / Russia;

²⁾Orel State Agrarian University named after N.V. Parakhin / Russia;

³⁾Russian State Agrarian University – Moscow Agricultural Academy named after K.A. Timiryazev / Russia;

⁴⁾Orel State University named after I.S. Turgenev / Russia

Tel: +79208289219; E-mail: kentury@yandex.ru

DOI: <https://doi.org/10.35633/inmateh-65-04>

Keywords: solar dryer, grain storage facilities, grain outflow

ABSTRACT

The construction of a solar dryer-grain storage facility is described in this paper. The design of a grain auger conveyor-distributor for its loading is made. The dependence of the width of the discharge opening in the casing of the auger conveyor-distributor on its length is obtained. The results of laboratory tests of the grain auger conveyor-distributor are presented. It is established that the minimum initial width of the drain opening for wheat grain should be not less than 9 mm. The conditions of grain uniform distribution grain by the auger conveyor-distributor are justified: the filling factor of the auger inter-turn space in its loading zone – 0.35; the length of the discharge opening of the charging hopper should be equal to the doubled value of the auger pitch size. In this case, the uneven distribution of grain along the discharge opening will be no more than 5%.

РЕЗЮМЕ

Описана конструкция гелиосушилки-зернохранилища. Предложена конструкция шнекового транспортера-распределителя зерна для ее загрузки. Получена зависимость ширины высыпного отверстия в кожухе шнекового транспортера-распределителя от его длины. Представлены результаты лабораторных испытаний шнекового транспортера-распределителя зерна. Установлено, что минимальная начальная ширина высыпного отверстия для зерна пшеницы должна составлять не менее 9 мм. Обоснованы условия равномерного распределения зерна шнековым транспортером-распределителем: коэффициент заполнения межвиткового пространства шнека в зоне его загрузки – 0.35; длина выходного отверстия загрузочного бункера должна быть равна удвоенному значению величины шага шнека. При этом, неравномерность распределения зерна вдоль высыпного отверстия составит не более 5%.

INTRODUCTION

Drying of freshly harvested grain is a necessary and energy-consuming operation, since the used drying installations consume on average 10 kg of liquid fuel per ton of grain while reducing its moisture content by one percent. The usage of high-capacity dryers for small amounts of grain production is especially inefficient, as the share of depreciation deductions from the cost of the drying unit, included in the grain cost, in this case significantly increases it. It is possible to reduce energy costs by using drying installations with non-traditional energy sources. We have conducted research on post-harvest drying of grain during its storage in a solar dryer-grain storehouse (fig. 1).

As a result of the experiment, the grain was dried to condition moisture content of 14% and stored well – no self-heating sources were observed. In spring, the crops had high germination rates (Kupreenko et al., 2011). However, the disadvantage of the experimental solar dryer-grain storage facility is the lack of mechanized loading and unloading of grain. Therefore, we have developed a design of mechanized solar dryer-grain storage facility. The main equipment for grain moving are auger conveyors (Pezo et al., 2015; Shimizu and Cundall, 2001; Orefice and Khinast, 2017; Rohatynskiy et al., 2019). Therefore, the usage of an auger conveyor was proposed to mechanize grain processing in the solar dryer-grain storage facility.

¹ Aleksey Kupreenko, Assoc. Prof. Dr. Eng.Sc.; Yury Kuznetsov, Prof. Dr. Eng.Sc.; Tatiana Bychkova, Assoc. Prof. Ph.D.; Igor Kravchenko, Prof., Dr. Eng.Sc.; Nikolay Aldoshin, Prof. PhD. Eng.Sc.; Larisa Kalashnikova L.V., Prof. Dr. Phil.Sc.

A number of works regard the study of auger conveyors operating modes (Hou et al., 2014; Tian et al., 2018; Hevko et al., 2019; Trokhaniak et al., 2020; Arkhangel'skii, 2019; Mashkov et al., 2018). At the same time, some scientists have also studied the process of grain outflow through various discharge openings (Han et al., 2017; Arkhangel'skii, 2019). However, they do not provide a uniform grain discharge along the length of the conveyor in its stationary position.

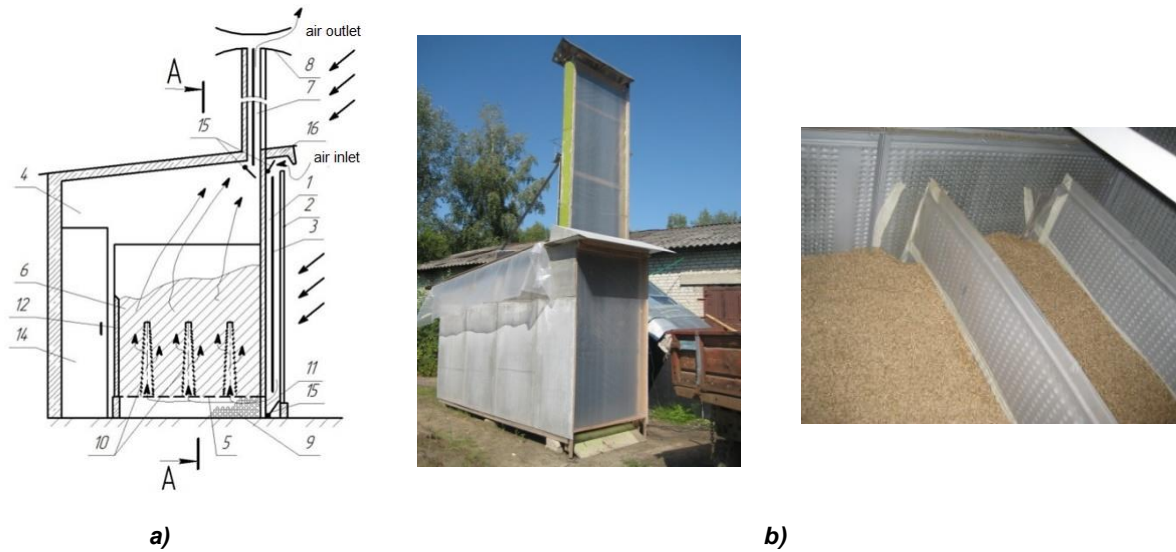


Fig. 1 - Scheme (a) and general view of the solar dryer-grain storage facility (b)
 1 - vertical solar collector; 2 - translucent coating; 3 - light-absorbing surface; 4 - drying chamber; 5 - perforated deck; 6 - dried grain; 7 - ventilation pipe; 8 - deflector; 9 - gravel accumulator; 10 - perforated air-distributing channels; 11 - openings in the grain storage facility walls; 12 - longitudinal partition; 13 - transverse partition; 14 - door; 15 - flaps; 16 - roof ridge

The purpose of the study is to justify the design of the grain auger conveyor-distributor, allowing to ensure uniform distribution of grain mass along the length of its discharge opening when loading rectangular tanks with a horizontal or sloping location of the bottom.

MATERIALS AND METHODS

The new design of the mechanized solar dryer-grain storage facility is shown in fig. 2. The usage of an auger conveyor-distributor was proposed to load grain on the perforated rectangular air-distributing trays, located in the drying chamber of the solar dryer-grain storage facility (Chashchinov et al., 2016).

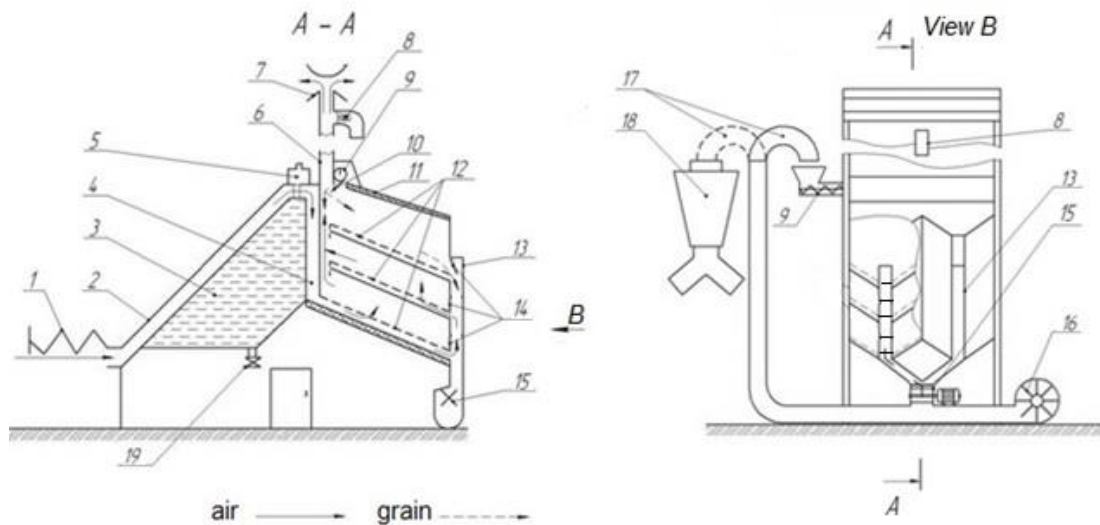


Fig. 2 - Mechanized solar dryer-grain storage facility
 1, 2 - retractable film and inclined solar collectors; 3 - water heat accumulator; 4 - main air channel; 5 - expansion tank; 6 - ventilation pipe; 7 - deflector; 8 - exhaust fan; 9 - loading auger conveyor-distributor; 10 - guide tray; 11 - drying chamber; 12 - perforated air-distributing trays; 13 - discharge channels; 14 - flaps; 15 - lock gate; 16 - pneumatic conveyor; 17 - rotary deflector; 18 - cyclone; 19 - drain cock

The design feature is the presence of a longitudinal slot (discharge opening) in the lower part of the auger conveyor-distributor casing. Through it the grain is discharged along the entire length of the casing (fig. 3) (Kupreenko et al., 2017).

A grain auger conveyor-distributor (fig. 3) works in the following way. Grain from the charging hopper 1 enters the casing 3 and auger 2 moves along the casing 3. Passing over the discharge opening 4, the grain begins to pour out of the auger casing. Due to the special shape of the discharge opening 4, the grain is discharged evenly along the entire length of the casing. There is a uniform loading of grain along the entire length of the hopper. The height of the grain layer along the length of the discharge opening decreases to zero at its end.

It was assumed that to ensure uniform grain distribution, the shape of the discharge opening in the auger casing should be as in fig. 3.

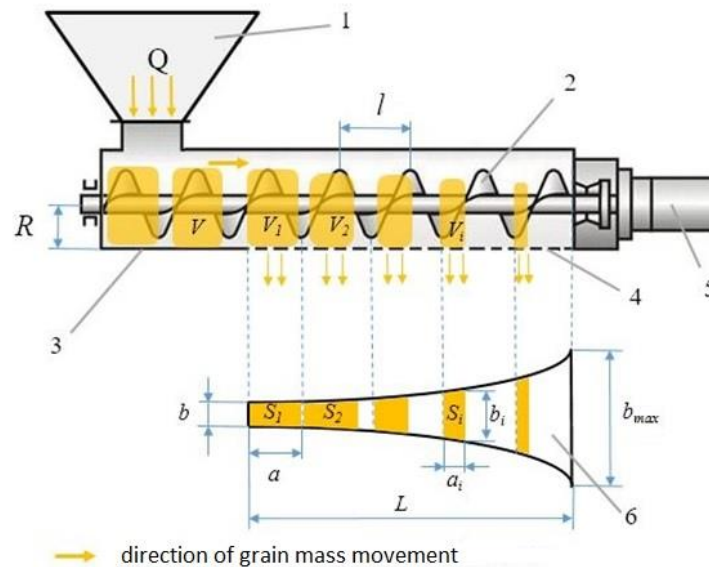


Fig. 3 - Construction and technological scheme of grain auger conveyor-distributor

1 - loading hopper; 2 - auger; 3 - auger casing; 4 - discharge opening; 5 - electric engine; 6 - type of discharge opening

Let's assume that within the auger inter-turn space, the discharge opening is rectangular in shape. The grain moves above the discharge opening in the auger casing. At any time it spills in the auger inter-turn space through the area $S = ab$, where a – the length of the area of the discharge opening, loaded with grain, b – the width of the discharge opening. In order to ensure a constant discharge volume V , it is necessary that the area S should be constant at each section of the discharge opening. As the grain moves along the auger casing, the grain volume in the auger inter-turn space decreases, which reduces the length a . Therefore, the width b must increase, so that the discharge area is constant.

During the time dt the inter-turn discharge opening will shift to $dx = v dt$, where v is the grain velocity within the auger casing. At the same time some grain volume will spill through the discharge opening in the inter-turn space. It will spill through the opening with the area:

$$S = a(x) \cdot b(x) \text{ [m}^2\text{]} \quad (1)$$

where: $a(x)$ and $b(x)$ depend on the value of the path traveled by the grain for the time t .

In this case, the grain outflow rate through the discharge opening in the inter-turn space will be:

$$q = k \cdot S \cdot v_{outflow} \text{ [m}^3\text{/s]} \quad (2)$$

where: k – coefficient of grain outflow through the opening;

$v_{outflow}$ – velocity of grain outflow through the discharge opening, [m/s].

Then in time dt the outflow rate through the discharge opening in the inter-turn space at the velocity of grain outflow from the auger casing $v_{outflow}$ with regard to expression (1) will be equal to:

$$q = k \cdot a(x) \cdot b(x) \cdot v_{outflow} \quad (3)$$

From expression (3), the specific grain outflow rate over time dt , per unit length of discharge opening $a(x)$, is:

$$\frac{q}{a(x)} = k \cdot b(x) \cdot v_{outflow} \quad (4)$$

The specific outflow rate of the grain mass at each section of the length of the discharge opening in the inter-turn space must be constant, i.e.

$$\frac{q}{a(x)} = const. \quad (5)$$

Then, from the expression (4)

$$b(x) = \frac{q}{k \cdot a(x) \cdot v_{outflow}} = \frac{Q}{k \cdot n_s \cdot a(x) \cdot v_{outflow}} \quad [m] \quad (6)$$

where: Q – conveyor-distributor capacity, [m³/s];

n_s – the number of auger inter-turn spaces over the entire length of the discharge opening.

The outflow coefficient depends linearly on the width of the discharge opening. Then, the dependence of the grain outflow velocity through the opening on its width can be represented as:

$$v_{outflow} = b \cdot C_1 + C_2 \quad (7)$$

where: C_1 and C_2 linear equation constants determined empirically ($C_1 = 0.0144$; $C_2 = -0.0621$).

Let us find the dependence of the discharge opening width b on its length. We consider the specific mass outflow rate Q_m :

$$Q_m = \rho \frac{Q}{L} \quad [kg/m \cdot s] \quad (8)$$

where: ρ – grain loading density, [kg/m³];

L – discharge opening length, [m].

Capacity Q is calculated as the product of the cross-sectional area of the spilling grain flow by the grain outflow velocity:

$$Q = S \cdot n_s \cdot v_{outflow} \quad (9)$$

Accordingly, the specific mass outflow rate with regard to expression (9) will be:

$$Q_m = \frac{\rho \cdot S \cdot n_s \cdot v_{outflow}}{L} = \frac{\rho \cdot a \cdot b \cdot v_{outflow}}{l} \quad (10)$$

where: l – grain loading density, [m].

Since the specific mass outflow rate is a constant, we find the dependence $b(a)$ from (10):

$$b = \frac{Q_m l}{(\rho \cdot a \cdot v_{outflow})} \quad (11)$$

Or considering expression (8):

$$b = \frac{Q_m l}{\rho \cdot a (b \cdot C_1 + C_2)} \quad (12)$$

After transforming expression (12) we obtain the equation:

$$C_1 \cdot b^2 + C_2 \cdot b - \frac{Q_m l}{\rho \cdot a} = 0 \quad (13)$$

The solution of equation (13) is:

$$b = \frac{-C_2 + \sqrt{C_2^2 + \frac{4C_1 Q_m l}{\rho \cdot a}}}{2C_1} \quad (14)$$

The value of the specific mass outflow Q_m through the construction-mode parameters of the auger conveyor-distributor is calculated by the formula:

$$Q_m = \frac{\rho \cdot f \cdot \pi \cdot R^2 \cdot l^2 \cdot n}{60L^2} \quad (15)$$

where:

f – filling factor of the auger inter-turn space;

R – auger radius, [m];

n – auger rotation frequency, [s⁻¹].

Let's substitute expression (15) into formula (14). We obtain the equation to find the discharge opening width at each of its sections:

$$b = \frac{-c_2 + \sqrt{c_2^2 + 4c_1 \cdot \frac{f \cdot \pi \cdot R^2 \cdot l^3 \cdot n}{60 \alpha L^2}}}{2c_1} \text{ [mm]} \quad (16)$$

RESULTS

To determine the construction and technological parameters of the auger conveyor-distributor, a laboratory installation was made (fig. 4.).

The installation has the following construction features. In the lower part of the casing 8 along its entire length there is the discharge opening (fig. 4b). Its width is regulated by plates 4. Adjustment of the width of the discharge opening is carried out by adjusting screws 6. Under the discharge opening there is a collecting tank 7, divided into equal compartments.

The experimental installation has the following geometrical dimensions, parameters and possible modes of operation: auger length – 1000 mm; auger pitch l – 65 mm; auger radius R – 55 mm; length of discharge opening L – 800 mm; width of discharge opening b varies from 10 mm to 24 mm along the length of the discharge opening; auger rotation frequency n – 309 and 364 min⁻¹.

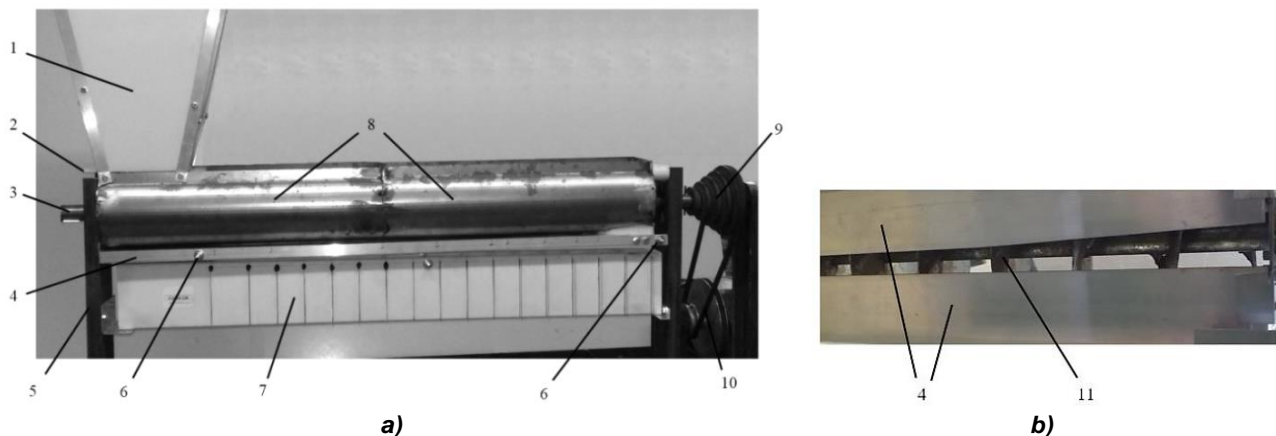


Fig. 4 - General view of the laboratory installation of the grain auger conveyor-distributor (a) and loading opening view from the bottom (b)

1 - loading hopper; 2 - flap; 3 - auger shaft; 4 - plates of discharge opening width adjustment;
5 - installation frame; 6 - adjustment screws of the discharge opening; 7 - collecting tank; 8 - auger casing;
9 - reducer; 10 - electric engine; 11 - auger

Grain of wheat variety "Moscow 39" (Russia) with the following characteristics: grain moisture – 12-18%; bulk density of grain – 750-760 kg/m³ was used as a bulk material. Studies have shown that changes in grain moisture within these limits do not affect the work of the auger conveyor-distributor.

The material was tested for compliance with the requirements for moisture and grain size distribution. In accordance with these requirements, the fractions of the studied material of class 3-2 mm should not exceed 5%, and the fractions of class 4-3 mm should not exceed 1% of the total mass of the aggregate of all fractions.

Studies have shown that with a constant area of the discharge opening, there is no effect of the layer height h above the discharge opening on the time and on the grain outflow velocity $v_{outflow}$ through the discharge opening accordingly.

During the experiment, it was found that the process of grain discharge stops when the width of the discharge openings $b \leq 7$ mm, and in the range of values b from 7 to 9 mm the process of grain outflow through the openings is unstable because of the presence of different impurities in the grain mass.

When the width of the discharge opening $b \geq 9$ mm, there is a linear character of the grain outflow process. Grain in free fall moves along parabolic trajectory. This gives uneven distribution of grain at the beginning and end of the rectangular tank (fig. 5a).

For uniform loading, the tank should be shifted relative to the beginning of the discharge opening towards its end by the value L_c . For example, in the case of loading height $h = 1$ m at the auger rotation frequency $n = 309 \text{ min}^{-1}$ $L_c = 130$ mm; at $n = 364 \text{ min}^{-1}$, $L_c = 156$ mm.

If the inclination of the loaded tank bottom to the angle of the horizon is equal to the angle of natural slope, then the tank will be filled with a uniform grain layer over the entire area of the bottom of the tank. Fig. 5b shows the scheme of loading air distribution trays of solar dryer-grain storage, located at an angle of natural slope of the grain to the horizon.

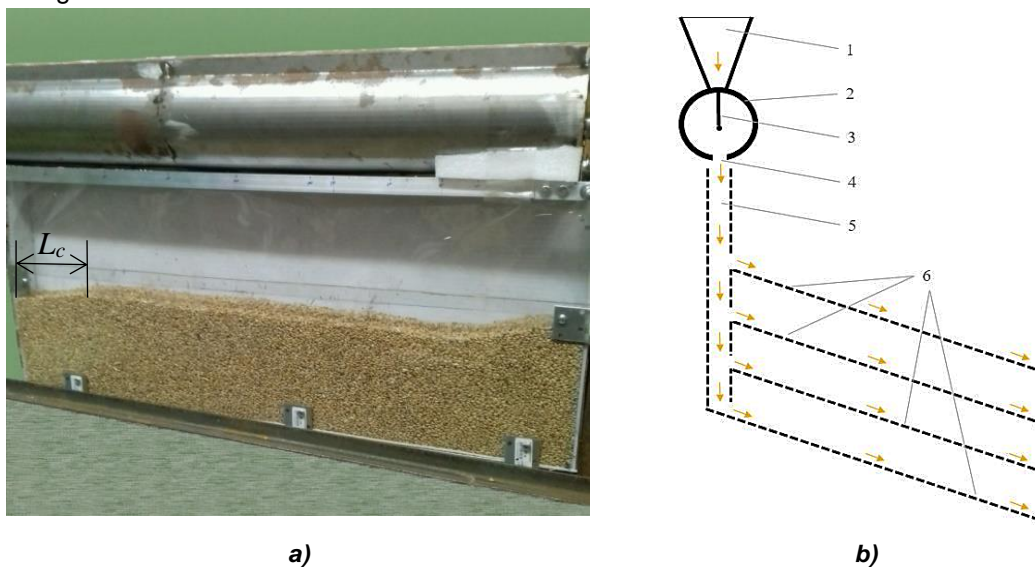


Fig. 5 - Example of loading a rectangular tank (a) and scheme of air-distributing trays of solar dryer-grain storage facility (b)

1 - loading hopper of auger conveyor-distributor; 2 - auger casing; 3 - auger; 4 - discharge opening; 5 - grain movement channel with perforated walls; 6 - perforated air-distributing trays

From the loading hopper 1 grain enters the casing 2 of auger 3. The auger 3 moves the grain to the discharge opening 4. First, the grain fills the bottom tray in an even layer – the layer thickness is limited by the gap between the wall of the vertical channel of grain movement 5 at the beginning of the tray and the bottom of the tray. Then, after filling the channel 5 between the lower and upper trays with grain, the second tray is filled similarly, and so on. The movement direction of grain mass in the scheme is shown by arrows.

In the laboratory installation a tank – analog of perforated air-distributing trays of solar dryer-grain storage facility was installed. Their angle to the horizon is equal to the angle of wheat grain natural slope – 30° (fig. 6a).

The studies confirmed the theoretical provisions. They showed the possibility of forming a uniform grain layer by the auger conveyor-distributor in rectangular tanks with the inclined bottom (fig. 6b).

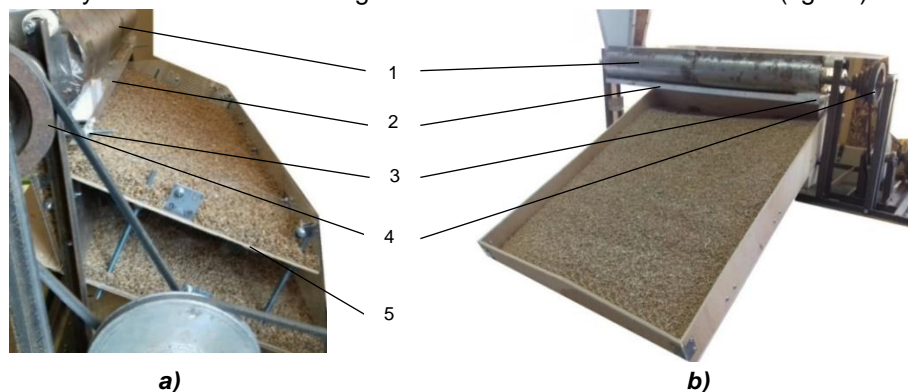


Fig. 6 - Layout loading: a) - perforated air-distributing channels of solar dryer-grain storage facilities; b) - inclined rectangular tank

1 - auger conveyor-distributor; 2 - plates, which set shaping of the discharge opening; 3 - screws for adjustment of discharge opening width; 4 - auger conveyor-distributor drive; 5 - perforated air-distributing channel

Additional conditions for uniform distribution of grain by the auger conveyor-distributor were determined: the filling factor of the auger inter-turn space in the loading area – 0.35; the length of the discharge opening of the hopper should be equal to the doubled value of the auger pitch size. In this case, the uneven grain distribution along the discharge opening was not more than 5%.

During the research, a nomogram for determining the parameters and modes of operation of the grain auger conveyor-distributor was obtained (fig. 7).

So when the auger rotation frequency $n = 400 \text{ min}^{-1}$ and auger diameter $D = 200 \text{ mm}$, the length of the discharge opening $L = 4 \text{ m}$, for $D = 250 \text{ mm}$, $L = 6 \text{ m}$.

To preserve grain quality when loading by auger conveyor-distributor one should use the rotation frequency $n = 300 \text{ min}^{-1}$. Under this condition, it is possible to load tanks up to 11 m wide.

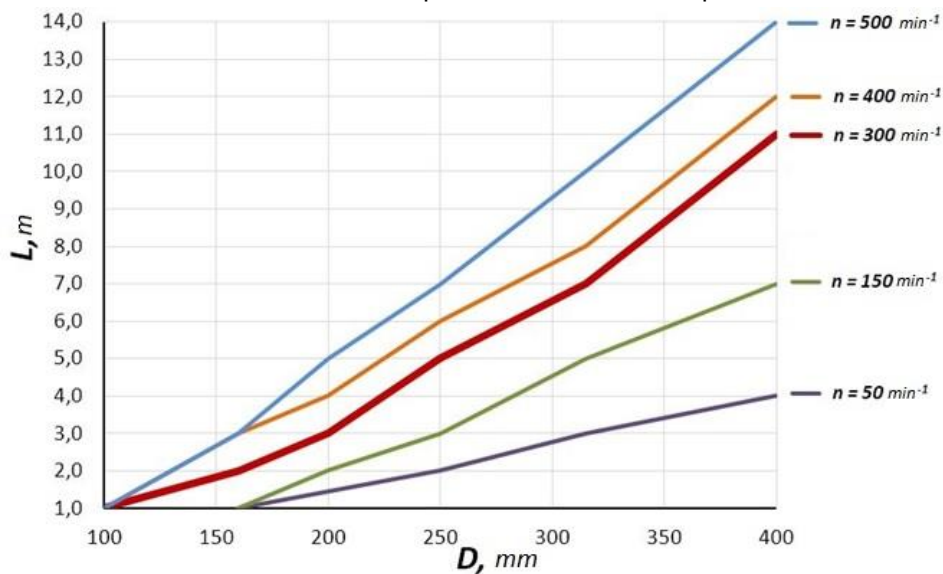


Fig. 7 - Nomogram for determining the parameters and modes of operation of the grain auger conveyor-distributor

CONCLUSIONS

The proposed auger conveyor-distributor provides mechanized loading of perforated air-distributing trays of solar dryer-grain storage facility with grain. The laboratory tests confirmed the adequacy of theoretical dependence (16) of the width of the discharge opening in the auger conveyor-distributor casing on its length. In the experimental studies, uniform distribution of grain mass over the entire surface in the rectangular tanks with horizontal and inclined position of the bottom was obtained. The above nomogram is convenient for practical use when choosing parameters and operating modes of auger conveyor-distributor taking into account the overall dimensions of the loaded tank.

In the future it is necessary to study the performance of the auger conveyor-distributor when loading the grain of small-seeded crops, as well as the grain with moisture above 18% and determine the appropriate dependency factor (16) to calculate the width of the discharge opening.

In addition, it is necessary to automate the adjustment of the discharge opening width for different production conditions.

REFERENCES

- [1] Arkhangel'skii, V. Y. (2019). Calculation of the sizes of output openings of gravity feeders for volumetric discrete dosing of powder bulk materials. *Chemical and Petroleum Engineering*, Vol. 55, Issue 7-8, pp. 525-535, Moscow/Russia.
- [2] Chashchinov, V. I., Kupreenko, A. I., Isaev, Kh. M., Baydakov, E. M., Chenin, A. N. (2016). *Helio dryer*. Patent No 159524. Russia.
- [3] Han, Y., Jia, F., Zeng, Y., Jiang, L., Zhang, Y., Cao, B. (2017). DEM study of particle conveying in a feed screw section of vertical rice mill. *Powder Technology*, Vol. 311, pp. 213-225, Amsterdam/Netherlands.

- [4] Hevko, R. B., Pohrishchuk, B. V., Dobizha, N. V., Zalutskyi, S. Z., Hladyo, Y. B., Tkachenko, I. G., Lyashuk, O. L., Pavlova, O. M., Trokhaniak, O. M. (2019). Determination of interaction parameters and grain material flow motion on screw conveyor elastic section surface. *INMATEH-Agricultural Engineering*, Vol. 57, Issue 1, pp. 123-134, Bucharest/Romania.
- [5] Hou, Q. F., Dong, K. J., Yu, A. B. (2014). DEM study of the flow of cohesive particles in a screw feeder. *Powder Technology*, Vol. 256, pp. 529-539, Amsterdam/Netherlands.
- [6] Kupreenko, A. I., Bychkov, I. E., Isaev, Kh. M. (2017). *Device for loading a container with bulk material*. Patent No 2016128176. Russia.
- [7] Kupreenko, A. I., Isaev, Kh. M., Baydakov, E. M. (2011). Results of testing the solar collector of a granary with a built-in heliodrying system (Результаты испытания солнечного коллектора зернохранилища со встроенной гелиосушильной системой). *Bulletin of the Bryansk State Agricultural Academy (Вестник Брянской государственной сельскохозяйственной академии)*, Issue 1, pp. 55-62, Bryansk/Russia.
- [8] Mashkov, S. V., Kuznetsov, M. A., Fatkhutdinov, M. R., Gridneva, T. S., Yudaev, I. V. (2018). Estimation of the Accuracy Parameters of Automatic Regulation of the Flow of Bulk Materials on Mobile Vehicles under Random External Influences. *Research Journal of Pharmaceutical, Biological and Chemical Sciences*, Vol.9, Issue 4, pp. 1077-1081, Jalpaiguri, West Bengal/India.
- [9] Orefice, L., Khinast, J. G. (2017). DEM study of granular transport in partially filled horizontal screw conveyors. *Powder Technology*, Vol.305, pp. 347-356, Elsevier BV, Netherlands.
- [10] Pezo, L., Jovanovic, A., Pezo, M., Colovic, R., Loncar, B. (2015). Modified screw conveyor-mixers – Discrete element modeling approach. *Advanced Powder Technology*, Vol.26, Issue 5, pp. 1391-1399, Amsterdam / Netherlands.
- [11] Rohatynskyi, R., Gevko, I., Diachun, A., Lyashuk, O., Skyba, O., Melnychuk, A. (2019). Feasibility study of improving the transport performance by means of screw conveyors with rotary casings. *Acta Technologica Agriculturae*, Vol. 22, Issue 4, pp. 140-145, Slovaca Universitas Agriculturae Nitriae, Nitra/Slovakia.
- [12] Shimizu, Y., A. Cundall, P. (2001). Three-Dimensional DEM Simulations of Bulk Handling by Screw Conveyors. *Journal of Engineering Mechanics*, Vol. 127, Issue 9, pp. 864-872, Reston/USA.
- [13] Tian, Y., Yuan, P., Gu, J., Chen, M., Cheng, Q., Yang, F., Tang, J., Su, Y., Ding, T., Zhang, K. (2018). Research on the principle of a new flexible screw conveyor and its power consumption. *Applied Sciences (Switzerland)*, Vol. 8, Issue 7, pp. 1038, Basel/Switzerland.
- [14] Trokhaniak, O. M., Hevko, R. B., Lyashuk, O. L., Dovbush, T. A., Pohrishchuk, B. V., Dobizha, N. V. (2020). Research of the of bulk material movement process in the inactive zone between screw sections. *INMATEH - Agricultural Engineering*, Vol. 60, Issue 1, pp. 261-268, Bucharest/Romania.

LONGITUDINAL COMPRESSING AND SHEARING PROPERTIES OF SILAGE CORN STALK IN NORTH CHINA PLAIN

华北平原青贮玉米秸秆纵向压缩剪切特性研究

Chen Meizhou¹⁾, Xu Guangfei¹⁾, Wei Maojian¹⁾, Song Zhicai¹⁾, Wang Wenjun¹⁾, Diao Peisong^{*1)} Teng Shaomin²⁾

¹⁾ School of Agricultural and Food Science, Shandong University of Technology, Zibo/China;

²⁾ Menoble Co., Ltd., Beijing/China

Tel: +86-13864306142; E-mail: dps2003@163.com

Corresponding author: Diao Peisong

DOI: <https://doi.org/10.35633/inmateh-65-05>

Keywords: silage corn stalks; compressing; longitudinal shearing; energy consumption

ABSTRACT

This paper aimed to optimize working quality and reduce energy consumption of the feeding and shearing device of the silage harvester by making a comprehensive analysis and experiment on the longitudinal compressing and shearing properties of the silage corn stalks. The main factors affecting the shearing energy consumption were obtained by compressing and shearing tests on internodes and nodes of silage corn stalk. The results of three-level and three-factor central combination experiments showed that the overall shearing energy consumption for nodes was much higher than that for internodes. Compressing the silage corn stalk to some extent before shearing at the loading direction of 0° and lower shearing speed was beneficial to saving energy.

摘要

本研究旨在通过对青贮玉米秸秆节间与节部的纵向压缩剪切性能分析，优化青贮收获机喂入与切碎装置的工作参数以降低作业能耗。根据青贮玉米秸秆的结构特性，分别对节间和节间压缩剪切试验，得出了影响剪切能量消耗的主要因素及水平。三因素三水平中心组合试验结果表明：秸秆节部的剪切能耗远大于节间的剪切能耗。以 0° 方向对青贮玉米秸秆进行压缩并以较低的剪切速率进行剪切有利于降低青贮玉米收获的能耗。

INTRODUCTION

Silage corn has been recognized as the highest quality roughage in the world, which has been used as basic feed for dairy cows and routine feed for beef cattle and sheep in countries with developed animal husbandry (Chattopadhyay et al., 1999; Chen et al., 2004). Silage corn accounts for about 8% of corn acreage in the United States and takes up about 80% of the corn planting area every year, among which France and Germany have the largest planting area, more than half of the European planting area (Chen et al., 2012; USDA-NASS, 2017). In China, about 78% of China's total demand for corn is used for animal husbandry and it's expected that by the year 2020, the demand for corn used for animal husbandry will reach more than 89.2% (Lan et al., 2019; Cheng et al., 2019; Shinnors et al., 2017). The silage corn cultivation in China is mainly concentrated in the Northeast, North China Plain and Southwest regions (Guo et al., 2016; Li et al., 2011; Liu et al., 2014). The silage corn planting area in the North China Plain accounts for one-third of the country (Jiang et al., 2017; Lan et al., 2019). Summer corn is the main silage variety in the North China Plain and its stalk leaf yield is high and the annual yield is low. According to the National Planting Structure Adjustment Plan (2016-2020), the planting area of corn will be reduced by more than 3.33 million ha approximately and the area of silage corn will be increased to 1.67 million ha. That is to say, plenty of silage corn stalk as the main component of whole-plant silage corn need to be ensiled every year.

The purpose of silage harvesting is to cut up the silage corn stalk to a degree for easy storage and fermentation, therefore, the longitudinal shearing process is the most critical step in silage harvesting. The silage corn stalk needs to be compressed by a feeding device of silage harvester before shearing. Consequently, the variation in the longitudinal shearing properties of silage corn stalk under different compressing conditions needs to be known to understand the behavior of the material with different operations. In this paper, the compressing and shearing tests were conducted for silage corn stalks to understand the longitudinal shearing characteristics properties of silage corn stalk after compressing. This study was focused on determining the shearing energy of silage corn stalk according to various compressing rates, loading

direction and shearing speed. The purpose is to provide a scientific basis for optimizing the feeding and cutting mechanism of the silage harvester with high efficiency and low energy consumption.

MATERIALS AND METHODS

This study is based on the existing feeding and cutting device of the silage harvester. During the silage harvest, the corn stalks may enter the feeding device at any angle. After being grabbed and compressed under the action of the toothed feeding roller blades, the corn stalks are cut up by the moving blades mounted on a rotating roller of the cutting device (Lu et al., 2018). Its operating process is shown in Fig. 1.

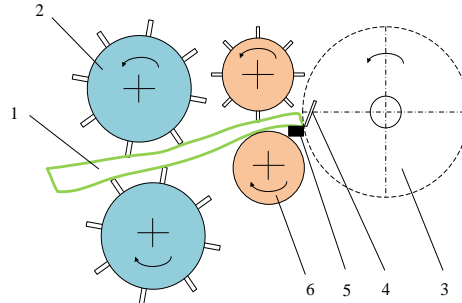


Fig. 1 - Feeding and shearing process of the silage harvester

1. Silage corn; 2. Toothed feeding roller; 3. Cutting device; 4. Moving blade; 5. Stationary blade; 6. Smooth feeding roller

Therefore, we firstly compressed the internodes and nodes respectively to investigate their compressing properties and obtained the range of loading direction and compressing rate affecting the shearing effect. Secondly, the compressed internodes and nodes were sheared to investigate the shearing properties and the range of shearing speeds were obtained. Finally, the Box-Behnken central composite experiments were carried out to obtain the best work parameters for lower shearing energy consumption.

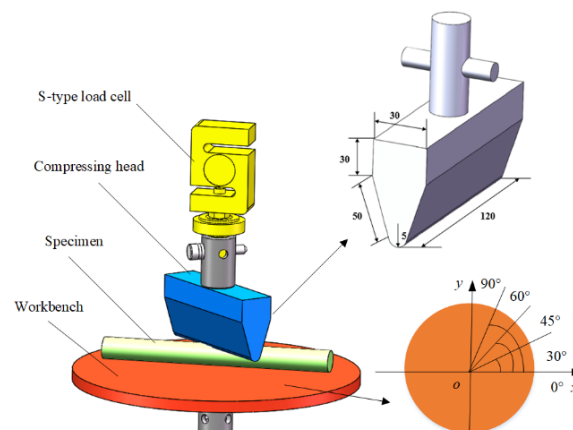


Fig. 2 - Stalk compressing schematic diagram

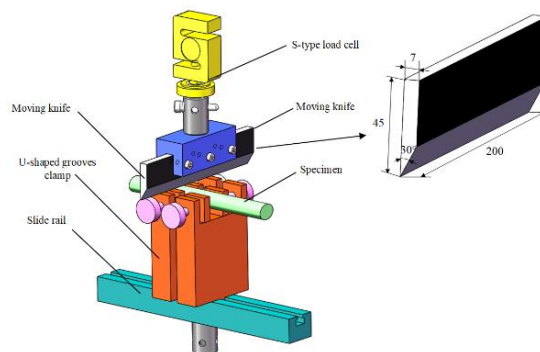


Fig. 3 - Stalk shearing schematic diagram

Compressing process: A compressing head was used to load in the vertical direction to simulate the feeding and compressing of the feeding roller blades with the test specimen axis consistent with the marked direction (0° , 45° and 90°) of workbench (Fig.2) (McRandal et al., 1980; Wang et al., 2019).

Shearing process: The crosscutting shear mode is adopted for the static shearing characteristic study. The custom moving blade fixed by a custom fixture was mounted to a beam of the UTM with a strain-gage load cell between them (Fig.3). In this study, perpendicular cutting was used to determine the shearing forces of silage corn (Kanafojiski et al., 1972; Sitkei et al., 1986; Persson et al., 1987; Chen et al., 2004).

Remark 1: as for the shearing test, a force-displacement curve was recorded up from the initial contact of the blade to the failure of the specimen, so the shearing energy was obtained using Eq.1.

$$W = \int_0^l F(x)dx \quad (1)$$

where:

W is the shearing energy required, [J]; l is the displacement from initial contact to shearing off the specimen, [mm]; $F(x)$ is the function of the shearing force-displacement curve, [N].

Materials

Silage corn, variety *Zhengdan 958* was used as test materials which was planted on May 1, 2020 and harvested in the middle of September 2020 from Experiment Station, Shandong University of Technology, Zibo. The fresh stalks with good growth and without holes, apparent cracks were selected. The moisture content of stalks on the test date ranged from 62% to 66% according to GB/T 1931-2009. The second section without node was selected as the internode specimen with a length of 90 mm–130 mm and the third node were selected as the node specimen with a length of 200 mm (Fig.4, 5).

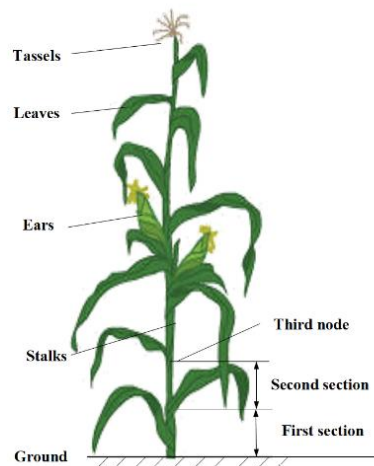


Fig. 4 -Sampling position



Fig. 5 - Partial specimens of silage corn stalk

The cross-section of stalks can be regarded as an ellipse (Igathinathane et al., 2006). The average dimensions of long axis (internode 24.5 mm, node 28.1 mm) and short axis (internode 18.8 mm, node 22.8 mm) were measured using digital calipers and the mean values were recorded. The compressing force and energy of the internode and node's short axis are higher than that of long axis in different loading forms including sing-point, direct pressure and three-point bending (Liu et al., 2014; Wang et al., 2010; Yan et al., 2020). Therefore, the short axis of specimens was selected as loading positions.

Compressing test

Fig. 6 shows examples of compressing processes in different loading directions. The shearing force and energy under different compressing rates and loading directions are the focus of our study (Zhao et al., 2010; Zhu et al., 2017).

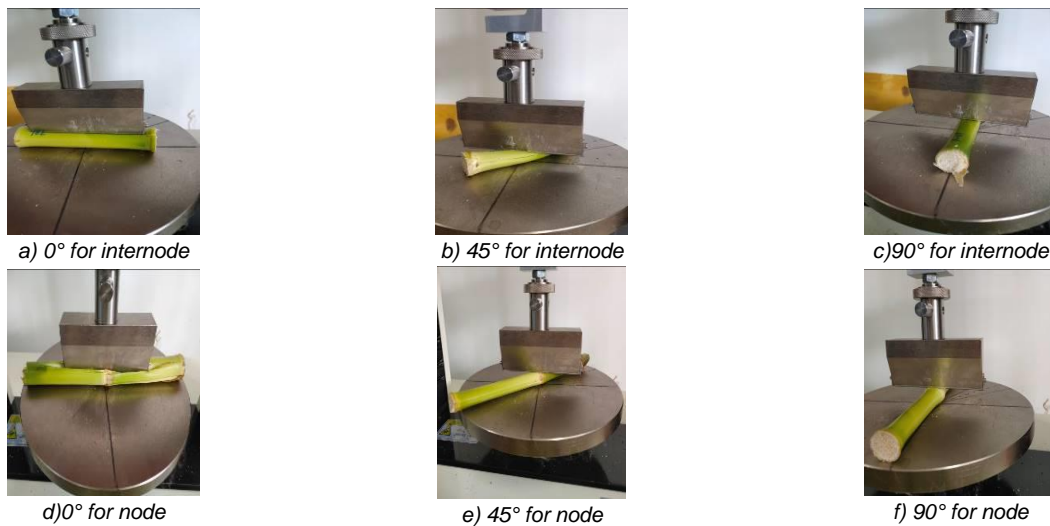


Fig. 6 - Compressing process for silage corn stalk specimen

The compressing rate is calculated using Eq.2,

$$\varepsilon = \frac{l}{d} \times 100\% \quad (2)$$

Where: ε is the compressing rate, [%]; l is the compressing displacement, [mm]; d is the diameter of the specimen at loading direction, [mm].

The compressing force increases at different growth rates by increasing the displacement respectively (Fig.7). On the stalk surface appears subsidence deformation and then cracks are produced at some point. However, the force-displacement curve of 0° is obviously different from that of other directions. Segment AB of 0° is the stage of extrusion deformation and the compressing force reaches its maximum values at point B, while the compressing rate is about 30%. The stalk epidermis is punctured with the compressing force larger than its damage strength. The compressing force correspondingly decreases quickly to point C, while the compressing deformation of the stalk core is dominant.

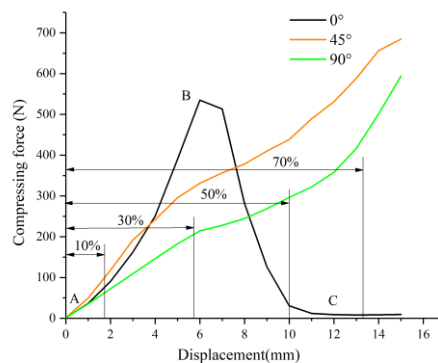


Fig. 7 - Compressing force versus displacement for internode of silage corn stalk

Fig. 8 shows that the heterogeneous morphology of stalks is the inner soft pith core covered with the thick tough skin. Based on direct observation, it was possible to identify three distinct regions to explain the deformation of the compressing process, which was similar to that of 45° loading direction.

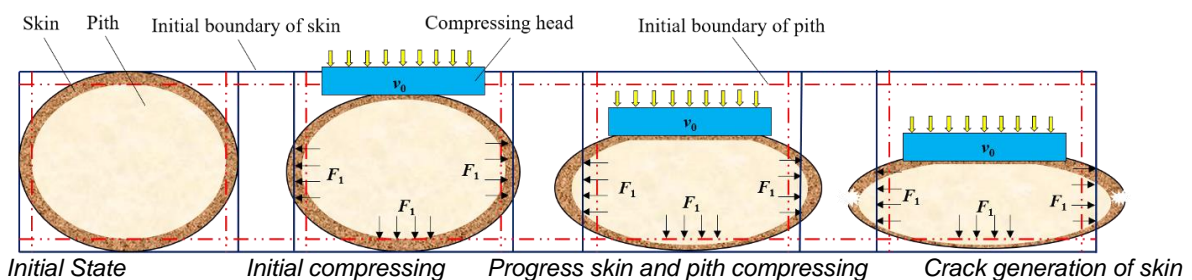


Fig. 8 - Compressing process of silage corn stalk internode in loading direction of 90°

Three distinct regions of 0° loading direction can also be identified to explain the deformation which was different significantly from the other two directions (Fig. 9).

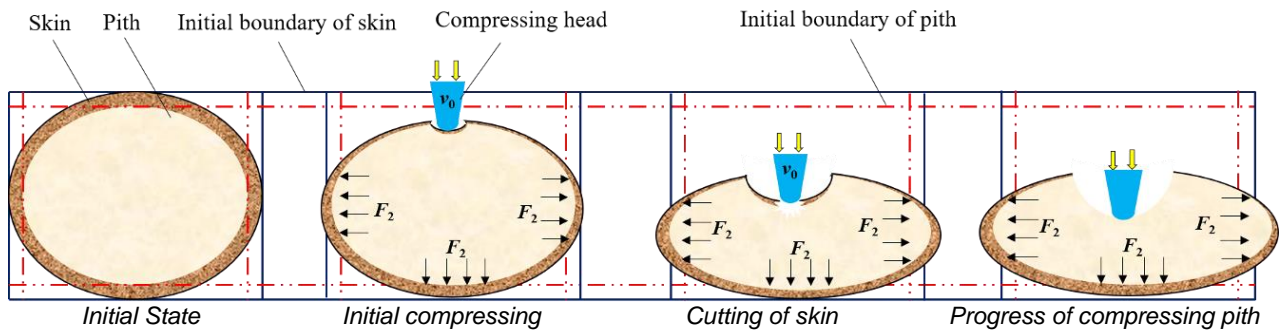


Fig. 9 - Compressing process of silage corn stalk internode in loading direction of 0°

Shearing test

This research emphasis is on the influence of the feeding mechanisms' operating parameters and shearing speed on shearing consumption, rather than chopping capacity and sectional form, although there are some evaluation indexes which are used to evaluate the effect of silage harvester, which might be one of the main points for our future studies.

The shearing process of internode and node were showed in Fig. 10.

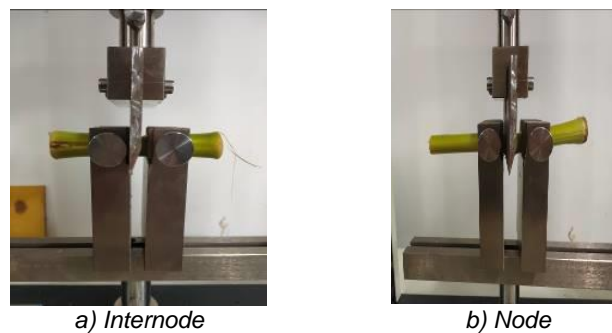


Fig. 10 - Shearing process for silage corn stalk specimen

Box-Behnken central composite experiment design

According to the previous study, the stalks showed obvious deformation with the compressing rate of 30%. Therefore, 10%, 30% and 50% were selected as different levels of compressing rates. The loading direction also had a significant effect on the deformation and force, especially at the direction of 0°. Various loading directions, selected for the shearing experiment were 0°, 45° and 90°. By referencing influences of cutter speed on corn straw for the minimum shearing force (Guo et al., 2016), the shearing speed was varied as 50, 100 and 150 mm/min. The Box-Behnken central composite experiment was adopted with three levels and factors. Each test group was repeated 3 times and their mean values, to reduce the random error, were applied as the final test result.

RESULTS AND DISCUSSION

In this section, the experiment data were processed using Design-Expert 8.0.6, the matching mathematical regression patterns were developed, the relation of salient factors was analyzed, the interaction of each factor was discussed and the parameters were optimized and validated.

Establishment of regression models and significance test

Table 1 presents the test results on the mean shearing energy of internode and node. The shearing energy for node is higher than internode (Zhu et al., 2017; Liu et al., 2014). Two quadratic polynomial response surface regression models for internode and node are shown as Eq.3 and Eq.4 respectively.

$$W_1 = 4.6 - 1.26A + 1.59B + 0.95C - 0.37AB - 0.44AC + 0.68BC + 1.51A^2 + 1.34B^2 + 0.47C^2 \quad (3)$$

$$W_2 = 8.19 - 0.92A + 1.24B + 0.83C - 0.015AB - 0.43AC + 0.64BC + 1.08A^2 + 0.99B^2 + 0.4C^2 \quad (4)$$

Table 1

Program and results of test quadratic rotation-orthogonal combination

NO.	Compressing rate (%)	Loading direction (°)	Shearing speed (mm/min)	Shearing energy (J)	
				Internode W_1	Node W_2
1	-1	-1	0	7.071	10.100
2	1	-1	0	4.827	8.095
3	-1	1	0	10.802	12.457
4	1	1	0	7.089	10.390
5	-1	0	-1	6.062	9.277
6	1	0	-1	4.874	8.482
7	-1	0	1	9.172	11.721
8	1	0	1	6.204	9.206
9	0	-1	-1	4.623	8.046
10	0	1	-1	6.618	9.407
11	0	-1	1	4.844	8.480
12	0	1	1	9.552	12.406
13	0	0	0	4.386	8.196
14	0	0	0	4.315	7.871
15	0	0	0	5.204	8.595
16	0	0	0	4.860	8.319
17	0	0	0	4.227	7.973

According to Table 2, on one hand, the p -value (< 0.0001) of the internode model indicated that the model was highly significant. The p -value (0.3932) of the “Lack of fit” indicated that no other major factors affected the indicators. The determination coefficient R^2 (0.9787) indicated that this model can explain more than 97% of the evaluation index. On the other hand, the p -value (< 0.0001) of the node model indicated that the model was also extremely significant. The p -value (0.6838) of the “Lack of fit” meant that no other major factors affected the indicators. The determination coefficient R^2 (0.9879) indicated that this model can explain more than 98% of the evaluation index. As a result, the model for internode and node can be used to evaluate the influence of the law of various factors on the shearing energy of silage corn stalks.

Table 2

ANOVA of regression model for shearing energy of internode and node

Source	Internode				Node			
	Sum of squares	Df	F-value	P-value	Sum of squares	Df	F-value	P-value
Model	63.08	9	35.70	0.0001**	37.66	9	63.54	0.0001**
A	12.78	1	65.12	0.0001**	6.81	1	103.36	0.0001**
B	20.15	1	102.63	0.0001**	12.35	1	187.37	0.0001**
C	7.21	1	36.74	0.0005**	5.45	1	82.65	0.0001**
AB	0.54	1	2.75	0.1414	9.610×10^{-4}	1	0.015	0.9073
AC	0.79	1	4.03	0.0845	0.74	1	11.22	0.0122*
BC	1.84	1	9.37	0.0183*	1.64	1	24.96	0.0016**
A²	9.59	1	48.83	0.0002**	4.90	1	74.28	0.0001**
B²	7.56	1	38.50	0.0004**	4.14	1	62.81	0.0001**
C²	0.93	1	4.75	0.0656	0.68	1	10.35	0.0147
Residual	1.37	7	-	-	0.46	7	-	-
Lack of fit	0.67	3	1.29	0.3932	0.13	3	0.53	0.6838
Pure error	0.70	4	-	-	0.33	4	-	-
Total	64.46	16	-	-	38.12	16	-	-

Notes: **Parameter coefficient significant at a 99% confidence level; *Parameter coefficient significant at a 95% confidence level.

Guo (2016) carried on longitudinal shear characteristics properties experiment of dried corn straw and found that the influence of shearing angel on shearing force is greater than that of shearing speed, which is consistent with the experiment results in this paper. The optimized regression model after eliminating the insignificant factors in the interaction terms for internode and node are shown in Eq.5 and Eq.6 respectively.

$$W_1 = 4.8 - 1.26A + 1.59B + 0.95C + 0.68BC + 1.53A^2 + 1.36B^2 \quad (5)$$

$$W_2 = 8.19 - 0.92A + 1.24B + 0.83C - 0.43AC + 0.64BC + 1.08A^2 + 0.99B^2 + 0.4C^2 \quad (6)$$

Analysis of the effect of each factor on the response value

The degree of influence of each factor on the model can be reflected by the size of the contribution rate K -value, which is proportional to the size of the impact degree. The results (Table 3) showed that the sequence of contribution rate of loading direction, compressing rate and loading speed on shearing energy for internode was in decreasing order, while the compressing rate, loading direction and loading speed for node was in increasing order. The calculation methods are shown in Eq. 7 and Eq.8

$$\delta = \begin{cases} 0 & F \leq 1 \\ 1 - \frac{1}{F} & F > 1 \end{cases} \quad (7)$$

$$\begin{cases} K_A = \delta_A + 0.5(\delta_{AB} + \delta_{AC}) + \delta_A^2 \\ K_B = \delta_B + 0.5(\delta_{AB} + \delta_{BC}) + \delta_B^2 \\ K_C = \delta_C + 0.5(\delta_{AC} + \delta_{BC}) + \delta_C^2 \end{cases} \quad (8)$$

Where:

δ is the assessment value of F -value; K is the sequence of the contribution rate.

Table 3

Analysis of the contribution rate of each factor for internode and node					
Sample	Response values	Compressing rate	Loading direction	Loading speed	Contribution rate
Internode	Shearing energy	2.66	2.73	2.58	$B > A > C$
Node		2.43	2.46	2.83	$C > B > A$

Response surface analysis of internode

According to Table 3, the interactive item (BC) of the loading direction and loading speed had a significant effect on shearing energy for the internode ($p=0.0183$). The effects of the other interactive items were not significant.

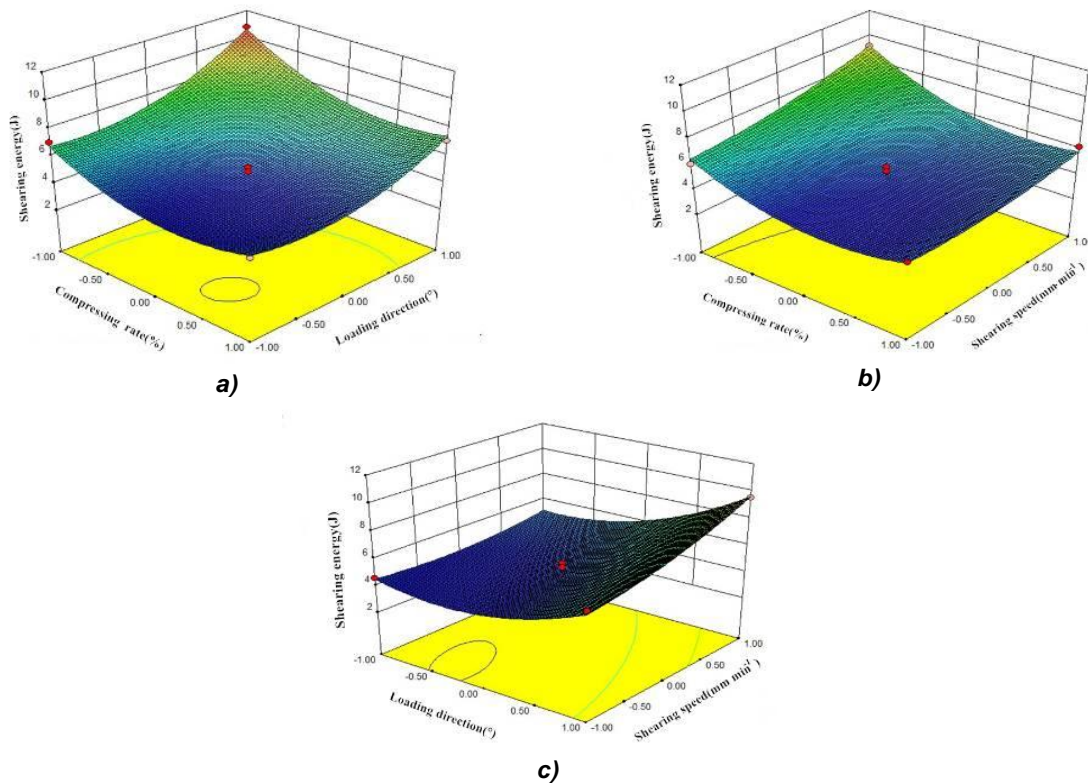


Fig. 11 - Influence of different factors on shearing energy for internode

Fig.11a showed that when the internode was compressed with the axis parallel or perpendicular to the compressing head, the effect of the compressing rate was a little greater than other orientation. Especially, the internode was split lengthwise with 0° loading direction and the internode became denser and easy to be cut while compressed to some extent. Therefore, the compressing rate was 50% and the loading direction was parallel to the compressing head, the shearing energy reached its minimum value (4.97 J). In this paper, the effect of the reduction rate is consistent with that of other radial compressing directions studied by other authors (Liu et al., 2014).

Fig.11b showed the shearing energy increased slowly with increase of the shearing speed (Zhao *et al.* 2010). When the shearing speed was high, the impact of the moving blade was the main reason for the increase in shearing energy. At the same time, the excessive impact caused the stalk to bend seriously and break away from the clamp. The shearing energy decreased gradually with the increase of the compressing rate. Therefore, it was helpful to reduce the shearing energy for internode by reducing the shearing speed and increasing the compressing rate. The effect of shearing speed on crop shearing strength and energy is consistent with Jiang's research (Jiang *et al.*, 2017).

Fig.11c showed the shearing energy changed little with the change of shearing speed at 0° loading direction, while the effect of the shearing speed was greater at 90° loading direction. When the shearing speed was high, the shearing energy increased rapidly with the loading direction from 0° to 90° loading direction. The epidermis of the internode was punctured at 0° loading direction. Therefore, the shearing energy of the soft pith was much less than that of the epidermis which was composed of cellulose and lignin, compressing at 0° loading direction before shearing was helpful to reduce the shearing energy. Igathinathane (2010) explained the nature of the cutting process of dried corn stalk by dividing the force-displacement into three identifiable regions. Deviation from the reported general force-displacement characteristics will occur due to the high moisture content of silage corn stalk, blade sharpness (Liu *et al.*, 2011).

Response surface analysis of node

According to Fig.12, the influence of experimental factors on the shearing energy of the node was similar to that of the internode. However, there were still some differences as the node was thicker than the internode for the material difference between internode and node.

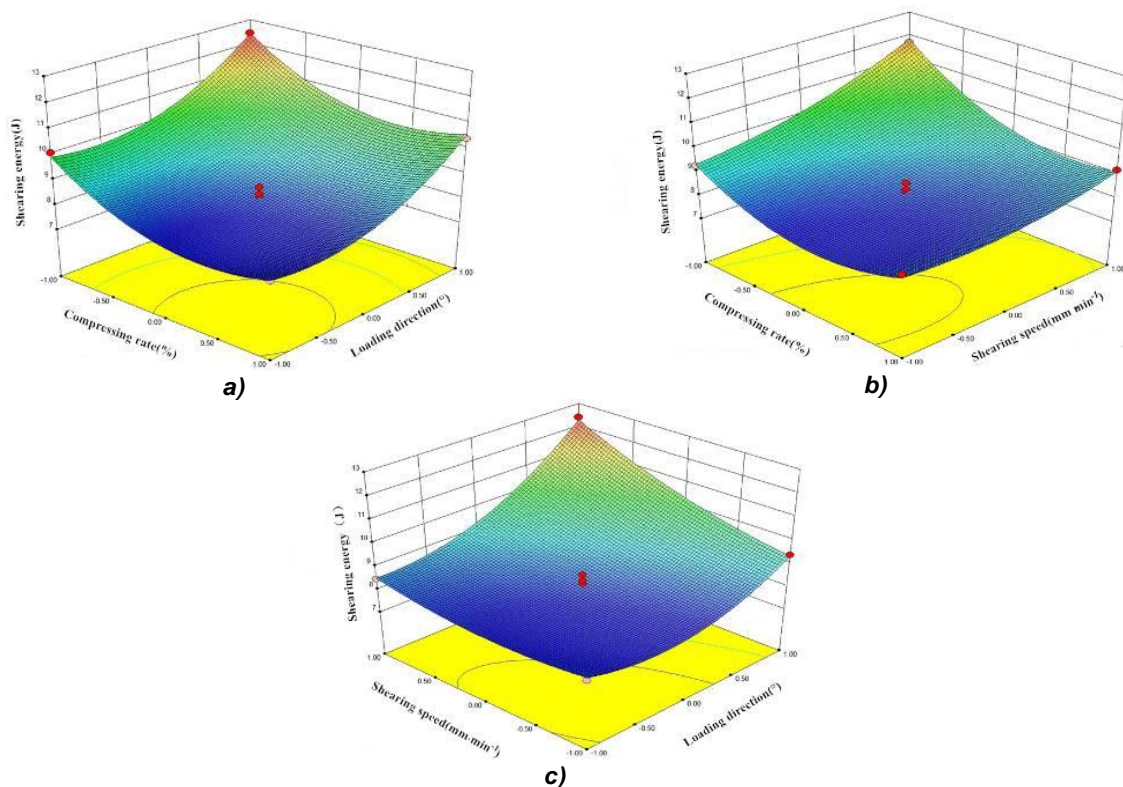


Fig. 12 - Influence of different factors on shearing energy for node

Fig.12a showed that the effect of the loading direction on shearing energy was greater than that of the compressing rate. The shearing energy was more easily affected by the compressing rate and decreased gradually with the increased compressing rate at 0° loading direction. At this time, the stalk epidermis was more easily damaged.

Fig.12b showed the interaction between the compressing rate and the shearing speed for the node was significant ($p < 0.05$). The effect of the compressing rate was greater than that of the shearing speed, *i.e.*, the shearing energy quickly decreased with the increase in compressing rate and increased with shearing speed.

Fig.12c showed the interaction between the shearing speed and the loading direction on shearing energy for the node was highly significant ($p < 0.01$). The shearing energy quickly rose with the increase in shearing

speed and the shearing energy reached its maximum (12.29J) at 90° loading direction with maximum shearing speed.

Parameter optimization and validation test

Based on the principle of low shearing energy consumption, the multi-objective optimization was carried out to obtain the optimal parameter combination of the compressing rate, the loading direction and the shearing speed, so the objective functions and constraints can be obtained as Eq.9,

$$\min W_1(A, B, C); \min W_2(A, B, C); -1 \leq A \leq 1; -1 \leq B \leq 1; -1 \leq C \leq 1 \quad (9)$$

It was concluded that the optimal parameter combinations were 36.08%, 25.4° and 73.39 mm/min. To verify the accuracy of the optimal results, ten parallel validations were carried out while the compressing rate, loading direction and shearing speed were chosen as 36%, 25° and 73 mm/min. It can be seen from the comparison of results (Table 4) that the experiment values were in good agreement with the theoretical optimal values and the relative error was both less than 4%, which confirmed that the optimized results were correct and credible.

Table 4

Comparison of average optimal and experimental value			
Project	Shearing energy for internode (J)	Shearing energy for node (J)	
Optimal value	3.82	7.55	
Average experimental value	3.97	7.81	
Relative error/%	3.95	3.43	

CONCLUSIONS

1. From the compressing test, the compressing force increased with increasing the displacement respectively at loading direction of 45° and 90°, while the compressing force decreased sharply as the compressing head pierced the epidermis of the silage corn stalk at 0° loading direction. This lower strength of the silage corn stalk at the loading direction of 0° can be exploited advantageously to develop feeding mechanisms.

2. From the Box-Behnken central composite experiments, the overall shearing energy consumption for shearing off the node was higher than that for internode due to different structural properties. The significant effects on shearing energy in a decreasing order was the loading direction, compressing rate and loading speed for internode and the loading speed, loading direction and compressing rate for node. The optimal parameter combinations were 36.08%, 25.4° and 73.39 mm/min.

3. In general, compressing the silage corn stalk to some extent before shearing at 0° loading direction and lower shearing speed were beneficial to saving energy during the process of shearing off the silage corn stalk. The reduced energy requirements of the silage corn stalk could be exploited advantageously to present new reference for the feeding and cutting mechanisms of silage harvester.

ACKNOWLEDGEMENTS

This work was supported by the National Key Research and Development Program, China (Grant No. 2016YFD0701302), Key Science and Technology Innovation Project of Shandong Province, China (Grant No. 2019JZZY020615)

REFERENCES

- [1] Chattopadhyay, P., & Pandey, K. (1999). Effect of the blade and operational parameters on energy requirement in flail forage harvesting. *Agricultural Engineering Research*, 73(1): 3–12.
- [2] Chen, Y., Chen, J., Zhang, Y., & Zhou, D. (2007). Effect of harvest date on shearing force of maize stems. *Livestock Science*, 111(1): 33–44.
- [3] Chen, Z., Wang, D., Li L.Q., & Shan R. (2012). Experiment on tensile and shearing characteristics of rind of corn stalk. *Transactions of the Chinese Society of Agricultural Engineering (Transactions of the CSAE)*, 28(21): 59–65.
- [4] Cheng, H., Jiang, F., Liu, D., Song, H., & Song, E. (2019). Current situation, existing problems and countermeasures of production and application of whole corn silage in Shandong province (山东省全株玉米青贮生产与应用现状、存在问题及对策). *China Cattle Science*, 45(6), 32–34.
- [5] Guo, Y., Cheng, Y., Ben, D., Yang, J., Wang, B., & Dong, L. (2016). Experiment of longitudinal shear

- characteristic properties of corn straw (玉米秸秆纵向剪切特性试验). *Journal of Chinese Agricultural Mechanization*, 37(2): 123–126.
- [6] Igathinathane, C., Womac, A. R., & Sokhansanj, S. (2010). Corn stalk orientation effect on mechanical cutting. *Biosystems Engineering*, 107(2): 97–106.
- [7] Igathinathane, C., Womac, A., Sokhansanj, S., & Pordesimo, L. (2006). Mass and moisture distribution in aboveground components of standing corn plants. *Transaction of the ASAE*, 49(1): 97–106.
- [8] Jiang, M., & Guo, Z. (2017). Effects of vertical pressure and shear velocity on direct shear strength and dilatancy properties of wheat (竖向压力和剪切速率对小麦直剪强度及剪胀特性的影响). *Transactions of the Chinese Society of Agricultural Engineering (Transactions of the CSAE)*, 33(6): 275–280.
- [9] Lan, J., Pan, B., Wang, B., Li, L., & Zhang, R. (2019). Analysis on current situation of silage maize quality in Northeast China (东北青贮玉米品质现状分析). *Heilongjiang Agricultural Sciences*, (10), 95–99.
- [10] Li, Y., Qin, T., Chen, J., & Zhao, Z. (2011). Experiments and analysis on mechanical property of corn stalk reciprocating cutting (玉米秸秆往复切割力学特性试验与分析). *Transactions of the Chinese Society of Agricultural Engineering*, 27(1): 160–164.
- [11] Liu, L., Bing, Y., Dong, X., Ai, M., & Yang, X. (2014). Effects of loading conditions on cracks of corn stalk and power consumption of machine (玉米秸秆压缩加载条件对其裂纹和机器功耗的影响). *Transactions of the Chinese Society of Agricultural Engineering*, 30(3), 163–169.
- [12] Lu, Y., Payen, S., Ledgard, S., Luo, L., & Zhang X. (2018). Components of feed affecting water footprint of feedlot dairy farm systems in Northern China. *Journal of Cleaner Production*, 183: 208–219.
- [13] McRandal, D., M., & McNulty, P. (1980). Mechanical and physical properties of grasses. *Transactions of the ASAE*, 23(4): 816–821.
- [14] Wang S., Du, J., Zhao, L., Jiao, L., Li, Z., & Xue, Z. (2019). Tensile and shearing strength properties of the stems of king grass (王草茎秆拉伸与剪切的强度特性). *Chinese Journal of Tropical Crops*, 40(6): 1188–1194.
- [15] Wang, G., Wang, D., Tabil, L., & Opoku, A. (2010). Shearing strength of timothy grass stem. *ASABE Annual International Meeting*. June 20–June 23, 2010 1009362. (doi:10.13031/2013.29861).
- [16] Yan, E., Wang, Z., Han, B., Xu, B., Chen, Y., & Qi, Z. (2020). Effect of water content and cutting sliding angel on straw cutting power consumption (含水率及切割滑切角对秸秆切割功耗影响规律). *Agricultural Mechanization research*, (2): 162–167.
- [17] Zhao, Z., Li, Y., Xu, L., & Song, S. (2010). Experiment on cutting mechanical property of single super rice stalk (超级稻单茎秆切割力学性能试验). *Transactions of the Chinese Society for Agricultural Machinery*, 41(10): 72–75.
- [18] Zhu, Z., Zhang, K., Li., & Zhang, H. (2017). Study on mechanical properties of corn stalk (玉米秸秆机械性能研究). *Jiangsu Agricultural Science*, 45(12): 178–181.

EXPERIMENTAL STUDY ON AIR FLOW FIELD CHARACTERISTICS OF SUCTION METERING DEVICE

气吸式排种器的气流场特性试验研究

Meng Zhang¹⁾, Zeqi Liu¹⁾, Yajun Zhuang¹⁾, Jie Han¹⁾, Yin Xiang^{1,3)}; Chen Yulong^{*1,2)}

1

¹⁾ School of Agricultural Engineering and Food Science, Shandong University of Technology, Zibo 255000, China;

²⁾ Research of Institute of Ecological Unmanned Farm, Shandong University of Technology, Zibo 255000, China;

³⁾ Shandong Provincial Key Laboratory of Dry-Farming Machinery and Informatization, Zibo 255000, China;

Tel: +86 15315206471; E-mail: 1097402292@qq.com

DOI: <https://doi.org/10.35633/inmateh-65-06>

Keywords: vacuum seed metering device, air flow field characteristics, experimental study, composite disc, vacuum chamber

ABSTRACT

The vacuum seed metering device absorbs seeds by using the negative pressure generated by vacuum air flow. Therefore, it is of great significance to study the variation law of pyrolysis gas flow field to improve its seed metering performance. In this paper, the common disc and composite disc were selected as the research objects and tested on the indoor test-bed. The negative pressure was measured by U-type barometer, and the effects of fan speed, suction hole size, seed hole structure and air chamber thickness on the air flow field were studied. Firstly, the influence of fan rotation frequency on vacuum chamber negative pressure is studied, and the variation law of negative pressure in vacuum chamber and fan port of common disc and composite disc under the same frequency is compared. Secondly, the suction holes in the vacuum chamber were numbered, the negative pressure distribution of the suction holes was measured, and the influence of the number and diameter of the suction holes on the negative pressure of the vacuum chamber was studied. Finally, the negative pressure was measured at the distance of 0 to 10 mm from the suction hole to study the effect of seed hole structure on the air flow field. Moreover, increase the additional thickness of the vacuum chamber from 0 to 40 mm to study the influence of the chamber thickness on the distribution of the gas flow field. This paper makes a comprehensive experimental analysis on the influencing factors of air flow field of air suction seed metering device, necessary for future design of air suction seed metering device.

摘要

气吸式排种器的利用真空气流产生负压吸取种子，了解气流场的变化规律对提高其排种性能具有重要意义。本文选取常规盘和复合盘作为研究对象，在室内试验台上进行试验，利用U型压力计对负压进行测量，对风机转速、吸孔尺寸、取种孔结构、气室的厚度对气流场的影响规律进行研究。首先通过变频器调节风机的转速，研究风机频率对气室负压的影响，对比相同频率下常规盘和复合盘的气室负压及风机口的负压变化；然后，对气室范围内的吸孔编号并测量吸孔的负压分布规律；以常规盘为对象研究吸孔的数量和直径对气室负压的影响；最后分别在距离吸孔0至10mm距离测量负压，研究取种孔结构对气流场的影响；并且增加气室的附加厚度分别为0至40mm，研究气室厚度对气流场的分布影响。本文对气吸式排种器的气流场影响因素进行全面的试验分析，试验结果对气吸式排种器的优化设计具有重要参考价值。

INTRODUCTION

The precision seed metering device (Yang et al., 2016) is the core component of the seeding machine, which seeds at a certain soil depth according to the optimal row and plant spacing in the agronomic requirements (Abdolahzare et al., 2018; Mao et al., 2015). The precision seed metering device can be divided into the mechanical (Chen et al., 2021; Liu et al., 2015; Wang et al., 2017), vacuum and air-pressure (Yang et al., 2016) type by the operating principle. Among others, the vacuum seed metering device features a simple structure, easy operation and maintenance and high seed suitability, becoming the most widely applied device (Liao et al., 2018). Such seed metering devices extract the air in the vacuum chamber with a fan, causing the chamber to vacuum. Then, they utilize the negative pressure to absorb seeds through the suction hole and

¹ Meng Zhang, M.S. Stud. Eng.; Zeqi Liu, M.S. Stud. Eng.; Yajun Zhuang, M.S. Stud. Eng.; Jie Han, M.S. Stud. Eng.; Yubin Lan, Prof. Ph.D. Eng.; Yulong Chen, Lecture Ph.D. Eng.

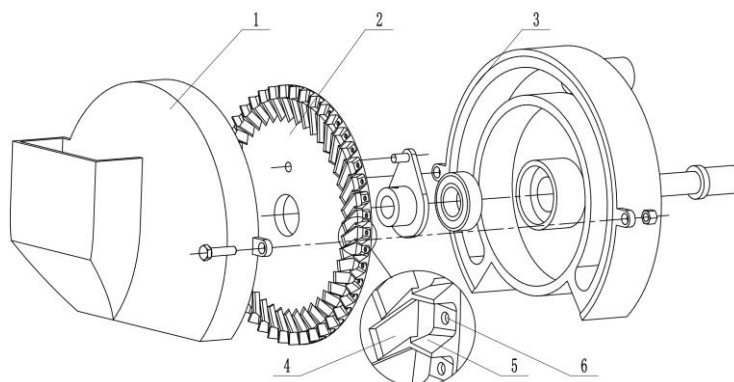
complete the seed filling. Many researchers have studied the vacuum seed metering device and established mathematical models of the vacuum seeding operation process (Cujbescu *et al.*, 2019). They further took advantage of cameras and photoelectric sensors to test the seeding performance and analyzed the performance with the bench test (Zhao *et al.*, 2015). The fluid simulation software has also been applied to simulate (Yu *et al.*, 2015; Zhang *et al.*, 2015) and analyze the airflow field of the seed metering device (Liu *et al.*, 2013; Yu *et al.*, 2014), thus optimizing the shape design of the suction hole and the seed disturbing mechanism (Dylan, S. J. *et al.*, 2013; Singh *et al.*, 2007; Xing *et al.*, 2020).

Based on the operating principle of the vacuum seed metering device, it can be found that the airflow field can greatly affect the seed filling performance. The existing researches on the vacuum seed metering device mainly focused on the seed-absorbing performance of the negative pressure airflow (Yu *et al.*, 2015; Zhang *et al.*, 2020), but neglected the impact of the fan speed, component structure near the suction hole and vacuum chamber structure on the airflow field. Therefore, in this paper, the above factors are applied in research so as to deeply explore the airflow field characteristics of vacuum seed metering devices.

MATERIALS AND METHODS

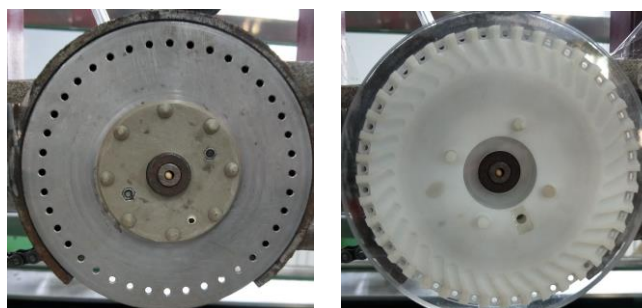
Vacuum seed metering device

Two different types of seed discs are installed with consistent shells and covers to make thorough experiment and study on the airflow field characteristics of the vacuum seed metering device. One of the discs is a common round flat steel disc (Singh *et al.*, 2007), 2 mm thick, with round suction holes evenly distributed along the circumference. The other disc is a composite plastic round disc (Jia *et al.*, 2018), 7 mm thick, designed by the author in early preparations. Several churning and filling grooves are evenly distributed along the circumference, and there are suction holes at the bottom of the filling groove.



a. Vacuum seed metering device with composite disc

b.



b. Common disc

c. Composite disc

Fig. 1 - Vacuum seed metering device and disc

1.Shell; 2.Disc; 3.Base; 4.Seed agitator; 5.Seed hole; 6.Suction hole

The common disc is further divided into soybean disc (SD) and corn disc (CD) as they differ in the diameter and number of the holes. The SD has 40 suction holes and the CD 20 holes; the hole diameter for the SD is 4 mm, and 5.5 mm for the CD. These two common seed discs are studied to find the impact of the number and diameter of suction holes on the airflow field.

Table 1

Design parameters of disc

Parameter	SD	CD
Diameter of disc[mm]	200.0	200.0
Thickness of disc [mm]	2.0	2.0
Number of suction holes [piece]	40.0	20.0
Diameter of suction hole[mm]	4.0	5.5

The vacuum chamber contained in the seed metering device is 20 mm deep and the coverage reaches 270° along the circumference. Suction holes are numbered from the lower-left corner, clockwise from left to right. The SD contains 30 holes in the coverage of the negative pressure chamber, but the CD contains only 15 holes.

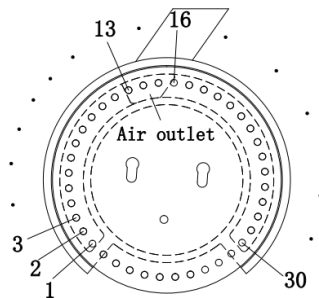


Fig. 2 - Distribution of suction holes on disc

Test plan

The experiment is carried out on an indoor bench (Zhang et al., 2015). The seed metering device is driven by a 3-phase AC motor and the negative pressure is generated by the centrifugal fan with the pressure value directly proportional to the fan speed. The fan speed is controlled by a frequency converter and the pressure at the fan outlet is displayed on the digital screen (Fig. 3).

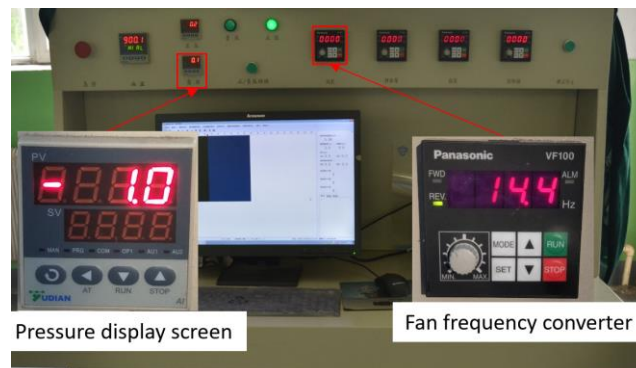


Fig. 3 - Control cabinet of test bench

The vacuum chamber pressure of the metering device is measured with a U-type barometer (Fig. 4 a). Then, the altitude difference of both liquid columns of the U-type barometer is applied to calculate the pressure difference in accordance with the Formula (1).

$$\Delta P = \rho \cdot g \cdot \Delta h / 1000 \tag{1}$$

where: ΔP is the column pressure difference of the barometer, kPa; Δh is the column altitude difference, m, twice the reading of the U-type barometer; ρ is the liquid density in U-shaped columns, water is applied in this paper as the pressure measuring media and the ρ is 1000 kg/m³.

Punching is carried out at the side of the vacuum chamber outlet and the outlet pressure is measured with the U-type barometer, as shown in Fig. 4 b.

As the circumference of the vacuum chamber is wide, different areas vary in the distance away from the outlet and the air pressure differs consequently. The U-type barometer is applied to measure the pressure values of suction holes at distinct sites respectively.

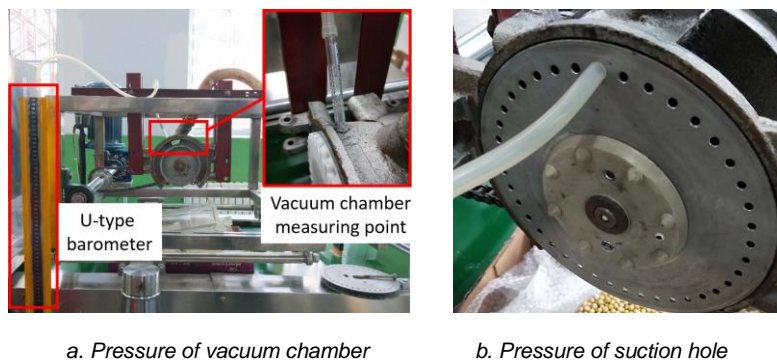


Fig. 4 - Measure the negative pressure with a U-type barometer

A vacuum chamber adjustment disc is installed based on the original coverage of the vacuum chamber to study the impact of vacuum chamber depth on the airflow field. The adjustment disc is composed of a 5 mm thick PMMA disc. With more adjustment discs added, additional vacuum chamber thickness will be modified to 5, 10, 15...40 mm respectively, as shown in Fig. 5.

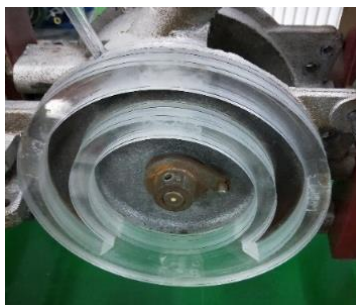


Fig. 5 - Adjustment of vacuum chamber thickness

RESULTS AND ANALYSIS

Fan speed and negative pressure of vacuum chamber

After adjustment of the fan speed and negative pressure with the frequency converter, the negative pressure readings on the screen are adjusted to be 1, 2, 3 kPa respectively. The frequency converter readings are recorded and the U-type barometer is applied to measure the outlet pressure. The results are shown in Table 1.

Table 1

Fan frequency and negative pressure		
Negative pressure on display	Fan frequency / Hz	
	Common disc	Composite disc
1.0	14.6±0.2a	14.4±0.3a
2.0	21.2±0.2a	21.0±0.2a
3.0	26.0±0.3a	25.6±0.2a
4.0	30.2±0.2a	30.0±0.3a
5.0	33.8±0.4a	33.6±0.2a

Note: When small letters in two columns and the same row resemble, it means the difference is not significant. However, when the small letters are different, the difference is significant.

Based on Table 1, it can be found that when the negative pressure values on the screen are the same, the small letter in all rows is a, indicating that two digits in each row are not significantly different. The fan frequencies corresponding to the common and composite discs respectively do not differ significantly, showing that the seed disc structure does not affect the fan outlet pressure greatly.

As the actual pressure value of the vacuum chamber changes according to the suction hole size and number as well as the number of seeds absorbed in the hole, it is unable to accurately control the negative pressure value of the vacuum chamber. Among multiple parameters related to the vacuum chamber pressure, only fan speed can be accurately controlled with the frequency converter. Therefore, in this paper, the fan frequency is adjusted to control its speed. The fan frequency values of the composite disc, 14.4, 21.0, 25.6, 30.0, 33.6, are applied as the benchmark for negative pressure regulation as mentioned below with the corresponding negative pressures, 1.0, 2.0, 3.0, 4.0, 5.0 kPa respectively.

The fan frequency is adjusted and the U-type barometer is used to measure the fan outlet and vacuum chamber pressure values of the common disc and composite disc. The results are shown in Fig. 6.

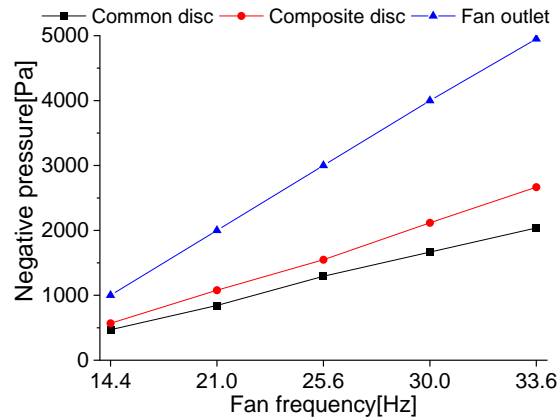


Fig. 6 - Relationship between fan frequency and pressure of vacuum chamber

From Fig. 6, the negative pressures of vacuum chambers for two seed discs are significantly lower than the negative pressures at the fan outlet, indicating that air pressure is greatly reduced in the delivery pipeline. The negative pressure of the composite disc is larger than that of the common disc. In addition, as the fan frequency grows, the negative pressure difference is also enlarged, showing that the pressure loss of the composite disc is lower than that of the common disc.

The following regression equation is obtained after conducting regression analysis of vacuum chamber negative pressures of the common and composite discs:

$$\begin{cases} y_1 = 416.23x, & R^2 = 0.9956 \\ y_2 = 530.27x, & R^2 = 0.9986 \end{cases} \quad (2)$$

where:

y_1 is the vacuum chamber negative pressure of the common disc;

y_2 is the vacuum chamber negative pressure of the composite disc and x is the fan frequency.

Negative pressure distribution in the vacuum chamber

For SD as the study object, the negative pressure value is measured with the U-type barometer at each suction hole in the vacuum chamber. The results are shown in Fig. 7.

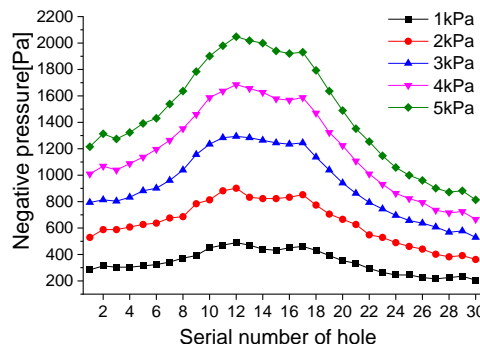


Fig. 7 - Negative pressure of each suction hole within the air chamber

The negative pressure at both ends of the vacuum chamber is relatively small. It increases as the distance with the outlet is smaller; while the suction holes 13-16 opposite to the outlet are not equipped with the maximum negative pressures, but slightly smaller than that of holes 12 and 17 nearby. The maximum negative pressure is measured near the outlet and the pressure at the outlet decreases slightly.

Airflow in the U-shaped vacuum chamber flows to the outlet in both directions and gathers at the middle position. Then, at the intersection, these airflows collide, forming cavitation where the airflow speed is slow. Therefore, the negative pressure near the vacuum chamber outlet is smaller than the pressure on both sides.

The negative pressures of suction holes 1-12 on the left of the outlet are smaller than those of holes 17-30 on the right. The static pressure at the left end of the vacuum chamber is significantly larger than that at the right end. Since the outlet is inclined by 45° on the left side, the air on the right side flows to the outlet smoother. However, air on the left side may be reversed when it flows to the outlet, leading to the airflow being obstructed.

Impact of suction hole parameters on the airflow field

The SD is taken as the research object to study the influence rules of hole number on negative pressure. SD has 30 suction holes in the vacuum chamber. Tape is used to seal 5 holes evenly per time to reduce the hole number in the chamber as 25, 20 and 15. Measured values of negative pressure of the vacuum chamber with different hole numbers and the results are shown in Fig. 8.

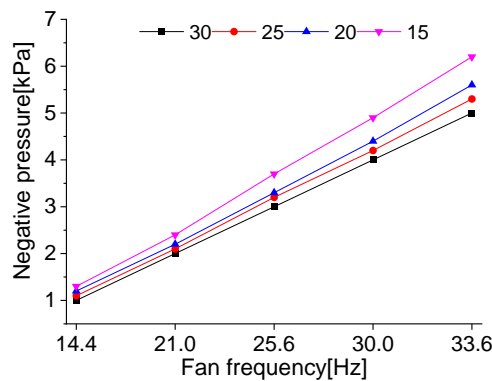


Fig. 8 - Effect of the number of suction holes on the pressure of vacuum chamber

From Fig. 8, it can be found that the hole number significantly influences the negative pressure value. Under the same fan frequency, the negative pressure of the vacuum chamber gradually increases with reduction of the hole number. Besides, the larger the frequency is, the more significant the growing tendency of the negative pressure is.

As the operation objects of the seed metering device vary, the hole diameter differs as well.

Generally, the larger seed size applies to larger hole diameter. SD and CD are applied to study the impact of suction hole diameter on the airflow field. To ensure consistent hole numbers, tapes are used to evenly seal 20 holes of the SD.

With the fan frequency adjusted as 14.4, 21.0, 25.6, 30.0 and 33.6 Hz, negative pressures of fan outlet and vacuum chamber of SD and CD are measured. The results are shown in Fig. 9.

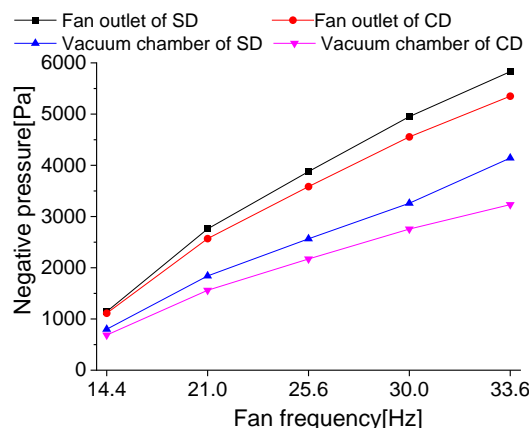


Fig. 9 - Effect of suction hole diameter on macro negative pressure

From Fig. 9, it can be found that the negative pressure of the SD fan outlet is larger than that of the CD fan and the negative pressures at outlets of the vacuum chamber are similar. This means that as the hole diameter increases, the vacuum chamber pressure decreases significantly and the decreasing tendency grows when the fan speed enlarges.

The hole negative pressure in the vacuum chamber is measured. Fifteen suction holes are in the vacuum chamber and they are numbered clockwise. The U-type barometer is used to measure the hole pressure one by one. The results are shown in Fig. 10.

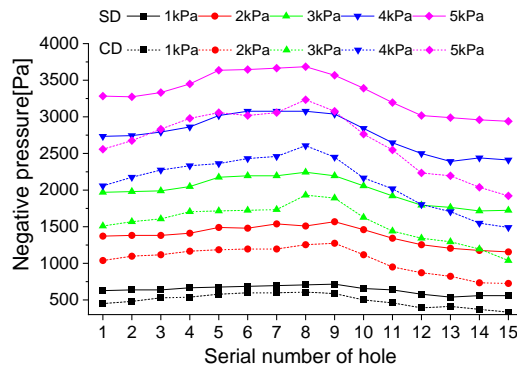


Fig. 10 - Influence of suction hole diameter on its negative pressure

From Fig. 10, it can be found that when the fan speed remains the same, the negative pressure of SD always outweighs that of CD and the pressure difference is larger as the fan speed is higher. This means that when the suction hole diameter is larger, the negative pressure grows as well.

Impact of seed hole structure on the negative pressure of suction hole

Common discs are flat and there is no other structure around the hole. On the contrary, outside the suction hole of the composite disc is a filling groove, which affects the airflow motion near the suction hole. When the negative pressure is 3 kPa, the pressures 0, 2, 4, 6, 8 and 10 mm away from the suction hole are respectively measured. Represented by holes 1, 6, 11, 16, 21 and 26 selected, the results are shown in Fig. 11.

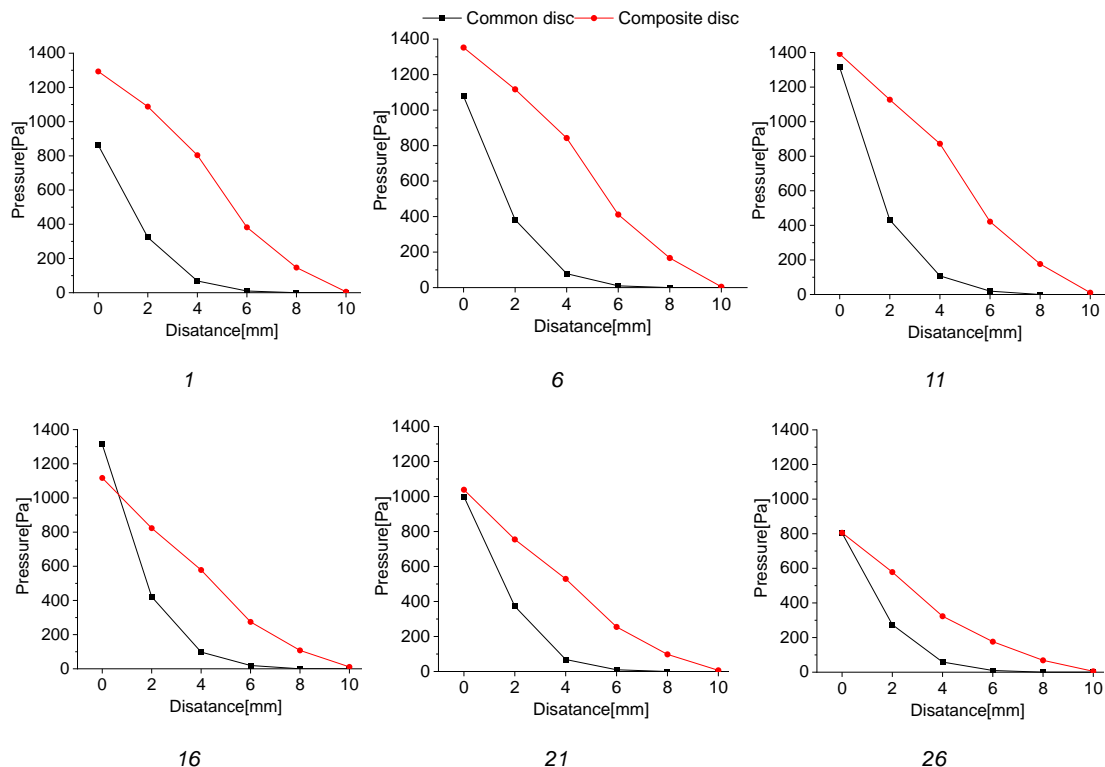


Fig. 11 - Effect of seed hole on negative pressure near suction hole

It can be found that as the distance enlarges, the negative pressure surrounding suction holes of the common disc decreases faster and the negative pressure changes at different areas of the vacuum chamber are similar. When the distance increases from 0 mm to 2 mm, the negative pressure decreases greatly; with the distance increasing from 2 mm to 4 mm, the pressure reduction slows down. The negative pressure approaches 0 when the distance reaches 6 mm and above. Namely, with the vertical distance between a seed and the hole being 6 mm, the suction force of airflow on the seed is negligible.

The negative pressure attenuation rate near suction holes of a composite disc is significantly slower than that of a common disc. In addition, with the same distance, the negative pressure of the composite disc is larger than that of the common disc except for individual holes. As the distance grows from 0 mm to 10 mm, the negative pressure attenuation of each suction hole in the vacuum chamber changes linearly. The negative pressure of each hole is larger than 0 when the distance is 6 mm and 8 mm. Namely, when the vertical distance between a seed and the suction hole is 8 mm, the airflow can intake the seed as well and filling operation is available. But the negative pressure approaches 0 when the distance reaches 10 mm. The suction force is unavailable in filling operation.

When the distance is 0 mm, the negative pressure difference between the common and composite discs is small. At holes 1 and 6, the negative pressure of the composite disc is slightly larger than that of the common disc. However, at holes 11, 21 and 26, the difference is insignificant. At hole 16, the common disc pressure is larger than the composite disc pressure. In addition, when the distance is larger than 0, the negative pressures of the common and composite discs vary significantly. The negative pressure at each hole of the composite disc is significantly larger than that of the common disc. As the distance remains 2 mm and 4 mm, the pressure difference increases. When the distance exceeds 6 mm, the difference narrows. As the distance reaches 10 mm, the negative pressure of the composite disc approaches 0.

The filling groove of the composite disc broadens the range of action of negative pressure and increases the air-suction filling performance of the suction hole, thus further improving the filling performance of the seed metering device at low negative pressure.

Impact of chamber thickness on air pressure

SD is taken as a research object to study the impact of chamber thickness on the airflow field. Additional thicknesses of the vacuum chamber adjustment disc are set as 0, 5, 10 to 40 mm. When the display screen shows 1.0, 2.0, 3.0 to 5.0 kPa, the corresponding frequency converter values are recorded. The results are shown in Table 2.

From Table 2, it can be found that as the additional disc thickness increases from 0 to 25 mm, the fan frequency does not change significantly with the fan outlet pressure remaining the same. This means that when the fan speed is fixed and the additional chamber thickness is not greater than 25 mm, the chamber thickness changes do not significantly influence the negative pressure at the fan outlet.

Table 2

Fan frequency corresponding to additional thickness of vacuum chamber									
	0 mm	5 mm	10 mm	15 mm	20 mm	25 mm	30 mm	35 mm	40 mm
1 kPa	14.4 c	14.3 c	14.5c	14.4 c	14.3c	14.5c	14.9b	15.4b	16.2a
2 kPa	21.1 d	21.0 d	21.4 d	21.2 d	21.3 d	21.2 d	21.6 c	22.3 b	22.8a
3 kPa	25.5 d	25.6 d	25.6 d	25.4 d	25.7 d	25.4 d	26.5 c	26.9b	27.4a
4 kPa	30.1 d	30.0 d	30.3 d	30.2 d	30.4 d	30.3d	30.8c	31.4b	32.1a
5 kPa	33.7 c	33.6 c	33.5 c	33.6 c	33.5 c	33.4c	33.9b	34.3b	35.2a

However, when the additional thickness reaches 30 mm and above, the fan frequency required to maintain the same negative pressure significantly enlarges with greater energy consumption. When the additional thickness exceeds 30 mm, the air pressure loss is significant. Therefore, the additional thickness may not exceed 25 mm.

When the additional thickness is from 0 to 25 mm and the negative pressure is 3 kPa, the negative pressures of suction holes 1, 6, 11, 16, 21 and 26 are measured. The measured results are shown in Fig.12.

From Fig. 12, it can be found that with different additional thicknesses, the negative pressure changes similarly at each suction hole. The pressure of hole 1 is relatively small, but as the hole number enlarges, the negative pressure increases as well and reaches the peak at hole 11 or 16. Furthermore, as the number

increases, the negative pressure decreases. So, the pressure at hole 26 is the minimum. The negative pressure at different areas of the chamber changes the most when the additional thickness is 0 mm (i.e., original vacuum chamber). The pressure difference is 563.5 Pa between hole 1 and hole 16. Between hole 26 and hole 16, it is 671.3 Pa. As the additional thickness increases, the pressure difference between different chamber areas is narrowed gradually. When the additional thickness is greater than 20 mm, the negative pressure difference at different areas is relatively small and the pressure distribution in the vacuum chamber is uniform. However, when the distance is 25 mm, the negative pressures at all suction holes are smaller than pressure with a distance of 20 mm. To enhance the uniform distribution of negative pressures in the vacuum chamber, the chamber thickness can be raised to 20 mm.

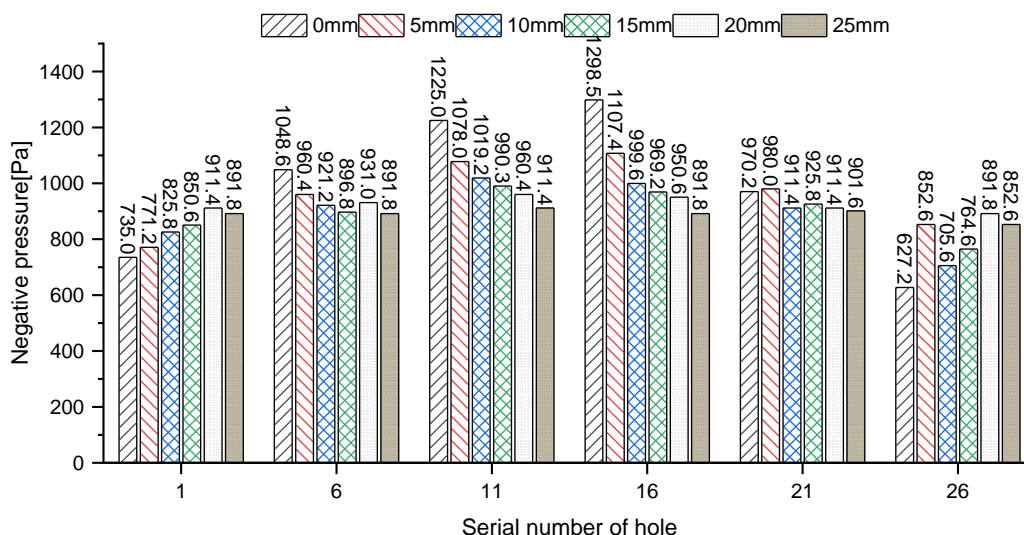


Fig. 12 - Effect of chamber thickness on suction hole pressure

CONCLUSIONS

(1) In the comparison of fan frequency between the common disc and composite disc, it can be found that the impact of seed disc structure on the fan outlet pressure is not significant. But the air pressure suffers great losses in the delivery pipeline and the pressure loss of composite disc is smaller than that of the common disc. At the same time, the regression equation between the negative pressure of the vacuum chamber and fan frequency is established.

(2) Negative pressures at both ends of the U-shaped vacuum chamber are relatively small, but the pressure value increases as the measured site is nearer the outlet. The negative pressures on both sides of the outlet are the maximum, but the pressure of suction holes opposite to the outlet is slightly reduced.

(3) The number and diameter of hole significantly influences the negative pressure value. As the hole number decreases, the negative pressure of the vacuum chamber gradually increases; with enlargement of the fan frequency, the negative pressure growing tendency is more significant. The chamber pressure significantly decreases with increase of the hole diameter and the decreasing tendency is enhanced as the fan frequency increases.

(4) Regulating the chamber thickness with the adjustment disc can enhance the negative pressure uniformity in the vacuum chamber. When the additional chamber thickness reaches 20 mm, the pressure uniformity in the vacuum chamber is optimal with the best negative pressure value.

ACKNOWLEDGEMENT

This work was supported by the National Natural Science Foundation of China (Grant No. 51905318), Shandong Provincial Colleges and Universities Youth Innovation Talent Induction Program (Smart Agriculture Research and Innovation Team), Top Talents Program for One Case One Discussion of Shandong Province ([2018]27), and Zibo School City Integration Project Academy of Ecological Unmanned Farm (Grant No. 2019ZBXC200).

REFERENCES

- [1] Abdolahzare, Z., & Mehdizadeh, S. (2018), Nonlinear mathematical modeling of seed spacing uniformity of a pneumatic planter using genetic programming and image processing, *Neural Computing and Applications*, vol.29, issue 2, pp. 363-375; <https://doi.org/10.1007/s00521-016-2450-1>

- [2] Chen, Y. L., Zhang, M., Liu, Z. Q., Lan Y. B., Yi, L. L., Peng, Q. J., & Yin, X. (2021), Design and experiment of seed agitator for vertical disk seed metering device, *INMATEH - Agricultural Engineering*, vol. 63, issue 1, pp.179-188;
- [3] Cujbescu, D., Matache, M., & Voicu, G. (2019), Mathematical model for sowing precision estimation of vacuum seed metering device, *UPB Scientific Bulletin, Series D: Mechanical Engineering*, vol.81, issue 3, pp. 225-234.
- [4] Dylan, S. J., Hesterman, D. C., & Guzzomi, A. L. (2013) Precision metering of Santalum spicatum (Australian Sandalwood) seeds, *Biosystems Engineering*, vol.115, issue 2, pp.171-183; <https://doi.org/10.1016/j.biosystemseng.2013.03.004>
- [5] Jia, H. L., Chen, Y. L., Zhao, J. L., Wang, J. X., Guo, M. Z., & Zhuang, J.(2018), Design and experiment of pneumatic-mechanical combined precision metering device for soybean, *Transactions of the Chinese Society for Agricultural Machinery*, vol.49, issue 4, pp. 75-86+139; <https://doi.org/10.6041/j.issn.1000-1298.2018.04.009>
- [6] Liao, Y. T., Liao, Q. X., Wang, L., Zheng, J., & Gao, L. P. (2018), Investigation on vacuum singulating effect influencing factors of pneumatic precision seed metering device for small particle size of seeds, *Transactions of the Chinese Society of Agricultural Engineering*, vol.34, issue 24, pp. 10-17; <https://doi.org/10.11975/j.issn.1002-6819.2018.24.002>
- [7] Liu, H. X., Guo, L. F., Fu, L. L., & Tang, S. F. (2015), Study on multi-size seed-metering device for vertical plate soybean precision planter, *International Journal of Agricultural and Biological Engineering*, vol.8, issue 1, pp.1-8; <https://doi.org/10.3965/j.ijabe.20150801.001>
- [8] Liu, Y. Q., Zhao, M. Q., & Hu, Y. W. (2013), Finite element analysis of airflow field for vacuum chamber in air-suction seed metering device of no-till seeder, *Applied Mechanics and Materials*, vol.275-277, pp.547-553; <https://doi.org/10.4028/www.scientific.net/AMM.275-277.547>
- [9] Mao, X., Yi, S. J., Tao, G. X., Yang, L., Liu, H. Y., & Ma, Y. C. (2015), Experimental study on seed-filling performance of maize bowl-tray precision seeder, *International Journal of Agricultural and Biological Engineering*, vol.8, issue 2, pp.31-38; <https://doi.org/10.3965/j.ijabe.20150802.1809>
- [10] Singh, R., Singh, G., & Saraswat, D. (2007), Design and operational parameters of a pneumatic seed metering device for planting of groundnut (*Arachis hypogaea*) seeds, *Indian Journal of Agricultural Sciences*, vol.77, issue 1, pp.40-42.
- [11] Wang, J. W., Tang, H., Wang, J. F., Li, X., & Huang, H. N. (2017), Optimization design and experiment on ripple surface type pickup finger of precision maize seed metering device, *International Journal of Agricultural and Biological Engineering*, vol.10, issue 1, pp. 61-71; <https://doi.org/10.3965/j.ijabe.20171001.2050>
- [12] Xing, H., Zang, Y., Wang, M. Z., Luo, W. X., & Fang, Y. L. (2020), Design and Experimental Analysis of a Stirring Device for A Pneumatic Precision Rice Seed Metering Device, *Transactions of the ASABE*, vol.63, issue 4, pp. 709-808; <https://doi.org/10.13031/TRANS.13096>
- [13] Yang, L., Yan, B. X., Yu, Y. M., He, X. T., Liu, Q. W., Liang, Z. J., Yin, X. W., Cui, T., & Zhang, D. X. (2016), Global overview of research progress and development of precision maize planters, *International Journal of Agricultural and Biological Engineering*, vol.9, issue 1, pp. 9-26.
- [14] Yu, J. J., Liao, Y. T., Cong, J. L., Yang, S., & Liao, Q. X. (2014), Simulation analysis and match experiment on negative and positive pressures of pneumatic precision metering device for rapeseed, *International Journal of Agricultural and Biological Engineering*, vol.7, issue 3, pp. 1-12.
- [15] Yu, H. L., Zhao, X. S., Liu, Z. L., Du, X., & Tian, C. (2015), Study on negative-pressure precision millet seed-metering device, *Advance Journal of Food Science and Technology*, vol.7, issue 2, pp.139-143; <https://doi.org/10.19026/ajfst.7.1282>
- [16] Zhang, G. Z., Zang, Y., Luo, X. W., Wang, Z. M., Zhang, Q., & Zhang, S. S. (2015), Design and indoor simulated experiment of pneumatic rice seed metering device, *International Journal of Agricultural and Biological Engineering*, vol.8, issue 4, pp. 10-18; <https://doi.org/10.3965/j.ijabe.20150804.1626>
- [17] Zhang, K. X., Sun, Y. Y., Liu, L., Liu, X. X., & Zhao, X. Y. (2020), Design and test of variable diameter pneumatic drum type bean seed metering device, *INMATEH - Agricultural Engineering*, vol.60, issue 1, pp.9-18; <https://doi.org/10.35633/INMATEH-60-01>
- [18] Zhao, Z., Wu, Y. F., Yin, J. J., & Tang, Z. (2015). Monitoring method of rice seeds mass in vibrating tray for vacuum-panel precision seeder, *Computers and Electronics in Agriculture*, vol.114, pp.25-31; <https://doi.org/10.1016/j.compag.2015.03.007>

STRENGTH TESTING OF STRIPPING CYLINDER'S TOOTH

ОПРЕДЕЛЕНИЕ ПРОЧНОСТИ ЗУБА ОЧЕСЫВАЮЩЕГО БАРАБАНА

Buryanov Alexey, Chervyakov Ivan, Kolin'ko Alexey¹

Federal State Budgetary Scientific Institution «Agricultural Research Centre «Donskoy» / Russia

Tel: +79515253806; E-mail: bern7771@rambler.ru

DOI: <https://doi.org/10.35633/inmateh-65-07>

Keywords: wheat, waste, stress, tooth, strength, reaper

ABSTRACT

When designing stripping headers, an important parameter is the value of the required strength of the stripping tooth. A method and means for measuring the forces acting on the stripping teeth, necessary for strength calculations, are proposed. To illustrate the application of the proposed method, an example of determining the force acting on a tooth when stripping winter wheat of the "Luchezar" variety with a moisture content of 10.7% under specific conditions is given.

РЕЗЮМЕ

При проектировании очесывающих жаток важным параметром является величина необходимой прочности очесывающего зуба. Предложена методика и средства для измерения усилий возникающих на очесывающих зубьях, необходимых для прочностных расчетов. В качестве иллюстрации применения предложенной методики приведен пример определения усилия, возникающего на зубе при очесе озимой пшеницы сорта Лучезар влажностью 10.7% в конкретных условиях.

INTRODUCTION

At present the technology of tow harvesting becomes more popular as there aren't enough combines in the farms because of their high cost. The adoption of No-Till technology promotes it too. Producers and scientists in many countries work at designing and producing stripping reapers, validating their parameters and modes of operation. The use of the towing technology for grain harvesting leads to reducing harvesting time and increasing the productivity of machines by 1.5–2.0 times (Dridiger V.K. et al., 2020). In addition, it allows reducing environment damage due to less emissions in the atmosphere since fuel consumption decreases to 40% (Dridiger V.K. et al., 2020; Chegini G.R. and Mirnezami S.V., 2016; Milyutkin V.A. et al., 2014; Siemens M.C. and Hulick D.E., 2007; Yuan J. and Lan Y., 2007).

There is no precise information for calculation of tooth strength taking into account safety factor (Lizhang X. and Yaoming L., 2011). There are some works in which either the scientists of our institute or other authors determine the stress for wheat ear stripping. But there has been determined only the stress per one plant, drawn through the slit manually. In this case the speed of ear drawing was rather lower than if it took place in the real process. The towing technology for grain harvesting is used not only for wheat harvesting but also for other grain crops, which differ either by inflorescences forms and sizes or by other characteristics (Aldoshin N.V. et al., 2016; Golpira H. et al., 2013).

Therefore, a number of scientists, who work at the adaptation of tow reaper for physical-mechanical properties of different crops and varieties and who suggest new forms and sizes of the stripping teeth and the stripping slit width, have to use the data about inflorescences destruction efforts that have been obtained by indirect methods (Alabushev A.V. et al., 2020; Buryanov A.I. et al., 2018; Egorov G.A., 1985; Chegini G.R., 2013). As a result, the construction of the stripping tooth has had either excess or insufficient strength. When the stripping teeth with insufficient strength are used, they are bent or broken, depending on the metal they are made of; this leads to harvesting loses as tooth angle of inclination has been changed.

¹ Alexey Buryanov – d. tech. sc., professor, main research officer; Ivan Chervyakov – junior research officer; Alexey Kolin'ko – junior research officer

The using of the stripping teeth with excess strength leads to the increasing of reaper's specific quantity of metal, its weight and, consequently, to cost increasing. In emergency situation, the holding teeth arrangement, including the stripping cylinder, may be broken because of the excess strength of the tooth. It involves the expensive repair or replacement of the stripping cylinder. Probably, there are a lot of things on the field that can lead to the damage of a reaper (Chegini G.R. and Mirnezami S.V., 2016; Savin V.Y., 2019; Savin V.Y., 2020).

Safety tests of the reaper with the teeth made of "soft" metal that is able to change its shape if a solid thing gets into the reaper have been performed. In this case their bending doesn't cause the structural damage of the stripping cylinder. In case when the teeth, made of excess strength steel 65G by 4 mm thickness, were used, the teeth had been broken and their sections had been cut off from the stripping cylinder and the cylinder itself had been partially broken. Moreover, neither the safety of the personnel nor that of the combine harvester is supported. The tests were carried out at the trailed tow reaper and they were recorded with the stationary video camera, fig.1.



Fig. 1 – Testing of the stripping unit safety using the excess strength tooth made of steel 65G

As you can see in fig.1, if the excess strength teeth collided with a solid thing, the integrity of the stripping cylinder was damaged, a number of teeth were cut off the cylinder, they flew out of the reaper and teeth parts could be reached at a distance of about 8 m. A deformation of the stripping cylinder was registered after inspection of the reaper's construction. One can say with certainty that using the excess strength teeth at the tow reaper is dangerous both for the personnel and for the other working parts of the harvester. Methods and means for measuring the stresses that appear on the stripping tooth, to further calculate the strength, are suggested.

MATERIALS AND METHODS

The laboratory setup was made for the experimentations; it was made on the basis of a laboratory setup for experimentations of grain stripping process which was patented as utility model (Buryanov A.I., et al., 2014), fig. 2.

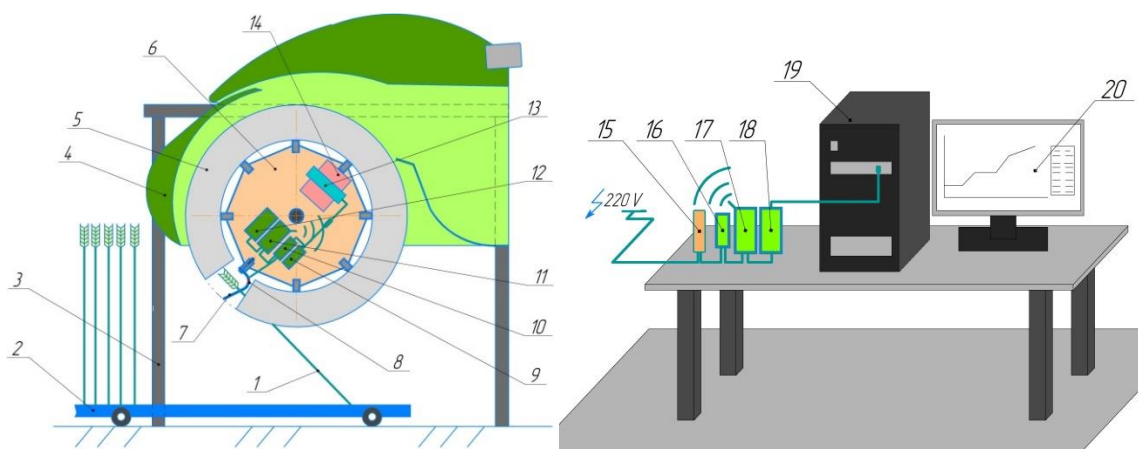


Fig. 2 – The laboratory setup drawing for determination of stripping tooth strength

Legend: 1 – stripped winter wheat plant (or other crop); 2 – movable field; 3 – laboratory setup supports; 4 – fairing; 5 – guide channel for combined plants; 6 – stripping cylinder; 7 – stripping tooth; 8 – strain sensor, fixed at the stripping tooth; 9-12 – measuring complex ZetLab; 13 – power element; 14 – counterweight for stripping cylinder's balancing; 15-18 – measuring complex ZetLab receiving the signal; 19 – personal computer (notebook); 20 – software package ZetLab

Laboratory setup (fig.2) consists of supports 3, fairing 4 which is fastened on them, stripping cylinder 6 with guide channel 5, measuring complex ZetLab which consists of 9, 10, 11, 12 blocks, power element 13 and stripping tooth 7 with strain sensor section 8. A signal of measuring is conveyed through radio channel to the ZetLab complex receiving part 15, 16, 17, 18 and then to the PC 19, where it is processed with ZetLab software package. A guide channel 5 is necessary for the plants to be headed strictly to the slit between the teeth after passing the tooth with the strain sensor 8. The channel is made of transparent material, which makes it possible to watch the measurements and record them with a high-speed video camera. The camera Sony DSCRX 100M5 was used in this case.

The sections of the measuring complex were adjusted before the experiment. The strain sensor had been calibrated with the interval 5 N to 100 N. A dynamometer MEGEON-03020 and mechanical dynamometer were used for calibration. The process of calibration was made using ZetLab software; it allowed getting the signal recording in such units of measurement such as newton, at once. Update rate of the measuring channel was 1000 Hz, which is the maximal one for the measuring unit.

There are four blocks in the measuring complex ZetLab, made by the company LLC “Electronic technologies and metrology systems” (fig.3): autonomous recorder ZET 71733, smart strain sensor with interface CAN ZET 7111, smart interface converter radio channel CAN ZET 7172-S, power converter ZETLab 7001. Lithium-ion cell, which is fixed on the cylinder, supplies with power all the blocks. Counterbalances were used to decrease cylinder beating.

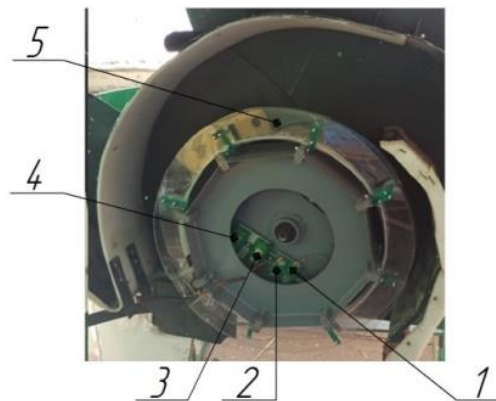


Fig. 3 – The laboratory setup drawing for testing the stripping tooth strength

1 – power converter ZET 7001, 2 – smart sensor with interface CAN ZET 7111; 3 – autonomous recorder ZET 7173; 4 – smart interface converter radio channel - CAN ZET 7172-S; 5 – guide channel

Autonomous recorder ZET 7173 (fig.3) makes it possible to record a signal in a file “.ana” during the measuring; a signal is recorded to internal memory with update rate 1000 Hz. The file of signal recording was copied on the PC for its further analysis in the software package “Statistica”, ZETLab, Excel.

For the experiment, the movable field 2 (fig.2) was filled with winter wheat plants. The plants of winter wheat had been prepared before. The part of the field was chosen at a distance no less than 50 m from forest belts and roads. Cut plants were shaped into a bundle; a number of plants was counted according to the number of tests and the quantity of plants needed to determine humidity.

Average humidity of grain was measured by means of “Willi 65” device right before the testing.

The field part length was 4 m. Plants have been chosen according to the fairing, stripping cylinder height; there were 90 pcs per 1 movable meter.

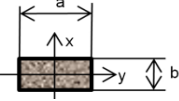
The stripping cylinder driver was turned on till its steady-state regime, then recording camera and driver of movable field were turned on, too.

It is possible to calculate the necessary tooth strength using the received data about the strength. Let us use simplified tabular procedure (Anuryev V.I., 1979) for this purpose, choosing the tabulated value for working stress when using alloyed hot-rolled steel 40CrNi (Anuryev V.I., 1979) of commercial quality at variable load from 0 to maximum and from maximum to 0 (pulsing) equal $\sigma_{bend} = 235.4 \text{ N/mm}^2$.

$$M_{bend} = F_{max} \cdot l_{st}, \text{ N}\cdot\text{mm} \quad (1)$$

where:

F_{max} is maximal strength at stripping tooth, N; l_{st} is distance acting on a tooth, mm.

Resisting moment W for a tooth, a load acting on the axis X  is (Anuryev V.I., 1979):

$$W_{res.} = \frac{a \cdot b^2}{6}, \text{ mm}^3 \quad (2)$$

where a is tooth width, mm.; b is tooth thickness, mm.

Acceptable bending moment $M_{ac.bend}$ is (Anuryev V.I., 1979):

$$M_{ac.bend} = \sigma_{bend} \cdot W_{res.}, \text{ N} \cdot \text{mm} \quad (3)$$

where σ_{bend} is working stress, N/mm²; $W_{res.}$ is resisting moment, mm³.

Load factor $K_{strength}$ then is (Anuryev V.I., 1979):

$$K_{strength} = \frac{M_{ac.bend}}{M_{bend}}. \quad (4)$$

The load factor must be greater than 1. Then the strength of the tooth will be sufficient for stable operation.

RESULTS

Method of determination of the optimal strength on stripping tooth was tested under the following conditions and modes of operation:

- movable field speed was 0.9 m/sec.;
- width of the combing slit 8.0 mm;
- winter wheat variety "Luchezar";
- a number of plants, placed on 1 m of the movable field, – 90 pcs;
- length of the field part, filled with plants, was 4 ± 0.1 m;
- winter wheat grains' humidity was $10.7 \pm 0.5\%$;
- 1000 grains mass 42.3 gm;
- plants' height up to ears was 0.77 ± 0.03 m;
- average length of an ear was 0.083 ± 0.004 m;
- height of the fairing low edge corresponded to the average height of plants to the ear 0.77 m;
- rotating frequency of the stripping cylinder – 40.1 sec.

Winter wheat plants were prepared before; the plants, having mentioned characteristics, were chosen so as to get average amount of strength, appeared at stripping.

The movable field speed and cylinder rotating frequency were chosen according to the measuring complex possibilities. Transit time of the stripped area – 4.3 sec. at the rotating frequency of the movable field 0.9 m/sec. and its length 4.0 m. Stripping cylinder performed 28 turns at rotating 40.1 sec., and stripping tooth met stripped plants 28 times, meanwhile the number of measuring points of the strength directly was 7; then the teeth moved the stripped heap. The length of the field's part was chosen according to the time of the video recording with the camera Sony DSC-RX100M5 at exposure 1/10000 and resolution (1920×1080 dpi). The results of tooth strength measured at mentioned parameters and plants characteristics are shown in fig.4.

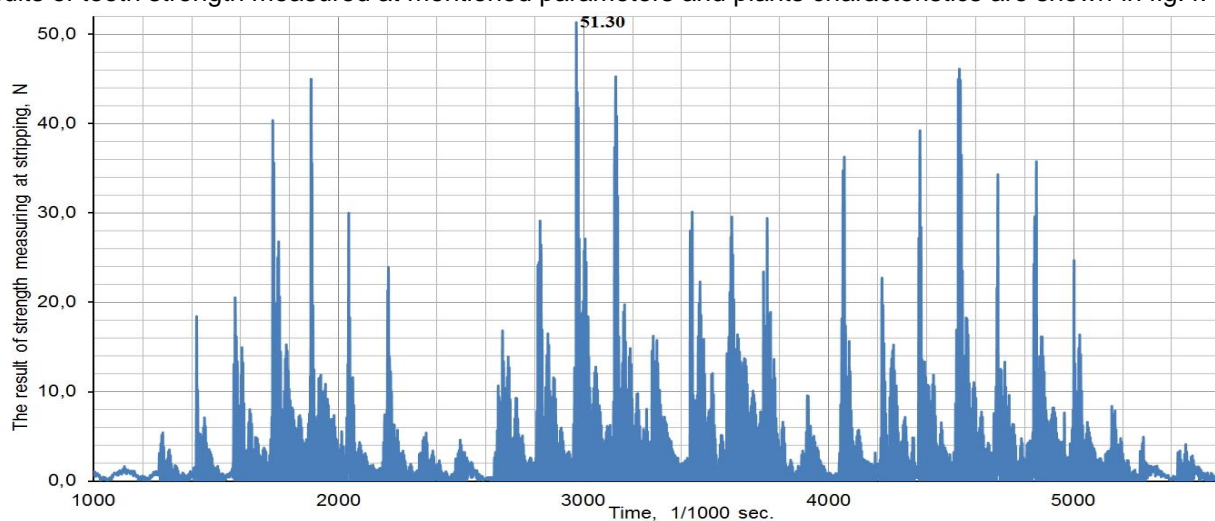


Fig. 4 – The result of stripping tooth strength measuring during winter wheat variety "Luchezar" stripping

The number of stripped plants was different and had random character at every cycle. Frames of speed video recording are shown in fig.5.

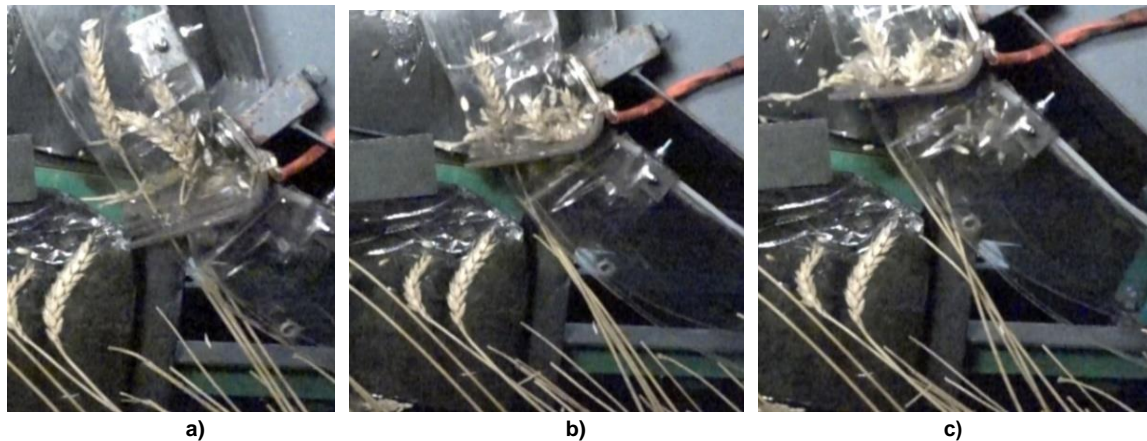


Fig. 5 – The frames of tow process

Legend: a – plants gripping with stripping teeth; b – winter wheat plants tow by teeth; c – stripped heap displacement by teeth

At maximal strength $F_{max} = 51.3$ N (fig.4), acting on a tooth at a distance $l_{st.} = 50$ mm from a tooth, assuming that a tooth is a straight beam which is rigid at one side, maximal bending moment M_{bend} is (1):

$$M_{bend} = F_{max} \cdot l_{st.} = 51.3 \cdot 50 = 2565 \text{ N}\cdot\text{mm}. \quad (5)$$

Resisting moment W for a tooth with a section $a=16$ mm, $b=2$ mm according to the formula (2):

$$W_{res.} = \frac{a \cdot b^2}{6} = \frac{16 \cdot 2^2}{6} = 10.7 \text{ mm}^3. \quad (6)$$

Acceptable bending moment $M_{ac.bend}$ according to the formula (3):

$$M_{ac.bend} = \sigma_{bend} \cdot W_{res} = 235.4 \cdot 10.7 = 2518.8 \text{ N}\cdot\text{mm}. \quad (7)$$

Then, the load factor is (4):

$$K_{strength} = \frac{M_{ac.bend}}{M_{bend}} = \frac{2518.8}{2565} = 0.98. \quad (8)$$

As the calculation indicates, the strength of a tooth made of strip of steel 40CrNi with 2 mm thickness, when a tooth width is 16 mm, will be insufficient. Considering almost equal meanings of acceptable bending moment and maximal strength on a bend, one can say that, increasing tooth thickness to 3 mm, acceptable bending moment elevation will be obtained and load factor will exceed 1.0.

If $a=16$ mm, $b=3$ mm then:

$$W_{res.} = \frac{a \cdot b^2}{6} = \frac{16 \cdot 3^2}{6} = 24.0 \text{ mm}^3, \quad (9)$$

$$M_{ac.bend} = \sigma_{bend} \cdot W_{res} = 235.4 \cdot 24.0 = 5649.6 \text{ N}\cdot\text{mm}, \quad (10)$$

$$K_{strength} = \frac{M_{ac.bend}}{M_{bend}} = \frac{5649.6}{2600} = 2.2. \quad (11)$$

In terms of the above, a stripping tooth, made of steel 40CrNi with 16 mm width and 3 mm thickness, is able to ensure the right working conditions. It should be noted that the strength of grain and ear bundle depends on humidity and variety of the crop that time; besides, it is necessary to repeat tests at different conditions. The suggested method and means of testing allow obtaining the necessary data to calculate the strength of the stripping tooth in all modes of operation and under different conditions. It will make it possible to achieve the required reliability and safety of the stripping unit without using the excessive solidity and metal intensity in the construction.

CONCLUSIONS

It is necessary to use a reliable information about occurring stresses on the stripping tooth making a calculation of stripping devices strength for qualitative and safe work. The stress should be obtained under different modes of operation and with different qualities of the harvested crops. The suggested methodology is recommended for strength determination that occurs at the cylinder's teeth of a reaper which is designed for a certain crop or their set, considering zonal conditions.

So, maximal stress on a tooth is 51.3 N when stripping winter wheat “Luchezar” with 10.7% humidity, feed 0.9 m/sec. rate, 40.1 sec⁻¹ cylinder rotary speed, and, for the effective process of stripping, a tooth can be made of steel 40CrNi with 16 mm width and 3 mm thickness.

REFERENCES

- [1] Alabushev, A.V.; Buryanov, A.I.; Pakhomov, V.I.; Kolinko, A.A.; Chervyakov, I.V., (2020), Development of a method to control threshing process based on properties of harvested crop variety and external factors, *IOP Conference Series: Earth and Environmental Science*, Vol. 422, no.1, 012005p, DOI: 10.1088/1755-1315/422/1/012005.
- [2] Aldoshin, N.V.; Zolotov, A.A.; Tsygutkin, A.A.; Lynin, N.A.; Malla, Bahaa, (2016), Harvesting of mixed crops of grain crops by the combing method, (Уборка смешанных посевов зерновых культур методом очёса), *Bulletin, (Вестник)*, no.1, pp. 7–13;
- [3] Anuryev, V.I., (1979), *Handbook of the designer - machine builder, (Справочник конструктора - машиностроителя)*, vol. 1, Mechanical Engineering, (Машиностроение), Moscow, 728p.
- [4] Buryanov, A.I.; Buryanov, M.A.; Dmitrenko, A.; Kolesnikov, G.E.; Chervyakov, I.V., (2014), *Laboratory installation for the study of parameters and modes of the process of stripping grain crops*, RU, No. 136743.
- [5] Buryanov, A.I.; Chervyakov, I.V.; Kolinko, A.A.; Pakhomov, V.I.; Ionova, E.V.; Khlystunov, V.F., (2018), Methods and results of determining the natural strength of the bond between grain and ear during ripening and full ripeness, (Методы и результаты определения естественной силы связи зерна с колосом в период созревания и полной спелости), *Grain economy of Russia, (Зерновое хозяйство России)*, Vol. 60, no 6, ISSN 2079-8725, pp. 21–25, DOI 10.31367/2079-8725-2018-60-6-21-25;
- [6] Chegini, G.R., (2013), Determine of Optimum Operating Conditions of Combine Harvester with Stripper-Header, *World Applied Sciences Journal*, Vol.23, no.10, pp.1399–1407, DOI: 10.5829/idosi.wasj.2013.23.10.1829;
- [7] Chegini, G.R.; Mirnezami, S. V., (2016), Experimental comparison of combine performance with two harvesting methods: stripper header and conventional header, (*CIGR Journal*), pp. 192–200;
- [8] Dridiger, V.K.; Gadzhumarov, R.G.; Yagovitova, E.A., (2020), Harvesting of winter wheat by the brushing method in the No-till technology, (Уборка озимой пшеницы методом очёса растений в технологии No-till), *Achievements of science and technology of the agro-industrial complex, (Достижения науки и техники АПК)*, no 10, ISSN 0235-2451, DOI 10.24411/0235-2451-2020-11012.
- [9] Egorov, G.A., (1985), *Technological properties of grain, (Технологические свойства зерна)*, Agropromizdat, (Агропромиздат), 334p.
- [10] Golpira, H.; Tavakoli, T.; Baerdemaeker, J.D., (2013), Design and development of a chickpea stripper harvester, *Spanish Journal of Agricultural Research (Span J Agric Res)*, Vol. 11, no 4, ISSN: 1695-971-X/eISSN: 2171-9292, DOI 10.5424/sjar/2013114-3393, pp. 929–934;
- [11] Lizhang, Xu; Yaoming, Li, (2011), Modelling and experiment to threshing unit of stripper combine, *African Journal of Biotechnology*, Vol.10, no 20, ISSN: 1684–5315, pp.4106–4113;
- [12] Milyutkin, V. A.; Strebkov, N. F.; Soloviev, S. A.; Makarovskaya, Z. V., (2014), Technical solutions for No-till and Strip-till technologies, (Технические решения для технологий No-till и Strip-till), *News of the Orenburg State Agrarian University, (Известия Оренбургского государственного аграрного университета)*, ISSN 2073-0853, pp.61–63;
- [13] Savin, V.Y., (2019), Determination of the force required for stripping the wheat ear, (Определение усилий, необходимых для очёса колоса пшеницы), *Mordovia University Bulletin, (Вестник Мордовского университета)*, Vol.29. no.3, Russia, ISSN: 2658-4123, DOI:10.15507/2658-4123.029.201903.456-466456–466;
- [14] Savin, V. Y., (2020), Determining the effort of barley stripping, (Определение усилия зачистки ячменя), *Gazette of the Moscow State Agricultural Engineering University named after V.P. Goretkin, (Вестник Московского государственного агроинженерного университета имени В.П. Горячкина)*, Vol.97, no.3, pp.17–21, DOI: 10.26897/2687-1149-2020-3-17-21;
- [15] Siemens, Mark C.; Hulick, Donald E., (2007), Development of an Alternative, Reaper/Flail Based Harvesting System for Biomass Collection and No-Till Seeding - 2nd Year, *Electronic-only Proceedings of the International Conference on Crop Harvesting and Processing*, no 701P0307e, 13p, Louisville, Kentucky USA, DOI 10.13031/2013.22592.
- [16] Yuan, J.; Lan, Y., (2007), Development of an Improved Cereal Stripping Harvester, *CIGR Ejournal*, Vol. 9.

WORKSPACE ANALYSIS OF A FLAME INTRA-ROW WEEDING ROBOT IN VEGETABLE FIELD AND NUMERICAL SIMULATION OF PROPANE COMBUSTION

蔬菜株间火焰除草机器人工作空间分析与丙烷燃烧数值模拟

Xu Bing¹⁾, Zheng Decong^{1)*}, Wang Jiaxin²⁾, Yang Youzhi³⁾

¹⁾ College of Agricultural Engineering, Shanxi Agricultural University, Taigu / China

²⁾ College of Mechanical and Electronic Engineering, Northwest A&F University, Yangling / China

³⁾ Quick Intelligent Equipment Co., Ltd, Changzhou / China

Tel: +86-0354-6288339; *E-mail: zhengdecong@126.com

DOI: <https://doi.org/10.35633/inmateh-65-08>

Keywords: *intra-row weeding, flame weeding, Delta mechanism, workspace, numerical simulation*

ABSTRACT

A flame intra-row weeding robot, based on the Delta mechanism, was designed to solve the problems of high labor intensity, low efficiency, easy-to-harm seedling and others. Simultaneously, the applicable robot kinematics model was established. Moreover, the method of exhaustion enabled us to obtain the full-scale robot workspace and analyze its smart workspace. When the nozzle diameter took different values, the numerical simulation on the propane combustion process in the burner was performed by the Fluent component transport model, analyzing the temperature distribution inside and out of the burner. The experimental results showed that the flame intra-row weeding robot was required to work on the condition that the radius of smart cylindrical space is $\Phi 400 \text{ mm} \times 359.8 \text{ mm}$ — when the length of the driving arm is 300 mm, the length of the driven arm is 800 mm, the radius of the static platform is 150 mm and the radius of the movable platform is 50 mm — the maximum temperature of propane flame reaches 1,830 K and the width of the high temperature zone reaches 27 mm — when the nozzle diameter is 1.6 mm.

摘要

针对蔬菜株间除草作业劳动强度大、效率低、易伤苗等问题，设计了一种基于 Delta 机构的株间火焰除草机器人，并建立了机器人运动学模型，利用穷举法得到了机器人全工作空间，并对其灵巧工作空间进行了分析；当喷嘴直径取不同值时，基于 Fluent 组分输运模型分别对燃烧器内丙烷燃烧过程进行了数值模拟，对燃烧器内部及出口温度分布进行了分析。结果表明，当主动臂长度为 300 mm、从动臂长度为 800 mm、静平台半径为 150 mm、动平台半径为 50 mm 时，其灵巧工作空间为 $\Phi 400 \text{ mm} \times 359.8 \text{ mm}$ 的圆柱形空间，当喷嘴直径为 1.6 mm 时，丙烷火焰最高温度达 1830 K，燃烧器出口高温区宽度达 27 mm，满足株间火焰除草的要求。

INTRODUCTION

Vegetables are one of the basic food sources for human being, providing vitamins, dietary fiber and minerals necessary for human health (Deng et al., 2018). China's vegetable production and consumption both rank first in the world, but the mechanization of vegetable production is still in the initial stage (Xiao et al., 2017). Easy-to-spread field weeds compete with crops for water, fertilizer and space, leading to a decline in the vegetable production. Therefore, field weeding is an essential part for vegetable production. Field weeds can be divided into the inter-row weeds and the intra-row weeds (Chen et al., 2015; Liu et al., 2017). The traditional cultivating implement is mainly applicable to the inter-row weeds, or when the distance between weeds and seedlings is relatively short, which requires a high demand in the weeding accuracy and thus improves the difficulty of weeding. The manual or the chemical method is often applied to the common weeding. The former is labor-intensive and low-efficiency, while the later reduces labor intensity but improves the weeding efficiency. Nevertheless, a large amount of herbicides not only cause the eutrophication of water bodies and the environmental pollution, but also lead to the pesticide residues in vegetables (Wu et al., 2019; Wang et al., 2018). Therefore, it is of great significance and urgency to develop the intelligent intra-row weeding device to improve the production efficiency and cut down on the use of pesticide in the context of the aging of the agricultural population, the reduction of labor force and the increasing demand for the quality of vegetable.

Bing Xu, As Lec. M.S. Eng.; Decong Zheng, Prof. Ph.D. Eng.; Jiaxin Wang M.S. Stud. Eng.; Youzhi Yang M.S. Eng.

Recently, researchers and scholars from various countries have done a lot of research on the intelligent intra-row weeding for different crops under different production conditions. The relevant studies at this stage mainly focus on the structure design, the recognition algorithm on the difference between weeds and seedlings and other key technologies for the intra-row weeding and the end-effector. *Hu Lian et al.* designed a claw-tooth intra-row weeding device that can kill weeds and get out of the way of seedlings by controlling the trochoid motion of claw-tooth (*Hu et al., 2012*). *Huang Xiaolong et al.* optimized the design on the end-effector and carried out the intra-row weeding robot experiment in vegetable field. The experiments results proved that the weeding rate was 95.4% when the plant spacing was 350 mm (*Huang et al., 2012*). The researchers also conducted the structural designs and had experiments on the intra-row weeding devices for crops, such as rice, corn, soybeans and grapes (*Jiang et al., 2020; Zhou et al., 2018; Han et al., 2020; Reiser et al., 2019*). *Kumar Satya Prakash et al.* presents development of a cost-effective mechatronic prototype for intra-row weeding operation. Preliminary field evaluations showed this system to be effective for intra-row weed (>65%) and plant damage control (<25%) (*Kumar et al., 2020*). For vegetable fields at the seedling stage, it is natural that seedlings are weak and the grass is strong. The existing intra-row weeding devices often kill weeds and get out of the way of seedlings by swinging or rotating weeding knives and weeding teeth. Because the distance between weeds and vegetable seedlings is short, this method is easy to harm the shallow root system of vegetable seedlings.

Some scholars tried physical methods to control weeds, such as electric, fire, microwave, steam and others. *Wang Jinwu et al.* designed a water jet weeding device and carried out a bench test, whose experiment results proved that the weeding rate is 90.62% when the water pressure of the device is 1.5 MPa (*Wang et al., 2021*). A flame weeder was applied to the production of organic corns by Serbian scholar *Rajković Miloš (Rajković et al., 2021)*. Generally, by methods of electric, fire, microwave, steam and others, it can reduce the damage to crop roots but can easily damage crop stems and leaves. Hence, it is urgent to improve the weeding rate and precision but reduce the damage rate of seedlings (*Raja et al., 2020a*).

The Delta mechanism is featured with the fast speed and the high precision. Based on this advantage, this paper designed a flame intra-row weeding robot in vegetable fields. It relied on the Delta mechanism and took the burner as the end-effector and the propane as fuel. Equipped with the self-propelled high-clearance platform and the Delta mechanism, it can meet the high-precision requirements of the intra-row weeding. The analysis on the weeding robot workspace and the numerical simulation on the temperature distribution of propane combustion flame by FLUENT confirmed that the Delta mechanism parameters and the burner nozzle diameter meet the requirements of the intra-row flame weeding.

MATERIALS AND METHODS

Flame Weeding Operation Environment and Requirements

Field investigations and relevant literature (*Trygve et al., 2018; Raja et al., 2020b; Kennedy et al., 2020*) inquiry enable us to know different vegetable cultivation modes, which help us determine the intra-row weeding operation environment in vegetable fields. It requires that the plant spacing is 300~500 mm, the plant height is 220~360 mm, and the row spacing is more than 200 mm. The flame weeding utilizes the fuel to produce high-temperature flames and destroy the weed cells and tissues, causing them to quickly lose water and die. The relevant studies indicate that the cytoderm of weeds will be destroyed when the flame temperature reaches 100 °C (about 375 K), which can control the growth of weeds. However, there has been a certain difference among and between different types of weeds and the same type of weeds at different growth stages (*Knezevic et al., 2014*). In order to make the burner have a better effect on most of weeds, the working temperature in the burner is above 600 K, namely the flame temperature is above 600 K. In addition to the flame temperature, the flame form also has an effect on the weed control to reduce its effectiveness and efficiency. The long and narrow flame can kill heat-sensitive weeds that grow in the vertical direction, while the short and wide flame has a good effect on weeds that creep on the ground and have more growing points to increase its weeding efficiency (*Guan et al., 2019; Fu et al., 2016*). On the whole, the flame width in the high temperature zone should be above 25 mm in designing the burner. In addition, the flame weeding should be performed in the condition of no wind or less wind, in which the wind speed is 0~0.2 m/s.

Structure and Principle of Flame Weeding Robot

The flame intra-row weeding robot is mainly composed of self-propelled high-clearance platform, Delta mechanism, vision system, fuel tank, pressure gauge, hose, burner and so on. The Delta mechanism includes mobile platform, driven arm, driving arm, motor and static platform.

The schematic diagram of the field operation of the flame weeding robot is shown in Figure 1. The Figure shows that L_1 represents the plant spacing and L_2 represents the row spacing.

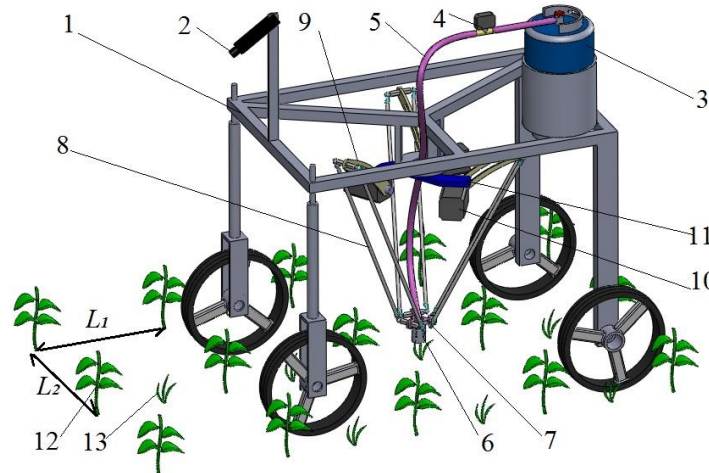


Fig. 1 - The schematic diagram of the field operation of the flame weeding robot

1- self-propelled high-clearance platform; 2- vision system; 3- fuel tank; 4- pressure gauge; 5- hose; 6- burner; 7- mobile platform; 8- driven arm; 9- driving arm; 10- motor ; 11- static platform; 12-crop; 13-weeds

The Delta mechanism is fixed on the frame of the self-propelled high-clearance platform by the static platform and the burner is fixed on the mobile platform. The burner is connected with the fuel tank fixed on the frame through the hose. When the weeding robot is working, the walking wheels on both sides of the self-propelled high-clearance platform respectively moved in adjacent crop rows, and the vision system identify crops and weeds to direct the driving arms to place the burner at different positions, killing the weeds and getting out of the way of seedlings.

Division of Intra-row Weeding Area

Vegetable seedlings divide the intra-row area into the intra-row weeding area and the protection area, as shown in Figure 2(a). The circular area with a radius of l represents the protection area and the other circular area with a diameter of (L_1-2l) represents the intra-row weeding area. The weeding operation of the flame weeding robot is composed of killing weeds and getting out of the way of seedlings. When the weeder is working, the burner, located in the intra-row weeding area, sprays the flame at a position of h above the ground. As shown in Figure 2(b), h is 50 mm. On the condition of getting out of the way of seedlings, the burner extinguishes the flame and raises a certain height to cross the protection area and enter into the next intra-row weeding area.

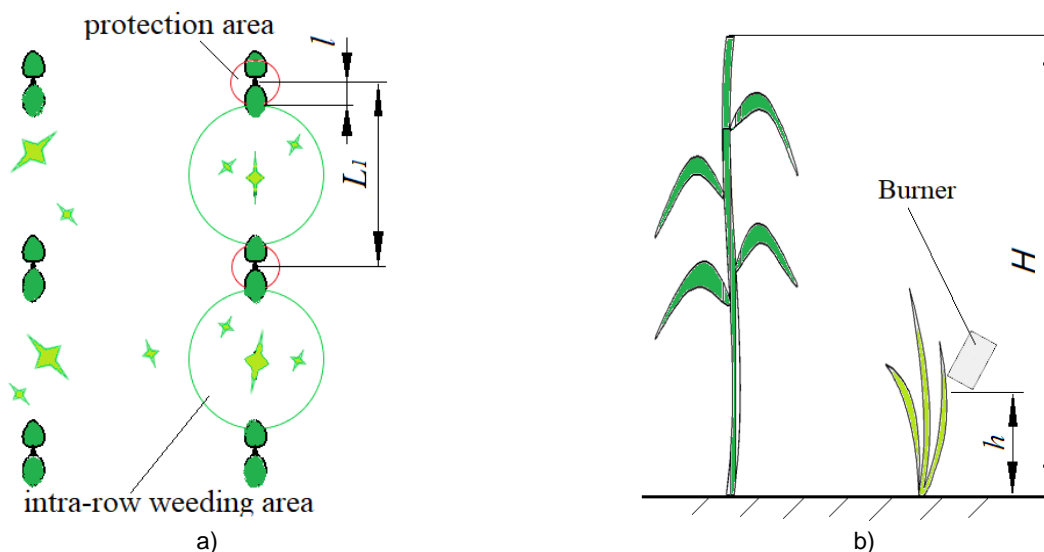


Fig. 2 - Schematic diagram of division of intra-row weeding area

Due to the discontinuous intra-row weeding area, it is easy to miss the weeds or harm the seedlings. Hence, the weeding rate and the damage rate of seedlings are two key indicators to measure the effectiveness of intra-row weeding.

The premise of increasing the weeding rate is that the end-effector, namely the burner workspace, can cover the intra-row weeding area to reduce the miss rate, when the weeding robot stays at the intra-row weeding area. To reduce the damage rate of seedlings simultaneously, the burner should be lifted above the height of crops, when the weeding robot leaves the intra-row weeding to pass the protection area.

The Delta mechanism full-scale workspace has a bowl-shaped enveloping space. In practical applications, it is generally applied to a cylindrical and smart workspace (Zhang et al., 2018). When the flame weeding robot is working, the burner is located on the flat surface, that is, the target working platform of the Delta mechanism and the bottom surface of the cylindrical smart workspace, at a position of h above the ground. The diameter of the bottom surface is represented by D . To make the burner workspace cover the intra-row weeding area, D should satisfy the formula (1). The maximum height that the burner can be lifted from the target working platform, namely the height of the cylindrical smart workspace H_1 , should satisfy the formula (2) to help the burner cross the crops and successfully get out of the way of seedlings.

$$D \geq L_1 - 2l \tag{1}$$

$$H_1 \geq H - h \tag{2}$$

To have a wider range, the plant spacing L_1 and the plant height H for the weeding robots are designed to be the maximum values respectively, namely $L_1=500$ mm and $H=360$ mm. Therefore, the bottom diameter D of the cylindrical smart workspace should be equal to or greater than 400 mm and the H_1 should be greater than 310mm to meet the operational requirements.

Kinematics Model of Delta Mechanism

The kinematic equation of the Delta mechanism should be established firstly, to obtain the workspace of the weeding robot. The schematic diagram of the Delta mechanism is shown in Figure 3. $A_1A_2A_3$ is the static platform and $C_1C_2C_3$ is the mobile platform. A_iB_i is the driving arm ($i=1,2,3$) and its length is presented by L_b . The field angle between the driving arm and the static platform is marked by θ_i . B_iC_i is the driven arm and L_a represents its length. Taking the static platform center O as the origin of coordinate, establish the static coordinate system $O-XYZ$ and make sure that the Y axis is perpendicular to A_1A_2 . Taking the mobile platform center O' as the origin of coordinate, establish the static coordinate system. OA_i represents the radius of the static platform, and its length is R . $O' C_i$ represents the radius of the mobile platform and its length is r . The included angle between OA_i and the X axis is defined as η_i .

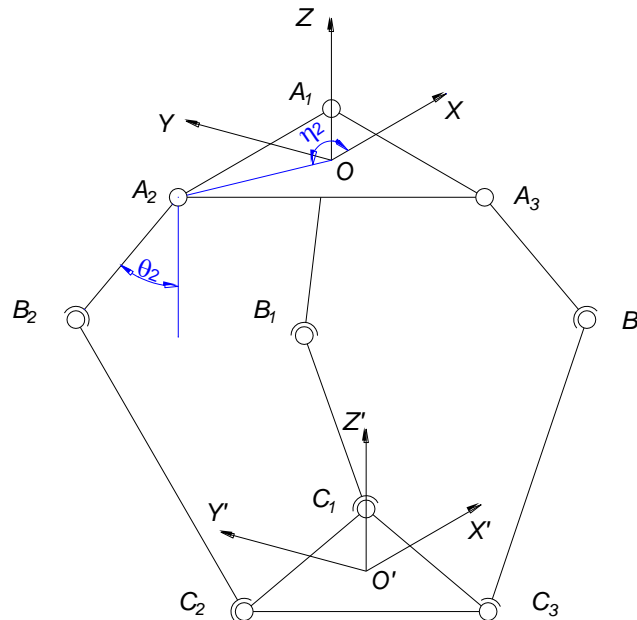


Fig. 3 - Sketch of Delta mechanism

The origin O' of the mobile coordinate system is represented by (x, y, z) on the dynamic coordinate system. In accordance with the geometric relationship, all parameters should satisfy the kinematic equation (3) (Zhang et al., 2018):

$$[(R + L_b \sin \theta_i - r) \cos \eta_i - x]^2 + [(R + L_b \sin \theta_i - r) \sin \eta_i - y]^2 + [-L_b \cos \theta_i - z]^2 = L_a^2 \tag{3}$$

Substitute η_i into the equation (3) to obtain the equation set (4).

$$\begin{cases} \left[\frac{\sqrt{3}}{2}(R + L_b \sin \theta_1 - r) - x \right]^2 + \left[\frac{1}{2}(R + L_b \sin \theta_1 - r) - y \right]^2 + [-L_b \cos \theta_1 - z]^2 = L_a^2 \\ \left[-\frac{\sqrt{3}}{2}(R + L_b \sin \theta_2 - r) - x \right]^2 + \left[\frac{1}{2}(R + L_b \sin \theta_2 - r) - y \right]^2 + [-L_b \cos \theta_2 - z]^2 = L_a^2 \\ x^2 + [-(R + L_b \sin \theta_3 - r) - y]^2 + [-L_b \cos \theta_3 - z]^2 = L_a^2 \end{cases} \quad (4)$$

The parameters of Delta mechanism are shown in Table 1.

Table 1

The parameters of Delta mechanism							
Symbol	L_a/mm	L_b/mm	R/mm	r/mm	η_1	η_2	η_3
Values	800	300	150	50	30°	150°	90°

There are three equations in the equation set (4). The forward kinematics analysis is carried out to obtain the workspace of the Delta mechanism. Taking the mobile platform center coordination (x, y, z) as the unknown quantities, the mobile platform center coordination can be resolved when the given value of each driving arm $(\theta_1, \theta_2, \theta_3)$ is determined. Within the value range of θ_i , the set of points of the Delta mechanism mobile platform can be obtained by the method of exhaustion (Liu et al., 2019; Zhang et al., 2019). The set of points can be densified in the three-dimensional coordinate system to get the Delta mechanism’s workspace.

Numerical Simulation of Propane Combustion

The burner, the key component of the flame weeding robot, is mainly composed of a base, a nozzle and a burner tip, whose diagram of real products is shown in Figure 4(a). When it is working, the propane is sprayed from the nozzle, which is mixed with air and burned in the burner. The burner tip diameter is determined to be 30 mm and its length is 75 mm according to the structure and the size of weeding robot, and its working environment. d represents the nozzle diameter and the two-dimensional model of burner is shown in Figure 4(b).

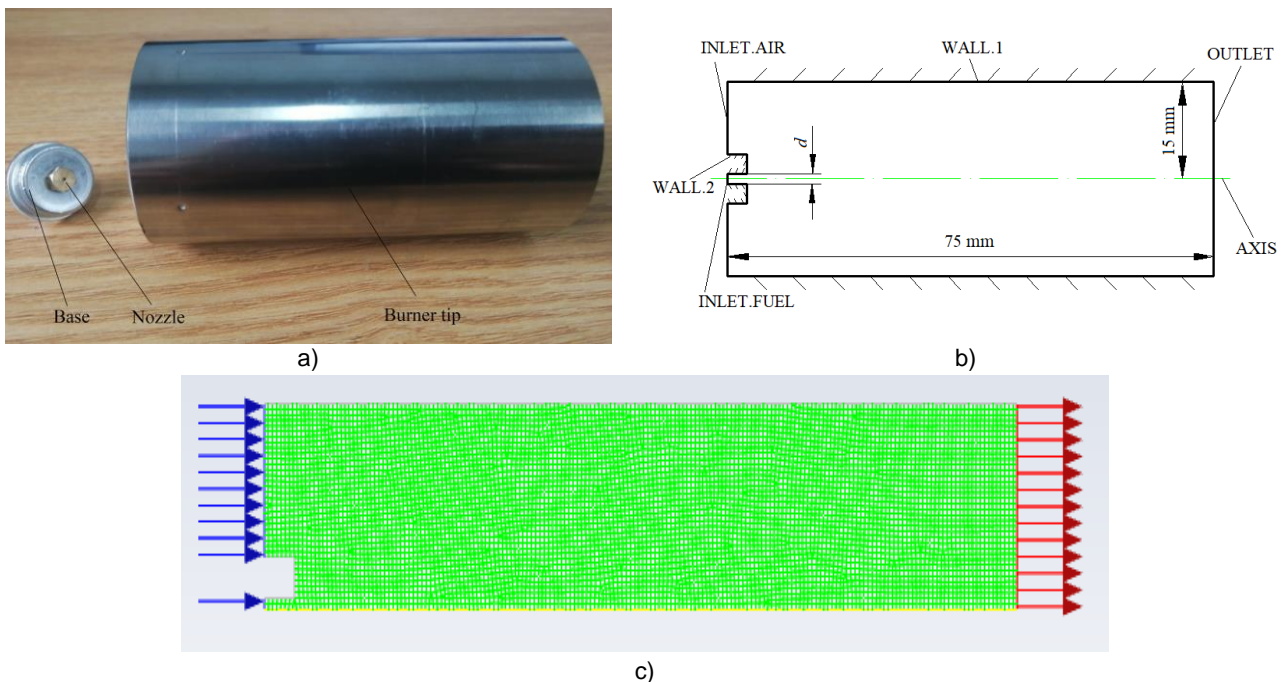


Fig. 4 - Burner model

The nozzle diameter directly affects the flame temperature distribution inside and out of the burner to further influence the effectiveness of weeding. There are a variety of nozzles with different diameters on the market.

To select the proper nozzle that is applicable to this weeder, the numerical simulation of propane combustion is carried out by Fluent on two burners whose diameters d are 0.8 mm and 1.6 mm, respectively. The main process is as follows. Firstly, the burner cross-section model is established by ANSYS ICEM CFD and is divided by the gridding, which is shown in Figure 4(c). Read the gridding and set up the solver parameters on the Fluent. Activate the option of Energy in the model settings (Tang et al., 2016). And then select the standard k-epsilon model for the turbulence model. In the dialogue box of the compositional model, activate the compositional transport and the option of the eddy-dissipation. Secondly, set up the boundary conditions and make sure that the fuel inlet velocity is set as 2.5 m/s and the air inlet velocity is set as 0.2 m/s. Lastly, the iterative computations is performed after the setting of iterative residual and the initialization of flow field.

RESULTS

Workspace Solutions and Analysis

The range of each field angle is determined to be $5^\circ \leq \theta_i \leq 110^\circ$ by the structure size of the flame weeding robot. The method of exhaustion is performed to program and solve the equation, drafting the Delta mechanism workspace in the three-dimensional coordinate system, as shown in Figure 5.

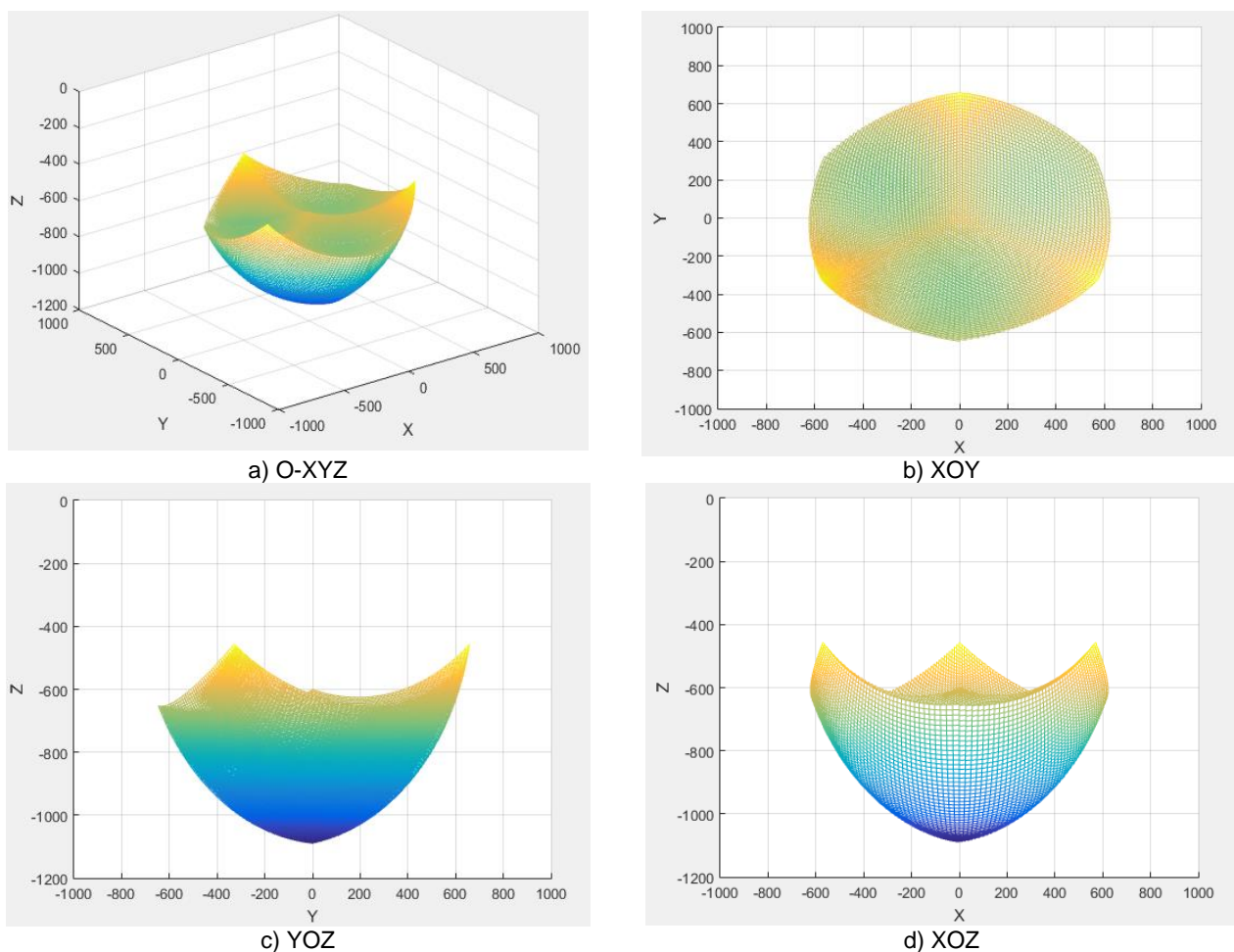


Fig. 5 - Workspace of Delta mechanism

The full-scale workspace of the Delta mechanism is the three-dimensional space in the enveloping surface, as shown in Figure 5 (a), and Figure 5 (b), (c) and (d) represent the projections of workspace on the planes of XOY, YOZ and XOZ, respectively. It can be seen from Figure 5(b) that the minimum value of x is -622.4 mm, the maximum value is 622.4 mm, the minimum value of y is -646.2 mm, and the maximum value is 658.2 mm. It can be known from Figure 5(c) and 5(d) that the minimum value of z is -1089 mm and the maximum value is -456.2 mm. The sectional view of XOZ plane is drawn by the full-scale workspace of the Delta mechanism, as shown in Figure 6. It can be seen from Figure 6 that the smart workspace can satisfy the formulas (1) and (2) simultaneously when its bottom surface diameter D is 400 mm and the height H_1 is 359.8 mm.

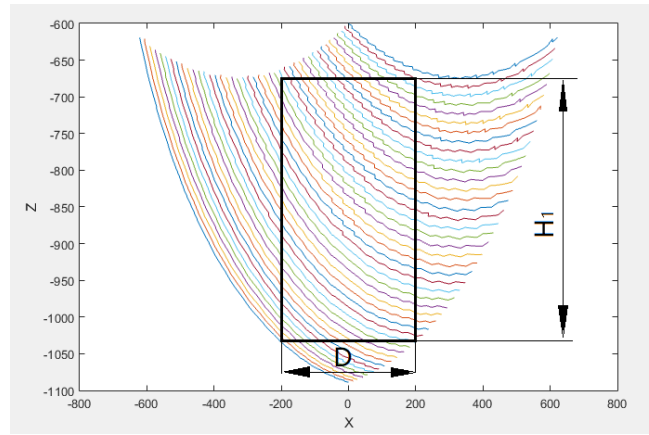


Fig. 6 –Workspace section

Numerical Simulation Results and Analysis

The flame temperature distribution diagrams of two combust with nozzle diameters of 0.8 mm and 1.6 mm are shown in Figure 7 (a) and (b) by the numerical simulation of the propane combustion process. It can be seen that the maximum flame temperature during the propane combustion is in or near the center of the burner, and the maximum temperature is 1,830 K.

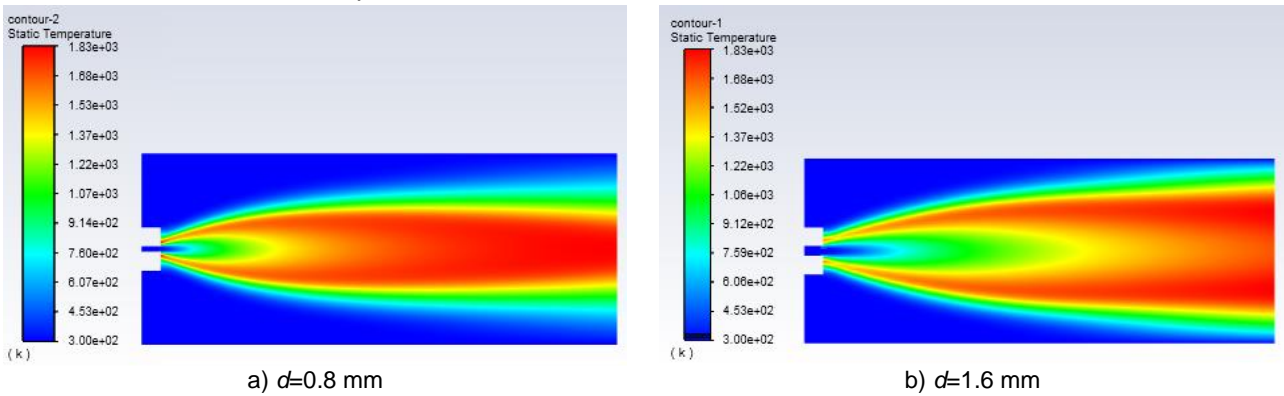


Fig. 7 - Temperature distribution inside burner

The CFD-Post module is utilized to have the post-process on the numerical simulation results to obtain the stereoscopic render effects of the flame temperature distributions in two burners, as shown in Figure 8 (a) and (b).

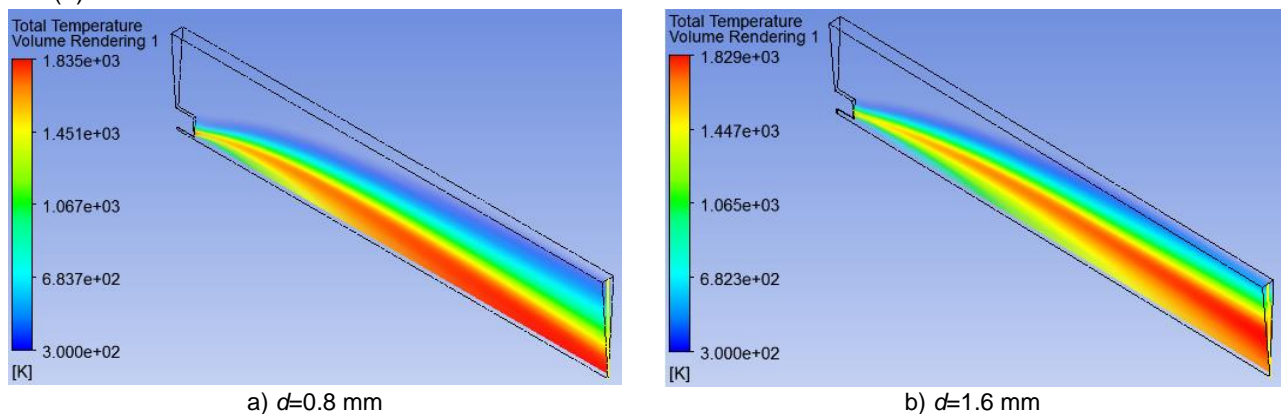


Fig. 8 -The stereoscopic render effects of the flame temperature distribution

To accurately obtain the burner outlet temperature distribution, it needs to take the center of the burner outlet as the starting point and draw a line segment that is perpendicular to the wall surface. Thus, the changing curve is displayed when each temperature on the output line segment changes with different positions. As shown in Figure 9 (a) and (b), the minimum scale value on the abscissa should be 0.5mm in accordance with the distance between the abscissa representative point and the center of the burner outlet, and the ordinate represents the temperature.

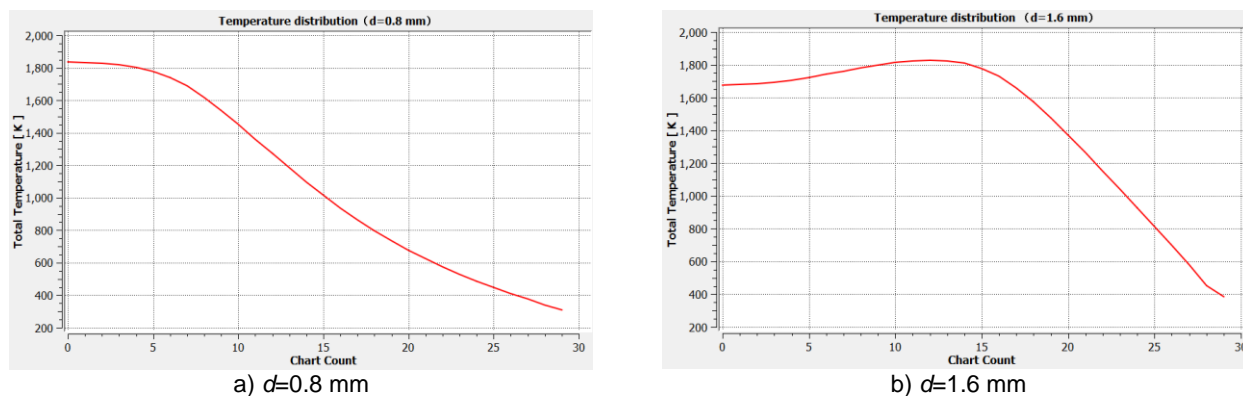


Fig. 9 - Burner outlet temperature variation curve

Comparing with Figure 9(a) and (b), it can be seen that the maximum flame temperatures are close at the outlets of two burners whose nozzle diameters are 0.8 mm and 1.6 mm, respectively. Owing to the symmetrical temperature distribution in the burner outlet, it can be deduced that the flame widths are 21.5 mm and 27 mm respectively when the temperatures at those two outlets are above 600 K, namely when the nozzle diameter is 1.6 mm, the burner outlet has a wider high temperature flame, which meets the requirements of the flame weeding.

CONCLUSIONS

(1) Taking vegetable seedlings as research object, a flame intra-row weeding robot was designed in this paper based on the Delta mechanism. The analysis on the workspace of the Delta mechanism shows that the smart workspace meets the weeding requirements on the condition that the length of the driving arm is 300 mm, the length of the driven arm is 800 mm, the radius of the static platform is 150 mm, and the radius of the mobile platform is 50 mm.

(2) The numerically simulation on the propane combustion process in the burner was performed by the Fluent component transport model. When the nozzle diameter took different values, the analysis on the temperature distribution inside and out of the burner showed that it meets the flame weeding technical requirements on the condition that the nozzle diameter is 1.6 mm, the highest temperature is 1,830 K, and the width of the high temperature zone is 27 mm.

ACKNOWLEDGEMENTS

This research, titled “Workspace Analysis of a Flame Intra-row Weeding Robot in Vegetable Field and Numerical Simulation of Propane Combustion”, was funded by the Science and Technology Innovation Fund of Shanxi Agricultural University (2017015), by project: “Major Special Projects for the Construction of China Modern Agricultural Industrial Technology System (Grant No. CARS-07-D-2)”.

REFERENCES

- [1] Deng M.Y., (2018), Mineral Content and Nutritional Value Evaluation and Risk Assessment in Vegetables (蔬菜中矿物质含量测定、营养评价及风险评估). *Food Research and Development*, Vol.39, Issue 9, pp.97-102, Tianjin / P.R.C.;
- [2] Xiao T.Q., (2017), Development status of vegetable production and its mechanization in China (我国蔬菜生产概况及机械化发展现状). *Journal of Chinese Agricultural Mechanization*, Vol.38, Issue 8, pp.107-111, Nanjing / P.R.C.;
- [3] Chen Z.W., (2015), Study review and analysis of high performance intra -row weeding robot (智能高效株间锄草机器人研究进展与分析). *Transactions of the Chinese Society of Agricultural Engineering*, Vol.31, Issue 5, pp.1-8, Beijing / P.R.C.;
- [4] Liu W., (2017), Research Status of Mechanical Intra—Row Weed Control in Row Crops (作物株间机械除草技术的研究现状). *Journal of Agricultural Mechanization Research*, Vol.39, Issue 01, pp.243-250, Harbin / P.R.C.;
- [5] Wu T., (2019), Analysis and Study on Intelligentized Technologies of Intra-row Weeding Mechanical Control (智能化作物株间机械除草技术分析与研究). *Journal of Agricultural Mechanization Research*, Vol.41, Issue 6, pp. 7- 12+18, Harbin /P.R.C.;

- [6] Wang H.C., (2018), Study Status of the End-actuator of Intra-row Weeding Machine. *Journal of Anhui Agricultural Sciences*, Vol. 46, Issue 17, pp.22-26+29, Hefei / P.R.C.;
- [7] Hu L., (2012), Development and experiment of intra-row mechanical weeding device based on trochoid motion of claw tooth (基于爪齿余摆运动的株间机械除草装置研制与试验). *Transactions of The Chinese Society of Agricultural Machinery*, Vol.28, Issue 14, pp. 10- 16, Beijing / P.R.C.;
- [8] Huang X.L., (2012), Optimal Design of Rotating Disc for Intra-row Weeding Robot (苗间锄草机器人锄草刀优化设计). *Transactions of the Chinese Society for Agricultural Machinery*, Vol.43, Issue 6, pp.42-46, Beijing / P.R.C.;
- [9] Jiang Y., (2020), Design and experiment of pneumatic paddy intra-row weeding device (气动式水稻株间机械除草装置研制). *Journal of South China Agricultural University*, Vol.41, Issue 6, pp.37-49, Guangzhou / P.R.C.;
- [10] Zhou F.J., (2018), Design and Experiment of Cam Rocker Swing Intra-row Weeding Device for Maize (凸轮摇杆式摆动型玉米株间除草装置设计与试验). *Transactions of the Chinese Society for Agricultural Machinery*, Vol.49, Issue 1, pp.84-92, Beijing / P.R.C.;
- [11] Han B., (2020), Design and Experiment of Soybean Intra-row Weeding Monomer Mechanism and Key Components (大豆株间除草单体机构及关键部件设计与试验). *Transactions of the Chinese Society for Agricultural Machinery*, Vol.51, Issue 06, pp.112-121, Beijing / P.R.C.;
- [12] Reiser D., (2019), Development of an Autonomous Electric Robot Implement for Intra-Row Weeding in Vineyards. *Agriculture*, Vol.9, Issue 1, pp. 18-29, Basel / Switzerland;
- [13] Kumar S.P., (2020), A fuzzy logic algorithm derived mechatronic concept prototype for crop damage avoidance during eco-friendly eradication of intra-row weeds. *Artificial Intelligence in Agriculture*, Vol.4, pp.116-126, Amsterdam / Netherlands;
- [14] Wang J.W., (2021), Design and Experiment of Jet-type Paddy Field Weeding Device between Plants (射流式水田株间除草装置设计与试验). *Transactions of the Chinese Society for Agricultural Machinery*, <http://kns.cnki.net/kcms/detail/11.1964.S.20210917.1058.004.html>. Beijing / P.R.C.;
- [15] Rajković M., (2021), Sustainable Organic Corn Production with the Use of Flame Weeding as the Most Sustainable Economical Solution. *Sustainability*, Vol.13, Issue 2, pp. 572-583, Basel / Switzerland;
- [16] Raja R., (2020a), Real-time weed-crop classification and localization technique for robotic weed control in lettuce. *Biosystems Engineering*, Vol.192, Issue 4, pp. 257-274, Amsterdam / Netherlands;
- [17] Trygve U., (2018), Robotic in-row weed control in vegetables. *Computers and Electronics in Agriculture*, Vol.154, Issue 11, pp. 36-45, Amsterdam/Netherlands;
- [18] Raja R., (2020b), Real-time robotic weed knife control system for tomato and lettuce based on geometric appearance of plant labels - ScienceDirect. *Biosystems Engineering*, Vol.194, Issue 6, pp. 152-164, Amsterdam / Netherlands;
- [19] Kennedy H., (2020), Crop signal markers facilitate crop detection and weed removal from lettuce and tomato by an intelligent cultivator. *Weed Technology*, Vol.34, Issue 3, pp. 342-350, Lawrence / USA;
- [20] Knezevic S. Z., (2014), Growth stage affects response of selected weed species to flaming. *Weed Technology*, Vol.28, Issue 1, pp. 233-242, Lawrence / USA;
- [21] Guan P., (2019), Research and realization of key Technology of Flame weeding Machine for Chinese Medicinal Materials (中药材火焰除草机关键技术研究及实现). Master Degree Dissertation, Shanxi Agricultural University, Taiyuan / P.R.C.;
- [22] Fu X.M., (2016), Review on Weed Management in Organic Orchards at Home and Abroad (国内外有机果园杂草管理技术研究综述). *Weed Science*, Vol.34, Issue 04, pp.7-11, Beijing / P.R.C.;
- [23] Zhang M.W., (2018), *Principle and application of industrial robot: DELTA parallel robot* (工业机器人原理及应用: DELTA 并联机器人), ISBN 9787560373171, Harbin University of Technology Press, P.R.C.
- [24] Liu L., (2019), Workspace simulation and trajectory planning for tomato sorting Delta robot, *INMATEH-Agricultural Engineering*, Vol. 58, Issue 2, pp.177-186, Bucharest / Romania.
- [25] Zhang X.C., (2019), Trajectory Planning for Product Sorting and Error Analysis of a Delta Parallel Robot (Delta 机器人产品分拣轨迹规划仿真). *Computer Simulation*, Vol.36, Issue 11, pp.295-299+364, Guangzhou / P.R.C.;
- [26] Tang J.P., (2016), *ANSYS fluent 16.0 super learning manual* (ANSYS FLUENT 16.0 超级学习手册), ISBN 9787115422040, Posts and Telecommunications Press, Beijing / P.R.C.

**WORK MOTION STUDY OF PIVOT TYPE TRAILER OPERATION
ON TWO WHEEL TRACTORS**
/
**STUDI GERAK KERJA PENGOPERASIAN TRAILER TIPE PIVOT
PADATRAKTOR RODA DUA**

Muhammad Dhafir¹⁾, Muhammad Idkham, Safrizal, Agus Arip Munawar

Agriculture Engineering Department Universitas Syiah Kuala / Indonesia

Tel: +628116810529.; E-mail: m.dhafir2001@gmail.com

DOI: <https://doi.org/10.35633/inmateh-65-09>

Keywords: ROM, pivot type trailer, two-wheel tractor, motion

ABSTRACT

This study aims to analyze the pivot type trailer operation with an ergonomic approach and the necessary interventions required to minimize work risks. Data collection was carried out using questionnaires and video recordings of the operators when the tractors as well as trailers were being operated at various conditions such as track, load, speed, straight motion or turn. Based on the Range of Motion (ROM) analysis, it was discovered that while operating this pivot type trailer, the upper body segments such as neck, shoulders, elbows and back of the operator felt comfortable while he was controlling the tractor. Meanwhile, in the lower body segments, such as the thighs and knees, the operator generally felt discomfort. Furthermore, the analysis of the operator's subjectivity perception showed that discomfort was felt at several segments of the upper and lower body, such as the hands and knees. Therefore, several ergonomic interventions are required to increase the comfort of operating this pivot type trailer.

ABSTRACT

Tujuan dari kajian ini adalah untuk menganalisis pengoperasian trailer tipe pivot dengan pendekatan ergonomi dan intervensi yang diperlukan untuk meminimalkan risiko kerja. Pengambilan dan pengumpulan data rekaman video operator dan kuisiner saat pengopearsaian traktor dan trailer dengan berbagai kondisi lintasan, muatan, kecepatan, gerakan lurus atau belokan. Hasil analisis natural Range of Motion (ROM) didapatkan bahwa secara umum pada pengoperasian trailer tipe pivot ini segmen tubuh bagian atas yaitu leher, bahu, siku, dan punggung operator dengan nyaman dapat mengendalikan traktor, sedangkan pada segmen bagian bawah tubuh yaitu paha dan lutut secara umum operator tidak nyaman karena lutut cenderung tertekuk sehingga perlu penyesuaian ketinggian tempat duduk. Analisis persepsi subjektifitas operator menunjukkan beberapa segmen tubuh atas dan bawah yang dirasakan kurang nyaman yaitu tangan dan lutut. Beberapa intervensi ergonomi diperlukan untuk meningkatkan kenyamanan pada pengoperasian trailer tipe pivot ini.

INTRODUCTION

Two-wheeled tractor is commonly used by farmers in Indonesia, both on paddy fields (wetlands) and dry land. This is because it is suitable for agricultural activities in the country, which generally has relatively small plots of land. Furthermore, from an economic point of view, it is relatively cheaper to purchase, operate and maintain compared to other types of tractors.

The two-wheeled tractor is actually not only meant for land cultivation but also used for other purposes when some parts are adjusted and added. For example, it is used in the fertilization process, by adjusting the width of the wheels and fertilizer coupling, as well as spraying process. Furthermore, it is used as a means of transporting the agricultural products.

The use of this tractor to tow conventional trailers as a means of transportation is widely applied. This is achieved by attaching the hitch end of the trailer to the hitch point of the tractor behind the gear box, while the operator sits a little backward on the trailer hitch. However, this conventional trailer has the disadvantage of turning, where the tractor handlebar moves away from the operator's control position. This is because the handlebars have turned to follow the body of the tractor, while the operator's seat is yet to turn. Consequently, the position of the handlebar becomes out of the operator's reach, therefore the operator has to bend over to get both control grips of the tractor handlebar.

For turns, especially over large radii, the operator has to get out of the seat to control the tractor. This causes fatigue, discomfort, difficulty, risk of injury and even work accidents for the operator.

Dhafir et al. (2019) modified the conventional trailer to be a pivot type. In this type of trailer, the axle is behind the operator, therefore it is possible to fully control the tractor in a straight line or turn (Figure 1a). The performance test results showed that it is better than conventional trailers, but it has never been tested on the aspect of safety and operator comfort.



(a) (b)
Fig. 1 - The position of the operator when turning 90°
 (a) pivot type trailer (b) conventional trailers (*Dhafiret al., 2019*)

Therefore, it is necessary to carry out an analysis of the operator's work motion, while operating a pivot-type trailer to determine the ergonomic risks related to its operation and modifications in order to minimize the risk of Musculoskeletal Disorder (MSD).

Musculoskeletal disorders (MSDs) are health problems involving joints, muscles, tendons, skeleton, cartilage, ligaments and nerves (*Van, 2016*). The level of this disorder ranges from the mildest to the most severe, which interferes with concentration at work, causes fatigue and ultimately reduces productivity (*Harcombe, 2014*).

Barnes (1980) stated that motion study is a branch of ergonomic studies commonly used to design an effective method, procedure or work method, with the least possible effort to obtain optimal results. Therefore, motion study may also be interpreted as a work method design.

Furthermore, *Syuaib (2015b)* carried out a motion and posture study of manual oil palm harvesters. The results of posture assessment using the Rapid Upper Limb Assessment (RULA) method showed that the work is outside the safe range. Meanwhile, work motion simulations produced work procedures that are able to minimize unsafe posture and musculoskeletal disorders (MSD). *Yadaf et al. (2010)* carried out a study of strength parameters in the design of manually operated agricultural equipment. These strength parameter data were very useful in designing equipment capable of providing the operator with comfort, safety and efficiency. Furthermore, *Toren (2001)* investigated muscle activity and range of motion for back rotation when driving a tractor in a sitting position. The results showed no significant difference due to the direction of back rotation performed. Therefore, the posture of the back that is twisted while driving the tractor is suspected to be a risk factor for low back pain.

This study aims to analyze the pivot type trailer operating activities with an ergonomic approach. The scope studied was a motion analysis to determine the safety and ergonomic risks of trailer operation based on the natural range of motion index and the operator's anthropometric suitability.

MATERIALS AND METHODS

Tools and Materials

The equipment used includes: (1) Yanmar two-wheeled tractor with Bromo DX model, a power of 8.5 HP, 2640 mm in length, 765mm in width, 1060cm in height, 250 kg in weight and a pivot type trailer, (2) a Handycam, (3) computer, (4) meter and calipers and (5) 18 MP digital camera.

Furthermore, some of the data processing and analysis software used include computer-aided design (CAD) 2013 software, spreadsheet and video to jpeg converter.

Study Stages

This study is generally described in the flow chart shown in Figure 2.

Study Subject

The subjects involved were two-wheeled tractor operators consisting of 4 (four) adult males. The selected subjects were quite close to the secondary anthropometric data of Indonesian society. Furthermore, they represented the three operator percentiles, namely the 5th, 50th and 95th percentiles. The trailer operation paths were paved roads and agricultural land on empty and full trailer load conditions with variations in the tractor forward speed of 4 and 6 km/hour.

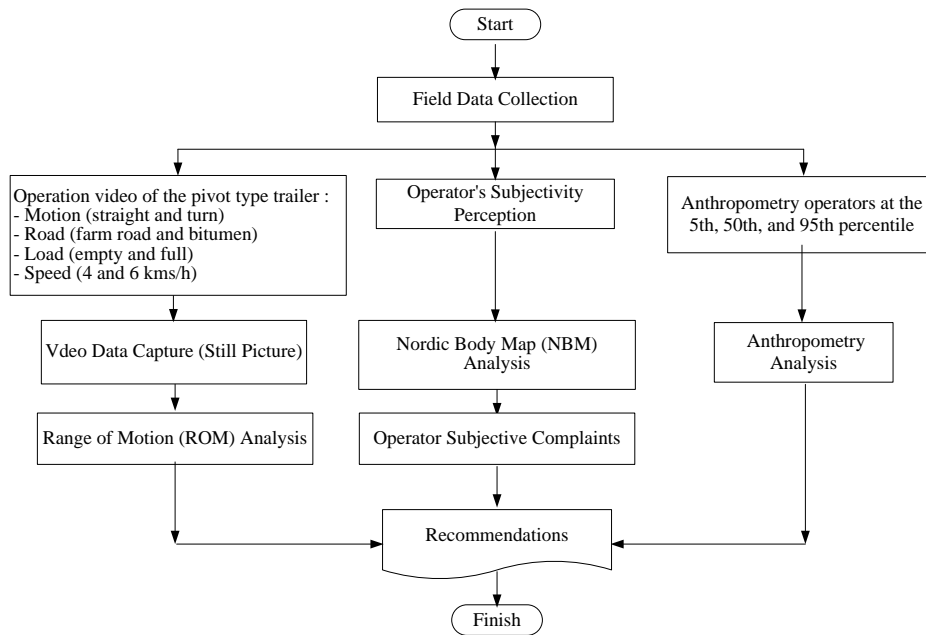


Fig. 2 - Study flow chart

Preliminary observations

The preliminary stages carried out were field observations, including primary and secondary data collection. Field observations include observing the operation of a two-wheeled tractor with a trailer. Primary data includes measurement of dimensions of two-wheeled tractors and trailers, while secondary data includes the anthropometric data of Indonesians according to *Syuaib (2015a)*.

Data Collection

Data collection for the pivot type trailer prototype was carried out by 4 (four) male subjects with each individual carrying out 4 repetitions. Furthermore, tests were carried out on operation in a straight and turning line on (a) paved and (b) agricultural land with (a) empty and (b) full load and at a tractor forward speed of 4 and 6km/hour. Figure 3 shows the line of the pivot-type trailer operation test.

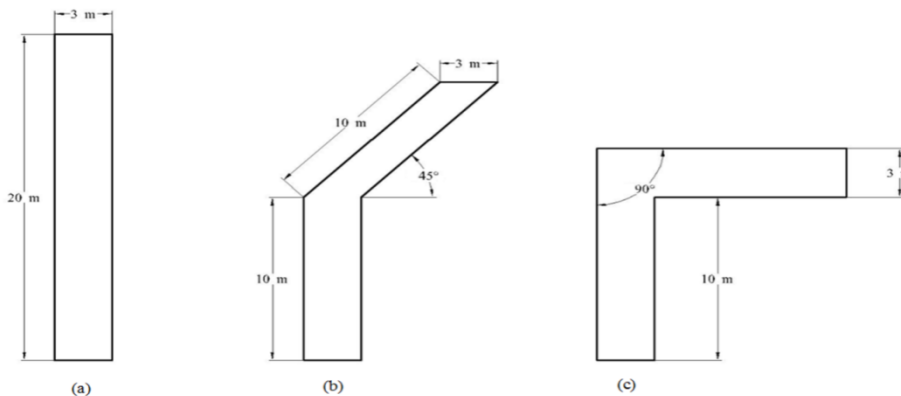


Fig. 3 - Line of trailer operation test
(a) straight (b) turn 45° and (c) turn 90°

Video cameras were used to record every movement from operating the tractor to analyzing its motion studies. The data obtained from these recordings were used as the main data source (quantitative data). Meanwhile, for motion study analysis, the video data (motion picture) was converted into still picture parts to be divided into motion elements. Furthermore, the range of motion data was obtained with the help of AutoCAD 2013 software.

The data collection design is shown in Figure 4. The data taken in this study were qualitative and quantitative. The quantitative data was in the form of a video recording while operating the two-wheeled tractor with a pivot type trailer. Meanwhile, the qualitative data was taken in the form of a questionnaire from the Nordic Body Map and distributed to the study subjects.

Data Analysis

The description of data analysis in this study is explained as follows.

a) Range of Motion (ROM)

Range of Motion (ROM) refers to the angles in the joints that normal humans are able to carry out in every segment of their body. The greater the range of motion angles carried out, the more the effort and risk incurred. Therefore, the working interval data for each element was analyzed by dividing it into four zones, namely the comfort, safe, alert and dangerous zone (*Openshaw, 2006*).

b) Nordic Body Map (NBM)

Nordic Body Map (NBM) is a method for obtaining complaints on Musculoskeletal Disorders (MSD) (*Sofyan and Amir, 2019*). It was used in the form of a questionnaire consisting of complaints regarding 27 body parts with four levels, which include no pain, mild, moderate and severe. The subjective perception of the operators was analyzed to determine which parts of the body experienced the greatest MSD complaints in relation to operation of the two-wheeled tractor. However, NBM cannot be used as a clinical diagnosis because it is subjective and specifically based on the subject's perception, not on a health diagnosis (*Suriyatmini, 2010*).

RESULTS

Operator Anthropometry

Ideally, the operator anthropometry chosen was one capable of representing the three percentiles of Indonesian society (5, 50, and 95%), but in reality, there were difficulties in fulfilling the proportional sample. Therefore, an operator close to the size of Indonesian society was chosen.

The anthropometric data for the operators of the trailer are shown in Table 1. As shown in the table, operator A represents the 5th percentile, operator B the 95th percentile, while operator C and D the 50th percentile. Furthermore, operator C was chosen to represent fat operators. Therefore, anthropometric data is very important as a basis in designing tools, equipment and work procedures in order for productivity compatibility to be optimal.

Table 1

Operator anthropometry for study subjects

No	Body Dimensions	Operator A (21 years)	Operator B (38 years)	Operator C (27 years)	Operator D (57 years)
1	Body Weight (kg)	62	59	91.2	69.3
2	Standing height	154	168.8	164	164.2
3	Eye height	142.8	158	153.2	153.4
4	Shoulder height	125.5	138.4	134.4	136.4
5	Elbow height	94.8	107.9	103.1	103.3
6	Wrist height	89.1	101.9	97.1	97.3
7	Knuckle height	65.1	77	72.2	72.4
8	Fingertip height	54.8	66.6	61.8	62
9	Hand stretch length	156.5	175	169	170
10	Elbow stretch length	78.4	93	87	88
11	Vertical hand reach	179.9	197.6	193.6	195.6
12	Horizontal grip reach	69	76	73	76

Table 1
(continuation)

No	Body Dimensions	Operator A (21 years)	Operator B (38 years)	Operator C (27 years)	Operator D (57 years)
13	Horizontal arm reach	80.2	87.5	84.5	87.5
14	Sitting height	84.3	84.8	82.7	79.8
15	Eye height when sitting	72.2	76.1	71.2	68.5
16	Shoulder height when sitting	52.9	57	55.8	52.2
17	Elbow height when sitting	20	23	23.6	19.7
18	Knee height	45.8	51.5	51.3	52.3
19	Upper limb length	53	55.5	55	52
20	Popliteal upper limb length	39	48	50	49
21	Popliteal	18.9	18.2	24.4	22
22	Chest width	36.1	44.2	54.9	47.2
23	Shoulder width	25.2	32.5	43.2	35.5
24	Hip width	29	35	32.2	33.7
25	Upper sleeve length	41	47	44	47
26	Hand length	16.7	18.2	17	18.7
27	Palm length	8.8	10.6	10.5	11.1
28	Hand width	3.5	4.2	4	4.7
29	Grip diameter (inside)	22	25.5	24	26
30	Foot length	8.4	10.2	9.3	13

Results of Work Motion Analysis in Pivot Type Trailer Operation

The work motion analysis was carried out by observing the working motion of the pivot-type trailer operation with reference to the body's Range of Motion (ROM). An example is taken from operator B for motion analysis as shown in Figure 4.

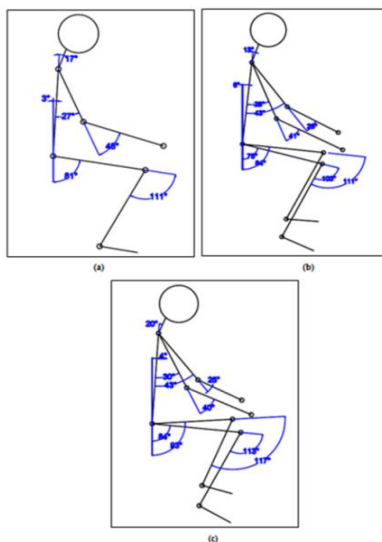


Fig. 4 - The work motion patterns of operator B on asphalt roads:
(a) go straight, (b) turn 45°, (c) turn 90°

Based on the results of the analysis of motion and natural range of motion (SAG) for each test element as a whole for operator B, the ergonomic risk is analyzable based on the aspect of work motion as presented in Table 2. It explains the risk of motion in each joint segment for each element of work accumulatively.

Zone-0 (white) and zone-1 (green) represent the safe zones for the subject's muscles and joints when working, zone-2 (yellow) is a zone that is still allowed but with a short time, the load is neither too heavy nor repetitive, but vigilance and care is required to work long and repetitive, while zone-3 (red) is a zone that should be avoided because it is dangerous for joints and muscles (Openshaw, 2006).

Table 2

Distribution of operator B Range of Motion for each body segment

Test number	Ef		Sf		Bf	Nf	Hf		Kf	
	R	L	R	L			R	L	R	L
B1	48	48	27	27	3	17	81	81	111	111
B2	41	25	28	43	6	13	75	84	103	111
B3	40	25	30	43	4	20	84	93	113	117
B4	46	46	27	27	22	19	86	86	113	113
B5	90	17		55	13	20	74	86	96	117
B6	73	33	11	46	14	16	78	90	100	101
B7	36	36	32	32	10	19	68	68	96	96
B8	60	42	16	30	10	17	70	84	99	103
B9	32	68	38	13	10	18	70	86	95	108
B10	45	45	27	27	3	19	68	68	102	102
B11	60	50	18	27	10	18	69	86	101	114
B12	55	37	21	32	14	20	73	83	92	101
B13	51	51	22	22	4	14	81	81	110	110
B14	53	47	26	30	3	19	80	100	108	118
B15	29	67	32	15	6	20	85	94	112	117
B16	57	57	26	26	9	10	83	83	108	108
B17	46	63	32	14	10	17	80	86	105	104
B18	43	36	29	36	15	14	82	88	106	111
B19	56	56	18	18	9	18	62	62	106	106
B20	66	49	19	35	16	16	83	88	102	113
B21	45	66	32	17	13	11	81	86	110	115
B22	73	73	20	20	21	16	76	76	106	106
B23	74	55	19	38	24	18	76	88	102	114
B24	75	60	33	20	24	18	76	85	101	102

	Road type	Load	Speeds (km/s)/h	Motion		Road type	Load	Speeds (km/s)/h	Motion
B1	Bitumen	Empty	4	Straight	B13	Farm road	Empty	4	Straight
B2	Bitumen	Empty	4	Turn 45°	B14	Farm road	Empty	4	Turn 45°
B3	Bitumen	Empty	4	Turn 90°	B15	Farm road	Empty	4	Turn 90°
B4	Bitumen	Empty	6	Straight	B16	Farm road	Empty	6	Straight
B5	Bitumen	Empty	6	Turn 45°	B17	Farm road	Empty	6	Turn 45°
B6	Bitumen	Empty	6	Turn 90°	B18	Farm road	Empty	6	Turn 90°
B7	Bitumen	Full	4	Straight	B19	Farm road	Full	4	Straight
B8	Bitumen	Full	4	Turn 45°	B20	Farm road	Full	4	Turn 45°
B9	Bitumen	Full	4	Turn 90°	B21	Farm road	Full	4	Turn 90°
B10	Bitumen	Full	6	Straight	B22	Farm road	Full	6	Straight
B11	Bitumen	Full	6	Turn 45°	B23	Farm road	Full	6	Turn 45°
B12	Bitumen	Full	6	Turn 90°	B24	Farm road	Full	6	Turn 90°

Observing the analysis results from the motion ergonomics perspective for operator B on the pivot type trailer operation, it is seen that that upper body segments, which include elbows (EF), shoulders (SF), back (BF) and neck (NF), of the operator were safe and comfortable while he was controlling the tractor. Meanwhile, the lower body segments, which include the thighs (HF) and knees (KF), were uncomfortable because the knees tend to bend.

To detect operator discomfort while working, the ROM method is applicable (Table 3). Therefore, for all operators (A, B, C, and D), the distribution of the operator's Range of Motion is summarized in Table 4.

Table 3

Range of Motion on several zones

	Movement	Range of movement zone (in°)			
		Zone 0	Zone 1	Zone 2	Zone 3
Neck (NF) *	Flexion	0 – 9	10 – 22	23– 45	46+
Shoulder (SF) *	Flexion	0 – 19	20 – 47	48– 94	95+
Elbow (EF) **	Flexion	0– 28	29– 62	63– 124	125+
Back (BF) *	Flexion	0 – 10	11 – 25	26– 45	46+
Thigh (HF) **	Flexion	0– 22	23– 50	51– 99	100+
Knee (KF) **	Flexion	0– 21	22– 48	49– 94	95+

Source: *) Chaffin (1999) and Woodson (1992) referred to in Openshaw (2006)

**) Processed based on data sourced from Houy 1983 referred to in Sanders and McCormick (1993)

Table 4

The results of operator ROM analysis on pivot type trailer operation

Parts of body	Movement	Summary of ROM values			
		A	B	C	D
Neck	Flexion (NF)	8 – 24°	10 – 20°	15 – 42°	10 – 49°
Shoulder	Flexion (SF)	11 – 59°	11 – 55°	6 – 53°	5 – 70°
Elbow	Flexion (EF)	21 – 113°	17 – 90°	11 – 78°	8 – 95°
Back	Flexion (BF)	0 – 32°	3 – 24°	0 – 17°	8 – 31°
Thigh	Flexion (HF)	43 – 80°	62 – 100°	57 – 93°	51 – 84°
Knee	Flexion (KF)	29 – 92°	92 – 118°	79 – 118°	76 – 115°

Tables 3 and 4 show the results of the analysis of potential risks of operator motion. The Range of Motion (ROM) analysis shows that in general, the upper body segments such as the neck (NF), shoulders (SF), elbows (EF) and back (BF) are in the safe zone for operators A, B and C. This implies that the upper body segment of the pivot-type trailer operation makes the operator comfortable while controlling the tractor.

However, operator D was an exception since the neck (NF) is often in the danger zone. This is because it is necessary to look down when turning to get the position of the auxiliary wheel which assists in turning and the D operator needs to adjust it longer for the use of this pivot type trailer. Therefore, some exercises and adjustments are needed for the operator in using this pivot type trailer.

Furthermore, the lower body segments of operator A such as thighs and knees (which represent the 5th percentile) were shown to be in a comfortable state, because the foot was well rested on the footrest and the knee was not bent. Meanwhile, operators B, C and D were generally in an uncomfortable condition, due to the tendency of the knee to bend during operation, especially for operator B (representing the 90th percentile) that always need to bend the knee during trailer operation because it has a different longer leg size.

The lower part of the body was influenced by the operator's seat height and foot seat. This is because when it is too high, it causes the foot to not tread properly and hang, while when it is too low, it causes the knees to bend and feel uncomfortable. Therefore, a mechanism capable of adjusting the operator's seat height (seat) is needed.

Operators Subjective Analysis Results

Subjective assessment was carried out in the form of filling out a questionnaire to obtain the complaints of the operator on body parts, pain, or discomfort, which is mostly felt when operating a pivot type trailer.

Figure 5 shows the distribution of musculoskeletal discomfort, and it was discovered that the operator experienced fatigue or musculoskeletal discomfort especially in the upper limbs which include the hands, forearms and upper arms by 42%. Furthermore, it was discovered that all operators felt pain in the right and left hands. According to the information obtained from the operators, these pains were due to the stiffness of the clutch lever, which consequently requires a lot of force to press it. Therefore, it is necessary to repair and maintain the clutch in order to solve the problem.

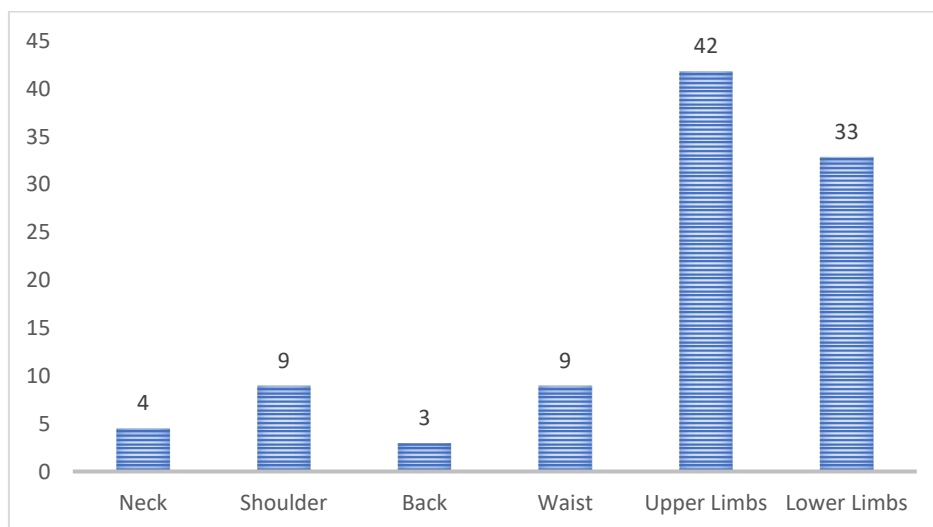


Fig. 5 - Operators subjective perception of complaints on body parts on the pivot type trailer operation

For the lower limbs, which include the thighs, knees, calves and feet, the percentage of discomfort felt by the operators was 33%.

Meanwhile, operator A did not experience any feeling of discomfort, while operators B, C and D experienced it, which may be due to the bending of the knee in order to adjust the seat height. However, this relatively short seat height was comfortable for Operator A, which represents the 5th percentile.

For the limb (waist) which includes the waist, and buttocks, the percentage of discomfort felt was 9%. This was due to the twisting motion on the back when the trailer is in a turning motion. Furthermore, the discomfort felt at the neck and back was 4 and 3%, respectively, due to the turning movements.

In general, the operators had the correct perception of the most uncomfortable body parts. Therefore, it can be used as a basis for making ergonomic interventions to reduce work risks which leads to increased productivity.

Ergonomic Intervention

According to Syaib *et al.* (2015), ergonomic interventions is carried out to reduce work risks and also increase productivity, by improving work procedures, improving tool design and using personal protective equipment/clothing.

Therefore, based on the analysis of motion and subjective perceptions above, to improve safety and comfort in operating a *pivot type trailer*, some ergonomic interventions are needed, namely:

1. Repairing and maintaining the clutch rotary lever to make it more comfortable for use.
2. Operator seat height (seat)

To increase the comfort during *pivot type trailer* operation, the seat height should be adjustable to the operators' anthropometry because of their different sizes. Therefore, an adjustable seat height mechanism is needed.

According to Nurmianto (2008), seat height based on anthropometric measurements of knee height (*popliteal*), is carried out by adding up the height of the shoes. According to Bendix (1987), the recommended seat height is about 30 to 50mm above the *popliteal* height. Therefore, the recommended adjustable seat design based on Table 5 is a minimum and maximum height of 410 and 490, respectively.

Table 5

Description	High(mm)	
	Fold height in knee (<i>popliteal</i>)	High seating design
Percentile 5	365	410
Percentile 50	405	440
Percentile 95	445	490

The recommended adjustment mechanism is shown in Figure 6. The mounting posts were connected to the mounting frame, while the fastener was fixed at the meeting point of the mounting post and frame. Furthermore, to adjust the seat height, the lock lever was relaxed. Therefore, it is possible to pull or press the seat posts axially with the seat frame to adjust the height as desired.

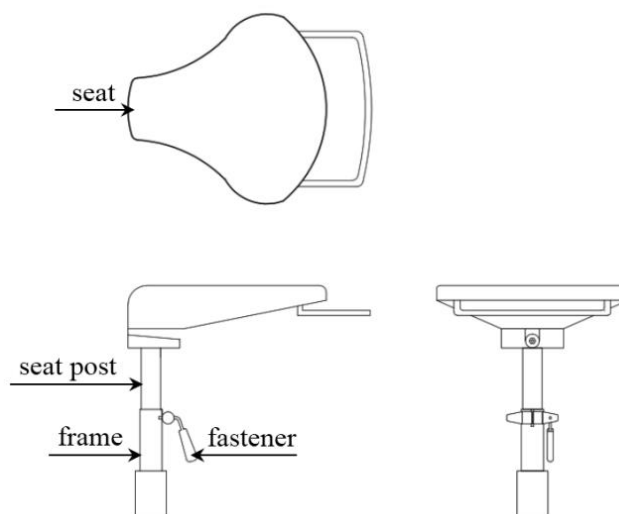


Fig. 6 - Adjustable mechanism on the operator's seat

CONCLUSIONS

1. The results of the motion hose operator analysis showed that in general the operation of the pivot type trailer for the upper body segment, namely neck, shoulder, elbows and back, is in a safe zone for all operators. Meanwhile, for the lower body segment, operators B, C and D's thighs and knees were uncomfortable, while operator A, representing the 5th percentile, was in a comfortable area.
2. The results of the subjective perception of the operators regarding complaints on the most uncomfortable pivot type trailer operating body parts were 42% and 33% for the upper and lower limb, respectively.
3. Ergonomic interventions that are capable of increasing safety and comfort during the operation of the pivot-type trailer include improving the clutch rotating lever, as well as the addition of a mechanism capable of adjusting to the seat height settings of operators.

REFERENCES

- [1] Barnes, R.M. (1980). *Motion and Time Study: Design and Measurement of Work*. [handbook, 7th ed.]. John Wiley & Sons. New York & Toronto.
- [2] Bendix T. (1987). *Adjustment of the seated workplace-with special reference to heights and inclinations of seat and table*. Dan. Med. Bull. 34(3):125-139.
- [3] Dhafir M, Mandang T, Hermawan W, Syuaib MF. (2019). Desain Ergonomis Sistem Penggunaan Trailer pada Traktor Roda Dua. *Jurnal Keteknik Pertanian* 7(1):99-106.
- [4] Harcombe H. (2014). *Musculoskeletal disorders Among Nurses Compared with Two Other Occupational Groups*. *Occup Me.* 64(8): 601-607.
- [5] Nurmianto E. (2008). *Ergonomi Konsep Dasar dan Aplikasinya*. Ed ke-2. Surabaya (ID): Guna Widya.
- [6] Openshaw S, Taylor E. (2006). *Ergonomics and Design A Reference Guide*. [e-book] Allsteelinc. [diunduh 2012 Mei 20]. Tersedia pada: <http://www.allsteeloffice.com/ergo>.
- [7] Sanders MS dan McCormick EJ. (1993). *Human Factors in Engineering and Design*. Ed ke-6. New York (US): McGraw-Hill. Inc.
- [8] Sofyan DK dan Amir. (2019). Determination of Musculoskeletal Disorders (MSDs) complaints level with Nordic Body Map (NBM). *IOP Conf. Ser.: Mater. Sci. Eng.* 505012033.
- [9] Suriyatmini S. (2010). *Review of ergonomic risk factors for musculoskeletal requests in manual handling activities for workers in the production division of PT Mitahun 2010 (Tinjauan factor risiko ergonomik terhadap keluhan musculoskeletal pada aktivitas manual handling pada pekerja di bagian produksi pt mitahun 2010)* [tesis]. Depok (ID): Universitas Indonesia.
- [10] Syuaib MF, Dewi NS, Sari TN. (2015). Study of Motion for Palm Oil Harvesting (Studi gerak pemanenan kelapa sawit secara manual). *Jurnal Keteknik Pertanian*. 3(1): 49-56.
- [11] Syuaib MF. (2015a). Anthropometric study of farm workers on Java Island, Indonesia, and its implications for the design of farm tools and equipment. *Applied Ergonomics*. 51 (2015): 222-235.
- [12] Syuaib MF. (2015b). Ergonomic of the manual harvesting task of oil-palm plantation in Indonesia based on anthropometric, postures and work motion analyses. *Agric Eng Int: CIGR Journal*. 17(3): 248-262.
- [13] Toren A. (2001). Muscle activity and range of motion during active trunk rotation in a sitting posture. *Applied Ergonomics*. 32:583–591
- [14] Van L. (2016). Prevalence of musculoskeletal symptoms among garment workers in Kandal Province. Cambodia (KH): *J Occup Health*. 58: 107-117.
- [15] Yadaf R, Nashik S, Patel NC, Gite LP. (2010). Analytical study of strength parameter of Indian farm workers and its implication in equipment design. *Agric Eng Int: CIGR Journal*. 12(2):49-54.

DESIGN AND EXPERIMENT OF A NEW ROTARY COATING MACHINE BASED ON LabVIEW

基于 LabVIEW 控制的新型旋转式包衣机的设计与试验

Xiwen Zhang, Zhanfeng Hou^{*}, Nianzu Dai

Inner Mongolia Agricultural University, College of Mechanical and Electrical Engineering, Inner Mongolia, China

Tel: 04714309215; Corresponding author E-mail: njau-hzf@163.com

DOI: <https://doi.org/10.35633/inmateh-65-10>

Keywords: seed coating; rotary coating machine; control system; LabVIEW; precise supply

ABSTRACT

In view of the problems of long coating time, complicated manual operation, high multi-seed rate of coated seeds, low qualified rate, and low degree of automation of control equipment in traditional rotary coating machine, a new type of rotary coating machine was designed while using LabVIEW with a complete electric control system, which can effectively improve the speed and quality of coating. The system uses single-chip microcomputer as the lower computer, LabVIEW as the upper computer, and uses programming electronic control technology to set seed coating parameters in advance, precisely control each part and achieve precise supply. Batch supply of powder and liquid greatly improves the automation and intelligence of the operating system, improves the coating efficiency, reduces the multi-seed rate and the seedless rate, and increases the coating pass rate. In order to improve the coating quality and the supply accuracy of the coating machine, the error analysis and calibration test of the seed supply system, powder supply system and liquid supply system were carried out. After the test verification, the supply error was controlled within 2% to meet the demand for precise supply. The test results show that the pass rate of the seeds coated by the new rotary coating machine is increased by 15% to 20% compared with the seeds coated by the traditional manual coating.

摘要

针对传统旋转式包衣机存在包衣时间长、人工操作复杂、包衣种子多籽率高合格率低、控制设备自动化程度低等问题,设计了一套新型旋转式包衣机的同时,运用 LabVIEW 设计了一套完整的电控系统,可有效提高包衣的速度和质量。该系统以单片机作为下位机, LabVIEW 做上位机,运用编程电控等技术,可提前设置种子包衣参数,精准控制各部分,对供种量、供粉量以及供液量实现精准供给。分批次供给极大提高了操作系统的自动化和智能化,提高了包衣效率的同时,降低了多籽率和无籽率,提高了包衣合格率。为提高包衣品质和包衣机的供给精度,分别对供种系统、供粉系统以及供液系统进行误差分析以及校准试验,经试验验证,供给误差控制在 2% 以内,满足精准供给的需求。试验结果表明:通过新型旋转式包衣机包衣的种子相比于传统人工添料包衣的种子包衣合格率提升 15% 到 20%。

INTRODUCTION

Seed coating technology is to use a specific coating process to make the surface of the seed and the coating agent evenly contact, and wrap it to form a smooth and firm film. Through mechanical processing, small spheres of uniform size and regular shape (including circle, ellipse, oblate, etc.) are made. The coating agent can contain a variety of components (Shao, 2018; Wu, 2017). According to specific environmental factors, proper adjustment of the dosage components can improve the ability of seeds to tolerate drought, cold, salt and alkali, and prevent soil-borne diseases. In addition, the coating technology achieves a uniform increase in seed particle size. The increase in particle size not only improves the fluidity of seeds in terms of physical properties, but also facilitates mechanized and precise seeding, thereby achieving the purpose of improving seeding efficiency and reducing seed waste. Therefore, how to use high-quality coating technology to achieve the diversity and functional specificity of coated seeds is an urgent and realistic demand (Qiu, 2017; Bai, 2020). Seed coating technology in China started in the 1980s, which is relatively late compared to some countries in the West. At present, the coating machine independently designed and produced in China has a low degree of intelligence and a relatively simple control system. The coating experience and operating proficiency of the operator directly affect the quality of the seed coating.

Considering how to optimize the coating process, select coating parameters, enrich the operating system to reduce the multi-seed rate and the seedless rate, and to increase the single-seed rate and the coating pass rate are the current mainstream research directions (Wang, 2021).

Aiming at the problems of uneven supply of powder and liquid in current seed coating technology, sticking pan, inconsistent coating formula, insufficient theoretical research of coating machine, low degree of automation, poor coating quality, etc., a new type of rotary type was researched and designed (Shu, 2017). The seed coating machine uses STM32 single-chip microcomputer as the lower computer, and the LabVIEW control system is designed as the upper computer to intelligently control the seed coating part, the powder supply part and the spray part. The automation of the coating machine is improved, and at the same time the precise supply of seeds, powders, and sprays is realized (P.T, 2016; Zhu, 2012). The modules operate in a coordinated and orderly manner to reduce the multi-seed rate and the seedless rate, increase the single-seed rate and the coating pass rate, and improve forming quality of coated seeds.

MATERIALS AND METHODS

OVERALL STRUCTURE

The seed coating machine designed this time consists of a seed supply system, a powder supply system, a liquid medicine supply system, a coating pot adjustment system and a host computer control system. The three-dimensional and two-dimensional diagrams of the overall structure are shown in Fig.1.

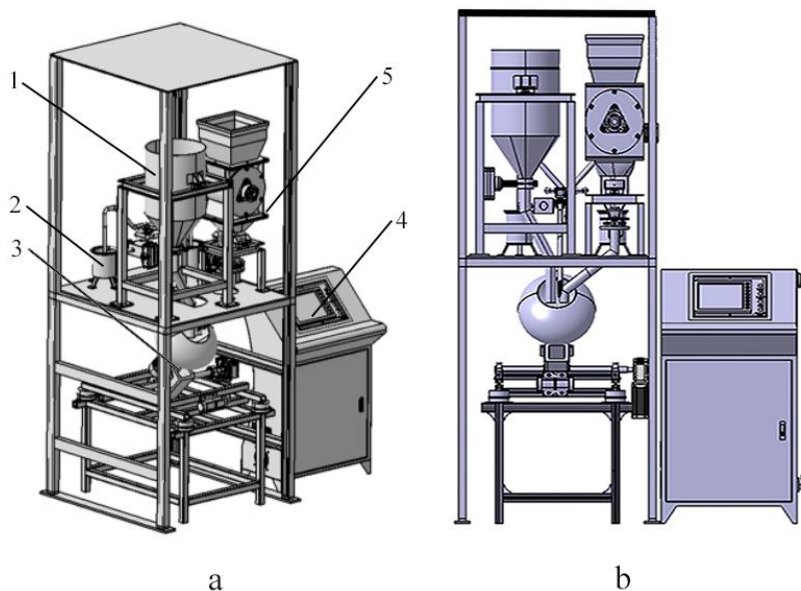


Fig. 1 - General structure

1-Seed supply system; 2-Liquid medicine supply system; 3-Coating pot adjustment system; 4-Host computer control system; 5-Powder supply system

Working principle of seed supply system

The seed supply system is mainly composed of seed charging barrel, load cell, pneumatic valve and solenoid valve. In this design, a high-precision piezoelectric weighing sensor with a range of 0-10 kg and an accuracy of less than 1 g is selected. After calibration, its combined error is <math><0.05\%</math>. It has the characteristics of high precision, easy operation, simple structure and strong anti-interference ability. Among them, the AD module uses HX711, which has 24-bit AD conversion and the accuracy level is C3. The specific seed supply process is as follows: fix two piezoelectric load cells on the tray of the seed hopper, real-time detection of the seed weight in the hopper, the weight information is converted from Digital-Analog Convert and transmitted to the single-chip microcomputer, then transmitted from the single-chip microcomputer to the upper computer. The weight is real-time display in the control system. First select the seed drop value in the control system, and then the system records the initial weight in the hopper. After starting to run, the single-chip microcomputer controls the relay to pull in, the solenoid valve opens, the pneumatic valve opens under the action of air, and the seeds begin to fall. During the falling process, the load cell detects the weight change in real time, and the control system calculates the weight loss in the hopper.

When the loss reaches the initial selected drop value, the microcontroller control relay will be disconnected, the solenoid valve will be closed, and the pneumatic valve will be closed to complete the entire drop. During the seed supply process, the seeds will fall into the coating pan and wait for coating. When the initially selected planting value is less than the weight value in the hopper, it prompts to add seeds. The system realizes accurate seed supply and continuous multi-batch operation. The three-dimensional and two-dimensional diagrams of the seed supply system is shown in Fig.2.

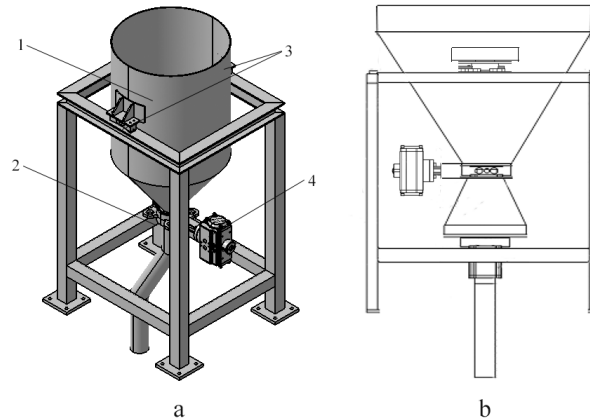


Fig. 2 - The three-dimensional diagram of the seed supply system
1- Seed charging barrel; 2- Load cell; 3- Pneumatic valve; 4- Solenoid valve

Working principle of the powder supply system

The powder supply system is mainly composed of charging barrel of powder, a stepping motor and an impeller metering disc. In order to realize the synchronous supply of powder and the precise amount of falling, a 42-line geared motor with a reduction ratio of 30 is selected to drive the impeller metering disc. This device can effectively improve the metering accuracy. The impeller metering disc is composed of 4 blades, and each blade has an angle of 90° . The volumetric method is used to control the powder supply weight. The right-angle volume between the two blades is calculated as 100 g by design. During the coating process, initially select the parameters in the control system, and set an appropriate seed-powder ratio according to the weight of the seed dropping. After starting and running, the stepping motor starts to rotate under the control of single chip microcomputer, and the impeller metering plate starts to rotate. The supply is completed every 90° rotation. The powder falls into the coating pan through the pipe under its own weight. The number of powder supply is calculated in the control system, and the cycle runs until the end of the powder supply. In order to prevent the powder from sticking and causing supply errors, the powder box is made of acrylic material, and the blade and shell of the impeller metering disc are 3D printed with PLA (Polylactic acid) material. When the shell and the impeller rotate, a large torque will be generated. The joint is designed with a fixed bearing to reduce the friction caused by rotation and reduce the error caused by the angle deviation. The three-dimensional and two-dimensional diagrams of the powder supply system is shown in Fig.3.

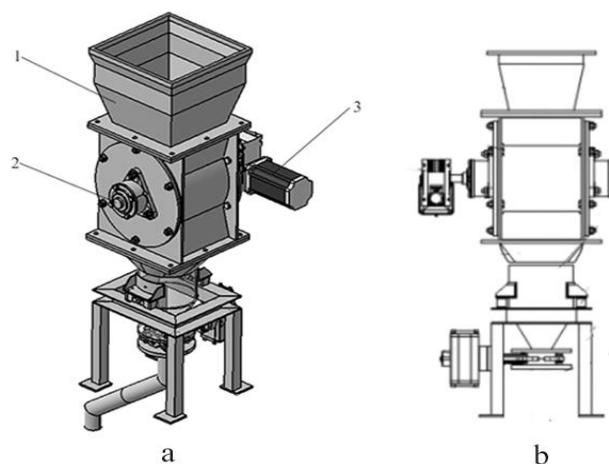


Fig. 3 - The three-dimensional diagram of the powder supply system
1- Charging barrel of powder; 2- Stepping motor; 3- Impeller metering disc

Working principle of the liquid supply system

The liquid supply system consists of a clear water barrel, a liquid medicine barrel, a peristaltic pump, a nozzle and pipeline. The working process of the liquid supply system is as follows: initially select the appropriate seed-liquid ratio in the control system, and according to the seed weight provided, the ratio 1g corresponds to 1 ml. After selecting the parameters, it starts to run, and the single-chip microcomputer controls the peristaltic pump to start working. The clean water and the liquid medicine are mixed through the water pipe and sprayed from the nozzle under the action of pneumatic force. The system calculates the required amount of liquid medicine through the seed weight provided and the selected seed-liquid ratio, and obtains the working time of the peristaltic pump through calculation, and performs timing in the system until the peristaltic pump stops running at the specified time. The liquid medicine is finally sprayed from the nozzle through the pipeline. The atomization nozzle chooses a gas-liquid two-phase flow nozzle, one end is connected to the air pump, one end is connected to the pipeline, and the nozzle position is aligned with the drop position of the seed in the pot. Under the action of air flow, the liquid medicine floats in the coating pan to form a moist mist environment, which is convenient for full contact with the seeds at the bottom and effective mixing to achieve an ideal coating state. According to the query atomization nozzle parameter table, when the flow rate is 9 L/h, the air flow rate is 45 L/min, which meets the atomization requirements required by the experiment. The three-dimensional and two-dimensional diagrams of the liquid supply system is shown in Fig.4.

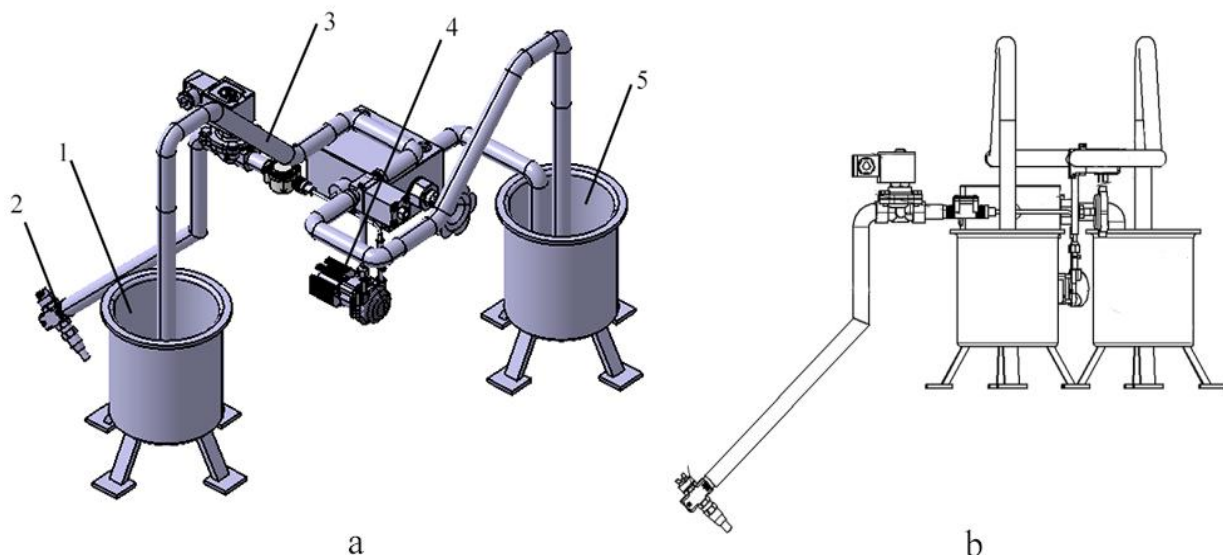


Fig. 4 - The three-dimensional diagram of the liquid supply system
1- Clear water barrel; 2- Nozzle; 3- Pipeline; 4- Peristaltic pump; 5- Liquid medicine barrel

Coating pot adjustment system

The coating pot adjustment system is composed of a coating pan, a frame, a driving motor and an inclination adjustment mechanism (Rogovskii I.L., 2020). Among them, the driving motor controls the rotating speed of the coating pan, and the rotating speed ranges from 0 r/min to 90 r/min, which meets the rotating speed requirements of normal rotary coating. The inclination adjuster is controlled by a NMRV turbo-worm gear stepper motor. The subdivision number is 3200.

The inclination angle is composed of the horizontal ground and the parallel line of the pot opening. When the pot opening is perpendicular to the ground, the inclination angle is 90°. The theoretical angle range is from 0° to 360°, but when the inclination angle exceeds 90° and is less than 180°, considering that the drive motor is placed above the rotating rod, long-term operation can easily cause the rotating rod to break and cause damage. When it exceeds 180°, the mouth of the pot is facing downwards, and coating cannot be carried out.

Usually, it is more appropriate to select a range between 20° and 60° for coating. The coating pan adjustment system satisfies the adjustment of the coating pan inclination and the coating pan rotation speed.

The three-dimensional and two-dimensional diagrams of the coating pan adjustment system is shown in Fig 5.

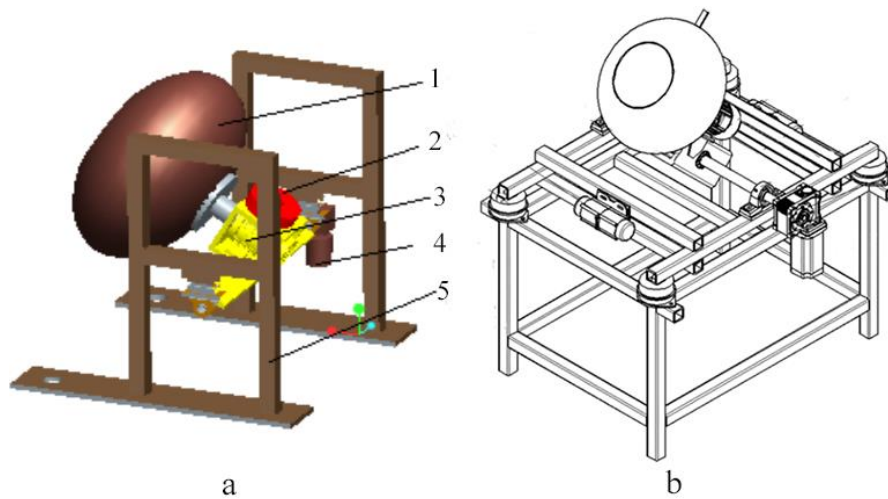


Fig. 5 - The coating pan adjustment system

1- Coating pan; 2- Driving motor; 3- Rotating rod; 4- Inclination adjustment mechanism; 5- Frame

Control System

Considering the low automation of domestic coating machine, a complete control system is designed by using LabVIEW. The control system is shown in Fig.6.

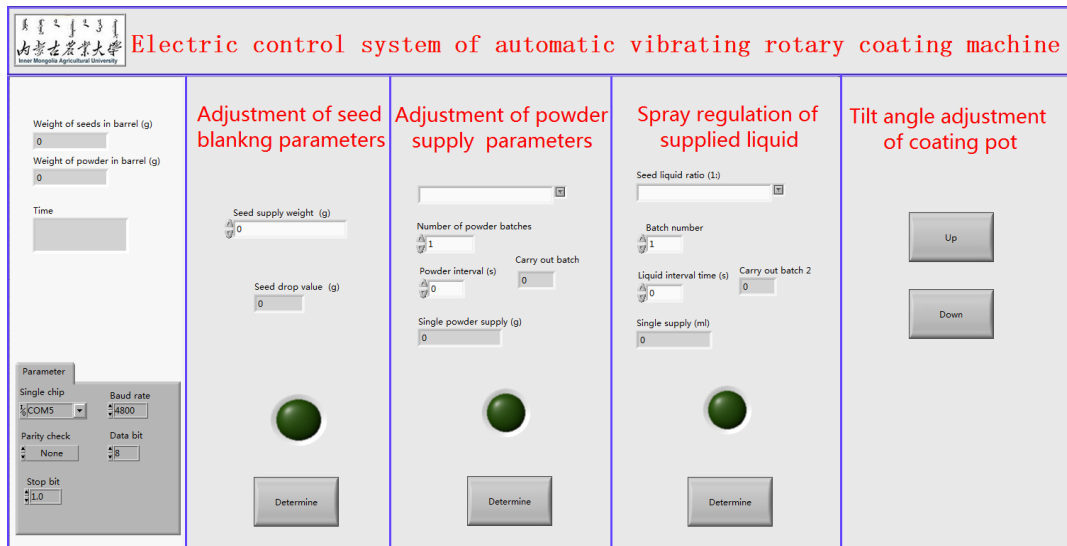


Fig. 6 - The control system

The control system consists of a front panel graphical user interface and a rear panel block diagram. The front panel is the control surface, which has functions such as sending operation instructions, parameter input, and data display. The block diagram of the rear panel uses graphical language to realize the logic control of the control system (Gülden, 2020).

The control system mainly realizes the precise control of the amount of seed supply, powder supply and liquid supply, as well as the adjustment of the inclination angle of the coating pan. At the same time, real-time detection of the weight change in the hopper to observe the margin.

Considering that the amount of coated seeds in a single time is too large, the function of supplying powder and liquid in batches is set up, which improves the intelligence of the system.

The specific control flow chart is shown in Fig.7.

First, the equipment is powered on, initialization adjustment and serial port selection are carried out. The appropriate single-chip serial port, baud rate, parity check, data bit and stop bit are adjusted. The default data can be adjusted to facilitate the next direct power on. During normal operation, the current seed and powder allowance will be displayed in real time, and the replenishment will be prompted if the allowance is insufficient. Before coating, select the parameters such as the ratio of seed to powder and the ratio of seed to powder liquid, adjust the dip angle of the coating pan, and adjust the rotary frequency converter to the appropriate speed of the coating pan.

If the supply is too much, batch supply can be selected. In the coating process, seed supply is carried out first, the valve of seed feeding system is opened, seeds in the seed charging barrel start to fall, and the weight information is transmitted by the load cell of seed feeding system to single chip computer in real time. After being converted by the Single Chip Microcomputer, the weight value is displayed in the upper computer control system in real time. Before operation, the system records the total weight of seeds in the seed charging barrel. During the seed feeding process, the system calculates the weight difference in real time. When the difference value reaches the set seed dropping value, the valve of seed feeding system closes, so as to complete the seed supply.

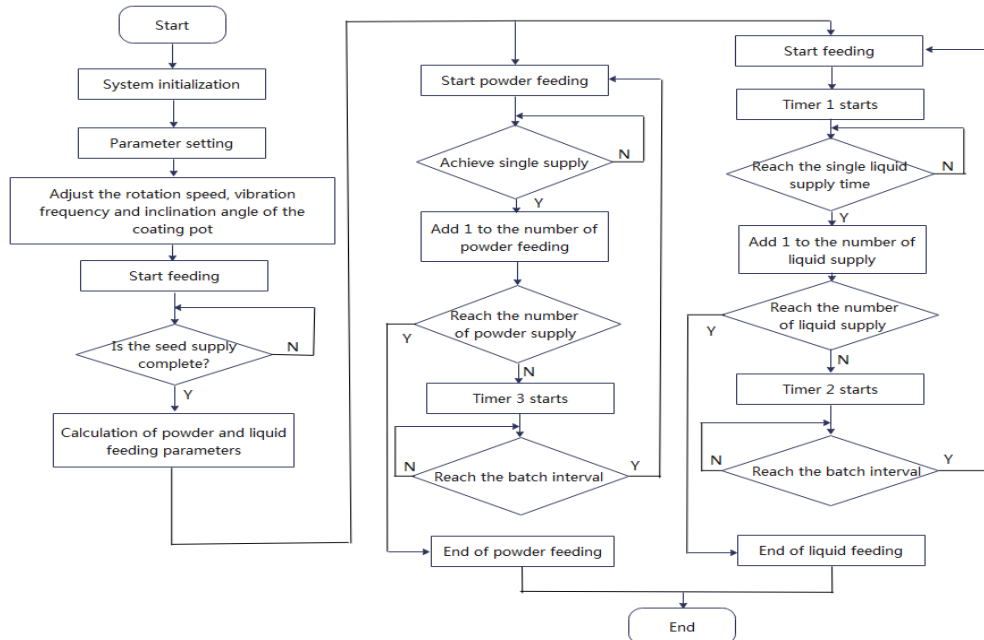


Fig. 7 - The specific control flow chart

After the seed supply is completed, the system records the supply amount, and calculates the single powder supply and single liquid supply by setting the seed powder ratio, seed liquid ratio, powder feeding batch, and liquid feeding batch. The single supply rotation angle of the stepping motor of the powder supply system is calculated through the calculation of a single supply of powder. After the calculation is completed, click Determine to start supplying. During the powder supply process, the indicator light will be on, indicating that the powder supply system is working. When the powder is supplied, the stepping motor of the powder supply system starts to rotate, and the powder in the powder container begins to fall. When the rotation angle of a single supply is reached, the number of powder supply increases by one. When the initial set powder supply batch is not reached, the powder supply system timer 3 starts to time, and when the set powder supply interval time is reached, the powder supply process is repeated. When the number of feeding times is equal to the initially set powder supply batch, the entire powder supply process is completed.

When supplying liquid, click Determine to start liquid supply, peristaltic pump starts to run, the liquid supply system timer 1 starts to time, during operation, indicator light is on, indicating that liquid supply is in progress. The system calculates the single working time by the spray amount per second of the nozzle and the single supply quantity of the setting. When the liquid supply system timer 1 reaches the single working time, the peristaltic pump stops running, and the number of liquid supply is added 1. At this time, the system compares the number of liquid supply and the initial set batch of liquid supply, and completes the whole liquid supply process when the batch reaches the liquid supply batch. When the batch of liquid supply is not reached, the liquid supply system timer 2 starts to time. When the liquid supply system timer 2 reaches the set liquid supply interval, the peristaltic pump starts to run and repeat the liquid supply process.

The upper computer communicates with the lower computer all the time to realize the functions of data transmission and module operation (Xiong, 2019). When the operation conditions are met, serial port communication is conducted through USB data line to control the high and low level of the CPU pin, so as to control the switch of relay and realize the switch control of specific modules. Finally, the whole coating process of rotary seed coating machine is completed. The circuit diagram of the system design is shown in Fig.8.

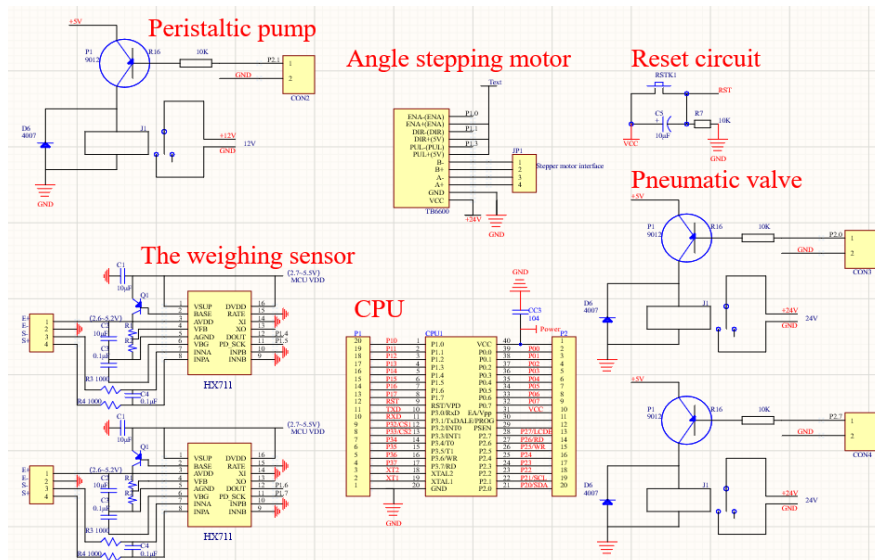


Fig. 8 - The circuit diagram of the system design

RESULTS AND DISCUSSIONS

ERROR ANALYSIS AND CALIBRATION TEST

In order to realize the precise supply of each module and meet the precision requirements during coating work, error analysis and calibration experiments were carried out on the seed supply system, powder supply system and liquid supply system. The physical picture of the coating machine is shown in Fig.9.



Fig. 9 - The physical picture of the coating machine

Calibration of seed supply error

The seed supply system uses a pneumatic valve to control the start and stop of the seed supply. The start and stop of the valve send instructions from the serial port to the microcontroller through the host computer. After the microcontroller receives it, the pin level is changed in real time, and the relay connected to the pin is used as a switch to control the pneumatic valve. The solenoid valve is turned on and off, and finally the valve opens and closes in real time. Considering that there is a time difference between the start and stop of the pneumatic valve, a small amount of excess seed drop is caused, which affects the precise supply of seeds and causes errors. In summary, choose the supply values of 100g, 500g, 1000g, 1500g and 2000g, and conduct multiple tests for comparison. The test results are shown in Table 1.

Table 1

Test value of feeding error			
Supply values (g)	Number of tests	Average value of seed drop (g)	Standard deviation
100	20	128.3	1.26
500	20	528.9	1.32
1000	20	1027.8	1.28
1500	20	1527.9	1.30
2000	20	2028.1	1.28

The error is calculated from the data in the table, and the average of the results of five times can be obtained. According to the experimental data, the error caused by the difference between the start and stop time of the pneumatic valve is about 28g, which is independent of the seed supply weight. Before coating, the system initially records the weight of seeds in the hopper. During operation, when the weight loss value in the hopper is equal to the selected value, it sends an instruction to close the valve and stop the seed supply. Taking into account the error value brought by the valve, when the weight loss value is set equal to the selected value minus 28g, the control system will stop the seed supply. Several tests were performed to analyse the errors, and the test results are shown in Table 2.

Table 2

Supply values (g)	Number of tests	Average value of seed drop (g)	Standard deviation
100	20	101.1	1.26
500	20	500.0	1.08
1000	20	1000.8	1.22
1500	20	1500.9	1.26
2000	20	2001.3	1.28

According to the data in Table 2, the error value of the seed supply after calibration is stable within 2%, which meets the design requirements.

Powder supply calibration design

During the coating process, the upper computer calculates the required powder supply amount through the weight of seed supply and the seed-powder ratio, and sends instructions to the lower computer through the upper computer. Each instruction controls the stepping motor to rotate 90°. At this time, the impeller metering disc rotates 90°, 100g powder supply, complete one-time powder supply. Times of powder feeding is calculated in the upper computer control system, and the cycle runs until the powder supply ends. In order to detect the error of the powder supply system, a number of tests were performed to analyse the error. The test results are shown in Table 3.

Table 3

Supply values (g)	Number of tests	Average powder drop value (g)	Error rate (%)
100	20	100.56	0.56

According to the experimental data, the error of the powder supply system is within 1%, which meets the design requirements.

Liquid supply calibration design

The amount of liquid supply depends on the operating time of the peristaltic pump. In order to achieve the effect of accurate liquid supply, the peristaltic pump needs to be accurately sprayed. The working voltage of the peristaltic pump selected in this design is 12 V, the rated current is between 4 and 6.5 A, and the spray volume depends on the current, which is 7 to 9 litres per minute. In the actual running process, the timing function is set on the upper computer, and the duration is calculated according to the liquid supply amount, and the liquid supply is completed by the arrival time. In order to accurately calculate the amount of sprayed liquid, choose to electrify for 10 s, 30 s, 60 s and 120 s, and perform multiple tests. The test results are shown in the Table 4.

Calculated value of liquid supply flow

Table 4

Liquid supply time (s)	Number of tests	Average value of liquid supply (ml)	Liquid supply per second (ml/s)
10	25	1063.2	106.3
30	25	3180.4	106.0
60	25	6390.6	106.5
120	25	12744.6	106.2

After calculation, the average value of multiple results can be obtained. The spray volume is 106 ml/s. When the actual liquid supply is 100 ml, it takes 0.94 s. In the control system, the cycle time is adjusted from 1000 ms to 940 ms, and 100 ml liquid is provided after one cycle.

Experimental results and analysis

In order to test the coating pass rate after the actual coating by the machine, the Agropyron seed are selected for the test. The powder is selected from soybean powder and diatomaceous earth mixed in a ratio of 4 to 6, and the pass rate of the coating after the traditional manual operation is used as the contrast, 50 sets of experiments were performed. Each group of seeds weighs 100g, choose the seed-powder ratio of 1:3 and the seed-liquid ratio of 1:2. When the seed coating agent is completely coated on the outer surface of the single seed is recognized as qualified as the coating, the qualified rate is calculated as the percentage of the number of qualified seeds in the total number of seeds tested. The test results are shown in Table 5.

Table 5

Coating qualification rate comparison table

Number	Traditional coating pass rate (%)	Instrument coating pass rate (%)	Difference	Number	Traditional coating pass rate (%)	Instrument coating pass rate (%)	Difference
1	71	89	18	26	69	88	19
2	69	88	19	27	72	89	17
3	70	89	19	28	70	90	20
4	70	86	16	29	68	86	18
5	68	85	17	30	66	85	19
6	68	86	18	31	71	89	18
7	71	89	18	32	72	87	15
8	68	85	17	33	69	88	17
9	70	88	18	34	70	88	18
10	72	87	15	35	73	88	15
11	71	90	19	36	71	86	15
12	67	86	19	37	67	83	16
13	69	84	15	38	66	84	18
14	70	87	17	39	69	86	17
15	67	85	18	40	70	85	15
16	71	86	15	41	71	87	16
17	74	90	16	42	73	90	17
18	66	83	17	43	69	84	15
19	65	82	17	44	66	86	20
20	69	85	16	45	68	87	19
21	71	89	18	46	70	88	18
22	68	83	15	47	68	85	17
23	72	89	17	48	69	84	15
24	73	90	17	49	66	82	16
25	70	88	18	50	71	86	15

The results show that the coating pass rate of the new type of rotary coating machine designed this time is 15%-20% higher than that of the traditional manual coating.

The difference of qualified rate of coating is shown in Fig.10.

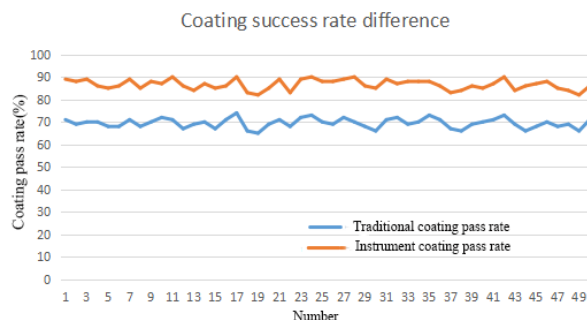


Fig. 10 - Contrast curve of coating success rate

CONCLUSIONS

This paper introduces the design structure of a new type of rotary coating machine, designs the electric control system of the coating machine by LabVIEW software, and controls it by MCU and other hardware modules. The automatic operation of coating process is realized, which can effectively improve the speed and quality of coating. On the premise of achieving the required function of coating process, the error calibration of each module was carried out, and the coating test of Agropyron seed was carried out.

The conclusion is as follows:

- 1) The error of seed feeding system, powder feeding system and liquid feeding system is controlled within 2% to meet the demand of precise supply.
- 2) Compared with the traditional manual coating, the qualified rate of the seeds coated by the new rotary coating machine increased by 15% to 20%.

ACKNOWLEDGEMENTS

We acknowledge that this work was financially supported by Inner Mongolia natural science foundation project (2018MS05023).

REFERENCES

- [1] Bai Y., Zhang C., Zeng L., (2020), Design of photoacoustic microscope system based on LabVIEW platform. *MATEC Web of Conferences*, Vol 309, Issue 4, pp. 4 -16, China;
- [2] Gülden G., Atalba M.C., Guler H., (2020), Chaotic Systems Based Real-Time Implementation of Visual Cryptography Using LabVIEW. *Traitement du Signal*, Vol 37, Issue 4, pp. 639 -645, Turkey;
- [3] Tamilselvi P., Manohar Jesudas., (2016), A Study on Physical Properties of Pelleted Carrot (*Daucus carota*. L) Seeds. *Advances in Life Sciences*, Vol 5, Issue 4, pp. 1220 -1224, India;
- [4] Qiu Y., Chen Z., Hou Z., Song T., Mi L., Shao Z., (2017), Numerical simulation and experiment on improving the effect of forage seed pellet coating by vibration force field. *Transactions of the Chinese Society of Agricultural Engineering*, Vol 33, Issue 19, pp. 86 -93, China;
- [5] Rogovskii I.L., Titova L.L., Trokhaniak V.I., Marinina L.I., Lavrinenko O.T., Bannyi O.O., (2020) Engineering management of machine for formation of artificial shell on seed vegetable cultures. *INMATEH - Agricultural Engineering*, Vol 61, Issue 2, pp. 165 -174, Ukraine;
- [6] Shao Z., Chen Z., Hou Z., Mi L., Qiu Y., (2018), Seed pelletizing movement characteristics of BYW-400 wheatgrass seed vibration pelletizing coating machine. *Transactions of the Chinese Society of Agricultural Engineering*, Vol 34, Issue 3, pp. 57-64, China;
- [7] Sun Z., Li S., Yuan Y., (2017), Design and experiment of pelleting device for tomato seed coating. *Agricultural Mechanization Research*, Vol 39, Issue 6, pp. 162-169, China;
- [8] Wang L., Hu C., He X., Guo W., Wang X., Hou S., (2021) A general modelling approach for coated cotton-seeds based on the discrete element method. *INMATEH - Agricultural Engineering*, Vol. 63, Issue 1, pp. 221-230, China;
- [9] Wu F., Zhang H., Xie H., Wang J., Qiu C., (2017), Overview and development considerations of seed coating machines in my country. *Chinese Journal of Agricultural Machinery Chemistry*, Vol 38, Issue 10, pp. 116 -120, China;
- [10] Xiong T., Lin Q., Feng X., (2019), Degradation dynamics of chlorfenapyr after pelleting and its control on *Phyllotreta striolata*. *Acta Entomologica Sinica*, Vol 56, Issue 4, pp. 826 -831, China;
- [11] Zhu M., Chen H., Li Y., (2012), Retrospect and prospect of seed processing industry in China. *Transactions of the Chinese Society of Agricultural Engineering*, Vol 28, Issue 2, pp. 1 -6, China.

MATHEMATICAL MODELING OF EAR GRAIN SEPARATION PROCESS DEPENDING ON THE LENGTH OF THE AXIAL FLOW THRESHING APPARATUS

MODELAREA MATEMATICĂ A PROCESULUI DE SEPARARE A SEMINTELOR DIN SPICE, FUNCȚIE DE LUNGIMEA APARATULUI DE TREIER CU FLUX AXIAL

Cujbescu D.¹⁾, Găgeanu I.^{*1)}, Iosif A.²⁾

¹⁾ INMA Bucharest / Romania;

²⁾ Herman Oilfield Inspection Service, Ploiești / Romania

E-mail: iulia.gageanu@gmail.com

DOI: <https://doi.org/10.35633/inmateh-65-11>

Keywords: modelling, separation, threshing, seeds, ears, axial threshing apparatus, rotor

ABSTRACT

Modelling the threshing and separation process involves the application of a method of description, analysis and analytical determination of system performance: threshing apparatus - working process. The modelling of the process of separating the seeds passing through an axial flow threshing device was performed taking into account that the separation function $s_s(x)$ is given depending on the length of the threshing apparatus. Then, models were made to describe the variation of the percentage (cumulative) of separated seeds $s_s(x=L)$, corresponding to the modification of the threshing apparatus functional parameters (depending on the peripheral speed of the rotor, the flow of straw parts and the moisture of straw parts).

REZUMAT

Modelarea procesului de treier și separare presupune aplicarea unei metode de descriere, analiză și determinare pe cale analitică a performanțelor sistemului: aparat de treier - proces de lucru. Modelarea procesului de separare a semințelor ce trec printr-un aparat de treier cu flux axial s-a realizat ținându-se cont că funcția de separare $s_s(x)$ este dată în funcție de lungimea aparatului de treier. În continuare s-au realizat modele care să descrie variația procentului (cumulat) de semințe separate $s_s(x=L)$, corespunzător modificării parametrilor funcționali ai aparatului de treier (în funcție de viteza periferică a rotorului, de debitul de părți păioase și de umiditatea părților păioase).

INTRODUCTION

The harvesting of straw cereals has been a major human activity throughout the history of civilization, and increasingly complex tools designed and made to facilitate this activity have given the process of creating them a significant place in all human activities (Ivan, 2014).

In general, the harvesting process of a cereal combine integrates the processes of harvesting, cutting, threshing, separation and cleaning, etc. (Hanna et al., 2013; Unakitan and Aydın, 2018). The threshing process represents an essential role in the operation of the combine, the seed losses occurring during harvesting being significantly influenced by the theory and technology of threshing (Ivan et al., 2015a; Ivan et al., 2015b; Fu et al., 2018; Khir et al., 2017). Natural losses are determined by weather conditions such as wind and rain (Audilakshmi et al., 2007; Gobbett et al., 2017). The degree of injury is another direct index of cereal threshing that negatively affects their market value and storage (Mirzazadeh et al., 2012; Khazaei et al., 2008) and depends on several factors, including the sieve separation regime (Pruteanu et al., 2018), the most common being the mechanical damage due to the impact of the seed kernel on the rigid surface of the threshing unit (Agelet et al., 2012; Zhu et al., 2016).

Modelling of the threshing and separation process emerged as a necessity to improve the quality of the threshing process. In the case of axial flow threshing apparatus, this was done later because of the fact that combines with longitudinal threshing apparatus appeared only after the 1970s. Shortly after this, the first researches in this field were made, continuing to this day when a sufficiently good modelling of the separation process has been reached (Li et al., 2017; Liang et al., 2017; Miu et al. al., 1997; Qirui et al., 2020; Sheychenko et al., 2018). This is also supported by the very good results obtained in operation with this type of threshing apparatus, the percentage of separated seeds often exceeding 99%. Experiments were performed in order to determine the constructive and functional characteristics of the combine based on a mathematical model of the displacement of the seed heap on the shaker (Ivan and Nedelcu, 2010).

The objective of this paper is to present a mathematical model that was made taking into account the input and output parameters of a working process carried out by an axial threshing apparatus.

MATERIALS AND METHODS

Input and output parameters of the system

The working process carried out by the threshing apparatus, regardless of its type, is very complex, being influenced by a series of parameters defined by:

- the material to be threshed;
- material feeding system of the threshing apparatus;
- its construction and working regime.

The mathematical model of the separation process developed in this paper takes into account the following input parameters:

- Material characteristics, represented by: seed moisture, u_s ; moisture of the straw parts, u_p ;
- Feeding system parameters: feeding width, l_a ; the height of the material layer when feeding takes place, h_a ; feeding speed, v_a ; feeding direction at angle γ ; material flow, q and the flow of straw parts, q_p .
- Construction of the threshing apparatus, characterized by: type: tangential or axial; beater (rotor) radius, R ; beater (rotor) length, L ; length of the concave's arc, l ; number of rails of the beater (rotor), z ; size on the radial direction of a rail, δ_R ; angle of the rails on the rotor to the generators, β_1 ; angle of the helical rails on the housing to the generators, β_2 .
- Operating regime, depending on: speed (angular speed, ω); peripheral speed of the beater (rotor), v ; beater (rotor) – concave (counter-rotor) spacing at the inlet δ_i ; beater (rotor) – concave (counter-rotor) spacing at the outlet δ_e .

Experimental installation and equipment used

The experimental researches performed on the axial flow threshing apparatus were carried out at INMA Bucharest on an axial flow thresher B-90 which is equipped with a threshing apparatus with a length of 2,000 mm. The thresher is actuated from the tractor's power take-off by means of a Cardan shaft which is coupled by a spring to the beater drive scutch.

The collection of the material heap separated by the concave was carried out using a matrix (10 x 5) of collecting boxes, a box having the dimensions: 200x200x100 [mm x mm x mm] (fig. 1).



Fig. 1 – Block of collecting boxes

Figure 2 shows a part of the constructive scheme of the experimental installation with axial flow threshing apparatus and Figure 3 a cross section of the threshing apparatus, under which the block of collecting boxes is mounted. Each line of boxes collects the material separated between two consecutive crossbars of the concave. The last line of boxes collects the heap separated in the transition area to the concave extension area.

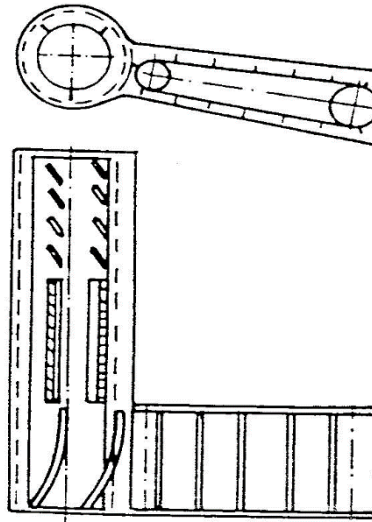


Fig. 2 - Constructive scheme of the experimental installation with axial threshing apparatus

The collection of the material evacuated at the outlet of the threshing apparatus (fragmented straw, unthreshed ears, unseparated seeds, chaff, etc.) was made on a tarpaulin with the dimensions of 2x3 sq. m, by means of two movable panels. Strain gauges were mounted on the beater shaft in order to measure the moment of resistance, by means of a specialized equipment.

The axial threshing apparatus has been fed tangentially in an area where the rotor is equipped with rails. In the same area, the housing of the threshing apparatus is provided with spiral rails, mounted at an angle of 60° to the axis of the rotor, which has a diameter of 560 mm. These rails are arranged on the housing, at an angle of 180° (Fig.2).

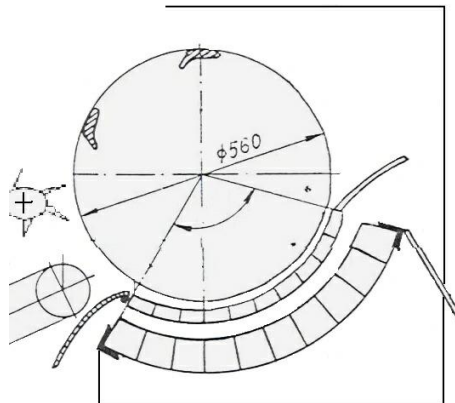


Fig. 3 – Cross section of the threshing apparatus

Figure 4 shows the constructive scheme of the axial flow threshing apparatus.

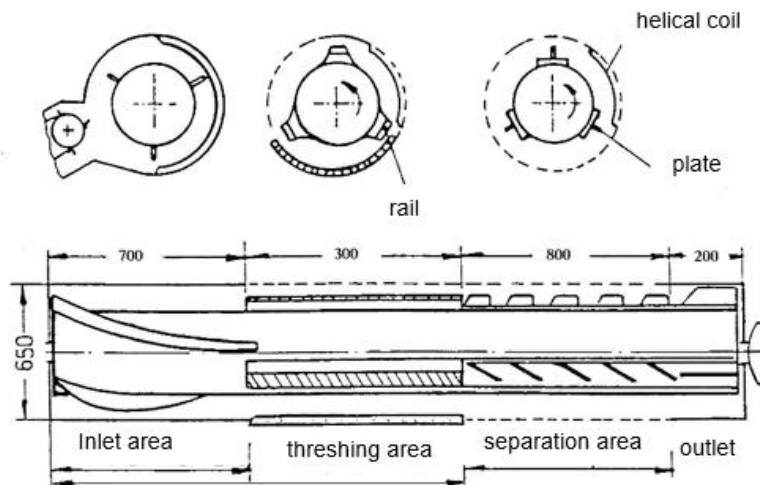


Fig. 4 – Constructive scheme of the axial flow threshing apparatus

The counter-rotor, with a winding angle of 110° has a construction similar to that of an ordinary tangential threshing apparatus, in the threshing area the rails are three in number and parallel to the rotor axis, in the separation area, on the same generators that the rails are mounted, the rotor being provided with three rows of separating plates, mounted inclined at an angle that can take the values of: 0° , 22.5° and 45° .

The housing of the threshing apparatus is provided entirely with holes measuring 20×40 mm, the active separating surface of the housing representing about 55% of its total surface. Helical rails 30 mm high and 500 mm long are mounted on the sides of the housing; they can be mounted at different angles: 60° ; 75° .

The main adjustable and measurable parameters taken into account, which influence the performance of the working process, were:

- beater speed n [rpm], adjustable within the limits of $600 \div 1200$ rpm; corresponding to this speed range, the peripheral speed of the beater being in the range $22 \div 32$ m/s;
- the material flow q [kg/s], was determined by weighing the sample of plant material and measuring the time in which the uniform feeding of the threshing apparatus was performed. The mass of material introduced into the apparatus was checked for each test with the mass of the components collected following the threshing process. During the tests the material flow corresponding to the width of the threshing apparatus was changed within the limits of $1.5 \div 4$ kg/s;
- the distance δ between the rails of the beater and the concave is variable, measured in the direction of material advance. Thus the distance δ can be varied as follows: $\delta_i = 12 \div 24$ mm at the inlet and $\delta_e = 3 \div 7$ mm at the outlet;
- the material feeding speed can be varied continuously by means of a speed variator, within the limits: $3.1 \div 4.65$ m/s;
- the material supply angle can vary within $15 \div 35^\circ$ and a clinometer is used to measure it.

Testing method

During the experiments, the values of several parameters were varied one by one, namely: the peripheral speed of the beater, the material flow, the S/PP ratio, the feeding speed, the distance between the beater and the concave.

The block of boxes for collecting the separated material is placed separately in the support guides on the chassis of the threshing apparatus module.

To collect the straw parts discharged, a tarpaulin and the movable panels for directing the material were properly placed so that it would not spread over the seeds.

The plant material required for the test was weighed and then placed on the feed conveyor belt, mainly with the ears positioned forward relative to the movement direction.

The thresher is put into operation by starting the tractor engine, the threshing apparatus being actuated from its power take-off, where the speed is checked and adjusted.

At the end of the experiment the material from the collecting boxes was then weighed separately as:

- separated seeds;
- unthreshed and separated seeds, namely seeds for the return circuit.

Samples were taken from the amount of separated seeds to determine the moisture of the seeds as well as to determine the percentage of damaged seeds.

The mass of material separated on the tarpaulin was weighed and recorded and then the block of collecting boxes was detached. The content of the 50 collecting boxes were placed in 50 numbered plastic or paper bags.

The material on the tarpaulin was processed manually, with great care, being separated in unthreshed ears (threshing loss), threshed and unseparated seeds (separation loss), discharged straw parts. A sample was taken from the discharged straw parts at each test to determine the moisture of the straw parts.

The separated material, from the 50 bags, was processed as follows: the material from each bag was separated after weighing into unthreshed but separated ears (seeds for the ear-return-spice circuit of the combine), separated seeds, separated straw parts. After manual separation of these components, the seeds separated in each collecting box were weighed with an electronic balance. Amounts of seeds were taken from the entire quantity of separated seeds, by the method of fractionation into quarters, to determine the moisture content of the seeds and to separate them into fractions of whole, broken and damaged seeds, which were weighed with the electronic balance.

The moisture of the seeds and the straw parts was determined by drying them in an oven at 105° .

RESULTS

The processing of the material separated in an experiment was done on the day of the experiment and during the following day. All data were entered in preliminary measurement tables.

Table 1

Den. no.	Separated seeds [g]					Sum
	A	B	C	D	E	
1.	12.4	23.4	27.5	16.5	4.9	84.7
2.	18.9	41.0	48.9	32.9	13.8	155.5
3.	23.3	43.9	51.1	33.9	12.4	164.6
4.	17.2	34.1	43.2	26.1	7.7	128.3
5.	16.6	34.6	39.5	29.5	8.1	128.3
6.	12.1	27.4	35.7	24.1	6.7	106.0
7.	10.4	22.2	27.2	24.6	6.4	90.8
8.	10.3	20.2	23.2	20.6	5.5	79.8
9.	7.6	16.2	23.7	15.2	3.8	66.5
10.	1.5	2.9	3.0	2.6	0.8	10.8
Sum	130.3	265.9	323.0	226	70.1	1015.3

The graphical representation of these data is shown in Figures 5-10.

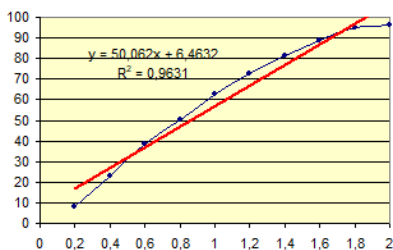


Fig. 5 - Linear function of seed separation

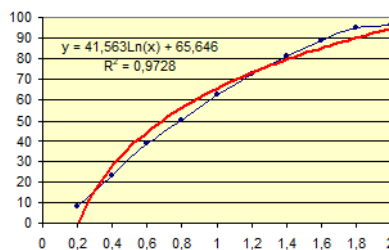


Fig. 6 - Logarithmic function of seed separation

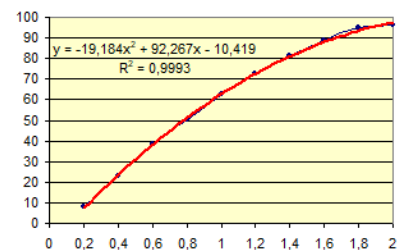


Fig. 7 – Second-degree polynomial function of seed separation

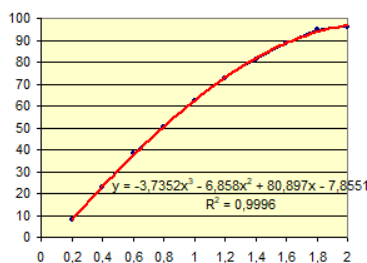


Fig. 8 – Third-degree polynomial function of seed separation

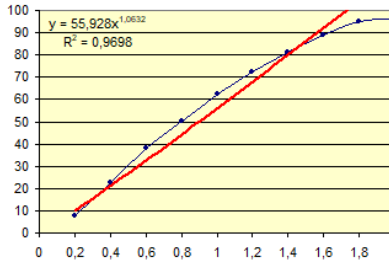


Fig. 9 - Power function of seed separation

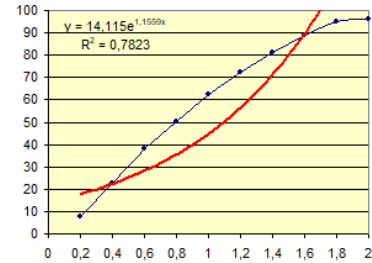


Fig. 10 - Exponential function of seed separation

— modelled function
— real function

Through the mathematical equations that compose it, the general mathematical model - in the case of the axial apparatus - describes mainly: the detachment of seeds from ears; separation of seeds by counter-rotor and housing; the size of losses at threshing and separation; separation of the straw parts.

On the length of the rotor $x \in (x \text{ takes the maximum value})$, the calculation expressions of the qualitative indices that characterize the threshing process of an axial device are obtained. The values of the coefficients β and λ used in this model, implicitly express the influences of all constructive, functional factors such as the physical and mechanical properties of the processed material.

Analysing the functions that model the separation process it can be observed that the polynomial functions of second and third degree best approximate the real function resulting from the data measured after performing the tests.

Thus, for *seed separation*, the second-degree polynomial function is of the form:

$$y = -ax^2 + bx - c \tag{1}$$

where: $a = 17.499 \div 26.752$;

$b = 88.322 \div 104.87$;

$c = 3.7228 \div 10.525$,

and the third-degree polynomial function is:

$$y = mx^3 - nx^2 + px - q \quad (2)$$

where: $m = -6.512 \div 3.7352$;

$n = 6.858 \div 48.162$;

$p = 80.897 \div 124.62$;

$q = 5.5671 \div 10.488$.

The second-degree polynomial function approximates well the real function, the correlation coefficient varying between $0.9985 \div 0.9996$, while the third-degree polynomial function has a correlation coefficient between: $0.9991 \div 0.9998$.

Considering that the third-degree polynomial function approximates the real function better than the second-degree polynomial function with a maximum of 1.1 per thousand, it is considered that the second-degree polynomial function (1) approximates the real function well enough.

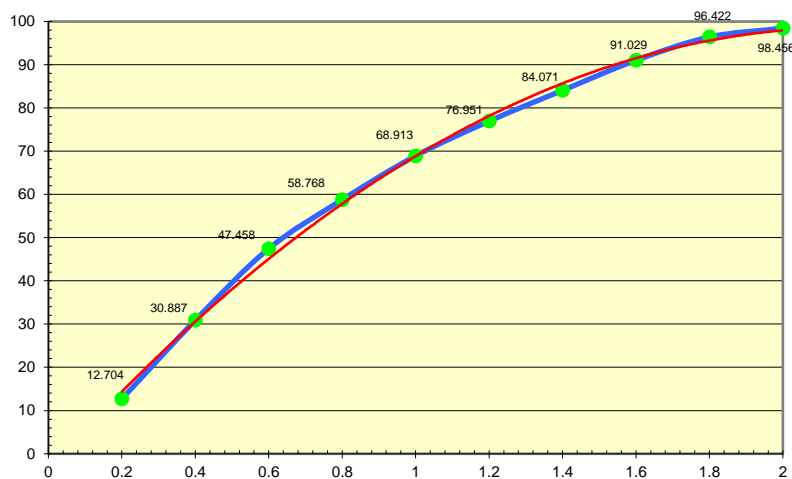


Fig. 11 – Seed separation depending on rotor length

In the case of this type of function, the range of values of a , b , and c is much narrower than in the case of the third-degree polynomial function, this highlighting the fact that the deviation from the real function is relatively small.

In the case of the axial apparatus, the separation of the seeds along the length of the threshing apparatus (threshing and separation areas) is described by:

- the cumulative frequency distribution function that quantifies the cumulative percentage of separated seeds for $x \in [0, L]$;
- seed separation density function that quantifies the frequency of seed separation over the length $x \in [0, L]$.

Next, models that describe the variation of the percentage (cumulative) of separated seeds $s_s(x = L)$, corresponding to the modification of the threshing apparatus functional parameters are proposed.

a) Seed separation depending on the peripheral speed of the rotor

The separation of seeds along the length of the axial threshing apparatus (threshing and separation areas) is described by a second-degree polynomial function of the form:

$$s_s(v_p) = -av_p^2 + bv_p - c \quad (3)$$

where: a , b , and c are experimentally determined values.

This function describes well the phenomenon of seed separation on the two areas (threshing and separation), taken separately or together.

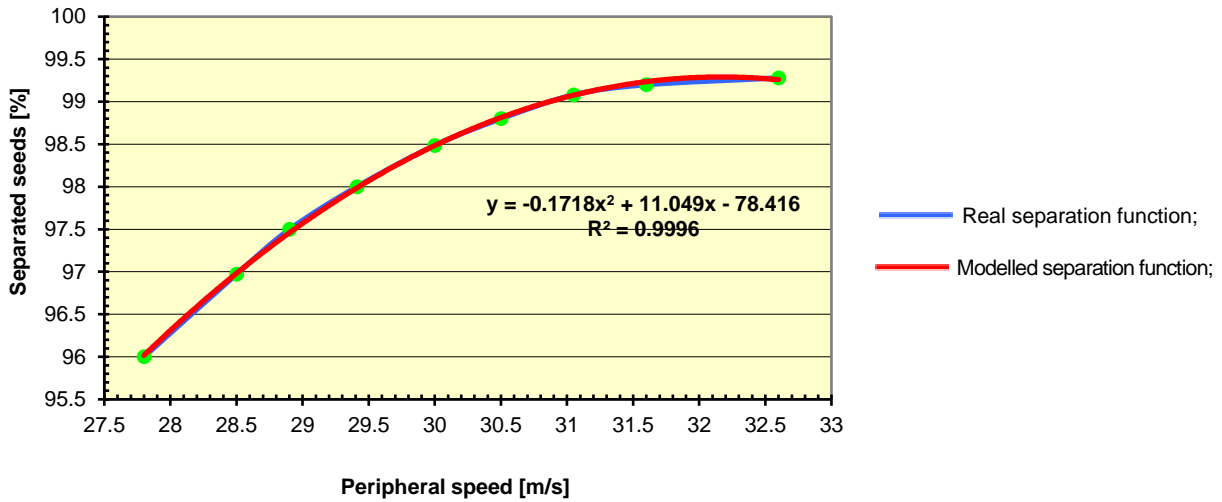


Fig. 12 – Seed separation depending on the peripheral speed of the rotor

The graph of this function (fig. 5) shows that at high peripheral speeds, the curves tend asymptotically towards a maximum separation of 100%.

It results that the dependence of the percentage of seeds separated by the peripheral speed of the rotor is described by a second-degree polynomial, whose maximum is obtained for:

$$v_p = \frac{b}{2c} \tag{4}$$

The detachment from the ears and the separation of the seeds through the counter-rotor and the housing take place due to the energy transmitted from the active elements (rails, plates, etc.) of the rotor, by impact. The higher the transmitted energy, the greater the separation of the seeds.

b) Seed separation depending on the flow of straw parts

In the case of the axial threshing apparatus tested for the variation of the flow of straw parts, there is a maximum of seed separation and with the increase of the flow of straw parts, the seed separation decreases continuously.

At low flow rates of straw parts, the distribution of the material in the space between the rotor and the housing is made in a thin layer, the material is more easily moved and therefore insufficiently processed; that is why the percentage of separated seeds decreases. At relatively high flow rates of straw parts, separation is hampered by the thick layer of material.

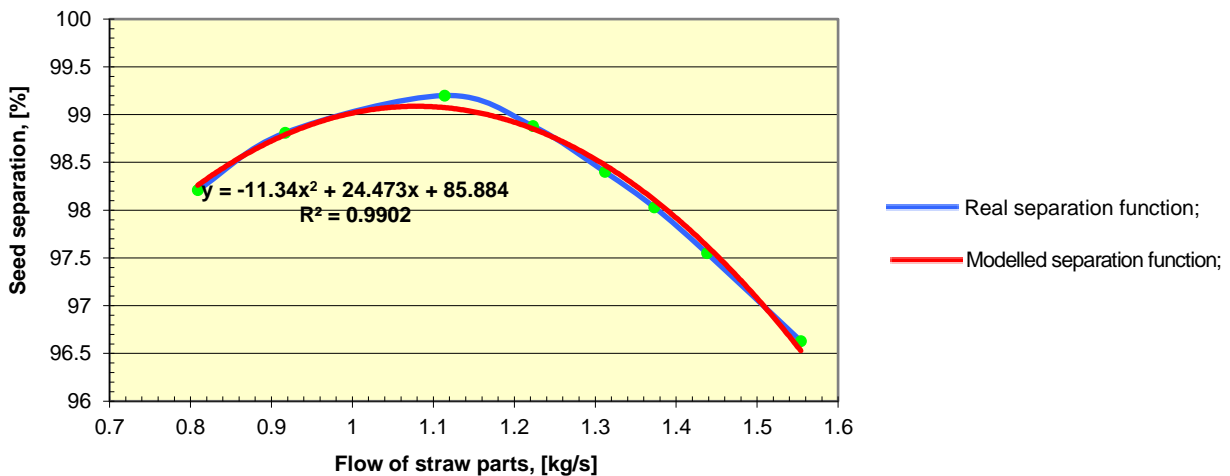


Fig. 13 – Seed separation depending on the flow of straw parts

$$s_s(q_p) = a + bq_p - cq_p^2 \tag{5}$$

where: a , b , and c are experimentally determined coefficients.

It results that the dependence of the percentage of seeds separated by the flow rate of straw parts is described by a second-degree polynomial, whose maximum is obtained for:

$$q_p = \frac{b}{2c} \tag{6}$$

c) Seed separation depending on straw parts moisture

Seed separation through the concave decreases with increasing the flow of straw parts almost linearly; at higher moisture, the percentage of separated seeds is higher. In the axial apparatus, seed losses (unseparated seeds) are higher when the material has a higher moisture content.

Data analysis suggests another way of interpreting the influence of moisture on seed separation. Due to the relatively long period of material remaining in the axial threshing apparatus, the moisture of the straw parts influences the separation of the seeds in two contradictory ways.

Thus, it can be said that at a low moisture of the straw parts, the detachment of the seeds is easy but the pronounced fragmentation of the straw prevents the separation of the seeds through the counter-rotor and the housing, which means that:

$$s_s = f(u_p) \tag{7}$$

where: u_p represents the moisture of the straw parts.

At a high moisture of the straw parts, threshing the material becomes more difficult, so

$$s_s = \frac{1}{f_2(u_p)} \tag{8}$$

A function that simultaneously describes the two modes of moisture influence can have the following form (fig. 7):

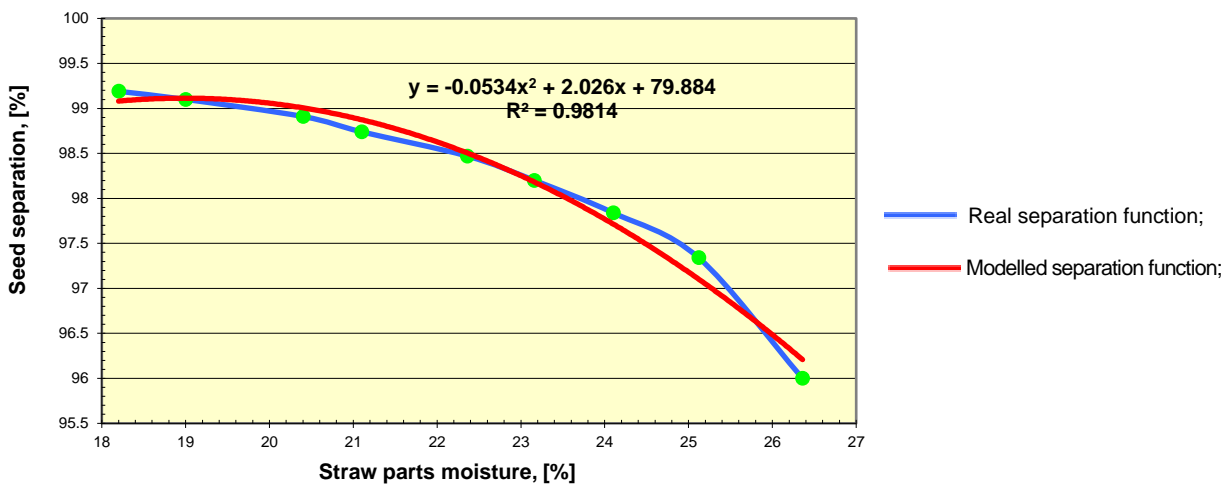


Fig. 14 – Seed separation depending on straw parts moisture

If:
$$\frac{ds_s}{du_p} = 0 \tag{9}$$

the value of the straw parts moisture for which the function (8) admits a maximum, respectively $u_p = \eta/\xi$, is obtained.

The function that best models the separation of seeds according to straw parts moisture also has a polynomial form of second-degree and is of the following form:

$$s_s(u_p) = -au_p^2 + bu_p + c \tag{10}$$

which has a maximum separation for:
$$u_p = \frac{b}{2c} \tag{11}$$

CONCLUSIONS

This paper presents a general mathematical model used to model the process of separating seeds from ears depending on the length of the threshing apparatus, seed separation being described by:

- the cumulative frequency distribution function for $x \in [0, L]$;
- seed separation density function over the length $x \in [0, L]$.

Then, models were proposed to describe the variation of the percentage of separated seeds $s_s(x)$, corresponding to the modification of the threshing apparatus functional parameters (seed separation depending on: peripheral speed of the rotor, the flow of straw parts and the moisture of straw parts).

Analysing the separation process, depending on these factors, the following observations can be distinguished:

- the separation of the seeds increases with the increase of the peripheral speed of the rotor, up to a limit speed of 32÷33 m/s; above this limit, the percentage of damaged seeds increases greatly;
- the separation of the seeds is done very well (reaches a maximum), for an average flow of the combine; at the limit (low or very high flow rates), the separation process is not performed satisfactorily;
- the moisture of the material entering the threshing apparatus and especially the moisture of the straw parts has a very big influence in the separation of the seeds; at a moisture higher than 18÷20%, the percentage of separated seeds begins to decrease.

To obtain these results, mathematical modelling was performed using the comparison of the results of the most used functions in the literature: linear, exponential, polynomial, power and logarithmic function, taking into account the function that best approximates the real separation function.

REFERENCES

- [1] Agelet, L. E., Ellis, D. D., Duvick, S., Goggi, A. S., Hurburgh, C. R., Gardner, C. A. (2012). Feasibility of near infrared spectroscopy for analysing corn kernel damage and viability of soybean and corn kernels. *Journal of Cereal Science*, 55(2), 160–165.
- [2] Audilakshmi, Aruna, S. C., Solunke, R. B., Kamatar, M. Y., Kandalkar, H. G., Gaikwad, P. (2007). Approaches to grain quality improvement in rainy season sorghum in India. *Crop Protection*, 2007; 26, 630–641.
- [3] Fu, J., Chen, Z., Han, L. J., Ren, L. Q. (2018). Review of grain threshing theory and technology. *Int J Agric & Biol Eng*, 2018; 11(3), 12–20.
- [4] Govindaraj, M., Masilamani, P., Asokan, D., Selvaraju, P. (2017). Effect of Different Harvesting and Threshing Methods on Seed Quality of Rice Varieties. *Int. J. Curr. Microbiol. Appl. Sci.*, 6, 2375–2383.
- [5] Gobbett D L, Hochman Z, Horan H. (2017). Yield gap analysis of rainfed wheat demonstrates local to global relevance. *The Journal of Agricultural Science*, 155(2), 282–299.
- [6] Hanna, H. M., Quick, G. R. (2013). Grain harvesting machinery. *Handbook of Farm, Dairy and Food Machinery Engineering*, Academic Press, 223–257.
- [7] Ivan, Gh. (2014). *Tangential treatment devices of grain harvesters*, Terra Nostra Iasi.
- [8] Ivan, Gh., Nedelcu, M. (2010). Theoretical study of pile displacement on straw walker of conventional combine harvesters, *INMATEH - Agricultural Engineering*, Vol. 31, No. 2, 5–10;
- [9] Ivan Gh., Vlăduț V., (2015), The intensification of shaking process to the conventional cereal harvesting combines, *Proceedings of the 43 International Symposium on Agricultural Engineering "Actual Tasks on Agricultural Engineering"*, vol. 43, 417÷430, Opatija – Croatia;
- [10] Ivan Gh., Vlăduț V., Ganea I., (2015), Improving threshing system feeding of conventional cereal harvesting combine, *Proceedings of the 43 International Symposium on Agricultural Engineering "Actual Tasks on Agricultural Engineering "Actual Tasks on Agricultural Engineering"*, vo. 43, 431÷440, Opatija – Croatia;
- [11] Khazaei, J., Shahbazi, F., Massah, J. (2008). Evaluation and modelling of physical and physiological damage to wheat seeds under successive impact loadings: mathematical and neural networks modelling. *Crop Science*, 48(4), 1532–1544.
- [12] Khir, R., Atungulu, G., Ding, C., Pan, Z. L. (2017). Influences of harvester and weather conditions on field loss and milling quality of rough rice. *Int J Agric & Biol Eng*, 10(4), 216–223.
- [13] Li, H., Wang, J. S., Yuan, J. B., Qian, Y. Z. (2017). Analysis of rice mixture separation through vibration screen using discrete element method. *Int J Agric & Biol Eng*, 10(11), 231–239.

- [14] Liang, Z., Li, Y., Xu, L., Zhao, Z., Tang, Z. (2017). Optimum design of an array structure for the grain loss sensor to upgrade its resolution for harvesting rice in a combine harvester. *Biosystems Engineering*, 157, 24–34
- [15] Mirzazadeh, A., Abdollahpour, S., Mahmoudi, A., Bukat, A. R. (2012). Intelligent modelling of material separation in combine harvester's thresher by ANN. *International Journal of Agriculture and Crop Sciences*, 2012; 4(23), 1767–1777.
- [16] Miu, P., Beck, F., Kutzbach, H.D. Mathematical modelling of threshing and separating process in axial threshing units, *ASAE Annual International Meeting, Mineapolis Convention Centre, Mineapolis, Minnesota, August 10-14*.
- [17] Pruteanu A., Vlăduț V., Ungureanu N., (2017), Characterization of chicory herb (*Cichorium intybus*) of separation process on length of flat vibrating sieves, *Proceedings of the 43 International Symposium on Agricultural Engineering "Actual Tasks on Agricultural Engineering "Actual Tasks on Agricultural Engineering"*, vol. 45, pp. 339÷350, Opatija – Croatia;
- [18] Qirui, W., Hanping, M., Qinglin. L. (2020). Modelling and simulation of the grain threshing process based on the discrete element method, *Computers and Electronics in Agriculture*, 178, ISSN 0168-1699. <https://doi.org/10.1016/j.compag.2020.105790>.
- [19] Sheychenko, V., Anelak, M., Kuzmych, A., Gritsaka, O., Dudnikov, I., Tolstushko, N. (2018). Investigation of the grain separation process in the three-drum threshing-separating device of a combine harvester, *Mechanization in agriculture & Conserving of the resources*, 64 (2), 42-45.
- [20] Unakitan, G., Aydın. B. (2018). A comparison of energy use efficiency and economic analysis of wheat and sunflower production in Turkey: A case study in Thrace Region. *Energy*, 149, 279–285.
- [21] Zhu, M., Shabala, S., Shabala, L., Fan, Y., Zhou, M. X. (2016). Evaluating predictive values of various physiological indices for salinity stress tolerance in wheat. *Journal of Agronomy and Crop Science*; 202(2), 115–124.

RESEARCH ON VISUAL NAVIGATION PATH DETECTION METHOD FOR DENSE PLUM GROVE

/ 密植李子树林视觉导航路径检测方法研究

Ren XiaoDan ¹⁾; Wang Haichao ^{*2)}; Shi Xin ²⁾ ¹

¹⁾Inner Mongolia Technical College of Mechanics and Electrics, Department of Electrical Engineering, Inner Mongolia/ China

²⁾Inner Mongolia Agricultural University, College of Energy and Transportation Engineering, Inner Mongolia/ China

Tel: +86 10 0471-4307822; ^{*} corresponding author E-mail address: ndwhc@imau.edu.cn

DOI: <https://doi.org/10.356.33/inmateh-65-12>

Keywords: Visual navigation, Plum grove, Path extraction, Otsu segmentation

ABSTRACT

Aiming at the field management of plum grove in Inner Mongolia of China, taking the dense planting plum groves in Bikeqi town of Hohhot City as the research object, this paper proposed a visual navigation path detection algorithm for plum grove. By processing the video image information of plum grove, comparing RGB and HSV color space model, HSV color model was selected to separate the plant and background in V channel. Homomorphic filtering was used to highlight the region of interest in the image, Otsu was selected to segment the image, the intersection of plum trunk and ground was extracted as feature points, and the least square method was used to fit the navigation path. Through the comparative analysis of detection rate under different detection conditions in one day, the verification test of route accuracy was carried out. The experimental results show that: for dense planting plum grove, the average path detection accuracy of the algorithm is 70% and 73.3% under the condition of front light and weak light, respectively. The detection accuracy and real-time meet the requirements of plum grove field management, and the navigation baseline can be generated more accurately, which provides a preliminary basis for the realization of mechanical vision navigation in plum grove field management.

摘要

针对中国内蒙古地区李子园田间管理，以呼和浩特市毕克齐镇密植李子园为研究对象，该研究提出一种李子园行内做视觉导航路径检测算法。通过处理李子园图像信息，对比 RGB 和 HSV 颜色空间模型，确定选用 HSV 颜色模型，在 V 通道进行植株与背景分离。使用同态滤波将图像感兴趣区域凸显出来，选择 Otsu 对图像进行分割，并将李子树干与地面交点作为特征点进行提取，采用最小二乘法拟合导航路径。通过在一天内不同检测条件下检测率的对比分析，对路线精度进行验证试验。试验结果表明：对于密植李子园在顺光和弱光检测条件下，该算法的路径检测准确率平均值分别为 70% 和 73.3%，检测准确性与实时性满足李子园田间管理要求，能够较准确生成导航基准线，为李子园田间管理机械视觉导航实现提供前期基础。

INTRODUCTION

Plum tree, also known as cherry plum, which can be planted in a variety of soil types because of its low requirements for climate and soil, is widely planted in Inner Mongolia of China. With the improvement of agricultural and forestry machinery, the planting and production efficiency of agricultural and forestry products has been greatly improved, and the agricultural and forestry products have been developed rapidly. However, for many reasons, most of the planting, management and harvesting operations in the dense plum grove were completed by manpower and a small part of machinery, which did not fully realize the mechanization of forestry equipment, which was time-consuming and laborious, and the cost was high. In the period of plum field management, the operators operated the machinery, which would expose them to dangerous pesticides, and their health was vulnerable to great threat. At the same time, working for a long time may reduce the operator's concentration, produce visual fatigue, and affect the observation and judgment.

¹ XiaoDan Ren, M.S. Assoc. Prof.; Haichao Wang, Ph.D.; Xin Shi, B.S.

Visual navigation has been widely used in various fields because of its high precision, wide signal detection range, good autonomy and real-time. With the continuous development of visual navigation, some scholars have developed automatic navigation systems for Kiwi (*Li, 2017*), citrus (*Liu, 2019*), jujube (*Peng et al., 2018*) and other plants.

According to the characteristics of orchard standard specification row planting, *Zhang* used image processing methods such as threshold segmentation, edge detection and centroid extraction to identify fruit trees from aerial top view of orchard, extracted fruit tree coordinate information and created orchard feature map. Hough transform and random sampling consistency algorithm were used to extract the straight line features of tree line, and the feasibility of the design was verified by simulation and field experiments (*Zhang, 2016*). *Ye et al.* used the offset algorithm to cluster the pixels of the original image to eliminate the diversity of pixels in the image, and then used the image segmentation algorithm based on graph theory to segment the processed image. On the basis of the binary image after edge detection, Hough transform was used to extract the boundary line between the tree and the ground, so as to obtain the robot's route (*Ye et al., 2017*). *Hou et al.* put forward a robot navigation system based on VC++ in 2008, which can carry out weed recognition application software. Camera was installed on the robot, and the perspective transformation principle was used to make the weeding robot carry out different pose changes (*Hou et al., 2008*). *An* took the lead in applying color constancy theory to machine vision navigation, so as to realize autonomous navigation of field agricultural robot (*An, 2008*). *Liu et al.* designed a navigation path generation algorithm based on the machine in the fruit tree grove in winter, which had good anti-interference and high robustness (*Liu et al., 2019*). *Zhang et al.* identified the tomato plants planted in the greenhouse from the complex background, extracted the navigation path feature points through the tomato position, and obtained the navigation path by using Hough transform, thus inventing a robot mainly used for timely image processing in the greenhouse (*Zhang et al., 2018*). *Peng et al.* used MFC (Microsoft Foundation Classes) and Opencv to create a visual navigation path extraction software for dense jujube garden (*Peng et al., 2018*). *Montalvo et al.* used the second Otsu method to segment images in high weed environment. Set the template in advance before the experiment, extracted the green pixels, separated the crops from the surrounding environment, and then compared it with the template to get the navigation center line after removing the noise (*Montalvo et al., 2012*). *Gu* used the combination of linear transformation and least square method to detect the navigation path when extracting the visual navigation parameters. This method can fuse the set of near distance points detected by the transform to fit the navigation path. The experiment showed that the false detection rate of this method was about 30% lower than that of using only transformation to detect the navigation path (*Gu, 2012*). According to the complex orchard navigation environment, *Feng* proposed an orchard navigation baseline generation algorithm based on image processing, which used two-dimensional Otsu algorithm to obtain the optimal segmentation threshold, binarized the color difference R-B component image, and used the least square method to fit the left and right boundary lines, extracted the center points of each line on the boundary line to generate the orchard navigation baseline (*Feng et al., 2012*). *Yang et al.* used the least square method to obtain the navigation line between rows of corn on the chassis of high gap plant protection machine. Experiments showed that the algorithm had good anti-jamming performance and could adapt to the more complex field environment (*Yang et al., 2020*). *Zeng et al.* used the least square method to fit the harvester operation navigation line to solve the problems of low contrast between the harvested area and the non-harvested area of mature wheat under strong light. The proposed method can accurately extract the wheat harvest sideline and get the harvester operation navigation line (*Zeng et al., 2020*). *Peng et al.* proposed an image processing method based on "row threshold segmentation" to segment the tree trunk and background for the complex environment of dwarf and dense planting jujube garden. According to the vertical gray distribution of the trunk, the floating window gray vertical projection method combined with morphological open close operation was used to extract the trunk region, and the left and right edges were fitted according to the principle of least square method, and the geometric center points of each line on the edge line were extracted to generate the navigation baseline of jujube garden. Many experiments showed that this method was feasible in a variety of complex environments (*Peng et al., 2017*).

The key to the accuracy of visual navigation is path recognition, which is always a difficult problem in unstructured environment. Therefore, according to the characteristics of inter row image of plum grove, an accurate path extraction algorithm is proposed to increase the safety of planting personnel and the production efficiency of plum plant, which lays a foundation for the realization of forestry equipment mechanization in plum grove.

MATERIALS AND METHODS

MATERIALS

Taking Bikeqi plum grove in Hohhot City as the research object, Canon EOS 6D digital camera was used to collect video image information. It mainly collected video information under different light conditions from April to May. The collected information was placed in the memory card to prevent the subsequent video image loss and facilitate the search for the required information.

Chose ASUS laptop with Intel Core i5 processor, 64 bit Win10 operating system, 2.50GHz main frequency and 4G memory. The software was mainly Matlab R2014a.

IMAGE PROCESSING

COLOR SPACE

RGB model is a color space often used in daily life, and there are many kinds of color description models in image processing. However, the three-dimensional coordinate form adopted by RGB color space model makes it very easy to understand, so it is widely used. R, G, B correspond to red, green, blue three color components, three different colors superimposed in RGB color space show different colors. RGB color space can be seen as a unit cube in a rectangular coordinate system. The color of any point is the accumulation of three color components.

The image collected in this study is RGB format, as shown in Fig.1.



Fig. 1 - Image collected in plum grove

HSV (Hue-Saturation-Value) color model is different from RGB color space model, which is generally represented by inverted cone. Although the visual effect of RGB color space model is better, it cannot reflect well the specific color information of the object, and HSV color space can very intuitively express the brightness, hue, and brightness of the color, which is convenient for color contrast and more conducive to image processing in later stage. Therefore, this paper chooses HSV color model for image processing based on the comparison of RGB and HSV color space models. The relation between them is shown in formulas (1) and (2).

$$\begin{cases} H = \begin{cases} \theta & B \leq G \\ 2\pi - \theta & B > G \end{cases} \\ S = \frac{\max(R, G, B) - \min(R, G, B)}{\max(R + G + B)} \\ V = \frac{\max(R, G, B)}{255} \end{cases} \quad (1)$$

$$\theta = \arccos\left\{ \frac{(R - G) + (R - B)}{2[(R - G)^2 + (R - G)(G - B)]^{1/2}} \right\} \quad (2)$$

HOMOMORPHIC FILTERING

In order to make the image clearly visible, highlight the key information, and make the image more conducive to observation and analysis, the image is enhanced. Image enhancement is generally divided into two parts according to its scope: spatial processing and frequency processing.

Homomorphic filtering combines gray-scale transformation with frequency filtering, takes the illuminance in the image as the basis of frequency-domain processing, and uses contrast enhancement and brightness range compression to improve image quality. In the homomorphic filtering, the gray value of the pixel is regarded as the result of the reflectivity and the illuminance. Therefore, if we deal with the relationship between the illuminance, the gray value of the pixel and the reflectivity well, the shadow area which is invisible to the naked eye can be shown.

Homomorphic filter makes the low frequency drop and the high frequency rise. It can reduce the illumination change and sharpen the edge details. At the same time, it is also a nonlinear filter. This technology is mainly based on the illumination reflection imaging in image formation, changing the gray range of the image to adapt to the new situation, so as to reduce or even disappear the uneven illumination in the image, eliminate the noise in the signal, protect the details in the image, and highlight the things in the beneficial area for the research.

In this paper, the dynamic Butterworth filter is selected, the expression is shown in formula (3).

$$H(u, v) = (\gamma_H - \gamma_L) / \left\{ 1 + c [D_0^n / D^m(u, v)]^2 \right\} + \gamma_L \quad (3)$$

In this formula, γ_H and γ_L represent high and low frequency gain respectively, and their value ranges are, $\gamma_H > 1$, $0 < \gamma_L < 1$; m and n are dynamic operators; C and D_0 are constants, which are used to control the slope of transition section of filter function and represent cut-off frequency respectively.

Fig. 2 shows the processing rendering and histogram after using Butterworth filter.

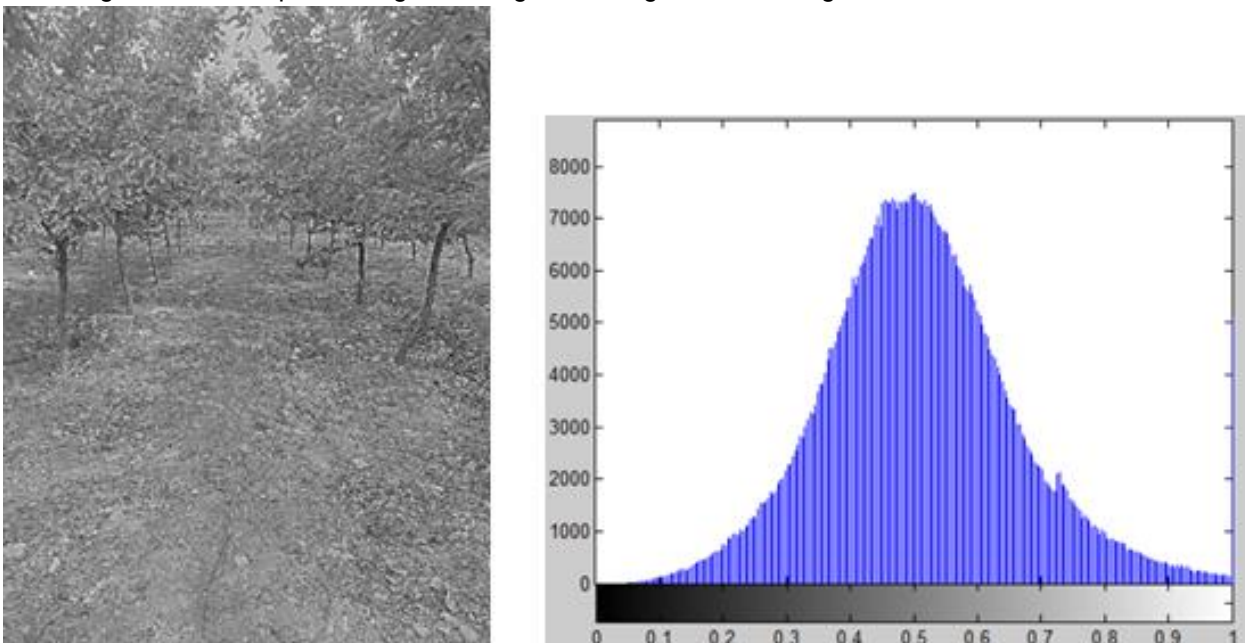


Fig. 2 - Processing rendering and histogram

Image segmentation

Image segmentation means that according to the characteristics of image gray, color, spatial texture and geometric shape, the image is divided into multiple regions by using appropriate image segmentation algorithm. The same region has the same property, and different regions are differentiated. In short, image segmentation is to separate the object from the background in a given image. As for the gray image, the pixels in the region generally have the property of gray similarity, and the pixels in the region edge or the outside show more gray discontinuity.

Image segmentation requires high level of technology and occupies a very large part in image processing, so many researchers have been studying and developing it since 1960s and 1970s.

But up to now, although there is not a perfect method for the problem of image segmentation, there are many methods and results that can be directly used, and these knowledge and rules about image segmentation have reached a consensus.

Threshold segmentation is an easy and efficient method in image segmentation. If the information needed in the image is obviously different from other information, threshold segmentation is often used. The guiding idea of Otsu is clustering idea, which divides the image into two parts: target and background according to the gray level. The variance of the same region is the smallest, and that of different regions is the largest. At present, the simplest algorithm in threshold segmentation is Otsu algorithm, which is easy to calculate and understand, and image contrast and illumination have little effect on it.

The image of threshold segmentation obtained by Otsu is as follows, which can be seen in Fig.3.



Fig. 3 - Otsu segmentation rendering

FEATURE POINT EXTRACTION

In the acquired image, the plum trunk was separated as the target, and then the feature points were extracted according to the segmented image, and the navigation path algorithm was designed according to the feature points.

Feature refers to the fact that a specific object in the part is different from other parts or is a collection of multiple features, which can be obtained by measurement and observation. For different images, each image has its own unique characteristics, which can be distinguished from other images. In an image, the brightness, color, spatial relationship, and edge and so on, which can be directly seen here, are called natural features, while the moment, histogram and other feature information of the image need further processing.

Generally speaking, the gray level on the edge of the image changes slowly, but the change on both sides is obvious, and the edge is the basic feature of the image. It mainly exists in the target, background and region. Therefore, it is the most important basis of image segmentation. The basic idea of edge detection is to first detect the edge points in the image, and then connect the edge points into a contour according to a certain strategy to form a segmentation region.

The edge of an image can be said to be the most basic feature. The main purpose of edge detection is to identify which brightness change is most easily seen in an image. At present, Sobel operator and Prewitt operator are widely used in edge detection. It can not only locate the boundary accurately, but also suppress the noise.

Sobel operator has better edge effect on the image with gradual change of gray level and noisier, simple calculation and fast operation speed. Therefore, this paper selects Sobel operator to detect the edge of plum grove image, as shown in Fig. 4.



Fig. 4 – Otsu feature point extraction

NAVIGATION PATH ALGORITHM GENERATION

After the image is processed by the above operations, the linear equation is obtained by path fitting. At present, the commonly used line fitting methods include least square method, Hough transform and its improved algorithm or vertical projection method (*Guan et al., 2020*). Because Hough transform is more robust, it is widely used. But the path algorithm fitted by the least square method is more accurate and faster. Therefore, in this paper, the least square method is used to fit the path information after obtaining the feature points.

In fact, the least square method fitting is that there is a corresponding Y under a given m sequences X . These corresponding sequences can be regarded as m points, and the coordinates of each point are (X, Y) . The least square method is to find a straight line with $y = kx + b$, so that the sum of squares of the distance between the m points and the straight line $y = kx + b$ (residual error is $\sum |y_i - f(x_i)|^2$) is the minimum. The solution of each coefficient is obtained by its derivation. The above m (X, Y) point sets are brought into the overdetermined equations, and the values of each coefficient are solved. The final equation expression is determined by the obtained coefficient values. The navigation baseline generation effect can be seen in Fig. 5 below.



Fig. 5 - Navigation baseline generation effect

EXPERIMENTAL RESULTS AND ANALYSIS

The resolution of the selected image was 3648 × 2432. The image was collected at different times of one day, and a total of 120 images were obtained. In these images, the plum trunk was used as the recognition target to process the images, and the results were sorted out as shown in the table below.

Table 1

Plum trunk recognition results			
Test conditions	Images number	Accurate detection	Accuracy
	[sheet]	[sheet]	[%]
Strong light	30	19	63.3
Weak light	30	22	73.3
Front light	30	21	70
Back light	30	17	56.7

From the analysis of the results in the above table, it can be seen that the detection rate of the algorithm is low under strong light and back light, while the detection rate can reach 70% or more under both front light and weak light. Under the strong light, the intensity of light in the plum grove is high and the light distribution is uneven, so the shadow of the image is large, and the difficulty of using the algorithm increases. In the case of back light, the image is not clear due to the influence of light, and the characteristic of plum trunk cannot protrude well. In conclusion, the algorithm performs better in weak light and front light environment, but the detection accuracy needs to be improved in strong light and back light environment, so the algorithm needs to be further optimized on the basis of the original research.

CONCLUSIONS

This paper took Bikeqi plum grove in Hohhot City as the research object to study the algorithm of visual path navigation in plum grove. After image acquisition in plum grove by camera, Matlab R2014a was used to process the image. The intersection of plum trunk and the ground was taken as the feature point, and the extracted feature points were fitted to obtain the main information about the navigation path. This paper mainly studies the following parts:

(1) The HSV color model was used to separate the plant from the background in the three HSV channels. The V channel was selected, and then homomorphic filtering was used to enhance the image.

(2) Otsu was selected to segment the image, and the intersection of plum trunk and ground was determined as the feature point of the image. So the feature information of intersection point can be extracted.

(3) According to the information of the feature points, the least square method was selected to fit the data to get the navigation algorithm, and the navigation algorithm was tested. The results show that the proposed algorithm can generate the navigation baseline more accurately. The detection rate of the algorithm is low under strong light and back light, and the detection rate can reach 70% or more under front light and weak light, which can provide a certain foundation for realization of mechanical vision navigation of plum field management.

ACKNOWLEDGEMENTS

We acknowledge that this work was financially supported by Inner Mongolia Autonomous Region Natural Science Foundation Project (2019BS06003) and Inner Mongolia Autonomous Region Scientific research projects of colleges and universities (NJZY19288).

REFERENCES

- [1] An Q., (2008), *Research on illumination issue and vision navigation system of agricultural robot*, PhD dissertation, Nanjing Agricultural University, Jiangsu / China;
- [2] Feng J., Liu G., Si Y.S., (2012), Algorithm Based on Image Processing Technology to Generate Navigation Directrix in Orchard, *Transactions of the Chinese Society for Agricultural Machinery*, vol.43, Issue 7, pp.184-189;
- [3] Gu B.X., (2012), *Research on intelligent mobile fruit picking robot*, PhD dissertation, Nanjing Agricultural University, Jiangsu / China;

- [4] Guan Z.H., Chen K.Y., Ding Y.C., Wu C.Y., Liao Q.X., (2020), Visual navigation path extraction method in rice harvesting, *Transactions of the Chinese Society for Agricultural Machinery*, vol.51, Issue 1, pp.19-28;
- [5] Hou X.G., Chen Y., Guo W.B., (2008), Machine vision-based navigation for a weeding robot, *Transactions of the Chinese Society for Agricultural Machinery*, vol.39, Issue 3, pp.106-108+112;
- [6] Li W.Y., (2017), *Research on the method of generating visual navigation path of kiwi picking robot*, MSc dissertation, Northwest A&F University, Shanxi / China;
- [7] Liu B., (2019), *Research on visual navigation system of citrus picking robot mobile platform*, MSc dissertation, Chongqing University of Technology, Chongqing / China;
- [8] Liu Y., Gao G.Q., (2019), Recognition of visual navigation directrix between winter fruit tree row, *Journal of Chinese Agricultural Mechanization*, vol.40, Issue 5, pp.160-166;
- [9] Montalvoa M., Pajares G., Guerrero J.M., et al, (2012), Automatic detection of crop rows in maize fields with high weeds pressure, *Expert Systems with Applications*, vol.39, Issue 15, pp.11889-11897.
- [10] Peng S.Z., Kan Z., Li J.B., (2017), Extraction of visual navigation directrix for harvesting operation in short-stalked and close-planting jujube orchard, *Transactions of the Chinese Society of Agricultural Engineering*, vol.33, Issue 9, pp.45-52;
- [11] Peng S.Z., Li J.B., (2018), Design and implementation of jujube garden visual navigation path extraction software, *Jiangsu Agricultural Sciences*, vol.46, Issue 10, pp.213-217;
- [12] Ye X.Q., Chen C., (2017), Autonomous navigation system for orchard working robot based on image boundary extraction, *Journal of Agricultural Mechanization Research*, vol.39, Issue 8, pp.202-206;
- [13] Yang Y., Zhang B.L., Zha J.Y., et al, (2020), Real-time extraction of navigation line between corn rows, *Transactions of the Chinese Society of Agricultural Engineering*, vol.36, Issue 12, pp.162-171;
- [14] Zhang Z.Y., (2016), *Research on the key technology of autonomous navigation for orchard mobile robot*, MSc dissertation, Huazhong University of Science and Technology, Hubei / China;
- [15] Zhang Q., Song J., Gao G.H., Yuan F.R., (2018), Path recognition algorithm and experiment of greenhouse robot by visual navigation, *Research and Exploration in Laboratory*, vol.37, Issue 5, pp.14-16+41;
- [16] Zeng H.W., Lei Z.B., Tao J.F., Zhang W., Liu C.L., (2020), Navigation line extraction method for combine harvester under low contrast conditions, *Transactions of the Chinese Society of Agricultural Engineering*, vol.36, Issue 4, pp.18-25.

RESEARCH OF A LATERAL REAMER BIT FOR DIGGING PLANTING HOLE IN ROCKY ABANDONED MINE AREA

面向废弃矿山地区造林挖坑的横向扩孔钻具研究

Luo Haifeng ^{*)}, Chen Chaoyu

Beijing Forest University, Beijing / China;
Tel: 8601062338144; E-mail: luohaifeng@bjfu.edu.cn
DOI: <https://doi.org/10.356.33/inmateh-65-13>

Keywords: rock, planting hole, lateral, reamer bit, metamorphic, digging

ABSTRACT

In the abandoned mine area with Karst landform in China, soils are few and thin but rocks are common, traditional planting hole diggers are unequal to work in rocks for vegetation restoration. A reamer bit with variable lateral drilling radius was designed based on the PDC (polycrystalline diamond compact) bit technology and metamorphic mechanism. Two lateral camber blades with PDC teeth were installed inside the bit body, a screw mechanism was employed as the actuation and a spatial double triangle mechanism was taken for the transmission. The curve of the camber blade was specially defined thus the reaming load was decentralized to 85.7% teeth on the blade. The kinematics of the lateral reamer bit was analysed, the mapping models from the actuation to the reaming radius and speed were established. Concrete samples were reamed indoors from 240mm to 407mm in diameter, the reaming cutting load and time length were measured and analysed. The lateral reamer bit was approved with the experiment results, this study provided equipment support for digging the planting hole in rocky abandoned mine areas and also expanded the PDC bit application.

摘要

中国岩溶地区废弃矿山缺乏土壤岩石大面积裸露，传统植树挖坑机无法在岩石中挖坑造林，生态恢复难度大，亟需研制岩石钻孔挖坑机。结合岩石 PDC 钻头技术及变胞机构理论，设计了横向可变钻削半径的扩孔钻头。钻头内对称布置了 2 个镶 PDC 齿的横向曲面刀翼，以螺旋传动机构为变径驱动，以空间双三角形机构为传动机构，为均衡扩孔载荷单独定义了曲面刀翼形状。分析建立了横向扩孔钻头的运动学模型，推导了驱动螺旋到输出扩孔半径及速度的映射模型。以混凝土试样为对象，进行了室内横向 240mm 至 407mm 直径的扩孔试验，测试分析了扩孔过程中的载荷曲线及时间。验证了横向岩石内部扩孔挖坑的可行性，本文的研究为岩溶地区废弃矿山的挖坑造林提供了装备支持，同时扩大了 PDC 钻具技术的应用场景。

INTRODUCTION

The abandoned mines affect and even destroy the regional ecosystem, making the ecological restoration of abandoned mine area an inevitable step of social civilization (Zhang J.D. et al., 2020). The abandoned mine in southwest China, combined with the landform of Karst stony desertification, brings serious challenge in vegetation restoration and commercial crop growing (Dai Q.H. et al., 2018). The soil layer is thin and few, whereas the rocks of big area are common, and the heavy rainfall washes the soil away yearly. The planting hole for vegetation, forestry sapling even fruit tree in this rocky area is not feasible to be dug by the traditional digging mechanism (Yoshida T. et al., 2013), as the rock is quite different with soil in material behaviour such as hardness and strength. The hole inside the rocks are drilled mostly by the PDC bit, which has a market share of about 85% (Scott D., 2015), the digging mechanism for the planting hole in rocky abandoned mine area is thus supposed to be constructed as a PDC bit type. The PDC bit for rocks is often with two or more blades, and the PDC teeth (shorten as tooth and teeth in the following text) are welded along the edge of the blades in a manner that all the teeth can cut the rock material one by one when the bit rotates and feeds forward. The shape and diameter of the holes made in the rock are directly determined by the bit blades and teeth on them, the existing blades on the bit are mostly fixed structure. The hole is thus a single straight cylinder shape with a constant diameter, which is equal to the cutting dimension of the bit teeth (Tang Q.Q. et al., 2018; Wang S.N. et al., 2014; Yang Y.X. et al., 2019). The hole in rock can be reamed by another bigger size bit which is installed behind the guiding bit, in the axis direction of hole and extends a long depth (Sun R.J. et al., 2017; Yang Y.X. et al., 2020).

Another type of drill bit for foundation stake in the civil engineering of rocky area is basically constructed with a metamorphic triangle blades, the hole with a cone shape for the stake is reamed by the teeth on the hypotenuse of triangle blades (Hu Z.H., 2020). The existing digging mechanism and PDC bit found in the literature are not competent in digging the planting hole directly in the rocky abandoned mine area.

A lateral reamer bit for digging the planting hole in rocky abandoned mine area was designed based on the PDC bit technology (Huang Z.Q. et al, 2017) and metamorphic mechanism (Wang R.G. et al., 2019), the blade of the reamer bit was evolved from traditional type (Akbari et al, 2016) to a camber shape. The curve of the blade was studied mainly with two relevant angles, a spatial double triangle mechanism was employed as the transmission mechanism for turning the blades. The resistance cutting load of the reamer bit were tested indoors with a lateral reamer bit prototype and concrete samples.

MATERIALS AND METHODS

Materials

In the rocky abandoned mine area with Karst landform, the soil is precious to grow vegetation, and it is more possible to be washed away by the heavy rainfall. The expected planting hole is preferred to have a big intra-rock space but a small neck channel to protect the soil from losing, as shown in Figure 1, which has an improved shape compared with the common planting hole in the rich soil area. The intra-rock planting hole is also able to contain more soil to improve survival rate of the sapling for forestry or even fruit tree. The variable diameters of the neck channel and intra-rock space demand a metamorphic structure for the new PDC digging bit (Wang R.G. et al., 2019). The new bit is expected to drill a hole with small diameter inside the rock first, and later ream the small hole to an intra-rock space, as indicated in Figure 1.

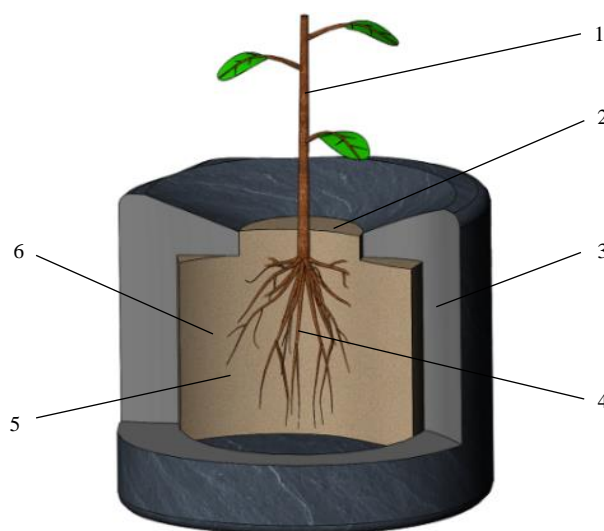


Fig. 1 - Planting hole in rock

1. Sapling; 2. Neck channel; 3. Rock; 4. Root; 5. Soil; 6. Intra-rock space

Methods

Mechanical structure of the reamer bit

To dig the intra-rock planting hole, the drill bit is expected to dig a straight hole of small diameter, and later the small hole is reamed laterally to a big space. The first step can be done by the existing drill bit without difficulty, the second step is the research target in this study. Figure 2. a shows the mechanical structure of the lateral reamer bit for digging the intra-rock planting hole. Two symmetrical camber blades are installed inside the main body via rotation joints R shown in Figure 2. c, the teeth are welded on the external surface of the camber blades to cut the side material of the small inner hole. The internal distal of the camber blade is drove with an universal joint pin (cross axis B and B'), which is further motivated by the upper push bar and lower push bar at joint B. The upper push bar and lower push bar are vertically connected to the upper slider and lower slider through joints A and C, which are further drove by the push rod and pull rod, the push rod and pull rod are linked to a screw joint D outside the guide column. The fixed handle is attached to the push rod, the drive handle and fixed handle are the actuation components to drive the screw joint D and following parts to unfold or withdraw the camber blades relative to the main body.

The transmission of a single lateral reamer bit is simplified and shown as Figure 2. b and c, the actuation triangle ΔABC is comprised of upper push bar (l_{AB}) and lower push bar (l_{BC} , $l_{AB}=l_{BC}$) at the side view, joints A and C are with a distance r_0 to the main body axis O and are drove symmetrically by the screw joint D. And the height h of the triangle ΔABC is the virtual part that actuates the camber blade through the universal joint B' at the top view. The unfolding triangle $\Delta ORB'$ for the camber blade is formed by OR (l_{OR} , structure distance of joint R to axis O), RB' ($l_{RB'}$, structure distance of joint R to joint B') and OB' ($l_{OB'}$, distance of joint O to joint B', $l_{OB'} = h + r_0$). The displacement of joint A and C are labelled as s_1 and s_2 ($|s_1|=|s_2|$). The final unfolding angle displacement of line RB' at joint R is marked as θ . With the spatial double triangle transmission mechanism, the actuation displacement s_1 from the screw joint D is transformed to the rotation angle θ of the camber blade, the reaming structure and related cutting radius of the reamer bit is thus varied and controlled.

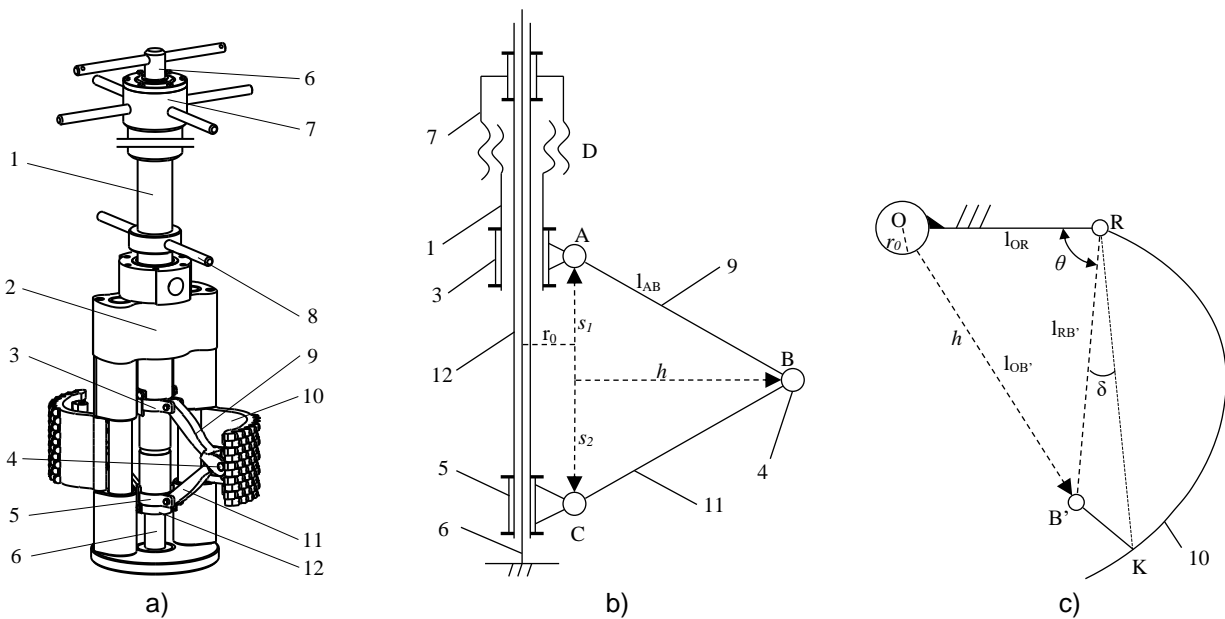


Fig. 2 - Metamorphic lateral reamer bit

a) Mechanical structure; b) Actuation triangle (side view); c) Unfolding triangle (top view)

1. Push rod; 2. Main body; 3. Upper slider; 4. Universal joint pin; 5. Lower slider; 6. Guide column; 7. Drive handle;
8. Fixed handle; 9. Upper push bar; 10. Camber blade; 11. Lower push bar; 12. Pull rod

With geometric model of the reamer bit shown in Figure 2. b and c, the height h of the actuation triangle ΔABC can be obtained as:

$$h = \sqrt{l_{AB}^2 - s_1^2} \tag{1}$$

In the unfolding triangle $\Delta ORB'$ it has:

$$\cos \theta = (l_{OR}^2 + l_{RB'}^2 - l_{OB'}^2) / 2l_{OR}l_{RB'} \tag{2}$$

And the unfolding joint angle θ is thus:

$$\theta = \arccos \frac{l_{OR}^2 + l_{RB'}^2 - (\sqrt{l_{AB}^2 - s_1^2} + r_0)^2}{2l_{OR}l_{RB'}} \tag{3}$$

Curve of the camber blade

The teeth are welded on the surface of camber blade, the cutting characteristic of the lateral reamer bit is directly determined by the curve of the camber blade. To decentralize the cutting load averagely to each teeth, the reaming cutting is designed to be started from the proximal tooth to the distal tooth on the camber blade. The curve of the camber blade is defined as following steps as shown in Figure 3. B_i ($i=1,2,\dots,9$) is the typical point on the camber blade curve RB_i , the tip of teeth T_i is welded and overlap with point B_i .

Step 1: an auxiliary line RK is defined through joint R, with an angle α_0 relative to the minus of OR. A series of concentric arcs with radius of r_i ($r_{i+1} = r_i + 5$) are intersected with line RK at points B_i' , B_i' is the reference cutting point of each cutting radius of r_i ;

Step 2: at the beginning of the anti-clock wise unfolding for the camber blade curve RB_i , the tooth T_1 on point B_1 is the first one to be rotated out and to cut the material, with the cutting point B_1' on line RK and a radius of r_1 . The cutting radius r_i of other teeth T_i on B_i ($i \neq 1$) is less than r_1 , the reaming cutting around radius of r_1 is done by the tooth T_1 ;

Step 3: the curve RB_i is then unfolded with an angle $\angle KRC_1$ ($\angle KRC_1 = \angle C_i RC_{i-1} = \beta$, $i = 2, \dots, 9$), the tooth T_2 on point B_2 is rotated to the position B_2' on line RK, the cutting radius is increased to r_2 . Tooth T_1 on the position B_1 is rotated to the radial line RC_1 , the cutting radius r_i of other teeth T_i ($i \neq 2$) is less than r_2 , the reaming cutting around radius of r_2 is done by the tooth T_2 ;

Step 4: the curve RB_i is unfolded step by step with an angle $\angle KRC_1$, each tooth T_i on point B_i is rotated to the position of B_i' on line RK, the related cutting radius becomes r_i . B_{i-1} is rotated to the radial line RC_{9+i-i} , the cutting radius r_j of other tooth T_j on B_j ($j \neq i$) is less than r_i , the reaming cutting around radius of r_i is done by tooth T_i on point B_i ;

Step 5: as the last point B_9 is unfolded to the line RK, the curve RB_i is formed mainly by the points B_i ($i=1,2, \dots,9$). The precise position of each B_i can be obtained from above steps.

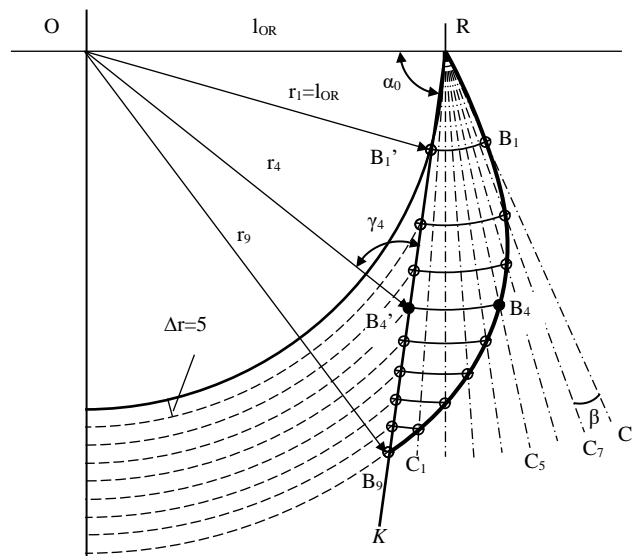


Fig. 3 - Camber blade curve

Take point B_4 as an example, in the triangle $\Delta ORB_4'$ it has:

$$\frac{l_{OR}}{\sin \gamma_4} = \frac{r_4}{\sin \alpha_0} \tag{4}$$

It deduces:
$$\gamma_4 = \arcsin \frac{l_{OR} \cdot \sin \alpha_0}{r_4} \tag{5}$$

For l_{RB_4} of RB_4' in the triangle $\Delta ORB_4'$ it also has:

$$\frac{l_{RB_4'}}{\sin(\pi - \alpha_0 - \gamma_4)} = \frac{r_4}{\sin \alpha_0} \tag{6}$$

Thus:
$$l_{RB_4} = l_{RB_4'} = \frac{r_4 \cdot \sin(\pi - \alpha_0 - \gamma_4)}{\sin \alpha_0} \tag{7}$$

With the l_{RB_4} and $\angle ORC_5 = \pi + \pi \cdot (\alpha_0 + (9-4) \cdot \beta) / 180$, the present coordination of B_4 are:

$$\begin{cases} x_{B_i} = l_{RB_4} \cdot \cos(\pi + \pi \cdot (\alpha_0 + (N-i) \cdot \beta) / 180) + l_{OR} \\ y_{B_i} = l_{RB_4} \cdot \sin(\pi + \pi \cdot (\alpha_0 + (N-i) \cdot \beta) / 180) \end{cases}, N=9, i=4 \quad (8)$$

The position of each point B_i ($i=1, \dots, 9$) on the curve RB_i in Figure 3 can be obtained similarly with equation (8), and the shape of the camber blade is thus determined. The curve RB_i is then rotated clock-wise with an angle of $(N-1)\beta$ to withdraw it inside the initial radius of r_1 . The coordination of each point B_i can be further deduced when the camber blade is unfolded again with a smaller step angle of $\beta/2$ in the normal reaming process as:

$$\begin{cases} x'_{B_{ij}} = l_{RB_i} \cdot \cos(\pi + \pi \cdot (\alpha_0 - (N-1) \cdot \beta + (N-i) \cdot \beta + j \cdot \beta/2) / 180) + l_{OR} \\ y'_{B_{ij}} = l_{RB_i} \cdot \sin(\pi + \pi \cdot (\alpha_0 - (N-1) \cdot \beta + (N-i) \cdot \beta + j \cdot \beta/2) / 180) \end{cases} \quad (9)$$

Here $N=9, i=1 \dots 9, j=1 \dots 16$, j is the serial number of step unfolding rotation for the camber blade, the cutting radius of each tooth T_i on B_i ($i=2, \dots, 9$) relative to the step rotation is thus:

$$r_{cT_{ij}} = \sqrt{(x'_{B_{ij}})^2 + (y'_{B_{ij}})^2} \quad (10)$$

And the max cutting radius of the camber blade on each step unfolding rotation is obtained as:

$$r_j(\alpha_0, \beta) = \max r_{cT_{ij}}, i=1, 2 \dots N, j=1, 2 \dots 16 \quad (11)$$

The parameters for camber blade curve RB_i can be further increased to $N=21, j=40$, $r_1=100, r_{21}=200$, the reaming cutting radius is thus varied from 100mm to 200mm. The instantaneous max reaming cutting radius r_j of each step unfolding rotation is related to a certain tooth T_i , and the relation between r_j and T_i is affected by the angles α_0 and β . The preferred parameters of them are determined as $\alpha_0=88^\circ, \beta=3.4^\circ$ finally to decentralize the cutting load to majority of teeth. And the reaming cutting radius r_j and related tooth number T_i are calculated with equation (10) to (11) and shown in Figure 4. a. Not exactly as expected, the camber blade cuts from tooth T_3 to T_{20} as it is unfolded, it means 85.7% of the teeth are functional in the reaming process, and each tooth T_i cuts about two or three step rotations of $\beta/2$ for the camber blade. The actual simplified camber blade curve and structure in this study is shown in Figure 4. b, 75 teeth are assembled row (7 teeth) by row (8 teeth) on one camber blade totally, to ream the rock hole from 220mm to 400mm in diameter. The back angle of each tooth T_i is set as 12 degrees relative to the curve normal at point B_i to ream with a low resistance load (Huang Z.Q. et al, 2017).

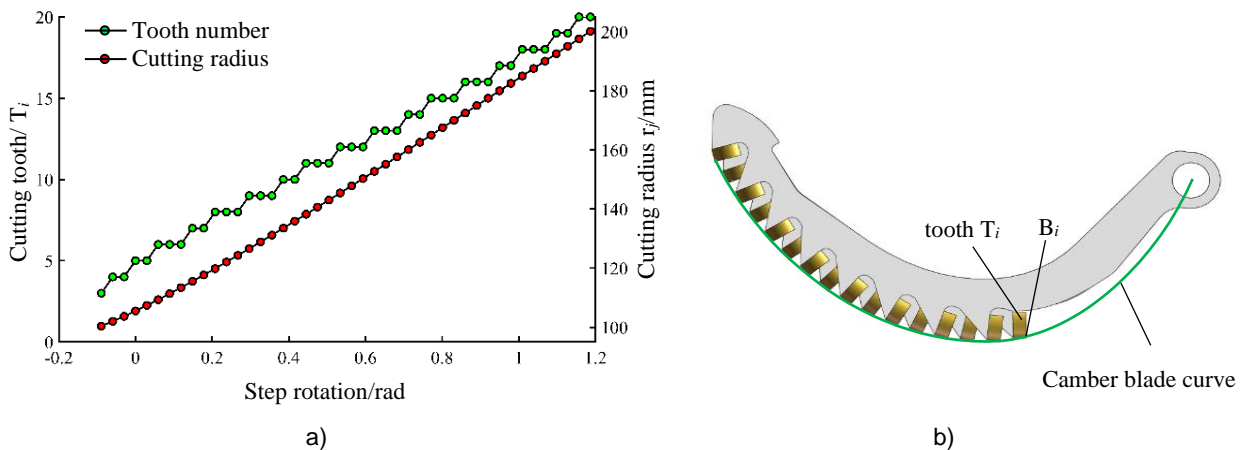


Fig. 4 - Cutting characteristic of camber blade
 a) Cutting radius and related tooth; b) Preferred camber blade curve and actual structure

Reaming cutting radius of the reamer bit

Joint the equations (11) and (3), the relation between the displacement s_1 of the actuation triangle ΔABC and the cutting radius r_j of the camber blade is deduced as:

$$r(s_1) = \max \left[\left(\frac{r_i \cdot \sin(\pi - \alpha_0 - a \sin \gamma_i)}{\sin \alpha_0} \cos\left(\pi + \pi \cdot \frac{\alpha_0 + \delta + \beta - i \cdot \beta}{180}\right) + a \cos \frac{l_{OR}^2 + l_{RB}^2 - (\sqrt{l_{AB}^2 - s_1^2} + r_0)^2}{2l_{OR}l_{RB}} \right) + l_{OR} \right]^2 + \left(\frac{r_i \cdot \sin(\pi - \alpha_0 - a \sin \gamma_i)}{\sin \alpha_0} \sin\left(\pi + \pi \cdot \frac{\alpha_0 + \delta + \beta - i \cdot \beta}{180}\right) + a \cos \frac{l_{OR}^2 + l_{RB}^2 - (\sqrt{l_{AB}^2 - s_1^2} + r_0)^2}{2l_{OR}l_{RB}} \right)^2 \right]^{1/2} \tag{12}$$

Where $i = 1, 2 \dots 21$, and $\delta = 2.93^\circ$ is the structure angle between RB' and auxiliary line RK in Figure 2. c. The variation of reaming cutting radius $r(s_1)$ of the bit is calculated with equation (12) and shown in Figure 5. a. The reaming radius $r(s_1)$ is increased rapidly at the beginning of the actuation displacement ($s_0 - s_1, s_0$ is the original position of s_1), and slows down in the latter process. Differentiating the equation (12) to time t , the reaming speed of the camber blade $v_{r(s_1)}$ can be deduced as:

$$v_{r(s_1)} = \frac{dr(s_1)}{dt} = \frac{dr(s_1)}{ds_1} \cdot \frac{ds_1}{dt} = r'(s_1) \cdot v_{s_1} \tag{13}$$

The $r'(s_1)$ is the derivative of the reamer radius $r(s_1)$ to s_1 , which is determined by the transmission parameters of the reamer bit, and the relationship between the actuation speed v_{s_1} and reaming speed $v_{r(s_1)}$ is reflected with it. As the reaming radius $r(s_1)$ is increased with a constant bit rotation speed, the relative speed of the tooth to the rock material will increase linearly. To maintain a constant cutting volume of the rock material in a time period for a tooth, the actuation speed v_{s_1} of the camber blade should be controlled as shown in Figure 5. b. The time length is calculated as about 3 hours, and the expected actuation speed v_{s_1} is increased from about 0.002mm/s to about 0.012 mm/s.

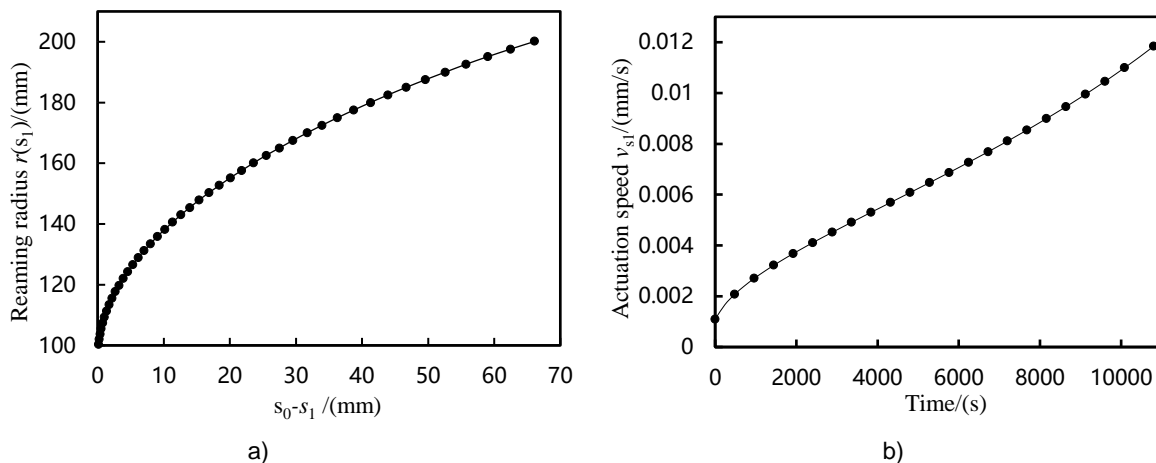


Fig. 5 – Reaming radius and actuation speed for camber blade

a) Reaming radius to actuation; b) Expected actuation speed to time

RESULTS

Prototype and indoor experiment

The prototype of the lateral reamer bit has been built and assembled as shown in Figure 6, and the reaming cutting experiments are carried out with it indoors. The max reaming dimension is designed as 400mm in diameter and 130 in height one time to ease the initial test process. The main body of the reamer bit is arranged to be still but the reaming target sample is drove to rotate by motor relative to the bit axis.

The reaming sample is made of concrete with small rocks around 10mm in dimension, as the standard cylindrical rock sample of 450mm in diameter is difficult to get. The concrete sample is rotationally installed on the frame under the reamer bit, four side supporters are arranged around it to improve the rotation precision of the sample, and also to make the concrete sample being coaxial with the reamer bit. The reamer bit is installed on a lifting board, which is drove by manual lift screw mechanism and guided with the guide rail, to land the reamer bit to the inside of the concrete sample. As mentioned above, this study puts emphasis on the reaming process, the concrete sample is constructed as a tubular shape with an inner hole of 240 mm in diameter. The reaming cutting torque of the bit is transformed to the pressure from the measure arm to the pressure sensor on the lift board. A displacement sensor is installed to the fixed handle to measure the motion of the push rod (s_1). A pump circulation system is employed to provide water flow to cool the reaming tooth and take away the drill cuttings made inside the concrete sample.

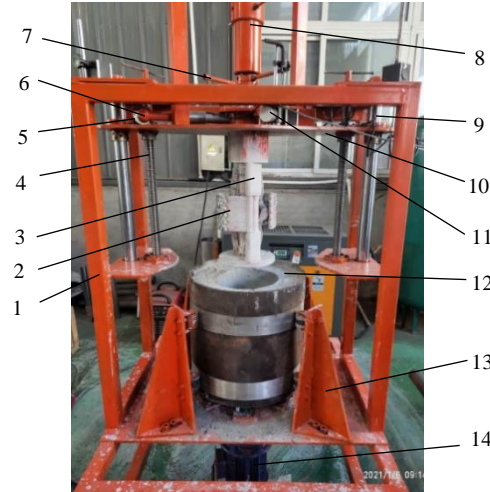


Fig. 6 - Experiment setup for lateral reaming bit

1. Frame; 2. Camber blade; 3. Main body; 4. Lift screw; 5. Pressure sensor; 6. Measure arm; 7. Fixed handle; 8. Drive handle; 9. Guide rail; 10. Lift board; 11. Displacement sensor; 12. Concrete sample; 13. Side supporter; 14. Motor

The parameters of the parts employed in the indoor reaming experiment are listed in Table 1. The experiment was firstly carried out with the concrete sample being rotated at speed of 24 rot/min (Dai X.W. et al., 2020; Zhu X.H. et al., 2020), and the initial actuation speed of the screw mechanism for the reaming of the camber blade was set as about 0.001 mm/s, as shown in Figure 5. b. The signals of the pressure sensor and displacement sensor, and the time length for a whole reaming process were both recorded, the speed for rotating the concrete sample was improved for each sample.

Table 1

Parameters of experiment parts

Item	Inner hole diameter of concrete sample [mm]	Diameter of concrete sample [mm]	Height of concrete sample [mm]	Range of displacement sensor [mm]	Precision of displacement sensor [mm]	Pump flow [m ³ /h]
Parameters	240	450	450	300	0.2	8
Item	Range of pressure sensor [N]	Precision of pressure sensor [N]	Power of motor [kW]	Speed of motor [rot/min]	Reaming height of bit [mm]	Min reaming diameter [mm]
Parameters	1000	1	3	0-60	130	220
Item	Max reaming diameter [mm]	Diameter of tooth [mm]	Total number of teeth	Back angle of tooth [degree]	Strength of concrete sample [MPa]	Number of concrete samples
Parameters	400	13.4	150	12	32	4

Experiment result and analysis

Four concrete samples were reamed in the indoor experiment, and the reaming result of the fourth concrete sample was shown in Figure 7. The concrete sample was constructed with an inner hole of 240mm

in diameter, as shown in Figure 7. a and b, and the inner hole was a little larger than the initial reaming diameter 220mm of the prototype bit to ease the preparation of experiment. The inner hole of the concrete sample was finally reamed to 407mm in diameter, as shown in Figure 7. c. The side face of the reamed hole was cut with corrugated shape, as shown in Figure 7. d and e, the corrugated shape was made by the serriated teeth rows on the camber blade. The enlarged view in Figure 7. e for the corrugated side face of the reamed hole indicated that the small rocks in the concrete sample were tightly fixed in the sample without breakage in the reaming process. And the small rocks are reamed layer by layer to the corrugated shape under the reaming cutting of the teeth, the concrete sample was considered to be qualified for the reaming cutting validation. The dimensions of the reamed inner hole in the fourth concrete sample was measured and shown in Figure 7. g, the max diameter of the reamed hole was measured as 407mm, and the height of the reamed hole was 195mm, which was combined with a whole height reaming and a half height reaming of the bit, and the height of the reamed hole could be further increased if the reamer bit was fed more along the height direction by the lift screw mechanism. During the reaming process of the concrete sample, no slag had been generated by the bit, all the materials in the cutting area were transformed to fines and then mixed with water into slurry, as shown in Figure 7. c. The transmission mechanism, camber blades, teeth were in good condition after reaming the four concrete samples, no macroscopic wear was found at the cutting edge of the teeth. As the flow magnitude of the pump was not powerful enough, the bit balling was found on the camber blades, as shown in Figure 7. f, which should be improved in the future.

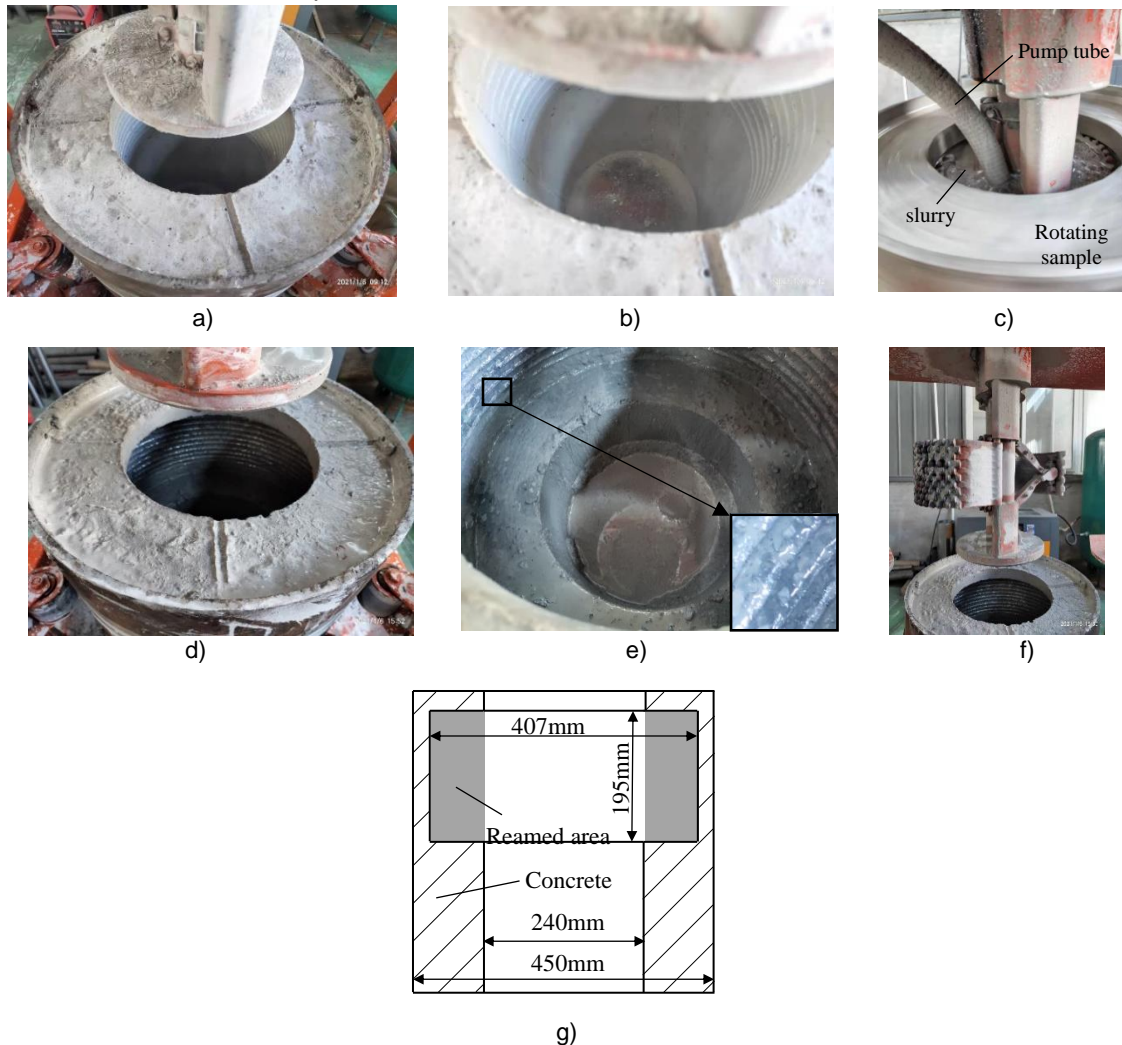


Fig. 7 - Reaming process of concrete sample

a) Sample before reaming; b) Inner hole before reaming; c) Reaming the sample; d) Reamed sample; e) Inside of reamed sample; f) Max reaming radius of the bit; g) Profiles of reamed sample

The displacement of the actuation screw mechanism for reaming the fourth concrete sample was measured and shown in Figure 8. a, the time length was totally about 6000s (1.6h). Due to the material fragility of the concrete sample, the reaming cutting was accompanied by the vibration between the tooth and the concrete sample, the signal of the displacement sensor was disturbed by the vibration of prototype machine,

as the impulse shown on the displacement curve. The actuation speed for the screw mechanism was further calculated with the displacement signals and shown in Figure 8. b, the actual actuation speed was increased from about 0.002 m/s to 0.025 m/s for the fourth concrete sample, it was about two times relative to the curve value in Figure 5. b., which had a similar curve shape but longer time period. The axis speed for the fourth concrete sample was set at about 60 rot/min.

The reaming cutting resistance load for the fourth concrete sample was measured and recorded as shown in Figure 8. c, the resistance torque for single teeth row on the camber blade waved around 10N.m due to the vibration of the reamer bit. The reaming cutting load and time length for reaming the four concrete samples were combined in Figure 8. d. As the rotation speed of the concrete sample was improved from 24rot/min to 36 rot/min, 48 rot/min and 60rot/min, the reaming cutting torque for single teeth row was reduced from about 20.5Nm to 13.3Nm, 11.3Nm and 9.6Nm as expected (Abugharara et al., 2019; Rostamsowlat et al., 2018), but the rate for torque decline became smaller. The time length for concrete sample reaming was also reduced from 4.1h to 3h, 2.3h and 1.6h, it was more efficient to ream the rock with higher rotations speed under the circumstances of device safety.

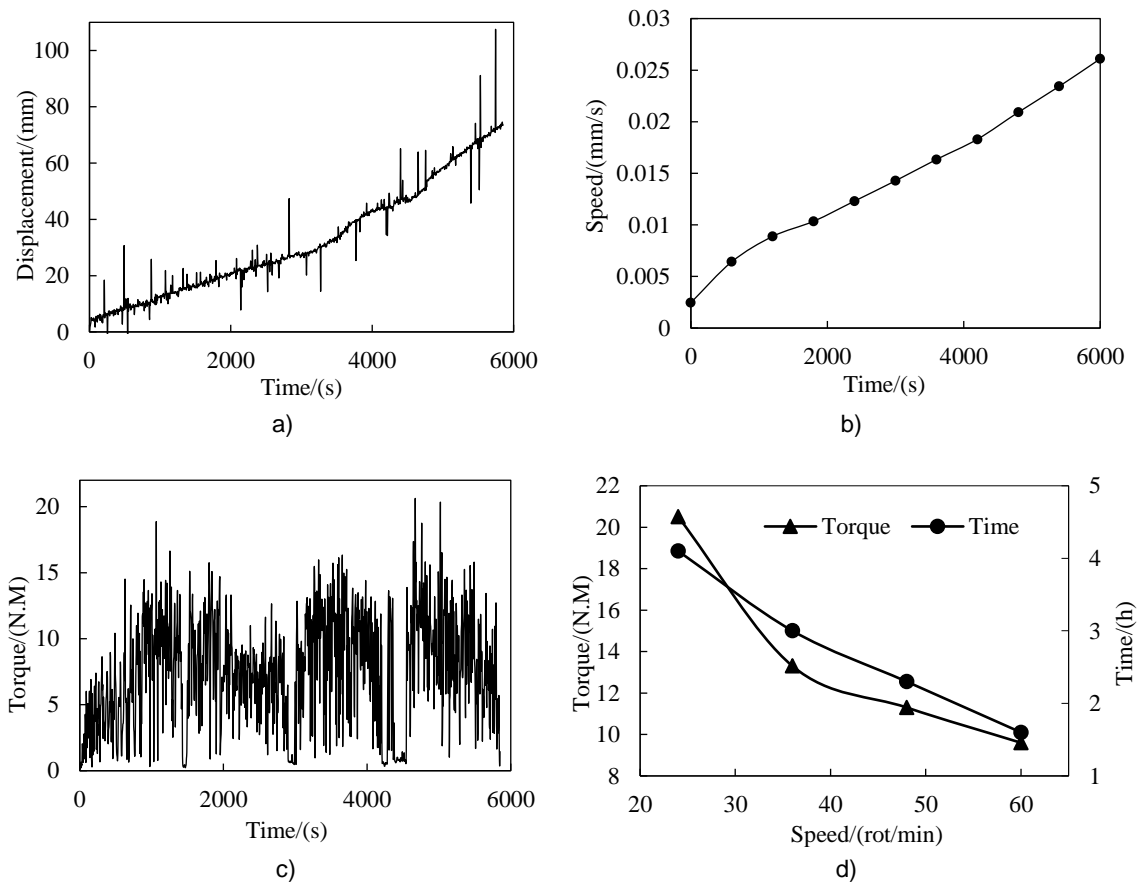


Fig. 8 - Reaming cutting parameters

a) Displacement of actuation; b) Speed of actuation; c) Resistance load; d) Resistance and time to actuation speeds

CONCLUSIONS

(1). To dig the planting hole in the rocky abandoned mine areas, a lateral reamer bit which integrated the PDC bit technology and metamorphic mechanism was proposed in this study. The mechanical structure of the lateral bit was designed mainly with two symmetrical lateral camber blades drove by the spatial double triangle transmission mechanism.

(2). The kinematics model for the transmission mechanism was established, to decentralize the reaming cutting load of the teeth on the camber blade, the curve of blade was defined mainly considering the angle α_0 of the auxiliary line RK and the step rotation angle β of the camber blade.

The preferred parameters were determined as $\alpha_0=88^\circ$ and $\beta=3.4^\circ$, with a utilization rate of 85.7% of the teeth on the camber blade. The mapping models from the actuation screw mechanism to the final reaming radius and speed were deduced.

(3). Four concrete samples were employed to test the lateral reamer bit indoors. The inner holes of the concrete samples were reamed from 240mm to 407mm in diameter. The concrete samples were reamed with lower resistance load and shorter time length as the rotation speed of the concrete sample was improved. The experiment result approved the lateral reaming method and bit design, and the planting hole was feasible to be dug with it for the vegetation restoration in abandoned mine area. Improvement is need for the present design of the lateral reamer bit to obtain better reaming cutting effect.

ACKNOWLEDGEMENT

This work is supported by the Fundamental Research Funds for the Central Universities (2017ZY46) and National Science Foundation (Grant numbers: 51705022)

REFERENCES

- [1] Akbari B, Miska S. (2016). The effects of chamfer and back rake angle on PDC cutters friction[J]. *Journal of Natural Gas Science and Engineering*, 33, 347-353.
- [2] Abugharara A.N, Mohamed B, Hurich C, Molgaard J. (2019). Experimental investigation of the effect of shale anisotropy orientation on the main drilling parameters influencing oriented drilling performance in shale[J]. *Journal of Energy Resources Technology-Transactions of the ASME*, 141(10).
- [3] Dai XW, Huang ZW, Shi HZ, Cheng Z. (2020). Rock failure analysis based on the cutting force in the single PDC cutter tests[J]. *Journal of Petroleum Science and Engineering*, 194.
- [4] Dai QH, Yan YJ. (2018). Advances in studies on rocky desertification and soil erosion in Karst regions in southwest China [J]. *Journal of Soil and Water Conservation*, 32(02), 1-10.
- [5] Hu ZH. (2020). Design and Construction of hydraulic reaming device [J]. *Construction Technology*, 49(01), 48-50.
- [6] Huang ZQ, Ma YC, Li Q, Xie D. (2017). Geometry and force modelling, and mechanical properties study of polycrystalline diamond compact bit under wearing condition based on numerical analysis[J]. *Advances in Mechanical Engineering*, 9(6).
- [7] Rostamsowlat I, Akbar B, Evans B. (2018). Analysis of rock cutting process with a blunt PDC cutter under different wear flat inclination angles[J]. *Journal of Petroleum Science and Engineering*, 171, 771-783.
- [8] Scott D. (2015). A bit of history: overcoming early setbacks, PDC bits now drill 90%-plus of worldwide footage. In: International Association of Drilling Contractors (IADC) (ed.) *Drilling contractor anthology series—DC drill bits*. Houston, TX: IADC, pp.1–7.
- [9] Sun RJ, Ju P, Shi ZJ. (2017). Simulation study of new directional drilling PDC bit used in coal mine[J]. *Geosystem Engineering*, 20(3), 142-148.
- [10] Tang QQ, Guo W, Gao K, Gao RF, Zhao Y, Sun Y, Zhou Y.(2018). Design and test of a self-adaptive bionic polycrystalline diamond compact bit inspired by cat claw[J]. *Advances in Mechanical Engineering*, 10(11).
- [11] Wang RG, Liao YF, Dai JS. (2019). The isomorphic design and analysis of a novel plane-space polyhedral metamorphic mechanism[J]. *Mechanism and Machine Theory*, 131, 152-171.
- [12] Wang SN, Niu QL, Shi BY, Jia W. (2014). Research and computer-aided design of deep-hole PDC reamer bit [J]. *Mineral exploration engineering (rock and soil drilling engineering)*, 41(08), 1-8.
- [13] Yang YX, Yang Y, Liu XM, Huang K, Ren HT. (2019). Optimized design and application of a directional reaming-while-drilling polycrystalline diamond compact bit[J]. *Engineering Failure Analysis*, 105, 699-707.
- [14] Yang YX, Yang Y, Ren HT, Qi QL, Chen XW. (2020). Research on the working mechanism of the PDC drill bit in compound drilling[J]. *Journal of Petroleum Science and Engineering*, 185.
- [15] Yoshida T, Koizumi T, Tsujiuchi N. (2013). Dynamic analysis of an excavator during digging operation. *SAE International Journal of Commercial Vehicles*, 6(2), 419-428.
- [16] Zhang JD, Xi FR. (2020). Study on ecological restoration of abandoned mines in China[J]. *Acta Ecologica Sinica*, 40(21), 7921-7930.
- [17] Zhu XH, Deng ZL, Liu WJ. (2020). Experimental Study on Energy Consumption of rock cutting under different groove geometry[J]. *Geotechnical Testing Journal*, 43(1), 151-170.

**THEORETICAL CONSIDERATIONS ON THE OPTIMIZATION OF THE WORKING
PROCESS OF VARIABLE WIDTH PLOUGHS**
/
**CONSIDERAȚII TEORETICE PRIVIND OPTIMIZAREA PROCESULUI DE LUCRU
AL PLUGURILOR CU LĂȚIME VARIABILĂ**

Nuțescu C.¹⁾, Gageanu I.*²⁾, Cujbescu D.*²⁾

¹⁾University Politehnica of Bucharest / Romania;

²⁾INMA Bucharest / Romania

E-mail: iulia.gageanu@gmail.com; dcujbescu@yahoo.com

DOI: <https://doi.org/10.35633/inmateh-65-14>

Keywords: *plough, qualitative indices, multivariable regression functions*

ABSTRACT

The paper presents theoretical research conducted for the optimization of the working process of variable width ploughs. Thus, were determined multivariable regression functions for the traction force of the plough with variable working function of the control parameters: working depth, working width and working speed. The use of these theoretical considerations of the optimal points sought lead to the opportunity of making assessments on the possibilities to conduct their experimental validation. Conditions for an experimental plan were formulated to highlight such optimal points and the theoretical results were validated through experiments.

ABSTRACT

Lucrarea prezintă cercetări teoretice realizate pentru optimizarea procesului de lucru al plugurilor cu lățime variabilă. Astfel, au fost determinate funcțiile de regresie multivariabilă pentru forța de tracțiune a plugului cu lățime de lucru variabilă în funcție de parametrii de control: adâncimea de lucru, lățimea de lucru și viteza de lucru. Utilizarea acestor considerații teoretice ale punctelor optime căutate duce la oportunitatea de a face evaluări cu privire la posibilitățile de efectuare a validării lor experimentale. Condițiile pentru un plan experimental au fost formulate pentru a evidenția astfel de puncte optime, iar rezultatele teoretice au fost validate prin experimente.

INTRODUCTION

Tillage is the primary and most energy consuming operation in farming operations. The purpose of tilling the land is to ensure favourable soil conditions by cutting and turning the soil for further seeding or transplanting (Mouli *et al.*, 2018). Tillage involves the operations starting from cutting and breaking, followed by turning or moving the top layer of soil, this normally being performed in a single pass. The aim is to create a desired final state from the initial conditions of the soil by mechanical manipulation. This mechanical operation requires a significant amount of energy, not only because of the large amount of the soil mass that must be moved but also because of the selection of the tillage tool and the fixation of its depth and speed of work (Ibrahimi *et al.*, 2017).

The mouldboard plough is normally the most used tillage equipment in the world. The variable width plough is a very useful farm equipment for performing the tillage work, being directly mounted on the tractor's PTO. It works on both the left and right side having a bilateral turnover mechanism that automatically reverses the plough position (Yin *et al.*, 2018). The mechanical function of ploughs is to cut the soil layer and turn it to the side. Thus, it is possible to incorporate and mix fertilizers and plant residues in the soil. The use of ploughs in wet seasons will prepare the soil for good ventilation, will help retain water and create furrows resistant to erosion (Luo *et al.*, 2019, Zhu *et al.*, 2016).

Researches were conducted by numerous researchers in the field, regarding the optimum working conditions for soil processing machinery (ploughs, chisels, loosening equipment) in the last years, from 2007-2016, studying the use of ante-mouldboard in the construction of ploughs (Biriș S.Șt. *et al.*, 2007), soil particles kinematics during the tillage working process using ante-mouldboard tools (Biriș S.Șt. *et al.*, 2008), determining the stress distribution that appears on the lamellar surface of the mouldboards for modelling and optimization (Bungescu S. *et al.*, 2008), nonlinear friction and resistance, generating sources of optimal points in the energy field of agricultural aggregates working process (Cârdei P. *et al.*, 2017), or the determination of subsoilers drag force influenced by different working depths and speed (Croitoru Șt. *et al.*, 2016).

Many attempts have been also made to have a better understanding of the complex nature of the tillage process using conventional or reversible ploughs (*Abbaspour-Gilandeh M. et al., 2020; Akbarnia et al., 2014; Godwin et al., 2007; Irshad Ali et al., 2015; Lortz et al., 2021*).

MATERIALS AND METHODS

The processing of experimental data is made in order to obtain multivariable regression functions of polytropic or polynomial form that allow the appreciation of the functional, energetic and qualitative indices of the plough with variable working width. During the experimental tests, independent variable elements were modified: travel speed, working depth and working width.

It was set out to determine the multivariable regression functions for the traction force of the plough with variable working width, dependent of slippage of the tractor's drive wheels, variation of working depth, variation of working width and variation of the working speed.

For their calculation, the analytical expressions of some multivariable functions will be determined, defined as a function of the type:

$$y=f(x_i, a_0, a_i, a_{ij}, a_{ij}) \quad (1)$$

expressing the dependence of the function y on the independent variables x_i and on the constants a_0, a_i, a_{ij}, a_{ij} . Due to the complexity of solving the problem, it is necessary to go through several stages: drawing up an adequate program for organizing experiments; determining the values of the constants; testing the significance of variables, testing the adequacy of the function's form (*Constantinescu I., 1980*).

The stages of a statistical program for organizing experiments are:

- formulating the problem and establishing the objectives of the experimental program;
- choosing independent variables that influence the dependent variable;
- establishing the range of variation (possible technologically) for each independent variable;
- choosing, in certain intervals, some values (called levels) that the independent variables will have;
- determining the size of the experimental error by repeating several experiments in the central point;
- execution of specific experiments in the program in a random order;
- measurement of the dependent variable for each experiment;
- statistical analysis of data and obtaining functional relationships between independent and dependent variables;

variables;

- interpretation of results of the statistical analysis.

The experimental research programs used to determine the function y are structured according to the following elements:

- the number n_* of experiments performed for different values of the independent variables, necessary for determining the regression coefficients;
- the number of experiments performed for identical values of the independent variables, necessary to determine the experimental error;
- levels of independent variables;
- the content of the experiments.

The total number of experiments is:

$$n=n_*+n_0 \quad (2)$$

where n_0 is the number of identical experiments required to determine the experimental errors.

The number of levels is calculated using the relation (*Constantinescu A., 2011*):

$$N \geq \sqrt[m_1]{n_*} \quad (3)$$

where m_1 is the total number of independent variables contained by the function.

Following is presented the calculation algorithm used to determine the regression coefficients using the least squares method.

To determine the values of the unknown regression coefficients, denoted generically with k_i , through linear mathematical regression, the functionals of the form $T(a_i, x_i)$ were formed, as a sum of the squares of the differences between the values obtained by applying the mentioned equations and the real values measured in experiments where $i = 1 \div n$, n being the number of unknown coefficients and $j = 1 \div m$, m being the number of measured quantities.

$$T = \sum (y(x_i) - y_i)^2 \quad (4)$$

where y_i is the vector of the independent variable measured in the experimental tests, and $y(x_i)$ is the vector of the independent variable calculated.

To determine the coefficients by mathematical regression, the least squares method was used, imposing the condition that the function T be minimal.

The minimum of the function T in relation to a_i is obtained by cancelling the partial derivatives of T_q with respect to the same coefficients, namely $\frac{\partial T}{\partial a_i} = 0$

The partial derivatives of the functional T were determined according to each of them and the unique determined system was created, of n equations with n unknowns:

$$\left\{ \frac{\partial T}{\partial a_i} = 0, \quad i=1 \div n \right. \quad (5)$$

To solve it numerically, the equations of the system were explained and the constants were eliminated to obtain the equivalent form that can be written as a matrix product:

$$ZY=X \quad (6)$$

where: Z is the matrix of the system, X is the matrix of free terms and Y is the matrix of unknown coefficients a_i , $Y=(a_i)$.

The determination of the vector Y formed by the unknown coefficients, was done by the numerical solving by mathematical regression of the equation (6) through the inverse matrix method, using the data strings obtained from the experiments.

$$Y=Z^{-1}X \quad (7)$$

To solve equation (6), a matrix calculation program in Mathcad was used. By replacing the coefficients in the analytical formulas, resulted the numerical forms of these functions.

Testing the significance of the coefficients is done using the Fischer Test which is a parametric test that verifies the equality of the dispersions of two normally distributed independent variables. To test the significance of the coefficients using the Fisher test, the sum of the squares of the experimental errors is calculated:

$$S_e = \sum_{i=n_*+1}^n \left(y_i + \sum_{i=n_*+1}^n \frac{y_i}{n_o} \right)^2 \quad (8)$$

The sums for the coefficients are:

$$S_o = n \cdot b_o^2 \quad (9)$$

$$S_j = a_j^2 \sum_{i=1}^n X_{ij}^2, \quad j = 1, 2, 3, \dots, m_1$$

The ratios are calculated:

$$F_0 = \frac{S_o(n_o-1)}{S_e} \quad (10)$$

$$F_j = \frac{S_j(n_o-1)}{S_e} \quad j = 1, 2, 3, \dots, m_1$$

If $F_0 \geq F(1-\alpha, 1, n_o - 1)$ and $F_j \geq F(1-\alpha, 1, n_o - 1)$ coefficient a_0 respectively coefficients a_j are significant. If this condition is not met, for one or more coefficients, the respective coefficients are equal to zero. Critical values $F(P = 1 - \alpha, k_1 = 1, k_2 = n_o - 1)$ are given (Reich R., 1978) for a level of significance $\alpha = 0.95$.

To test the adequacy of the form of the function with the Fisher test, the ratio is calculated:

$$F = \frac{(S-S_e)(n_o-1)}{S_e(n-n_o-m_1)} < F(1-\alpha, n_* - m_1, n_o - 1) \quad (11)$$

where n^* represents the number of different experiments, and m_1 is the number of function coefficients (without the coefficient a_0). If the condition is met then the form of the function is adequate (Popescu & Badescu, 2000).

RESULTS

Expression of traction force by multivariate polynomial functions

In order to determine the coefficients of the multivariable functions, the independent variables that influence the dependent variable and their variation interval were chosen:

- Working depth: $a = 0.1 - 0.3$ m;
- Working speed: $v = 0.9 - 1.9$ m/s;
- Working width: $B=0.8 - 1.2$ m, which corresponds to a working width of the plough body, $b = 0.2 \dots 0.4$ m.

The experimental test program for determining the multivariable functions for the traction force is presented in table 1.

Table 1

Experimental results for determining the traction force

Sample no.	Slippage coefficient δ_i [%]	Working width B [m]	Working depth a_i [m]	Speed v_i [m/s]	Average traction force F_t [N]
1	13.80	0.80	0.10	0.938889	17150
2	15.20	0.83	0.12	1.569444	17560
3	16.70	0.83	0.13	1.886111	17590
4	14.40	0.83	0.20	0.908333	20960
5	16.50	0.83	0.22	1.347222	21170
6	17.70	0.83	0.23	1.816667	22100
7	15.80	0.82	0.30	0.886111	23530
8	17.20	0.83	0.33	1.25	23850
9	18.80	0.83	0.32	1.469444	24130
10	14.60	1.01	0.10	0.891667	18240
11	15.80	1.04	0.12	1.472222	19150
12	17.90	1.03	0.13	1.861111	19970
13	15.20	1.04	0.20	0.877778	21760
14	17.70	1.04	0.21	1.294444	22060
15	18.30	1.04	0.23	1.733333	22950
16	16.20	1.04	0.30	0.805556	23560
17	20.40	1.04	0.31	1.188889	24320
18	23.70	1.04	0.32	1.597222	24480
19	15.70	1.20	0.10	0.869444	20980
20	18.00	1.23	0.12	1.447222	21160
21	19.10	1.23	0.11	1.741667	21440
22	16.80	1.23	0.20	0.875	24280
23	18.90	1.23	0.21	1.269444	24320
24	19.80	1.22	0.20	1.694444	24720
25	17.40	1.23	0.30	0.797222	26240
26	21.20	1.23	0.31	1.138889	26840
27	24.20	1.23	0.30	1.744444	28130

The matrix of the correlations of the process parameters measured during the experiments is given in Table 2. It was constructed by calculating the correlation coefficient for each pair of data strings representing the columns of Table 1.

Table 2

Matrix of correlation coefficients of the parameters measured during the experiments

	F [N]	a [m]	b [m]	v [m/s]	δ_v [%]
F [N]	1.000	0.839	0.486	-0.073	-0.717
a [m]	0.839	1.000	0.000	-0.223	-0.504
b [m]	0.486	0.000	1.000	-0.061	-0.449
v [m/s]	-0.073	-0.223	-0.061	1.000	-0.487
δ_v [%]	-0.717	-0.504	-0.449	-0.487	1.000

The values of the elements of the correlation matrix led to very important conclusions for the analysis of experimental data.

- The traction force is strongly correlated (directly) with the working depth and is significantly correlated (directly) with the working width, and strongly correlated (inversely) with the skidding;
- The traction force is not significantly correlated with the working speed, at least in the experimental interval.

The first form of the traction force function is the Goreachkin function (12), in which the values of coefficients f , k and ϵ , which are considered to be constant, will be numerically determined. Also, G , the weight of the plough-tractor unit used in the experiments, is constant.

$$F_t = fG + kaB + \epsilon aBv^2 \quad (12)$$

where: F_t the draft force, f is a coefficient of friction between metal and soil, k is a coefficient that characterizes the specific deformation resistance of the soil, a is the working depth, $B = nb$ is the plough working width where n is the number of mouldboards, ϵ is a coefficient that depends on the surface of the active shape of the mouldboard and to the soil properties, and v is the working speed.

To determine the values of the coefficients f , k and ε by linear mathematical regression, the functional $T(f, k, \varepsilon, G, a_i, B_i, v_i)$ was formed as a sum of the squares of the differences between the values obtained by applying equation (1) and the real values measured during experiments a_i, B_i, v_i from Table 1.

$$T = \sum (F - F_i)^2 = \sum (fG + ka_i B_i + \varepsilon a_i B_i v_i^2 - F_i)^2 \rightarrow \min \quad (13)$$

To determine coefficients f , k and ε , by mathematical regression, the condition was imposed that T expressed by equation (13) be minimal.

The minimum of the function T in relation to f , k and ε is obtained by cancelling the partial derivatives of T in relation to the same coefficients, namely $\frac{\partial T}{\partial f} = 0$, $\frac{\partial T}{\partial k} = 0$ and $\frac{\partial T}{\partial \varepsilon} = 0$.

The partial derivatives of the functional T were determined according to each of them and the unique determined system was created, of 3 equations with 3 unknowns:

$$\begin{cases} \frac{\partial T}{\partial f} = 2 \sum (fG + ka_i B_i + \varepsilon a_i B_i v_i^2 - F_i)G = 0 \\ \frac{\partial T}{\partial k} = 2 \sum (fG + ka_i B_i + \varepsilon a_i B_i v_i^2 - F_i)a_i B_i = 0 \\ \frac{\partial T}{\partial \varepsilon} = 2 \sum (fG + ka_i B_i + \varepsilon a_i B_i v_i^2 - F_i)a_i B_i v_i^2 = 0 \end{cases} \quad (14)$$

For the numerical solving of the system, the constants were eliminated and the equivalent form was obtained which can be written as a matrix product:

$$\begin{cases} f \sum G^2 + k \sum G a_i B_i + \varepsilon \sum G a_i B_i v_i^2 = \sum G F_i \\ f \sum G a_i B_i + k \sum a_i^2 B_i^2 + \varepsilon \sum a_i^2 B_i^2 v_i^2 = \sum F_i a_i B_i \\ f \sum G a_i B_i v_i^2 + k \sum a_i^2 B_i^2 v_i^2 + \varepsilon \sum a_i^2 B_i^2 v_i^4 = \sum F_i a_i B_i v_i^2 \end{cases} \leftrightarrow ZY = X \quad (15)$$

where:

$$Z = \begin{pmatrix} \sum G^2 & \sum G a_i B_i & \sum G a_i B_i v_i^2 \\ \sum G a_i B_i & \sum a_i^2 B_i^2 & \sum a_i^2 B_i^2 v_i^2 \\ \sum G a_i B_i v_i^2 & \sum a_i^2 B_i^2 v_i^2 & \sum a_i^2 B_i^2 v_i^4 \end{pmatrix} \quad (16)$$

$$X = \begin{pmatrix} \sum G F_i \\ \sum F_i a_i B_i \\ \sum F_i a_i B_i v_i^2 \end{pmatrix}$$

$$Y = \begin{pmatrix} f \\ k \\ \varepsilon \end{pmatrix}$$

The determination of the vector Y formed by the unknown coefficients (f, k, ε) that need to be calculated, was done by numerical solution through mathematical regression of equation (16), obtained from the matrix equation (15) by the inverse matrix method, using the data strings obtained from experiments.

$$Y = Z^{-1}X \quad (17)$$

Table 1 shows the values of the independent and dependent variables used in the mathematical regression operation performed using a calculation program in Mathcad.

The weight of the plough-tractor unit G was constant, 49830 N, corresponding to a mass of the tractor of 4480 kg and of the plough of 600 kg.

Using a calculation program in Mathcad, from equation (12) and the experimental data from table 1, coefficients (f, k, ε) were determined, resulting in the mathematical model (13) of the function.

$$F_t = 0.317G + 27850aB + 1188aBv^2 \quad (18)$$

where F_t represents the traction force.

The deviations of the calculated values from the experimental ones for the traction force are calculated with the relation:

$$A = \frac{|F_{ti} - F_{ci}|}{F_{ti}} \cdot 100, \quad [\%] \quad (19)$$

where F_{ci} is the vector of traction forces calculated using relation 13

Table 3 shows the values of the traction force measured during the experiments and the values of the traction force calculated using relation (19) and the deviation.

Table 3

Deviations of the calculated values from the experimental ones for the traction force

Sample no.	Average measured traction force, F_i [N]	Average calculated traction force, F_{ci} [N]	Deviation A [%]
1	17150	18108.655	5.59
2	17560	18862.062	7.415
3	17590	19257.692	9.481
4	20960	20582.413	1.801
5	21170	21275.614	0.499
6	22100	21861.364	1.08
7	23530	22876.921	2.776
8	23850	23932.717	0.347
9	24130	23874.419	1.059
10	18240	18705.061	2.55
11	19150	19593.696	2.317
12	19970	20076.665	0.534
13	21760	21779.665	0.09
14	22060	22313.546	1.149
15	22950	23311.649	1.576
16	23560	24725.883	4.949
17	24320	25316.234	4.096
18	24480	26072.942	6.507
19	20980	19246.519	8.263
20	21160	20274.505	4.185
21	21440	20052.263	6.473
22	24280	22871.204	5.802
23	24320	23484.382	3.436
24	24720	23423.814	5.243
25	26240	26351.243	0.424
26	26840	27002.596	0.606
27	28130	27406.275	2.573

The maximum deviation thus determined between the experimental data and the calculated data was 9.481%, resulting in a good accuracy of the proposed model. The correlation coefficient calculated using formula (12) in which the string X was replaced with F_i and the string Y with F_{ci} was 0.946, demonstrating a very strong correlation between the two strings.

If conditions are imposed that include some of the variables of the traction force, conditions from which a variable is removed, then, in some cases, functions that have extreme values depending on some of the remaining variables result. This was achieved using as an objective function the traction force (Goriachkin variant) and the condition to reach a given productivity.

Thus, we have the traction force resulting from the interpolation of the experimental data using the least squares method, as well as function (18) and the additional condition:

$$W = B \cdot v = \text{const} \quad (20)$$

By eliminating the working speed between relations (18) and (20), a traction force function is obtained depending on the working width of the plough with variable width and on the working depth.

$$F_t = 0.317G + 27850aB + \frac{1188aW^2}{B} \quad (21)$$

Figure 1 shows the variation of the traction force depending on the working width, for three fixed productivities and the working depth $a = 0.3$ m in the case of the plough with variable working width.

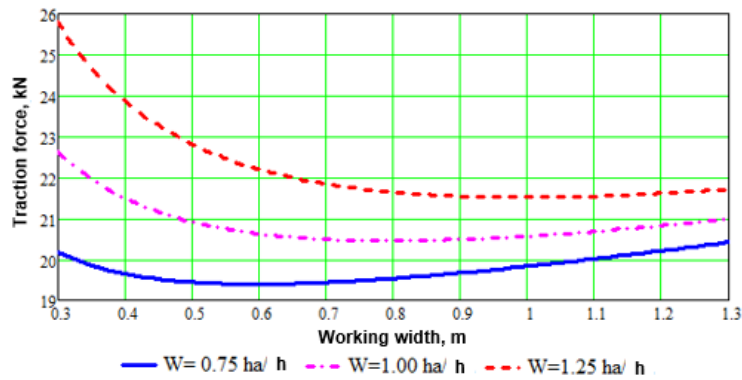


Fig. 1 - Variation of traction force with working width, for three productivities

It is observed that the minimum points of the traction force move with the increase of the programmed productivity, in the sense of increasing the optimal working width and, obviously, the optimal force.

The values of the optimal widths of the traction force and of the working width of the plough are calculated with relations:

$$F_{opt} = fG + 2aW\sqrt{k\varepsilon} \tag{22}$$

$$B_{opt} = W\sqrt{\frac{\varepsilon}{k}} \tag{23}$$

For the three productivities used (fig. 1), the optimal points are obtained with the coordinates given in table 4.

Table 4

Coordinates of the optimal points of the curves in Fig. 1

Productivity W [ha/h]	Optimal width B _{opt} [m]	Optimal traction width F _{opt} [N]
0.75	0.596	19391
1.00	0.794	20453
1.25	0.993	21516

Figure 2 shows in an orthogonal coordinate system the variation of the traction force as a function of the working width for the required working productivity.

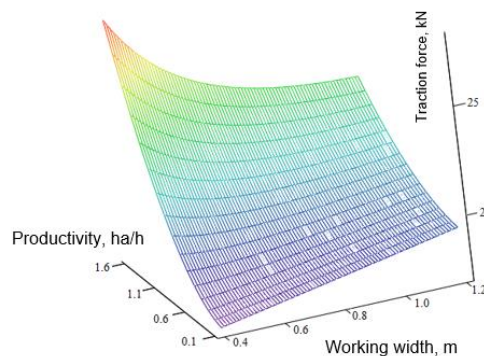


Fig. 2 - Variation of the traction force depending on the working width for the required productivity

As can be seen, the dependence of the traction force on the required productivity is not linear. It can also be seen that there is a linear dependence between the working width and the traction force.

Further, the traction force is presented as a second-degree polynomial function, dependent on working depth and width, working speed and slippage:

$$F_t = c_0 + c_1a + c_2B + c_3v + c_4\delta + c_{12}aB + c_{13}av + c_{14}a\delta + c_{23}Bv + c_{24}B\delta + c_{34}v\delta + c_{11}a^2 + c_{22}B^2 + c_{33}v^2 + c_{44}\delta^2 \tag{24}$$

where:

c₀, ..., c₄₄ are the regression coefficients;

- $a = 0.1 - 0.3$ m is the working depth;
 $B = 0.8 - 1.2$ m is the working width;
 $\delta = 13.8 - 24.2$ % is the coefficient of slippage of the tractor's drive wheels;
 $v = 0.9 - 1.9$ m/s is the working speed.

Table 1 shows the values of the independent variables and the dependent variable used in the calculation program in Mathcad, to determine the regression coefficients. After calculating the regression coefficients, the following multivariable polynomial function was obtained:

$$F_t = 39949.216 + 20545.854a - 37064.489B - 13259.116v - 102.292\delta - 77361.486aB - 23654.742av + 10539.344a\delta - 6712.583Bv + 2861.022B\delta + 1512.639v\delta - 143852.709a^2 + 10965.706B^2 - 136v^2 - 205.411\delta^2 \quad (25)$$

Next, the deviation of the traction forces calculated using relation (25) in relation to the traction forces measured in the experimental tests was calculated. Table 5 shows the values of the traction force measured during the experiments, the values of the traction force calculated using the relation (25) and the deviation.

The maximum error between the experimental data and the calculated data was 2.442%, thus resulting in a good accuracy of the proposed model. The correlation coefficient calculated in which the string X with F_i and the string Y with F_{ci} were replaced is 0.998, demonstrating a very strong correlation between the two strings.

The coordinates of the optimal point of the interpolation function (22), isolated (which is not located on the boundary of the definition domain), were identified by solving the linear system of equations obtained by cancelling the partial derivatives of the function.

Table 5

Measured traction forces, calculated traction forces and deviation

Sample no.	Average measured traction force F_i [N]	Calculated average traction force F_{ci} [N]	Deviation [%]
1	17150	17109.91	0.234
2	17560	17475.559	0.481
3	17590	18019.533	2.442
4	20960	21005.634	0.218
5	21170	20997.827	0.813
6	22100	21958.025	0.642
7	23530	23400.92	0.549
8	23850	23815.723	0.144
9	24130	24261.806	0.546
10	18240	18406.683	0.914
11	19150	19015.664	0.701
12	19970	19567.746	2.014
13	21760	21938.222	0.819
14	22060	21813.508	1.117
15	22950	23081.479	0.573
16	23560	23831.905	1.154
17	24320	24358.785	0.159
18	24480	24502.542	0.092
19	20980	20762.76	1.035
20	21160	21512.473	1.666
21	21440	21371.511	0.319
22	24280	24278.629	0.006
23	24320	24424.82	0.431
24	24720	24821.678	0.411
25	26240	25983.627	0.977
26	26840	26867.11	0.101
27	28130	28055.923	0.263

The second-degree polynomial function for the traction force, which interpolates the experimental data, can, however, be minimized in order to find an optimal point through a constraint minimization operation.

The function arguments are restricted in the experimental working range or at most in a slightly wider range, in the vicinity of an experimental point (sample 14: $a=0.21$ m, $B=1.04$ m, $v=1.29$ m/s, $\delta = 17.7$ %). The optimal coordinate point is obtained: $a_{opt} = 0.2$ m, $B_{opt} = 1$ m, $v_{opt} = 1.7333$ m/s, $\delta_{opt} = 18.33$, $F_{opt} = 20380.55$ N.

This optimal point is acceptable, but moving the starting point away from the experimental points may cause unacceptable results.

For the skidding of the tractor's motor wheels of 15%, the working speed $v=1.4$ m/s and three values of the working depth, were calculated the traction forces with relation (25), the data being presented in table 6.

Table 6

Working width B [m]	Traction force [daN]		
	a = 0.1 m	a = 0.2 m	a = 0.3 m
0.8	16238.6	20286	21456.4
0.85	16579.1	20239.7	21023.3
0.9	16974.4	20248.2	22655
0.95	17424.6	20311.6	22499.4
1	17929.6	20429.8	22398.6
1.15	19773.6	21113.4	22425.2
1.2	20497.9	21450.9	22543.8

Using the data from Table 6, the graph of the variation of the traction force, depending on the working width of the plough was represented (fig. 3).

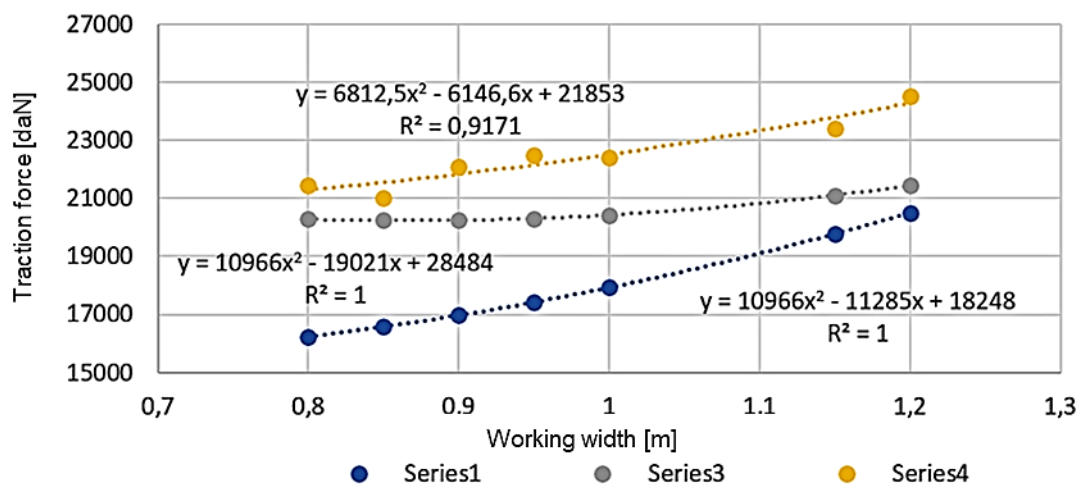


Fig. 3 - Variation of the traction force depending on the working width B , for the speed $v = 1.4$ m/s and for three values of the working depth: $a = 0.1$ m (series 1), $a = 0.2$ m (series 3) and $a = 0.3$ m (series 4)

Figure 3 shows that the traction force increases when increasing working depth and working width of the plough. The relations shown in figure 3 allow the calculation of the traction force for one of the working depths for any value of the working width $B = 0.8 - 1.2$ m.

CONCLUSIONS

The main results obtained consist in demonstrating that there are own optimal points in the working process of the tractor – plough with variable working width aggregate. In addition, the optimal points found have as abscissa not only the working speed, but also the working width, a parameter whose control defines this type of ploughs. Also, the optimality criteria used are natural, namely they have an intuitive meaning. From a physical point of view, the parametric structure of the coordinates of the optimal points leads to interesting conclusions, facilitated by the fact that these coordinates were found analytically and not numerically. Optimum points are confirmed in terms of working speed and working width in reference works in the field of agricultural machinery operation.

It is noted that of the four optimal operating points found, only one has an optimal working width as an abscissa, which minimizes the traction force (22) under conditions of a fixed productivity (21).

REFERENCES

- [1] Abbaspour-Gilandeh, M., Shahgoli, G., Abbaspour-Gilandeh, Y., Herrera-Miranda, M.A., Hernandez-Hernandez, J.L., Herrera-Miranda, I. (2020). Measuring and Comparing Forces Acting on Mouldboard Plow and Para-Plow with Wing to Replace Mouldboard Plow with Para-Plow for Tillage and Modelling It Using Adaptive Neuro-Fuzzy Interface System (ANFIS). *Agriculture*, 10, 633; doi:10.3390/agriculture10120633
- [2] Akbarnia, A., Mohammadi, A., Farhani, F., Alimardani, R. (2014). Simulation of draft force of winged share tillage tool using artificial neural network model. *Agric Eng. Int. CIGR J.*, 16, 57–65.
- [3] Biriş, S., Vlăduţ, V., Bungescu, S., Paraschiv, G., (2007), Researches regarding the utilization of ante-molboard in the ploughs building, *Proceedings of the 35 International Symposium on Agricultural Engineering "Actual Tasks on Agricultural Engineering"*, vol. 35, 85-96, Opatija / Croatia
- [4] Biriş, S., Maican, E., Vlăduţ, V., Paraschiv, G., Manea, M., Bungescu, S., (2008), Study regarding the soil particles kinematics during the ante-mouldboard tillage tools working process, *Proceedings of the 36 International Symposium on Agricultural Engineering "Actual Tasks on Agricultural Engineering"*, vol.36, 115-126, Opatija / Croatia.
- [5] Bungescu, S., Biriş, S., Vlăduţ, V., Paraschiv, G., (2008), Researches regarding the stress distribution determination appearing on the lamellar mouldboard surface with a view to modelling and optimization, *Proceedings of the 36 International Symposium on Agricultural Engineering "Actual Tasks on Agricultural Engineering"*, vol.36, 281-292, Opatija / Croatia
- [6] Cardei P., Matache M., Nutescu C., (2017), Optimum working conditions for variable width ploughs, https://www.researchgate.net/publication/318983573_Optimum_working_conditions_for_variable_widht_h_ploughs#fullTextFileContent
- [7] Constantinescu. I., (1980), *Processing of experimental data with numerical computers*, Technical Publishing House, Bucharest / Romania
- [8] Constantinescu, A. (2011), *Optimization of aggregates consisting of high-power tractors with agricultural machines for land preparation for sowing*. Doctoral thesis, Transylvania University of Brasov / Romania.
- [9] Croitoru, Şt., Vlăduţ, V., Marin, E., Matache, M., Dumitru, I. (2016), Determination of subsoiler's traction force influenced by different working depth and velocity, 15th International Scientific Conference "Engineering for Rural Development" Proceedings, vol. 15, pp. 817-825, Jelgava / Latvia
- [10] Godwin, R., O'Dogherty, M., Saunders, C., Balafoutis, A. (2007). A force prediction model for mouldboard ploughs incorporating the effects of soil characteristic properties, plough geometric factors and ploughing speed. *Biosyst. Eng.*, 97, 117–129.
- [11] Ibrahmi, A., Bentaher, H., Hamza, E., Maalej, A., Mouazen, A-M. (2017). 3D finite element simulation of the effect of mouldboard plough's design on both the energy consumption and the tillage quality. *The International Journal of Advanced Manufacturing Technology*, volume 90, 473–487, <https://doi.org/10.1007/s00170-016-9391-9>
- [12] Irshad Ali, M., Changying, J., Leghari, N., Ghulam Ali, B., Farman Ali, Ch., Chuadry Arslan, Ch. Sattar, A., Huimin, F. (2015). Analyses of 3-dimensional draught and soil deformation forces caused by mouldboard plough in clay loam soil. *Glob. Adv. Res. J. Agric. Sci.* 4, 259–26
- [13] Lortz, W., Govekar, E. (2021). Advanced modelling for grinding - from friction to ploughing and dynamic chip formation with temperatures, *Procedia CIRP*, volume 102, 79-84.
- [14] Luo, F., Zhu, L., Wei, M., Zhang, J-W., Zhu, D-Q., Jen, T-C. (2019). Tillage Condition Effects on Soil/Plow-breast Flow Interaction of a Horizontally Reversible Plow. *Procedia Manufacturing*, Volume 35, 980-985. <https://doi.org/10.1016/j.promfg.2019.06.045>
- [15] Mouli, K-C., Arunkumar, S., Satwik, B., Bhargava Ram, S., Rushi Tej, J., Sai Shaitanya A. (2018). Design of Reversible Plough Attachment, *Material Today*, vol.5, iss.11, 10.1016/j.matpr.2018.10.160
- [16] Popescu S., Badescu M. (2000). Methods and means used to determine the traction of wheeled tractors, *Mechanization of Agriculture*, no. 10, 16-23.
- [17] Reich, R. (1978). Measurement of the forces between the tractor and the device. *Grundl Agricultural Engineering*, 28, no. 4, 156-159
- [18] Yin, Y., Guo, S., Meng, Z., Qin, W., Li, B., Luo, C. (2018). Method and System of Plowing Depth Online Sensing for Reversible Plough. *IFAC-PapersOnLine*, Volume 51, Issue 17, 326-331. <https://doi.org/10.1016/j.ifacol.2018.08.199>
- [19] Zhu, L., Peng, S-S., Cheng X., Qi, Y-Y., Ge J-R., Yin C-L., Jen T-C. (2016). *Soil and Tillage Research* Volume 163, 168-175. <https://doi.org/10.1016/j.still.2016.06.002>

DESIGN AND TEST EVALUATION OF THE SUBSOILER EQUIPPED WITH TILLAGE DEPTH MONITORING AND CONTROL SUBSOILING ASSEMBLIES

耕深自动监测控制深松机深松单体设计与试验

Lou Shangyi¹⁾, He Jin^{*1)}, Li Hongwen¹⁾, Wang Qingjie¹⁾, Lu Caiyun¹⁾, Wu Yihang¹⁾, Liu Peng¹⁾, Li Hui²⁾

¹⁾ College of Engineering, China Agricultural University, Beijing 100080 / China;

²⁾ Shandong Academy of Agricultural Machinery Sciences, Jinan, 250100 / China

Tel: +8610 62737300; E-mail: hejin@cau.edu.cn

DOI: <https://doi.org/10.356.33/inmateh-65-15>

Keywords: subsoiler, hydraulic adjustment, stability of tillage depth, subsoiling quality, performance

ABSTRACT

Aiming at solving problems that the variation of tillage depth between rows and within rows caused by the surface undulation was great, the lateral stability of tillage depth obtained by the method of adjusting at the three-point suspension was poor, and lack of subsoilers with the function of accurate detection and adjustment of single row tillage depth, a method of independent control of single row tillage depth based on ultrasonic sensor detection and hydraulic adjustment was proposed. And the tillage depth monitoring and control subsoiling assembly and the subsoiler equipped with subsoiling assemblies were designed. The key structural parameters of the hydraulic cylinder and the model of the three-position four-way magnetic exchange valve were determined. The subsoiling quality and performance comparison tests were conducted, and the results showed that the mean value of the variable coefficient of soil hardness, looseness of soil and coefficient of soil disturbance were 52.23%, 32.55% and 62.15%, respectively, and the stability coefficient of tillage depth was 92.43%, which all met the subsoiling operation requirements. The standard deviation of tillage depth belonged to the method of independent adjustment of single row and unified adjustment of each row were 38.315mm and 51.521mm, respectively. The subsoiler equipped with tillage depth monitoring and control subsoiling assemblies designed in this paper was capable of significantly improving the stability of tillage depth between rows and within rows.

ABSTRACT

为了解决由于地表起伏造成的深松机行间、行内耕深变异较大，且整机调节方式得到的耕深横向稳定性较差，缺乏实现单行耕深精准检测与调节的深松机的问题，本文提出了一种基于超声波传感器检测与液压调节的独立控制单行耕深的方法，设计了耕深监测控制深松单体以及由多个单体组成的深松机，确定了液压缸的关键结构参数以及三位四通电磁换向阀的型号，开展了深松效果与性能对比试验，结果表明深松前后土壤硬度变化系数均值为 52.23%，土壤蓬松度均值为 32.55%，土壤扰动系数均值为 62.15%，耕深稳定性系数为 92.43%，各项指标均满足深松作业要求，单体调节与整机调节的耕深标准差分别为 38.315mm 和 51.521mm，本文设计的具有单行耕深独立检测与调节功能的深松机能够显著提高行间、行内耕深稳定性。

INTRODUCTION

Cultivated land is the important basis and guarantee of crop production, as well as the foundation to ensure food security (Poehlitz *et al.*, 2019). However, due to continuous ploughing and compaction, the soil compacted hardpan is formed, which prevents the roots from extending to the deeper soil, reduces the absorption of water and fertilizer by roots, hinders the flow of moisture and air, and thus decreases the crop yield (Somerville *et al.*, 2018; Hargreaves *et al.*, 2019; Kristoffersen *et al.*, 2005). Conservation tillage is capable of significantly improving soil properties, reducing wind and water erosion as well as surface runoff, and thus protecting the soil effectively (He *et al.*, 2018). The subsoiling technology is one of the key techniques of conservation tillage, which applies subsoiling machines to loosen the soil without turning over the soil (Singh *et al.*, 2019). Especially the loosening quality on the deeper layer is remarkable. Compared to the plough and rotary tillage, the subsoiling has several advantages, including breaking the soil compacted hardpan, reducing soil bulk density, improving soil porosity, enhancing water storage capacity, increasing soil fertility and water use efficiency, and thus improving crop yields (Feng *et al.*, 2018; Zhang *et al.*, 2015).

The subsoiling depth is a significant index affecting the subsoiling quality and energy efficiency, while it is also an important consideration basis for the government to carry out subsoiling subsidies in China. In the process of operation, subsoiling with insufficient depth cannot break the compacted hardpan completely, and thus the soil properties still need to be improved. Meanwhile, subsoiling with excessive depth increases power consumption and operation cost, resulting in the reduction of energy efficiency. Therefore, it is of prime importance to develop a subsoiler with the function of on-line detection and control of tillage depth.

At present, sensors used to detect tillage depth mainly include tilt sensors and ultrasonic sensors (Suomi *et al.*, 2015; Yin *et al.*, 2018; Mouazen *et al.*, 2004; Gao *et al.*, 2013), and the adjustment of tillage depth is mainly realized by applying the hydraulic mechanism or motor mechanism (Lee *et al.*, 1998; Zhao *et al.*, 2015; Ayiding *et al.*, 2013). The method, applying tilt sensor to measure the angle change of profiling mechanism and calculating the mathematical model to get the tillage depth, results in the mismatch between the adjustment completion point of tillage depth and the detection point, which caused by the profiling mechanism is generally placed behind the tillage component. While the ultrasonic sensor is commonly installed in front of the tillage component to complete the measurement of the distance between the soil surface and the frame, which avoids the inaccuracy caused by the profiling lagging. This method aims at adjusting the tillage depth of the whole machine or a group of tillage components of the combined scarification equipment, which is the same as the objective of mounting the tilt sensor on the three-point suspension to detect angle change of the lifting arm or drawbar. However, due to surface relief or soil resistance variation, there exists the problem of lateral instability of tillage depth of the machine with several shanks, which leads to the inconsistency of soil conditions in the lateral distribution. Therefore, it is necessary to develop a special assembly structure of subsoiling components that is capable of independently adjusting tillage depth of each row.

Hence, in order to avoid undesirable tillage depth of each shank and improve consistency of tillage depth between shanks during the subsoiler operation, in this paper, we proposed a method for independent adjustment of single row tillage depth based on ultrasonic sensor detection and hydraulic adjustment. And the single subsoiling assembly capable of monitoring and controlling tillage depth and the subsoiler equipped with subsoiling assemblies were designed. Furthermore, the subsoiling performance of the tillage depth monitoring and control subsoiler was evaluated by testing the qualified indexes, and the improvement effect of this subsoiler on the stability of single row tillage depth was verified by conducting the performance comparison test.

MATERIALS AND METHODS

Structure and working principle

The overall structure of the subsoiler is shown in Fig.1a); it consists of a frame and four tillage depth monitoring and control subsoiling assemblies. The tillage depth of each shank is independently detected, displayed, recorded and adjusted.

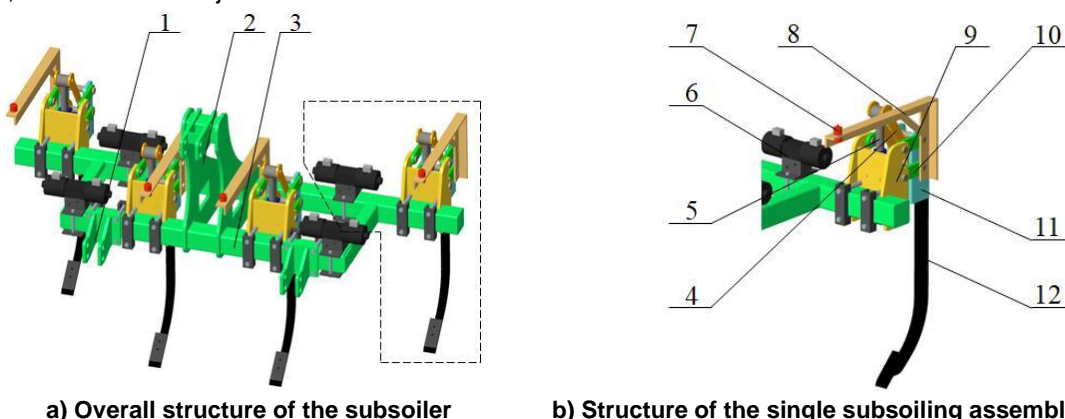


Fig. 1- Structure of the subsoiler equipped with tillage depth monitoring and control subsoiling assemblies
 1. Lower suspension point; 2. Upper suspension point; 3. Frame; 4. Hydraulic linkage; 5. Hydraulic cylinder; 6. Magnetic exchange valve; 7. Ultrasonic sensor; 8. Sensor bracket; 9. Fixed mount; 10. Swing rod; 11. Connect plate of the shank; 12. Subsoiler shank

The length, width and height of the subsoiler are 2200mm, 1130mm and 1492mm, respectively. The spacing of two lower suspension points is 982mm, the vertical spacing between the upper and lower suspension point is 624mm, and the range of operation row-spacing is 550~650mm.

The structure of the single subsoiling assembly is shown in Fig.1b); it is composed of a fixed mount, a hydraulic cylinder, two hydraulic linkages, four swing rods, a connect plate of the shank, a subsoiler shank, an ultrasonic sensor, a sensor bracket, and a magnetic exchange valve. The fixed mount was installed on the frame, other parts of the subsoiling assembly were fixed on or connected with the fixed mount, and the main body of the subsoiling assembly was integrated with the frame. The hydraulic cylinder was vertically fixed on the plant between the plates on both sides of the fixed mount. Swing rods were used to connect the fixed mount and the connect plate of the shank, and hydraulic linkages were used to connect the hydraulic cylinder and the connect plate of the shank. The subsoiler shank was fixed on the connect plate of the shank. This combined structure enables the shank to lift or lower in the vertical direction when the hydraulic cylinder is extended or shortened, and thus the tillage depth is reduced or increased to reach desirable value. The sensor bracket was mounted on the side of the connect plate of the shank, and the ultrasonic sensor applied to measure its distance from the soil surface was installed at the front of it, which ensures the synchronous up and down movement of the sensor and the shank. The magnetic exchange valve was fixed on the frame.

In addition to the ultrasonic sensor and magnetic exchange valve, the hardware of the control system of the subsoiler also included an analogue input module, a controller and an interactive touch screen. The analogue input module (S7-200SMART EM AI04, China) was applied in this study, which was used to convert the analogue signal outputted from the ultrasonic sensor into digital signal. The programmable logic controller (S7-200SMART, CPU ST40, China) and interactive touch screen (MT6071iP, China) were applied in this study. The PLC outputted control signal to the drive circuit of the magnetic exchange valve to adjust the tillage depth within the set range, which was inputted via the interactive touch screen. The real-time tillage depth was displayed via the interactive touch screen and recorded on a USB flash disk. The block diagram of monitoring and control system was shown in Fig.2.

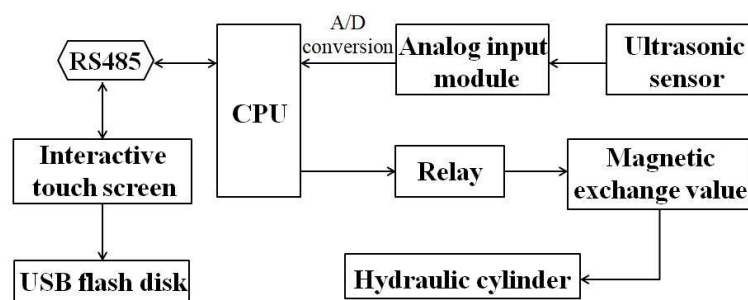


Fig. 2- Block diagram of monitoring and control system

The circuit elements, analogue input module, PLC and interactive touch screen, were placed in the tractor cab, which were powered by the on-board battery. The hydraulic cylinders of the tillage depth monitoring and control subsoiling assemblies were supplied by the tractor's hydraulic system, the hydraulic oil of which was transported through multiple hydraulic output ports. The driving circuit of the three-position four-way magnetic exchange valve controlled the valve position of the magnetic exchange valve to determine the flow direction of hydraulic oil. The desirable tillage depth was set via the interactive touch screen according to the local required depth value. During the subsoiling operation, ultrasonic sensors respectively detected their distance from the surface and sent corresponding signal to the control system. The magnetic exchange valves responded to the output signal of the control system, opening left or right valves or holding in middle position, to make the hydraulic cylinder complete the telescopic movement or remain unchanged. And thus, the tillage depth of each subsoiler shank was independently detected and adjusted to match the set range.

Design of key component parameters

Design of the subsoiler shank

The chisel subsoiler is adaptive for equipping with tillage depth monitoring and control system, so the subsoiler designed in this study initially adopted the common chisel shank, of which the optimization design had been conducted to achieve the purpose of reducing tillage resistance in the process of upper and lower adjustment. The chisel shank is composed of the handle and tip, and there are three kinds of handle that are commonly used, vertical column type, curved type and arc type. The first two type shanks are not suitable to be used in conservation field with more straw and stubble, while the arc type handle with front edge is capable of cutting on the stubble, so the object of optimization design of shank in this study is the chisel shank with arc type handle. Aiming at decreasing resistance of the shank during the subsoiling operation as well as lifting or

lowering adjustment, the force analysis of the shank in the process of operation was carried out, and the equivalent stress were analysed by the finite element method. Based on these, the sources increasing the tillage resistance caused by the structural parameters of the shank tip and shank handle were found out, and the optimization design of shank was conducted to reduce the tillage resistance. The resistance of the shank (F) was given by Eq.(1). The resistance of the shank tip was derived by the Eqs.(2)-(4), and the resistance of the shank handle was calculated by the Eq.(5) (Yu *et al.*, 2007).

$$F = F_1 + F_2 \quad (1)$$

where:

F_1 is the resistance of the shank tip, [N];

F_2 is the resistance of the shank handle, [N].

$$F_1 = \frac{G}{t_2} + \frac{t_1}{t_2 (\sin \beta + \mu_1 \cos \beta)} \quad (2)$$

$$t_1 = \frac{Cbd \left(1 + \tan \frac{\delta}{8} \right)}{\sin \beta} \quad (3)$$

$$t_2 = \frac{\cos \delta - \sin \delta}{\sin \delta + \cos \delta} + \frac{\cos \beta - \sin \beta}{\sin \beta + \cos \beta} \quad (4)$$

$$F_2 = 2N_2 \sin \frac{\alpha}{2} + 2N_2 \mu_2 \cos \frac{\alpha}{2} + 2N_3 \mu_2 \quad (5)$$

where:

F_1 is the resistance of the shank tip, [N];

F_2 - resistance of the shank handle, [N];

G - gravity of soil on the shank, [N];

α - cutting edge inclination, [°];

β - inclination of the front failure surface, [°];

δ - penetration angle of the shank, [°];

d - tillage depth, [cm];

b - shank width, [cm];

μ_1 - friction coefficient between the surface of the shank tip and soil;

μ_2 - friction coefficient between soils;

C - unit cohesion of soil, [N·cm⁻²];

N_2 - normal load on the front bevel of the shank handle, [N];

N_3 - normal load on the side of the shank handle, [N].

The soil bulk density was selected to be $1.45 \times 10^3 \text{ kg} \cdot \text{m}^{-3}$, the angle between the lower surface of the shank tip and the horizontal direction was 10° , the penetration angle of the shank was 23° , the width and length of the shank tip was 50mm and 165mm, respectively, the friction coefficient between the surface of the shank tip and soil was selected to be 0.6, the friction coefficient between soils was selected to be 0.3, and the unit cohesion of soil was selected to be $2 \text{ N} \cdot \text{cm}^{-2}$.

Aiming at obtaining tillage depth within the set range during the subsoiling operation, undesirable depth should be adjusted to meet the requirement. Setting that the desirable tillage depth was from 250 mm to 450 mm, and the initial tillage depth was selected as 350 mm. When the field surface was flat, the tillage depth remained roughly the same, and the system controlled the shank position unchanged. The F_1 calculated by the Eqs.(2)-(4) was 816 N when the tillage depth was 350mm, the F_2 calculated by the Eq.(5) was 3004 N, and the F calculated by the Eq.(1) was 3820 N. When the field surface was uneven, the tillage depth suddenly increased to about 500 mm, which was greater than the set maximum value, the shank needed to be raised, and until the tillage depth was about 250 mm, the maximum amount of lifting was achieved. When the tillage depth was about 500 mm, the calculated F_1 was 927 N, the calculated F_2 was 4021 N, and thus the calculated force F was 4948 N. When the tillage depth was about 250 mm, the calculated F_1 was 534 N, the calculated F_2 was 2680 N, and thus the calculated F was 3214 N. While when the tillage depth suddenly reduced from

350 mm to about 200 mm, which was less than the set minimum value, the shank needed to be lowered. Until the tillage depth was about 350 mm, the calculated F_1 was 850N, the calculated F_2 was 3147 N, and thus the calculated F was 3997 N.

The three-dimensional model of shank was imported into the finite element analysis software to solve the equivalent stress. The method of Fixed Support was used to add fixed constraint on the installation position of the shank, and the force was applied on the shank tip and handle according to the above calculated values. The results of solution showed that the maximum stress and deformation of the shank was 244.83MPa and 4.213mm, respectively. With the increase of tillage depth, the maximum stress of the shank increased with the raise of tillage resistance. Therefore, it is necessary to optimize the structure of the shank to reduce the tillage resistance during subsoiling operation, and slow down the stress increase of the shank in the process of lowering adjustment. According to Eqs.(2)-(5), the decrease of F_1 and F_2 is enabled by respectively reducing the value of G and N_2 . The width of the shank was optimized from 50mm to 40mm, as well as the length was optimized from 165mm to 155mm, to reduce the area of soil acting on the shank tip, which was capable of reducing the value of G . The bottom side of the shank handle was designed as a rhombus to decrease the value of N_2 , and thus reducing the force of the soil on the bottom of the shank handle. The finite element analysis was also carried out to solve the equivalent stress of the optimized shank, and the results showed that the maximum equivalent stress of the shank was 214.38 MPa, which is less than the 244.83 MPa. The equivalent stress and deformation distribution diagram of the unaltered shank and optimized shank were shown in Fig.3 and Fig.4, respectively.

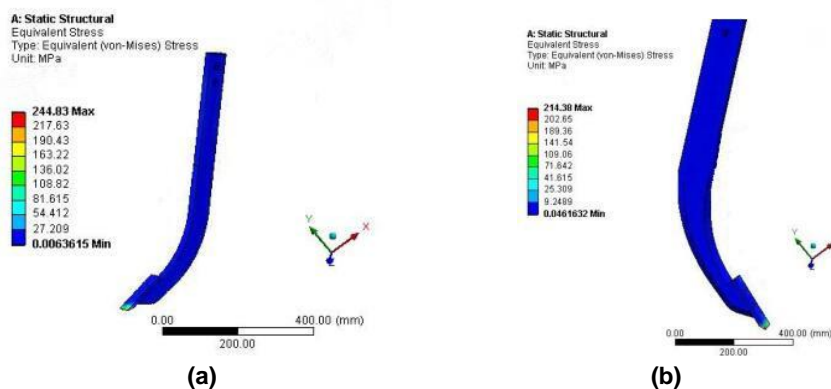


Fig. 3 - Comparison of equivalent stress distribution between the unaltered shank (a) and optimized shank (b)

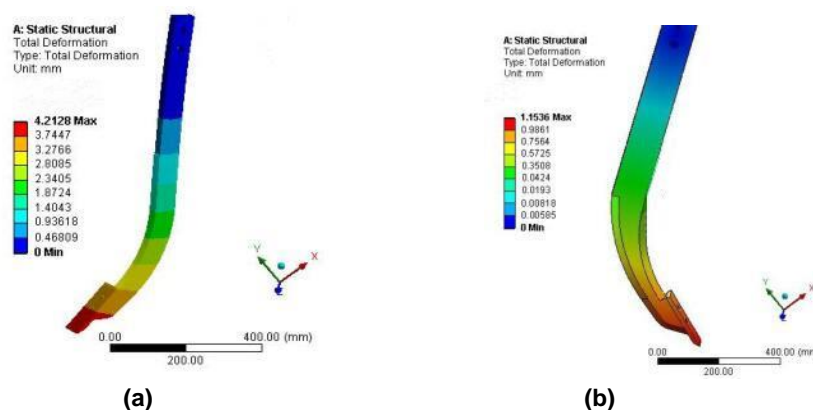


Fig. 4 - Comparison of deformation distribution between the unaltered shank (a) and optimized shank (b)

Design of the fixed mount and connect plate of the shank

The fixed mount and connect plate of the shank are the major components to fix the subsoiling assembly on the frame and enable good match between parts. The stability and reliability of these two components is the key to ensure efficient operation of the subsoiler. Two parallel four-bar mechanisms was respectively composed of a fixed mount, two swing rods and a connect plate of shank, which was capable of converting the telescopic movement of the hydraulic cylinder into the vertical up and down movement of the subsoiler shank.

According to the above structural and functional requirements, the basic structure of the fixed mount was designed, and its schematic diagram and force was shown in Fig.5. F_1 and F_2 were the support reaction of the swing rods, M_1 and M_2 were the flexural moment at the position of the hinge pins, P was the support reaction of the hydraulic mechanism, M_p was the flexural moment at the mounting hole of the U-bolt used to fix the hydraulic cylinder, F was the supporting force of the frame to the subsoiling assembly, and M was the flexural moment of the subsoiling assembly fixed on the frame. The fixed mount is made of No.45 steel, the elastic modulus of which is 2.09×10^{11} N/m and the yield strength is 355 MPa. The total weight of the subsoiling assembly was about 55 kg, and the support reaction of the swing rods was about 5460 N. The diameter of each hole and the distance between the hole and the boundary of the fixed mount were determined by Eqs.(6)-(7).

$$\tau = \frac{F}{A} \leq [\tau] \quad (6)$$

where:

τ is the shear stress, [MPa];

F - the shear force, [kN];

A - the shear area, [mm²].

$$\sigma_{r3} = \frac{\sqrt{M^2 + T^2}}{W} \leq [\sigma] \quad (7)$$

where:

M is the flexural moment, [kN·m];

T is the torque, [N·m];

W is the section modulus in bending, [mm³].

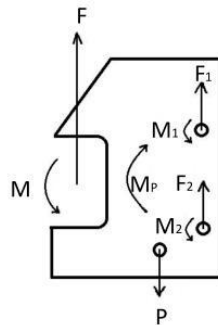


Fig. 5 - Schematic diagram of structure and force

The diameter of the hole for passing through the hinge pin used to install the swing rod was 20mm, and the distance of the hole from the boundary of the fixed mount must be greater than or equal to 16mm. Meanwhile, the diameter of the hole for passing through the hinge pin used to fix the hydraulic cylinder was 25mm and the diameter of the hole for inserting the u-bolt was 13mm, while the distance of the hole from the boundary of the fixed mount can't be less than 20mm. Furthermore, the overall dimension of the fixed mount was determined, including length, width and height.

Taking structural parameters and operating parameters into consideration, the distance between the front beam and the back beam of the frame was 400mm, the operation spacing ranged from 500mm to 700mm, and the maximum vertical displacement of the shank in the adjustment process was 200mm, the length, width and height of the fixed mount should not be larger than 250mm, 200mm and 360mm, respectively. In order to improve stiffness of the fixed mount, topology optimization was carried out using OptiStruct software, and the initial model in topology optimization was shown in Fig.6. The flexibility of the fixed mount was taken as the target response, the optimization region was taken as the design variable, and the volume ratio was set as the constraint. The volume ratio of 80%, 85% and 90% were selected as the upper limit for trial operation, and up to 85% of the volume belonging to the three-dimensional model was retained, which depends on the overall maximum stress that was considered as comparison parameter.

The positions of hinge holes and pin holes were changed, and the topology optimized model, the stress of which was reduced and the stiffness improved, was shown in Fig.7.

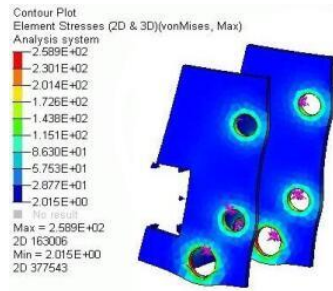


Fig. 6- Initial model



Fig. 7- Topology optimized model

The connect plate of the shank was stressed at the hinge holes and bolt holes, which were respectively used to connect the swing rods and fix the shank. It is made of No.45 steel, its material properties are the same as those of the fixed mount. The thickness of the steel plate used for the connect plate of the shank was 10 mm, and the diameter of the hinge hole was 25mm as well as of the bolt hole was 15mm. Static analysis results of the connect plate of the shank showed that its maximum stress was much less than the allowable stress, and the maximum deformation was 0.137mm. The material and structure of the connect plate of the shank met the request for utilization.

Design of the hydraulic linkage and swing rod

Each subsoiling assembly had four swing rods and two hydraulic linkages. One side of the swing rod was hinged with the fixed mount, and another side was hinged with the connect plate of shank. While one side of the hydraulic linkage was hinged with the hydraulic cylinder shaft, the other side was hinged with the lower swing rod. In this study, the stroke of the hydraulic cylinder was required to be 200mm, and the displacement of the upper and lower adjustment was 100mm, respectively. The relationship between the stroke of the hydraulic cylinder, the length of the swing rod and hydraulic linkage was presented in Eq.(8).

$$L=r(1-\cos\theta)+\frac{r^2}{l}(1-\cos2\theta) \tag{8}$$

where:

- L is the stroke of the hydraulic cylinder, [mm];
- r the length of the swing rod, [mm];
- l - the length of the hydraulic linkage, [mm];
- θ - the rotation angle of the swing rod, [°].

The required stroke of the hydraulic cylinder was 200mm, the rotation angle of the swing rod ranged from 45° to 125°, and the range of the rotation angle of the hydraulic linkage was 26°~35°. After calculation, the length of the swing rod and hydraulic linkage was 140mm and 383mm, respectively. The swing rod and hydraulic linkage were made of No.45 steel, and the thickness of the swing rod and hydraulic linkage was determined to be 10mm.

Determination of the hydraulic cylinder and magnetic exchange valve

The effective working area of the piston was derived by the Eqs.(9)-(10) (Cheng et al., 2008).

$$F = F_L + F_f + F_a \tag{9}$$

where:

- F is the total load applied on the hydraulic cylinder, [N];
- F_L - workload applied on the hydraulic cylinder, [N];
- F_f - frictional resistance applied on the hydraulic cylinder, [N];
- F_a - inertia load applied on the hydraulic cylinder, [N].

$$A = \frac{F}{P} \tag{10}$$

where:

- A is the effective working area of the piston, [mm²];
- F is the total load applied on the hydraulic cylinder, [N];
- P is the working pressure of the hydraulic cylinder, [MPa].

$$D = \sqrt{\frac{4A}{\pi}} \quad (11)$$

where D is the diameter length of the effective working area.

The subsoiler designed in this study had four rows of shanks, and each shank was separately equipped with a group of hydraulic transmission mechanism, the working pressure of which was determined to be 12MPa. The effective working area of the piston was calculated to be 583.33 mm², so the D was equal to 27.25mm.

According to the standard table, the inner diameter of the hydraulic cylinder was selected to be 32mm. Besides, the rod diameter of the hydraulic cylinder was 20mm, the outer diameter of the hydraulic cylinder was 55mm, and the stroke of the hydraulic cylinder was 200mm.

The type of the magnetic exchange valve was determined according to the working parameters and motion state of the hydraulic cylinder. In order to reduce the tillage depth when it's larger than the desirable value, increase the depth when it's less than the desirable value, and keep the depth unchanged when it's at the desirable value, the hydraulic cylinder needs to complete three actions, elongation, shortening and remaining unchanged. So, the three-position four-way magnetic exchange valve (DSG-03-3C60-DL-DC24) was applied in this study, which was controlled to open the left and right valves or keep the middle position to complete the telescopic movement of the hydraulic cylinder, and thus the desirable tillage depth was obtained by lifting or lowering the shank or keeping the position of the shank unchanged. The rated flow of this type of magnetic exchange valve is 60L/min, the maximum flow is 100 L/min, and the maximum working pressure is 24.5MPa.

Design of the sensor bracket

During the subsoiling operation, the speed of the tractor was about 3–5km/h, while the monitoring and control period of the system was 1s and the response time of the system was 0.4s. Within the response time, the advance distance of the subsoiler was given by Eq.(12).

$$S = v \times t \quad (12)$$

where:

S is the advance distance of the subsoiler, [m];

v - the speed of the tractor, [m/s];

T - the response time, [s].

Therefore, the range of advance distance in response time was 0.33–0.56m. In order to avoid profile lag, the ultrasonic sensor on the sensor bracket should be installed in front of the shank tip in the forward direction, and the distance between them basically enabled the same as the displacement of the subsoiler from current position to the detection point within the response time. The sensor bracket was fixed on the one side of the connect plate of the shank, which was capable of moving up and down synchronously with the shank, and the ultrasonic sensor was installed at the end of the forward extension part of it, as shown in Fig.8. To avoid the negative impact of vibration on the detection accuracy of tillage depth during the subsoiling operation, the forward extension distance of the sensor bracket was set as 500mm.

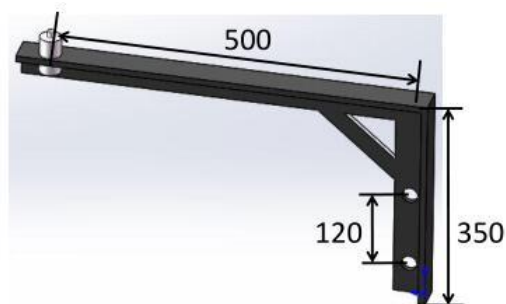


Fig. 8- Structure of the sensor bracket with the ultrasonic sensor

Evaluation experiment

Test arrangement

The field experiments were conducted to evaluate the subsoiling quality and operation performance of the subsoiler equipped with tillage depth monitoring and control subsoiling assemblies, and test indexes included the variable coefficient of soil hardness, looseness of soil, coefficient of soil disturbance and stability coefficient of tillage depth. Meanwhile, the comparison test of two adjustment methods was carried out, including independent adjustment of single row and unified adjustment of each row. The field experiments were carried out in Shenze County, Hebei Province, North China. Maize straw was returned to the field, and the soil type belongs to fluoro-aquil soil. The mean value of the soil moisture and soil bulk density was 15.4% and 1.45 g/cm³, respectively. The subsoiler equipped with tillage depth monitoring and control subsoiling assemblies was driven by the Levo TG series M1254-G tractor. The field experiment was shown in Fig.9.



Fig. 9 - Field experiments

1. Fixed mount; 2. Hydraulic cylinder; 3. Frame; 4. Magnetic exchange valve; 5. Sensor bracket; 6. Tractor; 7. Hydraulic linkage; 8. Ultrasonic sensor; 9. Swing rod; 10. Connect plate of the shank; 11. Subsoiler shank

Subsoiling quality test

Soil hardness is one of the important physical properties of soil. Comparing between subsoiled soil and unsubsoiled soil, the larger the variable coefficient of soil hardness is, the greater the change of soil hardness will be, and thus better subsoiling quality is obtained. The variable coefficient of soil hardness was given by Eq.(13). Looseness of soil, coefficient of soil disturbance and stability coefficient of tillage depth are significant indexes to evaluate subsoiling quality. Looseness of soil and coefficient of soil disturbance was respectively obtained by Eq.(14) and Eq.(15), and stability coefficient of tillage depth was derived by Eqs.(16) - (19).

$$C = \frac{H - H_i}{H} \times 100\% \quad (13)$$

where: C represents the variable coefficient of soil hardness, [%];
 H represents the soil hardness before subsoiling, [kg/cm²];
 H_i represents the soil hardness after subsoiling, [kg/cm²].

$$P = \frac{A_h - A_q}{A_q} \times 100\% \quad (14)$$

$$Y = \frac{A_s}{A_q} \times 100\% \quad (15)$$

where: P represents the looseness of soil, [%];

Y represents the coefficient of soil disturbance, [%];

A_h represents the section area between the theoretical curve of the furrow bottom and the surface curve of the subsoiled soil, [cm²];

A_q represents the section area between the theoretical curve of the furrow bottom and the surface curve of the unsubsoiled soil, [cm²];

A_s represents the section area between the actual curve of the furrow bottom and the surface curve of the subsoiled soil, [cm²].

$$a = \frac{\sum a_i}{n} \quad (16)$$

$$S = \frac{\sqrt{\sum (a_i - a)^2}}{n-1} \quad (17)$$

$$V = \frac{S}{a} \times 100\% \quad (18)$$

$$U = 1 - V \quad (19)$$

where:

a represents the average value of the tillage depth, [mm];

a_i represents the tillage depth of each measuring point, [mm];

n represents the number of the selected points measured manually;

S represents the standard deviation of tillage depth, [mm];

V represents the variation coefficient of tillage depth stability, [%];

U represents the stability coefficient of tillage depth, [%].

Three points were randomly selected from a row within the 50m length of the subsequent subsoiling operation section, and the soil hardness of each point at three soil layers was measured by the soil hardness instrument, including depth of 0~15cm, 15~30cm and 30~45cm. The position of each point was marked, the soil hardness data were recorded and the average soil hardness of each depth layer was calculated.

The subsoiler equipped with tillage depth monitoring and control subsoiling assemblies advanced 50m at the speed of 5 km/h, and the tillage depth range was set at 350~450 mm. After subsoiling, the soil hardness of three depth layers at three marked positions were measured and recorded, and the average soil hardness of each depth layer was obtained.

Therefore, the variable coefficient of soil hardness was solved by substituting the relevant data into Eq.(13). A part of the subsoiling area was selected to dig out the soil and show the furrow cross-section, and the surface curve of the unsubsoiled soil, the surface curve of the subsoiled soil and the curve of the furrow bottom were drawn with the same horizontal line in the furrow cross-section. A_h , A_q and A_s was calculated, and thus looseness of soil and coefficient of soil disturbance was respectively obtained by substituting the relevant value into Eq.(14) and Eq.(15).

Along the subsoiling operation route, 30 points were selected every 1.4m from the starting position and their tillage depth was measured manually. Substituting the relevant data into Eqs.(16)-(19), stability coefficient of tillage depth was calculated.

Performance comparison test

Performance comparison test was carried out on the subsoiler equipped with subsoiling assemblies under two adjustment modes of tillage depth, including automatic detection and adjustment of single row tillage depth controlled by the system and adjustment at three-point suspension by the tractor, to verify the improvement effect of the subsoiler equipped with tillage depth monitoring and control subsoiling assemblies on the stability of single row tillage depth. The tillage depth range was set at 250~450 mm. The subsoiler advanced 50 m at a speed of 5 km/h under the system operation state and the system stopped operation state, respectively. After the subsoiling operation, 10 measuring points were selected at equal distance from each operation route for manual measurement of tillage depth, and then these data were analysed and compared.

RESULTS AND DISCUSSION

Results of subsoiling quality test

Mean value of soil hardness of each soil layer at three marked points, and the variable coefficient of soil hardness of each soil layer before and after subsoiling were shown in Table 1, while looseness of soil and coefficient of soil disturbance were given in Table 2.

Table 1

Soil depth [cm]	Soil hardness before subsoiling [kg/cm ²]	Soil hardness after subsoiling [kg/cm ²]	Variable coefficient of soil hardness [%]
0~15	15.88	5.78	63.60
15~30	20.13	10.21	49.28
30~45	27.85	15.65	43.81
Mean value	21.29	10.55	52.23

Table 2

Set depth range [mm]	A_h [cm ²]	A_q [cm ²]	A_s [cm ²]	Looseness of soil [%]	Coefficient of soil disturbance [%]
350~450	42.74	32.31	20.06	32.55	62.15

According to the data in the Table 1, the mean value of the variable coefficient of soil hardness among the three depth layers was 52.23%, which illustrated that the soil hardness was significantly reduced after subsoiling operation of the subsoiler equipped with tillage depth monitoring and control subsoiling assemblies, which met the requirements of subsoiling operation. Meanwhile, the data in Table 2 showed that looseness of soil was 38.17% and coefficient of soil disturbance was 63.84%, and it indicated that the subsoiler designed in this paper was capable of obtaining good subsoiling quality and the soil which had been subsoiled met the standard requirement. Manually measured tillage depth at 30 selected points along the subsoiling operation route was shown in Fig.11, and the stability coefficient of tillage depth was 92.43% based on the derivation of Eqs.(16) - (19), which was more than 85% and met the requirement of depth stability in subsoiling operation.

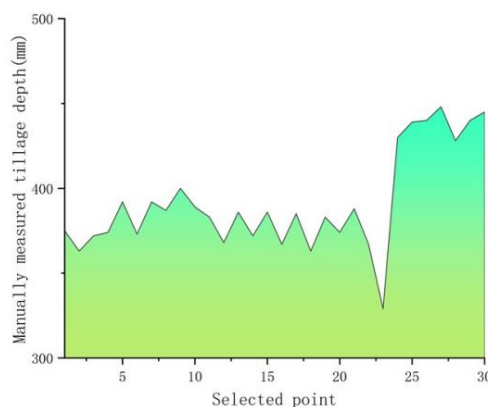


Fig. 10 - Manually measured tillage depth at 30 selected points

It was obvious in Fig.10 that the tillage depth between the first point and the 22nd point and between the 24th point and the 30th point basically remained unchanged. However, the tillage depth of the 23rd point was much smaller than that of the 22nd point. This might be due to the fact that there was depression on the surface, which made the tillage depth decrease greatly and led to the large difference of the tillage depth. Fortunately, the tillage depth monitoring and control system played a significant role in adjusting the tillage depth from 329mm to 430mm in time, which made the tillage depth meet the set range and improve the stability of tillage depth.

Results of performance comparison test

The tillage depth of 10 points selected equidistantly along each subsoiling route, which was respectively generated under the system operation state and the system stopped operation state, were shown in Fig.11. The standard deviation of tillage depth obtained by the method of adjusting the single shank was 38.315mm, while the standard deviation of tillage depth obtained by the method of adjusting the whole machine was 51.521mm, which indicated that the discreteness of the data obtained by the second method was greater than that by the first method. It was shown in Fig.11 that the minimum tillage depth was 221.5mm and the maximum tillage depth was 332.8mm, which were obtained by adjusting the single shank.

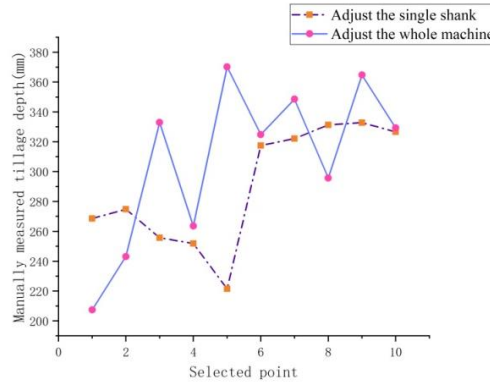


Fig. 11 - Comparison of tillage depth under two adjustment methods

The tillage depth of the first point to the fourth point was almost equal, and so was the tillage depth from the sixth point to the tenth point. These data were all within the set range of tillage depth. Nevertheless, due to the sunken surface between the fourth and fifth point, the tillage depth was reduced to 221.5mm and it was less than the minimum value of the set range, which was 250mm. The system controlled the hydraulic cylinder shortening to lower the shank so that the tillage depth was adjusted from 221.5mm to 317.5mm in time to make the tillage depth within the set range. Meanwhile, the minimum tillage depth was 207.4mm and the maximum tillage depth was 370.2mm, which were obtained by adjusting at the three-point suspension depending on the tractor driver, and tillage depth of four points were all outside the set range. The tillage depth at the first point was 207.4mm and at the second point was 243.1mm. It was obvious that when the tillage depth was outside the set range, this adjustment method was incapable of accurately adjusting the tillage depth to the desirable value. Besides, cross-section of partial subsoiling furrows belonging to these two adjustment methods were shown in Fig.12, which illustrated that compared with the method of adjusting the single shank, the variation of tillage depth obtained by the method of adjusting at the three-point suspension was larger. Hence, the stability of tillage depth obtained by this method was poor and the depth difference was great. It was proved that the subsoiler equipped with tillage depth monitoring and control subsoiling assemblies was capable of improving the tillage depth stability of single row.

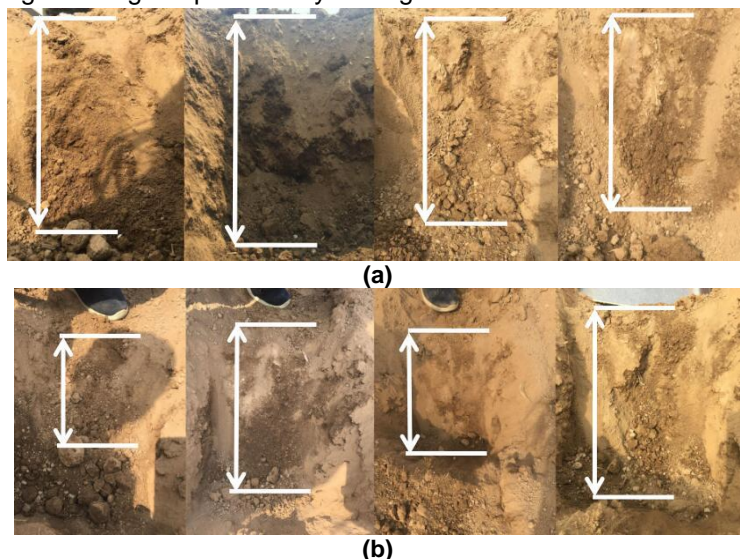


Fig. 12 - Cross-section of partial subsoiling furrows belongs to the method of adjusting the single shank (a) and adjusting at three-point suspension (b)

CONCLUSIONS

(1) A method for independent control of single row tillage depth based on ultrasonic sensor detection and hydraulic adjustment was proposed. The tillage depth monitoring and control subsoiling assembly and the subsoiler equipped with such assemblies were designed.

(2) Key structural parameters of the hydraulic cylinder were determined via the force analysis of subsoiling assembly. The inner diameter, rod diameter, outer diameter and stroke of the hydraulic cylinder were 32mm, 20mm, 55mm and 200mm, respectively. The three-position four-way magnetic exchange valve was applied to meet the requirement of three operation states of the hydraulic cylinder, including elongation, shortening and remaining unchanged.

(3) The subsoiling quality test was conducted and the results showed that the mean value of the variable coefficient of soil hardness, looseness of soil and coefficient of soil disturbance were 52.23%, 32.55% and 62.15%, respectively. The stability coefficient of tillage depth was 92.43%. The subsoiling quality of the tillage depth monitoring and control subsoiling assembly was good and all indexes met requirements.

(4) The performance comparison test was carried out, and the results indicated that the standard deviation of tillage depth belonging to the method of adjusting the single shank and adjusting at the three-point suspension were 38.315mm and 51.521mm, respectively. It was verified that the stability of single row tillage depth was significantly improved by applying the subsoiler equipped with tillage depth monitoring and control subsoiling assemblies.

ACKNOWLEDGEMENT

The author(s) disclosed receipt of the following financial support for the research, authorship, and/or publication of this article: This work was supported by the Modern Agricultural Industry Technology System (Grant No.CARS-03); The 2115 Talent Development Program of China Agricultural University.

REFERENCES

- [1] Ayiding, K., Wu, M.T., He, P.X., Liu, X.R., & Sun, B. (2013). The control system of automatic adjustment for ploughing depth (耕深自动调节控制系统). *Journal of Agricultural Mechanization Research*, 3, 160-163. <http://dx.doi.org/10.13427/j.cnki.njyi.2013.03.043>
- [2] Cheng, D.X., Wang, D.F., Ji, K.S., et al., (2008). Hand book of mechanical design (机械设计手册). *Chemical Industry Press*, Beijing/China.
- [3] Feng, X.M., Hao, Y.B., Latifmanesh, H., Lal, R., Cao, T.H., Guo, J.R., Deng, A.X., Song, Z.W., & Zhang, W.J. (2018). Effects of subsoiling tillage on soil properties, maize root distribution, and grain yield on Mollisols of Northeastern China. *Agronomy Journal*, 110(4), 1607-1615. <https://doi.org/10.2134/agronj2018.01.0027>
- [4] Gao, L., Yang, F., Wang, R.T., Jiang, L., Wang, D. (2013). Rotary cultivator digging depth design of detection system (旋耕机松土深度检测系统设计). *Journal of Agricultural Mechanization Research*, 5, 159-162. <http://dx.doi.org/10.13427/j.cnki.njyi.2013.05.034>
- [5] Hargreaves, P.R., Baker, K.L., Graceson, A., Bonnett, S., Ball, B.C., & Cloy, J.M. (2019). Soil compaction effects on grassland silage yields and soil structure under different levels of compaction over three years. *European Journal of Agronomy*, 109, 1-9. <https://doi.org/10.1016/j.eja.2019.125916>
- [6] He, J., Li, H.W., Chen, H.T., Lu, C.Y., & Wang, Q.J. (2018). Research progress of conservation tillage technology and machine (保护性耕作技术与机具研究进展). *Transactions of the Chinese Society for Agricultural Machinery*, 49(4), 1-18. <http://dx.doi.org/10.6041/j.issn.1000-1298.2018.04.001>
- [7] Kristoffersen, A.O., & Riley, H. (2005). Effects of soil compaction and moisture regime on the root and shoot growth and phosphorus uptake of barley plants growing on soils with varying phosphorus status. *Nutrient Cycling in Agroecosystems*, 72(2), 135-146. <https://doi.org/10.1007/s10705-005-0240-8>
- [8] Lee, J., Yamazaki, M., Oidab, A., Nakashimac, H., & Shimizub, H. (1998). Electro-hydraulic tillage depth control system for rotary implements mounted on agricultural tractor Design and response experiments of control system. *Journal of Terramechanics*, 35(4), 229-238. [https://doi.org/10.1016/S0022-4898\(98\)00026-3](https://doi.org/10.1016/S0022-4898(98)00026-3)
- [9] Mouazen, A.M., Anthonis, J., Saeys, W., & Ramon, H. (2004). An automatic depth control system for online measurement of spatial variation in soil compaction.1. Sensor design for measurement of frame height variation from soil surface. *Biosystems Engineering*, 89(2), 139-150. <http://doi.org/10.1016/j.biosystemseng.2004.06.005>

- [10] Poehlitz, J., Ruecknagel, J., Schlueter, S., Vogel, H.J., & Christen, O. (2019). Computed tomography as an extension of classical methods in the analysis of soil compaction, exemplified on samples from two tillage treatments and at two moisture tensions. *Geoderma*, 346, 52-62. <https://doi.org/10.1016/j.geoderma.2019.03.023>
- [11] Singh, k., Choudhary, O.P., Singh, H.P., Singh, A., & Mishra, S.K. (2019). Sub-soiling improves productivity and economic returns of cotton-wheat cropping system. *Soil & Tillage Research*, 189, 131-139. <https://doi.org/10.1016/j.still.2019.01.013>
- [12] Somerville, P.D., May, P.B., & Livesley, S.J. (2018). Effects of deep tillage and municipal green waste compost amendments on soil properties and tree growth in compacted urban soils. *Journal of Environmental Management*, 227, 365-374. <https://doi.org/10.1016/j.jenvman.2018.09.004>
- [13] Suomi, P., & Oksanen, T. (2015). Automatic working depth control for seed drill using ISO 11783 remote control messages. *Computers and Electronics in Agriculture*, 116, 30–35. <https://doi.org/10.1016/j.compag.2015.05.016>
- [14] Yin, Y.X., Wang, C., Meng, Z.J., Chen, J.P., Guo, S.X., & Qin, W.C. (2018). Operation Quality Measurement Method for Tilling Depth of Suspended Subsoiler (悬挂式深松机耕整地耕深检测方法研究). *Transactions of the Chinese Society for Agricultural Machinery*, 49(4), 68-74. <http://dx.doi.org/10.6041/j.issn.1000-1298.2018.04.008>
- [15] Yu, Y.C., Liu, W.Y., Zhao, Y.F., & Sun, J.Q. (2007). Force mathematical model and examination analysis of the column subsoiler (立柱式深松铲受力数学模型及试验分析). *Transactions of the Chinese Society of Agricultural Engineering*, 23(6), 109-113. <http://dx.doi.org/10.3969/j.issn.1002-6819.2007.06.005>
- [16] Zhang, R.F., Yang, H.S., Gao, J.L., Zhang, Y.Q., Wang, Z.G., Fan, X.Y., & Bi, W.B. (2015). Effect of subsoiling on root morphological and physiological characteristics of spring maize (深松对春玉米根系形态特征和生理特性的影响). *Transactions of the Chinese Society of Agricultural Engineering*, 31(5), 78-84. <http://dx.doi.org/10.3969/j.issn.1002-6819.2015.05.012>
- [17] Zhao, J.H., Liu, L.J., Yang, X.J., Liu, Z.J., Tang, J.X. (2015). Design and laboratory test of control system for depth of furrow opening (播种机开沟深度控制系统的设计与室内试验). *Transactions of the Chinese Society of Agricultural Engineering*, 31(6), 35-41. <http://dx.doi.org/10.3969/j.issn.1002-6819.2015.06.005>

EFFECT OF SEED FILLING AND RELEASING ANGLES ON THE PERFORMANCE OF COMPOUND VACUUM SEED METERING DEVICE

充种角度对复合气吸式排种器作业性能的影响规律

Liu Zeqi¹⁾, Zhang Meng¹⁾, Han Jie¹⁾, Zhuang Yajun¹⁾, Yin Xiang^{1,3)}, Chen Yulong^{*1,2)} ¹

¹⁾ School of Agricultural Engineering and Food Science, Shandong University of Technology, Zibo 255000, China;

²⁾ Research of Institute of Ecological Unmanned Farm, Shandong University of Technology, Zibo 255000, China;

³⁾ Shandong provincial key laboratory of dry-farming machinery and informatization, Zibo 255000, China;

Tel: +86 15315206471; E-mail: 1097402292@qq.com

DOI: <https://doi.org/10.35663/inmateh-65-16>

Keywords: vacuum seed metering device, filling angle, releasing angle, filling performance, metering performance

ABSTRACT

In this paper, taking compound air-suction seed metering device as the subject, the effect rule of seed filling angle and seed releasing angle on the performance of seed filling and seed metering is studied. An indoor test was conducted with a JPS-12 metering test bench and a high-speed camera system. The starting and ending angles of the air chamber were changed by adjusting the regulating plate, that is, the angles of seed filling and seed releasing, and the filling and seed metering performance was taken as evaluation indexes. The test results show that: the seed filling angle has significant effect on the seed filling effect, and the miss fill index decreases with the increase of the quality of fill index. When the seed filling angle exceeds 50°, they will stabilize gradually ending at the multiple fill index of 0%. The negative pressure and operating speed are interactive and have a significant effect on filling performance. The seed releasing angle has significant effect on the metering performance. With the increase of the angle, the quality of feed index increases firstly and then decreases. The multiple index and miss index are opposite to the quality of feed index which is the max at the seed releasing angle of 39.5°. The negative pressure and forward speed are interactive and have a significant effect on metering performance. The quality of feed index under the same condition is lower than that of fill index.

摘要

本文以气吸式复合排种器为对象，研究充种和投种角度对充种性能和排种性能的影响规律。利用 JPS-12 排种试验台和高速摄像系统开展室内试验；通过气室调整盘改变气室的起止角度，即充种和投种的角度，以充种性能和排种性能作为评价指标。结果表明：充种角度对充种效果具有显著影响，充种合格率逐渐增大，漏充率逐渐减小，当充种角大于 50° 后，二者逐渐稳定，而重充率始终为 0%，负压和作业速度对充种性能具有显著影响，且二者之间存在交互作用；投种角度对排种性能具有显著影响，随着角度的增大，合格率先升高后降低，重播率和漏播率与合格率呈现相反的变化规律，合格率最大时的投种角度为 39.5°，负压与前进速度对排种性能具有显著影响，且二者之间存在交互作用；相同条件下的排种合格率低于充种合格率。

INTRODUCTION

The seed metering device is a core part of precision seeding which is the main development direction of seeding technologies. By the principles, the seed metering devices can be divided into mechanical and pneumatic type devices, among which, the air-suction seed metering device is a research hotspot at present (Dylan et al., 2013; Jia et al., 2018; Singh et al., 2007; Wang et al., 2017; Yang et al., 2016). Most studies on air-suction seed metering device focus on the effect rule of the design of physical dimension of the seed-picking mechanism (Cujbescu et al., 2019; Liao et al., 2018), negative pressure value and forward speed and working parameters on the metering performance, or on optimizing seed metering devices for different seeds (Zhang et al., 2015; Zhang et al., 2020), such as corn, sunflower seeds, peanuts, rape seeds and millet seeds (Ding et al., 2018; Yu et al., 2014; Yu et al., 2015; Zhang et al., 2014).

¹ Zeqi Liu, M.S. Stud. Eng.; Meng Zhang, M.S. Stud. Eng.; Jie Han, M.S. Stud. Eng.; Yajun Zhuang, M.S. Stud. Eng.; Xiang Yin, As. Ph.D. Eng.; Yulong Chen, Lecture Ph.D. Eng.

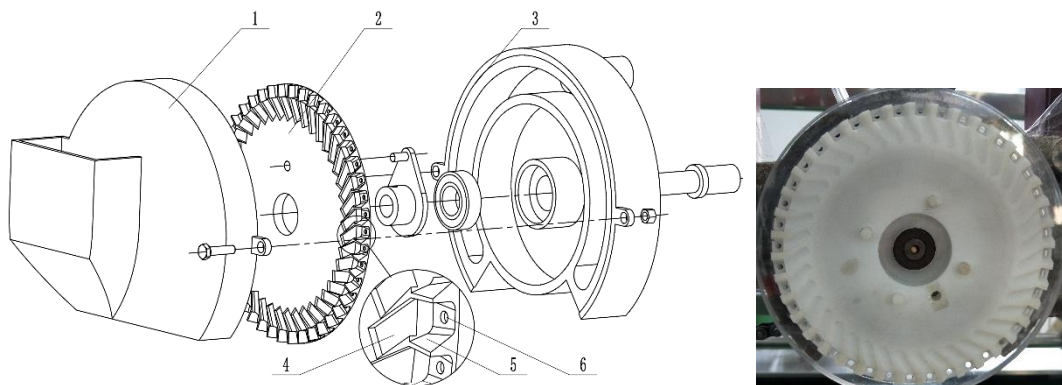
At the same time, some researchers focused on the process of seed falling and touching soil, and optimized the seed releasing angle and the shape of seed tube to improve the consistency of seed spacing (Abdolazare *et al.*, 2018; Karayel *et al.*, 2006; Zhao *et al.*, 2016). In the early stage, the author designed a compound air-suction seed metering device, optimized the seed hole mechanism, and reduced the negative pressure of the air-suction seed metering device (Chen *et al.*, 2021).

However, there are few in-depth studies on seed filling and releasing angles. The seed filling angle has significant effect on the filling effect and subsequent seed clearing, and the seed releasing angle has a significant effect on the height, speed and direction when seeds are released from the disk. The design of a suitable seed releasing angle is of great significance to improve the seed-metering performance. Therefore, the seed filling and releasing angles will be studied deeply in this paper by taking the compound air-suction seed metering device as the subject.

MATERIALS AND METHODS

Vacuum seed metering device

The compound air-suction seed metering device (Chen *et al.*, 2021) is equipped with an innovative disk which is a 7 mm thick plastic disk with several seed-stirring slots and seed-picking slots evenly distributed on the periphery (Fig. 1). There is a suction hole at the bottom of the seed-picking slot. The seed-picking structure of the disk is composed of seed-stirring slots, seed hole and suction hole. The seed-stirring slots are used to stir seeds to increase the dispersion degree of seed groups and to guide the movement of the seed hole. When the seed hole passes the seed group, seeds will enter the seed hole under the gravity and the internal force of the seed group, and the suction hole at the bottom of the seed hole will suck seeds under the negative pressure to fix seeds at the bottom of the seed hole. The structure can effectively improve the success rate of seed picking and reduce the negative pressure required during operation.



a. Structural diagram of vacuum seed metering device with composite disc

b. Physical diagram of composite disc

Fig. 1 - Vacuum seed metering device and composite disc

1. Shell; 2. Disc; 3. Base; 4. Seed agitator; 5. Seed hole; 6. Suction hole

Test plan

The test was carried out on the JPS-12 test bench (Fig. 2), which has been widely used in studies of seed metering devices (Zhang *et al.*, 2015; Zhao *et al.*, 2016).



Fig. 2 - Indoor test system



Fig. 3 - Adjustment of vacuum chamber thickness

By recording the position of seeds falling on the seed belt, the seed metering rule was calculated by image processing. However, due to the changes in the position and speed of seeds when they were released from the disk and in the process of falling, the seed metering information recorded by the test bench could not accurately reflect the filling performance of the seed metering device. To study the effect of seed filling angle and working parameters on the filling performance, a high-speed camera was used to record and count the seed filling information of the disk (Zhang *et al.*, 2015).

Previous studies have shown that the thickness and range of the air chamber can be changed by installing a regulating plate in the range of the original air chamber (Fig. 3). When the thickness of the regulating plate is 20 mm, the pressure uniformity of all parts within the air chamber is the best and the pressure drop is not obvious. Therefore, the 20 mm-thick regulating plate is used to change the starting and ending angles of the air chamber, then regulating the seed filling and releasing angles during seed metering, and studying the effect rule of seed filling and releasing angles on the seed-metering performance. The seed filling angle is set as 0° in the negative direction of the horizontal line and positive in the downward direction, and is increased by 10° from 0° to 90°. The seed releasing angle is set as 0° in the positive direction of the horizontal line, and positive in the downward direction, and is increased by 10° from 0° to 90°.

Studies at home and abroad have shown that the working parameters have an important effect on the metering performance. The main working parameters of the seed metering device include forward speed and negative pressure. Their effect on the filling and releasing performance was studied at the speed of 6, 8, 10 and 12 km/h, and the negative pressure of 1, 2, 3, 4 and 5 kPa.

Evaluating indicator

In accordance with GB/T 6973-2005 Testing Methods of Single Seed Drills (Precision Drills), each test shall be performed with 250 seeds and be repeated for 5 times, with the metering performance evaluation indexes of quality of feed index *A*, multiple index *D*, miss index *M* and precision index *C*. At the same time, to intuitively evaluate the effect of seed filling, the quality of fill index (*FA*), multiple fill index (*FD*) and miss fill index (*FM*) are set as the evaluation indexes of filling performance (Table 1).

Table 1

Evaluation index of working performance of seed metering device

Seed metering performance	Seed filling performance
$A = n_1/N \times 100$	$FA = h_1/H \times 100$
$D = n_2/N \times 100$	$FD = h_2/H \times 100$
$M = 100 - A - D$	$FM = 100 - FA - FD$
$C = \sigma \times 100$	

In Table 1: h_1 is the number of seed holes with a seed; h_2 is the number of seed holes with two or more seeds; H is the total number of seed holes counted; n_1 is the number of seeds with the seed spacing greater than 0.5 times the theoretical seed spacing and less than 1.5 times the theoretical seed spacing (the theoretical seed spacing herein is 10 cm); N is the number of seeds determined through test; n_2 is the number of seeds with the seed spacing less than 0.5 times the theoretical seed spacing; σ is the standard deviation of seed spacing.

RESULTS AND ANALYSIS

Effect of seed filling angle on filling performance

At first, the seed filling angle was tested, with the original seed releasing angle remaining unchanged. The test was conducted at the negative pressure of 3 kPa and forward speed of 8 km/h. The test results were recorded and counted by a high-speed camera (Table 2).

Table 2

Effect of seed filling angle on seed filling performance

Seed filling angle [°]	FA [%]	FD [%]	FM [%]
0	83.54	0	16.46
10	85.36	0	14.64
20	89.73	0	10.27
30	91.78	0	8.22
40	95.32	0	4.68
50	98.64	0	1.36
60	99.67	0	0.33
70	99.05	0	0.95
80	99.32	0	0.68
90	99.83	0	0.17

With the increase of the seed filling angle, *FA* increased continuously to approximately 100%, and *FM* decreased continuously to approximately 0%. When the seed filling angle increased from 0° to 50°, *FA* and *FM* changed significantly. After the seed filling angle exceeded 50°, *FA* and *FM* became stable gradually. By increasing the seed filling angle, the filling performance can be improved effectively to reduce the misses. In the change process of the seed filling angle, *FD* remained at 0% all along, indicating that the combined structure of seed hole and suction hole had a very obvious quantitative effect on seeds, and there were no multiple seeds filled into the seed hole at the same time, therefore, the clearing parts can be removed to simplify the seed metering mechanism.

After the regression analysis of *FA*, the mathematical models of *FA* and seed filling angle are obtained as below:

$$y_c = 7.19\ln(x) + 68.6, \quad R^2 = 0.96 \quad (1)$$

The effect of working parameters on the filling performance

As *FA* tends to be stable when the seed filling angle is greater than 50°, the forward speed and negative pressure were performed with the dual-factor test at the seed filling angle of 50°. The test results were recorded by a high-speed camera as well (Fig 4).

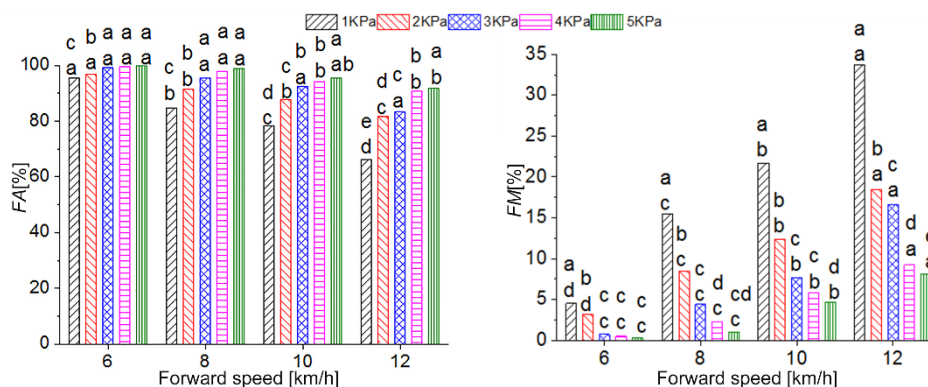


Fig. 4 - Effect of working parameters on seed filling performance

The upper and lower lowercase letters at the top of each group of data in the column chart represent the results of significance analysis of the data. Wherein, the upper letter represents the result of significance analysis of five negative pressures at each speed. If the two groups of data do not contain a same letter, it indicates that the two groups of data are significantly different. The lower letter represents the result of significance analysis of 4 speeds at a negative pressure, the same below.

The negative pressure and forward speed had no significant effect on *FD*. *FD* remained at 0% all along with the change of negative pressure and forward speed, further indicating that single seed quantitative seed picking can be achieved with the seed hole in an appropriate size without additional seed cleaning device.

At different speeds, negative pressure has a significant effect on *FA*. *FA* increases with the increase of negative pressure, with the increased amplitude changing with the increase of speed. At 6 km/h, the *FA* is 95.48% at 1 kPa and 99.60% at 5 kPa, with the increase ratio of 4.3%. At 12 km/h, the *FA* is 66.30% at minimum at 1 kPa and 91.86% at 5 kPa, with the increase ratio of 27.8%.

Under different negative pressures, *FA* decreases significantly with the increase of forward speed, which is the most significant at 1 kPa. *FA* is 95.48% at 6 km/h, and 66.3% at 12 km/h, with the decrease ratio of 30.6%. *FA* decreases slightly with the increase of negative pressure. Under the negative pressure of 5 kPa, the change of *FA* is the minimum; the *FA* is 99.67% at 6 km/h and 91.86% at 12 km/h, with the decrease ratio of 7.8%, indicating that the negative pressure is interactive with the forward speed.

Since *FD* is 0, *FM* is 100%-*FA*. Therefore, the change rule of *FM* is completely opposite to that of *FA*.

The effect of the seed releasing angle on the metering performance

The effect of the seed releasing angle on the metering performance was studied at the seed filling angle of 50°. The test was performed at the negative pressure of 3 kPa and forward speed of 8 km/h firstly. The data acquisition and processing system of JPS-12 metering test bench was used to record the test results automatically (Table 3).

Table 3

Effect of seed releasing angle on metering performance

Seed releasing angle [°]	A [%]	D [%]	M [%]	C [%]
0	81.61	13.14	5.25	21.85
10	86.32	11.27	2.41	21.12
20	92.03	6.95	1.02	18.65
30	93.65	5.67	0.68	15.48
40	98.48	1.01	0.51	11.05
50	97.53	1.34	1.13	13.62
60	92.61	2.96	4.43	19.84
70	85.42	9.48	5.10	21.22
80	76.33	16.37	7.30	24.87
90	73.12	18.28	8.60	25.32

At the seed releasing angle of 0°, *A* is 81.61%, which is low. When the seed releasing angle increases to 40°, *A* gradually increases to 98.48%. When the seed releasing angle is greater than 40°, *A* decreases gradually to 73.12% at 90°.

After the regression analysis of *A*, the regression equation of *A* about seed releasing angle is obtained.

$$y_q = -0.01x_t^2 + 0.79x_t + 80.60, \quad R^2 = 0.95 \quad (2)$$

Through the derivation of the regression equation, the seed releasing angle is 39.5° when *A* is at its maximum.

Different from *FD*, *D* is no longer 0%, and decreases first and then increases with the increase of the seed releasing angle. *D* is 18.28% (maximum) at 90° and 1.01% (minimum) at 40°.

The change rule of *M* is similar with that of *FD*. *M* decreases first and then increases with the increase of the seed releasing angle. *D* is 8.60% (maximum) at 90° and 0.51% (minimum) at 40°.

To further analyze the effect mechanism of the seed releasing angle on the metering performance, the states of motion of seeds when they are released from the disk at the seed releasing angles of 0, 39.5 and 90° were recorded with a high-speed camera (Fig.5).

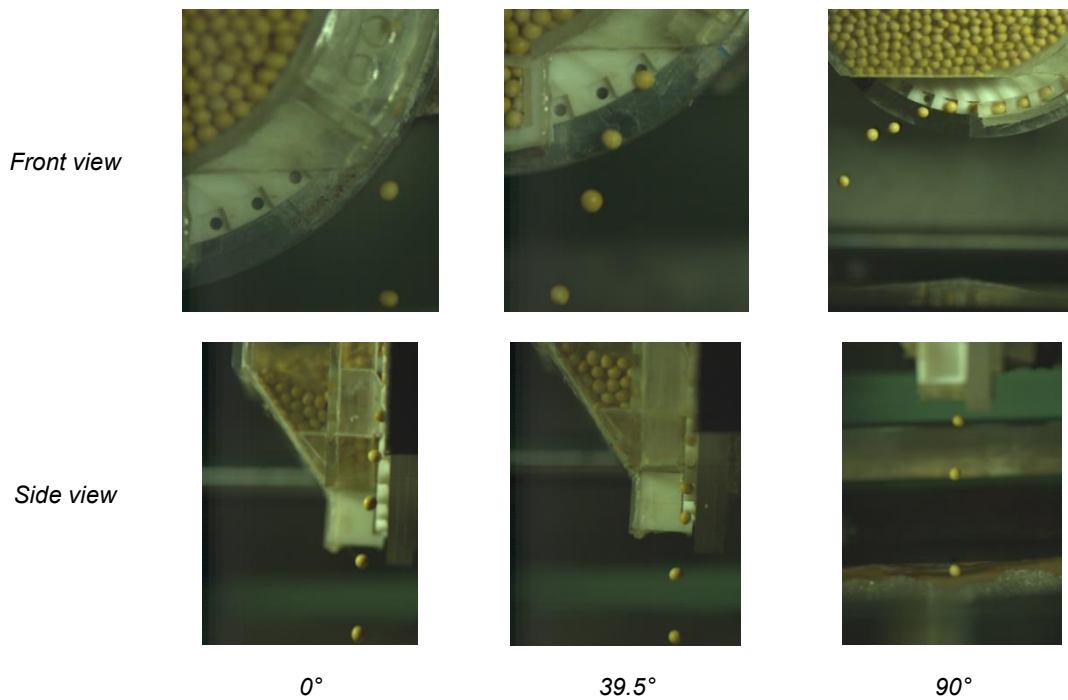


Fig. 5 - High speed photos of seed separation

At the seed releasing angle of 0° , when the speed is 6km/h, the initial speed of seed is vertically downward, and the gravity and speed are in the same direction after the negative pressure disappears. The acceleration of seed is large and the seed speed is greater than the linear speed of the disk. Therefore, the seeds collide with the front wall of the seed hole, and the seeds roll, resulting in the forward deviation of the falling track of seeds. As the front wall is inclined, the seeds have a large axial displacement, which reduces the metering performance and increases the precision index of seeds. With the increase of the speed, the linear speed at the edge of the disk increases, the collision between seeds and the front wall of the seed hole decreases gradually; the falling track of seeds shifts backward gradually, and the axial displacement decreases gradually. At the speed of 10 km/h, the linear speed of the disk is greater than the releasing speed. The seeds contact with the back wall of the seed hole, and then the back wall pushes seeds, resulting in backward deviation of the falling track of seeds. As the back wall is vertical, the axial deviation of seeds is small.

At the seed releasing angle of 39.5° , seeds can be released from the seed hole rapidly as the initial speed of the seeds is oblique to the lower left; the component of the acceleration of gravity in the speed direction is small; the horizontal component of velocity of the seeds is close to the linear velocity at the edge of the disk and the distance that the seeds move with the seed hole simultaneously before the seeds are released from the seed hole is short, after the negative pressure disappears, so that they will not contact with the front wall of the seed hole when being released from the seed hole, resulting in a small axial displacement of the seeds. When the speed varies from 6 to 10 km/h, the seeds don't contact with the front or back wall of the seed hole. Therefore, at the seed releasing angle of 39.5° , the metering performance is better and the precision index is lower.

At the seed releasing angle of 90° , the horizontal component of speed of seeds is theoretically consistent with the linear speed at the edge of the disk after the negative pressure disappears. Seeds will not contact with the back wall of the seed hole when they are released from the seed hole. However, actually, the horizontal component of velocity of the seeds is slightly less than the linear seed at the edge of the disk under the impact of friction with the wall of seed hole, air friction and other factors. Therefore, the seeds contact with the back wall of the seed hole. When being pushed by the back wall, with the seed hole moving upward, the seeds contact with the back wall at different points as they are not a standard sphere. As a result, the horizontal displacements of seeds are different when being pushed by the back wall, which reduces the metering performance and increases the precision index. At 6 km/h, the contact time between seeds and the back wall is short, and the difference of falling trajectory of seeds is small. With the increase of the speed, the thrust of the back wall on seeds increases, and the difference in the releasing trajectory of seeds increases. At the same time, as the back wall is vertical, the axial deviation of seeds in the falling process is small.

Effect of working parameters on the metering performance

At the seed releasing angle of 39.5° , forward speed and negative pressure were performed with the dual-factor test; the data processing and variance analysis were conducted; and a column chart was made (Fig.6).

The negative pressure has a significant impact on A , and A increases with the increase of the negative pressure. At the speed of 6 km/h, the negative pressure has no significant effect on A , which remains at about 95%. With the increase of speed, negative pressure has a more and more obvious effect on A . At the speed of 12 km/h, the negative pressure has the most significant effect on A . A is 60.88% at the negative pressure of 1 kPa. A increases significantly with the increase of the negative pressure. A is 81.62% at 5 kPa, with an increase ratio of 34.1%.

The forward speed has a significant effect on A . The lower the negative pressure is, the more significant the effect of forward speed on A is. Under the negative pressure of 1 kPa, A is 94.85% at 6 km/h and decreases with the increase of the speed. A decreases to 60.88% at 12 km/h, with the decrease ratio of 35.8%. When the negative pressure is large, the effect of forward speed on A becomes smaller. At the negative pressure of 5 kPa, A is 95.83% at 6 km/h and decreases to 81.62% at 12 km/h, with the decrease ratio of 14.8%.

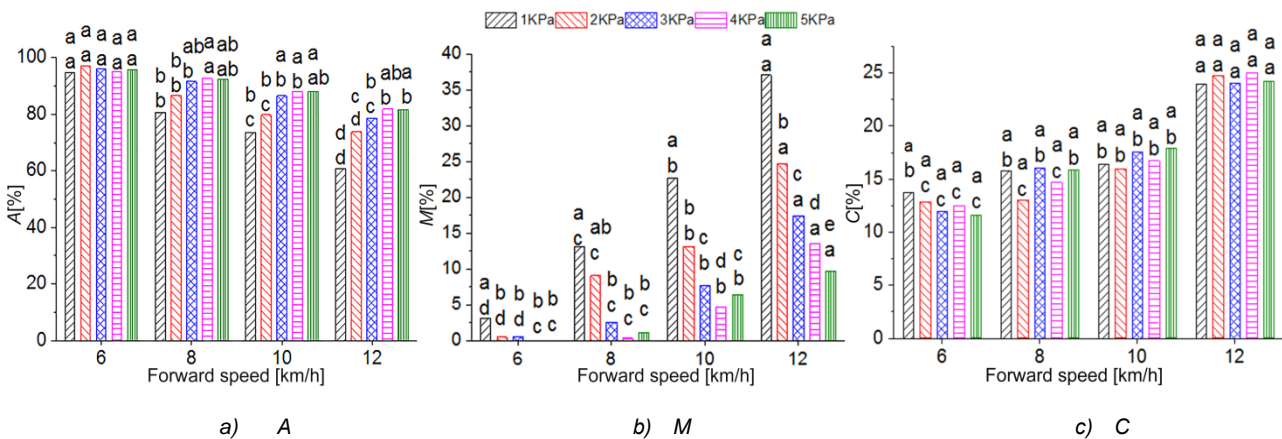


Fig. 6 - Effect of working parameters on the metering performance

The negative pressure has a significant effect on M , i.e., M decreases with the increase of the negative pressure. At the speed of 6 km/h, M is 3.16% at the negative pressure of 1 kPa.

When the negative pressure is greater than 2 kPa, M does not change significantly and tends to 0%. The effect of negative pressure on M becomes more and more significant with the increase of the speed.

When the speed increases to 12 km/h, M is 37.06% under the negative pressure of 1 kPa. M decreases significantly with the increase of negative pressure, and is 9.62% at 5 kPa, with the decrease ratio of 74.0%.

The forward speed has a significant effect on M , i.e., M increases with the increase of the forward speed. The miss index is the largest under the negative pressure of 1 kPa. M is 3.16% at 6 km/h and increases to 37.06% when the speed increases to 12 km/h, increasing by 10.7 times. With the increase of the negative pressure, the effect of the forward speed on M decreases. Under the negative pressure of 5 kPa, M is 0% at 6 km/h and increases to 9.62% at 12 km/h.

The negative pressure has no significant effect on the precision index. The precision index does not change significantly when the negative pressure changes in the range of 1-5 kPa. The forward speed has a significant effect on the precision index. Researchers at home and abroad have come to a similar conclusion that the precision index increases significantly with the increase of the speed.

Comparison of the filling performance and metering performance

The filling performance represents the seed picking capacity of the disk, and the metering performance represents the distribution rule of seeds in seeding ditch. FA and A under the same negative pressure and speed are compared (Fig.7).

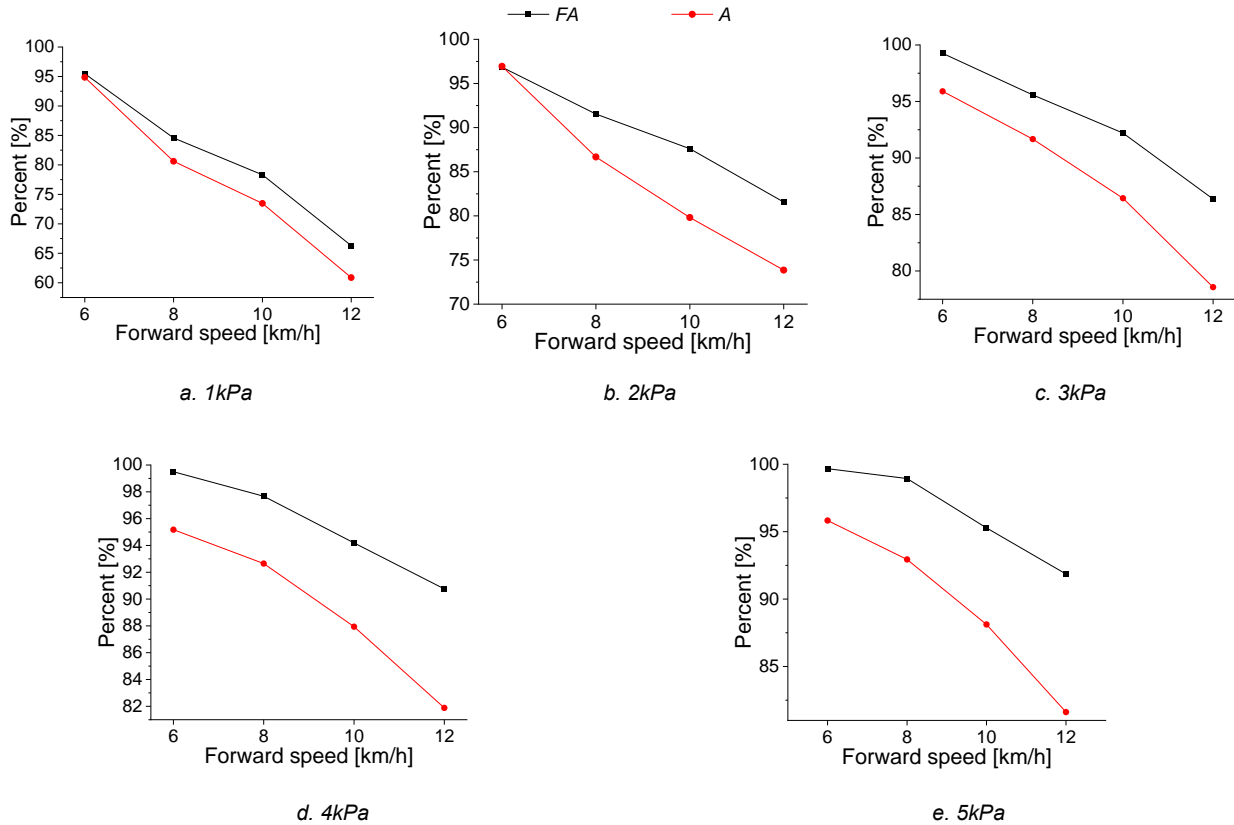


Fig. 7 - Comparison of the filling performance and metering performance

FA is obviously greater than A under the same negative pressure and speed. The difference between FA and A becomes more and more obvious with the increase of the forward speed.

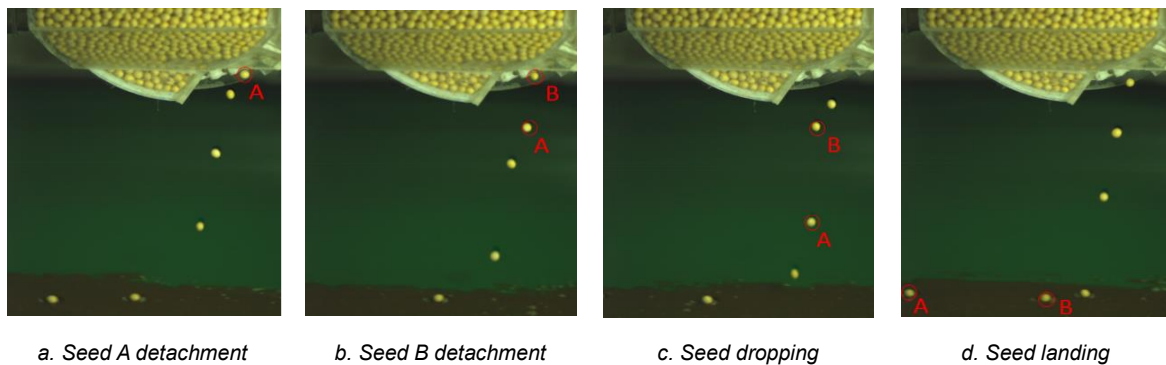


Fig. 8 - High speed picture of seed falling process

The state of motion of seeds in the process of falling and touching soil after they were released from the disk was observed with a high-speed camera (Fig.8).

When the seeds on the disk are released from the seed hole, the location and time of releasing of different seeds are different, and the releasing point, initial speed and angle of releasing cannot be kept completely consistent. In the process of falling, the position between seeds changes; the seed spacing in the seedbed decreases or expands, and the positions even change, resulting in the increase of multiple and miss seeds, and the decrease of A.

In order to improve the metering performance of the compound seed metering device, the seed releasing location shall be studied next to improve the consistency between the releasing position and time.

CONCLUSIONS

(1) The seed filling angle has significant effect on *FA* and *FM*, which are completely opposite in the change rule. With the increase of the seed filling angle, *FA* increases gradually, while *FM* decreases gradually. After the seed filling angle exceeds 50°, both of them tend to be stable gradually. In the change process of the seed filling angle, *FD* remains at 0% all along, indicating that a significant effect of single-seed picking can be achieved with the combined structure of seed hole and suction hole.

(2) The negative pressure and operating speed are interactive and have a significant effect on *FA* and *FM*. *FA* increases with the increase of the negative pressure and drops significantly with the increase of the forward speed. *FA* and *FM* are completely opposite in the change rule, while *D* remains at 0% all along.

(3) The seed releasing angle has a significant effect on the metering performance. *A* increases first and then decreases with the increase of the seed releasing angle, and reaches 98.48% (maximum) at 40°. The change rule of *D* and *M* is completely opposite to that of *A*. Through the regressive calculation, the seed releasing angle is 39.5° when *A* is at its maximum. Under different seed releasing angles, the positions of seeds colliding with the seed hole when they are released are different, which changes the state of motion of seeds when releasing and has effect on the metering performance.

(4) The negative pressure and forward speed are interactive and have a significant effect on the metering performance. With the increase of the negative pressure, *A* increases and *M* decreases; with the increase of the forward speed, *A* decreases and *M* increases. The negative pressure has no significant effect on the precision index, while the forward speed has a significant effect on the precision index. With the increase of the speed, the precision index increases significantly.

(5) Due to the differences in the time and position of seeds when they are being released from the seed hole, *A* is lower than *FA* under the same conditions. The releasing process shall be further studied next to improve the consistency between the releasing position and time.

ACKNOWLEDGEMENT

This work was supported by the National Natural Science Foundation of China (Grant No. 51905318), Shandong Provincial Colleges and Universities Youth Innovation Talent Induction Program (Smart Agriculture Research and Innovation Team), Top Talents Program for One Case One Discussion of Shandong Province ([2018]27), and Zibo School City Integration Project Academy of Ecological Unmanned Farm (Grant No. 2019ZBXC200).

REFERENCES

- [1] Abdolazare, Z., & Mehdizadeh, S. (2018), Nonlinear mathematical modeling of seed spacing uniformity of a pneumatic planter using genetic programming and image processing, *Neural Computing and Applications*, vol.29, issue 2, pp. 363-375; <https://doi.org/10.1007/s00521-016-2450-1>
- [2] Chen, Y. L., Zhang, M., Liu, Z. Q., Lan Y. B., Yi, L. L., Peng, Q. J., & Yin, X. (2021), Design and experiment of seed agitator for vertical disk seed metering device, *INMATEH - Agricultural Engineering*, vol. 63, issue 1, pp.179-188.
- [3] Cujbescu, D., Matache, M., & Voicu, G. (2019), Mathematical model for sowing precision estimation of vacuum seed metering device, *UPB Scientific Bulletin, Series D: Mechanical Engineering*, vol.81, issue 3, pp. 225-234.
- [4] Ding, L., Yang, L., Liu, S., Yan, B., He, X., & Zhang, D. X. (2018), Design of air suction high speed precision maize seed metering device with assistant seed filling plate, *Transactions of the Chinese Society of Agricultural Engineering*, vol.34, issue 22, pp. 1-11; <https://doi.org/10.11975/j.issn.1002-6819.2018.22.001>
- [5] Dylan, S. J., Hesterman, D. C., & Guzzomi, A. L. (2013) Precision metering of Santalum spicatum (Australian Sandalwood) seeds, *Biosystems Engineering*, vol.115, issue 2, pp. 171-183; <https://doi.org/10.1016/j.biosystemseng.2013.03.004>
- [6] Jia, H. L., Chen, Y. L., Zhao, J. L., Wang, J. X., Guo, M. Z., & Zhuang, J. (2018), Design and experiment of pneumatic-mechanical combined precision metering device for soybean, *Transactions of the Chinese Society for Agricultural Machinery*, vol.49, issue 4, pp. 75-86+139; <https://doi.org/10.6041/j.issn.1000-1298.2018.04.009>

- [7] Karayel, D., Wiesehoff, M., Ozmerzi, A., & Muller, J. (2006), Laboratory measurement of seed drill seed spacing and velocity of fall of seeds using high-speed camera system, *Computers and Electronics in Agriculture*, vol.50, issue.2, pp. 89-96; <https://doi.org/10.1016/j.compag.2005.05.005>
- [8] Liao, Y. T., Liao, Q. X., Wang, L., Zheng, J., & Gao, L. P. (2018), Investigation on vacuum singulating effect influencing factors of pneumatic precision seed metering device for small particle size of seeds, *Transactions of the Chinese Society of Agricultural Engineering*, vol.34, issue 24, pp. 10-17; <https://doi.org/10.11975/j.issn.1002-6819.2018.24.002>
- [9] Singh, R., Singh, G., & Saraswat, D. (2007), Design and operational parameters of a pneumatic seed metering device for planting of groundnut (*Arachis hypogaea*) seeds, *Indian Journal of Agricultural Sciences*, vol.77, issue 1, pp.40-42.
- [10] Wang, J. W., Tang, H., Wang, J. F., Li, X., & Huang, H. N. (2017), Optimization design and experiment on ripple surface type pickup finger of precision maize seed metering device, *International Journal of Agricultural and Biological Engineering*, vol.10, issue 1, pp. 61-71; <https://doi.org/10.3965/j.ijabe.20171001.2050>
- [11] Yang, L., Yan, B. X., Yu, Y. M., He, X. T., Liu, Q. W., Liang, Z. J., Yin, X. W., Cui, T., & Zhang, D. X. (2016), Global overview of research progress and development of precision maize planters, *International Journal of Agricultural and Biological Engineering*, vol.9, issue 1, pp. 9-26.
- [12] Yu, J. J., Liao, Y. T., Cong, J. L., Yang, S., & Liao, Q. X. (2014), Simulation analysis and match experiment on negative and positive pressures of pneumatic precision metering device for rapeseed, *International Journal of Agricultural and Biological Engineering*, vol.7, issue 3, pp. 1-12.
- [13] Yu, H. L., Zhao, X. S., Liu, Z. L., Du, X., & Tian, C. (2015), Study on negative-pressure precision millet seed-metering device, *Advance Journal of Food Science and Technology*, vol.7, issue 2, pp.139-143; <https://doi.org/10.19026/ajfst.7.1282>
- [14] Zhang, G. Z., Zang, Y., Luo, X. W., Wang, Z. M., & Li, Z. D. (2014), Line-churning tooth design and metering accuracy experiment of rice pneumatic precision hill-drop seed metering device on pregnant Japonica rice seed, *Transactions of the Chinese Society of Agricultural Engineering*, vol.30, issue 17, pp. 1–9; <https://doi.org/10.3969/j.issn.1002-6819.2014.17.001>
- [15] Zhang, G. Z., Zang, Y., Luo, X. W., Wang, Z. M., Zhang, Q., & Zhang, S. S. (2015), Design and indoor simulated experiment of pneumatic rice seed metering device, *International Journal of Agricultural and Biological Engineering*, vol.8, issue 4, pp. 10-18; <https://doi.org/10.3965/j.ijabe.20150804.1626>
- [16] Zhang, K. X., Sun, Y. Y., Liu, L., Liu, X. X., & Zhao, X. Y. (2020), Design and test of variable diameter pneumatic drum type bean seed metering device, *INMATEH - Agricultural Engineering*, vol.60, issue 1, pp.9-18; <https://doi.org/10.35633/INMATEH-60-01>
- [17] Zhao, Z., Li, Y., Chen, J., & Xu, L. (2010), Numerical analysis and laboratory testing of seed spacing uniformity performance for vacuum-cylinder precision seeder, *Biosystems Engineering*, vol.106, issue 4, pp. 344-351; <https://doi.org/10.1016/j.biosystemseng.2010.02.012>

THREE DIMENSIONAL SIMULATION OF OIL FLOW CHARACTERISTICS IN LUBRICATION SYSTEM OF ROTARY TILLAGE ENGINE

旋耕发动机润滑系统中的油流特性三维仿真研究

Junxiang Gao, Xiaoliang Gao^{*}, Wei Zou^{*}

¹⁾ Department of Automotive Engineering, Hunan Financial and Industrial Vocational-Technical College,
Heng'yang, Hunan, 421002 / China
These authors contributed equally.

Corresponding authors: Dr. Xiaoliang Gao (xqkiw75168@163.com), Dr. Wei Zou (hkpb57413@163.com)
DOI: <https://doi.org/10.356.33/inmateh-65-17>

Keywords: rotary tillage engine, lubrication system, performance optimization

ABSTRACT

Taking the lubrication system of rotary tillage engine as the research object, this paper makes a three-dimensional simulation study on the oil flow characteristics in the lubricating oil passage. The oil supply of the oil pump shall be greater than the circulating oil required by the lubrication system to ensure the lubrication of the rotary cultivator. Lubrication system is an important part to ensure the reliability and durability of rotary cultivator. The key component to achieve its performance is the oil pump. The geometric model of lubricating oil flow field in rotary tiller lubrication system is established by using FLUENT software. The results show that the pressure drop in the lubricating oil passage of the main bearing is the largest under the same working conditions. In the oil passage of the cylinder head, the pressure drop of the front main oil passage is the largest and the oil discharge is the largest. Add 1.6 mm oil pump rotor on the basis of the thickness of the original oil pump rotor, the oil flow at the connecting rod nozzle reaches the flow index of the original rotary cultivator, and there is no cylinder pulling phenomenon of the rotary cultivator.

摘要

本文以旋耕发动机润滑系统为研究对象，对润滑油道中的油流特性进行了三维仿真研究。油泵的供油量应大于润滑系统所需的循环油量，以保证旋耕机的润滑。润滑系统是保证旋耕机可靠性和耐久性的重要组成部分。实现其性能的关键部件是油泵。利用 FLUENT 软件建立了旋耕机润滑系统润滑油流场的几何模型。结果表明，在相同工况下，主轴承润滑油道中的压降最大。在缸盖的油道中，前主油道的压降最大，排油量也最大。在原机油泵转子厚度的基础上增加 1.6mm 油泵转子，连杆喷嘴处的油流量达到原旋耕机的流量指标，旋耕机不存在拉缸现象。

INTRODUCTION

At present, agricultural land resources are extremely rich, and there are many rural farmers. Promoting the stable development of agriculture is closely related to the improvement of the living standards of rural population. At the same time, the improvement of the quality of life of the rural population will also promote the prosperity of various industries (Savitska S., et al., 2020). The key task of the whole process of agricultural mechanization development is to focus on improving the comprehensive quality and benefit of agricultural mechanization of potato, corn, rice, soybean and other food crops. The core direction of the development of agricultural machinery industry is the intelligence and mechanization of agricultural machinery, which is also the main direction of realizing agricultural modernization (Bukhtiyarova T.I. et al., 2021; Handler A.M. et al., 2020). Rotary tiller, as an important tillage machine, it is one of the important equipment to improve the tillage quality when it is used in field operation. Although some achievements have been made in the research and development of average depth control of agricultural machinery in the world, there is still a big gap compared with developed countries, and it is still in a relatively backward stage.

In the development project of rotary tillage engine, in order to better achieve the strategic goal of sustainable development, reducing oil consumption should be the first problem to be solved in the development and research of rotary tillage engine (Siddique M. et al., 2021). Under any working conditions, the oil supply of the oil pump should be larger than the circulating oil required by the lubrication system to ensure the lubrication of the rotary tillage engine.

If the oil supply of the oil pump is insufficient, the main bearing and connecting rod bearing of the rotary tiller will be worn, and the cylinder of the rotary tiller will even be damaged. At the same time, lubricating oil will deteriorate and fail quickly, which will seriously affect the normal operation of equipment and agricultural production efficiency. Therefore, the rational and effective design of lubrication system is of great significance to improve the power, economy and reliability of crusher (*Mukhametshin I. et al., 2020; Shevchenko A.N. et al., 2018*).

Due to the complex structure and limited working environment of rotary tillage engine, we can't directly measure the lubrication parameters (such as crankshaft oil passage pressure, oil leakage, etc.) of some parts of the lubrication system through experiments. Using FLUENT simulation method to calculate and analyze the lubrication flow field of the lubrication system can not only get more accurate calculation results, but also save a lot of time and money and shorten its cycle (*Anand R. et al., 2021*). Based on this, this paper will optimize the performance of engine lubrication system for rotary tillage based on FLUENT software, ensure the lubrication of piston and other parts, and ensure the oil supply of oil pump is sufficient, thus effectively avoiding the occurrence of cylinder pulling phenomenon, greatly shortening the development cycle of oil pump products, reducing product cost and improving product quality.

Through the three-dimensional fluid simulation analysis of Aprilia diesel engine oil pump, the three-dimensional fluid simulation software pmplix is used to simulate, and the cavitation phenomenon of relevant fluid in the calculation is considered (*Chiavola O. et al., 2021*). They compare the experimental data obtained from the hydraulic test-bed with the simulation analysis results, and find that there is a good correlation between them. It can be proved that the oil pump can be simulated by 3D fluid simulation software when selecting or optimizing the oil pump. Flowmaster software can call models with different complexity in different internal combustion engine lubrication systems, and build and show the interaction of diesel engine fluid systems through these models, and then use one-dimensional fluid simulation software to complete different design tasks (*Samiezadeh S. et al., 2021*). When studying the oil pump and lubricating oil circuit, the researchers used the three-dimensional model of external gear pump and flow pulsation for experimental evaluation. (*Corvaglia A. et al., 2021*). Through the three-dimensional simulation model of oil pump, the internal structure of oil pump is optimized, the phenomenon of trapped oil and cavitation is improved, and the pressure loss at the corner and joint of complex casting oil channel is accurately predicted, which provides an important basis for the setting of oil pump (*Li D. et al., 2021*).

With the improvement of computer level, the numerical simulation method was used to study the flow characteristics of square section elbow, which provides a new method for the study of fluid in the pipe. In reference (*He M. et al., 2020*), the flow characteristics of gas-liquid two-phase flow in a 180° bend were studied by numerical simulation. The numerical results are in good agreement with the experimental results, which proves the correctness of the numerical method. The lubrication of crankshaft bearing in internal combustion engine lubrication system is deeply analyzed and studied, and put forward a complete set of software implementation scheme from mathematical modeling, analysis and calculation to simulation results, but unfortunately, only the crankshaft bearing was analyzed (*Zhang Y. et al., 2020*). With the development of a set of simulation analysis software for internal combustion engine lubrication system, *Simisinov et al.* put forward a brand-new graphical modeling method for internal combustion engine lubrication system by using modular programming idea (*Simisinov D. et al., 2020*). *Singh et al.* used FLUENT software in CFD tool to solve and analyze the pressure of sliding bearing, and calculated and analyzed the influence of bearing distribution and the size of upper and lower bearing slots on sliding bearing (*Singh R. et al., 2020*).

MATERIALS AND METHODS

Brief introduction of FLUENT solution process

Computational Fluid Dynamics (CFD) is a systematic analysis method and tool for simulating fluid flow, heat transfer and related transfer phenomena by computer. Because of complicated partial differential equations, most problems in fluid mechanics and heat and mass transfer cannot be solved accurately, and can only be dealt with by experience or experiment, which makes the application of fluid mechanics in engineering technology very limited. Among commercial CFD software packages, Fluent is the most popular, and its utilization rate is very high in countries with high design level such as America and Europe. FLUENT has developed a variety of flow simulation software, which can simulate various complex physical phenomena and meet the needs of various users. It is precisely because of its powerful function that greatly facilitates users and is welcomed by users.

The process of CFD simulation solution is complex. The solution process of different problems is roughly the same and can be divided into several steps. The solution process can be represented by flow chart as shown in Figure 1.

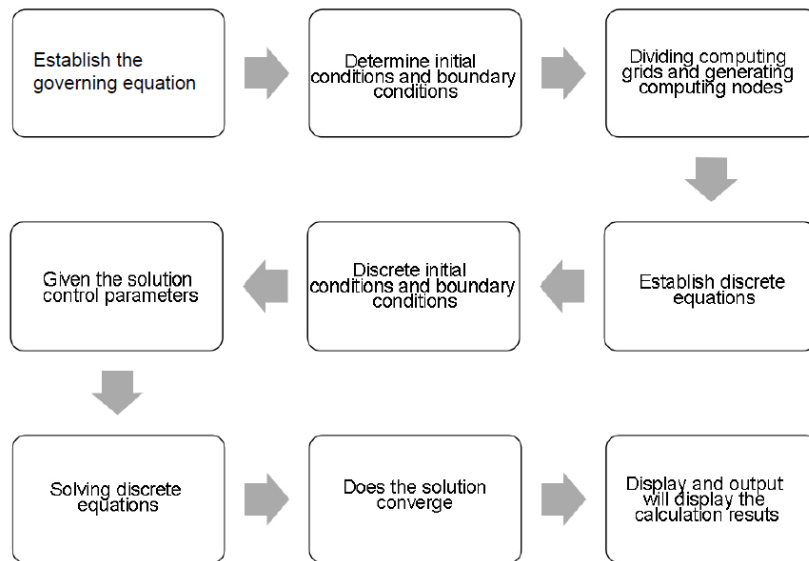


Fig. 1 - Flow chart of FLUENT analysis

Establishment of mathematical model of oil pump

Circulating oil quantity of oil pump is an important parameter of oil pump performance, and its size depends on the lubrication system of rotary tillage engine and the structural arrangement of rotary tillage engine. In the modern internal combustion engine, the circulating oil quantity of the oil pump is generally calculated by the heat transferred from the rotary tillage engine to the engine oil namely:

$$V_c = \frac{Q_o}{\gamma \cdot c \cdot \Delta t} \quad (1)$$

in which: V_c is the circulating oil quantity of oil pump, $L \cdot h^{-1}$; γ is the density of engine oil, $kg \cdot L^{-1}$; c is the specific heat capacity of engine oil, $k \cdot J \cdot (kg \cdot ^\circ C)^{-1}$; Δt is the temperature between the inlet and outlet of engine oil, $^\circ C$; Q_o is the heat absorption of engine oil, $kJ \cdot h^{-1}$. When there is no piston cooling nozzle, Q_o is 1.5% ~ 2.0% of the total fuel heat; piston cooling nozzle, Q_o is about 6.0% of the total fuel heat, where the total fuel heat is:

$$Q_f = \frac{3600 N_e}{\eta_e} \quad (2)$$

in which: N_e is the calibration power of internal combustion engine, kW; η_e is the effective efficiency of internal combustion engine.

Actually, the calculation of oil supply of the oil pump is determined according to the layout structure of the rotary tillage engine and the parts to be lubricated, that is, the oil supply of the oil pump is the sum of the lubrication flow required by each part.

Pipeline model

The flow of engine oil in pipeline belongs to viscous flow, and there are two different flow patterns in viscous flow: laminar flow and turbulent flow. These two flows have different natures and manifestations, and their velocity distribution, shear stress size and distribution, energy loss and diffusion properties are different under various specific boundary conditions. Therefore, first of all, it is necessary to determine the flow state of oil in the pipeline.

The along-way loss of engine oil is expressed by h_{λ} , which is caused by the along-way resistance, that is, the frictional resistance along the flow path. The characteristic of loss along the route is that the loss is evenly distributed along the process, and its size is proportional to the length of the process. Along-way loss analysis is to calculate the pressure loss of engine oil after passing through the pipeline according to the extracted structural parameters of the pipeline and the flow rate of engine oil in the pipeline.

When the fluid flows through various local obstacles, the movement pattern in the obstacle zone changes sharply, such as vortex, liquid flow deformation, velocity redistribution, impact and secondary flow, etc., and then the force hindering the fluid movement is generated, which is called local resistance.

The resulting energy loss is called local loss. Usually, the spoon is used to express the local head loss per unit weight of fluid, and its calculation formula is:

$$h_f = \xi \frac{v^2}{2g} \quad (3)$$

in which:

ξ -- local resistance coefficient;

h_f -- local resistance loss.

It can be seen from this formula that the key to calculate the local loss lies in how to determine the local resistance coefficient ξ . Generally speaking, ξ depends on the geometry of local obstacles and the Reynolds number R_e of flow. The relationship between the former and the latter is different in different areas divided by flow pattern, and its relationship is as follows:

(1) Laminar flow area, at this time, $\xi = A/R_e$; The A value needs to be determined by experiments, and it depends on the specific types of local obstacles.

(2) Smooth area, at this time, $\xi = B/R_e^{0.53}$; the value of B is determined by experiment.

(3) The resistance square area, in which the local loss coefficient has no relationship with R_e , but is only determined by the geometric shape of the local obstacle.

In this paper, according to the actual measurement of structural dimensions of related parts of rotary tillage engine, the oil circuit is simplified into a through pipe of corresponding size for convenience of drawing. The simplified oil circuit model of the engine lubrication system for rotary tillage is established by FLUENT (Figure 2). For the oil radiator and oil filter, because the internal structure is too complex, they are built into solid entities, and porous media are used instead in the calculation process. Because of the special structure and complicated flow, the bearings, intake and exhaust valves and lubricating oil passages of single pump are equivalent to oil drain holes.

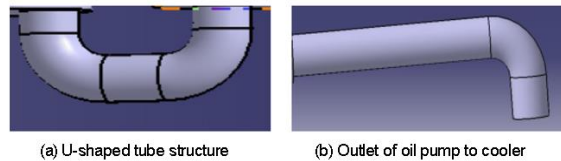


Fig. 2 - Special pipeline model

Calculation model of flow resistance of valve

There are two pressure limiting valves in the lubrication system of rotary tillage engine studied in this paper. The primary pressure limiting valve is installed at the outlet of the oil pump, and the secondary pressure limiting valve is installed at the outlet of the filter, which is connected in parallel with the whole lubricating oil circuit to limit the maximum oil pressure of the lubricating system. In the hydraulic valve, the influence of gravity is negligible. Because of $H_1 = H_2$, the influence of gravity potential energy is not considered. At the same time, the flow of fluid at the valve port is turbulent, and the kinetic energy coefficient is $a_1 = a_2 = 1$.

Therefore, Bernoulli equation of flow sections 1 and 2 is:

$$\frac{P_1}{\gamma} + \frac{v_1^2}{2g} = \frac{P_2}{\gamma} + \frac{v_2^2}{2g} + h_s \quad (4)$$

in which:

P_1, P_2 -- pressure of sections 1 and 2, MPa;

v_1, v_2 -- the velocity of sections 1 and 2, m/s.

The energy loss h_s can be expressed by the product of the resistance coefficient ξ of the valve port and the speed, i.e.:

$$h_s = \xi \frac{v_2^2}{2g} \quad (5)$$

$$\frac{P_1}{\gamma} + \frac{v_1^2}{2g} = \frac{P_2}{\gamma} + \frac{v_2^2}{2g} + \xi \frac{v_2^2}{2g} \quad (6)$$

According to the principle of fluid continuity

$$Q = A_1 v_1 = A_2 v_2 \quad (7)$$

where: A_1 is the area at the overcurrent section 1, m²;

A_2 is the area at the overcurrent section 2, m^2 .

Available:

$$\frac{v_1^2}{2g}(1+\xi) - \frac{v_1^2}{2g}\left(\frac{A_2}{A_1}\right)^2 = \frac{P_1}{\gamma} - \frac{P_2}{\gamma} \tag{8}$$

Solving equations:

$$v_2 = C_v \sqrt{\frac{2(P_1 - P_2)}{\rho}} \tag{9}$$

in which, $C_v = \frac{1}{\sqrt{1+\xi - (A_2/A_1)^2}}$. C_v is the velocity coefficient, and it is determined by experiments that $C_v=0.96-0.98$. It can be approximated as 1 in calculation. Add a shrinkage coefficient $C_0=A_2-A_1$, where A is the flow area at the valve port, then:

$$Q = A_2 v_2 = C_0 A_2 v_2 = C_v C_0 A \sqrt{\frac{2(P_1 - P_2)}{\rho}} = CA \sqrt{\frac{2(P_1 - P_2)}{\rho}} \tag{10}$$

In this formula, $C=C_v C_0$ is called flow coefficient. The flow coefficient is different for different orifice shapes. In hydraulic valves, slide valve type sliding port and cone valve port often appear. The flow coefficient $C \approx 0.65$ of the slide valve port is determined by experiments. Flow coefficient $C \approx 0.77-0.80$ of conical valve port. The cross-sectional areas in front of and behind the valve port are equal, so the relationship between pressure drop and flow rate of the valve is:

$$\Delta P = P_1 - P_2 = \left(\frac{Q}{CA}\right)^2 \frac{\rho}{2} \tag{11}$$

RESULTS

Analysis of lubrication system in cold start

At cold start, the rotational speed of the rotary tillage engine is 609r/min, and the measured pressure of the engine oil at the outlet of the filter is 0.15MPa. Fig. 3 shows the overall pressure nephogram of internal oil from the main oil passage to each outlet, and fig. 4 shows the oil pressure values of the main parts between the main oil passage and each oil injection point.

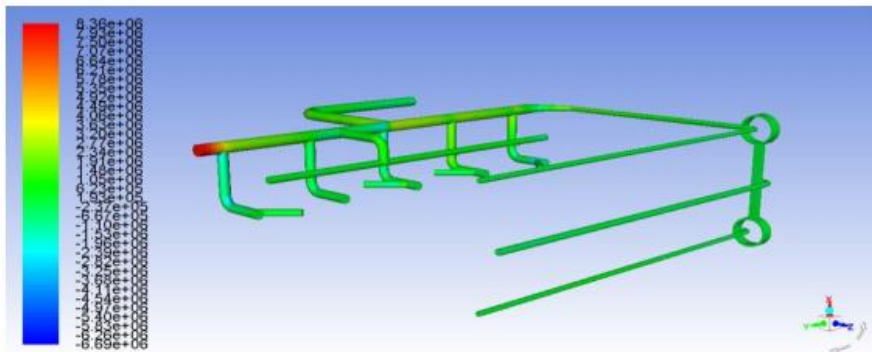


Fig. 3 - Pressure diagram at cold start

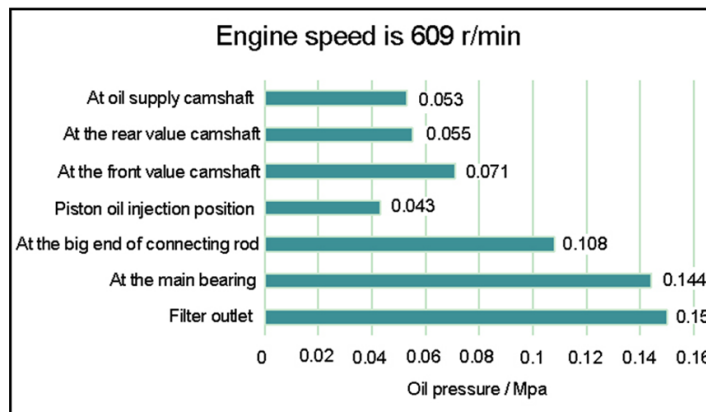


Fig. 4 - Pressure value of main parts

It can be seen from the data in the figure that the oil reaches the main bearing through a vertical elbow in the accessory bracket, and the oil pressure is 0.144 MPa. Part of the engine oil passes through the wetting place at the big end of the connecting rod connected with the main bearing, and the engine oil pressure is 0.108 MPa. At the nozzle of piston cooler, the pressure is 0.043 MPa. The engine oil passes through the nearby bracket and reaches the oil passage of the front valve camshaft, and the pressure is 0.071 MPa. In the oil passage of the rear valve camshaft, the pressure is 0.055 MPa. The pressure at the oil supply camshaft is 0.053 MPa.

According to the design experience, the circulating oil quantity of the rotary tillage engine with engine oil cooling piston, that is, the lubricating oil flow of the main oil passage, should meet $V_c = (0.42 - 0.57)N_e$, where N_e represents the power of the rotary tillage engine. Therefore, the circulating oil quantity of rotary tillage engine should be between 28-38L/min, while the oil supply quantity of oil pump is 54.3128L/min and the lubricating oil flow of main oil channel is 39.61L/min, which proves that the oil supply quantity of oil pump and the flow of main oil channel meet the design requirements. Fig. 5 shows the optimization process of engine lubrication system for rotary tillage.

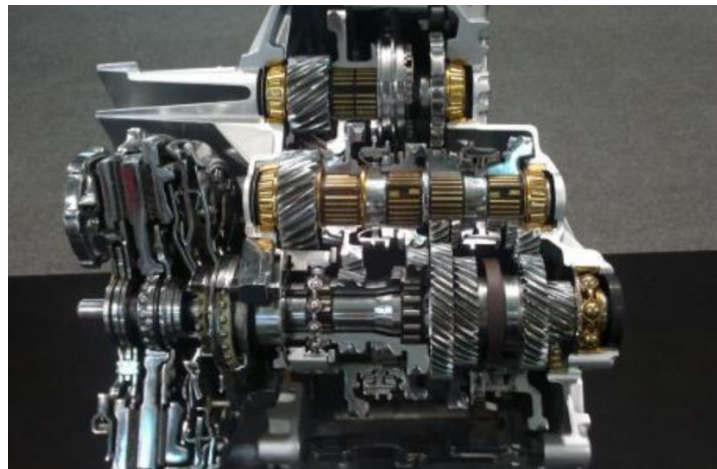


Fig. 5 - The optimization process of the engine lubrication system for rotary tillage

Fig. 6 is a graph showing the variation of lubricating oil distribution with rotating speed in several key parts, which lists the distribution of oil supply of oil pump, main oil passage flow, total flow of five main bearings, total flow of four connecting rod big end bearings and total flow of four cooling nozzles.

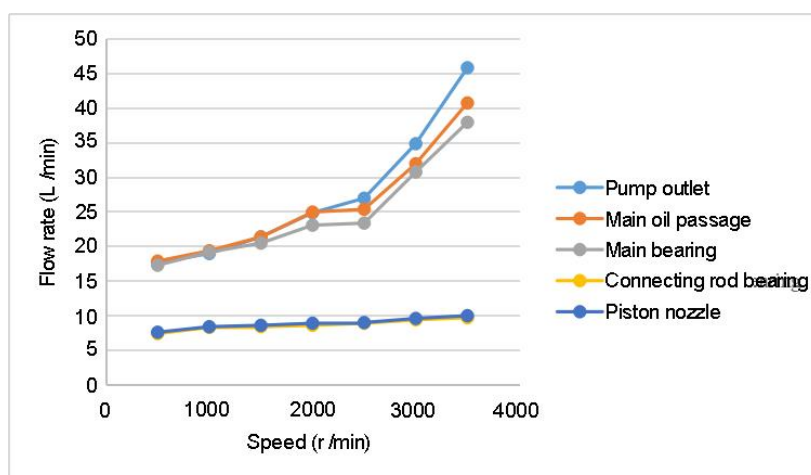


Fig. 6 - Variation diagram of lubricating oil distribution with rotating speed

Its distribution law has the following points:

- (1) Generally speaking, the oil distribution of each part increases with the increase of rotating speed;
- (2) In the medium and small speed range, the oil supply of oil pump increases linearly with the increase of speed, and its outlet flow all flows through the main oil passage without valve leakage.

In the middle and high speed region, the oil supply of the oil pump continues to increase linearly with the increase of the speed, but the oil supply of the main oil passage increases very little, because the pressure in the lubrication system has increased to the pressure of opening the safety valve at this time, and a large part of lubricating oil leaks back to the inlet of the oil pump through the safety valve when the safety valve is opened.

(3) Most of the lubricating oil after passing through the main oil passage is distributed to the main bearing, the rest is the connecting rod bearing and the piston nozzle again.

Optimization of lubrication system

Due to the complex structure, high manufacturing cost and high price of the raw oil pump, it cannot meet the economic requirements of the main oil passage, so a new pump is needed to replace the old one. The outlet pressure of the new oil pump is required to be greater than 2bar at the lowest speed. The minimum speed of oil pump is 425 r/min, and the maximum speed of oil pump is 1277 r/min. After improvement, it is required that the pressure in the main oil duct should be increased, and when the rotational speed of the rotary tillage engine reaches 1500 r/min, the pressure should be close to 0.7MPa. In this way, sufficient lubrication effect can be ensured, which not only reduces the friction between parts and the work lost due to friction, but also can better take away heat and adjust the temperature.

In normal operation, the engine oil inlet temperature for rotary tillage is 87.9-94.5°C, at which time the oil viscosity is 90-100SSU, 45-49SSU at 125.7 °C and 3600-8600SSU at 10 °C. There are two kinds of oil pumps that can be selected according to requirements: APV-5295-3 and APV-5183-3. These two kinds of oil pumps are respectively brought into the lubrication system model for simulation. For convenience of comparison, APV-5295-3 oil pump will be referred to as oil pump 1 and APV-5183-3 oil pump will be referred to as oil pump 2 hereinafter. Input the data of two new oil pumps into the model and run the module. The ratio of loss coefficient to Reynolds number of the introduced new oil pump is shown in Figure 7.

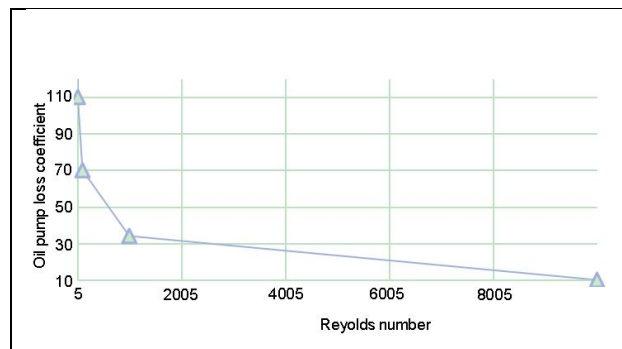


Fig. 7 - Ratio of oil pump loss coefficient to Reynolds number

The change of oil pump outlet pressure with rotary tillage engine speed is shown in Figure 8.

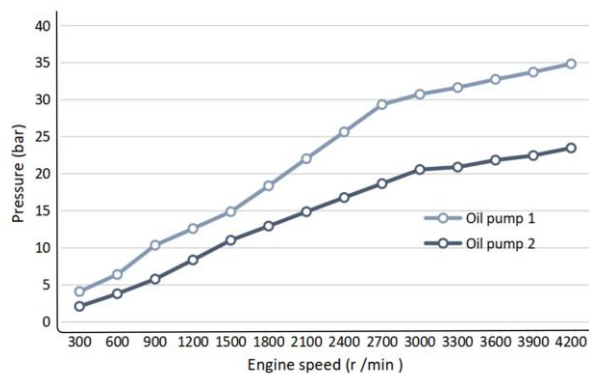


Fig. 8 - The change of oil pump outlet pressure with rotary tillage engine rotational speed

The change of oil pump flow rate with rotary tillage engine speed is shown in Figure 9.

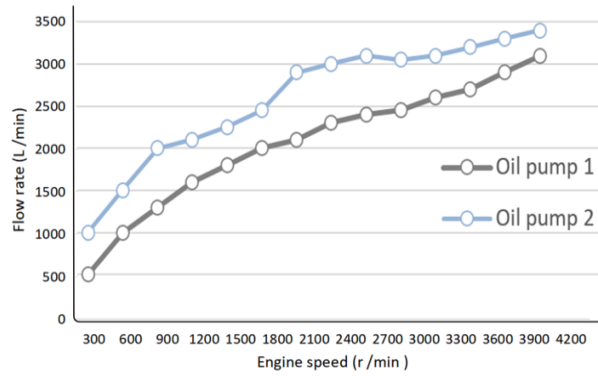


Fig. 9 - The change of oil pump flow rate with rotary tillage engine rotational speed

It can be seen from Figure 8 and Figure 9 that the changes of pressure and flow rate of both oil pumps increase with the increase of rotating speed. The increasing trend is approximately linear. This shows that the oil pump has good responsiveness, and can satisfy the lubrication of rotary tillage engine at various speeds, with corresponding changes. The No.1 oil pump is higher in pressure and flow than the No.2 oil pump, which is more effective and increases the amount of lubricating oil entering the main oil passage of the lubrication system. The analysis results are shown in Figure 10 and Figure 11.

Figure 10 is a comparison chart between the oil pressure test data of the main oil passage of the new rotary tillage engine using the new oil pump 2 and the simulation data. The error between the two is within 4%, and the maximum deviation is 0.02 MPa, which confirms that the simulation calculation model of the new rotary tillage engine is accurate.

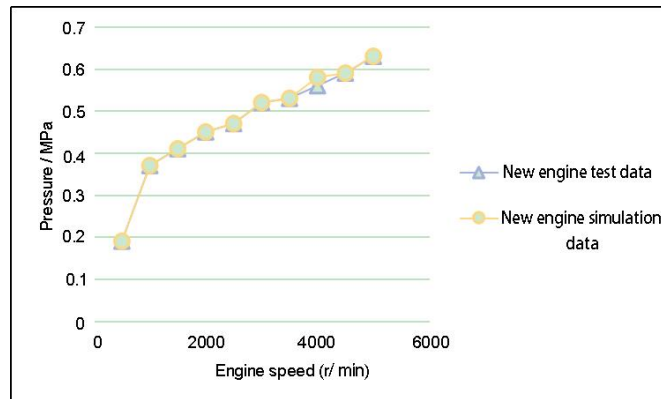


Fig. 10 - Comparison of pressure test and simulation data of main oil passage of rotary tillage engine

Figure 11 is a comparison between the flow rate of connecting rod nozzle produced by new rotary tillage engine at different speeds and the flow rate produced by original rotary tillage engine with original oil pump.

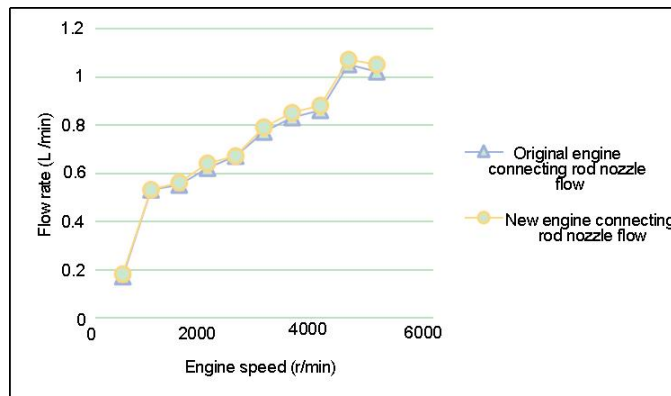


Fig. 11 - Comparison of connecting rod nozzle flow between original rotary tillage engine and new rotary tillage engine

It can be seen from Figure 11 that the flow rate of the connecting rod nozzle of the new rotary tillage engine is slightly lower than the original reference index at medium and low speed, which is mainly reflected in the three operating points of 1700 r/min, 2300 r/min and 3100 r/min. Therefore, according to these three speed operating points, the nozzle flow of the new oil pump connecting rods is simulated and calculated, and the results are shown in Table 1.

Table 1

Comparison of simulation results of nozzle flow of two new oil pump connecting rods			
Rotation speed (min)	Connecting rod nozzle flow rate (L·min) (Original pump)	Connecting rod nozzle flow rate (L·min) (New pump 1)	Connecting rod nozzle flow rate (L·min) (New pump 2)
1700	0.624	0.617	0.571
2300	0.775	0.779	0.736
3100	0.862	0.893	0.852

It can be seen from table 1 that the flow requirement of connecting rod nozzle is higher when the rotational speed of rotary tillage engine is 1700 r/min, because 1700 r/min is the low-speed torque point, and VVT (Variable Valve Timing) requires higher oil pressure at the low-speed torque point. Under this rotational speed of rotary tillage engine, the oil pump pumps less oil and the leakage at VVT is large, resulting in lower flow at connecting rod nozzle. For the new oil pump 2, when the rotational speed of the rotary tillage engine is 1700 r/min, the flow rate of the original oil pump connecting rod nozzle cannot be reached, but the new oil pump 1 meets the requirements.

CONCLUSIONS

In this paper, the lubrication system of rotary tillage engine is studied, and the lubrication system model of the engine is simulated by FLUENT software. According to the calculation results, the working condition of the engine lubrication system for rotary tillage was analyzed, and the optimization scheme was put forward. The research results show that: according to the data of the new oil pump, the curves of pressure and flow changing with rotating speed are made. The result is approximately linear, which indicates that the new oil pump has better response. The flow rate of engine oil at the connecting rod nozzle reaches the flow index of the original rotary tillage engine, which meets the requirements of the rotary tillage engine lubrication system and solves the cylinder pulling problem. The analysis and test results achieved by this optimization method are consistent, which provides a theoretical basis for the performance optimization and engineering application of the rotary tillage engine lubrication system, and reduces the production cost and development cycle.

In this paper, the simulation optimization of engine lubrication system for rotary tillage mainly focuses on the analysis of pressure and flow rate of main structure, and there is still some work to be further studied. For example, the branches of lubrication system, such as camshaft rocker arm and tappet, need to be studied. The lubricating oil flow of these components is small, so it is necessary to analyze the influence of its tiny flow.

REFERENCES

- [1] Anand R., Gupta Y., Desai J., (2021), Design and analysis of portable power hacksaw with coolant and lubrication system. *AIP Conference Proceedings*. AIP Publishing LLC, Vol. 2341, Issue 1, p.020001. United States;
- [2] Bukhtiyarova T.I., Semin A.N., Demyanov D.G., (2020), Competitiveness of rural areas: formation, assessment, growth reserves aspects. *IOP Conference Series: Earth and Environmental Science*. IOP Publishing, Vol. 548, Issue 2, pp. 022055. United States;
- [3] Chiavola O., Frattini E., Lancione S., (2021). Operation Cycle of Diesel CR Injection Pump via Pressure Measurement in Piston Working Chamber. *Energies*, Vol. 14, Issue 17, p. 5385. China;
- [4] Corvaglia A., Ferrari A., Rundo M., (2021), Three-dimensional model of an external gear pump with an experimental evaluation of the flow ripple. *Proceedings of the Institution of Mechanical Engineers, Part C: Journal of Mechanical Engineering Science*, Vol. 235, Issue. 6, pp. 1097-1105. England;
- [5] Handler A.M., Lonsdorf E. V., Ardia D. R., (2020), Evidence for red fox (*Vulpes vulpes*) exploitation of anthropogenic food sources along an urbanization gradient using stable isotope analysis. *Canadian Journal of Zoology*, Vol. 98, Issue 2, pp.79-87. Canada;

- [6] He M., Wang E., Zhang Y., (2020), Performance analysis of a multilayer thermoelectric generator for exhaust heat recovery of a heavy-duty diesel engine. *Applied Energy*, Vol. 274, pp. 115298. England;
- [7] Li D., Huang J., Huang L., (2021), High-performance three-dimensional aerogel based on hydrothermal pomelo peel and reduced graphene oxide as an efficient adsorbent for water/oil separation. *Langmuir*, Vol. 37, Issue 4, pp. 1521-1530. United States;
- [8] Mukhametshin I., Valiev A., Muhamadyarov F., (2020), Kinematic analysis of conical rotary subsoil loosener for tillage. *Engineering for Rural Development, 2020*, Issue 19, pp. 19-46. China.
- [9] Samiezadeh S., Qasemian A., Sohani A., (2021), Energy and environmental enhancement of power generation units by means of zero-flow coolant strategy. *International Journal of Energy Research*, Vol. 45, Issue 7, pp. 10064-10085. Switzerland;
- [10] Savitska S., Zaika S., Svystun L., (2020), Investment providing sustainable development of rural areas in Ukraine. *Independent Journal of Management & Production*, Vol. 11, Issue 8, pp. 571-586. England;
- [11] Shevchenko A. N., Krasnoshtanov S. Y., Ruuz M. V., (2020), Analysis of the roller bit lubrication system[C]/IOP Conference Series: Earth and Environmental Science. *IOP Publishing*, Vol. 408, Issue 1, p.012061. United States
- [12] Siddique M., Ayub A., Baek S. M., (2021), Simulation of Fuel Consumption Based on Engine Load Level of a 95 kW Partial Power-Shift Transmission Tractor. *Agriculture*, Vol. 11, Issue 3, p.276. Switzerland.
- [13] Simisinov D., Afanas'Ev A., Adas V., (2020), Lubrication system of a roller cone bit. *MATEC Web of Conferences*, Vol. 329, p.03006. China;
- [14] Singh R., Dureja J. S., Dogra M., (2020), Wear Behavior of Textured Tools Under Graphene-Assisted Minimum Quantity Lubrication System in Machining Ti-6Al-4V Alloy. *Tribology International*, p.145. United Kingdom;
- [15] Zhang Y., Chen G., Wang L., (2020), A calculation method for the journal bearing with a determined load based on response surface optimization. *Tribology Transactions*, Vol. 63, Issue 4, pp. 647-657. United States.

STUDY ON PRECISE FEEDING CONTROL OF DAIRY COWS BASED ON WIRELESS COMMUNICATION TECHNOLOGY AND DAIRY COW INFORMATION MANAGEMENT TECHNOLOGY

基于无线通信技术和奶牛信息管理技术的奶牛精确饲养控制研究

Bin Li*, Mingjun Ma, Chaoju Yang

Xinxiang Vocational and Technical College, Xinxiang, Henan, 453006 / China

*E-mail: oyyaic@163.com

DOI: <https://doi.org/10.356.33/inmateh-65-18>

Keywords: control system, feeding, cow

ABSTRACT

In order to improve the quality of modern dairy industry, it is an inevitable trend to implement intensive control feeding of dairy cows, which is also the development direction in the future. Different feeding methods have different important effects on the health of dairy cows. For example, calves grow and develop rapidly during lactation, their physiological structure changes rapidly, and their digestive function is not perfect. In the production of dairy farms, the scientific feeding mode of calves indirectly affects the overall benefits of dairy farms. Therefore, aiming at the above problems, this paper studies how to accurately control the quality of dairy cows. A cow precise feeding control system based on wireless communication technology and cow information management technology is studied, which solves the problems of wireless information transmission, automatic and accurate cow identification and dual-mode operation of feeder, and ensures the accurate supply of cow concentrate.

摘要

为了提升现代乳品工业质量，实行对奶牛集约化控制饲养是必然的趋势，这也是未来的发展方向。不同的饲养方式对奶牛的健康有着不同的重要影响。比如犊牛在哺乳期身体生长发育快，生理结构变化快，消化功能不完善。在奶牛场生产中，犊牛科学的饲养方式间接影响着奶牛场的整体效益。因此，针对上述问题，本文研究了如何精确控制奶牛质量的问题。研究了一种基于无线通信技术和奶牛信息管理技术的奶牛精确饲养控制系统，解决了无线信息传输、奶牛自动准确识别和喂料机双模运行等问题，保证了奶牛精饲料的准确供应。

INTRODUCTION

Agricultural production is the foundation of national economy in agricultural countries, which is related to the security of national economy and social stability. (Tian H. et al., 2020). The proportion of agriculture as the primary industry in the national economy has gradually declined (Minakov I. A. and Nikitin A. V., 2019). In the modern agricultural industrial structure, dairy industry is the most efficient industry, especially in the agricultural developed countries, the output value of dairy industry accounts for about 20% of the total agricultural output value (Rosa L. et al., 2020). In order to realize the healthy and rapid development of dairy industry, the implementation of dairy fine feeding technology is an inevitable trend, and it is also the main development direction of modern dairy industry (Pe'Er G. et al., 2019). From the perspective of system structure, the dairy industry structure is mainly composed of raw milk production, dairy products processing and marketing (Dong C. Y. et al., 2020). As the dairy industry is a part of the raw milk production system, the development of dairy industry is the basis for the development of dairy industry (Storm H. et al., 2020). The automatic feeding system of dairy cattle is one of the earliest and most effective fields in the application of advanced electronic technology in agricultural production. As the basis of automatic information management, cow automatic number recognition device was successfully developed in the mid-1970s and became a commercial product (Doss C. R., 2018). The reserve group of adult lactating cattle in dairy farm is calves. Different feeding methods of calves not only affect the healthy growth of calves, but also have an important impact on the later growth of calves and the performance of adult milk production. Therefore, it is very important to grow calves for the development of the whole dairy farm and even the whole dairy industry (Maleko D. et al., 2018).

With the development of agricultural science and technology, precision agriculture will become the development direction of modern agriculture. The per unit area yield of dairy cows has not increased significantly, and the development of dairy industry is still in the initial stage of extensive quantitative expansion (Igliński B. *et al.*, 2020). Calves in the lactation stage have rapid growth and development, rapid changes in physiological structure, strong plasticity, and incomplete digestive function (Van Damme M. *et al.*, 2018). With the rapid development of breeding industry, the feeding mode of calves is too simplistic, which affects the growth and development of calves (Qin Y. *et al.*, 2020). The reserve group of adult lactating cattle in dairy farm is calves. Different feeding methods of calves not only affect the healthy growth of calves, but also have an important impact on the later growth of calves and the performance of adult milk production (Costa J. H. C. *et al.*, 2021). Because the healthy growth of calves and low calf mortality can lay a solid foundation for the growth and development of dairy cows, calf feeding has become the primary task of dairy cattle production, and it is also an important link to create a high yield of cattle (Goulart R. S. *et al.*, 2020). For a long time, with the development of animal husbandry and beef cattle industry, people did not adopt a relatively strict calf culture method, which was more random and affected the normal growth and development of calves (Humer E. *et al.*, 2018). There is a large space for the development of dairy industry. Under the new situation of vigorously developing dairy industry, especially in the process of large-scale dairy farming, fine breeding based on individual information of dairy cows is the main research direction of modern dairy scientific breeding (Jensen M. B. *et al.*, 2017).

There is a large space for the development of dairy industry. In the new situation of vigorously developing dairy industry, especially in the process of large-scale dairy farming, fine feeding based on individual information of dairy cows is the main research direction of modern dairy scientific feeding. It is difficult to develop dairy farm automation equipment and computer integrated management system. At present, the development and application personnel of dairy automatic identification system pay less attention. Dairy farm equipment generally has the problems of single function, low efficiency and high failure rate. Most of the dairy farm management is still at the level of manual management. The self-propelled cow precise feeding technology provides the feed needed by individual cows according to the physiological characteristics of cows, implements the "distribution according to demand and quantitative milk" of cow feeding, and realizes the automation, refinement and intellectualization of cow breeding. With the rapid development of Internet of things technology, its application fields are penetrating into all fields of social life including agriculture. Internet of things technology refers to the use of local network or Internet and other communication technologies to connect sensors, controllers, machines, people and things together in a new way, forming a network of people and things, things and things, realizing informatisation, remote management and control and intelligence. This paper studies a self-propelled precision feeding control system based on wireless communication technology and cow information management technology, which solves the problems of wireless information transmission, automatic and accurate identification of individual cows and dual-mode movement of feeding machine in precision feeding technology of cows, and ensures the accurate supply of concentrate for cows.

Literature suggested that due to the improvement of internal nutrients and physical processing characteristics, and combined with the implementation of group feeding mode, the total mixed ration (TMR) feeding mode promoted the increase of per unit area yield of dairy cows in different degrees. However, the characteristics of feeding behaviour still adapt to the new feeding mode and management concept needs to carry out behavioural observation and research after the change of conditions in order to explore the new rules of feeding. In reference, a new design method is proposed. The intelligent precise feeding system of dairy cattle, combined with the corresponding mechanical structure, becomes a feeding robot, which is hung on the track, runs according to the designed program, runs along the track, automatically identifies the dairy cows, accurately proportions and mixes the feed for each dairy cow, realizes regular feeding for many times every day, and can change the feeding curve, memorize and download the delivery records. In reference, a self-propelled accurate feeding control system for dairy cows was proposed, which solved the problem of automatic identification of individual dairy cows, and the measurement error was controlled at about 2%. The measurement error of the latter has been improved obviously, but it is not enough to identify individual cows and record feed intake for further study of the feeding behaviour of cows. Under the automatic control of computer technology, calf feeding machine can accurately feed many calves. It can not only ensure the nutritional needs of different individual calves, but also find out the abnormal condition of calves in time, saving a lot of labour. In large-scale dairy farms with increasing workload and rising labour costs, such automatic calf feeding machinery is needed to ensure the operation and expansion of the pasture.

MATERIALS AND METHODS

With the transformation of dairy industry from scale and quantity type to quality type, it has become the development direction of cattle owners to improve individual milk yield and overall economic benefits of cattle, and it has become an inevitable trend for dairy farms to introduce computer management. The MCU control system receives the data sent by the information management software and stores the data in the external memory. When feeding, the SCM control system controls the dual-mode traveling mechanism to move forward. When the RFID card reader of the feeder identifies the tag installed on the cow's ear, the SCM control system receives the cow tag number sent by the card reader and controls the feeder to stop traveling. A PC is installed in the operator management office to realize the functions of man-machine conversation, data storage and processing, and given control commands. The feeding station includes milk storage tank, milk box, milk tank, electromagnetic valve, heater, ear tag reader, weighing scale, single chip microcomputer control box, etc. Single-chip microcomputer integrates microprocessor, random access memory, read-only memory, various I/O ports, interrupt systems and other input and output interfaces, and has been widely used in the field of industrial control, with strong functions, fast processing speed and low power consumption.

The designed MCU is the core part of the lower computer of calf feeding control system, which is responsible for communicating with the upper computer and controlling the action of the actuator and even the whole feeding process. Its performance stability, application field, self-contained resources, scalability, cost and compilation complexity, development environment and so on are several conditions that must be considered in the selection process. As shown in Figure 1, the whole feeding control system consists of six modules or systems: identification system, feeding console, weighing quality system, feeding system, feeding behaviour data cache system and data storage management and analysis system.

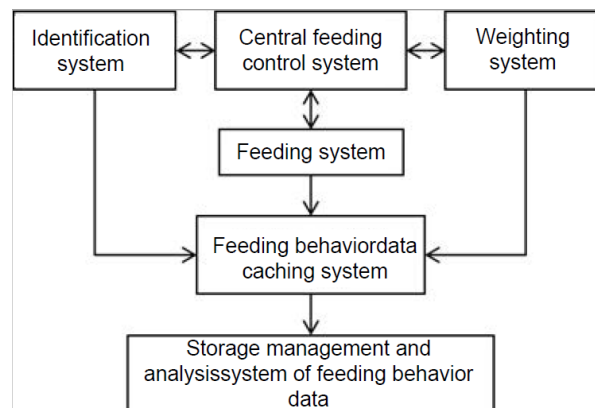


Fig. 1 - Feeding control and data acquisition system structure

Before feeding, the upper computer runs the cow information management software, and uses the software to call the physiological characteristic information data of the cow and process the information. The processed feeding data and the cow ID are sent to the MCU system through wireless transmission, and the MCU system receives and saves the data. The single chip microcomputer control system analyses the identified tag number to determine whether to feed. If the received tag number is a valid tag number, the single chip microcomputer control system controls the accurate feeding device to feed the cow through the stepping motor. When a calf with an ear tag comes to the milk trough to eat milk, the card reader in the feeding station recognizes the electronic ear tag worn by the calf, and transmits the electronic tag to the microcontroller. At the same time, the electronic scale begins to weigh the calf, and transmits the obtained ID number of the calf identification and the data of the weighing sensor to the upper computer through the RS-485 bus. The calf feeding control system is mainly composed of identification system, temperature control system, upper computer control system, peristaltic pump precise feeding system and communication system. When calves wearing ear tags approach the identification system, the machine matches the information of calves imported into the control system by identifying the ear tag ID, calculates the feeding amount, and sends the feeding amount to the MCU, which converts the feeding amount into pulses and transmits them to the servo motor driver to drive the peristaltic pump to feed accurately. The overall schematic diagram of the system is shown in Figure 2.

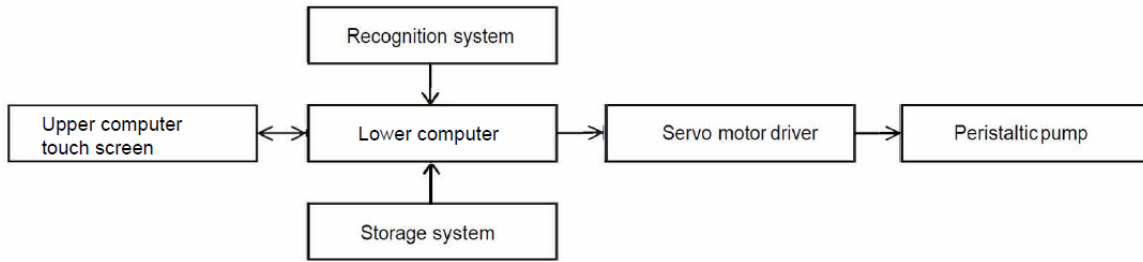


Fig. 2 - Feeding control system

Reader, i.e. radio frequency tag reading and writing equipment, is one of the two important components of radio frequency identification system. Generally speaking, the reading and writing equipment of radio frequency tags should be designed according to the reading and writing requirements and application requirements of radio frequency tags. When feeding, adjust the feeder to the manual control mode, manually operate the feeder to the tower of the cattle farm for feeding, and then drive the feeder to the pen to be fed, and adjust the feeder to the automatic control mode. Calves are sensitive to the changes of external feeding environment, and the most suitable temperature for feeding is 39°C. Too high or too low temperature is not conducive to the digestion and absorption of nutrients by calves. Excessive milk temperature will damage the intestinal mucosa of calves, reduce absorption capacity, cause nutritional diarrhoea and anorexia. If the temperature of milk is too low, the milk will be discharged in intestines and stomach, and the nutrition will not be absorbed completely, which cannot meet the needs of calf growth. With the development of radio frequency identification technology, some typical system realization modes have been formed for radio frequency tag reading and writing equipment. From the most basic principle point of view, radio frequency tag reading and writing equipment generally follows the basic mode. The main factor affecting the communication between the electronic tag and the reader is the working frequency, so the working frequency is determined according to the application requirements and the standards of various countries and regions.

The upper computer software control system calculates the milk feeding amount according to the formula of calf milk feeding amount, and converts the milk feeding amount into the required milk height in the milk box. The actual driving process of the automatic electromechanical control system is analysed, and a unified visual and behavioural model is formed, as shown in Figure 3.

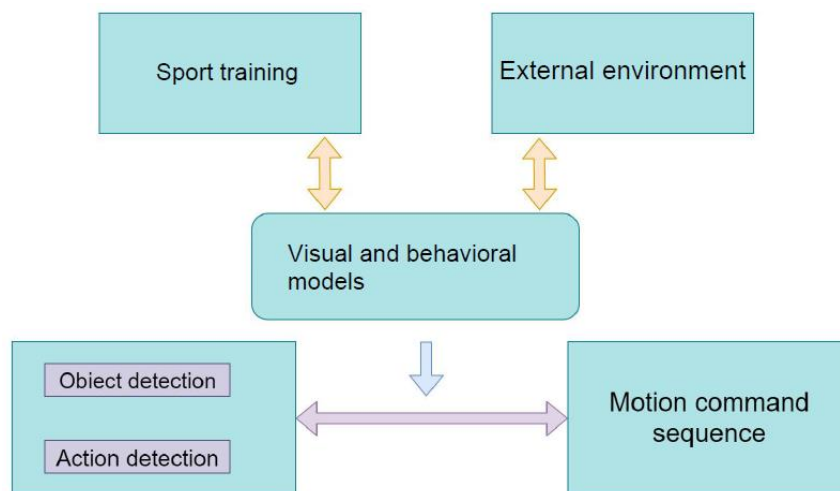


Fig. 3 - Vision and behaviour model

As the upper computer, PC stores, processes and analyses the data transmitted from the lower computer, and transmits various control commands to the lower computer through RS232/485 bus structure to realize centralized management and optimal control. Figure 4 is the flow chart of control system fault diagnosis algorithm.

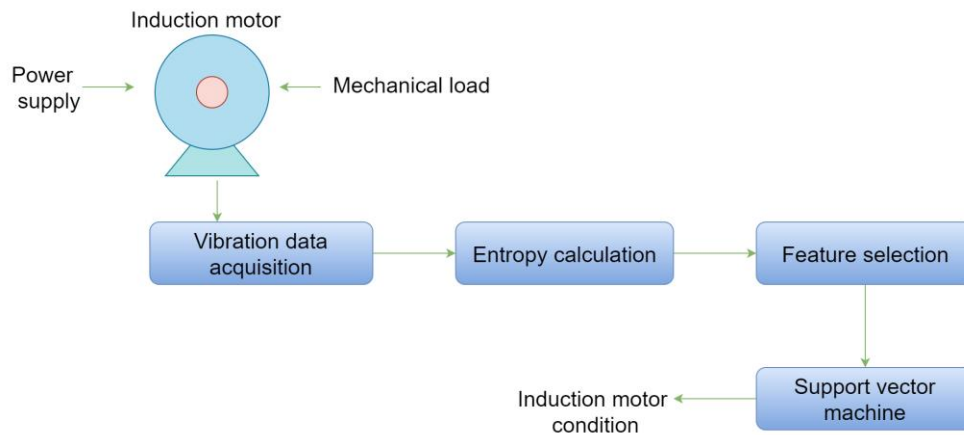


Fig. 4 - Control system fault diagnosis algorithm flow

The upper computer transmits the required milk height to the lower computer through the serial port, and starts the MCU control system to control the opening and closing of the solenoid valve and heater, thus realizing the scientific control of the temperature and milk quantity of feeding calf milk. When cows wearing electronic tags enter the reading range of reading and writing equipment, the recognition system can recognize that many cows wear electronic tags, but for cows, in order to ensure the correct supplementary feeding amount, the reader-writer is set in the fence of the channel, and the channel within the setting range in this direction is determined. The channel can only accommodate a single cow to eat, and the identification system can identify the information data of individual cows, thus avoiding confusion caused by multiple cows wearing electronic tags eating at the same time within the reading and writing range of the reader. In order to ensure the cleanness and hygiene of the normal milk processed by the equipment, water bath heating is designed, but there is a delay when the energy is transferred from water to the normal milk during heating, so the temperature control equipment system has great lag, the temperature is too high or too low to be accurately controlled, and even the pasteurization process is changed. The feeder automatically travels along the feeding trough under the control of the single chip microcomputer. When the feeder travels to the feeding area of dairy cows, the wireless radio frequency card reader identifies the tags worn on the ears of dairy cows in advance, and sends the identified tag numbers to the single chip microcomputer control system.

RESULTS

System function analysis

The foundation and key of the research and development of precision feeding control system for dairy cows is to identify individual dairy cows accurately and quickly. Only after accurately and quickly identifying the individual dairy cows who are taking food can the reasonable feeding amount of the individual dairy cows be determined according to the preset feeding strategy, and the feeding control of concentrated feed can be carried out on this basis. There are strict rules on the feeding amount of calves. At this stage, overeating calves will lead to over nutrition and diarrhoea, and in severe cases, the calves will suffer from diseases and die. If calves eat too little, they will not develop well, which will affect their later growth and development. In the case of a small number of animals, it is relatively easy to identify individual animals by these methods, and the identification process is relatively effective and intuitive. However, many of these traditional animal identification methods have shortcomings, which will cause discomfort or damage to individual animals, so these methods are difficult to be widely used in automatic management, so it is difficult to realize the scale of animal production. The MCU control system controls the feeder to stop moving forward, compares the identified tag number with the ID number in the memory, and after finding the corresponding ID number, calls the feeding data of dairy cows, starts the spiral feeding device, and puts the concentrated feed needed by dairy cows.

When working, the host computer circularly scans all data collectors to collect data, circularly scans the control mechanism to collect real-time feeding amount, displays timely data on the console, and sends information to the management platform to run the management software in real time. Figure 5 is the structure of the control system agent node.

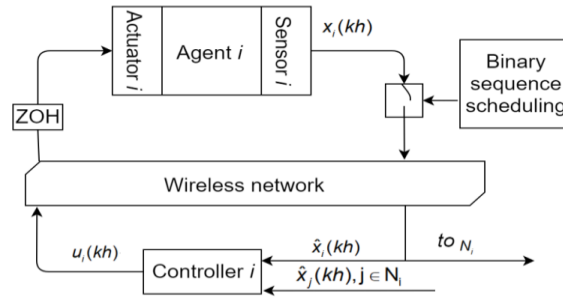


Fig. 5 - The structure of the intelligent body node of the automatic electromechanical control system

Data acquisition, visual positioning and data receiving modules transmit data through interfaces. The data format is shown in Table 1.

Table 1

Data format	
Name	Length
Start flag	4
Data length	6
Command word	7
Data part	12
Termination code	7

In the working environment of RFID system, if there are a lot of metals, water and other substances, the identification accuracy of electronic tags will be affected. Figure 6 shows the consistent distributed control state of agents.

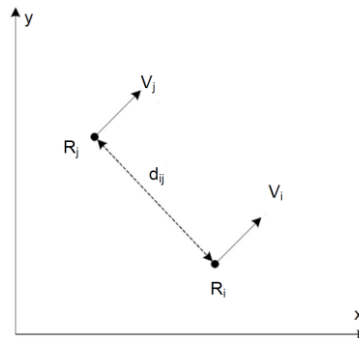


Fig. 6 - The state of consistent distributed control of the agent

Choose a 3-layer 5-input 5-output BP network controller, including 5 input nodes, 5 output nodes, and 1 hidden layer.

The calculation formula for the error of the p-th sample:

$$E_p = \left[\sum_i (t_{pi} - O_{pi})^2 \right] / 2 \tag{1}$$

In the formula, t_{pi} is the expected output value, and O_{pi} is the actual network output value. The input of the input node is x_j , and the output of the hidden node is:

$$y_i = f(\sum W_{ij}x_j - \theta_i) \tag{2}$$

In the formula, W_{ij} is the connection weight, and θ_i is the node threshold. The output node output O_l is:

$$O_l = f\left(\sum_i T_{ij}y_i - \theta_l\right) \tag{3}$$

In the formula, T_{ij} is the connection weight, and θ_l is the node threshold.

The speed response of the motor in the dynamic process is an oblique straight line, which shows that the motor is basically started with the maximum torque. When the speed reaches the target speed of 200rad/s, it stabilizes, and the motor torque stabilizes accordingly. The motor torque waveform is shown in Figure 7.

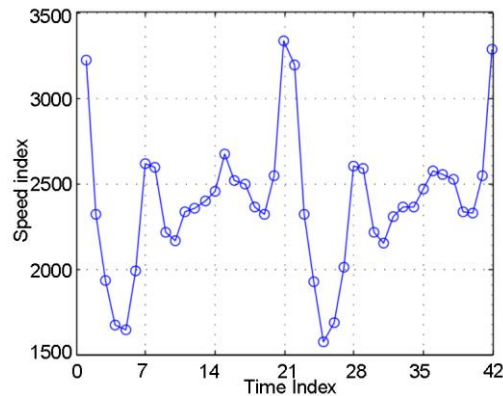


Fig. 7 - Motor torque waveform

The system administrator can run the management software from the management platform to input the basic information and various parameters of cows, and the computer can automatically calculate the concentrate feeding amount and feeding times according to the weight, stage, parity, pregnancy, physiological cycle, milk yield, milk quality and environmental factors of cows. The system uses PC as the feeding management platform to run the information management software. The information management software collects the physiological characteristic data of cows by calling the cow farm database, analyses and calculates these data, and finally sends the valid data to the MCU control system through the wireless transmission device. When working, all kinds of electrical equipment will radiate electromagnetic waves with different frequencies, and the RFID module will be interfered by electromagnetic waves, thus affecting the normal reading and writing recognition rate. In addition, other radio equipment will send out the same frequency wireless signals in the working environment, which will occupy the bandwidth of the radio frequency identification communication module, seriously affect the radio frequency identification module, and may even cause the system to fail to work normally.

System structure analysis

When in the state of system debugging, setting and correcting control parameters, and sending commands by the upper computer, the upper computer is always in the state of active communication, and the method used is query method, with sending before receiving. In practical work, with the application of radio frequency technology, it will be greatly affected when absorbing electromagnetic waves or hindering the transmission of electromagnetic waves. When the cow approaches the concentrate feeding trough, the cow identity automatic recognizer recognizes the identity of the cow and sends the information to the computer management system. After the computer processes the information, it sends a control command to the automatic feeder according to the preset value, and the automatic feeder accurately feeds according to the command. When feeding, the SCM control system controls the dual-mode traveling mechanism to move forward. When the RFID card reader of the feeder identifies the tag installed on the cow's ear, the SCM control system receives the cow tag number sent by the card reader and controls the feeder to stop traveling. Figure 8 shows the automatic feeding system of dairy farm.



Fig. 8 - Fully automatic feeding system for dairy farms

The whole communication process is in the form of polling, and the slave machine can send out a reply signal only when the PC accesses it. The slave is always waiting for the serial interrupt, and as soon as it receives the data, it immediately enters the serial interrupt to process the data. Establish a multi-mode cooperative working environment by using the existing technology. Collaborative work support platform with integrated multimedia mode. The operation flow of cooperative design is shown in Figure 9.

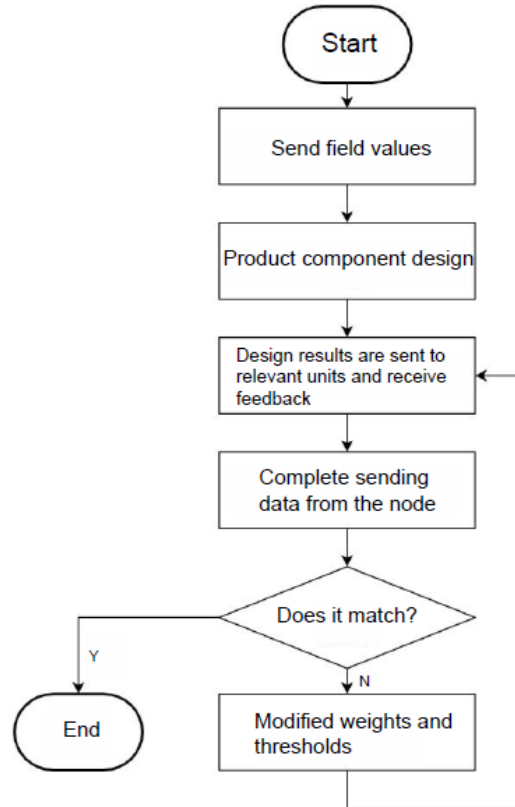


Fig. 9 - The operation process of mechanical processing cooperative design

According to the operational capability of power factor, each control strategy is different. Under the condition of constant resistance load resistance, the simulation results of each control strategy are shown in Figure 10(a). The simulation result curve under the condition of constant power load resistance is shown in Figure 10(b).

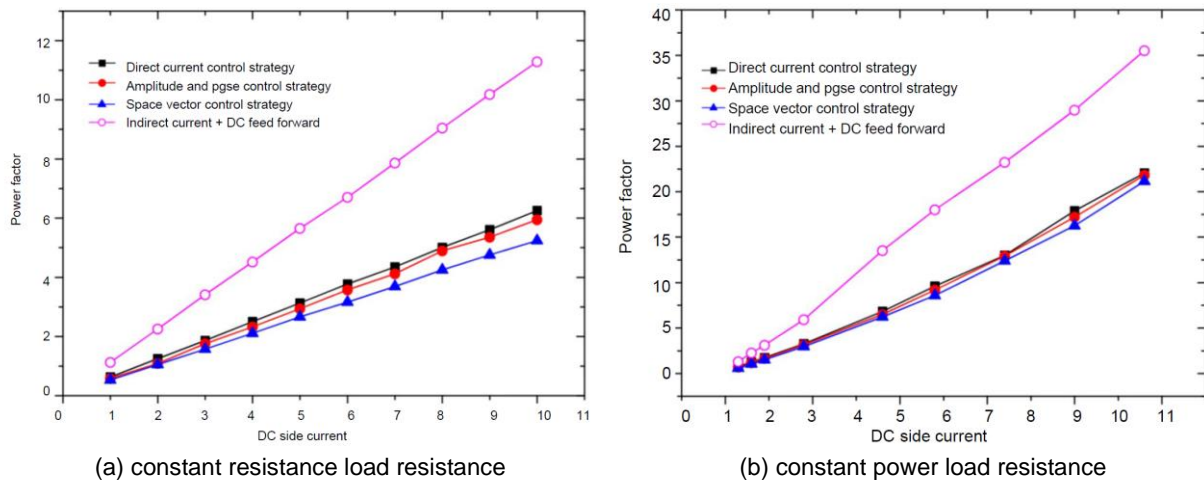


Fig. 10 - The power factor operation capability of each control strategy

When transmitting data, the ports of each MCU are inquired by the PC, and all the lower computers are always in the monitoring state, waiting for the upper PC to send instructions. The single chip microcomputer control system analyses the identified tag number to determine whether to feed.

If the received tag number is a valid tag number, the single chip microcomputer control system controls the accurate feeding device to feed the cow through the stepping motor.

In practical work, we should consider as much as possible to ensure the accessibility of reading and writing equipment and electronic tags, adjust the reader-writer distance, reader-writer power parameters and reduce the influence of working environment on the normal work of RFID module. The basic function of the system is to automatically identify the cow's identity, and automatically feed each cow with concentrated feed several times according to the set value. In addition, it can also realize the functions of milk cow yield monitoring, milk cow weight monitoring, milk cow activity monitoring, oestrus monitoring, output of various reports, analysis of milk cow conditions, etc., or expand other functions as required. When the upper PC sends instructions, all the lower PCs can receive and compare their addresses with the received address frames. If the two addresses are the same, the instructions or data will continue to be received, and if they are different, they will be ignored. After receiving the reply from the lower computer, the upper computer starts to prepare for receiving data, otherwise, it interrupts the line and continues to query the port of the next single-chip microcomputer until the end of receiving.

CONCLUSIONS

Self-propelled precise feeding technology for dairy cows is an advanced feeding technology for feeding dairy cows according to individual physiological information of dairy cows, and the corresponding feeding equipment has the characteristics of simple operation and high automation. The system uses PC as the feeding management platform to run the information management software. The information management software collects the physiological characteristic data of cows by calling the cow farm database, analyses and calculates these data, and finally sends the effective data to the MCU control system through the wireless transmission device. When transmitting data, the ports of each MCU are inquired by the PC, and all the lower computers are always in the monitoring state, waiting for the upper PC to send instructions. When working, all kinds of electrical equipment will radiate electromagnetic waves with different frequencies, and the RFID module will be interfered by electromagnetic waves, thus affecting the normal reading and writing recognition rate. On the basis of large-scale data analysis, we can obtain more general rules of dairy cows' feeding behaviour, and even refine the feeding behaviour characteristics of different lactation stages. With the continuous development of agricultural refinement, dairy cattle precision feeding technology will continue to promote the application in modern dairy farming.

ACKNOWLEDGEMENTS

Henan soft science research plan project, research on intelligent transformation of traditional manufacturing industry in Henan Province from the perspective of supply side structural reform (Project No.: 202400410344)

REFERENCES

- [1] Costa J. H. C., Cantor M. C., Neave H. W., (2021), Symposium review: Precision technologies for dairy calves and management applications. *Journal of Dairy Science*, Vol. 104, Issue 1, pp. 1203-1219. United States;
- [2] Dong C. Y., Ma B. B., Lu C. X., (2020), Spatio-temporal dynamics of feed grain demand of dairy cows in China. *Sustainability*, Vol. 12, Issue 2, pp. 663. Switzerland;
- [3] Doss C. R., (2018), Women and agricultural productivity: Reframing the Issues. *Development Policy Review*, Vol. 36, Issue 1, pp. 35-50. United Kingdom;
- [4] Goulart R. S., Vieira R. A. M., Daniel J. L. P., (2020), Effects of source and concentration of neutral detergent fibre from roughage in beef cattle diets on feed intake, ingestive behaviour, and ruminal kinetics. *Journal of animal science*, Vol. 98, Issue 5, pp. skaa107. United States;
- [5] Humer E., Petri R. M., Aschenbach J. R., (2018), Invited review: Practical feeding management recommendations to mitigate the risk of subacute ruminal acidosis in dairy cattle. *Journal of dairy science*, Vol. 101, Issue 2, pp. 872-888. United States;
- [6] Jensen M. B., Proudfoot K. L., (2017), Effect of group size and health status on behaviour and feed intake of multiparous dairy cows in early lactation. *Journal of dairy science*, Vol. 100, Issue 12, pp. 9759-9768. United States;

- [7] Lgliński B., Piechota G., Iwański P., (2020), 15 Years of the Polish agricultural biogas plants: their history, current status, biogas potential and perspectives. *Clean Technologies and Environmental Policy*, Vol. 22, Issue 2, pp. 281-307. Germany;
- [8] Maleko D., Msalya G., Mwilawa A., (2018), Smallholder dairy cattle feeding technologies and practices in Tanzania: failures, successes, challenges and prospects for sustainability. *International Journal of Agricultural Sustainability*, Vol. 16, Issue 2, pp. 201-213. United Kingdom;
- [9] Minakov I. A., Nikitin A. V., (2019), Agricultural market development: trends and prospects. *International journal of innovative technology and exploring engineering*, Vol. 9, Issue 1, pp. 3842-3847. India;
- [10] Pe'Er G., Zinggrebe Y., Moreira F., (2019), A greener path for the EU Common Agricultural Policy. *Science*, Vol. 365, Issue 6452, pp. 449-451. United States;
- [11] Qin Y., Abatzoglou J. T., Siebert S., (2020), Agricultural risks from changing snowmelt. *Nature Climate Change*, Vol. 10, Issue 5, pp. 459-465. United Kingdom;
- [12] Rosa L., Chiarelli D. D., Rulli M. C., (2020), Global agricultural economic water scarcity. *Science Advances*, Vol. 6, Issue 18, pp. eaaz6031. United States;
- [13] Storm H., Baylis K., Heckelei T., (2020), Machine learning in agricultural and applied economics. *European Review of Agricultural Economics*, Vol. 47, Issue 3, pp. 849-892. United Kingdom;
- [14] Tian H., Wang T., Liu Y., (2020), Computer vision technology in agricultural automation—A review. *Information Processing in Agriculture*, Vol. 7, Issue 1, pp. 1-19. China;
- [15] Van Damme M., Clarisse L., Whitburn S., (2018), Industrial and agricultural ammonia point sources exposed. *Nature*, Vol. 564, Issue 7734, pp. 99-103. United Kingdom;

DEM PARAMETERS CALIBRATION OF MIXED BIOMASS SAWDUST MODEL WITH MULTI-RESPONSE INDICATORS

混杂木屑离散元仿真模型的多响应参数标定

Gong Xun¹⁾, Bai XueWei¹⁾, Huang HaiBo¹⁾, Zhang FengYu¹⁾, Gong YuanJuan¹⁾, Wei DeSheng²⁾

¹⁾Shenyang Agricultural University, College of Engineering, Shenyang / China;

²⁾Sunbon Agricultural Machinery Manufacturing Company, Siping / China

Tel: +86-024-88487117; E-mail: bai-xuewei@syau.edu.cn

DOI: <https://doi.org/10.356.33/inmateh-65-19>

Keywords: mixed biomass sawdust, parameter calibration, DEM, constitutive property experiment

ABSTRACT

The Plackett-Burman factorial experiment was carried out by Design-Expert for 10 related factors. The simulation calibration experiment with JKR contact model was performed based on discrete element method (DEM) with mixed biomass sawdust as the research object. Taken the Box-Behnken experiment together with the steepest climbing test scheme, the parameters of the multi-response indicators were calibrated as follows: the Poisson's ratio of mixed biomass sawdust is 0.30; the density is 399.22kg·m⁻³; the recovery coefficient between sawdust particles is 0.47; the rolling friction coefficient between sawdust particles is 0.39 and the parameter of surface energy density between sawdust particles (JKR) is 0.29J·m⁻². The comparative verification experiments indicate that the relative error of the repose angle is 3.41% and the relative error of the stress-time response curve is less than 6.36%. These results verify the reliability of the calibration method and provide a theoretical reference for the study of the constitutive characteristics of biomass materials and the densification mechanism.

摘要

以混杂生物质木屑为研究对象，基于 DEM 离散元原理进行接触模型为 JKR 的仿真标定试验，利用 Design-Expert 针对 10 种相关因素进行 Plackett-Burman 析因试验，结合最陡爬坡试验方案，根据 Box-Behnken 试验，完成响应指标为堆积角、成型压制力、应力松弛时长的参数标定，其结果为：混杂木屑的泊松比 0.30，密度 399.22 kg·m⁻³，木屑颗粒间的恢复系数 0.47，木屑颗粒间的滚动摩擦系数 0.39，木屑颗粒间的 JKR 表面能密度 0.29 J·m⁻²。通过对比验证试验可知，堆积角的相对误差为 3.41%，应力-时间响应曲线的相对误差小于 6.36%，验证了该标定方法的可靠性，为生物质本构特性及致密成型机理的研究提供了理论参考。

INTRODUCTION

Mixed biomass sawdust is identified as a substitute of fossil energy for its inflammability, low ash content, low sulfur content, and high calorific value. Constitutive parameters of mixed biomass sawdust are of great significance for the development of pelleting machines (Chen *et al.*, 2020). Due to the wide divergence in the composition and morphology, and the high nonlinearity versus heterogeneity of the contact between components of sawdust, it is difficult to measure the mechanical constitutive parameters directly. Based on the dynamic relaxation theory, the discrete element method which analyzes integral subjects through discrete elements and takes Newton's second law as the basic theory, the parameters of nonlinearity materials by simplifying the material to particles can be calibrated. Therefore, the analysis method based on DEM is introduced to calibrate the constitutive parameters of mixed biomass sawdust (Liu *et al.*, 2019).

As reported, the parameters of mixed biomass sawdust which were calibrated by discrete element method are various. The values selected by different scholars are also quite different even on the same type of specimens of mixed biomass sawdust. Therefore, it is necessary to recalibrate the discrete element parameters of mixed biomass sawdust (Li *et al.*, 2019).

Recently, Horabik *et al.* calibrated the parameters of wheat particles by using the double stiffness Hertz contact model based on the DEM. The Poisson's ratio, the rolling friction coefficient, and the recovery coefficient are 0.25, 0.01, and 0.5 respectively, and the calibration error compared with physical experiment is 0.57% (Horabik *et al.*, 2020). Mostafa *et al.* calibrated the parameters of soil based on the discrete element principle combined with the contact model of hysteresis spring and linear cohesion (HS-LC).

The Poisson's ratio, the recovery coefficient, and the dynamic friction coefficient are 0.3, 0.6, and 0.5 respectively (Mostafa *et al.*, 2020). Kornél *et al.* calibrated the parameters of rapeseed based on the discrete element principle and uniaxial compression experiment. The results showed that the friction coefficient between particles is 0.5 and the local damping coefficient is 0.7 (Kornél *et al.*, 2015). Zhang *et al.* investigated and calibrated 15 factors including JKR parameter by referring to the data of concrete slump experiment. Using the accumulation height as the responding index combined with the analysis principle of discrete element, it was found that the static friction coefficient is 0.36, the rolling friction coefficient is 0.09 and the JKR parameter is $6.69\text{J}\cdot\text{m}^{-2}$ (Zhang *et al.*, 2020). Zhang *et al.* calibrated the parameters of blueberries by Plackett-Burman factorial experiment and central experiment with the angle of repose as responding index through discrete element simulation analysis. The results showed that the recovery coefficient is 0.06, the static friction coefficient is 0.56, the angle of repose is 24.66° , and the calibration error is 0.57% (Zhang *et al.*, 2020).

Extending from the above literatures, the parameters of response target in this study not only used repose angle as the single target value, but also included compaction force and stress relaxation time. Design-Expert was applied to investigate the Poisson's ratio, JKR parameter and other 10 factors based on Plackett-Burman factorial experiment, steepest ascent experiment and Box-Behnken experiment. The repose angle, molding compaction force and stress relaxation time were used as the response indicators in these experiments. Using the Hertz-Mindlin with JKR contact theory, combined with the DEM simulation analysis method, the Poisson's ratio, density, inter-particle recovery coefficient, inter-particle rolling friction coefficient and JKR parameter were calibrated for the mixed biomass sawdust.

MATERIALS AND METHODS

Materials

The mixed biomass sawdust of eucalyptus, arbores and other industrial production surplus was selected in this work. Sawdust samples of 200g were processed by screening out of stones and other industrial impurities by vibration sieve, according to the standard 'particle size distribution (GB / T14684 - 2001)'. The sawdust sample is gradually screened by standard test sieve. The size range of particle sample is shown in Table 1.

Table 1

Grading of sawdust particles	
Particle size /mm	Proportion /%
≤0.15	7.53
0.15~0.18	6.12
0.18~0.25	8.57
0.25~0.45	7.74
0.45~0.60	7.62
0.60~0.90	15.68
0.90~2.00	35.21
2.00≥	11.53
Total	100

According to the standard "Determination of moisture content of forestry biomass materials (GB/T36055-2018)", the moisture content of sawdust samples without impurities was determined. Random sawdust sample of 2.00g was weighed, put in a $(105\pm 2)^\circ\text{C}$ oven and weighed again after drying. Parallel tests were repeated in 8 groups, and the average moisture content of sawdust samples is $(8.5\pm 0.3)\%$.

Method

The parameters of mixed biomass sawdust were calibrated by simulation experiment and physical experiment. First, the repose angle of mixed biomass sawdust was measured, and then the stress-time response curve was obtained by single-mode hole compression experiment.

According to the Plackett-Burman factorial experiment, the factors with significant influence are selected from 10 related factors such as JKR and Poisson's ratio. Ultimately, the steepest ascent experiment was used to determine the optimal value range along the gradient direction of the response surface, and the variance analysis in the Box-Behnken experiment was used to optimize the target factors and to complete the parameter calibration of the related variables.

Measurement of mixed biomass sawdust repose angle

According to the measurement of the repose angle in the standard '(GB/T31057.2-2018) particle material physical properties experiment', the repose angle of mixed biomass sawdust was measured as shown in Fig.1, where the funnel taper is $60\pm 0.5^\circ$ and the outlet diameter is 10mm. The distance between the flow outlet surface and the tray surface is 80 ± 2 mm. The camera and the material tray plane were adjusted to the same level, photographed when the steady-state repose angle formed. Then, 20g mixed biomass sawdust samples were randomly weighed and used for the experiments. The parallel experiments were repeated for 5 times.



Fig. 1 - Measurement test of the repose angle of mixed biomass sawdust

As shown in Fig.2, the background was eliminated by using the method of image recognition, and it was transformed into a binary image and the contour of the repose angle was extracted. The angle between the fitted straight line and the horizontal plane is the repose angle. The average of repose angles obtained by five groups of parallel experiments is $32.40\pm 0.2^\circ$ (Peilin et al., 2020).

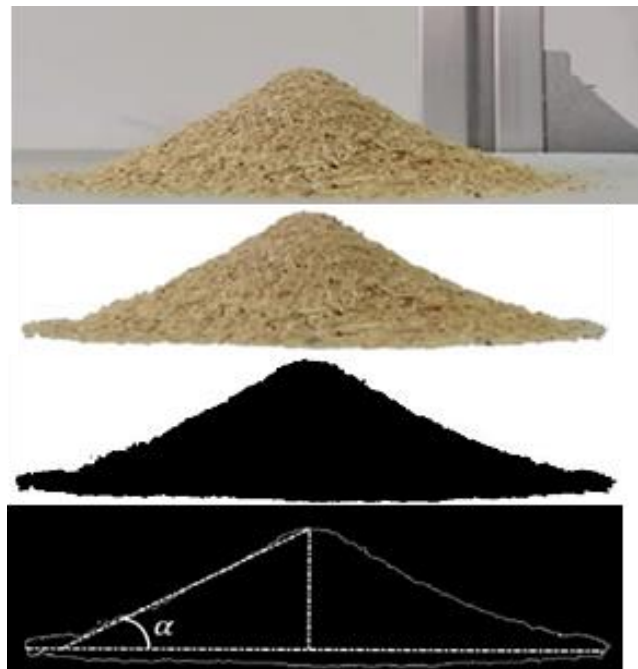


Fig. 2 - Image processing of repose angle

Compacting experiment of mixed biomass sawdust

As shown in Fig.3, the material of the mold is PLA which is produced by 3D-Printer. The compacting experiment was carried out by WDW-100A universal test bench.

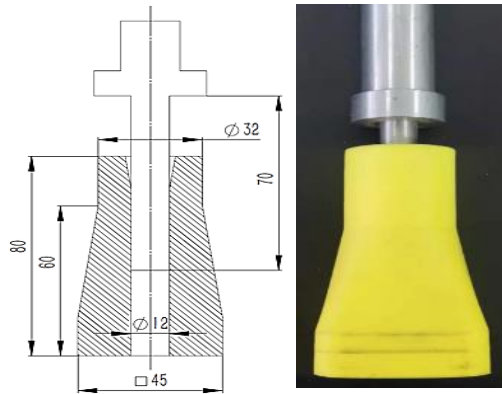


Fig. 3 - Forming test mold

Before compacting, the bottom surface of the pressing rod was aligned with the upper end of the mold, and the displacement count of the equipment was set to zero. At the beginning of compacting, the pressing rod was compressed downward at the speed of 15.00mm·s⁻¹ and stopped at 30.00mm. The current position was maintained for 60.00 s. During this period, the material entered the stress relaxation stage. Four groups of parallel tests were carried out and it was found that the average compacting force was 1436.30N and the average stress relaxation time was 43.60 s. The compressed pellets bar is shown in Fig.4.



Fig.4 - Compressed pellets bar

SIMULATION ANALYSIS BASED ON DISCRETE ELEMENT METHOD

Selection of contact model

In order to express the surface energy of particles, Hertz-Mindlin with JKR theory established the relationship between the normal elastic force, normal overlap and surface energy of the contact particles, reflecting the viscoelasticity and mechanical properties of particles, as Eq. (1-2):

$$F_{JKR} = -4\sqrt{\pi\gamma E^*} \alpha^{\frac{3}{2}} + \frac{4E^*}{3R^*} \alpha^3 \tag{1}$$

$$\delta = \frac{\alpha^*}{R^*} - \sqrt{\frac{4\pi\gamma\alpha}{E^*}} \tag{2}$$

where: F_{JKR} represents the normal elastic force of contact, γ represents the particle surface energy, E^* represents the equivalent elastic modulus, α represents the surface contact radius between particles, R^* represents the equivalent contact radius of particles, δ represents the normal overlap between particles.

The equivalent elastic modulus and contact radius can be obtained by the contact radius and Poisson's ratio of two contact particles as Eq. (3-4):

$$\frac{1}{E^*} = \frac{1-\nu_1^2}{E_1} + \frac{1-\nu_2^2}{E_2} \tag{3}$$

$$\frac{1}{R^*} = \frac{1}{R_1} + \frac{1}{R_2} \tag{4}$$

where: ν represents the Poisson's ratio of particles.

Hertz-Mindlin with JKR theory can show the mechanical properties of viscoelastic particles, so this contact model is selected for simulation test (Johnson et al., 1971; Mahdi et al., 2020).

Construction of simulation model and parameter setting

According to the screening results of mixed biomass sawdust, spherical particles with different sizes were created in the pre-processing module of EDEM. Six sections were created in size distribution module and set to the particle size range obtained by screening experiment. The funnel was created by geometries module. The inclination angle of the inner wall of the funnel is 60° , and the diameter of the outlet at the lower end is 10.00mm which is 80.00mm away from the horizontal plane. The Poisson's ratio of the model material is set to 0.3, the density is set to $7870.00 \text{ kg}\cdot\text{m}^{-3}$, and the shear modulus is $8.17 \times 10^7 \text{ MPa}$. The attribute parameters of the particles are set according to the factor values of the subsequent Plackett-Burman and Box-Behnken experiments.

The Hertz-Mindlin with JKR model was selected as the contact model, and the gravity acceleration is set to $9.81 \text{ m}\cdot\text{s}^{-2}$, and the direction is vertical downward. Ultimately, the analysis module was imported and set Rayleigh time step at 20%, the total simulation time at 10s, and the grid radius to three times of minimum radius. The simulation analysis process is shown in Fig.5 (Hao et al., 2020; Seunghyun et al., 2019).



Fig. 5 - Simulation test of repose angle

Referring to the experimental results according to compacting of mixed biomass sawdust, the compression model was created in the geometries module of EDEM as shown in Fig.6, and the speed of the compression plane was set to $15 \text{ mm}\cdot\text{s}^{-1}$, and the total time was set to 60s for simulation analysis (Hamid et al., 2020).

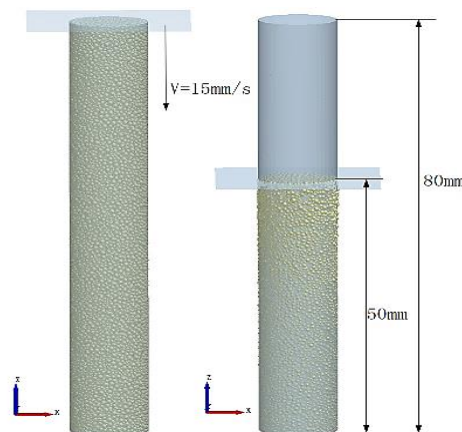


Fig. 6 - Simulation test of single-mode hole compacting

RESULTS

Plackett-Burman factorial experiment

Based on the requirements of Plackett-Burman factorial experiment, 10 variables including Poisson's ratio of mixed biomass sawdust, shear modulus, density, inter-particle recovery coefficient, inter-particle static friction coefficient, inter-particle rolling friction coefficient, inter-particle recovery coefficient with mold inner wall, inter-particle static friction coefficient with mold inner wall, inter-particle rolling friction coefficient with mold inner wall, and JKR parameter are selected for factor significance screening.

Due to the data of discrete element simulation models are quite different, therefore the range of above factors is determined according to the material library of EDEM and relevant papers. As shown in Table 2, the Poisson's ratio range of mixed biomass sawdust was found to be 0.1-0.5, the shear modulus range to be 1-10MPa, the particle density range to be 300-500kg·m⁻³, the recovery coefficient between particles to be 0.1-0.8, the static friction coefficient between particles to be 0.01-0.8, the rolling friction coefficient between particles to be 0.01-0.8, the recovery coefficient between sawdust and mold inner wall to be 0.1-0.8, the static friction coefficient between sawdust and mold inner wall to be 0.01-0.8, the rolling friction coefficient between sawdust and mold inner wall to be 0.01-0.8, and the JKR parameter is 0.05-0.5J·m⁻².

Table 2

Plackett-Burman test factor level table

Factor symbols	Factors	Factor levels		
		-1	0	1
T1	Poisson's ratio between particles	0.10	0.30	0.50
T2	Shear modulus between particles / MPa	1.00	5.50	10.00
T3	Particles density / kg·m ⁻³	300.00	400.00	500.00
T4	Recovery coefficient between particles	0.10	0.45	0.80
T5	Coefficient of static friction between particles	0.01	0.41	0.80
T6	Coefficient of rolling friction between particles	0.01	0.41	0.80
T7	Restoring coefficient with mold inner wall	0.10	0.45	0.80
T8	Static friction coefficient with mold inner wall	0.01	0.41	0.80
T9	Rolling friction coefficient with mold inner wall	0.01	0.41	0.80
T10	Parameter of surface energy density between particles (JKR) /J·m ⁻²	0.05	0.28	0.50

According to the factor level determined in table 2, factorial tests were carried out as shown in table 3, where T11 is an empty column; index Y1 is the repose angle; index Y2 is the molding pressing force (i.e., the peak stress of the compression plane at the end of compression); and index Y3 is the duration of stress relaxation (i.e., the duration of stress relaxation when the compression plane stops moving to 0).

Table 3

Plackett-Burman simulation test

Run No.	T1	T2	T3	T4	T5	T6	T7	T8	T9	T10	T11	Y1/°	Y2/N	Y3/s
1	1	1	1	-1	-1	-1	1	-1	1	1	-1	24.37	1402.63	39.18
2	1	1	-1	1	1	1	-1	-1	-1	1	-1	48.56	1536.84	41.21
3	1	-1	1	1	-1	1	1	1	-1	-1	-1	35.41	1237.87	45.32
4	1	-1	1	1	1	-1	-1	-1	1	-1	1	13.98	1168.94	29.73
5	-1	1	-1	1	1	-1	1	1	1	-1	-1	30.06	1654.31	19.13
6	-1	-1	1	-1	1	1	-1	1	1	1	-1	21.92	1099.36	16.36
7	1	-1	-1	-1	1	-1	1	1	-1	1	1	42.65	1264.82	20.96
8	-1	1	1	-1	1	1	1	-1	-1	-1	1	19.96	1374.98	22.98
9	-1	1	1	1	-1	-1	-1	1	-1	1	1	28.12	1498.11	48.54
10	-1	-1	-1	-1	-1	-1	-1	-1	-1	-1	-1	17.11	964.37	55.44
11	-1	-1	-1	1	-1	1	1	-1	1	1	1	32.49	953.22	65.71
12	1	1	-1	-1	-1	1	-1	1	1	-1	1	38.52	1934.76	14.65

Through the analysis on the experimental results of the response index as the repose angle shown in Table 4, the R² value adjusted by the model was 0.9978 with P value less than 0.05, suggesting the model is statistically validated for further analysis. The observation shows that the factors T1, T3, T6 and T10 are extremely significant; T2 and T4 are significant; and T1, T2, T4, T6 and T10 have positive effects on the repose angle, indicating the repose angle increases with the increase of the factor. The factor T3 has a negative effect on the repose angle, suggesting the repose angle decreases with the increase of the factor. Among them, T3, T1 and T10 have greater contributions to the repose angle results, while T2 and T4 have smaller contributions to the repose angle results. Similarly, the model is justified again by the R² value to be 0.9906 with the P value as 0.0625 when the response index is the molding compaction force. Factors T3 and T4 are extremely significant, while T1, T6, T10 and T8 are significant. Only factors T3, T10 had a negative effect on the molding force. By analyzing the test that the response index to be the stress relaxation time, the model demonstrated statistical significance with R² value adjusted by the model to be 0.9989 and the P value to be 0.0178.

Factors T10, T4 and T3 are extremely significant; T1, T6 and T5 are significant; only factors T10 and T4 had positive effect on stress relaxation time. In summary, T1, T3, T4, T6 and T10 are selected as the factors that have significant effects on indicators Y1, Y2 and Y3, and they are used as the factors for subsequent experimental investigations.

Table 4

Plackett-Burman simulation test analysis

Factors	Standardized effects	Contribution degree/%	Sum of mean squares	F-value	P-value
Model			1232.52	505.82	0.03**
T1	8.97	19.59	241.47	990.96	0.02**
T2	4.34	4.58	56.46	231.72	0.05*
T3	-10.94	29.12	358.94	1473.03	0.01**
T4	4.02	3.92	48.36	198.46	0.06*
T5	0.19	0.02	0.11	0.42	0.63
T6	6.76	11.13	137.16	562.89	0.02**
T7	2.79	1.89	23.32	0.72	0.56
T8	6.71	10.93	134.74	1.94	0.22
T9	-5.08	6.28	77.37	0.81	0.43
T10	7.18	12.54	154.59	634.39	0.02**

Note: $p \leq 0.05$ is extremely significant, expressed as "***"; $0.05 \leq p \leq 0.1$ is significant, expressed as "**"

Steepest ascent experiment

As shown in table 5, the significant factors filtered by Plackett-Burman are increased or decreased according to a certain step length, and the optimal range is determined according to the positive and negative effects of relative errors of each response index. The analysis shows that the repose angle index is bounded by the No.4 test, and the relative error decreases first and then increases. The compacting force index is bounded by the No.3 test, and its relative error decreases first and then increases. The stress relaxation time index is bounded by the No.4 test, and the relative error decreases first and then increases. Therefore, it is appropriate to select the values of the factors corresponding to experiment No.2 as the lower limit, and the values of the factors corresponding to experiment No.5 as the upper limit for Box-Behnken experiment, namely, T1 to be 0.18–0.42, T3 to be 340–460, T4 to be 0.24–0.66, T6 to be 0.17–0.62, and T10 to be 0.14–0.41.

Table 5

Analysis of the steepest ascent test

Run No.	Factors					Y1 relative error	Y2 relative error	Y3 relative error
	T1	T3	T4	T6	T10			
1	0.10	300	0.10	0.01	0.05	42.24%	33.83%	31.71%
2	0.18	340	0.24	0.17	0.14	37.11%	12.51%	25.63%
3	0.26	380	0.38	0.32	0.23	15.37%	4.72%	18.42%
4	0.34	420	0.52	0.47	0.32	9.23%	17.64%	5.14%
5	0.42	460	0.66	0.62	0.41	22.61%	29.76%	13.35%
6	0.50	500	0.80	0.80	0.50	38.12%	35.13%	27.84%

Calibration of simulation parameters and validation test

According to the factor value range of the steepest ascent experiment, 46 groups of Box-Behnken experiments including 6 groups of central experiments were carried out (Boikov et al., 2019). Through the analysis of the test with the repose angle as the index, the P value is found to be extremely significant at 0.012 with the adjusted R^2 value at 0.9954. However, the P value of the mismatch term is not significant at 0.2663, indicating that the model is well fitted. By analyzing the compacting force as the index of the test, the P value is significantly 0.0634 with the adjusted R^2 value at 0.9824, and the P value of the mismatch item at 0.1817 is not significant, indicating that the model is well fitted. The analysis of the test with compacting force as the index shows that the P value is extremely significant at 0.0156; the adjusted R^2 value is 0.9934; and the P value of the unfit term is not significant at 0.2216, indicating that the model is well fitted. Multi-objective optimization of the regression model is carried out by taking the repose angle of 32.4°, compacting force of 1436.3N, and stress relaxation time of 43.6s as the appropriate values.

The analysis shows that when the Poisson's ratio of mixed biomass sawdust is 0.30; the density is $399.22 \text{ kg}\cdot\text{m}^{-3}$; the recovery coefficient between particles is 0.47; the rolling friction coefficient between particles is 0.39, and the JKR parameter is $0.29 \text{ J}\cdot\text{m}^{-2}$, demonstrating that the response index is the most approach to the target value.



Fig. 7 - Comparison with simulation and physical experiment of repose angle

The calibrated parameters are imported into EDEM to carry out the single-hole compression simulation test as described above. The simulated data of stress versus time is plotted in the same coordinated system with the test data. Time duration is 45s, and the total number of data points investigated is 2000 as shown in Fig.8.

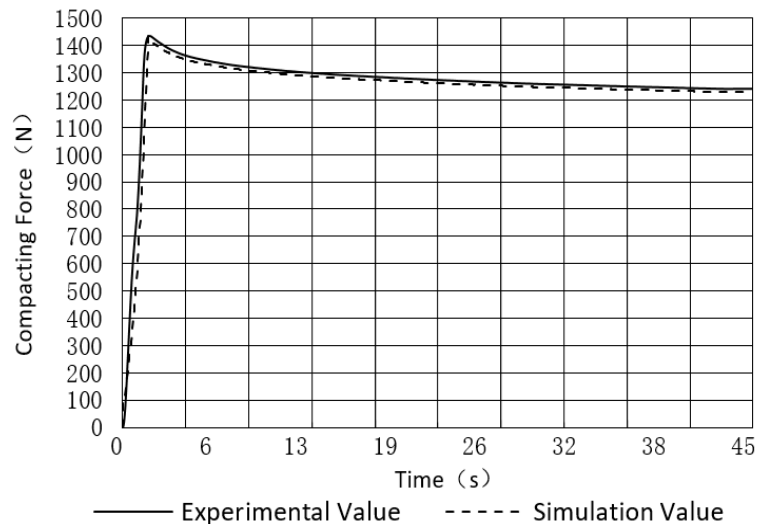


Fig. 8- Simulation versus experiment force data on time

The result shows that the maximum relative error between the actual value and the simulation value in the compacting process is 6.36%. By comparing with the compacting stage before the peak value of the pressing force and the stress relaxation stage after the peak value, it shows that the average relative error of the former is generally greater than that of the latter. This can be explained that the simulation test environment is ideal, and the compression mold inner wall does not affect each other, however, the actual test environment is relatively complicated. There is friction between the outer surface of the pressure rod and the inner wall of the mold, and there are differences in surface roughness between them. Therefore, friction is a variable with time. Once the influence of friction is eliminated when the movement of pressure rod stops and is in the stress relaxation stage, the fitting degree of the stress relaxation stage curve is the best.

CONCLUSIONS

(1) The mixed biomass sawdust of industrial surplus in the experiment shows the wet base moisture content at 8.50%, particle size less than or equal to 2mm, repose angle at 32.40° , compacting pressure to be 1436.30N, and the stress relaxation time to be 43.60s. Combined with the analysis method of discrete element method, the Hertz-Mindlin with JKR is used as the contact model, and the simulation analysis is carried out.

(2) Through the Plackett-Burman factorial experiment, ten factors including Poisson's ratio of mixed biomass sawdust, shear modulus, density, inter-particle recovery coefficient, inter-particle static friction

coefficient, inter-particle rolling friction coefficient, inter-particle recovery coefficient with mold inner wall, inter-particle static friction coefficient with mold inner wall, inter-particle rolling friction coefficient with mold inner wall, and JKR parameter are investigated. The factors that have significant effects on repose angle, compacting force and stress relaxation time are screened as follows: Poisson's ratio of mixed biomass sawdust, density, inter-particle recovery coefficient, inter-particle rolling friction coefficient, and JKR parameter.

(3) The steepest ascent test was used to determine the optimal range of target factors, and the multi-objective optimization was carried out through the Box-Behnken test with the repose angle of 32.40°, compacting pressure of 1436.30N and stress relaxation time of 43.60s. The obtained calibration parameters are as follows: the Poisson's ratio of mixed biomass sawdust to be 0.30, the density to be 399.22kg·m⁻³, the recovery coefficient between particles to be 0.47, the rolling friction coefficient between particles to be 0.39, and the JKR parameter to be 0.29J·m⁻².

(4) The calibrated parameters are compared with the results of the actual test. The relative error of the repose angle is 3.41%, and the maximum relative error of the stress-time response curve is less than 6.36%.

ACKNOWLEDGEMENT

The experimental equipment and experimental sites of this study are provided by Shenyang Agricultural University. The authors want to thank associate professor Xuwei Bai, Professor Yuanjuan Gong and Professor Yongkui Li for their academic guidance. Thanks also goes to Doctor Shuo Qiu in the laboratory for the technical support to this research. The authors gratefully acknowledge the financial support provided by Liaoning Provincial Education Department Fund (LSNQN201904) and Natural Science Foundation of China (51405311).

REFERENCES

- [1] Boikov A.V., Savelev R.V., Payor V.A. et al., (2019), DEM calibration approach: orthogonal experiment. *The Journal of Physics: Conference Series*. vol. 1210(1), Russia. <https://iopscience.iop.org/article/10.1088/1742-6596/1210/1/012025>
- [2] Chen G.Q., Yan J.X. et al., (2020), Simulation study on accumulation characteristics of maize particles by discrete element method (玉米颗粒堆积特性的离散元法模拟研究), *The Journal of light Industry Mechanics*. vol. 38(06), pp.11-14, Jiangsu/China. <https://kns.cnki.net/KCMS/detail/detail.aspx?dbcode=CJFD&filename=QGJX202006003>
- [3] Hamid Gilvari, Wiebren de Jong, Dingena L. Schott, (2020), Breakage behavior of biomass pellets: an experimental and numerical study. *The Journal of Computational Particle Mechanics*. vol.2020, pp. 1-14, Netherlands. <https://link.springer.com/article/10.1007/s40571-020-00352-3>
- [4] Hao Chen, Shiwei Zhao, Xiaowen Zhou, (2020), DEM investigation of angle of repose for super-ellipsoidal particles. *The Journal of Particuology*. vol. 50, pp. 53-66, China. <https://www.sciencedirect.com/science/article/abs/pii/S1674200119300975>
- [5] Horabik J., Wiącek J., Parafiniuk P. et al., (2020), Calibration of discrete-element-method model parameters of bulk wheat for storage, *The Journal of Biosystems Engineering*. vol.200, pp. 298-314, Lublin/Poland. <https://www.sciencedirect.com/science/article/pii/S1537511020302889>
- [6] Johnson K.L., Kendall K., Robert A.D., (1971), Surface energy and contact of elastic solids, *The Journal of Proceedings of the Royal Society of London*. vol.324, pp.301-313, United Kingdom. <https://royalsocietypublishing.org/doi/abs/10.1098/rspa.1971.0141>
- [7] Kornél Tamás, Bernát Földesi, János Péter Rádics et al., (2015), A Simulation Model for Determining the Mechanical Properties of Rapeseed using the Discrete Element Method, *The Journal of Periodica Polytechnica Civil Engineering*. vol. 59(4), pp. 575-582, Hungary. http://www.onacademic.com/detail/journal_1000041692106299_f7d4.html
- [8] Liu X.T., Gao Y.H. et al., (2019), Discrete element analysis of raw material geometry in biomass compacting process (生物质致密成型过程中原料几何形状的离散元研究), *The Journal of China Agricultural Machinery Chemistry*. vol. 40(09), pp.80-84, Baotou/China. https://kns.cnki.net/kcms/detail/detail.aspx?dbcode=CJFD&dbname=CJFDLAST2019&filename=GLJH201909015&uniplatform=NZKPT&v=0IRR2JQ23ZFrMOBo6EE-qBTj1j--a09p5x80cZb80tx1E-UM_6ljFqG3TGGYXe3g

- [9] Li Z. et al., (2019), Discrete element study on force chain evolution in densification process of Salix fine branch particles (沙柳细枝颗粒致密成型过程中力链演变的离散元研究), *The Journal of Acta Energiæ Solaris Sinica*. vol. 40(11), pp.3186-3195, Baotou/China.
<https://kns.cnki.net/kcms/detail/detail.aspx?dbcode=CJFD&dbname=CJFDLAST2019&filename=TYLX201911023&uniplatform=NZKPT&v=cOC7fu0rsHQE5ScNMEVeD6CapW6IDqYsnAOt6EJGrSfC0vEBDxVwgA7ju32YUSAg>
- [10] Mahdi Joulaei, Mojtaba Kolahdoozan, Mehdi Salehi, et al., (2020), Comparison of the adhesion forces in single and double layer coatings on the MEMS surfaces by JKR and DMT models. *The Journal of Surface and Interface Analysis*. vol. 52(1-2), pp. 34-41, Iran.
<https://analyticalsciencejournals.onlinelibrary.wiley.com/doi/full/10.1002/sia.6719>
- [11] Mostafa Bahrami, Mojtaba Naderi Boldaji, Davoud Ghanbarian et al., (2020), Simulation of plate sinkage in soil using discrete element modelling: Calibration of model parameters and experimental validation, *The Journal of Soil and Tillage Research*. vol. 203, Iran.
<https://www.sciencedirect.com/science/article/pii/S0167198720304827>
- [12] Peilin Li, Mustafa Ucgul, Sang-Heon Lee et al., (2020), A new approach for the automatic measurement of the angle of repose of granular materials with maximal least square using digital image processing, *The Journal of Computers and Electronics in Agriculture*. vol.172, Australia.
<https://www.sciencedirect.com/science/article/pii/S016816991932438X>
- [13] Seunghyun Lee, Junyoung Park., (2019), Standardized Friction Experiment for Parameter Determination of Discrete Element Method and Its Validation Using Angle of Repose and Hopper Discharge. 2019, *The Journal of Multiscale Science and Engineering*. vol. 1(3), pp. 247-255, Korea.
<https://link.springer.com/article/10.1007/s42493-019-00020-6>
- [14] Zhang K. et al., (2020), Parameter calibration of concrete discrete element based on JKR bond model (基于 JKR 黏结模型的混凝土离散元参数标定), *The Journal of Concrete*. vol. 2020(08), pp.46-50+55, Liaoning/China.
<https://kns.cnki.net/kcms/detail/detail.aspx?dbcode=CJFD&dbname=CJFDLAST2020&filename=HLTF202008012&uniplatform=NZKPT&v=RplydeDh1a7BjxRWjCfjpHw8O4eVUV08JuJBWE Ln-52eVMcXrMKUUoBX-8wXhwQY>
- [15] Zhang L.W. et al., (2020), Parameter calibration of blueberry discrete element based on response surface method (基于响应面法的蓝莓离散元参数标定), *The Journal of Shenyang Agricultural University*. Vol.51(05), pp. 540-548, Liaoning/China.
https://kns.cnki.net/kcms/detail/detail.aspx?dbcode=CJFD&dbname=CJFDLAST2020&filename=SYNY202005005&uniplatform=NZKPT&v=bd3CB3KQFIYcXn6_k_cVd2giaZcERycTHq3pj8o7eviOnex9_kl QndgIKdNYRkn2

DESIGN AND EXPERIMENT OF CENTRIFUGAL COLLISION TEST DEVICE FOR MILLET AND SWEET BUCKWHEAT GRAIN

谷子、荞麦籽粒离心式碰撞试验装置设计及试验

Sun Jingxin ¹⁾, Yang Liqin ²⁾, Xu Baohui ¹⁾, Guo Yuming ^{*3)}, Cui Qingliang ³⁾, Zhang Yanqing ³⁾ ¹

¹⁾ Department of Mechanical and Electrical Engineering, Yuncheng University, Yuncheng 044000, China;

²⁾ Planning Finance Office, Yuncheng University, Yuncheng 044000, China;

³⁾ College of Agricultural Engineering, Shanxi Agriculture University, Taigu 030801, China;

Tel: +86-0354-6286869; E-mail: quoyuming99@sina.com

DOI: <https://doi.org/10.356.33/inmateh-65-20>

Keywords: millet grain, sweet buckwheat grain, collision, crushing rate, threshing

ABSTRACT

This critical collision damage force of millet and sweet buckwheat grain and the shelling force of shelled granular materials are important basic data for research of threshing and shelling technology and equipment. In order to master the linear velocity and collision force of grain with different moisture content when collision damage occurs, a centrifugal collision test device is designed. Based on the dynamic and kinematic analysis of grain in the centrifugal rotary table, the collision force between grain and steel plate was measured by PVDF piezoelectric pressure sensor and data acquisition system. The results showed that: under the same moisture content, the higher the rotational speed, the higher the grain crushing rate; at the same rotational speed, with the increase of moisture content, the crushing rate first decreased and then increased. When the moisture content of Jingu-21 and Yuqiao-4 is 19.7% and 17.8%, respectively, the grain crushing rate was the lowest. In terms of the anti-collision ability of grain, the optimum moisture content of threshing is between 19.7% and 21% for millet. For sweet buckwheat, the optimum moisture content of threshing is 17.8% ~19%, while the optimum moisture content of shelling by centrifugal sheller is about 11%. The faster the rotational speed of centrifugal rotary table is, the greater the linear speed of grain is, and the greater the collision force is. When the linear velocity of grain was 8.32 m/s and 11.30 m/s respectively, the millet grain moisture content was 11.1% and 20.9% respectively, damage began to appear, and the corresponding collision force was about 5.51 N and 10.6 N, respectively. When the linear velocity of grain was 8.32 m/s and 11.30 m/s respectively, and the moisture content was 11.1% and 22.8% of the sweet buckwheat grain respectively, damage began to appear, the corresponding collision force was about 8.92 N and 12.79 N, respectively. When the rotating speed of rotary table was 910 r/min, the linear speed of grain was 27.05 m/s, the crushing rate of millet and sweet buckwheat grain in harvest period were 56.30% and 63.76%, respectively, and the crushing rate of millet and buckwheat grain with 11.1% moisture content were 86.27% and 89.4%, respectively. The research results can provide theoretical basis for design and optimization of millet and sweet buckwheat combine harvester, threshing device and shelling device.

摘要

谷子、荞麦籽粒的临界碰撞损伤力及带壳散体物料的破壳力是研究脱粒、脱壳技术及其装备的重要基础数据。为掌握不同含水率的籽粒出现碰撞损伤时的线速度、碰撞力等，该文设计了一种离心式碰撞试验装置，对籽粒在转盘内进行动力学及运动学分析的基础上，采用 PVDF 压电薄膜传感器及数据采集系统对籽粒与钢板的碰撞力进行了测定。结果表明：同一含水率下，转速越大，籽粒的破碎率越高；在同一转速下，随着含水率的增大，破碎率先减小后增大，晋谷 21 号、榆荞 4 号的含水率分别为 19.7%、17.8% 时，籽粒的破碎率最小；从籽粒的抗碰撞能力来说，对于谷子，脱粒的最佳含水率在 19.7%~21% 之间；对于甜荞麦，脱粒的最佳含水率在 17.8%~19% 之间，而采用离心式脱壳机脱壳时的最佳含水率在 11% 左右。离心式转盘的转速越快，籽粒的线速度越大，所受的碰撞力也越大；当籽粒的线速度分别是 8.32 m/s、11.30 m/s 时，含水率分别为 11.1%、20.9% 的谷子籽粒开始出现损伤，对应的碰撞力分别是 5.51N、10.6 N 左右；当籽粒的线速度分别是 8.32

¹ JingXin Sun, Lec. Ph.D. Eng.; Liqin Yang, Assis accoun. M.B.A.Eng.; BaoHui Xu, Prof. Ph.D. Eng.; YuMing Guo, Prof. Ph.D. Eng.; QingLiang Cui, YanQing Prof. Ph.D. Eng.; Zhang, Lec. Ph.D. Eng.

m/s、11.30 *m/s* 时，含水率为 11.1%、22.8% 的甜荞麦籽粒出现损伤，对应的碰撞力分别是 8.92N、12.79 N 左右；当转盘转速为 910 r/min 时，籽粒的线速度为 27.05*m/s*，收获期谷子、甜荞麦籽粒的破碎率分别为 56.30%、63.76%，含水率均为 11.1% 的谷子、甜荞麦籽粒的破碎率分别为 86.27%、89.4%。研究结果可为谷子和荞麦的联合收获机、脱粒装置及脱壳装置的设计、优化提供基础依据。

INTRODUCTION

Millet and sweet buckwheat are special grain crops and important economic crops to increase farmers' income in some areas of China (Ji et al., 2016; Domingos et al., 2021, Joshi et al., 2019; Rajasekaran et al., 2021). At present, the harvesting mechanization level of millet and sweet buckwheat is low (Du et al., 2018; Lu et al., 2020), and the special combine harvesters are few (Li et al., 2020). Most of them adopt the parameters and structure of improved grain and wheat combine harvester to harvest millet and sweet buckwheat (Du et al., 2018; Huang et al., 2018; Hyeon et al., 2015).

There are still some problems in mechanized harvest of millet and buckwheat, such as high loss of threshing and cleaning, high crushing rate of threshing and high impurity rate (Liang et al., 2015; Zhang et al., 2019; Lu et al., 2017). Through the development and test of cleaning test device, the suspension speed range of millet and Buckwheat under different moisture content, the optimal speed of fan and the loss rate of grain were determined (Hou et al., 2018; Li et al., 2018).

Grains are crushed and damaged by extrusion and impact of working parts during threshing of millet and buckwheat (Fan et al., 2019; Sun et al., 2017; Sun et al., 2018; Xu et al., 2013). There are studies that show very clearly that the friction coefficient had little effect on the collision dynamics of single grain, the maximum collision force between grain and tooth in normal and tangential directions is not synchronized, the higher the roller speed is, the greater the normal impact force is (Qian et al., 2017). The recovery coefficient of corn grain was determined by Wang based on high-speed camera system and the function derived from the velocity of corn grain in the direction of grain-grain collision contact force (Wang et al., 2018). The maximum impact forces of corn grain were reduced with the increase of the moisture content. Different internal structure and shape of corn seed lead to different ability of resisting impact rupture of different varieties (Li et al., 2009). The velocity of corn grain before and after collision was obtained through studying the motion state of corn grain after collision with threshing element and stalk in roller using high speed camera technique (Jiang et al., 2011). Lizhang Xu used HyperMesh pre-processing software and LS-DYNA dynamic analysis program to simulate and analyse the rice grain, and established the compression displacement and maximum stress distribution when rice grain collided with tooth (Xu et al., 2013). The critical velocity formula of impact damage between rice grain and threshing components can be deduced by *Contact Theory*, and the bench test of different varieties of rice grain is carried out. The test results are basically consistent with the calculation results (Xu et al., 2009). The varieties and moisture content of sunflower have significant effects on rupture (Li et al., 2018). Tao used the self-made centrifugal device to study the shelling of peony seeds, and obtained the optimal combination of motion parameters when the shelling rate was the highest and the kernel breaking rate was the lowest (Tao et al., 2018).

However, there are few reports about the determination of grain impact force of millet and buckwheat. Therefore, millet and buckwheat grains were tested on the self-made centrifugal collision test bench. By using PVDF piezoelectric pressure sensor to measure accurately the collision force between grain and steel plate, and taking grain crushing rate as index, rotating speed and moisture content as independent variables, the moisture content and rotating speed of grain crushing rate were obtained with the minimum grain crushing rate. These results can provide a basic basis for the development and improvement of threshing shelling techniques and equipment of millet and buckwheat.

MATERIALS AND METHODS

Test materials and equipment

The test samples are harvested from the test field during the suitable harvest period. In order to prevent mechanical damage, after the samples are manually rubbed and threshed, the intact and full seeds without insect damage are selected, sealed with double sealing bags and placed in low temperature ($1^{\circ}\text{C}\pm 0.5^{\circ}\text{C}$) environment. The variety of millet used in the test is Jingu-21, with moisture content of 11.1%, 15.2%, 17.5% and 20.9%. The variety of buckwheat used in the test is Yuqiao-4, with moisture content of 11.1%, 15.6%, 19.4% and 22.8%. The test equipment includes self-made centrifugal collision device and data acquisition system.

Overall structure and working principle

The centrifugal collision device is mainly composed of guide cone, centrifugal rotary table, centrifugal blade, collision baffle, retaining ring, adjustable speed motor, governor and frame. The power provided by the adjustable speed motor drives the spindle to rotate, and the spindle drives the centrifugal turntable to rotate. The speed of the centrifugal turntable is adjusted by the governor.

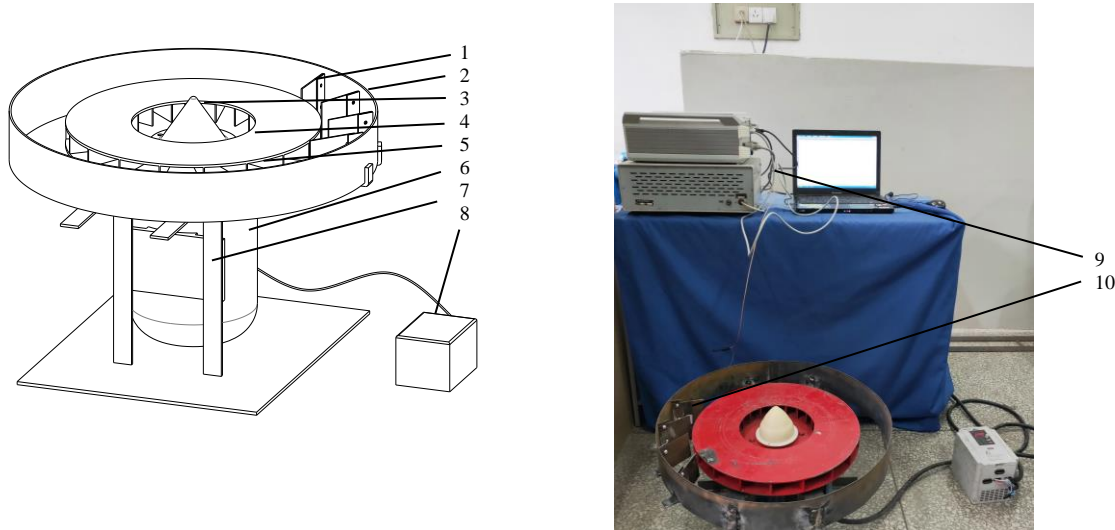


Fig. 1 - Structure diagram of centrifugal collision device

1 – Collision baffle; 2 – Retaining ring; 3 – Guide cone; 4 – Centrifugal rotary table; 5 – Centrifugal blade; 6 – Adjustable speed motor; 7 – Frame; 8 – Governor; 9 – Data acquisition system; 10 – PVDF piezoelectric pressure sensor

During measurement, turn on all power supply, adjust the rotary table speed to the designed speed of test by governor. After the rotating speed of the turntable is uniform, release the grain at 1cm above the guide cone at a still position, and place the receiving box under the impact plate, observe and record the voltage value in the data acquisition software.

Key component design

The adjustable structural parameters of centrifugal turntable mainly include the diameter of rotary table, the tilt angle of blades, the number of blades and the height of blades. According to the triaxial size and 1000 grain weight of buckwheat and millet (Sun et al., 2017; Sun et al., 2018), the parameters of centrifugal turntable were determined as follows: the outer diameter of centrifugal turntable is 400 mm, the inner diameter is 200 mm, the blade is installed in front 10°, the number of blades is 18, the blade height is 18 mm, the blade thickness is 2 mm, the structure diagram of centrifugal turntable is shown in figure 2.

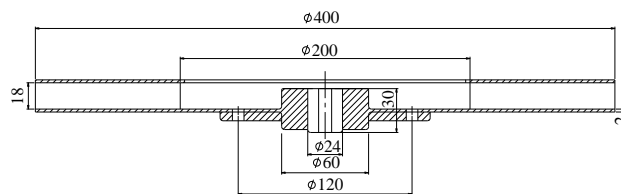


Fig. 2 - Structure diagram of centrifugal rotary table

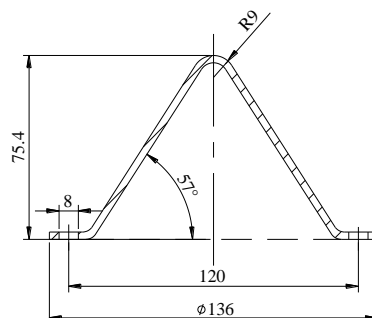


Fig. 3 - Structure diagram of guide cone

The guide cone mainly acts as buffer and shunt. When the grain falls along the surface of the guide cone, the grain enters the centrifugal turntable at a horizontal speed, which can effectively avoid the direct collision between the grain and the upper surface of the centrifugal turntable. The outer diameter of the guide cone is 136 mm, the height is 75.4 mm, and the sliding friction angle and rest angle between millet, buckwheat and Q235 steel plate are less than 40° according to the structure and size of the rotary table. For the grain to slide more easily, the angle between the guide plate and the horizontal plane is 57° , as shown in Figure 3.

Assume that the number of grains flying out of each pore is the same. There are four adjustable baffles installed on the outside of the rotary table. According to the calculated angle between the absolute velocity of grain leaving the rotary table and the circumference velocity φ_2 , the angle adjustment range is $40^\circ \sim 50^\circ$. A PVDF piezoelectric pressure sensor installed on one of the baffles to measure the load of grain colliding with steel plate. The collision baffle is shown in figure 4.

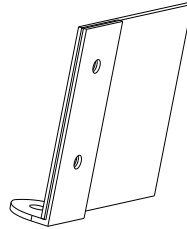


Fig. 4 - Structure diagram of collision baffle

Grain dynamics and kinematics analysis

After entering the centrifugal rotary table through the guide cone, the grain not only rotates around the axis at a constant speed with the rotary table, but also does linear motion along the blade away from the circle centre. Therefore, the grain of millet has a complex motion in the hole of the rotary table, and its motion trajectory is a complex curve. Force analysis of grain in the rotary table is shown in figure 5.

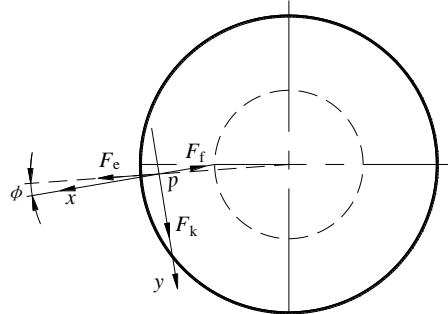


Fig. 5 - Force analysis diagram of grain in the rotary table

In order to analyse the force of the grain in the rotary table, the Cartesian coordinates xoy is established. The position of the grain in the rotary table is p , passing point p is X-axis along the blade direction and y-axis perpendicular to the blade direction. It can be obtained from Fig. 5.

$$\mathbf{F}_k + \mathbf{F}_e + \mathbf{F}_f = m\mathbf{a}_c \quad [\text{N}] \quad (1)$$

$$\mathbf{F}_k = m\mathbf{a}_k = 2m\omega v_c = 2m\omega \frac{dr}{dt} \quad [\text{N}] \quad (2)$$

$$\mathbf{F}_e = m\mathbf{a}_e = m\omega^2 r \quad [\text{N}] \quad (3)$$

$$\mathbf{F}_f = \mathbf{F}_1 + \mathbf{F}_2 \quad [\text{N}] \quad (4)$$

$$\mathbf{F}_1 = \mu mg, \quad \mathbf{F}_2 = \mu(\mathbf{F}_k - \mathbf{F}_e \sin \phi) \quad [\text{N}] \quad (5)$$

where: \mathbf{F}_k is Coriolis force on grain movement, [N];

\mathbf{F}_e is centrifugal force on grain movement, [N];

\mathbf{F}_f is friction on grain movement, [N];

\mathbf{F}_1 is friction caused by grain gravity, [N];

\mathbf{F}_2 is friction caused by Coriolis force and centrifugal force, [N];

m is quality of a grain, [kg];

- a_c is relative acceleration of grain in the rotary table, [m/s²];
- a_k is Coriolis acceleration, [m/s²];
- a_e is centrifugal acceleration, [m/s²];
- v_c is radial velocity vector of grain centre of gravity relative to the rotary table, [m/s];
- ω is angular velocity vector of the rotary table, [rad/s];
- r is the distance between grain centre of gravity and circle centre of the rotary table, [m];
- μ is friction coefficient between grain and rotary table blade;
- ϕ is the angle between centrifugal force and rotary table blade, [°].

The formula (1) is decomposed along the x-axis:

$$F_k \cos \phi - F_f = ma_c \tag{6}$$

Substitute (2), (3), (4), (5) into (6) to:

$$m\omega^2 r \cos \phi - \mu mg - 2\mu m\omega \frac{dr}{dt} + \mu m\omega^2 r \sin \phi = m \frac{d^2 r}{dt^2} \tag{7}$$

Simplified:

$$\omega^2 r \cos \phi - \mu g - 2\mu\omega \frac{dr}{dt} + \mu\omega^2 r \sin \phi = \frac{d^2 r}{dt^2} \tag{8}$$

According to the triangle cosine theorem, the absolute velocity of grain is:

$$v_0 = \sqrt{v_c^2 + v_e^2 - 2v_c v_e \cos \phi_1} \quad [\text{m/s}] \tag{9}$$

where: v_0 is the absolute speed of grain leaving the rotary table (p point), [m/s];

v_e is circumferential velocity of grain at p point, [m/s];

ϕ_1 is complementary angle at angles v_c and v_e , [°]

When the grain moves to the edge of the turntable, the speed diagram is shown in Fig. 6

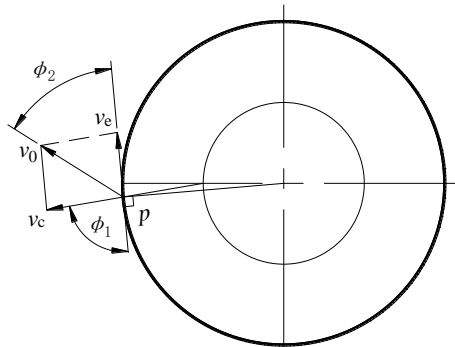


Fig. 6 - Speed diagram of grain at the edge of the rotary table

The ϕ_2 is the angle between v_0 and v_e , and its calculation formula is:

$$\phi_2 = \arctan \frac{v_c \sin \phi_1}{v_e - v_c \cos \phi_1} \tag{10}$$

The circumference velocity v_e of grain at p point as follows:

$$v_e = 2\pi Rn/60 \tag{11}$$

where: R is the calculated radius of the rotary table, [m]; n is rotating speed, [r/min];

According to the empirical formula of centrifugal sheller, the absolute velocity of grain is as follows:

$$v_0 = \pi Dn(1 + \delta)/60 \tag{12}$$

where: D is the calculated diameter of the rotary table, [m];

δ is the composite factor, 0.42;

When the grain leaves the turntable, the angle ϕ_2 between absolute velocity v_0 and the circumference velocity v_e is as follows:

$$\phi_2 = \arccos \frac{v_e}{v_0} = \arccos \frac{1}{1 + \delta} = 45.23^\circ \tag{13}$$

Method and Principle of Centrifugal Collision Test

The data acquisition system is composed of HT-1712H DC power supply (DC 12 V), TST high speed data collector and “DPA5.11” data acquisition software. The principle is to connect the amplifier signal to the data collector, and the collector uploads the signal to the computer through the TCP/IP protocol by Ethernet interface. The sampling frequency is 1 kHz. The advantages and disadvantages of piezoelectric ceramic sensor (Liang et al., 2016) and PVDF piezoelectric pressure sensor (Cao et al., 2019) are compared. Finally, it is determined that the force measuring device is composed of PVDF piezoelectric pressure sensor and VK101H charge amplifier (Output voltage ±5 V, sensitivity 10 pC/100mV, 1,2,4,8,11 times amplified by adjusting dial switch). The amount of charge can be calculated by the following formula:

$$C_{in} = \frac{V_{out} \cdot A_c}{G_{ain}} \tag{14}$$

where: C_{in} is the amount of charge that grain collide with the sensor, [pC] ($1C=1 \times 10^{12}$ pC);
 V_{out} is the voltage that grain collide with the sensor, [V];
 A_c is amplifier Sensitivity, [10 pC /100mV];
 G_{ain} is magnification of the amplifier setting

The collision force can be calculated by formula (15) to obtain:

$$F_p = C_{in} / 20 \tag{15}$$

where: F_p is collision force, [N];

RESULTS

Test results and analysis

The receiving box is installed under the collision plate, mainly to collect the grains that collide on the collision plate after being thrown out by the rotary table. After the experiment was completed, the crushing degree of grain was observed under stereomicroscope. Finally, according to the formula (21), the crushing rate of different moisture content under different speeds was calculated.

$$p = \left[m_1 / (m_1 + m_2) \right] \times 100\% \tag{16}$$

where: p is crushing rate, [%];
 m_1 is total quality of broken grains, [kg];
 m_2 is total quality of unbroken grains, [kg];

The voltage signal and time curve of single grain impact collected by data acquisition system is shown in figure 7.

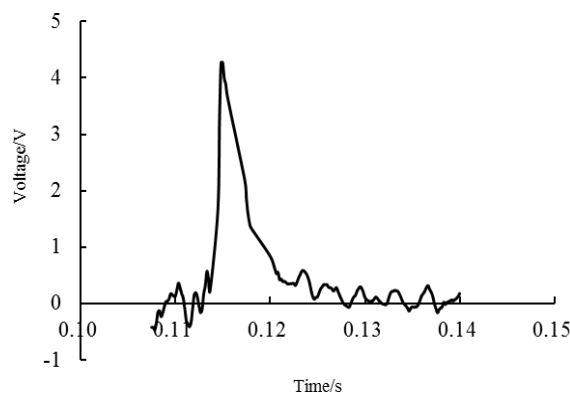


Fig. 7 - Curve of voltage value produced by single grain impact and time

Table 1

Experimental results of millet and buckwheat grains crushing rate under different speed

Variety	Moisture content/%	Speed						
		[r/min]						
		120	280	380	580	660	780	910
Crushing rate of Jingu-21	11.1%	0.0%	0.11%	5.77%	15.38%	41.03%	56.82%	86.27%
	20.9%	0.0%	0.0%	1.69%	12.21%	23.53%	29.46%	56.30%
Crushing rate of Yuqiao-4	11.1%	0.0%	2.58%	20.90%	29.29%	48.20%	68.08%	89.4%
	22.8%	0.0%	0.0 %	3.81%	16.14%	30.70%	39.02%	63.76%

It can be seen from Table 1 that under the same moisture content, the higher the rotational speed, the higher the grain crushing rate of millet and buckwheat grain, which is consistent with the results of Chen (Chen, 2019) and Guo (Guo et al., 2005). At the same rotational speed, the crushing rate of grain with high moisture content is smaller than that of low moisture content. This is due to the high hardness and low toughness of the grain when the moisture content is low, the elastic deformation is mainly occurred in the collision, and the deformation is small. When the moisture content is high, the grain hardness is small, the toughness is high, the plastic deformation occurs mainly during the collision, and the deformation is large. For the purpose of studying the variation of crushing rate with moisture content at the same rotational speed, at the rotary speed of 660 r/min, the centrifugal collision test was carried out on grain samples of Jingu-21 with moisture content 11.1%, 15.2%, 17.5%, 20.9% and Yuqiao-4 with moisture content 11.1%, 15.6%, 19.4% and 22.8% respectively. The relationship curve between crushing rate and moisture content is obtained by the test, as shown in figure 8.

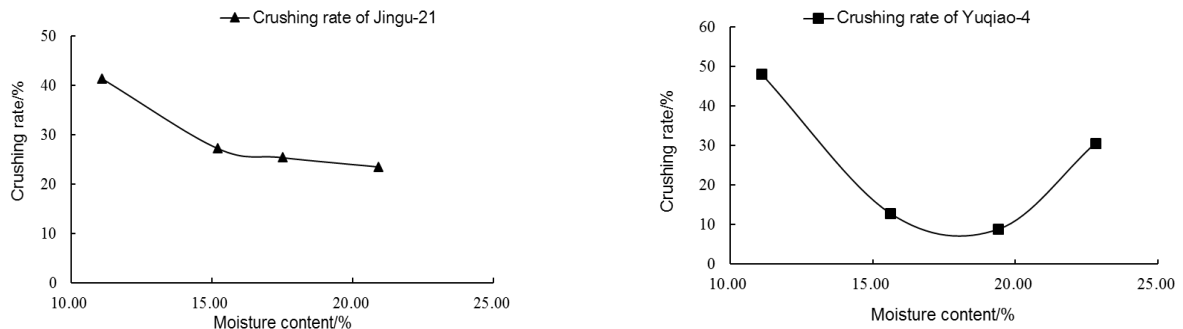


Fig. 8 - Relationship curve between crushing rate and moisture content

By fitting the relation curve in figure 8 with Matlab software, we get:

$$p_1 = 23.866x^2 - 9.3788x + 1.1555 \tag{17}$$

$$p_2 = 90.782x^2 - 32.326x + 2.9543 \tag{18}$$

where: p_1 is crushing rate of Jingu-21 at the rotary speed of 660 r/min, [%];
 p_2 is crushing rate of Yuqiao-4 at the rotary speed of 660 r/min, [%];
 x is moisture content, [%].

The relationship between breaking rate and moisture content is quadratic polynomial. The fitting accuracy is good (R^2 is 0.991, 0.9978 respectively).

According to the fitting formula, when the moisture content is 19.7% and 17.8%, the crushing rates p_1 and p_2 are the minimum, respectively. The test results showed that when the rotating speed of rotary table was 660 r/min, when the moisture content of Jingu-21 was 19.7%, the crushing rate was 21.9%; when the moisture content of Yuqiao-4 was 17.8%, the crushing rate was 7.1%. The test results were close to the model.

All peak voltages are recorded each time, and the collision force of millet and buckwheat at different rotational speeds is calculated according to formula (15). According to formula (12), the linear velocity of grain leaving the edge of rotary table is calculated, as shown in Table 2.

Table2

Collision force of millet and buckwheat grains under different rotating speed

Variety	Rotary speed						
	[r/min]						
	120	280	380	580	660	780	910
Linear velocity of grain [m/s]	3.57	8.32	11.30	17.24	19.62	23.19	27.05
Collision force of Jingu-21[N]	3.52	5.51	10.6	12.74	14.98	16.70	18.77
Collision force of Yuqiao-4[N]	5.27	8.92	12.79	15.59	18.72	20.15	22.07

It can be seen from Table 2 that the larger the rotating speed of the rotary table, the greater the linear velocity of the grain leaving the edge of the rotary table, and the greater the collision force of the grain. Compared with the literature of Sun (Sun et al., 2018) and Sun (Sun et al., 2017): it can be seen that under the same moisture content, the collision force of crushing damage of millet and buckwheat grains under dynamic load is less than that of static load compression.

Table 1 and Table 2 show that the collision force of crushing damage is about 5.51 N, 10.6N and the linear velocity of grain is about 8.32 m/s, 11.30m/s when the moisture content is 11.1% and 20.9% respectively. The collision force of crushing damage is about 8.92 N, 12.79N and the linear velocity is about 8.32 m/s, 11.30m/s when the moisture content is 11.1% and 22.8% respectively. When the rotating speed of is 910 r/min, the linear velocity of grain is 27.05 m/s, and the crushing rate of millet grain and sweet buckwheat grain is 56.30% and 63.76% respectively. And the crushing rate of millet grain and sweet buckwheat grain with moisture content of 11.1% is 86.27% and 89.4%, respectively.

CONCLUSIONS

1. This paper designs a centrifugal collision test device for millet, buckwheat and other grains. The adjustable speed motor is directly connected to the rotary table through the spindle, which has compact structure and can reduce the loss of mechanical energy. The angle of collision baffle is adjustable and the thickness and material of the baffle can be replaced. The PVDF piezoelectric pressure sensor can accurately determine collision force. The device can be used to determine the critical collision damage force of grain and shelling force of granular materials with shells (grain diameter ≤ 15 mm).

2. Under the same moisture content, the higher the rotational speed, the higher the crushing rate of millet and buckwheat grains. At the same rotational speed, the crushing rate decreases first and then increases with the increase of moisture content. When the moisture content of Jingu-21 and Yuqiao-4 is 19.7% and 17.8%, respectively, the grain crushing rate is the smallest. From the anti-collision ability of grain, the optimum moisture content of threshing is between 19.7%~21% for millet, 17.8%~19% for sweet buckwheat, and the optimum moisture content of centrifugal sheller is about 11%.

3. The higher the rotational speed of centrifugal rotary table, the greater the linear velocity of grain, the greater the collision force. At the same rotational speed, the collision force of millet and buckwheat is different. Under dynamic loading, the collision force of grain damage of millet and buckwheat is less than that of static load compression. The collision force of millet grain damage is about 5.51 N, 10.6 N when moisture content is 11.1% and 20.9% respectively. The collision force of sweet buckwheat grain damage is about 8.92N, 12.79N when moisture content is 11.1% and 22.8% respectively.

4. The research method and results of this article can provide theoretical basis for design and optimization of millet and sweet buckwheat combine harvester, threshing device and shelling device.

ACKNOWLEDGEMENTS

This research titled 'Design and experiment of centrifugal collision test device for millet and sweet buckwheat grain' was funded by the National Key Research and Development Plan of China (2016YFD0701801), Science and Technology Innovation Project of Shanxi Province (2020L0568) and Doctoral Research Start Project of Yuncheng University (YQ-2019020). The authors are grateful and honoured to have obtained support from the Laboratory of Agricultural Biomechanics.

REFERENCES

- [1] Cao R., (2019). *Research on signal processing system of multichannel PVDF piezoelectric thin film grain loss sensor based on DSP* (基于 DSP 的多通道 PVDF 压电薄膜谷物损失传感器信号处理系统研究). [Unpublished master's dissertation]. Zhejiang University, Zhejiang/China.
- [2] Chen W., (2019). *Experimental study on the mechanism of buckwheat kernel shelling and the performance of sheller based on low loss and high efficiency* (基于低损高效的荞麦籽粒剥壳机理及剥壳机性能试验研究). [Unpublished doctoral dissertation]. Inner Mongolia Agricultural University, Inner Mongolia /China.
- [3] Domingos I, Bilsborrow P.E., (2021). The effect of variety and sowing date on the growth, development, yield and quality of common buckwheat (*Fagopyrum esculentum Moench*) [J]. *European Journal of Agronomy*, 2021, vol.126, 126264, United Kingdom.
- [4] Du X., Ji J., Jin X., Li C., Yang X., (2018). Research on divider losses with high-speed photography for foxtail millet harvesting. *Future Generation Computer Systems*, vol.88, pp. 55-60, Henan/China.
- [5] Fan C., Cui T., Zhang D., Yang L., Qu Z., Li Y., (2019). Design and test of low-damage combined corn threshing and separating device (低损伤组合式玉米脱粒分离装置设计与试验). *Transactions of the Chinese Society for Agricultural Machinery*, vol.50, issue 4, pp. 113-123, Beijing/China.

- [6] Guo G., Lv X., Guo K., Dang G., (2005). Experimental study on the performance of rapeseed sheller (油菜籽脱壳机脱壳性能试验研究). *Transactions of the Chinese Society for Agricultural Machinery*, vol.36, issue 1, pp. 148-149, Shanxi/China.
- [7] Hou H., Cui Q., Guo Y., Zhang Y., Sun D., Lai S., Liu J., (2018). Design and test of air-sweeping suspension velocity testing device for cleaning threshed materials of grain and oil crops (气吹式粮油作物脱出物清选悬浮速度测量装置设计与试验). *Transactions of the Chinese Society of Agricultural Engineering*, vol.34, issue 16, pp. 43-49, Shanxi/China.
- [8] Huang X., Zhang W., Dang W., Zhang K., Feng S., Liu Z., Yang F., (2018). Research status and development trend of buckwheat harvester (荞麦收获机械研究现状及发展趋势). *Agricultural Machinery*, vol.850, issue 10, pp.84-90, Shanxi/China.
- [9] Hyeon J., Il S., Tae G., Yong C., Duck K., Choung K., (2015). Study on performance improvement of a head-feeding rice combine for foxtail millet harvesting. *Journal of Biosystems Engineering*, vol.40, issue 1, pp. 10-18, Jeonju/Korea.
- [10] Ji J., Li X., Jin X., Geng L., He Z., Li S., Pang J., (2016). Present situation, technical analysis and equipment demand of harvesting mechanization for characteristic coarse cereals (特色杂粮收获机械化现状、技术分析及装备需求). *Agricultural Engineering*, vol.6, issue 6, pp.1-3, Henan/China.
- [11] Jiang N., Yi S., Zhang K., (2011). Comparative analysis of grain movement and collision for different drum speeds axial flow device (不同滚筒转速轴流装置籽粒运动和碰撞对比分析). *Transactions of the Chinese Society for Agricultural Machinery*, vol.42, pp. 48-51, Heilongjiang/China.
- [12] Joshi D C, Chaudhari G V, Sood S, Kant L, Pattanayak A, Zhang K, Fan Y, Janovská D, Meglič V, Zhou M L, (2019). Revisiting the versatile buckwheat: reinvigorating genetic gains through integrated breeding and genomics approach [J]. *Planta*, vol.250, pp.783-801, India.
- [13] Liang S., Jin C., Zhang F., Kang D., Hu M., (2015). Design and experiment of 4LZG-3.0 millet combine harvester (4LZG-3.0 型谷子联合收获机的设计与试验). *Transactions of the Chinese Society of Agricultural Engineering*, vol.31, issue 12, pp. 31–38, Jiangsu/China.
- [14] Liang Z., Li Y., Xu L., Zhao Z., (2016). Sensor for monitoring rice grain sieve losses in combine harvesters. *Biosystems Engineering*, vol.147, pp. 51-66, Jiangsu/China.
- [15] Li X., Ma F., Gao L., (2009). Dropping impact experiment on corn seeds (玉米种子的跌落式冲击试验). *Transactions of the Chinese Society of Agricultural Engineering*, vol.25, issue 1, pp. 113-116, Henan/China.
- [16] Li X., Meng Y., Zhang J., Geng L., Ji J., (2018). Design and test of cleaning device for roller rubbing cylinder sieve of millet (辊搓圆筒筛式谷子清选装置设计与试验). *Transactions of the Chinese Society for Agricultural Machinery*, vol.49, issue 10, pp. 92-102, Henan/China.
- [17] Li H., Xue J., Wang B., Zhang Y., Wu X., Li X., Cui Q., Yang Z., (2020). Tensile properties of foxtail millet leaf sheath, leaf and leaf collar (谷子茎秆叶鞘叶片及其结合部位的拉伸力学性能). *Transactions of the Chinese Society of Agricultural Engineering*, vol.36, issue 18, pp. 11–17, Shanxi/China.
- [18] Li X., Yu Y., Geng L., Wang S., Pang J., Ji J., (2018). Study on collision test of sunflower seed (向日葵籽粒碰撞试验研究分析). *Journal of Agricultural Mechanization Research*, vol.7, issue 7, pp. 175-179, Henan/China.
- [19] Lu Q., Zheng D., Liu Y., Li L., Xu B., Ye S., (2020). Problems and thoughts on mechanized harvesting technology of buckwheat in China (我国荞麦机械化收获技术问题与思考). *Agricultural Engineering*, vol.10, issue1, pp. 6-9, Shanxi/China.
- [20] Lu W., Wang R., Deng Z., (2017). Development status and prospect of threshing technologies for coarse cereal (杂粮联合收获脱粒技术研究现状与展望). *Journal of Chinese Agricultural Mechanization*, vol. 38, issue 11, pp. 11-16, Henan/China.
- [21] Qian Z., Jin C., Ma Z., Zhang D., (2017). Multiple frictional impact dynamics of threshing process between flexible tooth and grain kernel. *Computers and Electronics in Agriculture*, vol.141, issue 9, pp. 276-285, Jiangsu/China.

- [22] Rajasekaran R, Francis N (2021). Genetic and genomic resources for improving proso millet (*Panicum miliaceum* L.): a potential crop for food and nutritional security [J]. *Nucleus (India)*, vol.64, pp.21-32, India.
- [23] Sun J., Yang Z., Guo Y., Cui Q., Wu X., Zhang Y., (2017). Compression mechanical properties and crack formation law of millet grain (谷子籽粒压缩力学性质及损伤裂纹形成机理). *Transactions of the Chinese Society of Agricultural Engineering*, vol.33, issue 18, pp. 306–314, Shanxi/China.
- [24] Sun J., Guo Y., Yang Z., Cui Q., Wu X., Zhang Y., (2018). Experimental study on biomechanical properties of buckwheat grain and viscoelastic properties of buckwheat powder (荞麦籽粒生物力学性质及内芯黏弹性试验研究). *Transactions of the Chinese Society of Agricultural Engineering*, vol.34, issue 23, pp. 287-298, Shanxi/China.
- [25] Tao M., (2018). Research on mechanical properties and shelling test of oil peony seeds (油用牡丹籽粒力学特性及脱壳试验研究). [Unpublished master's dissertation]. Henan University of Science and Technology, Henan/China.
- [26] Wang L., Wu B., Wu Z., Li R., Xin., (2018). Experimental determination of the coefficient of restitution of particle-particle collision for frozen maize grains. *Powder Technology*, vol.338, issue 10, pp. 263–273, Heilongjiang/China.
- [27] Xu L., Li Y., Ma Z., Zhao Z., Wang C., (2013). Theoretical analysis and finite element simulation of a rice kernel obliquely impacted by a threshing tooth. *Biosystems Engineering*, vol.34, issue 23, pp. 146-156, Jiangsu/China.
- [28] Xu L., Li Y., (2009). Critical speed of impact damage on a rice kernel (水稻谷粒冲击损伤临界速度分析). *Transactions of the Chinese Society for Agricultural Machinery*, vol.40, issue 8, pp. 54-57, Jiangsu/China.
- [29] Zhang Y., Cui Q., Guo Y., Li H., (2019). Experiment and analysis of cutting mechanical properties of millet stem (谷子茎秆切割力学特性试验与分析). *Transactions of the Chinese Society for Agricultural Machinery*, vol.50, issue 4, pp. 146–155, Shanxi/China.

EXHAUST NOISE ANALYSIS RESEARCH FOR A SINGLE-CYLINDER DIESEL ENGINE AND EVALUATION OF NOISE FILTRATION BY SIMULATION**STUDII ȘI CERCETĂRI PRIVIND ZGOMOTUL DE EVACUARE PENTRU UN MOTOR DIESEL MONOCILINDRIC ȘI EVALUAREA FILTRĂRII ZGOMOTULUI PRIN SIMULARE****Golgot Claudiu¹⁾; Filip Nicolae¹⁾ ¹**

Faculty of Road Vehicles, Mechatronics and Mechanics, Technical University of Cluj-Napoca / Romania

Tel: 0765429645; E-mail: golgot_claudiu@yahoo.com

DOI: <https://doi.org/10.356.33/inmateh-65-21>**Keywords:** *acoustic, exhaust noise, diesel engine, filter, audio***ABSTRACT**

The paper develops an analysis of exhaust noise for a single-cylinder diesel engine tested in laboratory conditions. The acoustic signal at the engine exhaust system, for the speed range 1,300 – 2,700 rpm was measured and recorded. The results of the noise recordings were subjected to a processing from which the variation of the noise level depending on the engine speed was obtained. Next, the physiological effect of acoustic filtrations for noise recordings was analyzed by simulation. This allowed the optimization of the exhaust noise, having identified the areas and the optimal attenuation effect. In the performed simulations, it was found that the low frequencies require the highest attenuation background.

REZUMAT

Lucrarea dezvoltă o analiză a zgomotului de evacuare pentru un motor diesel monocilindric testat în condiții de laborator. Semnalul acustic este măsurat și înregistrat la evacuarea motorului pentru intervalul variat de turații cuprins între 1.300 - 2.700 rpm. Măsurătorile de zgomot au fost supuse unor prelucrări acustice din care a rezultat variația nivelului de zgomot în funcție de viteza motorului. Efectul fiziologic al filtrărilor acustice a fost analizat prin simulări audio. Acest lucru a permis optimizarea zgomotului de evacuare, identificându-se zonele și efectul de atenuare optimă. Prin simulările efectuate, am constatat că nivelul de joasă frecvență necesită cea mai mare atenuare.

INTRODUCTION

Any pollutant that exceeds normal tolerance or absorption limits is a risk factor for the environment and human health. After the chemical pollution of the air, the noise produced by traffic is the most harmful pollutant in the urban environment (Colin, 2017). Exhaust noise is the main source of noise in internal combustion engines representing a percentage of 20% (Filip, 2000; Matthew, 2004).

Methods for reducing exhaust noise (Peter et al., 2015) by using an attenuator with an adaptable (flexible) internal structure were analyzed. This design allows the control of the acoustic waves according to the engine's functioning variations. With this type of attenuator, it achieved a transmission loss higher than 10 dB in the selected frequency band.

Another noise attenuation analysis using the transmission attenuation method is presented by numerical simulation of a circular attenuator (Wael A, 2020; Wei and Li, 2016). This type of attenuator consists of a resonance chamber and a perforated tube. In this case increasing the exhaust gas flow generally increases the transmission attenuation property and decreases the amplitude of the resonant frequency.

Similarly, to improve the performance of an attenuator mounted to the exhaust of a diesel engine, software simulation was studied and compared to experimental laboratory measurements (Jung et al., 2015). The conclusion was that for the frequency range less than 3,000 Hz the error level between software simulation and physical measurements is very small.

For a minimal influence on the internal combustion engine power, it was analyzed an attenuator with a volume six times larger than the volume of the engine cylinder, a diameter of two and a half times the diameter of the exhaust pipe and a length of four times the size of the diameter (Babu and Amba, 2014).

¹ Golgot Claudiu, Ph.D. Stud.; Filip Nicolae, Prof. M.S. Eng

In the attenuation calculation, the attenuator was equipped with a series of perforated plates of different properties. This type of simulations was performed avoiding the natural resonance frequency of the system, thus obtaining attenuation from 86.77 dB to 74.44 dB.

In an analysis of the exhaust noise level and the back pressure level (*Mohiuddin et al., 2005*), according to various constructive forms of the attenuator, results that the back pressure level is the difference between the exhaust pipe pressure and the atmospheric pressure. Concluding, the number of components (pipes, resonating chambers and perforated orifices) directly influences the flow of exhaust gases through the attenuator. High noise level attenuation means high back pressure, thus influencing the performance of the engine, which is undesirable. For this reason, a sizing calculation is necessary considering the low, medium and high frequency range.

Generally, the most common attenuators used to reduce attenuation noise are composed of several resonant chambers (reactive type). The characteristics of these types of resonators are well presented in the acoustic literature (*Munjaj, 2014*). Further reducing exhaust noise and improving fuel consumption are also proposed in studies using an electromagnetic audio speaker as a noise generator (*Rossi, 2002*). Changing the dimensions of the resonant chambers changes the resonant frequency and the amplitude of pressure in the resonator cavity (*Myonghyon, 2008*).

A theoretical calculation analysis predicting the attenuation of acoustic intensity by transmission loss (TL) uses the transfer matrix method (TMM) compared to experimental tests (*Mihai and Ovidiu, 2006*). For the experimental testing of the acoustic transmission loss (TL) of the attenuator in the absence of a noise generated by the exhaust gas, the stand is composed of equipment's such as: audio signal generator; signal power amplifier; omnidirectional audio speakers; capacitive microphones; data acquisition board and data storage unit, computer (PC).

According to experimental tests the mathematical model does not show major differences (except for certain areas of the frequency spectrum) so it can be considered a reliable method in calculating noise attenuators. The acoustic behavior of a double-chamber circular exhaust system and its effects depends on various changes such as the attenuator material, the number of resonant chambers and their size (*Erkan et al., 2021; Selamet et al., 2003*). In this situation, the acoustic attenuation performance can be significantly improved because of these effects.

Similarly, an optimization study of an attenuator composed of several resonant chambers positioned in a cascade, each with different characteristic properties of transmission loss (TL) was analyzed (*Lee J. et al., 2020; Xiang Yu et al., 2015; Fang et al., 2009*). To improve the level of attenuation (TL) from the perspective of increasing the frequency range in the operation of the attenuator, an analysis on the effect of changing the internal geometric parameters compared to the initial stage is presented. Also, in this case the test stand consists of a pulse generator speaker, a power amplifier, piezoelectric microphones, data acquisition board, computer unit (PC) and cone-shaped sound-absorbing material at the end of the piping.

In this paper, it is aimed at developing a method for identifying the characteristic of exhaust noise measured in a single-cylinder diesel engine and presenting a technique for optimizing it by simulation. The novelty of the research lies in the fact that a simulation of the noise filtrations was performed compared to the physiological audio effect. Also, the identification of frequencies to attenuate the sound pressure level is the basic information necessary to design efficient noise attenuators.

MATERIALS AND METHODS

Noise measurements were performed on the exhaust system of a single-cylinder diesel engine code KM186FA (four stroke, $P_{max} = 5.7$ kW / 3,000 rpm), without a noise attenuation system attached, for a wide range of engine speeds at-load free mode. All measurements are in linear frequency bands without acoustic weighting. The value of the engine speed was measured using a digital laser tachometer with a tolerance of 1%. The equipment used to configure the experimental stand are the computer unit, the Solo-01dB sound level meter. The schematic configuration of the experiment configuration is shown in Fig. 1. The time interval for each measurement (at each engine speed) was 60 seconds. For a comparison check of the equivalent noise level L_{eq} , two acoustic sound level meters, initially calibrated (Solo-01dB and Norsonic-12 equipment) were used. The Solo-01dB equipment allows a more detailed visualization and processing of noise variation in frequency bands.

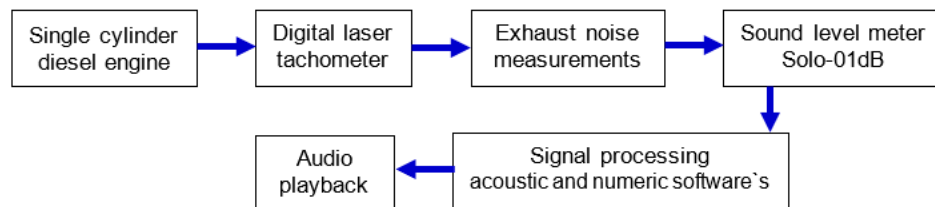


Fig. 1 - Schematic configuration of the experiment setup

The proposed research method requires several stages. These are shown in the block diagram in Fig. 2. The first stage was to collect data by performing noise measurements at the engine exhaust positioning the sound level meters at a distance of 0.5 m, height of 1 m and at 45 ° from the exhaust. The signal was recorded in the real time with a fixed period of 60 seconds set in the sound level meters. The acoustic signal was recorded directly on the PC unit using software specific to the sound level meters. Due to the very large number of recorded values, the signal was processed in several stages (3,072,000 units with a purchase period of 1,953·e-0.5 seconds).

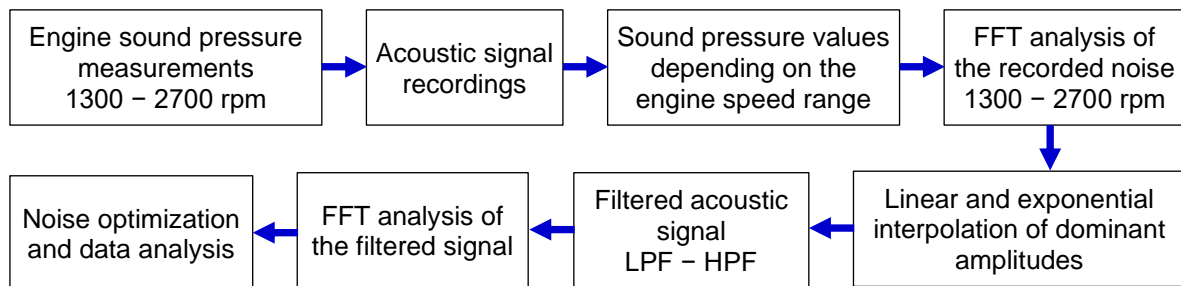


Fig. 2 - Schematic configuration with the main stages of the experiment

The second stage was the decomposition into FFT (Fast Fourier Transform) series where the level of the dominated amplitudes and their occurrence frequencies were determined depending on the engine's speed. Following the results obtained, a calculation of linear and exponential interpolation of the dominant amplitudes of order 1, order 2 and order 3 depending on the engine speed was performed. In the third stage, numerical processing, and acoustic filtration (LPF and HPF) of the recorded acoustic signal were performed, through which the noise-generating components and the resulting physiological effect were determined. For a more detailed analysis, the filtered sound pressure values were also decomposed into FFT series.

In the fourth stage, following the experimental determinations obtained previously, it was achieved attenuation by selectively combining the two types of acoustic filters (LPF and HPF) in frequency bands. From the results, the efficiency of acoustic filters and the possibility of experimental determination of the frequency range, for which the attenuator has the expected efficiency, were identified.

SOUND PRESSURE OF THE EXHAUST NOISE

For a detailed visualization of the acoustic signal recorded following the acoustic measurements, the time required to perform three engine cycles depending on speed was sampled. To determine the value of the sample, Equation (1) was used (Filip and Candale, 2002)

$$\Delta_t = \frac{K}{\frac{n}{60} \cdot \frac{2}{\delta}}, \text{ [sec]} \quad (1)$$

where:

Δ_t is the time interval [sec], K is the number of complete engine cycles (three cycles), δ is the number of engine strokes (four strokes) and n is the measured engine operating speed [rpm].

To calculate the x number of values recorded for three engine cycles from the range of values, the Equation (2) was used

$$x = \Delta_t \cdot f_{aq}, \quad (2)$$

where:

f_{aq} is the acquisition frequency of the sound level meter, for the speeds at which the acoustic signal was recorded (in our case 51,200 values / sec).

The calculated values using Equation (1) and Equation (2) are presented in Table 1 where it can be seen, the time interval calculated for three engine cycles at 2700 rpm is 0.14 seconds.

Table 1

Calculated values, depending on engine speed

Engine Speed [rpm]	1,300	1,600	1,900	2,100	2,400	2,700
Time interval Δt [sec]	0.30	0.24	0.20	0.18	0.15	0.14
Number of value x	15,360	12,288	10,240	9,216	7,680	7,168

RESULTS

Fig. 3a shows the variation of the sound pressure recorded for a calculated interval of 0.14 seconds measured at the evacuation of the single-cylinder engine for the speed of 2,700 rpm (at load-free mode). A maximum sound pressure level of 12 Pa can be observed. Analyzing the variation of the sound pressure level measured at the engine speed stabilized at 2,700 rpm confirmed that three engine cycles were captured and the noise measurements performed are correct. Those three tips represent the reference points corresponding to the opening of the engine exhaust valve. For more details, the complex acoustic signal was decomposed into FFT frequency series for each range of idling engine speeds to determine the dominant frequencies and amplitude level. In Fig. 3b it was represented the level of FFT amplitudes at the speed of 2,700 rpm for the low frequency range (200 Hz) where a maximum value of over 2 Pa resulted. Analyzing the amplitude level, in the low frequency range, a linear increase from 0 to 45 Hz and an exponential decrease with increasing frequency were observed.

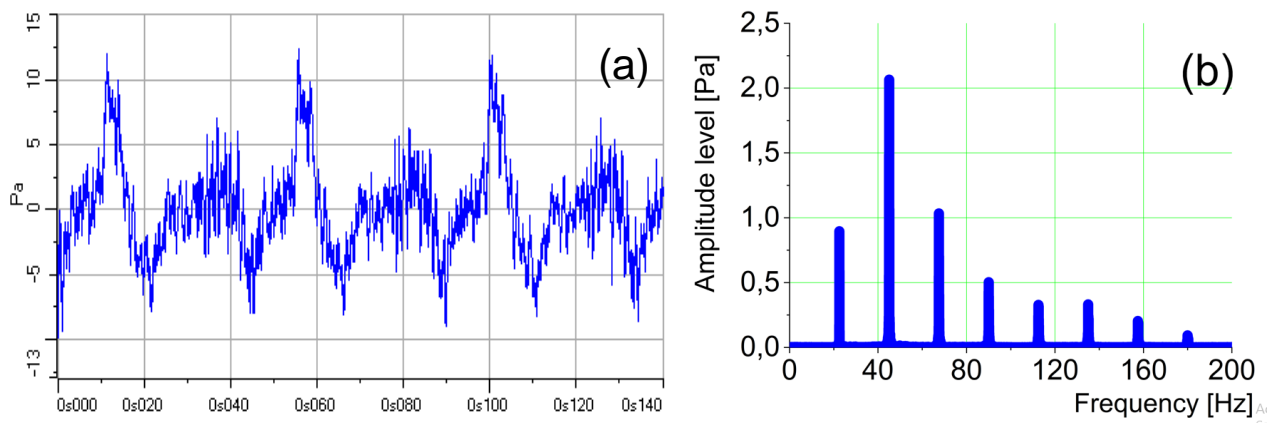


Fig. 3 - Acoustic signal measured at the engine exhaust for the speed range 2,700 rpm
 (a) Acoustic pressure for 3 engine cycles, time = 0.14 sec. at load-free mode,
 (b) Detailed FFT analysis in the low frequency range

From the FFT analysis, the variation of the first three dominant amplitudes and their frequency of occurrence (Table 2) were extracted. The maximum measured values were obtained at a speed of 2,700 rpm, 2.6 Pa. The acquisition frequency of this sound level meter at which the acoustic signal was recorded is 51,200 values / sec. It is observed how the amplitude level decreases with increasing frequency and the maximum measured values are around frequencies lower than 12,000 Hz. Above the frequency of 16 kHz (ultrasound area) the measured noise is not found in the human audibility zone.

Table 2

Data extracted from the FFT analysis of the acoustic signals recorded at the engine exhaust

Engine Speed [rpm]	Amplitude order [Pa]			Amplitude frequency [Hz]		
	A ₁	A ₂	A ₃	f ₁	f ₂	f ₃
1,300	0.18	0.40	0.41	13.00	27.00	40.50
1,600	0.17	0.54	0.49	13.50	27.00	41.00
1,900	0.24	0.45	0.68	15.80	31.50	47.30
2,100	0.20	0.44	0.48	17.30	35.00	52.00
2,400	0.46	1.13	0.40	20.00	40.00	60.00
2,700	0.88	2.60	1.03	22.40	45.00	68.00

For the validation of the measurements, identifying the main oscillation frequency of the pressure wave evolving in the exhaust system, derived from Equation (1), depending on the engine speed was calculated by:

$$f_1 = \frac{n \cdot z}{60} \cdot \frac{2}{\delta}, \quad [\text{Hz}] \quad (3)$$

and

$$f_2 = f_1 \cdot 2, \quad [\text{Hz}] \quad (4)$$

where: δ is the number of engine strokes (four strokes), n is measured engine operating speed, z is the number of engine cylinders, f_1 is first degree frequency and f_2 is second degree frequency.

By comparing the measured data values with the calculated values Equation (3, 4) of the first two dominant frequencies (f_1 and f_2), they are almost identical except for the frequencies measured at 1,300 rpm. Thus, it is confirmed that the measurements performed in the laboratory are correct. By mathematical interpolation, the sound pressure level of the first two dominant amplitudes respects an exponential increase with increasing speed (Fig. 4a. and Fig. 4b.). In the case of third order amplitudes (Fig. 4c.) the amplitudes show a very large pressure variation, especially for frequencies between 1,900 Hz and 2,400 Hz, which is why linear or exponential interpolation for third order amplitude cannot be considered.

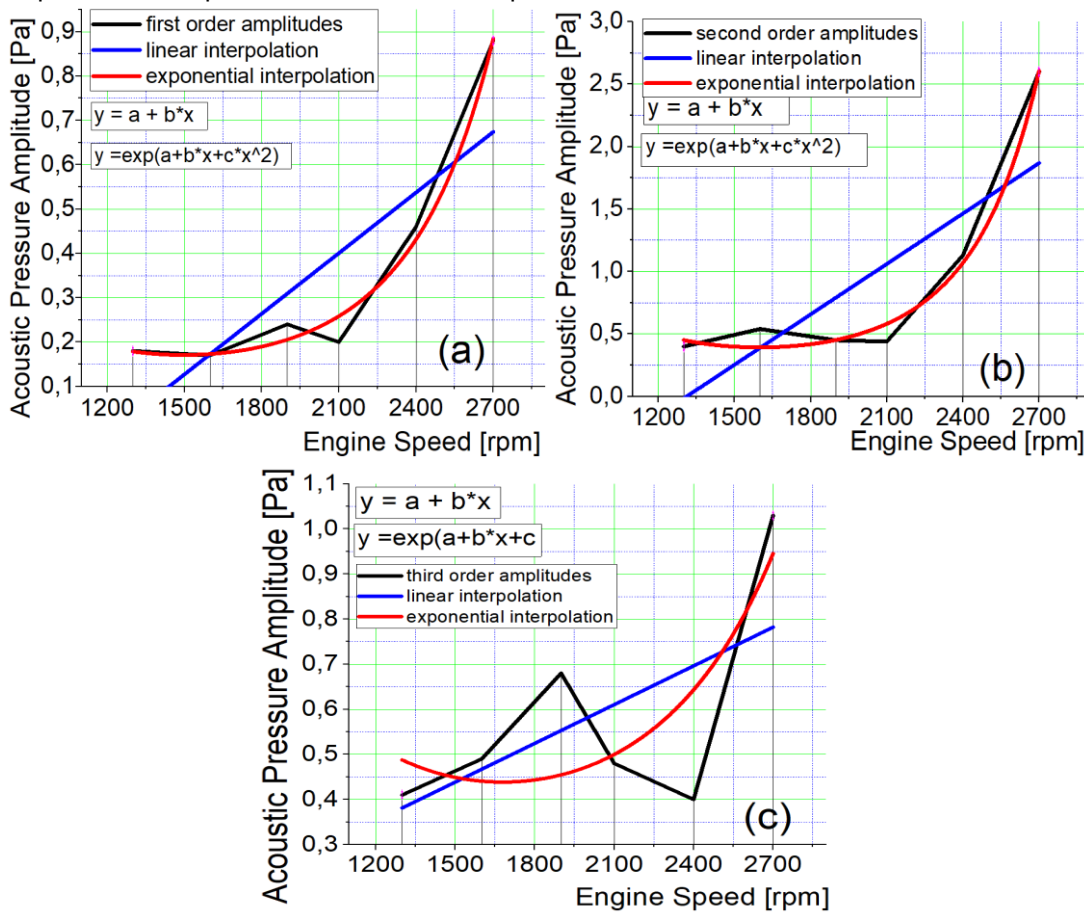


Fig. 4 - Linear and exponential FFT amplitude interpolation, for the dominant frequencies
 (a) first order amplitudes, (b) second order amplitudes, (c) third order amplitudes

SIMULATION ANALYSIS OF THE EFFECT OF ACOUSTIC FILTERS

To simulate the effects of acoustic filtering, the initially measured signal and the filtered signal are transformed into a "waveform audio file format ". The acoustic filters used in the simulation are low pass filter LPF for high frequency attenuation and high pass filter HPF for low frequency attenuation. These types of filters were chosen because they are most often used in the field of acoustics. For a more detailed image of the component spectral elements, the obtained pressure values are transformed into a series of FFT type amplitudes. In this case the operating frequencies of the acoustic filters are in the range of 50 Hz – 20,000 Hz depending on the human audibility threshold relative to the low, medium and high frequency range. For low pass filter attenuation LPF shown in Fig. 5a. and Fig. 5b., it can be seen how the number of components of the attenuated signal decreases along with the attenuation frequency.

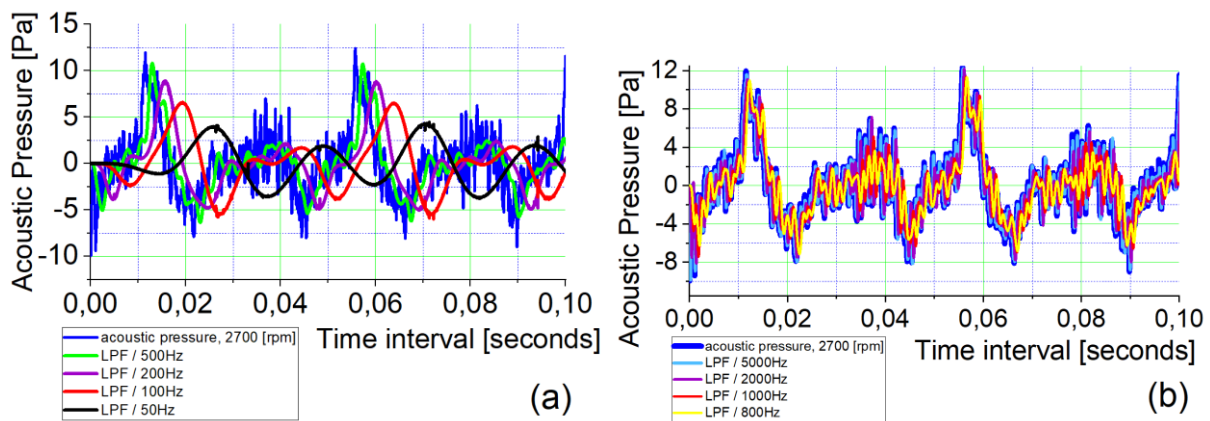


Fig. 5 - Comparison between the sound pressure of the initial signal (2,700 rpm) and the signal filtered by LPF
(a) at 50 Hz, 100 Hz, 200 Hz and 500 Hz, (b) at 800 Hz, 1,000 Hz, 2,000 Hz and 5,000 Hz

After the attenuation LPF by audio playback of the processed signal, from the auditory point of view the perceived noise decreases with the reduction of the attenuation frequency within the limits of the audibility range. For attenuation at 50 Hz, 100 Hz and 200 Hz LPF the noise is difficult to perceive auditorily, but it is present in the form of high amplitude pulsations. These pulsations increase in number of spectral elements as the attenuation frequency increases. After the filters for each attenuation frequency, an FFT type analysis was performed. From this, amplitudes of noise-generating components and their frequency were obtained.

By comparing the FFT analysis of the initial unfiltered signal (Fig. 3b.) and the analysis of the filtered signal by LPF, depending on the actuation frequency (Fig. 6a. and Fig. 6b.), a significant attenuation is observed in the case of 50 Hz filtering. The attenuation of the dominant amplitudes decreases by increasing the actuation frequency.

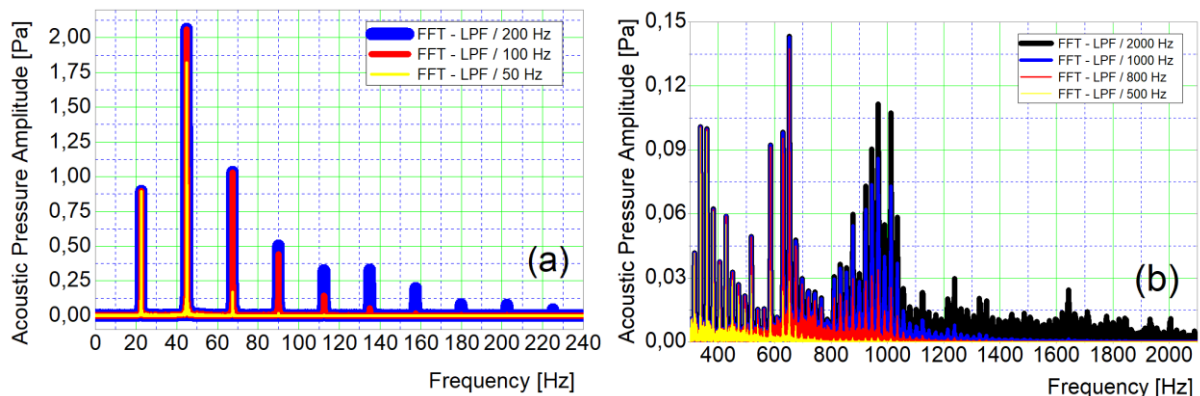


Fig. 6 - FFT diagram of the signal filtered by the LPF method for engine speed of 2,700 rpm
(a) at 50 Hz, 100 Hz and 200 Hz, (b) at 500 Hz, 800 Hz, 1,000 Hz and 2,000 Hz

For the attenuation at 500 Hz LPF, in addition to the pulsations present in the low frequency range, there is a noise specific to internal combustion engines but much lower in intensity. By attenuating at 800 Hz LPF, the perception of the annoying auditory noise begins, being close to the threshold of the painful sensation (120 dB). As the attenuation LPF frequency increases, the noise is composed of an increasing number of component elements (high frequency amplitudes) making it more disturbing auditorily (1,000 Hz, 2,000 Hz, 5,000 Hz, 8,000 Hz, and 10,000 Hz). From the FFT diagrams it can be seen how the acoustic filter LPF works depending on the operating frequency at 500 Hz, 800 Hz, 1,000 Hz and 2,000 Hz. An increase in the number of unfiltered FFT amplitudes can be observed by increasing the actuation frequency. In terms of high frequency LPF works best up to a frequency of 500 Hz. The attenuation effect of the LPF filter above the frequency of 10,000 Hz compared to the initial recorded signal is very difficult to perceive because it approaches the upper limit of the high frequencies heard by the human ear (20 kHz).

In the case of HPF attenuation in Fig. 7a., the number of component elements of the attenuated signal increases with the reduction of the attenuation frequency. From the variation of the acoustic pressure of the attenuated signal, a higher level of acoustic pressure is observed in the frequency range between 50 Hz and 2,000 Hz. In the case of the FFT analysis for HPF filtration shown in Fig. 7b., it can be seen how the number of amplitudes decreases by increasing the actuation frequency. For the attenuation at 50 Hz HPF, compared

to the initial signal (FFT analysis, Fig. 3b.), a significant attenuation of the first two dominant amplitudes (22.4 Hz and 45 Hz) is observed. In this case the level of maximum linear sound pressure was reduced from 12 Pa (initial signal) to 8 Pa.

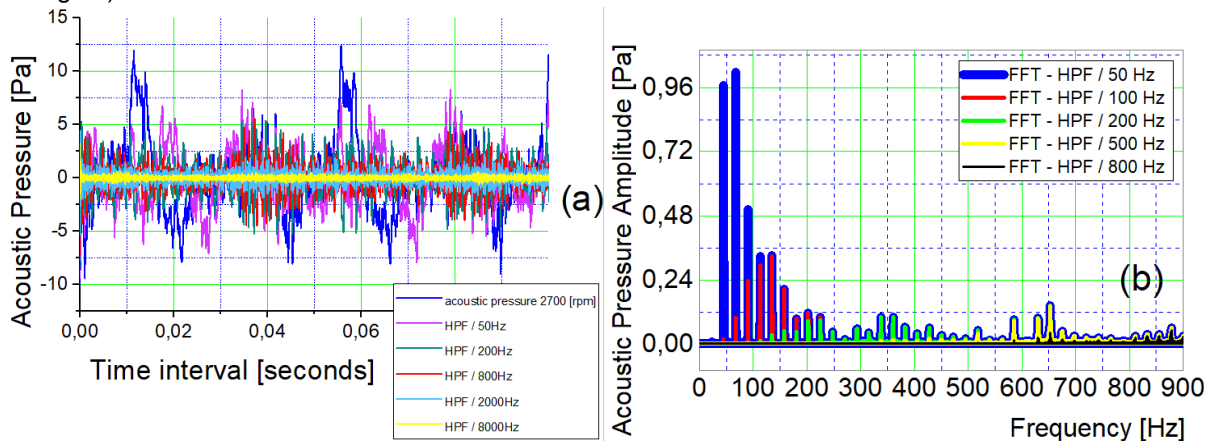


Fig. 7 - HPF attenuation of the initial signal at 2,700 rpm

(a) Acoustic pressure of the signal filtered by HPF at 50 Hz, 200 Hz, 800 Hz, 2,000 Hz and 8,000 Hz
 (b) FFT diagram of the signal filtered at 50 Hz, 100 Hz, 500 Hz and 800 Hz HPF

From an auditory point of view, for the attenuation HPF by audio playback of the signal saved in audio format, the perceived noise decreases significantly with the increase of the actuation frequency, especially by the attenuation of low and medium frequencies (20 Hz – 1,600 Hz). For attenuation HPF at 50 Hz, 100 Hz, 200 Hz, 500 Hz and 800 Hz, high-amplitude pulses are completely attenuated, but the perceived noise still contains high-pitched amplitudes that are disturbing to the ear. By attenuation HPF at 1,000 Hz, auditory noise is significantly reduced compared to the initial measured signal but still contains enough amplitudes of medium frequency that are disturbing. By attenuating HPF to 2,000 Hz, the noise has a very low level of sound pressure level being less disturbing auditorily. By attenuating at 5,000 Hz, 8,000 Hz and 10,000 Hz HPF, an almost complete reduction of the unfiltered signal measured at 2,700 rpm was obtained. From the audio playback, the resulting sound has small amplitude, so a significant audio amplification is needed to be able to perceive the difference between the three filters. Above the frequency of 10,000 Hz, the resulting noise can no longer be perceived by the human ear.

OPTIMIZATION OF MEASURED NOISE

According to the analysis performed, it is possible to identify the main frequency ranges containing FFT spectral components producing dominant noise and the physiological effect signaled when playing audio files as follows (Fig. 8.):

- attenuation zone 1 between 0 Hz - 200 Hz
- attenuation zone 2 between 300 Hz - 400 Hz
- attenuation zone 3 between 550 Hz - 700 Hz
- attenuation zone 4 between 900 Hz – 1,050 Hz
- attenuation zone 5 between 2,000 Hz – 25,600 Hz

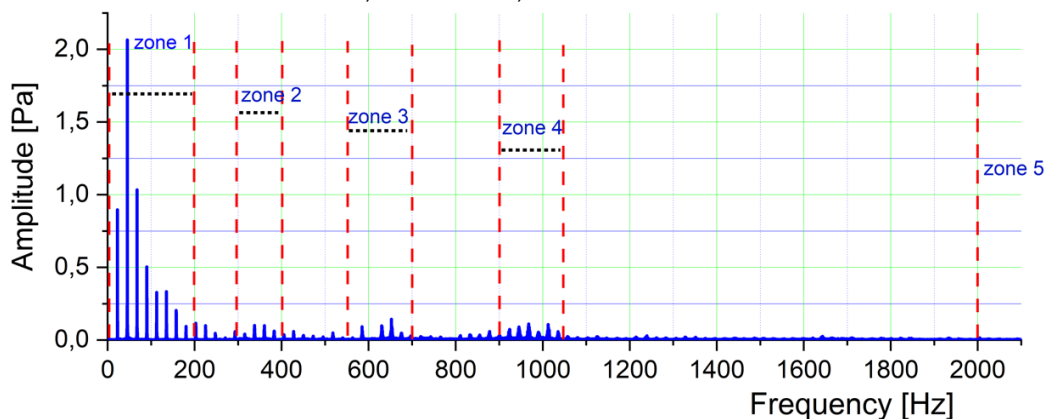


Fig. 8 - FFT diagram of the initial acoustic signal measured at 2700 rpm and filtered frequency areas

Within the acoustic processing software, these attenuation limits were chosen experimentally based on the level of the maximum FFT amplitudes in the low frequency, medium frequency, high frequency range and the specific stamp of the sound resulted from the audio files. In the case of exhaust noise, measured at 2,700 rpm, for this selective attenuation of high amplitude frequency ranges, the following LPF and HPF filters are applied as indicated:

- filtering HPF / 200 Hz and LPF / 300 Hz
- filtering HPF / 400 Hz and LPF / 550 Hz
- filtering HPF / 700 Hz and LPF / 900 Hz
- filtering HPF / 1,050 Hz and LPF / 2,000 Hz

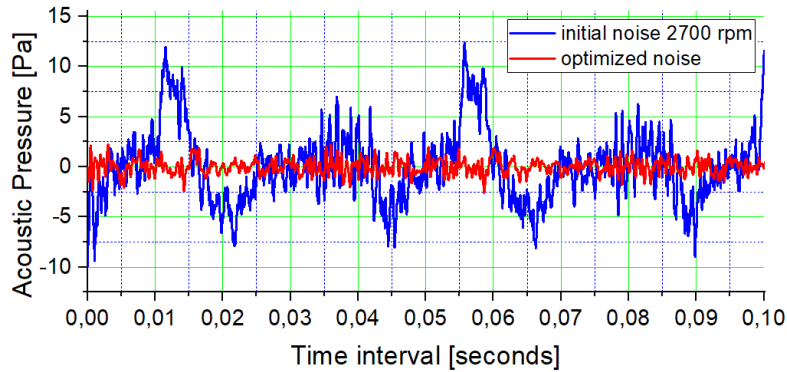


Fig. 9 - Comparison between the acoustic pressure of the initial signal (2,700 rpm) and the signal, optimized by selective filtering (LPF - HPF)

After the filtering, the audio files were generated separately. Final signal from these selective filtering contains all audio files combined (Fig. 9.). Fig. 10a. shows the FFT analysis of the signal attenuated by LPF and HPF compared to the initial signal (FFT analysis, Fig. 3b.). A complete attenuation of amplitudes lower than 200 Hz is observed so the high amplitude pulsations are significantly reduced especially in the low frequency range. The maximum value of the acoustic pressure amplitude of 2 Pa is reduced to 0.1 Pa for optimized signal.

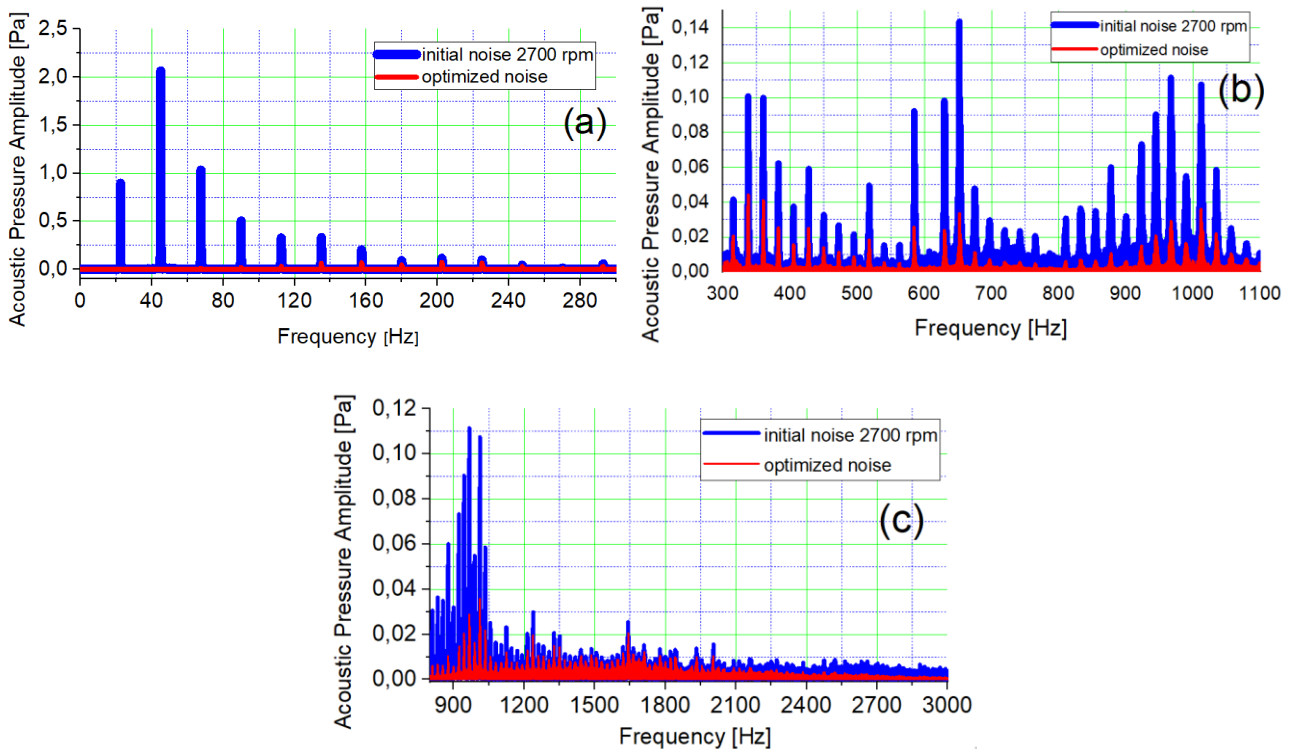


Fig. 10 - Comparison of FFT analysis, initially measured signal and signal optimized by LPF and HPF (2,700 rpm) (a) frequency range 0 Hz - 300 Hz, (b) frequency range 300 Hz – 1,100 Hz, (c) frequency range 750 Hz – 3,000 Hz

From the FFT analysis for the frequency range 300 Hz – 1,100 Hz (Fig. 10b.), the optimized signal is close in shape to the initial signal but the amplitude level is much lower and the resulting noise is less disturbing auditorily. By audio playback of the attenuated signal, the resulting noise is close to the stamp of the initially measured sound and at a much lower level. The tone of the noise did not change significantly, but its intensity decreased. **Error! Reference source not found.**c. shows the FFT analysis for the 750 Hz – 3,000 Hz frequency range of the attenuated signal / initial signal, where an almost complete attenuation of the high frequency range is observed.

CONCLUSIONS

The result and the audio effect obtained from the acoustic filters can be highlighted only by playing audio files made in waveform audio files format. Following the attenuation and optimization stages, the audio playback of the generated effect is achieved by using an amplifier, a speaker and a sound level meter. According to the experimental optimization, the need to attenuate the measured noise at the exhaust (for this type of engine) for the 20 Hz – 3,000 Hz frequency range is confirmed.

The audio files are generated and processed separately for each type of attenuation applied, resulting in an audio signal containing data values representing the variation of the optimized sound pressure level. The optimization by the selective combination in frequency bands of the low pass filters (LPF) and high pass filters (HPF) was obtained after a total summation of the filtering effects in a single audio file. The main frequency ranges, containing dominant noise generating FFT spectral components in this processing, are presented compared to the initial noise depending on the resulting specific stamp, transmission frequency and amplitude level.

Due to experimental results obtained, the efficiency can be confirmed by the selective combination of the two types of acoustic filters, thus determining the frequency range in which they have an effect. The attenuated frequency range and the optimized method applied require an individual approach depending on the type of internal combustion engine and its operating speed range.

By using this method of analysis, it was possible to make a classification of the attenuation effects generated according to the version of the attenuator chosen in correlation to the analysis of the primary noise supplied / produced by the engine without attenuation system and components. Even if the noise attenuation effects and optimizations in the frequency bands are auditorily similar to the actual situation, it should be specified that in this case the gas flow is considered equal to zero.

It should be noted that the proposed noise attenuation approach technique has an obvious degree of novelty. This method of analysis is less found as research in the literature. This has an obvious applicability in establishing the optimal parameters for the design of noise attenuators. The fact that the audio playback indicated that the stamp of the sound does not change, we suggest, possibly a new applicability regarding the generation of low intensity fake noise inside cars equipped with electric motors to simulate a variation of noise in relation to specific driving conditions.

This function of reproducing a false noise inside electric vehicles could be activated and controlled by the driver, who can choose the specific sound of the internal combustion engine, according to preferences, from a wide range of processed sounds. In this case, the possibilities of selecting and audio playback of sounds specific to internal combustion engines could be unlimited, varying by type of simulated engine, type of simulated vehicle and driving conditions, respectively acceleration, deceleration, engine speed, vehicle speed, engine torque etc.

REFERENCES

- [1] Babu, A.R., Amba, P.R., (2014), Simulation of new design muffler to reduce noise in exhaust system of SI engine, *International journal of mechanical and production engineering*, vol.2, no.11, ISSN 2320-2092, pp. 5-9;
- [2] Colin, H., Con, D., Kristy, H., (2017), *Fundamentals of acoustics and frequency analysis*, Publishing House Wiley;
- [3] Erkan, S., Hakan, A., Burak, B., (2021), A statistical design optimization study of a multi-chamber reactive type silencer using simplex centroid mixture design, *Journal of low frequency noise, vibration and active control*, vol.40(1), SAGE Journals, pp. 626-638;
- [4] Fang, J., Zhou, Z., Hu, X., Wang, L., (2009), Measurement and analysis of exhaust noise from muffler on an excavator, *International journal of precision engineering and manufacturing*, vol.10, no.5, ISSN 1392-8716, pp. 59-66;

- [5] Filip, N., Candale, L., (2002), Researches regarding the noise conversion from tractor engine in order to reduce the intake manifold noise, (Cercetări de conversie a zgomotului la un motor de tractor pentru a reduce zgomotul din colectorul de admisie), *40th Symposium actual tasks of agricultural engineering*, vol.8, Croatia, ISSN 1333-2651, pp. 311-318;
- [6] Filip, N., (2000), *Vehicle noise, (Zgomotul la autovehicule)*, Publishing House Toderescu, Cluj-Napoca / Romania, ISBN 973-99659-9-7;
- [7] Jun, F., Wei, C., Yuan, T., Wenhua, Y., Guangming, L., And Yu, L., (2015), Modification of exhaust muffler of a diesel engine based on finite element method acoustic analysis, *Advances in mechanical engineering*, vol.7, no.4, SAGE Journals, pp. 1-11;
- [8] Lee, J. K., Oh, S. K., Lee, J. W., (2020), Methods for evaluating in-duct noise attenuation performance in a muffler design problem, *Journal of sound and vibration*, vol.464, Elsevier, ISSN 0022-460X;
- [9] Matthew, H., (2004), *Vehicle refinement controlling noise and vibration in road vehicles*, vol.1, Butterworth-Heinemann, United Kingdom, ISBN 9780080474755;
- [10] Mihai, B., Ovidiu, V., (2006), The mufflers modeling by transfer matrix method, (Modelarea atenuatorului de evacuare prin metoda matricei de transfer), *10th WSEAS International conference on applied mathematics*, Dallas, Texas, pp. 476-483;
- [11] Mohiuddin, A.K.M., Mohd, R., Shukri, M., (2005), Experimental study of noise and back pressure for silencer design characteristics, *Asian network for scientific information*, vol.5, no.7, ISSN 1812-5662, pp. 1292-1298;
- [12] Munjal, M., (2014), *Acoustics of ducts and mufflers*, Publishing House Wiley, ISBN 978-1-118-44312-5;
- [13] Myonghyon, H., (2008), *Sound reduction by a Helmholtz resonator*, PhD. Thesis, Lehigh University, Pennsylvania;
- [14] Peter, S., Mirko, C., Primoz, L., Jurj, P., (2015), Adaptive muffler based on controlled flow waves, *Journal of the acoustical society of America*, vol.137, no.6, pp. 503-509;
- [15] Rossi, F., (2002), Active noise control technique to improve engine efficiency, Energy and environment, centro interuniversitario di ricerca sull'inquinamento e sull'ambiente, pp. 1-12;
- [16] Selamet, A., Denia, F.D., Besa, A.J., (2003), Acoustic behavior of circular dual-chamber mufflers, *Journal of sound and vibration*, vol.265, no.5, ISSN 1095-8568, pp. 967-985;
- [17] Wael, A, A., (2020), An exact solution for acoustic simulation based transmission loss optimization of double-chamber silencer, *Sound & Vibration*, Tech Science Press, vol.54, no.4, ISSN 1541-0161, pp. 215-224;
- [18] Wei, F., Li-Xin, G., (2016), An investigation of acoustic attenuation performance of silencers with mean flow based on three-dimensional numerical simulation, *Shock and Vibration*, Hindawi Publishing Corporation, vol.2, ISSN 1070-9622, pp. 1-12;
- [19] Xiang, Y., Yuhui, T., Li, C., Jie, P., (2015), Sub-chamber optimization for silencer design, *Journal of sound and vibration*, vol. 351, no.8, Elsevier, ISSN 0022-460X, pp. 57-67.

DESIGN AND PARAMETER OPTIMIZATION OF LAYERED FERTILIZATION OPENER FOR WHEAT, BASED ON EDEM

基于 EDEM 的小麦分层施肥开沟器设计及参数优化

Zhilong Zhang^{1,2)}, Jinlong Zheng¹⁾, Aijun Geng^{1,2)}, Ji Zhang^{1,2)}, Abdalla N. O. Kheiry³⁾, Ang Gao¹⁾ ¹

¹⁾ College of Mechanical and Electronic Engineering, Shandong Agricultural University, Tai'an /China;

²⁾ Shandong Provincial Engineering Laboratory of Agricultural Equipment Intelligence, Tai'an;

³⁾ College of Agricultural Studies, Sudan University of science and Technology, Khartoum, Sudan;

Tel:+86-0538-8242500 E-mail: gengaj@sdau.edu.cn

DOI: <https://doi.org/10.356.33/inmateh-65-22>

Keywords: agricultural machinery; layered fertilization opener; EDEM; parameter optimization

ABSTRACT

Applying different types of fertilizers to different depths of soil according to demand is advantageous in that it can optimize the distribution of nutrients in arable soil, adjust the nutrient supply of each growth stage of wheat, and increase grain yield. In the study, a layered fertilization opener that could realize the layered fertilization was developed. The interaction model between the opener, fertilizer and soil was established using EDEM simulation software. A response surface analysis was used to determine the optimal parameters of the opener. Specifically, the horizontal distance between the fertilizer drop openings was 140 mm, the machine speed was 1.05 m/s, and the angle of the opener was 37°. Furthermore, field experiments demonstrated that the average depth of upper layer was 8.39 cm, the average depth of middle layer was 16.465 cm, the average depth of lower layer was 24.025 cm, the average spacing of upper layer was 8.075 cm, and the average spacing of lower layer was 7.6 cm. The corresponding findings demonstrated that the layering effect of the opener met the requirements of the fertilization standard.

摘要

将不同种类的肥料根据需求量分层施入不同深度土层，可优化养分在耕层土壤中的分布，调节小麦各生长发育阶段的养分供给，进而提高籽粒产量。本文设计了一种分层施肥开沟器并进行了参数优化。利用 EDEM 仿真软件建立施肥装置与土壤相互作用模型，分析了机具行进速度、落肥口之间的水平距离、开沟器倾斜角等参数对土壤回流以及肥料分层效果的影响。利用响应面分析各因素对分层施肥效果的影响，并得到最优参数为落肥口水平距离为 140 mm，机具行进速度为 1.05 m/s，开沟器倾角为 37°。对样机加工并进行田间试验，试验得出上层施肥平均深度 8.39 cm，中层施肥平均深度 16.465 cm，底层施肥平均深度 24.025 cm，上层施肥间距平均 8.075 cm，下层分层施肥间距平均 7.6 cm。整机分层效果较好，符合分层施肥作业标准要求。

INTRODUCTION

The utilization of granular fertilizers is an important method in increasing crop yields in agricultural production (Li B et al, 2021). In China, fertilizers are used at early and later stages, and fertilizers are usually applied on the soil surface manually or mechanically (Yang Q et al, 2020). This mode of fertilization can improve the fertilizer utilization rate, which has been widely adopted in practice. However, late topdressing increased the number of machines entering the field, resulting in problems such as soil compaction.

In order to improve fertilizer utilization, various research has been conducted that focused on the deep application of fertilizers (Bautista E et al, 2001; Quinn D et al, 2020). The deep application of fertilizers involves using fertilizer machinery to place fertilizers to the lower side of the seed in a quantitative and uniform manner. This method of fertilization can improve fertilizer utilization while reducing environmental pollution (Kargbo M. et al, 2016; Min J et al, 2021). Layered fertilization involves applying the fertilizer required by the crop into the soil at a time suitable to meet the nutrient requirements of the crop in different growth periods, which can increase the fertilizer utilization rate and yield (Abbas A. et al, 2014). In order to achieve a good layered fertilization effect, some studies focused on the design and analysis of layered fertilization opener. Yang R et al. (2018) proposed layered fertilization technology based on surface drainage and V type anti-blocking structure, and developed a layered fertilization opener for potato planter. While, some studies optimized the parameters of the layered fertilization device by using simulation method.

¹ Zhilong Zhang, Ph.D.; Jinlong Zheng, B.D.; Aijun Geng, Ph.D.; Ji Zhang, Ph.D.; Abdalla N. O. Kheiry, Ph.D.; Ang Gao, B.D.

Yang Q. *et al.*, (2020), researched the working process of the layered fertilization device based on EDEM, the relationship between the amount of fertilizer discharged of the upper and middle fertilizer outlets and the factors such as front-end width, rear-end width and installation angle of fertilization adjustment piece was determined. Wang Y. *et al.*, (2016), investigated the trend of fertilizer distribution ratio for different lift angles and working length of fertilization-piece based on the DEM. Ding S. *et al.*, (2018), studied the layer fertilization device and developed an integrated model to simulate the metering and banding processes of the dual-band applicator using the DEM. Fertilizer fertilization involves the interaction of soil, fertilizer, and machinery. However, the above studies rarely involve the effect of soil return on the layering effect of fertilizers.

The objective of the present study is to design a layered fertilization opener to attain precise layered fertilization, develop a simulation model to study the motion of granular fertilizer following fertilization, analyze the speed of the machine and horizontal distance between the openings on the effect of layered fertilization, determine the optimal parameters, and verify the layered effect through field experiments.

MATERIALS AND METHODS

STRUCTURE DESIGN OF THE LAYERED FERTILIZATION OPENER

Studies have shown that applying fertilizers in the subsoil layers of 8 cm, 16 cm, and 24 cm according to demand of wheat optimizes the distribution of nutrients in the soil and regulates the nutrient supply at each growth stage of wheat, thereby increasing the yield (Wen Y *et al.*, 2017). In order to provide the nutrients necessary for different growth periods of wheat, the layered fertilization device should be able to apply different types of fertilizers in layers, while ensuring that the layer spacing is 8 cm.

The layered fertilizer opener was mainly made up of a shovel point, shank, fertilizer grooves and fertilizer drop opening, as shown in Fig.1(a). The fertilizer grooves and fertilizer metering device were connected through three independent fertilizer tubes to ensure that fertilizers with different nutrients may be applied to each layer. The three fertilizer openings were distributed in a ladder shape to allow a certain horizontal distance between the openings to increase soil fall time. As shown in Fig.1(b), according to the agronomic requirements of layered fertilization for wheat, the fertilization depth h_3 was 24 cm, and the width w of the opener was 2.6 cm. The vertical spacing h_1 between the bottom and middle fertilizer drop opening, as well as that of h_2 between the middle and the upper fertilizer drop opening, were both 8 cm. In order to ensure that the effect of stratification was obvious, the horizontal distance d_1 between the bottom and middle fertilizer drop opening and the horizontal distance d_2 between the middle and upper fertilizer drop opening should be greater than 11.5 cm. In order to meet the requirements of having a compact structure, the angle α should be selected within the range of $20^\circ\sim 50^\circ$ (Zhang J. *et al.*, 2014).

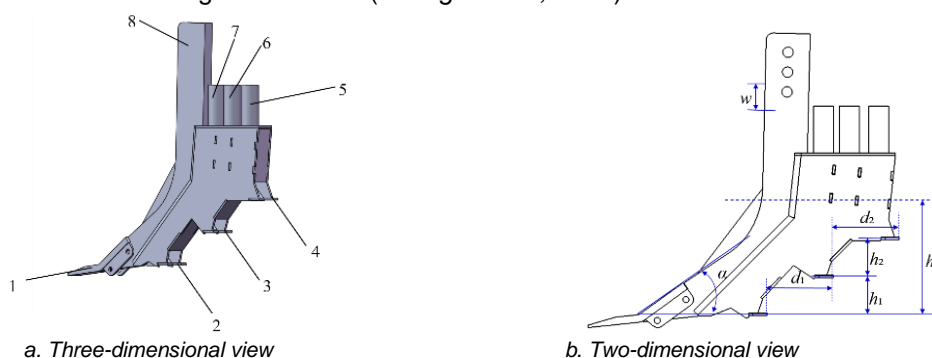


Fig. 1 - Layered fertilization opener

1. Shovel point; 2. Lower fertilizer drop opening; 3. Middle fertilizer drop opening; 4. Upper fertilizer drop opening; 5. Upper fertilizer tube; 6. Middle fertilizer tube; 7. Lower fertilizer tube; 8. Shank

SIMULATION AND PARAMETER OPTIMIZATION OF LAYERED FERTILIZATION OPENER

Establishment of the simulation model

(1) Establishment of the soil particle model

According to the earlier soil collection results, 0-12 cm was the depth of rotary tillage, in which the soil following rotary tillage was found to have large porosity, good air permeability and small soil particles. The soil below 12 cm had little disturbance, large soil particles and irregular shapes. The shape of soil particles was usually cluster, nucleus, block and so forth (Michele M. *et al.*, 2015). Therefore, the upper soil particles were replaced by spherical particles, the deep soil was built in two layers, the middle soil particles were replaced by nucleated particles, and the bottom soil particles were replaced by massive particles.

The established soil particle model was shown in Fig.2. The contact model between soil particles adopted the Hertz-Mindlin with JKR model after which the value of JKR was set. In this paper, the JKR value was determined to be 2 after calibration test.

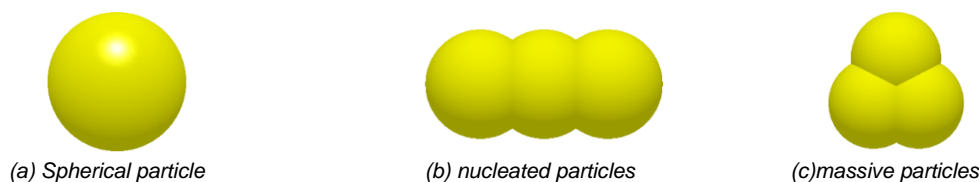


Fig. 2 - Soil particle model

(2) Establishment of the soil tank model

The particles were defined, and a soil tank was established with length of 1000 mm, width of 500 mm, and height of 300 mm. The soil tank was built in three layers, of which the upper layer was 12 cm. In addition, the lower soil was built in two layers, in which the middle and bottom layers were each 9 cm. The bottom layer was made of massive particles with a total of 23,000 particles, while the middle layer was made of nucleated particles with a total of 73,000 particles and the upper layer was made of spherical particles with a total of 270,000 particles. The time step was set to 20% of the Rayleigh time step, the grid size was 3 times the minimum particle radius, and the total time was 4 s. The soil particles were generated within 3 s and settled to 4 s. The corresponding soil tank was shown in Fig.3.

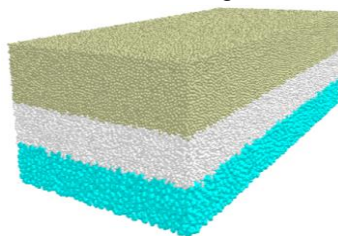


Fig. 3 - Soil tank model

(3) Establishment of the fertilizer particle model

According to the measurement of the compound fertilizer, the density was 1527 g/cm³, equivalent diameter was 4.03 mm, and sphericity rate was 93.02%. The spherical particles were used instead of fertilizer particles, and the particle radius was set to 2 mm. The contact model between fertilizer particles, the contact model between the fertilizer and opener were all set to Hertz-Mindlin (no-slip) (Coskun M. et al, 2006).

(4) Establishment of the opener model

SolidWorks software was used to establish a three-dimensional model of the opener at a ratio of 1:1. After the 3D model of the opener was created, it was saved in the 'igs.' format and imported into EDEM software.

(5) Parameter settings of the simulation model

The furrow depth was set to 24 cm, and the pellet factory was established on the top of the three fertilizer tubes of the opener. Fertilizer particles were then generated at a speed of 0.05 kg/s, and the gravity acceleration of fertilizer particles was set to 9.81 m/s² along the negative direction of the Z axis. The opener and pellet factory were then set to run together along the positive direction of the Y axis.

RESULTS

Determination of key parameters for the layered fertilization opener

(1) The effect of horizontal distance between the fertilizer openings and machine speed on soil falling

Given that the machine speed was 0.8 m/s, and the speed direction was along the positive direction of the Y-axis. The Slice function in the Clipping option was used to slice the simulation results. The soil falling section after slicing was shown in Fig.4.

By selecting any time on the time axis randomly and placing the slice boundary at the position where the soil had yet to fall, point A was determined. The time axis moved, the opener advanced, the soil began to fall, and the falling height h was measured. When the height of the soil falling was 80 mm, it was considered to be point B. At this time, the distance from point A that has yet to fall to point A' under the opener was 96 mm. Here, no movement trend of certain soil particles from point A to A' was observed, as shown in Fig.5.

Essentially, when the horizontal distance between the lower and middle fertilizer drop opening was set to 96 mm, the fertilization interval achieved was 80 mm. When the soil fell from 80 mm to 160 mm, the opener traveled 80 mm. Specifically, when the horizontal distance between the middle and upper fertilizer drop opening was 80 mm, the fertilizer layer spacing became 80 mm.

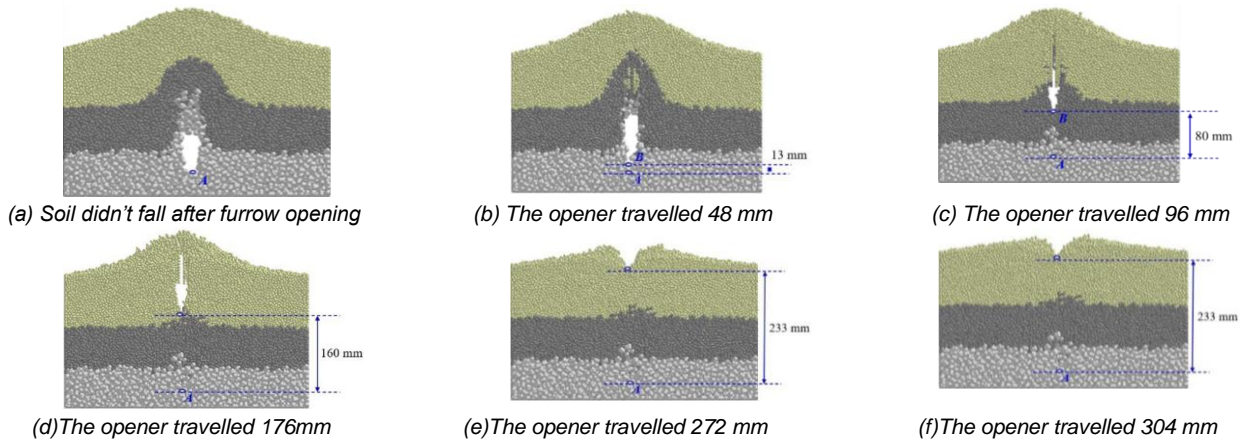


Fig. 4 - Cross section of soil falling

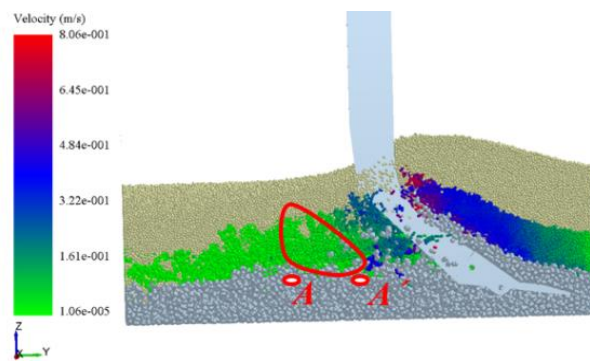


Fig. 5 - Soil particle velocity change

In order to analyze the change in soil falling height under different speeds, the speed was set to 0.8 m/s, 1.05 m/s, and 1.3 m/s and the result was shown in Fig.6. When the speed was 0.8 m/s, the horizontal distance between the lower and middle fertilizer drop opening was 96 mm, and the horizontal distance between the middle and the upper fertilizer drop opening was 80 mm. When the speed was 1.05 m/s, the horizontal distance between the lower and the middle fertilizer drop opening was 126 mm, and the horizontal distance between the middle and the upper fertilizer drop opening was 75 mm. When the speed was 1.3 m/s, the horizontal distance between the lower and middle fertilizer drop opening was 140 mm, and the horizontal distance between the middle and upper fertilizer drop opening was 77 mm. In summary, the horizontal distance between the lower and middle fertilizer drop opening should be greater than 140 mm, and the horizontal distance between the middle and the upper fertilizer drop opening should be greater than 80 mm.

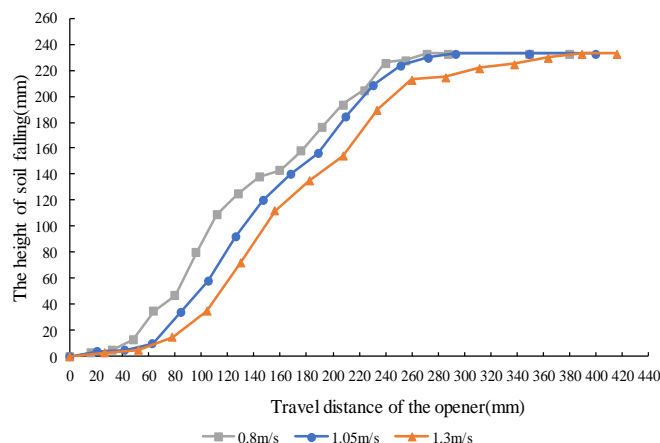


Fig. 6 - Variations of the height of soil falling with the travel distance of the opener under different speeds

(2) The effect of the inclination angle of the opener on soil falling

A simulation analysis was conducted on soil falling after ditching with the opener placed at different angles. The inclination angles of the openers were set as 20°, 30°, 40° and 50°, respectively. The cross sections of the openers at different angles were shown in Fig.7. The height of soil falling was measured according to the above method; when the height of soil falling was 80 mm, the travel distance of the opener, that was the horizontal distance between the fertilizer drop openings, was measured. The relationship between the horizontal distance between the fertilizer drop openings and inclination angle was shown in Fig.8. Here, according to the trend line function, the inclination angle of the opener was 37° when the horizontal distance between the fertilizer openings was the smallest.

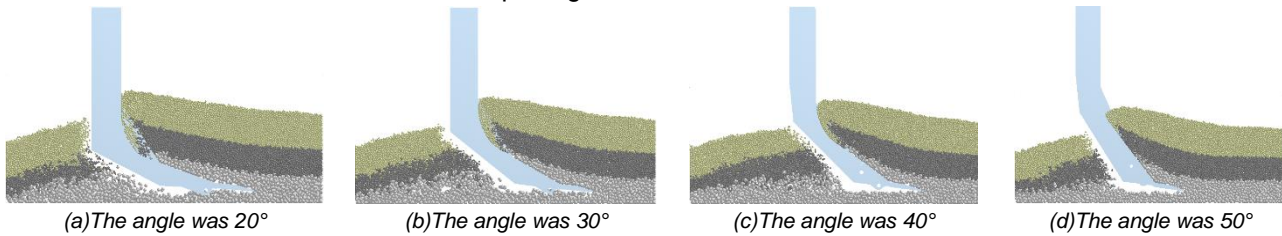


Fig. 7 - The cross section of the soil under different inclination angles of the openers

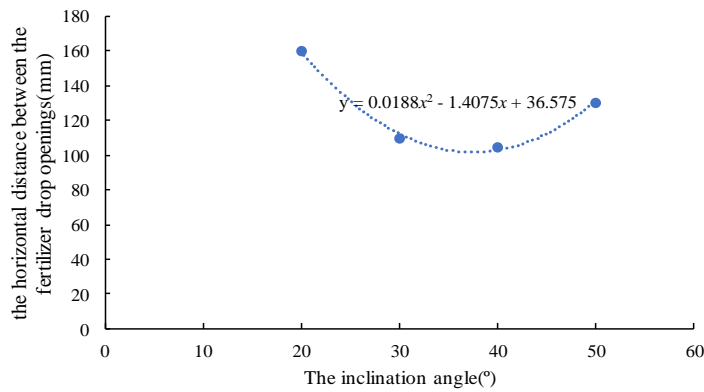


Fig. 8 - The relationship between the horizontal distance and the inclination angle

(3) The effect of the horizontal distance between the fertilizer drop openings on fertilizer layering

According to the above analysis, the horizontal distance between the lower and middle fertilizer drop opening should be greater than 140 mm, while the horizontal distance between the middle and upper fertilizer drop opening should be greater than 80 mm.

The simulation was performed when the horizontal distance between the lower and middle fertilizer drop opening was 120 mm, 140 mm, and 160 mm. Meanwhile, the inclination angle of the opener was 37° and the speed was 0.8 m/s. The distance from the middle position of the lower fertilizer layer to the middle position of the middle fertilizer layer was then measured, in which the effect of fertilizer layering was shown in Fig.9. When the horizontal distance was 120 mm, the interval between middle fertilizer and lower fertilizer was 46 mm, the interval between fertilizer layers was 79 mm when the horizontal distance was 140 mm, and the interval between fertilizer layers was 80 mm when the horizontal distance was 160 mm. The vertical distribution height of the middle fertilizer layer was 11 mm, and the vertical distribution height of the bottom fertilizer layer was 14 mm. The stratification effect was observed to be obvious.

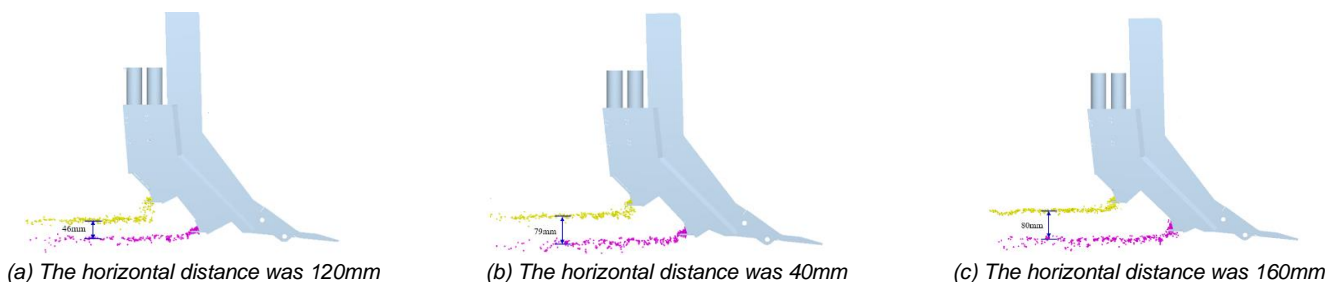


Fig. 9 - The effect of middle and lower fertilizer layering

The simulation was carried out when the horizontal distances between the middle and upper fertilizer drop openings were set to 80 mm, 100 mm, 120 mm, 140 mm, and 160 mm, respectively. The spacing between the upper fertilizer layer and middle fertilizer layer was measured, and the effect of fertilizer layering was obtained, as shown in Fig.10. The vertical distribution height of the upper fertilizer layer was 22 mm. Evidently, the layer spacing of the upper layer fertilizer was found to rise along with the horizontal distance between fertilizer drop openings until the distance reached 140mm. Meanwhile, the layer spacing was constant when the distance was bigger than 140 mm.

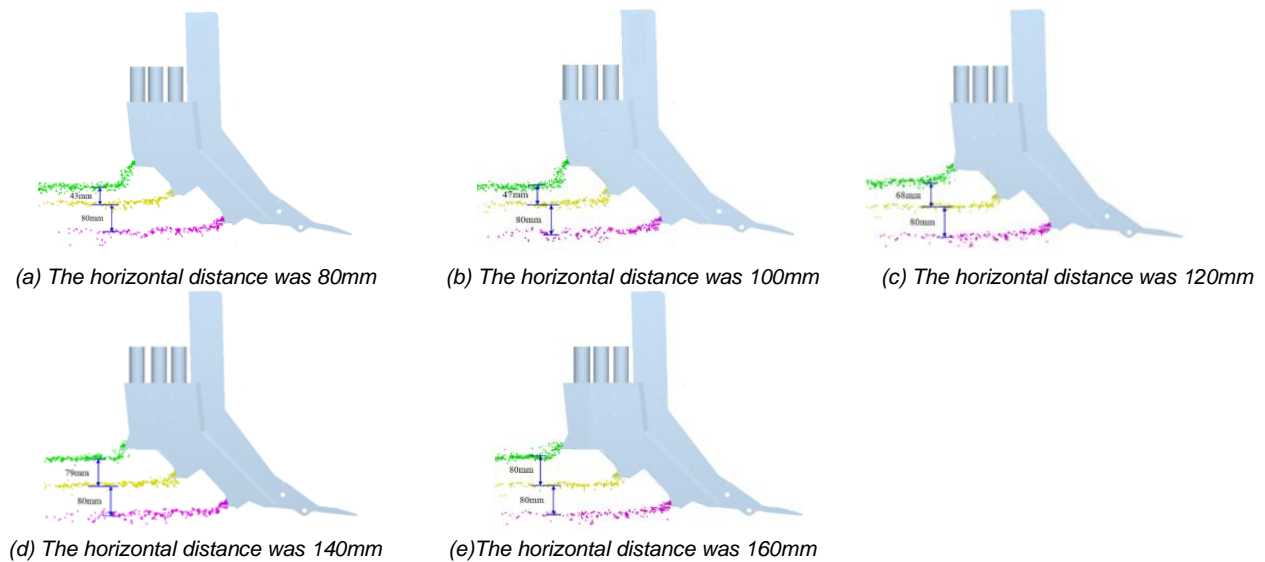


Fig. 10 - The effect of middle and upper fertilizer layering

(4) The effect of machine speed on the fertilizer layering

The simulation of fertilizer layering was conducted when the horizontal distance between the fertilizer drop openings was 140 mm, the inclination angle of the opener was 37° , and the speed was 0.8 m/s, 1.05 m/s, and 1.3 m/s, respectively. The effect of layered fertilization corresponding to different speeds was shown in Fig.11. According to the results, when the speed was 0.8 m/s and 1.05 m/s, the layer spacing was noted to be stable at 80 mm and the vertical distribution height of fertilizers in each layer was 18 mm. When the forward speed was 1.3m/s, the layer spacing was 70 mm. This occurred because, as the other parameters were constant, the faster the speed, the greater the distance traveled, and the less the amount of soil return that could cause the fertilizer to move downward.

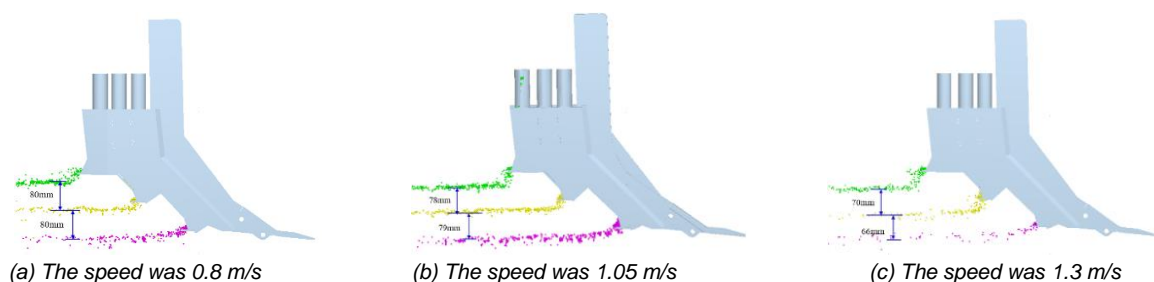


Fig. 11 - Effect of fertilizer layering at different speeds

Parameter optimization of layered fertilizer opener

(1) Test factor coding

The simulation optimization test regarded the inclination angle of the opener, the machine speed and the horizontal distance between the fertilizer drop openings as the test factors. In addition, the upper fertilizer layer spacing and lower fertilizer layer spacing were taken as evaluation indicators. Quadratic regression orthogonal test with three-factor three-level was designed using Design-Expert. According to the results of the previous simulation test, the range of the inclination angle of the opener was found to be $30^\circ\sim 44^\circ$, while the machine speed was 0.8~1.3 m/s and the horizontal distance between the fertilizer drop openings was 120~160 mm. The factors and levels of the simulation optimization test was shown in Table 1.

Table 1

Factors and levels of simulation test

Levels	Factors		
	The inclination angle of the opener a (°)	Machine speed b (m/s)	The horizontal distance between the fertilizer drop openings c (mm)
-1	30	0.8	120
0	37	1.05	140
1	44	1.3	160

(2) Analysis of test results

The tests were performed according to the designed plan and the results were shown in Table 2.

Table 2

Simulation test results

No.	Inclination angle A (°)	Machine speed B (m/s)	Horizontal distance C (mm)	Upper fertilizer layer spacing Y1 (mm)	Lower fertilizer layer spacing Y2 (mm)
1	0	-1	-1	64	51
2	1	0	-1	60	46
3	-1	0	1	78	73
4	0	0	0	78	76
5	-1	0	-1	60	43
6	1	1	0	60	47
7	0	0	0	80	77
8	0	0	0	81	77
9	-1	-1	0	75	70
10	0	0	0	76	74
11	0	1	1	73	65
12	0	1	-1	55	42
13	1	0	1	75	68
14	1	-1	0	70	60
15	-1	1	0	63	53
16	0	-1	1	80	80
17	0	0	0	78	74

The Design-expert 8.0 software was used to perform binary regression fitting on the experimental data, in which the following regression equations of each factor with the upper fertilizer layer spacing and lower fertilizer layer spacing were obtained:

$$Y1=78.60-1.37A-4.75B+8.38C-0.5AB-0.75AC+0.5BC-5.68A^2-5.93B^2-4.67C^2 \quad (1)$$

$$Y2=75.60-2.25A-6.75B+13.00C+1.0AB-2.0AC-1.5BC-10.05A^2-8.05B^2-8.05C^2 \quad (2)$$

The results of the variance analysis of the regression equation were shown in Tables 3. The *P* value of the regression model of the upper and lower fertilization layer spacing was found to be less than 0.01, indicating that the regression model was significant. The *P* value of the lack-of-fit item was noted to be greater than 0.05, indicating that the model possessed a high fit degree. The determination coefficient of the two models was close to 1, signifying that this regression model had high reliability.

Table 3

Variance analysis of quadratic polynomial model of upper fertilizer layer spacing

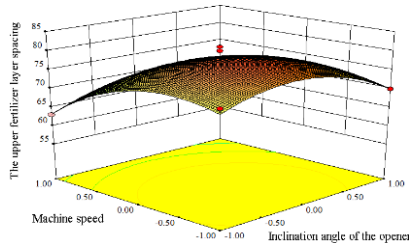
Item	Sources	Mean square	Freedom	Sum of squares	P value
Quadratic polynomial model of upper fertilizer layer spacing	Model	1179.99	9	131.11	<0.0001**
	A	15.13	1	15.13	0.0688
	B	180.50	1	180.50	0.0001**
	C	561.13	1	561.13	<0.0001**
	AB	1.00	1	1.00	0.5979
	AC	2.25	1	2.25	0.4348

Table 3
(continuation)

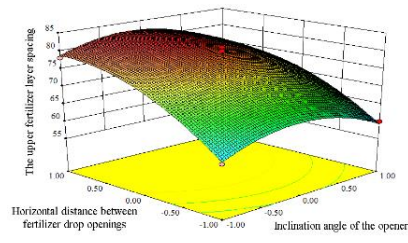
Item	Sources	Mean square	Freedom	Sum of squares	P value
	BC	1.00	1	1.00	0.5979
	A ²	135.60	1	135.60	0.0004
	B ²	147.81	1	147.81	0.0003
	C ²	92.02	1	92.02	0.0011
	Residual	22.95	7	3.28	
	Lack of Fit	7.75	3	2.58	0.6088
	Pure Error	15.20	4	3.80	
	Cor Total	1202.94	16		
Quadratic polynomial model of lower fertilizer layer spacing	Model	2869.33	9	318.81	<0.0001**
	A	40.50	1	40.50	0.0296*
	B	364.50	1	364.50	<0.0001**
	C	1352.00	1	1352.00	<0.0001**
	AB	4.00	1	4.00	0.4203
	AC	16.00	1	16.00	0.1306
	BC	9.00	1	9.00	0.2399
	A ²	425.27	1	425.27	<0.0001
	B ²	272.85	1	275.85	0.0002
	C ²	272.85	1	275.85	0.0002
	Residual	38.20	7	5.46	
	Lack of Fit	29.00	3	9.67	0.0996
Pure Error	9.20	4	2.30		

** represents highly significant (P<0.01); * represents significant (P<0.05).

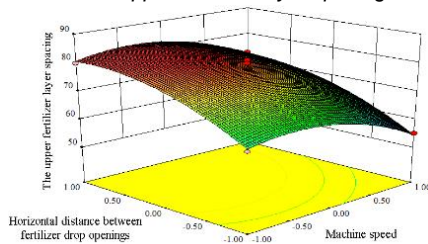
According to the analysis of the regression model, Design-expert 8.0 was used to plot the response surface graph, as shown in Fig.12.



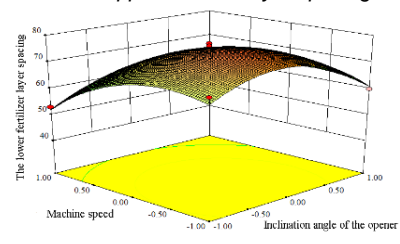
(a) The influence of machine speed and inclination angle on the upper fertilizer layer spacing



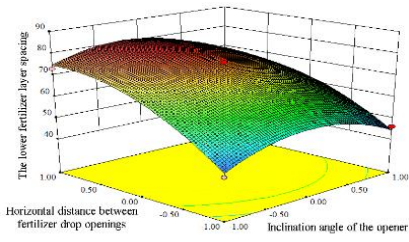
(b) The influence of horizontal distance and inclination angle on the upper fertilizer layer spacing



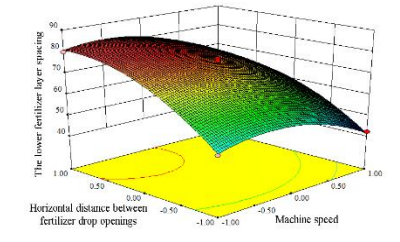
(c) The influence of horizontal distance and machine speed on the upper fertilizer layer spacing



(d) The influence of machine speed and inclination angle of on the lower fertilizer layer spacing



(e) The influence of horizontal distance and inclination angle on the lower fertilizer layer spacing



(f) The influence of horizontal distance and machine speed on the lower fertilizer layer spacing

Fig. 12 - Response surface between different factors and fertilizer layer spacing

As shown in Fig.12 (a) and (d), the machine speed was kept constant. In addition, the fertilizer layer spacing was found to initially increase and then decrease as the inclination angle of the opener increased. The inclination angle of the opener was unchanged, and the fertilizer layer spacing was found to decrease as the machine speed rose. This was because as the machine speed increased, the amount of returned soil decreased, and the distance between the two fertilizer layers decreased.

As shown in Fig.12 (b) and (e), the horizontal distance between the fertilizer drop openings remained unchanged, in which the fertilizer layer spacing initially rose and then decreased as the inclination of the opener increased. The inclination angle of the opener was constant, and the fertilizer layer spacing increased as the horizontal distance between the fertilizer drop openings increased. When the horizontal distance rose more than 140mm, the increasing trend of the layer spacing decreased until it no longer rose.

As shown in Fig.12 (c) and (f), the horizontal distance between the fertilizer drop openings remained constant, and the fertilizer layer spacing decreased as the machine speed rose. This was because the machine speed increased, the amount of returned soil decreased, and the distance between the two fertilizer layers decreased. The machine speed was constant, and the fertilizer layer spacing increased as the horizontal distance between the fertilizer drop openings rose. When the horizontal distance rose beyond 140 mm, the increasing trend of the layer spacing decreased until it no longer rose.

Parameter optimization

In order to achieve the ideal layered fertilization effect, the upper and lower fertilization spacing were taken as the performance index, and influencing factors, such as the inclination angle of the opener, the horizontal distance between the fertilizer drop openings, and the machine speed, were then optimized. Design-expert 8.0 was used to optimize the parameters. The optimal parameters were obtained: the inclination angle of the opener was 37°, the horizontal distance between the fertilizer drop openings was 140 mm, and the machine speed was 1.05m/s. The optimized layered fertilization opener was shown in Fig.13.



Fig. 13 - Layered fertilization opener

FIELD TESTS

Test equipment and methods

In order to determine the fertilization depth and fertilizer layer spacing, tools such as shovels, tape measures were used to collect the experimental data. The test was carried out in Yanzhou District, Jining City, Shandong Province in September 2020. This paper took “GB/T 20346.2-2006 Fertilization Machinery Test Method” and “DB23/T1208-2008 Layered Fertilization Operation Quality Standard” as standards. The planter was driven by the tractor at a speed of 2-5 km/h. The test procedure was shown in Fig.14.



Fig. 14 - The test process of the prototype

The five-point method was used, and five testing points were randomly selected. In each testing point area, a shovel was used to dig a section of each fertilizer ditch vertically. The shovel was then used to clean the surrounding soil, gently scrape the surface soil, find easily observable fertilizer, and measure the fertilization depth. After the fertilization depth was measured, the data was recorded as shown in Fig.15.



Fig. 15 - Field data measurement and fertilization effect

According to operating standards, the fertilization depth (H) was qualified when the fertilization depth was $H \pm 2$ cm, and the fertilizer layer spacing (S) was qualified when the fertilizer layer spacing was $S \pm 2$ cm. The qualified rate of fertilization depth Q_1 as well as the qualified rate of fertilizer layer spacing Q_2 were calculated according to Formulas (3-4).

$$Q_1 = \frac{n_1}{N} \times 100\% \tag{3}$$

$$Q_2 = \frac{n_2}{N} \times 100\% \tag{4}$$

where, Q_1 was the qualified rate of fertilization depth, %; Q_2 was the qualified rate of fertilizer layer spacing, %; n_1 referred to points of fertilization depth which is qualified; n_2 referred to points of fertilizer layer spacing which is qualified; N was the total number of points measured.

Test results

A ruler was used to measure the fertilization depth, for which the data was given in Table 4.

Table 4

		Fertilization depth						
	Fertilization row	Point 1 (cm)	Point 2 (cm)	Point 3 (cm)	Point 4 (cm)	Point 5 (cm)	Mean (cm)	Qualified rate (%)
First row	upper layer	9.0	7.3	8.2	8.7	8.5	8.34	100
	middle layer	16.2	15.7	16.0	16.2	16.8	16.18	100
	lower layer	23.5	23.3	24.0	23.5	24.3	23.72	100
Second row	upper layer	8.7	8.4	8.3	8.3	8.5	8.44	100
	middle layer	16.8	16.8	16.5	16.7	16.7	16.70	100
	lower layer	24.4	24.7	23.8	24.0	24.6	24.30	100
Third row	upper layer	7.2	8.2	7.8	8.1	9.3	8.12	100
	middle layer	14.8	16.2	15.8	16.4	17.3	16.10	100
	lower layer	21.6	23.8	23.5	24.3	25.2	23.68	80
Forth row	upper layer	7.8	8.7	8.9	9.4	8.5	8.66	100
	middle layer	16.2	16.5	18.0	17.1	16.6	16.88	100
	lower layer	23.7	24.2	25.1	24.6	24.4	24.40	100
Mean	upper layer	8.390						
	middle layer	16.465						
	lower layer	24.025						

It was calculated that the average fertilization depth of upper layer was 8.39 cm, the average fertilization depth of middle layer was 16.465 cm, and the average fertilization depth of bottom layer was 24.025 cm. It could be seen from Table 4 that the qualified rate of the average fertilization depth of upper layer and middle layer was 100%, and the qualified rate of the average fertilization depth of lower layer qualified rate was 95%, and the fertilization depth met the requirements of layered fertilization operations.

The measured spacing of fertilizer layer was shown in Table 5.

Table 5

Fertilization row		Point 1 (cm)	Point 2 (cm)	Point 3 (cm)	Point 4 (cm)	Point 5 (cm)	Mean (cm)	Qualified rate (%)	
First row	upper layer	7.2	8.4	7.8	7.5	8.3	7.84	100%	
	lower layer	7.3	7.6	8.0	7.3	7.5	7.50	100%	
Second row	upper layer	8.1	8.4	8.2	8.4	8.2	8.26	100%	
	lower layer	7.6	7.9	7.3	7.3	7.9	7.60	100%	
Third row	upper layer	7.6	8.0	8.0	8.3	8.0	7.98	100%	
	lower layer	6.8	7.6	7.7	7.9	7.9	7.58	100%	
Forth row	upper layer	8.4	7.8	9.1	7.7	8.1	8.22	100%	
	lower layer	7.5	7.7	7.1	7.5	7.8	7.52	100%	
Mean	upper layer	8.075							
	lower layer	7.600							

According to Table 5, the average fertilizer spacing of the upper layer was 8.075 cm, and the maximum spacing error was 1.1 cm; the average fertilizer spacing of lower layer was 7.6 cm, and the maximum spacing error was 1.2 cm. Therefore, the fertilizer spacing satisfied the operating requirements.

CONCLUSIONS

(1) In this study, according to the agronomic requirements of the layered fertilization of wheat, a layered fertilization opener was designed, which comprised of a shovel point, shank, fertilizer grooves and fertilizer drop openings.

(2) The interaction model between the opener, the soil and fertilizers were then established, and soil falling and fertilizer falling simulation experiments were carried out to determine the main parameters of the opener. The optimal parameters were obtained: horizontal distance between the fertilizer drop openings of 14 cm, machine speed of 1.05 m/s, and opener inclination angle of 37°.

(3) The field test results signified that the average depth of upper layer fertilization was 8.39 cm, the average depth of middle layer fertilization was 16.465 cm, and the average depth of lower layer fertilization was 24.025 cm. Furthermore, the average spacing of the upper fertilizer layer was found to be 8.075 cm, while the average spacing of the lower fertilizer layer was 7.6 cm, thus satisfying the requirements of the layered fertilization standard.

ACKNOWLEDGEMENT

We would like to thank the support of the Shandong Provincial Key Science and Technology Innovation Engineering Project (2019JZZY010716), Key R & D project of Shan-dong Province (2019GNC106089) and Shandong Provincial Engineering Laboratory of Agricultural Equipment Intelligence.

REFERENCES

- [1] Abbas A., Zaman Q., Schuman A. et al., (2014), Effect of split variable rate fertilization on ammonia volatilization in wild blueberry cropping system, *Applied Engineering in Agriculture*, Vol.30, pp.619-627, American Society of Agricultural and Biological Engineers, North Carolina State / USA;
- [2] Bautista E., Koike M., Suministrado D., (2001), PM-power and machinery: mechanical deep placement of nitrogen in wetland rice, *Journal of Agricultural Engineering Research*, Vol.78, pp. 333-346, Elsevier, Amsterdam / Netherlands;
- [3] Coskun M., Yalcin I., Oezarslan C., (2006), Physical properties of sweet corn seed (*zea mays saccharata sturt.*), *Journal of Food Engineering*, Vol.74, pp.523-528, Elsevier, Amsterdam/Netherlands;
- [4] Ding S., Bai L., Yao Y. et al., (2018), Discrete element modelling (DEM) of fertilizer dual-banding with adjustable rates, *Computers and Electronics in Agriculture*, Vol.152, pp.32-39, Elsevier, Amsterdam / Netherlands;
- [5] Kargbo M., Pan S., Mo Z. et al, (2016), Physiological basis of improved performance of super rice (*oryza sativa l.*) to deep placed fertilizer with precision hill-drilling machine, *International Journal of Agriculture and Biology*, Vol.18, pp.790-804, Friends Science Publishers, Faisalabad / Pakistan;

- [6] Li B., Wang G., Chen Z. et al, (2021), Effects of layered fertilization on yield and water use efficiency of winter wheat under different irrigation conditions, *Journal of Soil and Water Conservation*, Vol.35, pp.326-332.
- [7] Michele M., Hugh S., (2015), Discrete element method (DEM) for industrial applications: comments on calibration and validation for the modelling of cylindrical pellets, *Kona Powder and Particle Journal*, Vol.32, pp.236-252, Hosokawa Powder Technology Foundation, Osaka / Japan;
- [8] Min J., Sun H., Wang Y. et al, (2021), Mechanical side-deep fertilization mitigates ammonia volatilization and nitrogen runoff and increases profitability in rice production independent of fertilizer type and split ratio, *Journal of Cleaner Production*, Vol.316, pp.128370, Elsevier, Amsterdam / Netherlands;
- [9] Quinn D., Lee C., Poffenbarger H., (2020), Corn yield response to sub-surface banded starter fertilizer in the U.S.: a meta-analysis, *Field Crops Research*, Vol.254, pp.107834, Elsevier, Amsterdam / Netherlands;
- [10] Wang Y., Liang Z., Cui T. et al, (2016), Design and experiment of layered fertilization device for corn, *Transactions of the Chinese Society for Agricultural Machinery*, Vol.47, pp.163-169, Chinese Society for Agricultural Machinery, Beijing / China;
- [11] Wen Y., Wang D., (2017), Basal fertilization in strips at different soil depths to increase dry matter accumulation and yield of winter wheat, *Journal of Plant Nutrition and Fertilizers*, 2017, Vol. 23, pp. 1387-1393, Chinese Society of Plant Nutrition and Fertilizer, Beijing / China;
- [12] Yang Q., Wang Q., Li H. et al, (2020), Development of layered fertilizer amount adjustment device of pneumatic centralized variable fertilizer system, *Transactions of the Chinese Society of Agricultural Engineering*, 2020, Vol. 36, pp. 1-10, Chinese Society of Agricultural Engineering, Beijing / China;
- [13] Yang R., Yang H., Lian Z. et al, (2018), Design and experiment of separated layer fertilization furrow opener for potato planter, *Transactions of the Chinese Society for Agricultural Machinery*, Vol. 49, pp. 104- 113, Chinese Society for Agricultural Machinery, Beijing / China;
- [14] Zhang J., Tong J., Ma Y., (2014), Design and experiment of bionic anti-drag subsoiler, *Transactions of the Chinese Society for Agricultural Machinery*, Vol. 45, pp. 141-145, Chinese Society for Agricultural Machinery, Beijing / China.

STUDY ON ACTIVE ANTI ROLLOVER CONTROL AND MODEL TEST OF TRACTOR MOMENTUM FLYWHEEL

拖拉机动量飞轮主动防侧翻控制与模型试验研究

Weihong Qiao^{*)}, Qihong Wei

Xinxiang Vocational and Technical College, Xinxiang, Henan, 453006, China

*E-mail: mmmkwom@163.com

Corresponding authors: Dr. Weihong Qiao

DOI: <https://doi.org/10.356.33/inmateh-65-23>

Keywords: tractor, momentum flywheel, rollover prevention control method, roll angle

ABSTRACT

The tractor working environment is complex and changeable, and the dynamic variation range of the center of gravity position of the tractor body is large. In order to avoid rollover accident, an active anti rollover control method of tractor momentum flywheel and its model test are proposed in this paper. The tractor dynamic system model and control strategy are verified by a 1:16 scale tractor model. The research results show that when the model tractor crosses the trapezoidal obstacle B, the roll angle of the whole machine is temporarily stable near 35°, indicating that at this time, the tires on one side of the whole machine are in actual contact with the obstacle, showing a short stable state of the whole machine. When the pavement roughness reaches F-H level, without any active anti rollover control, the evaluation index EP shows a divergence trend when it is greater than 1, and the simulation calculation is terminated due to the occurrence of rollover of the whole machine. The test data and simulation results under two different driving speeds are in good agreement, which verifies the effectiveness and reliability of the tractor rollover dynamic system model and the momentum flywheel active stabilization system.

摘要

拖拉机作业环境复杂多变，拖拉机机体重心位置动态变化范围较大，为避免发生侧翻事故，本文提出拖拉机动量飞轮主动防侧翻控制方法及其模型试验。通过 1:16 比例模型拖拉机对拖拉机动力学系统模型及控制策略进行验证。研究结果当模型拖拉机翻越梯形障碍 B 时，整机侧倾角短暂稳定在 35° 附近，说明此时整机一侧轮胎均与障碍物实际接触，表现为短暂的整机稳定状态。当路面粗糙度进入 F-H 级时，在没有任何主动防侧翻控制的条件下，评价指标 EP 大于 1 后呈发散趋势，仿真计算均因整机侧翻的发生而终止。两种不同行驶速度工况下的测试数据和仿真结果吻合度较高，验证了拖拉机侧翻动力学系统模型及动量飞轮主动回稳系统的有效性和可靠性。

INTRODUCTION

With the development of economy, the application scope of agricultural machinery is more and more extensive, but its accident rate is also on the rise. Especially, tractor rollover accidents frequently occur (Vahdanjoo M. et al., 2020). The causes of rollover accidents are mainly due to design defects and quality problems of tractors, and also due to improper operation of users. Whether the tractor is working in the field or on the road, once a rollover accident occurs, it is inevitable to cause casualties and economic losses (Karakulak S. S. et al., 2020). Therefore, the detection of tractor's maximum stable inclination angle is a very important project. Tractor rollover test is a test to exam the stable angle and maximum stable inclination angle of tractor rollover. It is a necessary item for tractor supervision, inspection and popularization appraisal (Song H. S. et al., 2020). Passing the tractor rollover test is of great significance for controlling the height of the tractor's center of gravity, driving safely or operating safely in the field, which can not only improve the stability and safety of the tractor, but also reduce the incalculable accidents of the tractor during operation. Tractor itself is a complex system with large delay, high nonlinearity, time-varying and uncertainty. Moreover, it is difficult to establish an accurate mathematical model because of poor farmland conditions and complex interaction process between tires and ground. When the controlled object is affected by uncertain factors such as parameter perturbation and external interference, it will reduce the control quality of the system. Disadvantages such as increased oscillation and long transition time occur (Elsayed A.T. et al., 2016).

Therefore, it is necessary to fully mine the vehicle state information contained in the vehicle model and select the appropriate control algorithm to improve the navigation system performance (Shamsuddin P. et al., 2020). The necessary condition for tractor rollover is that the vertical line of the tractor's center of gravity crosses the fulcrum between the overturned tire and the ground. Therefore, the tractor can be prevented from turning over as long as the stable moment formed by the tractor's center of gravity on both sides of the tire and the ground fulcrum is greater than the dumping moment formed by other forces on the tire and the ground fulcrum, and the direction is opposite to the stable moment (Hu Y. et al, 2016). When it's turning, the tractor speed should not be too fast, and the turning should not be too fast (Stroganov Y N. et al., 2020). Because when it's turning, the tractor will produce an outward centrifugal force. The centrifugal force is directly proportional to the tractor's mass, directly proportional to the square of the tractor's traveling speed and inversely proportional to the turning radius. Therefore, when turning too fast, the centrifugal force of the tractor may be increased, and the centrifugal force will form a dumping moment on the fulcrum between the steering outer tire and the ground. When the dumping moment is greater than the stable moment formed by tractor gravity, the tractor will roll over. The center of gravity of loading should be low, and unbalanced loading should be prevented during loading. For example, the tractor is equipped with a bucket or combine, etc. (Jang B. E. et al., 2021).

The centrifugal force acting on the center of gravity or the tilting force formed on the slope will increase the dumping moment due to the increase of the force arm (the height of the center of gravity is increased), which is easy to cause rollover. Due to the eccentric load, the center of gravity shifts to one side tire, which reduces the stabilizing moment formed by gravity against the side tire, and also easily causes the tractor or trailer to roll over (Li S. et al., 2018). There are two reasons that cause the tractor to turn back. The first is the torque and traction resistance of the rear axle, and the second is that the tractor's center of gravity or the vertical line of the center of gravity moves backward, which causes the tractor's stable torque to decrease and causes it to turn over. When the clutch is engaged, the engine transmits the torque to the rear axle. If the rear wheels can't rotate for some reason, for example, the tires of the rear wheels are frozen on the ground or the tractor pulls too much, the driving torque will make the tractor rotate around the rear axle and make the front wheels leave the ground. If the engine has enough power, and the ground adhesion coefficient is good, it will cause the tractor to turn back, because the rear wheels cannot slip or roll forward in situ, and the torque of the rear wheels will make the tractor turn back. Tractor's center of gravity or vertical line of center of gravity moves backward, which causes the tractor's stabilizing moment to decrease and makes it turn backward. When a tractor climbs a hill, the front wheel should be weighted or the reverse gear should be hung. The method of retreating uphill, because when the tractor goes uphill, the action line of gravity leans towards the rear wheel, which increases the danger of the tractor turning backwards. Reduce the height of hitch point of trailer on tractor. Because the higher the towing point is, the greater the backward turning moment formed by the towing resistance of the trailer on the tractor, which is easy to cause the tractor to turn backward. The towing point of the trailer should be selected on the towing plate of the tractor. It can't be attached to other parts of the tractor, and the wrong attachment method may reduce the load of the front wheel of the tractor, make the operation fail, and even cause an accident of rollover. According to this research, Bauer M. et al. proposed that to prevent high-speed emergency braking, unilateral braking should be prohibited, speed should be reduced first when turning, and driving at low speed on snow, ice and muddy roads should make trailer braking precede tractor braking, etc. When the tractor skids during running, the skidding force will act on the center of gravity of the tractor, forming a dumping moment on the fulcrum between the tire and the ground, which will make the tractor slip into the ditch or roll over, turn on its side in the drain as shown in Figure 1 (Rogov P. S. et al., 2020).



Fig. 1 - Tractor overturned in the gutter

Elsayed *et al* thought that tractor drivers should be extra careful when driving on a cross slope (Elsayed A.T. *et al.*, 2016). Because the action line of gravity of the tractor on the transverse slope leans towards the fulcrum between the tire and the ground on the inclined side, the stabilizing moment on this side becomes smaller, and the greater the slope of the ground, the smaller the stabilizing moment becomes. Therefore, when driving on a cross slope, the speed must be slow to prevent the ground from bumping and avoid turning on the slope (Liao C. *et al.*, 2018). Zhang L. *et al.* believe that when the tractor runs in dangerous areas such as ditch embankment and dam edge, the tractor should be a certain distance away from the ditch edge, and the driver must concentrate on driving the tractor (Zhang L. *et al.*, 2021).

On the basis of the current research, this paper puts forward the active anti-rollover control method of tractor momentum flywheel and its model test, and verifies the above tractor dynamic system model and control strategy by means of a 1:16 scale model tractor. The tractor dynamic system model established in this paper can accurately reflect the course of tractor obstacle crossing and rollover behavior, and the active stabilization system is effective and reliable. Tractor rollover dynamics system model and momentum flywheel active stabilization system are effective and reliable.

MATERIALS AND METHODS

System Modeling and Stability Evaluation

As shown in Figure 2, a mechanism independent of the main engine, the swingable front axle of tractor plays a role in improving the stability and obstacle-surmounting ability of the whole engine. In the modeling process, the front axle and the main engine have six degrees of freedom, namely, longitudinal, lateral, vertical, roll, pitch and yaw. The six-degree-of-freedom motion of the front axle is restricted by the motion of the engine body, except for the roll motion. Therefore, seven degrees-of-freedom can describe the dynamic behavior of tractors except tires (Wu X. *et al.*, 2017).

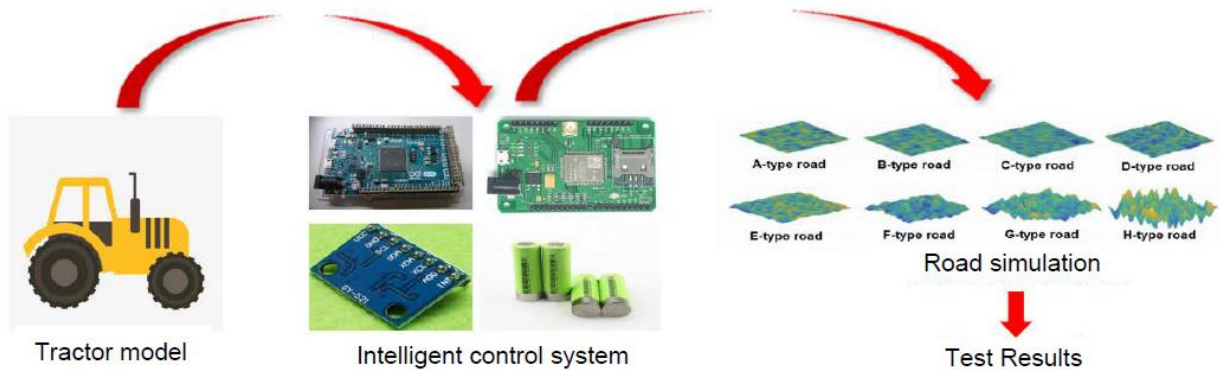


Fig. 2 - Schematic diagram of experimental simulation

The tractor runs at a constant speed along the X axis of the slope contour line, and the translational motion equations of its main engine along the Y and Z axes are shown in Formula (1).

$$\begin{aligned}
 m\ddot{y} &= mg \sin \alpha + F_{py} - F_{y3} - F_{y4} \\
 m\ddot{z} &= F_{pz} + F_{z3} + F_{z4} - mg \cos \alpha
 \end{aligned}
 \tag{1}$$

The roll, pitch and yaw motion equations of the airframe around x, y and z axes are shown in formulas (2), (3) and (4) respectively.

$$I_{xr} \ddot{\phi}_r = (F_{z3} - F_{z4}) \frac{B_r}{2} + (F_{y3} + F_{y4}) H_r - F_{py} e_{rz}
 \tag{2}$$

$$I_{yr} \ddot{\theta}_r = F_{pz} L_{r1} - (F_{z3} + F_{z4}) L_{r2}
 \tag{3}$$

$$I_{zr} \ddot{\gamma}_r = (F_{y1} + F_{y2}) L_f - (F_{y3} + F_{y4}) L_r
 \tag{4}$$

The independent roll motion equation of the front axle around the X axis is shown in (5).

$$I_{xf} \ddot{\theta}_f = M_{xf}
 \tag{5}$$

Formula (1)-(5) symbol description is shown in Table 1.

Table 1

Formula (1)-(5) symbol description

m	the mass of the whole machine
g	the acceleration of gravity
α	the lateral slope angle
F_{py}	the lateral force of the hinge point of the front axle
F_{pz}	the vertical stress of the hinge point of the front axle
F_{yi}	the wheel lateral force N, $i=1-4$
F_{zi}	the wheel vertical force N, $i=1-4$
I_{xr}	rotational inertia of the main body around the x axis
I_{yr}	rotational inertia of the main body around the y axis
I_{zr}	rotational inertia of the main body around the z axis
ϕ_r	represents the overall roll angle
B_r	the rear wheel track
H_r	height of center of gravity (COG_r) from the ground
e_{rz}	the vertical distance between the center of gravity of the machine body and the pivot of the front axle
L_{r1}	horizontal distance from COG_r to hinge point of front axle
L_{r2}	horizontal distance from COG_r to rear wheel
L_r	horizontal distance from COG_r to rear axle
L_f	horizontal distance from COG_r to front axle
γ_r	horizontal distance from COG_r to hinge point of front axle
I_{xf}	the moment of inertia of the front axle around the x axis
θ_f	front axle pitch angle
M_{xf}	surrounded by the front bridge

In the process of tractor running, all external forces (ignoring air resistance) on the machine body come from the contact between tires and the ground, so establishing a relatively accurate tire model is the basis for the whole machine dynamic model to reflect the real tractor state. In this paper, Fiala tire model 201 is selected, and the tire vertical force can be expressed as shown in formula (6).

$$F_{zi} = -k_{f/r} \Delta z_{f/r} - c_{f/r} \Delta \dot{z}_{f/r} \quad (i = 1-4) \tag{6}$$

$c_{f/r}$ is the tire vertical damping, $k_{f/r}$ is the tire vertical stiffness, $\Delta z_{f/r}$ is the vertical deformation of the tire.

The lower corner mark f represents the front wheel and r represents the rear wheel. Considering the tractor-momentum flywheel system, ignoring the friction when the flywheel rotates around the motor shaft and the dissipation force in the process of tractor stabilization, the Lagrange method can be obtained as shown in Formula (7).

$$(I_x^* + I_w) \ddot{\phi} - \frac{B}{2} (m + m_w) g \sin \phi = -I_w \ddot{\zeta} \tag{7}$$

where I_w is the flywheel moment of inertia, I_x^* is moment of inertia of the whole machine around the x axis, and B is track coefficient, m_w is flywheel mass, ζ is flywheel angle, ϕ represents the overall roll angle.

The lateral stability evaluation index is an important symbol and control basis for reflecting the stability of the whole machine. The instability boundary exists in the tractor rollover process, which is determined by whether the projection of the center of gravity of the whole machine in the vertical direction crosses the roll axis. Therefore, this paper introduces the lateral stability evaluation index EP based on the extreme posture position in the rollover process, and its calculation formula is as follows (8).

$$EP = \frac{2H_{coc} mg \sin(|\phi + \alpha|)}{Bmg \cos(|\phi + \alpha|)} \tag{8}$$

H_{coc} is the height of gravity center of the whole machine. With 1 as the instability threshold, when the tractor is in a stable state, the lateral component of gravity is small, and at this time EP is less than 1. With the increase of the roll angle of the whole machine, EP continues to increase until EP reaches 1 when the center of gravity is directly above the roll axis, and the whole machine is in a critical unstable state. When the center of gravity of the whole machine crosses the roll axis, EP is greater than 1. If there is no outside intervention, a rollover accident will occur. This index is the basis for dynamic evaluation, monitoring and active control of lateral stability of the whole machine (Zong, Z. et al., 2019).

Scale Model Test Platform to Build a Model Tractor

Considering the high risk of using real vehicles for rollover test, this paper verifies the above tractor dynamic system model and control strategy through a 1:16 scale model tractor. Considering the test function of the model tractor, the model tractor is mainly composed of control unit, drive unit, flywheel-motor unit, fuselage shell, chassis and front axle. The control unit consists of ArduinoDUE control module, HC-05 Bluetooth data transmission module, MPU6050 six-axis gyroscope and 12V lithium battery. The driving unit is composed of ZS-H1B double H-bridge DC motor driving module, permanent magnet DC driving motor, gear reducer and herringbone pattern model tire.

The flywheel-motor unit is composed of reaction torque flywheel, driving motor and Hall encoder, etc. The momentum flywheel is placed in the front of the tractor, which can replace the traditional static counterweight and actively provide anti-rollover torque, and build the completed 1:16 scale model. To further verify the effectiveness and universality of active rollover control of momentum flywheel system under complex road conditions, combining the relationship between displacement power spectral density (PSD) and spatial frequency in formula (9), the system excitation is provided for the simulation and verification of the active control system under the full-scale road surface.

$$G_q(n) = G_q(n_0) \left(\frac{n}{n_0} \right)^{-w} \quad (9)$$

where $G_q(n)$ is displacement power spectral density, $G_q(n_0)$ is road roughness coefficient, n is the spatial frequency, n_0 is the reference spatial frequency.

RESULTS

Determine the Test Verification of Active Stabilization System under Obstacles

Figure 3 and Figure 4 show the change trend of the whole machine's roll angle during the obstacle crossing process of the model tractor at different speeds. By using Matlab/Simulink software, the effectiveness of PID control is simulated and analyzed during the stabilization process of the reaction flywheel. According to the time domain definition of the two obstacle-crossing processes of the whole machine in Figure 3 and Figure 4, the lateral attitude of the whole machine fluctuates twice in different degrees during the process of the model tractor crossing the obstacle A. This is because the front axle can swing freely within a certain angle, so that the lateral attitude change of the whole machine caused by the obstacle crossing of the front wheel is less than the influence of the obstacle crossing of the rear wheel, which is in line with the actual working condition of the tractor. When the model tractor climbs over the trapezoidal obstacle B, the side inclination of the whole machine is temporarily stable near 35, which indicates that the tires on one side of the whole machine are actually in contact with the obstacle at this time. It shows a short stable state of the whole machine. The test data under two different driving speeds are in good agreement with the simulation results, which verifies the validity and reliability of the tractor rollover dynamic system model and the momentum flywheel active stabilization system.

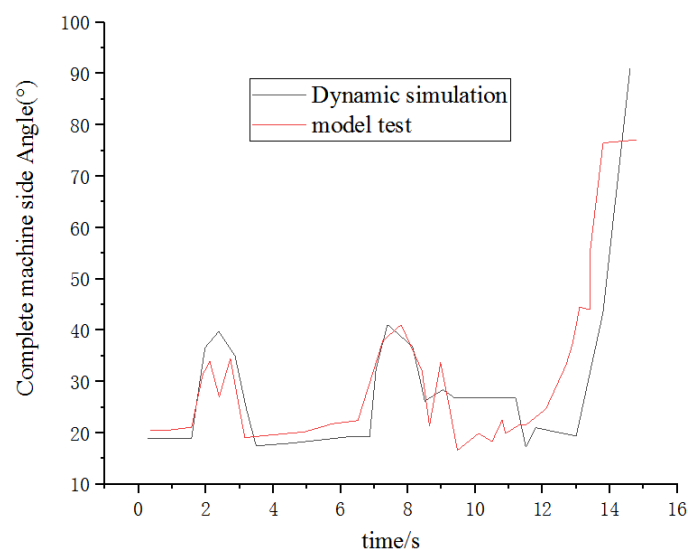


Fig. 3 - Change curve of roll angle of the whole machine at 0.1 m/s

The anti-rollover verification of momentum flywheel system is carried out by applying tractor dynamic system model verified above and full-scale random road surface, and the change rule of lateral stability evaluation index of the whole machine under F and H roads as shown in Figure 5 and Figure 6 is obtained.

When the tractor runs on a relatively flat road surface, the lateral stability evaluation index EP of the whole machine is always less than 1, and the whole machine does not show a rollover trend. This is consistent with the actual situation that the tractor has relatively good stability when running on the road surface with small fluctuation and low roughness.

When the roughness of pavement enters F-H level, under the condition of no active anti-rollover control, the evaluation index EP is greater than 1, and then it tends to diverge, and the simulation calculation is terminated due to the occurrence of the whole machine rollover. Under the condition of active control, despite the rollover tendency of tractors in different directions, the tractors are stabilized under the active intervention of momentum flywheel system, which can make the tractors run safely and smoothly on the road with large fluctuation and high roughness.

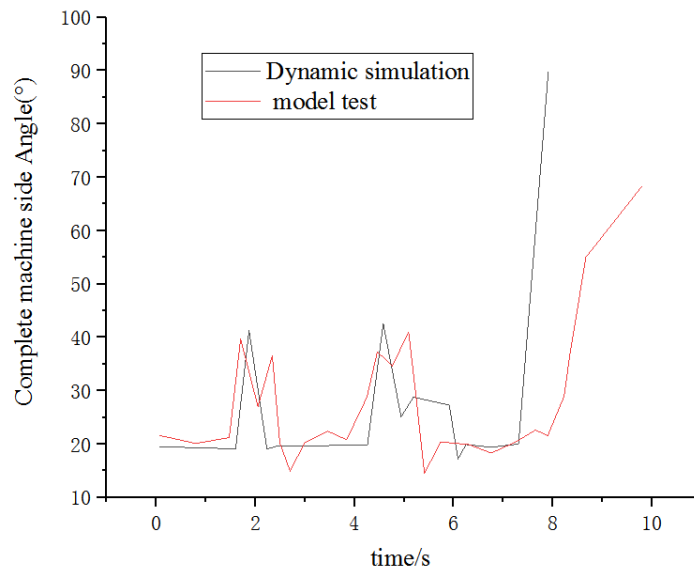


Fig. 4 - Change curve of roll angle of the whole machine at 0.2 m/s

Simulation and verification of effectiveness of momentum flywheel system under random road excitation.

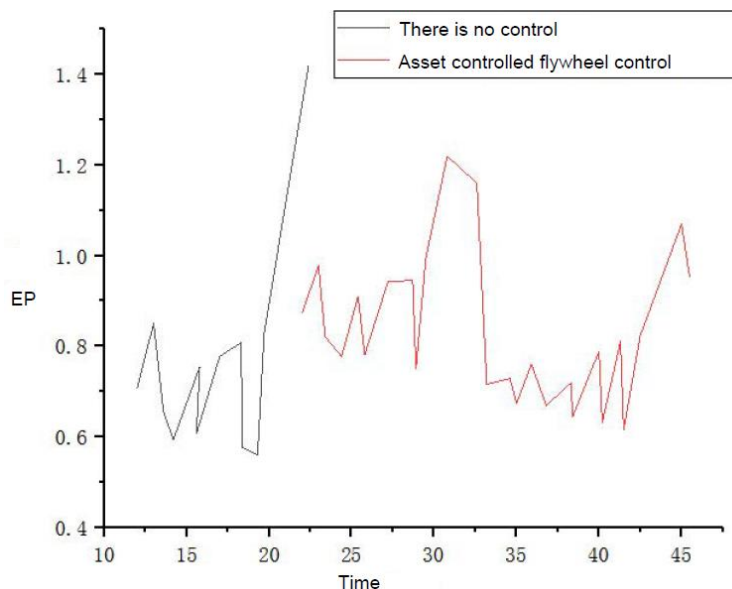


Fig. 5 - Variation law of lateral stability evaluation index of the whole machine under F level pavement

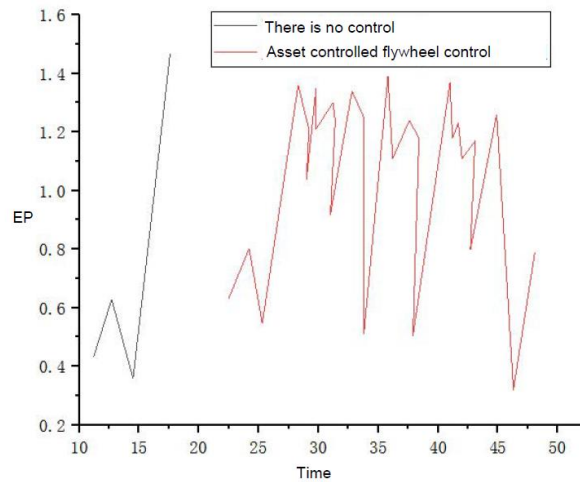


Fig. 6 - Variation law of lateral stability evaluation index of the whole machine under 4H grade pavement

The working state of the tractor momentum flywheel active anti-rollover control system is shown in Figure 7.



Fig. 7 - Anti-rollover control system for tractor

CONCLUSIONS

In this paper, the active anti-rollover control method of momentum flywheel is proposed, and the model and road test platform are built. The effectiveness of the active control system and dynamic model is verified by simulation. The tires on one side of the whole machine are actually in contact with obstacles, showing a short-term stable state of the whole machine. Test data and simulation results under two different driving speeds are in good agreement. The validity and reliability of tractor rollover dynamic system model and momentum flywheel active stabilization system are verified. The fact that the tractor has relatively good stability when running on the road with small undulation and low roughness coincides with the actual situation. The tractor rolls in different directions, but with the active intervention of the momentum flywheel system, they are stable, which enables it to drive safely and stably on the road with large fluctuation and high roughness. The method proposed in this paper can effectively suppress the rollover behavior of tractor under extreme working conditions.

REFERENCES

- [1] Elsayed, A. T., Youssef, T. A., & Mohammed, O. A. (2016). Modeling and control of a low speed flywheel driving system for pulsed load mitigation in DC distribution networks. *IEEE Transactions on Industry Applications*, Vol. 52, Issue 4, pp. 3378-3387. United States;
- [2] Hu, Y., Chen, M., Xu, S., & Liu, Y. (2017). Semi-active inerter and its application in adaptive tuned vibration absorbers. *IEEE Transactions on Control Systems Technology*, Vol. 25, Issue 1, pp.294-300. United States;

- [3] Jang B. E., Chowdhury M., Ali M., (2021). Stability and vibration analysis of a tractor-mounted Chinese cabbage collector // *IOP Conference Series: Earth and Environmental Science*. IOP Publishing, Vol. 733, Issue 1, pp. 01. United States;
- [4] Karakulak S. S., Yetkin E., (2020), Agricultural Tractor Cabin Safety Analysis and Test Correlation. *International Journal of Automotive Science and Technology*, Vol. 4, no. 1, pp. 1-9, 2020. South Korea;
- [5] Li, S., Liu, X., & Feng, X. (2018). Study of anti-rollover control strategy on pickup truck with active suspension. *Wuhan Ligong Daxue Xuebao (Jiaotong Kexue Yu Gongcheng Ban)/Journal of Wuhan University of Technology (Transportation Science and Engineering)*, Vol. 42, Issue 3, pp. 383-387. China;
- [6] Liao, C., Sun, Y. C., Li, M. S., & Li, M. (2018). Study on modeling and integrated anti-rollover control of automotive differential braking and active suspension. *IPPTA: Quarterly Journal of Indian Pulp and Paper Technical Association*, Vol.30, Issue8, pp. 793-799. China;
- [7] Rogov P. S., Orlov L. N., (2020), Determination of the most efficient bus rollover computer simulation technique according ECE R66. *International Journal of Heavy Vehicle Systems*, Vol. 27, Issue 4, pp. 422-440. United States;
- [8] Shamsuddin P., Mansor M. A., Ramli r. M., (2020). Development of navigation system for unmanned surface vehicle by improving path tracking performance. *Journal of Engineering Science and Technology*, Vol. 15, Issue 2, pp. 1371-1383. England;
- [9] Song H. S., Kim Y. Y., (2020), Determination of the Properties of the Rubber Mounted Under the Agricultural Tractor Rollover Protective Structure Cabin Using a Hyperelastic Tensile Test and Finite Element Analysis. *Journal of Biosystems Engineering*, Vol. 45, Issue 3, pp. 188-196. England;
- [10] Stroganov Y. N., Pampura E. M., (2020), Increase in linear motion steadiness of tractor-trailers using stabilizing towing couplers // *IOP Conference Series: Materials Science and Engineering*. IOP Publishing, Vol. 966, Issue 1, pp. 012123. United States;
- [11] Vahdanjoo M., Madsen C. T., Sørensen C. G., (2020), Novel Route Planning System for Machinery Selection. Case: Slurry Application. *AgriEngineering*, Vol. 2, Issue 3, pp. 408-429. Switzerland;
- [12] Wu, X., Zhou, B., & Wen, G. (2017). A study on anti-roll control of half-car model active interconnected suspension with consideration of actuator dynamics. *Journal of Vibration and Shock*, Vol. 36, Issue 12, pp.150-154. China;
- [13] Zhang L., Tan B., Liu T., (2021), Research on recognition of dangerous driving behavior based on support vector machine // *Twelfth International Conference on Graphics and Image Processing (ICGIP 2020)*. *International Society for Optics and Photonics*, 11720: 117201L, 2021. Switzerland;
- [14] Zhong, G., Deng, H., Kobayashi, Y., & Wang, H. (2015). Theoretical and experimental study on remote dynamic balance control for a suspended wheeled mobile manipulator. *Nonlinear Dynamics*, Vol. 79, Issue 2, pp. 851-864. U.S.A.;
- [15] Zong, Z., Sun, Y., & Jiang, Y. (2019). Experimental study of active t-foil control of longitudinal motions of a trimaran hull in irregular waves. *Journal of Ship Research*, Vol. 63, Issue 3, pp.165-181. China;

**METHOD OF THEORY OF DIMENSIONS
IN EXPERIMENTAL RESEARCH OF SYSTEMS AND PROCESSES**
/ **МЕТОД ТЕОРІЇ РОЗМІРНОСТЕЙ
В ЕКСПЕРИМЕНТАЛЬНИХ ДОСЛІДЖЕННЯХ СИСТЕМ І ПРОЦЕСІВ**

Dmytriv V.T.¹⁾, Dmytriv I.V.¹⁾, Horodetskyi I.M.²⁾, Horodniak R.V.¹⁾, Dmytriv T.V.³⁾ ¹⁾

¹⁾ Lviv Polytechnic National University, Institute of Mechanical Engineering and Transport, Lviv, Ukraine

²⁾ Lviv National Agrarian University, Faculty of Mechanic, Power Engineering and Information Technologies, Lviv-Dubliany, Ukraine

³⁾ Lviv Polytechnic National University, Institute of Computer Technologies, Automation and Metrology, Lviv, Ukraine

* E-mail: Dmytriv_V@ukr.net

DOI: <https://doi.org/10.356.33/inmateh-65-24>

Keywords: *technological process, dimension theory, experiment, Galileo criterion, Euler number, coefficient of friction, mathematical model.*

ABSTRACT

The method and parameters of experimental modelling of systems and processes in mechanical engineering are substantiated. The theory of similarity and dimensionality is used as an intermediate link between theory and experiment. The dimension of the factor space depends on the number of factors. The set of factors is grouped into dimensionless similarity criteria. The selected criteria are in certain dependence, such as the Galileo test, Euler and Reynolds numbers. Examples of application in experimental studies are given. The use of dimension theory in a factor-planned experiment allows reducing the number of factors, simplifies the mathematical interpretation of the response criterion and provides a graphical representation in the form of 3-D model.

РЕЗЮМЕ

Обґрунтовано методу та параметри експериментального моделювання систем і процесів в галузевому машинобудуванні. Використано теорію подібності і розмірності, як проміжну ланку між теорією і експериментом. Розмірність факторного простору залежить від числа факторів. Сукупність факторів згрупована в безрозмірні критерії подібності. Вибрані критерії знаходяться у визначеній залежності, наприклад критерій Галілея, числа Ейлера і Рейнольдса. Приведено приклади застосування в експериментальних дослідженнях. Використання теорії розмірності при факторному планованому експерименті дозволяє скоротити кількість факторів, спрощує математичну інтерпретацію характеру критерію відгуку і забезпечує графічне представлення у вигляді 3-D моделі.

INTRODUCTION

Nowadays, many technological processes and technical systems are evaluated by a large number of parameters that are mutually consistent and affect the indices of control or measurement. These indicators characterize the optimality of the system or process (Dmytriv V.T. et al, 2020). Modelling in the traditional form of a statistical model is one of the more scalable methods, which takes into account a large number of parameters, a significant amount of sample data and a significant range of variation. There are experimental research methods that reduce both the number of parameters and the amount of sample data. Such methods are as follows: analysis of basic parameters and its variants (Kettaneha N. et al, 2005; Elgamal T. and Hefeeda M., 2015), clustering methods (Bouveyron C. and Brunet-Soumard C., 2014), variational selection by checking the independence of factors (Fan J. and Lv J., 2008; Fan J et al, 2011) and the smallest angular regression (Efron B. et al, 2004).

For large data types, other methods have been developed, such as sequential updates for streaming data (Schifano E.D. et al, 2016) or matrix adjustments (Liberty E., 2013). These methods are aimed at simplifying data processing, reducing the characteristics of processes to linear functional dependences, but do not simplify the number of factors for multifactorial processes, where each parameter affects the optimization criterion.

¹⁾ Dmytriv V.T., Prof., PhD.Sc.Eng.; Dmytriv I.V., Assoc. prof., PhD.Eng.; Horodetskyi I.M., Assoc. prof., PhD.Eng.; Gorodnyak R. V., PhD.Eng.; Dmytriv T.V., Student.

For a large number of variables in the experiment it is more appropriate to use the totality of the methods of the dimensional analysis and modern statistical modelling of experiments (Islam M.F. and Lye L.M., 2009; Woods D. C. et al, 2017). The dimensional method is widely used to analyse the various processes, for this the Buckingham Pi theorem is used (Hu P. and Chang C.-kan, 2020). On the example of a significant number of parameters, which are grouped by functional characteristics, the method of dimensional functions shows the possibility of implementing the model on the measured data in real time (Wang Y. et al, 2019).

Experimental and analytical modelling of processes at the level of physical phenomena and patterns, including technical, technological and at the level of operational control of processes, requires a significant number of factors to be taken into account. These factors characterize the relationship between the parameters of the technological process and the physical and mechanical characteristics of the components involved in the technological process. To generalize and determine the characteristics of the technological process, it is advisable to have structured dependencies that describe in the first approximation the physics of the process and will give possibility to determine the critical limits of factors.

The purpose of this study is to develop methods for the theory of similarity and dimensionality, criterion values, as an intermediate component between theory and experiment. This will ensure a functional relation between whole sets of quantities that characterize the process at the level of the physical model and simplify the planned experiment for processes and systems characterized by a significant number of factors.

MATERIALS AND METHODS

Transformation of factor space by methods of dimension theory

The analysis of theoretical and experimental researches allows to conclude that in the theory of experiment planning the choice of process parameters is the most important. The accepted parameters should reflect all the main factors of the technological process, and their number should be minimal for the planned experiment. Reducing the number of factors reduces the number of experiments and increases the reliability of the response criterion.

The dimension of factor space depends on a number of factors, so to simplify the problem the method of dimension theory, namely the π -theorem, is used. The essence of this theorem is that the whole set of factors can be grouped into dimensionless similarity criteria of $\pi_1, \pi_2, \dots, \pi_i$ (Sonin A.A., 2001; Shen W., and Lin D. K. J., 2019; Albrecht M. C. et al, 2013; Jónsson D., 2014).

The application of methods of the theory of similarity and dimensionality, criterion quantities, as an intermediate component between theory and experiment, provides a functional relationship between whole sets of quantities that characterize the process at the level of the physical model.

The application of the proposed technique is as follows. The whole set of factors is grouped into dimensionless similarity criteria. To find these quantities, the basic units of measurement are chosen and through them - the dimension of all other quantities. For example, the number of factors is n values, and r is the number of values that have independent dimensions, respectively, $n - r$ similarity criteria are obtained. The selected criteria are in a certain dependence.

For example, modelling of hydropneumodynamic processes is considered (Dmytriv V. et al, 2018; Dmytriv V.T. et al, 2019; Dmytriv V. et al, 2019). Galileo's criterion, Euler's and Reynolds numbers were an analogue of the momentum of kinetic energy, the specific indicator of the equivalent of energy consumption was the equivalent factor of profitability or productivity, the scale factor and others were used in study. Similarly for other modelling, for example, is considered the process of mixing a multicomponent mixture with the indices as follows. The analogue of the kinetic energy momentum of the bulk material particle is justified as a ratio of $p \cdot g / (\mu \cdot \omega)$, where: g – acceleration of gravity, m/s^2 ; μ – dynamic flow viscosity of the bulk component, $kg/(m \cdot s)$, ω - angular speed, s^{-1} , p – pressure in the mixing chamber of the components, kg/m^2 .

All selected parameters must have a physical meaning and be controlled during the experiment, meet the requirements of compatibility and independence. The correct choice of these parameters is confirmed by a determinant consisting of the dimensions of these parameters, which should not be equal to zero.

Transformation of a multifactor space into a two-factor planned experiment

It is considered the transformation of multifactor space into a two-factor planned experiment on the example of air transportation in the vacuum pipeline of the milking machine. The process can be subjected to the method of proportionality and a combination of similarity numbers through the equation of relations:

$$\lambda = f(\Delta p, u, g, v, \rho, i_p, d) \quad (1)$$

where: λ - coefficient of friction; Δp – pressure drop at the section, Pa; v – air velocity, m/s; g – acceleration of gravity, m/s²; η – kinematic viscosity of the mixture, m²/s; ρ – air density at a given pressure, kg/m³; i_p – piezometric slope of the pipeline; d – diameter of the milk pipeline, m.

To find these quantities, the basic units of measurement are chosen and through them the dimension of all other quantities are expressed. In this case, $n=7$ quantities, and $r = 3$ is the number of quantities having independent dimensions, respectively, $n - r = 4$ similarity criteria are obtained. The selected criteria are in a certain dependence. Basic units of dimension are: mass, length, time (Table 1). The main parameters of air movement are $\Delta p, \eta, d$.

Table 1

Dimensionality of the parameters of the equation for milk-air mixture transporting through the milk pipeline of the milking machine

Operation factors	λ	Δp	v	g	η	ρ	i_p	d
M	0	1	0	0	0	1	0	0
L	0	-1	1	1	2	-3	0	1
T	0	-2	-1	-2	-1	0	0	0

The correct choice of parameters is confirmed by the determinant, which consists of the dimension of these parameters, which should not be equal to zero:

$$\Delta = \begin{vmatrix} \Delta p & \eta & d \\ M & 1 & 0 & 0 \\ L & -1 & 2 & 1 \\ T & -2 & -1 & 0 \end{vmatrix} = 1 \neq 0$$

Taking into consideration the choice of basic units, the equation (1) can be written as:

$$\lambda = F((\Delta p^{\alpha v} \cdot \eta^{\beta v} \cdot d^{\gamma v})/v; (\Delta p^{\alpha g} \cdot \eta^{\beta g} \cdot d^{\gamma g})/g; (\Delta p^{\alpha \rho} \cdot \eta^{\beta \rho} \cdot d^{\gamma \rho})/\rho; 1) \tag{2}$$

The coefficients of $\alpha v, \dots, \beta g, \dots, \gamma \rho$ were determined on the condition that each complex is dimensionless quantity. The values of $\alpha U, \beta U, \gamma U$ were determined in the way of:

$$\frac{\Delta p^{\alpha v} \cdot \eta^{\beta v} \cdot d^{\gamma v}}{v} = \frac{(M^1 \cdot L^{-1} \cdot T^{-2})^{\alpha U} \cdot (L^2 \cdot T^{-1})^{\beta U} \cdot (L^1)^{\gamma U}}{L^1 \cdot T^{-1}} = M^{\alpha v} \cdot L^{-\alpha v + 2\beta v + \gamma v - 1} \cdot T^{-2\alpha v - \beta v + 1} = 1 \tag{3}$$

From the equation (3) a system of equations of the power expressions is composed and solved by finding the values of powers at their parameters:

$$\begin{cases} \alpha v = 0 \\ -\alpha v + 2\beta v + \gamma v - 1 = 0 \\ -2\alpha v - \beta v + 1 = 0 \end{cases} \rightarrow \begin{cases} \alpha v = 0 \\ \gamma v = -1 \\ \beta v = 1 \end{cases} \tag{4}$$

Accordingly, the similarity criterion for velocity was determined by the ratio:

$$\Pi_v = \frac{\eta}{d \cdot v} \tag{5}$$

By analogy for other criteria, the values of indicators are found and the ratio for other similarity criteria is written:

$$\Pi_g = \frac{\eta^2}{d^3 \cdot g}, \quad \Pi_\rho = \frac{\Delta p \cdot d^2}{\eta^2 \cdot \rho} \tag{6}$$

Instead of the parameters in equation (1), the following criteria will be substituted:

$$\lambda = f\left(\frac{\eta}{d \cdot v}, \frac{\eta^2}{d^3 \cdot g}, \frac{\Delta p \cdot d^2}{\eta^2 \cdot \rho}, i_p\right) \tag{7}$$

In the equation of (7), the first component is the inverse of the Reynolds number (1/Re), the second component is the inverse of the Galilean criterion (1/Ga), and the third component is the Euler number (Eu), in which the η^2/d^2 ratio has an explicit physical content of the mixture velocity.

In equation (7), the kinematic viscosity is repeated in the first and second terms, so the inverse of the Galilean criterion is multiplied by the Euler number and the result is the second and third terms. After these transformations, the following equation is obtained:

$$\lambda = f\left(\frac{\eta}{d \cdot v}, \frac{\Delta p}{d \cdot \rho \cdot g}, i_p\right) \tag{8}$$

The third term of the (8) equation is a constant value during the experiment, so it is neglected. The (8) criterion equation will take the form of:

$$\lambda = f(\text{Re}, Eu); \frac{1}{\text{Re}} = \frac{\eta}{d \cdot v}; Eu = \frac{\Delta p}{d \cdot \rho \cdot g}. \tag{9}$$

For the planned experiment, where the response criterion is the coefficient of friction, there were two factors, the Reynolds number and the Euler number. These criteria take into account the main parameters on which the coefficient of friction is depended.

Transformation of a multifactor space into a three-factor planned experiment

The technological process of bulk material mixing in a low vacuum environment is considered. The dependence of homogeneity and energy efficiency on the determining parameters can be represented by the connection equations:

$$v_m = f(\omega, g, R_\rho, R_D, \alpha, m_b, \rho_{10}, \mu_{10}, Q, p); \tag{10}$$

$$N_m = f(\omega, g, R_\rho, R_D, \alpha, m_b, \rho_{10}, \mu_{10}, Q, p), \tag{11}$$

where ω – angular speed of rotation of the dosing and mixing disk, [s⁻¹]; g – acceleration of gravity, [m/s²]; R_ρ – radius of the curvature of agitator, [m]; R_D – disk radius, [m]; α – the angle of inclination of the generating line of disk, [grad]; m_b – number of blades or agitators on the disk, pcs.; ρ_{10} – density of bulk material, [kg/m³]; μ_{10} – the dynamic viscosity of bulk material flow, [kg/(m·s)]; Q – productivity of the mixing component, [kg/s]; p – vacuum in the chamber of the components mixing, [kg/m²].

In this case, $n = 10$ quantities, and $r = 3$ is the number of quantities having independent dimensions, respectively, $n - r = 7$ similarity criteria are obtained. The selected criteria are in certain dependence. Length, mass and time were accepted as basic units. The dimensions of the required and defining parameters of the work process are given in Table 2.

Table 2

The dimension of the parameters of the mixer of the feed mixture micro-components

Operation factors	v_{3M}	N_{3M}	ω	g	R_ρ	R_D	α	m_b	ρ_{10}	μ_{10}	Q	p
M	0	1	0	0	0	0	0	0	1	1	1	1
L	0	0	0	1	1	1	0	0	-3	-1	0	-2
T	0	0	-1	-2	0	0	0	0	-	-1	1	0

From Table 2 the basic units of measurement for the considered technological process are chosen. As the main parameters ω, ρ_{10}, p were considered. The correct choice of these parameters is confirmed by the determinant, which consists of the dimension of these parameters, which should not be equal to zero. Once such a determinant is solved, the following is obtained:

$$\Delta = \begin{vmatrix} \omega & \rho_{10} & p \\ M & 0 & 1 & 1 \\ L & 0 & -3 & -2 \\ T & -1 & 0 & 0 \end{vmatrix} = -1 \neq 0$$

Taking into consideration the choice of basic units the equation (10) can be written as:

$$v_m = \Phi(1; g / (\omega^{\beta g} \rho^{\gamma g} p^{\lambda g}); R_\rho / (\omega^{\beta h} \rho^{\gamma h} p^{\lambda h}); R_D / (\omega^{\beta d} \rho^{\gamma d} p^{\lambda d}); 1; \mu_{10} / (\omega^{\beta \mu} \rho^{\gamma \mu} p^{\lambda \mu}); 1). \tag{12}$$

The coefficients of $\beta g, \gamma h, \dots, \lambda \mu$ were determined on the condition that each complex is dimensionless quantity. The values of $\beta g, \gamma g, \mu g$ were determined in the way of:

$$\begin{aligned}
 g / (\omega^{\beta g} \rho^{\gamma g} p^{\lambda g}) &= L^1 \cdot T^{-2} \sqrt{\left[|T^{-1}|^{\beta g} |M^1 \cdot L^{-3}|^{\gamma g} |M^1 \cdot L^{-2}|^{\lambda g} \right]} = \\
 &= L^1 \cdot T^{-2} / (T^{-\beta g} \cdot M^{\gamma g + \lambda g} \cdot L^{-3\gamma g - 2\lambda g}) = T^{-2 + \beta g} \cdot M^{-\gamma g - \lambda g} \cdot L^{1 + 3\gamma g + 2\lambda g} = 1 \\
 &- 2 + \beta g = 0, \text{ whence } \beta g = 2 \\
 &-\gamma g - \lambda g = 0, \text{ whence } \gamma g = -1 \\
 &1 + 3\gamma g + 2\lambda g = 0, \text{ whence } \lambda g = 1
 \end{aligned}$$

Accordingly, this similarity criterion was determined by the ratio:

$$\Pi_g = \frac{\omega^2 p}{g \rho_{10}} \quad (13)$$

In a similar manner the other criteria were determined:

$$\Pi_{R_p} = \frac{R_p p}{\rho_{10}}; \quad \Pi_D = \frac{R_D p}{\rho_{10}}; \quad \Pi_\mu = \frac{\mu_{10} p^2 \omega}{\rho_{10}} \quad (14)$$

Taking into consideration the criteria of (13) and (14), equation (10) is written as follows:

$$v_m = \Phi(\Pi_g, \Pi_h, \Pi_d, \Pi_\mu, \alpha, m_b) \quad (15)$$

The product of criteria (13) and (14) or their division gives the new criteria, respectively:

$$\Pi_h : \Pi_d = \frac{R_p}{R_D}, \quad Q : \Pi_\mu \cdot \Pi_g = \frac{Q \cdot \omega}{\mu_{10} \cdot p \cdot g}$$

After the transformations, a new criterion equation is obtained:

$$v_m, N_m = \Phi\left(\frac{Q \cdot \omega}{\mu_{10} \cdot p \cdot g}; \frac{R_p}{R_D}; \alpha; m_b\right) \quad (16)$$

where: $\frac{Q \cdot \omega}{\mu_{10} \cdot p \cdot g}$ – dimensionless factor of feeding of a blending agent on mixing;

R_p/R_D – the scale factor; α, m_b – dimensionless factors.

Since the number of blades on the disk is constant, the m_b factor is not taken into account during the experiment.

When the vacuum changes from 0 to 6 kPa, the dynamic flow viscosity is constant.

At atmospheric pressure the vacuum is 0, so the division by 0 in the dimensionless factor gives infinity. Instead of a vacuum, a coefficient that is calculated as a ratio is introduced:

$$K_p = \frac{p_{atm}}{p_{abs}}, \quad (17)$$

where: p_{atm} – atmospheric pressure, kPa; p_{abs} – absolute pressure in the mixing chamber, kPa;

$$p_{abs} = p_{atm} - p_v.$$

Accordingly, at atmospheric pressure $K_p = 1.0$ at $p_v = 3$ kPa; $K_p = 1.031$ at $p_v = 6$ kPa; $K_p = 1.064$.

Thus, the derived similarity criteria in their physical content are as follows: $Q \cdot \omega / (K_p \cdot g)$ – analogue of the momentum of the kinetic energy of a particle adding into the mixture of bulk material; R_p/R_D – scale factor; α – the angle of the generating line of the disk, the dimensionless factor.

RESULTS

The results of experimental studies of the coefficient of friction

The nature of the change in the coefficient of friction of air depending on the Reynolds and Euler numbers according to (9) criterion equation is considered. Reynolds and Euler numbers are calculated from experimental data of parameters: the volume air flow of vacuum pipeline $V = 0.0015-0.0060$ m³/s; the loss of vacuum gage pressure of the vacuum pipeline $\Delta p = 0.6-2.2$ [kPa]; the inner diameter of the vacuum pipeline $d = 0.022-0.038$ m.

The regression equation in natural values has the form of:

$$\lambda = 4.4218 - 1.3104 \cdot 10^5 \cdot \frac{1}{Re} + 0.0029 \cdot Eu + 9.265 \cdot 10^7 \cdot \left(\frac{1}{Re}\right)^2 + 24.032 \cdot \frac{1}{Re} \cdot Eu - 3.9655 \cdot 10^{-7} \cdot Eu^2 \quad (18)$$

The calculated value of the Cochran test is $G_{cal} = 0.2601$, which is less than the tabular of $G_T = 0.2624$. Accordingly, the experiment is reproduced.

The calculated value of the F -criterion is $F_{cal} = 0.2111$, which is much lower than the tabular $F_T = 2.3$. Accordingly, the model is adequate.

The graphical representation of the regression equation is presented in the form of a three-dimensional plane (Fig. 1).

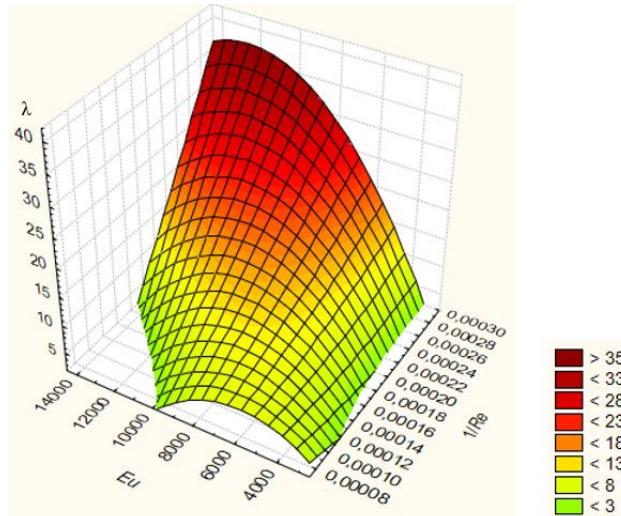


Fig. 1 – Dependence of the coefficient of friction λ of air in vacuum pipeline on the Euler and Reynolds numbers

The results of experimental studies of the homogeneity of bulk materials mixing

The results of a planned experiment are considered to study the homogeneity of mixing by the meter-mixer using the following factors: analogue of the kinetic energy impulse (x_1) – $Q \cdot \omega / (K_p \cdot g)$, the angle of the generating line of the metering disk α (x_2), scale factor of (x_3) – R_p / R_D . The response criterion is the homogeneity of the mixing of the meter-mixer.

The regression equation, which characterizes the dependence of the mixing homogeneity of the meter-mixer on the analogue of the kinetic energy impulse, the angle of the generating line of the metering disk and the scale factor in natural values, is as follows:

$$y = 0.0883921 \cdot \frac{Q \cdot \omega}{K_p \cdot g} + 0.088567 \cdot \alpha - 0.0990177 \cdot \frac{R_p}{R_D} \tag{19}$$

The calculated value of the Cochran-criterion is $G_{cal} = 0.09497$ which is less than the tabular of $G_T = 0.1377$, accordingly, the experiment is reproduced.

The calculated value of the F -criterion is $F_{cal} = 1.5882$, which is less than the tabular $F_T = 1.6$, which confirms the adequacy of the model. The graphical representation of the regression equation is presented in the form of four-dimensional plane (Fig. 2).

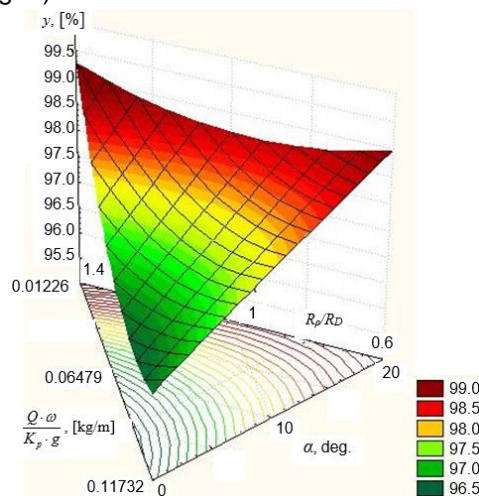


Fig. 2 - The dependence of the y mixing homogeneity of the meter-mixer on the analogue of the kinetic energy impulse of $Q \cdot \omega / (K_p \cdot g)$, the R_p / R_D scale factor and the α angle of the generating line of the metering disk

CONCLUSIONS

Analysis of the results of experimental studies of the friction coefficient where the factors are Reynolds and Euler numbers, showed the identity to the theoretical studies. The coefficient of friction is within the same limits. With vacuum and excess pressures, with decreasing of Reynolds number and increasing of Euler number, the gas friction coefficient increased. As the pressure loss and the diameter of the pipeline are increased the friction coefficient increased as well. An increase in the Reynolds number characterizes an increase as follows: the dynamic parameters of gas flow, velocity and flow modes - from laminar to turbulent, which consequently leads to an increase in Mach number.

The use of dimension theory in a factor-planned experiment allows reducing the number of factors, simplifies the mathematical interpretation of the response criterion and provides a graphical representation in the form of 3-D model. Fundamental similarity numbers confirm the validity of the model and expand the number of factors that directly through the similarity numbers characterize the physical essence of the processes. The use of the research results allows optimal tasks control according to specified criteria.

Using the method of the theory of similarity and dimensionality, criterion values, as an intermediate component between theory and experiment ensures a functional relationship between whole sets of quantities that characterize the process at the level of the physical model.

REFERENCES

- [1] Albrecht M. C., Albrecht T. A., Nachtsheim C. J. and Cook R. D., (2013), Experimental Design for Engineering Dimensional Analysis, *Technometrics*, Vol. 55(3), pp. 257–270. <http://www.jstor.org/stable/24587346> ;
- [2] Bouveyron C. and Brunet-Saumard C., (2014), Model-based clustering of high-dimensional data: A review, *Computational Statistics & Data Analysis*, Vol. 71, pp. 52–78. <https://doi.org/10.1016/j.csda.2012.12.008> ;
- [3] Dmytriv V.T., Dmytriv I.V., Horodetskyi I.M. et al, (2020), Adaptive cyber-physical system of the milk production process, *INMATEH - Agricultural Engineering*, Vol. 61, No. 2, pp. 199 - 208, Bucharest / Romania. DOI: 10.35633/inmateh-61-22 ;
- [4] Dmytriv V.T., Dmytriv I.V. and Yatsunskiy P.P., (2019), Experimental pulse generator combined with the milking machine collector, *INMATEH - Agricultural Engineering*, vol. 59(3), pp. 219-226. DOI: 10.35633/INMATEH-59-24 ;
- [5] Dmytriv V., Dmytriv I., Horodetskyi I. and Dmytriv T., (2019), Analytical dynamic model of coefficient of friction of air pipeline under pressure, *Diagnostyka*, Vol. 20(4), pp. 89–94. DOI: 10.29354/diag/114334 ;
- [6] Dmytriv V., Dmytriv I. and Dmytriv T., (2018), Research in thermoanemometric measuring device of pulse flow of two-phase medium, *17th International Scientific Conference: Engineering for Rural Development*, Jelgava / Latvia, vol. 17, pp. 894-904. DOI: 10.22616/ERDev2018.17.N200 ;
- [7] Elgamal T. and Hefeeda M., (2015), Analysis of PCA algorithms in distributed environments. Preprint. Available at : [arXiv:1503.05214v2](https://arxiv.org/abs/1503.05214v2) ;
- [8] Efron B., Hastie T., Johnstone I. and Tibshirani R., (2004), Least angle regression. *The Annals of Statistics*, Vol. 32 (2), pp. 407 – 499. <https://doi.org/10.1214/009053604000000067> ;
- [9] Fan J., Feng Y. and Song R., (2011), Nonparametric independence screening in sparse ultra-high dimensional additive models. *Journal of the American Statistical Association*, Vol. 106(494), pp. 544 - 557. DOI: 10.1198/jasa.2011.tm09779 ;
- [10] Fan J. and Lv J., (2008), Sure independence screening for ultrahigh dimensional feature space. *Journal of the Royal Statistical Society: Series B (Statistical Methodology)*, Vol. 70(5), pp. 849 - 911. <https://doi.org/10.1111/j.1467-9868.2008.00674.x> ;
- [11] Hu P. and Chang C.-kan, (2020), Research on optimize application of Buckingham Pi theorem to wind tunnel test and its aerodynamic simulation verification, *Journal of Physics: Conference Series*, vol. 1507(8). <https://doi.org/10.1088/1742-6596/1507/8/082047> ;
- [12] Islam M.F. and Lye L.M., (2009), Combined use of dimensional analysis and modern experimental design methodologies in hydrodynamics experiments, *Ocean Engineering*, Vol. 36(3-4), pp. 237-247. DOI: 10.1016/j.oceaneng.2008.11.004 ;
- [13] Jónsson D., (2014), Dimensional Analysis: A Centenary Update. *arXiv: 1411.2798* ;
- [14] Kettaneha N., Berglund A. and Wold S., (2005), PCA and PLS with very large data sets, *Computational Statistics & Data Analysis*, Vol. 48(1), pp. 69–85. <https://doi.org/10.1016/j.csda.2003.11.027> ;

- [15] Liberty E., (2013), Simple and deterministic matrix sketching. *In Proceedings of the 19th ACM SIGKDD International Conference on Knowledge Discovery and Data Mining*, (August 2013), pp. 581–588. ACM, New York. <https://doi.org/10.1145/2487575.2487623>;
- [16] Schifano E. D., Wu J., Wang C., Yan J. and Chen M.-H., (2016), Online updating of statistical inference in the big data setting. *Technometrics*, Vol. 58(3), pp. 393–403. DOI: 10.1080/00401706.2016.1142900;
- [17] Shen W., and Lin D. K. J., (2019), Statistical theories for dimensional analysis, *Statistica Sinica*, Vol. 29(2), pp. 527–550. <https://www.jstor.org/stable/26705477> ;
- [18] Sonin A.A., (2001), *The Physical Basis of Dimensional Analysis*. 2nd Edition, Department of Mechanical Engineering, MIT, Cambridge. <http://goo.gl/2BaQM6> ;
- [19] Tsoutsouras V., Willis S. and Stanley-Marbell Ph., (2021), Deriving equations from sensor data using dimensional function synthesis, *Communications of the ACM*, Vol. 64(7), pp. 91–99. <https://doi.org/10.1145/3465216> ;
- [20] Wang Y., Willis S., Tsoutsouras V. and Stanley-Marbell Ph., (2019), Deriving Equations from Sensor Data Using Dimensional Function Synthesis, *ACM Transactions on Embedded Computing Systems*, Vol. 18(5s), Article No.: 84, pp. 1–22. <https://doi.org/10.1145/3358218> ;
- [21] Woods D. C., Overstall A. M., Adamou M. and Waite T. W., (2017), Bayesian design of experiments for generalized linear models and dimensional analysis with industrial and scientific application, *Quality Engineering*, Vol. 29(1), pp. 91-103. <https://doi.org/10.1080/08982112.2016.1246045> .

**DEVELOPMENT AND TESTING OF BED FORMER IMPLEMENT
POWERED BY HAND TRACTORS**
/
**PENGEMBANGAN DAN PENGUJIAN IMPLEMEN PEMBUAT GULUDAN DENGAN
SUMBER DAYA TRAKTOR TANGAN**

Mustaqimah ¹⁾, Ramayanty Bulan ^{*1)}, Syafrandi ¹⁾, Reza Imanda ¹⁾, Uzair ¹⁾, Dewi Sartika T. ²⁾, Agustami Sitorus ³⁾

¹⁾ Department of Agricultural Engineering, Syiah Kuala University/ Indonesia;

²⁾ Department of Civil Engineering, Nusa Putra University/ Indonesia;

³⁾ Research Centre for Appropriate Technology, National Research and Innovation Agency (BRIN) / Indonesia;

Tel: +62 812-8343-9334; E-mail: ramayantybulan@gmail.com

DOI: <https://doi.org/10.356.33/inmateh-65-25>

Keywords: agriculture engineering, appropriate technology, machinery, soil tillage, upland conservation

ABSTRACT

Soil tillage, like making raised beds, is time-consuming and labour-intensive if it is done without the help of mechanization. Therefore, this study aims to develop and test a bed former powered by a hand-tractor for upland. It was carried out in the experimental field (sandy clay loam texture) at a furrow depth of 15 cm and 20 cm with a tractor forward speed of 0.5 m/s. The bed's former design results have dimensions of length, width, and height of 1200×1000×820 mm. The performance test results showed an increase in tillage depth resulted in increased bed height, bed width, bed width, and slip. However, field capacity decreases with increasing tillage depth. The bed former's performance was found to be satisfactory in general.

ABSTRAK

Pengolahan tanah, seperti membuat guludan, memakan waktu dan tenaga jika dilakukan tanpa bantuan mekanisasi. Oleh karena itu, penelitian ini bertujuan untuk mengembangkan dan menguji alat pembentuk guludan yang ditarik oleh traktor tangan untuk lahan kering. Penelitian ini dilakukan pada plot percobaan (tekstur tanah lempung berpasir) pada kedalaman pengolahan tanah 15 cm dan 20 cm dengan kecepatan maju traktor 0.5 m/s. Hasil desain alat pembentuk guludan memiliki dimensi panjang, lebar, dan tinggi masing-masing sebesar 1200×1000×820 mm. Hasil uji performansi menunjukkan peningkatan kedalaman pengolahan mengakibatkan peningkatan tinggi guludan, lebar atas guludan dan lebar bawah guludan serta slip. Namun, kapasitas lapangan menurun dengan bertambahnya kedalaman pengolahan tanah. Kinerja pembentuk guludan secara umum sangat memuaskan.

INTRODUCTION

The raised beds are places for cultivated plants to grow by elevating the soil and giving special treatment. The purpose of making the raised beds is to make planting easier, both in terms of overcoming weeds, runoff and providing nutrition in the hope of producing maximum yields. According to Govaerts *et al.* (2006), the size and shape of the raised beds made by the bed former machine will determine the commodity to be planted.

Bed forming can have an average length of 20-30 m depending on the area of land being cultivated. Raised beds can have an average bed height between 25 and 30 cm with an average bed width of 30-40 cm (Figure 1). As a result, the process of making raised beds requires a lot of time and energy in the process (Dixit *et al.*, 2018; Kato *et al.*, 2007; Zhang *et al.*, 2018). Therefore, there are several researchers and engineers who have attempted to carry out the design of this machine. However, very few studies have focused on the developed bed former machine for upland crops until today.

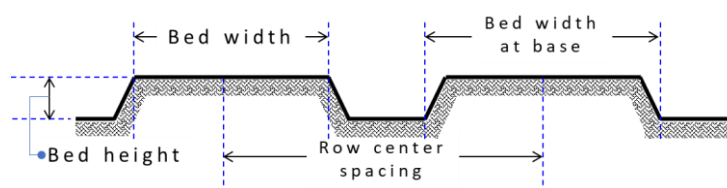


Fig. 1 - View of the raised beds for growing crops

Dixit *et al.*, (2018), have studied developing and testing a wide-bed former for vegetables towed by a 50 HP 2WD four-wheel tractor. The field capacity of this machine is reported as 0.31 ha/h with a forward speed of 2.75-5.25 km/h.

Another study from Saha *et al.* (2018) has carried out research on the performance of a bed former integrated with the planter and powered by a 52 kW 4WD four-wheel tractor. Bed width and bed height of bed former made are 1200mm, 200mm, respectively. Field capacity from this implement is reported to be 0.35 ha/h.

Besides, Awad, (2016), conducted the manufacture of a prototype of a raised-bed planter for wheat. This study suggests using a speed of 1.21 m/s in making raised beds for silty loam soil texture. This implement is also integrated with a planting device which is both pulled by a 2WD four-wheel tractor. The power required to pull these implements is reported to be in the range of 3.03 to 5.65 kW.

In addition, He *et al.*, (2009), have investigated the design of bed former for permanent raised beds. This study reports that his bed-former design can work more effectively. Unfortunately, the tractor power and field capacity of the designed implementation are not specifically reported.

To the best of our knowledge, the entire developed bed former uses a four-wheeled tractor to pull the bed former implements. So far, no other studies have been reported developing a bed former that was pulled using a hand tractor. In fact, hand tractors are more commonly used in Indonesia. Therefore, this study aims to develop and test the bed former with 10.5 HP hand tractors.

MATERIALS AND METHODS

The conceptual design of the bed former as an implement is presented in Figure 2. The bed-forming equipment's main components are the furrower unit, bed former unit, third wheel unit, and mainframe unit. The furrower unit functions to make soil grooves and drain them to the bed former unit. Bed former functions to form raised beds. The third wheel will function to adjust the depth of soil tillage.

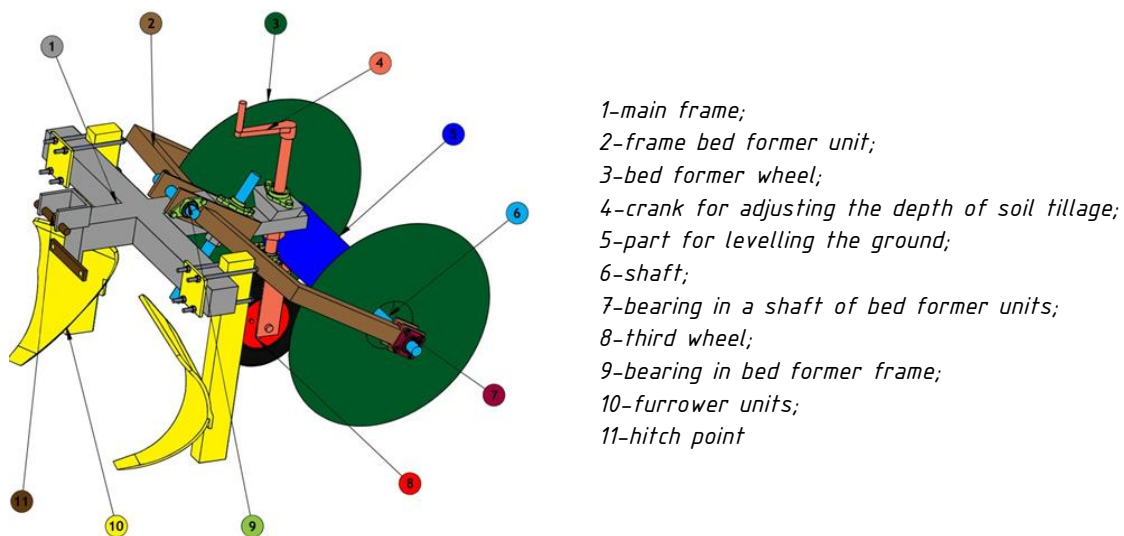


Fig. 2 - Isometric design of bed former as an implement for hand tractor

This analysis is used to determine the criteria for the material used in the bed's former machine's design. This estimation is to determine the maximum load that can be pulled by a hand tractor using Equation 1. Material flexibility is analysed using Equation 2 (Bulan *et al.*, 2019).

$$\sigma = \frac{F}{A} \quad (1)$$

$$\sigma = \frac{M_L}{W_L} \quad (2)$$

where:

σ - tensile strength (MPa);

F - force (N);
 A - cross-sectional area of the specimen (m²);
 σ_L - bending stress (Kg/cm²);
 M_L - bending moment (Kg/cm);
 W_L - linear moment (cm³).

The frame is the most important component of a machine that functions as a holder for other components. The frame also functions as a load-bearing so that the frame is not deflected. To calculate this effect, Equation 3 is used. The deflection caused by the loading is compared to the approval deflection calculated using Equation 4 (Slaitas and Valivonis, 2021).

$$\delta = \frac{PL^3}{48EI} \quad (3)$$

$$\delta_{izin} = \frac{1}{300}L \quad (4)$$

where:

δ - deflection that occurs (mm);
 P - power (watt);
 L - centre point (mm);
 E - modulus of elasticity (kg/mm²);
 I - moment of inertia (mm⁴);

Analysis of hand tractor power requirements is estimated by calculating each tractor power requirement and the power required to move the bed former. The power requirement of the tractor can be estimated using Equation 5. The power requirement to pull the implement bed former can be calculated using Equation 6 (Usaborisut and Prasertkan, 2019).

$$P_T = C_{rr} \cdot F_T \cdot V_t \quad (5)$$

$$P_{BF} = \mu \cdot F_{BF} \cdot V_t \quad (6)$$

$$P_a = P_T + P_{BF} \quad (7)$$

where:

P_T - tractor power requirements (Watt);
 C_{rr} - rolling resistance coefficient;
 F_T - weight of hand tractor (N);
 V_t - tractor forward speed (m/s);
 P_{BF} - power requirements to pull implements (Watt);
 μ - pull force coefficient;
 F_{BF} - weight of bed former (N);
 P_a - total power requirement of the tractor (Watt).

The type of tractors used in this research is YZC series, 10.5 HP, 2400 RPM hand tractor. Hand tractor has a field capacity of up to 0.11 ha/h. The tractor speed applied in this research is 0.5 m/s. The slips that occur during tillage are also measured using Equation 8 (Shafaei *et al.*, 2021).

$$S = \frac{D_t - D_r}{D_t} \times 100\% \quad (8)$$

where: S - Slip (%); D_t - theoretical distance (m); D_r - real distance (m).

Field testing was carried out on a plot of land measuring 12 m × 10 m. The length of the track in one trial was 9.2 m. The bed former is tested at furrower depths of 15 cm and 20 cm. The test was carried out with three repetitions. The theoretical field capacity, effective field capacity, and efficiency are calculated using Equation 9 to Equation 11, respectively (Kumar *et al.*, 2013).

$$F_{CT} = \frac{W_i \times V_t \times 3.6}{10^5} \quad (9)$$

$$F_{CE} = \frac{D_T \times W_t \times 3.6}{t \times 10^5} \quad (10)$$

$$E_F = \frac{F_{CE}}{F_{CT}} \times 100\% \quad (11)$$

where:

F_{CT} - theoretical capacity field (ha/h);

W_i - width implement (cm);

V_t - tractor forward speed (m/s);

F_{CE} - effective field capacity (ha/h);

D_T - bed track length (cm);

W_t - tillage width (cm);

t - time of making the raised beds (s);

E_F - effectiveness (%).

The shape and height bed from the designed machine are measured using a relief meter. Soil physical properties such as soil moisture content and bulk density were measured before and after making the raised beds. Soil moisture content was measured using the gravimetric method and calculated using Equation 12 and soil bulk density was measured using Equation 13. Soil sampling was carried out as 10 points from the experimental plot.

$$S_w = \frac{m_{sw} - m_{sd}}{m_{sd}} \times 100\% \quad (12)$$

$$B_D = \frac{m_{sd}}{V_{ol}} \quad (13)$$

where:

S_w - soil moisture content (% d.b.);

m_{sw} - wet soil mass (g);

m_{sd} - dry soil mass (g);

B_D - bulk density (g);

V_{ol} - soil volume (cm³).



Fig. 3 - Measurement of raised beds with a relief meter

RESULTS

The bed former (Figure 4) is designed with dimensions of length, width, and height of 1200, 1000, 820 mm, respectively. The total weight of this implement is 96.7 kg. The bed former unit has a diameter of 600 mm with a steel plate material with a thickness of 3 mm. The total length of the bed former unit is 700 mm.

A connecting rod 25.4 mm in diameter is connected at the hitch point of a hand tractor. The total height and width of the furrower are 400 mm, 350 mm, respectively. The width of the bottom of the furrower is 44 mm with an angle of 45°. The thickness of the plate used in the furrower was 12 mm. A third wheel with a turning crank is used to adjust the depth of tillage. All parts are attached to the mainframe made of UNP iron measuring 80×45×6 mm.



- 1-hitch point;
- 2-hand tractor (10.5 HP);
- 3-handle soil tillage depth adjustment;
- 4-bed former unit;
- 5-third wheel;
- 6-furrower unit

Fig. 4 - Bed former powered by hand tractors

The soil composition in the test area has a sand content of 55%, silt 16%, and clay 28%. This shows that the soil texture for this implement test is sandy clay loam. The moisture content before making the raised beds was 27.91%. The moisture content after the process of making the raised beds was 24.58%. These results indicate that the moisture content has decreased after making the raised beds. The moisture content after tillage decreases because of evaporation generated by soil disturbance.

The result of bulk density measurement before making the raised beds is 1.26 g/cm³. After making the raised beds is carried out, the average value of bulk density is 0.89 g/cm³. These results indicate a decrease in bulk density after making raised beds by 29.37%. This phenomenon is in line with several studies (Osunbitan *et al.*, 2005; Evans *et al.*, 1996; Li *et al.*, 2019) that state that the denser the soil the higher the bulk density. Besides, tillage will provide a lower bulk density value where the best bulk density for upland crop growth should be less than 1.53 g/cm³ (Xiu *et al.*, 2019; Bilgili *et al.*, 2017; Kundu *et al.*, 2019).

The relief of raised beds formed from furrower as deep as 15 cm are presented in Figure 5. It can be seen that the formed bed height has an average of 19.66±0.58 cm. The formed bed width and bed width at base were 46.33±1.53 cm, 65.66±1.54 cm, respectively. This bed height has followed several studies (Niu *et al.*, 2007; Jolliffe and Gaye, 1995; Simpson *et al.*, 2019), which state that bed height should be in the range of 15-23 cm. Besides, the effective field capacity of the tool with this treatment is 0.13 ha/h with an efficiency of 78.41%. It is smaller than the research results of Saha *et al.* (2018) and Dixit *et al.* (2018) which use a four-wheeled tractor as their power source.

The relief of raised beds from furrower treatment as deep as 20 cm are presented in Figure 6. It can be seen that the formed bed height has an average of 23.67±0.58 cm. Also, formed bed width and bed width at base was 41.67±1.15 cm, 67.33±0.58 cm, respectively. The effective field capacity with this treatment is 0.11 ha/h with an efficiency of 65.91%.

Bed former slip can reduce field efficiency and supply traction from the tractor used as a power source. The average slip for a furrower with a depth of 15 cm is 15.17±1.19%. At a furrower depth of 20 cm, the average slip that occurred was 23.0±0.67%. This slip is greater than the results of Awad, (2016), which reported that the maximum slip that occurs in testing the prototype of a raised-bed planter for wheat, towed using a 2WD tractor, is less than 15%. On the other hand, Syahri *et al.* (2019) also reported more significant slip (23.04%) from this study's results when using a hand tractor in traversing an inclined plane.

However, *Pranav et al., (2012)*, explained that the slip in soil tillage activities is still within normal limits if it occurs in the range of 14% to 23%.

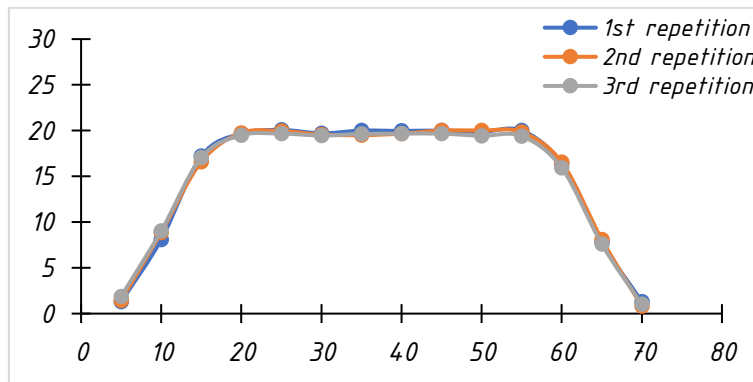


Fig. 5 - Relief of raised beds at a furrow depth of 15 cm

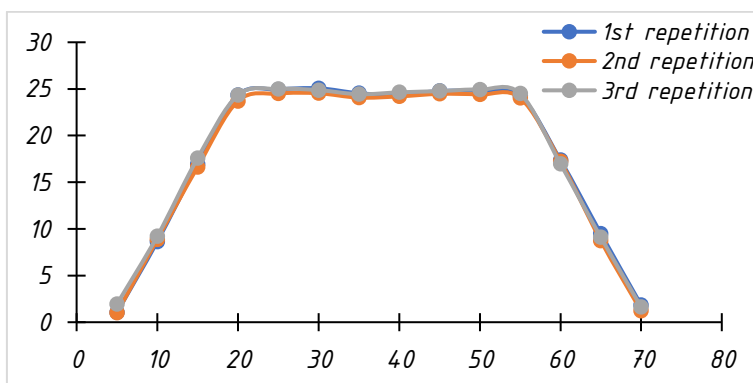


Fig. 6 - Relief of raised beds at a furrow depth of 20 cm

CONCLUSIONS

A bed-former powered by 10.5 HP hand tractors has been designed and tested successfully for performance. Overall, this implement has dimensions of length, width, height, and weight of 1200 mm, 1000 mm, 820 mm and 96.7 kg, respectively. Field testing showed a decrease in soil bulk density by 29.37% after making raised beds on sandy clay loam soil types.

The implement's performance shows that the furrower depth of 15 cm and 20 cm produces raised beds with an average height of 19.66 ± 0.58 cm, 23.67 ± 0.58 cm, respectively. The bed width formed at a furrower depth of 15 cm and 20 cm is 46.33 ± 1.53 cm, 65.66 ± 1.54 cm. At a furrow depth of 15 cm and 20 cm, the bed width at base is 41.67 ± 1.15 cm, and 67.33 ± 0.58 cm, respectively. During the test, the slips with a depth of 15 cm and 20 cm were 15.17%, 23.0%, respectively. This indicates that bed height, bed width, bed width at base increase with increasing tillage depth. It is inversely proportional to the effective field capacity of the tool, which decreases with increasing soil cultivation depth. The maximum efficiency achieved in this test is 78.41%. The bed former's overall performance was considered to be satisfactory.

REFERENCES

- [1] Awad, M., (2016), Fabricated Prototype of Raised-Bed Planter for Wheat, *Journal of Soil Sciences and Agricultural Engineering*, Vol.7(12), pp.921-927.
- [2] Bilgili, A. V., Küçük Ç., Van Es H. M., (2017), Assessment of the quality of the Harran Plain soils under long-term cultivation, *Environmental monitoring and assessment*, Vol.189(9), pp.1-15.
- [3] Bulan, R., Yasar M., Nata Y., Sitorus A., (2019), Design and construction of chopper machine AE02-type for oil palm frond, *INMATEH-Agricultural Engineering*, Vol.57(1), pp.165-172.
- [4] Dixit, A., Khurana R., Verma A., Singh A., Manes G., (2018), Development and Evaluation of a Wide-Bed Former for Vegetable Cultivation in Controlled Tractor Traffic, *Journal of The Institution of Engineers (India): Series A*, Vol.99(3), pp.449-452.

- [5] Evans, S., Lindstrom M., Voorhees W., Moncrief J., Nelson G., (1996), Effect of subsoiling and subsequent tillage on soil bulk density, soil moisture, and corn yield, *Soil and Tillage Research*, Vol.38(1-2), pp.35-46.
- [6] Govaerts, B., Sayre K. D., Ceballos-Ramirez J., Luna-Guido M., Limon-Ortega A., Deckers J., Dendooven L., (2006), Conventionally tilled and permanent raised beds with different crop residue management: effects on soil C and N dynamics, *Plant and Soil*, Vol.280(1), pp.143-155.
- [7] He, J., Li H., Zhang X., Li W., Zhang X., (2009), Design and experiment of 1QL-70 bed former for permanent raised beds, *Nongye Jixie Xuebao= Transactions of the Chinese Society for Agricultural Machinery*, Vol.40(7), pp.55-60.
- [8] Jolliffe, P. A., Gaye M.-M., (1995), Dynamics of growth and yield component responses of bell peppers (*Capsicum annuum* L.) to row covers and population density, *Scientia Horticulturae*, Vol.62(3), pp.153-164.
- [9] Kato, Y., Kamoshita A., Yamagishi J., (2007), Evaluating the resistance of six rice cultivars to drought: restriction of deep rooting and the use of raised beds, *Plant and Soil*, Vol.300(1), pp.149-161.
- [10] Kumar, V., Saharawat Y. S., Gathala M. K., Jat A. S., Singh S. K., Chaudhary N., Jat M., (2013), Effect of different tillage and seeding methods on energy use efficiency and productivity of wheat in the Indo-Gangetic Plains, *Field Crops Research*, Vol.142, pp.1-8.
- [11] Kundu, C., Das H., Ghosh P., (2019), Soil organic carbon sequestration potential and economic profitability of perennial forage crops under different mulching environments, *Range Management and Agroforestry*, Vol.40(1), pp.83-88.
- [12] Li, Y., Li Z., Cui S., Jagadamma S., Zhang Q., (2019), Residue retention and minimum tillage improve physical environment of the soil in croplands: A global meta-analysis, *Soil and Tillage Research*, Vol.194, pp.104292.
- [13] Niu, G., Rodriguez D. S., Aguiniga L., (2007), Growth and landscape performance of ten herbaceous species in response to saline water irrigation, *Journal of environmental horticulture*, Vol.25(4), pp.204-210.
- [14] Osunbitan, J., Oyedele D., Adekalu K., (2005), Tillage effects on bulk density, hydraulic conductivity and strength of a loamy sand soil in southwestern Nigeria, *Soil and Tillage Research*, Vol.82(1), pp.57-64.
- [15] Pranav, P. K., Tewari V. K., Pandey K. P., Jha K. R., (2012), Automatic wheel slip control system in field operations for 2WD tractors, *Computers and Electronics in Agriculture*, Vol.84, pp.1-6.
- [16] Saha, K., Singh D., Jat D., Singh K., (2018), Performance Evaluation of Tractor Operated Rotary Assisted Broad Bed Former-cum-seeder for Wheat Sowing, *Journal of Agricultural Engineering*, Vol.55(3), pp.1-11.
- [17] Shafaei, S., Loghavi M., Kamgar S., (2021), Fundamental realization of longitudinal slip efficiency of tractor wheels in a tillage practice, *Soil and Tillage Research*, Vol.205, pp.104765.
- [18] Simpson, C. R., Melgar J. C., Nelson S. D., Sétamou M., (2019), Growth and yield responses under different grove floor management strategies for water conservation in young grapefruit trees, *Scientia Horticulturae*, Vol.256, pp.108567.
- [19] Slaitas, J., Valivonis J., (2021), Concrete cracking and deflection analysis of RC beams strengthened with prestressed FRP reinforcements under external load action, *Composite Structures*, Vol.255, pp.113036.
- [20] Syahri, C. I., Tineke M., Wawan H., (2019), Modification of Two Wheel Tractor Handlebar for Ease of Climbing Fields Slope, *INMATEH-Agricultural Engineering*, Vol.58(2), pp.293-302.
- [21] Usaborisut, P., Prasertkan K., (2019), Specific energy requirements and soil pulverization of a combined tillage implement, *Heliyon*, Vol.5(11), pp.e02757.
- [22] Xiu, L., Zhang W., Sun Y., Wu D., Meng J., Chen W., (2019), Effects of biochar and straw returning on the key cultivation limitations of Albic soil and soybean growth over 2 years, *CATENA*, Vol.173, pp.481-493.
- [23] Zhang, Y.-L., Feng S.-Y., Wang F.-X., Binley A., (2018), Simulation of soil water flow and heat transport in drip irrigated potato field with raised beds and full plastic-film mulch in a semiarid area, *Agricultural Water Management*, Vol.209, pp.178-187.

OPTIMUM WORKING CONDITIONS FOR VARIABLE WIDTH PLOUGHS

CONDIȚII OPTIME DE LUCRU PENTRU PLUGURI CU LĂȚIME VARIABILĂ

Cârdei P.¹⁾; Nuțescu C.*²⁾; Matache M.¹⁾; Cristea O.¹⁾

¹⁾ INMA Bucharest / Romania; ²⁾ U.P. Bucharest;

Tel: 0727.260.414; E-mail: cristiannutescu@yahoo.com

DOI: <https://doi.org/10.356.33/inmateh-65-26>

Keywords: *variable working width plough, optimal working regime*

ABSTRACT

In this paper, a few assessments of the optimal parametric combinations in the operating regime of agricultural aggregates with ploughs of variable width are made. The starting point was from a classic expression of the tillage draft force required for traction. In order to find optimal points, some problems of constrained extreme have been formulated. Extremes provided by the optimal working width and speed have been found. Such optimal points have existed in the literature, for about half a century. Using these theoretical estimates of the optimal points sought, assessments of the possibilities for their experimental validation were made. Basic conditions for an experimental plan are formulated to highlight such optimal points.

REZUMAT

În această lucrare se realizează câteva evaluări ale combinațiilor optime de parametri în regimul de funcționare a agregatelor agricole cu pluguri cu lățime variabilă. S-a pornit de la o expresie clasică a forței de tracțiune necesară lucrării de arat. Pentru a găsi punctele optime, am formulat câteva probleme ale extremelor de constrângere. S-au găsit extreme oferite de lățimea și viteza optimă de lucru. Astfel de puncte optime există în literatura de specialitate, de aproximativ jumătate de secol. Folosind aceste estimări teoretice ale punctelor optime căutate, se fac evaluări ale posibilităților de validare experimentală a acestora. Sunt formulate condițiile de bază ale unui plan experimental pentru a evidenția astfel de puncte optime.

INTRODUCTION

With the improvement of the ploughing machines, there has naturally been the concern to optimize their working processes. Such optimization problems are frequently mentioned in the literature (Dobrescu, 1981; Sandru et al., 1983; Sandru et al., 1982, Stanciu et al., 2011). The solutions are almost all theoretical in the literature. Experimental research or validation of optimal theoretical solutions are few and incomplete (Khaffaf A.A. and Khadr, 2008; Deyao Tan, 2015). Optimal ideas have not changed significantly over time. There has always been the purpose to minimise draft force, power consumption or energy consumed to carry out the work (Dobrescu, 1981; Sandru et al., 1983; Sandru et al., 1982, Stanciu et al., 2011).

In the field of use of the tillage machines, ideas were expressed regarding the optimal moisture for soil tillage, and regarding the problem of increasing the working speed in order to increase productivity. With the development of the variable working width ploughs (the end of the seventh decade of the past century), besides working speed, the working width has become another important optimization parameter (Adel El Titi, 2003; Cronk et al., 1987).

Researchers have used various approaches to predict the draft force, using analytical and numerical methods (Almaliki et al., 2018). Some dynamometers measure all force components acting on the implements. In some other designs, only the horizontal and vertical forces are measured (Mohammadreza A.-G., et al., 2020). The obtained characteristics make it possible to optimize the structural and technological parameters of the working parts of machines using computer simulation (Mudarisova S.G., et al., 2019). The predictions from one proposed artificial neural network (ANN) model were very satisfactory, based on comparisons with other reported results using multiple linear regression and the mean absolute errors between the measured and predicted values using the ANN model were 0.99 kN and 2, respectively, 39 kWh / ha (Abdulrahman A.-J., et al., 2020).

The conclusions presented by Shafaei S.M., et al., 2019 can contribute both to academic knowledge and to practical applications to properly manage the energy indices of the tractor during soil tillage operations to optimize energy consumption and dissipation in tillage systems.

Also, researches regarding optimum working conditions for tillage equipment (ploughs, shears, loosening equipment) were carried out in the period 2007-2016 by numerous researchers, who studied:

- utilization of ante-mouldboard in the construction of ploughs (Biriş S.Şt. et al., 2007),
- soil particles' kinematics during the ante-mouldboard tillage tools working process (Biriş S.Şt. et al., 2008),
- stress distribution determination appearing on the lamellar mouldboard surface with a view to modelling and optimization (Bungescu S. et al., 2008),
- nonlinear friction and resistance, generating sources of optimal points in the energy field of agricultural aggregates working process (Cârdei P. et al., 2013), respectively
- determination of the subsoiler traction force influenced by different working depth and velocity (Croitoru Şt. et al., 2016).

MATERIALS AND METHODS

Possible objective function and components of the objective functions

For optimal calculus, it was started from a well-known form of the plough draft force – V.P. Goryachkin's equation. Equation (1) describes the traction (draft) force mathematically:

$$F = f \cdot G + n \cdot k \cdot ab + n \cdot \varepsilon \cdot ab \cdot v^2 \quad (1)$$

where: F is the draft force, f is a coefficient of friction between metal and soil, G is the plough weight, n is the number of plough mouldboards, k is a coefficient that characterizes the specific deformation resistance of the soil, a is the working depth, b is the mouldboard working width, ε is a coefficient that depends on the surface of the mouldboard active shape and on the soil properties, and v is the working speed.

It is considered that the working speed is constant and the expression of the power consumed for traction is obtained, using the following formula:

$$P = F \cdot v \quad (2)$$

Let's assume that the conditions are fulfilled so that the energy required for the tractor to trail the plough on a surface with area A , is given by the following formula:

$$E = F \cdot L = F \frac{A}{n \cdot b} \quad (3)$$

The theoretic productivity (the real productivity, which includes the turns and other working specific times, will be considered in a later stage) is considered in the working process:

$$W = n \cdot b \cdot v \quad (4)$$

Taking into consideration that without adding some additional conditions (restrictions) to the basic formulas from which it was started, the chances of finding extreme local points are very small or null (Al-Janobi A.A. and Al-Suhaibani S.A., 1998; Cârdei P. et al., 2013), the productivity as value, W , was set constant, and then from relation (4) the working speed can be expressed:

$$v = \frac{W}{n \cdot b} \quad (5)$$

Introducing (5) in (1), the following form of the draft force is obtained:

$$F = f \cdot G + n \cdot k \cdot ab + \frac{\varepsilon \cdot a \cdot W^2}{n \cdot b} \quad (6)$$

The function F from (6) depending on the working width b , has a positive extremum point, which is characterised by the following coordinates:

$$b_{opt} = \frac{W}{n} \sqrt{\frac{\varepsilon}{k}}, \quad F_{opt} = f \cdot G + 2 \cdot a \cdot W \sqrt{k\varepsilon} \quad (7)$$

which is a minimum point for the function F from (6).

A similar solution can be obtained, using the working speed, v , similarly expressed by (5):

$$b = \frac{W}{n \cdot v} \quad (8)$$

Operating just like parameter v , for function (1), the optimal point is obtained, having the following coordinates:

$$v_{opt} = \sqrt{\frac{k}{\varepsilon}}, \quad F_{opt} = f \cdot G + 2a \cdot W \sqrt{k \cdot \varepsilon} \quad (9)$$

For power function (2) and energy function (3), there were no optimal points obtained (or optimal points of their own have negative coordinates, which does not have any physical sense in the studied process).

Also, as objective functions, to optimize working speed or working width (considering that a variable working width plough is used), other functions, such as the *draft force specific to the unit of productivity* f_w , can be considered:

$$f_w = \frac{F}{W} = \frac{fG}{n \cdot b \cdot v} + \frac{k \cdot a}{v} + \varepsilon \cdot a \cdot v \quad (10)$$

The power required for traction, specific to the unit of productivity

$$p_w = \frac{P}{W} = \frac{fG}{n \cdot b} + k \cdot a + \varepsilon \cdot a \cdot v^2 \quad (11)$$

and the mechanical energy specific to the productivity unit, required for plough traction:

$$e_w = \frac{E}{W} = \frac{A}{n^2} \left(\frac{fG}{b^2 v} + \frac{nka}{bv} + \frac{n\varepsilon v}{b} \right) \quad (12)$$

The objective function (10) has an optimal point (minimum) only in relation to the working speed with the coordinates:

$$v_{opt} = \sqrt{\frac{k}{\varepsilon} + \frac{fG}{n \cdot \varepsilon \cdot ab}}, \quad f_{wopt} = \sqrt{\frac{\varepsilon \cdot a}{n \cdot b} (f \cdot G + n \cdot k \cdot ab)}. \quad (13)$$

The objective function (11) has no optimal points in relation to variables b or v . The objective function (12) has an optimal point (minimum) only in relation to the working speed v :

$$v_{opt} = \sqrt{\frac{k}{\varepsilon} + \frac{fG}{n \cdot \varepsilon \cdot ab}}, \quad e_{wopt} = \frac{2A}{n^2 b^2} \sqrt{n \cdot \varepsilon \cdot ab (f \cdot G + n \cdot k \cdot ab)}. \quad (14)$$

RESULTS

The main results prove that there are optimal points in the working process of the unit formed by tractor and the variable working width plough. In addition, the optimal points found have as abscissa not only the working speed but also the working width, a control parameter defining this type of ploughs, which according to (<http://www.ploughmen.co.uk/about-us/history-of-the-plough>), were introduced at the end of the 1970s. There are also other points of view regarding the optimization of working width for ploughs for which this parameter is adjustable. One is suggested in (McKyes E., 1985) and the term energy efficiency is introduced. In addition, the optimality criteria used are natural, meaning intuitive.

From a physical point of view, the parametric structure of the coordinates of the optimal points leads to interesting conclusions, facilitated by the fact that these coordinates were found in the analytical and not numerical way. They confirm the optimal points, in terms of working speed and working width, found from reference works in the field of agricultural machinery exploitation (Al-Janobi A.A and Al-Suhaibani S.A, 1998; Almaliki et al., 2018; Biriş S. et. al, 2007; Biriş S. et. al, 2008).

Analytical results

In concrete terms, the assertions about the obtained results refer to the coordinates of the optimal points given in (7), (9), (13), and (14).

It is noted that of the four optimal operating points found, only one has as abscissa an optimal working width, which minimizes the draft force (6) in the conditions of a fixed productivity (5). The same draft force, with the same productivity, is achieved with the optimal speed from (9).

It is interesting that the two optimal points (7) and (9) lead to the same expression of the minimum draft force. This means that the two optimal conditions (can be ascertained by calculation) are fulfilled simultaneously. The optimal common speed of the optimal points given in (13) and (14) minimizes the power and power functions specific to the unit of productivity.

It should be mentioned that the optimal speeds are characterized by a quantity that will be noted as a critical process speed:

$$v_{cr} = \sqrt{\frac{k}{\varepsilon}} \quad (15)$$

The critical speed (15) is equal to the optimal speed given in (7) and (9), and the optimal speed given in (13) and (14), can be written as in the following formula:

$$v_{wopt} = v_{cr} \sqrt{1 + \frac{f \cdot G}{n \cdot k \cdot ab}} \quad (16)$$

From (15), it results that the square of the critical speed, v_{cr} , is the ratio of constants describing the soil structure, k and ε . Optimal speeds (16) differ from critical speed v_{cr} , through the ratio of the frictional force to the static component of the traction resistance.

According to the data from (Letosnev M. N., 1959), for the usual values of the k and ε model constants, the critical speed is limited in the range between 2 m/s and 9 m/s. The optimal speed that minimizes the power and energy specific to the productivity unit (16) is greater than the critical speed that minimizes draft force, (9).

It should also be noted that the critical speed, v_{cr} , is also included in the expression of the optimal working width (7).

Numerical results

In order to facilitate a wider understanding of the possibilities of optimal choice of working regime for variable working ploughs, as considered in this research, some numerical results in the specific case of a variable working width plough are presented.

A variable working width plough equipped with $n = 3$ mouldboards, with a mass of 600 kg, working depth set at 0.3 m, working width between 0.15 m and 0.45 m (to better highlight the optimum value) was considered. Soil characterized by the parameter values $f=0.45$, $k= 25000$ Pa, $\varepsilon= 1992$ kg/m³ was considered.

To obtain the curves of figures 1 - 4, a value of $W=1.08$ ha/hour (3 m²/s) for productivity was used and $A=1$ ha, the surface for energy calculation, was considered.

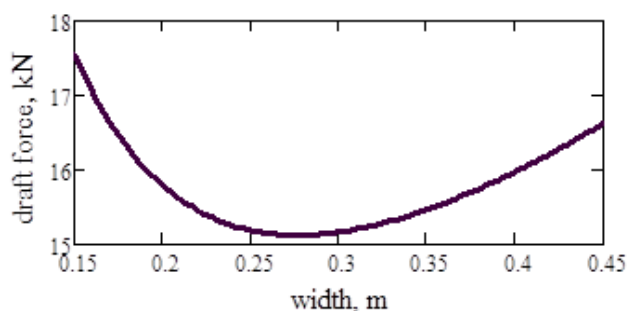


Fig. 1 - Optimum point of the *draft force* in relation to the working width

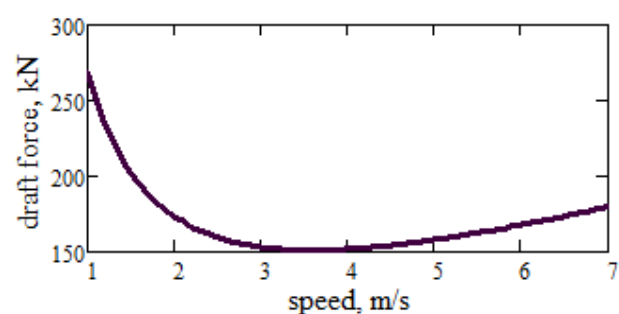


Fig. 2 - Optimal point of the *draft force* in relation to the working speed

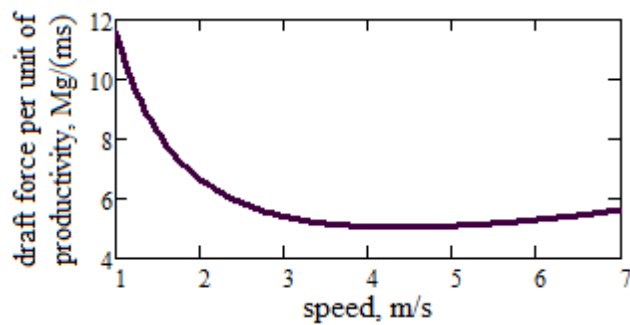


Fig. 3 - Optimum point of the *draft force specific to the unit of productivity*, in relation to the working speed

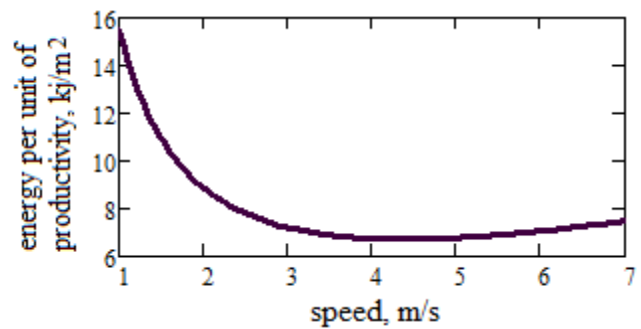


Fig. 4 - Optimum point of the *energy required for traction, specific to the productivity unit*, in relation to the working speed

It can be seen that the numerical study materialized in the curves in figures 1 - 4 confirms the theoretical results, both qualitatively and quantitatively.

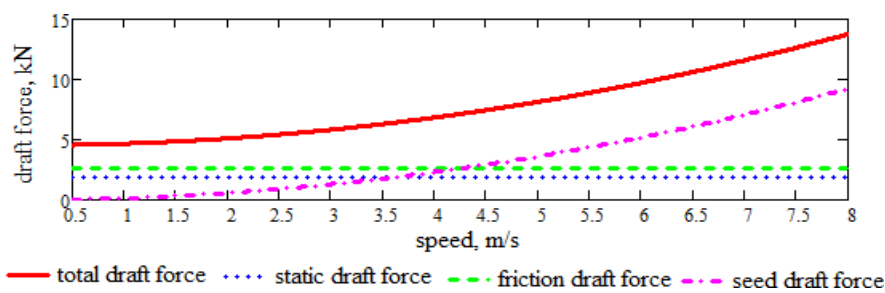


Fig. 5 - Dependence of draft force and its components on the working speed

It can be seen that for the numerical case analysed in this paper, at working speeds higher than 3.5 m/s, the component of the draft force dependent on the working speed, gradually exceeds each of the other components. At working speeds higher than 4 m/s, this component becomes dominant. At a working speed of 5.7 m/s, the total draft force doubled due to the speed dependent component, and at the speed of 8 m/s tripled. In such experiments, in which all the power of a tractor with a large reserve of power was used, there were cases of failure of the plough bearing structure.

As a result of these observations, it is useful to include a structural verification of the plough's resistance in the experimental plan providing high intensity tests. The complexity of designing a load bearing structure of the plough also results, considering the high traction capabilities of modern tractors, as well as some deficiencies in operation (failure to observe working speed limitations). Practically, having very powerful traction means, it is often important to finish soil works as quickly as possible so that the aggregate is used at the maximum tangible speed.

CONCLUSIONS

- Without complicated numerical analysis, it is noted that both the optimal working width, the b_{opt} , or the optimal working speed, the v_{opt} , and the objective functions that they minimize, depend on the parameters that encapsulate the intrinsic environment, k , ϵ and on the interaction parameter between the environment and the working machine: f . This dependence expresses that the coordinates of the optimal point vary depending on the soil and implicitly on the meteorological parameters involved.
- The existence of optimal points in the working regime of agricultural machines for soil works is obtained by a classic, very used expression of draft force, (1). The widespread use of this formula, perhaps not the most accurate, is due to its simplicity and physical significance that is easily accepted, although the meaning, is not very well known (the traction force formula (1) is also easy to use in calculating the dynamics of the tractor - plough aggregate).
- In addition, the fact that formula (1) uses only three constants with which it characterizes the soil in the interaction with the machine (f , k and ϵ), is an advantage, considering the tabulation of these values over about one hundred years of use for various types of soils.

- From an experimental point of view, however, literature (at least the wide circulation literature) does not mention the existence of the optimal points that the theory recommends.
- It is obvious that without the experimental validation, the optimal points whose coordinates are given in (7), (9), (13) and (14), remain pure theory. In order to be able to validate these optimal points experimentally, it is necessary to achieve the appropriate experiences. This means that within the variation range of the working width and the working speed of the aggregate, the optimal values predicted by the theory must be included.

$$b_{\min} \leq \frac{W}{n \cdot v_{cr}} \leq b_{\max} \quad (17)$$

where b_{\min} and b_{\max} are the minimum working width, and maximum working width achievable by the plough, respectively

$$v_{cr_{\min}} \leq v \leq v_{cr_{\max}} \quad (18)$$

are the minimum value, and maximum value of the critical speed value, (15), possible to increase at the minimum and maximum critical speeds (16).

Taking into account the minimum and maximum values of soil characteristic constants, k and ε , given in the literature, the minimum and maximum values of critical speed (15), 2 m/s and 8 m/s, are obtained. As a result, if speeds of less than 2 m/s are applied, the existence of optimal working speeds cannot be validated. As regards the validation of an optimal working width, this could be observed if the minimum and maximum achievable plough width would have the expressions related to the soil characteristics:

$$b_{\min} = \frac{W}{n \cdot v_{cr_{\max}}}; \quad b_{\max} = \frac{W}{n \cdot v_{cr_{\min}}} \quad (19)$$

From this reasoning, it results the need to include in the experimental plan for the validation of optimal working widths or working speeds, the estimates (17) - (19). Otherwise, it is very likely that validation of such optimal points will receive a (experimental) negative response, although their existence may be a real one.

The realization of the speed regimes necessary for the experimental validation of the optimal working regimes for the variable width ploughs is also conditioned by a very important decision of the experimenter. Increasing the working speed over certain limits leads to increased draft force and strongly stresses the plough bearing structure, which can lead to irreversible damage. Therefore, a plough prepared for such tests must be designed with a sufficiently strong bearing structure (the weight of the plough will increase as well as the optimal type speed (16)).

Investigating the problem of the actual existence of optimal points in the working regime is even more complicated by the fact that the three constants that characterize the soil in (1) depend on the soil moisture and its internal structure (physical and chemical components, layer structure, etc.). If the moisture is well quantified, the physical and chemical structure (component) is deficiently quantified and deeply dependent on depth. The random nature of the physical and chemical structure makes it difficult to be considered in the modelling process. The influence of moisture is quite simple to consider, provided that significant values of this parameter are used. Besides, the existence of optimal working moisture for agricultural machines for soil tillage, has, by long, been supported by specialists, but without giving clear numerical evidence. The introduction of moisture in the optimal calculation makes it necessary to consider the tractor's slippage.

ACKNOWLEDGEMENT

This work was supported by "NUCLEU" Programme, developed with the support of MCID, project no. PN 19 10 01 02.

REFERENCES

- [1] Abdulrahman A.-J., Saad Al-H., Abdulwahed A., Almajhadi Y., (2020), Modelling of draft and energy requirements of a mouldboard plough using artificial neural networks based on two novel variables, *Scientific Paper, Agricultural Machinery Management, Eng. agric. (Online)* 40 (3), <https://doi.org/10.1590/1809-4430-Eng.Agric.v40n3p363-373/2020>;
- [2] Adel El Titi, (2003), *Soil Tillage in Agroecosystems*, CRC Press;

- [3] Al-Janobi A.A., Al-Suhaibani S.A., (1998), Draft of primary tillage implements in sandy loam soil, Applied Engineering in Agriculture, *American Society of Agricultural Engineers*, vol. 14(4): 343-348;
- [4] Almaliki S., Himoud M.S., Muhsin S.J., (2018), A stepwise regression algorithm for prognostication draft requirements of disk plough, *International Conference on Promotion of Scientific & Regional Cooperation on Food and Agricultural Sciences*, Mashhad;
- [5] Biriş S., Vlăduţ V., Bungescu S., Paraschiv G., (2007), Researches regarding the utilization of ante-mouldboard in the ploughs building, *Proceedings of the 35 International Symposium on Agricultural Engineering "Actual Tasks on Agricultural Engineering"*, vol. 35, pp 85÷96, Opatija – Croatia;
- [6] Biriş S., Maican E., Vlăduţ V., Paraschiv G., Manea M., Bungescu S., (2008), Study regarding the soil particles kinematics during the ante-mouldboard tillage tools working process, *Proceedings of the 36 International Symposium on Agricultural Engineering "Actual Tasks on Agricultural Engineering"*, vol. 36, pp. 115÷126, Opatija – Croatia;
- [7] Bungescu S., Biriş S., Vlăduţ V., Paraschiv G., (2008), Researches regarding the stress distribution determination appearing on the lamellar mouldboard surface with a view to modelling and optimization, *Proceedings of the 36 International Symposium on Agricultural Engineering "Actual Tasks on Agricultural Engineering"*, vol. 36, pp. 281÷292, Opatija – Croatia;
- [8] Cârdei P., Alexiou Al., Badescu M., Marin E., (2013), Nonlinear Friction and Resistance, Generating Sources of Optimal Points in the Energy Field of Agricultural Aggregates Working Process, *Conference Proceedings of the 2013, International Conference on Energy, Environment, Ecosystems and Development (EEED 2013)*, Rhode Islands, Greece;
- [9] Croitoru Şt., Vlăduţ V., Marin E., Matache M., Dumitru I., 2016, Determination of subsoiler's traction force influenced by different working depth and velocity, *15th International Scientific Conference "Engineering for Rural Development"*, *Proceedings*, vol. 15, pp. 817-825, Jelgava, Latvia;
- [10] Cronk B. J., Williams, T.H., Krishnan, P., Kemble, L.J., (1987), Optimal width equations for various tillage implements, *American Society of Agricultural Engineers*;
- [11] Deyao Tan, (2015), Engineering Technology, Engineering Education and Engineering Management, CRC Press Taylor & Francis Group, p. 436;
- [12] Dobrescu C., (1981), Optimization of the parameters of agricultural aggregates to reduce energy consumption, Ministry of Agriculture and Food Industry, *Centre for Agricultural Teaching Material and Propaganda*, Bucharest;
- [13] Khaffaf A.A. Khadr, (2008), Effect of some primary tillage implement on soil pulverization and specific energy, *Journal of Agricultural Engineering*, 25(3): 731-745;
- [14] Letosnev M. N., (1959), Agricultural machinery, *Agro-Silvica de Stat Publishing House*, Bucharest;
- [15] McKyes E., (1985), Soil Cutting and Tillage, *Developments in Agricultural Engineering 7, Elsevier*;
- [16] Mohammadreza A.G., Gholamhossein S., Gilandeh Y, Apolonio M., Hernández J.L., Miranda I., (2020), Measuring and comparing forces acting on mouldboard plough and para-plough with wing to replace mouldboard plough with para-plough for tillage and modelling it using adaptive neuro-fuzzy interface system (ANFIS), *Agriculture*, vol. 10(12), 633, <https://doi.org/10.3390/agriculture10120633>;
- [17] Mudarisova S.G., Gabitova I. I., Lobachevskyb Y. P., Mazitovc N. K, Rakhimovd R. S., Khamaletdinova R. R., Rakhimova R., Farkhutdinova A.M., (2019), Modelling the technological process of tillage, *Soil and Tillage Research*, vol. 190, pp. 70-77, <https://doi.org/10.1016/j.still.2018.12.004>;
- [18] Sandru A., Badescu M., Sandru L., (1982), Energy consumption reduction through rational usage of agricultural aggregates, *Scrisul Românesc Publishing House*, Craiova;
- [19] Sandru A., Popescu S., Cristea I., Neculaiasa V., (1983), Agricultural equipment exploitation, *Didactic and Pedagogical Publishing House*, Bucharest;
- [20] Shafaei S.M., Loghavi M., Kamgar S., (2019), Prognostication of energy indices of tractor-implement utilizing soft computing techniques, *Information Processing in Agriculture* 6(1):132-149.
- [21] Stanciu L., Cardei P., Voicu Gh., Vartukapteinis K., (2011), Studies on Optimization of Trailed Corn Harvesting Combines Working Regimes, *INMATEH - Agricultural Engineering*, Vol. 33(1), pp.29-36;
- [22] <http://www.ploughmen.co.uk/about-us/history-of-the-plough>;
- [23] https://www.researchgate.net/publication/314154209_Researches_regarding_the_Motion_Equation_of_the_Tractor_in_Aggregation_with_the_Machines_f_or_Soil_Processing.

CALIBRATION OF BONDING MODEL PARAMETERS FOR COATED FERTILIZERS BASED ON PSO-BP NEURAL NETWORK

基于 PSO-BP 神经网络的包膜肥料 Bonding 模型参数标定

Xin Du, Cailing Liu*, Meng Jiang, Hao Yuan, Lei Dai, Fanglin Li, Zhanpeng Gao

College of Engineering, China Agricultural University, Beijing 100083/ China;

Tel: 0086-010-62737502; E-mail: cailingliu@163.com

Corresponding author: Cailing Liu

DOI: <https://doi.org/10.356.33/inmateh-65-27>

Keywords: Coated fertilizer; Parameter calibration; Proxy Model; PSO-BP Neural Network

ABSTRACT

In this paper, the ultimate crushing displacement Y_1 and load Y_2 of the coated fertilizer granules were obtained by uniaxial compression test as 0.450 mm and 58.668 N, respectively. The Plackett-Burman and Steepest ascent tests were taken to determine factors that had significant effects on the results and their ranges of values, respectively. Finally, the Particle Swarm Optimization - Back Propagation (PSO-BP) neural network was trained, and the correlation coefficients of training, validation, testing and overall performance were obtained as 0.98057, 0.95781, 0.96724 and 0.97459, respectively. The Y_1 and Y_2 are 0.450 mm and 58.703N, with a relative error of 0.06% from the actual value.

摘要

采用 PSO-BP 神经网络模型为代理模型对 Bonding 模型参数进行标定, 首先通过单轴压缩试验得到包膜肥料颗粒的极限破碎位移和极限破碎载荷分别为 0.450 mm 和 58.668 N。建立包膜肥料的 DEM 模型, 分别采取 Plackett-Burman 和 Steepest ascent test 确定对结果影响显著的因素及其取值范围。采用全因素试验数据训练 PSO-BP 神经网络, 得到训练过程、验证过程、测试过程和整体性能的相关系数分别 0.98057、0.95781、0.96724 和 0.97459, 表明训练后的 PSO-BP 神经网络拟合效果良好, 可以预测极限破碎位移和极限破碎载荷。PSO-BP 神经网络预测结果显示, 当法向刚度 X_1 、切向刚度 X_2 、切向极限应力 X_4 和粘结半径 X_5 分别为 $1.006E+10 \text{ N/m}^2$ 、 $1.021E+10 \text{ N/m}^2$ 、 1200000 Pa 和 0.20 mm 时, 压缩位移 Y_1 和压缩载荷 Y_2 分别为 0.450 mm 和 58.703 N, 与实际值相对误差最小为 0.06%。

INTRODUCTION

Fertilizers play a significant role in increasing crop yields, and China uses a large amount of chemical fertilizers with low fertilizer utilization rates (Chojnacka et al., 2020). Controlled release fertilizer adopts polymer coating, which can quantitatively control the amount and period of fertilizer nutrient release, so that the effect of fertilizer saving and efficiency is significant (Xiang et al., 2017). The nutrient release characteristics of wrapper fertilizers are closely related to the material and structure of the wrapper layer (Chen et al., 2018), mechanical damage can cause damage to the envelope layer and thus affect the nutrient release characteristics of the fertilizer. In order to study the principle of mechanical damage of wrapped fertilizer, the discrete element method is proposed to be used for numerical simulation of the crushing process.

The calibration process of numerical simulation parameters directly affects the accuracy of simulation results (Coetzee, 2017). Researchers have tried many methods to calibrate or measure discrete component parameters. One is to measure the parameters of the particle directly by experiment, which is applicable to the parameters that reflect the nature of the particle itself such as Poisson's ratio, density, shear modulus, etc.; the other is to measure the macroscopic phenomenon of the particle by experiment and then reversely calibrate it. In the inverse calibration process, the traditional method is "trial and error", which is inefficient and inaccurate (Chen, 2017). To remedy these deficiencies, Zhao (Zhao et al., 2012) attempted to explore the complex relationships between micro- and macro-mechanical behaviors and parameters through empirical or theoretical formulations.

Xin Du, Ph.D. Stud.; Cailing Liu*, Prof. Ph.D.; Meng Jiang, Ph.D. Stud.; Hao Yuan, Ph.D. Stud.; Lei Dai, Ph.D. Stud.; Fanglin Li, Ph.D. Stud.; Zhanpeng Gao Ph.D. Stud.

During the calibration process, samples were generated using design of experiments methods, such as Yoon (Yoon, 2007) using central combined design (CCD), Hanley (Hanley et al., 2011) using Taguchi method and orthogonal tests, Rackl (Rackl and Hanley, 2017) using Latin hypercube sampling and Kriging methods. Optimization algorithms were then used to process the data and obtain calibration results, such as Do (Do et al., 2018) using genetic algorithms, Benvenuti (Benvenuti et al., 2016) using artificial neural networks, and Zhou (Zhou et al., 2018) using radial basis neural network method. However, the above studies still have some shortcomings. On the one hand, the above calibration methods simplify the parameters, and there are few studies on multi-parameter multi-objectives. On the other hand, the accuracy of the obtained models is low, and it is difficult to predict the combination of simulation parameters accurately.

In this paper, the ultimate crushing load and loading displacement of wrapped fertilizer particles were measured by uniaxial compression test, and by establishing the same simulation model as the real test, the number of factors was gradually reduced and the range of factor values was narrowed by using PB design and the most rapid ascent method, and then the PSO-BP neural network was trained by using the full-factor test to predict the Bonding model parameter combinations with the well-fitted network model, and the obtained parameter combinations were validated. The Bonding model parameters of the envelope fertilizer were accurately calibrated.

MATERIALS AND METHODS

Bonding Model

In the Bonding model, the material being crushed (particles, blocks, etc.) it consists of a number of small particles, which are held together by bonded cements. Bonded cements have mechanical properties similar to those of the finite element method and are subject to deformation (tension, compression, torsion) under external forces. When the force or moment generated by the deformation of bonded cements reaches a certain level, the cements break and the small particles separate from each other. The Bonding model assumes that the cement between two particles is a virtual flat plate (cylinder), as shown in Figure 1. When the relative motion of two particles occurs, the flat plate (cylinder) is subjected to tension, bending and shear, and the mile generated by the bond can be obtained according to the following equation.

$$\begin{cases} \delta F_n = -v_n S_n A \delta t \\ \delta F_t = -v_t S_t A \delta t \\ \delta M_n = -\omega_n S_t J \delta t \\ \delta M_t = -\omega_t S_n \frac{J}{2} \delta t \end{cases} \quad (1)$$

where: δF_n and δF_t are the normal and tangential forces respectively; v_n and v_t are the normal and tangential velocities of the particles respectively; S_n and S_t are the normal stiffness and tangential stiffness respectively; δt is the simulation time step; A is the contact area between the particles of "fraction"; δM_n and δM_t are respectively tangential moment and normal moment; ω_n , ω_t are the normal and tangential angular velocities, respectively; J is the polar moment of inertia of the cement.

$$\begin{cases} A = \pi R_B^2 \\ J = \frac{1}{2} \pi R_B^4 \end{cases} \quad (2)$$

where: R_B is the bonded radius of the cement. It can be seen from formulas (1) and (2) that the bonded radius R_B has a direct effect on the force and moment.

When the force and moment reached the limit value or the distance between the "fraction" particles is greater than the setting contact radius, the bonded cement will break. The normal and tangential shear force calculation formulas are as follows:

$$\begin{cases} \sigma_{\max} < \frac{-F_n}{A} + \frac{2M_t}{J} R_B \\ \tau_{\max} < \frac{-F_t}{A} + \frac{M_n}{J} R_B \end{cases} \quad (3)$$

where: σ_{\max} is the normal shear force; τ_{\max} is the tangential shear force.

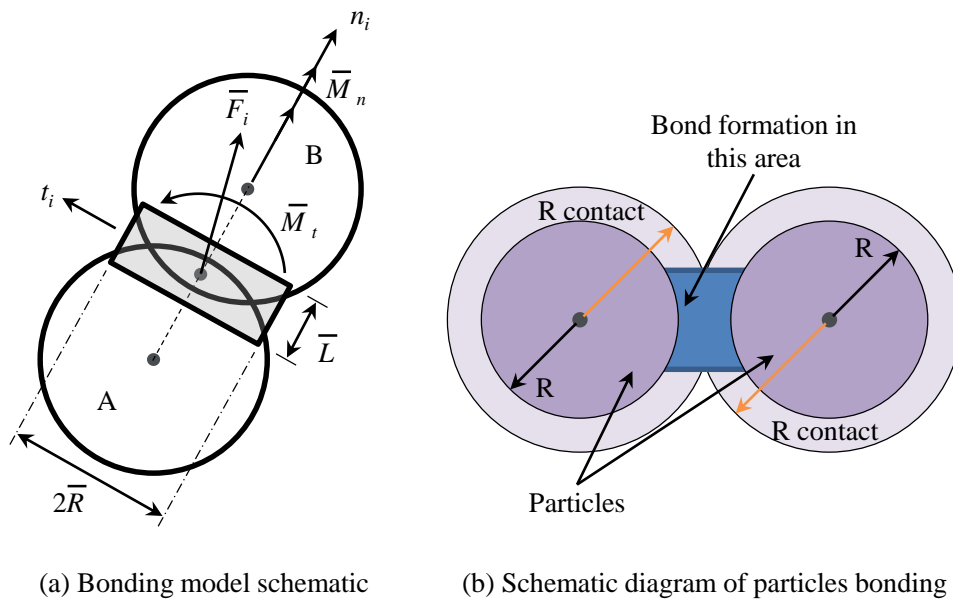


Fig. 1 – Bonding model schematic

F_i is the contact force vector, which can be resolved into normal and shear components; M_n and M_t denote the axial- and shear- directed moments, respectively; n_i and t_i are the unit vectors that define the contact plane; L and R_i are the length and parallel-bond radius of the cement; A and B denote two particles in contact; R and R_{contact} denote the radius and contact radius between two particles, respectively.

Material parameters

In this paper, the coated controlled-release fertilizers were sourced from Shandong Nongyang Biological Technology Co., Ltd., China. The moisture content, true density, average triaxial size, equivalent diameter and sphericity of fertilizer are 0.88%, 1.46 g/cm³, 4.08 mm×3.97 mm×3.89 mm, 3.98 mm and 0.975, respectively. Select fertilizers (as shown in Fig. 2(a) (b)) whose length, width and height are similar to the equivalent diameter to establish a contour model. To study the fertilizer particle fragmentation characteristics, the bonded particle method (BMP) was used to build a discrete element model of fertilizer particles (as shown in Fig. 2(c)).

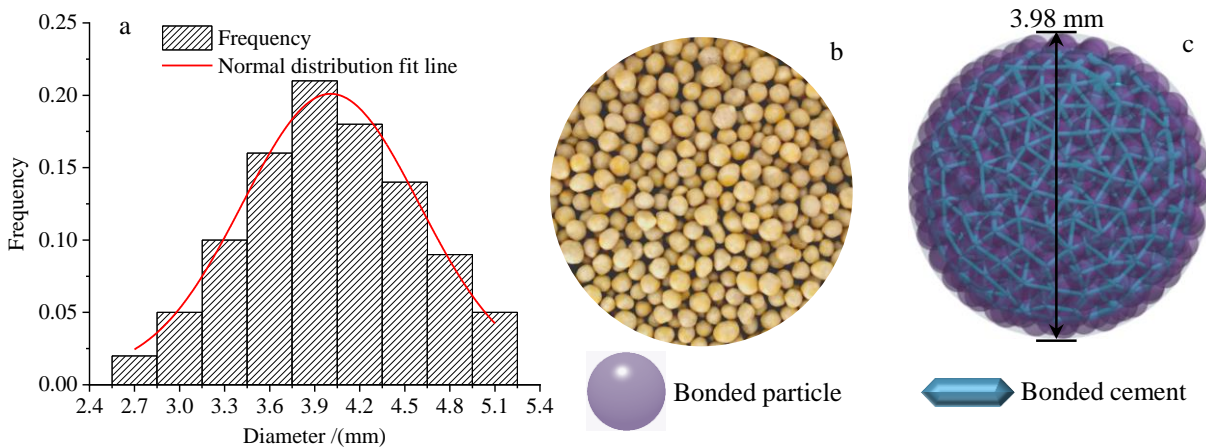


Fig. 2 – Fertilizers and discrete element model

Uniaxial compression test (actual)

Select fertilizer particles with a diameter of 3.98 mm, and use a universal tester to perform a uniaxial compression test on the fertilizer particles, and load them at a speed of 0.05 mm/s until the sample is damaged, as shown in Fig. 3(a). The experiment was repeated 20 times and the average value was taken, then the displacement load curve of the fertilizer particles was obtained as shown in Fig. 3(b).

As can be seen from Fig. 3, the ultimate crushing displacement and ultimate crushing load of the coated fertilizer granules were obtained by uniaxial compression test as 0.450 mm and 58.668 N, respectively.

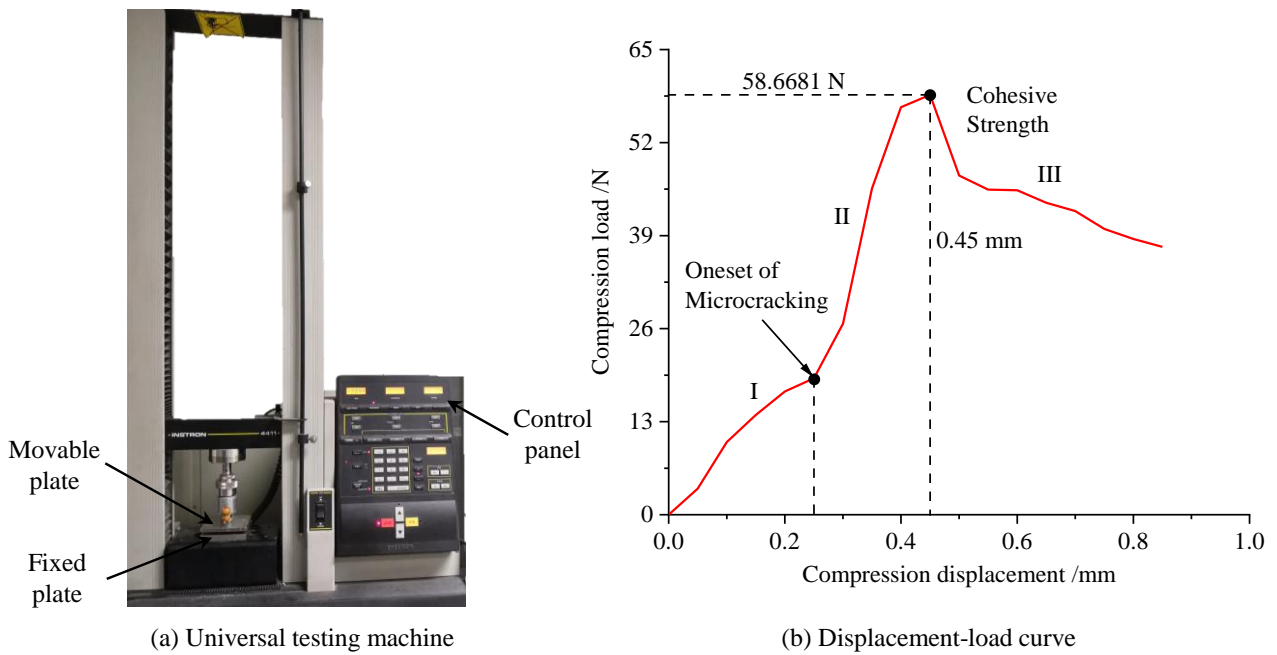


Fig. 3 – Uniaxial compression test

Uniaxial compression test (simulation)

The discrete element software EDEM2018 was used to establish a uniaxial compression simulation test consistent with the actual test, as shown in Fig. 4. The constitutive and contact parameters of the coated fertilizer particles used in the simulation refer to related literature (Du Xin et al., 2019; Liu Cailing et al., 2018), and the values are shown in Table 1.

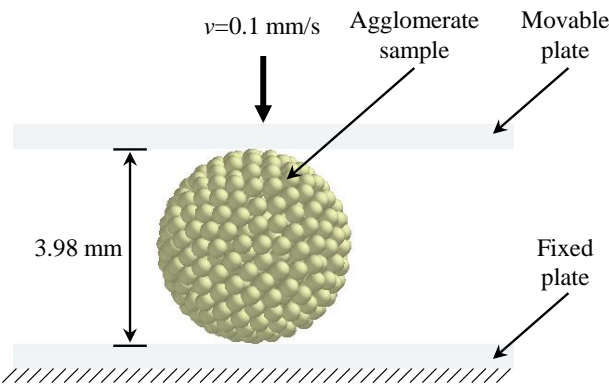


Fig. 4 – Simulation diagram of uniaxial compression test

Table 1

Simulation parameters		
Parameter	Fertilizer	ABS
Poisson's ratio	0.225	0.394
Real density (kg/m ³)	2474	1060
Shear modulus (Pa)	1.528×10 ⁸	8.9×10 ⁸
Collision recovery factor	0.654	0.47
Coefficient of static friction	0.189	0.42
Rolling friction coefficient	0.034	0.095

PSO-BP neural network

The standard BP neural network (three-layer model) structure is used, i.e., input layer, implicit layer and output layer. The BP neural network uses the gradient correction method for learning the weights and thresholds. Suitable parameters can effectively improve the overall performance of the system. Two important factors that affect the learning quality of BP neural networks are: the number of implicit nodes and the size of learning rate. The increase in the number of implicit nodes accelerates the decrease in error, but the computational effort also increases and the learning time of the system becomes longer, which reduces the usefulness of the system. The number of implicit neurons is estimated using the following formula:

$$j = \sqrt{i+k} + z \quad (4)$$

where j is the number of neurons in the hidden layer, i is the number of neurons in the input layer, k is the number of neurons in the output layer, and z is the empirical value ($1 \leq z \leq 10$).

The learning rate determines the size of the change in weights and thresholds during each iteration. Decreasing the learning rate can reduce the probability of the system falling into local convergence and make the system eventually converge globally; too small a learning rate results in a small change in each iteration, leading to an increase in the number of iterations and a longer training and learning time.

Different combinations of the number of implied nodes and learning rate are used to form different network structures and compare the final error output of the system. Considering the learning time and the final error of the network, the best learning ability of the BP neural network is obtained when the number of implicit nodes of this system is 10 and the learning rate is 0.3.

The standard BP neural network can approximate any nonlinear continuous function, but the algorithm has the defects of slow convergence and easily falling into local minima. In order to find better network weights and threshold values for BP neural networks and minimize their global errors, the PSO algorithm is used to optimize the BP neural networks.

The PSO algorithm is an evolutionary search technique proposed based on birds' predatory behavior and movement patterns. Each bird is equivalent to a particle in the model, representing the solution of the optimization problem, and their range and direction depend on the velocity of each particle in the particle swarm, and the best adaptation value is obtained by the optimal particle searching in the solution space for the global optimal solution.

Assuming that there are M particles forming a particle population in a D -dimensional search space, the main computational derivation of the PSO algorithm is:

$$\begin{cases} v_{id}^{(t+1)} = u \times v_{id}^{(t)} + c_1 r_1 (P_{id} - x_{id}^{(t)}) + c_2 r_2 (P_{gd} - x_{id}^{(t)}) \\ x_{id}^{(i+1)} = x_{id}^{(t)} + v_{id}^{(t+1)} \end{cases} \quad (5)$$

where: $v_i = (v_{i1}, v_{i2}, \dots, v_{id})$ denotes the velocity of the i -th particle; $x_i = (x_{i1}, x_{i2}, \dots, x_{id})$, ($i = 1, 2, \dots, M$) denotes the position of the particle in space; $P_i = (P_{i1}, P_{i2}, \dots, P_{id})$ denotes the historical best position passed by the i -th particle in space; $P_g = (P_{g1}, P_{g2}, \dots, P_{gd})$ denotes the historical best position passed by the whole population in space; c_1, c_2 denote the learning acceleration coefficients, which usually take the value of 2.0; r_1, r_2 are random numbers varying between $[0, 1]$; u denotes the inertia weights.

The weights and thresholds of the BP neural network are regarded as particles, and the training process of the system is completed by mutual learning between particles, then the change of the weights is:

$$\Delta W_{ij} = c_1 r_1 (W_{ij}(p) - W_{ij}) + c_2 r_2 (W_{ij}(g) - W_{ij}) \quad (6)$$

where $W_{ij}(p)$ denotes the individual optimal value of the corresponding particle; $W_{ij}(g)$ denotes the global optimal value of the whole network.

The flow chart of BP neural network weights modified by PSO algorithm is shown in Fig. 5. The specific training process of the network is as follows.

(1) Initialize the PSO algorithm parameters. Determine the initial and ending weights according to the structural characteristics of the BP neural network, learn the acceleration coefficients and the initial positions of the particle population.

(2) The PSO algorithm corresponds to the BP neural network. A D -dimensional vector is created, which represents a particle in the PSO algorithm and includes the weights and thresholds of the implicit and output layers in the BP network.

(3) Calculate the fitness of the particles. In order to measure the goodness of the particle position, the fitness function needs to be established, using the error function in the BP network as the fitness function.

(4) Update individual optima and global optima. Compare the fitness function values of each particle at time $t-1$ with those at time t . If the fitness of the particle is better at time t , the individual optimum of the corresponding particle is updated. Similarly, compare the fitness function values of the population at time $t-1$ with those at time t . If the fitness of the population is better at time t , then the global optimum of the population is updated.

(5) Update the position and velocity of the particles. The velocity and position information of the particles are recalculated according to Eqs. (2) and (4), and the weights and thresholds of each layer are updated.

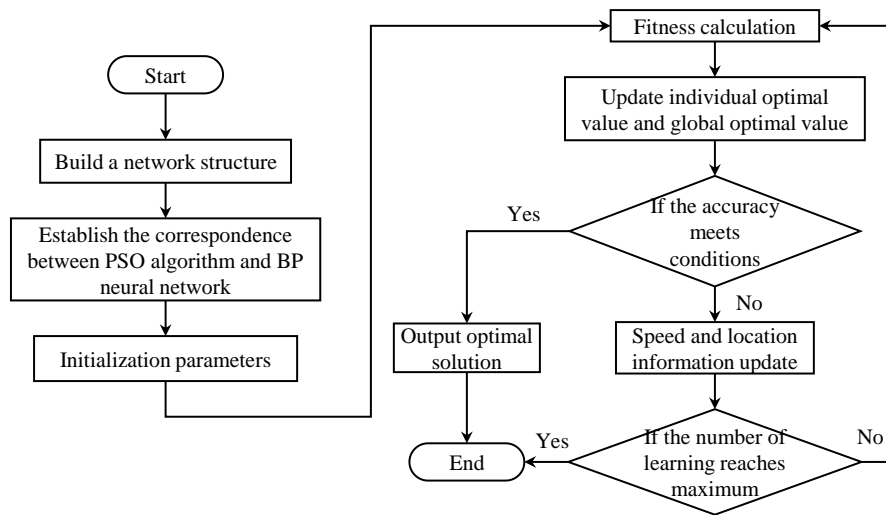


Fig. 5 – Fertilizer granule crushing test

RESULTS

Plackett-Burman test

The normal stiffness, tangential stiffness, normal ultimate stress, tangential ultimate stress and bonded radius were used as the five factors (X_1, X_2, X_3, X_4, X_5) of the Plackett-Burman test, and two levels of each factor were selected.

The Plackett-Burman design with $N=11$ was chosen for the test, and six dummy terms were reserved for error analysis, and the Plackett-Burman test protocol and results are shown in Table 2, and the ANOVA and t-test were performed separately for each factor effect using Design-Expert 8.0.6 software, and the results are shown in Table 3.

Table 2

Plackett-Burman test results

No.	X_1	X_2	X_3	X_4	X_5	Y_1	Y_2
1	9.60E+09	1.28E+10	6.00E+05	1.20E+06	0.16	0.395	37.274
2	9.60E+09	1.28E+10	4.00E+05	8.00E+05	0.24	0.521	85.528
3	6.40E+09	1.28E+10	4.00E+05	1.20E+06	0.16	0.355	31.243
4	9.60E+09	1.92E+10	6.00E+05	8.00E+05	0.16	0.348	39.621
5	9.60E+09	1.92E+10	4.00E+05	8.00E+05	0.16	0.348	39.621
6	6.40E+09	1.92E+10	6.00E+05	8.00E+05	0.24	0.428	75.203
7	6.40E+09	1.92E+10	6.00E+05	1.20E+06	0.16	0.363	40.406
8	9.60E+09	1.28E+10	6.00E+05	1.20E+06	0.24	0.530	97.275
9	6.40E+09	1.92E+10	4.00E+05	1.20E+06	0.24	0.475	91.781
10	6.40E+09	1.28E+10	4.00E+05	8.00E+05	0.16	0.357	31.481
11	6.40E+09	1.28E+10	6.00E+05	8.00E+05	0.24	0.484	79.520
12	9.60E+09	1.92E+10	4.00E+05	1.20E+06	0.24	0.488	94.295

Table 3

Analysis of significance of parameters in Plackett-Burman test

Source	Compression Displacement					Compression Load				
	Sum of Squares	df	Mean Square	F Value	p-value	Sum of Squares	df	Mean Square	F Value	p-value
Model	0.055	5	0.011	42.07	0.0001*	8046.936	5	1609.387	73.06	< 0.0001*
X_1	0.002	1	0.002	9.02	0.0239*	159.034	1	159.034	7.22	0.0362*
X_2	0.003	1	0.003	11.81	0.0139*	27.941	1	27.941	1.27	0.3031
X_3	0.000	1	0.000	0.01	0.9439	1.581	1	1.581	0.07	0.7978
X_4	0.001	1	0.001	4.62	0.0753	144.188	1	144.188	6.55	0.0430*
X_5	0.048	1	0.048	184.92	< 0.0001*	7714.192	1	7714.192	350.17	< 0.0000*
Residual	0.002	6	0.000			132.178	6	22.030		
Cor Total	0.056	11				8179.114	11			

Notes: *Shows that the term is significant (i.e., $P < 0.05$).

Steepest ascent test

According to the Plackett-Burman test results, the initial values of the selected factors X_1 , X_2 , X_4 and X_5 were 8.00×10^9 N/m², 1.60×10^{10} N/m², 1.00×10^6 Pa and 0.18 mm, and the step length was 0.80×10^9 N/m², - 0.16×10^{10} N/m², 0.10×10^{10} Pa and 0.01 mm, respectively. Based on the above description, a steepest ascent test was carried out to further find the parameters combination that approximates the true value. The steepest ascent test plan and results were shown in Table 4.

Table 4

Steepest ascent test plan and results

No.	X_1	X_2	X_4	X_5	Y_1	Y_2
1	8.00E+09	1.60E+10	1.00E+06	0.18	0.409	52.517
2	8.80E+09	1.44 E+10	1.10E+06	0.19	0.420	57.086
3	9.60E+09	1.28E+10	1.20E+06	0.20	0.446	63.534
4	1.04E+10	1.12E+10	1.30E+06	0.21	0.498	75.726
5	1.12E+10	9.60E+09	1.40E+06	0.22	0.510	78.411

From the test results in Table 5, it can be seen that the error between the compressive displacement and load in the simulation test and the real value first decreases and then increases, combined with 2.3.1, it can be seen that the actual uniaxial compressive displacement and load of fertilizer granules are 0.45 mm and 58.668 N respectively, and the compressive displacement Y_1 and load Y_2 of the 3rd group test are closest to the real value.

PSO-BP neural network

As can be seen from Table 5, the actual loading displacement and ultimate load are between the results of Scheme 1 and Scheme 4, therefore, the factor ranges of Scheme 1 and Scheme 4 were selected to complete the full-factor test with 4 factors and 4 levels, and the test factor level ranges are shown in Table 5.

Table 5

Table of test factor levels

Factor	Level			
	1	2	3	4
X_1	8.00E+09	8.80E+09	9.60E+09	1.04E+10
X_2	1.60E+10	1.44 E+10	1.28E+10	1.12E+10
X_4	1.00E+06	1.10E+06	1.20E+06	1.30E+06
X_5	0.18	0.19	0.2	0.21

The objectives to be optimized in this paper are compression displacement Y_1 and compression load Y_2 . According to the importance of each objective, the linear weighted combination method is used to transform the multi-objective optimization problem into a single-objective optimization problem, and the index conversion and weighting formulas are as follows.

$$\begin{cases} \min \sum_{i=1}^2 w_i y_i(x) \\ y_i = \left| \frac{Y_{ij} - Y_{io}}{Y_{io}} \right| \times 100\% \quad j \in [1, 256] \end{cases} \quad (7)$$

where:

w_i is the weighting factor, $w_1 = w_2 = 0.5$ in this paper; y_i is the relative error of each index and the actual value; Y_{ij} is the simulation result of each index of each scheme; Y_{io} is the actual value of each index, where $Y_{1o} = 0.45$ mm, $Y_{2o} = 58.668$ N.

There are 256 sets of simulation results, 180 sets are randomly selected as training network, and the other data are used as validation and testing network performance, and the correlation coefficients of training process, validation process, testing and overall performance of PSO-BP neural network are obtained as 0.98057, 0.95781, 0.96724 and 0.97459, respectively (as shown in Fig. 6). In general, a correlation coefficient greater than 0.9 is considered a good network fit (Dong et al., 2020).

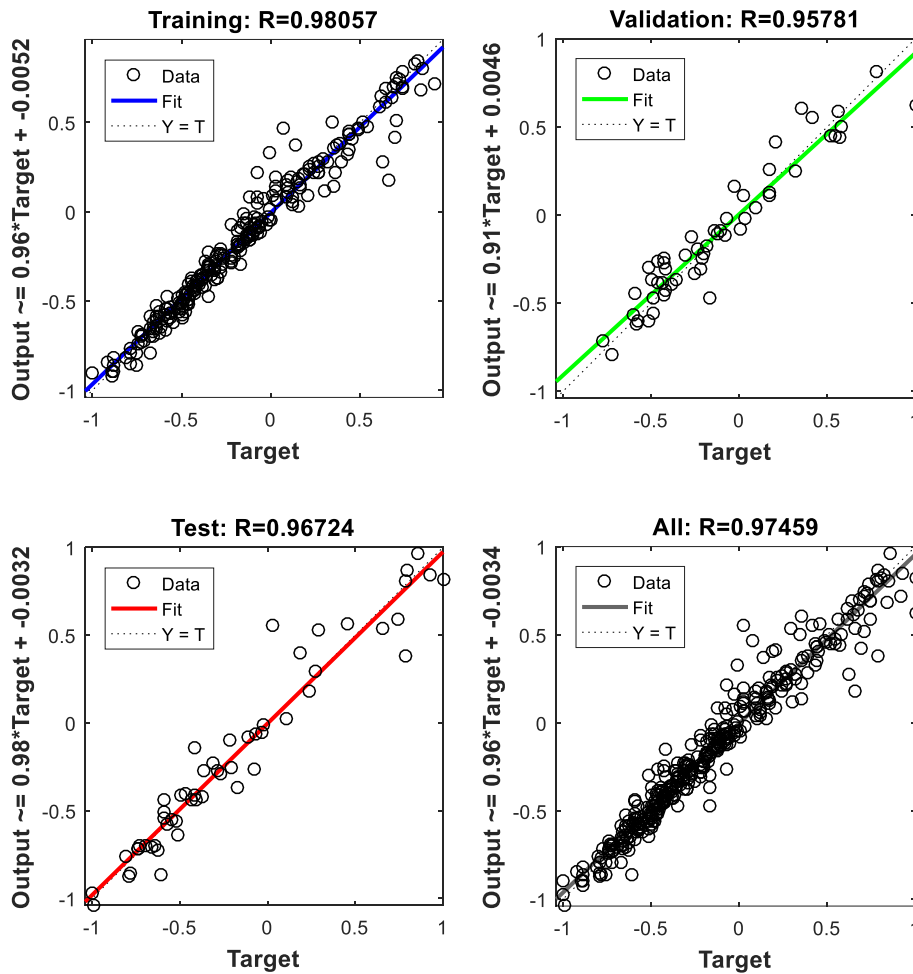


Fig. 6 – Simulation diagram of fertilizer particle crushing during fertilizer discharge process

Combined with the relative error between the validation set, test set and the real value from Fig. 7, it can be concluded that the PSO-BP neural network fitted in this paper can realistically predict the fertilizer granule crushing.

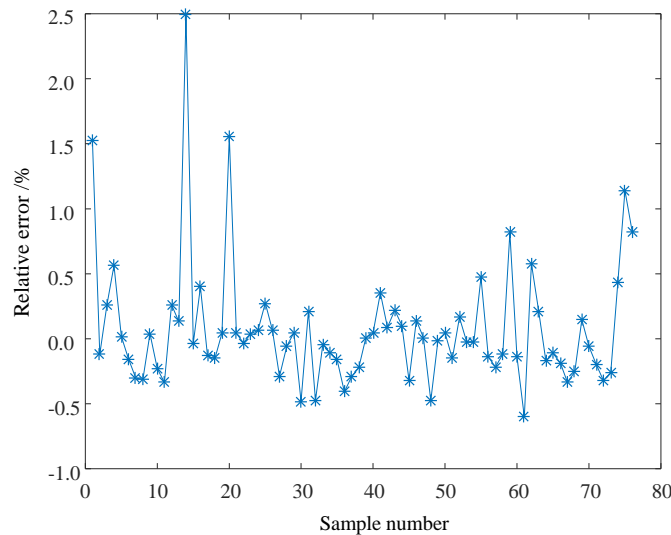


Fig. 7 – Relative error of validation set, test set and true value

With the above trained PSO-BP neural network model as the objective function, the compression displacement Y_1 and compression load Y_2 are optimized, and the network input that makes the network output 0 (with zero relative error to the true value) is solved to obtain a series of parameter combinations, which are inverted and substituted into EDEM to verify the rationality of the parameter combinations (as shown in Table 6).

Table 6

Parameter combination verification results

No.	X_1	X_2	X_4	X_5	Y_1	Y_2	y_1	y_2	y
1	9.979E+09	1.036E+10	1200000	0.20	0.455	59.524	1.111	1.459	2.570
2	1.006E+10	1.021E+10	1200000	0.20	0.450	58.703	0.000	0.060	0.060
3	1.008E+10	1.019E+10	1200000	0.20	0.451	58.594	0.222	0.126	0.348
4	9.948E+09	1.031E+10	1200000	0.20	0.452	58.941	0.444	0.466	0.910
5	1.003E+10	1.038E+10	1200000	0.20	0.452	59.395	0.444	1.238	1.683

The simulation results of the five parameter combinations in Table 7 show that the relative error y is 0.06%~2.57%, which indirectly proves that the PSO-BP neural network model fits well. When the normal stiffness X_1 , tangential stiffness X_2 , tangential ultimate stress X_4 and bonded radius X_5 are 1.006E+10 N/m², 1.021E+10 N/m², 1200000 Pa and 0.20 mm, respectively, the compression displacement Y_1 and compression load Y_2 are 0.450 mm and 58.703 N, respectively, with the minimum relative error of 0.06%.

CONCLUSIONS

The ultimate crushing displacement and ultimate crushing load of the encapsulated fertilizer granules were obtained by uniaxial compression tests as 0.450 mm and 58.668 N, respectively. The PSO-BP neural network model was used as a proxy model to calibrate the Bonding model parameters, and the factors with significant effects on the results and their value ranges were determined by the Plackett-Burman and Steepest ascent tests, respectively. The full-factor test data were used to train the PSO-BP neural network, and correlation coefficients of 0.98057, 0.95781, 0.96724 and 0.97459 were obtained for the training process, validation process, testing process and overall performance, respectively. The prediction results of PSO-BP neural network show that when the normal stiffness X_1 , tangential stiffness X_2 , tangential ultimate stress X_4 and bonded radius X_5 are 1.006E+10 N/m², 1.021E+10 N/m², 1200000 Pa and 0.20 mm, respectively, the compression displacement Y_1 and compression load Y_2 are 0.450 mm and 58.703 N, with a minimum relative error of 0.06% from the actual value.

ACKNOWLEDGEMENT

This work was financially supported by National Key Research and Development Plan of China (2017YFD0700703).

REFERENCES

- [1] Benvenuti, L., Kloss, C., Pirker, S., (2016). Identification of DEM simulation parameters by Artificial Neural Networks and bulk experiments. *Powder Technology*, 291:456-465.
- [2] Chen, P.Y., (2017). Effects of Microparameters on Macroparameters of Flat-Jointed Bonded-Particle Materials and Suggestions on Trial-and-Error Method. *Geotechnical and Geological Engineering*, 35 (2):663-677.
- [3] Chen, S., Yang, M., Ba, C., et al, (2018). Preparation and characterization of slow-release fertilizer encapsulated by biochar-based waterborne copolymers. *Science of the Total Environment*, 615:431-437.
- [4] Chojnacka, K., Moustakas, K., Witek-Krowiak, A., (2020). Bio-based fertilizers: A practical approach towards circular economy. *Bioresource Technology*, 295:122223.
- [5] Coetzee, C.J., (2017). Review: Calibration of the discrete element method. *Powder Technology*, 310:104-142.
- [6] Do, H.Q., Aragón, A.M., Schott, D.L., (2018). A calibration framework for discrete element model parameters using genetic algorithms. *Advanced Powder Technology*, 29 (6):1393-1403.
- [7] Dong, Y., Fu, Z., Peng, Y., et al, (2020). Precision fertilization method of field crops based on the Wavelet-BP neural network in China. *Journal of Cleaner Production*, 246:118735.
- [8] Du, X., Liu, C., Jiang, M., et al, (2019). Design and experiment of self-disturbance inner-filling cell wheel maize precision seed-metering device. (自扰动内充型孔轮式玉米精量排种器设计与试验) *Transactions of the Chinese Society of Agricultural Engineering*, 35 (13):23-34.
- [9] Hanley, K.J., O'Sullivan, C., Oliveira, J.C., et al, (2011). Application of Taguchi methods to DEM calibration of bonded agglomerates. *Powder Technology*, 210 (3):230-240.

- [10] Liu, C., Wei, D., Song, J., et al, (2018). Systematic Study on Boundary Parameters of Discrete Element Simulation of Granular Fertilizer. (颗粒肥料离散元仿真边界参数系统化研究) *Transactions of the Chinese Society for Agricultural Machinery*, 49 (09):82-89.
- [11] Rackl, M., Hanley, K.J., (2017). A methodical calibration procedure for discrete element models. *Powder Technology*, 307:73-83.
- [12] Xiang, Y., Ru, X., Shi, J., et al, (2017). Preparation and properties of a novel semi-IPNs slow-release fertilizer with the function of water retention. *Journal of Agricultural and Food Chemistry*.
- [13] Yoon, J., (2007). Application of experimental design and optimization to PFC model calibration in uniaxial compression simulation. *International Journal of Rock Mechanics and Mining Sciences*, 44 (6):871-889.
- [14] Zhao, G., Dai, B., Ma, C., (2012). Study of effects of microparameters on macroproperties for parallel bonded model. *Yanshilixue Yu Gongcheng Xuebao/Chinese Journal of Rock Mechanics and Engineering*, 31 (7):1491-1498.
- [15] Zhou, H., Hu, Z., Chen, J., et al, (2018). Calibration of DEM models for irregular particles based on experimental design method and bulk experiments. *Powder Technology*, 332:210-22

RESEARCH PROGRESS OF AGRICULTURAL IMPLEMENT GUIDANCE SYSTEMS. A REVIEW

/

农机自动驾驶技术的研究进展. 综述

Zhenguo Zhang^{1,2)}, Jin He^{*1)}, Hongwen Li¹⁾, Qingjie Wang¹⁾, Wenchao Yang¹⁾, Quanyu Wang¹⁾

¹⁾ College of Engineering, China Agricultural University, Beijing 100083, China;

²⁾ College of Mechanical and Electrical Engineering, Xinjiang Agricultural University, Urumqi 830052, China

Tel: +86010 62737300; E-mail: hejin@cau.edu.cn

DOI: <https://doi.org/10.356.33/inmateh-65-28>

Keywords: agricultural implement, implement guidance systems, passive implement, active implement

ABSTRACT

Automatic navigation system for agricultural vehicles have become a widely used technology in precision agriculture over the last few decades. More and more sophisticated tractor control systems, however, revealed that exact positioning of the actual implement is equally or even more important. Based on literature sources and patent databases, the aim of this review is to introduce implement guidance systems and describe its current application in agricultural implement. Agricultural implement guidance is an essential technology for autonomous vehicle operations. In addition, applications and new technologies associated with navigation sensors on passive and active implement guidance are analyzed. Finally, challenges and future perspectives of agricultural implement systems are summarized and forecasted. This study can enrich the application of automatic navigation sensors on agricultural implements and provide a reference for the application of automatic navigation on more field operations.

摘要

农业机械自动驾驶技术已经成为精准农业中广泛应用的技术之一。然而，田间地表情况复杂多变，及时、准确地农具的精准定位对提升机具作业质量具有重要的现实意义。在总结了目前作业农具研究现状的基础上，本文旨在重点介绍农具自动驾驶系统，并描述其目前在农业实施中的应用。农具自动驾驶技术是农业机械主动导航的一项重要技术。此外，还分析了导航传感器在被动和主动农具导航上的应用和新技术。最后，对自动驾驶技术在作业机具上的应用所面临的挑战和未来前景进行了总结和预测。本研究可以拓展自动驾驶技术在农具上的应用，为自动驾驶在更多田间作业上的应用提供参考。

INTRODUCTION

Agriculture is the foundation of human existence (Ding et al., 2018). As the World's population continue to grow and will reach nearly 10 billion by 2050, the need for food and agricultural products is growing at the same time. However, the growing demand for food has resulted in a significant shortage of labor for agriculture. So, precision agriculture is considered to be one of the key technologies to ensure food security and reduced labor intensity (Loures et al., 2020). Combined with an ever-declining rural labor force it causes the need for greater efficiencies and inevitably leads to increasing levels of in-field automation (Mavridou et al., 2019). In addition, long hours and repetition easily result in operators' fatigue, which in turn causes safety issues and decrease operation efficiency (Reid et al., 2004). Therefore, the automatic navigation technology of agricultural machinery is the basis for the implementation of precision agriculture, which can effectively reduce the labor intensity of agricultural machinery operators, improve the operation accuracy and efficiency. (Zhang et al., 2004; Li et al., 2009; Mousazadeh, 2013; Dong et al., 2017).

¹ Zhenguo Zhang, Ph.D. Stud.; Jin He, Prof.; Hongwen Li, Prof.; Qingjie Wang, Prof.; Wenchao Yang, Ph.D. Stud.; Quanyu Wang, Ph.D. Stud.

Tractor-mounted agricultural implements are rarely involved in navigation and positioning systems in the field. A recent expansion to the area of automatic vehicle guidance is the use of automatic implement guidance (Werner, 2015). It is a natural extension because, after all, the implement is the actual device doing the fieldwork.

Agricultural implement guidance system controls tractor steering and position and sometimes implement steering to achieve accurate positioning of the implement rather than the tractor itself (Oksanen et al., 2016). Agricultural Implement guidance continues to evolve, improving field performance, and providing capabilities beyond solely tractor guidance. The application to implement guidance systems to agriculture can yield significant productivity and efficiency benefits (Balafoutis et al., 2017; Fue et al., 2020). Therefore, automatic control of agricultural implements such as cultivators and planters that are attached to the tractors is essential for automated or autonomous operations (Han, et al., 2018).

There is a long history of creating automatic navigation guidance systems in agriculture. Mousazadeh, (2013) described a technical review on navigation systems of agricultural autonomous off-road vehicles. Han et al., (2018) gave a review of recent development in autonomous vehicles, including localization, navigation control, mission planning, perception and safeguarding, and implement control. But no summary of implement guidance system uses in agricultural applications has been reported. In this review, implement guidance systems are used mainly in agricultural applications such as soil cultivation implements, planting machines. These applications in implement guidance systems are presented. The challenges and future perspectives of implement guidance systems are discussed. Finally, the conclusions are drawn.

RESULTS OF THE STUDY

Agricultural implement guidance system

Currently, there are two types of implement guidance systems: passive and active (Fig. 1). Passive implement guidance does not require a steering mechanism on the implement, and the drift of the implement path is corrected by adjusting the tractor path. Active implement guidance system requires a localization sensor for the implement (e.g., GNSS or Machine Vision) and a steerable implement. Both the tractor and the implement follow the desired path.

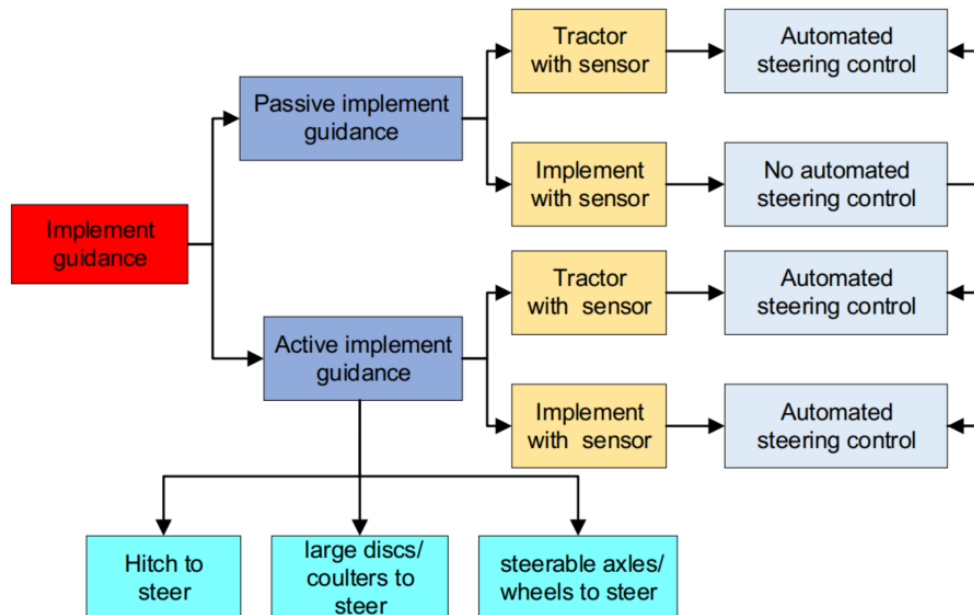


Fig. 1 - Agricultural implement guidance systems

Passive implement guidance systems

The most popular implement guidance solution is passive guidance (Fontanelli, et al., 2015). Passive implement guidance system that monitors and corrects the position of the implement by moving the tractor (Fig. 2). However, passive implement steering means that the implement does not have its own steering mechanism. Instead, it can be kept on-line by moving the tractor away from the desired line.

Typically, two GNSS/Vision receivers are used, one mounted on the cab and one on the implement. The receiver will keep the implement on-track based on tractor heading and equipment geometry or dynamics.

This type of implement guidance solution is cheaper compared to its active counterpart. However, one disadvantage of passive implement guidance is that the tractor must steer the implement, which means that the tractor may be operating off of the guidance path.

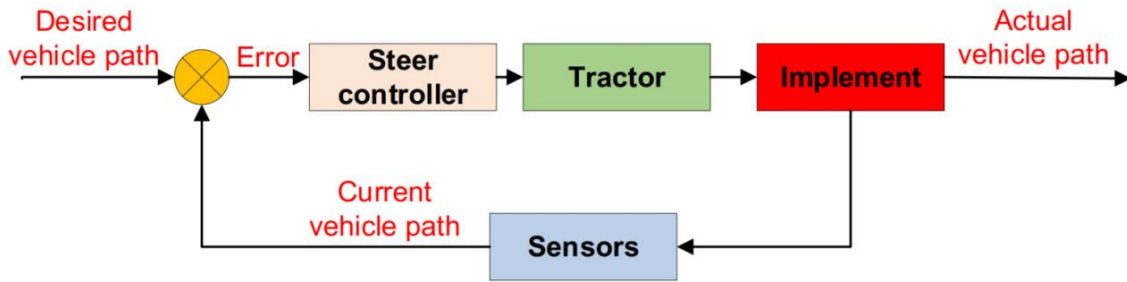


Fig. 2 - Control flow chart for passive implement guidance systems

Active implement guidance systems

Active implement guidance, in which the implement is steered independently of the tractor, may be particularly useful within an autonomous system, allowing implement guidance to operate somewhat independently of the vehicle guidance system (Thomasson, et al., 2018). These systems guide the implement independently of the tractor. Active guidance describes when an implement is being guided independently of the tractor or prime mover (Fig. 3). A second GNSS/Vision receiver is mounted on the implement along with components depending upon the type of implement guidance system. The significant advantage of active over passive guidance is seen when operating in growing crops, ridges, or beds where both the tractor and implement will remain on the desired guidance path, preventing damage (Feng, et al., 2005, Jessie, 2015). However, active guidance comes at a higher cost since it requires “active” technology to steer the implement independently of the tractor. Still, the extra accuracy may be warranted to improve cropping returns (Jack, 2017).

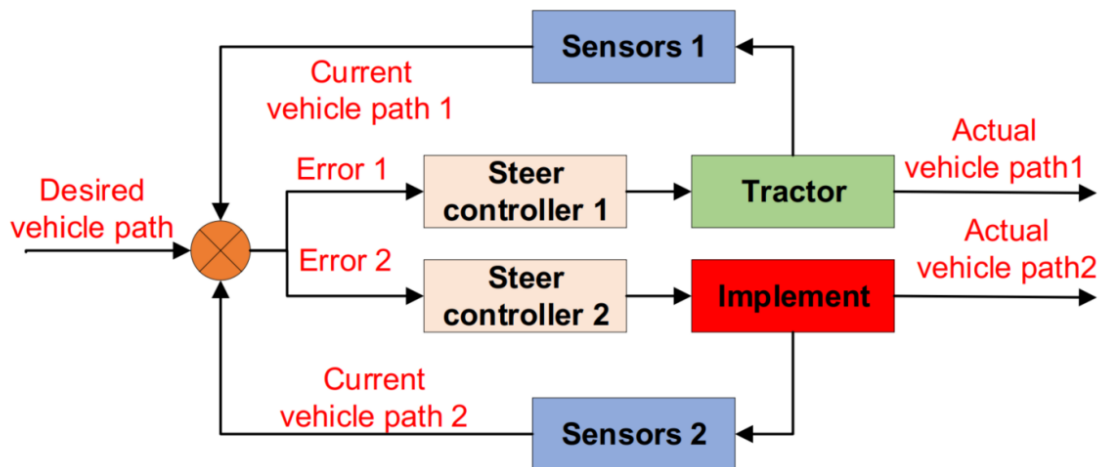


Fig. 3 - Control flow chart for active implement guidance

Application in agricultural implement systems

Automatic control of agricultural implements such as cultivators and planters that are attached to the tractors is essential for automated or autonomous operations (Han, et al., 2018). Agricultural implement guidance continues to evolve, improving field performance, and providing capabilities beyond solely tractor guidance. Due to the implement drift caused by varying soil conditions as well as gravity in sophisticated agricultural field applications, the implement path should be different from the tractor path. It is possible for the vehicle to follow the desired path but have the implement completely off its desired path (Han et al., 2018). The cause for this is side forces acting on the implement caused by operation on a side slope, vehicle attitude, and slip, and unevenness of the ground drag on the implement. Therefore, implement guidance systems can keep the implement on the desired path.

Application in passive implement guidance system

As shown in Fig. 4, the weight of pull-type implement will cause it to drift downhill in uneven terrain and on slopes. A shared-signal second StarFire Receiver installed on the implement communicates the implement's exact position to the tractor's AutoTrac system (John Deere, 2020a). The tractor then changes its path to compensate for the implement drift and will get a perfect pass-to-pass result. Regardless of the terrain, AutoTrac Implement Guidance - Passive can now achieve the highest precision standards in all seeding, planting, and tillage operations.



Fig. 4 - Automatically compensate implement drift

As shown in Fig. 5, control the implement with the Trimble TrueGuide implement guidance system (Trimble, 2020), a passive guidance system that monitors and corrects the position of the implement with compensation from the tractor. With TrueGuide, the implement's position is dependent on the tractor. When implement drifts, TrueGuide signals the tractor's Autopilot system to pull the implement on-line. TrueGuide provides passive implement guidance through integration with the tractor guidance system. The guided position of the tractor is adjusted to position the implement correctly. TrueGuide Implement Guidance System reduces uncontrolled drift of the implement by more than 50% over guiding the tractor alone, minimizes draft and results in more consistent guess rows, and increases precision with input placement.



Fig. 5 - TrueGuide implement guidance system

Application in active implement guidance

Active implement guidance is based on dedicated 'auto-steering' systems for the implement, of which there are three main types.

Hitch correction

Hitch correction is where the tractor drawbar or the implement hitch tongue is hydraulically adjusted side-to-side to guide the implement (Jack, 2017). Different compensation techniques are required, depending on whether the implement is mounted on a three-point hitch or towed behind the tractor (Hou, 2010).

Implements are particularly susceptible to lateral drifts for various reasons. In this case, it is best if the implement is also controlled, not just the tractor. A system controller reacts to GNSS/Vision receiver position data from the implement itself or data from a stubble row or furrow/ridge tracking sensor fitted to the implement.

This approach adjusts the implement position up to a maximum offset but without correcting any skew angle (Heraud et al., 2009; Rovira-Más, 2010). Therefore, typically, an implement controller is used in addition to a tractor controller. The advantage of implement control becomes immediately evident on rolling hills.

(1) Tongue Steer

As an implement tongue connection, tongue Steer (e.g., Laforge DynaTrac CLASSIC) is ideal for pulled implements to the left or right. The guided hitch allows a semi-mounted (2-point) planter and applicator to follow the GPS-RTK guidance line with a high level of accuracy in flat fields and on hillsides (Fig. 6.a).

The hitch replaces the crossbar on planters, and adapters for other implements and nutrient applicators are available. The system gives users the same RTK repeatable sub-inch accuracy on tractors with the implement (Fig.6.b).

By automatically steering the planter, it compensates for planting side-hill drift and makes perfect end-rows to maximize yields. It also helps to prevent crop damage and improve efficiency in subsequent field operations (Laforgegroup, 2020).



Fig. 6 - Laforge Guided Hitch System (a) DynaTrac CLASSIC(b) The DynaTrac CLASSIC is used on towed tongue implements to allow lateral movement of the implements

(2) 3-point hitch system providing real-time lateral or side-shift adjustment

Perez-Ruiz et al. (2012) developed and evaluated an innovative machine for weed control in inter-row and intra-row areas, with a unique combination of inter-row cultivation tooling and intra-row band spraying and an electro-hydraulic side-shift frame (Fig. 7.a) controlled by an RTK-GPS system. Band spraying with mechanical weed control using RTK-GPS (Fig. 7.b) enabled the comparison between treatments from the perspective of cost savings and efficacy in weed control for a sugar beet crop. During one season, the herbicide application rate ($112 \text{ L}\cdot\text{ha}^{-1}$) of band spraying with mechanical weed control using RTK-GPS was approximately 50% of the conventional method. Thus, a significant reduction in the operating costs of weed management was achieved.

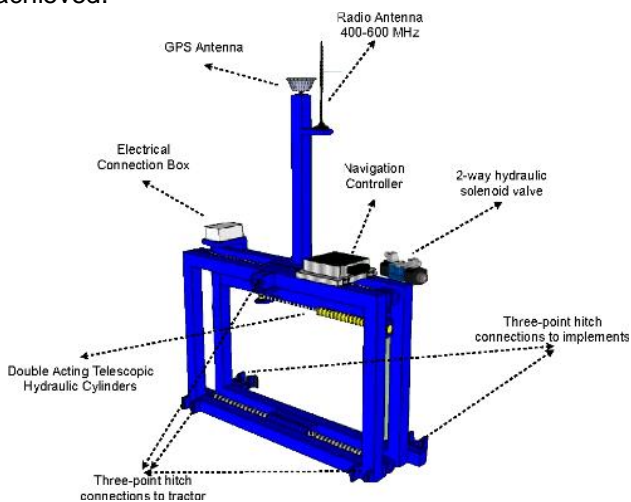


Fig. 7 - Combined cultivator and band sprayer with a Row-Centering RTK-GPS guidance system
(a) Schematic diagram of the side-shift frame system by an RTK-GPS geo-positioning system;
(b) The prototype of six-row mechanical weed control cultivator

Stehle et al. (2015) examines the work economic effects of a Garford camera system steering the hoeing tools attached to a hydraulic side shift frame (Fig. 8.a). The crop plant losses, type and number of weeds, and the standard deviation of the hoe were recorded. Based on the calculated standard deviation of the hoe, the proper settings for the distance between the hoeing tool and the plant row were calculated to minimize crop plant losses.

Contrary to expectations, the speed had no significant effect on the working accuracy of the camera control. Robocrop also has a crop imaging system which achieves excellent row following by viewing multiple crop rows over a large area. A stereo vision camera is mounted on the side shifting frame of Robocrop guided hoes (Fig. 8.b). Utilizing the Robocrop grid matching technique accurate row following is possible even on narrow row cereals and multi-line rows. Images are analyzed at a rate of 30 frames per second, and the direction of the hoe adjusted via a hydraulic side shift with anti-backlash action. The accuracy of the visual navigation system is typically 15 mm, and the machine can travel at speeds of up to 12 km/hr (*Garford Farm Machinery Ltd., 2020*).

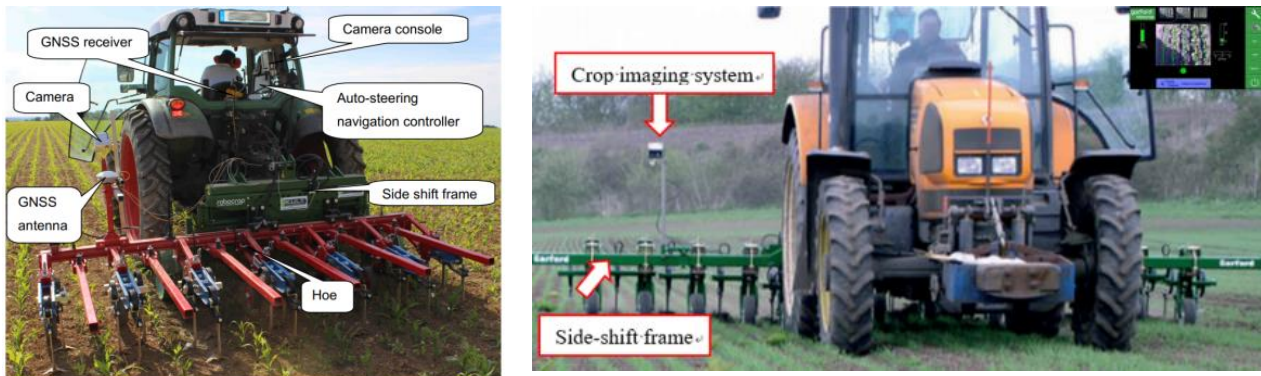


Fig. 8 - Robocrop Side Shift System. (a) GNSS guidance system. (b) Crop imaging system

(3) Portable hitch

Portable hitch attaches (e.g., Sunco Acura Trak) directly to the tractor and control all of the hitches mounted equipment with one portable solution (Fig. 9.a). The Sunco Hitch efficiently steers the implement from a leading position instead of a trailing position. In situations standard feedback options are not possible and implement accuracy is critical (such as strip-till, precision fertilizer placement, or drip tape installation), GPS implement guidance is a great option. The Sunco Implement Guidance Hitch, when used in conjunction with Sunco Stabilizers and John Deere's Active Implement Guidance System or Trimble's TrueTracker Implement Guidance System (Fig. 9.b), can solve many of the issues with current implement guidance products (*Sunco Farm Equipment, 2020*).

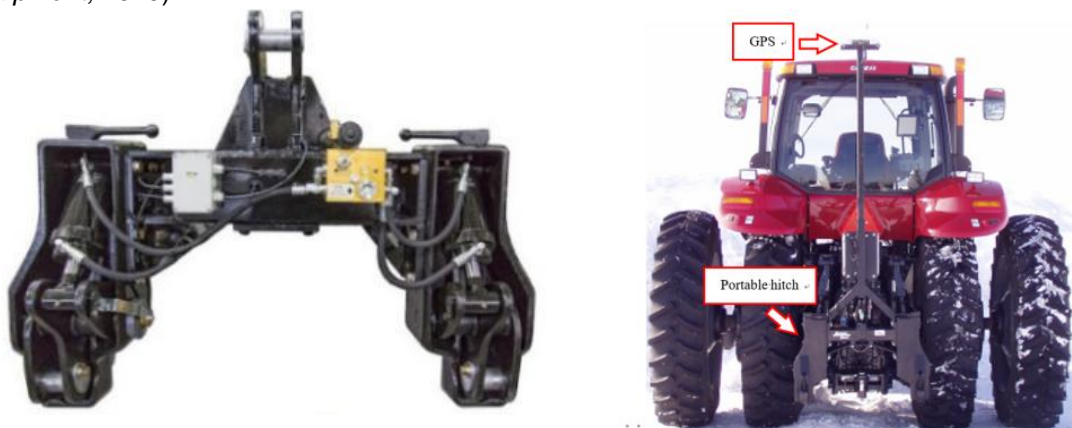


Fig. 9 - Acura Trak (a) Sunco AcuraTrak (b) Sunco AcuraTrak with an active implement guidance system

Using large discs/coulters to steer the implement

Using large discs/coulters to steer the implement develop to provide industry-leading precision guidance for drawn and 3-point mounted row crop units. For example, Orthman's Tracker IV system (Fig. 10) easily mounts onto the implement and is fully compatible with GNSS/Vision guidance systems. Available with ground-engaging steering blades, the system design features a single hydraulic cylinder that pivots all the blades simultaneously for consistent implement-tracking correction. Sub-inch implement guidance allows year-over-year repeatability of fertilizer and seeding operations, eliminates crop damage from implement drift, and reduces input cost by reducing seed and chemical overlap.

Implement guidance was shown to dramatically improve crop yields by precisely placing the seed and fertilizer closer to each other in separate field passes. Yields increased 13% when seed/fertilizer was placed with sub-inch accuracy compared to the crop planted at an 8-inch offset, and 5% higher when compared to the 4-inch offset (Orthman Manufacturing, Inc. 2020).

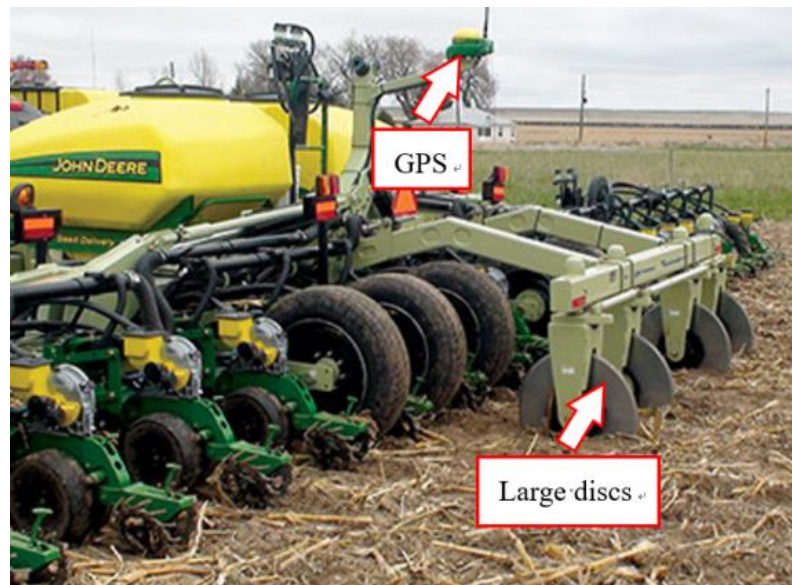


Fig. 10 - Orthman's Tracker IV system

Steerable axles or wheels on the implement

Load bearing wheel actively directs the implement frame over the guidance path using steerable wheels or disc blades to generate a corrective force (Fig. 11). Their action is controlled by GPS position data from both the implement and the tractor. Automatically steer implements with factory steering options for dramatic in-row precision. Active Implement Guidance helps optimize the use of inputs by increasing accuracy at the implement and facilitating seamless, repeatable passes throughout the growing season. Active Implement Guidance can help to reduce input costs in a variety of applications. Potato producers and other specialty crop producers that make frequent passes through the field have seen the value of active Implement Guidance as they precisely plant and care for their crops. Additionally, producers employing strip-till practices are better able to align their seed placement with their fertilizer placement, maximizing the uptake of their valuable nutrients (John Deere, 2020b).



Fig. 11 - Load bearing wheel with active implement guidance

Challenges and future perspectives

Agricultural automatic navigation technology has become increasingly mature after years of development. Navigation sensor technology based on vision and GNSS has become the leading technology of automatic navigation system of agricultural vehicles (Hu et al., 2015; Dong et al., 2017).

Automatic navigation sensors of agricultural implements have been widely used in agricultural production practice (Han *et al.*, 2018). However, there are still many challenges in the automatic navigation technology of agricultural implements that need further research.

The sole control of the path of the tractor without controlling the path of the agricultural implements cannot meet the needs of today's precision operations. Passive and active implement guidance systems can deliver additional accuracy and cost-effective guided agricultural machinery practices in challenging conditions. Although implement guidance system has been explored extensively for weed removal, field spraying, and seeding in cultivated soils, no-till seeding in restricted rows has not yet been addressed (Chen, 2018). Therefore, the application of implement guidance systems in the mechanization of the agricultural process needs to be further explored.

The steering controller is a compulsory module for implement guidance systems. The steering controller is the actuator that converts a control signal from a feedback controller to an appropriate mechanical adjustment in the steering angle (Reid *et al.*, 2000). Steering controller design needs for agriculture differ from that of on-highway vehicles due to operating conditions of the vehicle in the field. Agricultural equipment often operates on unprepared, changing, and unpredictable terrain, ranging from asphalt to spongy topsoil in the field (Han *et al.*, 2018). In the case of automatic or autonomous operation, steering controllers should be able to provide appropriate steering actions in response to the variations in equipment operation states, traveling speed, tire cornering stiffness, ground conditions, and many other parameters influencing steering dynamics (Zhang *et al.*, 1998). Therefore, a steering controller suitable for problematic agricultural practices is essential for implement guidance systems.

In addition, the cost of agricultural navigation sensors, as well as the cost and safety of using and maintaining the implement guidance systems (Mousazadeh *et al.*, 2013), still need to be further addressed in future research.

CONCLUSIONS

This review has briefly discussed the current development of automatic navigation system and its application in agricultural implements. Despite many reviews of automatic navigation sensors and their development in an automatic guidance system, no summary of implement guidance systems uses in agricultural applications has been reported.

In this article, we have roughly described that implement guidance systems is an essential technology for autonomous vehicle operations. In addition, applications and new technologies associated with navigation sensors on passive and active implement guidance are analyzed. Finally, challenges and future perspectives of navigation sensor use on agricultural implement are summarized and forecasted.

ACKNOWLEDGEMENT

This study was supported by Modern Agricultural Industry Technology System Construction Project - National Wheat Industry Technology System (CARS-03), Ministry of Education Innovative Team Development Program (IRT13039). We are grateful to all members of the Conservation Tillage Research Center for their suggestions for this paper.

REFERENCES

- [1] Balafoutis, A., Beck, B., Fountas, S., Vangeyte, J., Wal, T., Soto, I., & Eory, V. (2017). Precision Agriculture Technologies Positively Contributing to GHG Emissions Mitigation, Farm Productivity and Economics. *Sustainability*, Vol. 9, Issue 8, p.1339.
- [2] Bechar, A., Vigneault, C. (2017). Agricultural robots for field operations. Part 2: Operations and systems. *Biosystems Engineering*, Vol. 153, pp.110-128.
- [3] Catania, P., Comparetti, A., Febo, P., Morello, G., Orlando, S., Roma, E., & Vallone, M. (2020). Positioning Accuracy Comparison of GNSS Receivers Used for Mapping and Guidance of Agricultural Machines. *Agronomy*, Vol. 10, Issue 7, p. 924.
- [4] Chen, W.Z. (2018). *Study on Maize Stubble Avoidance Technology Based on Machine Vision for Row-follow No-till Seeder* (基于机器视觉的免耕播种机对行避茬技术研究). PhD dissertation, China Agricultural University, Beijing/ China.
- [5] Choi, C. H. (1988). *Automatic guidance system for farm tractor*. PhD dissertation, Iowa State University, Iowa/ USA.

- [6] Ding, Y., Wang, L., Li, Y., & Li, D. (2018). Model predictive control and its application in agriculture: A review. *Computers and Electronics in Agriculture*, Vol. 151, pp.104-117.
- [7] Dong, S., Yuan, Z., Gu, C., & Yang, F. (2017). Research on intelligent agricultural machinery control platform based on multi-discipline technology integration (基于多学科技术融合的智能农机控制平台研究综述). *Transactions of the Chinese Society of Agricultural Engineering*, Vol. 33, Issue 8, pp. 1-11.
- [8] Emmi, L., Gonzalez-de-Soto, M., Pajares, G., & Gonzalez-de-Santos, P. (2014). Integrating Sensory/Actuation Systems in Agricultural Vehicles. *Sensors*, Vol. 14, Issue 3, pp. 4014-4049.
- [9] Feng, L., He, Y., Bao, T. & H. Fang (2005). Development of trajectory model for a tractor implement system for automated navigation applications. *Instrumentation and Measurement Technology Conference, Ottawa, Canada, May*, pp.17-19.
- [10] Fontanelli, D., Giannitrapani, A., Palopoli, L., & Prattichizzo, D. (2015). A passive guidance system for a robotic walking assistant using brakes. *In 2015 54th IEEE Conference on Decision and Control (CDC)*, pp. 829-834.
- [11] Fue, K., Porter, W., Barnes, E., & Rains, G. (2020). An Extensive Review of Mobile Agricultural Robotics for Field Operations: Focus on Cotton Harvesting. *AgriEngineering*, Vol. 2, Issue 1, pp.150-174.
- [12] Gan-Mor, S., Clark, R. L., & Upchurch, B. L. (2007). Implement lateral position accuracy under RTK-GPS tractor guidance. *Computers and Electronics in Agriculture*, Vol. 59, Issue 2, pp. 31-38.
- [13] Garford Farm Machinery Ltd. (2020). Robocrop Guided Hoes Gallery. <https://garford.com/gallery/robocrop-guided-hoes/>
- [14] González-García, J., Gómez-Espinosa, A., Cuan-Urquizo, E., García-Valdovinos, L. G., Salgado-Jiménez, T., & Cabello, J. A. E. (2020). Autonomous Underwater Vehicles: Localization, Navigation, and Communication for Collaborative Missions. *Applied Sciences*, Vol. 10, Issue 4, pp. 1256.
- [15] Guo, L., Zhang, Q., & Han, S. (2002). Sensor fusion method for off-road vehicle position estimation, *Proc. SPIE, Unmanned Ground Vehicle Technology IV*, pp. 4715.
- [16] Han, S., He, Y., & Fang, H. (2018). Recent development in automatic guidance and autonomous vehicle for agriculture: A Review. (农机自动导航及无人驾驶车辆的发展综述). *Journal of Zhejiang University (Agriculture and Life Sciences)*, Vol. 44, Issue 4, pp. 381-391.
- [17] Heraud, J. A., & Lange, A. F. (2009). Agricultural Automatic Vehicle Guidance from Horses to GPS: How We Got Here, and Where We Are Going. *ASABE Distinguished Lecture*, Vol. 33, pp. 1-67. <https://elibrary.asabe.org/abstract.asp?aid=25819>
- [18] Hu, J., Gao, L., Bai, X., Li, T., & Liu, X. (2015). Review of research on automatic guidance of agricultural vehicles [J]. *Transactions of the Chinese Society of Agricultural Engineering*, Vol. 31, Issue 10, pp. 1-10.
- [19] Jack, D. (2017). Seeder Tracking & Guidance for Precise Planting. <https://www.striptillfarmer.com/articles/2288-seeder-tracking-guidance-for-precise-planting>.
- [20] John Deere. (2020a). *AutoTrac Implement Guidance - Passive*. <https://www.deere.co.uk/en/agricultural-management-solutions/guidance-automation/autotrak-implement-guidance-passive/>
- [21] John Deere. (2020b). John Deere Active Implement Guidance Base. <https://www.martindeerline.com/inventory/v1/Current/John-Deere/Precision-Agriculture/Guidance/Active-Implement-Guidance/Base--0---14105001>
- [22] Jessie, S. (2015). *Passive vs. Active Implement Guidance-Successful Farming*. https://www.agriculture.com/machinery/farm-implements/passive-vs-active-implement-guidance_225-ar49802.
- [23] Laforgegroup. (2020). DynaTrac® CLASSIC. <https://www.laforgegroup.com/en/products/dynatrac>.
- [24] Li, M., Imou, K., Wakabayashi, K., & Yokoyama, S. (2009). Review of research on agricultural vehicle autonomous guidance. *International Journal of Agricultural and Biological Engineering*, Vol. 2, Issue 3, p.1.
- [25] Li, Q., Queralta, J. P., Gia, T. N., Zou, Z., & Westerlund, T. (2020). Multi-Sensor Fusion for Navigation and Mapping in Autonomous Vehicles: Accurate Localization in Urban Environments. *Unmanned Systems*, Vol. 8, Issue 3, pp. 229-237.
- [26] Ljungblad, J., Hök, B., Allalou, A., & Pettersson, H. (2017). Passive in-vehicle driver breath alcohol detection using advanced sensor signal acquisition and fusion. *Traffic Injury Prevention*, Vol. 18, Issue sup1, pp. 31-36.

- [27] Loures, L., Chamizo, A., Ferreira, P., Loures, A., Castanho, R., & Panagopoulos, T. (2020). Assessing the Effectiveness of Precision Agriculture Management Systems in Mediterranean Small Farms. *Sustainability*, Vol. 12, Issue 9, pp. 3765.
- [28] Mavridou, E., Vrochidou, E., Papakostas, G. A., Pachidis, T., & Kaburlasos, V. G. (2019). Machine Vision Systems in Precision Agriculture for Crop Farming. *Journal of Imaging*, Vol. 5, Issue 12, pp. 89.
- [29] Meng, Q., Qiu, R., He, J., Zhang, M., Ma, X., & Liu, G. (2015). Development of agricultural implement system based on machine vision and fuzzy control. *Computers and Electronics in Agriculture*, Vol. 112, pp. 128-138.
- [30] Mousazadeh, H. (2013). A technical review on navigation systems of agricultural autonomous off-road vehicles. *Journal of Terramechanics*, Vol. 50, Issue 3, pp. 211-232.
- [31] Noguchi, N., Reid, J. F., Will, J., Benson, E. R., & Stombaugh, T. S. (1998). Vehicle automation system based on multi-sensor integration. *ASAE paper*, pp. 983111.
- [32] Orthman Manufacturing, Inc. (2020). GPS TRACKER® IV. <http://www.orthman.com/our-products.aspx?pagename=Product%20Details&itemid=2056&prodid=12238&pagetitle=Implement+Guidance>
- [33] Pérez Ruiz, M., y Upadhyaya, S. (2012). GNSS in Precision Agricultural Operations. *In New Approach of Indoor and Outdoor Localization Systems. Spain: Intech*. ISBN/ISSN. 978-953-51-0775-0.
- [34] Reid, J. F., Zhang, Q., Noguchi, N., & Dickson, M. (2000). Agricultural automatic guidance research in North America. *Computers and Electronics in Agriculture*, Vol. 25, Issue 1, pp. 155-167.
- [35] Rovira-Más, F. (2010). Sensor Architecture and Task Classification for Agricultural Vehicles and Environments. *Sensors*, Vol. 10, Issue 12, pp. 11226-11247.
- [36] Sahlholm, P., Jansson, H., Kozica, E., & Johansson, K. H. (2007). A sensor and data fusion algorithm for road grade estimation. *IFAC Proceedings Volumes*, Vol. 40, Issue 10, pp. 55-62.
- [37] Stehle, T., Griepentrog, H. W., Holpp, M., & Anken, T. (2015). Study on a machine vision based guidance system for hoeing in row crops. *Land Technik AgEng 2015, 6.-7. VDI-Verlag, Düsseldorf, Germany*, pp.493-498.
- [38] Sunco Farm Equipment. (2020). Sunco Acura Trak. <https://www.farm-equipment.com/articles/18139-sunco-farm-equipment-sunco-aurac-trak>.
- [39] Thomasson, J. A., Baillie, C. P., Antille, D. L., McCarthy, C. L., & Lobsey, C. R. (2018). *A review of the state of the art in agricultural automation. Part II: On-farm agricultural communications and connectivity*. 2018 Detroit, Michigan July 29 - August 1.
- [40] Tian, H., Wang, T., Liu, Y., Qiao, X., & Li, Y. (2019). Computer Vision Technology in Agricultural Automation--a review. *Information Processing in Agriculture*, Vol. 7, Issue 1, pp. 1-19.
- [41] Tillett, N. D. (2006). Video camera-based precision guidance: Development and applications to field crops. *Journal of the Royal Agricultural Society of England*, p. 167.
- [42] Trimble. (2020). TrueGuide Implement Guidance System. [https:// agriculture.trimble.com/ product/trueguide-implement-guidance-system/](https://agriculture.trimble.com/product/trueguide-implement-guidance-system/)
- [43] Werner, R. (2015). *Centimeter-Level Accuracy Path Tracking Control of Tractors and Actively Steered Implements. Doctoral dissertation*. PhD dissertation, Technische Universität Kaiserslautern, Kaiserslautern/ Germany.
- [44] Zhang, Q., Reid, J. F., & Noguchi, N. (1999). Agricultural vehicle navigation using multiple guidance sensors. *Proceedings of the international conference on field and service robotics*, pp. 293-298.
- [45] Zhang, M, Ji Y., Li S., Cao R., Xu H., & Zhang Z. (2020). Research Progress of Agricultural Machinery Navigation Technology (农业机械导航技术研究进展). *Transactions of the Chinese Society for Agricultural Machinery*, Vol. 51, Issue 4, pp. 1-18.

DEVELOPMENT OF TECHNOLOGIES FOR OBTAINING COMPOSITE MATERIALS BASED ON THE USE OF OILSEED FLAX FIBERS

РОЗРОБКА ТЕХНОЛОГІЙ ОДЕРЖАННЯ КОМПОЗИЦІЙНИХ МАТЕРІАЛІВ НА ОСНОВІ ВИКОРИСТАННЯ ВОЛОКОН ЛЬОНУ ОЛІЙНОГО

Olga Gorach ¹⁾, Olena Dombrovska ²⁾, Anastasiia Tikhosova ²⁾

¹⁾ Kherson State Agrarian and Economic University, Kherson / Ukraine;

²⁾ Kherson National Technical University, Kherson / Ukraine;

Tel: +38 (050) 537-98-42; E-mail: olga_gorach@ukr.net

DOI: <https://doi.org/10.356.33/inmateh-65-29>

Keywords: oilseed flax, straw, bast, chemical processing, fiber, composite materials.

ABSTRACT

The article examines the ways to solve the problem of developing a scientific basis for obtaining composite materials of different functional purposes from oilseed flax fibers. The paper covers theoretical and experimental research in the area of processing flax raw materials. The purpose of the study is to provide scientific substantiation of developing the technologies for obtaining fillers to reinforce composite materials. In order to do it, modification of oilseed flax fiber was performed and a technology for processing oilseed flax straw with regulated technological and performance characteristics was developed. The article also presents the results of the research on determining causes of low wettability of oilseed flax bast. In order to find out the causes of low bast wettability, research on examining chemical composition and anatomy of straw stems was conducted. The formulation for preparing the fiber aimed to be used as a filler for reinforcement of composite materials is offered. The study suggests evaluation of the quality of composite materials produced based on using modified oilseed flax fibers.

РЕЗЮМЕ

Статтю присвячено вирішенню проблем розвитку наукових основ одержання композиційних матеріалів різного функціонального призначення з волокон льону олійного. Стаття містить теоретичні та експериментальні дослідження в галузі переробки лляної сировини. Завданням роботи є наукове обґрунтування створення технологій одержання наповнювачів для армування композиційних матеріалів. Для цього в результаті досліджень було проведено модифікацію волокна льону олійного та розроблено технології переробки соломи льону олійного з регульованими технологічними та експлуатаційними властивостями. У статті також наведено результати досліджень з визначення причин низької змочуваності лубу льону олійного. Для цього були проведені дослідження з вивчення хімічного складу та анатомічної будови стебел соломи. Подано рецептуру підготовки волокна з метою застосування його в якості наповнювачів для армування композиційних матеріалів. Надано оцінку якості одержаним композиційним матеріалом виготовлених на основі застосування модифікованого волокон льону олійного.

INTRODUCTION

Oilseed flax is a valuable industrial crop of versatile use. Its botanical name *Linum usitatissimum* means “early maturing”. According to the FAO data, the sown areas of oilseed flax cover almost 3.5 million hectares over the globe (FAO et al, 2000). Flax is grown in many countries of the world. Oilseed flax takes more than 70% of sown areas in the world. Recently, oilseed flax production has been intensively developed in Canada and the USA.

Analysis of the global oilseed flax production shows that the leading producers of oilseed flax in the world are Canada, China, India, Argentina, the USA and Russia. The total gross seed yield in these countries makes 1.2 million tons. In Ukraine this crop has not been paid attention over many past years due to social and political processes occurring in our country in the course of centuries. Nowadays oilseed flax returns to Ukraine. A wide range of varieties, their diversity and high profitability contribute to rapid spreading and annual growth of sown areas for this crop cultivation.

In Ukraine flax seeds are processed to obtain oil in small volumes, and most of them are exported. The crop stems are rarely processed and largely burnt in the fields. The research conducted at Kherson National Technical University (Ukraine) showed that oilseed flax stems contain a sufficient amount of fiber similar by its structure to short fiber of linen flax (*Tikhosova H.A. et al, 2011; Zhivetin V.V. et al, 2000*).

Oilseed flax stems, like linen flax stems, contain cellulose fiber in their bast. However, oilseed flax fiber has not been used in the global industry so far. After separating seeds, straw residues have been mostly burnt and mixed into soil, i.e. they were applied as fertilizer. Recently the issues of using oilseed flax have been paid much attention over the globe, but these studies are mainly aimed at processing seeds. Only few of them investigate the processing of oilseed flax stems to obtain fiber (*Gorach O. et al, 2018*). The article introduces the results of experimental studies on obtaining composite materials of different functional purposes from modified oilseed flax fibers. Examination and generalization of the results of the modern theoretical research in the area of production of composite materials allowed formulating the main hypothesis of the study: modification of oilseed flax fiber must result in the formation of its quality indexes, determined by physical-mechanical and chemical properties, parameters and modes of processing raw materials that can be considered as a complex criterion affecting final characteristics of composite materials of different functional purposes obtained from oilseed flax fiber (*Gorach O. et al, 2016; Chursina L. et al, 2017*). Confirmation of this hypothesis will support scientific development of innovative technologies for obtaining composite materials of different functional purposes by using oilseed flax fiber.

Application of oilseed flax straw will allow using annually renewable, environmentally friendly and safe raw materials, in particular, oilseed flax fiber to manufacture fillers for reinforcement of composite materials (*Gorach O.O., Hureieva S.S., Shot V.E. et al, 2019*). In order to determine suitability of the obtained bast for production of industrial textile, in particular, fillers for composite materials, production trials were carried out at the state enterprise “Plastmas” (Ukraine).

After reaching full maturity of oilseed flax straw stems and their mechanical processing by means of hackling, bast completely gets rid of its woody parts: phloem, xylem, parenchyma, and cuticle is left on the exterior of fibers, that adds hydrophobic properties to fibers. Cuticle is structureless transparent covering existing between fibers in the form of hairs. Cuticle consists of substances called cutins. As the study of Ordina N.A. proves, cutins are high molecular fatty acids, oxyacids, waxes and fats. They are resistant to the effects of strong chemical reagents such as concentrated acids and alkali. Cutins do not dissolve in sulfuric and chromic acids and even in copper-ammonia solution in which cellulose dissolves. It is availability of cutins on oilseed flax bast that causes its low wettability and a lack of adhesion to polymeric matrix (*Ordina N.A. et al, 1978*).

MATERIALS AND METHODS

Scientists from different countries of the world, namely, Langer E. (Germany), Kathleen V.D.V. (Belgium) carried out research on using natural fibers, in particular, oilseed flax fiber to obtain internal panels for cars. There are studies of Ton-That MT, Denault J. (Canada) on applying fibers to manufacture products for technical purposes. The papers of Mieleniak B., Bagley C., d'Anselme T., Guyader J. (USA) evidence that oilseed flax is traditionally grown on 700-800 thous. ha in the west of Canada. Annual yield of oilseed flax straw is nearly 1 million tons, and only 15-20% of this straw is used in production, mainly, to manufacture cigarette paper. Factories producing pulp and paper are located in the states North Carolina and New Jersey (USA). The studies of Pallesen (Denmark) highlight that fiber obtained by the technology of Rome research center (IPZS), after enzymatic treatment, extracting, active warm ventilation and carding process are used to produce composite materials, and shives – to produce chipboards. Zelenetskyi S. (Russia) succeeds in conducting research on modification of natural fibers to produce polymeric composite materials with natural fibers as fillers (*Mieleniak B. et al, 1985; Bagley C., d'Anselme T., Guyader J. et al, 1997; Guillyay R., 1997; Joly C, Gauthier R., Chabert B. et al, 1996; Kathleen V.D.V. et al, 1998; Langer E. et al, 1998*).

Three varieties of oilseed flax – Evryka, Liryna and Aisberh were selected to conduct research and carry out experiments. They were significantly different from each other by technological characteristics. These varieties were grown in the climatic conditions of the South of Ukraine. Flax oilseed straw was obtained at the state enterprise “Research Farm “Askaniiske” of the National Academy of Agrarian Sciences of Ukraine.

The variety Evryka has been included in the List of Plant varieties of Ukraine since 2004. It was created by the Institute of Irrigated Agriculture of the NAAS of Ukraine using the method of hybridization with further individual-family selection. The variety is designed to obtain oil for food and industrial needs and protein meal to feed animals. The plant height is 57-62 cm. The stem is rounded. Its thickness equals 3-4 mm.

It has branches in its lower and upper parts. The length of the growing season is 81 days. The inflorescence is umbellate, 25-32 cm long. The fruit is a rounded capsule with 7-10 seeds. The seeds are black. The weight of 1000 seeds is 7-8 g. It is resistant to lodging, capsule cracking and seed shedding. The variety is stable in terms of yields. It is medium-resistant to pests and diseases, suitable for all growing zones. The seed productivity is 2880 kg/ha. Seed oil content is 39.4 %.

The variety Aisberh has been included in the List of plant varieties of Ukraine since 2001; it was created by the Institute of oilseed crops of the UAAS by the method of induced mutagenesis of Tsian variety seeds through irradiation with gamma-rays. The plant height is 54-57 cm, the duration of the growing season is 86-88 days. The variety is characterized by drought and lodging resistance. In the field experiments of the Institute of Agriculture of the Southern region of the UAAS (2004) its seed profitability was 2080-2180 kg/ha.

The variety Liryna has been included in the List of plant varieties of Ukraine since 2002; it was created by the German plant breeders of "Deutsche Saatveredelung AG". The variety is of an intensive type of usage. It generates high stable yields – 2500-2900 kg/ha. The growing season lasts 107-128 days. A large number of capsules with seeds ensure high yields even under low seeding density. The plant height is 58-78 cm. The weight of 1000 seeds is 5.6-7.2 g. Oil content is 44.3-46.1 %. Plants are characterized by uniform maturation. It is recommended for growing in forest-steppe and steppe zones.

In order to obtain fiber, the straw stems were mechanically processed using a modernized flax-scutching machine without a technological operation of flax straw preparation. The main reason for not preparing flax straw lies in the fact that agricultural enterprises are not interested in producing oilseed flax straw. It is related to additional financial, energy and labor costs, which agricultural producers cannot afford because of a lack of stable market for selling flax straw.

Having studied all the available methods for purifying bast to remove extraneous substances and waxes, the scientists of Kherson National Technical University developed a number of techniques to obtain cellulose from oilseed flax bast and fiber (Gorach O. et al, 2016). The most effective technique is acidification that ensures high cellulose output (Gorach O.O., Hureieva S.S., Shot V.E. et al, 2019).

This technique was used in boiling oilseed flax bast of the varieties under study obtained after double hackling.

The composition of boiling solutions and modes are given in Table 1.

Table 1

Modes and formulations for boiling oilseed flax bast to remove incrust and cutins from fiber

Technological operation	Composition of boiling solution, g/l	Mode of boiling
1. Oxidation boiling	Hydrogen peroxide (100%) – 4.0	1. Boiling at 100 °C – 60-180 min.
	Sodium hydroxide – 10.0	2. Rinsing with cold water – 10 min.
	Calcined soda – 2.0	3. Acidification with sulfuric acid (2 g/l) – 10 min.
	Sodium silicate – 5.0	4. Rinsing with cold water – 20 min.
sodium tripolyphosphate – 1.0		
	Wetting agent – 0.3	
2. Fiber pressing out and drying	-	Pressing out to moisture content of 60% and drying at 100 °C

In order to find out the cause of such low wettability, the chemical composition of oilseed flax bast (Table 1) and the anatomy of oilseed flax stems were examined.

RESULTS

After processing straw stems of oilseed flax using a modernized flax-scutching machine, samples of the obtained bast were selected and its physical-mechanical properties were determined: a mass portion of shives and impurities, breaking load, bast output (Kathleen V.D.V. et al, 1998; Langer E. et al, 1998).

Analysis of the obtained results showed that bast, obtained from oilseed flax straw stems, has a high mass portion of shives – 27.2-30.6 % and low strength – 3.9-5.0 daN. However, bast output after mechanical processing by a modernized flax-scutching machine is sufficiently high: with the average stem length of 32.9-

36.0 cm, this index amounts to 32.4-39.4 %. Thus, we can draw a conclusion that bast-fiber raw materials with such high indexes of a mass portion of shives and impurities does not meet the requirements of producers of industrial textile for different purposes. Therefore, in the further research bast was additionally purified from shives by means of the operation of machine hackling.

The experimental research resulted in obtaining bast with high quality indexes due to optimization of the modes and parameters of mechanical processing of oilseed flax straw stems. After the second hackling by the hackling machines with the rotational frequency of the main cylinder of 555 min^{-1} and the opening between it and the knife of 1.5 mm, bast with the following physical-mechanical characteristics was obtained: the staple length – 18.10 mm; the mass portion of shives and impurities – 0.01 %; linear density – 0.35 tex. In order to determine suitability of the obtained bast for manufacturing fillers for reinforcement of composite materials, production trials were carried out at the state enterprise “Plastmas” (Ukraine). As it is known, the main index of filler adhesion to phenol formaldehyde resins is wettability. Currently at the enterprise “Plastmas” cotton lint with the wettability of 120 g is used as a filler. Therefore, the wettability of oilseed flax bast of the three varieties (Aisberh, Evryka and Liryna) was determined. The results of the experimental research showed that the average values of this index ranged from 5.0 to 6.3. Analysis of the obtained results indicate that bast fiber of oilseed flax has wettability that is 24 times less than that of cotton lint. According to the requirements of the regulating documents, a filler for phenoplasts should have wettability of 116-120 g. Therefore, oilseed flax bast, obtained after mechanical processing of straw stems is unsuitable for producing fillers to reinforce composite materials on the basis of phenol formaldehyde resins because of its low wettability (Gorach O.O., Hureieva S.S., Shot V.E. et al, 2019).

After mechanical processing of straw stems using a modernized flax-scutching machine and hackling machines, cuticle remained on fiber. It is evidenced by micro-photos of the cross sections of oilseed flax bast of the varieties under study obtained as a result of mechanical processing (Fig. 1-3). Microphotographs were taken using microscopes.

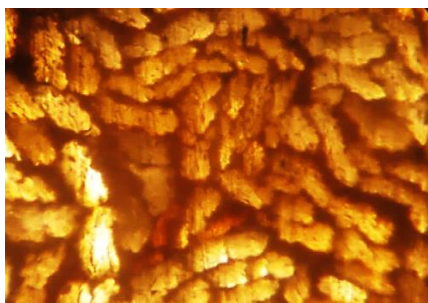


Fig. 1 - Micro-photo of the cross section of oilseed flax bast of the variety Aisberh



Fig. 2 - Micro-photo of the cross section of oilseed flax bast of the variety Evryka

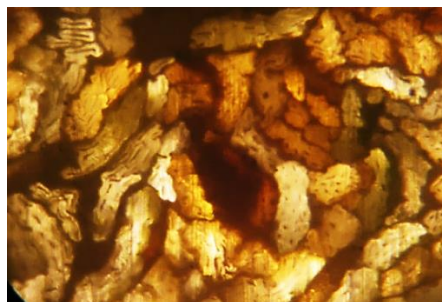


Fig. 3 - Micro-photo of the cross section of oilseed flax bast of the variety Liryna

Thus, the results of experimental research allowed establishing that after mechanical processing of straw stems of oilseed flax by means of a modernized flax-scutching machine and double hackling of the obtained bast using a hackling machine to remove incrusts and cutins, it is necessary to perform chemical processing (boiling) of bast.

Therefore, the second stage of developing the technology for obtaining fillers to reinforce composite materials from oilseed flax is chemical modification, i.e. purifying fibers to remove cellulose and substances accompanying cutin – high molecular fatty acids, oxyacids, waxes and fats. The chemical composition of oilseed flax bast of the varieties under study prior to boiling is given in Table 2.

Table 2

The chemical composition of oilseed flax bast of the varieties under study prior to boiling

Oilseed flax variety	Content of chemical components, %				
	cellulose	lignin	pectin substances	wax substances	mass proportion of hemicellulose
Aisberh	82.27	1.62	4.21	3.85	6.47
Evryka	81.37	1.31	4.03	3.74	6.77
Liryna	82.12	1.34	4.15	3.82	6.72

Table 1 shows that oilseed flax bast has a high content of lignin – 1.31-1.62 %, pectin substances – 4.03-4.21 %, wax substances – 3.74-3.85 % and hemicellulose – 6.47-6.77 %. Thus, oilseed flax bast is hardly suitable for using in production industries because of a high content of substances accompanying cellulose, therefore, in order to increase its wettability and adhesion, bast was boiled.

Table 3 presents the results of the research on wettability and chemical composition of oilseed flax fiber of the variety Aisberh after boiling for 1, 2 and 3 hours. The results of the chemical analysis of oilseed flax fiber composition of the three varieties under study allowed establishing that different varieties of oilseed flax have similar content of chemical components. Therefore, we used mediated values of the experimental research of the oilseed flax variety Aisberh.

Table 3

Physical-chemical indexes of fiber quality of the oilseed flax variety Aisberh

Number of experiments	Physical-chemical indexes of oilseed flax fiber					
	Duration of boiling, hours					
	1		2		3	
	wettability, g	mass portion of α -cellulose, %	wettability, g	mass portion of α -cellulose, %	wettability, g	mass portion of α -cellulose, %
1	104.88	87.32	105.92	87.78	122.80	90.96
2	104.45	86.67	104.86	88.28	123.50	89.64
3	105.22	86.83	105.76	87.53	119.70	90.04
4	104.98	87.06	105.58	87.22	124.70	89.76
5	105.15	86.54	104.84	87.58	123.20	89.67
Average value	104.94	86.88	105.39	87.68	122.78	90.01

Analysis of the data in Table 3 shows that boiling oilseed flax bast of the variety Aisberh according to the mode given in Table 2 for 1, 2 and 3 hours allowed obtaining fiber which meets the requirements for wettability of fillers set by the enterprise "Plastmas". In the course of the previous research it was determined that this index for oilseed flax bast was only 5.0-6,3 g, and due to the technological operation of boiling the fiber, wettability increased to the necessary indexes – 104.94-122.78 g, a mass proportion of α -cellulose rose from 76.88 % in the control variant (without boiling) to 86.88-90.01 %.

The results of the research on bast chemical composition in the control variant and oilseed flax fiber of the variety Aisberh after boiling for 1, 2 and 3 hours are given in Table 4. According to the methods for conducting experiments, we considered the average mean of five parallel measurements of the content of cellulose, lignin, pectin and wax substances and the mass portion of hemicellulose to be the result of the trial.

Table 4**Chemical composition of oilseed flax fiber**

Time of boiling, hrs	Content of chemical components, %				
	cellulose	lignin	pectin substances	wax substances	Mass portion of hemicellulose
control	82.27	1.62	4.21	3.85	6.47
1	91.27	0.31	-	0.04	3.77
2	93.22	0.64	-	0.02	3.72
3	94.06	0.68	-	0.01	3.05

Analysis of the data in Table 4 shows that boiling oilseed flax bast of the variety Aisberh according to the mode given in Table 2 for 1, 2 and 3 hours allowed obtaining fiber rich in cellulose and free of wax pectin substances. Cellulose content increased from 82.27 % to 91.27 % after boiling bast for 1 hour, to 93.22 % – after boiling for 2 hours and to 94.06 % – after boiling for 3 hours. The mass proportion of hemicellulose fell from 6.47% to 3.05%, and wax substances were almost removed. The index of their content in bast – 3.85%, and after chemical processing it dropped to 0.01-0.04%. However, by the relative breaking load and the relative breaking extension, flax fiber is significantly inferior to cotton fiber.

After examining physical-mechanical indexes of oilseed flax fiber and cotton fiber, comparative analysis of physical-mechanical properties of phenoplasts, reinforced with cotton and flax fibers, was performed. In order to do that, in the course of the experiment at the laboratory LLC “RDS IL” (Ukraine), were made experimental samples of the composite materials in which oilseed flax and cotton fibers were used as fillers.

The quality of the obtained phenoplasts, reinforced with oilseed flax and cotton fibers was evaluated according to the requirements of TU U 25.2-32512498-001-2004 with amendments 1, 2, 3, 4 “Pressing phenolic mass” (*TU U 25.2-32512498-001-2004 with amendments 1, 2, 3, 4. et al, 2004*). The obtained composite materials were compared by their color, appearance, fluidity, notch-toughness by Charpy impact test on the samples without a cut and electrical robustness. Physical-mechanical quality indexes of the phenoplasts Y1-301-07, reinforced with cotton fiber and oilseed flax fiber are given in Table 5.

Table 5**Quality indexes of phenoplasts reinforced with oilseed flax and cotton fibers**

№	Quality indexes	Type of a filler					
		standard indexes	control variant	oilseed flax fibers of the variety Aisberh after boiling for, hrs			cotton
				1	2	3	
1.	Color	from light-brown to dark-brown	complies	complies	complies	complies	complies
2.	Fluidity, mm	40-140	200	185-190	180-190	200	125
3.	Appearance of pressed samples	without cracks and blisters	does not comply	complies	complies	complies	complies
4.	Notch-toughness by Charpy on the samples without a cut, kJ/m ² (daN·cm/cm ²), not less	8.8 (9.0)	16.43	9.5	11.3	8.2	12.38

Table 5
(continuation)

№	Quality indexes	Type of a filler					
		standard indexes	control variant	oilseed flax fibers of the variety Aisberh after boiling for, hrs			cotton
				1	2	3	
5.	Bending stress under damage, MPa (daN·cm/cm ²), not less	58.8 (600)	632.55	571	562	706	692
6.	Specific volume electric resistivity, Ω ·cm	1 · 10 ⁹	-	2.89 · 10 ¹²	1.96 · 10 ¹³	6.9 · 10 ¹³	5.0 · 10 ⁹
7.	Electric robustness, kW/mm	6.0	-	10.8	10.6	12.0	-

Analysis of the quality indexes of the obtained composite materials given in Table 7 evidences appropriateness of reinforcing phenoplasts with oilseed flax fibers on the basis of using thermosetting resin. Boiled for 1 and 2 hours, oilseed flax fiber of the variety Aisberh complies with the requirements of TU U 25.2-32512498-001-2004 by all the indexes under study except bending stress under damage. It equals to 571 daN/cm² after 1 hour of boiling and 562 daN/cm² after 2 hours of boiling, i.e. a bit less than the standard index that must be not less than 600 daN/cm², which is determined by low strength of oilseed flax fiber.

CONCLUSIONS

Oilseed flax fiber can be used as fillers to reinforce composite materials after mechanical processing and chemical modification. The results of the research on chemical composition of bast obtained after mechanical processing and analysis of the anatomy of oilseed flax stem structure allowed determining that high hydrophobic behavior and low wettability of bast are caused by the presence of cuticular layer on fiber. It consists of high molecular fatty acids, wax substances and fats, and their average content in bast equals to 3.85%. It was established that in order to use oilseed flax bast for reinforcing composite materials, in addition to mechanical purifying to remove extraneous substances and shives, it is necessary to perform chemical cleaning of cellulose to remove incrusts, i.e. lignin and pectin substances, and also high molecular fatty acids, wax substances and fats.

Experimental analysis of the advantages and disadvantages of different methods for obtaining cellulose was performed. A new acidification method was chosen for purifying bast to remove substances accompanying cellulose. The research results showed that after boiling oilseed flax bast of the variety Aisberh for 3 hours were obtained samples of phenoplast that complied with the requirements of TU U 25.2-32512498-001-2004 by all the indexes except for notch toughness which was 8.2 kJ/m², whereas the standard index equals not less than 8.8 kJ/m². The samples of phenoplast obtained by means of oilseed flax bast without boiling, i.e. the control variant, complied with TU U 25.2-32512498-001-2004 by physical-mechanical properties, but the disks had numerous blisters and cracks, that did not make it possible to test these samples by electric indexes.

Thus, analyzing the results of the experimental research, can be drawn the conclusion that oilseed flax fiber after boiling according to the suggested method can be used as a reinforcing component to produce composite materials on the basis of thermosetting resin individually or in combination with other types of cellulose fiber. Therefore, scientific development of innovative technologies for obtaining composite materials from oilseed flax fibers of different functional purposes will allow using annually renewable, environmentally-friendly and safe raw materials that will contribute to the development of resource-saving technologies and will allow improving the environment and supplying the global market with new commodities of different functional purposes.

REFERENCES

- [1] Bagley C., d'Anselme T., Guyader J., (1997), Properties of Flax Fiber-Reinforced Composite, *Works of INF*, pp. 385-386. USA;
- [2] Cappelletto P.L., (1997), Fiber valorization of oilseed flax. Flax and other Bast Plants, Symposium, 30 September and 1 October. *Institute of Natural Fibers*, pp. 150-151. Poznan / Poland;
- [3] Chursian L.A., Gorach O.O., (2017), Processing of oilseed flax stems for industrial textile on the basis

- of modern technologies, *Quality management in education and industry: experience, problems and prospects: abstracts of the III International scientific-practical conference in memory of Professor Peter Stolyarchuk*, pp. 50–51. Lviv / Ukraine;
- [4] Chursina L., Tihosova G., Gorach O., (2017), The scientific justification for the use of fiber flax oil to produce technical textiles. *National Science Review, (Oxford University Press)*, Issue 4 (2). Vol. 4. pp. 1344-1450.
- [5] DSTU 4149-2003., (2004), Flax Straw. Technical conditions. 14 p. Kyiv / Ukraine;
- [6] DSTU 5015-2008., (2008), Short flax fiber. Technical conditions. 16 p. Kyiv / Ukraine;
- [7] Information bulletin of the FAO European Cooperative research Network on flax and other bast Plants, (2000). № 2 (14), December, Poznan / Poland;
- [8] Gorach O., Tihosova H., (2016), Scientific development of innovative technologies for technical textiles of different functions (Науковий розвиток інноваційних технологій одержання технічного текстилю різного функціонального призначення), *Contemporary Science and Education in Americas, Africa and Eurasia. The X International Academic Congress*. pp. 289-296. Rio de Janeiro / Brazil;
- [9] Gorach O., Bogdanova O., (2018), Perspective technologies of cellulosis reception flax fiber. *International Review of Education and Science Engineering Studies, Issue 3(2), vol.9, №.1. (14), Vol. VIII.*, pp.213-221. Ottawa / Canada;
- [10] Gorach O., Tihosova G., (2016), Scientific development of innovative technologies for technical textiles of different functions. *Contemporary Science and Education in Americas, Africa and Eurasia. The X International Academic Congress*. pp. 289-296. Rio de Janeiro / Brazil;
- [11] Gorach O.O., Hureieva S.S., Shot V.E., (2019), Research on wettability of oilseed flax bast and hemp (Дослідження змочуваності олійного льону та конопель), *Merchandising bulletin*. Issue 1. pp. 89-96. Lutsk / Ukraine;
- [12] Guillaud R., (1997), Nonwoven application of natural fibers. *Flax and other Bast Fibrous Symposium*, France 30 September. France;
- [13] Joly C, Gauthier R., Chabert B., (1996), Physical Chemistry of the Interface in Polypropylene, Cellulosic-Fiber Composites, *Composites Science and Technology*. 56. pp. 761-765.
- [14] Kozłowski R., (1999), Composite materials strengthened by plants natural fibers for motor industry, *FAO Intercessional Consultation on Fibers*. 15-16 November. Poznan / Poland;
- [15] Kathleen V.D.V., (1998), Research on the use of flax as reinforcement for thermoplastic pultruded composites. *The 1st Nordic Conference on flax and hemp processing*. Belgium;
- [16] Langer E., (1998), Flax in Germany – new technical and textile applications, *The 1-st Nordic Conference on flax and hemp processing*, Germany;
- [17] Mieleniak B., (1985), Low-cost «Compak» board based on vegetable fiber, *Wood Bas. Pan. Int.* № 1. Poznan / Poland;
- [18] Ordina N.A., (1978), Structure of blast fiber plants and its changes in processing, *Light industry*. 273 p. Moscow / Russia;
- [19] Tikhosova H.A., Chursina L.A., Gorach O.O., Yanyuk T.I., (2011), Scientific foundations of complex processing of oilseed flax seeds and stems (Наукові основи комплексної переробки стебел та насіння льону олійного), monograph. *Oldi-plius*. 356 p. Kherson / Ukraine;
- [20] Tikhosova H.A., Gorach O.O., Kniaziev O.V., (2016), Analysis of the development of industrial textile in the world (Аналіз розвитку промислового текстилю у світі), *Promising technologies and equipment*. pp. 25-29. Lutsk / Ukraine;
- [21] Tikhosova H.A., Gorach O.O., Kniaziev O.V., (2016), Analysis of the development of industrial textile in the world, *Promising technologies and equipment*. pp. 25-29. Lutsk / Ukraine;
- [22] TU U 25.2-32512498-001-2004 with amendments 1, 2, 3, 4., (2004), Phenolic pressing mass (Maca пресувальна фенольна), *The State Committee of Ukraine for standardization, meteorology and certification*. 10 p. Chernihiv / Ukraine;
- [23] Yeneke Michael, (2010), Global market of industrial textile. Impact of crisis, tendencies and prospects, *Industrial textile*. № 29. pp. 81-87. Vienna / University of East Anglia;
- [24] Zhivetin V.V., (2000), Oilseed flax and its complex development (Масличный лён и его комплексное развитие), *TsNILKA*. 389 p. Moscow / Russia.

DEVELOPMENT AND TEST OF FREQUENCY SUBSECTION REGULATION SYSTEM FOR COMBINE HARVESTER HEADER CUTTER

联合收获机割台切割器频率分段调控方法及试验

Li Ying¹⁾, Guan Zhuohuai^{1, *)}, Chen Yisong²⁾

¹⁾Nanjing Institute of Agricultural Mechanization, Ministry of Agriculture and Rural Affairs, Nanjing, 210014, China

²⁾Mechanical Engineering, Jiangsu University, Zhenjiang, 212013, China

Tel: +86 15295798587; E-mail: Guan_zh@foxmail.com

DOI: <https://doi.org/10.356.33/inmateh-65-30>

Keywords: Combine harvester, header, cutter frequency, segmented regulation, missed cutting

ABSTRACT

Aiming at the problems that the cutter frequency of combine harvester is difficult to be adjusted adaptively with the forward speed, and that the missed cut or repeated cut may cause the harvesting loss to increase and the operation effect to fluctuate greatly, the system is designed to regulate the cutter frequency of combine harvester by sections. By constructing the cutter trajectory equation, the influence of the relationship between the forward speed of the harvester and the cutting frequency on the cutting area is analysed, and the optimum cutting frequency range at different operating speeds is determined. The results show that the error between the actual cutting frequency and the desired frequency of the cutter is less than 0.8Hz, and the maximum relative error is less than 8.6%; the average steady-state adjustment time of the system is 1.3s when the input cutting frequency of the device changes abruptly. The research class provides technical support for the improvement of the combine harvester handling system and the increase of the machine automation level.

摘要

针对目前联合收获机割台切割器频率在收获过程中通常保持不变,容易产生秸秆的重割或漏割现象,造成谷物收割损失增大、作业性能不稳定等问题,设计了联合收获机割台切割器频率分段调控装置,该装置主要由信号采集及调理模块、按键模块、控制模块和显示模块等组成。对切割图进行理论分析,确定了不同动刀片刃部高度与机器作业速度条件下切割频率范围。调控装置根据实时监测的联合收获机作业速度和切割频率,运用调控算法实现切割器频率的分段调控。测试结果表明,装置调整切割频率偏差保持在 $\pm 0.8\text{Hz}$ 以内,最大相对误差为-8.6%。在装置输入切割频率阶跃信号情况下,系统平均稳定调节时间为1.3s;田间试验表明,使用该切割器频率分段调控装置后,未出现漏割穗现象,且短小茎秆数量明显减少,重复切割的情况得到改善。

INTRODUCTION

The cutter cuts the straw through the movement of the cutter, which is one of the main working parts of the grain combine harvester. In the process of harvester operation, the forward speed needs to be adjusted according to the grain yield, density and moisture content. However, because the traditional combine harvester generally adopts mechanical transmission, the frequency of the cutter is constant, and it is difficult to adjust it adaptively with the forward speed, resulting in a large number of missed cutting or repeated cutting, which increases the loss of grain harvesting, and the short stalks will enter the cleaning system with the cut crops, increase the cleaning load of the machine, increase the cutter wear, affect the service life of the machine (Chaab et al., 2020; Hirai et al., 2004; Song et al., 2012; Chuan-Udom, 2010). Guarnieri et al., (2007), established a lumped mass mathematical model of reciprocating single blade harvester rod with crank slider mechanism, and numerically analysed the motion equation. Kwag and Chung, (1994), studied the basic characteristics of the torque of the cutter rod drive shaft when the traditional standard single cutter form is replaced by double cutters. The optimal cutting frequency at different forward speeds is typically made based on the cutting pattern (Copur et al., 2017). Xu et al., (2014), Chen et al., (2011) and He, (2012), tested and analysed the vibration of combine header.

¹⁾Li Ying, Assistant Research Fellow.Ph.D.; Guan Zhuohuai, Assistant Research Fellow. Ph.D.; Chen Yisong, Master.

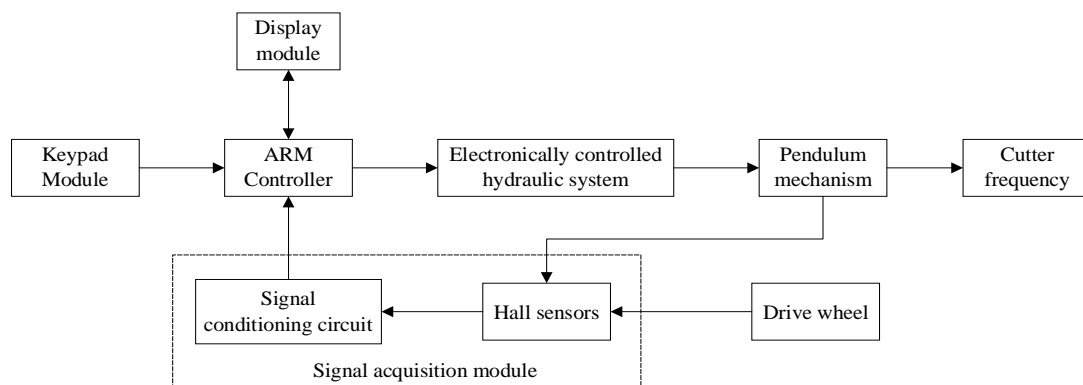
Chai (2013), Xia et al. (2007) and Xiang et al., (2015), analysed the cutting diagram theoretically. Guan et al. (2019) proposed bidirectional electric drive side knife for rape combine harvester and a cutting speed adaptive control system, compared to the fixed speed cutting, header loss was reduced by 14.05% and side knife loss was reduced by 34.76% (Copur et al., 2017). However, there are few reports on the application of frequency control of machine cutter.

In this paper, aiming at the problem that the frequency of combine header cutter is difficult to adjust adaptively with the forward speed, the frequency segment control device of combine harvester cutter is designed. By constructing the cutter trajectory equation, the influence of the relationship between forward speed and cutting frequency on the cutting area is analysed, and the optimal cutting frequency range under different operating speeds is determined. The segmented regulation is beneficial to reduce the loss of grain harvesting, reduce the power consumption of the machine, reduce the labour load of the operator, and improve the intelligent level of the machine.

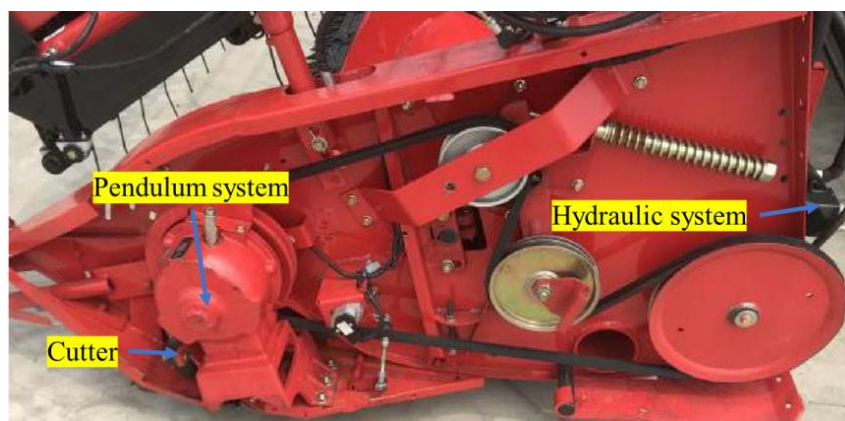
MATERIAL AND METHODS

OVERALL STRUCTURE OF CONTROL SYSTEM

As shown in Fig. 1a, the frequency segment control system of the cutter mainly includes signal acquisition and conditioning module, cutting frequency control module and cutter drive actuator (as shown in Fig. 1b). Hall sensor monitors the speed of the cutter drive swing ring and the speed of the harvester drive wheel to obtain the frequency of the cutter and the forward speed of the harvester. ARM embedded controller as the core of the control system, receives the filtered and reshaped sensor signal, calculates the frequency value and working speed of the cutter, outputs the control signal, and controls the electro-hydraulic proportional valve to adjust the cutting frequency. The composition of the cutter drive actuator is shown in Fig. 1, mainly including hydraulic system, pulley, swing ring box and cutter. The main parameters of cutter include: the stroke displacement of cutter is 76.2mm, the height of moving blade is 502mm, 542mm, and the width of bottom edge of moving knife is 76.2mm.



a. Frequency subsection regulation system



b. Cutter drive actuators

Fig. 1 - Structure of frequency subsection regulation system

CUTTING AREA ANALYSIS MODEL

The absolute motion of cutter is the combination of reciprocating cutting motion and forward motion of harvester, and its motion trajectory can be regarded as simple harmonic motion (Guarnieri et al., 2007; Pang et al. 2019). The cutting diagram is shown in Fig. 2. For the crop in area I, the passive blade is pushed to the edge of the adjacent fixed blade and cut.

After cutting, the stubble of the crop in area II is repeatedly touched by another cutting edge, resulting in repeated cutting. The crops in Area III are not touched when the blade moves to the right. They are only pushed by the front axle and adjacent blades. However, they cannot be cut off because they are not close to the blade edge of the fixed blade. They need to be cut off in bundles by the moving cutter when they return. Due to the large cutting resistance of bunch cutting, it is possible to break the stem and miss cutting, which will affect the harvesting effect. Therefore, the miss cutting area and re-cutting area should be minimized in the process of harvesting.

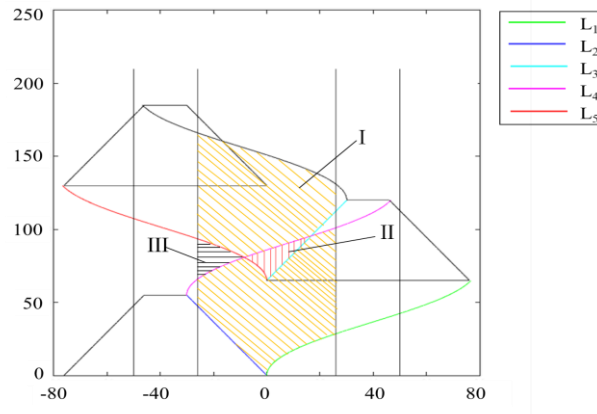


Fig. 2 - Reciprocating cutter cutting diagram

As shown in Fig. 3, the motion path of the swing ring driving mechanism is shown:

$$x = -L \sin \alpha \cos \omega t \times \frac{1}{\cos \alpha \sqrt{1 + \tan^2 \alpha \cos^2 \omega t}} \tag{1}$$

$$L = \frac{r}{\sin \alpha} \tag{2}$$

L is the length of swing rod (mm); r - half stroke displacement of cutter (mm); ω - angular velocity of swing ring driving shaft (rad/s); α - swing angle ($^\circ$).

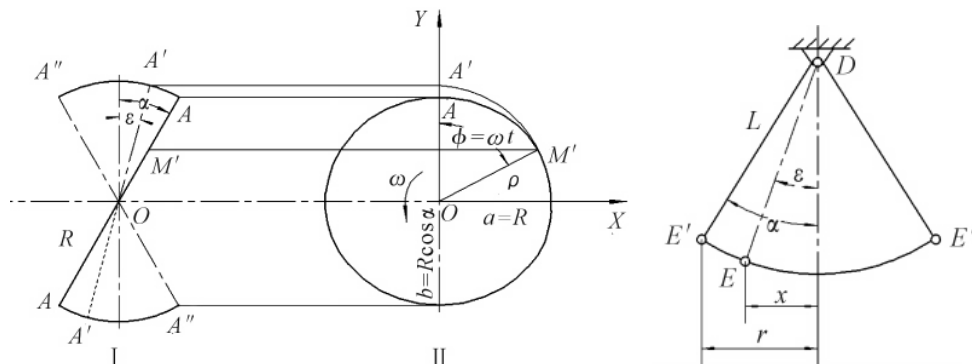


Fig. 3 - Schematic diagram of pendulum movement

According to the machine speed, the motion equation of cutter in longitudinal direction is obtained as follows:

$$y = v_m t \tag{3}$$

The curve equation of moving tool path can be obtained by combining (1), (2) and (3):

$$x = -L\sin\alpha\cos\frac{\omega y}{v_m} \frac{1}{\cos\alpha\sqrt{1+\tan^2\alpha\cos^2\frac{\omega y}{v_m}}} \quad (4)$$

where:

X is the transverse displacement of cutter (mm);

y - the longitudinal displacement of cutter (mm);

v_m - the machine operation speed (mm/s).

Because the blade is translational, the motion trajectory of each point on the blade is the same. In the same coordinate system, the equation of each point of the moving blade can be obtained by translating formula (3). Similarly, the trajectory equation of the moving knife in return motion can be obtained by turning and translating formula (3).

The equations of L1, L2, L3, L4 and L5 were established:

$$\begin{aligned} L_1 : x &= -L\sin\alpha\cos\frac{\omega y}{v_m} \frac{1}{\cos\alpha\sqrt{1+\tan^2\alpha\cos^2\frac{\omega y}{v_m}}} + L\sin\alpha \\ L_2 : x &= -0.55y \\ L_3 : x &= 0.55(y-H) \\ L_4 : x &= -L\sin\alpha\cos\frac{\omega(y-h)}{v_m} \frac{1}{\cos\alpha\sqrt{1+\tan^2\alpha\cos^2\frac{\omega(y-h)}{v_m}}} + L\sin\alpha - \frac{a-b}{2} \\ L_5 : x &= L\sin\alpha\cos\frac{\omega(y-H)}{v_m} \frac{1}{\cos\alpha\sqrt{1+\tan^2\alpha\cos^2\frac{\omega(y-H)}{v_m}}} - L\sin\alpha \end{aligned} \quad (5)$$

where:

h - the height of moving blade (mm);

a - the width of the moving edge (mm);

b - the front axle width of moving cutter (mm);

H - the cutter advance (mm).

Cutter advance refers to the forward distance of the machine within the time of cutter completing one stroke. The calculation formula is as follows:

$$H = v_m \frac{\pi}{\omega} \quad (6)$$

ANALYSIS OF INFLUENCING FACTORS OF CUTTING AREA

According to the cutter motion trajectory modelling, the parameters that affect the area of the three areas in the cutting diagram are machine operation speed, angular velocity of swing ring driving shaft, moving blade height, swing ring angle, swing rod length, bottom edge width and front axle width. The swing rod length can be calculated by cutter travel displacement and swing ring angle. According to the national standard of reciprocating cutter and cutter parameters, the range of parameters is determined. The displacement of cutter stroke is 76.2mm, the height of moving blade is 50.2mm and 54.2mm, the width of moving blade bottom is 76.2mm, and the inclination angle of swing ring is generally 15°~16°. In this paper, the angle of inclination is 10°, 15° and 20°. The results were analysed. In the above parameters, in order to facilitate the subsequent expression, the angular velocity of the swing ring driving shaft is converted into the cutting frequency value in the program, and because the width of the bottom edge of the moving blade and the width of the front axle of the moving blade have no significant influence on the cutting area, this paper mainly analyses the influence of the machine operation speed, the cutter frequency and the swing ring inclination angle on the cutting area.

In order to further analyse the influence of the relationship between harvester forward speed V and cutting frequency h on each cutting area, numerical simulation analysis was carried out. Figure 4 shows the relationship between the cutting frequency and the area of each cutting area under different forward speeds.

According to the figure, the area of each cutting area changes significantly with the cutting speed and cutting frequency. The area of re-cutting area increases with the increase of cutter frequency, the area of missed cutting area decreases with the increase of cutter frequency, and the area of primary cutting area also decreases. In order to get a suitable range of cutter frequency at a certain machine speed, the relationship between the areas of these three characteristic areas should be comprehensively considered: (1) The area of missed cutting area should be as small as possible; (2) Under the same parameters, the area of primary cutting area should be as large as possible; (3) In order to maintain the cutting quality of the cutter, the area of the missed cutting area should be smaller than that of the re-cutting area.

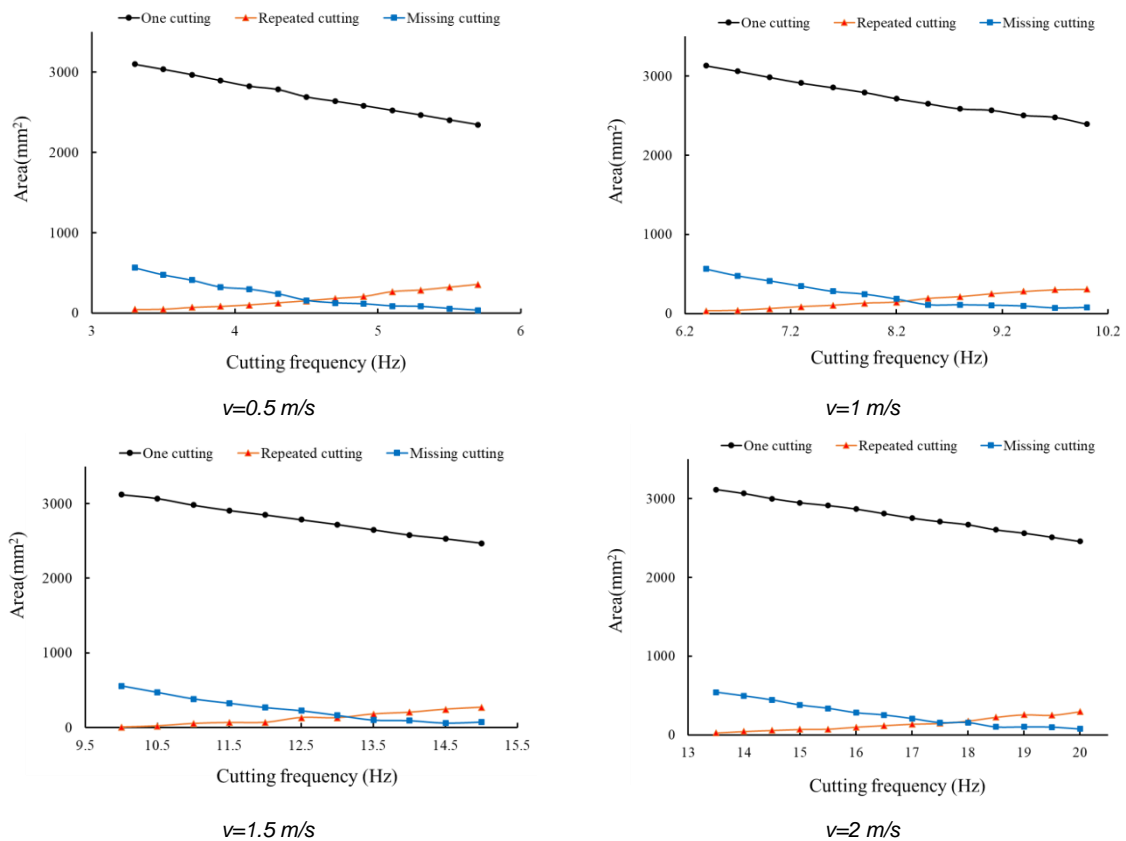


Fig. 4 - The curve of the area of each area of the cutting graph with the cutting frequency under different machine operating speeds

Under the condition of the same cutting area s , the comprehensive evaluation formula is designed according to the above conditions:

$$\begin{cases} B = \frac{S_2 + S_3}{S_1} \\ S_2 > S_3 \end{cases} \quad (7)$$

where: S_1 - area of primary cutting area (mm);
 S_2 - re cutting area (mm);
 S_3 - area of missed cutting area (mm).

According to the area data of each area in the cutting map and the above evaluation formula, when the crop density is basically the same and there is no lodging, when the working speed is 0.5 m/s, the frequency of the cutter is 4.3~5.0 Hz. Similarly, when the operating speed is 1.0 m/s, it is 8.8~9.5 Hz; when the operating speed is 1.5 m/s, it is 13.3~14.2 Hz; when the operating speed is 2.0 m/s, it is 17.8~18.8 Hz.

Because the frequency of the combine doesn't need to change in real time with the change of the working speed of the machine, and the cutting operation is required to be fast and efficient, this paper adjusts the cutting frequency according to the working speed of the machine. When the working speed of the machine is 0~1.0 m/s, the cutting frequency is 8.5~9.2Hz. When the working speed of the machine is 1.0~1.5m/s, the cutting frequency is 13.0~13.9Hz. When the working speed of the machine is 1.5~2.0 m/s, the cutting frequency is 17.5~18.5Hz. When the working speed of the machine is greater than 2.0m/s, the cutting frequency value is 18.8~23.7Hz, of which 23.7Hz is the maximum cutting frequency value provided by the combine harvester.

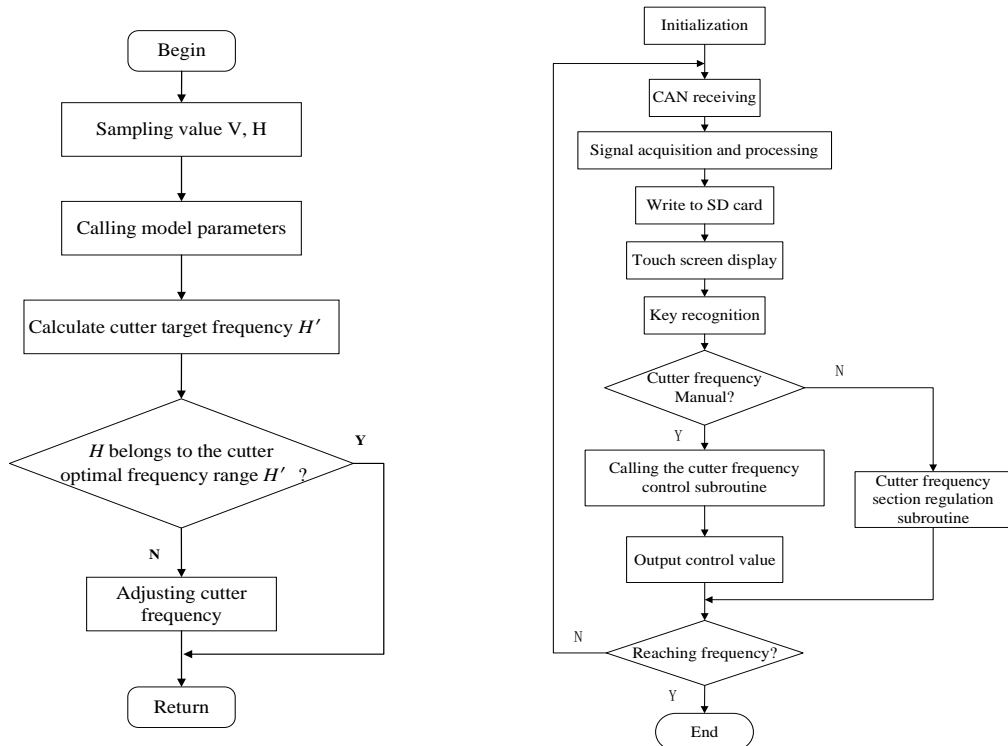
When the machine is working, due to the different density of crops in the field, the frequency value of the cutter can be adjusted. When the grain density is large, in order to reduce the number of missed cut grains, the frequency of the cutter should be increased appropriately to reduce the area of the blank area; When the grain density is small, in order to reduce the area of re-cutting area and the cutting power consumption of the machine, the frequency value of the cutter can be appropriately reduced. The cutting frequency range under different working speeds is shown in Table 1.

Table 1

Frequency range of cutter under certain operating speed	
Machine operating speed (m/s)	Cutter frequency (Hz)
0~1.0	8.0~8.5
1.0~1.5	12.2~13.0
1.5~2.0	16.4~17.0
>2.0	17.3~23.7

DESIGN OF SEGMENTED FREQUENCY CONTROL ALGORITHM FOR CUTTER

The segmented regulation process of cutter frequency is shown in Fig. 5a. The optimal cutting frequency of the cutter is obtained by harvesting forward speed. The actual value of current cutter frequency is compared and adjusted. The flow chart of control program is shown in Fig. 5b.



a. Flow chart of frequency regulation of cutter

b. Flow chart of main program of cutter frequency segmentation control device

Fig. 5 - System programming

After the system started and initialized, the basic data of the harvester is obtained from the CAN bus. The working speed is indirectly obtained by measuring the speed of the driving wheel. The speed of the swing ring spindle is collected by the speed sensor, and processed by filtering and shaping. Then the signal is input into the arm controller to calculate the current speed of the swing ring mechanism spindle and the speed of the driving wheel. It is converted into the actual cutter frequency and operation speed, written into the SD card and displayed on the touch screen. The manual and automatic mode can be switched by key recognition. In the automatic mode, the frequency subsection control subroutine of the cutter is called, and the cutting frequency control value is calculated according to the input value of the control algorithm. By outputting PWM control signal, the electro-hydraulic proportional valve is controlled, and then the speed of the hydraulic motor is controlled to realize the frequency subsection control of the cutter. When the automatic mode program of the control device is wrong or manual operation is necessary, the device can be in manual control mode by manual automatic switching module to realize the manual intervention of the cutting frequency of the cutter.

RESULTS

TEST AND ANALYSIS

As shown in Fig. 6, the actual object of the segmented frequency control system of the cutter is integrated into GK100 wheel type full feeding combine to carry out field test.

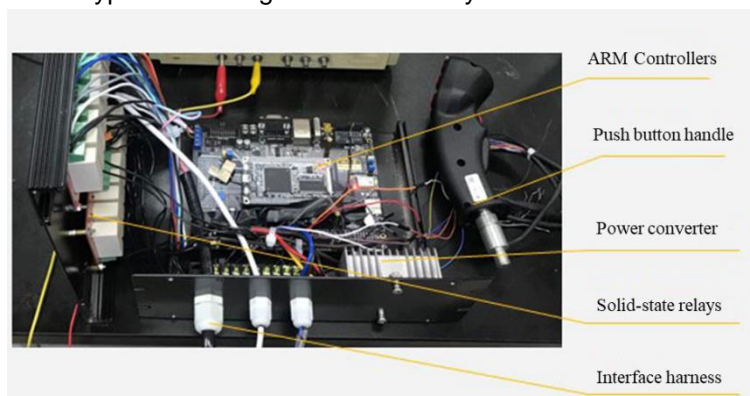


Fig. 6 - Hardware diagram of the control device

The frequency control value of cutter is sent to the controller by computer and the target value is taken as the target value, and the data displayed on the display screen is taken as the measurement value. Use stopwatch to record the time required for the cutter frequency to change from the beginning to the relative stability, which is used as the system adjustment time data, and record the relevant data. The cutting frequency control accuracy and adjustment time test data are shown in Table 2.

Table 2

Control accuracy and adjustment time test data table

Serial number	Target value (Hz)	Measurements (Hz)	Relative error (%)	Adjust the time (s)
1	3.8	3.5	-8.6	1.2
2	5.2	5.6	7.1	1.4
3	6.4	6.7	4.5	1.1
4	8.1	8.6	5.8	1.5
5	11.2	10.7	-4.7	1.2
6	14.9	14.1	-5.7	1.2

According to table 2, the deviation of cutting frequency of device adjustment is kept within $\pm 0.8\text{Hz}$, and the maximum relative error is -8.6% . Due to the nonlinearity of hydraulic system, there is error in data fitting between the speed of hydraulic motor and input signal of electro-hydraulic proportional valve, which may be the main reason for the change of relative error. When the cutting frequency step signal is input, the average stable adjustment time of the system is about 1.3s, which meets the design requirements.

In November 2019, the frequency segment control device of cutter was installed on GK100 wheel type full feeding combine harvester, and the field test of device installation was carried out in Changyinsha farm, Zhangjiagang City, Jiangsu Province. The harvested rice variety was "Changyou 998", with natural height of 120 cm, ear length of 19.6 cm and yield of $716\text{kg} / 667\text{m}^2$.

Taking the harvester to maintain a relatively stable speed through the 20 meters calibration area as a group of test samples, 10 groups were set up in the test, of which the first four groups did not turn on the frequency segment control system of the cutter as a comparative test, and the last six groups turned on the control system as a functional verification test. In this paper, the control effect test of the cutter is based on whether there are missing ears and the number of short stalks in a certain range of the ground after harvest.

In the field function test, because of the high grain density in the field, the grain density level is set to 1. The basic parameters are set in the arm controller program in advance, and then the harvester passes through the 20 meters calibration area at different operating speeds. The time of each passing through the calibration area is recorded with a stopwatch, and the average operating speed is calculated as the test data. The cutting frequency data is obtained from the SD card of the control device. Five data are randomly selected, and the average value is taken as the test data of the cutting frequency. The materials produced by the cleaning system of the harvester are manually caught with oilcloth to keep the ground in the state after cutting by the cutter, which is convenient for counting the number of short stalks and missing grains. 30 cm in each group \times The number of short stalks in the 30cm box was counted for 5 times, and the average value was taken as the test data, as shown in Figure 7. In the process of 10 groups of tests, there was no phenomenon of missing cut grain, so the missing cut grain data was not shown in the test data table. The comparison test data is shown in Table 3, and the function verification test data is shown in Table 4.



a. Field test site

b. Stem quantity statistics

Fig. 7 - Control effect test

Table 3

Comparison test data table

Serial number	Average operating speed (m/s)	Cutting frequency value (Hz)	Number of short stalks
1	0.4	14.7	28
2	0.67	15.1	23
3	0.81	15.0	20
4	1.06	14.7	17

Table 4

Functional verification test data table

Serial number	Average operating speed (m/s)	Cutting frequency range (Hz)	Number of short stalks
1	0.54	8.0~8.5	13
2	0.71	8.0~8.5	9
3	0.87	8.0~8.5	6
4	0.91	8.0~8.5	7
5	1.02	12.2~13.0	12
6	1.10	12.2~13.0	10

It can be seen from table 2 and table 3 that when the frequency segmented control system of the cutter is not turned on, the machine harvests at a higher cutting frequency, the number of short stalks is at a higher value, and the re-cutting phenomenon is serious, resulting in a waste of cutting power. With the increase of machine operation speed, the number of short stalks shows a downward trend, which is in line with the theoretical analysis. After turning on the segmented control system of cutting frequency, the number of short stalks decreased significantly under the condition of approximate working speed, and there was no phenomenon of missing cutting rice ears in the process of harvesting, which indicated that the segmented control system of cutting frequency of the cutter had significantly improved the cutting effect.

CONCLUSIONS

(1) In view of the problems of inconvenient control and poor cutting effect, the paper compiles the analysis program of reciprocating cutter working characteristics based on MATLAB, analyses the factors affecting the area of cutting drawing, determines the cutting frequency and machine working speed as the main influencing factors. The range of cutting frequency under different machine operating speed conditions is determined by using comprehensive evaluation formula. The frequency segment control algorithm of the cutter is designed to realize the segmented control of the frequency of the cutter.

(2) The test results show that the adjustment cutting frequency deviation of the control device is kept within 0.8 Hz, and the maximum relative error is -8.6%. Under the condition of input cutting frequency step signal, the average stable adjustment time of the system is about 1.3s.

(3) After the frequency segment control system of cutter is opened, the number of short and small stalks decreases obviously under the condition of approximate operating speed, and there is no leakage in the process of harvesting. There cutting and missing cutting are improved during the cutting process.

When the machine type and harvested grain are changed, the number of short stalks and missing panicles may be changed, but the number of short stalks and missing panicles will be reduced and the cutting effect will be improved compared with that when the frequency segment control device of the cutter is not turned on. More comparative experiments are needed to analyse the specific situation.

ACKNOWLEDGEMENT

This research was supported by Research Project of Jiangsu Science and Technology Association (JSKXKT 2021029); and Special Fund for Basic Scientific Research Business of Chinese Academy of Agricultural Sciences (S202118-02).

REFERENCES

- [1] Badretdinov I., Mudarisov S., Lukmanov R., et al. (2019). Mathematical modelling and research of the work of the grain combine harvester cleaning system. *Computers and Electronics in Agriculture*, 165: 104966.
- [2] Chaab R.K., Karparvarfard S.H., Rahmadian-Koushkaki, H. et al. (2020). Predicting header wheat loss in a combine harvester, a new approach. *Journal of the Saudi Society of Agricultural Sciences*, 19(2): 179-184. <https://doi.org/10.1016/j.jssas.2018.09.002>
- [3] Chai H.W. (2013). Research on the performance of the reciprocating cutter of the combine harvester. *Agricultural Machinery*, 10: 131-136. DOI: 10.16167/j.cnki.1000-9868.2013.10.015
- [4] Chen S.R., Lu Q., Qiu H.Z. (2011). Vibration test and analysis of the header of cereal combine harvester based on LabVIEW. *Journal of Agricultural Machinery*, 42: 86-89.
- [5] Chuan-Udom S. (2010). Development of a cutter bar driver for reduction of vibration for a rice combine harvester. *Asia-Pacific Journal of Science and Technology*, 15(7): 572-580.
- [6] Copur H., Bilgin N., Balci C., et al. (2017). Effects of different cutting patterns and experimental conditions on the performance of a conical drag tool. *Rock Mechanics and Rock Engineering*, 50: 1585-1609. <https://doi.org/10.1007/s00603-017-1172-8>
- [7] Gharakhani H, Alimardani R and Jafari A. (2017). Design a new cutter-bar mechanism with flexible blades and its evaluation on harvesting of lentil. *Eng Agric Food Environ*, 10(3): 198-207.
- [8] Guan Z.H., Wu C.Y., Wang G. et al. (2019). Design of bidirectional electric driven side vertical cutter for rape combine harvester. *Transactions of the Chinese Society of Agricultural Engineering*, 35(3): 1-8.

- [9] Guarnieri A., Maglioni C., Molari G. (2007). Dynamic Analysis of Reciprocating Single-Blade Cutter Bars. *Transactions of the ASABE*, 50(3): 755-764. Doi: 10.13031/2013.23130
- [10] He C.X. (2012). Test and analysis of the vibration of the header of the wheat combine harvester. *Agricultural Machinery*, 07: 107-108. DOI: 10.16167/j.cnki.1000-9868.2012.07.009
- [11] Hirai Y., Inoue E. and Mori K. (2004). Application of a Quasi-static Stalk Bending Analysis to the Dynamic Response of Rice and Wheat Stalks gathered by a Combine Harvester Reel. *Biosystems Engineering*, 88(3): 281-294. <https://doi.org/10.1016/j.biosystemseng.2004.04.010>
- [12] Jumiyatun J., Mustofa M. (2018). Controlling dc-dc buck converter using fuzzy-PID with DC motor load. *IOP Conference Series Earth and Environmental Science*, 156(1): 012013.
- [13] Kwag B.C., Chung C.J. (1994). Dynamic Characteristics of the Reciprocating Cutter-bar of Combine Harvester. *Journal of the Korean society for agricultural machinery*, 19(3): 175-184.
- [14] Lenaerts B., Aertsen T., Tijssens et al. (2014). Simulation of grain-straw separation by discrete element modelling with bendable straw particles. *Computers and Electronics in Agriculture*, 101: 24-33.
- [15] Pang J., Li Y.M., Ji J.T., et al. (2019). Vibration excitation identification and control of the cutter of a combine harvester using triaxial accelerometers and partial coherence sorting. *Biosystems Engineering*, 185: 25-34. <https://doi.org/10.1016/j.biosystemseng.2019.02.013>
- [16] Song Z.H., Tian F.Y., Zhang S.F. et al. (2012). Simulation and experiment of reciprocating cutter dynamics of cotton stalk under no-load. *Transactions of the Chinese Society of Agricultural Engineering*, 28(16): 17-22.
- [17] Tofanica B.M., Cappelletto E., Gavrilescu D. et al. (2011). Properties of rapeseed stalks fibres. *JNat Fibres*, 8(4): 241-262.
- [18] Toshikaza M., Tatsuro S. (2017). The evaluation of harvest loss occurring in the ripening period using a combine harvester in a shattering-resistant line of common buckwheat, *Japanese Journal of Crop Science*, 86(1): 62-69.
- [19] Xia P., Yin S., Chen L. Q., Zhu D. Q., Li B. (2007). Numerical Simulation and Simulation of Cutting Diagram of Reciprocating Cutter of Harvesting Machinery. *Journal of Agricultural Machinery*, 03: 65-68.
- [20] Xiang Y., Luo X. W., Zeng S., Zang Y., Yang W. W. (2015). Analysis of working characteristics of reciprocating cutters based on visual programming. *Transactions of the Chinese Society of Agricultural Engineering*, 31(18): 11-16.
- [21] Xu L.Z., Li Y.M., Sun P.P., Pang J. (2014). Vibration test and analysis of crawler-type full-feed rice combine harvester. *Transactions of the Chinese Society of Agricultural Engineering*, 30(08): 49-55.

MECHANIZATION DEVICES FOR HANDLING BRANCHES IN MODERN ORCHARDS

/ 现代果园枝条机械化处理装置

Li Hui^{1,2)}, Yang Xin¹⁾, Yang Aiqian²⁾ ¹¹⁾ College of Mechanical and Electrical Engineering, Hebei Agricultural University, Baoding, 071000/China;²⁾ Research Institute of Mechanical and Electronic, Hengshui University, Hengshui, 053000/China;

*E-mail: yangxin@hebau.edu.cn

DOI: <https://doi.org/10.356.33/inmateh-65-31>**Keywords:** Branch; Gathering; Picking-up; Optimization; Simulation; Orchard**ABSTRACT**

In most parts of China, pruned branches in orchards are still treated manually. In order to reduce the intensity and labor cost, this paper provides a mechanical solution for branches collection, which mainly includes the gathering device, picking device, and smashing device. A simulation platform with a human-computer interaction was developed in Matlab. It can set optimization goals based on human practical experience and optimize the main influencing parameters, and both the gathering device and the picking device achieve the design simulation on this platform. Furthermore, this method helps to quickly obtain the data of key components in the core device. Firstly, the shape of the Slide-way shell of the gathering device can be obtained quickly through different gathering ranges. Secondly, a group of angle and motion trajectory of the picking device with lower height was obtained from the simulation design. Furthermore, the performance of the improved picking device under four different laying conditions was tested. The results showed that, under $R=38-42$ r/min and $V=0.80-0.95$ m/s, the success rate of the picking device was 94.2%, 92.5%, 61.0% and 30.8%, respectively. The field test demonstrated that there are no significant differences between the simulated test results and practice test results.

摘要

在中国的大部分地区，果园里修剪过的树枝仍然是主要依靠人工处理的。为了降低劳动强度和管理成本，本文提出了一种机械化处理枝条的方案，主要包括聚拢装置、捡拾装置和粉碎装置。在 Matlab 中开发了具有人机交互功能的仿真平台。它可以根据人类的实践经验设定优化目标，对主要影响参数进行优化。聚拢装置和捡拾装置均在此平台上实现了模拟仿真运动。该方法有助于快速获取核心设备中关键部件的数据。首先，通过聚拢范围的不同，能够快速获得聚拢装置滑道壳体上滑道的形状。其次，能够得到了一组合理的捡拾装置的角度和运动轨迹。此外，还对改进后的拾取装置在四种不同铺设条件下的性能进行了试验。结果表明，在 $R=38-42$ r/min、 $V=0.80-0.95$ m/s 条件下，采摘装置的成功率分别为 94.2%、92.5%、61.0% 和 30.8%。场地试验结果表明，模拟试验结果与实际试验结果无显著差异。

INTRODUCTION

Apple is one of the most widely planted fruits in northern China. In 2018, the planting area was about 2.54 million ha and the fresh output reached 39 million tons, accounting for more than 40% of the world. Growers general prune branches twice per year, and a large amount of branch residues are produced in orchards (Abdallah et al., 2011).

These residues from orchards or forests are renewable biomass resources that can be recycled to compensate for the shortage of fuel in remote areas (Leszek et al., 2014; Paweł et al., 2016). In China, the branch residues scattering on the ground is commonly manual picking-up, which is labor-intensive and costly (Bussemaker et al., 2015).

This traditional operation mode urgently needs new technological support to handle with these residues. In order to meet the requirements of growers, there is an urgent need for innovative mechanized devices to replace the traditional manual way.

¹ Hui Li, Ph.D. Stud.; Xin Yang, Prof. Ph.D.; Aiqian Yang, Lecturer

Agricultural machinery manufacturers from Europe, America, Canada and Australia have developed several types of shredders. They are one of the commonly used machines for mechanization treatment of orchard pruning residues (Dyjakon, 2018a).

The agricultural machinery technology of residues collection is relatively mature (Dyjakon, 2018b; Gong et al., 2020). The general residues collection mainly includes collecting, picking-up, feeding, smashing and recovering (Guerra et al., 2018; He et al., 2016).

At present, various types of gathering devices have been developed and widely used in pastures. An aggregator was used to convert the scattered straw into straight stripes for drying and recycling (Florian et al., 2014). For example, Rolabar 256 rotary drum tedder and WR10 series of finger wheel tedder of the United States, RT 13 finger wheel tedder of Italy and Liner series horizontal rotary rake of Germany (Kumar et al., 2015). In addition, engineers from Whitlands developed a tool harrow with adjustable angle, which was mainly used to recycle vineyard pruning residues. RX series rotary brush gathering device produced by Fa.ma of Italy was installed on the tractor head, which can also collect pruned grape-vines scattered on the ground to the center of the row (McEniry et al., 2008).

Luigi et al., (2018) reported that the research team of Poznan University in Poland cooperated with a local fruit growing farm to develop a collection device with three rotating iron sheets, which is similar to the reinforcement version of rotary brush. However, there are few studies on the structural design and working principle of the gathering device for branch residues, as well as the evaluation and test of its performance.

In order to make full use of these pruning residues, some growers suggest collecting them by machine and then storing them to substitute some wood as fuel or energy sources (Pari et al., 2018). A round baler was developed and tested by the New Holland Company, which proved the feasibility of using baler to collect pruning residues.

Florian et al., (2014) designed and tested a new mini-baler for hilly areas to recover vineyard pruning residues that were inaccessible to traditional tractors (Naujoks B., 2011). However, the test performance and mechanical design of the baler picking system are rarely mentioned and specified.

Yu et al., (2018) tested the picking performance index of optimal parameter combination of the spring-finger cylinder harvester for green forage and corn stalks.

Xu et al., (2016), optimized the primary parameters of spring finger picker according to the biophysical characteristics of peanut stalks (Qiang et al. (2018)) (Ren et al., 2020). However, there are few researches on the spring finger picking mechanism for hard-stalk crops collection, and the application of other pickers on hard stem crops is also rare. In view of the differences between soft-straw crops and hard-stalk crops, the design of picking mechanism for pruning residues is carried out.

The main purpose is to design a mechanical device for collecting branch pruning residues by comprehensively considering the critical influence factors of collecting and picking-up. The objectives are design and analysis of the critical parts of the whole machine, including gathering device, picking device and smashing device. Then, the picking performance of the machine is tested under different laying conditions of branch residues. The relations between the laying orientation of branches and the picking success rate are evaluated.

MATERIALS AND METHODS

A mechanized processing device suitable for pruning branches in orchards is studied. The process mainly includes gathering, picking-up, smashing and collecting. The structural design and parameters optimization of both gathering and picking-up are completed with human-computer interaction to improve the efficiency of design.

STRUCTURE DESIGN

The whole machine is applied for processing the branches in orchard, which mainly includes gathering device, picking device, smashing device and a collection bin with a filter, as shown in Figure 1 (Spinelli et al., 2014). Among them, the gathering device collects the branches in the middle of rows; the picking device picks the residues on the ground, and the smashing device works in an almost close shell. It not only uses hammer claw to crush most of the residues, but also uses rotary blade mechanism to cut branches with large diameters. The collection bin with filter is used to collect residues or collect them in bags or containers.

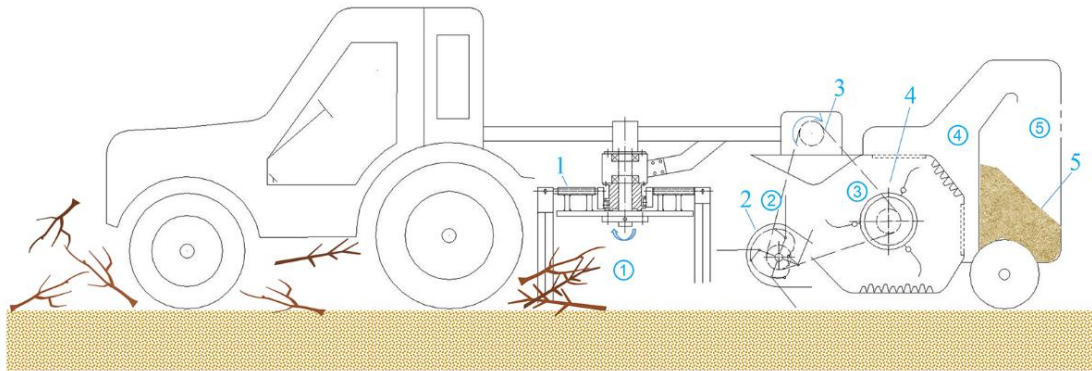


Fig. 1 - Machine structure

1, gathering device; 2, picking device; 3, driving system; 4, smashing device; 5, collection bin.

① to ⑤ represent the handling steps of branch residues. The pruning residues of the orchard branches are collected at position ① and the smashed residues are finally collected in the dustbin at position ⑤.

Gathering device

The gathering device is mainly composed of hydraulic motor, rotary chassis, shell with track and a set of crank connected machinery, as shown in Figure 2. Hydraulic power comes from a tractor. A set of implement mechanism fixed on the rotary chassis mainly includes swing crank, swing connecting rod, axle sleeve, spring teeth and crank bearing. The axle sleeve is welded on the surface of the chassis. The swing connecting rod is connected with a spring teeth through the shaft sleeve, and the other end is connected with the swing crank. A bearing is installed on the other end of the swing crank and it slides in the track of the shell. The movement trajectory of the spring teeth is limited by the slide-way shape of the shell. It makes complex movements, including rotary movement around the hydraulic motor and swing movement around the axle sleeve.

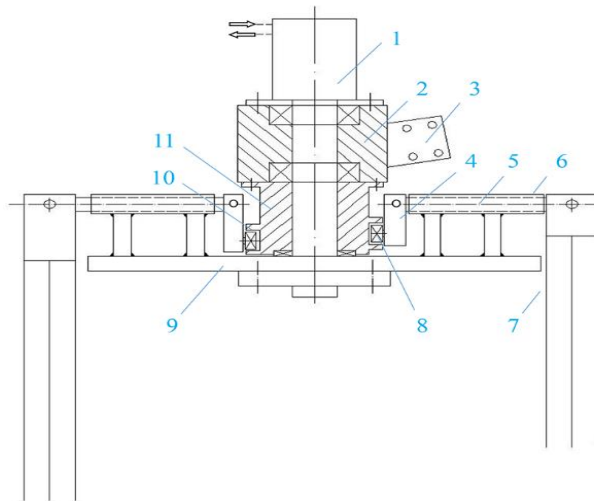


Fig. 2 - The structure of gathering device

1. Hydraulic motor; 2. Upper end shell; 3. Fixed end; 4. Swing crank; 5. Swing connecting rod; 6. Axle sleeve; 7. Spring-tooth combination; 8. Crank bearing; 9. Rotation chassis; 10. Track; 11. Shell with slide-way

In order to facilitate the kinematic analysis of the collecting mechanism, its structure schematic is drawn as Figure 3. Where, α_1 represents the rotation angle of spring tooth around point O; β_1 represents the swing angle of spring tooth around line OK; P1, P2 and P3 of the diagram represent the dividing point of different actions during the whole collecting process. P1P2, P2P3 and P3P1 represent the collecting phase, departing phase and return to original phase respectively. Based on the kinematic analysis, a mathematical model of collecting mechanism is established and an optimization design platform is developed. The whole running process of the collecting mechanism is simulated on the platform, as shown in Figure 4. The data value of the mechanism is optimized by means of human-computer dialogue and expert experience under the guidance of parameter optimization (Xiudan, 2015; Ye et al., 2013).

Slide-way shell is a core component of the gathering device. The track shape controls the implement mechanism movement and impacts the effect of collecting directly. According to the swing angle of spring teeth in different processes, an effective slide-way (point J) is obtained by using the optimization design platform, as shown in Figure 5 (Tao et al., 2016).

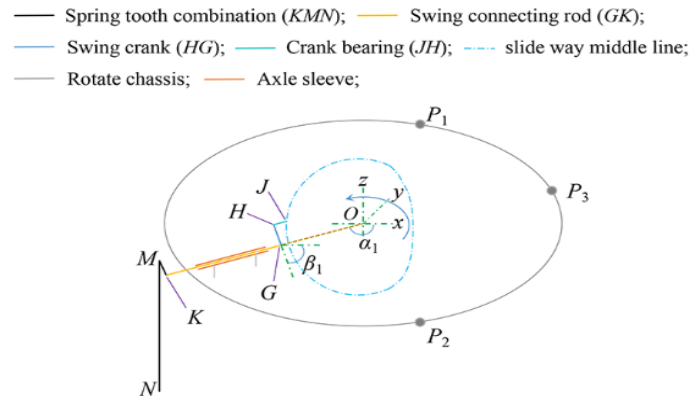


Fig. 3 - The motion schematic diagram of gathering device

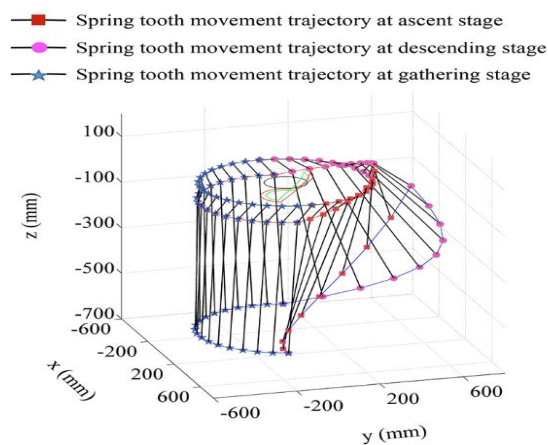


Fig. 4 - The static movement simulation trajectory of gathering device

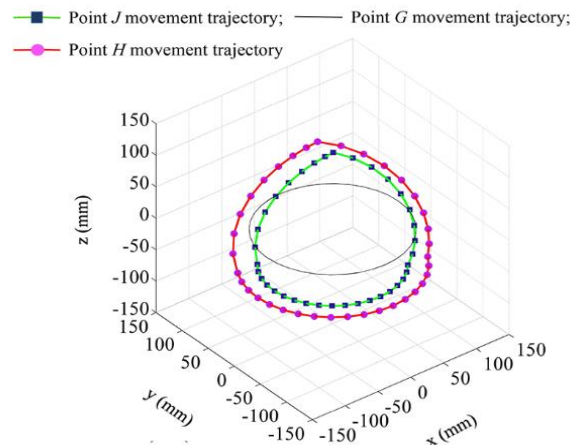


Fig. 5 - The slide-way middle line (green) of the shell of gathering device

Picking-up device

The working principle of the spring finger-cylinder picking device is described as follows, mainly consists of link_1, crank_2, spring fingers_3, central axis_5, cam disk_6, and guard plate_7. In Figure 6, link_1 makes a circular movement around point O. At the same time, the spring finger_3 follows link_1 to make circular movement and make swing movement under the limitation of cam disk_6. The mechanism adjusts the posture of the spring finger by changing the shape of the cam disk to meet the requirements of picking pruning residues.

Link_1 rotates one full turn around point O. The entire cycle is divided into five phases: stacking, lifting, transporting, feeding, and separating and recovering according to the attitude of the spring finger in space. F represents the action force of spring finger to branch pruning residue_4. F1 and F2 are F-branch forces in the horizontal direction and the vertical direction respectively. The coordinate system defines point O as the center of the mechanism. x is the horizontal coordinate axis and y is the vertical coordinate axis. $\Delta A1B1C1$, $\Delta A2B2C2$, $\Delta A3B3C3$, $\Delta A4B4C4$ and $\Delta A5B5C5$ are different positions of the picking mechanism in the running process. A1-A5 represents the top end of the link; B1-B5 represents the top end of the crank, and C1-C5 represents the top end of the spring finger. H is the distance between A3C3 and the ground in the lifting phase, that is, the picking height of the device.

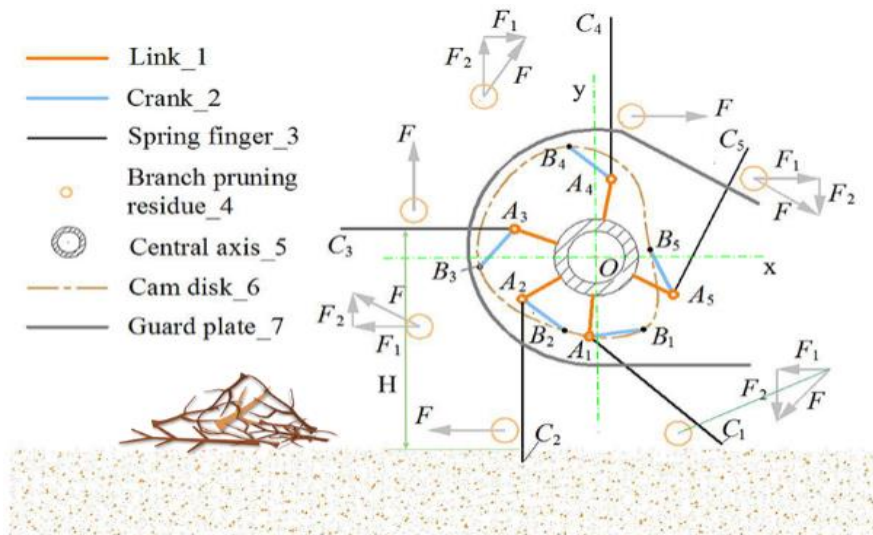


Fig. 6 - Kinetic analysis of spring finger picking device

The kinetic analysis results of the picking device are shown in Table 1.

Table 1

Kinetic analysis of each phase in an entire cycle

Each phase	Branches forced				α (°)	β (°)	
	F_1 (N)		F_2 (N)			Starting	Ending
Stacking	x-	↑	y-	↓	$\alpha_1 = \angle A_1OA_2$	A_1C_1 (45°)	A_2C_2 (90°)
Lifting	x-	↓	y+	↑	$\alpha_2 = \angle A_2OA_3$	A_2C_2 (90°)	A_3C_3 (180°)
Transporting	x+	↑	y+	↓	$\alpha_3 = \angle A_3OA_4$	A_3C_3 (180°)	A_4C_4 (270°)
Feeding	x+	↓	y-	↑	$\alpha_4 = \angle A_4OA_5$	A_4C_4 (270°)	A_5C_5 (315°)
Separating and recovering					$\alpha_5 = \angle A_5OA_1$	A_5C_5 (315°)	A_1C_1 (45°)

Note that the picking-up device rotates clockwise as positive direction. α represents the rotation angles of the middle central axis; β represents an angle between the spring finger and the horizontal coordinate axis in the coordinate system; '↑' represents the gradual increase, and '↓' represents the gradual decrease. In the coordinate system, 'x+' represents the positive direction of the x-axis; 'x-' represents the negative direction of the x-axis; 'y+' represents the positive direction of the y-axis, 'and y-' represents the negative direction of the y-axis.

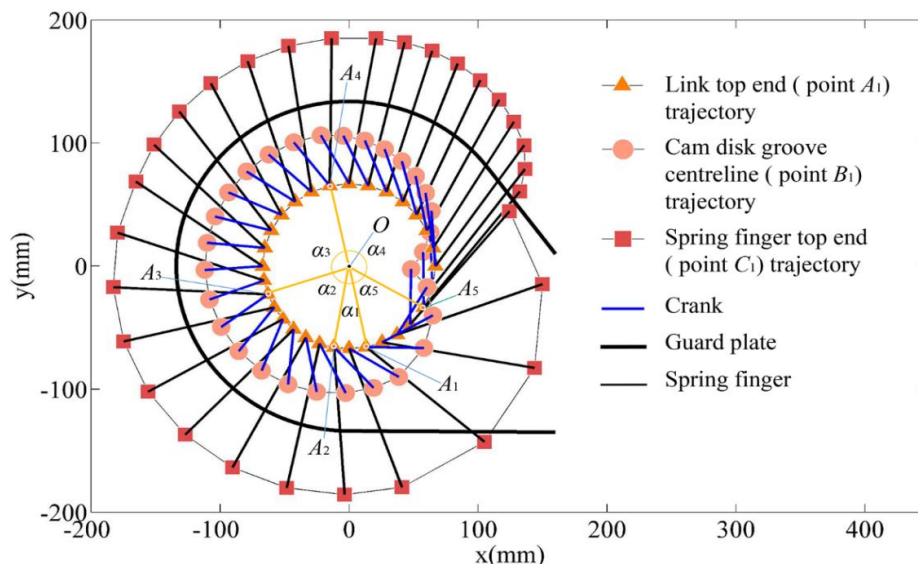


Fig. 7 - Static simulation movement trajectory of the picking device

In Figure 7, the picking device runs clockwise in its positive direction throughout the cycle. Based on the structure of the picking device, the mathematical model is established, the static programs are written and the simulation platform is developed in Matlab environment. In this platform, human-computer interaction is employed to optimize the primary parameters of the mathematical model.

As shown in the optimization objective, the angle (β) of the spring finger contacting with scattering branches is maintained in the range of 40° - 50° in the stacking stage. The angle α_1 should be decreased as much as possible to avoid 'congestion'. In the lifting phase, α_2 should maintain a minimum angle so as to obtain a low picking height. In the transporting phase, the spring finger should reach the vertical attitude soon to strengthen the followed feeding. In the feeding phase, α_4 should be increased to prolong the distance of feeding (Ye *et al.*, 2013). In the separating and recovering phase, the spring finger should be pulled out gradually along the vertical direction of the top of the guard plate to avoid clamping branches. As shown in Table 3, according to these optimization objectives, the main structural parameters of the picking device are optimized on the movement trajectory simulation platform.

Smashing device

The smashing device is the main part of the machine that is used for crushing pruning residues. It mainly includes the driving end, smashing part, chipping part, shell, filter net, fixed blade and main shaft. In order to meet the resistance required for crushing residues, chain drive is selected. The hammer claws of the smashing mechanism are arranged alternately, so that the machine can crush the residues smoothly, as shown in Figure 8 (Yu *et al.*, 2018).

The chips on the right side are used to handle the branches manually with a large diameter and feed into the crushing cavity from entrance to become particles. The chip function consists of a stationary blade fixed on the shell and a moving blade installed on a heavy rotating base (Zhao *et al.*, 2018).

The rotating base can also be used as a counterweight, thereby improving the crushing ability of the hammer claw only the inlet and outlet are reserved in the shell. These repeated hammering residues become smaller particles than the filter mesh in the shell cavity, and then enter the container chamber along the discharge pipe.

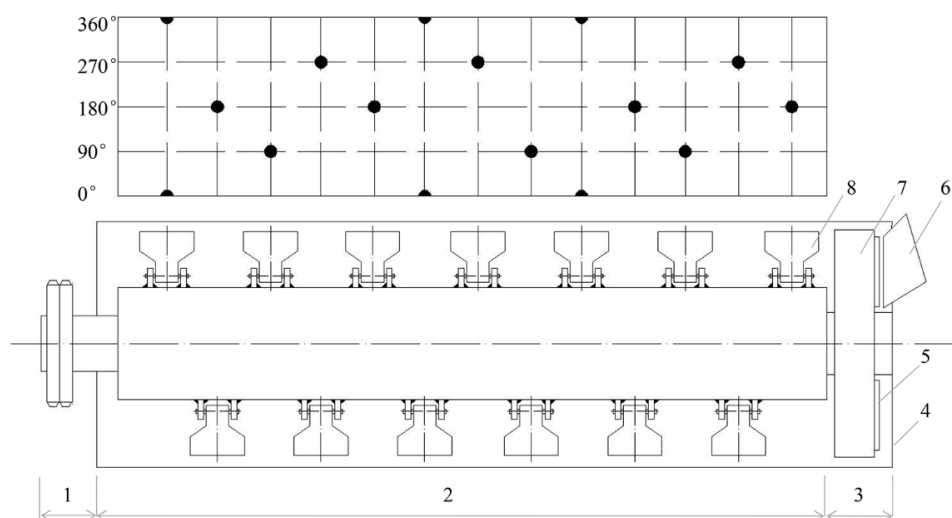


Fig. 8 - Smashing device

1. Driving end; 2. Smashing part; 3. Chipping part; 4. Smashing shell; 5. Moving blade; 6. Entrance for chipping;
7. Rotation base; 8. Hammer claw combination

OPEN FIELD TEST

Picking-up device prototype test

In order to test the performance of the picking device, a baler with spring finger picking is used to collect the ground residues. To evaluate the influence of different postures of branches on the ground, four conditions are set.

Figure 9 (a-d) shows disordered branches, horizontal branches and longitudinal branches, including the first contact between the treetop and the spring fingers or the first contact between the thick stem of the branch and the spring fingers.



Fig. 9 - The improved picking device is tested under four different conditions.

(a-d) showed the disordered state of the exchange direction between the end of canopy and thick stem of trunk, the transverse laying state perpendicular to the straight road, and the laying state along the straight road respectively

Collection efficiency

The success rate of branch residues collection is defined as the percentage of branch residues successfully collected in the total weight. The picking success rate is determined by Eq. (1).

$$\eta_2 = \frac{W - W_r}{W} \times 100 \tag{1}$$

Where, η_2 is the picking success rate; W_r is the weight of residues loss, and W is the weight of total branch residues scattered on the ground in each test.

Under these four different conditions, branch pruning residues are collected 14 times. According to the plan, three tests are carried out in each case, and two of them fail because the tractor is out of control. The average picking success rate is calculated as follows:

$$\eta_2' = \frac{\sum_{k=1}^n \eta_{2(k)}}{n} \tag{2}$$

where, η_2' is the average picking success rate, and k is the number of test for each condition and $n=3$.

The test results are shown in Table 5.

RESULTS AND DISCUSSION

OPTIMIZATION PARAMETERS RESULTS

Based on the simulation technology, the moving trajectory of the gathering device and the picking-up device are simulated and optimized. The optimization results are obtained as shown in Table 3 and Table 4.

Table 3

Optimized parameters of gathering device

Parameter	Unit	Symbol	Value
Length of swing crank	mm	L_{GH}	80
Depth of crank bearing	mm	L_{HJ}	30
Length of swing connecting rod	mm	$L_{GK} = L_{OK} - L_{OG}$	300
	mm	KM	100
Spring tooth	mm	KN	650
	°	$\angle MKN$	35
	°	$P_1P_2 (\alpha_1)$	-90-60
Rotation angle of the rotating chassis (clockwise rotation on the left)	°	$P_2P_3 (\alpha_1)$	60--25
	°	$P_3P_1 (\alpha_1)$	-25--90
	°	$P_1P_2 (\alpha_1)$	-90-120
Rotation angle of rotating chassis (rotate counterclockwise on the right)	°	$P_2P_3 (\alpha_1)$	120--155
	°	$P_3P_1 (\alpha_1)$	-155--90
	°	β_1	-45-45

Table 4

Optimization parameters of picking-up device		
Structural parameters	Coordinate (mm)	α (°)
$OA_1= OA_2= OA_3= OA_4= OA_5= 67$ mm, Length of the crank_2 = 45 mm, Length of the spring finger_3 = 120 mm, $\angle B_1A_1C_1= \angle B_2A_2C_2= \angle B_3A_3C_3= \angle B_4A_4C_4= \angle B_5A_5C_5= 39^\circ$	A_1 (11.36, -65.98)	$\alpha_1=25^\circ$
	A_2 (-16.45, -64.95)	$\alpha_2=50^\circ$
	A_3 (-61.36, -26.91)	$\alpha_3=86^\circ$
	A_4 (-29.07, 60.36)	$\alpha_4=147^\circ$
	A_5 (60.72, -28.32)	$\alpha_5=52^\circ$

EXPERIMENT RESULT OF PROTOTYPE

This experiment is carried out in an open field located at BoYo Agriculture Equipment Co. LTD in China (114.71°N, 38.01°W). Firstly, four straight strips of 15 m (L) long and 1.8 m (Wi) wide are drawn. Secondly, the weighed branch residues are laid on the ground and the height is maintained at 100-250 mm. Secondly, the weighed tree dreys are placed on the ground, and the height is maintained at 100-250mm. In addition, the auxiliary equipment is Dongfanghong-MF604. The laser tachometer (SW-6234C) is used to measure the rotation speed of the picking device. The scales (Edberg NK/HP and G&G/Shuang Jie SW-6234C) are used to measure the total weight of branch residues before the experiment and that of weight losses after the experiment. Total three tests are carried out for each condition and the time (T) of each test is recorded. The results are shown in Table 5.

Table 5

Data analysis of the practical experiments								
Branch conditions	t (sec)	L (mm)	V=L/t (mm/s)	R (r/min)	Weight (kg)		η_2 (%)	Average η_2 (%)
					W	W _r		
Figure 9a	15.8	15000	950	40±2	15±0.2	0.84	94.4	94.2
	16.5		910			0.57	96.2	
	17.2		870			1.21	91.9	
Figure 9b	17.0		880			1.30	91.3	92.5
	16.1		930			0.79	94.7	
	16.3		920			1.28	91.5	
Figure 9c	17.9		840			4.72	68.5	61.0
	16.9		890			7.32	52.2	
	17.0		880			5.65	62.3	
Figure 9d	16.5		910			9.22	38.5	30.8
	16.0	940	11.30	24.7				
	15.8	950	10.62	29.2				

The optimization results in Table 3 show that the effective working range of spring teeth is extended from original 180° to 210°, but the range of returning is shortened to 65°, which is more conducive to bring the branches to the middle of orchard rows. In order to verify the practicability of the picking mechanism simulation platform, a rectangular baler with spring finger is used as the test carrier. The measured data are input into the man-machine dialogue window to optimize these parameters and can get α_2 , α_4 , and a lower H as shown in Table 4. The central line equation of the core part cam disc is obtained on the platform window. It can use MATLAB to process the data of cam disk. According to the data processing results, the cam disk is redesigned and its supporting parts are improved and get a new cam disk, as shown in Fig 9. Finally, the picking device is tested in an open field.

Table 5 shows the test comparison of four pruning residues scattering on the ground. When the rotation speed of the picking device is 38–42r/min and the moving speed is 0.80–0.95m/s, the success rate of picking in Figure 9a is 94.2%, which proves the effectiveness and potential of the method. The picking success rate of Figure 9b is close to Figure 9a under the same V and R. The reason is that the spring finger starts to push the transverse laid branches forward, finally stack together in a disordered state. Figure 9c and Figure 9d have a lower picking success rate of 61.0% and 30.8% respectively. Figure 9c shows that the branches moved to the side of the picking device and there were some branch losses.

Figure 9d makes it difficult to pick because the thick stem of the branch is inserted directly into the gap, which makes the spring finger unable to operate the branch effectively. The experiments confirmed that if the thick end of branch stems is drilled into the bottom of the picking device, most of them will be lost. Therefore, the situation of Figure 9d should be avoided.

CONCLUSIONS

In this paper, the mechanized treatment path and related equipment of orchard pruning residue are studied, and a human-computer dialogue design method is used to optimize the main devices structural parameters of mulching machine. Through the field test about the optimized picking-up device, the practicability and accuracy of the design method are verified. The conclusions are as follows. Through the simulation platform about the gathering device, a group of parameters are obtained quickly and accurately. The effective working range of spring teeth is extended and the return phase of spring teeth are shortened in the entire gathering period, which is more suitable to the gathering branches operation. Similarly, a set of suitable spring finger angle and lower picking-up height of spring finger are obtained quickly and accurately from the simulation platform about the picking-up device. A prototype of picking-up device is developed according to the optimized parameters. The success rate of the prototype is 94.2% under the optimal conditions. Field experiments show that the improved device can significantly improve the success rate of pruning residues picking that can meet the requirements of operation.

This study showed a promising and proper mechanical solution or idea for collecting residues in orchard. The machine will be tested in an orchard and applied to the farm in the future. The research results can provide basic data for the design of harvesting machine to collect pruning residues and the human-computer interaction design method can also be applied to other mechanisms.

ACKNOWLEDGEMENTS

This research was partially supported in part by Special project for the construction of modern agricultural industrial technology system in China (CARS-27); Funding projects for the introduction of overseas students in Hebei Province (C20200355).

REFERENCES

- [1] Abdallah R., Auchet S., Méausoone P.J., (2011), Experimental study about the effects of disc chipper settings on the distribution of wood chip size. *Biomass and Bioenergy*, 35(2): 843–852. <https://doi.org/10.1016/j.biombioe.2010.11.009>
- [2] Bussemaker M.J., Day K., Drage G., Franjo C., (2015), A Value Chain Optimization Model for a Biorefinery with Feedstock and Product Choices. *Computer Aided Chemical Engineering*, 37(June): 1883-1888. <https://doi.org/10.1016/B978-0-444-63576-1.50008-X>
- [3] Dyjakon A., (2018a), Harvesting and baling of pruned biomass in apple orchards for energy production. *Energies, MDPI, Open Access Journal*, 11(7): 1-14. RePEc:gam:jeners:v:11:y:2018:i:7:p:1680-d:154835
- [4] Dyjakon A., (2018b), The influence of the use of windrowers in Baler machinery on the energy balance during pruned biomass harvesting in the apple orchard. *Energies, MDPI, Open Access Journal*, 11(11): 1-15.
- [5] Florian A., Arkadiusz D., Paweł F., Leszek R., (2014), Conception of Machine for Pressing Branches with Pruning Fruit Tree. *Journal of Research and Applications in Agricultural Engineering*, 59(2): 5-9.
- [6] Gong I., Lee K., Kim J., Min Y., Shin K., (2020), Optimizing Vehicle Routing for Simultaneous Delivery and Pick-up Considering Reusable Transporting Containers: Case of Convenience Stores. *Appl. Sci.* 10, 4162. DOI: 10.3390/app10124162
- [7] Guerra S.P.S., Oguri G., Denadai M.S. et al., (2018), Preliminary trials of the BioBaler working in Brazilian eucalypt plantations. *Southern Forests*, 80(2): 131-135. <https://doi.org/10.2989/20702620.2017.1292441>
- [8] He L., Fu H., Karkee M. et al., (2016), Effect of fruit location on apple detachment with mechanical shaking. *Biosystems Engineering*, 49(16): 293-298. <https://doi.org/10.1016/j.ifacol.2016.10.054>
- [9] Kumar I.M.S., Kumar D.T.R.H., (2015), Design and Development of Agricultural Waste Shredder Machine. *International Journal of Innovative Science, Engineering & Technology*, 2(10): 164-172.

- [10] Leszek R., Arkadiusz D., Florian A., Piotr F., (2014), Problems with deriving the fruit tree pruned biomass for energy use. *Agricultural Engineering*, 3(157): 157-167. DOI:10.14654/IR.2014.151.068
- [11] Luigi P., Alessandro S., Angelo D.G., Antonio S., Enrico S., (2018a), Influence of chipping system on chipper performance and wood chip particle size obtained from peach pruning. *Biomass and Bioenergy*, 112(January): 121-127. <https://doi.org/10.1016/j.biombioe.2018.01.002>
- [12] McEniry J., O’Kiely P., Clipson N.J.W. et al., (2008) The microbiological and chemical composition of silage over the course of fermentation in round bales relative to that of silage made from unchopped and precision-chopped herbage in laboratory silos. *Grass and Forage Science*, 63(3): 407-420. <https://doi.org/10.1111/j.1365-2494.2008.00645.x>
- [13] Pari L., Suardi A., Frąckowak P. et al., (2018b) Two innovative prototypes for collecting pruning biomass: Early performance tests and assessment of the work quality. *Biomass and Bioenergy*, 117: 96-101. <https://doi.org/10.1016/j.biombioe.2018.07.010>
- [14] Paweł F., Florian A., Grzegorz W., Michał S., Arkadiusz D., Luigi P., Alessandro S., (2016), A prototype machine for harvesting and baling of pruning residues in orchards: first test on apple orchard (*Malus Mill.*) in Poland. *Journal of Research and Applications in Agricultural Engineering*, 61(3): 88-93.
- [15] Naujoks B., (2011), Project final report. ETICA EU Project, (December): 1-89.
- [16] Qiang M., Jiang L., Hang Z., Yamei W., Qian G., Ling Z., (2021), Design and simulation Analysis of Trussing Jujube Remnant Crusher. *Journal of Agricultural Mechanization Research*, (1): 101-108.
- [17] Ren D., Zhongxian Z.H., Jiadong L., Qikai M., Bowei S., Lili T., (2020), Kinematics Analysis on Elastic Tooth of Horizontal Rotating Rake. *Mechanical Engineer*, 3: 1-4.
- [18] Spinelli R., Lombardini C., Pari L., Sadauskienec L., (2014), An alternative to field burning of pruning residues in mountain vineyards. *Ecological Engineering*, 70: 212-216. <https://doi.org/10.1016/j.ecoleng.2014.05.023>
- [19] Tao X., Yongzhe S., Lianxing G., Xudong Z., Changyi L., Zhixia L., (2016), Spring-finger Peanut Pickup Mechanism Based on Two-stage Harvest. *Transactions of the Chinese Society for Agricultural Machinery*, 47(3):90-97,111
- [20] Xiudan M., (2015), Development Situation of Raker Machine in Foreign Countries.7-10.
- [21] Ye B.L., Liu A., Yu G.H., Luo C.X., (2013), Parameters optimization with human-computer interaction method and experiment of vegetable seedling pick-up mechanism. *Nongye Jixie Xuebao/Transactions of the Chinese Society for Agricultural Machinery*, 44(2): 57-62.
- [22] Yu Z.H., Huai S.C., Wang W.M., (2018) Leakage rate and optimization of working parameters for cylinder pickup collector based on spring-finger trajectory. *Nongye Gongcheng Xuebao/Transactions of the Chinese Society of Agricultural Engineering*, 34(4): 37-43.
- [23] Zhao Z., Huang H., Yin J., Simon X. Yang, (2018), Dynamic analysis and reliability design of round baler feeding device for rice straw harvest. *Biosystems Engineering*, 174: 10-19. <https://doi.org/10.1016/j.biosystemseng.2018.06.014>

EXPERIMENTAL RESEARCH AND CFD MODELING OF MODULAR POULTRY BREEDING

/

ЕКСПЕРИМЕНТАЛЬНЕ ДОСЛІДЖЕННЯ ТА CFD МОДЕЛЮВАННЯ МОДУЛЬНОГО ВИРОЩУВАННЯ ПТИЦІ

Trokhaniak V.I.¹, Spodyniuk N.A.¹, Antypov I.O.¹, Shelimanova O.V.¹, Tarasenko S.V.¹, Mishchenko A.V.¹ ¹

¹ National University of Life and Environmental Sciences of Ukraine / Ukraine;

Tel: +380673513082; E-mail: Trohaniak.v@gmail.com

DOI: <https://doi.org/10.356.33/inmateh-65-32>

Keywords: poultry, module for poultry breeding, CFD, infrared heater, ventilation system.

ABSTRACT

For high-quality and simultaneous breeding of different ages of poultry a modular keeping is proposed. The heating system of the module is a panel infrared heater. It is intended for local heating of technological area. Design dimensions of the module were determined for reasons of qualitative course of technological process, namely the stocking density of poultry. Experimental studies of the temperature regime of poultry breeding area were carried out. Body temperature of the poultry was within acceptable limits, up to 41.5°C. In addition, the surface temperature of the feathers did not exceed 29.1°C, which fully complies with sanitary and hygienic standards. For a better representation of temperature regime in the module, CFD modeling was performed. Fields of velocities, pressures and temperatures were obtained. The air temperature near poultry in the module reached 18.6°C, and the average velocity did not exceed 0.75m/s.

РЕЗЮМЕ

Для якісного і одночасного різновікового вирощування птиці запропоновано модульне утримання. Системою теплозабезпечення модуля служить панельний інфрачервоний нагрівач. Він призначений для локального нагріву технологічної зони. Конструктивні розміри модуля визначалися з міркувань якісного перебігу технологічного процесу, а саме щільності посадки птиці. Проведено експериментальні дослідження температурного режиму зони вирощування птиці. Температура тіла птиці знаходилася в допустимих межах, до 41,5°C. А температура поверхні пір'я не перевищувала 29,1°C, що повністю відповідає санітарно-гігієнічним нормам. Для отримання більш якісного представлення температурного режиму в модулі проведено CFD моделювання. Отримано поля швидкостей, тисків і температур. Температура повітря поблизу птиці у модулі сягала 18,6 °C, а середня швидкість не перевищувала 0,75 м/с.

INTRODUCTION

Intensive poultry farming in industrial conditions is carried out mainly in limited livestock facilities, equipped with mechanical ventilation systems. Frequency of heat stress of the body is constantly increasing due to poor regulation of microclimate parameters. This in turn affects the productivity of the poultry, namely, daily weight fluctuation, mortality, feed conversion rate and others (Vitt R. et al., 2017).

Traditional heating systems are not able to fully satisfy the temperature parameters in the poultry's location area at the same time providing a dynamic thermal regime. Alternative to them may be local heating systems, such as infrared heating systems.

With the correct placing of infrared emitters, heating occurs only in the area where the poultry is located. This feature allows to avoid the necessity to heat the entire volume of the poultry house. In addition, the heaters are easy in adjusting and provide the required air temperature, which changes with the growth of poultry. With additional application of the automation kit, together with the infrared heating system, significant economic effect can be obtained (Voznyak O. et al., 2021).

¹ Trokhaniak V.I., Assoc. Prof. Ph.D. Eng.; Spodyniuk N.A., Assoc. Prof. Ph.D. Eng.; Antypov I.O., Acting Head of Dep. Ph.D. Eng.; Shelimanova O.V. Assoc. Prof. Ph.D. Eng.; Tarasenko S.V., Assoc. Prof. Ph.D. Eng.; Mishchenko A.V., Assoc. Prof. Ph.D. Eng.

From a sanitary and hygienic point of view, infrared radiation has a positive effect on the physiological condition of poultry, especially on young stock. Radiation heat transfer occurs at the absence of intermediate environment between two surfaces at different temperatures. Thus, nature of the surface coating plays an important role in the absorption of infrared rays (*Amanowicz Ł. and Wojtkowiak J., 2018*).

Diffuse nature of the radiation heat transfer is shown *Brown K.J. et al., (2016)*, where the example of infrared heater with a power of 600 W describes a method of studying the heat flow distribution. It is indicated that efficiency of the emitter raises up with initial increase of electric power and stabilizes at 52%. It is also proved that the uniformity of the radiant heat flow distribution improves with distance from the heater.

Linhoss J.E. et al., (2017) presents in his paper the results of a study of radiant heat flow at the heights of heater from 1.22 to 1.98 m above the measuring plane. Authors *Ermolaev A.N. et al., (2018)* presented the results of studies of a light infrared emitter. This heater has wide range of capacities and it is located at heights from 4 to 10 m. Numerous studies in this direction prove that the choice of infrared heater's type depends directly on geometric dimensions of the room, geometric location of equipment, heat sources, size of irradiation area (*Kuznetsov G.V. et al., 2018; Semenov B.A. et al., 2018*). These facts confirm the influence of many factors on the formation of temperature regime in the irradiation area.

Sufficient attention is paid to the design of heater. Additional reflectors will increase the efficiency of radiation. *Lee E.H. and Yang D.Y. (2015)* made an experimental-numerical analysis of a parabolic reflector with a radiant heat source and different input widths, the effects of which on the temperature distribution are presented. In the paper *Maznoy A. et al., (2020)* is proposed a heater with using an annular cylindrical radiant burner mounted inside a stainless steel conical reflector. The item not only refocuses the directed radiant flow of the burner, but also participates in heat exchange with the flue gases and emits additional radiation flux. All these features show effectiveness of the application of infrared emitters in agriculture, in particular in poultry houses.

Authors *Gorobets V.G. et al., (2018b)* proposed a new cooling system in the poultry house using heat exchangers of special design (*Gorobets V.G. et al., 2018a*). They performed CFD modeling of air flows and heat and mass transfer in the poultry house, using water from underground wells as a cooler. In addition, recommendations for the choice of ventilation systems in poultry houses are given. In continuation of these studies (*Gorobets V.G. et al., 2018c*), authors optimized the height of the exhaust fans. It was shown that the ventilation equipment should be installed at a height of 1.5 m. This reduces the sizes of stagnant areas and the uneven distribution of air velocity near the poultry.

In order to reduce energy consumption and improve air quality while providing the necessary conditions for breeding of young poultry (*Trokhaniak V.I. et al., 2019*) authors conducted experimental studies and numerical simulations. In the process of research, a reduction in energy consumption was achieved to ensure the microclimate parameters during the breeding of broilers. In addition, the air quality of poultry houses was improved. This made it possible to reduce feed costs and losses of poultry and, as a result, increase the economic efficiency of production and the quality of finished products.

In the paper *Trokhaniak V.I. et al., (2020)*, the construction of the poultry house was modernized. CFD modeling was performed and the effective location of supply valves for the side ventilation system was found. Authors noted that the supply valves should be installed not lower than at a height of 200 mm from the floor level. Scientists recommended that this be further taken into account at the design stage of the side ventilation system.

Authors *Kiktev N. et al., (2021)*, *Lysenko V. et al., (2019)*, *Korobiichuk I. et al., (2017)* investigated the feasibility of using IoT technology in agricultural production and developing an energy-efficient method of controlling a modular electrical complex.

MATERIALS AND METHODS

Based on the principle of sectional poultry breeding, modular keeping of broiler chickens is proposed. The heating system of the module is a panel infrared heater, designed for a local heating of the technological area. To ensure a constant supply of fresh air and assimilation of hazards is provided a supply and exhaust ventilation system in the module.

This method of poultry breeding has a number of advantages. First of all, it is possible to use modules both in industrial breeding and within individual farms. The industrial method of poultry breeding involves the accumulation of large number of it in one poultry house, so the emergence and rapid spread of

infectious diseases is possible. Due to the local microclimate, provided in the module, this negative phenomenon can be prevented. In addition, it is possible to keep different age groups of poultry in one poultry house, changing the temperature regime with the growth of poultry.

Infrared heating and ventilation systems provide normalized air temperature in the irradiation area when the air temperature in the module changes from +16 to +35 °C, air velocity - from 0.2 to 0.3 m/s and there is quality regulation of these parameters (Spodyniuk N. and Lis A., 2021). At the same time, the required temperature conditions change while the poultry is growing.

Design dimensions of the module were determined for reasons of qualitative course of technological process, namely, ensuring maximum indexes of production yield in the poultry house, taking into account normalized stocking density of poultry $n_{norm} = 0.035 \text{ m}^2$ per 1 head and normalized intensity of floor irradiation $q_{norm} = 174... 290 \text{ W/m}^2$ (DSTD-AIC-04.05, 2005).

Table 1 shows the results of solving the problem of choosing rational parameters of the module for poultry breeding.

Rational geometric parameters of the module

Table 1

Module area $F, \text{ m}^2$	Module length $a, \text{ m}$	Module width $b, \text{ m}$	Module height $H, \text{ m}$	Dimensions of the infrared heater $a_{heat} \times b_{heat}, \text{ m}$	Irradiation area $F_{irrad}, \text{ m}^2$
0.96	1.2	0.8	1.5	0.1x0.54	3.26

On the basis of defined rational parameters of the module for poultry breeding, experimental installation in full size, shown in Fig. 1, was mounted.

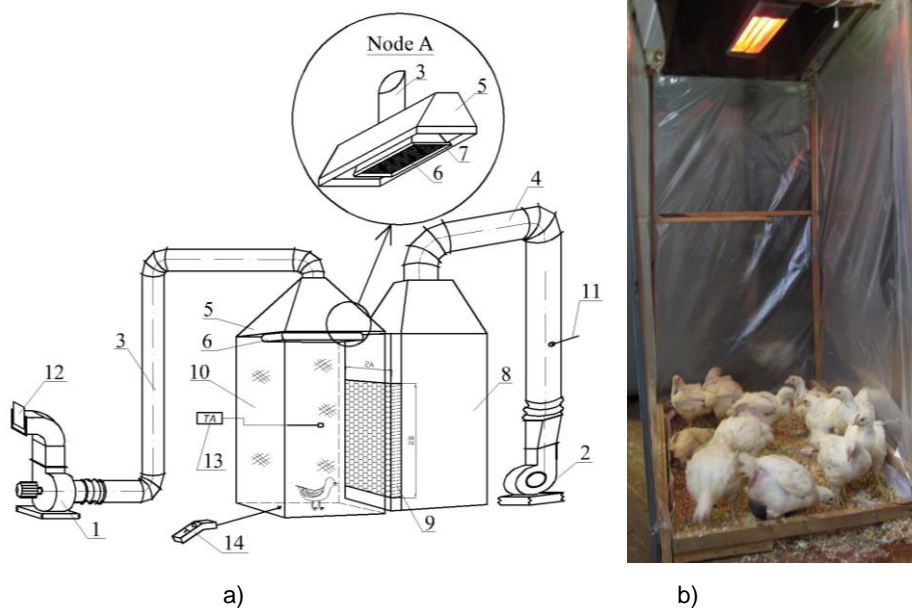


Fig. 1 – Scheme (a) and a photo (b) of experimental installation for studying the temperature regime of technological area of module for poultry breeding

1 – exhaust fan; 2 – supply fan; 3 – exhaust air duct; 4 – supply air duct; 5 – exhaust outlet; 6 – infrared heater QH 1500; 7 – reflector; 8 – static pressure chamber; 9 – uniform air distributor; 10 – module for poultry breeding; 11, 12 – dampers; 13 – thermoanemometer ATT - 1004; 14 – pyrometer "Nimbus-530/1"

The experimental installation was built for reasons of quality provision the microclimate parameters in module and was represented as a complex of heating and ventilation system. Study of the temperature regime was carried out as follows. Poultry was located in the module in accordance with sanitary and hygienic standards of stocking density. The infrared heater 6 was intended for local heating of technological area of the module. Through the uniform air distributor 9 and the static pressure chamber 8, fresh air was supplied to technological area of the module. Exhaust outlet 5 removed polluted air from the module. Air flow was regulated with the dampers 11 and 12. The temperature in the module was measured with a thermoanemometer ATT – 1004 13. The surface temperature on the poultry's feathers was measured with a pyrometer "Nimbus-530/1" 14.

For a better assessment of thermal state in the module and microclimate in general, numerical simulations were performed. To save computer calculation time, numerical simulations were performed only in module for poultry breeding 10. Prepared geometric model with the selected boundary conditions is presented in fig. 2 a.

Mathematical model is based on the Navier-Stokes equations (Gorobets V.G. et al., 2018b; Khmelnik S.I., 2018), the energy transfer equations for convective flows and the continuity equations. The Spalarta-Allmarasa turbulence model (Allmaras S.R. et al., 2012) and the Discrete Ordinates radiation model (ANSYS, 2017) were used in the calculations.

Air consumption of supply and exhaust air was 800 m³/h (0.02722 kg/s). Irradiation intensity of the infrared heater was 7238 W/m². Blackness degree of the heater surface was 0.7. Temperature of the poultry was 41°C.

Numerical model of hydrodynamics and heat and mass transfer used the finite element method. The method of local grid control was used in construction of grid for the module area (Fig. 2 b). The quality index of the Orthogonal Quality grid corresponds to about 0.274. The minimum size of the element was 0.005 m, the maximum - 0.02 m. Number of elements - 1747410, number of nodes - 2381752. The protruding grid is clearly visible in the section, thus it is possible to estimate better quality and shortcomings of the grid. In addition, it can be noticed a thickening of the grid near infrared heater.

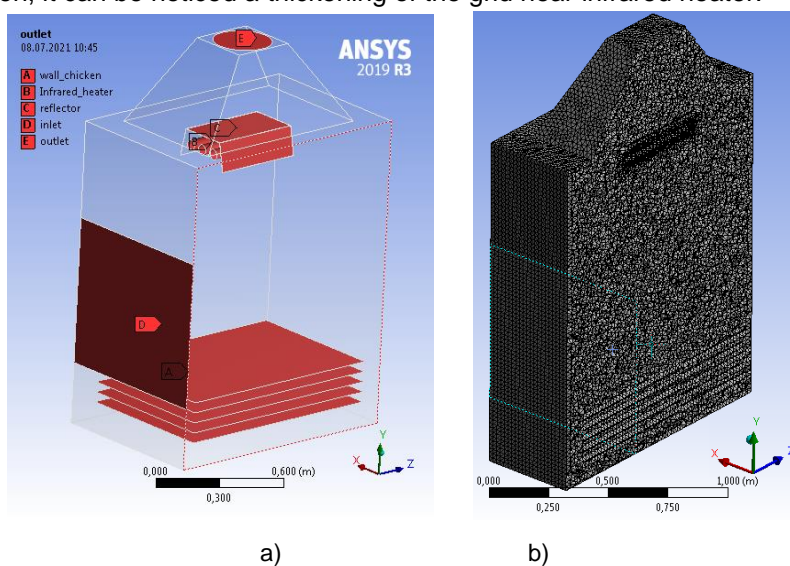


Fig. 2 – Geometric model (a) and a grid (b) of area of the module for poultry breeding

RESULTS

Temperature regime is a complex phenomenon that combines air temperature and ambient surface temperature. As it is known that the main parameters that affect its formation in module are power of infrared heater and height of its installation, that is, these values were chosen as input and variable factors. The thermal power Q_{heat} varied from 500 to 1500 W, and the installation height of the heater H was chosen as the most optimal for the module - 1.5 m. Temperature regime in the module also depended on background temperature in the room, and this value was also taken into account. In the cold period of the year, indoor air temperature was 15 - 18 °C.

Research results of the temperature regime of module for poultry breeding were compared with the normalized values, according to sanitary and hygienic standards [20] and numerical simulations (Table 2).

The air in the module was heated due to convective heat transfer between the heated surface of the poultry's body, other surrounding surfaces and the surrounding air. Therefore, air temperature in the module was the resulting temperature and it took into account temperatures of all surfaces, feather surface temperature and indoor air temperature.

For a more thorough study of the effects of infrared radiation on poultry's body, which was placed under the heater for a long time, the body temperature of poultry was determined. As can be seen from the table, body temperature is within acceptable limits, according to sanitary and hygienic standards (DSTD-AIC-04.05, 2005), therefore, the body does not overheat and infrared radiation has a positive effect on young animals.

Therefore, in a comprehensive experimental study obtained the total air temperature in the module for poultry breeding, which was changed with increasing of infrared heater's power. The obtained temperature values satisfied the internal microclimate parameters in poultry's location areas. The use of heating and ventilation system made it possible to change air temperature in the module quickly and dynamically by adjusting the power of heater. Changing the power by one position allowed increasing the air temperature in poultry's location area by 7.2%.

Figures 3-9 show the results of numerical simulations. Figures 3-4 show the velocity field in the module for poultry breeding. Maximum velocity in the boundary area "exit" reaches 10.427 m/s (Fig. 3b). Average air velocity near the poultry is 0.75 m/s, which fully complies with the standards of poultry farming. Velocity at the boundary area "entrance" is 0.2 m/s. In figure 4, flow turbulence can be observed in the upper part of module. The air flow is slowly directed to the end wall, opposite the boundary area "entrance" and rises up.

Results of experimental research and numerical modeling of the temperature regime of module for poultry breeding

Table 2

Results	Thermal power of the heater Q_{heat}, W	Installation height of the heater H, m	Indoor air temperature $t_{in}, ^\circ C$	Body temperature of the poultry $t_{body}, ^\circ C$	Feather surface temperature $t_{feath}, ^\circ C$	Air temperature in module $t_{mod}, ^\circ C$
Experiment	500	1.5	15	40.9	26.1	19.5
	1000	1.5	15	41.0	27.4	20.7
	1500	1.5	15	41.5	29.1	22.3
CFD	1000	1.5	15	41.0	-	19.124
Standards for poultry breeding (DSTD-AIC-04.05, 2005)	400...1500	1...1.7	15...18	40...42	23...35	16...35

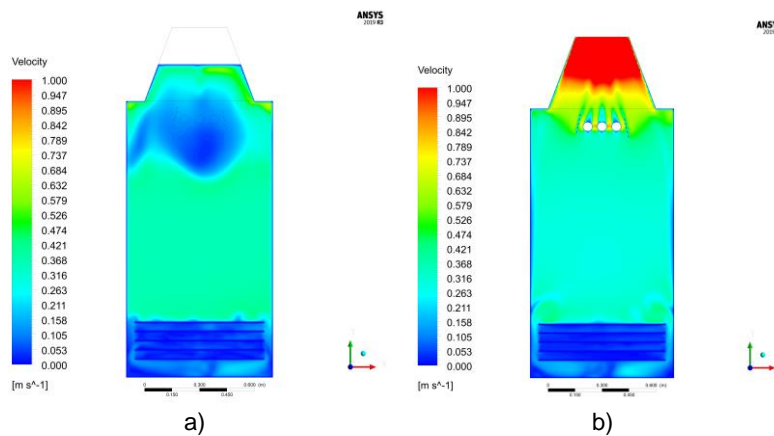


Fig. 3 – Velocity field (m/s) in the module for poultry breeding on the axis xy
a – 0.3 m from the wall; b – 0.6 m from the wall

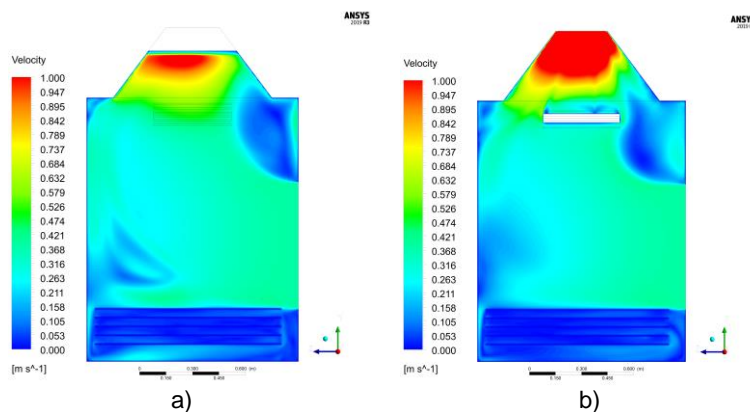


Fig. 4 – Velocity field (m/s) in the module for poultry breeding on the axis zy
a – 0.2 m from the wall; b – 0.4 m from the wall

Figures 5-6 showed the pressure field in the module. The maximum pressure drop reaches 10 Pa. At the boundary area "output", a slight vacuum of up to 5 Pa is created in the module. Observed phenomenon is insignificant and does not affect the poultry breeding as a whole.

Figures 7-8 show the temperature field in the module. The maximum temperature is observed near the infrared heater - 154 °C. An infrared emitter heats the poultry of modular breeding. At the same time, air flow passes around the poultry in the module. The heat is extracted from the surface of poultry's body and moves up. Average temperature in the module is 18.6°C, which fully meets the standards of poultry farming.

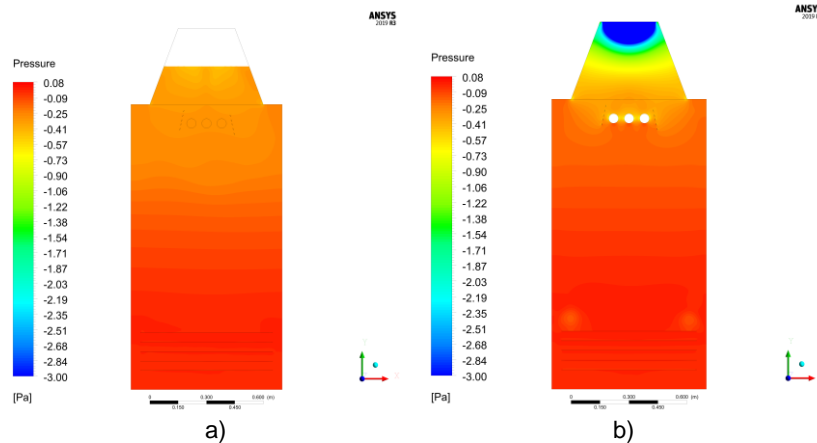


Fig. 5 – Pressure field (Pa) in the module for poultry breeding on the axis xy
a – 0.3 m from the wall; b – 0.6 m from the wall

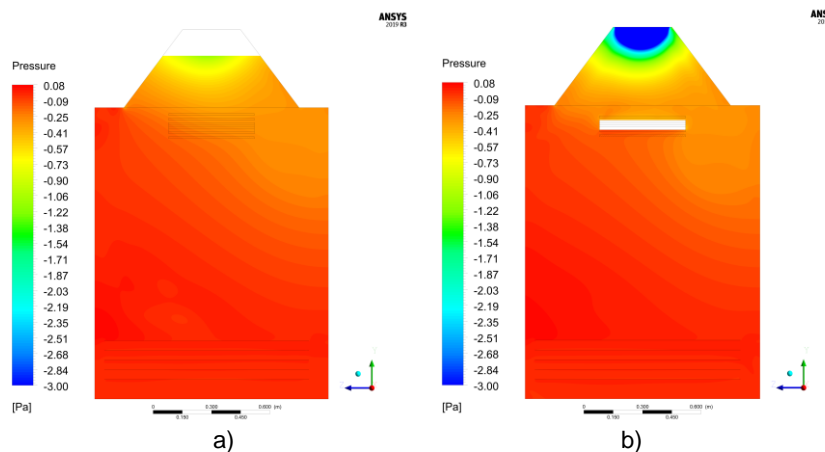


Fig. 6 – Pressure field (Pa) in the module for poultry breeding on the axis zy
a – 0.2 m from the wall; b – 0.4 m from the wall

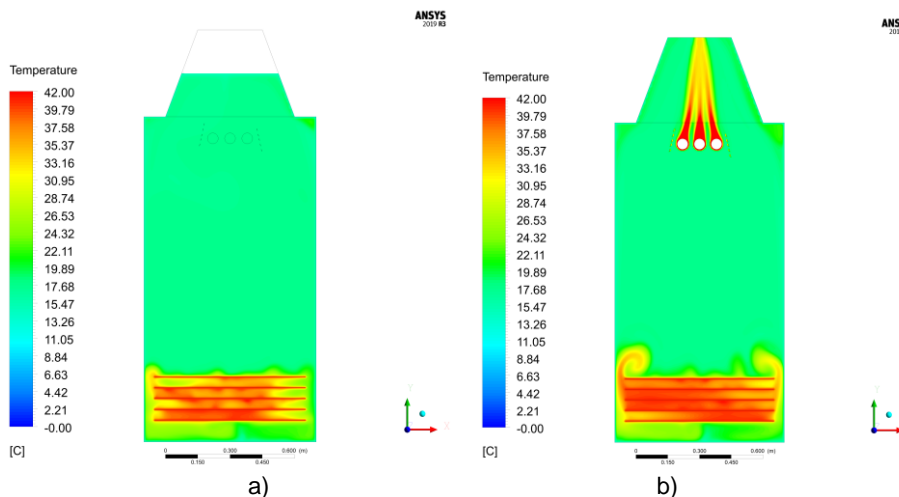


Fig. 7 – Temperature field (°C) in the module for poultry breeding on the axis xy
a – 0.3 m from the wall; b – 0.6 m from the wall

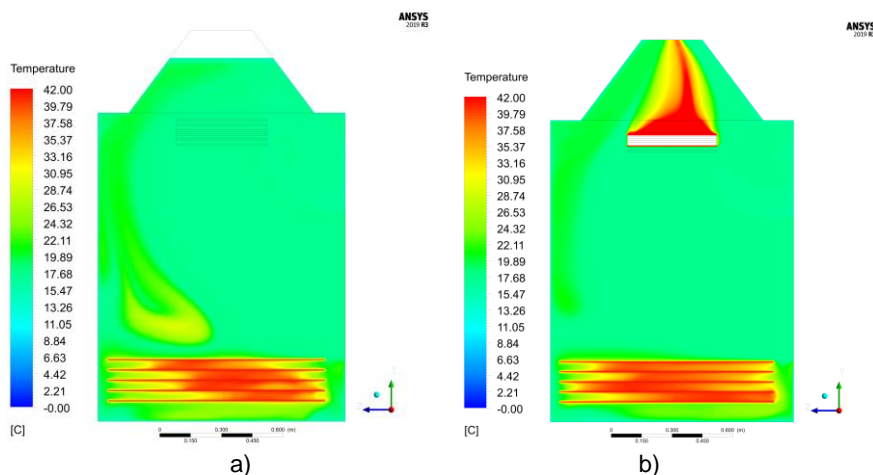


Fig. 8 – Temperature field (°C) in the module for poultry breeding on the axis zy
a – 0.2 m from the wall; b – 0.4 m from the wall

Below are the current lines, m/s (Fig. 9 a), air velocities, m/s (Fig. 9 b) and air temperatures, °C (Fig.9c) in the module for poultry breeding in 3D display. From these images, it is possible to estimate in more detail and qualitatively the formation of a microclimate in the module and its influence on the poultry's organism.

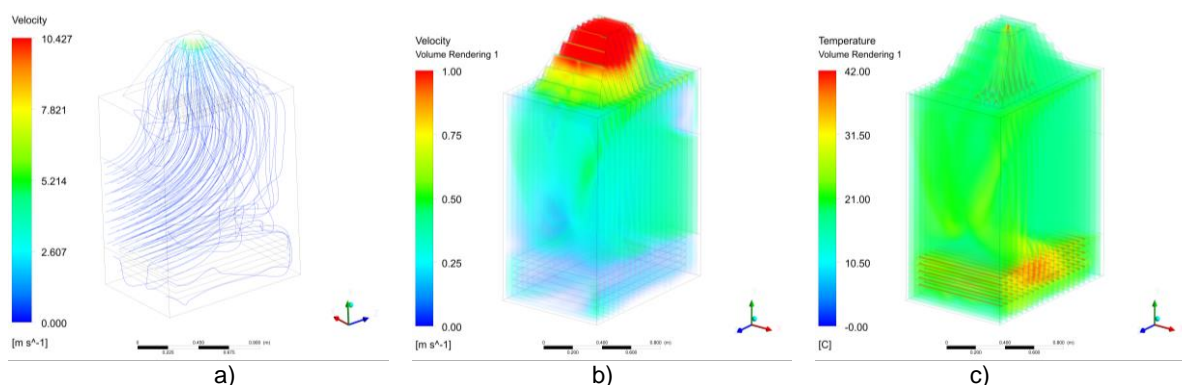


Fig. 9 –Current lines, m/s (a), air velocities, m/s (b) and air temperatures, °C (c) in module for poultry breeding in 3D display

CONCLUSIONS

Based on the principle of sectional poultry breeding, modular keeping of broiler chickens is proposed. Design of a module for poultry breeding with an infrared heater has been developed. The proposed design is energy efficient and it is recommended for installation in poultry houses.

Experimental researches of a temperature regime in the module at change of thermal power of the heater were carried out. Air temperature in the module, as well as the thermal state of the poultry's organism were within acceptable values, according to sanitary standards of poultry farming. The use of infrared heater allows changing the air temperature in module dynamically according to the technological process.

Numerical modeling of the module for poultry breeding was carried out. Fields of velocities, pressures and temperatures were obtained. The microclimate in the module was analyzed. The air temperature near the poultry in the module reached 18.6°C, and the average velocity did not exceed 0.75m/s.

REFERENCES

- [1] Allmaras S.R., Johnson F.T., Spalart P.R., (2012), Modifications and Clarifications for the Implementation of the Spalart-Allmaras Turbulence Model, *7th International Conference on Computational Fluid Dynamics*, pp. 9-13, Big Island/Hawaii;
- [2] Amanowicz Ł., Wojtkowiak J., (2018), Experimental investigations of thermal performance improvement of aluminum ceiling panel for heating and cooling by covering its surface with paint, *E3S Web of Conferences*, vol. 44, 00002. <https://doi.org/10.1051/e3sconf/20184400002>, Polanica-Zdrój/Poland;
- [3] ANSYS, (2017), ANSYS Fluent Theory Guide. Release 18.2, Published in the USA, 832 p.
- [4] Brown K.J., Farrelly R., O'shaughnessy S.M., Robinson A.J., (2016), Energy efficiency of electrical infrared heating elements, *Applied Energy*, vol. 162, pp. 581-588, <https://doi.org/10.1016/j.apenergy.2015.10.064>, United Kingdom;
- [5] DSTD-AIC-04.05, (2005), Departmental standards of technological design. Poultry enterprises (Відомчі норми технологічного проектування. Підприємства птахівництва), Ministry of Agrarian Policy of Ukraine (Міністерство аграрної політики України), 90 p., Kyiv/Ukraine;
- [6] Ermolaev A.N., Khaustova O.V., Turaev I.A., (2018), Simulating a convective heat transfer in buildings with radiant gas heating, *MATEC Web Conferences*, vol. 194, 01025, <https://doi.org/10.1051/matecconf/201819401025>, Tomsk/Russia;
- [7] Gorobets V.G., Bohdan Yu.O., Trokhaniak V.I., Antypov I.O., (2018a), Experimental studies and numerical modelling of heat and mass transfer process in shell-and-tube heat exchangers with compact arrangements of tube bundles, *MATEC Web of Conferences*, vol. 240, 02006, <https://doi.org/10.1051/matecconf/201824002006>, Cracow/Poland;
- [8] Gorobets V.G., Trokhaniak V.I., Antypov I.O., Bohdan Yu.O., (2018b), The numerical simulation of heat and mass transfer processes in tunneling air ventilation system in poultry houses, *INMATEH: Agricultural Engineering*, vol. 55, no. 2, pp. 87-96, Bucharest/Romania;
- [9] Gorobets V.G., Trokhaniak V.I., Rogovskii I.L., Titova L.L., Lendiel T.I., Dudnyk A.O., Masiuk M.Y., (2018c), The numerical simulation of hydrodynamics and mass transfer processes for ventilating system effective location, *INMATEH: Agricultural Engineering*, vol. 56, no. 3, pp. 185-192, Bucharest/Romania;
- [10] Khmelnik S.I., (2018), Navier-Stokes equations. On the existence and the search method for global solutions, *Mathematics in Computers – MiC*, 134 p., Bene-Ayish/Israel;
- [11] Kiktev N., Lendiel T., Osypenko V., (2021), Application of the internet of things technology in the automation of the production of compound feed and premixes, *CEUR Workshop Proceedings*, Vol. 2833, pp. 24-133, Kyiv/ Ukraine;
- [12] Korobiichuk I., Lysenko V., Reshетиuk V., Lendiel T., Kamiński M., (2017), Energy-efficient electrotechnical complex of greenhouses with regard to quality of vegetable production, *Advances in Intelligent Systems and Computing*, vol. 543, pp. 243-251. https://doi.org/10.1007/978-3-319-48923-0_30, Warsaw/Poland;
- [13] Kuznetsov G.V., Kurilenko N.I., Nee A.E., (2018), Mathematical modelling of conjugate heat transfer and fluid flow inside a domain with a radiant heating system, *International Journal of Thermal Sciences*, vol. 131, pp. 27-39. <https://doi.org/10.1016/j.ijthermalsci.2018.05.010>. Nantes/France;
- [14] Lee E.H., Yang D.Y., (2015), Experimental and numerical analysis of a parabolic reflector with a radiant heat source, *International Journal of Heat and Mass Transfer*, vol. 85, pp. 860-864, <https://doi.org/10.1016/j.ijheatmasstransfer.2015.02.042>, United Kingdom;
- [15] Linhoss J.E., Purswell J.L., Davis J.D., Fan Z., (2017), Comparing Radiant Heater performance using spatial modeling, *Applied Engineering in Agriculture*, vol. 33, no. 3, pp. 395-405. <https://doi.org/10.13031/aea.12108>, USA;
- [16] Lysenko V., Lendiel T., Komarchuk D., (2019), Phytomonitoring in a greenhouse based on Arduino hardware, *Paper presented at the 2018 International Scientific-Practical Conference on Problems of Infocommunications Science and Technology, PIC S and T 2018 - Proceedings*, 365-368. <https://doi.org/10.1109/INFOCOMMST.2018.8632030>, Kharkiv/Ukraine;
- [17] Maznoy A., Kirdyashkin A., Pichugin N., Zambalov S., Petrov D., (2020), Development of a new infrared heater based on an annular cylindrical radiant burner for direct heating applications, *Energy*, vol. 204, 117965, <https://doi.org/10.1016/j.energy.2020.117965>, United Kingdom;

- [18] Semenov B.A., Pashchenko D.I., Mitenev S.A., (2018), Mathematical modelling of heat transfer in a gas radiant of “dark” type, *Journal of Physics: Conference Series*, vol. 1111, 012008. <https://doi.org/10.1088/1742-6596/1111/1/012008>, United Kingdom;
- [19] Spodyniuk N., Lis A. (2021), Research of Temperature Regime in the Module for Poultry Growing, *Lecture Notes in Civil Engineering*, vol. 100, pp. 451-458. https://doi.org/10.1007/978-3-030-57340-9_55, Lviv/Ukraine;
- [20] Trokhaniak V.I., Rogovskii I.L., Titova L.L., Dziubata Z.I., Luzan P.H., Popyk P.S., (2020), Using CFD simulation to investigate the impact of fresh air valves on poultry house aerodynamics in case of a side ventilation system, *INMATEH Agricultural Engineering*, vol. 62, no. 3, pp. 155-164, <https://doi.org/10.35633/inmateh-62-16>, Bucharest/Romania;
- [21] Trokhaniak V.I., Rutylo M.I., Rogovskii I.L., Titova L.L., Luzan O.R., Bannyi O.O., (2019), Experimental studies and numerical simulation of speed modes of air environment in a poultry house, *INMATEH Agricultural Engineering*, vol. 59, no 3, pp. 9-18, <https://doi.org/10.35633/INMATEH-59-01>, Bucharest/Romania;
- [22] Vitt R., Weber L., Zollitsch W., Hortenhuber S.J., Baumgartner J., Niebuhr K., Piringner M., Anders I., Andre K., Hennig-Pauka I., Sch€onhart M., Schaubberger G., (2017), Modelled performance of energy saving air treatment devices to mitigate heat stress for confined livestock buildings in Central Europe, *Biosystems Engineering*, vol. 64, pp. 85-97. <https://doi.org/10.1016/j.biosystemseng.2017.09.013>, San Diego/USA;
- [23] Voznyak O., Spodyniuk N., Savchenko O., Sukholova I., Kasynets M., (2021), Enhancing energetic and economic efficiency of heating coal mines by infrared heater, *Naukovyi Visnyk Natsionalnoho Hirnychoho Universytetu*, vol. 2, pp. 104-109, <https://doi.org/10.33271/nvngu/2021-2/104>, Dnipro/Ukraine.

THEORETICAL ANALYSIS OF STRENGTH RESISTANCE TO DISPLACEMENT OF IMPROVED DIGGING WORKING BODY OF POTATOE HARVESTING COMBINE

ТЕОРЕТИЧНИЙ АНАЛІЗ СИЛ ОПОРУ ПЕРЕМІЩЕННЮ УДОСКОНАЛЕНОГО ПІДКОПУЮЧОГО РОБОЧОГО ОРГАНУ КАРТОПЛЕЗБИРАЛЬНОГО КОМБАЙНА

Nalobina O.O.¹⁾, Shymko A.²⁾, Bundza O.Z.¹⁾, Holotiuk M.V.¹⁾, Herasymchuk O.²⁾, Puts V.S.²⁾, Shovkomyd O.²⁾¹

¹⁾National University of Water and Environmental Engineering / Soborna str.11, Rivne, Ukraine;

²⁾Lutsk National Technical University / Lvivska str., 75, Lutsk, Ukraine;

Tel: +380960825360; E-mail: o.z.bundza@nuwm.edu.ua

DOI: <https://doi.org/10.356.33/inmateh-65-33>

Keywords: *digging working body, potato harvesting, resistance, energy consumption.*

ABSTRACT

The amount of energy required to perform technological processes in agriculture largely depends on the size of the resistance to the displacement of the working bodies of machines. The main factor of energy consumption performing the technological process of potato harvesting is the resistance to the displacement of the digging working body. In order to reduce the resistance to displacement an improved design of the digging body is proposed. An analytical study was conducted to determine the problem of moving the working body in the soil environment. The strength of the soil resistance is determined and the regularity of the influence on its change of parameters and the shape of the blade and separation parts of the digging working body is established. Calculations are made using the Mathematica application program. The graphic dependences and contours of the isocline of the traction flange of the working body ploughshare part are obtained. Analysis of the calculations allowed to set the parameters of the instrument panel surface, of which provide a minimum of traction resistance. The schedule and contours of isoclines of the change of the total resistance to the displacement of soil mass with the tubers on the working body separation surface depending on the distance between the bars and the size of their intersection are also obtained. Analysis of the dependence of soil resistance and tubers on the separation surface indicates that an increase in the size of the geometric size of rods intersection leads to a significant increase in the resistance of the medium. The material presented in the article can be used for analytical determination of the resistance of the digging working body of potato harvesting machines of arbitrary geometric shape in the soil medium with tubers.

РЕЗЮМЕ

Величина енергії, потрібна для виконання технологічних процесів у сільському господарстві, значним чином залежить від величин опорів переміщенню робочих органів машин. Основним чинником витрати енергії при виконанні технологічного процесу збирання картоплі є опір переміщенню викопуючого робочого органу. З метою зменшення опору переміщенню запропоновано удосконалену конструкцію викопуючого робочого органу. Виконано аналітичне дослідження, спрямоване на визначення опору переміщення робочого органу у ґрунтовому середовищі. Визначено силу опору ґрунту та встановлено закономірність впливу на її зміну параметрів і форми лемішної та сепарувальної частин викопуючого робочого органу. Розрахунки виконано з використанням прикладної програми Mathematica. Отримано графічні залежності та контури ізоліній зміни тягового опору лемішної частини робочого органу. Аналіз отриманих розрахунків дозволив встановити параметри поверхні лемішної частини, які забезпечують мінімум тягового опору. Отримано також графік та контури ізоліній зміни повного опору переміщенню маси ґрунту з бульбами по сепарувальній поверхні робочого органу у функції відстані між прутками та розміру їх перетину. Аналіз залежності опору ґрунту з бульбами, що знаходяться на сепарувальній поверхні свідчить про те, що збільшення величини геометричного розміру перетину прутків призводить до суттєвого зростання опору середовища. Матеріал, викладений у статті може бути використаний для аналітичного визначення опору переміщення викопувального робочого органу картоплезбиральних машин довільної геометричної форми у ґрунтовому середовищі з бульбами.

¹ Nalobina O.O., Prof. Ph.D. Eng.; Shymko A.; Bundza O.Z., Ph.D. Eng.; Holotiuk M.V., Ph.D. Eng.; Herasymchuk O., Ph.D. Eng.; Puts V.S., Ph.D. Eng.; Shovkomyd O., Ph.D. Eng.

INTRODUCTION

Potato is one of the most popular vegetable in the world with high yields (Negar N. et al., 2015). Ukraine consumes 136 kg of potatoes per person each year, Russia, Poland - 131 kg, Rwanda - 125 kg, UK -102 kg. The producers of potatoes enrol about 130 countries. Among the most powerful potato producers are New Zealand (average yield of 502 pounds per hectare), the Netherlands (447 pounds/ha), Germany (423 pounds/ha), France (432 pounds/ha), England (405 pounds/ha) (<https://kartofan.org/skolko-sobirayut-kartoshki-v-rossii-i-mire.html>).

Not only the volumes of produced products but also their high qualitative indices and the level of material and energy costs for growing and harvesting potatoes are important for successful competing in the world market. The formation of the above mentioned factors has a significant influence on the performance of machines for potato harvesting, in particular their traction-performance indicators, which are conditioned by the construction of working bodies, kinematic parameters.

This statement is proved by theoretical and experimental investigations of many scientists (Amare D. et al, 2015; Popov A.A., 1984; Petrov D.G., 1989; Baio F.H.R. and al, 2004).

In addition, the process of collecting potatoes and its parameters is influenced by the nature of the interaction of the working bodies of machines and soil, physical and mechanical properties of soil (Kushnariov A.S., 1980; Kovbasa V.P., 2001; Frentisek V. et al., 2013). The design of the working bodies affects not only the conditions of operation of the machines but also the forces of soil treatment, thus, determining the energy costs for technological processes implementation (Kosolapov, V.V. et al., 2019; Engin O. et al., 2017); Simdyankin A.A. et al., 2015). The solution to the problem of the working body interaction with the soil by establishing the relationship between the geometric parameters and modes of operation of the working body itself with the change of soil properties, as well as, the component of traction resistance is an urgent task that needs to be solved.

MATERIALS AND METHODS

In order to achieve the goal of reducing the energy intensity of the process of picking up potato tubers an improved digging working body for potato harvesting machines (A. Shymko, O. Nalobina, 2018) was developed and manufactured and is presented in Fig. 1.

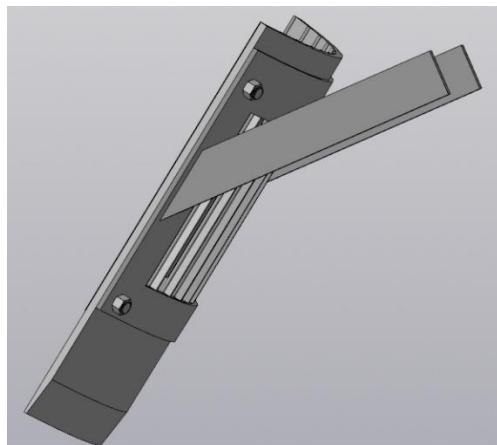


Fig. 1 - Undercutting working body

Schematically, the working body is presented in the form of a structure shown in Fig. 2. Studies on the interaction process of the working body provide a mathematical description of the surfaces of the working body constituent parts and the soil space of the field. With this in mind, two coordinate systems were introduced: xyz which corresponded to the soil space of the field and $\xi\eta\zeta$, which is adopted to describe the surface equations of the working body constituent parts. Coordinate system $\xi\eta\zeta$ idem xyz coincides with the coordinate system of the soil half-space. Axis direction x coincides with the direction of the velocity vector V_m of working body. Axis z is directed into the depths of the soil space, and the axis y is perpendicular to the movement direction of the working body and coincides with the surface $z = 0$. This system is adopted to describe the equations of the surfaces of the working body components.

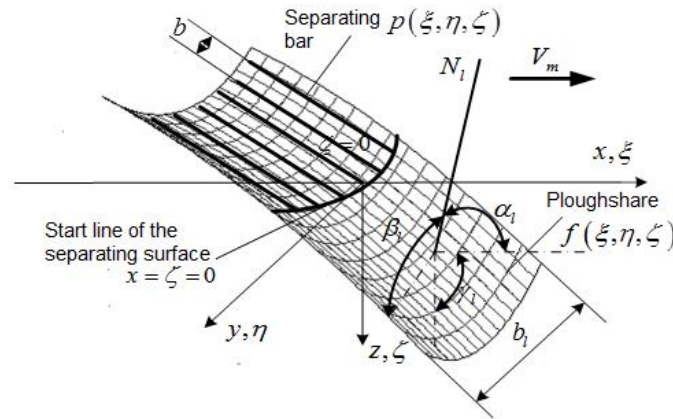


Fig. 2 - General scheme of digging-separating working body

Note: In the figure 2, the notations are: $f(\xi, \eta, \zeta)$ - container surface equation, $p(\xi, \eta, \zeta)$ - the equation of the surface of the separating rod, b - the step of placing the separating bars in the transverse direction, i.e. in the y -axis direction, N_1 - normal to the surface of the ploughshare, α_1 - the angle of inclination of the normal to the surface of the container to the axis ξ idem x , β_1 - the angle of inclination of the normal to the surface of the container to the axis η idem y , γ_1 the angle of inclination of the normal to the surface of the ploughshare to the axis ζ idem z , V_m - the speed of movement of the working body in the direction of axis x .

To formalize the surfaces of the working body parts, the equation of the surfaces of its constituent parts was recorded in the coordinate system $\xi\eta\zeta$. The equation of the surface of the ploughshare and the surface in which the separating rods are placed is presented in the form of a hyperbolic paraboloid in an implicit form:

$$f_l = \zeta - \left(d + c \left(\frac{((\phi\xi) + s)^2}{a} - \frac{(\kappa\eta)^2}{b} \right) \right) \quad (1)$$

where ϕ, s, a, κ, b - coefficients characterizing the shape of the location and the parameters of the curvature of the surface of the ploughshare part, which then turns into a bar separating part (Shymko A., Nalobina O., 2018). The change of these coefficients leads to a change in the configuration and geometric parameters of the working body (Shymko A., Nalobina O., 2018). They will be called form-forming parameters. In solving the problem of the working body interaction to separate the soil chunk from the tubers and further destroy its integrity, a soil model in the form of a viscoelastic medium was adopted, which can be formalized by the Kelvin-Voigt model. The mechanical model of such an environment is shown in Fig. 3. According to this model, due to the application of load, there is a viscoelastic deformation of the material, in which with the increasing speed of load application, the rate of deformation increases in proportion to the decrease in the modulus of viscosity.

For such a mechanical model, the physical equations of stress-strain relationship have the form:

$$\begin{aligned} \sigma_x &= \frac{4}{9} e^{\frac{Gt}{2\eta(1+\nu)}} \eta(1+\nu\dot{\epsilon}) (6\dot{\epsilon}_x - 3(\dot{\epsilon}_y + \dot{\epsilon}_z)) - \frac{e^{\frac{Gt}{\eta(1+\nu)}} (1+\nu)\dot{\epsilon}}{-1+2\nu} \\ \sigma_y &= \frac{4}{9} e^{\frac{Gt}{2\eta(1+\nu)}} \eta(1+\nu) (-3(\dot{\epsilon}_x - 2\dot{\epsilon}_y + \dot{\epsilon}_z)) - \frac{e^{\frac{Gt}{\eta(1+\nu)}} (1+\nu)\dot{\epsilon}}{-1+2\nu} \\ \sigma_z &= \frac{4}{9} e^{\frac{Gt}{2\eta(1+\nu)}} \eta(1+\nu) (-3(\dot{\epsilon}_x + \dot{\epsilon}_y - 2\dot{\epsilon}_z)) - \frac{e^{\frac{Gt}{\eta(1+\nu)}} (1+\nu)\dot{\epsilon}}{-1+2\nu} \\ \tau_{xy} &= 2e^{\frac{Gt}{2\eta(1+\nu)}} \eta(1+\nu) \dot{\gamma}_{xy}, \quad \tau_{yz} = 2e^{\frac{Gt}{2\eta(1+\nu)}} \eta(1+\nu) \dot{\gamma}_{yz}, \\ \tau_{xz} &= 2e^{\frac{Gt}{2\eta(1+\nu)}} \eta(1+\nu) \dot{\gamma}_{xz} \end{aligned} \quad (2)$$

where:

- $\sigma_x, \sigma_y, \sigma_z, \tau_{xy}, \tau_{xz}, \tau_{yz}$ – components of normal deformations and shear deformations, Pa;
- G – shear module, Pa; $G = E/(2(1 + \nu))$;
- E – modulus of elasticity of linear deformations, Pa;
- ν – Poisson's ratio;
- $\dot{\epsilon} = 1/3(\dot{\epsilon}_x + \dot{\epsilon}_y + \dot{\epsilon}_z)$, where $\dot{\epsilon}_x, \dot{\epsilon}_y, \dot{\epsilon}_z$ – components of linear deformations, s^{-1} ;
- $\dot{\gamma}_{xy}, \dot{\gamma}_{xz}, \dot{\gamma}_{yz}$ – shear deformation components, s^{-1} ;
- η – shear modulus of shear deformations, Pa·s;
- t – deformation time, s

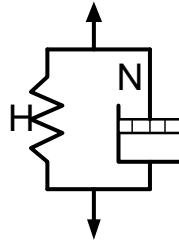


Fig. 3- Mechanical model of viscoelastic medium (soil).
H – elastic element (Hooke's body), I- viscous element (Newton's body)

It is known that the main factor in energy consumption is the resistance to movement of the working body during the process. Equilibrium equation on the contact surface of the working body with the soil, according to the solution of the elastic equilibrium problem of an anisotropic body (Kovbasa V. P., Shvajko V. M., Gucol O.P., 2015), has the form:

$$\left. \begin{aligned} \sigma_x l + \tau_{xy} m + \tau_{xz} n &= \bar{X}; \\ \sigma_y m + \tau_{yz} n + \tau_{xy} l &= \bar{Y}; \\ \sigma_z n + \tau_{xz} l + \tau_{yz} m &= \bar{Z}; \end{aligned} \right\} \quad (3)$$

where:

- l, m, n – guide cosines of the external normal to the surface that limits the environment, i.e. the contact surface (the surface of the working body);
- $\bar{X}, \bar{Y}, \bar{Z}$ -components of projections of forces distributed on the contact surface on the corresponding coordinate axes;
- $\sigma_x, \sigma_y, \sigma_z, \tau_x, \tau_y, \tau_z$ - components of normal deformations and shear deformations, Pa.

To analyse the influence of parameters and modes of operation of the ploughshare part of the working body, it is necessary to determine the relationship of dynamic quantities, including stresses in the soil depending on their mechanical properties and geometric parameters and modes of operation of the ploughshare. Such dynamic quantities are the components of stresses in the soil environment. These components are determined by the dependences (2), which describe the relationship of the stress components with the components of the strain rates both normal and tangential. In equations (2) the following notations are accepted: for stress components $\sigma_{xl} \rightarrow \sigma_x, \sigma_{yl} \rightarrow \sigma_y, \sigma_{zl} \rightarrow \sigma_z, \tau_{xyl} \rightarrow \tau_{xy}, \tau_{xzl} \rightarrow \tau_{xz}, \tau_{yzl} \rightarrow \tau_{yz}$, and for the components of the relative strain rates - $\dot{\epsilon}_{xl} \rightarrow \dot{\epsilon}_x, \dot{\epsilon}_{yl} \rightarrow \dot{\epsilon}_y, \dot{\epsilon}_{zl} \rightarrow \dot{\epsilon}_z, \dot{\gamma}_{xyl} \rightarrow \dot{\gamma}_{xy}, \dot{\gamma}_{xzl} \rightarrow \dot{\gamma}_{xz}, \dot{\gamma}_{yzl} \rightarrow \dot{\gamma}_{yz}$. In this case, the values of the stress components in the soil will be determined by the dependencies:

$$\left\{ \begin{aligned} \sigma_x &= \frac{\frac{GL}{\sqrt{2\eta}} \frac{1}{\sqrt{\rho-2\nu\rho}} \eta_1 (\dot{\tau}_{xl}(5-7\nu)+2(\dot{\tau}_{yl}+\dot{\tau}_{zl})(-2+\nu))}{9(-l+\nu)} \\ \sigma_y &= \frac{\frac{GL}{\sqrt{2\eta}} \frac{1}{\sqrt{\rho-2\nu\rho}} \eta_1 (\dot{\tau}_{yl}(5-7\nu)+2(\dot{\tau}_{xl}+\dot{\tau}_{zl})(-2+\nu))}{9(-l+\nu)} \\ \sigma_z &= \frac{\frac{GL}{\sqrt{2\eta}} \frac{1}{\sqrt{\rho-2\nu\rho}} \eta_1 (\dot{\tau}_{zl}(5-7\nu)+2(\dot{\tau}_{xl}+\dot{\tau}_{yl})(-2+\nu))}{9(-l+\nu)} \\ \tau_{xyl} &= 2e \frac{\frac{GL}{\sqrt{2\eta}} \frac{1}{\sqrt{\rho-2\nu\rho}} \dot{\gamma}_{xyl} \eta_1}{\sqrt{\rho-2\nu\rho}} \\ \tau_{yzi} &= 2e \frac{\frac{GL}{\sqrt{2\eta}} \frac{1}{\sqrt{\rho-2\nu\rho}} \dot{\gamma}_{yzi} \eta_1}{\sqrt{\rho-2\nu\rho}} \end{aligned} \right. \quad (4)$$

where:

l - distance distribution of waves in the soil

L - the distance of propagation of stress waves in the soil.

Based on the equilibrium equations on the surface, the constituents of the resistance that arise in the contact interaction look like this (in accordance with equation (2)):

$$\left. \begin{aligned} \sigma_{xl}l_l + \tau_{xyl}m_l + \tau_{xzl}n_l &= dF_x; \\ \sigma_{yl}m_l + \tau_{yzi}n_l + \tau_{xyl}l_l &= dF_y; \\ \sigma_{zl}n_l + \tau_{xzl}l_l + \tau_{yzi}m_l &= dF_z; \end{aligned} \right\} \quad (5)$$

where:

dF_x, dF_y, dF_z are components of projections of forces, which are assigned to the unit of contact area.

Thus, in order to obtain the components of the soil resistance to the movement of the ploughshare part of the working body, the components dF_x, dF_y, dF_z are necessary to integrate in corresponding planes that are perpendicular to the distributed forces for dependencies:

$$\left. \begin{aligned} F_{xli} &= \int_0^h \int_{-b_l}^{b_l} (\sigma_{xl}l_l + \tau_{xyl}m_l + \tau_{xzl}n_l) d\eta d\zeta, \\ F_{yli} &= \int_0^h \int_{L_l}^0 (\tau_{xyl}l_l + \sigma_{yl}m_l + \tau_{yzi}n_l) d\xi d\zeta, \\ F_{zli} &= \int_0^h \int_{L_l}^0 (\tau_{xyl}l_l + \tau_{yzi}m_l + \sigma_{yl}n_l) d\xi d\zeta, \end{aligned} \right\} \quad (6)$$

where:

h – the depth of the ploughshare of the working body into the ground;

L - the distance of propagation of stress waves in the soil;

b_l - the half-width of the working body.

The components of the resistance forces act on the surface of the working body in three mutually perpendicular directions. To determine the total resistance force acting in the direction of motion, it is necessary to take into account the component of the resistance force in the direction of motion and take into account the external friction on the surface of the working body:

$$F_{xl} = F_{xli} + \left(\sqrt{F_{xli}^2 + F_{yli}^2 + F_{zli}^2} \right) \cdot tg[\psi], \quad (7)$$

where:

$tg[\psi]$ is the coefficient of external friction of the soil on the material of the working body.

The resistance forces that occur on the separation surface are determined in a similar way. At the same time there is one difference, which consists in the fact that the forces of resistance consist of the sum of the bars. Expressions for the determination of forces have the form:

$$\left. \begin{aligned} F_{xli} &= 2 \sum_{n_p=1}^{n_p} \int_{-\chi/2}^{\chi/2} \int_{\zeta_0}^{\zeta_k} (\sigma_{xp} l_p + \tau_{xyp} m_p + \tau_{xzp} n_p) d\zeta d\chi, \\ F_{yypi} &= 2 \sum_{n_p=1}^{n_p} \int_{\zeta_0}^{\zeta_k} \int_{\xi_0}^{\xi_k} (\tau_{xyp} l_p + \sigma_{yp} m_p + \tau_{yzp} n_p) d\xi d\zeta, \\ F_{zpi} &= 2 \sum_{n_p=1}^{n_p} \int_{-\chi/2}^{\chi/2} \int_{\xi_0}^{\xi_k} (\tau_{xzp} l_p + \tau_{yzp} m_p + \sigma_{zp} n_p) d\xi d\chi, \end{aligned} \right\} \quad (8)$$

where:

χ is geometric dimension of the bar of the working surface of the working body (the size of their diameter),

n_p - is the number of bars.

Limits of integration in equations (8) are defined as follows: the lower limit of integration on the height of the separating surface for each specific rod ζ_0 due to the need to locate the rod in the middle of the surface at $\eta = 0$ that it should not be below the surface of the field, therefore $\zeta_0|_{(\zeta-b_p n_{pp}) \rightarrow 0, n_{pp}=\{-1,1\}} = 0$. The upper limit

of integration ζ_k due to the need to raise the middle part of the surface to ensure the movement of soil with tubers and ensure a minimum clearance h_p , so $\zeta_k|_{(\zeta-b_p n_{pp}) \rightarrow 0, n_{pp}=\{-1,1\}} = h_p$. Since the separation surface is a

continuation of the ductile surface, the parameters characterizing its geometric shape remain unchanged. Therefore, the only variable values of the separating surface remain the geometric size of the bar (diameter) χ and the distance between the bars on the surface b_p (Shymko A., Nalobina O., 2018).

The general resistance to the displacement of soil mass with the tubers on the separation surface has the form:

$$F_{xp} = F_{xpi} + \left(\sqrt{F_{xpi}^2 + F_{yypi}^2 + F_{zpi}^2} \right) \cdot tg[\psi]. \quad (9)$$

The results of theoretical research have been proven in experiments. For this purpose, three variants of the working body with the following shaping parameters are proposed: the first: $c=0.95$; $b=1.5$; $\phi=0.25$; second: $c=1.05$; $b=1.5$; $\phi=0.25$; third: $c=0.95$; $b=1.5$; $\phi=0.15$. Rational values of shaping parameters have been established by the authors in previous studies (Shymko A., Nalobina O., 2018) on the condition of the greatest loosening of the soil.

According to these shaping parameters, 3D models are built, which are the basis for the manufacture of physical models of the working body. A laboratory soil channel was used for research (Fig.4). The working body was fixed on the frame of the tensometric trolley, which was moved along the channel with the soil and the value of traction resistance was fixed.



Fig. 4 - A laboratory soil channel was used for research

RESULTS

On the received dependencies the calculation has been made. The value of the parameters of the working body was obtained by the authors in the course of the previous theoretical studies and is partly presented in the authors' work (Shymko A., Nalobina O., 2018). Calculations are made using the Mathematica application.

In fig. 4 is shown a graphical solution of function (4), depending on changes in the parameters of the separating part of the working body.

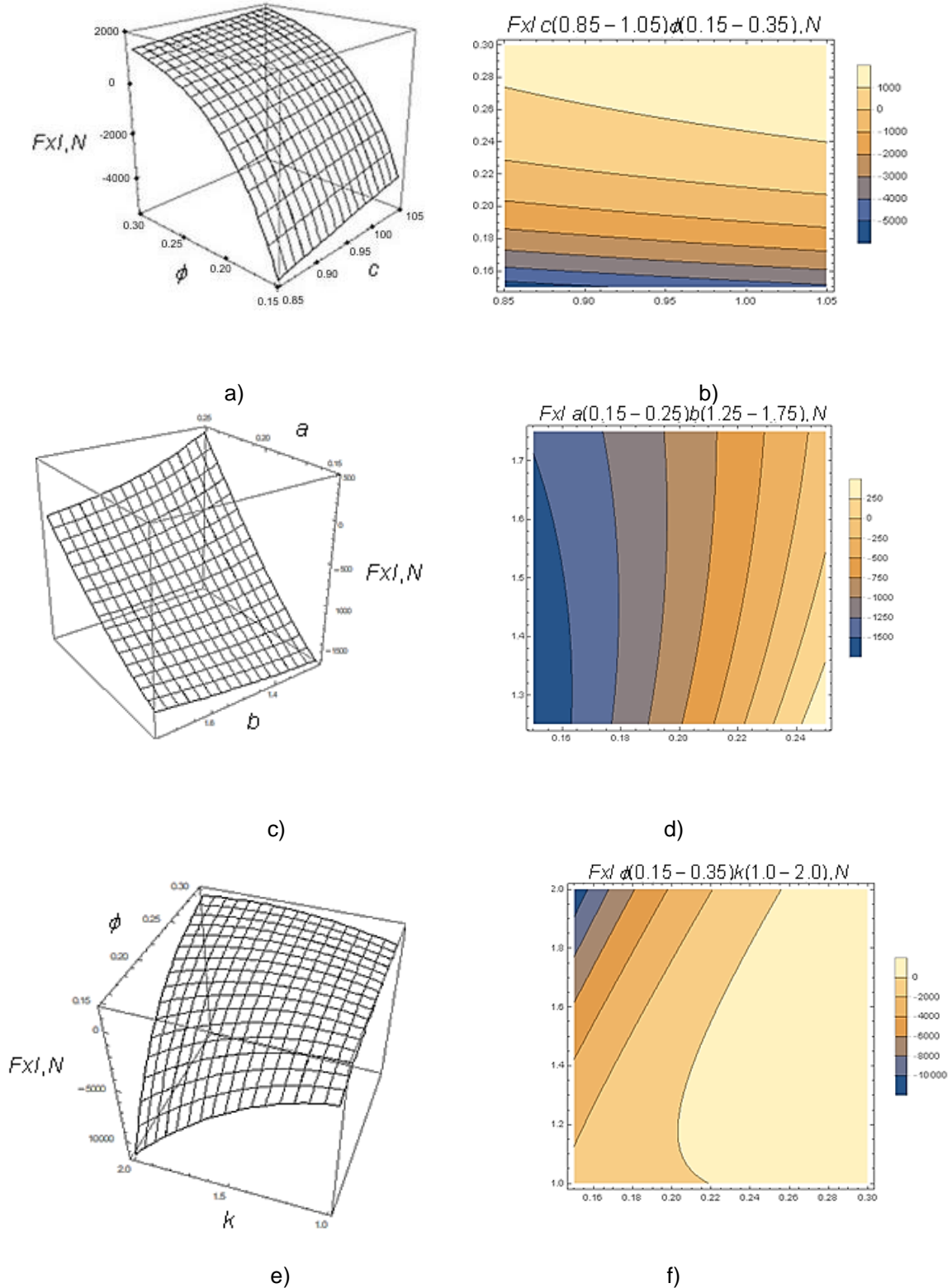


Fig. 5 - Graphical dependencies of traction resistance changes F_{xI} at various parameters of the shape of the working body surface c, a, b, ϕ, k

By analysing the dependence of the resistance on the displacement of the working platform of the excavator in the soil (Fig. 5), one can conclude that the minimum traction resistance can be achieved with the use of a working body with surface parameters: $c \rightarrow 0.95$, $\phi \rightarrow 0.25$, $b \rightarrow 0.20$, $k \rightarrow 1.50$.

Graphically, the dependence of full resistance F_{xp} displacement of soil mass with tubers by separation surface depending on the distance between bars b_p and the size of their intersection χ on a one-sided number of bars 13 is shown in Fig. 6

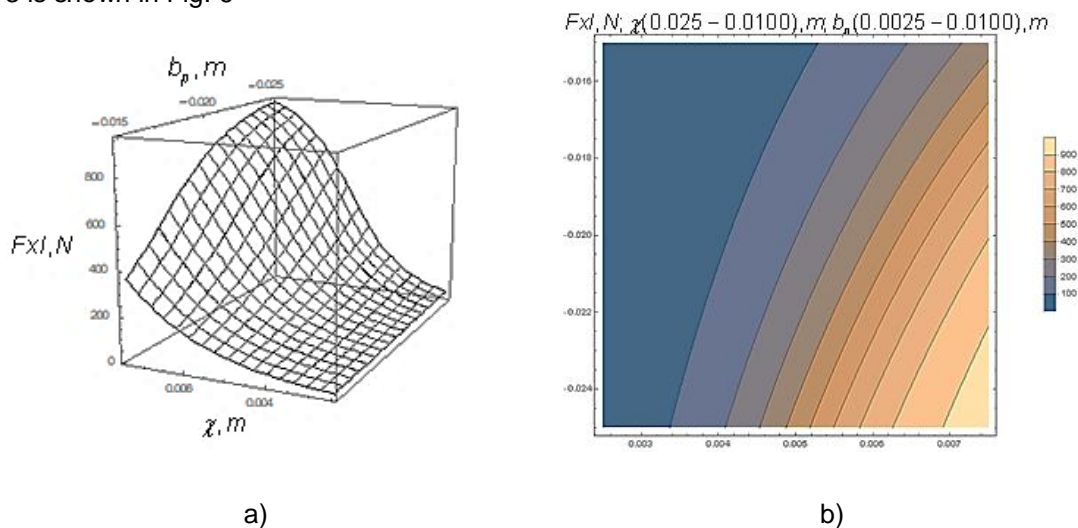


Fig. 6 - Chart and contours of isocline change of full resistance F_{xp} displacement of soil mass with tubers by separation surface depending on the distance between bars b_p and the size of their intersection χ on a one-sided amount of the number of bars 13 by one-sided amount of bars $n_p = 13$, $V_m = 1.0 \frac{m}{s}$

CONCLUSIONS

The minimum traction resistance is provided by means of a working body with the parameters of the ploughshare surface: $c \rightarrow 0.95$, $\phi \rightarrow 0.25$, $b \rightarrow 0.20$, $k \rightarrow 1.50$. These values of the parameters coincide with the values of these parameters, which provide soil loosening. This is explained by the fact that under such parameters there is a destruction of the soil in the maximum possible area before the working body, therefore the resistance of the soil to the displacement of the working body is reduced. This has been proven by experimental studies. The use of a working body with the following shaping parameters provided: minimum traction resistance.

Analysis of the dependence of soil resistance and tubers on the separation surface indicates that an increase in the size of the geometric size of the intersection of bars χ leads to a significant increase in environmental resistance. At the same time increasing the distance between the axes of bars b_p has insignificant influence on the change of resistance movement at small values χ but this resistance increases significantly at higher values χ .

REFERENCES

- [1] Amare D., Kidanemariam G., Endalew W., Yilma S., (2015), Potato Harvester for Smallholder Producers. *In International Journal of Mechanical Engineering and Applications*, Vol. 3, no. 6, pp. 103-108. DOI:10.11648/j.ijmea.20150306.11, Bahir Dar / Ethiopia;
- [2] Baio F.H., Antuniassi U.R., Balastreire L.A., Caixeta Filho J.V. (2004), Modelo de programacao linear para selecao de pulverizadores agricolas de barras, *Engenharia Agrícola*, Jaboticabal, v.24, n.2, p.355-363, Pádua Dias / Spain;
- [3] Hafezi N., Sheikhdavoodi M. J., Sajadiye S. M. (2015), Study of energy consumption of potato slices during drying process, *In Acta Technologica Agriculturae*, Vol. 2, pp. 36–41. DOI: 10.1515/ ata-2015-0008, Nitra / Slovak Republic;
- [4] Engin Özgöz, Ebubekir Altuntas, Murat Asilturk, (2017), Effect of soil tillage on energy in potato farming in Central Anatolia of Turkey. *In Energy*, vol. 141, pp. 1517–1523, Istanbul / Turkey;
- [5] František Varga, Miroslav Mojžiš, Rudolf Abrahám, (2013), Soil resistance and its impact on tillage depth, *In Acta Technologica Agriculturae*, vol. 1, pp. 26–30. DOI: 10.2478 / ata-2013-0007, Warsaw / Poland;
- [6] Kosolapov V.V., Kosolapova E.V., Igoshin D.N., Skorokhodov A.N., Rudenko A.A., (2019), *In Acta Technologica Agriculturae*, vol. 1, pp. 31–37. DOI: 10.2478 / ata-2019-0006, Warsaw / Poland;

- [7] Kovbasa V. P., Shvajko V. M., Gucol O.P. (2015), *Mechanics of agricultural materials and environments (Механіка сільськогосподарських матеріалів та середовищ)*, Kiev, Lysenko, 536 p., ISBN 978-617-640-175-9, Kiev / Ukraine;
- [8] Kushnariov A.S. (1980), *Mechanical and technological bases of the process of impact of working bodies of tillage machines and tools on the soil (Механико-технологические основы процесса воздействия рабочих органов почвообрабатывающих машин и орудий на почву)*, (PhD Thesis), Melitopol, 329p., Melitopol / Ukraine;
- [9] Petrov D. G. (1989), *Improving the efficiency of agricultural units by equipping trailed agricultural machines with propulsion systems (for example, a potato harvester) (Повышение эффективности сельскохозяйственных агрегатов за счет оснащения прицепных сельскохозяйственных машин двигателями (на примере картофелеуборочного комбайна))*, (PhD Thesis), Moscow, 22p., Moscow / Russia;
- [10] Popov A. A., (1984), *Improving the quality of the friction separators of potato machines (Повышение качества работы фрикционных сепараторов картофелеуборочных машин)*, (PhD Thesis), Cheliabinsk Institute of Agricultural Mechanization, 22 p., Cheliabinsk / Russia;
- [11] Simdiakin A.A., Kostenko M.Y., Rembalovich G. K., Kiryushin I.N. and all, (2015), Issues of improving potato technology (Актуальные вопросы совершенствования картофелеуборочной техники), *In the Scientific Journal of the Kuban State Agrarian University (Научный журнал Кубанского государственного аграрного университета)*, vol. 114(10), pp. 1–16., Krasnodar / Russia
- [12] Shymko A., Nalobina O., (2018), Analysis of the influence of the lemporary part of the working body on the grain-tu properties change, *In Współpraca Europejska*, vol. 6(37) 2018, p. 21-35, ISSN (PRINT) 2449-7320, Warsaw / Poland.

DESIGN OF DEEP-FERTILIZATION MECHANISM WITH DEFORMED GEARS AND PERFORMANCE TESTS

变形齿轮式深施机构设计与施肥性能试验

Feng Jinlong^{1,2,3)}, Yi Shujuan^{1*)}, Li Qichao³⁾

¹⁾ College of Engineering, Heilongjiang Bayi Agricultural University, Heilongjiang Daqing 163319, China

²⁾ Quality Supervision and Testing Center for Agricultural Processed Products of the Ministry of Agriculture (Daqing), Heilongjiang Daqing 163319, China

³⁾ College of Mechanical and Electrical Engineering, Lingnan Normal University; Zhanjiang 524048, China

*E-mail: yishujuan_2005@126.com

DOI: <https://doi.org/10.356.33/inmateh-65-34>

Keywords: deformed gear; deep-fertilization mechanism; fertilizer amount; test

ABSTRACT

Deep-fertilization mechanism is a key part of deep-fertilization liquid fertilizer applicator. To obtain a good-performance deep-fertilization mechanism, this study developed a deep-fertilization mechanism with deformed gears and designed a deformed gear fertilization test bench. Single-factor and central composite design tests were performed with the planet carrier, spray hole size and pump pressure as the test factors, and the fertilizer amount as the test index. The results of the single-factor test showed a linear functional relationship between fertilizer amount and pump pressure, an exponential functional relationship between planet carrier velocity and fertilizer amount, and an exponential relationship between spray hole size and fertilizer amount. The rotating and perpendicular test data were analyzed and optimized using Design-Expert 8.0.5 software. The result of the optimization is: 10.5 ml of fertilizer amount with pump pressure 0.36 MPa, planet carrier velocity 82 r/min, and spray hole size 2 mm. The test result can meet the agronomic requirements.

摘要

深施机构是深施型液态施肥机的关键部件,为得到具有较好施肥性能的深施机构,设计了变形齿轮式深施机构,研制了变形齿轮施肥试验台。采用单因素和正交旋转试验方案,以行星架转速、喷孔直径和泵的压力为试验因素,以施肥量为试验指标。单因素试验结果表明,施肥量与液泵压力呈线性函数关系,行星架转速与施肥量呈指数函数关系,喷孔直径与施肥量呈指数关系。运用 Design-Expert 8.0.5 软件对正交旋转试验数据进行分析和优化。最优结果:液泵压力 0.36MPa,行星架转速 82r/min,喷孔直径为 2mm 时,施肥量 10.5ml。试验结果满足农艺要求。

INTRODUCTION

Liquid fertilizer deep-fertilization technology is an agricultural technology which applies fertilizer at the root of crops by means of deep-fertilization mechanism. This method can directly deliver the nutrient composition of liquid fertilizer to the root system of crops, promote their absorption of nutrients, improve the utilization and reduce the run-off of fertilizer, which can lower the cost of agricultural production and protect the environment (*da Silva et al., 2017; Jagvir et al., 2018; Zhou et al., 2016*). Deep-fertilization mechanism is a key part of liquid fertilizer deep-fertilization applicator; hence it is very necessary to develop a liquid fertilizer deep-fertilization applicator suitable for Chinese situations. Currently there are mainly three types of deep-fertilization applicators, namely crank rocker mechanism, planetary elliptic gear mechanism, and all planetary elliptic gear mechanism. For crank rocker mechanism, the trajectory of the pricking is too forward, making it hard to control the inertia of the mechanism, enlarging the hole in the soil, and causing a waste of fertilizer (*Zhang et al., 2018a*). The planetary elliptic gear mechanism and all planetary elliptic gear mechanism can optimize the mechanism parameters by writing visual aids and using human-machine interaction method, which can improve the entering and exiting trajectory of the hole pricking mechanism, reducing the hole size and the waste of fertilizer (*Zhang et al., 2018b; Wang et al., 2013; Zhao et al., 2005*).

¹⁾Feng Jinlong, Lecturer, Ph.D.; Yi Shujuan, Professor, Ph.D.; Li Qichao, Associate professor, Ph.D.

However, the fertilizer loss of the above deep-fertilization applicators is still very high. Therefore, this paper proposed a liquid fertilizer injection deep-fertilization mechanism with deformed gears. As deformed gears can realize the vertical and horizontal changes of transmission ratio (Da Silva et al., 2017; Jin et al., 2018; Thomas, 2002), this type of deep-fertilization mechanism can improve the perpendicularity to the soil and further reduce the fertilizer loss. Then, bench test was performed on the deep-fertilization mechanism with deformed gears. By identifying a reasonable combination of working parameters, this study aimed to provide reference for the design and optimization of liquid fertilizer deep-fertilization applicator.

MATERIAL AND METHODS

STRUCTURE AND WORKING PRINCIPLE OF DEEP-FERTILIZATION MECHANISM WITH DEFORMED GEARS

Deep-fertilization mechanism is an important executive component of deep-fertilization liquid fertilizer applicator. According to the working characteristics of deep-fertilization liquid fertilizer applicator, the deep-fertilization mechanism was designed with deformed gears, which include five congruent deformed gears, one gearbox (planet carrier), two pairs of rocker arms and spray fertilizer needles, as shown in Fig. 1. The planet carrier is coaxially arranged with the central deformed gear. The planetary deformed gear is consolidated with the rocker arm with screw to be one component. When the mechanism is working, the central deformed solar gear stays fixed (similar to the sun wheel in epicyclic gear train), the planet carrier rotates and drives two intermediate deformed gears through meshing transmission to revolve around the central deformed solar gear, and meanwhile the planetary deformed gears at two sides would make cyclical movements through the meshing transmission with the intermediate deformed gears. The compound motion of the rocker arms and spray fertilizer needles, the clockwise rotational movement of the planetary deformed gears and the swing with the planetary deformed gears have constituted the special trajectory of the spray fertilizer needles and a whole process of fertilization is thus completed. According to agronomic requirements, the fertilization depth of liquid fertilizer should be around 80 mm. Therefore, a 20 mm long needle tip was welded at the lower part of the spray part to facilitate the entering of the spray fertilizer needles into the soil and avoid attaching soil when the mechanism is working. Each spray needle is designed with two liquid hole to reduce the number of sprays needs and improve the working efficiency.

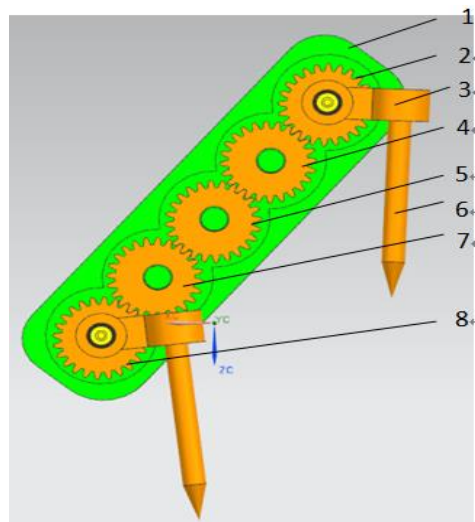


Fig. 1 - Structure of deep-fertilization mechanism with deformed gears

1. Planet carrier
2. Upper planetary deformed gear
3. Rocker arm
4. Upper intermediate deformed gear
5. Deformed solar gear
6. Spray fertilizer needle
7. Lower intermediate deformed gear
8. Lower planetary deformed gear

FERTILIZATION PERFORMANCE TESTS OF DEEP-FERTILIZATION MECHANISM WITH DEFORMED GEARS

Test equipment

In order to study the fertilization quality of deep-fertilization mechanism with deformed gears under certain combination of working parameters, a fertilization performance test was conducted on a self-built test bench of deep-fertilization mechanism with deformed gears. The structure of the test bench is shown in Fig. 2.

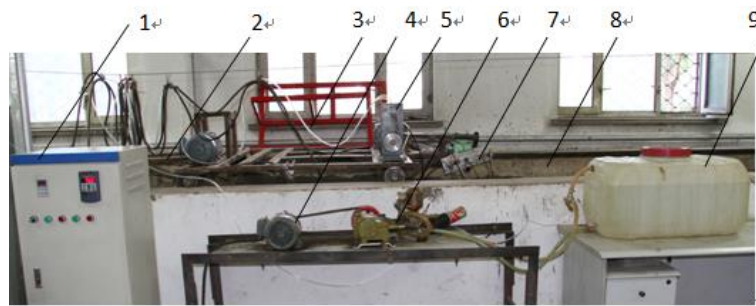


Fig. 2 - Test bench of deep-fertilization mechanism

1. Frequency converter; 2. Trolley; 3. Fertilization line; 4. Motor; 5. Distributor; 6. Liquid fertilizer pumps;
7. Deep-fertilization mechanism; 8. Test soil bin; 9. Liquid fertilizer container

As shown, the test bench mainly consists of frequency converter, trolley, fertilization line, motor, distributor, liquid fertilizer pump, deep-fertilization mechanism, test soil bin, and liquid fertilizer container, of which the deep-fertilization mechanism with deformed gears is the major working part. The working process is as follows: (1) Adjust the frequency converter to make the planet carrier speed and the executive mechanism movement satisfy the requirement; (2) Start the three-phase asynchronous motor to drive the liquid pump; (3) When the liquid pump works under a stable pressure, the trolley would be driven into the test area and the spray fertilizer needles of the deep-fertilization mechanism would prick into the soil in the test soil bin; (4) The distributor delivers certain liquid fertilizers with proper pressure into the spray fertilizer needles, which were sprayed into the soil from the spray hole; (5) The trolley keeps moving, the distributor stops delivering liquid fertilizer and the spray fertilizer needle stops fertilizing; (6) The deep-fertilization mechanism drags the spray fertilizer needles from the soil, and a deep-fertilization application of liquid fertilizer is therefore completed. As for the measurement of fertilizer amount, we start the liquid pump, adjust the planet carrier speed through the frequency converter, wait until the liquid pump becomes stable, and take the mean value of sprayed fertilizer as the fertilizer amount. A measuring cylinder was applied to get 10 times of fertilizer amount, and the average amount was used as the single-factor test data.

Test design

Fertilizer amount is an index to evaluate the fertilizing performance of deep-fertilization mechanism. The major working parameters that affect the fertilization performance include planet carrier speed, spray hole size and pump pressure. These three parameters were defined as the test factors of fertilization performance. A three-factor, five-level quadric rotating perpendicular test design was adopted. Table 1 shows the coding of factor levels. Design expert 8.0.1 software was adopted to process the test data and analyze the influence law of different factors on the fertilizer amount of the deep-fertilization mechanism (Wang *et al.*, 2017; Wang *et al.*, 2018; Viei *et al.*, 2015).

Table 1

Coding of factor levels			
Coded value	Planet carrier speed ($r \cdot \text{min}^{-1}$)	Liquid pump pressure (MPa)	Spray hole size (mm)
1.68	63	0.23	1
1	70	0.3	1.5
0	80	0.4	2
-1	90	0.5	2.5
-1.68	96	0.57	3

RESULTS AND ANALYSIS

Single-factor test

Impact of pump pressure on fertilizer amount

Single-factor test was performed on the pump pressure under the condition of 2.5 mm spray hole size and 80 r/min planet carrier speed with fertilizer amount as the index. Results were shown as Fig.3.

The curve regression fitting of pump pressure and fertilizer amount showed a nice goodness of fit of the linear functional relationship. The fitted equation and coefficient of determination were shown in Fig. 3. The results showed that the fertilizer amount and the pump pressure presented a significant linear functional relationship. As shown, the fertilizer amount satisfies the agronomic requirement of 5-20 ml when the pump pressure is controlled in the range of 0.3-0.5MPa. Therefore, the 0.3-0.5MPa pump pressure is initially defined as the reference pressure of subsequent tests.

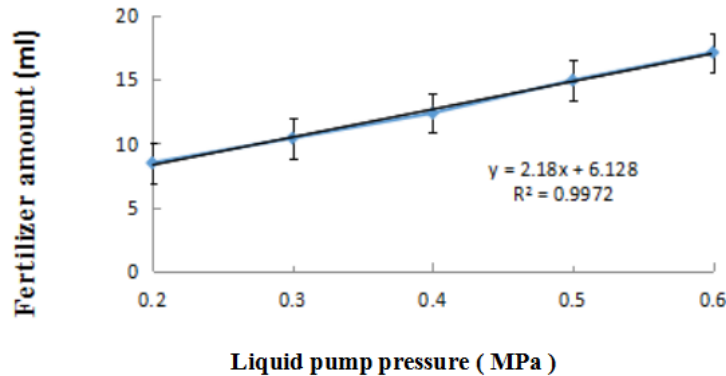


Fig. 3 - Impact of pump pressure on fertilizer amount

Impact of planet carrier speed on fertilizer amount

Single-factor test was performed on the planet carrier speed under the condition of 2 mm spray hole size and 0.4 MPa pump pressure with fertilizer amount as the index. Results were shown as Fig.4.

The curve regression fitting of planet carrier speed and fertilizer amount showed a nice goodness of fit of the linear functional relationship. The fitted equation and coefficient of determination were shown as Fig. 4. The results showed that the fertilizer amount and the planet carrier speed presented a significant logarithmic functional relationship. As shown, the fertilizer amount satisfies the agronomic requirement of 5-20 ml when the planet carrier speed is controlled in 70–90 r/min. Therefore, the 70–90 r/min of planet carrier speed is initially defined as the reference speed of subsequent tests.

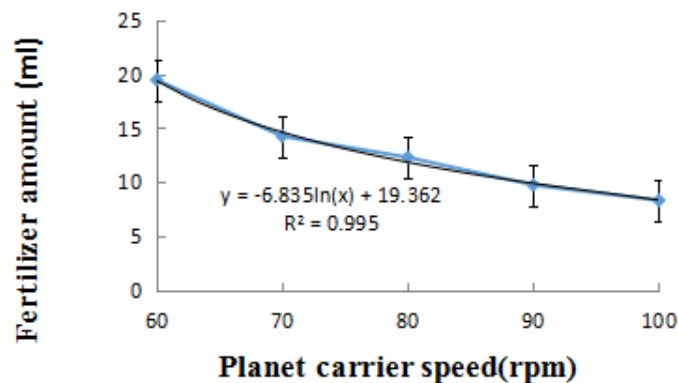


Fig. 4 - Impact of planet carrier speed on fertilizer amount

Impact of spray hole size on fertilizer amount

Single-factor test was performed on the spray hole size under the condition of 80r/min planet carrier speed and 0.4 MPa pump pressure with fertilizer amount as the index. Results were shown as Fig.5.

The curve regression fitting of spray hole size and fertilizer amount showed a nice goodness of fit of the power functional relationship. The fitted equation and coefficient of determination were shown as Fig. 5. The results showed that the fertilizer amount and the spray hole size presented a significant power functional relationship. As shown, the fertilizer amount satisfies the agronomic requirement of 5-20 ml when the spray hole size is controlled in 1.5-2.5 mm. Therefore, the 1.5-2.5 mm of spray hole size is initially defined as the reference size of subsequent tests.

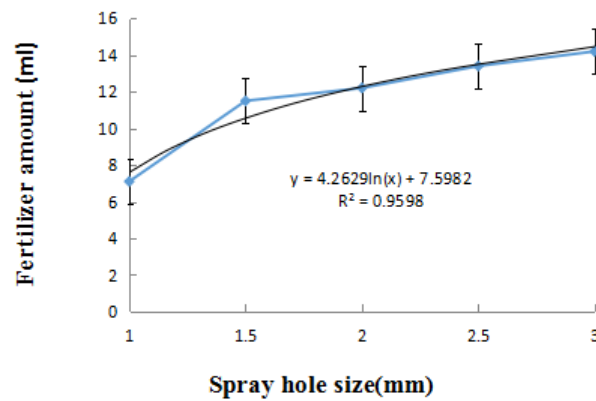


Fig. 5 - Impact of spray hole size on fertilizer amount

Multi-factor test

An orthogonal rotation test was performed on the basis of a single factor. The test scheme and results are shown in Table 2. Design-Expert 8.05 software is applied to analyze the test data in Table 2 to obtain the hydraulic pump pressure and the nozzle-hole diameter.

Table 2

Test plan and results

Number	Test factors			Performance index	
	Planet carrier speed x_1 (r·min ⁻¹)	Liquid pump pressure x_2 (MPa)	Spray hole size x_3 (mm)	Fertilizer amount y_1 (ml)	Fertilizer loss rate y_1 (%)
1	-1	-1	-1	10.6	1.6
2	-1	1	-1	17.2	3.3
3	-1	-1	1	12.5	1.6
4	-1	1	1	21.1	4.9
5	1	-1	-1	6.2	4.7
6	1	1	-1	6.8	3.6
7	1	-1	1	7.8	2.2
8	1	1	1	13.1	5
9	0	-1.68	0	6.5	3.2
10	0	1.68	0	18.4	6.5
11	0	0	-1.68	4.3	1.5
12	0	0	1.68	13.5	4.5
13	-1.68	0	0	25.7	1.5
14	1.68	0	0	7.3	5.5
15	0	0	0	12.3	2.9
16	0	0	0	12.3	3.1
17	0	0	0	12.3	2.9
18	0	0	0	12.4	2.9
19	0	0	0	12.4	3
20	0	0	0	12.3	3.1
21	0	0	0	12.4	2.9
22	0	0	0	12.3	3
23	0	0	0	12.3	2.9

The response surfaces are depicted in Figure 6, Figure 7 and Figure 8 to reflect the influences of the hydraulic pump pressure and the rotational speed of the planet carrier, as well as the nozzle-hole diameter and the rotational speed of the planet carrier, on the fertilization amount, and the multi-factor analysis of variance is shown in Table 3. Also, the response surfaces are depicted in Figure 9, Figure 10, and Figure 11, to reflect the influences of the hydraulic pump pressure and the nozzle-hole diameter, the hydraulic pump pressure and the rotational speed of the planet carrier, as well as the nozzle-hole diameter and the rotational speed of the planet carrier on the loss rate of fertilizer, and the multi-factor analysis of variance is exhibited in Table 4 (Otto et al., 2014; Fan et al., 2006; Xu et al., 2010).

At the significance level of $F_{0.05}$, it can be seen from Table 3 that x_2 , x_3 , x_1 , x_1x_2 , x_3^2 and x_1^2 have a significant influence on the fertilization amount and are the significant terms of the model. After removing insignificant terms, the fitted regression equation is:

$$y_1 = 51.68 - 2.08x_1 + 123.1x_2 + 26.08x_3 - 1.16x_2x_1 - 5.45x_3^2 + 0.01x_1^2 \quad (1)$$

Table 3

Analysis of variance for the influence of factors to the fertilization amount

Source	Sum of squares (ml)	Degree of freedom (ml)	F-value (ml)	Significance level (P>F) (ml)
Model	511.13	9	32.9	<0.0001
x_2	123.77	1	71.70	<0.0001
x_3	62.32	1	36.10	<0.0001
x_1	250.12	1	144.90	<0.0001
x_2x_3	5.61	1	3.25	0.0946
x_1x_2	10.81	1	6.26	0.0265
x_1x_3	0.55	1	0.32	0.5816
x_2^2	0.19	1	0.11	0.7476
x_3^2	29.54	1	17.11	0.0012
x_1^2	27.84	1	16.13	0.0015
Error	22.44	13		
Sum	533.57	22		

It is clear from Table 3 that the F value reflecting the effect of hydraulic pump pressure on the fertilization amount y_1 is 71.7, while the F value reflecting the effect of nozzle-hole diameter on the fertilization amount y_1 is 36.1. As thus, compared to nozzle-hole diameter, hydraulic pump pressure has a greater effect on fertilization amounts.

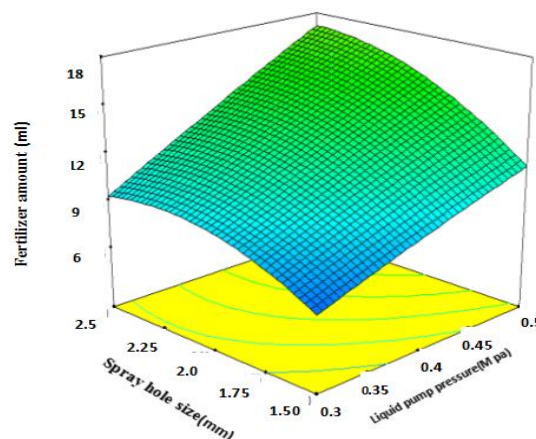


Fig. 6 - Impact of liquid pump pressure and spray hole size on fertilizer amount

Figure 6 shows that when the nozzle-hole diameter remains constant and the hydraulic pump pressure varies in the range 0.3-0.5 MPa, the fertilization amount will gradually increase with increasing hydraulic pump pressure; on the other hand, when the pressure at the hydraulic pump remains constant and the nozzle-hole diameter varies in the range 1.5-2.5 mm, the fertilization amount gradually increases with increasing nozzle-hole diameter. The response surface changes faster in the direction of hydraulic pump pressure than in the direction of nozzle-hole diameter.

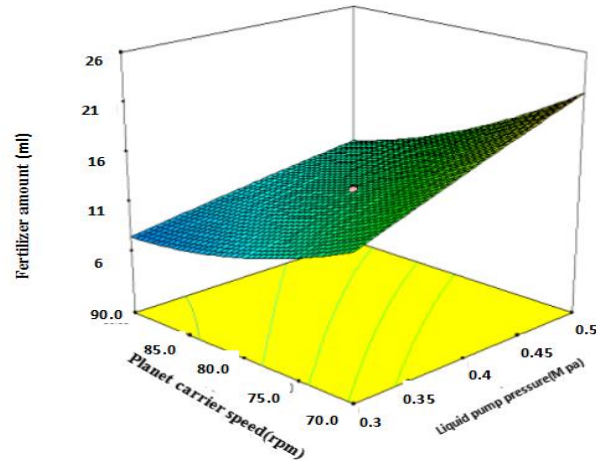


Fig. 7 - Impact of liquid pump pressure and planet carrier speed on fertilizer amount

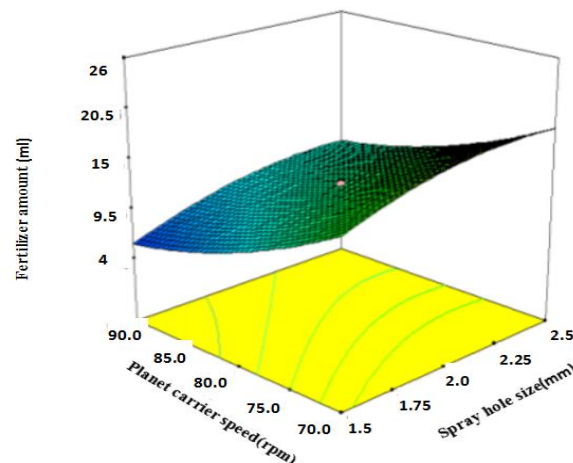


Fig. 8 - Impact of spray hole size and planet carrier speed on fertilizer amount

Figure 7 visibly demonstrates that when the pressure at the hydraulic pump remains constant and the rotational speed of the planet carrier varies in the range 70-90 r/min, the fertilization amount will gradually decrease with an increase in rotational speed; on the other hand, when the rotational speed of the planet carrier remains constant and the pressure at the hydraulic pump varies in the range 0.3-0.5 MPa, the fertilization amount will gradually increase with an increase in pressure. The response surface changes faster in the direction of the rotational speed of the planet carrier than in the direction of the pressure at the hydraulic pump. As per Table 3, the F value reflecting the effect of the rotational speed of the planet carrier on the fertilization amount y_1 is 144.90, while the F value reflecting the effect of the pressure at the hydraulic pump on the fertilization amount y_1 is 71.7. As thus, compared to the pressure at the hydraulic pump, the rotational speed of the planet carrier has a greater effect on fertilization amounts.

It can be seen from Figure 8 that when the nozzle-hole diameter remains constant and the rotational speed of the planet carrier varies in the range 70-90 r/min, the fertilization amount will gradually decrease with increasing rotational speed; on the other hand, when the rotational speed of the planet carrier remains constant and the nozzle-hole diameter varies in the range 1.5-2.5 mm, the fertilization amount will gradually rise with declining diameter.

The response surface changes more slowly in the direction of the rotational speed of the planet carrier than in the direction of the nozzle-hole diameter. According to Table 3, the F value reflecting the effect of the rotational speed of the planet carrier on the fertilization amount y_1 is 112.56, while the F value reflecting the effect of the nozzle-hole diameter on the fertilization amount y_1 is 36.10. As thus, compared to the nozzle-hole diameter, the rotational speed of the planet carrier has a greater effect on fertilization amounts.

At the significance level of $F_{0.05}$, it can be seen from Table 4 that $x_2, x_3, x_1, x_1x_2, x_3^2$ and x_1^2 have a significant influence on the fertilization loss rate and are the significant terms of the model. After removing insignificant terms, the fitted regression equation is:

$$y_2 = 30.37 - 0.77x_1 + 13.71x_2 + 1.69x_3 - 0.55x_1x_2 + 51.9x_2^2 + 0.0053x_1^2 \quad (2)$$

Table 4

Analysis of variance for the influence of factors on fertilization loss rate

Source	Sum of squares (ml)	Degree of freedom (ml)	F-value (ml)	Significance level (P>F) (ml)
Model	62.03	9	22.10	< 0.0001
x_2	17.25	1	55.34	< 0.0001
x_3	9.84	1	31.55	< 0.0001
x_1	22.38	1	71.77	< 0.0001
x_2x_3	0.72	1	2.31	0.1525
x_1x_2	2.42	1	7.76	0.0154
x_1x_3	0.60	1	1.94	0.1870
x_2^2	4.28	1	13.72	0.0026
x_3^2	0.013	1	0.043	0.8384
x_1^2	4.57	1	14.67	0.0021
Error	4.05	13		
Sum	66.08	22		

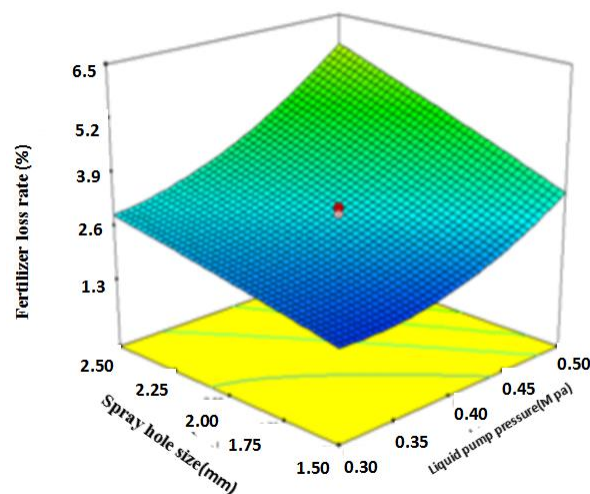


Fig. 9 - Impact of liquid pump pressure and spray hole size on fertilizer loss rate

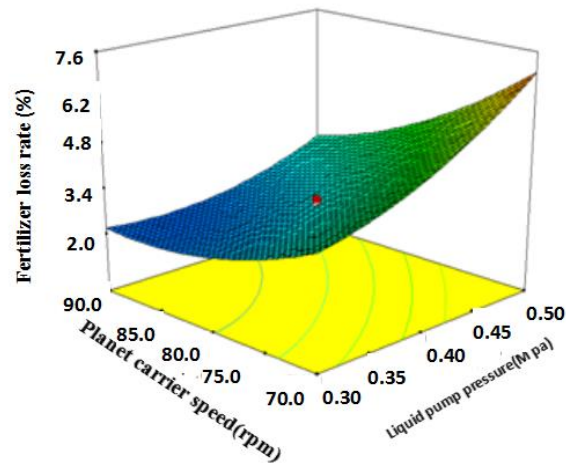


Fig. 10 - Impact of liquid pump pressure and planet carrier speed on fertilizer loss rate

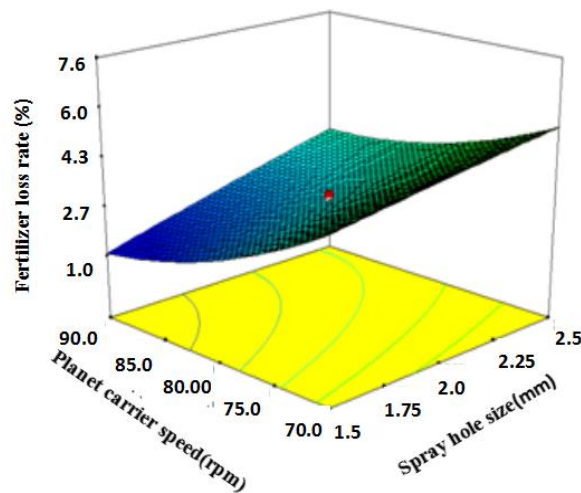


Fig. 11 - Impact of spray hole size and planet carrier speed on fertilizer loss rate

Figure 9 shows that when the nozzle-hole diameter remains constant and the pressure at the hydraulic pump varies in the range 0.3-0.5 MPa, the fertilization loss rate will gradually increase with increasing hydraulic pump pressure; on the other hand, when the pressure at the hydraulic pump remains constant and the nozzle-hole diameter varies in the range 1.5-2.5 mm, the fertilization loss rate gradually increases with increasing nozzle-hole diameter. The response surface changes faster in the direction of hydraulic pump pressure than in the direction of nozzle-hole diameter. Table 4 indicates that the F value reflecting the effect of hydraulic pump pressure on the fertilization loss rate y_2 is 55.34, while the F value reflecting the effect of nozzle-hole diameter on the fertilization loss rate y_2 is 31.55. Hence, compared to nozzle-hole diameter, the pressure at the hydraulic pump has a greater effect on the fertilization loss rate.

Figure 10 exhibits that when the pressure at the hydraulic pump remains constant and the rotational speed of the planet carrier varies in the range 70-90 r/min, the fertilization loss rate will gradually decrease with increasing rotational speed; on the other hand, when the rotational speed of the planet carrier remains constant and the pressure at the hydraulic pump varies in the range 0.3-0.5 MPa, the fertilization loss rate will gradually increase with increasing pressure. The response surface changes fast in the direction of the rotational speed and it changes slowly in the direction of the hydraulic pump pressure. As per Table 4, the F value reflecting the effect of the rotational speed of the planet carrier on the fertilization loss rate y_2 is 71.77, while the F value reflecting the effect of the pressure at the hydraulic pump on the fertilization loss rate y_2 is 55.34. Hence, compared to the pressure at the hydraulic pump, the rotational speed of the planet carrier has a greater effect on fertilization loss rates.

In accordance with Figure 11, when the nozzle-hole diameter remains constant and the rotational speed of the planet carrier varies in the range 70-90 r/min, the fertilization loss rate will gradually decrease with increasing rotational speed; on the other hand, when the rotational speed of the planet carrier remains constant and the nozzle-hole diameter varies in the range 1.5-2.5mm, the fertilization loss rate will gradually rise with an increase in the nozzle-hole diameter. The response surface changes fast in the direction of the rotational speed of the planet carrier and it changes slowly in the direction of the nozzle-hole diameter. It is clear from Table 4 that the F value reflecting the effect of the rotational speed of the planet carrier on the fertilization loss rate y_2 is 71.77, while the F value reflecting the effect of the nozzle-hole diameter on the fertilization loss rate y_2 is 31.55. Hence, compared to the nozzle-hole diameter, the rotational speed of the planet carrier has a greater effect on fertilization loss rates.

Test optimization and verification

In order to find the optimal combination of parameters for hydraulic pump pressure, nozzle-hole diameter and rotational speed of the planet carrier, this study uses fertilization amount and fertilization loss rate as performance indicators, and the constraint conditions of agronomic requirements as boundary conditions in order to analyze the regression equation of fertilization amount and fertilization loss rate and get a mathematical model of nonlinear programming:

$$\begin{cases} y_1 \in (10,20) \\ y_2 \in (0,2.5) \\ s.t. 70 \leq x_1 \leq 90 \\ 0.3 \leq x_2 \leq 0.5 \\ 1.5 \leq x_3 \leq 2.5 \end{cases} \quad (3)$$

where the objective function for parameter optimization is

$$\begin{cases} y_1 = 51.68 - 2.08x_1 + 123.1x_2 + 26.08x_3 - 1.16x_1x_2 - 5.45x_3^2 + 0.01x_1^2 \\ y_2 = 30.37 - 0.77x_1 + 13.71x_2 + 1.69x_3 - 0.55x_1x_2 + 51.9x_1^2 + 0.0053x_1^2 \end{cases} \quad (4)$$

In this study, Design-Expert 8.05 software is applied for parameter optimization, and the optimal combination of parameters for hydraulic pump pressure, nozzle-hole diameter and rotational speed of the planet carrier is gained: the rotational speed of the planet carrier at 82.15 r/min, the pressure at the hydraulic pump at 0.36 MPa, the nozzle-hole diameter at 2.04 mm, the output fertilization amount at 10.5 mL and the fertilization loss rate at 2.3%, and this combination has met the fertilization performance requirements.

Table 5

Verification of testing results

Rotational speed of the planet carrier $x_1 / \text{r}\cdot\text{min}^{-1}$	Factor		Performance indicators	
	Hydraulic pump pressure x_2 / MPa	Nozzle-hole diameter x_3 / mm	Fertilization amount $y_1 / \text{mL}\cdot\text{s}^{-1}$	Fertilization loss rate $y_2 / \%$
82	0.36	2	10.5	2.31
			10.6	2.35
			10.4	2.33
			10.4	2.28
			10.6	2.36

Five sets of verification testing were carried out based on the optimal value optimal combination of parameters, i.e. the rotational speed of the planet carrier at 82 r/min, nozzle-hole diameter at 2mm and hydraulic pump pressure at 0.36 MPa.

The verification testing results are illustrated in Table 5. It can be seen from Table 6-13 that as per the test results, for the fertilization amount, the maximum is 10.6 mL, the minimum is 10.4 mL, the average is 10.5 mL; for the fertilization loss rate, the maximum is 2.36%, the minimum is 2.28%, and the average is 2.33%. These results have proved that the optimal combination of parameters can meet the performance standards required by fertilization.

CONCLUSIONS

(1) A test bench of deep-fertilization mechanism with deformed gears was established. Single-factor test showed that the fertilizer amount presented a linear function increase trend with the increase of the pump pressure, an exponential function decrease trend with the increase of planet carrier speed, and an exponential function increase trend with the increase of spray hole size.

(2) A quadric rotating perpendicular test design was adopted to establish a mathematical model of fertilization performance index and test factors, and the impacts of interaction relationship on the fertilization index were analyzed.

(3) The test results were analyzed and optimized using Design-Expert 8.0.5 software. Results show that an optimal fertilizing performance can be achieved with following parameter combination: liquid pump pressure: 0.36 MPa; spray hole size: 2 mm; planet carrier speed: 82r/min. The fertilizer amount was 10.5 mL and fertilizer loss rate was 2.33%, with this combination, which can meet the agronomic requirement of fertilization.

ACKNOWLEDGMENTS

Thank you for Postdoctoral Science Foundation of Heilongjiang Province of China (Grant No. LBH-Z18254), Heilongjiang Bayi Agricultural University Support Program for San Heng San Zong (TDJH201803), Special project for doctoral talents of Lingnan Normal University (ZL2021019)

REFERENCES

- [1] Da Silva M.J., Magalhães P.S.G. (2017). A liquid injection dosing system for site-specific fertilizer management. *Biosystems Engineering*. 163:150-158. doi.org/10.1016/j.biosystemseng.2017.09.005
- [2] Da Silvamj, Franco H.C.J., Magalhes P.S.G. (2017). Liquid fertilizer application to ratoon cane using a soil punching method. *Soil & Tillage Research*, 165: 279-285.
- [3] Edathiparambil Vareed Thomas. (2002). Development of a mechanism for transplanting rice seedlings. *Mechanism and Machine Theory*, 37(4): 395-410. https://doi.org/10.1016/S0094-114X(01)00071-4
- [4] Fan C.J., Xiong G.M., Zhou M.F. (2006). *Application and advancement of ADAMS*. Beijing: China Machine Press.
- [5] Jagvir Dixit, Vinay Kumar, Mudasir Ali. (2018). Development and Evaluation of a Single Row Manual Vegetable Transplanter. *Agricultural Engineering Today*. 42(2): 58-66.
- [6] Jin S.J., Frank G.O., Jae M.J. et al. (2018). A study on improving the performance of the planting device of a vegetable transplanter. *Journal of Biosystems Engineering*, 43 (3): 202-210.
- [7] Otto R., Franco H.C.J., Faroni C.E. et al. (2014). The role of nitrogen fertilizers in sugarcane root biomass under field conditions. *Agricultural Sciences*, 5(14): 1527-1538.
- [8] Viei R.A., Megda M.X., Mariano E., Leite J.M. et al. (2015). Contribution of fertilizer nitrogen to the total nitrogen extracted by sugarcane under Brazilian field conditions. *Nutrient Cycling in Agroecosystems*, 101(2): 241 -257.
- [9] Wang J.F., Wang J.W., Ju J.Y. et al. (2013). Research progress on pricking hole mechanism of deep-fertilization liquid fertilizer applicator. *Journal of Northeast Agricultural University*, 44(05): 157-160. DOI: 10.19720/j.cnki.issn.1005-9369.2013.05.030
- [10] Wang J.W., Zhou W.Q., Bai H.C. et al. (2018). Design and experiment of differential-type bidirectional distribution device for fertilizer supply for deep-fertilizer liquid fertilizer application. *Transactions of the Chinese Society for Agricultural Machinery*, 49 (6): 106-111. DOI: 10.6041/j.issn.1000-1298.2018.06.012.
- [11] Wang J.W., Zhou W.Q., Wang X. et al. (2017). Oblique type pricking hole mechanism based on Lagrange curve for cubic fitting trajectory. *Transactions of the Chinese Society for Agricultural Machinery*, 48(5):79-85. DOI:10.6041/j.issn1000-1298.2017.05.009.

- [12] Xu X.H., He M.Z. (2010). *Experimental design and application of Design-Expert and SPSS*. Beijing: Science Press.
- [13] Zhang L.B., Cai Z.X., Wang Li Wei (2018). Coupled Eulerian-Lagrangian finite element method for simulating soil-tool interaction. *Biosystems Engineering*, 175: 96-105.
- [14] Zhang L.B., Cai Z.X., Liu H.F. (2018). A novel approach for simulation of soil-tool interaction based on an arbitrary Lagrangian–Eulerian description. *Soil and Tillage Research*, 178: 41-49. <https://doi.org/10.1016/j.still.2017.12.011>
- [15] Zhao Y., Yu G.H., Wu C.Y. (2005). *Numerical analysis and synthesis of mechanism*. Beijing: China Machine Press.
- [16] Zhou C.J., Hu B., Chen S.Y. (2016). Design and analysis of high-speed cam mechanism using Fourier series. *Mechanism and Machine Theory*, 104: 118-129.

DESIGN AND EXPERIMENTAL STUDY OF FLEXIBLE THRESHING UNIT FOR CHINESE CABBAGE SEEDS

大白菜种子柔性脱粒装置设计与试验

Wang Shengsheng^{1,2)}, Chen Pan¹⁾, Ji Jiangtao^{1,2)}, Lu Mengqing¹⁾

¹⁾ College of Agricultural Equipment Engineering, Henan University of Science and Technology, Luoyang; 471003, China;

²⁾ Collaborative Innovation Center of Machinery Equipment Advanced Manufacturing of Henan Province, Luoyang; 471003, China

*Email: wangsheng5288@126.com

DOI: <https://doi.org/10.356.33/inmateh-65-35>

Keywords: Chinese cabbage, seeds harvested, flexibility threshing unit, experiment

ABSTRACT

In order to solve the problems of low efficiency of artificial harvesting method and high breakage rate and undepurated rate of traditional threshing method, a new flexible threshing device of Chinese cabbage seeds was designed, which was composed of flexible round head nail teeth and circular tube concave plate. Hertz contact collision theory was used to analyze and determine the structural parameters of the new threshing unit. The interaction force of different threshing elements materials were analyzed by using EDEM. The feasibility of the flexible threshing unit was verified by the comparison test of the distribution of threshed mixture. Finally, the orthogonal test was carried out to study the influence of the movement parameters of each structure on the cleaning rate and the rate of undepurated, and the weight matrix method was used to optimize it. The results indicate that under the condition the rotating speed of the threshing cylinder 750 rpm, the concave clearance 20 mm, and the feeding rate 1.4 kg/s, the threshing performance of the flexible threshing unit was the best. At this time, the breaking rate was 0.064%, and the un-threshing rate was 0.67%, which both met the relevant industry standards.

摘要

针对大白菜种子人工收获方式效率低、传统脱粒方式存在破碎率及未脱净率较高的问题，设计了一种新型的柔性圆头钉齿和圆管凹板组合的大白菜种子柔性脱粒装置。采用 Hertz 接触碰撞理论确定了柔性圆头钉齿及圆管凹板的结构参数，采用离散元仿真软件 EDEM 对比分析了不同脱粒元件及凹板与物料接触时的受力情况，结合脱出物分布对比试验结果进一步验证了该柔性脱粒装置的可行性。最后以滚筒转速、脱粒间隙及喂入量为试验因素，以种子破碎率、未脱净率为试验指标，开展正交试验，采用权矩阵法优化得到了该脱粒装置的最佳工作参数组合。结果表明：当脱粒滚筒转速为 750r/min，脱粒间隙为 20mm，喂入量为 1.4kg/s 时，该柔性脱粒装置的脱粒性能达到最佳，此时破碎率为 0.064%，未脱净率为 0.67%，满足国家相关行业标准。

INTRODUCTION

Chinese cabbage has excellent taste and high nutritional value. It is one of the vegetables with high domestic demand. In recent years, with the diversity of consumer demand, the Chinese cabbage breeding industry has also developed rapidly, and the planting area has grown rapidly (Li et al, 2018). The manual harvesting method of direct seed harvesting is low in efficiency and cannot meet the large-area harvesting requirements of the breeding base; when the existing harvesting models on the market are used for operation, the structure or working parameter configuration is not good, which may easily cause a higher seed breakage rate and greater loss (Wu et al, 2014; Ji et al, 2020; Steponavicius et al, 2018). Therefore, there is an urgent need to solve the problem of mechanized harvesting of Chinese cabbage seeds, and the threshing device is the core working component of the cabbage seed combine harvesting equipment. Improving its threshing performance has become a key issue restricting the development of Chinese cabbage seed combine harvesting equipment.

At present, domestic and foreign research on low-loss threshing devices for Chinese cabbage seeds is still a blank field. Generally speaking, there are currently two ways to reduce the threshing loss of grains. One is to use intelligent control and automation technology to adjust the working parameters of the threshing device in combination with the crop attributes and the operating conditions of the machine, so as to reduce

¹ Shengsheng Wang, Lecturer, Ph.D.Stud.; Pan Chen, M.S.Stud.; Jiangtao Ji, Prof.; Mengqing Lu, M.S.Stud.

the crushing rate and loss rate (Rahman et al, 2019; Jahanbakhshi et al, 2017; Badretdinov et al, 2019; Bello et al, 2019). The second is to improve the threshing effect by improving the structure and material of the threshing and separating device, such as the structure and material of the threshing element, the structure of the concave plate and the size of the sieve hole. For example, Pužauskas et al, (2016), conducted theoretical analysis, simulation and verification tests on three different shapes of concave grids, and obtained the conclusion that the inclined concave grids are more effective for corn ear threshing. Dhananchezhiyan et al., (2013), designed a kind of flexible spikes, established a dynamic model of the flexible threshing process of rice, and verified through experiments that the flexible spikes can meet the needs of rice separation while effectively reducing the seed breakage rate and have good adaptability.

Based on the above theory and experimental research, in order to solve the problem of low-loss threshing of Chinese cabbage seeds and combine the characteristics of Chinese cabbage seed harvesting, this paper proposes the use of flexible round-head spikes and round tube concave plates for flexible low-loss threshing of Chinese cabbage seeds. Taking the collision contact and mechanical analysis between the material and the threshing element as the starting point, the contact force of the flexible threshing element and the concave plate is studied and analyzed, the structural parameters are determined, the EDEM simulation analysis and the bench test results are combined, and the matrix weight is adopted. Method optimization obtained the optimal structure and working parameter combination of the flexible threshing device, which proved the feasibility of the flexible threshing device.

MATERIAL AND METHODS

OVERALL STRUCTURE AND WORKING PRINCIPLE

The overall structure of the Chinese cabbage seed flexible threshing device is shown in Figure 1; it is mainly composed of threshing drum, guide plate, top cover and concave plate.

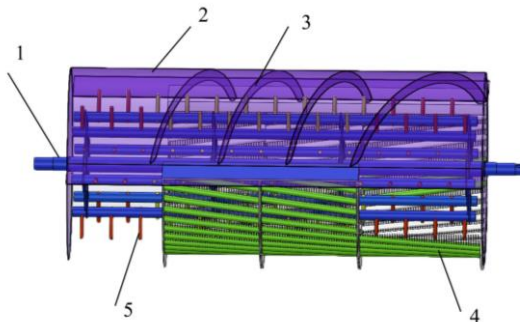


Fig.1- Key structure of Chinese cabbage seed threshing device
1. Threshing drum; 2. Top cover; 3. Deflector; 4. Concave plate; 5. Threshing element

When working, the power is provided by the frequency conversion motor, which drives the threshing drum to rotate through the drum main shaft. The Chinese cabbage plant enters the threshing chamber under the force of the rigid spike-teeth at the feeding entrance to complete the feeding process. Chinese cabbage seed silques spiral backward under the combined action of drum threshing elements and top cover deflector. In this process, the silique completes the threshing process under the action of the threshing element and the concave plate to hit, collide and knead. In this area, the threshing element is a flexible round head spike, and the concave plate is a round tube concave plate. This structure can effectively reduce the rigid impact on the seeds, reduce mechanical damage, and prevent the seeds from staying on the concave plate. The removed Chinese cabbage seeds are separated from the long stalks, silques and other sundries through the concave plate of the round tube to complete the separation process and be collected by the receiving device; In this process, the contact area between the concave plate of the round tube and the exudates is large, and the contact time is long, which is beneficial to the timely separation of seeds and reduces the entrainment loss; the long stalks are discharged through the grass discharge opening under the action of the rigid long spikes at the tail of the drum. Complete the cleaning process.

DESIGN OF THE KEY PARAMETER

Structure Design of Threshing Drum

The length of the horizontal axial flow threshing drum is closely related to its own threshing and separation capacity, The longer the threshing drum, the greater the amount of material that can be fed, but the power consumption and seed breakage rate of threshing also increase.

The increase of stalks, siliques and other miscellaneous residues caused excessive cleaning load. The calculation formula for the length of the horizontal axial flow threshing drum is:

$$L \geq q/q_0 \quad (1)$$

where L is the length of the threshing drum, m; q is the feed amount of the threshing device, kg/s; q_0 is the allowable feed amount per unit length of the threshing drum, generally 1.5~2.0 kg/s. The feeding amount of the flexible threshing device is calculated based on the maximum feeding amount of 2 kg/s, and the length range of the threshing drum is 1~1.3m. Taking into account that the length of the drum is restricted by the configuration and structural dimensions of the combined food harvester, this paper takes the length of the threshing drum as 1.2m.

The diameter of the horizontal axial flow threshing drum is:

$$D_z \geq D_g + 2h_z \quad (2)$$

In the formula, D_g is the diameter of the threshing element, mm; h_z is the height of the threshing element, mm.

Because the diameter of the threshing drum is too small, it is easy to entangle the crop and reduce the separation area of the concave plate. However, if the diameter of the drum is too large, the power consumption of threshing will increase, usually D_g is greater than 300 mm. Based on comprehensive consideration, the barrel diameter of the threshing drum is determined to be 320 mm. The working height of spike-tooth threshing element is generally 50~100 mm. In order to ensure a suitable threshing line speed, the height of the threshing element in the feeding and threshing section in this study is 70 mm. In order to facilitate more thorough grass removal, the threshing element height in the trash removal section is 75 mm, so the roller diameter ranges from 460 to 470 mm.

Design of Threshing Element

Arrangement of threshing elements

The Chinese cabbage seed threshing drum adopts a three-stage combined structure, as shown in Figure 2. The feeding section uses rigid spike-tooth threshing elements to improve the ability of the threshing elements to grasp and feed plants. In order to reduce the seed damage during the threshing process, the nails of the threshing separation section are made of polyurethane rubber materials to reduce the rigid impact on the Chinese cabbage seeds during the threshing process and reduce seed damage. The tail has a long rigid spike-tooth structure to enhance the ability to discharge long stems and other debris outwards.

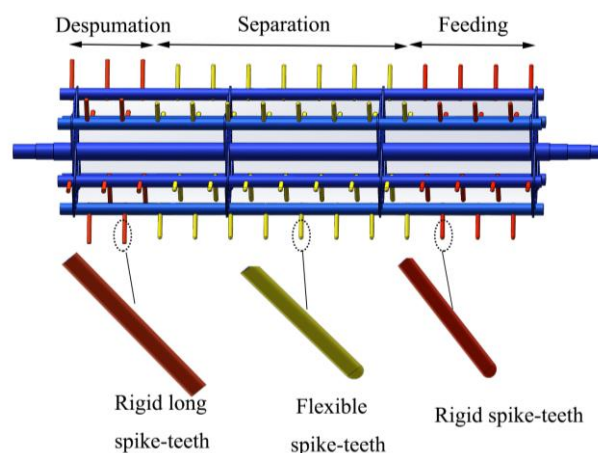


Fig. 2 - Threshing drum structure of Chinese cabbage seed

The common value of spike-tooth trace distance is 25~50 mm, 42 mm is selected for this design (Guan *et al*, 2020). In order to realize the turning and backward movement of materials in the cycle threshing process, each threshing element is arranged in a spiral line. In order to increase the number of impacts of the threshing element per unit length on the material, the number of screw heads $K=3$ is selected. The number of spike-tooth rows is usually 6-12, and the tooth pitch is usually 50-100 mm. If the distance is too small, the stalk will be severely broken, and the threshing power consumption will increase. In this design, the number of tooth rows is 6, and the tooth pitch $l=84$ mm.

Spike-tooth collision analysis and optimization design

Compared with rigid spikes, flexible threshing spikes made of polyurethane materials will deform during the threshing process. From contact with the material to the completion of the threshing action, the angle of rotation is greater than that of rigid spikes, thus prolonging the contact time with the material. According to the friction and movement characteristics of peanut pods, we determined that the Angle of sliding screen was 40° based on experiment of test-bed under the condition that material is not congested during the decline of materials. When the rotating speed of the drum is constant, since the quality of the flexible threshing tooth is constant, the impulse to the seed is constant, from the momentum theorem; it can be known that with a constant impulse, the impact force for increasing the contact time must be reduced. Therefore, the use of flexible materials for threshing spikes can reduce the impact force on the Chinese cabbage seeds and reduce the seed breakage rate.

In references, the mechanical analysis of the contact between the spike and the seed is carried out from the two positions of the tip and the side of the spike, without considering the sharp collision with too small contact area (Fan et al, 2019). In actual working conditions, the tooth tip edges and corners also collide with the seeds, and the damage to the seeds is more serious. In general, when the contact and collision force between the seed and the different threshing elements is equivalent (that is, the difference is not large), a larger contact area can weaken the stress concentration phenomenon, thereby reducing damage.

In order to further reduce the damage caused by the tip angle of the spike to the seed, the structure of the flexible spike was optimized. Based on the Hertz contact theory, a theoretical analysis of the impact process of Chinese cabbage siliques and two kinds of threshing elements before and after structural optimization (Chuan-udom et al, 2011) was made. The process of collision and contact between two kinds of spikes and Chinese cabbage seeds is shown in Figure 5. In order to facilitate comparative analysis, the incident angle of the collision between the Chinese cabbage seeds and the spike teeth is taken as 45° , the seeds in Figure 3 are simplified as spheres, and the model in the schematic diagram is enlarged.

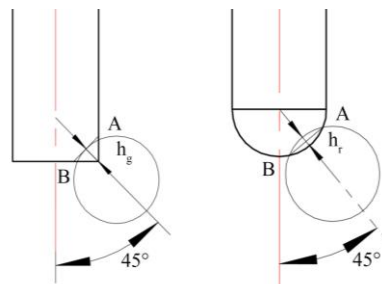


Fig. 3- Collision diagram

In Figure 3, before and after the optimization of the spike-tooth structure, the contact area with Chinese cabbage seeds is:

$$S_1 = 2h_g r \quad (3)$$

$$S_2 = \pi \left[R^2 - (R - h_r)^2 \right] \quad (4)$$

Among them, r represents the diameter of the Chinese cabbage seed ball, which is taken as 2.2 mm; h_g , h_r respectively represent the compression amount of the Chinese cabbage seed when it collides with the conventional spikes and the optimized spikes, mm; R represents the diameter of the optimized spikes, mm.

Through previous compression experiments, it was obtained that when the Chinese cabbage seeds (variety Jincai No. 3) with a moisture content of 28.39-30.25% were compressed, the compression deformation range for the seeds to break was 0.4-0.6 mm. In order to prevent the seeds from breaking, this paper takes the minimum compression $h_{\min} = 0.4$ mm.

In the two contact modes,

$$S_2 - S_1 = \pi \cdot (2R - h_r) \cdot h_r - 2h_g \cdot r \quad (5)$$

$$h_r = h_g = h_{\min} \quad (6)$$

Then, there are $S_2 - S_1 = h_{\min} (2\pi R - \pi h_{\min} - 2r) > 0$ constants established. Therefore, the contact area between the spike-tooth and the seed after the structure optimization is always larger than that before the

structure optimization. Therefore, the structure-optimized round-head spikes can reduce the impact on Chinese cabbage seeds, thereby reducing threshing damage.

Comprehensively considering the threshing requirements, structural dimensions, and the difficulty of the actual processing technology, the diameter of the round head spike and the round head diameter of the final threshing separation section are both 8 mm. In order to ensure the smooth progress of the feeding and discharging process, the diameter of the rigid spikes in the feeding section and discharging section is 10 mm.

Parameter design of concave plate structure

Based on the problems of the conventional grid-type intaglio plate in the mechanized harvesting process of Chinese cabbage seeds, a round tube-shaped de-parting concave plate was optimized, as shown in Figure 4.

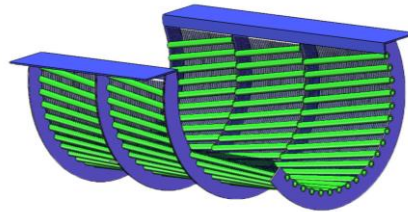


Fig. 4- Round tube for plates

Considering the requirements of the whole machine structure size and guaranteeing the performance of threshing operation, the round-tube threshing concave plate uses a round steel pipe with an outer diameter of 18 mm and a thickness of 3 mm instead of the horizontal grid plate in the grid-type concave plate. Chinese cabbage siliques are fatigued and fractured under multiple cycles of threshing elements and round tube concave plates, rather than one-time fracture, in order to achieve the purpose of reducing the rate of seed breakage. In order to further improve the possibility of the material on the circular tube-shaped concave plate, the circular tube is installed along the axis of the concave plate at an offset of 10° from the axis, which is consistent with the direction of the material's spiral movement in the axial direction when the threshing drum is working, so as to facilitate the backward pushing of the material.

The collision force between the Chinese cabbage silique and the round tube under the two installation methods is shown in Figure 5. Assume that the silique collides with the tube at the center of speed v .

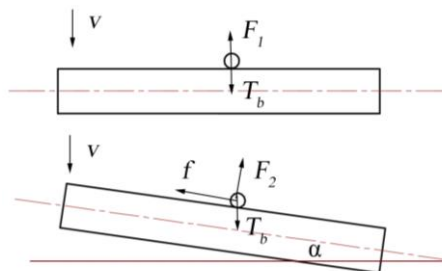


Fig. 5- Schematic diagram of collision between pod and concave tube

As can be seen from the figure, the collision reaction force of the silique by the tube is as follows:

$$F_1 = T_b \quad (7)$$

$$F_2 = T_b \cdot \cos \alpha \quad (8)$$

Among them, F_1 is the collision reaction force of the silique when the tube is installed directly, N; F_2 is the collision reaction force of the silique when the tube is installed obliquely, N; T_b is the force of gravity on the silique, N; α is the installation angle of the circular tube deviating from the axial direction of the concave plate.

Because $F_1 - F_2 = T_b \cdot (1 - \cos \alpha) > 0$, so $F_2 < F_1$. Under the same conditions, the collision reaction force of the round tube straight-mounted threshing concave plate on the cabbage silique is greater than the collision

reaction force of the round tube inclined threshing concave plate on the silique. Therefore, the concave plate with the round tube inclined installation method is adopted. It helps reducing the collision reaction force to the silique and reducing the rate of seed breakage. At the same time, there is friction f when the silique interacts with the oblique-mounted round tube, and the friction f has a certain rubbing effect on the silique to ensure the removal rate and improve the quality of threshing.

CONTACT MECHANICS SIMULATION OF THRESHING PROCESS BASED ON EDEM

Model creation and parameter setting

Using SolidWorks software, the simplified models of threshing devices under two combined forms were established and imported into EDEM software. Considering that the materials in the Chinese cabbage plant threshing drum mainly include seeds, stalks and cabbage siliques, referring to the relevant literature and combining with the previous testing of the physical properties of the various components of the Chinese cabbage plant, under the premise of ensuring the consistency of the model appearance characteristics, are established their own discrete element models by manual multi-ball filling, as shown in Figure 6 (Wang *et al*, 2018). Among them, cabbage seeds are spherical with a diameter of 2.2 mm. The triaxial dimensions of siliques are 52.40 mm (length), 4.55 mm (width) and 3.14 mm (height) respectively. The long stem is a circular arc with a diameter of 9.80 mm and a length of 70 mm; Hertz-Mindlin (No Slip) contact was selected on the Globals panel in combination with the results of the previous physical property test and relevant literature, and the threshing device, material properties and mechanical property parameters of the model were set as shown in Table 1 and Table 2 (Lu, Ma, & Qi, 2016).

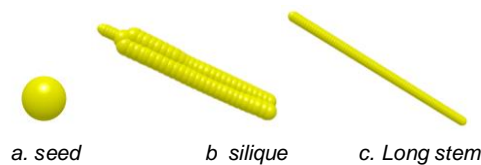


Fig. 6- Discrete element model

Table 1

Model material parameters			
Materials	Poisson's ratio	Shear modulus/[MPa]	Density/[kg·m ⁻³]
Seed	0.25	52	880
Silique	0.35	0.8	300
Stalk	0.45	4.4	550
Steel	0.30	75000	7850
Polyurethane (PU)	0.33	174	1072

Table 2

Model material contact parameters			
Contact form	Recovery factor	Static friction coefficient	Coefficient of rolling friction
Seed - steel	0.62	0.46	0.08
Seed - PU	0.29	1.05	0.15
Silique - steel	0.2	0.8	0.12
Silique - PU	0.29	1.05	0.16
Stalk - steel	0.2	0.8	0.12
Stalk - PU	0.29	1.05	0.16

In the Factories panel, the motion form and parameters of the threshing cylinder are set. The feeding amount of the two simulation models was set as 1.2 kg/s, and the dynamic generation method was adopted. The mass of seeds, long stalks and nuts were respectively 0.4 kg/s, 0.6 kg/s and 0.2 kg/s. The particle factory was set above the conveyor belt entrance in the form of Box. In the simulation, the threshing drum is set as rotation, the drum speed is 700 r/min, the conveyor belt is set as plane movement, and the speed is 1 m/s. The whole threshing device was gridded. The basic grid size was 3 times of the minimum particle size. During simulation, Rayleigh time step was 25% of the total step size. The total simulation time was set as 8 s, and the material entered the threshing device after 1.6 s. The threshing simulation model was finally obtained, as shown in Figure 7.

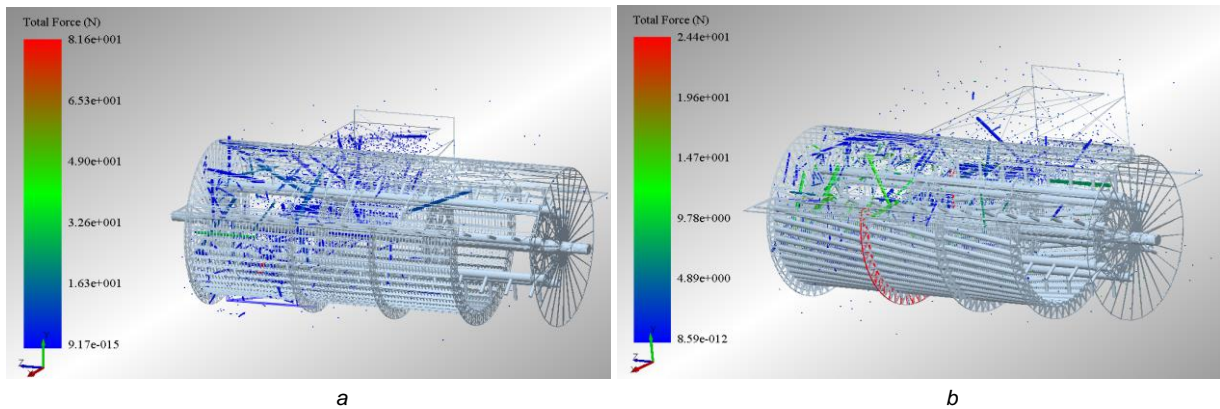


Fig. 7 - Threshing simulation model of thresher

a. Threshing simulation model of conventional threshing device b. Threshing simulation model of flexible threshing device

Simulation results and analysis

The EDEM solver is used to simulate the two kinds of threshing device models respectively. According to the simulation animation, when seeds, nuts and stalks enter the drum, they move towards the end of the drum under the action of flexible spike-tooth and concave pipe plate, and the process of feeding and straw discharge is smooth, which can realize the process of material threshing and separation. After the simulation is completed, the contact collision force between the two threshing elements and the concave plate and the material is extracted for analysis, and the results are shown in Figure 8.

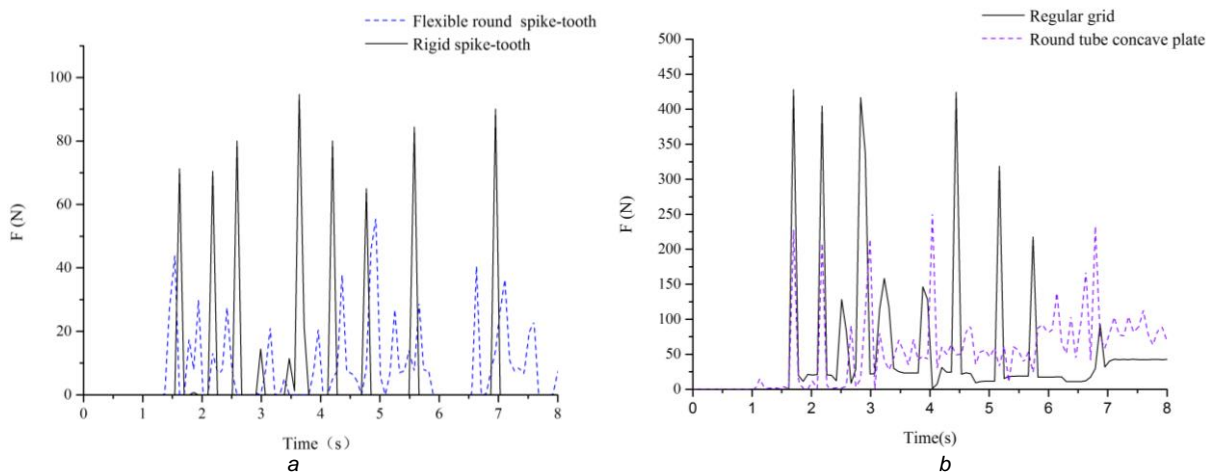


Fig. 8 - Threshing device and material stress

a. Contact force between flexible round head spike-teeth and conventional spike-teeth and materials
b. Contact force between concave tube and conventional grid and material

It can be seen from Figure 8 that the Chinese cabbage material within 0~1.6 s was produced by the particle factory and entered into the threshing drum through the conveyor belt, starting to produce contact behavior. From the peak of contact force, it can be seen that at the same roller speed, the impact force between the flexible spike-tooth and the pipe concave plate and the material is lower than that between the spike-tooth and the grid concave plate. Among them, the range of contact force between conventional rigid spike-tooth and material is 61-94n, while the range of contact force between flexible circular head spike-tooth and material is 18-52n, which reduces by 44% to 70.5%. The range of contact force between conventional grid concave plate and material is 100~425n, and that between pipe concave plate and material is 50~250n, reducing by 41.2%~50%. Therefore, the selection of flexible round head spike-teeth and pipe concave plate can effectively reduce the impact of threshing device on seeds and so on, thus reducing the effect of threshing damage.

RESULTS

EXPERIMENTAL RESULTS AND OPTIMIZATION

Experimental material and methods

The threshing experiment was carried out in Jiyuan City, Henan province. The designed flexible low loss threshing device was used to carry out relevant indoor threshing experiments on Chinese cabbage seeds in the suitable harvest period. The Chinese cabbage variety Jincai No. 3 was used in the experiment, and the characteristics of some materials of this variety were measured before the experiment, as shown in Table 3.

Table 3

Material characteristics of Chinese cabbage seed plants	
parameter	quantity
Plant height [mm]	880~1200
Cuticle diameter [mm]	560~860
Average moisture content of the fruit [%]	13.16
Average moisture content of seeds [%]	28.39
Average stem moisture content [%]	40.12
Weight of 1000-seeds [g]	3.08~3.25
Ratio of grain to straw	0.3~0.6
Yield [kg·acre ⁻¹]	123~160

The test shall be carried out in accordance with General Provisions on Determination Methods for Test Conditions of Agricultural Machinery GB/T 5262-2008 and Thresher Test Methods GB/T 5982-2005. The test instruments and equipment mainly include VC6234P digital display tachometer and electronic balance. Before the beginning of the test, the cabbage plants were evenly spread on one side of the conveyor belt, and an acceleration adjustment zone of 5 m was left. Start the threshing device and adjust the speed of conveying device and threshing drum to the required value through frequency converter. After stable operation of the threshing device, start the conveyor belt to complete the process of conveying, feeding, threshing and feeding. The test site is shown in Figure 9a.

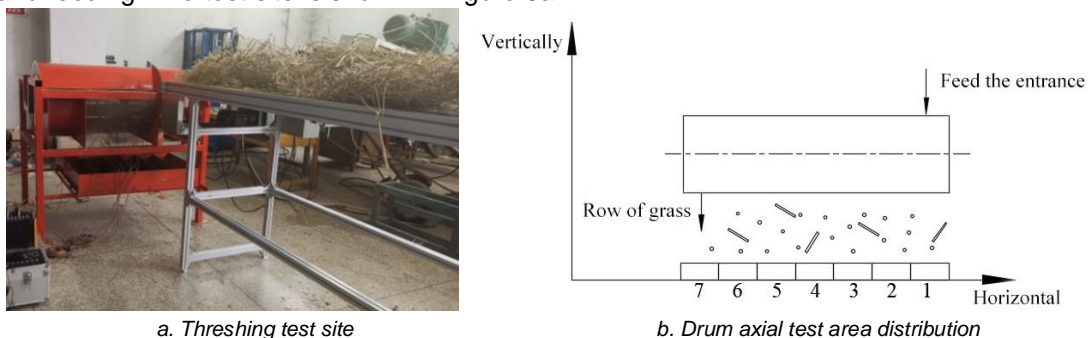


Fig. 9 - Threshing test site and Axial survey area distribution

Comparative test of threshing mixture distribution

To explore the release distribution of the flexible threshing device, the receiving device was divided into 7 test areas along the axial direction of the threshing drum, as shown in Figure 10. After the end of the test, the distribution of impurities, seeds and broken seeds in the outcrops in each test area was counted respectively, and the test was repeated for 3 times to take the mean value. Under the threshing condition with fixed feeding rate of 1.6 kg/s, drum speed of 750 r/min, and threshing clearance of 20 mm, the results were compared with those of conventional spike-tooth - grid concave plate threshing device under the same working condition. The distribution of the outfalls in each test area is shown in Figure 9b.

It can be seen from Figure 10 that under the two threshing conditions, the accumulations of seeds, miscellaneous seeds and broken seeds distributed along the axial direction of the drum were significantly different, but the distribution rules were similar. Diagram indicated that the conventional threshing components had a greater impact on the seed of Chinese cabbage, the seed breakage rate was higher, and the excessive impurity increased the cleaning load; the flexible threshing element has less impact on Chinese cabbage seed, but it also has stronger ability of threshing and separating. According to the test results, the threshing performance of flexible circular head spike-tube concave plate is better than that of conventional spike-grid concave plate, which can meet the demand of Chinese cabbage seed threshing.

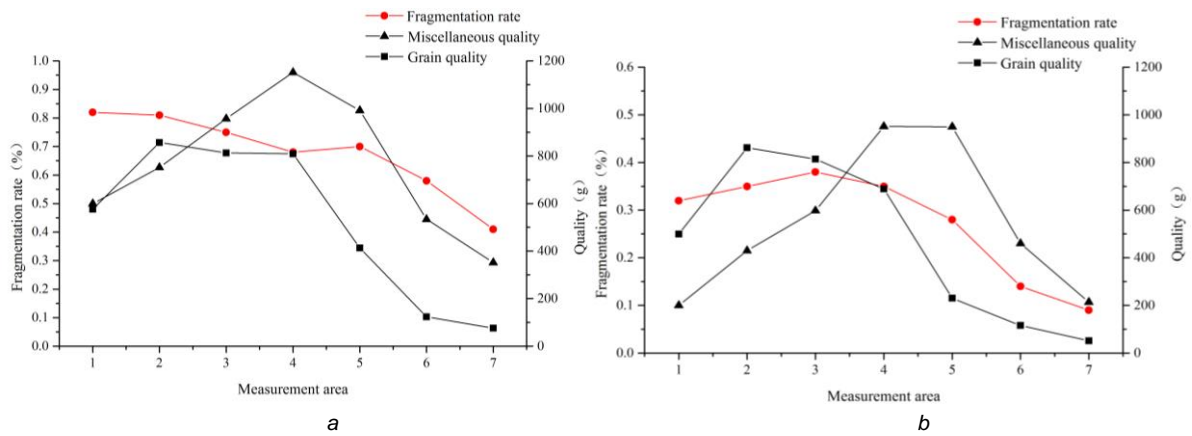


Fig. 10- Comparison of distribution of extract

a. Distribution of extracts from conventional threshing equipment b. Distribution of extracts from flexible thresher

Orthogonal experiment

In order to explore the optimal working parameters of the flexible threshing device, the roller speed A (r/min), the concave clearance B (mm) and the feeding amount C (kg/s) which have great influence on the threshing quality are selected as the experimental factors. The orthogonal experiment of three factors and three levels was carried out with seed crushing rate and unclean rate as test indexes. The test factor levels and their coded values are shown in Table 4.

Table 4

Factor Level Coding Table			
Level	Factor		
	Drum rotation speed (A)	Threshing clearance (B)	Feed quantity (C)
	[r•min ⁻¹]	[mm]	[kg•s ⁻¹]
1	750	15	1.2
2	850	20	1.4
3	950	25	1.6

Table 5

Orthogonal test results						
Test number	Factor			Vacant column	Y ₁ / Damage rate [%]	Y ₂ / Loss rate [%]
	A	B	C			
1	1	1	1	1	0.115	0.821
2	1	2	2	2	0.064	0.672
3	1	3	3	3	0.235	0.894
4	2	1	2	2	0.134	0.813
5	2	2	3	3	0.289	0.772
6	2	3	1	1	0.249	0.796
7	3	1	3	3	0.352	0.715
8	3	2	1	1	0.245	0.584
9	3	3	2	2	0.172	0.613

Table 6

Variance analysis					
Index	The source of variance	Quadratic sum	Degree of freedom	F	Significance
Y ₁	A	0.382	2	16.881	*
	B	0.022	2	0.535	
	C	0.001	2	32.128	**
	Error	0.001	2		
Y ₂	A	0.050	2	23.268	**
	B	0.020	2	9.165	*
	C	0.013	2	6.227	
	Error	0.002	2		

The results of orthogonal test and variance analysis are shown in Table 5 and Table 6. According to the results of variance analysis, the influences of various factors on the damage rate were as follows: extremely significant feeding amount, significant drum speed, and insignificant threshing gap. The influences of various factors on the loss rate of seeds were as follows: roller speed was very significant, threshing clearance was significant, and feeding amount was not significant.

Orthogonal experiment

In the optimization problem of orthogonal test, the subjective weighting method is often used to determine the weight of multiple indexes, which requires a lot of calculation and has some human factors. Therefore, this study uses matrix analysis to calculate the influence degree of each experimental factor on the index, and quickly determines the primary and secondary order of each factor according to the weight, which can well solve the optimal scheme selection problem of multi-index orthogonal experimental design (Wei et al, 2010).

According to the orthogonal test scheme, the three-layer structure model (Table 7) is established, which is respectively the index layer, the factor layer and the horizontal layer. Suppose l is the number of test factors in an orthogonal experiment, m is the level of each factor. Where, k_{ij} represents the average value of the test index at the j -the level of factor A_i . If the test result is larger, the better, let $K_{ij}=k_{ij}$; otherwise, let $K_{ij}=1/k_{ij}$. Establish the following matrix formula:

Table 7

Matrix structure			
Structural layer			
1	Test index		
2	Factor A_1	Factor A_2	Factor A_i
3	$A_{11} A_{12} \dots A_{1m}$	$A_{21} A_{22} \dots A_{2m}$	$A_{i1} A_{i2} \dots A_{im}$

Establish the index layer matrix for test investigation:

$$M = \begin{bmatrix} K_{11} & 0 & 0 & \dots & 0 \\ K_{12} & 0 & 0 & \dots & 0 \\ \dots & \dots & \dots & \dots & \dots \\ K_{1m} & 0 & 0 & \dots & 0 \\ 0 & K_{21} & 0 & \dots & 0 \\ 0 & K_{22} & 0 & \dots & 0 \\ \dots & \dots & \dots & \dots & \dots \\ 0 & K_{2m} & 0 & \dots & 0 \\ \dots & \dots & \dots & \dots & 0 \\ 0 & 0 & 0 & \dots & K_{i1} \\ 0 & 0 & 0 & \dots & K_{i2} \\ \dots & \dots & \dots & \dots & \dots \\ 0 & 0 & 0 & 0 & K_{im} \end{bmatrix} \tag{9}$$

Let $T_i = 1 / \sum_{j=1}^m K_{ij}$, establish the factor layer matrix:

$$T = \begin{bmatrix} T_1 & 0 & 0 & 0 \\ 0 & T_2 & 0 & 0 \\ \dots & \dots & \dots & \dots \\ 0 & 0 & 0 & T_l \end{bmatrix} \tag{10}$$

In the orthogonal experiment, the range of factor A_i is S_i . Let $S_i = s_i / \sum_{i=1}^l s_i$

Establish the horizontal layer matrix:

$$S = \begin{bmatrix} S_1 \\ S_2 \\ \dots \\ S_l \end{bmatrix} \quad (11)$$

The weight matrix affecting the test index value is:

$$\omega = MTS \quad (12)$$

$$\omega^T = [\omega_1 \quad \omega_2 \quad \dots \quad \omega_m] \quad (13)$$

The weight of each index is calculated by Formula 13. In this orthogonal test, both the crushing rate and the uncleanness rate should be taken into account in the investigation index, and it can be calculated as follows:

$$\begin{aligned} \omega_1 &= [A_1, A_2, A_3, B_1, B_2, B_3, C_1, C_2, C_3]^T = \\ & [0.1628, 0.1121, 0.1107, 0.0160, 0.0180, 0.0291, 0.1805, 0.2115, 0.1584]^T \\ \omega_2 &= [A_1, A_2, A_3, B_1, B_2, B_3, C_1, C_2, C_3]^T = \\ & [0.1364, 0.1370, 0.1709, 0.0932, 0.1079, 0.0952, 0.0873, 0.0914, 0.0806]^T \end{aligned}$$

In this orthogonal experiment, the total weight matrix of the index is the average value of the weight matrix of the two index values, which can be calculated as follows:

$$\begin{aligned} \omega &= [A_1, A_2, A_3, B_1, B_2, B_3, C_1, C_2, C_3]^T = \\ & [0.2992, 0.2491, 0.2816, 0.1092, 0.1259, 0.1243, 0.2678, 0.3029, 0.2390]^T \end{aligned}$$

Based on the above calculation results, the primary and secondary order (primary → secondary) of the influence of each factor on the orthogonal test index value is CAB. Factors C₂, A₁ and B₂ have the largest weight. The optimal scheme of this orthogonal experiment is A₁B₂C₂, that is, when the threshing drum speed is 750 r/min, the threshing gap is 20 mm, and the feeding amount is 1.4 kg/s, the threshing performance of the flexible threshing device is the best, the crushing rate is 0.064%, and the under-threshing rate is 0.67%, which meets the national industry standard.

CONCLUSIONS

1. The test bed of low loss flexible threshing device for Chinese cabbage seeds was designed. The structure and parameter determination method of key parts of the threshing device were studied.
2. The simulation models of conventional and flexible threshing systems were established by EDEM software, and the contact forces between threshing elements and concave plates and Chinese cabbage seed plant materials were analyzed. The results showed that the flexible threshing device could effectively reduce the impact on seeds. Finally, the feasibility of the flexible threshing form was verified through the comparative test of the distribution of threshing matter.
3. The orthogonal test, and the weighting matrix method were adopted according to the results of the experiment optimization to determine the optimal structure and working parameters of threshing device combination, namely the threshing cylinder rotation speed of 750 r/min, threshing clearance of 20 mm, feed rate of 1.4 kg/s, the device threshing performance index respectively, the seed damage rate was 0.064%, loss rate was 0.67%, the threshing effect was good and met the national industry standard.

ACKNOWLEDGEMENT

This research was supported by The China's Natural Science Foundation (No.52005163) and the China's National Key Research and Development Program (No.2017YFD0701204-02) and the Experimental Technology Development Foundation of Henan University of Science and Technology (No.SY2122006).

REFERENCES

- [1] Badretdinov I., Mudarisov S., & Lukmanov R., (2019). Mathematical modeling and research of the work of the grain combine harvester cleaning system. *Computers and Electronics in Agriculture*, 165:104966. DOI: 10.1016/j.compag.2019.104966
- [2] Bello B., Tokan A, Jiya D, Musa A., (2019). Design Model of Automated Groundnut Threshing Machine, *Majlesi Journal of Mechatronic Systems*, 8(1):19-24.
- [3] Chuan-udom S., Chinsuwan W. (2011), Effects of operating factors of an axial flow rice combine harvester on grain breakage. *Sonklanakarin Journal of Science and Technology*, 33(2): 221-225.
- [4] Dhananchezhyan P., Parveen S., Rangasamy K., Shridar, B.; Kumar, A. S., (2013), Development of a nylon rasp bar threshing cylinder for portable paddy thresher and its performance evaluation, *Madras Agricultural Journal*, 100:623-626.
- [5] Guan Z.H., Zhang Z., Jiang T. et al., (2020). Development and test of speed control system for combine harvester threshing and cleaning device. *INMATEH-Agricultural Engineering*, 61(2): 305-314. <https://doi.org/10.35633/inmateh-61-33>.
- [6] Fan C.L., Cui T., Zhang D.X., Yang L., Qu Z., Li Y.H., (2019). Design and Test of Low-damage Combined Corn Threshing and Separating Device. *Transactions of the Chinese Society for Agricultural Machinery*, 50(04):113-123. DOI:10.6041/j.issn.1000-1298.2019.04.013
- [7] Jahanbakhshi A., Ghamari B., Heidarbeigi K., (2017). Assessing acoustic emission in 1055I John Deere combine harvester using statistical and artificial intelligence methods. *International Journal of Vehicle Noise and Vibration*, 13(2):105-117. DOI: 10.1504/IJNVN.2017.087906
- [8] Ji J.T., Hu J.P., Wang S.S., Zhang R.H., Pang J., (2020). Vibration and impact detection of axial-flow threshing unit under dynamic threshing conditions. *INMATEH-Agricultural Engineering*, 60(1):183-192. DOI : 10.35633/inmateh-60-21.
- [9] Li H.D., (2018). Research and Preliminary Design of Single-row Chinese Cabbage Harvester (单行大白菜收获机的研究与初步设计). *Mechanization of rural pastoral areas*, (5): 5-18.
- [10] Lu F.Y., Ma X., Qi L., Tan Y X., Jiang L.K., Sun G.D., (2016). Parameter optimization and experiment of vibration seed-uniforming device for hybrid rice based on discrete element method. *Transactions of the Chinese Society of Agricultural Engineering (Transactions of the CSAE)*, 32(10):17-25. DOI:10.11975/j.issn.1002-6819.2016.10.003
- [11] Pužauskas E., Steponavičius D., & Jotautienė E., (2016). Substantiation of concave crossbar shape for corn ear threshing. *Mechanics*, 22(6): 553-561. DOI:10.5755/j01.mech.22.6.16370
- [12] Rahman M.M., Ishii K., Noguchi N., (2019). Optimum harvesting area of convex and concave polygon field for path planning of robot combine harvester. *Intel Serv Robotics* 12, 167-179. DOI: 10.1007/s11370-018-00273-4
- [13] Steponavicius D., Puzauskas E., Spokas L., Jotautienė E., Kemzūraitė A., Petkevičius S., (2018), Concave Design for High-Moisture Corn Ear Threshing. *Mechanics, Design and Optimization of Mechanical Systems*, 24(1):80-91. DOI: <https://doi.org/10.5755/j01.mech.24.1.18345>
- [14] Wu C.Y., Xiao S.Y., Jin M., (2014). Comparison on rape combine harvesting and two-stage harvesting. *Transactions of the Chinese Society of Agricultural Engineering (Transactions of the CSAE)*, 30(17): 10-16. DOI: 10.3969/j.issn.1002-6819.2014.17.002
- [15] Wan X.Y., Shu C.X., Xu Y., Xu Y., Yuan J.C., Li H.T., Liao Q.X., (2018). Design and experiment on cylinder sieve with different rotational speed in cleaning system for rape combine harvesters. *Transactions of the Chinese Society of Agricultural Engineering (Transactions of the CSAE)*, 34(14): 27-35. DOI:10.11975/j.issn.1002-6819.2018.14.004
- [16] Wei X.L., Xue B.J., Zhao Q., (2010). Optimization design of the stability for the plunger assembly of oil pumps based on multi-target orthogonal test design. *Journal of Hebei University of Engineering (Natural Science Edition)*, 27(3): 95-99. DOI:10.3969/j.issn.1673-9469.2010.03.024

DESIGN AND TEST OF SELF-PROPELLED STRADDLE-TYPE LYCIUM BARBARUM L. SPRAYING MACHINE

自走式跨行枸杞喷药机设计与试验

Gao ZeNing¹⁾; Chen QingYu¹⁾; Hu GuangRui¹⁾; Chen Chao¹⁾; Li ChuanLin¹⁾; Chen Jun^{*1)}

¹⁾ College of Mechanical and Electronic Engineering, Northwest A&F University, Yangling 712100, China

Tel: +86 13572191773; E-mail: chenjun_jdxy@nwsuaf.edu.cn

DOI: <https://doi.org/10.35633/inmateh-65-36>

Keywords: *Lycium barbarum L.*, spraying, self-propelled straddle-type, phytosanitary liquid recovery, double-layer fence planting

ABSTRACT

According to the planting agronomy of *Lycium barbarum L.* in Ningxia, a self-propelled straddle-type sprayer was designed. The aim was to reduce the labour requirements, improve the spraying effect to the middle and lower parts of the canopy, reduce the influence of natural wind on droplet drift, and recycle excess phytosanitary liquid to reduce environmental pollution. Tests showed that the coverage rate of phytosanitary liquid on the leaf surface and back of the leaf peaked at 84.2% and 48.3%, respectively, when spraying pressure was high. Under different spraying distances, the coverage rate of phytosanitary liquid on leaf surface and back of leaf reached 73.3% and 38.3% at the shortest distance. The uniformity of the spray droplet distribution was good, the use error was less than 10%, and the excess liquid was effectively recovered.

摘要

针对宁夏地区的双层篱架式枸杞种植农艺, 设计了一种自走式跨行枸杞喷药机。目的在于减轻劳动强度, 提高树冠中下部的喷药效果, 减少自然风对液滴漂移的影响, 并将多余药液进行回收以减少对环境的污染。试验结果表明: 在不同的喷药压力下, 叶面和叶背的药液覆盖率可达 84.2% 和 48.3%; 在不同的喷药距离下, 叶面和叶背的药液覆盖率可达 73.3% 和 38.3%。整机喷药的雾滴分布均匀性良好, 施药量误差均在 10% 以内, 并且可以有效的对多余药液进行回收。

INTRODUCTION

Lycium barbarum L. is a deciduous shrub with infinite inflorescence, which is characteristic of *Lycium* in the Solanaceae family (Chen et al., 2018; Zhao et al., 2021a, 2021b, 2021c, 2021d). *L. barbarum L.* is mainly produced in Ningxia, Qinghai, Gansu, Tibet, and Inner Mongolia (Chang, 2020; Li, 2021). *L. barbarum L.* has both high medicinal value and high economic value (Li et al., 2017). In recent years, intelligent technologies have been widely used in planting, spraying and harvesting (Hu et al., 2021). Importantly, spraying of artificial phytosanitary liquid/chemicals to protect *L. barbarum L.* is still common practice in China, but this practice has many problems, including high labour costs, low efficiency, uneven spraying, and environmental pollution caused by excess chemicals (Qi, 2017; Hu et al., 2021).

In recent years, in order to improve the efficiency in spraying *L. barbarum L.*, some large plantations have sprayed using unmanned aerial vehicles or orchard air-driven sprayers. Although the spraying efficiency is markedly improved by these methods, the effective utilization rate of phytosanitary liquid is very low. To address this, the Institute of Plant Protection, Ningxia Academy of Agriculture and Forestry Sciences designed a windproof spraying machine by covering the top and side of the spraying machine with a curtain. This reduced the influence of natural winds on droplet drift and improved the utilization rate of the phytosanitary liquid, but did not improve the spraying effect (Zheng, 2015). Following this, Ningxia University designed a windproof *L. barbarum L.* spraying machine in 2019 that reduced the influence of natural wind on droplets and used a three-dimensional spray rod configuration to even out the distribution of droplets deposited in the middle and lower parts of the canopy. Their sprayer also used pneumatic devices to provide kinetic energy for the droplets. However, these machines still do not consider the impact of excess phytosanitary liquid on the environment, and in the case of pneumatic devices, the droplets were less likely to attach to leaves and more likely to float into the air, which further increased the waste of phytosanitary liquid (Hu, 2019).

¹ Zening Gao, M.S. Stud. Eng.; Qingyu Chen M.S. Stud. Eng.; Guangrui Hu M.S. Stud. Eng.; Chao Chen M.S. Stud. Eng.; Chuanlin Li M.S. Stud. Eng.; Jun Chen, Prof. Ph.D. Eng.

In order to solve the above problems, this study designed a self-propelled straddle-type *L. barbarum* L. spraying machine to suit the double-layer hedgerow planting agronomy of *L. barbarum* L. utilized in Ningxia. This machine can effectively reduce the labour requirements, improve the spraying quality in the middle and lower parts of the canopy, reduce the influence of natural winds on droplet drift, and recycle excess phytosanitary liquid to reduce environmental pollution.

MATERIALS AND METHODS

Overall structure and working principle

The primary components of the machine include the windproof baffle, frame, phytosanitary liquid tank, wheels, universal wheels, stepping motor, phytosanitary liquid recovery baffle, phytosanitary liquid recovery tank, diaphragm pump, spraying distance adjusting device, pressure regulating valve, nozzle, spraying pipeline, and solenoid valve, as shown in Figure 1. The windproof baffles were fixed around the frame to form a relatively enclosed space. The phytosanitary liquid tank, diaphragm pump, pressure regulating valve, nozzle, injection pipeline, and solenoid valve constitute the injection system that sprays the liquid. The stepping motor, wheels, and universal wheels were installed under the frame to make the platform mobile.

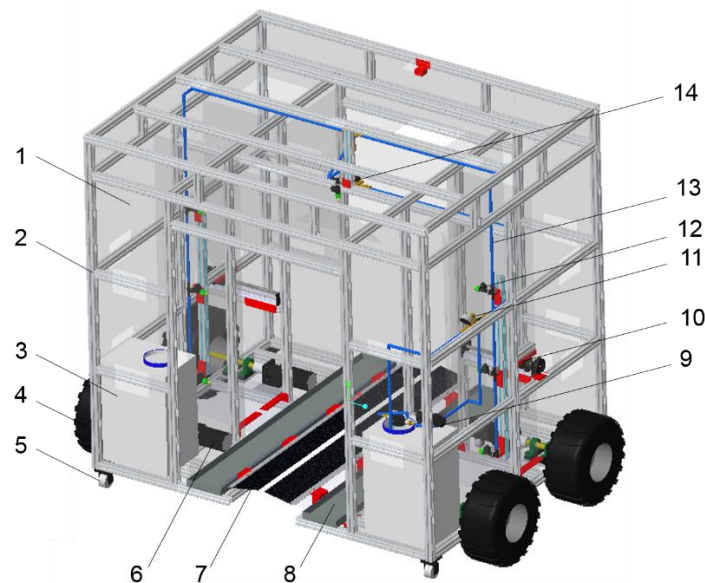


Fig. 1 - Schematic diagram of the machine

1) Windproof baffle; 2) frame; 3) phytosanitary liquid tank; 4) wheels; 5) universal wheel; 6) stepping motor; 7) phytosanitary liquid recovery baffle; 8) phytosanitary liquid recovery tank; 9) diaphragm pump; 10) spraying distance adjusting device; 11) pressure regulating valve; 12) nozzle; 13) spraying pipeline; 14) solenoid valve

During operation, the operator uses the controller to remotely direct the machines movements, either forward or backward over the crown of the *L. barbarum* L. plants. If there is any deviation in the traveling direction, the speed of wheels on both sides can be adjusted using the handle to realize differential steering. When spraying, the solenoid valve is kept open while the diaphragm pump provides the kinetic energy that drives droplets through the nozzle, which creates an even spray distribution, and the three-dimensional configuration of spraying rods effectively improves the spraying effectiveness for the middle and lower parts of the canopy. The windproof baffles surrounding the sprayer effectively reduce the influence of natural winds on the phytosanitary liquid drift and any droplets that do not attach to the blades will be collected and returned to the phytosanitary liquid recovery tank via the phytosanitary liquid recovery baffles. This significantly reduces the excess phytosanitary liquid allowed to enter and pollute the environment. In addition, the spraying pressure of the spraying machine can be adjusted using the pressure regulating valve, and the spraying distance can be specified by adjusting the nozzles on both sides to achieve the optimal spraying effect.

Design requirements and technical parameters

This study was conducted at the ecological *Lycium barbarum* L. science and technology demonstration base of the Zhengqihong *Lycium barbarum* L. Industry Development Co. Ltd. in Guyuan, Ningxia. The demonstration base utilizes the double-layer hedgerow planting mode, which is designed to encourage *L. barbarum* L. plants grow high and stably for a long time, improve fruit quality, reduce pests and diseases, and facilitate management (Wu *et al.*, 2016). The *L. barbarum* L. variety used in the experiment was Keqi No. 2.

According to measurements, the planting agronomy of this variety was: row spacing of 3000 mm, plant spacing of 1100 mm, plant heights of 1320 mm~1640 mm, and canopy diameters of 750 mm~1200 mm. The machine was designed according to the planting agronomy and its main technical parameters are shown in Table 1.

Table 1

Main technical parameters of the spraying machine

Technical parameter	Value	Unit
Overall dimensions (length × width × height)	1600×2500×2000	mm
Overall weight	360	kg
Working speed	0.2~1.0	m·s ⁻¹
Track	2300	mm
Wheelbase	760	mm
Stepping motor torque	12.5	N·m
Reduction ratio	6	-
Maximum working height	1700	mm
Maximum working width	1000	mm
Ground clearance	120	mm

Key design components

Moving steering device and kinematic model

The moving steering device was mainly composed of the frame, tires, transmission shaft, bearing with seat, coupling, reducer, stepping motor, driver, single chip microcomputer, and remote controller, as shown in Figure 2. In order to simplify the steering mechanism, reduce the weight of the machine, and improve the field traversing performance, a "four-wheel drive and differential steering" driving mode was adopted for the moving steering device.

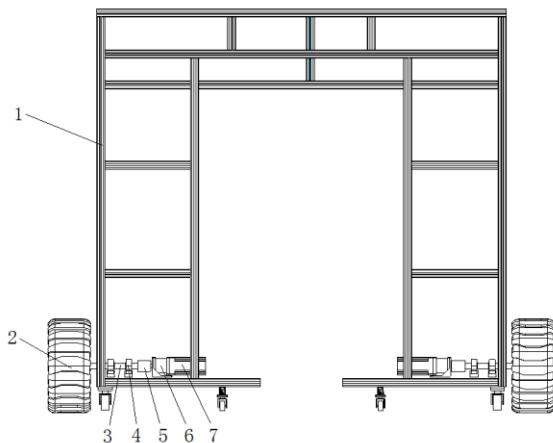


Fig. 2 - Schematic diagram of moving steering device

1) Frame; 2) tires; 3) transmission shaft; 4) bearing with seat; 5) coupling; 6) reducer; 7) stepping motor

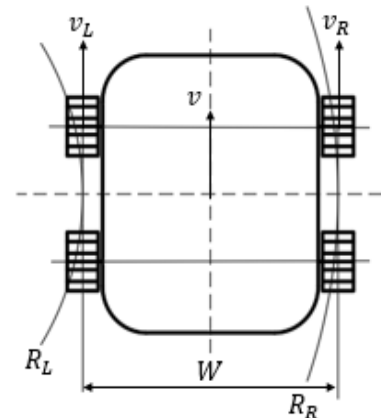


Fig. 3 - Kinematics model

Because the speeds of wheels on either side of the moving steering device were the same, the simplified two-wheel differential motion model could be used, as shown in Figure 3.

The linear speed is:

$$v_L = r \cdot u_L \quad (1)$$

$$v_R = r \cdot u_R \quad (2)$$

The angular velocity $\dot{\theta}$ of rotation around point O is:

$$\dot{\theta} = \frac{v_L}{R_L} = \frac{v_R}{R_R} \quad (3)$$

According to the relationship between R_R and R_L , R_L is:

$$\frac{v_L}{R_L} = \frac{v_R}{R_L + W} \tag{4}$$

$$R_L = \frac{v_L \cdot W}{v_R - v_L} \tag{5}$$

The angular velocity $\dot{\theta}$ can be obtained by bringing R_L into the equation as follows:

$$\dot{\theta} = \frac{v_R - v_L}{W} \tag{6}$$

The linear velocity v of the machine is:

$$v = \frac{v_R + v_L}{2} \tag{7}$$

The motion equation of the machine is:

$$\begin{cases} \dot{x} = v \cdot \cos\theta \\ \dot{y} = v \cdot \sin\theta \\ \dot{\theta} = \frac{v_R - v_L}{W} \end{cases} \tag{8}$$

The simplified model is:

$$\dot{q} = \begin{bmatrix} \dot{\theta} \\ \dot{x} \\ \dot{y} \end{bmatrix} = \begin{bmatrix} -\frac{r}{W} & \frac{r}{W} \\ \frac{r}{2} \cos\theta & \frac{r}{2} \cos\theta \\ \frac{r}{2} \sin\theta & \frac{r}{2} \sin\theta \end{bmatrix} \begin{bmatrix} u_L \\ u_R \end{bmatrix} \tag{9}$$

where:

point O is the centre point of the turning radius; R_L is the turning radius of the left wheel, mm; R_R is the turning radius of the right wheel, mm; r is the wheel radius, mm; u_L is the angular velocity of the left wheel, rad/s; u_R is the angular velocity of the right wheel, rad/s; v is the linear speed of the machine, m/s; v_L is the linear speed of the left wheel, m/s; v_R is the linear speed of the right wheel, m/s; θ is the rotation angle of the machine, °; and W is the left and right wheel track, mm.

Control device

The control circuit diagram is shown in Figure 4. An Arduino single chip microcomputer was selected as the lower computer and a DC5V battery was used as the power supply. An 86 closed-loop stepping motor was selected as the driving motor and a ZDM-2HA860 driver powered by a DC72V battery was selected as the driver. A PS2 Bluetooth controller was used as the remote control. Two single-chip microcomputers communicate through TX and RX pins. The single-chip microcomputer 1 was connected to the Bluetooth receiving module to receive the remote control signals from the controller and, after signal processing, the control instructions are transmitted to the single-chip microcomputer 2. The single-chip microcomputer 2 then controls the four stepping motors and uses different pulse frequencies to control the rotation speeds of the stepping motors. This process controls the vehicle speed and direction.

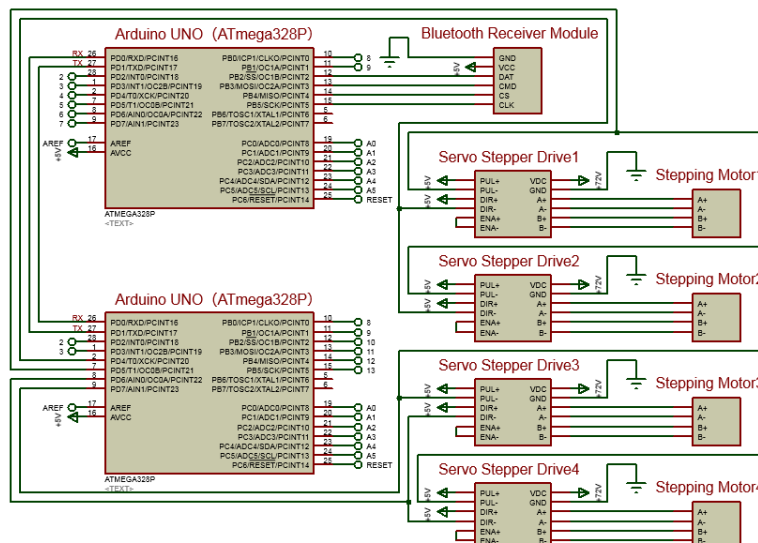


Fig. 4 - Control circuit diagram

Spray device

The schematic diagram of the spraying device is shown in Figure 5. It mainly consisted of the phytosanitary liquid tank, filter, diaphragm pump, check valve, nozzle, solenoid valve, pressure gauge, pressure regulating valve, and pressure relief valve, all of which were connected by pipelines and pipeline joints. After being pressurized by the diaphragm pump, the phytosanitary liquid flows out of the phytosanitary liquid tank and passes through the filter. The phytosanitary liquid then passes through the pressure regulating valve before reaching the solenoid valve. When the spraying operation starts, the solenoid valve opens and the phytosanitary liquid is sprayed from the nozzle at a constant pressure. A pressure gauge was installed at the outlet of the pressure regulating valve in the phytosanitary liquid pipeline to display the main pipeline pressure. When the pressure of the main pipeline is too high, the pressure relief valve relieves the pressure and any discharged phytosanitary liquid is returned back to the phytosanitary liquid tank, which is stirred.

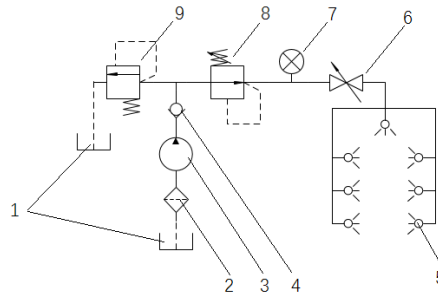


Fig. 5 - Schematic diagram of spraying device

- 1) Phytosanitary liquid tank; 2) filter; 3) diaphragm pump; 4) check valve; 5) nozzle; 6) solenoid valve; 7) pressure gauge; 8) pressure regulating valve; 9) pressure relief valve

In order to improve the uniformity of phytosanitary liquid coverage across the crown of the *L. barbarum* L. plants, a three-dimensional spray configuration was adopted wherein three nozzles were spaced evenly on each side. ARAG anti-drift nozzles, which were made in Italy and have a spray with a 110° sector shape (Qi, 2021), were used as shown in Figure 6. In order to ensure that the sprayed phytosanitary liquid covered the canopy of the *L. barbarum* L. plants, a minimum spraying distance was established according to the layout of the nozzles, calculated according to the following formula:

$$\frac{H}{6D} = \tan \frac{\theta}{2} \quad (10)$$

$$D = \frac{H}{6 \tan \frac{\theta}{2}} \quad (11)$$

where: H is plant height, mm; D is the minimum spraying distance, mm; and θ is the included angle of spraying the fan-shaped surface, °.

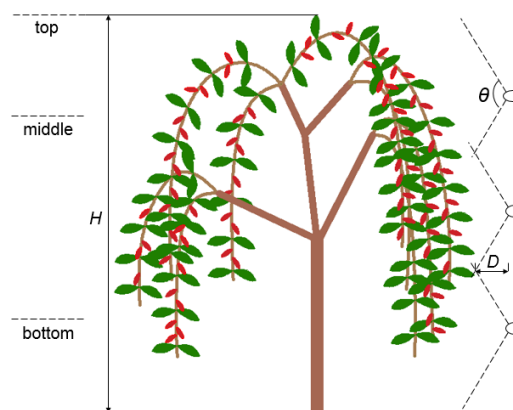


Fig. 6 - Schematic diagram of single side nozzle layout

The machine has a spraying position adjusting device which connects the three-dimensional spraying rods on each side with the modified GX80 sliding table, and the spraying distance can be adjusted within a range of 180 mm to 340 mm, as shown in Figure 1. The pressure adjusting valve was used so that the spraying pressure could be adjusted between 0.15 MPa and 0.35 MPa, as shown in Figure 1. The phytosanitary liquid recovery device which is positioned under the crown of *L. barbarum* L. when working, was designed to collect the phytosanitary liquid that did not attach to leaves, as shown in Figure 1.

Test conditions and design

From July 5th to 10th, 2021, a field experiment was conducted at the *L. barbarum* L. base of Zhengqihong Lycium barbarum L. Industry Development Co. Ltd., Yuanzhou District, Guyuan City, Ningxia, as shown in Figure 7. The test field was located at the coordinates 106.11 E and 36.29 N, and there was no rain or dew during the test. The temperature was 28–30°C, the wind speed was 1.6–2.0 m/s, and the spraying machine speed was 0.5 m/s.



Fig. 7 - Field trials

Nozzle test

The test instruments and materials included a stopwatch, measuring cup, electronic scale, and purified water. Each nozzle was labelled in turn and the spraying pressures were set to 0.15 MPa, 0.20 MPa, 0.25 MPa, 0.30 MPa, and 0.35 MPa in turn. The diaphragm pump was turned on and the liquid from each nozzle was collected with a measuring cup which was then put on the electronic scale for weighing after 1 min, this test process was repeated for three times (Liu, 2019).

Spraying effect test

Instruments and materials included water-sensitive test paper, purified water, and an electronic scale. A row of *L. barbarum* L. was randomly selected from the field and 10 evenly spaced *L. barbarum* L. trees within that row had 20 mm × 50 mm water-sensitive test papers fixed at their tops, middles (3/4 height), and bottoms (1/4 height) for observation, as shown in Figure 6.

Single factor experimental designs were used. First, at a spraying distance of 260 mm, spraying pressures of 0.15 MPa, 0.20 MPa, 0.25 MPa, 0.30 MPa and 0.35 MPa were tested. Next, the spraying pressure was fixed at 0.25 MPa and spraying was carried out at distances of 180 mm, 220 mm, 260 mm, 300 mm and 340 mm. Each of the above tests were repeated three times and the experimental water-sensitive test paper was taken back to the laboratory for quantification. The quantification indexes mainly included the coverage by phytosanitary liquid, the deposition density of droplets, and the uniformity of droplet distribution. The coverage of phytosanitary liquid was measured as the percentage of the total area covered with phytosanitary liquid. Droplet deposition density was calculated as the number of droplets per unit area. The degree of uniformity of droplet distribution was expressed by its coefficient of variation.

Application error and liquid recovery test

Test instruments and materials included a stopwatch, phytosanitary liquid tank, electronic scale, and purified water. Application error and liquid recovery were tested by operating the spraying machine for 1 min at spraying pressures of 0.15 MPa, 0.20 MPa, 0.25 MPa, 0.30 MPa and 0.35 MPa. The weight of the phytosanitary liquid tank before and after spraying and the weight of the liquid in the phytosanitary liquid recovery tank were recorded. Each test was repeated three times. Then the application error and recovery rates were calculated through the following formula:

$$U = \frac{q - q_0}{q_0} \times 100 \quad (12)$$

$$G = \frac{w}{q} \times 100 \quad (13)$$

where: U is the error rate of application rate, %; q is the actual dosage of phytosanitary liquid, L/min; q_0 is the predetermined dosage, L/min; G is the recovery rate of phytosanitary liquid, %; and w is the amount of recovered phytosanitary liquid, L/min.

RESULTS AND ANALYSIS

During the test, the spraying machine ran smoothly, the remote control device exhibited stable and reliable operation, the spray was uniform, and there were no out-of-control periods or rollover events during driving. At the same time, the spraying pressure and spraying distance was easily manually adjusted and consistent, and the overall performance was good. As a test prototype, initial observations showed that the spraying machine met the design requirements.

Nozzle test

The nozzle test results are shown in Table 2. The coefficient of variation was used as a measure of uniformity of nozzle spray. When the spraying pressure increases, the spray volume from the nozzle will also increase. The minimum variation coefficient was 0.331 and occurred when the spraying pressure was increased to 0.35 MPa, indicating that the uniformity of spray from each nozzle was the best at this pressure.

Table 2

Spray rate test results of nozzle

Nozzle number	Pressure (MPa)				
	0.15	0.20	0.25	0.30	0.35
1	277.79	316.51	341.28	361.79	378.41
2	284.89	323.57	352.29	373.06	382.39
3	260.16	297.50	321.33	342.51	358.04
4	259.23	296.69	319.98	343.47	361.53
5	258.38	295.74	318.55	338.95	369.99
6	285.74	325.74	347.40	372.26	388.88
7	284.61	328.69	350.07	370.81	388.11
Total spraying amount / ml	1910.79	2184.44	2350.90	2502.85	2627.35
Standard deviation / ml	13.10	14.89	15.26	15.39	12.41
Average value / ml	272.97	312.06	335.84	357.55	375.34
Coefficient of variation / %	0.0480	0.0477	0.0454	0.0430	0.0331

Spraying effect test

The spray test results under different spraying pressures are shown in Table 3. The droplet deposition density on the leaf surface and the back of the leaf peaked at 0.35 MPa, which indicated that with the increasing spray pressure the atomization effect was improved and droplet diameter decreased. The coverage rate of the phytosanitary liquid on the leaf surfaces peaked at 0.30 MPa, which indicated that when the spraying pressure is less than 0.30 MPa, the droplet particles had larger diameters and did not easily adhere to the leaves; but when the spraying pressure is greater than 0.30 MPa, the droplet particles have small diameters and droplet drift occurs, resulting in fewer droplets adhering to the leaves. The coefficients of variation of both the fronts and backs of the leaves were about 1%, which showed good uniformity of droplet distribution.

Table 3

Test results of spraying effect under different spraying pressure

Pressure (MPa)	Leaf	Canopy	Droplet coverage rate (%)		Droplet deposition density (pcs/cm ²)		Uniformity of droplet distribution (%)	
0.15	front	top	72.5	65	16	18	0.84	0.94
		middle		77.5		14		1.00
		bottom		75		16		0.59
	back	top	42.5	35	9	10	0.86	0.71
		middle		47.5		8		0.92
		bottom		45		8		0.94

Table 3
(continuation)

Pressure (MPa)	Leaf	Canopy	Droplet coverage rate (%)		Droplet deposition density (pcs/cm ²)		Uniformity of droplet distribution (%)	
0.20	front	top	75.8	60	18	20	0.27	0.86
		middle		82.5		17		1.51
		bottom		85		18		0.96
	back	top	42.5	42.5	9	12	1.03	0.81
		middle		42.5		8		1.23
		bottom		42.5		7		1.06
0.25	front	top	80.0	70	18	19	1.26	0.99
		middle		85		17		1.10
		bottom		85		19		1.68
	back	top	46.7	42.5	8	9	1.27	1.13
		middle		52.5		7		1.18
		bottom		45		8		1.49
0.30	front	top	84.2	80	19	19	1.09	1.09
		middle		87.5		17		0.96
		bottom		85		20		1.24
	back	top	48.3	45	9	11	1.00	1.11
		middle		50		7		1.03
		bottom		50		8		0.87
0.35	front	top	77.5	70	21	23	1.00	1.14
		middle		85		19		0.86
		bottom		77.5		21		1.01
	back	top	47.5	45	10	12	0.73	0.80
		middle		50		8		0.74
		bottom		47.5		11		0.65

The test results at different spraying distances are shown in Table 4. The droplet deposition density on the leaf surface and back of the leaf was highest when the distance was shortest, 180 mm. This indicated that, with increasing spraying distance, fewer droplets attach to the leaves due to insufficient kinetic energy. The coverage rate of the phytosanitary liquid on the leaf surface and back of the leaf peaked at 340 mm, but the deposition density of droplets was the lowest at this distance, indicating that at large distances the spray overlap will allow small droplets to converge into larger droplets and attach to the leaves, thus improving the coverage of phytosanitary liquid. The coefficients of variation of both the fronts and backs of leaves were about 1%, which showed good uniformity of droplet distribution.

Table 4**Test results of spraying effect under different spraying distance**

Distance (mm)	Leaf	Canopy	Droplet coverage rate (%)		Droplet deposition density (pcs/cm ²)		Uniformity of droplet distribution (%)	
180	front	top	70.0	65.0	27	28	1.46	1.33
		middle		67.5		27		1.75
		bottom		77.5		27		1.31
	back	top	34.2	35.0	12	15	1.22	1.50
		middle		35.0		12		1.10
		bottom		32.5		9		1.07

Table 4
(continuation)

Distance (mm)	Leaf	Canopy	Droplet coverage rate (%)		Droplet deposition density (pcs/cm ²)		Uniformity of droplet distribution (%)	
220	front	top	66.7	55.0	25	24	1.00	0.76
		middle		70.0		28		1.50
		bottom		75.0		22		0.75
	back	top	30.8	25.0	12	14	1.07	1.63
		middle		37.5		14		0.86
		bottom		30.0		9		0.71
260	front	top	65.0	57.5	25	24	1.24	1.17
		middle		67.5		26		1.23
		bottom		70.0		26		1.31
	back	top	30.8	30.0	11	12	0.95	1.03
		middle		32.5		11		0.84
		bottom		30.0		9		0.98
300	front	top	68.3	57.5	23	24	1.08	1.16
		middle		75.0		22		1.10
		bottom		72.5		24		0.99
	back	top	31.7	32.5	12	13	1.05	0.79
		middle		35.0		12		1.46
		bottom		27.5		12		0.88
340	front	top	73.3	62.5	19	20	1.10	1.61
		middle		77.5		18		1.00
		bottom		80.0		18		0.71
	back	top	38.3	35.0	10	12	1.05	1.29
		middle		37.5		10		0.98
		bottom		42.5		8		0.90

Application error and liquid recovery test

The error in the application amount and the phytosanitary liquid recovery test are shown in Table 5. When working in the field, the error in the application amount under different spraying pressures remained within 10% and the phytosanitary liquid recovery device was able to collect the droplets that did not attach to the leaves. From the test results of the phytosanitary liquid recovery rate, it was also found that with increasing of spraying pressure, the phytosanitary liquid recovery rate gradually decreased. This indicated that more droplets had attached to the leaves and the phytosanitary liquid utilization rate was improved.

Table 5**Application error and liquid recovery test results**

Pressure /MPa	Scheduled dosage / (L/min)	Average dosage / (L/min)	Error rate /%	Average recovery / (L/min)	rate of recovery /%
0.15	1.911	1.775	7.12	0.867	48.85
0.20	2.184	2.047	6.27	0.807	39.43
0.25	2.351	2.557	8.76	1.035	40.48
0.30	2.503	2.740	9.47	1.027	37.47
0.35	2.627	2.706	3.01	0.974	36.00

CONCLUSIONS

Considering the specific requirements of the double-layer hedgerow planting mode of *Lycium barbarum* L., a self-propelled straddle-type phytosanitary liquid spraying machine was designed, the key components and parameters of the machine were determined, and a prototype was made. The machine adopted the "four-wheel drive and differential steering" driving mode, which is a simple steering mechanism that reduces machine weight and has good field traversal performance and operability. The three-dimensional spraying configuration with spray rods on both sides effectively improved the spraying of the middle and lower portions of the *L. barbarum* L. and made the spraying more uniform over the entire plant. The phytosanitary liquid recovery device effectively recovered most of the phytosanitary liquid that was not attached to the leaves and reduced the pollution to the environment.

ACKNOWLEDGEMENT

The authors would like to acknowledge Zhengqihong *Lycium barbarum* L. Industry Development Co. Ltd. for their support during field testing.

REFERENCES

- [1] Chang, X. M. (2020). Pollution-free cultivation of *Lycium barbarum* L.. *Agricultural Technology and Equipment*, (03), 149-150.
- [2] Chen, J., Zhao, J., Chen, Y., Bu, L. X., Hu, G. R., & Zhang, E. Y. (2019). Design and experiment on vibrating and comb brushing harvester for *Lycium barbarum* L.. *Transactions of the Chinese Society of Agricultural Machinery*, 50(01), 152-161+95.
- [3] Hu, G. R., Kong, W. Y., Qi, C., Zhang, S., Bu, L. X., Zhou, J. G., & Chen, J. (2021). Optimization of the navigation path for a mobile harvesting robot in orchard environment. *Transactions of the Chinese Society of Agricultural Engineering*, 37(09), 175-184.
- [4] Hu, X. D. (2019). *Design and research of windproof plant protection machine*. [Master dissertation, Ningxia University]. CNKI.
- [5] Hu, X. D., Zhang, D. F., He, J., Hu, C. & Bai, F. (2021). Development and test of wind-proof wolfberry plant protection machine. *Journal of Agricultural Mechanization Research*, 43(01), 119-124+145.
- [6] Li, J. H. (2017). *Design of directional air-blowing wolfberry sprayer*. [Master dissertation, Ningxia University]. CNKI.
- [7] Li, X. P. (2021). Study on utilization value and cultivation technology of *Lycium barbarum* L.. *Seed Science and Technology*, 39(05), 24-25.
- [8] Liu, L. M., Zhang, X. H., Shi, G. Z., Jiang, H. H., Bai, P., & Li, J. (2019). Design and test of polymorphic automatic target air-blast spray test-bed. *Jiangsu Agricultural Sciences*, 47(13), 260-263.
- [9] Qi, C. (2021). *Variable spraying control system for sprayer*. [Master dissertation, Northwest A&F University]. CNKI.
- [10] Qi, P. (2017). Introduction of common plant protection machinery. *Scientific Farming*, (08), 61-62.
- [11] Wu, Z. S., Ma, M. C., & Ma, M. R. (2016). Management techniques of trellis cultivation for organic *Lycium barbarum* L. in Qaidam area of Qinghai province. *Protection Forest Science and Technology*, (08), 16-18+33.
- [12] Zhao, J., & Chen, J. (2021). Detecting maturity in fresh *Lycium barbarum* L. fruit using colour information. *Horticulturae*, 7(5).
- [13] Zhao, J., Ma, T., Inagaki, T., Chen, Q. Y., Gao, Z. N., Sun, L. J., Cai, H. X., Chen, C., Li, C. L., Zhang, S. X., Tsuchikawa, S., & Chen, J. (2021). Finite element method simulations and experiments of detachments of *Lycium barbarum* L. *Forests*, 12(6).
- [14] Zhao, J., Ma, T., Inagaki, T., Chen, Y., Hu, G. R., Wang, Z. W., Chen, Q. Y., Gao, Z. N., Zhou, J. G., Wang, M. H., Tsuchikawa, S., & Chen, J. (2021). Parameter optimization of vibrating and comb-brushing harvesting of *Lycium barbarum* L. based on FEM and RSM. *Horticulturae*, 7(9).
- [15] Zhao, J., Tsuchikawa, S., Ma, T., Hu, G. R., Chen, Y., Wang, Z. W., Chen, Q. Y., Gao, Z. N., & Chen, J. (2021). Modal analysis and experiment of a *Lycium barbarum* L. shrub for efficient vibration harvesting of fruit. *Agriculture-Basel*, 11(6).
- [16] Zheng, Q. W. (2015). Ningxia academy of agriculture and forestry sciences has achieved remarkable results in the transformation of windproof machinery for *Lycium barbarum* L. disease and insect control. *Pesticide Market News*, (25), 51.

THEORETICAL INVESTIGATION OF HEAT PRODUCTION FEASIBILITY BY MEANS OF WIND MECHANICAL PLANTS

ТЕОРЕТИЧНЕ ДОСЛІДЖЕННЯ МОЖЛИВОСТІ ВИРОБНИЦТВА ТЕПЛОВОЇ ЕНЕРГІЇ ЗА ДОПОМОГОЮ ВІТРОМЕХАНІЧНИХ УСТАНОВОК

Holovko Volodimir ^{1), 2)}, Kohanevich Volodimir ¹⁾, Shikhailov Mikola ¹⁾, Sukmaniuk Olena ³⁾, Kukharets Savellii³⁾

¹⁾ Renewable Energy Institute of NAS of Ukraine / Ukraine

²⁾ National Technical University of Ukraine «Igor Sikorsky Kyiv Polytechnic Institute» / Ukraine

³⁾ Department of mechanical and engineering agroecosystems, Polissia National University / Ukraine,

Tel: +380676653548, E-mail: kikharets@gmail.com

DOI: <https://doi.org/10.356.33/inmateh-65-37>

Keywords: wind energy, force moment, mechanical energy, pump, fan

ABSTRACT

A widespread use of wind turbines can fully or partly provide energy for the consumers, but with due regards to certain investments and instability of energy generation. Technologies of using wind energy imply the conversion of the mechanical energy of a wind flow into the electrical or heat energy. The work is concerned with the estimation of the amount of heat in the process of heating liquid coolants and heat-transfer fluids when using wind mechanical plants. In the paper was made a numerical analysis of the temperature rise of the liquid which circulates in a closed loop of a gear-type pump, whose productivity is 3 l/m and which is driven by a wind turbine 5 kW of power capacity under a nominal wind speed of 7 m/s and under cycle duration of 2 s. The analysis showed that the temperature increased by 0.290 °K/s. If such wind speed is observed during one hour, the temperature of 100 kg of water will increase by 8.1 °C. Heating of a heat-transfer fluid with a supply of mechanical energy to a working part can be achieved by a centrifugal fan. Assuming that the given process occurs without supplying and removing heat energy (it is adiabatic), for the capacity of 1.5 kW and under the revolution in a range of 1000...3000 r/m, the changes in temperature will range from 0.38 to 0.87 °K/s, but for the capacity of 7.5 kW and under 750 – 1500 r/m, the changes in temperature will range from 0.56 to 1.23 °K/s.

АБСТРАКТ

Широке використання вітроенергетичних установок може дати повну або часткову енергозабезпеченість споживача, але при врахуванні певних капіталовкладення та нестабільності вироблення енергії. Сучасні технології використання енергії вітру передбачає перетворення механічної енергії потоку вітру в електричну з подальшим перетворенням, за вимогою споживача, в механічну або в теплову енергію. Однісі із таких є технологія прямого перетворення механічної енергії, що надходить з валу ротора вітроустановки, в теплову.

Робота присвячена оцінці кількості теплоти в процесі нагрівання рідинних та газоподібних теплоносіїв при застосуванні вітромеханічних установок. За даною методикою проведено чисельний аналіз підвищення температури рідини, що циркулює за замкненим контуром шестеренчастого насосу продуктивністю 3 л/хв, привід якого здійснює вітроустановка потужністю 5 кВт за номінальної швидкості вітру 7 м/с та тривалістю циклу 2с. Аналіз показав, що підвищення температури становить 0,29°K/с. Якщо така швидкість вітру буде спостерігатися протягом години, то температура 100 кг води підніметься на 8,1°С. Нагрівання газоподібного теплоносія за рахунок підведення тільки механічної енергії до робочого органу, що здійснює його перемішування (рух), можливе за допомогою відцентрового вентилятора. Припускаючи, що даний процес проходить без підведення та відведення теплової енергії, тобто є адіабатним, для потужності 1,5кВт за зміни обертів в діапазоні 1000...3000об/хв., зміна температури складе 0,38...0,87 °K, а для потужності 7,5кВт за обертів 750...1500об/хв. – 0,56...1,23°K.

INTRODUCTION

The production of clean energy in the world increases. The goal of this process is to reduce the level of greenhouse gas emissions (Golub et al, 2017). Besides, the energy strategy of each country is focused on providing with technically reliable, cost effective and ecologically safe energy resources in order to guaranty the improvement of population well-being (Liu et al, 2021). During the period of 2015–2020, the cost indices of heat and electric energy which comes from traditional sources increased as compared with those which use the sunlight and the wind energy, the energy of biofuel, the energy of waste gases utilization of waste heat and of geothermal heat and other types of a renewable energy (Doytch et al, 2021; Cole et al, 2021).

Paying attention to everything mentioned above, the use of wind turbines in the world increases (Gönül *et al*, 2021; Li *et al*, 2021). The use of wind turbines can fully or partially provide the consumer with energy (Lawan *et al*, 2017). But the development of wind turbines requires significant capital expenditures (Zwarteveen *et al*, 2021). Besides, in the process of wind turbines exploitation it is necessary to consider the wind factor and, as a result, an inconsistent energy production (Dolara *et al*, 2017). Modern technologies of using the energy of the wind implies the conversion of a mechanical energy of a wind flow into the electrical one with further conversion, by the consumer's demand, into mechanical or heat energy (Aziz *et al*, 2017; Ali *et al*, 2021). Such systems have a very low coefficient of using the wind energy – up to 30% (Devashish, 2017; Niu, *et al*, 2018). Thus, the scientific research for improving the efficiency of using the energy of wind are numerous.

The technology of the conversion of the mechanical energy, which comes from rotor shaft of a wind turbine, into the heat energy is one of the research lines. One of the variants of such a conversion is using waste heat from the wind turbine generators; e.g. the authors Rostamzadeh *et al*, (2020) suggest using waste heat in the demineralized water generator systems. Such systems have a somewhat higher efficiency factor. For example, a system of heating and cooling on the basis of waste heat with an efficiency factor of 45% is suggested (Khalilzadeh *et al*, 2020). But such systems are rather complicated as because they contain regenerators, heaters, absorbers, heat exchangers. Besides, they have a low efficiency factor.

Using of heat carriers is one more way of producing heat energy by means of wind turbines. But the complexity and a high cost of such heat pumps are the drawbacks of such systems (Rieck *et al*, 2020).

One more interesting technology lies in creating a store of pressed air, whose energy is already used, but the complexity and unreliability of the systems on using pressed air for energy needs are the drawbacks of it (Mohammadi *et al*, 2017).

All above mentioned systems are not systems with a direct generation of heat energy. According to the research analysis, there are no investigations as to a direct conversion of mechanical energy, which comes from a rotor shaft of a wind turbine, into heat energy.

That is why the research on the feasibility of producing heat energy by means of wind turbines or by wind mechanical plants with a direct conversion of mechanical energy into heat energy is extremely important.

MATERIALS AND METHODS

The generation of heat energy when using wind mechanical plants is possible owing to the displacement of liquid in a closed space or by throttling of motive fluids through a choke or a safety valve. In the first case motive fluids are heated by the friction of fluid layers, and in the second case – by a sudden pressure jump during throttling.

The wind turbine for heat production, which is suggested by us, consists of a rotor with a hub which is firmly fastened on a shaft, 3 (Golovko *et al*, 2014). A positive displacement pump 4 (fig. 1) which is located in a sealed ribbed tank 5 with motive fluids (mineral olive), is firmly joined to the same shaft.

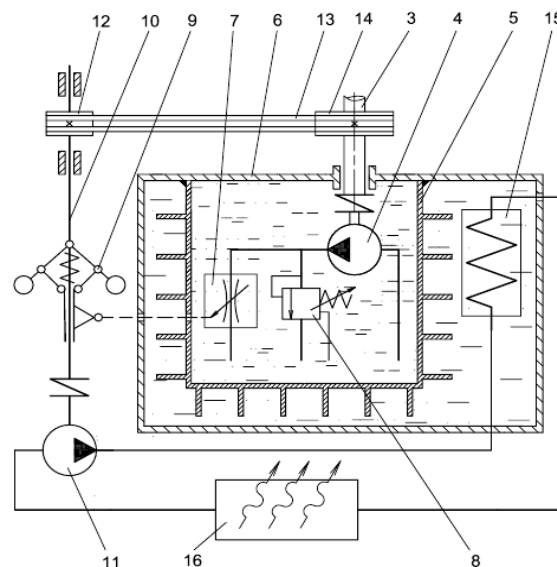


Fig. 1 - Wind mechanical plant for generating heat
(the explanation of positions is in the text)

Tank 5, in its turn, is located in a container with a heat-transfer fluid 6 (water). A controlled choke 7 is subsequently installed in the pump-discharge line 4. A safety valve 8 is installed in front of the controlled choke 7. A regulating unit of the controlled choke 7 is kinematically connected with the movable part (sensitive element) of the centrifugal corrector 9 with weights which is installed on the shaft of the circulating pump 10. On the same shaft 10, are installed the circulating pump 11, and the sheave 12, which, by means of a wedge-shaped belt 13, is cinematically connected with a low-speed pulley 14, which is tightly installed on the main shaft 3.

A heat exchanger 15 is installed in a container with a heat-transfer fluid 6, the inlet into the heat exchanger is hydraulically connected with an outlet of the circulating pump 11, and the outlet is connected with the consumer 16 of the generated heat energy, for example with a radiator of a hot-water heating. A starting Savonius rotor (*Yahya et al, 2021*) is tightly joined to the hub 2.

The wind turbine on heat production works in the following manner. When the wind speed is sufficient (2.5...3 m/s) a rotary moment occurs on a starting rotor, under the action of this rotary moment the rotor starts running up to the design speed. Herewith, a hub 2, the main shaft 3 and a shaft of a positive displacement pump 4 rotate. The positive displacement pump 4 produces the amount of fluid which is proportional to a rotor speed 1. This fluid, coming through a controlled choke 7 loses a considerable part of energy which turns into heat. Thus, motive fluids from tank 5 will be heated. To remove the generated heat from the motive fluids, tank 5 is made with ribs and is installed in a container with a heat-transfer fluid 6. A heat transfer fluid is heated as well, and the generated heat is supplied to the consumer 16 by a circulating pump 11, which is driven by the shaft 3, by means of a V-belt transmission 14, 13, 12, as well as by the shaft of a circulating pump 11. A centrifugal corrector 9, whose movable joint responds to the rotations of the shaft 3, is fastened on this shaft as well.

Its location is proportional to the deviation of the rotor rotations from rated values, that is why under the deviations of rotor rotations 1 it can move along the shaft 11 and, having a kinematic connection with the regulating unit of the controlled choke 7, it can change its conductivity. When the rotor rotations increase, the conductivity decreases and additional resistance to passage of liquids is created, which results in the rise of the temperature. To avoid pressure increase under the increase of rotor rotation 1 in the pump-discharge line 4, the safety valve 8 is installed. Under transfer of fluid through this valve the motive fluids is heated because the safety valve is also like a throttle. Thus, beside this, the rotor rotations of a wind turbine as well as its capacity are regulated, because when the rotor rotations increase, the loading on it increases due to the increase of resistance of the controlled choke.

Temperature rise per one closed cycle in a tight system will equal to (*Pratima Bajpai, 2018*):

$$\Delta t = \frac{P}{\rho C Q} = \frac{981 H}{\eta C} \quad (1)$$

where:

- P – pump capacity;
- C – specific weight of motive fluids;
- Q – pump efficiency;
- H – pump pressure;
- η – pump efficiency factor;
- ρ – specific density of heat-carrying fluid.

At the same time a driving moment on a pump shaft can be determined as:

$$M = \frac{30 \cdot Q H \gamma}{102 \mu \pi n} \quad (2)$$

where:

- n – shaft speed of a pump;
 - γ – fluid density.
- Rotor shaft moment of the wind turbine equals (*Zhao et al, 2019*):

$$M = \overline{M} \pi R^3 \frac{\rho_n v^2}{2} \quad (3)$$

where:

\bar{M} – rotor shaft moment of the wind turbine, which can be determined by the results of the calculations of a rotor characteristic line;

R – rotor radius;

v – wind speed;

ρ_n – specific air density.

Speed rate on a rotor shaft:

$$n = \frac{30zv}{\pi R} \tag{4}$$

where:

z – rotor speed whose rate is determined by a characteristic line $\bar{M} = f(z)$.

RESULTS

After building a characteristic line $M=f(n)$ under v from initial values to reference values (controlled), these values are conformed to the multiplier parameters (fig. 2).

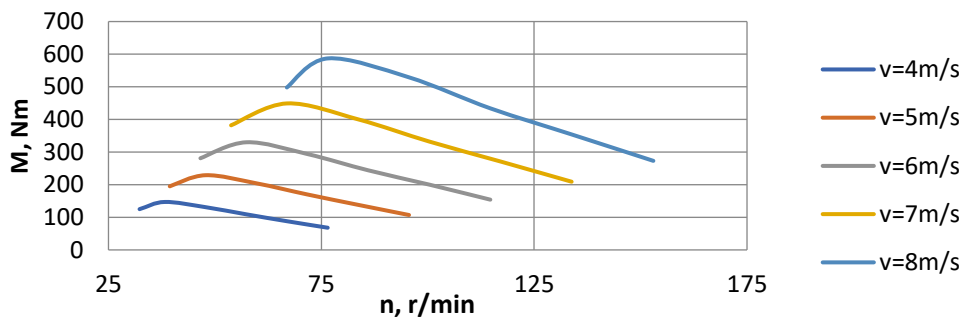


Fig. 2 - The dependence of a moment (M , Nm) on a rotor shaft on its speed (n , r/min), v – wind speed

The estimation of a temperature rise of the fluid, which circulates in a closed tube of a gear-type pump, whose productivity is 3 l/min and which is driven by a wind turbine 5 kW of power capacity under a nominal wind speed of 7m/s (fig. 3) and under cycle duration of 2 s, equals 0.29°K/s.

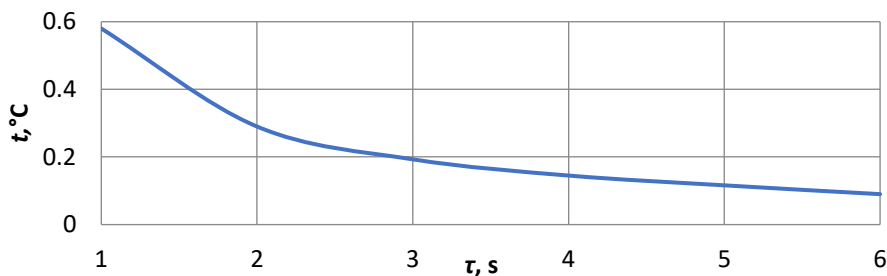


Fig. 3 - The dependence of a temperature rise of heat-transfer liquid (t , °C) on the technological cycle duration (τ , s)

Suppose, we need to determine by how many degrees the temperature of 100 kg of water will rise during one hour of heating under different rates of the wind speed. Suppose, during one hour the wind speed rate changes very little and the heat losses are not significant. Using previous dependences (fig. 2, 3) we will get as follows: under the wind speed of 8 m/s and the cycle duration of 2 s during the period of one hour, the temperature of 100 kg of water will rise by 8.1°C. The results of calculations under other conditions are given in fig. 4.

The process of heating of heat-transfer fluid by supplying only mechanical energy to the working part which makes it move (movement) is possible due to the centrifugal fan if the inlet and the outlet fittings are closed.

If we suppose that this process goes on without supplying and removing heat, that is the process is adiabatic, (under occurrence and non-occurrence of heat exchange with the environment), the parameters relationship of the body which is being heated will equal (Rosa et al, 2021):

$$\frac{T_1}{T_2} = \left(\frac{p_1}{p_2} \right)^{\frac{k-1}{k}} \tag{5}$$

where:

T_1, T_2 – the inlet- and outlet temperature respectively during one cycle;

p_1, p_2 – the environmental pressure and the pressure in a functional area of a fan respectively;

k – the adiabatic index (for dry air in the range from 20 to 100°C it equals from 1.4 to 1.401).

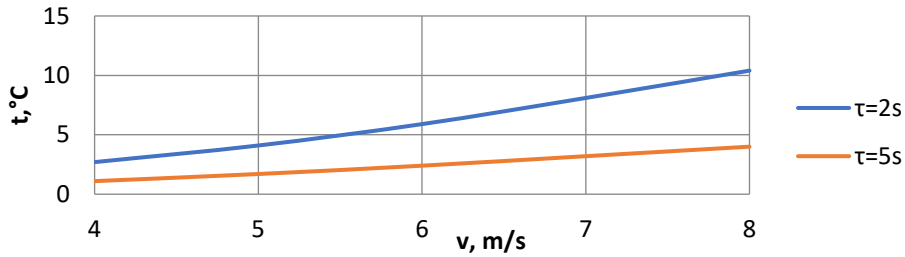


Fig. 4 - The dependence of the temperature rise ($t, ^\circ\text{C}$) of 100 kg of water on different rates of wind speed ($v, \text{m/s}$) and cycle duration (τ, s)

According to a given formula, the temperature at the outlet will depend on the pressure in a functional area that is on a drive capacity as well as on the number of rotations of the fan shaft. For example, for the capacity of 1.5 kWt and under the rotations change in the range from 1000 to 3000 r/m, the temperature change will equal 0,38...0,87°K, and for the capacity of 7.5 kWt under the rotations change in the range from 750 to 1500 r/m, the temperature change will equal to 0.56...1.23°K.

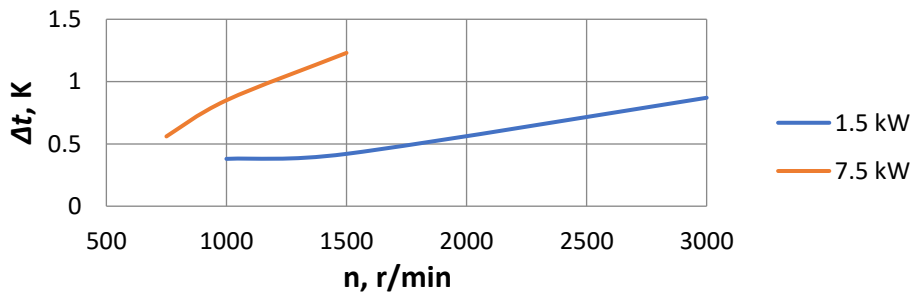


Fig. 5 - The dependence of the temperature rise ($\Delta t, \text{K}$) of a heat-transfer fluid on the rotation speed ($n, \text{r/min}$) of the fan shaft

Thus, it is principally important to use wind mechanical plants in order to provide the consumers' heat needs. But it should be taken into account, that under a low energy density of wind speed up to 8m/s, it is necessary to increase the size dimension of a wind turbine in order to increase the technological efficiency of heating. It should be mentioned that a twofold increase of a rotor diameter results in a fourfold increase of capacity on a shaft, but specific material costs per unit of capacity increase as well. The use of wind turbines is expedient on the areas with high potential, as a twofold increase of wind speed results in the eightfold capacity increase.

CONCLUSIONS

The amount of heat in the process of heating liquid coolants and heat-transfer fluids when using wind mechanical plants was estimated during the research. A numerical analysis of the temperature rise of the liquid which circulates in a closed loop of a gear-type pump, whose productivity is 3 l/min and which is driven by a wind turbine 5 kW of power capacity under a nominal wind speed of 7 m/s and under cycle duration of 2s, was made.

The temperature increased by 0.29°K/s. If such wind speed is observed during one hour, the temperature of 100 kg of water will increase by 8.1°C. Heating of a heat-transfer fluid with a supply of only mechanical energy to a working part, which makes it drive (movement), can be achieved by a centrifugal fan. Under the assumption that the given process occurs without supplying and removing heat energy (is adiabatic), then, for example, for the capacity of 1.5 kW under the revolutions changes in a range of 1000...3000 r/m, the changes in temperature will range from 0.38 to 0.870 K, and for the capacity of 7.5 kW under 750...500 r/min the changes in temperature will range from 0.56 to 1.230 K.

REFERENCES

- [1] Aziz, M. S., Mufti, G. M., & Ahmad, S., (2017), Wind-hybrid Power Generation Systems Using Renewable Energy Sources – A Review, *International Journal of Renewable Energy Research*, vol. 7, no.1, pp.111-127.
- [2] Ali, R. B., Bouadila, S., Arıcı, M., & Mami, A., (2021), Feasibility study of wind turbine system integrated with insulated Greenhouse: Case study in Tunisia, *Sustainable Energy Technologies and Assessments*, vol. 47, 101333.
- [3] Cole, W., Gates, N., & Mai, T., (2021), Exploring the cost implications of increased renewable energy for the U.S. power system, *The Electricity Journal*, vol. 34, issue 5, 106957.
- [4] Devashish, J., (2017), A Comprehensive Review on Wind Energy Systems for Electric Power Generation: Current Situation and Improved Technologies to Realize Future Development, *International Journal of Renewable Energy Research*, vol.7, no.4, pp.1786-1805.
- [5] Dolara, A., Gandelli, A., Grimaccia, F., Leva, S., & Mussetta, M., (2017), Weather-based machine learning technique for Day-Ahead wind power forecasting, *IEEE 6th International Conference on Renewable Energy Research and Applications (ICRERA)*, pp. 206-209, doi: 10.1109/ICRERA.2017.8191267.
- [6] Doytch, N., & Narayan, S., (2021), Does Transitioning towards Renewable Energy Accelerate Economic Growth? An Analysis of Sectoral Growth for a Dynamic Panel of Countries, *Energy*, 121290.
- [7] Gönül, Ö., Duman, A.C., Deveci, K., & Güler, Ö., (2021), An assessment of wind energy status, incentive mechanisms and market in Turkey, *Engineering Science and Technology, an International Journal*, (Available online 21 April 2021 In Press).
- [8] Golovko V.M., Kohanievych V.P., & Shyhailov M.O., (2014), Wind Turbine on Heat Production, *Utility model patent of Ukraine №90974, published in a bulletin №11*.
- [9] Golub G.A., Kukharets S.M., Yarosh Y.D, Kukharets V.V., (2017), Integrated use of bioenergy conversion technologies in agroecosystems, *INMATEH – Agricultural Engineering*, Vol.51, Issue 1, pp.93–100
- [10] Khalilzadeh, S., & Nezhad, A. H., (2020), Using waste heat of high capacity wind turbines in a novel combined heating, cooling, and power system, *Journal of Cleaner Production*, vol. 276, 123221.
- [11] Lawan, M. M. G., Raharijaona, J., Camara, M. B., & Dakyo, B., (2017), Power control for decentralized energy production system based on the renewable energies — using battery to compensate the wind/load/PV power fluctuations, *IEEE 6th International Conference on Renewable Energy Research and Applications (ICRERA)*, pp. 1132-1138.
- [12] Li, J., Chen, S., Wu, Y.g, Wang, Q.i, Liu, X., Qi, L., Lu, X., & Gao, L., (2021), How to make better use of intermittent and variable energy? A review of wind and photovoltaic power consumption in China, *Renewable and Sustainable Energy Reviews*, vol. 137, 110626.
- [13] Liu, X., Zhao, T., Chang, C.-Ter, & Fu, C. J., (2021), China's renewable energy strategy and industrial adjustment policy, *Renewable Energy*, vol. 170, pp. 1382-1395.
- [14] Mohammadi, A., Ahmadi, M. H., Bidi, M., Joda, F., Valero, A., & Uson, S., (2017), Exergy analysis of a Combined Cooling, Heating and Power system integrated with wind turbine and compressed air energy storage system, *Energy Conversion and Management*, vol. 131, pp. 69-78.
- [15] Niu, B., Hwangbo, H., Zeng, L., & Ding, Y., (2018), Evaluation of alternative power production efficiency metrics for offshore wind turbines and farms, *Renewable Energy*, vol. 128, part A, pp.81-90.
- [16] Rosa, Aldo V. da, & Ordóñez, J. C., (2021), A Minimum of Thermodynamics and of the Kinetic Theory of Gases, *Fundamentals of Renewable Energy Processes (Fourth Edition)*, Academic Press, ch. 2, pp. 49-104.

- [17] Rostamzadeh, H., & Rostami, S., (2020), Performance enhancement of waste heat extraction from generator of a wind turbine for freshwater production via employing various nanofluids, *Desalination*, vol. 478, 114244.
- [18] Rieck, J., Taube, L., & Behrendt, F., (2020), Feasibility analysis of a heat pump powered by wind turbines and PV - Applications for detached houses in Germany, *Renewable Energy*, vol. 162, pp. 1104-1112.
- [19] Pratima Bajpai, (2018), Hydraulics, Biermann's Handbook of Pulp and Paper (Third Edition), ch. 23, pp. 455-482.
- [20] Yahya, W., Ziming, K., Juan, W., Qurashi, M. S., Al-Nehari, M., & Salim, E., (2021), Influence of tilt angle and the number of guide vane blades towards the Savonius rotor performance, *Energy Reports*, vol. 7, pp. 3317-3327.
- [21] Zhao, D., Han, N., Goh, E., Cater, J., & Reinecke, A., (2019), General introduction to wind turbines, *Wind Turbines and Aerodynamics Energy Harvesters*, Academic Press, ch. 1, pp. 1-20.
- [22] Zwartveen, J. W., Figueira, C., Zawwar, I., & Angus, A., (2021), Barriers and drivers of the global imbalance of wind energy diffusion: A meta-analysis from a wind power Original Equipment Manufacturer perspective, *Journal of Cleaner Production*, vol. 290, 125636.

MACHINE LEARNING TECHNIQUES IN PLANT DISEASE DETECTION AND CLASSIFICATION – A STATE OF THE ART

/

MACHINE LEARNING

ഉപയോഗിച്ചുള്ളവിളകളിലെരോഗനിർണ്ണയവുംകണ്ടെത്തലും – ഒരുപഠനം

Sreya John¹⁾, Arul Leena Rose^{*1)} 1

¹⁾ Department of Computer Science, College of Science and Humanities, SRM Institute of Science and Technology, Kattankulathur, Chennai -603203 / India;
E-mail: leena.rose527@gmail.com
DOI: <https://doi.org/10.356.33/inmateh-65-38>

Keywords: Plant disease detection, Machine Learning, Convolutional Neural Network, Classification

ABSTRACT

As we belong to a developing country, the agricultural importance is a known criterion. Majority of the Indians depend on agriculture for their basic living. It also serves as the backbone of the Indian economy. Therefore this sector should be considered important and taken care of. Diseases affecting the plants and pest are the two major threats of agriculture production. Naked eye observation followed by the addition of chemical fertilizers is the traditional method adopted by most of the farmers to avoid plant diseases. But the main limitation to this method is that it works only in the case of small scale farming. In order to tackle this issue many automatic plant disease detection systems have been developed from the early 70s. This paper is intended to survey some of the existing works in plant disease recognition that include various procedures, materials and approaches. They use different machine learning algorithms, image processing techniques and deep learning methods for disease detection. This paper also compares and suggests novel methods to recognize and classify the various kinds of infections affecting agricultural plants.

ABSTRACT

ഇന്ത്യയിൽവളരെയധികംപ്രാധാന്യമർഹിക്കുന്നഒരുമേഖലയാണ്കാർഷികമേഖല. പകുതിയിലധികംവരുന്നരാജ്യത്തെപൗരന്മാർഇന്നുംകാർഷികമേഖലയെആശ്രയിച്ചാണ്ജീവിക്കുന്നത്. അതുകൊണ്ട്തന്നെഈവിഭാഗംനേരിടുന്നഎല്ലാവിധവെല്ലുവിളികളുംപ്രാധാന്യമർഹിക്കുന്നതുംഗൗരവത്തോടെകാണേണ്ടതുമാണ്. കാർഷികവിളകളെബാധിക്കുന്നരോഗങ്ങൾഒരുപ്രധാനവെല്ലുവിളിതന്നെയാണ്. ഇവമൂലംഉണ്ടാവുന്നനഷ്ടങ്ങളുംവളരെകൂടുതലാണ്. അതിനാൽ 70 കൾമുതൽഇതിനുപ്രതിവിധിയെന്നോണംപലരോഗനിർണ്ണയ applications ഉംനിലവിൽവന്നു. Machine learning ഉപയോഗിച്ചുള്ളപലപുതിയരോഗനിർണ്ണയരീതികളുംഅവയുടെപ്രാധാന്യവുമാണ്ഈപഠനത്തിലൂടെവ്യക്തമാക്കുന്നത്.

INTRODUCTION

A developing country like India depends on the agricultural sector to a large extent. Around 70% of its population rely upon agriculture for food and livelihood. Also, this sector has a vital role in contributing to the Indian Economy. Recent studies show that several types of diseases and pest infections are causing serious yield losses across the farmlands. Therefore, it requires great care and attention during the whole cultivation process. Naked eye observation followed by the addition of chemical fertilizers is the traditional method adopted and practiced by most of the farmers. The main limitation to this method is that it works only in small scale farming. Also many farmers are unaware of the different diseases affecting the agricultural crops and their respective control measures.

¹ Sreya John, Arul Leena Rose, Dr. P.J.

Manually observing plants and expertise in plant diseases is a time consuming, tedious process. For these reasons, it has become important to automatically detect diseases and classify them accordingly.

Hence, this paper gives an idea about the latest methods and techniques introduced in the plant disease detection and classification. Also the established existing techniques such as image processing, MATLAB, Machine learning algorithms, Neural networks etc. are studied and compared accordingly. Image processing is a vast and highly recommended area. This approach includes many steps such as data collection, image pre-processing, image segmentation, selected feature extraction and disease classification. Pre-processing is nothing but improving the input image data by suppressing the unwanted noises or distortions and also enhancing the image features that are necessary for further processing. After pre-processing the image is segmented or simplified into something that is easier for the system to analyze. Further, the features are extracted, so that when an unknown image is given, the system can identify whether it is a diseased or healthy image. There are many classification techniques to classify the various diseases affecting the plants. These techniques are compared, analyzed and discussed in this paper in terms of its performance level and accuracy.

RELATED WORKS

This area of study deals with some of the works associated with the plant disease recognition and classification using machine learning techniques and they are presented below.

Azim et al., (2021), developed a feature extracting method for the rice plant leaf disease classification. In this work, 3 types of diseases affecting the rice leaves are detected. The unwanted parts of the image are separated using saturation threshold and the diseased areas are segmented using hue threshold. Extreme gradient boosting decision tree ensemble is used in this system for its better performance. This system shows an accuracy of 86.58% for the rice leaf image dataset collected from UCI. *Bisen D., (2021)*, developed a plant species recognition system using deep convolutional neural network. The CNN classifier used here study the features of leaves through hidden layers such as convolutional layer, max pooling layer, dropout layers and fully connected layers. This system makes use of the extracted features from the leaves for the species detection process. The features are collected using Swedish leaf dataset which consist of 15 tree classes and results in 97% accuracy. *Andhare et al., (2020)*, compared several machine learning techniques namely clustering, classification, regression etc. in their work and a detailed study on different plant disease detection systems are also done. Data collection using real time images and wireless sensor networks are also discussed in this work. *Hassan et al., (2021)*, developed a deep convolutional neural network system for the recognition of plant species utilizing the plant leaf images. Due to the similarity in the morphological features of plant species, it is difficult to classify using the traditional techniques. Features such as shape, size, color etc. are considered in this work to recognize the leaf species. *Poonguzhali et al., (2019)*, developed a crop assessment system using machine learning. It stresses on the assessment of the crop condition with the help of its leaves. In this work, K-means clustering is used for segmentation. TensorFlow and machine learning algorithms are the techniques adopted in classification. The images of diseased and healthy leaves are taken directly from the real time environment in order to assess the crops. *Badage. A., (2018)*, suggested a plant disease recognition model using machine learning algorithms. The aim of this work is early detection of diseases. The identification of crop diseases is done using the canny edge detection algorithm. *Goel et al., (2021)*, outlined a system to automate farming by interconnecting agricultural systems with Big Data and Internet of Things, which can also provide rapid data analysis. Study of different technologies and models are also done in this work for areas such as yield estimation, crop sowing dates etc.

Singh V. et al., (2017), developed an algorithm for image segmentation technique. The proposed algorithm is tested on 10 species such as sapota, banana, jackfruit, tomato, lemon, potato, beans and mango. *Singh T. et al., (2021)*, discussed various algorithms such as ANN and image processing tools that are used by researchers in plant disease detection. *Vashisht et al., (2021)*, analyzed different machine learning approaches that are adopted in the plant disease detection. This paper also explains the functioning and comparative measures of many algorithms with other technologies. *Singh. A et al., (2021)*, proposed a method for the recognition of potato leaf diseases. In this paper, the classification of diseases is done using SVM and grey-level co-occurrence matrix. *Kadoli V. et al., (2021)*, developed a dissimilar disease recognition system using machine learning tools by taking the leaf images as the input data. This approach aims at the early detection of plant diseases. Classification is done using the two machine learning algorithms, K-means clustering and support vector machine.

Rahman et al., (2020), developed a rice disease detection system based on the image processing techniques such as data segmentation, feature extraction and classification using the convolutional neural networks. *Kumar R. et al., (2021)*, introduced a model to locate the fungal blast disease in rice seed using the classifiers such as random forest, SVM, decision tree, logistic regression and Naïve Bayes. Here, the results from the traditional classifiers are taken and compared using transfer learning. *Mohapatra et al., (2021)*, developed a rice disease detection system using the Naïve Bayes algorithm. This system uses both machine learning and image processing technologies. In this work, the classification is done using Convolutional neural networks.

Aliyu. M. A et al., (2020), in their work used large diseased plant leaf image datasets to compare support vector machine, a machine learning technique with deep learning. Factors such as architecture, the amount of training data and computational power are considered to evaluate the two. *Sethy P.K et al., (2020)*, displayed a study on the development of the rice plant disease detection using image processing techniques by referring various research papers. This work also discusses the limitations, achievements and suggestions for future work in this area. *Karthik R. et al., (2020)*, developed a tomato leaves disease detection system based on deep residual network. Two different deep architectures are used for the disease recognition and classification. *Sharma P. et al., (2020)*, proposed a solution to the fatal flaw of the deep learning models that when tested once on the unseen dataset, their performance diminishes. This problem can be rectified using segmented images to train the convolutional neural network models. *Singh V. et al., (2020)*, illustrated a study on various computer vision approaches and imaging tools utilized in the plant disease detection. This paper also discusses the challenges and current trends in this field. *Panigrahi et al., (2020)* focused on supervised machine learning techniques to develop a disease detection system for the diseases affecting maize leaves. Decision Tree, Naïve Bayes, KNN, Random Forest and SVM are the classification techniques analyzed and compared here. Also it concluded that RF algorithm shows an accuracy of 79.2% when compared with the other classification methods.

Iniyar S. et al., (2020), developed a model to detect and classify the diseases using machine learning algorithms such as SVM and artificial neural network. This paper also discusses on the pros and cons of methods used. *Sreehari R. et al., (2020)*, illustrated a system in which the work is done on a web portal. Traditional wholesale services are discussed in this work. The plant disease identification is done using image processing tools and machine learning. *Sujatha R. et al., (2021)*, compared the performance of deep learning and machine learning in terms of citrus plant leaf diseases. This paper also discusses the advantages and disadvantages of machine learning over deep learning. *Ganatra N. et al., (2020)*, developed a multi class disease recognition system. Plant leaf images of various classes are taken and two different datasets are being used here. Many classification techniques are taken for comparison and Random Forest gives the highest accuracy. *Wei et al., (2020)*, used Random forest algorithm to build a carrot yield mapping system. The databases used in this model are satellite spectral data and carrot ground-truth yield sampling. *Abdullahi et al., (2017)*, developed a plant image recognition and classification system with an accuracy of 99.58%. Here the datasets are collected using remote sensing techniques. Features are extracted and segmented using the image processing techniques. Classification techniques such as SVM, CNN, fuzzy logic and neural networks are compared and evaluated. *Deepalakshmi P. et al., (2021)*, introduced a plant disease detection model. The feature extraction and classification is done using DCNN. The model produced an accuracy of 94.5%. *Oo Y.M et al., (2018)*, developed a model to classify diseases such as Powdery Mildew, Bacterial Blight, Cercospora leaf spot and Rust. The major algorithms used in this system are Local binary pattern, SVM and KNN. In this work, Histogram Equalization is done to enhance the image context. K-means clustering is utilized to segment the leaf images. GLCM and LBP features are extracted after applying K-means clustering. *Dhingra. G et al., (2018)*, did a comprehensive study on image processing techniques such as segmentation, feature extraction of the dataset and classification in the field of plant disease detection. An analysis of previously proposed works is also done in this paper. *Sambasivam G et al., (2021)*, developed a model using CNN and Rectifier Linear Unit to detect and validate the diseases affecting Cassava with an imbalanced dataset. The system provides an accuracy of 93%. *Huang. Z. et al., (2020)*, developed a system to identify and classify grape leaf disease by using four modified deep learning models. Based on 3 pre-trained machine models VGG-16, AlexNet and MobileNet, transfer learning technique has been used here. *Dahiya S. et al., (2020)*, reviewed the recent studies in which machine learning has been applied to detect and classify various plant diseases. They had also discussed about CNN and its various parameters, transfer learning and factors that can affect the performance level of the deep learning model. *Sivasangari et al., (2021)*, used Standard Area Diagrams (SADs) to show the seriousness of the plant disease in terms of percentage using image processing and neural

networks. This model is based on TensorFlow and MobileNet architectures. *Vashisht et al., (2021)*, analyzed the predictive measures for the better understanding of existing architectures of commonly used artificial neural networks in the recognition and classification of plant diseases. In this work, they had proposed a Gaussian filter as a predictive measure or value to improve the efficiency of trained model at minimal computational costs.

Ferentinos K.P., (2018), used 90 thousand images as datasets and 58 classes of plant varieties in his Plant disease detection and diagnosis system. DCNN is used to build this model. *Türkoğlu M. et al., (2019)*, proposed a system which utilizes transfer learning and deep feature extraction methods. The system is built using 9 architectures of deep neural networks. The classification is done using KNN, SVM and extreme learning machine. *Ramcharan et al., (2017)*, trained a deep convolutional neural network model by applying transfer learning to identify the three commonly occurring diseases and 2 types of pest damage. In order to avoid the complex feature extraction step, transfer learning from CNN inception V3 is used here.

Francis J. et al., (2016), developed a pepper plant leaf disease identification system by applying image processing tools and MATLAB. The proposed system identifies and informs the user if any variation from the characteristic features of the plant parts is observed. *Ngugi. L.C. et al., (2021)*, reviewed the recent development achieved in the area of crop pest and disease identification utilizing both image processing and machine learning tools. This work is narrowed to those methods designed for pest and disease identification using visible light images (RGB). They conducted an experiment to study about ten commonly used CNN architectures and concluded that ResNet-101, DenseNet201 and VGG16 are the high accuracy performers when compared to the other deep learning models. *Shruthi U et al., (2019)*, through their work concluded that Convolutional Neural Networks provides better accuracy than the other techniques and detects large number of diseases. This paper gives an insight about the various stages of plant disease detection and their comparative studies. *Vishnoi V.K et al., (2020)*, used image processing tools such as segmentation, image preprocessing, feature extraction and classification to detect the diseases affecting the agricultural crops. This paper also summarizes the difficulties during the feature extraction module. *Golhani et al., (2018)*, studied and compared the varieties of artificial neural networks that are applied in the plant disease recognition using hyper spectral data. This work gives a detailed review on the different mechanisms, types and many other features of the neural networks. *Giraddi S. et al., (2020)*, proposed an automated system to detect the fungal diseases affecting the maize leaves. This model uses the image processing techniques for extracting features and segmenting. Deep learning algorithms are followed in the disease classification.

Ashok S. et al., (2020), reviewed about the different levels of plant disease identification system and did a comparison between various machine learning classification algorithms. This paper also concludes that CNN provides better accuracy than others and detects a large number of diseases. *Venkataramanan A. et al., (2019)*, introduced a model that uses multi stage classification in order to provide better accuracy. Here, a leaf from the input image set is extracted using a YOLOv3 object detector. Many ResNet18 layers which are trained using the transfer learning are used to analyze the extracted leaf. One of the layers detects the disease type and the rest classify the leaf type. *Singh V. et al., (2015)*, developed a system to detect the unhealthy region of plant leaves. In this work, the image segmentation is done using generic algorithm. *Mukhopadhyay S. et al., (2021)*, developed a system that utilizes the image clustering algorithm NSGA-II to detect the diseased area in the tea leaves.

Patidar S. et al., (2020), introduced a rice leaf disease recognition model. Deep residual learning is the algorithm used here to detect the 3 common rice plant diseases. *Ramya R. et al., (2020)*, used MATLAB and cloud computing for the fruit disease detection and classification. K-means clustering and support vector machine are the techniques used for the disease classification. *Geetharamani et al., (2019)*, implemented a system that uses 6 data augmentation methods and deep CNN model with thirty nine varieties of plant leaves classes and their background images. Data augmentation is used in order to improve the conduction of the model. *Nandhini et al., (2021)*, focused on the diseases affecting tomato, corn and apple leaf diseases. The implemented CNN architecture consists of 5 layers. *Shrestha G. et al., (2020)*, illustrated a simulation study and analysis in terms of the area of infected region and time complexity. Around 15 diseases are identified and classified using the image processing. *Bedi P et al., (2021)*, proposed a model using the deep learning architecture LeNet -5. Peach plant leaves are considered in this paper. Discussions on many CNN architectures such as AlexNet etc. are also done here. *Goncharov P. et al., (2018)*, used deep Siamese convolutional neural network, a deep learning tool to detect three main types of diseases that infect the grape leaves. *Hussein M.A et al., (2019)*, developed a computer based model to detect the diseases affecting the plant leaves.

Here the preprocessing is done using the cropping, filtering and histogram equalization techniques. The classification process of the diseases is done using SVM. *Gunasekaran S. et al., (2021)*, introduced delta tributary network, a novel deep learning technique that can replace the bottleneck DCNN architectures for plant disease detection and classification. *Nihar V. et al., (2021)* proposed a novel neural network ModCNN that produces an accuracy of 97.69% in finding the common diseases affecting the plant leaves.

Ghorai A.K. et al., (2021), illustrated a model to detect the nutritional deficiencies and diseases affecting the plant leaves. In this paper, pre-processing is done using color space models. The major filtering techniques followed here are Gaussian, Mean, Rank, Laplacian and Bilateral. *Selvaraj M.G. et al., (2019)*, introduced a DCNN based detection system to detect the diseases and pests infecting banana plants. A deep transfer learning is used here to develop a network that can make accurate predictions. ResNet50, InceptionV2 and MobileNetV1 are the three architectures used in this system.

Lin H. et al., (2021), developed a model that can process the leaf disease image using the color features compositing and detection method for the lesion segmentation. PCA method is used to remove the features and simplify them. *Afzaal. H et al., (2021)*, explained a system to investigate the Early Blight disease in potato plant throughout its growing stages. Deep Learning models mainly GoogLeNet, VGGNet and EfficientNet are trained using the PyTorch framework. *Brenes et al., (2021)*, proposed a system to detect the diseases infecting horticultural crops. Tomato and bell pepper leaves are taken to perform the experiment. In order to classify the diseases a custom created model classifier along with a pre trained DenseNet-161 classifier is implemented. *Gargade A. et al., (2021)* introduced an automated computer based model to detect the nutritional deficiencies and some of the leaf diseases in custard apple plant. The algorithms applied for the classification are SVM and K Nearest neighbor. Supervised machine learning is adopted in this work using image processing tools. *Kartikeyan P. et al., (2021)*, reviewed some of the emerging trends in the area of plant disease identification and classification. This paper discusses the established techniques used for the extraction of features and image segmentation. Some classification techniques such as SVM, ANN, and KNN are studied and compared based on the accuracy and performance. *Patel A. et al., (2021)*, made a brief report on the image processing tools and machine learning algorithms that are used to identify the variety diseases affecting the banana plant. The other methods and technologies used in the detection and classification processes are also analyzed and discussed.

Patil A. et al., (2021), developed a system that uses SVM and KNN algorithms for the classification of diseases. The feature extraction technique used here is GLCM (5). Comparison with the existing traditional methods is also done in this paper so as to prove the high efficiency of the proposed system. *Dalal T. et al., (2021)*, illustrated a study of leaf disease recognition and classification using multiple CNN algorithms. A comparative study on various training methods and feature extraction techniques are also done in this work. *Xiao et al., (2021)*, introduced a CNN based model to identify the diseases affecting strawberry plant leaves. The architecture of this model is based on ResNet50. *Anagnostis et al., (2021)*, proposed a system that can detect and classify anthracnose infected trees from the walnut orchards. A deep learning methodology is followed and achieved an accuracy of 87%. *Shah et al., (2021)*, illustrated a model utilizing image processing techniques such as segmentation, feature extraction and disease classification to detect the infections affecting the plants. Cotton leaves images are considered for the process. *Maheshwari K. et al., (2021)*, introduced a model to analyze the performance of diseases affecting the mango leaves using machine learning techniques. This model is based on the LeNet architecture. Here the classification is done using KNN and CNN algorithms. *Nandhini et al., (2021)*, developed a model that utilizes CNN approach to classify bacterial spot, Septoria leaf spot, late blight, and Tomato mosaic virus, four types of diseases affecting the tomato leaves without any manual intervention. The model achieved an accuracy of 99%. *Hasan M.Z. et al., (2021)*, proposed a system that is able to detect and classify the diseases affecting the Betel Vine leaves by applying machine learning tools. Various computer vision and machine learning approaches are compared here. *Yadav S. et al., (2021)*, developed a bacteriosis detection and evaluation system in peach leaves. Here the image processing technique, segmentation of the leaves images is done automatically. This model achieved an accuracy of 98.75% on 240 testing images.

Islam M.A. et al., (2021) introduced a paddy leaf disease recognition system using deep convolutional neural networks. This system detected four different types of diseases affecting the paddy leaves. Four architecture models VGG-19, Inception- ResNet –V2, ResNet-101, Xception are analyzed and computed in this paper. Inception – ResNet – V2 gives an accuracy of 92.68%, which is the highest. *Tiwari et al., (2021)* illustrated a plant disease detection system that uses deep convolutional neural networks to classify the diseases.

In this work, six crops of twenty seven categories are considered to check laboratory and on field conditions. *Pandey C. et al., (2021)*, developed a system that consists of fully automatic segmentation of plant leaves which is followed by spatial domain feature extraction and SVM to predict the diseases. *Bhargavi K. et al., (2021)*, reviewed the common CNN architectures that are used for plant disease recognition such as AlexNet, ZFnet, VGGNet, ResNet, GoogleNet, and LeNet. They are compared using the design and advantages. In terms of accuracy and error rate ResNet and ZFnet gives higher efficiencies.

Hu G. et al., (2021), proposed a tea leaf blight identification system that uses a deep learning technology also called faster region based convolutional neural network. It improves the recognition performance of the blurred images. The severity of the TLB is accurately classified using the VGG16 deep learning model.

RESULTS AND DISCUSSIONS

This survey provides an overview of the latest works done in the plant disease recognition and classification field using machine learning techniques. We have taken 80 research papers that used various machine learning techniques for the comparison study. Articles (*Bisen D., 2021; Badage, 2018; Singh. V., 2017; Kadoli V., 2021; Singh V., 2020; Ganatra N., 2020; Abdullahi H.S., 2017; Deepalakshmi P., 2021; Oo, Y.M., 2018; Geetharamani, 2019; Nandhini S., 2021; Shrestha G., 2020; Gunasekaran S., 2021*) have taken many varieties of plant leaves as the input data (Table1). The performances of these models are studied with the other papers that are focusing on some particular plants and diseases. Also the accuracy rates of these models are very high. Convolutional neural network, Support vector machine, K-means clustering and random forest are the common architectures followed in most of the recent works.

Among these architectures, VGG16, ResNet50 and LeNet5 of Convolutional Neural Network provide high efficiency systems. This is described in article *Huang Z., (2020); Ngugi. L.C, (2020); Bedi P., (2021); Lin H., (2021); Xiao, (2021); Islam M.A, (2020); Bhargavi, (2021)*. In most of the papers, we can see that the crop leaf images are used as the input dataset. This should be rectified in the future research works by including other plant part images also as the datasets. The crops considered for disease detection in these 80 research papers are listed in Fig 1. From this graph we can say that only few works have been done in some plants (*Xiao et al., 2021; Anagnostis et al., 2021*). Equal care and importance should be given to all plants so that we can improve the agricultural sector.

Table 1

Summary of the review papers in terms of Architecture and Accuracy

Article	Architecture and Validation	Leaf type	Accuracy
[7]	Extreme gradient boosting decision tree (XGBOOST)	Rice Leaf	86.58%
[11]	CNN	15 classes of leaves are considered.	97%
[53]	TensorFlow, ANN	Paddy leaf images	
[8]	Canny Edge Detection	Wheat, Cotton	
[64]	Grey level Co-occurrence, SVM	Potato	95.99%
[35]	K-Means Clustering, SVM	many varieties	85%-88%
[38]	SVM, Logistic Regression, Decision Tree, Naïve Bayes, Random Forest.	Rice Leaf	90%
[54]	CNN	Rice Leaf	90%
[60]	Deep Residual Neural Network	Tomato	98%
[67]	CNN	many varieties	98.60%
[49]	Naïve Bayes, Decision Tree, KNN, SVM, Random Forest	Maize	79.23%
[19]	DCNN	many varieties	88.80%
[1]	ANN, SVM, Fuzzy logic, CNN	many varieties	99.58%
[15]	CNN	many varieties	94.50%
[47]	K-Means Clustering, SVM, Local Binary Pattern	many varieties	89%
[57]	CNN, ReLU	Cassava	93%
[55]	DCNN	Cassava	93%
[21]	DCNN	39 Leaf varieties	96.46%
[44]	CNN	Tomato, corn, apple	96%- 98%
[62]	CNN	many varieties	88.80%
[9]	LeNet-5	Peach	90%

Table 1
(continuation)

[26]	Deep Siamese CNN	Grape	90%
[27]	Delta Tributary Network	many varieties	96%
[39]	PCA and Machine Learning	Pumpkin	97.30%
[20]	KNN, SVM	Custard	99.50%
[30]	VGG16, Faster Region based CNN	Tea leaf	95.74%

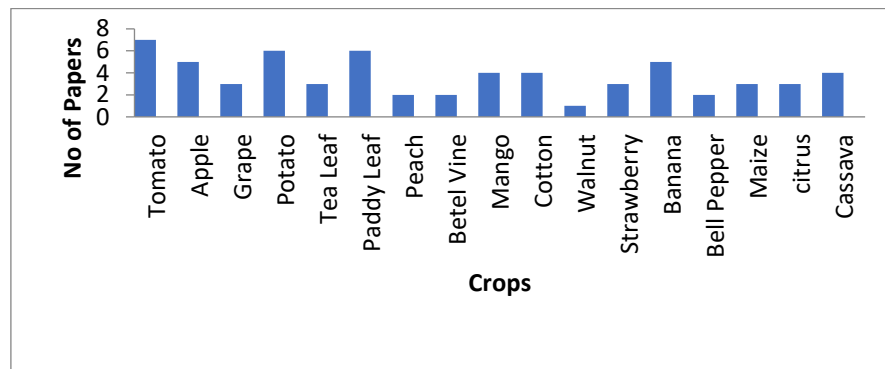


Fig. 1 -Agricultural crops considered for the computer based automated plant detection system

CONCLUSIONS

This survey gives an idea about the importance of the plant disease detection and also about the adverse effects if it is not done on time. Early recognition of the disease and subsequent treatment is the best solution to adopt in such cases. For this, we need accurate automated plant disease detection systems. With the help of such technologies the plant disease detection system automatically detects the symptoms that are visible on leaves and stem of the plant and helps in nurturing healthy plants of the farmland. Thus increases the yield and quality of the agricultural products. In this paper, study on the existing systems have been done and compared in terms of the time and accuracy. The architectures that are used to build the models are also studied and analyzed based on the performance and accuracy.

ACKNOWLEDGEMENT

I would like to thank my Supervisor, Dr.P.J. Arul Leena Rose, for her support and guidance throughout this work.

REFERENCES

- [1] Abdullahi, H. S., Sheriff, R., Mahieddine, F. (2017). Convolution neural network in precision agriculture for plant image recognition and classification. In *2017 Seventh International Conference on Innovative Computing Technology (INTECH)*, Vol. 10. IEEE.
- [2] Afzaal, H., Farooque, A. A., Schumann, A. W., Hussain, N., McKenzie-Gopsill, A., Esau, T., Acharya, B. (2021). Detection of a potato disease (early blight) using artificial intelligence. *Remote Sensing*, 13(3), 411.
- [3] Aliyu, M. A., Mokji, M. M. M., Sheikh, U. U. U. (2020). Machine learning for plant disease detection: an investigative comparison between support vector machine and deep learning. *IAES International Journal of Artificial Intelligence*, 9(4), 670.
- [4] Anagnostis, A., Tagarakis, A. C., Asiminari, G., Papageorgiou, E., Kateris, D., Moshou, D., Bochtis, D. (2021). A deep learning approach for anthracnose infected trees classification in walnut orchards. *Computers and Electronics in Agriculture*, 182, 105998.
- [5] Andhare, S., Wankhade, S. (2020, May). Identification of Plant Diseases Using Machine Learning: A Survey. In *International Conference on Image Processing and Capsule Networks*, pp.411-421. Springer, Cham.
- [6] Ashok, S., Kishore, G., Rajesh, V., Suchitra, S., Sophia, S.G, and Pavithra, B., (2020, June), Tomato Leaf Disease Detection Using Deep Learning Techniques, in *2020 5th International Conference on Communication and Electronics Systems (ICCES)*, pp.979-983, IEEE.

- [7] Azim, M. A., Islam, M. K., Rahman, M. M., & Jahan, F. (2021). An effective feature extraction method for rice leaf disease classification. *Telkomnika*, 19(2), 463-470.
- [8] Badage, A. (2018). Crop disease detection using machine learning: Indian agriculture. *Int. Res. J. Eng. Technol. (IRJET)*, 5(9), 866-869.
- [9] Bedi, P., Gole, P., Agarwal, S.K. (2021). 18 Using deep learning for image-based plant disease detection. In *Internet of Things and Machine Learning in Agriculture*, pp.369-402, De Gruyter.
- [10] Bhargavi, K., & Babu, B. S. (2021). Application of Convoluted Neural Network and Its Architectures for Fungal Plant Disease Detection. In *Artificial Intelligence and IoT-Based Technologies for Sustainable Farming and Smart Agriculture*, pp. 314-324, IGI Global.
- [11] Bisen, D. (2021). Deep convolutional neural network based plant species recognition through features of leaf. *Multimedia Tools and Applications*, 80(4), 6443-6456.
- [12] Brenes, J. A., Eger, M., & Marín-Raventós, G. (2021). Early Detection of Diseases in Precision Agriculture Processes Supported by Technology. *Sustainable Intelligent Systems*, 11.
- [13] Dahiya, S., Gulati, T. (2020). An Application of Machine Learning in Plant Leaves Disease Detection and Classification. *Journal of Computational and Theoretical Nanoscience*, 17(6), 2645-2652.
- [14] Dalal, T., Singh, M. (2021). Review Paper on Leaf Diseases Detection and Classification Using Various CNN Techniques. In *Mobile Radio Communications and 5G Networks*, pp.153-162. Springer, Singapore.
- [15] Deepalakshmi, P., Lavanya, K., Srinivasu, P. N. (2021). Plant Leaf Disease Detection Using CNN Algorithm. *International Journal of Information System Modeling and Design (IJISMD)*, 12(1), 1-21.
- [16] Dhingra, G., Kumar, V., Joshi, H.D. (2018). Study of digital image processing techniques for leaf disease detection and classification. *Multimedia Tools and Applications*, 77(15), 19951-20000.
- [17] Ferentinos, K. P. (2018). Deep learning models for plant disease detection and diagnosis. *Computers and Electronics in Agriculture*, 145, 311-318.
- [18] Francis, J., & Anoop, B. K. (2016, March). Identification of leaf diseases in pepper plants using soft computing techniques. In *2016 conference on emerging devices and smart systems (ICEDSS)*, pp.168-173. IEEE.
- [19] Ganatra, N., Patel, A. (2020). A multiclass plant leaf disease detection using image processing and machine learning techniques. *Int. J. Emerg. Technol*, 11(2), 388421.
- [20] Gargade, A., Khandekar, S. (2021). Custard Apple Leaf Parameter Analysis, Leaf Diseases, and Nutritional Deficiencies Detection Using Machine Learning. In *Advances in Signal and Data Processing*, pp. 57-74. Springer, Singapore.
- [21] Geetharamani, G., Pandian, A. (2019). Identification of plant leaf diseases using a nine-layer deep convolutional neural network. *Computers & Electrical Engineering*, 76, 323-338.
- [22] Ghorai, A.K., Mukhopadhyay, S., Kundu, S., Mandal, S. N., Barman, A.R., De Roy, M., Dutta, S. (2021), *Image Processing Based Detection of Diseases and Nutrient Deficiencies in Plants*. Research Gate
- [23] Giraddi, S., Desai, S., Deshpande, A. (2020). Deep Learning for Agricultural Plant Disease Detection. In *ICDSMLA 2019*, pp.864-871. Springer, Singapore.
- [24] Goel, R. K., Yadav, C. S., Vishnoi, S., Rastogi, R. (2021). Smart agriculture—Urgent need of the day in developing countries. *Sustainable Computing: Informatics and Systems*, 30, 100512.
- [25] Golhani, K., Balasundram, S. K., Vadamalai, G., Pradhan, B. (2018). A review of neural networks in plant disease detection using hyperspectral data. *Information Processing in Agriculture*, 5(3), 354-371.
- [26] Goncharov, P., Ososkov, G., Nechaevskiy, A., Uzhinskiy, A., Nestsiaenia, I. (2018). Disease detection on the plant leaves by deep learning. In *International Conference on Neuroinformatics*, pp.151-159. Springer, Cham.
- [27] Gunasekaran, S., Gunavathi, K. (2021). Delta tributary network—An efficient alternate approach for bottleneck layers in CNN for plant disease classification. *IET Image Processing*.
- [28] Hassan, S.M., Maji, A.K. (2021). Identification of Plant Species Using Deep Learning. In *Proceedings of International Conference on Frontiers in Computing and Systems*, pp.115-125. Springer, Singapore.
- [29] Hasan, M.Z., Zeba, N., Malek, M.A., Reya, S.S. (2021). A Leaf Disease Classification Model in Betel Vine Using Machine Learning Techniques. In *2021 2nd International Conference on Robotics, Electrical and Signal Processing Techniques (ICREST)*, pp.362-366. IEEE.
- [30] Hu, G., Wang, H., Zhang, Y., Wan, M. (2021). Detection and severity analysis of tea leaf blight based on deep learning. *Computers & Electrical Engineering*, 90, 107023.

- [31] Huang, Z., Qin, A., Lu, J., Menon, A., Gao, J. (2020, November). Grape Leaf Disease Detection and Classification Using Machine Learning. In *2020 International Conferences on Internet of Things (iThings) and IEEE Green Computing and Communications (GreenCom) and IEEE Cyber, Physical and Social Computing (CPSCom) and IEEE Smart Data (SmartData) and IEEE Congress on Cybermatics (Cybermatics)*, pp.870-877. IEEE.
- [32] Hussein, M.A., Abbas, A.H. (2019). Plant Leaf Disease Detection Using Support Vector Machine. *Al-Mustansiriyah Journal of Science*, 30(1), 105-110.
- [33] Iniyar, S., Jebakumar, R., Mangalraj, P., Mohit, M., Nanda, A. (2020). Plant Disease Identification and Detection Using Support Vector Machines and Artificial Neural Networks. In *Artificial Intelligence and Evolutionary Computations in Engineering Systems*, pp.15-27. Springer, Singapore.
- [34] Islam, M., Shuvo, M., Rahman, N., Shamsojjaman, M., Hasan, S., Hossain, M., Khatun, T. (2021). *An Automated Convolutional Neural Network Based Approach for Paddy Leaf Disease Detection*. DOI:10.14569/IJACSA.2021.0120134
- [35] Kadoli, V., Gull, K. C., Gull, S. C. (2021). Dissimilar Disease Detection Using Machine Learning Techniques for Variety of Leaves. In *Sustainable Communication Networks and Application*, pp.57-71. Springer, Singapore.
- [36] Karthik, R., Hariharan, M., Anand, S., Mathikshara, P., Johnson, A., Menaka, R. (2020). Attention embedded residual CNN for disease detection in tomato leaves. *Applied Soft Computing*, 86, 105933.
- [37] Kartikeyan, P., Shrivastava, G. (2021). Review on emerging trends in detection of plant diseases using image processing with machine learning. *International Journal of Computer Applications*, 975, 8887.
- [38] Kumar, R., Baloch, G., Pankaj, A. B. B., Bhatti, J. Fungal Blast Disease Detection in Rice Seed using Machine Learning.
- [39] Lin, H., Sheng, H., Sun, G., Li, Y., Xiao, M., Wang, X. (2021). Identification of pumpkin powdery mildew based on image processing PCA and machine learning. *Multimedia Tools and Applications*, 80(14), 21085-21099.
- [40] Maheshwari, K., Choure, P.K., Birchha, V. *Performance Analysis of Mango Leaf Disease using Machine Learning Technique*. International Journal for Research in Applied Science & Engineering Technology. Volume 9, Issue 1, 856-862.
- [41] Mohapatra, D., Tripathy, J., & Patra, T. K. (2021). Rice Disease Detection and Monitoring Using CNN and Naive Bayes Classification. In *Soft Computing Techniques and Applications*, pp.11-29. Springer, Singapore.
- [42] Mukhopadhyay, S., Paul, M., Pal, R., De, D. (2021). Tea leaf disease detection using multi-objective image segmentation. *Multimedia Tools and Applications*, 80(1), 753-771.
- [43] Nandhini, S., Ashokkumar, K. (2021). Improved crossover based monarch butterfly optimization for tomato leaf disease classification using convolutional neural network. *Multimedia Tools and Applications*, 80(12), 18583-18610.
- [44] Nandhini, S., Suganya, R., Nandhana, K., Varsha, S., Deivalakshmi, S., Thangavel, S.K. (2021). Automatic Detection of Leaf Disease Using CNN Algorithm. In *Machine Learning for Predictive Analysis*, pp. 237-244. Springer, Singapore.
- [45] Ngugi, L. C., Abelwahab, M., & Abo-Zahhad, M. (2021). Recent advances in image processing techniques for automated leaf pest and disease recognition—A review. *Information processing in agriculture*, 8(1), 27-51.
- [46] Nihar, F., Khanom, N. N., Hassan, S. S., Das, A. K. (2021). Plant Disease Detection through the Implementation of Diversified and Modified Neural Network Algorithms. *Journal of Engineering Advancements*, 2(01), 48-57. doi:10.38032/jea.2021.01.007
- [47] Oo, Y. M., Htun, N.C. (2018). Plant leaf disease detection and classification using image processing. *International Journal of Research and Engineering*, 5(9), 516-523.
- [48] Pandey, C., Baghel, N., Dutta, M. K., Srivastava, A., Choudhary, N. (2021). Machine learning approach for automatic diagnosis of Chlorosis in Vigna mungo leaves. *Multimedia Tools and Applications*, 80(9), 13407-13427.
- [49] Panigrahi, K.P., Das, H., Sahoo, A.K., Moharana, S.C. (2020). Maize leaf disease detection and classification using machine learning algorithms. In *Progress in Computing, Analytics and Networking*, pp.659-669. Springer, Singapore.
- [50] Patel, A., Agravat, S. (2021). Banana Leaves Diseases and Techniques: A Survey. In *Data Science and Intelligent Applications*, pp.209-215. Springer, Singapore.

- [51] Patil, A., Lad, K. (2021). Chili Plant Leaf Disease Detection Using SVM and KNN Classification. In *Rising Threats in Expert Applications and Solutions*, pp.223-231. Springer, Singapore.
- [52] Patidar, S., Pandey, A., Shirish, B.A., and Sriram, A., (2020), Rice plant disease detection and classification using deep residual learning, *In International Conference on Machine Learning, Image Processing, Network Security and Data Sciences*, pp.278-293. Springer, Singapore.
- [53] Poonguzhali, R., Vijayabhanu, A. (2019) Crop Condition Assessment using Machine Learning., *International Journal of Recent Technology and Engineering (IJRTE)*. Volume 7, Issue-6S2.
- [54] Rahman, M.A., Shoumik, M.S.N., Rahman, M.M., Hena, M.H. (2021). Rice Disease Detection Based on Image Processing Technique. In *Smart Trends in Computing and Communications: Proceedings of SmartCom 2020*, pp.135-145. Springer, Singapore.
- [55] Ramcharan, A., Baranowski, K., McCloskey, P., Ahmed, B., Legg, J., Hughes, D.P. (2017). Deep learning for image-based cassava disease detection. *Frontiers in plant science*, 8, 1852.
- [56] Ramya, R., Kumar, P., Sivanandam, K., Babykala, M. (2020). Detection and Classification of Fruit Diseases Using Image Processing & Cloud Computing. In *2020 International Conference on Computer Communication and Informatics (ICCCI)*, pp.1-6. IEEE.
- [57] Sambasivam, G., Opiyo, G.D. (2021). A predictive machine learning application in agriculture: Cassava disease detection and classification with imbalanced dataset using convolutional neural networks. *Egyptian Informatics Journal*, 22(1), 27-34.
- [58] Selvaraj, M.G., Vergara, A., Ruiz, H., Safari, N., Elayabalan, S., Ocimati, W., Blomme, G. (2019). AI-powered banana diseases and pest detection. *Plant Methods*, 15(1), 1-11.
- [59] Sethy, P.K., Barpanda, N.K., Rath, A.K., Behera, S.K. (2020). Image Processing Techniques for Diagnosing Rice Plant Disease: A Survey. *Procedia Computer Science*, 167, 516-530.
- [60] Sharma, P., Berwal, Y.P.S., Ghai, W. (2020). Performance analysis of deep learning CNN models for disease detection in plants using image segmentation. *Information Processing in Agriculture*, 7(4), 566-574.
- [61] Shah, Z., Vania, R., Vegad, S. (2021). Disease Prediction in Plants: An Application of Machine Learning in Agriculture Sector. In *Data Science and Intelligent Applications*, pp.105-111. Springer, Singapore.
- [62] Shrestha, G., Das, M., Dey, N. (2020). Plant Disease Detection Using CNN. In *2020 IEEE Applied Signal Processing Conference (ASPCON)*, pp.109-113. IEEE.
- [63] Shruthi, U., Nagaveni, V., Raghavendra, B.K. (2019). A review on machine learning classification techniques for plant disease detection. In *2019 5th International Conference on Advanced Computing & Communication Systems (ICACCS)*, pp.281-284. IEEE.
- [64] Singh, A., Kaur, H. (2021). Potato Plant Leaves Disease Detection and Classification using Machine Learning Methodologies. In *IOP Conference Series: Materials Science and Engineering*, Vol.1022, No.1, p.012121). IOP Publishing.
- [65] Singh, V., Misra, A.K. (2017). Detection of plant leaf diseases using image segmentation and soft computing techniques. *Information processing in Agriculture*, 4(1), 41-49.
- [66] Singh, V., Misra, A.K. (2015). Detection of unhealthy region of plant leaves using image processing and genetic algorithm. In *2015 International Conference on Advances in Computer Engineering and Applications*, pp.1028-1032. IEEE.
- [67] Singh, V., Sharma, N., Singh, S. (2020). A review of imaging techniques for plant disease detection. *Artificial Intelligence in Agriculture*.
- [68] Singh, T., Kumar, K., Bedi, S.S. (2021). A Review on Artificial Intelligence Techniques for Disease Recognition in Plants. In *IOP Conference Series: Materials Science and Engineering*, Vol.1022, No.1, p. 012032. IOP Publishing.
- [69] Sivasangari, A., Kishore, M.S., Poornesh, M., Gomathi, R.M., Deepa, D. (2020). Plant Disease Detection and Classification Using Image Processing and Neural Networks. *Journal of Computational and Theoretical Nanoscience*, 17(11), 4920-4924.
- [70] Sreehari. R., and Mahalakshmi. B., (2020), Plant disease detection using machine learning. *International Educational Applied Research Journal*, 4(4), pp.17-21.
- [71] Sujatha, R., Chatterjee, J.M., Jhanjhi, N.Z., Brohi, S.N. (2021). Performance of deep learning vs machine learning in plant leaf disease detection. *Microprocessors and Microsystems*, 80, 103615.
- [72] Türkoğlu, M., Hanbay, D. (2019). Plant disease and pest detection using deep learning-based features. *Turkish Journal of Electrical Engineering & Computer Sciences*, 27(3), 1636-1651.

- [73] Tiwari, V., Joshi, R.C., Dutta, M.K. (2021). Dense convolutional neural networks based multiclass plant disease detection and classification using leaf images. *Ecological Informatics*, 63, 101289.
- [74] Vashisht, S., Kumar, P., Trivedi, M.C. (2021). Design of a Predictive Measure to Enhance Neural Network Architecture for Plant Disease Detection. In *Proceedings of International Conference on Big Data, Machine Learning and their Applications*, pp.137-150. Springer, Singapore.
- [75] Vashisht, S., Kumar, P., Trivedi, M.C. (2021). Machine Learning Approaches for Accurate Image Recognition and Detection for Plant Disease. In *Smart Innovations in Communication and Computational Sciences*, pp.157-165. Springer, Singapore.
- [76] Venkataramanan. A., Honakeri D.K.P. and Agarwal. P., (2019) Plant disease detection and classification using deep neural networks, *International Journal on Computer Science and Engineering (IJCSE)*, 11(08), pp.40-46.
- [77] Vishnoi. V.K., Kumar. K., Kumar. B., (2020). Plant disease detection using computational intelligence and image processing, *Journal of Plant Diseases and Protection*, pp.1-35.
- [78] Wei, M.C.F., Maldaner, L.F., Ottoni, P.M.N., Molin, J.P. (2020). Carrot Yield Mapping: A Precision Agriculture Approach Based on Machine Learning. *AI*, 1(2), 229-241.
- [79] Xiao, J.R., Chung, P.C., Wu, H.Y., Phan, Q.H., Yeh, J.L.A., Hou, M.T.K. (2021). Detection of Strawberry Diseases Using a Convolutional Neural Network. *Plants*, 10(1), 31.
- [80] Yadav, S., Sengar, N., Singh, A., Singh, A., Dutta, M.K. (2021). Identification of disease using deep learning and evaluation of bacteriosis in peach leaf. *Ecological Informatics*, 61, 101247.

EVALUATION OF THE PLACES FOR CREATION OF APIARIES AND OPTIMAL DISTRIBUTION OF THE BEE COLONIES

ОЦЕНКА НА МЕСТАТА ЗА СЪЗДАВАНЕ НА ПЧЕЛИНИ И ОПТИМАЛНО РАЗПРЕДЕЛЕНИЕ НА ПЧЕЛНИТЕ КОЛОНИИ

Atanasov Atanas ^{*1)}, Georgiev Ivan ²⁾

¹⁾ University of Ruse, Agro-industrial Faculty / Bulgaria;

²⁾ University of Ruse, Faculty of Natural Sciences and Education, Department of Applied Mathematics and Statistics / Bulgaria

Tel: +359 885 497 406; E-mail: aatanasov@uni-ruse.bg

DOI: <https://doi.org/10.356.33/inmateh-65-39>

Keywords: honey bee, multicriteria model, Pareto optimality, location assessment, overpopulation, carrying capacity, malnourishment

ABSTRACT

An approach for evaluation of the places for creation of apiaries and optimal distribution of bee colonies formed on the basis of the feeding capacities of the areas with flowering plants, the distances between these sites and the feeding areas is proposed. A multicriteria model with two main criteria is considered. The first maximizes the sum of the products of the weights for a given place multiplied by the number of colonies that will be positioned at that place. This criterion is divided into two sub-criteria, including the “subjective” and “objective” assessment of place preferences, respectively. The second criterion aims to minimize malnourished bee colonies. The model, with the proposed approach for “objective” assessment of potential distribution sites, can be applied both for cases without overpopulation of the area with bee colonies and for areas with overpopulation.

РЕЗЮМЕ

Предложен е подход за оценка на местата за създаване на пчелини и оптимално разпределение на формираните пчелни колонии на базата на хранителните капацитети на площите с цъфтящи растения, разстоянията между тези площи и местата за хранене. Разглежда се многокритериален модел с два основни критерия. Първият максимизира сумата от произведенията на теглата за дадено място, умножена по броя на колонии, които ще бъдат позиционирани на това място. Този критерий е разделен на два подкритерия, включващи съответно „субективна“ и „обективна“ оценка на предпочитанията за място. Вторият критерий цели минимизиране на недохранените пчелни семейства. Моделът, с предложения подход за „обективна“ оценка на потенциалните места за разпространение, може да се приложи както за случаи без пренаселеност с пчелни колонии, така и за райони с пренаселеност.

INTRODUCTION

Providing sufficient quantity and quality of food resources to bee (*Apis mellifera macedonica*) colonies is essential for their optimal biological development. The selection of areas with appropriate bee pasture is a difficult task in terms of the variable location of areas with agricultural crops, the variable number of bee colonies in the area over the years, the regulations governing beekeeping, etc. All these factors can affect the sustainability of bee products in different years. It is very important for bee colonies to find the best location for setting up an apiary in a certain area in such a way that each colony has sufficient food resources and at the same time minimizes the proportion of colonies that will not be fed due to overpopulation. The food resources are very important for the honey bee population and its dynamics has been studied in a number of papers, see e.g.: Atanasov & Georgiev, (2021), Georgiev & Vulkov, (2021), including unhealthy dynamics (Atanasov et al., 2021).

The social behaviour of bees in a colony allows them to be considered as a very well-structured biological unit subordinated to a common goal. The study of social animals and social insects has led to the creation of mathematical models seeking an optimal solution to a problem (Todorov & Dimov, 2020; Dimov et al., 2015) satisfying one or more objective functions, under conditions of a set of constraints.

In order to avoid competition between bee colonies, many publications discuss optimal models for the distribution of bee colonies in predetermined locations (Ramon *et al.*, 2010; Rebysarah *et al.*, 2011; Yuce *et al.*, 2013; Maica *et al.*, 2014). These places have connections with fields of flowering plants to feed bee colonies. Different fields have different nectar secretion potentials (Al-Ghamdi *et al.*, 2016). Some studies solve an optimization task aimed to optimize the beekeeper's preferences for individual places including accessibility and ease of maintenance, features related to the terrain, transport distances to settlements, security and surveillance, quality infrastructure and more (Saritha & Vinod Chandra, 2017). The optimization model in the article allows the possibility of overpopulation in the area, which leads to malnutrition of some bee colonies. In the presence of such a part, the optimization model minimizes it.

A similar problem has been solved by Aderinto *et al.*, (2020), where the distribution of bees in the apiary is optimized to improve honey production, which in turn maximizes profits and minimizes the cost of maintaining hives in terms of nutrition, labour and storage. Other studies have considered a similar problem for optimal distribution of bee colonies, optimizing several criteria simultaneously (Atanasov & Georgiev, 2021). When simultaneously optimizing several criteria, the Pareto optimal set of solutions is sought, after which one is chosen (Triantaphyllou, 2013). In the optimization models considered so far (Maica *et al.*, 2014; Atanasov & Georgiev, 2021), the constraints are:

$$\begin{aligned}
 \text{Constraint 1)} & \quad \sum_{j \in C_i}^p x_{ij} - X_i = 0 \quad \forall i = 1, \dots, m \\
 \text{Constraint 2)} & \quad \sum_{i \in F_j}^m x_{ij} - b_j \leq 0 \quad \forall j = 1, \dots, p \\
 \text{Constraint 3)} & \quad \sum_{k=1}^n z_{ki} - E_i - X_i = 0 \quad \forall i = 1, \dots, m \\
 \text{Constraint 4)} & \quad \sum_{i=1}^m z_{ki} \leq d_k \quad \forall k = 1, \dots, n
 \end{aligned} \tag{1}$$

where:

m - is the number of relocation sites,

p - the number of plants or plants clusters,

n - number of colonies,

X_i - number of colonies to be relocated at site i , $i = 1, \dots, m$; $X_i \in Z^+$,

x_{ij} - fraction of colonies of X_i (relocation of in site i , which feed on a plant cluster j , that can be accommodated by plant cluster j , $i = 1, \dots, m$, $j = 1, \dots, p$; $x_{ij} \in Z^+$

b_j - carrying capacity of plant cluster j ; $b_j \in R^+$

w_i - priority weight given to site i ; $w_i \in Z^+$

z_{ki} - number of hives from the k -th apiary, that can be relocated at site i , $k = 1, \dots, n$, $i = 1, \dots, m$; $z_{ij} \in Z^+$

d_k - number of hives from the k -th apiary; $d_k \in Z^+$

E_i - number of hives distributed in the i -th site that will not be fed; $E_i \in R^+$

$j \in C_i$ - plant cluster j is connected to site i

$i \in F_j$ - if site i is connected to plant cluster j

Constraint 1 represents the distribution of the number of colonies relocated at a site connected to the connected plant clusters. *Constraint 2* represents the contribution of a site (in terms of number of colonies) to the carrying capacity of the connected plant cluster. *Constraint 3* shows how the number of colonies will be relocated to the sites with the assurance that the colony will not be subdivide into parts. *Constraint 4* allows, part or all of the hives to be relocated in different sites.

The objective functions are:

$$\text{Max} f_1(X) = \sum_{i=1}^m w_i X_i \wedge \text{Min} f_2(E) = \sum_{i=1}^m E_i \tag{2}$$

Important aspects in formulating the mathematical model are the distances of a potential location of apiaries to the fields with flowering vegetation (food source), the nectar secretion capacities of these fields, as well as the competition with the other locations of apiaries.

In the considered models the assessment, which puts the beekeeper in the separate places for apiaries location, is to a large extent subjective and insufficiently substantiated.

Our study aims to complement the proposed models by proposing a solution to more accurate assessment in the individual places.

MATERIALS AND METHODS

A model for estimating the potential site has been designed

A model has been designed to assess the potential location M_i , $i=1\dots m$, where hives can be placed, comparable to a coefficient characterizing the extent to which this place is desired. When constructing this coefficient, the following will be taken into account:

- 1) the distance c_{ij} from place M_i to the source of feeding S_j , $j=1\dots m$;
- 2) carrying capacity of plant cluster b_j , $j=1\dots m$ (measured in the number of bee colonies that can be fed);
- 3) competition with other places.

One of the important factors that determine the choice of bees to carry nectar and pollen from the source of feeding to the bee colony is the distance and the energy spent by the bees in flight. Since the energy consumed by the bee per flight is linearly increasing and in practice after 2500m, the bee consumes energy equivalent to the food supply it has collected, this linearity will be taken into account when determining the efficiency factor. Let us construct a linear function f , matching a number $c_{ij} \in [0,1]$ at any distance between a place M_i and given source of feeding S_j . If a potential place is located on the area of a source of nectar (rather the distance between them is negligibly small), then on, c_{ij} the number 1 is compared. If the distance between the potential site and the source of nectar is 2500 m or more, the number 0 is compared. Let this number c_{ij} , let's call it "useful distance", it takes the value 0 at no utility of the real distance (above 2500m) and 1 at maximum utility (when the location of the apiary and the location of the food source coincide). The function f has the following form:

$$f(x) = \begin{cases} \frac{-x}{2500} + 1, & x \in [0; 2500] \\ 0, & x \notin [0; 2500] \end{cases} \quad (3)$$

We will determine the "value" of given field source of feeding, S_j , concerning a place M_i , taking into account the "useful distances", the capacity b_j and the competition between the other places. Because given source of feeding can be accessed by places other than M_i , the "value" of the place source of feeding S_j , about place M_i can be defined as part of the capacity b_j , proportional to the square of the "useful distance" and inversely proportional to the sum of all "useful distances" to the location of the source of feeding S_j . The latter is motivated by the fact that if a feeding place has a connection with only one apiary place, then the "value" of this feeding place for the given apiary place is expressed by the part of the food stocks at that feeding place, which does not have to be spent on flight- $b_j c_{ij}$. This part is weighted on average in terms of "useful distances" with other places. The "value" of a place of feeding S_j , for given place for apiary M_i , this is the part of the capacity b_j , which remains after taking into account the competition (potential sharing) with other places and the energy spent by the bees to fly to that place. In order to obtain a final coefficient ρ_i , preferably in a given place, the sum of the "values" of all feeding places in relation to the given apiary place is taken:

$$\rho_i = \sum_{j=1}^n b_j c_{ij} \frac{c_{ij}}{\sum_{k=1}^m c_{ik}} = \sum_{j=1}^n \frac{b_j c_{ij}^2}{\sum_{k=1}^m c_{ik}} \quad (4)$$

In determining the coefficient ρ_i , the preferences of the beekeeper were not taken into account when assessing the potential locations for bee colonies. For the purpose of the numerical experiment, when choosing a place in accordance with the wishes of the beekeeper, priority weights w_i^1 , are given, taking into account the proximity of the apiary to the main road, the proximity to the settlement, the possibility of guarding and monitoring the apiary. With these requirements in mind, the following "subjective" priority weights have been identified:

$$w_1^1 = 4; w_2^1 = 3; w_3^1 = 5; w_4^1 = 6; w_5^1 = 1; w_6^1 = 7; w_7^1 = 7;$$

We propose a practical technological solution for evaluation of the places for creation of 7 apiaries with different numbers of bee hives as follows: $d_1 = 100$; $d_2 = 30$; $d_3 = 22$; $d_4 = 96$; $d_5 = 34$; $d_6 = 10$; $d_7 = 25$, with 317 total number, spaced at a certain distance from fields with flowering vegetation's with caring capacity of plant cluster $b_1 = 64$; $b_2 = 14$; $b_3 = 66$; $b_4 = 10$; $b_5 = 7$; $b_6 = 20$ and $b_7 = 218$ shown in (Table 1.).

Using formula (3) and (4), the "objective" priority weights are also calculated:

$$w_1^2 = 0.4347; w_2^2 = 0.3745; w_3^2 = 0.1185; w_4^2 = 0.0101; w_5^2 = 0.0466; w_6^2 = 0.0085; w_7^2 = 0.0071.$$

The total priority weight w_i is designed as a convex linear combination of the “subjective” w_i^1 and “objective” w_i^2 priority weights:

$$w_i = \mu w_i^1 + (1 - \mu)w_i^2 \tag{5}$$

where $\mu \in [0,1]$. At $\mu = 0$, full priority is given to the “objective” priority weights, at $\mu = 1$, full priority is given to the “subjective” priority weights. When setting intermediate values to μ : $0 < \mu < 1$, the “subjective” and “objective” priorities with different weight are taken into account. As a result, different objective functions $f_1(X)$, are obtained, which would lead to different solutions of problem (1)-(2). Criteria $f_1(X)$ a set of two sub-criteria in which the subjective assessment of the beekeeper for on-site preferences and the objective assessment for on-site preferences are calculated by formulas (3)-(4). These two criteria are combined into one - $f_1(X)$, by selecting the parameter μ .

The study was conducted in 2019, based on the assessment existing bee forage resources as Acacia (*Robinia pseudoacacia*), Sunflower (*Helianthus annuus*) and the number of bee colonies kept in the Northeast part of Bulgaria in village Batishnica. Geographical location of experimental apiaries in Batishnica are $m_1, m_2, m_3, m_4, m_5, m_6, m_7$ – 43°32'21.53"N, 25°50'33.58"E; 43°33'17.02"N, 25°49'27.51"E; 43°33'22.91"N, 25°48'57.99"E; 43°32'13.69"N, 25°52'26.25"E; 43°31'46.43"N, 25°52'17.40"E; 43°31'35.65"N, 25°51'59.15"E; 43°31'34.93"N, 25°52'10.88"E and at an altitudinal range of 288 m. In the region major honey source plants are *Robinia pseudoacacia* with total land area 6.3 ha and *Helianthus annuus* with total land area 317.7 ha.

These two major crops determined the main honeybee pasture in the study area. Other vegetation types are vineyards (*Vitis*), oak (*Quercus*), maize (*Zea mays*), wheat (*Triticum*), barley (*Hordeum vulgare*), soybeans (*Glycine max*). If all the factors remain constant, the productivity of the bee colonies is in correlation with nectar secretion potential of bee forage species and the existing honeybee colony density. It is very important for the proper development of bee colonies to find the best location of a bee hive in the certain study area.

The distance between an apiaries site and a plant cluster is consistent with the maximum flight distance D , of the bee species *Apis mellifera macedonica*, which has a productive distance of up to 2500 m. This distribution was made to investigate the flight of bees to the extent that they were productive in collecting nectar and pollen and transporting it to the colony.

Table 1

The distance between an apiaries site and a plant cluster
 (d_k – number of hives from the k -th apiary, b_j – carrying capacity of plant cluster j , kg/h;
 D - flight distance, m)

	b₁	b₂	b₃	b₄	b₅	b₆	b₇
d₁	1737	2103	876	1533	1408	1214	0
d₂	1490	654	1880	D >2500	D >2500	D >2500	0
d₃	1600	1285 m	D >2500	D >2500	D >2500	D >2500	1214
d₄	D >2500	D >2500	D >2500	1417	2280	1370	2500
d₅	D >2500	D >2500	1982	1080	1602	730	1985
d₆	D >2500	D >2500	D >2500	1882	1840	1385	D >2500
d₇	D >2500	D >2500	D >2500	1998	1884	1468	D >2500

In the particular case, specific numbers of hives were placed on the places and the solution of the problem redistributed to the same places. The matrix of connections is represented by the following graph (Fig.1.).

The rectangles show the number of relocation sites m , the circles show the number of plants clusters p with Acacia and Sunflower. The apiaries m_1 and m_2 are located in a circle of plant cluster p_7 , which does not take into account the influence of the distances between the locations of the apiaries m_1 and m_2 and plant cluster p_7 .

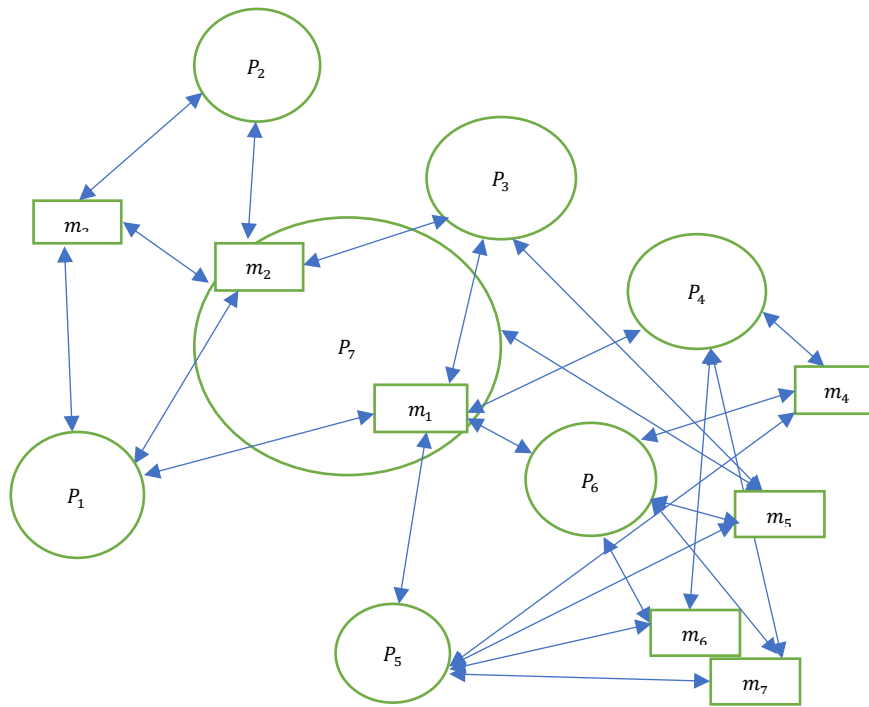


Fig. 1 - Matrix of connections

m - number of relocation sites; *P* - number of plants or plants clusters

A graph is composed of nodes and edges. Two kinds of nodes will be considered – the possible relocation of sites of beehives and clusters of plants. The distance between a relocation site and a plant cluster is consistent with the maximum flight distance of the bee species *Apis mellifera macedonica*.

This distribution was made to investigate the flight of bees to the extent that they were productive in collecting nectar and pollen and transporting it to the colony. The maximum flight distance for bees to search for food is taken into account in the assessment of each apiary location. This reduces the stress in the colony of the lack of supply of nectar and pollen into the hive. Food sources are various flowering plant species around the apiaries. The productivity of the various forage species depends on the nectar secretion potential of each plant.

RESULTS

The ability of flowering plant fields to feed bee colonies is defined by the name “carrying capacity of a plant cluster”. The carrying capacity of a plant cluster depends on the nectar secretion potential of each plant and the area occupied by flowering plants. The preference of the beekeeper and feeding of bee colonies over the location sites can also be considered by giving each site a priority weight. In constructing the proposed mathematical model, we estimated the places for creation of apiaries based on main pastures of *Robinia pseudoacacia* and *Helianthus annuus*. The role in feeding bees from other flowering plants in the study area is too small and was not taken into account in the site assessment in our model.

The problem is solved via Matlab software operations research capabilities. The aim in our experiment is to find the Pareto optimal solutions (Blunter et. al., 2004) of problem (1) - (2).

For this purpose, a generalized criterion is constructed:

$$F(X) = \lambda f_1(X) + (1 - \lambda)f_2(X), \tag{6}$$

where $\lambda \in [0,1]$.

From the fact that the constraints (1) are linear, it follows that the permissible range is convex. Criteria (2) are also linear and to find the Pareto optimal solutions can be obtained by setting a set of different values of the parameters $\lambda \wedge \mu$. Different numerical experiments were performed (at different values of $\lambda \wedge \mu$). Different solutions have been obtained. The beekeeper can choose a solution depending on the specific situation and the characteristics of the beekeeping area. Some of the results are shown in Table 2, 3, 4, 5.

Table 2

Number of hives from the k -th apiary that can be relocated at site i , at $\lambda = 0.5, \mu = 0.5$
 (d_k – number of hives from the k -th apiary, m_k – number of relocation sites)

z_{ki}	m_1	m_2	m_3	m_4	m_5	m_6	m_7
d_1	100	0	0	0	0	0	0
d_2	30	0	0	0	0	0	0
d_3	22	0	0	0	0	0	0
d_4	96	0	0	0	0	0	0
d_5	34	0	0	0	0	0	0
d_6	10	0	0	0	0	0	0
d_7	25	0	0	0	0	0	0

Table 3

Number of hives from the k -th apiary that can be relocated at site i , at $\lambda = 0.5, \mu = 0.1$
 (d_k – number of hives from the k -th apiary, m_k – number of relocation sites)

z_{ki}	m_1	m_2	m_3	m_4	m_5	m_6	m_7
d_1	100	0	0	0	0	0	0
d_2	30	0	0	0	0	0	0
d_3	19	0	0	0	0	3	0
d_4	96	0	0	0	0	0	0
d_5	0	0	0	0	0	34	0
d_6	10	0	0	0	0	0	0
d_7	25	0	0	0	0	0	0

Table 4

Number of hives from the k -th apiary that can be relocated at site i at $\lambda = 0.1, \mu = 0$
 (d_k – number of hives from the k -th apiary, m_k – number of relocation sites)

z_{ki}	m_1	m_2	m_3	m_4	m_5	m_6	m_7
d_1	0	0	93	0	0	7	0
d_2	0	0	0	0	0	0	30
d_3	0	0	22	0	0	0	0
d_4	0	0	96	0	0	0	0
d_5	0	0	34	0	0	0	0
d_6	0	0	10	0	0	0	0
d_7	0	0	25	0	0	0	0

Table 5

Number of hives from the k -th apiary that can be relocated at site i at $\lambda = 1, \mu = 0.9$
 (d_k – number of hives from the k -th apiary, m_k – number of relocation sites)

z_{ki}	m_1	m_2	m_3	m_4	m_5	m_6	m_7
d_1	0	100	0	0	0	0	0
d_2	0	3	0	20	0	0	7
d_3	0	0	22	0	0	0	0
d_4	0	84	12	0	0	0	0
d_5	0	0	34	0	0	0	0
d_6	0	0	10	0	0	0	0
d_7	0	0	0	0	25	0	0

In all the obtained solutions there is a complete feeding of the bee colonies, which is a prerequisite for obtaining honey. Regardless of which solution the beekeeper chooses, each of them is applicable.

The model (1)-(2) is also applicable when the number of colonies exceeds the capacity of the food stocks of the areas with flowering plants. Then there will certainly be malnourished bee colonies. If the capacity of plant cluster decreases: $b_1 = 32; b_2 = 7; b_3 = 33; b_4 = 5; b_5 = 4; b_6 = 10; b_7 = 109$, and the remaining parameters are retained, the following results are obtained and shown in the Table 6, 7, 8, 9.

Table 6

Number of hives from the k -th apiary that can be relocated at site i at $\lambda = 0.5, \mu = 0.5$
 (d_k – number of hives from the k -th apiary, m_k – number of relocation sites)

z_{ki}	m_1	m_2	m_3	m_4	m_5	m_6	m_7
d_1	100	0	0	0	0	0	0
d_2	30	0	0	0	0	0	0
d_3	0	0	0	0	0	0	22
d_4	35	61	0	0	0	0	0
d_5	0	0	0	0	0	0	34
d_6	10	0	0	0	0	0	0
d_7	25	0	0	0	0	0	0

Table 7

Number of hives from the k -th apiary that can be relocated at site i at $\lambda = 0.5, \mu = 0.1$
 (d_k – number of hives from the k -th apiary, m_k – number of relocation sites)

z_{ki}	m_1	m_2	m_3	m_4	m_5	m_6	m_7
d_1	100	0	0	0	0	0	0
d_2	30	0	0	0	0	0	0
d_3	0	0	0	0	0	0	22
d_4	16	80	0	0	0	0	0
d_5	0	0	0	0	0	19	15
d_6	10	0	0	0	0	0	0
d_7	25	0	0	0	0	0	0

Table 8

Number of hives from the k -th apiary that can be relocated at site i at $\lambda = 0.1, \mu = 0$
 (d_k – number of hives from the k -th apiary, m_k – number of relocation sites)

z_{ki}	m_1	m_2	m_3	m_4	m_5	m_6	m_7
d_1	0	100	0	0	0	0	0
d_2	0	0	0	0	0	0	30
d_3	0	0	22	0	0	0	0
d_4	0	0	96	0	0	0	0
d_5	0	0	28	0	0	6	0
d_6	8	0	2	0	0	0	0
d_7	25	0	0	0	0	0	0

Table 9

Number of hives from the k -th apiary that can be relocated at site i at $\lambda = 1, \mu = 0.9$
 (d_k – number of hives from the k -th apiary, m_k – number of relocation sites)

z_{ki}	m_1	m_2	m_3	m_4	m_5	m_6	m_7
d_1	0	100	0	0	0	0	0
d_2	0	0	0	0	0	0	30
d_3	0	0	22	0	0	0	0
d_4	0	79	17	0	0	0	0
d_5	0	0	0	0	0	0	34
d_6	0	10	0	0	0	0	0
d_7	0	0	0	0	25	0	0

In all considered decisions the number of the malnourished colonies is 117, regardless of the distribution in the individual places. The distribution of colonies that can be fed is optimal according to the relevant criteria with selected parameters $\lambda \wedge \mu$, and for those that cannot be fed it is necessary to find another solution. Possible solutions are: relocation of the malnourished colonies to places other than the designed ones, increasing the area of the flowering plants, the type of the sown crops, improving the nectar-releasing potential of the crops, by applying good agrotechnical practices, etc.

CONCLUSIONS

An approach for “objective” assessment of the potential distribution sites of bee colonies formed on the basis of the feeding capacities of the areas with flowering plants, the distances between these sites and the feeding areas is proposed.

A multicriteria model with two main criteria is considered. The first maximizes the sum of the products of the weights for a given place multiplied by the number of colonies that will be positioned at that place. This criterion is divided into two sub-criteria, including the “subjective” and “objective” assessment of place preferences, respectively. The second criterion aims to minimize malnourished bee colonies.

The given model, with the proposed approach for "objective" assessment of potential distribution sites, can be applied both for cases without overpopulation of the area with bee colonies and for areas with overpopulation.

ACKNOWLEDGEMENT

This research is supported by Bulgarian National Science Fund under Project KP-06-PN 46-7 "Design and research of fundamental technologies and methods for precision apiculture".

REFERENCES

- [1] Aderinto O. Y., Azagbaekwue A., Bamigbola M. O., Oke M. O., Obayomi A. A., Salaudeen O. L., & Aliu O. T. (2020). Optimization of Honey Bee Production, *International journal of mathematical models and methods in applied sciences*, 56-61. doi: 10.46300/9101.2020.14.13
- [2] Al-Ghamdi, A., Adgaba, N., Getachew, A., & Tadesse, Y. (2016). New approach for determination of an optimum honey bee colony's carrying capacity based on productivity and nectar secretion potential of bee forage species, *Saudi Journal of Biological Sciences*, Vol. 23 (1), 92-100.
- [3] Atanasov A.Z. & Georgiev I.R. (2021). A Multicriteria Model for Optimal Location of, Honey Bee Colonies in Regions without Overpopulation. *AIP Conference Proceedings* 2333, 090008.
- [4] Atanasov A.Z., Georgiev S.G. & Vulkov L.V. (2021). Numerical parameter identification of a three-dimensional honeybee-mite model. *47th International Conference Application of Mathematics in Engineering and Economics. AMEE '21. To appear in AIP Conference Proceedings.*
- [5] Atanasov A.Z. & Georgiev S.G. 2021b. Adjoint state optimization algorithm for prediction of honeybee population losses. Reported at *15th Annual Meeting of the Bulgarian Section of SIAM. BGSIAM '20. To appear in Advanced Computing in Industrial Mathematics, Studies in Computational Intelligence*, Springer.
- [6] Blunter, R., Bezuidenhout, A., Breheny, R., Glucksberg, S., Happé, F. (2004). *Optimality Theory and Pragmatics*, Publisher Palgrave Macmillan UK.
- [7] Dimov I., Georgieva R., Todorov V. (2015). Balancing of Systematic and Stochastic Errors in Monte Carlo Algorithms for Integral Equations. In: Dimov I., Fidanova S., Lirkov I. (eds) *Numerical Methods and Applications. NMA 2014. Lecture Notes in Computer Science*, vol. 8962. Springer, Cham. https://doi.org/10.1007/978-3-319-15585-2_5
- [8] Georgiev, S.G. & Vulkov, L.V. (2021). Parameter identification approach for a fractional dynamics model of honeybee population. Reported at *13th International Conference on Large-Scale Scientific Computations. LSSC '21. To appear in Lecture Notes in Computer Science*, Springer.
- [9] Maica K.A. G., Jomar F. R. & Cleofas R. C. (2014). Mathematical Programming Models for Determining the Optimal Location of Beehives. *Bulletin of Mathematical Biology* 76: 997-1016.
- [10] Ramon J. P. E., Michael C. V. & Jomar F.R. (2010). Determining the optimal distribution of bee colony locations to avoid overpopulation using mixed integer programming. *Journal of Nature Studies*, 79-82.
- [11] Reby Sarah S. T., Jomar F. R., Ramon J. P. E. & Michael C. (2011). Villadelrey Prediction of migration path of a colony of bounded-rational species foraging on patchily distributed resources. *Advanced Studies in Biology*, Vol. 3. (7), 333–345.
- [12] Todorov V. & Dimov I. (2020). Efficient Stochastic Approaches for Multidimensional Integrals in Bayesian Statistics. In: Lirkov I., Margenov S. (eds) *Large-Scale Scientific Computing. LSSC 2019. Lecture Notes in Computer Science*, Vol. 11958. Springer, Cham. https://doi.org/10.1007/978-3-030-41032-2_52
- [13] Saritha R. & Vinod Chandra S. S. (2017). Multi-Dimensional Honey Bee Foraging Algorithm Based on Optimal Energy Consumption. *Journal of the Institution of Engineers (India): Series B, Electrical, Electronics & Telecommunication and Computer Engineering*, 98(5):527–531.
- [14] Triantaphyllou E. (2013). Multi-criteria decision making methods: a comparative study. *Springer Science and Business Media*. Vol. 49, 5-21.
- Yuce B., Packianather M. S., Mastrocinque E., Pham T. D., & Lamiase A. (2013). Honey bees inspired optimization method: the Bees Algorithm. *Insects* 4 (4), 646-662.

NEW METHOD FOR DOSING LIQUID MIXTURE'S COMPONENTS BY MEANS OF OVERPRESSURE

METODA NOUĂ DE DOZARE A COMPONENTELOR AMESTECURILOR LICHIDE CU UTILIZAREA SUPRAPRESIUNII

Cerempei Valerian¹⁾, Molotcov Iurii²⁾, Popa Lucretia³⁾ ¹

¹⁾ UASM Chişinău / Republic of Moldova; ²⁾ ITA Mecagro Chişinău / Republic of Moldova; ³⁾ INMA Bucharest / Romania

Tel: (373) 796 777 28 E-mail: cerempeivalerian@gmail.com

DOI: <https://doi.org/10.35633/inmateh-65-40>

Keywords: liquid mixtures, dosage, overpressure, installation, parameters

ABSTRACT

The results of the bibliographic and theoretical studies on methods of dosing liquid substances using hydropneumatic systems are presented in this article. Based on these studies, the multicomponent continuous dosing method and installation were developed in order to obtain high quality liquid mixtures (including biofuels) at minimal cost. In the proposed installation "Biomixt-Pres" the flow of liquid components is ensured by overpressure in the dispenser tank. Theoretical analysis and experimental research of this installation allowed to argue the values of constructive and hydrodynamic parameters (overpressure in the working tank $\Delta p = 0.2- 0.5$ MPa; diameter of the working tank $D \approx 0.625 H$ (H is the height of the tank), liquid level and the installation height of the maximum, minimum liquid level transducers in the working tank), which ensures the required ratio of components with the error $\delta \leq 0.2\%$.

REZUMAT

În prezentul articol sunt prezentate rezultatele studiilor bibliografice și teoretice privind metode de dozare a substanțelor lichide cu utilizarea sistemelor hidropneumatice. În baza acestor studii au fost elaborate metoda și instalația de dozare continuă multicomponentă, cu scopul de a obține amestecuri lichide (inclusiv, biocombustibili) de înaltă calitate cu cost minim. În instalația propusă „Biomixt-Pres”, curgerea componentelor lichide este asigurată de suprapresiune în rezervorul dozatorului. Analiza teoretică și cercetările experimentale ale acestei instalații au permis argumentarea valorilor parametrilor constructivi și hidrodinamici (suprapresiunea în rezervorul de lucru $\Delta p = 0,2-0,5$ MPa; diametrul rezervorului de lucru $D \approx 0,625H$ (H este înălțimea rezervorului), nivelul lichidului și înălțimea instalării traductoarelor de nivel maxim / minim al lichidului în rezervorul de lucru), care asigură raportul necesar al componentelor cu eroarea $\delta \leq 0,2\%$.

INTRODUCTION

Obtaining high-quality, reasonably priced liquid mixtures, including biofuels, is an important technical-scientific problem in various branches of the world economy (chemical, pharmaceutical, energy, food, etc.). Therefore, methods and equipment for dosing and mixing liquid components are the subject of research of many specialists (Başta et al., 2010; Băieşu, 2012; Bezmenov, 2011; Cori-Fill TM, 2020; Gheorghişor, 2012; Globin and Krasnov, 2012; Maşumura Takehico and Utino Iosihico, 2014). The known liquid mixing dosing machines in most cases provide the high dosing accuracy of each component, which increases the complexity of these machines. In many technological processes it is important to obtain liquid mixtures with a high precision of the ratio between the components.

In order to streamline the technological process of dosing-mixing liquid components in a mixture, for example, biofuel, a method and an installation with the name "Biomixt" were developed (Cerempei and Molotcov, 2019; Hăbăşescu et al., 2011). The proposed method is based on the flow of liquid components through holes or calibrated individual pipes, under the action of a negative pressure difference Δp (aspiration) at the inlet to the metering pump. In the Biomixt installation, the multichannel dosing with common electronic control of the actual process is performed.

The long-term tests of the Biomixt installation have shown that it ensures a relatively high accuracy of the ratio between the components of the mixture ($\delta \leq 0.5\%$). However, the mentioned installation, having some

¹ Cerempei Valerian, D.Hab.Eng.; Molotcov Iurii, Ph.D.Eng.; Popa Lucretia, Ph.D.Eng

advantages (constructional simplicity, small dimensions), ensured the necessary precision under certain conditions. In reality, liquid mixtures, including biofuels, are produced under various conditions, respectively their production is characterized both by different productivity and by the composition of the mixture, dosing accuracy, etc. Achieving these goals is possible due to certain constructive peculiarities. In order to deal with this situation, the analysis of the hydrodynamic parameters that influence the liquid flow process and, implicitly, the precision of the dosing of the components was performed.

The dosing error δ of each component and the ratio between them in a liquid mixture can be expressed by the formula (Cerempei and Molotcov, 2019):

$$\delta = \frac{Q - Q_r}{Q} \cdot 100\% = \left[1 - \sqrt{1 + \frac{\Delta h}{h + \frac{\Delta p}{\rho g}}} \right] \cdot 100\% \quad (1)$$

where:

Q and Q_r are the flow rates, respectively, the nominal and the real ones (for the constant values of the working section S of the pipe and of the flow coefficient μ), [m^3/s];

h - height of the liquid column at the inlet of the outlet hole, [m];

Δh - variation range of the height h , [m];

Δp - the pressure difference at the inlet and outlet of the dosing system ($p_1 > p_0$), [Pa];

g - gravitational acceleration, [m^2/s];

ρ - density of the dosed liquid, [kg/m^3].

Therefore, in practice, the dosing error δ of each component and of the ratio of components in the fuel mixture depends on the accuracy of maintaining the height of the liquid column (Δh), the difference in pressure Δp at the inlet and outlet of the dosing system, and the height h . At present there are high capacities for decreasing the fluctuation of the height of the liquid h , i.e. it is possible that $\Delta h \rightarrow 0$ (Băieşu, 2012; Bezmenov, 2011). For economic reasons, it is not rational to increase the height h of the liquid in the working tank. Therefore, there is only one rational way left: to increase the value of the pressures difference Δp . However, in the Biomixt installation there are limited possibilities to increase Δp , because in this case the pressure difference consists in difference between the atmospheric pressure p_0 in the working tank and the inlet pressure p_1 at the inlet to the dosing pump.

Thus, analysing formula (1) it was found that in order to increase the dosing accuracy it is necessary to increase the difference Δp between the inlet pressure and the outlet pressure in the outlet. This condition can be achieved if the liquid flows from an airtight tank with a pressure of $p_1 > p_0$. Generally, installations operating according to the mentioned principle are known (Başta et al., 2010; Bezmenov, 2011; Cori-Fill TM, 2020; Globin and Krasnov, 2012; Maşumura Takehico and Utino Iosihico, 2014; Nistoran et al., 2007). The typical functional diagram is shown in Figure 1.

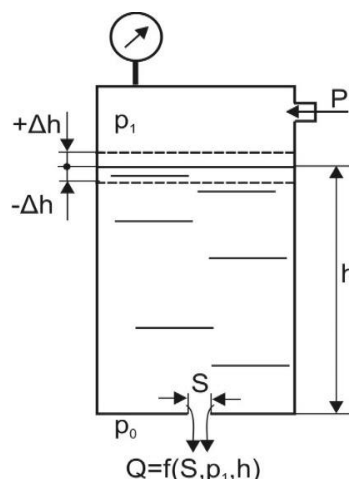


Fig 1 - Functional diagram of the liquid flow dispenser through the calibrated hole with section S

In the working tank, the required pressure ($p_1 \pm \Delta p_1$) is maintained with the help of compressed air from the pneumatic system. In order to achieve the described conditions, it is necessary that the flow rate Q through the orifice calibrated with section S be in the range $Q \pm \Delta Q$, where ΔQ represents the error of the flow rate.

The results of the monographic researches show that in the existing installations for continuous dosing of liquids (fig.1), there are difficulties in the simultaneous regulation of the liquid level in the tank $h \pm \Delta h$ and of the pressure in the tank $p_1 \pm \Delta p_1$. One of the causes of the difficulties is that with the completion of the liquid in the working tank in the dosing process, the overpressure Δp can increase uncontrollably, exceeding the set value. Therefore, in this case, the flow rate Q also increases, so that additional dosing errors occur simultaneously.

Therefore, existing liquid dosing facilities have certain shortcomings and a narrow field of use, the information from existing bibliographic sources is not sufficient for the design and use in production of the installation with continuous dosing of several liquid components, especially for the production of biofuels. Therefore, it is necessary to carry out a complex of theoretical and experimental research activities, with the aim of developing the method and installation to ensure the continuous and concomitant dosing of several liquid components with precise compliance of the ratio between them and the minimum cost of the mixture production.

MATERIALS AND METHODS

After conducting bibliographic studies, as well as experimental research of the Biomixt installation (*Cerempei and Molotcov, 2019*), technical solutions were submitted aimed at streamlining the dosing process of liquid mixtures, including biofuels, which require theoretical and experimental research to achieve the stated goal. Therefore, the following activities were performed:

1. Design, development of the method and installation for the dosing and mixing of components in order to obtain high quality liquid mixtures. Verification of the conformity of the functional parameters of the installation presented for tests to those established in the design phase;
2. Carrying out the theoretical analysis of the hydrodynamic parameters, which influences the dosing error δ of the components in the liquid mixture. Determining the flow rate dependence of the components depending on the pressure in the dispenser working container. Estimation of possible dosing errors, resulting from the theoretical calculation, and their comparison with the real ones obtained on the pilot installation.
3. Long-term testing of the procedures for adjusting the ratio between the components of the liquid mixture.

As a result of the activities from the first stage, the method and installation "Biomixt-Pres" for the preparation of liquid mixtures was developed (fig.2) (*Hăbășescu et al., 2011, 2014*).

The experimental installation (fig.2) works in the following way.

After connection, pumps 12 and 13 initiate the supply of liquid to the working tanks 2 of the dispensers. The pressure inside the pumps starts to increase and after reaching the installed value, the pressure transducer 11 sends the signal of the electronic command and control system SECC with panel 8, which controls the opening of the distributors 4 in the exhaust channels. The process of continuous dosing of the A, B components of the liquid mixture starts. Transducers 9 and 10 monitor the level of components A, B in the tanks 2, and transducer 11 monitors the value of the working pressure in the pneumatic system.

The pressure in the working tanks 2 is automatically maintained by supplying the liquid components in the respective working containers or by pumping the compressed air by a compressor. Each component (A, B, etc.) of the liquid mixture, passing through the fixed section of the discharge nozzle 5, under the action of the overpressure Δp in the working container, flows with the flow given in the storage tank 6. Due to the fact that the nozzles of the mixing device are inclined towards each other, the diffused jets merge into one, forming the expected mixture. It is then sent to the storage container from where it is delivered to the consumer with the special pump 7.

The conformity check of the developed installation was performed by comparing the initial design requirements with the actual parameters of the installation, determined by visual examination and measurements. Water was used as the initial stage dosing component. To test the safety of the installation, the control valves of the exhaust channels 4 were positioned arbitrarily, then the installation was started. When the pressure set in the containers was reached, the solenoid valves of the exhaust channels opened and a stable jet of both liquids formed in the storage container. Each experiment lasted at least 20 minutes.

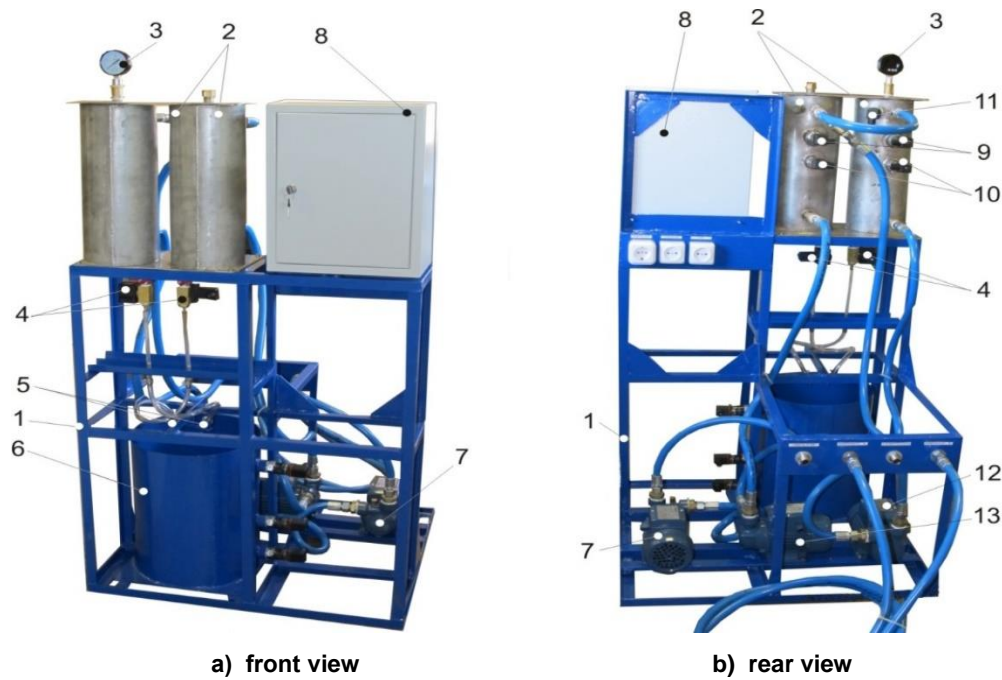


Fig. 2 - Biomixt-Pres installation for the preparation of liquid mixtures (Hăbășescu et al., 2011, 2014)

1 - frame; 2 - working tanks; 3 - control manometer; 4 - hydraulic distributors; 5 - exhaust nozzles; 6 - storage tank; 7 - pump for taking the ready liquid mixture; 8 - control panel; 9 - maximum level transducers; 10 - minimum level transducers; 11 - pressure transducer; 12 - pump for supplying component A; 13 - pump for supplying component B.

To evaluate the dosing accuracy of the components, the installation worked continuously for 15 min, in each experiment. This period ensured the stabilization of the operating regimes of all component systems. The control valve in the drain of the base component was fully opened ($Q_A = \max$), and the valve of the drain of the component B for each experiment was positioned so as to ensure the following ratios of the constituents of the mixture: $Q_B / Q_A = 10/90; 20/80; 30/70; 40/60; 50/50$.

The accuracy of the Q_i flow rate measurement of each component was ensured by using calibrated fuel measurements and by repeating the measurements 10 times according to the standard SM 226: 2002-“Automotive gasoline used in the Republic of Moldova. Technical conditions for conformity assessment”.

Using the stopwatch, the time required to fill the container to the mark line was measured and the flow rate Q_i (l/min) was calculated for each channel in the following relationship:

$$Q = \frac{60 \cdot V}{\tau} \quad (2)$$

where:

V is the volume of the calibrated container, [l]; τ - the filling time of the container, [s].

Based on the measurement results, the average value of the flow rate was determined:

$$Q_m = \frac{1}{n} \sum_{i=1}^n Q_i \quad [\text{l/min}] \quad (3)$$

where:

Q_i is the result of the measurement and flow rate, [l/min]; n - number of experiments performed.

Next, the deviation Δ_i was calculated for each measurement of Q_i from Q_m , taking into account the sign. This allowed the determination of the relative dosing error for each measured flow rate:

$$\delta_i = \frac{\Delta_i}{Q_m} \cdot 100 \quad [\%]. \quad (4)$$

The evaluation of the reproducibility of the established flow rates was performed, repeating one of the experiments described above for 96 hours, without changing the position of the control valve. In this case, for each series of long-term experiments the mean value of the flow rate Q_{mi} was calculated and was compared with the overall mean value Q_m previously obtained according to formula (2).

RESULTS

The analysis of formula (1) shows that the accuracy of the component dosing and the error value of the flow rate ΔQ are determined by the sum of the errors that occur when maintaining the overpressure Δp and the level Δh . The degree to which Δp and Δh influence the dosing accuracy can be determined from the analysis of formula (1), from which it follows that the relative dosing error decreases with decreasing Δh and increasing Δp . So, $\lim_{p_1 \rightarrow \infty} \delta = 0$

Theoretical calculations based on formula (1) and the results of experimental research with the Biomixt installation, allowed to establish the dependence of the dosing error δ depending on the pressure drop Δp in the working tank for different heights of the liquid column h and the deviation Δh with a fixed value (fig. 3).

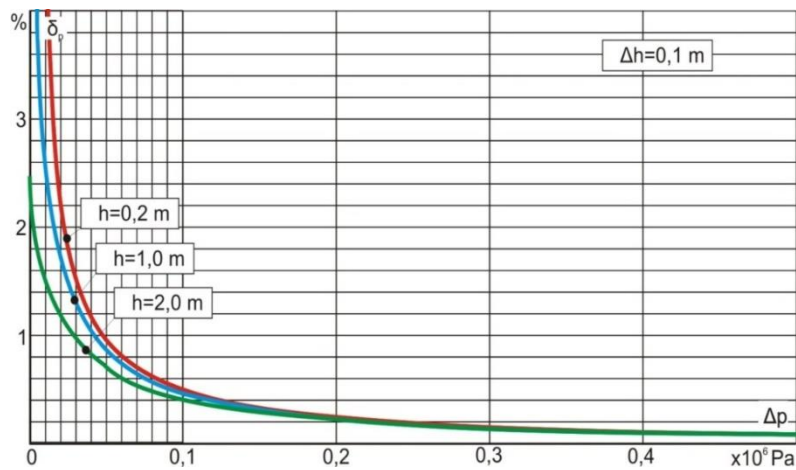


Fig. 3 – Dosing error δ depending on the overpressure Δp in the working tank for different heights h of the liquid column

The graph shows that, for $\Delta p > 0.2$ MPa, the initial height of the liquid column h practically does not influence the error δ , which becomes dependent only on the absolute values Δp and Δh (fig. 4).

For comparison, the dependence formula $\delta = f(\Delta h)$ for $\Delta p = 0$ is presented, ie for the case when the pressure in the working tank is equal to the atmospheric pressure. In this case the size δ depends a lot on Δh and can be determined from the relation:

$$\delta \approx 49 (\Delta h / h) \text{ [%]} \tag{5}$$

Increasing the pressure drop Δp to 0.2MPa, this dependence becomes much lower, namely:

$$\delta \approx 2.3 (\Delta h / h) \text{ [%]} \tag{6}$$

At pressure drop $\Delta p = 0.5$ MPa:

$$\delta \approx 1 (\Delta h / h) \text{ [%]} \tag{7}$$

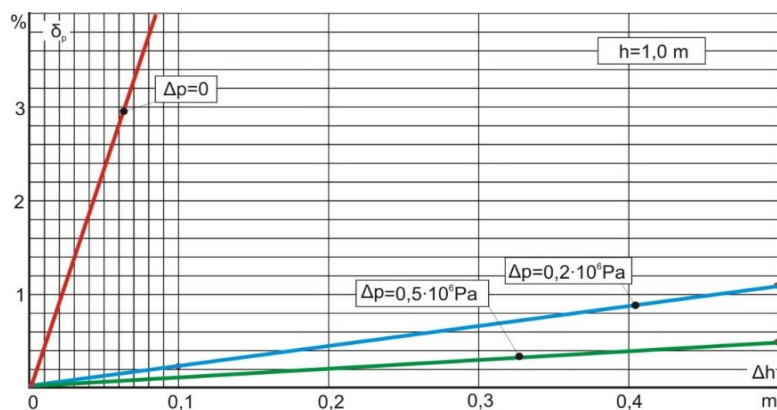


Fig. 4 – Influence of deviations of the liquid column height (Δh) on the dosing error δ , for different values of the overpressure Δp in the working tank

Therefore, it can be said that with increasing pressure, the dependence $\delta = f(\Delta h)$ becomes smaller and when $\Delta p \rightarrow \infty$ the relative dosing error $\delta \rightarrow 0$ and a little depends on the magnitude of the fluctuation Δh . It follows that in the working tank for pressure p_1 with high values ($\Delta p > 0.5$ MPa) (fig.3), the dosing error δ depends only on the errors of maintaining the given pressure.

For practically assuring the results obtained from the theoretical and experimental researches, the dispenser was elaborated (fig.5), in which the pressure p_1 is maintained by a combined method, namely by supplying in the working tank the dosed liquid or the compressed air. To switch from one mode to another and to control the liquid level in the tank, maximum and minimum level transducers have been installed on the side wall of the working tank.

Safe operation of the dispenser shown in figs. 2 and 5 is conditioned by the correct choice of geometric parameters and installation coordinates of level transducers.

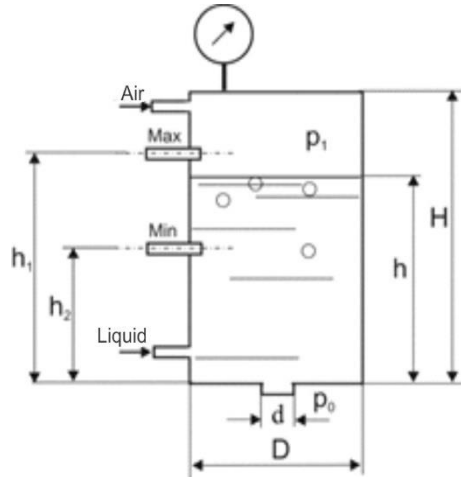


Fig. 5 – Schematic of the combined continuous-acting dispenser for maintaining overpressure in the working tank

The basic dimension H (height of the working tank, fig.5) is required according to the general scheme of the device in which the dispenser will be installed. In this case, the total volume of the tank will be expressed by the formula:

$$V = S_t H = \pi D^2 H / 4 \quad [\text{m}^3] \tag{8}$$

where: S_t is the cross-sectional area of the working tank regardless of shape, m^2 ; D , H - respectively the diameter and height of the working tank, m .

Volume V is occupied by air until the liquid is supplied to the working tank. In this case the pressure inside the tank is equal to the atmospheric pressure p_o (overpressure $\Delta p = 0$). When the liquid is supplied to the tank, the air is compressed to the volume V_g and its absolute pressure p_1 increases according to the Boil-Mariott law ($p_1 V_g = \text{const}$, for constant values of gas mass and temperature) (Ratbil, 2010). However, in this case, if the increase of the compression temperature is neglected, according to the mentioned law, the proportion will take place:

$$\frac{V}{V_g} = \frac{p_1}{p_o} = \frac{\Delta p + p_o}{p_o}, \tag{9}$$

whence:

$$V_g = V \cdot \frac{p_o}{\Delta p + p_o} \quad \text{or} \quad V_g = \frac{V}{\left(\frac{\Delta p}{p_o} + 1\right)}, [\text{m}^3] \tag{10}$$

where: V_g is the volume of compressed air.

Substituting the value V from formula (8) into formula (9), the following is obtained:

$$V_g = \frac{\pi D^2 H}{4 \left(\frac{\Delta p}{p_o} + 1 \right)} \quad [\text{m}^3] \quad (11)$$

Knowing the volume of compressed air V_g and taking into account the fact that the liquid occupies the rest of the volume of the working tank, the following can be written:

$$V_l = \frac{\pi D^2 H}{4} - V_g = \frac{\pi D^2 H}{4} \left(1 - \frac{1}{\left(\frac{\Delta p}{p_o} + 1 \right)} \right) \quad [\text{m}^3] \quad (12)$$

From expression (12) is determined the height h , at which the liquid rises in the working tank when the given overpressure is reached Δp :

$$h = H \left(1 - \frac{1}{\left(\frac{\Delta p}{p_o} + 1 \right)} \right) \quad [\text{m}] \quad (13)$$

The formula is valid for containers with a constant cross-sectional area.

As shown in formula (13), the level of liquid h in the working tank of the dispenser does not depend on the shape and dimensions of its cross section, but only on the total height of the tank H and the value of the overpressure Δp .

The height h_1 (fig.5), at which the maximum liquid level transducer is installed, is established by adding to the height h (calculated from formula (13)), the size $\Delta = \frac{H-h}{2}$. In this case, the metered liquid acts on the maximum level transducer. This state serves as a signal for the transfer of the control system into operation, in which the working pressure p_l is maintained due to the supply of metered air in the tank. This excludes overloading the tank and blocking the dispenser.

The height h_2 (fig.5), at which the minimum liquid level transducer is installed, is established, based on the requirement that the duration τ in which the liquid level is lowered from h_1 to h_2 is greater than 10 seconds. Otherwise ($\tau < 10$ s) the liquid supply pump in the working tank will operate intermittently, which significantly reduces its working durability.

The results of the monographic research showed that the optimal value is $\tau > 15$ s. In this way, the value of h_2 can be chosen from the condition:

$$h_2 \leq h_1 - \tau Q / S_t \quad (14)$$

where S_t is the cross-sectional area of the working container, $[\text{m}^2]$.

From here, for the round section tank:

$$h_2 \leq h_1 - \frac{4\tau Q}{\pi D^2} \quad (15)$$

where Q is the flow rate of the component, $[\text{m}^3 \text{ s}^{-1}]$; D - inside diameter of the working tank, $[\text{m}]$;

τ - standby time in the feed pump operation, $[\text{s}]$.

From formula (15) results that increasing the diameter D of the working container tank reduces the difference h_2-h_1 and, at the limit, becomes zero. But for small values of D it can happen that the difference on the right side of the formula (15) becomes negative. In this case it is necessary to increase D or decrease τ .

When choosing the working tank diameter D , it must also be taken into account that, for constant values of the difference Δp , increasing the diameter D , for the given flow rate Q , leads to an increase in the working tank volume which, implicitly, increases the time for filling the tank τ .

The pressure, developed by the pump for supplying the metered liquid in the working tank, must be higher than $(1.5 \dots 2.0) \Delta p$ (Δp the overpressure imposed in the working container). This will allow the pump to maintain Δp at the calculated level, exceeding the resistance of the connecting pipes.

The pump flow rate must be within the range $(4 \dots 5)Q$. If this interval is exceeded, in the process of maintaining the given pressure, the phenomenon of significant "over-adjustment"² may arise, which may initiate additional dosing errors. At the same time, the lower flow rate can adversely affect the operating speed of the pressure regulating system in the working tank.

The results of the research on the flow of liquid through the calibrated orifice under the action of overpressure, presented in this article, served as a basis for the development of the pilot model of the liquid mixture preparation installation, including biofuels (trade name "Biomixt-Pres") (Hăbășescu et al., 2011, 2014).

The Biomixt-Pres installation (fig.6) is composed of the working tanks 1 and 2 of the dispensers of components A, B. Through one-way valves SSU 1 and SSU 2; (pos. 3, 4), the tanks are connected to pumps 5 and 6, which supply the liquid components A, B in a dosed manner. Module 7, consists of an air filter, an air pressure regulating valve, a manometer and a compressed air distributor block.

In the same time, using the manometer 9 of the air preparation module, the pressure in the working vessels is controlled by means of the pressure transducer 10, which converts the pressure value into an electrical signal, being transmitted in the automatic control system SAR1.

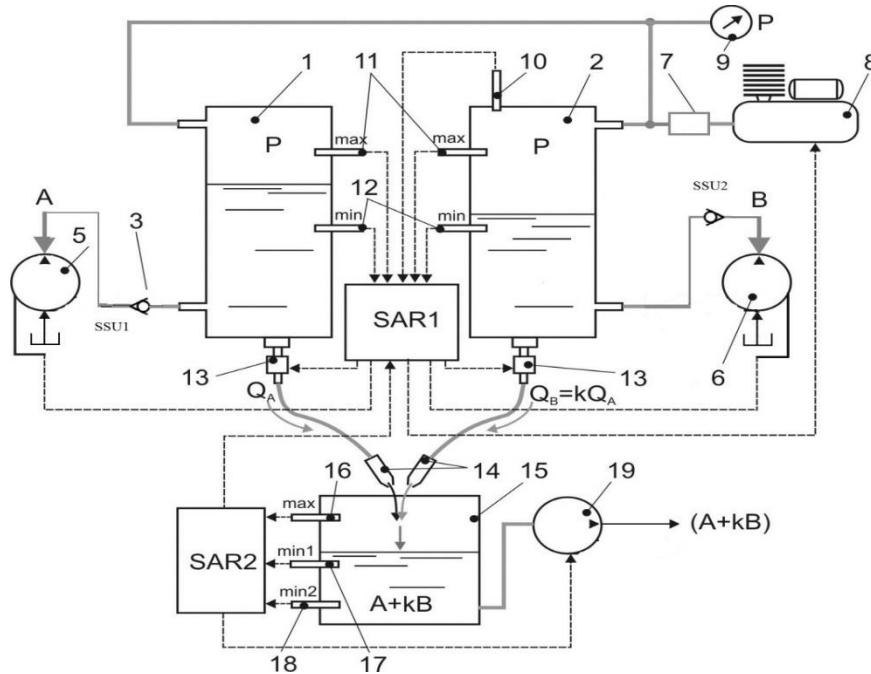


Fig. 6 – Schematic of the "Biomixt-Pres" pilot model for the preparation of liquid mixtures

1,2- tanks; 3,4-valves; 5,6- supply pumps; 8- air preparation module; 9- manometer; 10- pressure transducer; 11,12,16, 17, 18- level transducers; 13- evacuation devices; 14- nozzles; 15- storage tank; 19- mixture drain pump

On the side walls of the working tank are installed the maximum level 11 and the minimum level 12 transducers, and on the lower bottom of both tanks are connected an outlet channel 13 equipped with a hydraulic distributor which, if necessary, blocks the outlet channel. The section of the outlet channel of component B is adjustable, and that of component A - fixed at the maximum level.

The sizes Δp and Δh are set automatically by a steering system specially designed for this purpose. By modifying the section of the outlet channel of component B, the mixture can be prepared with the necessary composition $A + kB$, where k – the coefficient, which determines the ratio of components B and A in the mixture:

$$k = \frac{Q_B}{Q_A} \quad (16)$$

The components A and B with the given ratio, through the outlet channels 13, move in the mixing device, which consists of two nozzles 14, inclined to each other at a certain angle. The $A + kB$ mixture reaches the

² Overadjustment - quantitative characteristic of the oscillation property of the system; is denoted by the letter σ and is determined as a percentage in relation to the value stabilized according to the expression (Băieșu, 2012; Bezmenov, 2011):

storage tank 15, equipped with the level transducers 16, 17 and 18, connected to the pump 19 for taking the prepared mixture.

The SAR2 automatic control system manages the operation of pump 19. It is connected to the SAR1 system, which forms a unique SECC command and control system, which ensures the stable operation of the installation in all working conditions, including accidental one.

Therefore, the research carried out allowed the development of a method and, respectively, of the “Biomixt-Pres” installation that ensures the continuous and concomitant dosing of several liquid components with a high precision: the error of maintaining the ratio between the components δ was less than 0.2 %, which is sufficient in many technological processes in the food, chemical, liquid biofuel production industry (mixtures of monohydric alcohols with gasoline, esters of vegetable oils with diesel).

The tests of the developed method and of the “Biomixt-Pres” installation carried out in the Experimental Center of the Mecagro Institute of Agricultural Technology confirmed the results obtained in the theoretical and experimental research, as well as high values of reliability and durability of the Biomixt-Pres installation.

CONCLUSIONS

✓ Based on the bibliographic study, the analysis of hydrodynamic parameters and experimental research, a method of dosing and mixing the components of liquid mixtures was developed, for the realization of which an installation equipped with a SECC command and control system was developed. Its operation is based on the principle of liquid flow through a calibrated outlet channel (orifice or pipe) under the action of overpressure.

✓ It was theoretically argued and experimentally confirmed the efficiency of using in the “Biomixt-Pres” installation the principle of liquid flow, at controlled overpressures, through holes calibrated with the delivery of components by separate pumps. The flow of liquids in each dosing channel was stable. This minimized the dosing error ($\delta \leq 0.2\%$) for wide ranges of liquid flow rate.

✓ Based on the calculations and researches, the main construction parameters of the “Biomixt-Pres” installation were established, among which are: overpressure in the working tank $\Delta p = 0.2 \dots 0.5$ MPa; working tank diameter $D \approx 0.625H$ (H is the height of the tank); the level of the liquid in the working tank depending on the pressure p_1 of the liquid in the same tank, the atmospheric pressure p_0 and the height of the tank H ; the height of the installation of the maximum and minimum liquid level transducers in the working tank.

✓ The functions of the electronic command and control system SECC for the dosing-mixing installations of liquid mixtures were determined, namely: automatic maintenance of the pressure in the working tank with the indication of the current pressure value; automatic opening and closing of solenoid valves in component exhaust pipes; automatic control of the components delivery pumps and discharge of the prepared mixture from the storage tank; protection against accidental working conditions.

REFERENCES

- [1] Bașta T.M., Rudnev S.S., Necrasov B.B. et al. (2010). *Hydraulics, machines and hydraulic drives (Гидравлика, гидромашины и гидроприводы)*. Alians, 423p.; ISBN 978-5-903034-88-8, Moscow / Russia;
- [2] Băieșu A.S. (2012). *Automatic adjustment technique (Tehnica reglării automate)*, Matrixrom, 214p., ISBN: 9789737558152. Bucharest / Romania;
- [3] Bezmenov V. (2011). *Pneumatic automated liquid dosing systems. Principles and methods of design (Пневматические системы автоматизированного дозирования жидкостей. Принципы и методы построения)*. LAP LAMBERT Academic Publishing, 168 p., ISBN 13: 978-3-8454-0174-4; ISBN-10: 3845401745;
- [4] Cerempei V., Molotcov Iu., (2019). Elaboration of dosing method for liquid biofuel components. *INMATEH – Agricultural Engineering*, vol. 58, no.2, pp.27-36. ISSN 2068-2239. Bucharest / Romania;
- [5] Gheorghîșor M. (2012). *Motor fuels and lubricants*. Tiparg, 276 p., ISBN: 978-973-735-642-0. Bucharest / Romania;
- [6] Globin A.N., Krasnov I.N. (2012). *Dispensers (Дозаторы)*. FGBOU VPO ACGAA-Zernograd, 348p. ISBN 978-5-91833-073-9; Rostov/Russia;
- [7] Hăbășescu I., Cerempei V., Molotcov Iu. (2011). *Liquid dosing and mixing device (Dispozitiv pentru dozarea și amestecarea lichidelor)* Patent no. 363 Y, Republic of Moldova;

- [8] Hăbășescu I., Cerempei V., Molotcov Iu. (2011). *Continuous liquid dosing system (variants) (Instalație de dozare continuă a lichidului (variante))*. Patent no. 411 Z, Republic of Moldova;
- [9] Hăbășescu I., Cerempei V., Molotcov Iu. (2014). *Installation and process for continuous dosing of the liquid (Instalație și procedeu de dozare continuă a lichidului)*. Patent no. 765 Z, Republic of Moldova;
- [10] Mațumura Takehico, Utino Iosihico (2014). *Liquid mixing device (Устройство для смешивания жидкостей)*. Patent no. 2 529 242, Russia;
- [11] Nistoran D.E., Moatăr Fl., Manoliu M., Ionescu Gr. (2007). *Technical hydraulics (Hidraulică tehnică)*. Printech, 226p. ISBN 978-973-718-661-4; Bucharest / Romania;
- [12] Ratbil E. (2010). *Boyle-Mariotte's law (Закон Бойля-Мариотта)*. Drofa, 159p., Moscow / Russia;
- [13] Cori-Fill TM Coriolis Mass Flow Meter Based Compact Fluid Dosage Assembly (quoted 27.09.2021); <https://www.bronkhorst.com/int/service-support-1/technologies/cori-fill-technology/>

RESEARCHES ON THE TESTING IN LABORATORY CONDITIONS OF AN ECOLOGICAL CLIMATE SYSTEM USED FOR SELF-PROPELED AGRICULTURAL MACHINES

CERCETĂRI PRIVIND TESTAREA ÎN CONDIȚII DE LABORATOR A UNUI SISTEM DE CLIMATIZARE ECOLOGIC FOLOSIT LA MAȘINILE AGRICOLE AUTOPROPULSATE

Găgeanu Iuliana, Cujbescu Dan*, Dumitru Cristinel

INMA Bucharest / Romania;

*E-mail: dcujbescu@yahoo.com

DOI: <https://doi.org/10.35633/inmateh-65-41>

Keywords: ecological climatization, operator comfort, water-air flow, evaporation

ABSTRACT

Nowadays, cooling the air by means of climate maintenance systems is achieved, in most cases, using installations based on freon or other substances that cause pollution. Taking into account the fact that the EEC standards and regulations increase the emphasis on ensuring the quality, labour safety, health and environment, finding a solution for air conditioners that do not use a substance that causes pollution, has become a necessity. As a great part of farming work is done in the warmest periods of the year, temperatures being frequently over 35°C, it is necessary to equip the agricultural machines with air conditioners in order to achieve a thermic comfort in the cab. For this purpose, an air conditioner based on the process of water evaporation was designed, made and tested. The installation is able to cool the air that enters into the cab through the evaporation process that takes place in the special filling, with an efficiency of the mixing process more than 90%. Air passing sections are calculated so that they can assure both the quantity needed for climate maintenance in the cab (about 3.5 - 4 m³/min) and the relative speed between air and water in the filling, in order for the evaporation process to be conducted in the best conditions that were theoretical established.

ABSTRACT

În zilele noastre, răcirea aerului prin sistemele de menținere a climei se realizează, în majoritatea cazurilor, folosind instalații bazate pe freon sau alte substanțe care provoacă poluare. Ținând cont de faptul că standardele și reglementările CEE sporesc accentul pus asupra asigurării calității, siguranței muncii, sănătății și mediului, găsirea unei soluții pentru aparatele de aer condiționat care nu utilizează o substanță care provoacă poluare, a devenit o necesitate. Deoarece o mare parte a muncilor agricole se face în perioadele cele mai calde ale anului, temperaturile fiind frecvent peste 35°C, este necesar să se echipeze utilajele agricole cu aparate de aer condiționat pentru a obține un confort termic în cabină. În acest scop, a fost proiectat, realizat și testat un aparat de aer condiționat bazat pe procesul de evaporare a apei. Instalația este capabilă să răcească aerul care intră în cabină prin procesul de evaporare care are loc în umplutura specială, cu o eficiență a procesului de amestecare mai mare de 90%. Secțiunile de trecere ale aerului sunt calculate astfel încât să poată asigura atât cantitatea necesară pentru întreținerea climatică a cabinei (aproximativ 3.5 - 4 m³/min), cât și viteza relativă dintre aer și apă în umplutură, pentru ca procesul de evaporare să se desfășoare în cele mai bune condiții stabilite teoretic.

INTRODUCTION

The main functions of agricultural machinery cabs are to provide a comfortable environment for operators and to protect them from vibrations, noise and other adverse influences. Since the conditions inside self-propelled machinery cabs (agricultural tractors and other equipment) affect the health, performance and comfort of the operator, it is important to find solutions for improving these conditions (Ruzic & Casnji, 2012).

The most important factors influencing thermal comfort of humans operating in vehicle cabs are air velocity, temperature, clothing style, relative humidity, and level of activity of the occupants (Afzal et al., 2020; Simion et al., 2016).

Ensuring the comfort of the person operating the equipment is achieved both by using an ergonomic car seat and by creating a pleasant environment by air conditioning inside the cab with the help of special equipment (Oh et al., 2020).

In general, air-conditioning systems are complicated, they must provide the air with previously set conditions for all its characteristic parameters, thus creating an imposed artificial climate. Certain well-defined climatic conditions correspond to each organism in order to develop in optimal conditions or to give a maximum efficiency in the work process.

Thus, the amount of exterior air received by a person should not be less than 30 m³/h, in order to avoid fatigue, headaches and nausea, caused by the lack of oxygen. Comfort conditions regarding temperature and relative humidity depending on the season must fit with some precision between the limits listed in Table 1 (ISO 14269-2:1997; Ivanescu et al., 2010).

Table 1

Comfort conditions regarding temperature and relative humidity

Season	Lower limit		Upper limit	
	Temperature (°C)	Relative humidity (%)	Temperature (°C)	Relative humidity (%)
Winter	16÷17	70	21÷24	70
Summer	18÷20	30	26.5÷27	70

It can be stated in principle that for a certain state of comfort, with the increase of humidity, a decrease in temperature can be admitted. The movement of air occurs both as a result of ventilation and because of temperature differences between the air layers. It is obvious that as the air speed increases, the same degree of comfort is reached at a higher temperature. For example, the effect felt in the case of an unventilated cab (resting air), where the air has 24°C and 50% humidity is the same as the effect that would be created if the air had 30°C, 50% humidity and a speed of air of 1.5 m/s² (Kaufman et al., 1979).

An air-conditioner (AC) system for a motor vehicle cab has the disadvantage that it is the largest power consumer, excluding the vehicle propulsion system. The power consumption of the AC in small tractors can reach 10-100% of the actual engine power and the highest values occur during the engine idling (Ruzic D., 2018; Leighton & Ruth, 2016).

Permanent change of air in the cab is necessary to replace the oxygen consumed by the driver and at the same time remove the combustion products (gases, vapours). The minimum amount of fresh air required by a person is 0.25 m³/min (Martinho et al., 2004).

The comfort requirements are:

- degree of humidity in the range: 40...70%;
- the relative speed of the air must have values between 0.15...0.25 m/s, in the case of laboratory tests;
- for an outdoor temperature of 27...30°C, the limit of natural regulation by transpiration is reached;
- at a temperature higher than 35°C cardiovascular changes occur;
- at a temperature of about 40°C the person is exposed to syncope;
- the allowed comfort temperature is within the limits of 22...28 (30)°C, being strongly dependent on the air circulation speed (ISO 14269-2:1997).

The paper presents an ecological alternative to the classic air conditioning systems, being able to carry out the cooling of the air entering the cab through the evaporation process that takes place in the special type filling.

MATERIALS AND METHODS

Starting from the theoretical bases of the thermal and hydro-pneumatic process, an experimental model was developed that ensures a nominal flow of at least 4 m³/min, necessary for the conditioning of the cabs of combine harvesters.

The proposed air conditioning system differs from the others used by renowned companies from abroad (in the country, the self-propelled tractors and self-propelled agricultural machineries are not equipped with an air conditioning system as such), due to the fact that it is an environmentally-friendly installation (it does not use freon or other pollutants), it is a relatively simple construction, the temperature difference achieved is, under normal conditions, 1...18 °C (above average), the installation can be used successfully even when the air humidity is high, due to the use of hygroscopic substances that retain moisture in the air, the cooled air having a low humidity.

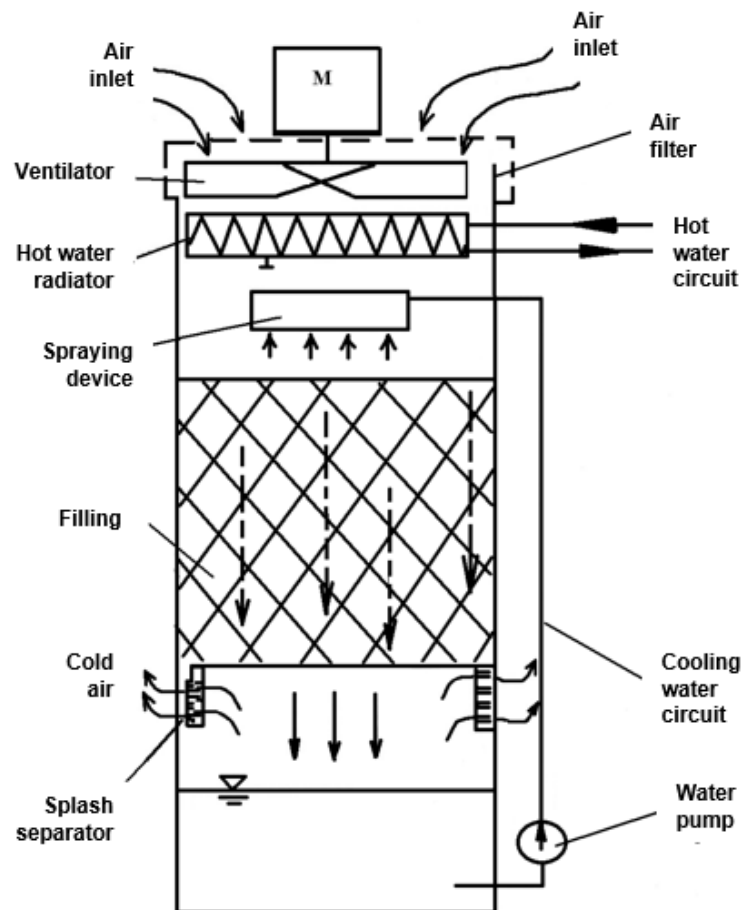


Fig. 1 - Scheme of the air conditioning system

The installation is capable of cooling the air entering the cab through the evaporation process that takes place in the special type filling, with a mixing process efficiency of over 90%.

The air passage sections are calculated so as to be able to ensure both the quantity necessary for the cab conditioning (approximately 3.5 - 4 m³/min) and the relative speed between air and water in the filling, necessary for carrying out the evaporation process in the optimal conditions theoretically established.

Filling - an important component of this installation is the filling, chosen for this device so that it can be controlled in terms of behaviour in these conditions, through a set of mathematical relations. It is made of PVC corrugated sheets arranged on top of each other.

Fan - the air circuit of the installation presents numerous changes of the flow direction as well as local resistances, which implies the choice of a type of medium pressure fan (100...250 mm Hg). A fan whose nominal flow rate, without pneumatic resistances on the route, is 240 m³N/hour was chosen. Taking into account that the maximum flow rate required for cab ventilation is 360 m³N/hour, it was necessary to use two such fans.

Water pump - was chosen for the following reasons: the minimum pressure required is 0.7 m H₂O, the only significant pressure loss being the spraying device; the minimum flow of recirculated water is calculated in relation to the minimum flow of treated air and must be 7.5 l/min.

Considering these particularities, a centrifugal pump was used and a DC motor supplied at 24 V was adapted to it. Under these conditions the pressure can exceed 2.5 m H₂O and the flow rate reaches up to 28 l/min.

Spraying device - is placed in the way of the air jet, therefore its shape and dimensions must be calculated so as to oppose as little resistance as possible. On the other hand, too small dimensions lead to non-compliance with the condition of uniform spraying of the filling. Unlike other air conditioning systems based on the same operating principle, fine water spraying is not required here, so the diameter of the device holes is calculated only for reasons of flow rate and uniformity of spraying.

Water tank - The water tank has a capacity of 18 l and is made of a thermal insulation material, as well as the entire air and water circuit. The efficiency of the entire installation depends very much on the heat transfer coefficient between the environment and the water, respectively the air flowing through the installation.

Measured parameters

During the experimental determinations, the aim was first of all to measure the parameters of the air conditioning compared to those of the air admitted in the installation. It was considered to comply with the specific comfort requirements imposed by domestic and international standards, according to the comfort requirements listed above.

The following were determined:

- tank water temperature variation;
- water consumption (by periodically measuring the water level in the tank);
- water flow rate through the spraying device (indirectly, by measuring the direct current voltage applied to the motor terminals driving the water pump).

Measuring apparatus and devices

The outside air temperature was measured in the shade using a 1°C mercury thermometer. It was placed at a distance of 2 m from the ground, in a well-ventilated weather enclosure. A mercury glass thermometer with divisions of 0.5°C was used for the tank water temperature.

In order to accurately observe the temperature changes of the air conditioning, which occurred during the experiments with variable water/air flows, two electronic multimeters were used to which a thermocouple, respectively a thermal probe was attached. An electronic thermometer was placed in the cab in the operator's head area. An electronic anemometer was used to determine the air flow rate of the fan.

The water level in the tank was determined with a ruler placed on the transparent plexiglass wall of the basin, in an area where the water surface did not show turbulence caused by the operation of the pump or the free fall of water from the humidification chamber.

The humidity of the unconditioned and conditioned air, respectively, was measured with two mechanical hair hygrometers with drum recording.

The determinations were performed both at normal temperatures for the summer period in Romania and at extreme temperatures, rarely found in our country (40...41°C in the shade).

The installation was mounted successively on two cabs:

1. classic U-650 tractor cab, not equipped for conditioning;
2. C-110 P combine cab also not equipped to create thermal comfort (unsealed, no metal wall insulation, no thermal glass)

RESULTS

1. U-650 tractor cab, not equipped for air conditioning, without operator on board

Initial conditions:

• outdoor air temperature, °C:	40
• outdoor air humidity, %:	34
• temperature in the cab, °C:	47
• tank water temperature, °C:	28
• tank water level, mm:	200
Ceiling sheet temperature, °C:	51
Water consumption resulting from experiments, l/hour:	2.96

Exposed to solar radiation in conditions of outdoor temperatures of 40°C in the shade, without air conditioning or ventilation, 37°C were recorded in the cab (with the door open) at head level.

According to the experimental results it is observed that for outdoor temperatures of 40.5-41.5°C and humidity of 34%, 24.7-25.3°C were achieved at the outlet, while at the level of the operator's head were recorded 37°C and a relative humidity of 56-58% (Table 2, figures 2 - 5). The temperature of the cab ceiling was 51°C.

Table 2

Results obtained from determinations on the U-650 cab

Environment		Air conditioning					Tank water temperature (°C)	Time of determination (hour:min)	Voltage at pump terminals (V)	Water level in the tank (mm)
T _{dry} (°C)	U _{rel} (%)	t _{dry.cab} (°C)	t _{dry. air cond.} (°C)	t _{usc.env. - t_{dry. air cond.}} (°C)	V _{air} (m/s)	U _{rel} (%)				
40.5	34	38	25.3	15.2	16	58	23.0	13:20	18	188
41.0	34	37	24.8	16.2	16	56	22.7	13:30	20	184
41.0	34	38	24.3	16.7	16	57	23.0	13:40	20	179
41.5	34	37	24.7	16.8	16	56	23.0	13:50	20	172
41.5	34	37	24.8	16.7	16	58	23.0	14:00	24	167
41.5	34	37	24.7	16.8	16	58	23.0	14:10	18	163

Legend:

T_{dry} = outside temperature; u_{rel} = relative humidity;
 t_{dry.cab} = temperature inside the cab before using air conditioning;
 t_{dry. air cond.} = temperature using air conditioning system

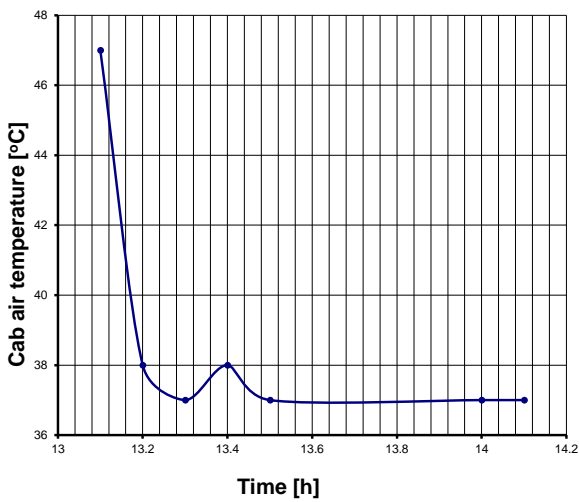


Fig. 2 - Variation of cab air temperature depending on time

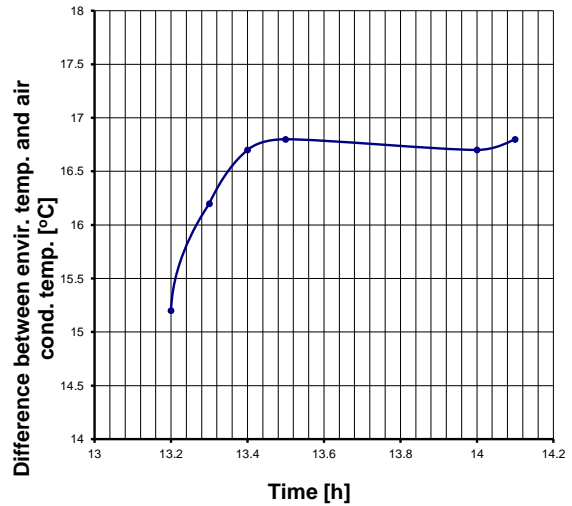


Fig. 3 - Temperature difference generated by the air conditioning system

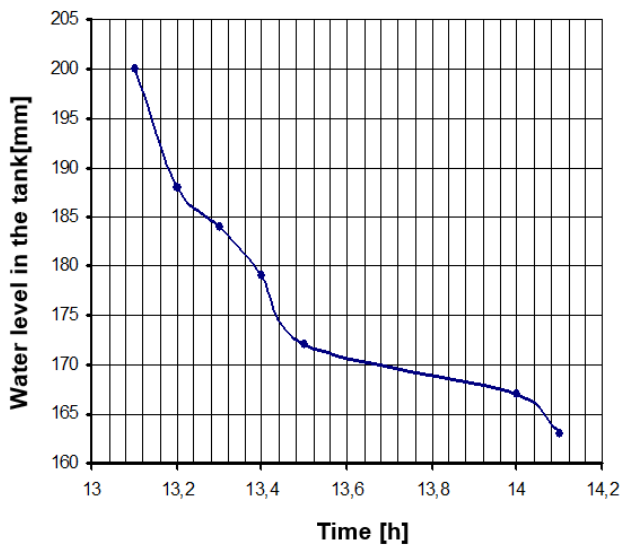


Fig. 4 - Water level variation in the tank depending on time

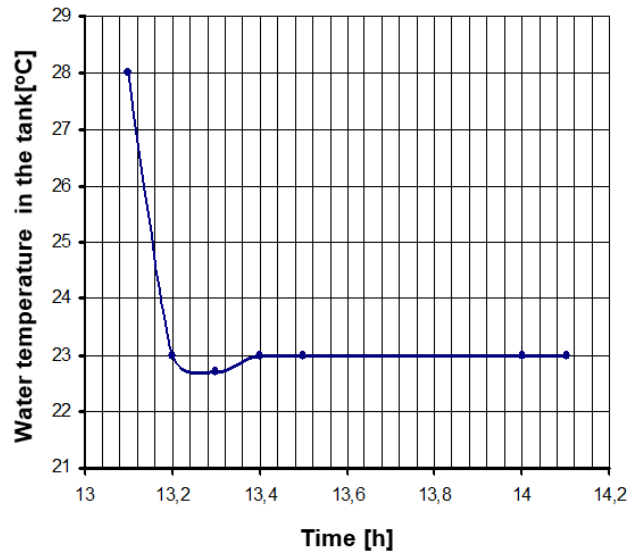


Fig. 5 - Water temperature variation in the tank depending on time

2. C 110P combine cab

In the case of a C 110P combine cab (which, compared to the U-650 tractor cab, also has a roof padding), for outdoor air temperatures of 40-41°C in the shade, but with a relative humidity of 48-52%, temperatures 21-25°C were recorded at the device outlet, while at the level of the operator’s head 33-35°C and a relative humidity of 59-63% were measured (Table 3, figures 6-9).

Initial conditions:

- outdoor air temperature, °C: 40
- outdoor air humidity, %: 48
- temperature in the cab, °C: 47
- tank water temperature, °C: 28
- tank water level, mm: 200

Ceiling temperature, °C: 48
 Water consumption resulting from experiments, l/hour: 2.43

Table 3

Results obtained from determinations on the C 110P cab

Environment		Air conditioning					Tank water temperature (°C)	Time of determination (hour:min)	Voltage at pump terminals (V)	Water level in the tank (mm)
T _{dry} (°C)	U _{rel} (%)	t _{dry.cab} (°C)	t _{dry. air cond.} (°C)	t _{usc.env. – t_{dry. air cond.}} (°C)	V _{air} (m/s)	U _{rel} (%)				
40	48	35	23.2	16.8	16	59	23.0	14:40	18	170
41	48	33	21.2	19.8	16	61	23.0	14:50	18	166
41	48	33	20.8	20.2	16	61	22.8	15:00	18	160
41	48	34	20.7	20.3	16	62	22.6	15:10	16	156
41	48	33	20.7	20.3	16	62	22.6	15:15	24	154
41.5	34	37	24.7	16.8	16	58	23.0	15:20	18	163

Legend:

- T_{dry} = outside temperature; u_{rel} = relative humidity;
- t_{dry.cab} = temperature inside the cab before using air conditioning;
- t_{dry. air cond.} = temperature using air conditioning system

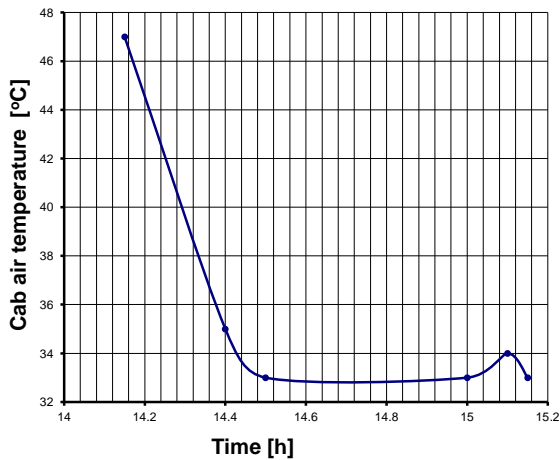


Fig. 6 - Variation of cab air temperature depending on time

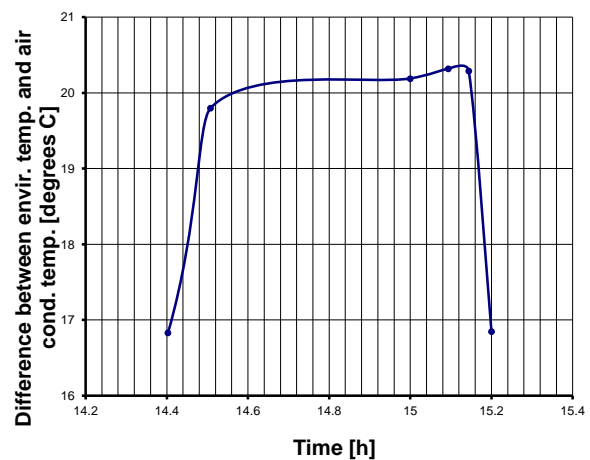


Fig. 7 - Temperature difference generated by the air conditioning system

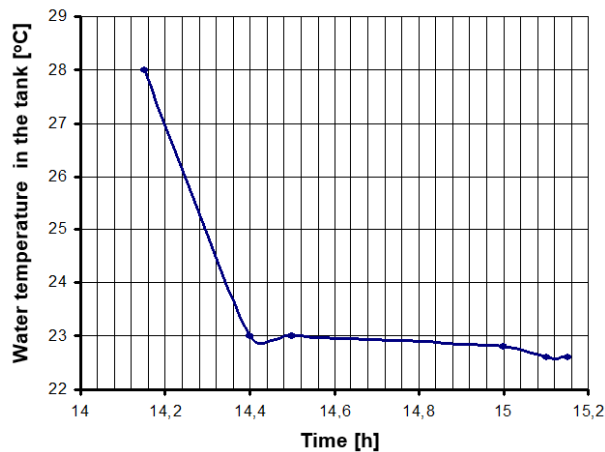


Fig. 8 - Water level variation in the tank depending on time

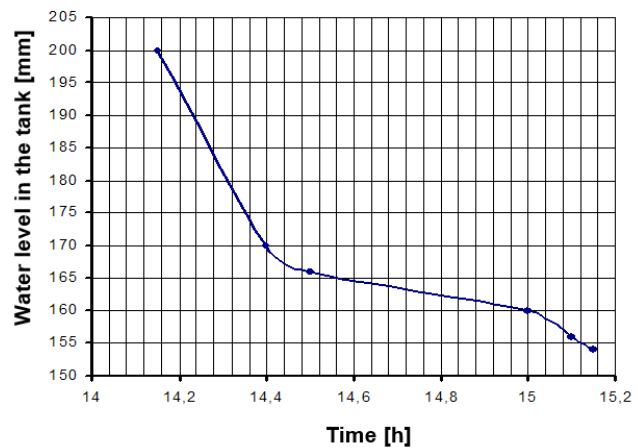


Fig. 9 - Water temperature variation in the tank depending on time

The results obtained demonstrate the efficiency of the created experimental model, but also the need to fit out the cab so as to contribute through the constructive parameters to:

- reducing the level of thermal radiation that enters the cab;
- preventing air currents from entering the interior through areas other than those designed for this purpose (sealing);
- good air circulation at the level of the operator's head, chest and legs, without exceeding the maximum speeds allowed by the domestic and international norms in force.

CONCLUSIONS

As most of the agricultural work is carried out in the warmest period of the year, with temperatures frequently reaching 38°C and even more, it is necessary to equip agricultural machines with air conditioning systems to achieve thermal comfort in the cab.

For this purpose, an air conditioner was designed, made and tested based on the water evaporation process, which has the following advantages over similar freon installations:

- constructive simplicity;
- very low-cost price (1/3 - 1/5 of the price of a refrigeration installation);
- high reliability;
- simple in terms of maintenance and repairs, even performed by non-specialists;
- does not require special marketing licenses as it does not use freons;
- low energy consumption (0.2-0.5 kW);
- quiet during operation;
- non-polluting;
- the large amounts of outside air circulated do not allow the accumulation of particulate matter or pollutants;
- humidification of the air removes the danger of dehydration, which can lead to the appearance of respiratory diseases over time;
- by washing the air (laboratory technique) it removes biological contaminants (pollen, spores, fine dust particles that cannot be retained by ordinary filters, bacteria), gases and smoke (including carbon monoxide in the flue gases), wide variety of chemical vapours (formaldehyde, benzene, toluene, etc.).

Disadvantages include:

- the possibility of achieving lower thermal differences from the external environment than in freon-based installations;
- is dependent on the relative humidity of the ambient air.

In the case of a U-650 tractor cab exposed to solar radiation in conditions of outdoor temperatures of 40°C in the shade, without conditioning or ventilation, 47°C were recorded at the operator's head level (in the cab, the door being open).

The water consumption of the installation was close to the value of 2-3 l/hour, which shows the need to increase the capacity of the water tank for a continuous operation, without refuelling during the working day.

Tank water temperature was 21-23°C, 2-3°C higher than the air conditioning at the outlet of the installation.

The connection between the device and the fan was ensured by means of a flexible aluminium hose with a length of 1.5 m.

Under these conditions, by measuring the temperatures at both ends of the hose, a temperature loss of approximately 3°C was found, having a negative influence on the air parameters in the cab. It is therefore necessary to use a flexible hose made of thermal insulation material (plastic), or the existing one to be thermally insulated.

REFERENCES

- [1] Afzal, A., Saleel, A., Badruddin, I-A., Khan, T.M.Y., Kamangar, S., Mallick, Z., Samuel, O-D., Soudagar, M-E. (2020). Human thermal comfort in passenger vehicles using an organic phase change material–an experimental investigation, neural network modelling, and optimization. *Building and Environment*, Volume 180, 107012, <https://doi.org/10.1016/j.buildenv.2020.107012>;
- [2] Ivanescu, M., Neacsu, C.A., Tabacu, I. (2010). Studies of the thermal comfort inside of the passenger compartment using the numerical simulation. *International Congress Motor Vehicles & Motors*, MVM2010-026;
- [3] ISO 14269-2, 1997, *Tractors and Self-Propelled Machines for Agriculture and Forestry – Operator Enclosure Environment. Part 2: Heating, Ventilation and Air-conditioning Test Method and Performance*
- [4] Kaufman, K.R., Turnquist, P.K., Swanson, R.N., (1979). Thermal comfort in an air-conditioned tractor cab. *Transactions of the American Society of Agricultural Engineers*, Volume 22, Issue 4, 694-698, 701;
- [5] Leighton, D., Ruth, J. (2016). *Increasing EDV Range through Intelligent Cabin Air Handling Strategies*, Annual Progress Report, National Renewable Energy Laboratory USA
- [6] Martinho, N.A.G., Silva, M.C.G., Ramos, J.A.E. (2004). Evaluation of thermal comfort in a vehicle cabin. *Proceedings of the Institution of Mechanical Engineers, Part D: Journal of Automobile Engineering*, Volume 2018, Issue 2, 159-166;
- [7] Oh, J., Choi, J., Son, G., Park Y-J., Kang, Y-S., Kim, Y-J. (2020). Flow analysis inside tractor cabin for determining air conditioner vent location. *Computers and Electronics in Agriculture*. Volume 169, 105199, <https://doi.org/10.1016/j.compag.2019.105199>
- [8] Ruzic, D., Casnji, F. (2012). Thermal Interaction between a Human Body and a Vehicle Cabin. Heat Transfer Phenomena and Applications, Salim N. Kazi, IntechOpen, DOI: 10.5772/51860;
- [9] Ruzic, D. (2018). Airflow and thermal management in farm tractor cab. IOP Conference Series: *Materials Science and Engineering*, Volume 393, 012026, doi:10.1088/1757-899X/393/1/012026;
- [10] Simion, M., Socaciu, L., Ungureanu, P. (2016). Factors which influence the thermal comfort inside of vehicles. *Energy Procedia* 85, 472–480, <https://doi.org/10.1016/j.egypro.2015.12.229>.

THE FUNCTIONAL CONTROLLABILITY OF MILK EJECTION OF THE ADAPTIVE MILKING SYSTEM

ФУНКЦІОНАЛЬНА КЕРОВАНІСТЬ МОЛОКОВІДДАЧЕЮ АДАПТИВНОЇ ДОЇЛЬНОЇ СИСТЕМИ

Dmytriv I.V.¹

¹ Lviv Polytechnic National University, Institute of Engineering Mechanics and Transport, Lviv / Ukraine

E-mail: Dmytriv_V@ukr.net

DOI: <https://doi.org/10.356.33/inmateh-65-42>

Keywords: *adaptive system, milking unit, milk ejection, Pearson distribution, microcontroller*

ABSTRACT

The concept of functional controllability of the milk ejection is considered, which makes it possible to predict the intensity of milk ejection in the online mode of the milking machine. The architecture of the functional controllability by intensity of milk ejection is developed. Input and output parameters of the structural-functional scheme of adaptive control of milk ejection intensity are described. An analytical model of milk ejection intensity based on Pearson's distribution is developed. The milk ejection intensity for different productivity and duration of cows milking is modelled. The microprocessor unit is designed using a single-chip microcontroller. It ensures the algorithm set by the central computer and implements a step of changing the pulsation frequency of 0.1 Hz, the ratio between the cycles of 0.25%, the phase shift step of 0.1 s.

РЕЗЮМЕ

Розглянуто концепцію функціональної керованості молоковіддачею, яка уможливорює прогнозування інтенсивності молоковіддачі в режимі он-лайн роботи доїльного апарата. Наведено архітектуру функціональної керованості інтенсивністю молоковіддачі. Описані вхідні і вихідні параметри структурно-функціональної схеми адаптивного керування інтенсивністю молоковіддачі. Розроблена аналітична модель інтенсивності молоковіддачі на основі розподілу Пірсона. Проведено моделювання інтенсивності молоковіддачі для різної продуктивності і тривалості доїння корови. Наведена функціональна реалізація адаптивної доїльної системи та її загальний вигляд. Мікропроцесорний блок з використанням однокристалного мікроконтролера забезпечує алгоритм роботи, який задається центральним комп'ютером та реалізовує крок зміни частоти пульсації 0.1 Гц, співвідношення між тактами 0.25 %, крок зсуву фаз 0.1 с.

INTRODUCTION

The adaptive system of cow machine milking implements the "machine-animal" biotechnical system, provides realization of functional controllability of milk ejection intensity of animal. The effectiveness of functional controllability of milk production depends on the parameters that ensure the quality and efficiency of technological functions.

The adaptive milking machine must ensure the adaptation of the parameters of the technical system to the physiology of milk ejection of the cow. The implementation of such a system is possible through self-regulation of technological characteristics of machine milking, which allows predicting the intensity of milk ejection of cows (Dmytriv V.T. et al, 2020). However, predicting the intensity of milk ejection during milking is an unrealized task. Accordingly, the prediction of technological parameters for the next cycle of the technical milking system without the parameter of milk ejection of the system is incorrect.

The relevance of predicting the intensity of milk ejection in the online mode of the milking machine is confirmed by a significant number of studies, which can be roughly attributed to the partial solution of the problem. Thus, individual variations of daily milking and duration of single milking depending on the duration of the milking interval are quantified, models of random factors are used to describe the impact of individual milking interval on daily milk yield and duration of single milking (Andre G. et al, 2010). It is established that the value of vacuum should be variable in the process of milk ejection.

¹ Dmytriv I.V., Assoc. prof., Ph.D.Eng.

Adjusting the vacuum during milking the cow increases the intensity of milk production and reduces the duration of a single milking (*Reinemann D. J. et al, 2021*).

A number of researchers believe that the basis is the cow's lactation curve, which characterizes the productivity of the animal and the influence of key factors on the milk production process. They investigate lactation curves, which represent the theoretical dynamics of milk yield using an iterative procedure that corresponds to Wood's model based on daily milk data, and the influence of various factors on its characteristics (*Adriaens I. et al, 2020; Ben Abdelkrim A. et al, 2021*). Such modelling of the cow's lactation curve has a limitation, which is that to comply with the typical lactation curve the short-term disturbances are ignored, i.e. the significant deviations of the quantitative parameters of milk from the lactation curve are not taken into account (*Adriaens I. et al, 2018*). But the characteristics of the disturbances are important for the analysis of milk productivity of cows and, accordingly, decisions on the functional controllability of the process (*Elgersma G.G. et al, 2018*). Taking into consideration the disturbances (the amount of milk is outside the lactation curve) that occur during lactation, models of lactation with perturbation are developed that capture contrasting characteristics, from a sharp and short decline in milk yield to a long and slow decline in milk yield (*Sadoul B. et al, 2015; Nguyen Ba H. et al, 2020; Revilla M. et al, 2019*).

A detailed analysis of the impact of technical and technological parameters on the functional controllability of milk ejection is given in the review article: setting up of milking machines, the condition of teats and the efficiency of cows milking (*Odorčić M. et al, 2019*).

One of the parameters of the functional controllability of milk production is the fluctuations of the vacuum in the suction phase (sucking stroke). It is revealed that the amplitude of fluctuations is higher with increasing of the milk ejection; this characteristic is important for the adaptation of the system in the suction phase (*Ströbel U. et al, 2016*). It is important to determine the characteristics of the interaction amongst the compression of the teat cup liner, the milking vacuum and the duration of the pulsation b-phase. It is revealed that the increase in excessive pressure increases the hyperkeratosis, especially in highly productive cows, which are milked three or more times a day. Increasing the vacuum causes more teats congestion than increasing the b-phase in the most common range. And changes in average milk ejection are much smaller than changes in peak milk ejection, so an increase in peak milk ejection did not reflect a corresponding reduction in milking time (*Reinemann D.J. et al, 2010; Bade R. D. et al, 2009*). The combination of high levels of vacuum and the open phase of teat cup liner increases the potential for congestion at the tips of the teats (*Perry J.F. et al., 2017*). Conversely, a lower vacuum reduces the intensity of milk ejection and increases the duration of a single machine milking, but there is less effect on the teat tissue (*Besier J. and Bruckmaier R.M, 2016*). The determining factor in the intensity of milk ejection is the vacuum in the sucking phase and its different levels during machine milking (*Besier J. and Bruckmaier R.M., 2016*). The vacuum at the end of the sucking phase affects the teat tissue at the beginning and end of milking. Therefore, the availability of the mathematical model of vacuum change makes it possible to conduct simulation tests of the controllability of the machine milking process (*Golisz E. et al, 2021*).

Among these studies, investigations of vacuum changes in the milking system have a special place (*Achkevych O. et al, 2020; Medvedskiy O., 2018*), and this is the main technical parameter of the milking machine. The vacuum loss and fluctuations in the milking machine reduce the efficiency of milking and are factors that affect the health of the udder of cows. They cause reverse flows of milk-air mixture, which can reach significant velocities in the certain designs of the milking machine (*Dmytriv V., 2020*).

The pulsator is a component of the adaptive milking machine system. The pulsation system of the milking machine affects the intensity of milk production, the duration of milking, the condition of the teats and the milk amount. Therefore, the study of the influence of the pulsation coefficient on daily milk yield, milk production intensity and duration of milking are directly related to the functional controllability of milk ejection (*Dmytriv V.T. et al, 2019*). The milking process in the milking parlor with the MultiLactor milking system has been studied, the peculiarity is that each quarter of the udder is milked separately. It is established that the pulsation coefficient of the milking process is a parameter of adaptation and allows functional controllability of milk ejection (*Kaskous S., 2018*).

Both the irregular pulses of vacuum during milking in combination with the frequency of pulsations and high value of vacuum at the end of the teat increase the likelihood of infection of the teats and reduce the flow rate of milk (*Besier J. et al, 2016*). A higher vacuum at the end of the teat reduces the peak intensity of milk production; on teats the milking cups are moved more intensively that can lead to injuries of tips of teats, cause an infection of an udder, and also lead to accumulation of liquid and obstruction of channels on tips of teats (*Perry J.F. et al, 2017; Wieland M. et al, 2017*).

A number of researchers analyzed the factors that have influence on the vacuum in the milking machine, they also simulated the processes under the condition of changing the vacuum pulsations and changes in the intensity of milk production (Enokidani M. et al, 2016; Enokidani M. et al, 2016). Other scientists have studied the effect of vacuum on the efficiency of machine milking and the condition of teats depending on milk ejection (Besier J., Bruckmaier R.M., 2016; Stauffer C., et al, 2020; Parilová M. et al, 2010).

The analysis of researches shows that functional controllability of milk ejection is realized by parameters of vacuum, pulsation frequency and off-duty factor of impulses as a function of intensity of the milk ejection of a cow. These parameters must be set by the system in advance of the next pulse cycle. Therefore, the prediction of the next interval of milk intensity is possible at the presence of a model of the curve of milk intensity ejection for a concrete cow. Analysis of research has shown the absence of such models.

The purpose of this study is to develop models of the intensity of milk ejection of cows and a system of functional controllability of milk ejection, which will enable the implementation of an adaptive milking system and is relevant for improving the efficiency of milking systems.

MATERIALS AND METHODS

The concept of functional controllability of milk ejection

To date, the intensity of milk ejection has been characterized as a parameter of the biological state of the animal and the functional influence of the parameters (vacuum gage pressure, pulsation frequency, ratio of cycles) of the technical system. The influence of these factors on the biological intensity of milk ejection (velocity and amount of milk) was evaluated as a probabilistic process.

To implement the adaptation of the machine milking system it is necessary to consider the functional controllability of the intensity of milk ejection by the technical system. At the reflex level, technical parameters act as stimuli that affect sensation and physical action, as well as technological parameters of the process (fig. 1).

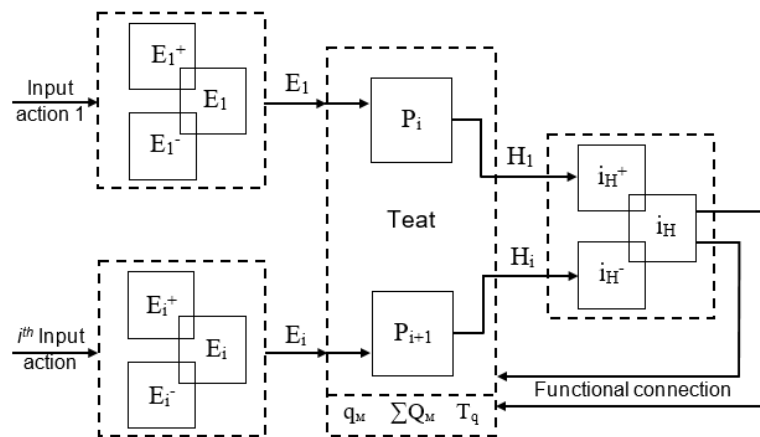


Fig. 1 - Architecture of the functional controllability of milk ejection intensity

$E_1^+, E_1^-, E_1^+, E_1^-$ – limits of input parameters of the technical system; E_1, E_i – optimal values of input parameters of the technical system; P_i, P_{i+1} – receptors that are affected by input parameters; H_1, H_i – quantitative parameter of feedback self-descriptiveness; i_H^+, i_H^- – limits of the effective self-descriptiveness; i_H – information of functional connection on technological parameters of milk ejection

Mathematically, the characteristic of the functional controllability of the intensity of milk ejection is formed as the dependence of the intensity of milk ejection on the technological and technical parameters of the system:

$$q_m = f(P, \tau, \tau(t), K_{\tau_i}) \tag{1}$$

where P – the vacuum gage pressure; τ – the pulsation frequency;

$\tau(t)$ – the off-duty factor of impulses (ratio of cycles);

K_{τ_i} – the coefficient of the constant of time of vacuum gage pressure increase and decrease in the inter wall space of the milking or teat cup.

The coefficient $K_{\tau_{cc}}$ of the constant of time of vacuum increase (transition from the compression stroke to the suction stroke):

$$K_{\tau_{cc}} = f(P, \tau, \tau(t), F_H) \tag{2}$$

and the coefficient $K_{\tau_{ct}}$ of the constant of time of atmospheric pressure increase (transition from the suction stroke to the compression stroke):

$$K_{\tau_{CT}} = f(P, \tau, \tau(t), F_H) \tag{3}$$

where F_H – the force of mounting tension of the teat cup liner in the teat cup shell.

Acceleration of closing and opening of the teat cup liner:

$$a_{\omega} = f(P(t), F_H) \tag{4}$$

where $P(t)$ – function of the pressure change over time (for 1 cycle of the pulsator work).

According to the above factors of the architecture of functional control, the structure of the technological system will be developed, which will allow intensity control, as a functional adaptation to the physiology of the process of milk ejection (Fig. 2). Functional controllability of milk ejection by the technical system is realized by three groups of parameters: input (technological) parameters, are realized by the technical system and control the work of the pulsator and the control chamber of the milking or teat cup; output (information) parameters of functioning of the "teat – milking teat cup" system; information parameters, which are implemented by algorithmic-hardware methods through the microcontroller and displayed on the information board of the milking machine operator, on the central computer of the dispatcher and in the database.

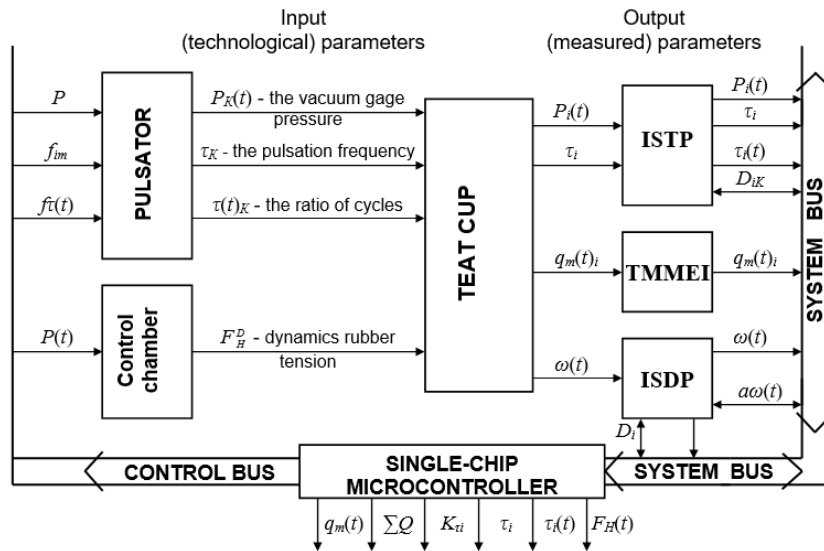


Fig. 2 - Structural and functional scheme of adaptive control of milk ejection intensity

ISTP – information system for technological parameters determining; ISDP – information system for dynamic parameters determining; TMMEI – thermoanemometric measurer of milk ejection intensity; τ_i – pulsation frequency in the i -th moment of time; $P_i(t)$ – pressure in the i -th moment of time; D_{iK} – address data, form the number of the cow; $q_m(t)_i$ – milk ejection intensity in the i -th moment of time; $\omega(t)$ – speed of closing and opening of teat cup liner; $a_{\omega}(t)$ – acceleration of closing and opening of teat cup liner.

The model of milk ejection, as an element of functional controllability of milk election intensity, is described mathematically and it is possible to predict it on the basis of a perspective assessment of this parameter at the $i + 1$ time of milking.

Mathematical model of milk ejection intensity

The intensity of the milk ejection is denoted as q by the variable of y ; the duration of milk ejection will be denoted as T , which corresponds to the duration of milking. Accept $x \rightarrow t$ condition as current value of time. Let the milk ejection curve have the form shown in Fig. 3.

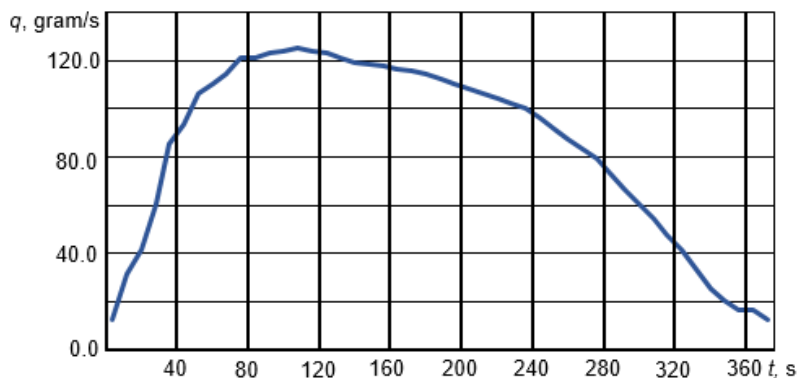


Fig. 3 – The curve of milk ejection

Considering the fact that x is a time parameter and Δx is a quantization period corresponding to the condition of $\Delta x = \text{const}$, the interval of integration of milk ejection intensity will be as follows:

$$t = k_i \cdot \Delta x \tag{5}$$

where k_i – the number of measurements for time t , which can be defined as $k_i = t/\Delta x$.

Then

$$n_i = y_i = \int_{x_i - \frac{t}{2}}^{x_i + \frac{t}{2}} y(x) \cdot dx = y(x_i, b_0, b_1, b_2) \tag{6}$$

To describe the milk ejection curve, Pearson distribution is used (Korn G. et al, 1977), which is subject to the differential equation:

$$\frac{dy}{y} = \frac{x - a}{b_0 \cdot x^2 + b_1 \cdot x + b_2} \cdot dx \tag{7}$$

The coefficients of b_0, b_1, b_2 are determined and the equation (7) is rewritten as follows:

$$x^n \cdot (b_0 \cdot x^2 + b_1 \cdot x + b_2) \cdot dy = -y \cdot x^n \cdot (x - a) \cdot dx. \tag{8}$$

After integrating the left side of (8) equation, the following is obtained:

$$\begin{aligned} [x^n \cdot (b_0 \cdot x^2 + b_1 \cdot x + b_2) \cdot y]_{-\infty}^{\infty} - \int_{-\infty}^{\infty} ((n+2) \cdot b_0 \cdot x^{n+1} + (n+1) \cdot b_1 \cdot x^n + \\ + n \cdot b_2 \cdot x^{n-1}) \cdot y \cdot dx = - \int_{-\infty}^{\infty} x^{n+1} \cdot y \cdot dx + a \int_{-\infty}^{\infty} x^n \cdot y \cdot dx \end{aligned} \tag{9}$$

Let the expression in square brackets of equation (9) be zero at the ends of the distribution curve, which characterizes the milk ejection curve, which corresponds to reality.

$$\lim_{y \rightarrow \pm\infty} x^{n+2} \cdot y \rightarrow 0 \tag{10}$$

The milk ejection curve is probabilistic, respectively, the moment of distribution relative to zero of the parameter of milk ejection intensity is written as follows:

$$\mu_j = \int_0^{\infty} x^j \cdot y(x) \cdot dx \tag{11}$$

where $j = 0, 1, 2, \dots, n$.

The moment of μ_j distribution relative to zero is a numerical characteristic of a random variable $y(x)$.

Taking into account the dependence (11) and condition (10) the equation (9) will take the form:

$$(1 - n + 2 \cdot b_0) \cdot \mu_{n+1} - ((n+1) \cdot b_1 + a) \cdot \mu_n - n \cdot b_2 \cdot \mu_{n-1} = 0 \tag{12}$$

Expression (11) is analyzed for a random distribution that characterizes the cow's milk ejection graph as the probability distribution of a random variable. For $j = 0$ from dependence (11) results:

$$\mu_0 = \int_0^{\infty} y(x) \cdot dx = \sum_{i=0}^n y_i(x) / \sum_{i=0}^n y_i(x) = 1 \tag{13}$$

Mathematical expectation is the average value that characterizes the center of distribution:

$$\mu_1 = \int_0^{\infty} x \cdot y(x) \cdot dx = \frac{\sum_{i=0}^n x_i \cdot y_i(x_i)}{\sum_{i=0}^n y_i(x_i)} \tag{14}$$

Then the j -th moment relative to the point a , where the point a is the value of x_i , which corresponds to y_{imax} is defined as:

$$\mu_{aj} = \int_0^{\infty} (x - a)^j \cdot y(x) \cdot dx = \frac{\sum_{i=0}^n ((x_i - a)^j \cdot y_i(x_i))}{\sum_{i=0}^n y_i(x_i)} \tag{15}$$

The central moment of the j order of the $y(x)$ distribution is the following equality:

$$\mu_j = \frac{1}{\sum_{i=0}^n y_i(x_i)} \cdot \sum_{i=0}^n y_i(x_i) \cdot (x_i - \bar{x})^j \quad (16)$$

There is a relationship between the central and initial moments; taking into account the equations of (13), (14), (15) and (16), it can be written:

$$\mu_j = \sum_{j=0}^n (-1)^j \cdot C_n^j \cdot \mu_{aj} \cdot (\bar{x} - a)^j \quad (17)$$

Taking of $j = 0, 1, 2, 3, 4$ from (17) dependence, the following equations are obtained:

$$\begin{aligned} \mu_0 &= 1; \mu_1 = 0; \mu_2 = \mu_{a2} - (\bar{x} - a)^2 \\ \mu_3 &= \mu_{a3} - 3 \cdot \mu_{a2} \cdot (\bar{x} - a) + 2 \cdot (\bar{x} - a)^3 \\ \mu_4 &= \mu_{a4} - 4 \cdot \mu_{a3} \cdot (\bar{x} - a) + 6 \cdot \mu_{a2} \cdot (\bar{x} - a)^2 - 3 \cdot (\bar{x} - a)^4 \end{aligned} \quad (18)$$

The (7) parabola equation coefficients are determined from the (12) dependence by substituting of $n = 0, 1, 2, 3$ and taking into account that $\mu_0 = 1, \mu_1 = 0$ a system of equations is obtained:

$$\left. \begin{aligned} n = 0: & \quad b_1 + a = 0; \\ n = 1: & \quad 3 \cdot b_0 \cdot \mu_2 + b_2 - \mu_2 = 0; \\ n = 2: & \quad 4 \cdot b_0 \cdot \mu_3 + 3 \cdot b_1 \cdot \mu_2 + a \cdot \mu_2 - \mu_3 = 0; \\ n = 3: & \quad 5 \cdot b_0 \cdot \mu_4 + 4 \cdot b_1 \cdot \mu_3 + 3 \cdot b_2 \cdot \mu_2 + a \cdot \mu_3 - \mu_4 = 0 \end{aligned} \right\} \quad (19)$$

From the system of equations (19), the coefficients of b_0, b_1, b_2 are calculated:

$$\begin{aligned} b_0 &= \frac{2 \cdot \mu_4 \cdot \mu_2 - 3 \cdot \mu_3^2 - 6 \cdot \mu_2^3}{2 \cdot (5 \cdot \mu_4 \cdot \mu_2 - 6 \cdot \mu_3^2 - 9 \cdot \mu_2^3)} \\ b_1 &= \frac{\mu_3 \cdot \mu_4 + 3 \cdot \mu_3 \cdot \mu_2^2}{2 \cdot (5 \cdot \mu_4 \cdot \mu_2 - 6 \cdot \mu_3^2 - 9 \cdot \mu_2^3)} \\ b_2 &= \frac{4 \cdot \mu_4 \cdot \mu_2^2 - 3 \cdot \mu_2 \cdot \mu_3^2}{2 \cdot (5 \cdot \mu_4 \cdot \mu_2 - 6 \cdot \mu_3^2 - 9 \cdot \mu_2^3)} \end{aligned} \quad (20)$$

After determining the coefficients of (7) equation, the differential equation is integrated:

$$\int \frac{dy}{y} = - \int \frac{x - a}{b_0 \cdot x^2 + b_1 \cdot x + b_2} \cdot dx \quad (21)$$

To do this, the (21) equation is decomposed in the denominator of the differential into a multiplier as follows:

$$b_0 \cdot x^2 + b_1 \cdot x + b_2 = b_0 \cdot \left(x^2 + \frac{b_1}{b_0} \cdot x + \frac{b_2}{b_0} \right) = b_0 \cdot (x + k_1) \cdot (x - k_2) \quad (22)$$

where k_1, k_2 – the roots of the equation and

$$k_{1,2} = \frac{-\frac{b_1}{b_0} \pm \sqrt{\left(\frac{b_1}{b_0}\right)^2 - 4 \cdot \frac{b_2}{b_0}}}{2}$$

Assume that the roots of k_1, k_2 are natural numbers, and one of them can have a negative value. Then, the subintegral expression of (21) dependence is written in the following form:

$$-\frac{x - a}{b_0 \cdot x^2 + b_1 \cdot x + b_2} = \frac{1}{b_0} \cdot \left(\frac{A_1}{x + k_1} + \frac{A_2}{x - k_2} \right) \quad (23)$$

where $A_1 = -\frac{a + k_1}{k_1 + k_2}; A_2 = \frac{a - k_2}{k_1 + k_2}$.

After entering the notation of $q_1 = A_1/b_0$; $q_2 = A_2/b_0$ the (21) dependence will take the following form:

$$\int \frac{dy}{y} = \int \frac{q_1}{x+k_1} \cdot dx + \int \frac{q_2}{x-k_2} \cdot dx, \quad \ln y = q_1 \cdot \ln(x+k_1) + q_2 \cdot \ln(x-k_2) + C. \quad (24)$$

Let $x = 0$; $y = y_0$, then the constant integration will be equal:

$$C = \ln \frac{y_0}{k_1^{q_1} \cdot (-k_2)^{q_2}} \quad (25)$$

Then, after minor transformations, the equation of the parabola is obtained:

$$y = y_0 \cdot \left(1 + \frac{x}{k_1}\right)^{q_1} \cdot \left(1 - \frac{x}{k_2}\right)^{q_2} \quad (26)$$

In (26) equation the y_0 is unknown. We will integrate by x :

$$\int_{-k_1}^{k_2} y \cdot dx = \sum_{i=0}^A y_i, \quad \text{accordingly } \int_{-k_1}^{k_2} y_0 \cdot \left(1 + \frac{x}{k_1}\right)^{q_1} \cdot \left(1 - \frac{x}{k_2}\right)^{q_2} \cdot dx = \sum y_i \quad (27)$$

The values in the equation are substituted:

$$z = \frac{k_1 + x}{k_1 + k_2} \Rightarrow x = z \cdot (k_1 + k_2) - k_1, \quad dz = \frac{dx}{k_1 + k_2} \Rightarrow dx = dz \cdot (k_1 + k_2)$$

Under $x = -k_1 \Rightarrow z = 0$; $x = k_2 \Rightarrow z = 1$

Then, the integral of (27) will take the form:

$$\frac{y_0 \cdot (k_1 + k_2)^{q_1 + q_2 + 1}}{k_1^{q_1} \cdot k_2^{q_2}} \cdot \int_0^1 z^{q_1} \cdot (1 - z)^{q_2} \cdot dz \quad (28)$$

The subintegral expression of the (28) dependence is an Euler integral that has such a solution:

$$\int_0^1 z^{q_1} \cdot (1 - z)^{q_2} \cdot dz = B \cdot (q_1 + 1, q_2 + 1) \quad (29)$$

where $B \cdot (q_1 + 1, q_2 + 1)$ – beta function:

$$B \cdot (q_1 + 1, q_2 + 1) = \frac{\Gamma \cdot (q_1 + 1) \cdot \Gamma \cdot (q_2 + 1)}{\Gamma \cdot (q_1 + q_2 + 2)} \quad (30)$$

where Γ – gamma function.

Gamma functions are determined by the classical method (Korn G. et al.1977). Taking into consideration the dependences of (27), (28), (29) and (30), the dependence to determine the value of y_0 is obtained:

$$y_0 = \frac{\sum y_i \cdot k_1^{q_1} \cdot k_2^{q_2}}{(k_1 + k_2)^{q_1 + q_2 + 1}} \cdot \frac{\Gamma \cdot (q_1 + q_2 + 2)}{\Gamma \cdot (q_1 + 1) \cdot \Gamma \cdot (q_2 + 1)} \quad (31)$$

With the dependence of (31), the (26) expression will look like:

$$y = \frac{\sum y_i \cdot k_1^{q_1} \cdot k_2^{q_2}}{(k_1 + k_2)^{q_1 + q_2 + 1}} \cdot \left(1 + \frac{x}{k_1}\right)^{q_1} \cdot \left(1 - \frac{x}{k_2}\right)^{q_2} \cdot \frac{\Gamma \cdot (q_1 + q_2 + 2)}{\Gamma \cdot (q_1 + 1) \cdot \Gamma \cdot (q_2 + 1)} \quad (32)$$

The equation (32) characterizes the milk ejection curve of a cow at the process of milking.

RESULTS

Realization of the milk ejection intensity model

To realize the model of milk ejection intensity in the form of the (32) function, an arbitrary graphical dependence is considered in (Fig. 3). This graphical dependence of milk ejection can be interpreted as follows. The milk ejection interval is divided evenly by 5 s, the total duration of milk ejection at cow milking is 378 s, or 6.3 min. Accordingly, x_i is the middle of the x time interval. Then the intensity of milk ejection in the x time interval will correspond to x_i and will be $y(q)_i$, gram/s, respectively. In fact, $y(q)_i$ characterizes the weight quantitative coefficient of the x_i argument. Then the \bar{x} average value is calculated by dependence:

$$\bar{x} = \frac{1}{\sum y(q)_i} \cdot \sum (y(q)_i \cdot (x_i - a)) + a \tag{33}$$

where a – arbitrary value of x .

Under the condition of $a = 67.5$ at $x = 5$ s is obtained $\bar{x} = 74.746$. Accordingly, the moments with respect to zero will be as follows: $\mu_0 = 1$; $\mu_1 = 0$; $\mu_2 = 3949.956$; $\mu_3 = 192861.042$; $\mu_4 = 28023477.44$.

Due to the known values of the central moments of the $\mu_0, \mu_1, \mu_2, \mu_3, \mu_4$, orders, the coefficients of the parabola equation are calculated by the dependences of (20).

The coefficients of the equation are $b_0 = 0.46384$; $b_1 = -31.81023$; $b_2 = -1644.10432$.

The (34) equation of the parabola is solved, assuming that $y = 0$:

$$y = 0.46384 \cdot x^2 - 31.81023 \cdot x - 1644.10432 \tag{34}$$

The roots of the (34) quadratic equation are as follows: $K_1 = 102.995$; $K_2 = -34.415$. According to the calculation results, the following values were obtained: $q_1 = -5.36$; $q_2 = 3.204$; Gamma functions: $\Gamma(q_1+q_2+1) = -7.16827$; $\Gamma(q_1+1) = -0.08295$; $\Gamma(q_2+1) = 7.7975$. Then the (32) equation will look like:

$$y(q) = 0.08356 \cdot \sum y_i \cdot \frac{(34.415+t)^{3.204}}{(102.995+t)^{5.36}} \tag{35}$$

where $\sum y_i$ – the maximum amount of milk moved out by the milking machine for the duration of milking, gram;

t – running time of the milking, s;

$y(q)$ – milk ejection intensity, gram/s.

For the total amount of milk for one milking of a cow $\sum y_i = 4000$ grams and duration of one-time milking by the milking machine $\sum t_i = 300$ s, according to (35) dependence the graph of milk ejection corresponds to fig. 4,a.

For the total amount of milk for one milking of $\sum y_i = 16000$ gram and milking time of $\sum t_i = 780$ [s] the parabolic equation is derived (36) and milk production graph is constructed (fig. 4,b)

$$y(q) = 2.63 \cdot 10^4 \cdot \sum y_i \cdot \frac{(26.708+t)^{0.703}}{(361.555+t)^{3.201}} \tag{36}$$

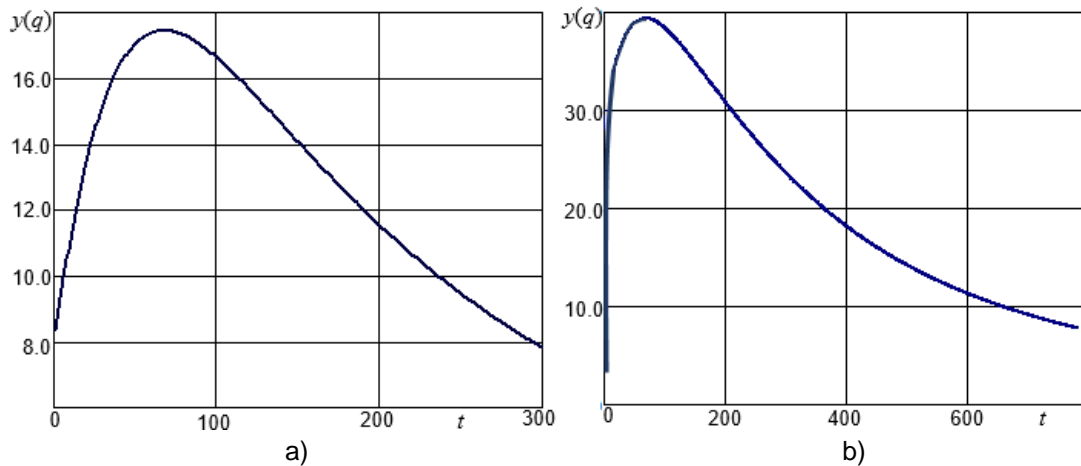


Fig. 4 – Graphical realization of milk ejection intensity described by equations: a – (35); b – (36)
 $y(q)$ – intensity of milk ejection, gram/s; t – time of milking, s

The realization of functional controllability of the adaptive milking system

Functional controllability of milk ejection is realized on the basis of adaptive milking system. The intensity of milk ejection was measured with a thermoanemometric meter and compared with the calculated one. The adequacy of the parameters of the milking process was evaluated. Vacuum in the inter wall chamber of teat cup and in the under teat space (milking chamber of teat cup), the pulsations frequency and the off-duty factor of impulses were set on the basis of forecasting the intensity of milk ejection per stroke of the milking machine. These parameters create the mode of operation which is adequate to the intensity of milk ejection.

The functional scheme of the adaptive milking system is shown in Fig. 5 (Dmytriv V.T. et al, 2020). A general view of the hardware implementation for the study of functional controllability of the milk ejection intensity of the technical system is shown in Fig. 6.

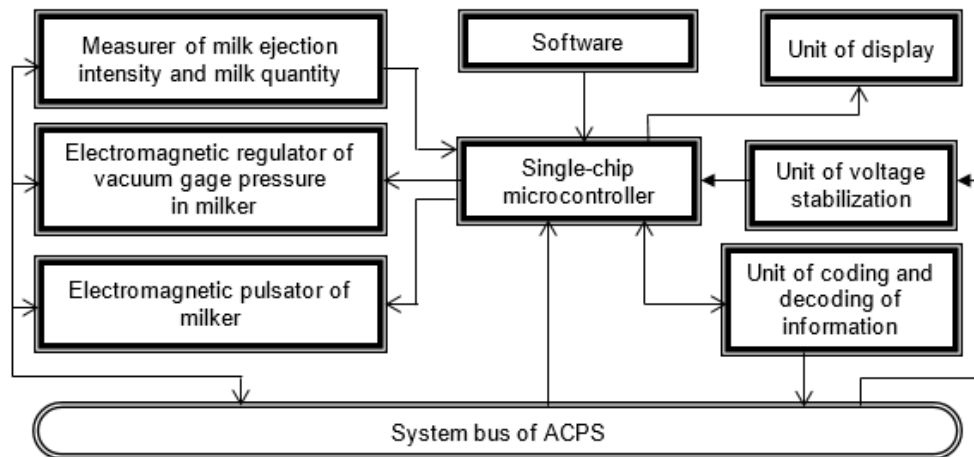


Fig. 5 – Functional implementation of adaptive milking system

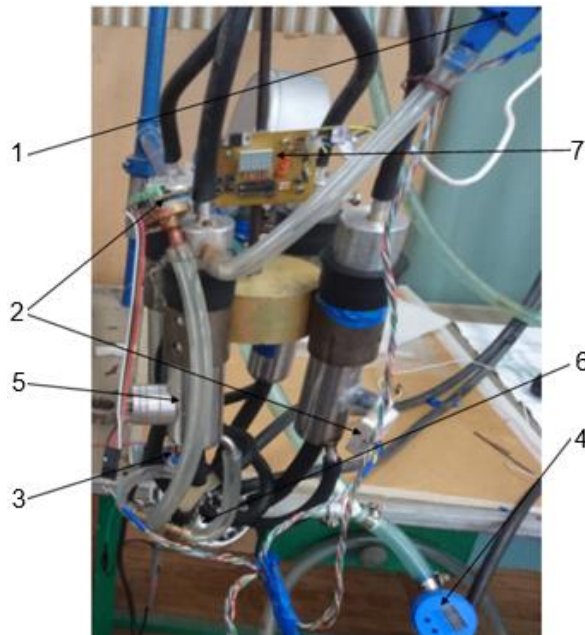


Fig. 6 – General view of an adaptive milking system for the study of the controllability by milk ejection

1 – pressure sensor in the artificial udder; 2 – pressure sensor in the inter wall chamber of the milking (teat) cup; 3 – pressure sensor in the milking chamber of the teat cup; 4 – pressure sensor in the milk hose; 5 – adaptive teat cup; 6 – claw of the milker; 7 – microprocessor control unit

The microprocessor unit is designed using the Atmel single-chip microcontroller. It ensures the algorithm set by the central computer and implements a step of changing the pulsation frequency of 0.1 Hz, the ratio between the cycles of 0.25%, the phase shift step of 0.1 s.

A digital control system was used to implement the selection of optimal modes. The functional scheme of the adaptive control unit with a search engine for self-tuning is implemented on base of the three single-chip microcontrollers (OMK). The distribution of functions is as follows: the first OMK - the functions of the mathematical model, the identification of the object of control, evaluation of the quality of control and the formation of control tasks; the second OMK - direct control of the process of machine milking, distribution of functions among other OMK; the third OMK - removal of the information on parameters of control object, optimization of parameters of adjustment of the executive elements, adjustment of parameters, data transfer, indication of the operational parameters.

CONCLUSIONS

The considered aspects of functional controllability of milk ejection of the adaptive milking system allow to state that the new generation of milking systems will be based on the new organizational and technological decisions with use of the cybernetic principles of organization of hardware-programmed functional autonomous technological elements.

Adaptation of the milking system is carried out in an automated mode, based on the parameters of the milk ejection. For each cow, an individual algorithm for the intensity of milk ejection is selected. The flexible relationship between the intensity of milk ejection of the cow and the design and technological parameters of the milking system is provided that allows an individual approach to the function of milk ejection for each cow separately.

The use of digital control systems based on single-chip microcontrollers provides the implementation of digital controllers, which significantly simplifies the hardware. The process of determining the optimal parameters for adjusting the controllers is carried out by mathematical dependence, which reduces the over-regulation of the parameters of the controllers.

REFERENCES

- [1] Achkevych O., Achkevych V., Bratishko V. and Potapova S., (2020), Justification of rational design parameters of milking machine for installations with milk line system, *20th International Scientific Conference: Engineering for Rural Development*, Jelgava / Latvia, vol. 20, pp. 1313–1318. DOI: 10.22616/ERDev.2020.19.TF329 ;
- [2] Adriaens I., Huybrechts T., Aernouts B. et al., (2018), Method for short-term prediction of milk yield at the quarter level to improve udder health monitoring, *Journal of Dairy Science*, vol. 101(11), pp. 10327–10336 ;
- [3] Adriaens I., van den Brulle I., D'Anvers L. et al., (2020), Milk losses and dynamics during perturbations in dairy cows differ with parity and lactation stage, *The preprint server for biology*: bioRxiv 2020.07.01.182568. <https://www.biorxiv.org/content/biorxiv/early/2020/07/02/2020.07.01.182568.full.pdf> ;
- [4] Andre G., Berentsen P. B. M., Engel B. et al., (2010), Increasing the revenues from automatic milking by using individual variation in milking characteristics, *Journal of Dairy Science*, vol. 93(3), pp. 942-953. <https://doi.org/10.3168/jds.2009-2373> ;
- [5] Bade R. D., Reinemann D. J., Zucali M. et al., (2009), Interactions of vacuum, b-phase duration, and liner compression on milk flow rates in dairy cows, *Journal of Dairy Science*, vol. 92(3), pp. 913-921. DOI:10.3168/jds.2008-1180 ;
- [6] Ben Abdelkrim A., Puillet L., Gomes P. et al., (2021), Lactation curve model with explicit representation of perturbations as a phenotyping tool for dairy livestock precision farming, *Animal: The international journal of animal biosciences*, vol. 15(1), p. 100074. DOI: 10.1016/j.animal.2020.100074;
- [7] Besier J. and Bruckmaier R.M., (2016), Vacuum levels and milk-flow-dependent vacuum drops affect machine milking performance and teat condition in dairy cows, *Journal of Dairy Science*, vol. 99(4), pp. 3096–3102. DOI: <http://dx.doi.org/10.3168/jds.2015-10340> ;
- [8] Besier J., Lind O., Bruckmaier R.M., (2016), Dynamics of teat-end vacuum during machine milking: types, causes and impacts on teat condition and udder health - a literature review, *Journal of Applied Animal Research*, vol. 44(1), pp. 263–272. DOI: <https://doi.org/10.1080/09712119.2015.1031780> ;
- [9] Dmytriv V.T., Dmytriv I.V., Horodetskyi I.M. et al., (2020), Adaptive cyber-physical system of the milk production process, *INMATEH - Agricultural Engineering*, Vol. 61, No. 2, pp. 199 - 208, Bucharest / Romania. DOI: 10.35633/inmateh-61-22 ;
- [10] Dmytriv V., (2020), Model of forced turbulence for pulsing flow, *Diagnostyka*, vol. 21(1), pp. 89–96. DOI: <https://doi.org/10.29354/diag/118651> ;
- [11] Dmytriv V.T., Dmytriv I.V., Yatsunskyi P.P., (2019), Experimental pulse generator combined with the milking machine collector, *INMATEH - Agricultural Engineering*, vol. 59(3), pp. 219-226. DOI: 10.35633/INMATEH-59-24 ;
- [12] Dmytriv V., Dmytriv I., Dmytriv T., (2018), Research in thermoanemometric measuring device of pulse flow of two-phase medium, *17th International Scientific Conference: Engineering for Rural Development*, Jelgava / Latvia, vol. 17, pp. 894-904. DOI: 10.22616/ERDev2018.17.N200
- [13] Elgersma G.G., de Jong G., van der Linde R., Mulder H.A., (2018), Fluctuations in milk yield are heritable and can be used as a resilience indicator to breed healthy cows, *Journal of Dairy Science*, vol. 101(2), pp. 1240–1250;

- [14] Enokidani M., Kawai K., Shinozuka Y. and Watanabe A., (2016), Milking performance evaluation and factors affecting milking claw vacuum levels with flow simulator. *Anim. Sci. J.*, vol. 88(8), pp. 1134–1140. DOI: <https://doi.org/10.1111/asj.12741> ;
- [15] Enokidani M., Kuruhara K., Kawai K., (2016), Analysis of factors affecting milking claw vacuum levels using a simulated milking device. *Anim. Sci. J.*, vol. 87(6), pp. 848–854. DOI: <https://doi.org/10.1111/asj.12489> ;
- [16] Golisz E., Kupczyk A., Majkowska M. et al., (2021), Simulation Tests of a Cow Milking Machine-Analysis of Design Parameters, *Processes in Enterprises and Circular Economy concerning Conventional Energy and Renewable Energy*, vol. 9(8), pp. 1358. DOI: <https://doi.org/10.3390/pr9081358>
- [17] Kaskous S., (2018), Optimization of the Pulsation Ratio During the Course of Milk Removal after using A Quarter Individual Milking System “MultiLactor”, *International Journal of Agriculture Innovations and Research*, vol. 6(6), pp. 284-289 ;
- [18] Korn G., Korn T., (1977), A mathematics reference book for scientists and engineers/Справочник по математике для научных работников и инженеров, Moscow/Москва, Science/Наука, 831 p. ;
- [19] Medvedskiy O., Kukharets S., Golub G. and Dmytriv V., (2018), Installation of equilibrium pressure of milking machine vacuum system, *17th International Scientific Conference: Engineering for Rural Development*, Jelgava / Latvia, vol. 17, pp. 143-148. DOI: 10.22616/ERDev2018.17.N173 ;
- [20] Nguyen-Ba H., van Milgen J., Taghipoor M., (2020). A procedure to quantify the feed intake response of growing pigs to perturbations, *Animal: The international journal of animal biosciences*, vol. 14(2), pp. 253-260. DOI: <https://doi.org/10.1017/S1751731119001976> ‘
- [21] Odorčić M., Rasmussen M. D., Paulrud C. O. et al., (2019), Review: Milking machine settings, teat condition and milking efficiency in dairy cows, *Animal: The international journal of animal biosciences*, vol. 13(S1), pp. 94-99. DOI: <https://doi.org/10.1017/S1751731119000417> ;
- [22] Parilová M., Ježková A., Stádník L. and Štolc L., (2010), Effect of milking vacuum and overmilking on selected milking characteristics, *Cattle Research*, vol. 3, pp. 35–42 ;
- [23] Penry J.F., Upton J., Mein G.A., et al., (2017), Estimating teat canal cross-sectional area to determine the effects of teat-end and mouthpiece chamber vacuum on teat congestion. *Journal of Dairy Science*, vol. 100(1), pp. 821–827. DOI: <https://doi.org/10.3168/jds.2016-11533> ;
- [24] Reinemann D. J., van den Borne B. H. P., Hogeveen H. et al., (2021), Effects of flow-controlled vacuum on milking performance and teat condition in a rotary milking parlor, *Journal of Dairy Science*, vol. 104(6), pp. 6820-6831. <https://doi.org/10.3168/jds.2020-19418> ;
- [25] Reinemann D.J., Mein G., (2010), Review of milking biomechanics research, *IDF Mastitis Conference: Mastitis Research into Practice*.
https://www.researchgate.net/publication/316119771_Review_of_milking_biomechanics_research ;
- [26] Revilla M., Friggens N.C., Broudiscou L.P. et al., (2019), Towards the quantitative characterization of piglets' robustness to weaning: a modelling approach, *Animal: The international journal of animal biosciences*, vol. 13(11), pp. 2536-2546. DOI: <https://doi.org/10.1017/S1751731119000843> ;
- [27] Sadoul B., Martin O., Prunet P., Friggens N.C., (2015), On the use of a simple physical system analogy to study robustness features in animal sciences. *PLoS ONE*, vol. 10(8), e0137333. <https://doi.org/10.1371/journal.pone.0137333> ;
- [28] Stauffer C., Feierabend M., Bruckmaier R.M., (2020), Different vacuum levels, vacuum reduction during low milk flow, and different cluster detachment levels affect milking performance and teat condition in dairy cows, *Journal of Dairy Science*, vol. 103(10), 9250–9260. DOI: <https://doi.org/10.3168/jds.2020-18677> ;
- [29] Ströbel U., Rose-Meierhöfer S., Öz H. et al., (2016), Evaluation of teat-end vacuum conditions as affected by different pulsation settings in a quarter-individual milking system, *Landbauforsch, Appl Agric Forestry Res*, vol. 66(2), pp. 228-239. DOI: 10.3220/LBF1478788111000 ;
- [30] Wieland M., Nydam D.V., Virkler P.D., (2017), A longitudinal field study investigating the association between teat-end shape and two minute milk yield, milking unit-on time, and time in low flow rate. *Livestock Science*, vol. 205, pp. 88–97. DOI: <https://doi.org/10.1016/j.livsci.2017.09.011> .

PARAMETER OPTIMIZATION AND EXPERIMENT OF SLIDER-HOLE-WHEEL SEED-METERING DEVICE BASED ON DISCRETE ELEMENT METHOD

基于离散元法的滑片型孔轮式排种器参数优化与试验

Xiaoshuang Zhang¹⁾, Dequan Zhu^{*1,2)}, Kang Xue¹⁾, Lanlan Li¹⁾, Jianjun Zhu¹⁾, Shun Zhang¹⁾, Juan Liao¹⁾

¹⁾ School of Engineering, Anhui Agricultural University, Hefei 230036, China;

²⁾ Anhui Province Engineering Laboratory of Intelligent Agricultural Machinery and Equipment, Hefei 230036, China;

^{*} Corresponding author, E-mail: zhudequan@ahau.edu.cn

DOI: <https://doi.org/10.35663/inmateh-65-43>

Keywords: Seed-metering device, Parameter optimization, Seeding performance, Slider-hole-wheel, Test

ABSTRACT

To improve the adaptability and precision of the slider-hole-wheel seed-metering device to meet the requirements of precision sowing, the single factor simulation experiments and the three factors three levels of orthogonal simulation experiments were carried out based on the discrete element method. The rotation speed of the seeding shaft, the shape of the hole, and the depth of the hole were set as experiment factors. The results of simulation experiments showed that the qualified rate was the highest when the rotation speed of the seeding shaft was 30 r/min, the shape of the hole was oval, and the depth of the hole was 9 mm. The qualified rate, replay rate, and miss-seeding rate were 89.09%, 3.64%, and 7.27%, respectively. The hybrid rice seeds of Zhongnong 2008, Chuangliangyou 4418, and Gangyou 898 were chosen as the materials for the bench and field seeding performance tests to verify the reliability of the simulation results. The test results showed that the qualified rate of Zhongnong 2008, Chuangliangyou 4418, and Gangyou 898 seed in bench tests were 85.07%, 85.20%, and 82.13%, and the qualified rate of Zhongnong 2008, Chuangliangyou 4418, and Gangyou 898 seed in field tests were 82.13%, 82.27%, and 80.53%. The seeding performance with the three kinds of rice seeds could meet the agronomic requirements for precision sowing of hybrid rice. The paper provided the basis for the structure optimization and seeding performance improvement of the slider-hole-wheel seed-metering device.

摘要

为了提高滑片型孔轮式排种器的适应性和排种精度, 满足水稻精量穴播要求, 采用离散元法, 以排种轴转速、型孔形状、型孔深度为试验因素, 开展了单因素仿真试验和3因素3水平正交仿真试验。仿真结果表明, 在排种轴转速为30 r/min、型孔形状为椭圆形、型孔深度为9 mm时, 排种合格率最高, 合格率、重播率、漏播率分别为89.09%、3.64%、7.27%。为了验证仿真结果的可靠性, 以中农2008、创两优4418和冈优898为试验材料, 进行了排种器台架性能试验和田间播种试验。试验结果表明, 中农2008、创两优4418、冈优898种子台架试验排种合格率分别为85.07%、85.20%、82.13%, 中农2008、创两优4418、冈优898种子田间试验播种合格率分别为82.13%、82.27%、80.53%, 3种水稻种子的排种性能均能满足杂交水稻精量播种的农艺要求。该研究为滑片型孔轮式排种器结构优化及排种性能提升提供了依据。

INTRODUCTION

Rice precision hill-direct-seeding is a light and simple planting technology with saving costs and improving efficiency (Zhang et al., 2018). In recent years, rice precision hill-direct-seeding has become a development trend (Xing et al., 2018; Tian et al., 2021). The seed-metering device is the core working part of the hole direct broadcast machine, and its performance directly determines the seeding quality (Jia et al., 2018; Ye et al., 2021; Chen et al., 2021).

¹⁾Xiaoshuang Zhang, As. M.S. Stud. Eng.; Dequan Zhu, Prof. Ph.D. Eng.; Kang Xue, As. Ph.D. Stud. Eng.;

Lanlan Li, As. M.S. Stud. Eng.; Jianjun Zhu, As. M.S. Stud. Eng.; Shun Zhang, Lec. Ph.D. Eng.; Juan Liao, Lec. Ph.D. Eng.

The discrete element method is used as a new numerical method to deal with discontinuous media problems which are developing these years, and is used in many fields (Ketterhagen, 2011; Liu *et al.*, 2020; Xu *et al.*, 2021). The EDEM software can be used to simulate the seed-metering device process, which can conveniently and accurately test the seeding performance, determine its structural parameters and working parameters, and reduce the number of bench tests and field tests (Xue *et al.*, 2019; Wang *et al.*, 2021). EDEM software was used to analyze the filling process of the cell-belt rice precision seed-metering based on friction, and obtain influence rules of the filling performance with cell-belt velocity, cell-belt inclined angle, and seed layer thickness (Liu *et al.*, 2019).

EDEM software was used to simulate and optimize the structure parameters and working parameters of the spoon taking seed and the piston pricking hole for the seed-metering device (Zhou *et al.*, 2018). EDEM software was used to simulate and analyze four kinds of the groove wheel seeding devices, and obtained the optimal structural parameters of the devices (Xu *et al.*, 2018).

EDEM software was used to simulate the seed-metering device seeding process of three kinds of sphericity rice seeds at six seeding wheel speeds, and the seeding performance change law of rice seeds at different seeding wheel speeds was obtained (Zhu *et al.*, 2018). These application studies have achieved satisfactory research results on the optimization of the seed-metering device working parameters and the improvement of the seeding performance. However, the above studies simply consider the effects of working parameters on the seeding performance of the seed-metering device and have not comprehensively optimized structural parameters and working parameters of the seed-metering device.

Therefore, according to the agronomic requirements of precision hill-direct-seeding of hybrid rice, EDEM software was used to simulate the seeding performance of the self-developed slider-hole-wheel seed-metering device and comprehensively optimize the structure and working parameters of the seed-metering device. Chuangliangyou 4418 rice seeds with moderate seed sphericity were selected as material, the rotation speed of the seeding shaft, the shape of the hole, and the depth of the hole were used as test factors, and the qualified rate, the replay rate, and the miss-seeding rate were taken as evaluated indicators. The single factor simulation tests and three factors three levels of orthogonal simulation tests were performed to determine the optimal parameter combination for seeding performance. Finally, the reliability of simulation results was verified by bench tests and field tests based on the test materials of Zhongnong 2008, Chuangliangyou 4418, and Gangyou 898 rice seeds.

MATERIALS AND METHODS

Structure and working principle

The slider-hole-wheel seed-metering device is composed of a seeding wheel, eight slip sheets, a cleaning brush, a cleaning shaft, a shield shell, two convex blocks, a seed limiting plate, a seed pipe, a seeding shaft, and two flanges, as shown in Fig. 1. During the operation, rice seeds are filled into the seed chamber composed of the seed-metering device shell and seed limiting plate. The seeds in the seeding chamber flow into the filling area under the action of gravity, and the inclined structure at the bottom of the seeding chamber ensures that the seeds continuously flow into the filling area. In the filling area, the seeding wheel and slip sheets embedded in the seeding wheel are driven by the seeding shaft which made a circular movement with the seeding shaft, and rice seeds are filled into the hole of the seeding wheel.

The seeds in the hole are taken into the seed cleaning area by the seeding wheel, and the excess seeds outside the hole will be removed by the cleaning brush, and the cleared seeds will go in the filling area for secondary seeding. The seeds in the hole are entered in the seed protection area with the seeding wheel.

When the slip sheet is rotated with the seeding wheel to end point A of the cleaning brush working area, it touches the bump on the inner side of the right flange, and the slip sheet is pushed to the other side to cover the hole, so as to ensure that the seeds will not fall out of the hole at the seed protection stage, which plays the role of seed protection. As the slide sheet rotates with the seeding wheel to point B, the slide sheet is pushed to its original position by the convex block on the inner side of the left flange, which fits into the hole. At this time, the seeds enter the dropping area, and the seeds fall from the seed pipe into the seed groove by gravity and centrifugal force to complete the precision sowing (Zhu *et al.*, 2018). The schematic diagram of the seeding process is shown in Fig. 2.

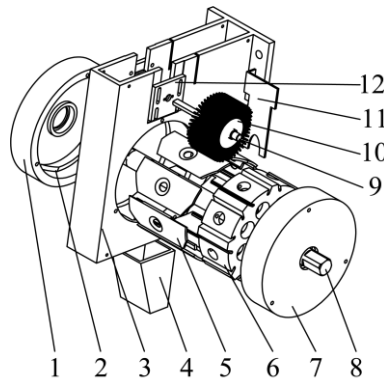


Fig. 1 - Structural diagram of the seed-metering device

- 1) Left flange; 2) Convex block; 3) Shield shell; 4) Seed pipe; 5) Slip sheet; 6) Seeding wheel; 7) Right flange; 8) Seeding shaft; 9) Cleaning shaft; 10) Cleaning brush; 11) Seed limiting plate; 12) Fixed plate

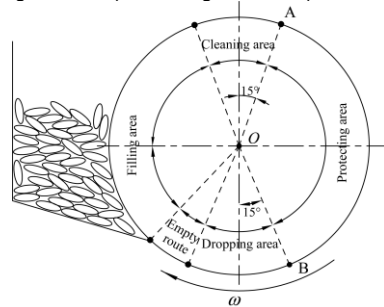


Fig. 2 - Structural diagram of seeding process

Test method

The EDEM software was used to analyze the factors affecting the seeding performance of the seed-metering device. Chuangliangyou 4418 rice seeds were taken as material, the rotation speed of the seeding shaft, the shape of the hole, and the depth of the hole were taken as test factors, and the qualified rate, the replay rate, and the miss-seeding rate were taken as evaluation indexes. The single factor simulation tests and three factors three levels of orthogonal simulation tests were carried out to determine the optimal parameter combination for seeding performance. Taking Zhongnong 2008, Chuangliangyou 4418, and Gangyou 898 rice seeds as experimental materials, the reliability of the simulation results were verified by bench tests and field tests.

Tests evaluation index

According to the agronomic requirements of precision hill-direct-seeding of hybrid rice, and referring to the standard of testing methods of single seed drills, the qualified rate Y_1 , replay rate Y_2 , miss-seeding rate Y_3 , injury rate I , and variation coefficient of hill spacing V were selected as the test indicators (Shi *et al.*, 2014), and these indicators can be calculated as follows:

- 1) When the number of seeds per hole is 2 to 4, it is qualified, then the qualified rate Y_1 is

$$Y_1 = \frac{n_1}{N} \times 100\% \quad (1)$$

- 2) When the number of seeds per hole is greater than (or equal to) 5, it is replay, then the replay rate Y_2 is

$$Y_2 = \frac{n_2}{N} \times 100\% \quad (2)$$

- 3) When the number of seeds per hole is less than (or equal to) 1, it is miss-seeding, then the miss-seeding rate Y_3 is

$$Y_3 = \frac{n_3}{N} \times 100\% \quad (3)$$

- 4) When the seed is broken, it is the seed injury, then the seed injury rate I is:

$$I = \frac{n_4}{N} \times 100\% \quad (4)$$

- 5) The variation coefficient of hill spacing V can be calculated from the acupoint distance and standard deviation, and the calculation formula is:

$$\bar{x} = \frac{\sum x_i}{N} \quad (5)$$

$$S = \sqrt{\frac{\sum (x_i - \bar{x})^2}{N-1}} \quad (6)$$

$$V = \frac{S}{\bar{x}} \times 100\% \quad (7)$$

Where:

N is the number of theoretical seeds; n_1 is the number of qualified seeds; n_2 is the number of replay seeds; n_3 is the number of miss-seeding seeds; n_4 is the number of broken seeds; \bar{x} is the average hill spacing, [mm]; S is the standard deviation, [mm].

Simulation tests

In EDEM software, the particle-particle and particle-geometric boundary contact models were all non-sliding contact models (*Khatchaturian et al., 2014*). The slip sheets were set to rotation and translation. The seeding wheel and the cleaning brush were rotated, the rotation speed of the cleaning brush was three times the rotation speed of the seeding wheel. The direction of gravity acceleration was set to the negative direction of the Y-axis, and the value was 9.80 m/s². According to the function and processing requirements of the seed-metering device, all parts of the seed-metering device were set as stainless steel, except for the cleaning brush of plastic.

The physical parameters of rice seeds, cleaning brush, and stainless steel, which include shear modulus, density, and Poisson's ratio were setting as shown in Table 1.

The physical mutual contact mechanical parameters setting of each component material are shown in Table 2 (*Wen, 2018*).

Table 1

Physical parameters

Material	Shear modulus (Pa)	Density (kg·m ⁻³)	Poisson's ratio
Rice seeds	1.8×10 ⁸	1200	0.30
Cleaning brush	1.0×10 ⁸	1500	0.40
Stainless steel	7.9×10 ⁷	7850	0.28

Table 2

Contact mechanical parameters

Material	Coefficient recovery coefficient	Static friction coefficient	Rolling friction coefficient
Rice-rice	0.30	0.56	0.15
Rice-cleaning brush	0.45	0.50	0.20
Rice-stainless steel	0.52	0.50	0.10

The shape of the rice seeds is spindle-shaped, with narrow ends at both ends, wide and thick in the middle, and there is no cohesion between particles. This paper used Chuangliangyou 4418 rice seed (9.00 mm×2.30 mm×1.84 mm) as material. To simplify the grain model and reflect the shape of rice grains more realistically in the EDEM software, a multi-sphere combination filling method was used to establish a combination model with a shape similar to the Chuangliangyou 4418 rice seed. The model consists of a total of 24 spherical spindles with the same triaxial size as the actual triaxial size of the Chuangliangyou 4418 rice seeds, as shown in Fig. 3.

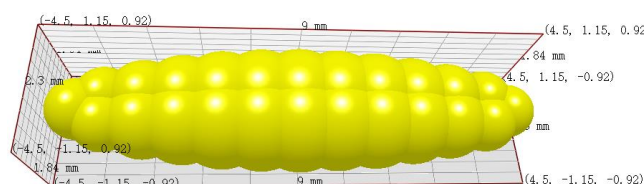


Fig. 3 - The rice model

SolidWorks software was used to build the three-dimensional model of the seed-metering device, and the model of the seed-metering device saved as IGES format was imported into EDEM software. To ensure continuous filling seeds, a certain amount of seeds should be stored in the seed filling room. The total number of particles generated by the particle factory was set to 4000, the time for particles to generate was 1 s, and the seeding wheel starts to move at 1.5 s. The total simulation time was set to 30 s (Liu *et al.*, 2021), as shown in Fig. 4.

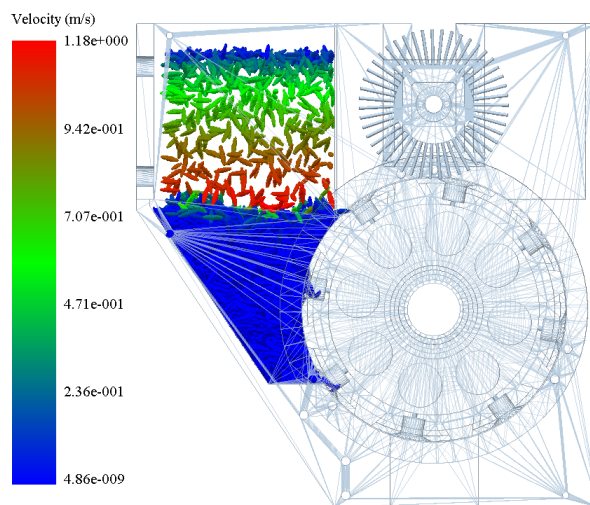


Fig. 4 - The seed-metering device simulation process in EDEM

(1) Single factor simulation tests

a) Effect of the rotation speed of the seeding shaft on seeding performance

When the shape of the hole was set as cylindrical (diameter 10 mm) and the depth of the hole was set as 8 mm, the rotation speeds of the seeding shaft were respectively set as 15 r/min, 20 r/min, 25 r/min, 30 r/min, 35 r/min, and 40 r/min for the simulation tests of the seeding performance. Through the simulation experiments of the seeding performance of the device under different rotation speeds of the seeding shaft, the qualified rate, replay rate, and miss-seeding rate of the whole number were calculated.

b) Effect of the shape of the hole on seeding performance

When the rotation speed of the seeding shaft was set as 30 r/min and the depth of the hole was set as 8 mm, the shapes of the hole were respectively set as diamond (long side diagonal 12 mm \times short side diagonal 10 mm), oval (long axis 14 mm \times short axis 8 mm), and cylindrical (diameter 10 mm) for the simulation tests of the seeding performance. Through the simulation experiments of the seeding performance of the device under the different shapes of the hole, the qualified rate, replay rate, and miss-seeding rate of the whole number were calculated.

c) Effect of the depth of hole on seeding performance

When the shape of the hole was set as oval and the rotation speed of the seeding shaft was set as 30 r/min, the depths of the hole were respectively set as 7 mm, 8 mm, 9 mm, 10 mm, and 11 mm for the simulation tests of the seeding performance. Through the simulation experiments of the seeding performance of the device under the different depths of the hole, the qualified rate, replay rate, and miss-seeding rate of the whole number were calculated.

(2) Orthogonal simulation tests

Based on the results of the single factor simulation tests, the rotation speed of the seeding shaft, the shape of the hole, and the depth of the hole were selected as test factors. Each factor was set at 3 levels, and three factors three levels of orthogonal tests were performed. The orthogonal factors and levels table was shown in Table 3.

Table 3

Orthogonal factors and levels table

Level	A Rotating speed (r·min ⁻¹)	B Shape of the hole (mm)	C Depth of the hole (mm)
1	25	Diamond	8
2	30	Cylindrical	9
3	35	Oval	10

Without considering the interaction between the three factors, the $L_9 (3^4)$ three factors three levels orthogonal table were used in these experiments. There was one empty column in the $L_9 (3^4)$ orthogonal table, and the orthogonal tests scheme was shown in Table 4.

Table 4

Orthogonal tests scheme

Test number	Factors			
	A	B	Empty column	C
1	1	1	1	1
2	1	2	2	2
3	1	3	3	3
4	2	1	2	3
5	2	2	3	1
6	2	3	1	2
7	3	1	3	2
8	3	2	1	3
9	3	3	2	1

Bench tests

To verify the reliability of the simulation results, bench tests of the seed-metering device on the seeding performance was conducted. The test site was in the precision seeding laboratory of Anhui Agricultural University. The test equipment was the JPS-12 type seed-metering device performance test bench which was developed by the Heilongjiang Agricultural Machinery Engineering Research Institute. The seed-metering device was fixed on the bracket, the seeding shaft was driven by the test bench chain, and the speed of the seed bed belt was adjusted according to the speed of the seeding shaft. The seeds fall into the oil belt on the seed bed belt to prevent the seeds from bouncing during the falling process, as shown in Fig. 5.

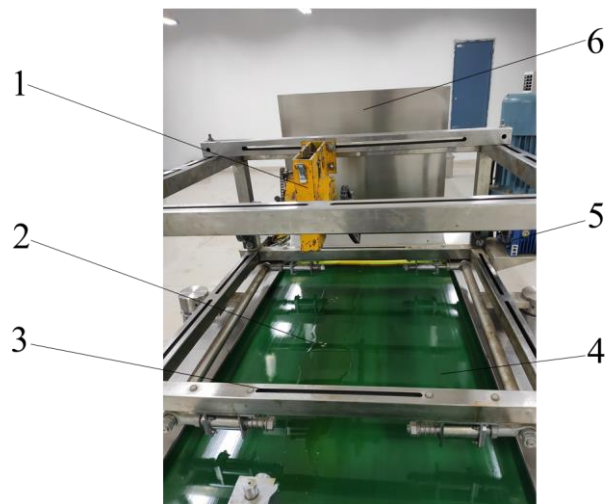


Fig. 5 - Seed-metering device bench tests

1) Seed-metering device; 2) Seeds; 3) Bracket; 4) Seedbed belt; 5) Motor; 6) Lighting device

Field tests

To test the field seeding performance of the seed-metering device, which was installed on a precision dry-seeding-sowing machines, and these field seeding tests were carried out in the agricultural field of Anhui Agricultural University, in May, 2020. Before these tests, the field soil was plowed with a rotary tiller to make it loose and level. The average plowing depth was 11.2 cm, and the average soil solidity was 390.8 kPa. These rice varieties of Zhongnong 2008, Chuangliangyou 4418, and Gangyou 898 were selected in turn for sowing tests, and these tests were conducted in accordance with national standards (*Press, 2006*). During these tests, the forward speed of the unit was about 4.5 km/h, the rotation of the seed-metering device was driven by the direct-current motor, and the average working speed of the seed-metering device was about 30 r/min.

RESULTS AND ANALYSIS

Simulation tests

Single factor simulation tests

(1) Effect of the rotation speed of the seeding shaft on seeding performance

When the shape of the hole was cylindrical and the depth of the hole was 8 mm, the relationship curves between the rotation speeds of the seeding shaft and the evaluation indexes are shown in Fig. 6.

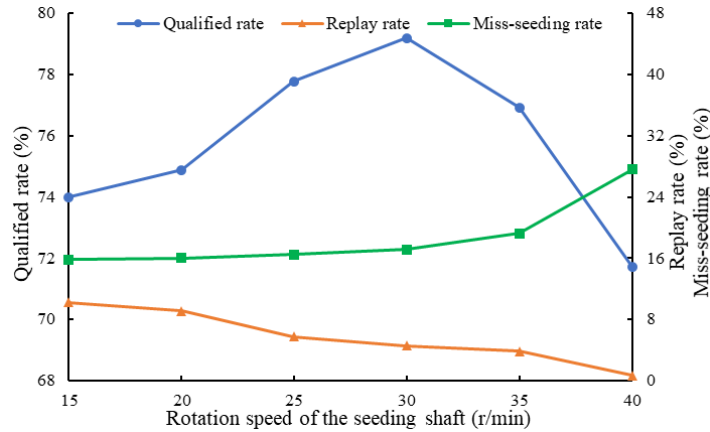


Fig. 6 - Relationship curves between rotation speeds of the seeding shaft and evaluation indexes

As shown in Fig. 6, when the rotation speed of the seeding shaft increased, the qualified rate increased first, and then decreased. The miss-seeding rate was on the rise as a whole. The replay rate generally decreased. In the beginning, the rotation speed of the seeding shaft was low, and the time for the hole to pass through the filling place was longer, so the seeds were easier to be filled into the hole, and the replay rate was higher. As the rotation speed of the seeding shaft increased, the time for the hole to pass through the filling place became shorter, the probability of the seeds to fill in the hole decreased, and at the same time, the centrifugal force of the rice seeds increased, and the seeds were easily detached from the hole, which resulted in missing. When the rotation speed of the seeding shaft was 30 r/min, the qualified rate of the seeding performance was the highest, and the qualified rate, replay rate, and miss-seeding rate were 79.19%, 4.54%, and 16.37%, respectively.

(2) Effect of the shape of the hole on seeding performance

When the rotation speed of the seeding shaft was 30 r/min and the depth of the hole was 8 mm, the relationship curves between the shapes of the hole and the evaluation indexes are shown in Fig. 7.

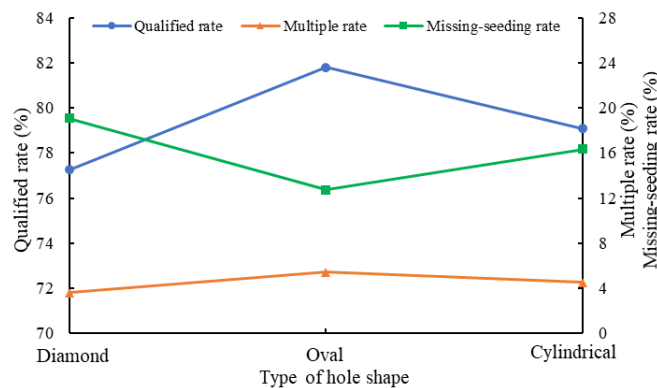


Fig. 7 - Relationship curves between shapes of the hole and evaluation indexes

As shown in Fig. 7, the qualified rate of the oval hole was the highest and the qualified rate of the diamond hole was the lowest, so the oval hole was suitable for sowing rice seeds of this size. Because the oval hole was similar to the outer contour of the rice seeds, it was easier for the rice seeds to fill the oval hole. The qualified rate of the oval hole was the highest, and the qualified rate, replay rate, and miss-seeding rate were 81.81%, 5.45%, and 12.74%, respectively.

(3) Effect of the depth of the hole on seeding performance

When the rotation speed of the seeding shaft was 30 r/min, the relationship curves between the depths of the hole and the evaluation indexes for oval hole are shown in Fig. 8.

As shown in Fig. 8, with the increase of the depth of the hole, the qualified rate increased first and then decreased, the replay rate increased in the whole curve, while the miss-seeding rate decreased in the whole curve. With the increase of the depth of the hole, the depth of the hole has better performance in the seed filling area. However, when the hole cavity was too large, the replay rate increased and the miss-seeding rate decreased. When the depth of the hole was 9 mm, the qualified rate of the seeding performance was the highest, and the qualified rate, replay rate, and miss-seeding rate were 89.09%, 3.64%, and 7.27%, respectively.

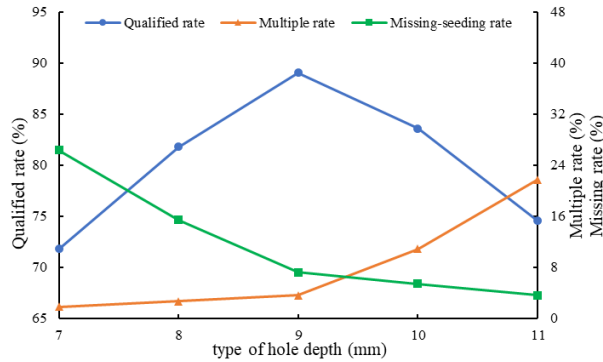


Fig. 8 - Relationship curves between depths of the hole and evaluation indexes for oval hole

Orthogonal simulation tests

The orthogonal tests scheme and results were shown in Table 5. The test results were analyzed by the range and variance analysis, as shown in Table 6 and Table 7, respectively.

Table 5

Results of orthogonal tests

Test number	Factors				Tests results		
	A	B	Empty column	C	Qualified rate (%)	Replay rate (%)	Miss-seeding rate (%)
1	1	1	1	1	74.44	5.56	20.00
2	1	2	2	2	84.44	6.67	8.89
3	1	3	3	3	83.33	8.89	7.78
4	2	1	2	3	82.72	7.27	10.01
5	2	2	3	1	79.09	4.54	16.37
6	2	3	1	2	89.09	3.64	7.27
7	3	1	3	2	82.31	3.84	13.85
8	3	2	1	3	83.08	6.92	10.00
9	3	3	2	1	77.69	3.07	19.24

Table 6

Range analysis

Index	Analysis items	A	B	Empty column	C	
Qualified rate	k_1	80.74	79.82	82.20	77.07	
	k_2	83.63	82.20	81.62	85.28	
	k_3	81.03	83.37	81.58	83.04	
	Range R	2.90	3.55	0.63	8.21	
	Order			C>B>A		
	Optimal scheme			C ₂ B ₃ A ₂		
Replay rate	k_1	7.04	5.56	5.37	4.39	
	k_2	5.15	6.04	5.67	4.72	
	k_3	4.61	5.20	5.75	7.69	
	Range R	2.43	0.84	0.38	3.30	
	Order			C>A>B		
	Optimal scheme			C ₁ A ₃ B ₃		

Miss-seeding rate	k_1	12.22	14.62	12.42	18.54
	k_2	11.21	11.75	12.71	10.00
	k_3	14.36	11.43	12.67	9.26
	Range R	3.15	3.19	0.29	9.27
	Order	C>B>A			
Optimal scheme		C ₃ B ₃ A ₂			

From the analysis in Table 6, it can be seen that the order of factors affecting the seeding qualified rate was the depth of the hole, the shape of the hole, and the rotation speed of the seeding shaft, and the optimal scheme was C₂B₃A₂. The order of factors affecting the seeding replay rate was the depth of the hole, the rotation speed of the seeding shaft, and the shape of the hole, and the optimal scheme was C₁A₃B₃. The order of factors affecting the seeding miss-seeding rate was the depth of the hole, the shape of the hole, and the rotation speed of the seeding shaft, and the optimal scheme was C₃B₃A₂. From the analysis in Table 7, it can be seen that the depth of the hole had a highly significant effect on the seeding qualified rate. The rotation speed of the seeding shaft and the shape of the hole had a significant effect on the seeding qualified rate. The rotation speed of the seeding shaft and the depth of the hole had a significant effect on the seeding replay rate. The rotation speed of the seeding shaft, the shape of the hole, and the depth of the hole had a highly significant effect on the seeding miss-seeding rate. When the rotation speed of the seeding shaft was 30 r/min, the shape of the hole was oval and the depth of the hole was 9 mm, the qualified rate was the highest. The qualified rate, replay rate, and miss-seeding rate were 89.09%, 3.64%, and 7.27%, respectively.

Table 7

Variance analysis

Evaluated indicator	Variation source	Standard deviation square	Degrees of freedom	Mean square	F - Value	P - Value
Qualified rate	A	15.269	2	7.635	20.68	0.046*
	B	19.604	2	9.802	26.55	0.036*
	C	107.993	2	53.997	146.24	0.007**
	Error column	0.738	2	0.369		
Replay rate	A	9.769	2	4.884	40.29	0.024*
	B	1.075	2	0.538	4.43	0.184
	C	19.879	2	9.940	81.99	0.012*
	Error column	0.243	2	0.121		
Miss-seeding rate	A	15.494	2	7.747	106.50	0.009**
	B	18.498	2	9.249	127.15	0.008**
	C	159.360	2	79.680	1095.34	0.001**
	Error column	0.145	2	0.073		

Note: “*” indicates significance at 0.05 level, “**” indicates the highly significance at 0.01 level.

Bench tests

According to the results of the single factor simulation tests and the orthogonal simulation tests, the seed-metering device was installed on the experimental table, and the tests were carried out under the condition of the seeding shaft was 30 r/min and an oval hole depth was 9 mm. Zhongnong 2008, Chuangliangyou 4418, and Gangyou 898 rice seeds were selected for bench tests in turn, and the 250 consecutive holes were counted after the seed-metering device worked stably, and each group of tests was repeated three times. The average value was taken as the results of the tests, and the results were shown in Table 8.

Table 8

Results of bench tests

Varieties	Qualified rate (%)	Miss-seeding rate (%)	Replay rate (%)	Injury rate (%)	Hill spacing (mm)	Variation coefficient of hill spacing (%)
Zhongnong 2008	85.07	5.47	9.46	0.33	206.32	8.13
Chuangliangyou 4418	85.20	6.40	8.40	0.30	205.56	7.03
Gangyou 898	82.13	12.40	5.47	0.41	209.31	11.43

As shown in Table 8, under the conditions of the rotation speed of the seeding shaft was 30 r/min, the shape of the hole was oval, and the depth of the hole was 9 mm, the Chuangliangyou 4418 rice seed qualified rate was the highest of 85.20%, and the Gangyou 898 rice seed qualified rate was the lowest of 82.13%. The error between the Chuangliangyou 4418 rice seeds simulation tests and the bench tests were less than 5%, which proved that the simulation tests were reliable.

Field tests

In each group of field tests, the number of seeds and the hill spacing in 250 holes was counted continuously, and each group of tests was repeated three times. The average value was taken as the field test results. The test results are shown in Table 9.

As shown in Table 9, under the working conditions of the average speed of the seed-metering device of 30 r/min and the forward speed of the unit of 4.5 km/h, Chuangliangyou 4418 seeds had the highest seeding qualified rate of 82.27%, and Gangyou 898 seeds had the lowest seeding qualified rate of 80.53%, and the injury rate was below 0.5%. The range of hill spacing distributes from 208 to 211 mm, and the variation coefficient of hill spacing among sowing points was lower than 16%. The slider-hole-wheel seed-metering device had good adaptability to rice seeds of different shapes, and can meet the agronomic requirements for rice precision hill-direct-seeding. However, the qualified rate of the three rice varieties was lower than that of the bench tests, mainly due to the impact of field vibration on the seed-metering device.

Table 9

Results of field tests

Varieties	Qualified rate (%)	Miss-seeding rate (%)	Replay rate (%)	Injury rate (%)	Hill spacing (mm)	Variation coefficient of hill spacing (%)
Zhongnong 2008	82.13	3.07	14.80	0.35	209.38	12.36
Chuangliangyou 4418	82.27	4.93	12.80	0.31	208.45	11.28
Gangyou 898	80.53	8.80	10.67	0.43	210.52	15.37

CONCLUSIONS

In this study, the rotation speed of the seeding shaft, the shape of the hole, and the depth of the hole were taken as experiment factors, and the qualified rate, replay rate, and miss-seeding rate were taken as the evaluation indicators. The single factor experiments and three factors three levels of orthogonal simulation experiments were carried out, and the results shows as follows. Single factor simulation tests showed that the seeding performance was the best when the rotation speed of the seeding shaft was 30 r/min, and the qualified rate was 79.19% under the conditions that the shape of the hole was cylindrical and the depth of the hole was 8 mm. The seeding performance was the best when the shape of the hole was oval, and the qualified rate was 81.81% under the conditions that the rotation speed of the seeding shaft was 30 r/min and the depth of the hole was 8 mm. The seeding performance was the best when the depth of the hole was 9 mm, and the qualified rate was 89.09% under the conditions that the rotation speed of the seeding shaft was 30 r/min and the shape of the hole was oval. Three factors and three levels of orthogonal simulation tests showed that the qualified rate was the highest under the rotation speed of seeding shaft was 30 r/min, the shape of the hole was oval and the depth of the hole was 9 mm, and the qualified rate, replay rate, and miss-seeding rate were 89.09%, 3.64%, and 7.27%, respectively. The bench tests showed that the seeding qualified rate of Zhongnong 2008, Chuangliangyou 4418, and Gangyou 898 rice seeds were 85.07%, 85.20%, and 82.13%, respectively. Field tests showed that the seeding qualified rate of Zhongnong 2008, Chuangliangyou 4418, and Gangyou 898 rice seeds were 82.13%, 82.27%, and 80.53%, respectively. The seed-metering device had good adaptability to rice seeds in different shapes and sizes and can meet the agronomic requirements of precision hill-direct-seeding in rice fields.

ACKNOWLEDGEMENT

This work was supported by the Major Scientific and Technological Special Project of Anhui Province (No. 17030701045) and the Funding Project of Scientific Research Activities for Academic and Technical Leaders and Reserve Candidates in Anhui Province (No. 2019D223).

REFERENCES

- [1] Chen Y.L., Liu Z.E., Zhang M., et al. (2021). Research of seed group structure characteristics of vertical disc metering device based on discrete element method. *INMATEH-Agricultural Engineering*, Vol. 64, Issue 2, pp. 488-496.
- [2] Jia H.L., Chen Y.L., Zhao J.L., et al. (2018). Design and key parameter optimization of an agitated soybean seed metering device with horizontal seed filling. *International Journal of Agricultural and Biological Engineering*, Vol. 11, Issue 2, pp. 76-87.
- [3] Ketterhagen W. R. (2011). Modeling the motion and orientation of various pharmaceutical tablet shapes in a film coating pan using DEM. *International Journal of Pharmaceutics*, Vol. 409, Issue 1-2, pp. 137-149.
- [4] Khatchaturian O. A., Binelo M. O., de Lima R. F. (2014). Simulation of soya bean flow in mixed-flow dryers using DEM. *Biosystems Engineering*, Vol. 123, pp. 68-76.
- [5] Liu C.L., Wang Y.L., Du X., et al. (2019). Filling performance analysis and verification of cell-belt rice precision seed-metering based on friction and repeated filling principle. *Transactions of the Chinese Society of Agricultural Engineering*, Vol. 35, Issue 4, pp. 29-36.
- [6] Liu F., Li D.P., Zhang T., et al. (2020). Analysis and calibration of quinoa grain parameters used in a discrete element method based on the repose angle of the particle heap. *INMATEH-Agricultural Engineering*, Vol. 61, Issue 2, pp. 77-86.
- [7] Liu J., Zhu D.Q., Tai, Q.L., et al. (2021). Design and experiment of adjustable socket-wheel precision fertilizer apparatus for dry direct-seeding rice. *INMATEH-Agricultural Engineering*, Vol. 63, Issue 1, pp. 121-130.
- [8] Operating quality of film-covering hill-drop drill. (2006) In GB/T 25418-2010.
- [9] Shi L.R., Wu J.M., Sun W., et al. (2014). Simulation test for metering process of horizontal disc precision metering device based on discrete element method. *Transactions of the Chinese Society of Agricultural Engineering*, Vol. 30, Issue 8, pp. 40-48.
- [10] Tian L.Q., Xiong Y.S., Ding Z., et al. (2021). Design and performance test of direct seed metering device for rice hill. *INMATEH-Agricultural Engineering*, Vol. 64, Issue 2, pp. 257-268.
- [11] Wen S. Design and experimental study of rice precision hill direct seed metering device. Master thesis of Anhui Agricultural University. 2018.
- [12] Wang Y.B., Li H.W., Wang Q.J., et al. (2021). Experiment and parameters optimization of seed distributor of mechanical wheat shooting seed-metering device. *INMATEH-Agricultural Engineering*, Vol. 63, Issue 1, pp. 29-40.
- [13] Xu B., Zhang Y.Q., Cui Q.L., et al. (2021). Construction of a discrete element model of buckwheat grain and calibration of parameters. *INMATEH-Agricultural Engineering*, Vol. 64, Issue 2, pp. 175-184.
- [14] Xu H., Tao D.C., Tao Y.H., et al. (2018). Simulation and experimental research on rice seed metering device based on EDEM. *Journal of Agricultural Science and Technology*, Vol. 20, Issue 3, pp. 64-70.
- [15] Xing H., Wang Z.M., Luo X.W., et al. (2018). Design of an active seed throwing and cleaning unit for pneumatic rice seed metering device. *International Journal of Agricultural and Biological Engineering*, Vol. 11, Issue 2, pp. 62-69.
- [16] Xue P., Xia X., Gao P., et al. (2019). Double-setting seed-metering device for precision planting of soybean at high speeds. *Transactions of the Asabe*, Vol. 62, Issue 1, pp. 187-196.
- [17] Ye S.B., Zheng D.C., Li W., et al. (2021). Design and test of negative pressure chamber rotary buckwheat seed metering device. *INMATEH-Agricultural Engineering*, Vol. 64, Issue 2, pp. 185-194.
- [18] Zhu D.Q., Li L.L., Wen S.C., et al. (2018). Numerical simulation and experiment on seeding performance of slide hole-wheel precision seed-metering device for rice. *Transactions of the Chinese Society of Agricultural Engineering*, Vol. 34, Issue 21, pp. 17-26.
- [19] Zhou F.J., Li X.L., Yin B.X. (2018). Design and experiment of seeding apparatus with spoon taking seeds and piston pricking hole for rice. *Journal of Northeast Agricultural University*, Vol. 49, Issue 8, pp. 73-82.
- [20] Zhang M.H., Wang Z.M., Luo X.W., et al. (2018). Review of precision rice hill-drop drilling technology and machine for paddy. *International Journal of Agricultural and Biological Engineering*, Vol. 11, Issue 3, pp. 1-11.

MATERIAL MOVEMENT WITHIN A SINGLE-SCREW EXTRUDER / ДВИЖЕНИЕ МАТЕРИАЛА В ОДНОШНЕКОВОМ ЭКСТРУДЕРЕ

Dorokhov A.S.¹), Zagoruiko M.G., Maradudin A.M., Bashmakov I.A. ¹

FSBSI "Federal Scientific Agronomic and Engineering Centre VIM" / Moscow / Russia

Tel: +79645843518; E-mail: sazonov_nikolay@mail.ru

Corresponding author: Dorokhov A.S.

DOI: <https://doi.org/10.356.33/inmateh-65-44>

Keywords: extruder, screw, friction, rate of rotation, temperature gradient

ABSTRACT

In present-day economic conditions, extrusion is one of the advanced feedstuffs and food production processes involving intensive manifold heat and force action. During extrusion, the main function is performed by a compression mechanism which includes a forcing screw unit built into the cylinder (cowling). The forcing mechanism performs the task of transferring material while concurrently compressing it up to a required pressure and increasing the material's temperature due to compression and friction against the cowling's sides. The temperature affects the quality of the resulting product. Thus, the research aims at obtaining a heat balance equation to optimize the extrusion process and the operating parameters of the extruder itself.

РЕЗЮМЕ

В современных экономических условиях одним из прогрессивных технологических процессов в производстве кормов и продуктов питания является экструдирование, при котором материал подвергается мощному комплексному тепловому и силовому воздействию. Главную функцию при экструдировании выполняет прессовочный механизм, который включает в себя нагнетающий шнековый блок, смонтированный в цилиндр (кожух). Задача прессовочного механизма, перемещать, одновременно сжимая материал до необходимого давления, повышая температуру от сжатия и трения о стенки кожуха. Температура влияет на качество получаемой продукции. Таким образом исследования направлены на получение уравнения теплового баланса с целью оптимизации процесса экструзии и рабочих параметров самого экструдера.

INTRODUCTION

In present-day economic conditions, extrusion is one of the advanced feedstuffs and food production processes involving intensive manifold heat and force action. During extrusion, the main function is performed by a compression mechanism which includes a forcing screw unit built into the cylinder (cowling). The forcing mechanism performs the task of transferring material while concurrently compressing it up to a required pressure and increasing the material's temperature due to compression and friction against the cowling's sides.

When analyzing material movement within the screw, the authors use the scientific abstraction approach, i.e., instead of using an actual material body they use its simplified model. This approach uses two main techniques. In the first case, the actual arrangement is replaced by movement of the material within "a channel with a floating lid", or between parallel planes with one of the planes moving (Sagirov. S.N., 2011).

After that, the Navier-Stokes equation is resolved for the case of movement of a Newtonian liquid, together with the continuity equation under various assumptions and with various representations of the obtained solution (Barsukov V.G., Grakholskaya E.V., Volk O.S., et al., 2009; Mikulionok I., Gavva O., Kryvoplias-Volodina L., et al., 2018). Further development of this technique lies in the analysis of the extruded material which has properties different from Newtonian liquid, and the problem is viewed as a one-dimensional, two-dimensional, and even three-dimensional problem (Didyk T.A., 2005; Kryuchkova L.G., Dotsenko S.M., Burmağa A.V., Cheredov A.V., et al., 2014).

¹ Dorokhov A.S., Prof. PhD. Eng.Sc.; Zagoruiko M.G., PhD. Eng.Sc.; Maradudin A.M., PhD. Eng.Sc.

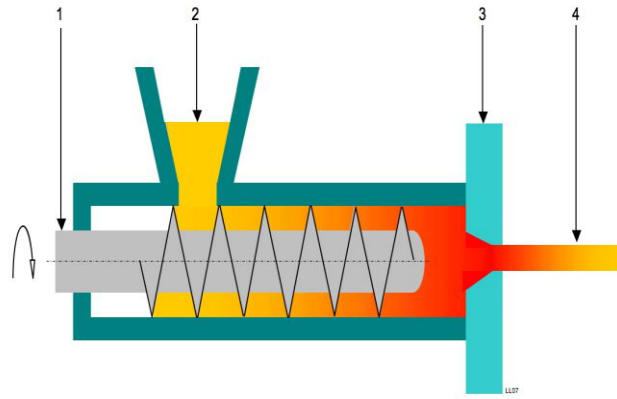


Fig. 1 – Extruder operation process flow diagram
1 – effector (screw); 2 – loaded raw material; 3 – forming die; 4 – finished product

MATERIALS AND METHODS

The second technique views the compressed material as a flowing medium (either continuous or granular) throughout the screw's length (Adigamov K.A., Chernenko A.V., 2010; Zubkova T.M., Kolobov A.N., 2015). An extension of this technique is an approach which attributes both flowing and pseudoplastic body properties to the material (Ostrikov A.N., Ospanov A.A., Vasilenko V.N., et al., 2019). In this case, the use of the continuous model of a flowing medium is more advisable since the differential body equilibrium equations are similar to the equation of the theory of elasticity and plasticity. This approach, when used in analyzing stress condition of the compressed mass, allows to substitute all the actual forces acting on specific particles at points of contact with other particles with assumptive forces distributed uniformly along an arbitrary section of the material (Wu M., Sun C.H., Bi F. et al., 2019). Therefore, this makes it possible to make a transition from a material particle to a system of particles that collectively make up the flowing medium.

In our view, the first technique is appropriate when a material which is moving within the compression area is in viscous-flow state. The second technique is optimal for theoretical description of areas of loading, transportation, and compression (melting) where the working pressure is maintained.

In his research, Grigoryev A.M. developed a system of motion equations of a material particle resting on the surface of an inclined screw and pressed against its wall (Fig. 2) (Evstratova N.N., Apachanov A.S., Grigoryev V.I., 2009):

$$\begin{cases} N_1 \cos \alpha - f_1 N_1 \sin \alpha - ma \left(\frac{d^2 \varphi}{dt^2} \right) - G \cos \gamma - f_2 N_2 \sin \beta = 0 \\ G \cos \gamma \sin \varepsilon + f_2 N_2 \cos \beta - f_1 N_1 \cos \alpha - N_1 \sin \alpha - mr \left(\frac{d^2 \varphi}{dt^2} \right) = 0 \\ G \sin \gamma \cos \varepsilon + mr \omega_0^2 + mr \left(\frac{d\varphi}{dt} \right)^2 - N_2 - 2mr \omega_0 \left(\frac{d\varphi}{dt} \right) = 0 \end{cases} \quad (1)$$

where:

N_1 is the normal response of the inclined plane, [N];

f_1 - the coefficient of friction of the material against the screw blade;

m - the weight of the material element [kg];

α - the elevation angle of the screw section of the screw [rad];

ω_0 - the angular rate of rotation of the screw [s^{-1}];

G - the weight of the material element [N];

γ - the angle of inclination of the screw shaft axis to the vertical axis [rad];

N_2 - the normal response of the cowling [N];

f_2 - the coefficient of friction of the material against the cowling wall;

φ - the angle of deflection of a particle when rotating at a constant rate of angular rotation ω_0 ;

$\frac{d\varphi}{dt}$ - the rate of angular rotation of relative movement of a material point, [s^{-1}];

ε - the angle which determines the position of the point against the vertical plane; $\varepsilon = \omega_0 t + (-\varphi)$;

r - the outer radius [m];

$mr \left(\frac{d^2 \varphi}{dt^2} \right)$ - the tangential inertia force [N];

$mr \omega_0^2$ - the centrifugal inertia force of the translation motion [N];

- $mr \left(\frac{d\varphi}{dt}\right)^2$ - the centrifugal inertia force of the relative movement [N];
- $2mr\omega_0 \left(\frac{d\varphi}{dt}\right)$ - the Coriolis force [N];
- $ma \left(\frac{d^2\varphi}{dt^2}\right)$ - the axial inertia force [N].

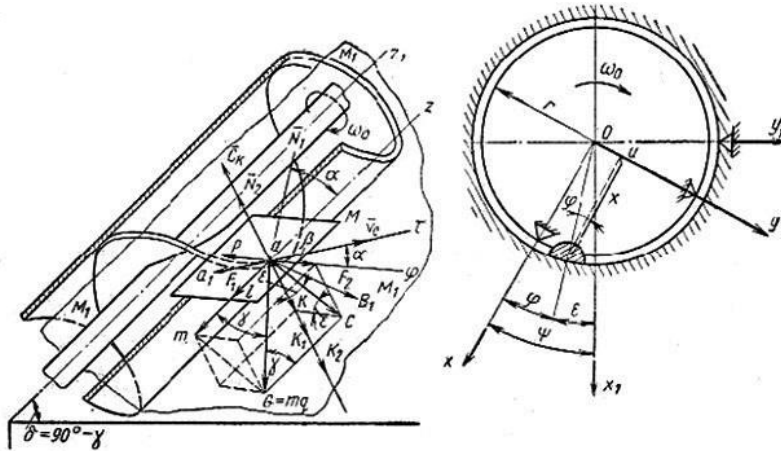


Fig. 2 – The diagram of forces applied to a material point which moves along the screw, as well as of the locations of the moving and fixed reference systems

The author notes that during the screw operation, the period of non-steady movement is minute, lasting several fractions of a second to several seconds, after which the movement steadies (this is characterized by stable values of average axial velocity and absolute angular rate of rotation ω).

Thus, during the steady mode of operation of the screw with $\frac{d\varphi}{dt} = \text{const}$ and $\frac{d^2\varphi}{dt^2} = 0$, when the rotation axis of the screw is horizontal (i.e., $\gamma = 90^\circ$), the equation system (1) could be written as follows:

$$\begin{cases} N_1 \cos \alpha - f_1 N_1 \sin \alpha - f_2 N_2 \sin \beta = 0 \\ f_2 N_2 \cos \beta - f_1 N_1 \cos \alpha - N_1 \sin \alpha = 0 \\ G \cos \varepsilon + mr\omega_0^2 - N_2 - 2mr\omega_0 \left(\frac{d\varphi}{dt}\right) = 0 \end{cases} \quad (2)$$

After the reduction and translation, this gives us the following:

$$N_2 = m \left(g \cos \varepsilon + r\omega_0^2 - 2r\omega_0^2 \frac{\text{ctg } \alpha - f_1}{\text{ctg } \alpha + \text{tg } \alpha} \right) \quad (3)$$

$$N_1 = m \left(g \cos \varepsilon + r\omega_0^2 - 2r\omega_0^2 \frac{\text{ctg } \alpha - f_1}{\text{ctg } \alpha + \text{tg } \alpha} \right) \frac{f_2 \cos \beta}{f_1 \cos \alpha + \sin \alpha} \quad (4)$$

Based on the expressions (3) and (4), forces of friction of the material against the screw and cowlng surfaces, respectively, may be determined as follows:

$$F_1 = m \left(g \cos \varepsilon + r\omega_0^2 - 2r\omega_0^2 \frac{\text{ctg } \alpha - f_1}{\text{ctg } \alpha + \text{tg } \alpha} \right) \frac{f_2 \cos \beta}{\cos \alpha + \sin \alpha} \quad (5)$$

$$F_2 = m \left(g \cos \varepsilon + r\omega_0^2 - 2r\omega_0^2 \frac{\text{ctg } \alpha - f_1}{\text{ctg } \alpha + \text{tg } \alpha} \right) f_2 \quad (6)$$

Movement of the compressed material along the screw chamber of the screw, its compression and liberation of moisture occurs due to the difference of the positive force of friction F_2 and negative force of friction F_1 (Bostandzhiyan S.A., Stolin A. M., 1965; Roland W., Marschik C., Krieger M. et al., 2019).

In accordance with the expressions (5) and (6), the difference of the effective and the negative force of friction could be written as follows:

$$\Delta F = F_2 - F_1 = mf_2 \left(g \cos \varepsilon + r\omega_0^2 - 2r\omega_0^2 \frac{\text{ctg } \alpha - f_1}{\text{ctg } \alpha + \text{tg } \alpha} \right) \left(1 - \frac{\cos \beta}{\cos \alpha + \sin \alpha} \right) \quad (7)$$

An analysis of the resulting expression makes it possible to conclude that the friction force difference affecting the material particle depends on the weight of the compressed material m , travel time parameters of the screw operation (the angular rate of rotation ω_0 and the angle β), geometric parameters of the screw (the diameter of the screw, the elevation angle of the screw section α). The difference in friction forces is also affected by the physical and mechanical properties of the transported material, the extrusion machine's screw and ring (the coefficients of friction f_1 and f_2). It should be noted that the dependency on the angular rate of rotation has an exponential form (Wu M., Sun C.H., Bi F. et al., 2018).

Let us consider the dependency of the friction force difference ΔF on the travel time property of the screw operation ω_0 . In order to exclude the effect of particle weight on the final value, let us analyze the specific difference of friction forces $\Delta F/m$.

Let us determine the critical value of angle β using the following formula (Kryuchkova L.G., Dotsenko S.M., Burmaga A.V., et al., 2014):

$$\beta = 90^\circ - (\alpha + \varphi_1) \quad (8)$$

where:

φ_1 is the angle of friction of the transported material against the screw metal [degrees].

Based on the results of analysis of the resulting graph (Fig. 3) it could be seen that at the considered interval of angular rate of rotation $\omega_0 = 1 \dots 10 \text{ s}^{-1}$ (the value of the screw rotation rate interval $n = 9.6 \dots 95.5 \text{ min}^{-1}$), with the increase of ω_0 the effective difference of friction forces F_1 and F_2 decreases, while at the angular rate of rotation of $\omega_0 \approx 9.3 \text{ s}^{-1}$ ($n = 88.8 \text{ min}^{-1}$) their values become the same. During the following increase ω_0 , the difference between friction forces increases, on the contrary, towards F_1 . Thus, the increase of the screw rate of rotation impairs the effectiveness of the processes of compression of the transferred material and squeezing of the liquid fraction. This may result in a situation where the movement of the material relative to the screw stops and instead the material rotates together with the screw.

The optimal difference of the specific friction forces ΔF is comparatively small. This difference may be improved by making the interior surface of the screw cowl ribbed (Ostrikov A.N., Platov K.V., Sokolov I.Y., 2004).

This would result in a different friction factor f_2 . As can be seen from the diagram, changes of the friction factor within the range of $f_2 = 0.4$ to $f_2 = 0.5$ result in the increase of specific friction force difference by 25%, while changing it from $f_2 = 0.5$ to $f_2 = 0.6$ results in a 20% increase, with the screw angular rate of rotation of $\omega_0 = 1 \text{ s}^{-1}$. With the increase of the angular rate of rotation, the effectiveness achieved by increased friction factor f_2 reduces, and at $\omega_0 = 9.3 \text{ s}^{-1}$ levels out completely. Thus, it is advisable to make the interior surface of the screw cowl ribbed if the extruder's screw operates at low rotation rates.

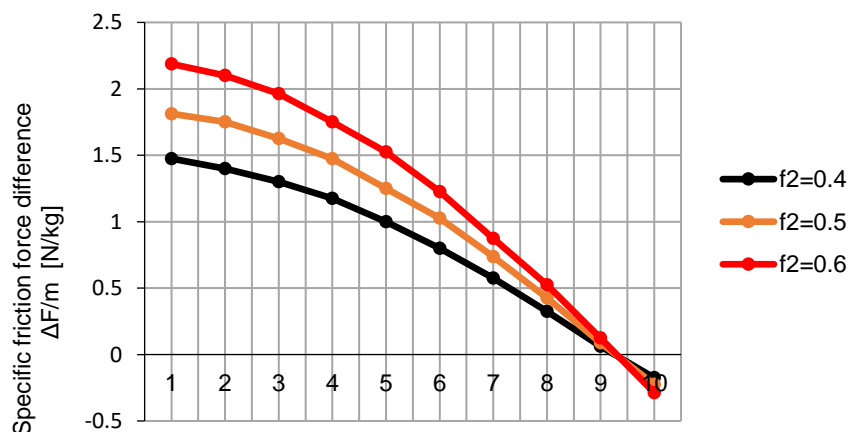


Fig. 3 – The diagram of dependency of friction forces of transported material at the cowl and screw surfaces on the angular rate of rotation of the screw at different friction coefficient f_2 values

Apart from affecting the advance of the material inside the extruder, the friction forces also affect the rate of heat generation within the extruded material (*Rauvendaal K., 2008*) as follows:

$$\dot{Q} = F_{tr} \cdot \Delta v \quad (9)$$

where:

\dot{Q} is the rate of heat generation [W/s];

F_{tr} - the force of friction [N];

Δv - the relative velocity of the transported material against the cylinder [m/s].

$$\Delta v = v_c \frac{\sin \alpha}{\sin(\theta + \alpha)} \quad (10)$$

where:

v_c is the annular velocity of the extruder's screw [m/s];

α - the elevation level of the screw section of the screw [rad];

θ - the solid material feed angle (the angle between the velocity vectors $\Delta \bar{v}$ and \bar{v}_c).

The annular velocity of the cylinder is

$$v_c = \omega_0 \frac{D_c}{2} \quad (11)$$

where:

ω_0 is the angular rate of the screw rotation [s^{-1}];

D_c is the screw cylinder diameter [m].

The solid material feed angle may be determined using the following formula:

$$\theta = \arcsin \left[\frac{(1+f_1^2-x^2)^{0.5}-f_1x}{1+f_1^2} \right] - \alpha \quad (12)$$

where:

$$x = \frac{H}{f_2 z} \ln \frac{P}{P_0} + \frac{f_1}{f_2} \left(1 + \frac{2H}{W} \right) \quad (13)$$

where:

H is the blade height [m];

z - the screw channel length [m];

P - the pressure at the considered point [Pa];

P_0 - the initial pressure at $z = 0$ [Pa];

W - the screw channel width [m].

All the heat generated under the action of friction forces within the solid material is transferred due to thermal conductivity and is distributed between the material itself, the cylinder walls and the screw (*Subbotin E.V., Trufanova N.M., Scherbinin A.G., 2012*).

The rate of thermal conduction within the material is described by the Fourier's law as follows:

$$\dot{Q}_z = -k_z A_z \frac{\partial T}{\partial z} \quad (14)$$

where:

\dot{Q}_z is the thermal flux (the rate of thermal conduction) [W/s];

k_z - the thermal conduction coefficient [W/m·C];

A_z - the area perpendicular to the flux [m^2]; $A_z = W \cdot H$; $\frac{\partial T}{\partial z}$ is the temperature gradient.

By equating the expressions (9) and (14) and after the reduction and translation this gives us the following:

$$\frac{\partial T}{\partial z} = - \frac{F_{tr} \omega_0 D_c \sin \alpha}{2k_z W H \sin(\theta + \alpha)} \quad (15)$$

The resulting expression makes it possible to estimate the variation of the temperature against the screw channel length.

Based on the equations (5) and (6) developed previously, we obtain the distribution of temperature within the area of contact of the material with the screw.

$$\frac{\partial T_a}{\partial z} = -\frac{m\omega_0 D_c \sin \alpha}{2k_z WH \sin(\theta+\alpha)} \left(g \cos \varepsilon + r\omega_0^2 - 2r\omega_0^2 \frac{\text{ctg } \alpha - f_1}{\text{ctg } \alpha + \text{tg } \alpha} \right) \frac{f_2 \cos \beta}{\cos \alpha + \sin \alpha} \quad (16)$$

as well as within the area of contact of the material with the cowling wall.

$$\frac{\partial T_c}{\partial z} = -\frac{m\omega_0 D_c \sin \alpha f_2}{2k_z WH \sin(\theta+\alpha)} \left(g \cos \varepsilon + r\omega_0^2 - 2r\omega_0^2 \frac{\text{ctg } \alpha - f_1}{\text{ctg } \alpha + \text{tg } \alpha} \right) \quad (17)$$

RESULTS AND DISCUSSION

The heat generation resulting from friction forces acting upon the material depends mainly on the weight of the compressed material *m*, traveltime parameters of the screw operation, geometrical parameters of the screw, the friction factors *f₁* and *f₂*, as well as the material’s thermal conduction coefficient *k_z*.

Let us make a graphical representation of the dependencies (16) and (17) (Fig. 4). The diagrams make it possible to conclude that the major part of temperature is generated due to the action of friction forces when the screw rate of rotation is $\omega_0 = 5 \text{ s}^{-1}$. Further increase of angular rate of rotation of the screw causes the temperature gradient to decrease since the amount of friction forces decreases.

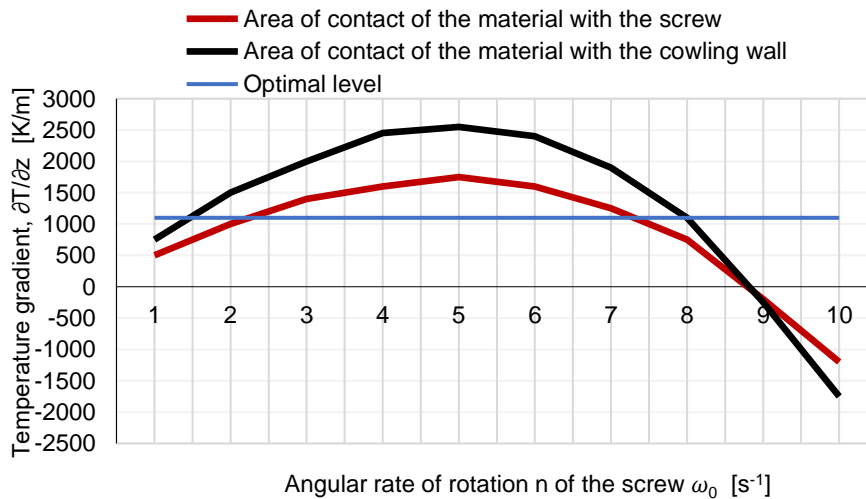


Fig. 4 – Diagram of temperature gradient change depending on the angular rate of rotation of the screw

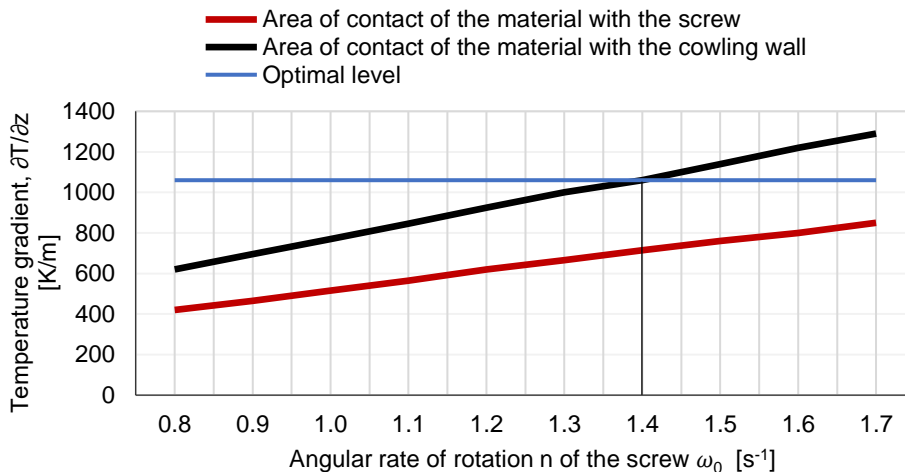


Fig. 5 – Diagram of temperature gradient change depending on the angular rate of rotation of the screw

Experimentally it was determined that when extruding lentils, the optimal temperature within the pre-die area was 105°C to 115°C. This conforms to the data of other experiments (Jiang, Q.H., Wu K., Sun Y., 2019; Orisaleye, J.I., Ojolo S.J., 2019). If the initial raw material temperature is assumed to be 20 °C, and the total length of the loading, transportation and compression (melting) areas is assumed to be 0.7*L*, where *L* is the length of the screw channel, then the optimal level of the temperature gradient is approximately 1080K/m.

At lower values of the gradient, the melting temperature within the pre-die area decreases, at higher values it increases resulting in product overheating. In both cases, maintenance of the optimal temperature regime requires additional heat supply or extraction, which is not effective.

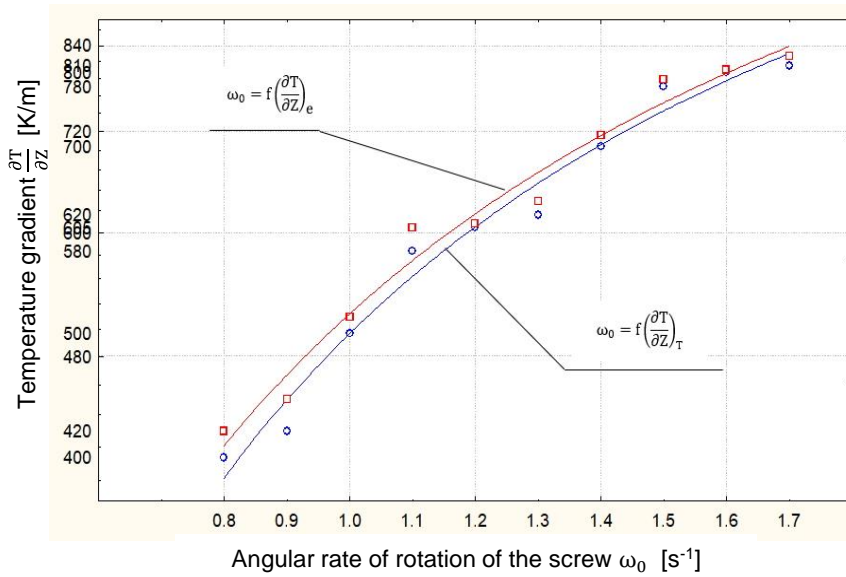


Fig. 6 – The diagram of dependency of the theoretical $\left[\left(\frac{\partial T}{\partial z}\right)_T\right]$ and experimental $\left[\left(\frac{\partial T}{\partial z}\right)_e\right]$ temperature gradients within the area of contact of the material with the screw with the angular rate of rotation of the screw

If we consider the resulting dependencies in more detail (Fig. 5), we will see that the optimal angular rate of rotation of the screw is approximately $\omega_0 \approx 1.4 \text{ s}^{-1}$. This conforms to the data obtained experimentally and the results of experiments conducted earlier.

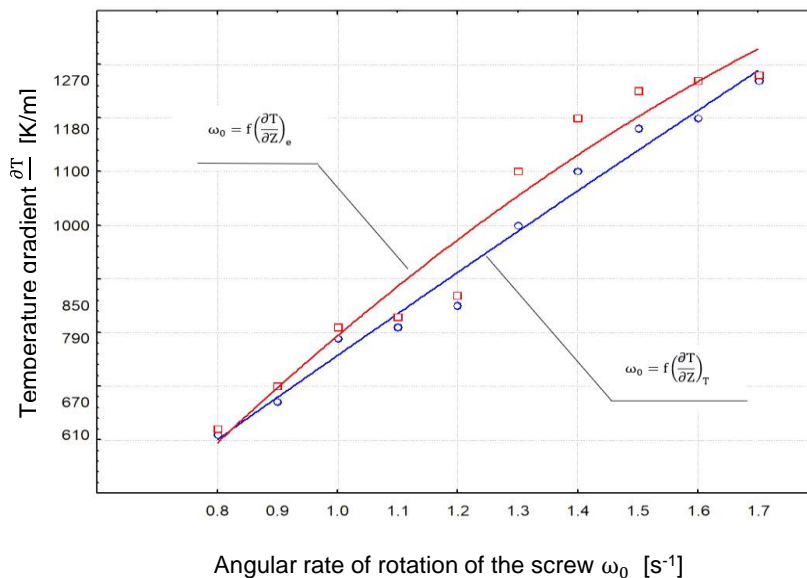


Fig. 7 – The diagram of dependency of the theoretical $\left[\left(\frac{\partial T}{\partial z}\right)_T\right]$ and experimental $\left[\left(\frac{\partial T}{\partial z}\right)_e\right]$ temperature gradients within the area of contact of the material with the cowling wall on the angular rate of rotation of the screw

CONCLUSIONS

To sum the above information up, optimal level of the temperature gradient is approximately 1080 K/m. At lower values of the gradient, the melting temperature within the pre-die area decreases, at higher values it increases resulting in product overheating. The optimal angular rate of rotation of the screw is approximately $\omega_0 \approx 1.4 \text{ s}^{-1}$. This is corroborated by the diagram shown in Figure 4 and Figure 5.

Conducted experiments showed good repeatability of theoretical and experimental data (the deviation amounted to no more than 3%). This is corroborated by the diagram shown in Figure 6 and Figure 7.

Also, as a result of the conducted studies, expressions were obtained that allow us to estimate the temperature distribution inside the screw channel with the specified basic parameters.

ACKNOWLEDGEMENTS

Consequently, the results of the study can be used when composing the heat balance equation in order to optimize the extrusion process and the operating parameters of the extruder itself.

REFERENCES

- [1] Adigamov K.A., Chernenko A.V., (2010), The effect of cowlng elevation angle on the performance of vertical screw conveyor (Влияние угла подъема ребра кожуха на производительность вертикального шнекового конвейера) *Fundamental and applied problems of machinery and processes Science and Technical Journal*, Issue number 2/3 (280), pp. 20–22, Eagle / Russia;
- [2] Barsukov V.G., Grakholskaya E.V., Volk O.S., (2009), The effect of the angle at the screw blade tip on extruder performance (Влияние угла при вершине гребня витка на работоспособность шнека экструдера), *Brest State Technical University Gazette. Ser. Mechanical Engineering*, Issue number 4(58), pp. 87–91, Brest / Belarus;
- [3] Bostandzhiyan S.A., Stolin A.M., (1965), Flow of Newtonian liquid between two parallel planes (Течение неньютоновской жидкости между двумя параллельными плоскостями), *Proceedings of AS of the USSR Mechanical Engineering*, Issue number 1, pp. 185–188, Moscow / Russia;
- [4] Didyk T.A., (2005), Reducing energy consumption of the extrusion process using screw extruder (Снижение энергетических затрат процесса экструдирования в шнековом пресс-экструдере) *FSEI HPE N. I. Vavilov Sraratov State Agricultural University*, Issue number 15(13), 13 p, Saratov / Russia;
- [5] Evstratova N.N., Apachanov A.S., Grigoryev V.I., (2009), A mathematical model of the process of movement of clay body within the screw channel of the screw press during ceramic brick manufacturing (Математическая модель процесса движения глиняной массы в винтовом канале шнекового пресса при производстве керамического кирпича), *News of higher educational institutions. The North Caucasus region. Technical sciences*, Issue number 5, pp. 85–88, Stavropol / Russia;
- [6] Helmig J., Behr M., Elgeti S., (2019), Boundary-conforming finite element methods for twin-screw extruders: Unsteady - temperature-dependent - non-Newtonian simulations. *Computers Fluids*. Vol. 190, pp. 322–336, Aachen / Germany;
- [7] Jiang, Q.H., Wu K., Sun Y., (2019), Modeling and analysis of pelletization process based on a multi-hole pelletizing device, *Int J Agric Biol Eng*, Issue number 4, pp. 17–23. Beijing / China;
- [8] Kryuchkova L.G., Dotsenko S.M., Burmaga A.V., Cheredov G.V., (2014), *Scientific bases for improving the efficiency of the processes of preparing and distributing feed mixtures to pigs (Научные основы повышения эффективности процессов приготовления и раздачи кормовых смесей свиньям)*, Monograph, *FGBOU VO FAR EASTERN GAU*, 275 p, Blagoveshchensk / Russia;
- [9] Kushnir V., Gavrilov N., Kim S., (2017), Experimental Studies on Grain Material Extruding Process. *Procedia Engineering*. Vol. 206, pp. 1611–1617, Kostanay / Kazakhstan;
- [10] Luo C., Wanga X., Miglerb K.B., Seppalab J.E. (2020), Effects of feed rates on temperature profiles and feed forces in material extrusion additive manufacturing. *Additive Manufacturing*, Vol. 35, 101361, Gaithersburg / USA;
- [11] Mikulionok I., Gavva O., Kryvoplias-Volodina L., (2018), Modeling of melting process in a single screw extruder for polymer processing, *Eastern-European Journal of Enterprise Technologies*, Issue number 5-92, pp. 4–11. Kharkiv / Ukraine;
- [12] Orisaleye, J.I., Ojolo S.J., (2019), Parametric analysis and design of straight screw extruder for solids compaction, *Journal of King Saud University - Engineering Sciences*, Issue number 31, pp. 86–96. Riyadh / Saudi Arabia;
- [13] Ostrikov A.N., Ospanov A.A., Vasilenko V.N., Muslimov N.Zh., Timurbekova A.K., Jumabekova G.B., (2019), Melt flow of biopolymer through the cavities of an extruder die: Mathematical modelling, *Mathematical Biosciences and Engineering*, Issue number 16, pp. 2875–2905. Arizona / USA;
- [14] Ostrikov A. N., Platov K. V., Sokolov I. Y., (2004), Study of the process of lentil stick extrusion (Исследование процесса экструзии чечевичных палочек), *Fundamental studies*, Issue number 4, pp. 55–56, Moscow / Russia;

- [15] Rauwendaal C., (2019), How an Extruder Works, *Understanding Extrusion*, Issue number 3, pp. 77–121 / USA;
- [16] Rauwendaal K., (2008), Polymer extrusion, (Экструзия полимеров), *Professiya*, 768 p., Saint-Petersburg / Russia;
- [17] Roland W., Marschik C., Krieger M., Löw-Baselli B., Miethlinger J., (2019), Symbolic regression models for predicting viscous dissipation of three-dimensional non-Newtonian flows in single-screw extruders, *Journal of Non-Newtonian Fluid Mechanics*, Issue number 268, pp.12–29, Liverpool / UK;
- [18] Sagirov. S.N., (2011), Study and simulation of the process of movement of polymer within a single-screw extruder (Исследование и моделирование процесса движения полимера в одношнековом экструдере), *Fundamental studies*, Issue number 12, pp. 179–183, Vladimir / Russia;
- [19] Subbotin E.V., Trufanova N. M., Scherbinin A. G., (2012), Computational study of flows of polymer liquids within the channel of a screw extruder based on the one- and bi-dimensional models (Численное исследование течений полимерных жидкостей в канале шнекового экструдера на основе одно- и двухмерных моделей), *Computational mechanics of continuous media*, Issue number 4, pp. 452–460, Perm / Russia;
- [20] Wang H., (2021), Construction and discrete processing of screw extruder based on three-dimensional spiral model. *Microprocessors and Microsystems*, Vol. 82. 103946. Liaoning / China;
- [21] Wu M., Sun C.H., Bi F., Ji B.R., Li J.J., (2018), Xing Effects of extrusion conditions on the physicochemical properties of soy protein/gluten composite, *International Journal of Agricultural and Biological Engineering*, Issue number 11, pp. 230–237, Beijing / China;
- [22] Zubkova T.M., Kolobov A.N., (2015), Optimization of geometrical parameters of extruder to manufacture products with predetermined quality characteristics (Оптимизация геометрических параметров экструдера для получения продукции с заданными показателями качества), *Orenburg State University Gazette*, Issue number 4(179), pp. 197–204, Orenburg / Russia.

EXPERIMENTAL STUDIES OF THE INTERACTION OF TRACTOR DRIVE WHEELS WITH THE SOIL IN THE PLOWED FIELD

ЕКСПЕРИМЕНТАЛЬНІ ДОСЛІДЖЕННЯ ВЗАЄМОДІЇ ПРИВОДНИХ КОЛІС ТРАКТОРА ІЗ ҐРУНТОМ НА ЗОРАНОМУ ПОЛІ

Gennadii Golub^{*1)}, Viacheslav Chuba¹⁾, Yaroslav Yarosh²⁾, Oleksandr Solarov³⁾, Nataliya Tsyvenkova^{1,2)}

¹⁾ National University of Life and Environmental Sciences of Ukraine / Ukraine;

²⁾ Polissia National University / Ukraine;

³⁾ Sumy National Agrarian University / Ukraine

Tel: +380953115050; E-mail: gagolub@ukr.net

DOI: <https://doi.org/10.356.33/inmateh-65-45>

Keywords: soil deformation, tire, the contact area of the wheel, support surface

ABSTRACT

The article defines the influence of structural and operational parameters of a machine-tractor unit on changes in the hardness of freshly plowed soil due to deformation and compaction of the soil by wheeled running systems. An experimental model of the effect of pressure in the pneumatic chamber of the wheel, working width, and speed of the unit on changes in soil hardness in the area of operation of running systems is obtained. The obtained mathematical models make it possible to reduce the negative impact on the soil by optimally completing, configuring, and selecting a machine-tractor unit operating mode.

РЕЗЮМЕ

У статті визначено вплив конструкційних та експлуатаційних параметрів машинно-тракторного агрегату на зміну твердості свіжозораного ґрунту внаслідок деформації та ущільнення ґрунту колісними ходовими системами. Отримано експериментальну модель впливу тиску в пневматичній камері колеса, ширини захвату та швидкості руху агрегату на зміну твердості ґрунту в зоні дії ходових систем. Отримані математичні моделі дозволяють зменшити негативний вплив на ґрунт ходових систем за рахунок оптимального комплектування, налаштування та вибору режиму роботи машинно-тракторного агрегату.

INTRODUCTION

In the context of the intensification of agricultural production, more and more attention is paid to the issues of soil conservation and reducing the negative impact on the environment (Jimenez et al., 2021; Usowicz et al., 2017). Current trends in Mechanical Engineering consist in increasing the productivity of machine-tractor units (MTU) by increasing the working width and increasing power. As a result of the action of running systems, deformation, compaction and changes in the porosity of the soil occur, the processes of air and moisture permeability are disrupted (Peth et al., 2010; De Lima et al., 2017). Under the influence of cyclic loads, there is a change in the soil structure (Pulido-Moncada et al., 2019) and a shift in soil layers (Huang et al., 2021), which has a more negative impact than deformation and compaction. As a result, the conditions for the development of plant root systems worsen (Nawaz et al., 2013; Batey, 2009), which leads to a decrease in crop productivity and yield (Mueller et al., 2010; Golub et al., 2019). Taking into account global trends, the issue of reducing soil degradation under the influence of running systems is an urgent task.

Most of the studies performed on the influence of contact interaction of running systems with the ground can be divided into two main areas. The first direction of this study is related to determining the influence of a certain factor of contact interaction of the wheel with the fertile soil layer. In (Carman, 2002; Taghavifar, H. et al., 2015), the influence of vertical load from tractor weight on the process of soil degradation is considered. The authors (Pulido-Moncada et al., 2019; De Pue et al., 2020) found out that as a result of the action of traction force the soil is destroyed in the horizontal direction. However, the process of changing the properties of the fertile soil layer cannot be limited to analyzing changes in the soil condition as a result of certain loads. In (Kurjenluoma et al., 2019; Carman, 2002; Vennik et al., 2019), diverse studies were performed to determine the structural parameters of tires and vertical loads on soil compaction, rolling resistance, and track formation.

One of the most important indicators of the interaction of the wheel with the soil is sliding (Mason et al., 2016; Gray et al 2016; Damanauskas, 2015), which directly affects the effective performance of MTU and leads to the destruction of the fertile soil layer. The data obtained as a result of such studies allows obtaining regression models suitable for modeling the influence of certain factors on the parameters of wheel interaction with the ground. These studies give a complete picture of the effect of a particular factor and the consequences that this factor entails. However, the practical application of such studies is limited by the fact that when the wheel interacts with the ground, all factors act in a complex way, affect each other and have certain relationships. In (Taghavifar, H. et al., 2015; Golub et al., 2017), the factors of contact interaction are combined on the basis of the effect on the traction power of the power tool. However, studies (Taghavifar, H. et al., 2015; Golub et al., 2017) do not fully take into account the parameters of the soil environment and their changes under the influence of loads.

The second area of research is related to the creation of mathematical models that allow linking the parameters of the soil environment and the parameters of contact interaction of running systems with the soil and are aimed at reducing the negative impact on the soil. In (Défossez et al., 2002; Smith et al., 2000), the soil is considered as a certain homogeneous elastic element. The use of such models for determining deformations and compaction of the soil is somewhat limited by the fact that the soil has a heterogeneous structure and the effect of contact loads exceed the elasticity of the soil. A number of analytical models of VTI (Vehicle Terrain Interface) have been developed to determine the indicators of soil deformation and track formation (Carman, 2002; Vahedifard et al., 2016; Golub et al., 2019). The use of analytical models requires a significant amount of experimental data on determining the parameters of the agrotechnological environment. There are a certain number of finite element models (FEM) (González Cueto et al., 2016; Silva et al., 2018) that take into account the contact interaction of running systems and allows determining soil deformations. However, most finite element models focus on determining the effect of soil environment properties on the stress distribution and deformation of the soil. The use of FEM models to take into account the design parameters of running systems and MTU operating modes requires the search for partial solutions to the interaction of the corresponding parameters and the determination of a certain number of initial parameters. The SoilFlex model (Keller et al., 2007) and the varieties obtained on its basis (Keller et al., 2015; Lozano et al., 2013) are most widely used for predicting soil deformations. These models allow combining the parameters of the contact interaction of the wheel with the soil, take into account the properties of the soil and allow determining the volume of the soil deformation in different directions. However, these models are not yet suitable for determining the optimal effective indicators and operating modes of the MTU.

The volume of research performed to date provides an understanding of the influence of various factors of contact interaction of running systems on the fertile soil layer. However, the obtained results do not make it possible to perform a comprehensive simulation of the impact of MTU running systems on the fertile soil layer and search for optimal driving modes. When modeling the impact of running systems, it is necessary to understand that the load-bearing capacity of the soil and its ability to deform significantly depends on the composition of structural elements, the content of substances, porosity and moisture of the soil.

The purpose of the research is to determine the relationship between the operational parameters of the MTU due to the settings of wheel running systems and their impact on the fertile soil layer. A freshly plowed soil layer was chosen as the soil medium for conducting experimental studies. In this phase, the soil is loosened as much as possible and is maximally exposed to the negative effects of running systems. The change in the forces of contact interaction of the wheel with the ground was modeled by a change in the pressure in the pneumatic chamber of the wheel, a change in the gripping width of the working unit, and a change in the speed of movement. These factors directly affect sliding, rut formation, and changes in soil parameters. This combination made it possible to determine the influence of the design and operational parameters of the MTU on the indicators of changes in the soil environment and determine the effective performance of the MTU.

MATERIALS AND METHODS

Studies of the effect of wheel thrusters on the fertile soil layer were performed using a multi-factor experiment according to the *D*-optimal Box-Behnken design for the three studied factors (Golub et al., 2018). The adequacy of the obtained regression equations was evaluated by the Fischer criterion. Statistical estimation of the level of variance of the obtained results was carried out according to the Cochran criterion for a 95% confidence probability level. The intervals of values and levels of variation of variable factors that were used in the research are shown in Table 1.

When performing experimental studies, a Kyi-14102 tractor with a total weight of 37.5 kN and a PRO-3 plow weighing 8.5 kN were used (Fig. 1, a, b). To determine the influence of the studied factors on changes in soil hardness, a rectangular section of the field with a length of 150 m and a width of 100 m was previously plowed to a depth of 30 cm.

Table 1

Intervals of values and variation levels of research factors

Name of the factors	Marking	Factor levels			Variation intervals
		-1	0	+1	
Driving speed, [km/h]	V_T	4.6	6.4	8.2	1.8
Pressure in the pneumatic chambers of the wheel, [atm]	P_P	1.4	1.8	2.2	0.4
Working width of the unit, [m]	L_U	0.35	0.70	1.05	0.35

The change in the traction resistance applied to the tractor was modeled by changing the width of the plow grip (the number of installed plow housings was changed). Before starting the research, the plow was set up so that all its housings were evenly buried by 30 cm when the tractor was moving on a horizontal surface. After setting the appropriate pressure in the pneumatic chambers of the wheels and adjusting the width of the plow grip, the tractor was driven through freshly plowed soil. The change in soil hardness was determined by measuring the taper index of the soil profile.

The taper index of the freshly plowed soil profile was measured using a DATAFIELD manual electronic penetrometer (Fig. 1, c), in the range of soil profile depth from zero to 30 cm in 25 mm increments. Measurement of the taper index in the track from the contact interaction of the wheel with the ground was carried out to a depth of 30 cm from the horizontal surface of the field.

Fuel consumption was measured by a portion fuel flow meter, which was connected to the tractor fuel system using two three-way cranes. Thanks to the parallel connection of the fuel flow meter in the fuel supply and return line from the high-pressure fuel pump, it was possible to instantly switch the engine power from the standard fuel supply system to the batch fuel flow meter.

Wheel slip was defined as the path that the wheel passes in one complete turn. To determine the amount of rotation, the wheel was divided into eight equal sectors, each of which had neodymium magnets placed on the wheel rim. A bracket with a reed switch connected to the pulse counter was installed on the tractor fender. During the passage of the control section of a given length, the number of pulses was measured, which made it possible to determine the actual path travelled by the wheel during the passage of the control section.

Using a measuring tool, the depth of the track was recorded after the tractor passed through. The experiments were performed in threefold repetition.



Fig. 1 - Equipment used in conducting experimental studies:

a – preparation of the field for conducting experimental studies; b – plow with a variable number of housings for modeling the tractor load; c – manual electronic penetrometer for measuring the taper index of the soil profile

To estimate the change in soil hardness after the tractor wheels passing, the soil hardness coefficient was applied, which was determined by the following expression:

$$k = \frac{\sum_{i=1}^n \frac{T_{Bi}}{n}}{\sum_{i=1}^m \frac{T_{Ai}}{m}} \text{ [rel. un.]} \quad (1)$$

where:

k_H – soil hardness coefficient, [rel. un.]; T_{Ai} – hardness of the soil profile of freshly plowed soil at the appropriate depth, [kPa], m – number of measurements of the hardness of a freshly plowed soil profile; T_{Bi} – hardness of the soil profile in the track at the appropriate depth, [kPa], n – number of soil profile hardness measurements in the track.

To determine the change in the hardness of the soil profile, a 5-fold measurement of the taper index in the track of the corresponding experiment was performed and its average value was determined.

RESULTS

As a result of mathematical processing of experimental research data, regression equations were obtained, which are given in table 2.

Table 2

Regression equations obtained as a result of mathematical processing of experimental data

Indicator name	Regression equation	Number
Soil profile hardness coefficient, k_H , [rel. un.]	$k_H = 8.06667 + 1.31061V_T + 1.38863P_P + 3.12633L_U + 0.563635V_T^2 - 0.53096P_P^2 - 0.16071L_U^2 - 0.02792V_T P_P - 0.14897V_T L_U - 0.125P_P L_U$	(1)
Track depth, h_k , [mm]	$h_k = 172.028 - 3.7158V_T - 108.2558P_P + 0.1072L_U + 0.8128V_T^2 + 38.2813P_P^2 - 0.0008L_U^2 - 0.5671V_T P_P + 0.0134V_T L_U + 0.1548P_P L_U$	(2)
Wheel sliding, δ , [rel. un.]	$\delta = 8.7787 - 0.0498V_T - 10.0464P_P + 0.0632L_U + 0.0175V_T^2 + 3.6279P_P^2 - 0.0003L_U^2 + 0.0152V_T P_P + 0.0011V_T L_U$	(3)
Fuel consumption, G , [kg/h]	$G = 21.0211 - 1.4247V_T - 19.0972P_P - 0.0993L_U + 0.1475V_T^2 + 5.5259P_P^2 + 0.0004L_U^2 + 0.3306V_T P_P + 0.0074V_T L_U + 0.0251P_P L_U$	(4)

A graphical interpretation of equations (1-4) is shown in Fig. 2-5.

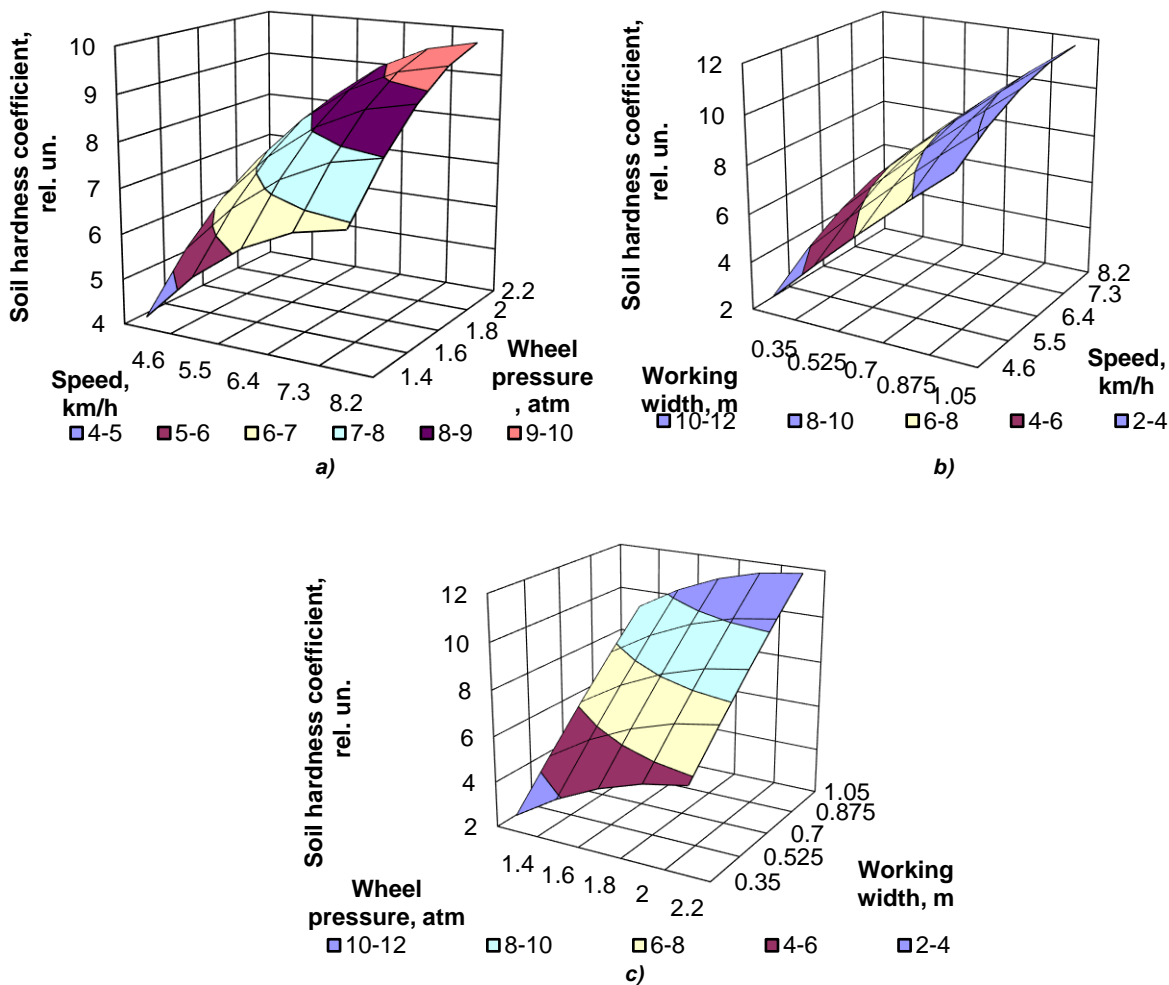


Fig. 2 - Graphical dependence of the soil hardness coefficient on:

- a - driving speed and pressure in the pneumatic chambers of the wheel with a working unit working width of 70 cm;
- b - driving speed and working width of the unit at a pressure in the pneumatic chambers of the wheel of 1.8 atm;
- c - pressure in the pneumatic chambers of the wheel and the working width of the unit at a speed of 6.4 km/h.

It should be noted that the value of the hardness coefficient of the soil profile after plowing in relation to the untilled field was 42.8. Based on the obtained data, it can be stated that the maximum soil hardness in the track after the tractor passes reaches almost 25% of the field hardness before plowing.

With a working width of a working unit of 0.7 m, the minimum value of the soil hardness coefficient is obtained at a speed of 4.6 km/h, and the pressure in the pneumatic chamber of the wheel is 1.4 atm, namely 4.273. Increasing the speed of the tractor to 8.2 km/h leads to an increase in the hardness coefficient by 61.3%. Pressure increase to 2.2 atm. at a speed of 8.2 km/h leads to the increase of the soil hardness coefficient by 40.3%. Changes in the speed of movement and pressure in the pneumatic chamber of the wheel have almost the same effect on the soil hardness coefficient, since the difference between the values of the change Δk_H is less than 6%.

At a pressure in the pneumatic chamber of the wheel of 1.8 atm, the minimum value of the soil hardness coefficient is obtained with a working unit working width of 0.35 m and a driving speed of 4.6 km/h, namely 2.756. Increasing the tractor speed to 8.2 km/h leads to a 106% increase in the hardness coefficient. Increasing the working unit working width to 1.05 m at a speed of 8.2 km/h increases the soil hardness coefficient by 105%. A change in the working width (an increase in traction resistance) has a more significant effect on soil compaction than the speed of movement, since the difference between the values of the change Δk_H is about 124.4%.

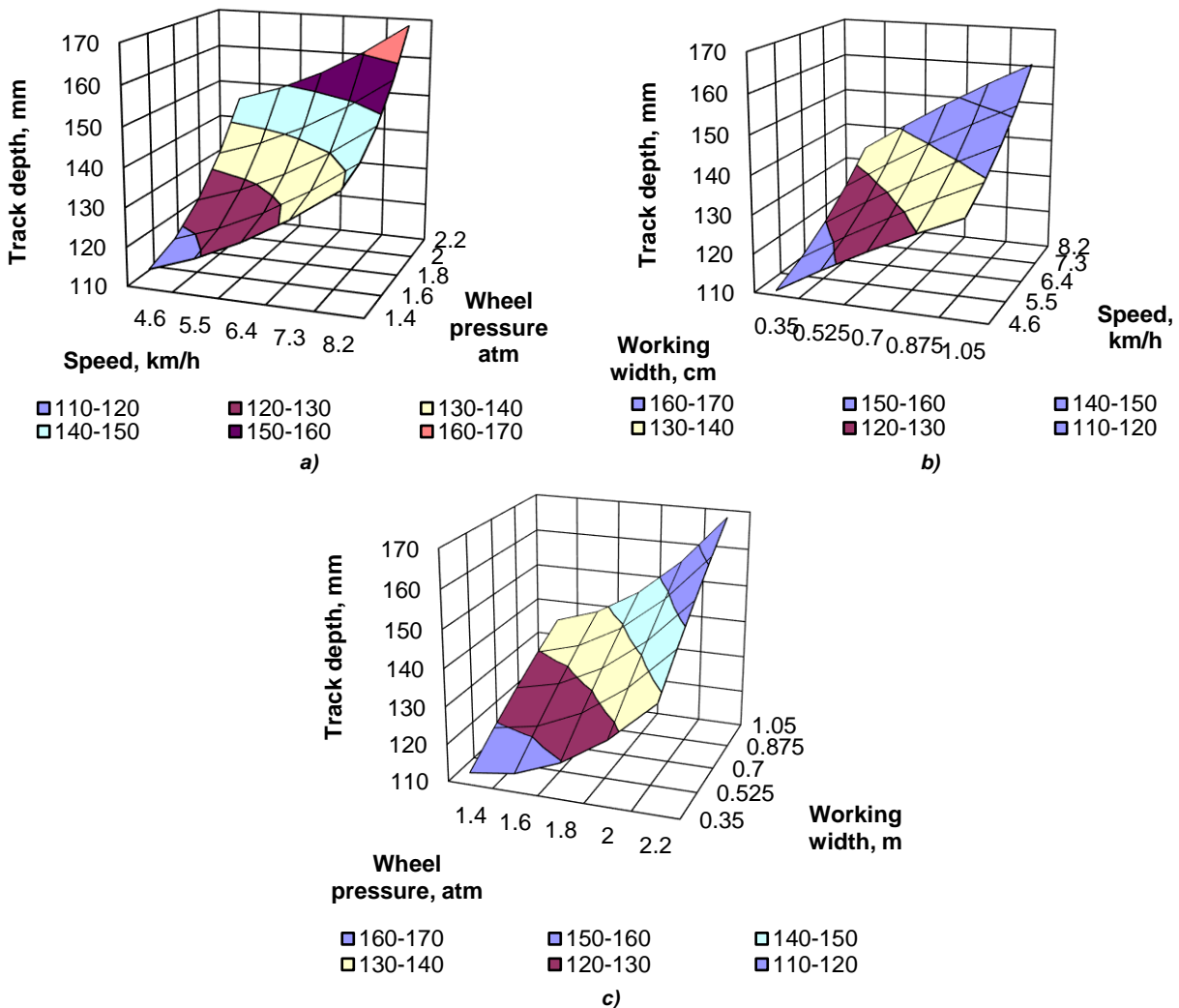


Fig. 3 - Graphical dependence of the track depth on:

- a - driving speed and pressure in the pneumatic chambers of the wheel with a working unit working width of 70 cm;
- b - driving speed and working width of the unit at a pressure in the pneumatic chambers of the wheel of 1.8 atm;
- c - pressure in the pneumatic chambers of the wheel and the working width of the unit at a speed of 6.4 km/h.

At a tractor speed of 6.4 km/h, the minimum value of the soil hardness coefficient is obtained with a working unit working width of 0.35 m and a pressure in the pneumatic chamber of 1.4 atm, namely 2.735.

An increase in the pressure in the pneumatic chamber to 2.2 atm leads to an increase in the hardness coefficient by 110.7%. Increasing the working unit working width to 1.05 m at a pressure in the pneumatic chamber of 2.2 atm leads to an increase in the soil hardness coefficient by 104.2%. A change in the working width (an increase in traction resistance) has a more significant effect on soil compaction than the pressure in the pneumatic chamber of the wheel, since the difference between the values of the change Δk_H is about 114.8%.

In the studied range, the simultaneous action of the maximum values of parameters in comparison with the minimum values for the pressure in the pneumatic chamber and the speed of movement leads to an increase of 126.3% in the coefficient of soil hardness, working width and speed of movement – by 322%, working width and pressure in the pneumatic chamber – by 330%. The obtained data show that the traction force that the tractor implements when performing a technological operation has a significant impact on soil compaction and changes its hardness. It should also be noted that an important factor affecting the compaction of soil and changes in its hardness is the area of contact interaction of the wheel with the soil, which disproportionately changes with changes in pressure in the pneumatic chamber.

With a working unit working width of 0.7 m, the minimum track depth value is obtained at a driving speed of 4.6 km/h. and the pressure in the pneumatic chamber of the wheel is 1.4 atm, namely 115 mm. Increasing the tractor speed to 8.2 km/h increases the track depth by 21.7%. Increasing the pressure in the pneumatic chamber of the wheel to 2.2 atm at a speed of 8.2 km/h leads to an increase in the track depth by 20.7%. The pressure in the pneumatic chamber of the wheel has a slightly greater effect on the formation of the track than the change in the speed of movement, since the difference between the values of the change Δh_K is about 20%.

At a pressure in the pneumatic chamber of the wheel of 1.8 atm, the minimum value of the track depth is obtained with a working unit working width of 0.35 m and a driving speed of 4.6 km/h, namely 111 mm. Increasing the tractor speed to 8.2 km/h results in a 19.8% increase in track depth. Increasing the working unit working width to 1.05 m at a speed of 8.2 km/h increases the track depth by 20.3%. Changes in the operating width (an increase in traction resistance) and the speed of movement affect the formation of the track to almost the same extent, since the difference between the values of the change Δh_K is about 9%.

At a tractor speed of 6.4 km/h, the minimum track depth value is obtained with a working unit working width of 0.35 m and the pressure in the pneumatic chamber of 1.4 atm, namely 113 mm. An increase in the pressure in the pneumatic chamber to 2.2 atm leads to an increase in the track depth by 22%. Increasing the working unit working width to 1.05 m at a pressure in the pneumatic chamber of 2.2 atm leads to an increase in the track depth by 21.7%. The change in pressure in the pneumatic chamber of the wheel has a slightly greater effect on the formation of the track than the working width (increase in traction resistance), since the difference between the values of the change Δh_K is about 19%.

In the studied range, the simultaneous action of the maximum values of parameters in comparison with the minimum values for the pressure in the pneumatic chamber and the speed of movement leads to an increase in the track depth by 46.1%, the working width and speed of movement – by 44%, the working width and pressure in the pneumatic chamber – by 32.7%.

The obtained patterns show that the pressure in the pneumatic chamber of the wheel has a slightly greater effect on the formation of the track than changes in the working width and the speed of movement. An increase in the track depth with an increase in pressure in the pneumatic chamber of the wheel is associated with a decrease in the area of the contact spot of the wheel with the ground and, as a result, an increase in the contact load. An increase in the speed of movement and the working width leads to an increase in the traction resistance of the working unit, which in turn leads to an increase in traction forces in the contact zone of the wheel with the ground and, as a result, an increase in soil deformation occurs.

With a working unit working width of 0.7 m, the minimum wheel sliding value is obtained at a speed of 4.6 km/h. and the pressure in the pneumatic chamber of the wheel is 1.4 atm, namely 5.32%. Increasing the speed of the tractor to 8.2 km/h leads to an increase in wheel sliding by 18.5%. Increasing the pressure in the pneumatic chamber of the wheel to 2.2 atm at a speed of 8.2 km/h leads to an increase in wheel sliding by 39.8%. The change in pressure in the pneumatic chamber of the wheel has a greater impact on the change in wheel sliding than the speed of movement, since the difference between the values of change $\Delta \delta$ is about 60.5%.

At a pressure in the pneumatic chamber of the wheel of 1.8 atm, the minimum value of wheel sliding was obtained with a working unit working width of 0.35 m and a driving speed of 4.6 km/h, namely 4.73%. Increasing the speed of the tractor to 8.2 km/h leads to an increase in wheel sliding by 18.39%. Increasing the working unit working width to 1.05 m at a speed of 8.2 km/h results in a 35.77% increase in wheel sliding. A change in the working width (an increase in traction resistance) affects the change in the wheel sliding index to a greater extent than a change in speed, since the difference between the values of the change $\Delta\delta$ is 130.95 %.

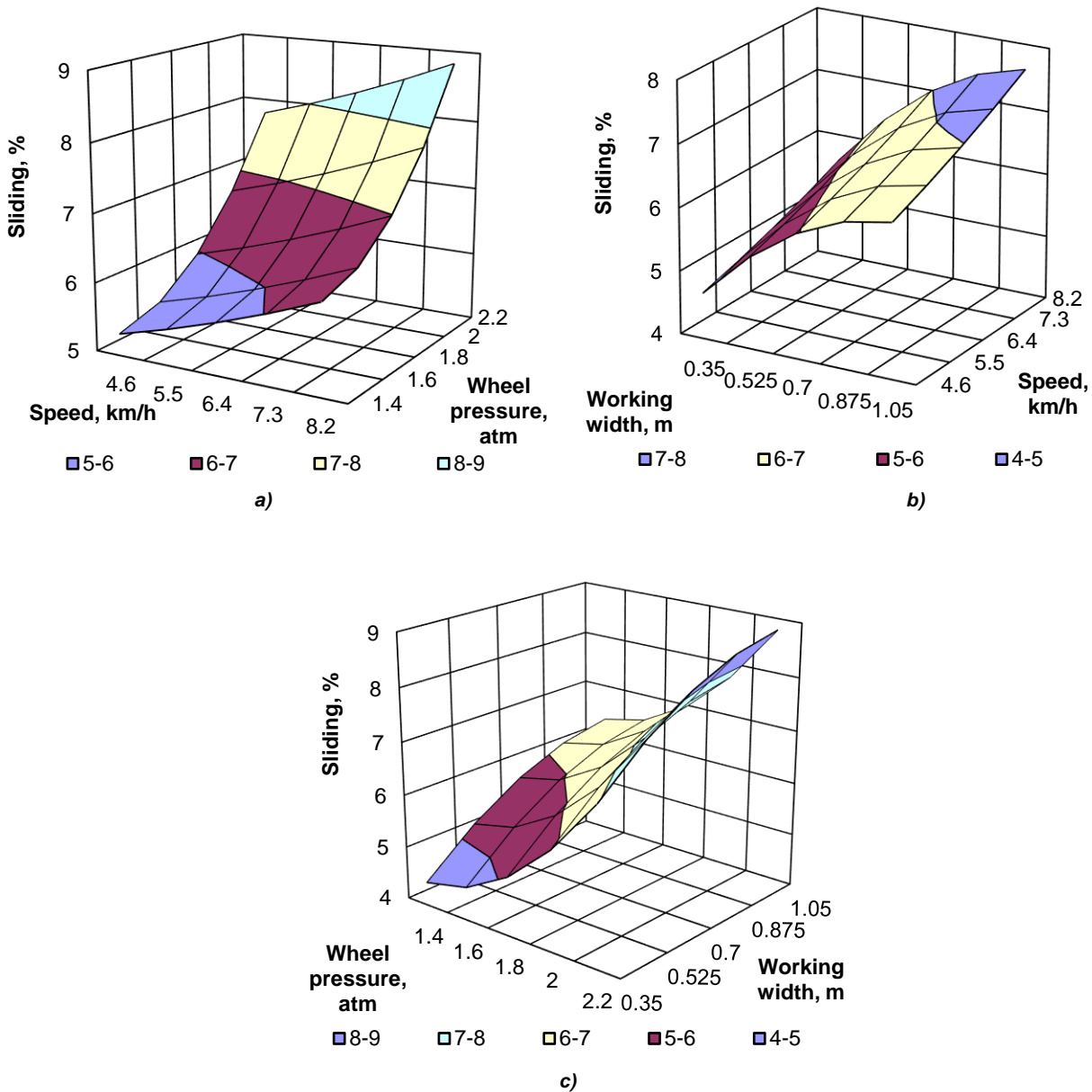


Fig. 4 - Graphical dependence of wheel sliding on:

- a - driving speed and pressure in the pneumatic chambers of the wheel with a working unit working width of 70 cm;
- b - driving speed and working width of the unit at a pressure in the pneumatic chambers of the wheel of 1.8 atm;
- c - pressure in the pneumatic chambers of the wheel and the working width of the unit at a speed of 6.4 km/h.

At a tractor speed of 6.4 km/h, the minimum wheel sliding value is obtained with a working unit working width of 0.35 m and the pressure in the pneumatic chamber of 1.4 atm, namely 4.43%. An increase in the pressure in the pneumatic chamber to 2.2 atm leads to an increase in wheel sliding by 56.02%. Increasing the working unit working width to 1.05 m at a pressure in the pneumatic chamber of 2.2 atm leads to an increase in wheel sliding by 41.82%. The change in pressure in the pneumatic chamber of the wheel has a slightly greater effect on the sliding of the wheels than the working width (increase in traction resistance), the difference between the values of the change $\Delta\delta$ is about 33.91%.

In the studied range, the simultaneous action of the maximum values of parameters in comparison with the minimum values for the pressure in the pneumatic chamber and the speed of movement leads to an increase in wheel sliding by 60.51%, the working width and speed of movement – by 60.74%, the working width and pressure in the pneumatic chamber – by 97.86%. When the pressure in the pneumatic chamber of the tire increases, the contact area of the wheel with the ground decreases, which leads to an increase in the amount of contact forces on the support surface. As a result of increasing contact forces, there is an increase in the process of ground deformations in the longitudinal direction, and as a result, there is an increase in wheel sliding. An increase in the working unit working width, as well as the driving speed, leads to an increase in traction power, realization of which must be provided by the driving wheels. As a result of increasing the traction power, the amount of contact forces in the contact zone of the wheel with the ground increases. As a result, the load on the ground increases, its deformation increases, and the volume of wheel sliding increases.

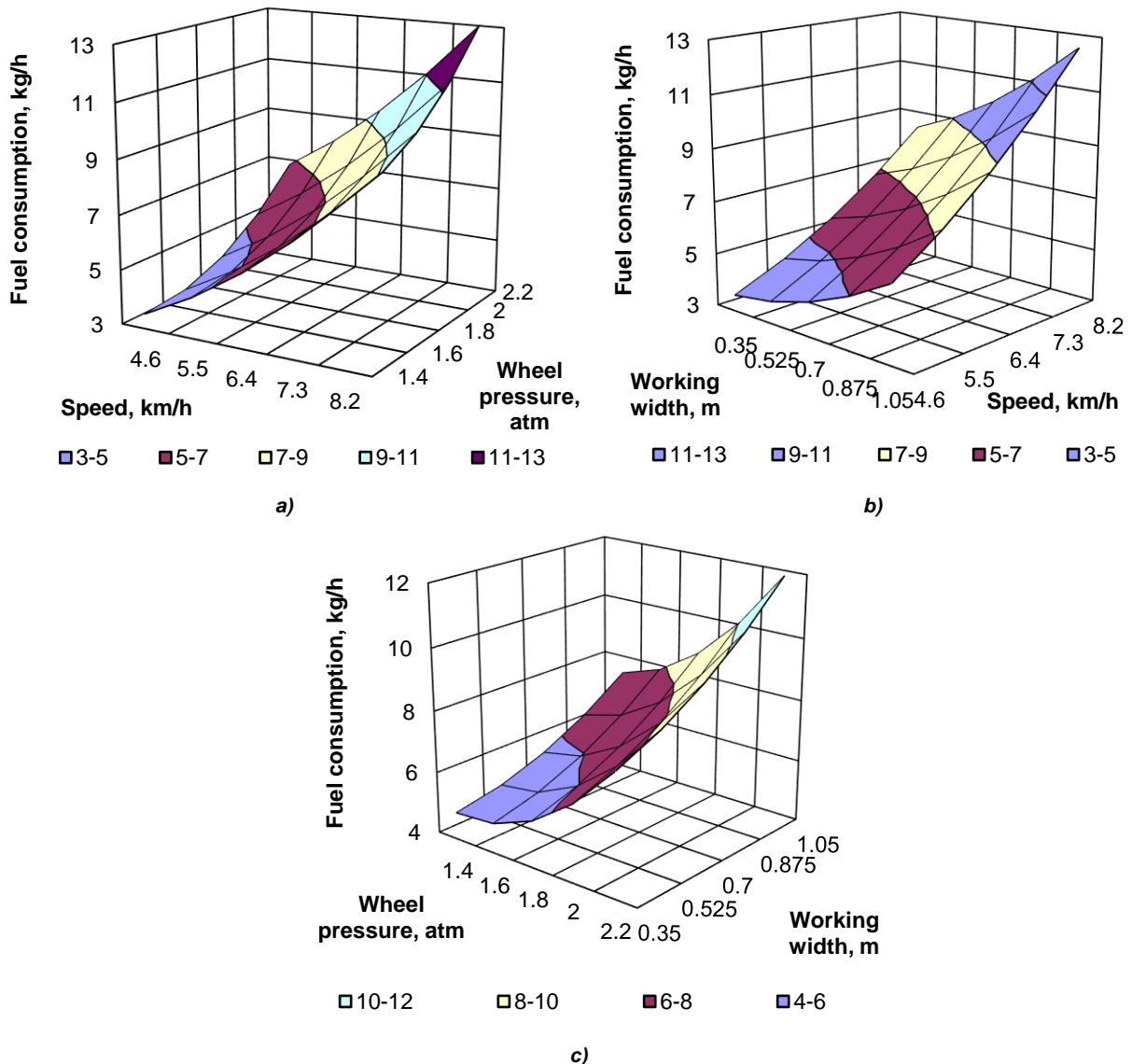


Fig. 5 - Graphical dependence of fuel consumption on:

- a - driving speed and pressure in the pneumatic chambers of the wheel with a working unit working width of 70 cm;
- b - driving speed and working width of the unit at a pressure in the pneumatic chambers of the wheel of 1.8 atm;
- c - pressure in the pneumatic chambers of the wheel and the working width of the unit at a speed of 6.4 km/h.

With a working unit working width of 0.7 m, the minimum fuel consumption value is obtained at a speed of 4.6 km/h. and the pressure in the pneumatic chamber of the wheel is 1.4 atm, namely 3.552 kg/h. Increasing the tractor speed to 8.2 km/h results in a 146.37% increase in fuel consumption. Increasing the pressure in the pneumatic chamber of the wheel to 2.2 atm at a speed of 8.2 km/h leads to an increase in fuel consumption by 48.12%.

A change in driving speed has a greater impact on the change in fuel consumption than the pressure in the pneumatic chamber of the wheel, since the difference between the values of the change ΔG is about 59.5%.

At a pressure in the pneumatic chamber of the wheel of 1.8 atm, the minimum fuel consumption value is obtained with a working unit working width of 0.35 m and a driving speed of 4.6 km/h, namely 3.614 kg/h. Increasing the tractor speed to 8.2 km/h results in a 131.22% increase in fuel consumption. Increasing the working unit working width to 1.05 m at a speed of 8.2 km/h results in a 49.78% increase in fuel consumption. A change in driving speed affects the change in fuel consumption to a greater extent than the working width (an increase in traction resistance), since the difference between the values of the change ΔG is 130.95%.

At a tractor speed of 6.4 km/h, the minimum fuel consumption value is obtained with a working unit working width of 0.35 m and a pressure in the pneumatic chamber of 1.4 atm, namely 4.875 kg/h. An increase in the pressure in the pneumatic chamber to 2.2 atm leads to an increase in fuel consumption by 62.21%. Increasing the working unit working width to 1.05 m at a pressure in the pneumatic chamber of 2.2 atm leads to an increase in fuel consumption by 49.68%. The change in pressure in the pneumatic chamber of the wheel has a slightly greater impact on fuel consumption than the working width (increase in traction resistance), the difference between the values of the change ΔG is about 29.54%.

In the studied range, the simultaneous action of the maximum values of parameters in comparison with the minimum values for the pressure in the pneumatic chamber and the speed of movement leads to an increase in fuel consumption by 264.93%, the working width and speed of movement – by 246.29%, the working width and pressure in the pneumatic chamber – by 330.16%. An increase in the speed of the tractor and the working unit working width leads to an increase in the forces of resistance to movement of the working unit and rolling resistances. Therefore, increasing the speed and working width of the working unit requires an increase in traction power, which leads to an increase in fuel consumption. The increase in fuel consumption with increasing pressure in the pneumatic chamber of the wheel is due to an increase in rolling resistance associated with an increase in track depth and an increase in tractor wheel sliding.

CONCLUSIONS

✓ The conducted studies have shown that in the process of compaction of the soil by running systems, the intensity of changes in soil hardness gradually decreases due to the fact that it is necessary to spend more effort to change the hardness of more compacted soil. It should be noted that a decrease in the soil hardness coefficient due to a decrease in pressure in pneumatic chambers practically corresponds to a decrease in the soil hardness coefficient obtained by reducing the speed.

✓ Experimental studies for the given intervals of variable factors have shown that changes in the speed of movement and the width of the working unit have almost the same effect on the formation of the track. Based on the obtained results of track formation and taking into account the influence of the studied factors on the productivity of the tractor, it is advisable to increase the area of contact of the running systems with the ground and increase the working unit working width.

✓ The results of these studies allow stating that the sliding of wheels largely depends on the parameters of the contact interaction of the wheel with the ground. A significant influence on the sliding of the wheels is played by the size of the contact zone of the wheel with the ground, as well as the traction power that the driving wheels realize. It is these two parameters that affect the amount of contact interaction of the wheel with the soil environment. An increase in the forces of contact interaction leads to an increase in the deformation that the ground undergoes and, as a result, there is an increase in the driving wheels sliding.

✓ Analysis of changes in fuel consumption when working on decompressed soil, for the specified intervals of the studied factors, indicates the feasibility of operating the tractor at low pressures in pneumatic chambers. In order to fully utilize the traction power of the tractor and increase the productivity of its operation, it is more advisable to use an increase in the working unit working width than an increase in the speed of movement.

REFERENCES

- [1] Batey, T. (2009). Soil compaction and soil management - a review. *Soil Use and Management*, 25, 335–345. <https://doi.org/10.1111/j.1475-2743.2009.00236.x>
- [2] Carman, K. (2002). Compaction characteristics of towed wheels on clay loam in a soil bin. *Soil Till Res.*, 65 (1), 37–43. [https://doi.org/10.1016/S0167-1987\(01\)00281-1](https://doi.org/10.1016/S0167-1987(01)00281-1)

- [3] Damanauskas, V. (2015). Algirdas Janulevičius, Differences in tractor performance parameters between single-wheel 4WD and dual-wheel 2WD driving systems. *In Journal of Terramechanics*, 60, 63–73. <https://doi.org/10.1016/j.jterra.2015.06.001>.
- [4] De Lima, R. P., da Silva, A. P., Giarola, N. F. B. da Silva, A. R. & Rolim, M. M. (2017). Changes in soil compaction indicators in response to agricultural field traffic. *Biosystems Engineering*, 62, 1–10, United States. <https://doi.org/10.1016/j.biosystemseng.2017.07.002>
- [5] De Pue, J., Lamandé, M. & Cornelis W.M. (2020). DEM simulation of stress transmission under agricultural traffic Part 2: Shear stress at the tire-soil interface. *Soil and Tillage Research*, 203. <https://doi.org/10.1016/j.still.2020.104660>
- [6] Défossez, P. & Richard, G. (2002). Models of soil compaction due to traffic and their evaluation. *Soil Till Res.*, 67, 41–64. [https://doi.org/10.1016/S0167-1987\(02\)00030-2](https://doi.org/10.1016/S0167-1987(02)00030-2)
- [7] Golub G.A., Kukharets S.M., Tsyvenkova N.M., Golubenko A.A. & Kalenichenko P.S. (2018). Research on a boiler furnace module effectiveness working on small fracture wastes. *INMATEH-Agricultural Engineering*, 55 (2), 9–18.
- [8] Golub, G., Chuba, V. & Kukharets, S. (2017). Determining the magnitude of traction force on the axes of drive wheels of self-propelled machines. *Eastern European Journal of Enterprise Technologies*, 4 (7), 50–56. <https://doi.org/10.15587/1729-4061.2017.107192>
- [9] Golub, G.A., Chuba, V.V., Kukharets, S.M., Yarosh, Y.D., & Tsyvenkova, N. (2019). Calculation of a track formation process during wheel-ground interaction. *INMATEH - Agricultural Engineering*, 59 (3), 69–76.
- [10] González Cueto, O., Iglesias Coronel, C.E., López Bravo, E., Recarey Morfa, C.A. & Herrera Suárez, M. (2016). Modelling in FEM the soil pressures distribution caused by a tire on a Rhodic Ferralsol soil. *Journal of Terramechanics* 63, 61–67. <https://doi.org/10.1016/j.jterra.2015.09.003>
- [11] Gray, J.P., Vantsevich, V.V. & Paldan, J. (2016) Agile tire slippage dynamics for radical enhancement of vehicle mobility. *Journal of Terramechanics*, 65, 14–37. <https://doi.org/10.1016/j.jterra.2016.01.002>
- [12] Huang, X., Horn, R., & Ren, T. (2021). Deformation and pore water pressure change during static and cyclic loading with subsequent shearing on soils with different textures and matric potentials. *Soil and Tillage Research*, 209. <https://doi.org/10.1016/j.still.2020.104909>
- [13] Jimenez, K.J., Rolim, M.M., de Lima, R.P., Cavalcanti, R.Q., Silva, Ê. F. F. & Pedrosa, E. M. R. (2021). Soil Physical Indicators of a Sugarcane Field Subjected to Successive Mechanized Harvests. *Sugar Tech* 23, 811–818. <https://doi.org/10.1007/s12355-020-00916-w>
- [14] Keller, T., da Silva, A.P., Tormena, C.A., Giarola, N.F.B., Cavalieri, K.M.V., Stettler, M. & Arvidsson, J. (2015). SoilFlex-LLWR: Linking a soil compaction model with the least limiting water range concept. *Soil Use and Management*, 31(2), 321–329. <https://doi.org/10.1111/sum.12175>
- [15] Keller, T., Défossez, P., Weisskopf, P., Arvidsson, J. & Richard, G. (2007). SoilFlex: A model for prediction of soil stresses and soil compaction due to agricultural field traffic including a synthesis of analytical approaches. *Soil and Tillage Research*, 93(2), 391–411. <https://doi.org/10.1016/j.still.2006.05.012>
- [16] Kurjenluoma, J., Alakukku, L. & Ahokas, J. (2009). Rolling resistance and rut formation by implement tires on tilled clay soil. *Journal of Terramechanics*, 46(6), 267–275. <https://doi.org/10.1016/j.jterra.2009.07.002>
- [17] Lozano, N., Rolim, M.M., Oliveira, V.S., Tavares, U.E. & Pedrosa, E.M.R. (2013). Evaluation of soil compaction by modeling field vehicle traffic with SoilFlex during sugarcane harvest. *Soil & Tillage Research*, 129, 61–68. <https://doi.org/10.1016/j.still.2013.01.010>
- [18] Mason, G. L., Vahedifard, F., Robinson, J. D., Howard, I. L., McKinley, G. B. & Priddy, J. D. (2016). Improved Sinkage Algorithms for Powered and Unpowered Wheeled Vehicles Operating on Sand. *Journal of Terramechanics*, 67, 25–36. <https://doi.org/10.1016/j.jterra.2016.07.001>
- [19] Mueller, L., Schindler, U., Mirschel, W., Shepherd, T. G., Ball, B. C., Helming, K., Rogasik, J., Eulenstein, F. & Wiggering, H. (2010). Assessing the productivity function of soils: a review. *Agronomy for sustainable development*, 30 (3), 601–614, France <https://doi.org/10.1051/agro/2009057>
- [20] Nawaz, M.F., Bourrié, G. & Trolard, F. (2013) Soil compaction impact and modelling. A review. *Agronomy for Sustainable Development*, 33 (2), 291–309. <https://doi.org/10.1007/s13593-011-0071-8>
- [21] Peth, S., Rostek, J., Zink, A., Mordhorst, A., & Horn, R. (2010). Soil testing of dynamic deformation processes of arable soils. *Soil and Tillage Research*, 106(2), 317–328. <https://doi.org/10.1016/j.still.2009.10.007>

- [22] Pulido-Moncada, M., Munkholm, L. J. & Schjønning P. (2019). Wheel load, repeated wheeling, and traction effects on subsoil compaction in northern Europe. *Soil and Tillage Research*, 186, 300–309. <https://doi.org/10.1016/j.still.2018.11.005>
- [23] Silva, R.P., Rolima, M.M., Gomes, I.F., Pedrosa, E.M.R., Tavares, U.E. & Santos, A.N. (2018) Numerical modeling of soil compaction in a sugarcane crop using the finite element method. *Soil & Tillage Research*, 181, 1–10. <https://doi.org/10.1016/j.still.2018.03.019>
- [24] Smith, R., Ellies, A. & Horn, R. (2000). Modified Boussinesq's equations for nonuniform tire loading. *In Journal of Terramechanics*, 37 (4), 207–222. [https://doi.org/10.1016/S0022-4898\(00\)00007-0](https://doi.org/10.1016/S0022-4898(00)00007-0)
- [25] Taghavifar, H. & Mardani, A. (2015). Net traction of a driven wheel affected by slippage, velocity and wheel load. *Journal of the Saudi Society of Agricultural Sciences*, 14 (2), 167–171. <https://doi.org/10.1016/j.jssas.2013.11.002>
- [26] Usowicz, B. & Lipiec J. (2017). Spatial variability of soil properties and cereal yield in a cultivated field on sandy soil. *Soil and Tillage Research*, 174, 241–250. <https://doi.org/10.1016/j.still.2017.07.015>
- [27] Vahedifard, F., Robinson, J.D., Mason, G.L., Howard, I.L. & Priddy, J.D. (2016). Mobility algorithm evaluation using a consolidated database developed for wheeled vehicles operating on dry sands. *Journal of Terramechanics*, 63, 13–22. <https://doi.org/10.1016/j.jterra.2015.10.002>
- [28] Vennik, K., Kukk, P., Krestein, K., Reintam, E. & Keller, T. (2019) Measurements and simulations of rut depth due to single and multiple passes of a military vehicle on different soil types. *Soil and Tillage Research*, 186, 120–127. <https://doi.org/10.1016/j.still.2018.10.011>

CREEP PROPERTIES AND PREDICTION MODEL OF PADDY SOIL UNDER COMPRESSION

/ 水稻土受压蠕变特性及预测模型构建

Guoyang Liu¹⁾, Junfang Xia^{1,2)}, Kan Zheng^{*1,2)}, Jian Cheng¹⁾, Liu Jiang¹⁾, Liwei Guo¹⁾

¹⁾ College of Engineering, Huazhong Agricultural University, Wuhan 430070 / China

²⁾ Key Laboratory of Agricultural Equipment in Mid-lower Reaches of Yangtze River, Ministry of Agriculture and Rural Affairs, Wuhan 430070 / China

Tel: +86 15271890761; E-mail: zhengkan@mail.hzau.edu.cn

DOI: <https://doi.org/10.356.33/inmateh-65-46>

Keywords: constitutive equation; stress level; creep model; viscoplasticity; strain; paddy soil

ABSTRACT

In order to study the compressive creep properties and laws of paddy soil, multi-stress creep experiments of paddy soil with different moisture content were carried out. The results show that the creep deformation of paddy soil, subjected to compressive loads effect, develops stably and the paddy soil is not destructed under the yield strength when the stress is low. When the stress level is higher than the yield strength, the internal damage of paddy soil would be caused at the moment of loading. With the extension of creep time, the cracks would gradually expand, resulting in the soil to yield, break and disintegrate. According to the analysis of the deformation properties of paddy soil under compression and the change trend of creep curve, the nonlinear viscoelastic-plastic model was composed of the nonlinear viscoplastic model and Burgers model in series. The creep test curve was introduced into the model for fitting, and the coefficient of determination reached more than 0.96. Based on the model, the strain composition, strain proportion, and strain rate of paddy soil were studied. Finally, the nonlinear model was compared with Burgers model by verification test. The fitting accuracy of the nonlinear model was better than Burgers model, and the coefficient of determination and relative error were 0.997 and 0.437%, respectively, which proved the rationality and correctness of the nonlinear viscoelastic-plastic model. This study can provide a theoretical basis for the optimization of tillage machinery structure and the simulation analysis of soil tillage and compaction.

摘要

为研究水稻土受压蠕变性能，探究其蠕变规律，以不同含水率的水稻土为试验对象进行多应力蠕变试验。试验结果表明水稻土在持续受压载荷作用下，应力水平较低时，蠕变变形发展稳定，不会发生失效破坏；应力水平大于屈服强度时，加载瞬间就会导致土壤内部损伤，随着蠕变时间延长，裂纹逐渐扩展致使土壤受压屈服破坏解体。通过分析水稻土受压变形特征和蠕变曲线变化趋势，将非线性黏塑性模型与 Burgers 模型串联组成非线性黏弹塑性模型，并将蠕变试验曲线引入该模型进行拟合，决定系数均达到 0.96 以上。基于推导的模型探究了水稻土受压蠕变各应变组成、应变占比以及应变速率规律，最后通过验证试验将该非线性模型与 Burgers 模型进行对比，结果表明非线性模型拟合精度优于 Burgers 模型，其决定系数和相对误差分别为 0.997、0.437%，证实了所建立的非线性黏弹塑性模型的合理性与正确性。本研究可为耕作机械结构优化及土壤耕作、压实等相关仿真分析提供理论依据。

INTRODUCTION

Soil is the main operation object for tillage machinery (Romaneckas, & Jasinskas, 2017). Due to the complexity of soil physical composition (Schmalz et al., 2013), dynamic factors of tillage machinery (Zeng, Chen, & Zhang, 2017), and adhesion of soil particles (Wang et al., 2019), the tillage process is very complicated. As a kind of complex rheological body, soil rheology presents the properties of deformation and flow under the action of external force. Therefore, soil rheology is essential in the research and development of tillage machinery and formulation of agronomy. The results of such can provide some new ideas for optimal design of tillage machinery with the aim to reduce resistance and traction performance improvement.

¹ Guoyang Liu, Ph.D. Stud. Eng.; Junfang Xia, Prof. Ph.D.; Kang Zheng, Lec. Ph.D. Eng.; Jian Cheng, M.S. Stud. Eng.; Liu Jiang, M.S. Stud. Eng.; Liwei Guo, M.S. Stud. Eng.

Creep model plays an important role in the theoretical research of rheological mechanics properties, which can be used to accurately reflect and predict the rheology of materials. For example, *Kong et al.* studied the mechanical properties of seed cotton compression and stress relaxation process and constructed its constitutive model. This finding can provide a profound theoretical basis to simulate seed cotton compression in most cotton picking areas (*Kong et al., 2021*). It has been proposed that both temperature and moisture content affect the tensile creep and recovery by influencing the formation and fracture of hydrogen bonds according to Norway spruce creep tests (*Engelund and Salmen, 2012*). In addition to using creep model to characterize the mechanical properties of materials, researchers have also developed creep model to make it suitable for the prediction and evaluation of material rheology in multiple environments. Combing the test results of creep deformation properties of frozen soil with the theory of binary medium model, *Wang et al.* analysed the creep fracture mechanism of frozen soil in detail and proposed a new binary medium creep constitutive model (*Wang et al., 2021*). Meanwhile, a new fractional creep model of soft soil was established by introducing Almeida fractional derivative into the classical elastic-viscoplastic model. The fractional creep model required fewer material parameters and state variables than the traditional model. It exhibited higher accuracy and convenience (*Xiang et al., 2021*).

The soil in the middle and lower of the Yangtze River, alternates between dry and wet all year round, resulting in soil sticking and hardening. The physical state of soil was related to the form of soil deformation during cultivating in the field (*Zheng et al., 2019; Zhu et al., 2020*). From the perspective of soil deformation, the soil with strong viscoplasticity could withstand large plastic deformation without little fracture and fragmentation. When tillage machinery was working in such paddy fields, the straw burial rate and surface flatness would be decreased (*Zhu et al., 2019*). Therefore, how to accurately predict and evaluate the rheology and creep process of the soil has become a research point of agricultural machinery.

In this study, we carried out compression creep tests on paddy soil with different moisture content in multi stress load. The nonlinear viscoelastic-plastic creep model was established based on creep test curves, and creep model parameters and deformation laws were obtained. It is expected to provide a theoretical basis for the research on high efficiency and low consumption design of agricultural equipment, related simulation parameter selection of tillage machinery.

MATERIALS AND METHODS

Experimental materials

The soil used in the experiment was taken from the paddy field in the Modern Agricultural Science and Technology Experimental Base of Huazhong Agricultural University (30°28'N, 114°21'E). The annual double-crop rotation system (rice - wheat and rice - rape) is the domain planting pattern. During the experiment, the surface rice stubble and weeds in the sampling area were removed, and the soil of tillage layer was collected by five point sampling method. The soil moisture content is 27.16%; the dry density is 1.48 g/cm³; the organic matter content is 20.31 g/kg, and the mass fractions of clay (< 0.002 mm), powder (0.002-0.05 mm) and sand (0.05-2.0 mm) are 41.36%, 50.73% and 7.91% respectively.

The above experimental field was sampled again at an interval of 30 days, and the measured moisture content of the second sampling soil was 21.51%. Soil samples were collected to conduct creep test by a cylindrical ring knife with a diameter of 70 mm and a height of 52 mm. We took the average compressive strength obtained from the same batch of soil compression test as the stress reference value of creep test, and regarded 15%, 30%, 45%, 60% and 75% of compressive strength as the stress level. In order to conveniently describe the experiment process and results, the above two soils were called w_1 and w_2 soil respectively. We numbered it w_{1015} - w_{2075} according to the stress level.

Table 1

Numbers of soil creep samples under compression										
Moisture content [%]	27.61					21.51				
Number	w1015	w1030	w1045	w1060	w1075	w2015	w2030	w2045	w2060	w2075
Stress level [%]	15	30	45	60	75	15	30	45	60	75
Stress [MPa]	0.016	0.032	0.048	0.064	0.080	0.017	0.034	0.051	0.068	0.085

Experimental methods

The TMS-PRO texture analyser (American FTC company) was used as the creep test equipment, which could provide a maximum test force of 1000 N and accuracy of $\pm 1\%$ (Fig. 1). A disk-shaped probe with the diameter of 75 mm was selected to conduct compression creep tests. The sample was placed and fixed on the test bench. After setting predetermined load, the disk moved downward at the velocity of 20 mm/min. When reaching the predetermined load, the pressure was maintained for 900 s. When the pressure holding time was over, the disk returned automatically. The force, displacement and time during the experiment were automatically recorded and saved with sampling frequency of 50 Hz. The soil strain was the ratio of the displacement difference collected by the sensor to the soil initial height (52 mm).

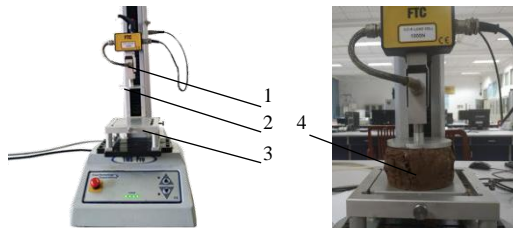


Fig. 1 - Creep test bench

1 – sensor; 2 – disc indenter; 3 – support; 4 – soil sample



Fig. 2 - Creep failure of soil under compression

RESULTS AND DISCUSSIONS

Soil compression creep properties

After the soil was removed from the test bench, the soil strain recovered slightly. With the extension of time, the greater the recovery value of strain was, the smaller the recovery speed was (Fig. 2). However, there was still permanent deformation of soil after long-time recovery, and it could not return to the initial state before loading. The final shape was waist drum shape, and the increase of applied stress had positive effect on the creep deformation. When the stress of soil was between elastic strength and yield strength, the soil would produce elastic deformation. Creep deformation gradually increased with the increase of creep time. Therefore, the soil with 15% and 30% stress levels only deformed in the whole creep process, and there was no crack on the surface. Because the applied stress was close to the yield strength of the soil, there was deformation and surface cracks of the samples with 45% and 60% stress levels in the creep process. The waist drum position of these samples deviated from the centre and was close to the bottom. Although the soil sample had cracks, it did not disintegrate. The waist drum shape of the sample at 75% stress level was located in the top. The appearance of the sample looked rough with destructive soil particles protruding from its surface. The reason was that the soil was an anisotropic material with inconsistent internal strength. If a certain position of soil reached the yield strength, the cracks would occur. With the increase of creep time, the internal damage gradually accumulated, and finally the internal and external cracks penetrated to form macro cracks. Moreover, the soil was destroyed under plastic deformation, and the angle between the soil failure section and the horizontal plane α was about 45° . It showed that the soil firstly reached the shear stress strength and then was damaged.

In order to study the law of soil compression creep deformation under different stress levels, taking the instantaneous strain of reaching the predetermined load as the starting point, we calculated the growth rate (ζ_t) of each time relative to this point in the pressure holding time. The calculation formula was as follows:

$$\zeta_t = \frac{\varepsilon_t - \varepsilon_0}{\varepsilon_0} \times 100\% \quad (1)$$

Where, ζ_t is the growth rate of strain at time t , %; ε_t is the strain at time t , %; ε_0 is the instantaneous strain, %.

As shown in Fig. 3, the initial instantaneous strain and final steady state strain increased with the increase of stress level, and the creep curve was consistent and similar. All the samples produced instantaneous strain during loading. Because the loading time was shorter than the later creep time, it could be considered that the elastic deformation occurred instantaneously. After elastic deformation, the strain of the soil initially increased linearly with the increase of creep time, and then the creep rate decreased gradually. The overall creep curve showed nonlinear characteristics. Although the creep strain at 15% and 30% stress levels increased with time, the creep rate almost approached 0 at the later stage of creep. The soil strain at 45% and 60% stress levels changed more obviously with time. In the later stage of creep, the strain increased approximately linearly with time, and the creep deformation rate was high.

The creep curve was steeper than that at low stress level. For soils subjected to 75% stress level, the strain and strain rate increase rapidly after compression, and the value was higher than that of other stress levels.

Since the stress of the soil under 75% stress level exceeded its yield strength, the time to reach creep failure in the pressure holding process was shorter. The strain rate of the soil was faster and its growth rate was greater than 1, so the strain growth rate curve at 75% stress level was not drawn in Fig. 3. The strain growth rate of each sample increased with the increasing time, and the strain growth rate decreased gradually. Generally speaking, the strain growth rate of two groups of soil samples with different moisture content initially increased rapidly, and gradually increased slowly after 100 s. The nonlinear relationship was more and more obvious, showing the stages of instantaneous creep and attenuation creep.

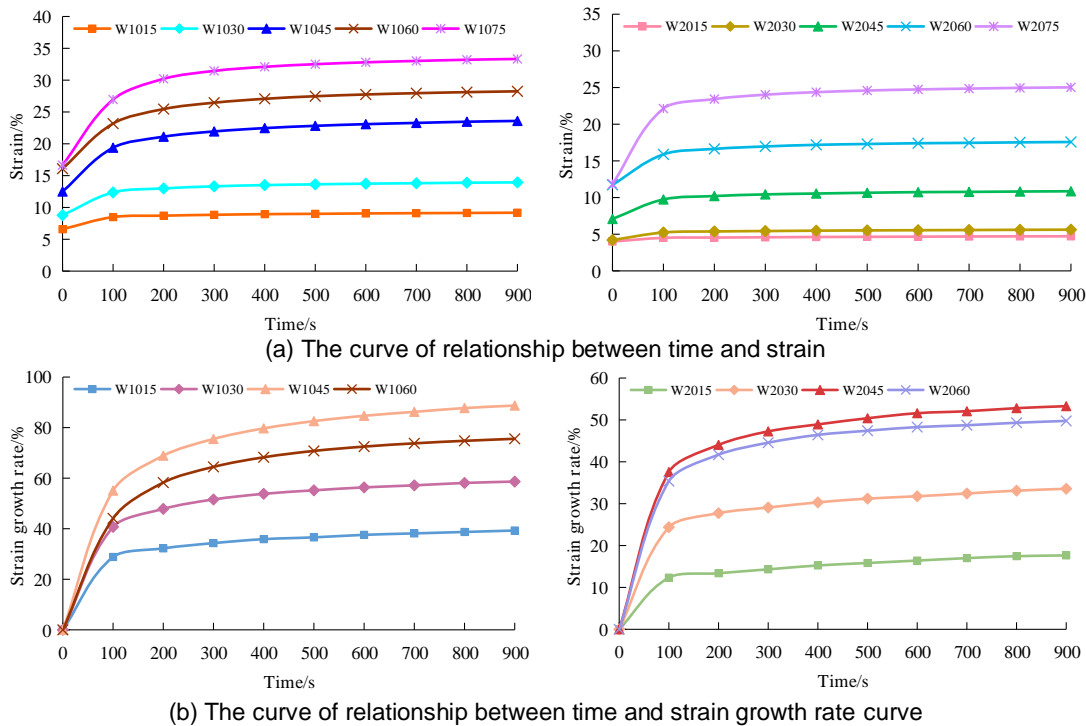


Fig. 3 - Creep characteristic curve of soil under different stress levels

For the initial strain, steady state strain and strain rate of the sample, the change trend of the two groups of soil with different moisture content was the same, which increased with the increase of stress level (Table 2). However, the final strain growth rate of 60% stress level was lower than that of 45% stress level in two sets of test samples. It may be that the applied stress of 60% stress level was high, which could destroy some fragile areas in the soil interior. The force applied during the pressure holding process could gather and compact the evacuated soil particles, resulting in the increase of deformation resistance and the decrease of deformation. After the stress level was greater than 30%, the trend of steady state strain was non convergent continuous growth. In addition, the strain growth rate of soils at 60% and 75% levels was also the trend until soil failure.

Table 2

Creep strain and strain growth rate of soil			
Number	Initial strain [%]	Steady state strain [%]	Final strain growth rate [%]
w1015	6.59	9.18	39.29
w1030	8.79	13.94	58.64
w1045	12.50	23.59	88.71
w1060	16.09	28.24	75.57
w1075	16.65	33.33	/
w2015	4.01	4.72	17.65
w2030	4.21	5.62	33.56
w2045	7.08	10.86	53.28
w2060	11.74	17.58	49.76
w2075	11.85	25.03	/

Construction of nonlinear viscoelastic plastic creep model

From the above analysis, it could be seen that the deformation of soil under different stresses was also different. In order to establish the creep constitutive equation of paddy soil under multi stress environment, it was necessary to further analyse the deformation process and properties of soil. On the one hand, from the perspective of relationship between time and strain, the deformation increased rapidly in the initial stage of loading, and tended to be stable. After unloading, the soil rebounded slightly, but there was still residual deformation. On the other hand, from the perspective of relationship between time and strain rate, the strain rate decreased gradually with time and tended to 0. These results showed that the paddy soil conformed to the loading and unloading laws of viscoelastic materials and viscoplastic materials. Therefore, paddy soil could be regarded as a viscoelastic-plastic material. In addition to a single elastic, viscous and plastic strain, there are also complex coupling strains in the deformation process, such as viscoplastic and elastic-plastic strain. For such materials, it was difficult to accurately describe their nonlinear creep properties by traditional Kelvin, Maxwell and other models (Aleksandar *et al.*, 2020; Zou *et al.*, 2013).

Burgers model (Fig. 4a) was one of the common linear models, which could well describe the properties of soil instantaneous elastic deformation, delayed elastic deformation and viscous flow. However, when the creep time exceeded a certain time, the viscoelastic strain contributed by Maxwell model in the model had reached the maximum. Since then, the strain increment only came from viscous strain, which led to the linear growth trend of the predicted creep curve in the later stage. The phenomenon deviated from the objective fact that the creep curve tended to be stable (Tia *et al.*, 2009). Therefore, such a linear model could not characterize the plastic deformation of soil. This kind of linear model could only meet the fitting requirements, and could not theoretically analyse the influence of multi stress load on soil creep deformation, which was not convenient for its application in numerical simulation.

Nonlinear viscoelastic-plastic creep model

Based on the experimental curve, a two-element nonlinear viscoplastic model composed of nonlinear damper and friction block was established (Fig. 4b). The soil compression creep curve was fitted by the correction method that the viscosity coefficient changed according to the law of power function, and the equation was:

$$\varepsilon = \varepsilon_0 + kt^n \quad (2)$$

When $\sigma > \sigma_s$, the two-element nonlinear viscoplastic creep model was triggered, and the relationship between strain and time was shown in equation (3). Combining equation (2) with equation (3), we defined $(\sigma - \sigma_s) / \eta_0 = k$. The expression of nonlinear damper η_s could be obtained:

$$\varepsilon = \varepsilon_0 + \frac{\sigma - \sigma_s}{\eta} t \quad (3)$$

$$\eta(\eta, t) = \eta_0 \frac{t_0^{n-1}}{t^{n-1}} = \frac{\eta_0}{t^{n-1}} \quad (4)$$

where, t_0 is the reference time, 1; η_0 is the initial viscosity coefficient, MPa·s; σ is the applied stress, MPa; σ_s is the yield strength, MPa.

According to the above derivation process, the creep constitutive equation of the nonlinear viscoplastic model could be obtained.

$$\varepsilon(t) = \frac{H(\sigma - \sigma_s)}{\eta_{(n,t)}} t = \frac{H(\sigma - \sigma_s)}{\eta_{(n,t)}} t^n = \begin{cases} 0 & (\sigma \leq \sigma_s) \\ \frac{\sigma - \sigma_s}{\eta_{(n,t)}} t^n & (\sigma > \sigma_s) \end{cases} \quad (5)$$

Nonlinear viscoelastic-plastic creep model

Considering the complexity of soil compression deformation, the Burgers model was modified in this study. The nonlinear viscoplastic model was connected with it to form the six-element nonlinear viscoelastic-plastic creep model of soil (Fig. 4c). When the model was subjected to constant stress σ that was less than the soil yield strength, the six-element nonlinear viscoelastic-plastic creep model would degenerate into a four-element Burgers model. When the soil was subjected to constant stress σ that was greater than the soil yield strength, the nonlinear viscoplastic model was triggered. The model stress passed through the friction block σ_s was attenuated and transferred to Burgers model.

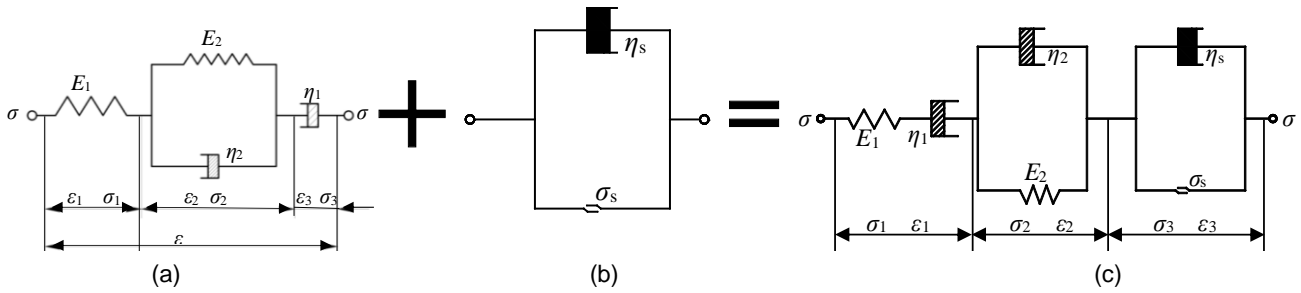


Fig. 4 - Nonlinear viscoelastic plastic model

When the stress applied to the model was less than the soil yield strength, the two-element nonlinear viscoplastic model would not be triggered. At this time, the model was still Burgers model, and the constitutive equation was as follows:

$$\varepsilon = \frac{\sigma}{E_1} + \frac{\sigma}{\eta_1}t + \frac{\sigma}{E_2} \left(1 - e^{-\frac{E_2}{\eta_2}t}\right) \quad (6)$$

When the stress applied to the model was greater than the soil yield strength, the model was a six-element nonlinear viscoelastic-plastic creep model. All elements in the model participated in deformation, and the relationship between stress and strain meet the following equations. The constitutive equation was as follows:

$$\eta_1 \frac{d\varepsilon}{dt} + \frac{\eta_1\eta_2}{E_2} \frac{d^2\varepsilon}{dt^2} = \sigma + \left(\frac{\eta_1}{E_2} + \frac{\eta_1 + \eta_2}{E_2} + \frac{\eta_1}{\eta_0}t^n + \frac{2\eta_1\eta_2nt^{n-1}}{E_2\eta_0}\right) \frac{d\sigma}{dt} + \left(\frac{\eta_1\eta_2}{E_2E_2} + \frac{\eta_1\eta_2}{E_2\eta_0}t^n\right) \frac{d^2\sigma}{dt^2} + \frac{(\sigma - \sigma_s)\eta_1nt^{n-2}}{\eta_0} \left(t + \eta_2 \frac{n-1}{E_2}\right) \quad (7)$$

The creep equation (8) of the soil nonlinear viscoelastic-plastic model could be obtained by Laplace transform and inverse Laplace transform of equation (7).

$$\varepsilon = \frac{\sigma}{E_1} + \frac{\sigma}{\eta_1}t + \frac{\sigma}{E_2} \left(1 - e^{-\frac{E_2}{\eta_2}t}\right) + \frac{\sigma - \sigma_s}{\eta_0}t^n \quad (8)$$

Parameter identification and property analysis

Creep compliance of nonlinear viscoplastic model

When the viscoelasticity of materials was described by creep model, the creep compliance $J(t)$ was usually used to represent the creep energy of materials. It represented the creep strain of materials under unit stress (Chen et al., 2021). Its general expression was:

$$J(t) = \varepsilon(t) / \sigma = J_e + J_v(t) + J_{ve}(t) + J_{vs}(t) \quad (9)$$

The creep compliance composition of the nonlinear viscoelastic-plastic model was derived. Where J_e stands for elastic compliance; $J_e = 1/E_1$; $J_v(t)$ represents viscosity compliance; $J_v(t) = t/\eta_1$; $J_{ve}(t)$ represents the viscoelastic compliance; $J_{ve}(t) = [1 - \exp(-E_2t/\eta_2)]/E_2$; $J_{vs}(t)$ represents the viscoplastic compliance; $J_{vs}(t) = (\sigma - \sigma_s)t^n/\sigma\eta_2$. σ is the applied stress on the material, and t was time of applied stress. According to the expression of creep compliance $J(t)$, the elastic compliance J_e is the instantaneous elastic deformation under the stress applied to paddy soil, which does not change with time. The coefficient of viscosity compliance $J_v(t)$, which increases slowly and linearly with time, is the reciprocal of the coefficient viscosity η_1 , where the creep curve shows the creep rate of uniform creep stage of the soil. The viscoelastic compliance $J_{ve}(t)$ is influenced by the delay elastic modulus E_2 and delay viscosity coefficient η_2 . As time increases, the viscoelastic compliance $J_{ve}(t)$ gradually increases, then the growth rate slows down to a fixed value. The creep curve illustrates the attenuation creep stage of paddy soil. The viscoplastic compliance $J_{vs}(t)$ represented the viscoplastic strain of soil under unit stress.

Due to the above analysis and equation (8), the fitting of soil nonlinear viscoelastic-plastic model was realized by MATLAB software. The parameters of creep model can be obtained by the fitting equation 8 (Table 3). The determination coefficients of the fitted equations were greater than 0.985, and the coefficient of variation was less than 0.011. The nonlinear viscoelastic-plastic creep model deduced in this study could accurately describe creep properties of paddy soil under multi stress environment.

Table 3

Fitting parameters of soil creep model

Number	Instant elastic modulus E_1 [MPa]	Viscosity coefficient η_1 [MPa·s]	Delay elastic modulus E_2 [MPa]	Delay viscosity coefficient η_2 [MPa·s]	η_0 [MPa·s]	R^2
w1015	0.243	2062.121	0.814	1.244	/	0.992
w1030	0.364	1881.246	0.836	0.915	/	0.984
w2045	0.384	1059.369	0.633	0.635	/	0.975
w1060	0.398	1203.460	0.789	0.821	/	0.963
w1075	0.486	109140.518	4.984	9.758	0.249	0.986
w2015	0.424	6724.684	3.450	14.898	/	0.995
w2030	0.808	7951.356	3.192	6.958	/	0.992
w2045	0.720	4253.545	1.791	2.453	/	0.984
w2060	0.579	3837.472	1.517	5.780	/	0.983
w2075	0.719	8719737.382	2.336	3.240	0.130	0.997

As shown in Table 3, when the stress level increased from 15% to 75%, the instantaneous elastic modulus and delay elastic modulus of w_1 paddy soil ranged 0.243 - 0.486 MPa and 0.633 - 4.984 MPa with average values of 0.375 and 1.611 MPa, respectively. For w_2 paddy soil, the instantaneous elastic modulus and delay elastic modulus ranged 0.424 - 0.808 MPa and 1.517 to 3.450 MPa with average values of 0.650 MPa and 2.457 MPa, respectively. The paddy soil will produce instantaneous elastic deformation at the moment of loading. The instantaneous elastic modulus and delay elastic modulus represent the elastic mechanical properties of paddy soil. The instantaneous elastic modulus represents the ability of soil to resist instantaneous deformation. The delay elastic modulus stands for the slow degree of elastic change of paddy soil in the stable creep stage. The above analysis showed that in the internal structure of w_1 paddy soil and w_2 paddy soil, the elastic deformation resistance of the spring element E_1 in Maxwell model was less than that of spring element E_2 in the Kelvin model.

The viscosity coefficient represents the fluidity of paddy soil. A larger value indicates a stronger anti-deformation viscosity resistance and poor fluidity. For w_1 paddy soil, the viscosity coefficient and delayed viscosity coefficient ranged 1059.369-109140.518 MPa·s and 0.635-9.758MPa·s with average values of 23069.343 MPa·s and 2.675 MPa·s, respectively. In comparison, w_2 paddy soil exhibited a viscosity coefficient of 3837.472-9414.022 MPa·s (average of 1748500.888MPa·s) and delayed viscosity coefficient of 1.369-4.318 MPa·s (average of 2.613 MPa·s). The above results showed that the viscous resistance to deformation of the viscous element η_1 in Maxwell model was stronger than the delayed viscous element η_2 in the Kelvin model.

Analysis of creep deformation process

By fitting the creep test data according to equations (8), the variation laws of strain, strain rate and strain acceleration during creep deformation could be obtained. The results were shown in Table 4.

Table 4

Fitting equation of soil creep model

Strain fitting	Strain rate fitting	Strain acceleration fitting
$\epsilon_1=0.066+7.759 \times 10^{-6} t+0.020 \times (1-e^{-0.654 t})$	$v_1=7.759 \times 10^{-6}+0.013 e^{-0.654 t}$	$a_1=0.013 e^{-0.654 t}$
$\epsilon_2=0.088+1.701 \times 10^{-5} t+0.038 \times (1-e^{-0.913 t})$	$v_2=1.701 \times 10^{-5}+0.035 e^{-0.913 t}$	$a_2=0.035 e^{-0.913 t}$
$\epsilon_3=0.125+4.531 \times 10^{-5} t+0.076 \times (1-e^{-0.996 t})$	$v_3=4.531 \times 10^{-5}+0.076 e^{-0.996 t}$	$a_3=0.076 e^{-0.996 t}$
$\epsilon_4=0.161+5.318 \times 10^{-5} t+0.081 \times (1-e^{-0.962 t})$	$v_4=5.318 \times 10^{-5}+0.078 e^{-0.962 t}$	$a_4=0.078 e^{-0.962 t}$
$\epsilon_5=0.165+7.330 \times 10^{-7} t+0.016 \times (1-e^{-0.511 t})+0.040 t^{0.201}$	$v_5=7.330 \times 10^{-7}+8.176 \times 10^{-3} e^{-0.511 t}+8.040 \times 10^{-3} t^{0.799}$	$a_5=-4.178 \times 10^{-3} e^{-0.511 t}-6.424 \times 10^{-3} t^{-1.799}$
$\epsilon_6=0.040+2.528 \times 10^{-6} t+0.005 \times (1-e^{-0.232 t})$	$v_6=2.528 \times 10^{-6}+1.160 \times 10^{-3} e^{-0.232 t}$	$a_6=1.160 \times 10^{-3} e^{-0.232 t}$
$\epsilon_7=0.042+4.276 \times 10^{-6} t+0.011 \times (1-e^{-0.459 t})$	$v_7=4.276 \times 10^{-6}+5.049 \times 10^{-3} e^{-0.459 t}$	$a_7=5.049 \times 10^{-3} e^{-0.459 t}$
$\epsilon_8=0.071+1.199 \times 10^{-5} t+0.028 \times (1-e^{-0.730 t})$	$v_8=1.199 \times 10^{-5}+0.020 e^{-0.730 t}$	$a_8=0.020 e^{-0.730 t}$
$\epsilon_9=0.117+1.772 \times 10^{-5} t+0.045 \times (1-e^{-0.263 t})$	$v_9=1.772 \times 10^{-5}+0.012 e^{-0.263 t}$	$a_9=0.012 e^{-0.263 t}$
$\epsilon_{10}=0.118+9.748 \times 10^{-9} t+0.036 \times (1-e^{-0.721 t})+0.039 t^{0.136}$	$v_{10}=9.748 \times 10^{-9}+0.026 e^{-0.721 t}+5.304 \times 10^{-3} t^{0.864}$	$a_{10}=0.019 e^{-0.721 t}-4.583 \times 10^{-3} t^{-1.864}$

$\epsilon_1 - \epsilon_{10}$, $V_1 - V_{10}$ and $a_1 - a_{10}$ were the corresponding strain, strain rate and strain acceleration of w_{1015} - w_{2075} samples respectively. It could be seen that when the stress level was below 75%, the total creep deformation of the two groups of paddy soil was composed of elastic strain $\epsilon_e(t)$, viscous strain $\epsilon_v(t)$ and viscoelastic strain $\epsilon_{ve}(t)$. When the load at 75% stress level was applied, the total strain of paddy soil included viscoplastic strain $\epsilon_{vs}(t)$ in addition to the above three strains.

The proportion of each strain in the total strain was further analysed using the following formula.

$$P_i(t) = \frac{\epsilon_i(t)}{\epsilon(t)} \times 100\% = \frac{J_i(t)}{J_e(t) + J_v(t) + J_{ve}(t) + J_{vs}(t)} \times 100\% \quad (10)$$

Fig. 5 showed the variation law of strain proportion with time under unit stress. The proportion of elastic strain in total strain (P_e) decreased nonlinearly with time. The proportion of viscous strain to total strain (P_v) increased with creep time. The proportion of viscoelastic strain in the total strain (P_{ve}) first increased and then decreased with time. The elastic strain increased with the increase of stress level. When the applied stress did not reach the yield strength, the variation trend of viscosity and viscoelastic strain was the same as that of elastic strain. When the stress exceeded the yield strength, an opposite trend can be observed for the viscous and viscoelastic strain. When the stress level increased from 10% to 45%, the proportion of elastic strain (P_e) decreased with it; the viscous and viscoelastic strains (P_v and P_{ve}) increased with it. When the stress level increased from 45% to 60%, this law of change was opposite to the previous one. Under each stress level, the smallest proportion of each strain was viscous strain. When the stress level increased to 75%, the proportion of viscous strain would decrease sharply. The reason was that its proportion was replaced by the viscoplastic strain. The general trend of strain and proportion of w_1 soil and w_2 soil with time and stress level was the same, which did not change with the varying of soil moisture content.

The proportion of each strain in the steady state strain of soil

Table 5

Number	ϵ_1	ϵ_2	ϵ_3	ϵ_4	ϵ_5	ϵ_6	ϵ_7	ϵ_8	ϵ_9	ϵ_{10}
ϵ_e [%]	6.60	8.80	12.50	16.10	16.50	4.00	4.20	7.10	11.70	11.80
ϵ_v [%]	0.70	1.53	4.08	4.79	0.07	0.02	0.04	1.08	1.59	8.77×10^{-4}
ϵ_{ve} [%]	2.00	3.80	7.60	8.10	1.60	0.05	1.10	2.80	4.50	3.60
ϵ_s [%]	/	/	/	/	15.70	/	/	/	/	9.84
P_e [%]	70.98	62.27	51.70	55.54	48.72	84.61	73.88	64.67	65.75	46.76
P_v [%]	7.51	10.83	16.87	16.51	0.19	4.81	6.77	9.83	8.96	3.48×10^{-3}
P_{ve} [%]	21.51	26.89	31.43	27.94	4.72	10.58	19.35	25.50	25.29	14.26
P_{vs} [%]	/	/	/	/	46.36	/	/	/	/	38.98

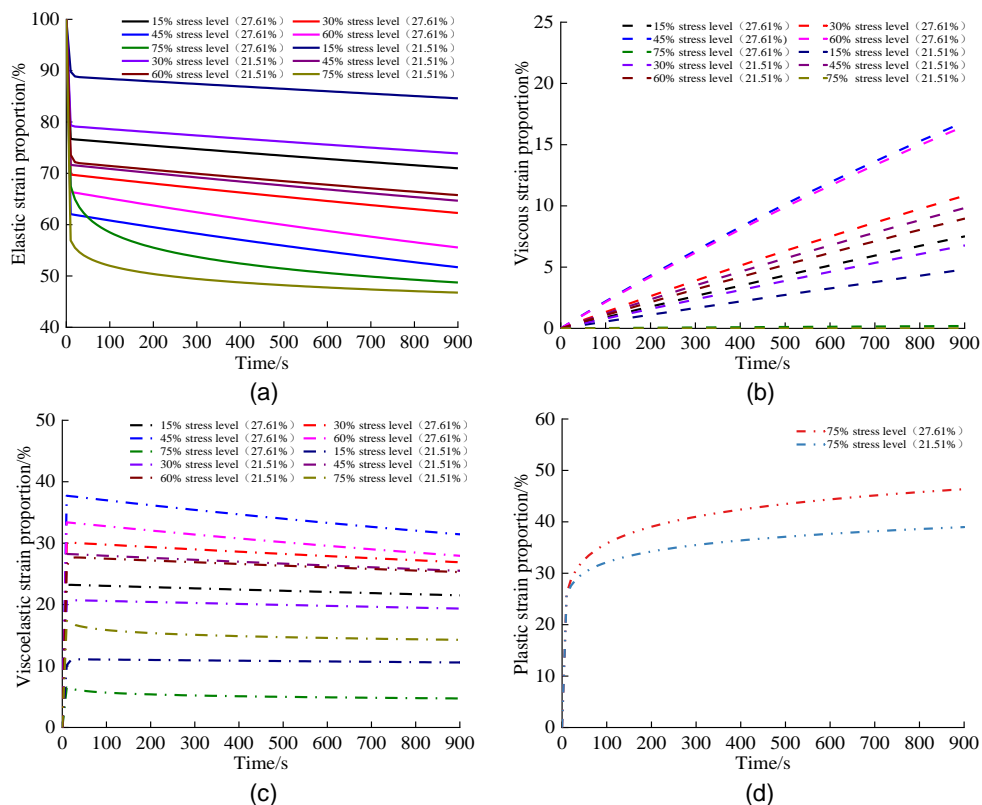


Fig. 5 - The curve of strain proportion with time

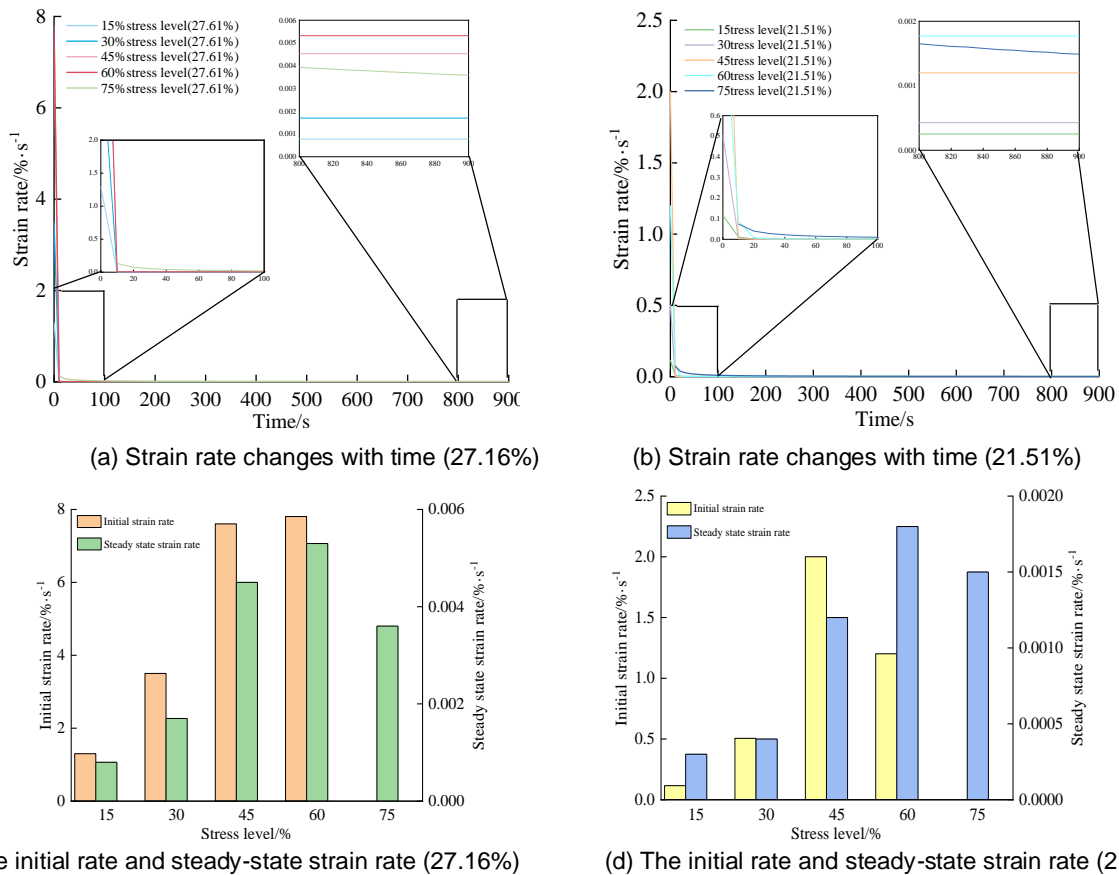


Fig. 6 - Soil creep rate under different stresses

When the applied stress was less than the yield strength, the strain rate of paddy soil was composed of viscous strain rate and viscoelastic strain rate. After the applied stress exceeded the yield strength, the strain rate included viscoplastic strain rate in addition to the above two rates (Fig. 6). In the creep process, all samples show obvious differences in the initial stage. According to Table 4 and equation (8), when $0 < n < 1$, the creep rate was greater than 0 and the creep acceleration was less than 0. The paddy soil at each stress level showed instantaneous creep stage, attenuation creep stage and steady state creep stage in the process of compression creep. Due to the mathematical definition of strain expression at 75% stress level, the initial strain rate cannot be deduced according to the formula. Therefore, the steady state strain rates of w1015, w1030, w1045, w1060 and w1075 were 0.0008, 0.0017, 0.0045, 0.0053 and 0.0351%·s⁻¹ respectively, with initial strain rates of 1.3008, 3.5017, 7.6045 and 7.8053%·s⁻¹. The steady state strain rates corresponding to w2015, w2030, w2045, w2060 and w2075 were 0.003, 0.0004, 0.0012, 0.0018 and 0.0015 %·s⁻¹ respectively, with initial strain rates of 0.1163, 0.5053, 2.0012 and 1.2018%·s⁻¹.

Creep model verification

According to the creep constitutive equations of the two models, the difference of the models would be reflected when the loading stress was above the yield strength. Therefore, based on the above experimental method, the soil of the same paddy field was taken again. The measured moisture content was 19.65%, and the compressive strength was 0.136 MPa. The 75% stress level creep test was carried out on the soil, and the creep steady stage strain was 22.699%. The derived nonlinear creep model and Burgers model were used to fit and analyse the creep test data respectively (Fig. 7).

The determination coefficients of the fitting equations of the nonlinear viscoelastic-plastic model and the Burgers model were 0.997 and 0.989 (Table 5). The variation law of the nonlinear viscoelastic-plastic model was generally consistent with the creep test curve, and the model exhibited better regularity and accuracy than Burgers model. Although the fitting accuracy between Burgers model and creep test value was good in the initial creep stage, it was because the nonlinear viscoelastic-plastic model introduced viscoplastic deformation, resulting in the small instantaneous strain of the initial creep stage.

However, with the extension of creep time, the fitting effect between nonlinear viscoelastic-plastic model and creep test data was obviously better than Burgers model. Especially in the steady state creep stage, the difference was more obvious. The creep steady state strains of nonlinear model and Burgers model were 22.796% and 22.887% respectively, with the relative errors of 0.437% and 0.827%. The creep curve predicted by Burgers model showed a linear growth trend in the later stage of creep, which deviated from the creep test curve. The result was consistent with the above theoretical analysis. In conclusion, the nonlinear viscoelastic-plastic creep model established in our study was scientific and reasonable, and could more accurately reflect the whole creep process of paddy soil.

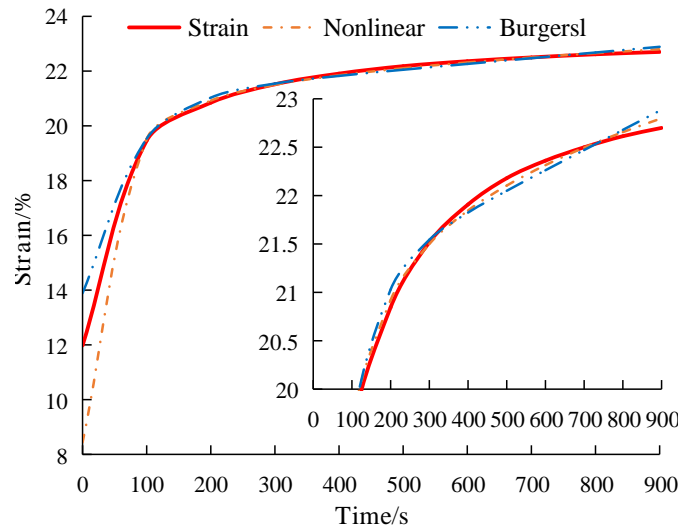


Fig. 7 - Comparison of fitting result

Table 5

The proportion of each strain in the steady state strain of soil

Model	Steady stage strain [%]	E_1 [MPa]	η_1 [MPa·s]	E_2 [MPa]	η_2 [MPa·s]	η_0 [MPa·s]	Relative error [%]	R^2
Nonlinear	22.799	0.142	1111111.111	0.276	17.922	0.046	0.437	0.997
Burgers	22.887	0.734	4899.135	1.432	99.553	/	0.827	0.989

CONCLUSIONS

- (1) The compression creep properties of paddy soil were analysed, and a two-element nonlinear viscoplastic model modified by power function was established. By connecting the nonlinear viscoplastic model with Burgers model in series, a six-element creep model which could fully reflect the nonlinear viscoelastoplastic creep properties of paddy soil was derived.
- (2) According to the test data, the parameters of the nonlinear viscoelastoplastic model were identified, and the fitting determination coefficients of creep curves at each stress level were more than 0.96. The creep curves of paddy soil with moisture content of 19.65% were compared and predicted at 75% stress level. The determination coefficient and relative error were 0.997% and 0.437% respectively. It showed that the model was feasible to predict the creep properties and deformation behaviour of paddy soil.
- (3) The creep process was the transition of the internal structure of paddy soil from unbalanced state to equilibrium state after applied stress. The time when the deformation reached the steady state was mainly affected by the viscosity, elasticity, plasticity and their coupling effects in the soil. When the damage caused by the force applied to the soil accumulates to a certain extent, the soil will be destroyed.

ACKNOWLEDGEMENT

This study was financially supported by a program of China’s National Natural Science Foundation Project (No. 31901412), the National Key Technology R&D Programme (No. 2017YFD0301300) and the Special Fund for Agro-scientific Research in the Public Interest (No. 201503136).

REFERENCES

- [1] Vaitauskien K., Arauskis E., Romaneckas K. et al., (2017), Design, development and field evaluation of row-cleaners for strip tillage in conservation farming. *Soil & Tillage Research*, vol. 174, pp. 139-146.
- [2] Schmalz H., Taylor R., Johnson T. et al., (2013), Soil morphologic properties and cattle stocking rate affect dynamic soil properties. *Rangeland Ecology & Management*, vol. 66, pp. 445-453.
- [3] Zeng Z., Chen Y., Zhang X., (2017), Modelling the interaction of a deep tillage tool with heterogeneous soil. *Computers and Electronics in Agriculture*, vol. 143, pp. 130-138.
- [4] Wang X., Zhang S., Pan H. et al., (2019), Effect of soil particle size on soil-subsoiler interactions using the discrete element method simulations. *Biosystems Engineering*, vol. 182, pp. 138-150.
- [5] Kong F., Wu T., Chen C. et al., (2021), Mechanical properties and construction of constitutive model for compression and stress relaxation of seed cotton (籽棉压缩与应力松弛力学特性及模型构建). *Transactions of the Chinese Society of Agricultural Engineering*, vol. 37, Issue 7, pp. 53-60.
- [6] Wang, P., Liu, E., Song, B. et al., (2019). Binary medium creep constitutive model for frozen soils based on homogenization theory. *Cold Regions Science and Technology*, vol.162, pp. 35-42.
- [7] Engelund E., Salmen L. (2012), Tensile creep and recovery of Norway spruce influenced by temperature and moisture. *Holzforschung*, vol. 66, pp. 959-965.
- [8] Xiang, G., Yin, D., Cao, C. et al., (2021), Creep modelling of soft soil based on the fractional flow rule: simulation and parameter study. *Applied Mathematics and Computation*, vol. 403. <https://doi.org/10.1016/j.amc.2021.126190>.
- [9] Zheng K. (2019), Research status and prospect of soil anti-adhesion technology for tillage equipment. (耕整机械土壤减粘脱附技术研究现状与展望). *Journal of Anhui Agricultural University*, vol. 46, Issue 4, pp. 728-736.
- [10] Zhu Y., Xia J., Zeng R. et al., (2020), Prediction Model of Rotary Tillage Power Consumption in Paddy Stubble Field Based on Discrete Element Method (基于离散元的稻板田旋耕功耗预测模型研究). *Transactions of the Chinese Society for Agricultural Machinery*, vol. 51, Issue 10, pp. 42-50.
- [11] Zhu Y., Zhang J., Zeng R. et al., (2019), Design and experiment of herringbone type rotary blade roller for burying stubble in paddy field and dry land (人字型水旱两用旋埋刀辊设计与试验). *Transactions of the Chinese Society for Agricultural Machinery*, vol. 50, Issue 4, pp. 49 - 57.
- [12] Zou L., Wang S., Lai X., (2013), Creep model for unsaturated soils in sliding zone of Qianjiangping landslide. *Journal of Rock Mechanics and Geotechnical Engineering*, vol. 5, Issue 2, pp. 162-167.
- [13] Aleksandar S., Okuka., Dušan Z., (2020), Fractional Burgers models in creep and stress relaxation tests. *Applied Mathematical Modelling*, vol. 77, Issue 2, pp. 1894-1935.
- [14] Liu J., Bai X., Li P., (2013), Modified Burger's model for describing creep behaviour of tomato fruits (番茄果实蠕变特性表征的 Burger's 修正模型). *Transactions of the Chinese Society of Agricultural Engineering*, vol. 29, Issue 9, pp. 249-255.
- [15] Chen S., Wei Y., Zhao K. et al., (2021), Creep performance and prediction model of bamboo scrimber under compression (重组竹顺纹受压蠕变性能及预测模型). *Acta Materiae Compositae Sinica*, vol. 38, Issue 3, pp. 44-952.

SIMULATION OF DESIGN VARIABLES EFFECT ON PERFORMANCE OF A COMMON BEANS (*Phaseolus vulgaris* L) PORTABLE THRESHER

KUBASHIRI VIGEZO HUSIKA NA ADHARI ZAKE KWA UTENDAKAZI WA MTAMBO UNAYOJULIKANA WA KUPORA MAHARAGWE

Patrick W. Wamalwa¹⁾, Christopher L. Kanali²⁾, Erick K. Ronoh²⁾, Gareth M. Kituu²⁾

¹⁾ Egerton University, Faculty of Engineering, Agricultural Engineering Department, P.O. Box 536-20115 Egerton/Kenya

²⁾ Jomo Kenyatta University of Agriculture and Technology, Department of Agricultural and Biosystems Engineering, P.O. Box 62000 – 00200 Nairobi/Kenya

Correspondent author's contacts: Tel: +254728920918 E-mail: patrick.wamalwa@egerton.ac.ke

DOI: <https://doi.org/10.356.33/inmateh-65-47>

Keywords: Common beans, portable thresher, modelling, simulation, grain damage, efficiency

ABSTRACT

In Kenya, threshing of common beans is mainly made by traditional method using sticks and animal tramping, which are slow, inefficient and tedious. Consequently, there is a need to develop portable threshers locally available on the market for small and medium-scale farmers. The objective of this study was to simulate design variables effect on the performance of a common beans portable thresher. Sizing of design variables and parameters was the key in the development of the bean thresher. This could be achieved by costly experiments or use of prediction mathematical model equation. The later method was used by developing mathematical models from combination of Buckingham Pi theorem and reference to other similar works in literature. The predicting equation for power requirement, grain losses, grain damages, efficiency and throughput capacity were developed and validated using experimental thresher from the same study. The results showed that there was a positive correlation with R^2 of 0.9. Based on actual data and 10% absolute residual error interval, the prediction performance of the developed models was above 77%. The results noted that increase in cylinder peripheral speed of the pegs resulted in the increase in power requirement, bean grains damage, threshing efficiency and throughput capacity. Also increase in effective cylinder diameter caused increase in threshing efficiency and grain damage.

ABSTRACT

Nchini Kenya kupura kwa maharagwe yanayojulikana na wakenya wengi hufaywa kwa njia ya kitamaduni inayohusisha matumizi ya vijiti na wanyama kukanyaga maharagwe. Mbinu hii ina udhahifu kwani ni ya pole, si njia ya kupeana matokeo ya ufanisi na huchosha. Hata hivyo kuna haja ya kubuni mtambo unaobebeka wa kupura maharagwe na upatikane mashinani kwa wakulima wa kiwango kidogo na wastani. Lengo la utafiti huu ilikua ni kubashiri kigezo husika na adhari zake kwa utendakazi wa mtambo unayojulikana wa kupora maharagwe. Idadi ya vigezo mahususi na msingi ya kutumia vigezo hivyo ilikua ni msingi mkuu katika uundaji wa mtambo wa kupora. Hii ilifanywa kwa ujaribati wenye gharama ya juu au kwa kutumia mtindo wa kubashiri wa hesabu unaotokana na nadharia ya Buckingham pi na matumizi ya kazi zingine za kifasihi. Nadharia tete za mahitaji ya umeme, dhana bashiri ya umeme unaohitajika, nafaka ambazo zitaharibika, kiwango cha ufanisi na uwezo wa huru vilibuniwa kwa kutumia mtambo wa kupura wa ujarabati. Matokeo yalionyesha kuwa, kulikuwa na na uhusiano chanya wa nadharia tete na matokeo ya ujarabati yaani uhusiano wa kiwango cha asilimia 90% kwa kuzingatia data halisi na dhana ya mfumo wa ukosefu wa uhalisia ya asilimia 10% na ubashiri wa utendakazi wa miundo maalum ulikuwa Zaidi ya asilimia 77%. Matokeo yalidhihirisha kuwa ongezeko la mzunguko wa kipengo na kasi ya mishalee iliongeza mahitaji ya umeme, uharibifu wa nafaka ya maharagwe, ufanisi wa kuporwa na uwezo wa mtambo. Aidha, ongezo la upana wa kipenyo ulizidisha ufanisi wa kupura na uharibifu wa nafaka.

INTRODUCTION

Common beans (*Phaseolus vulgaris* L) are the second most important staple food crop after maize in most African developing countries Kenya included (Kiptoo et al., 2016). The crop provides a cheap source of protein and is rich in the essential amino acid element lysine, which is found in fewer quantities in maize and other grains (Mutuku et al., 2018). It is also an appetite suppressant because it digests slowly and causes a low sustained increase in sugar levels hence it is good for weight reduction.

The production is mainly at the subsistence level by small-scale farmers with limited commercialization, especially during bumper harvest. The crop is grown in almost all regions in Kenya. However, Eastern, Nyanza, Central, Western, and Rift Valley are the major bean-growing regions (Wortmann, 1998). Historically, beans are grown for sustenance; however, they have become an important source of income for small-scale Kenyan farmers. As a result of the increase in population, there has been an increasing demand of common beans of over one million metric tonnes against production of 750,000 tonnes in Kenya. The use of traditional human power is one reason for low production coupled with a minor subdivision of land. Therefore, farm mechanization is key towards smart, efficient farming to improve beans production in Kenya (Groote *et al.*, 2020).

In Kenya, post-harvest losses are reported at 20% for cereal grain crops. Drying, threshing, cleaning, packaging, and storage are the primary post-harvest practices (Mwangi *et al.*, 2017). The conventional threshing methods involve beating them with a rod or stick and animal treading, which are tedious, time-consuming, inefficient, and require much energy to the extent of causing blister (Joshi, 2006). Grain combine harvesters were popular in overcoming such difficulties associated with the traditional method of threshing harvested beans. However, the existing cost-effective structure of agricultural production and the small scale of farms in Kenya make their use uneconomical. The traditional threshing of common beans problem can therefore be addressed by portable threshers, which are not readily available in the market hence the need for design and development (Duke, 2012; Ndirika, 1997).

The design and development of cereal grain threshers is not entirely a new area of study. Various cereal stationary threshers exist for different crops like sorghum, rice, cashew nuts, and millet. However, there is scanty information on common beans thresher. Reported findings have mainly been based on experimental data and few theoretical modelling of the threshing unit. Desta and Mishra, (1990), developed and evaluated the performance of an experimental sorghum thresher. Their results focused mainly on the optimum operating speeds and average threshing efficiency was 98% at 400 revolutions per minute (RPM). Singh *et al.*, (2015), developed a multi-crop thresher and evaluated the effect of cylinder speed on threshing efficiency. The results indicated that an increase in the level of drum speed had a significant effect on the threshing efficiency of the thresher.

To understand the effect of machine and crop parameters on performance of common beans thresher, simulation is necessary using a mathematical model. Modelling and simulation is the use of physical, mathematical, or logical representation of a system or process to generate performance data (Law *et al.*, 2000). Muna *et al.*, (2016), developed threshing efficiency and optimization models for spike tooth mechanical cereal threshers using dimensional analysis and predictive validation methods. The model was fit when the threshing speed was in the range of 14.3 to 20 ms^{-1} , the feed rate was in the range of 0.1 to 0.2 kgs^{-1} , and moisture content was 10.6 to 15.8 % wet basis. Experimental data used for validation was from millet crop thresher, and the mechanical damage model was not developed, which is a cross-cutting issue in various studies. Comprehensive modelling and simulation of rasp bar cereal thresher were also presented by Osueke, (2011). Threshing efficiency, power requirement, threshing loss, and grain damage models were developed. However, the model was validated with published threshing performance data, which was not clear on the type of crop. The established results were found to fit well, taking R^2 values equal to or greater than 0.9, which were highly significant ($\alpha=0.05$).

The cylinder/concave threshing mechanism is by far the most commonly used. Its universal adoption appears to be due to its ability to thresh a wide range of crops and high threshing efficiency with a low degree of injury to the seeds if used skilfully (Ramteke and Sirohi, 2003). The threshing mechanism adopted for common thresher in this study was the spike or peg tooth type. Ndirika, (1997), modelled the performance of stationary spike tooth grain thresher using dimensional analysis and Buckingham Pi theorem. Model development considered moisture content which is very critical on the performance of grain threshers. The formulated models were verified and validated with experimental data from stationary mechanical sorghum and millet thresher. The models were found to correlate and fit well with the experimental data with R^2 values greater than 0.91 at a 0.001 level of significance. Considering the assumptions made, this study has used Ndirika (1997) models with little calibration for simulating the performance of common beans thresher.

Simulation can be achieved by setting up a model of a real system and performing experiments on it for design and evaluation. Softwares like Visual Basic and Python can use mathematical model equations for simulation (Dysarz, 2018). Researchers have in the past used these software to simulate the performance of machines before full-scale development and, after that, only construct the most promising design. Osueke, (2011), simulated operating parameters using visual Basic computer-aided software to determine and identify

the performance characteristic of least threshing loss due to grain damage, incomplete threshing, and threshing efficiency. The software was designed to determine the effect of a range of varied machine and crop parameters on the performance of a cereal thresher and hence select the best set of parameters. In this study, Python was selected because it is free and open-source, object-oriented, simple and easy to use, has many libraries including Numpy, Scipy, and Sympy for manipulating mathematical and numerical expressions, constants, and multi-dimensional matrices (Hart *et al.*, 2011). In this study, mathematical model equations with a set of assumptions concerning the operation of the common beans thresher were coded. The execution of models represented by a computer program was meant to answer questions that were dynamic in nature through quantitative ways.

MATERIALS AND METHODS

1.1 Theoretical models relating to the performance of common beans thresher

The models' development was based on past researchers' mathematical explications to form distinct model expressions for an ideal threshing unit. Dimensional analysis using the concept of Buckingham's Pi theorem and mechanic theory was mainly used. Figure 1 shows the schematic diagram of the modelled threshing unit for the common beans thresher.

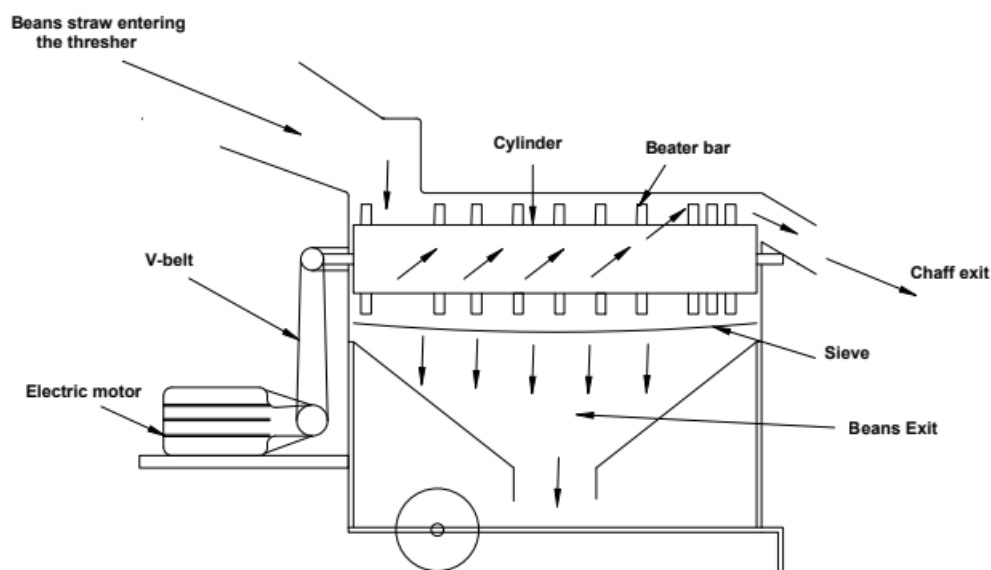


Fig. 1 - Schematic diagram of common beans thresher

The modelled threshing unit consisted of a cylinder drum with the pegs attached in a spiral configuration, concave that forms part of the sieve, and concave clearance. When the common beans were fed in at the concave entrance, it formed a crop stream which was accelerated by the spike tooth during impact. The common beans were detached from the panicles by a combination of rubbing and impact action. The action involved the application of tensile, compressive, bending, and twisting forces on a head of grain. Threshing was also achieved by the impact occurring when the cylinder pegs strike the bean pods. Separation of the threshed grain from the straws was accomplished through the radial motion of grains relative to the crop streams under the action of gravity and centrifugal force (Huynh *et al.*, 1982; Ndirika, 1997). The key models used to describe the threshing unit were; power requirement, threshing efficiency, threshing loss, grain damage, and output capacity.

The power requirement model was a sum of power required to overcome friction, the power required to detach the grains from the pods, and the power required to turn the unloaded cylinder. In determining the power required to overcome friction, the pressure of the crop stream on the concave surface was assumed to be uniformly distributed over the entire length and width of the concave. The power required to detach the grains from the pods was determined by first defining the energy required to detach the grains from the panicles. Let's assume that the variables of importance are the crop velocity, crop bulk density (wet basis), feed rate, concave clearance, concave length, and cylinder diameter. The power required to run the unloaded cylinder was based on the rotational speed without load and the torque required to run the cylinder without

load. Therefore Equation 1 was used to predict the total power required for threshing common beans (Huyhn *et al.*, 1982; Osueke 2011 and Ndirika, 1997).

$$P_T = K_a \left(\frac{V_p^{1/2} Q_r^{3/2} V_p}{\rho_w^{1/2} L_c} \right) + K_b Q_r V_p^2 + \frac{2\pi M_c Y N (g' + 2V_p / D)}{60} \quad (1)$$

where: P_T is total power required for threshing; K_a is slippage factor for cylinder pegs; V_p is the peripheral velocity of the pegs; Q_r is feed rate of common beans; ρ_w is bulk density of common beans (wet basis); L_c is concave length; K_b is a dimensional constant relating to motion resistance of the material; M_c is mass of the cylinder; Y is the radius of the driven pulley; N is cylinder RPM without load; g' is the acceleration due to gravity and D is the effective diameter of the cylinder.

The threshing process has been defined by an exponential function (Huyhn *et al.*, 1982; Gregory, 1988). Therefore, the exponential probability density function was considered for describing and predicting the process performance and various variables influencing threshability.

The process was considered a probability of equal likely events that assumed that any bean grains had an equal chance of being threshed at any time and had an equal chance of reaching the concave surface at a given position. Equation 2 was used to predict the threshing efficiency of common beans thresher.

$$T_e = 1 - e^{-\left[\frac{1.4 \times K_T \times \rho_d \times w \times D \times V_p^2 L_c}{(1-\beta) Q_r} \right]} \quad (2)$$

where:

T_e is the threshing efficiency of the thresher; K_T is the threshing Constant; ρ_d is the dry bulk density of common beans; w is the concave length, and β is the moisture content of common beans.

Threshing loss T_L is defined in Equation 3, the fraction of unthreshed common beans expressed in percentage.

$$T_L = 1 - T_e \quad (3)$$

Substituting T_e in Equation 2 into Equation 3 resulted into Equation 4, which was used to predict threshing loss.

$$T_L = -e^{-\left[\frac{1.4 \times K_T \times \rho_d \times w \times D \times V_p^2 L_c}{(1-\beta) Q_r} \right]} \quad (4)$$

The damage frequency or the mean rate of grain damage was determined using dimensional analysis and applying Buckingham's Pi theorem. The crucial variables influencing damage parameters were assumed to be cylinder velocity, crop bulk density, feed rate, cylinder diameter, and minimum velocity to cause grain damage. Fraction of damaged common beans was further defined based on integral exponential probability density function within dwell time in the threshing zone (Huyhn *et al.*, 1982; Gregory, 1988).

Equation 5 was used to express the fraction of the damaged common beans after impact by the pegs. D_b is the fraction of damaged common beans grains in the equation, and K_d is the damaged constant.

$$D_b = e^{-\left[\frac{-0.5 K_d \rho_d D V_p w L_c}{(1-\beta) Q_r} \right]} \quad (5)$$

All damaged and unthreshed grains were considered as a loss in the modelling of the total grain loss. This is because damaged grains may result in poor seed germination, and cracked kernels may result in dockage when sold for milling purposes. Furthermore, unthreshed heads retained for re-threshing often result in damaged kernels, and small kernel fragments resulting from damaged grain are likely to be lost totally during pneumatic separation. Therefore, the total grain loss in the threshing unit was presented as the sum of the threshing loss and grain damage loss.

The model used in calculating common beans thresher throughput capacity was expressed in Equation 6 (Ndirika, 2006; Gregory, 1988; Vas and Harrison, 1969), where: C_T is the output capacity of the thresher; K_m is the yield factor; Z is the grain straw ratio; λ_1 is the mean rate of threshing; λ_2 is the grain migration parameter; λ_3 is concave separation parameter, and t_d is the dwell time in the threshing zone.

$$C_T = K_m Q_r Z \left\{ 1 - \frac{\left[\lambda_1 \lambda_3 (\lambda_3 - \lambda_1) e^{-\lambda_2 t_d} + \lambda_2 \lambda_1 (\lambda_1 - \lambda_2) e^{-\lambda_3 t_d} + \lambda_2 \lambda_3 (\lambda_2 - \lambda_3) e^{-\lambda_1 t_d} \right]}{\left[(\lambda_1 - \lambda_2) (\lambda_3 - \lambda_2) (\lambda_3 - \lambda_1) \right]} \right\} \quad (6)$$

1.2 Simulation of the performance of common beans thresher

In developing a simulation model, the best framework and language were chosen among the following: Visual Basic, web-based simulation model (Js), Matlab, and Python, among many others. The mathematical model equation were coded in the software, and to effectively manipulate the equations and computations, several dependencies using the pip command were installed. The user is requested to enter all the input parameters shown in Table 1-3. This is followed by a series of arithmetic manipulations.

Table 1

Fixed crop and machine input parameters into the model	
Parameter	Dimensions
Radius of the driven pulley, Y	0.045 m
Mass of threshing cylinder, M_c	5 kg
Centre line distance between adjacent concave rods, a_1	0.04 m
Concave rod diameter, a_2	0.0018 m
Centre line distance between adjacent concave bar, b_1	0.06 m
Width of concave bars, b_2	0.0085 m
Grain straw ratio, Z	0.9
Spherical size of common beans	0.016 m

Table 2

Crop and machine variables used for simulation	
Variable	Variations
Moisture content of common beans, β (%)	15, 17.5, 20, 22.5, 25.
Feed rate, Q_r (kg/s)	0.01, 0.02, 0.03, 0.04, 0.05
Peripheral velocity of the pegs, V_p (m/s)	2, 4, 6, 8, 10, 12
Concave clearance, c (m)	0.018, 0.02, 0.022, 0.024, 0.028
Concave length, L_c (m)	0.25, 0.5, 0.75, 1

Table 3

Constants used in the applicable mathematical models	
Constants	Values
Acceleration due gravity, g	9.8
Slippage factor, K_a	0.35
Threshing constant, K_T	0.002
Damage constant, K_d	8×10^{-3}
Yield factor, K_m	0.7

1.3 Model testing and validation

Crop and machine parameters were entered individually and then simulated to view performance results. Parameters in Table 1 and 3 were kept constant, while those in Table 2 were varied to ascertain their effect on the thresher performance. A common beans thresher was then developed using design equations. Measured data from the developed thresher was used to validate the performance models by plotting graphs, student t -test, and residual analysis. The line of best fit, correlation coefficient, and coefficient of determination R^2 were used to measure how well the regression equation fits the data. To establish the repeatability of experimental data, the mean and standard deviations of the data were also established.

The absolute residual error ε_r was determined as shown in Equation 7 (Uluko et al., 2006; Kanali, 1997), in which ψ_p and ψ_a are the predicted and actual values, respectively. The prediction performance (η_{um}) of the model at $\varepsilon_r\%$ residual error interval was determined by equation 8, where ζ_w and ζ_t represent the number of data within the interval and the total trial data, respectively. The simulated results of each performance model were validated with measured experimental outputs.

$$\varepsilon_r = \left| \frac{\psi_p - \psi_a}{\psi_a} \times 100 \right| \tag{7}$$

$$\eta_{um} = 100 \times \frac{\zeta_w}{\zeta_t} \tag{8}$$

RESULTS

2.1. Validation of simulated data

This study was meant to use a simulation method in the design of common beans thresher. This was intended to reduce the cost of design since most of the experiments are carried out on the model system and optimization. Therefore, the results from the model had to be verified with measured experimental data for validation purposes. The effect of peripheral speed on the performance of common beans thresher was carried out. The machine minimum drum speed was 400 RPM which was the start velocity for running loaded bean thresher. Based on preliminary experiments, any speed below the minimum could not operate the thresher with the load of unthreshed common beans. The maximum cylinder speed was identified to be 1200 RPM for purposes of safety and vibration of the machine. Therefore, at an interval of 100 RPM, the performance of the developed thresher using design equations was calculated from measured outputs. The same input parameters and variables used for the experimental thresher were fed into the simulation model that represents the common bean thresher. The output performance was calculated based on the developed model equations and recorded. The correlation coefficient of regression R, and the coefficient of determination R² were used to evaluate the relationship between the model and experimental results. The correlation coefficient numerically varies between -1 and 1, indicating negative, zero, or positive correlation between the model and measured results. Since the coefficient of determination must also have a statistical meaning, a statistical significance test at $\alpha = 5\%$ was also done to ascertain how the sample data sets represent the whole population adequately.

2.1.1. Analysis of effect of pegs velocity on power required for threshing

The performance indicators for common thresher were power requirement, damaged grain, threshing efficiency, and throughput capacity. Figure 2 shows a comparison of experimental and computed power requirements for common beans thresher under different peripheral speeds of pegs.

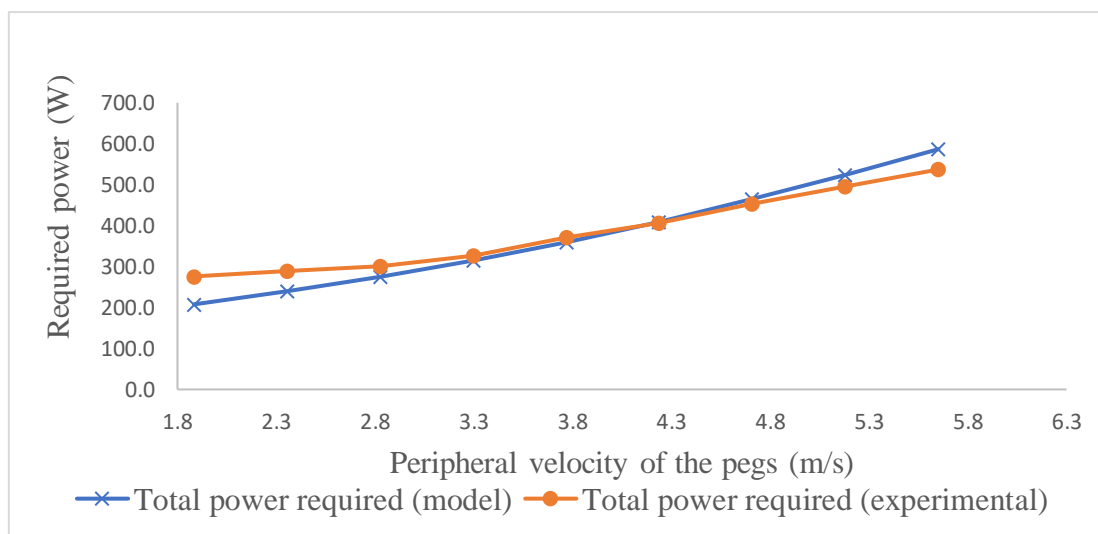


Fig. 2 - Comparison of experimental and computed power required for threshing common beans

Power required for threshing depends on detachment of the grain from the pod, frictional power, and power required to run the unloaded cylinder. As observed from Figure 2, there was an increase in power requirement for threshing common beans with an increase in peripheral velocity of the pegs in both the computed and experimental data. This is justified since power is mainly a function of velocity, cylinder revolution per minute, and cylinder mass. Therefore, increasing speed will result in increased power required for threshing. R^2 was 0.99 and 0.99 for experimental and computed power, respectively, required for threshing beans. This shows there is a positive correlation between the two data sets. Hence, the model can be used for simulating the power requirement for threshing. Similarly, when the student *t*-test for paired two sample means was conducted the *t*-statistics at 5% = 0.69 was less than *t*-critical = 1.89, a further indication that there was no statistically significant difference between the two data sets. This is also true because the computed data sets had a mean of 375.5 W power use within the speed range. In contrast, experimental results had a mean of 384 W. Generally, a farmer will prefer a machine with a low power requirement because of the reduced production cost.

The absolute residual error analysis (Kanali, 1997) between the simulated and the mean experimental observed power required for threshing for the 9 data ranged from 0.7% to 9.2%, with a mean value of 4.4%. This implies that there were discrepancies between the simulated and actual data on a few peripheral velocities of the pegs, which were slightly above the 5% residual error interval but on average, were within 10% residual error interval. This could be explained by the higher overall efficiency of the three-phase asynchronous motor than the single-phase used in the experimental thresher. At 10% absolute residual error interval, the prediction performance of the power requirement model was 78%.

2.1.2. Analysis of effect of pegs velocity on grain damage

Grain damage is a critical performance indicator for cereal thresher (Osueke, 2014). It has a direct effect on the germination of seeds and the market value of beans. In this case, it was determined by visual examination of any chipped, cracked or broken common beans grains expressed as a percentage of threshed bean grains. The extent and type of bean grain damage depend on machine and variety characteristics. The nature of damage experienced in large red kidney bean types during measured threshing was split into two halves due to impact action and rubbing against the concave surface. Figure 3 shows the results of measured and computed damaged grains of a bean thresher under different peripheral speeds of the peg.

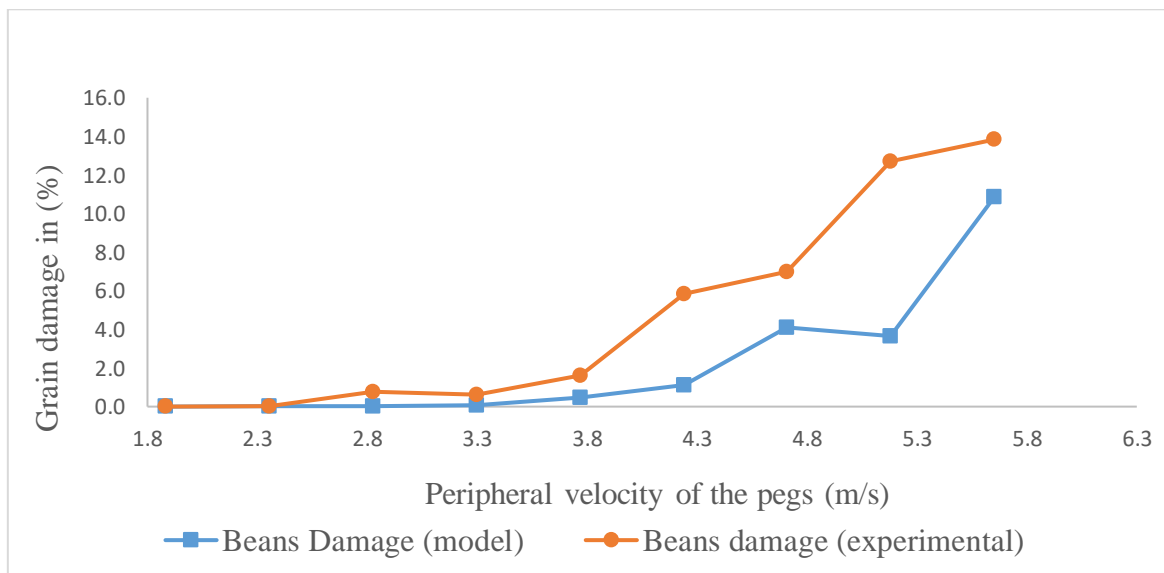


Fig. 3 - Measured and computed damaged grains of common beans thresher under different peg peripheral speeds

The computed damaged bean grains had a mean of 2.3% of threshed gains in all the evaluated peg peripheral speeds. This would be the ideal and recommended output for common bean thresher since the objective is to minimize grain damage. There was a slight increase of beans grain damage with an increase in peripheral velocity of the cylinder pegs. This was expected since an increase in cylinder pegs' peripheral velocity results in increased impact force enough to cause some grain damage.

The trend was different for experimental measured damaged bean grains under different cylinder speeds. The fraction of damaged grain was below 5% of threshed grain up to a maximum peg peripheral velocity of 3.8 ms^{-1} and increased drastically to 13.8% at a speed of 5.7 ms^{-1} . It was clear that at low speed, the damages were low since the impact force was low. The high bean grain damages at high speed for experimental thresher was a result of a design problem. The shape of the cylinder pegs needs to be smoothed instead of the bolts used, and sieve size increased to allow free fall of the beans grains through the concave surface. The absolute residual error analysis (Kituu *et al.*, 2010) between the simulated and the mean experimental observed fraction of the damaged grains for the 9 data ranged from 0.2% to 18.6%, with a mean value of 7.2%. This implies some disparities between the simulated and actual data on a few peripheral velocities of the pegs, which were above 5% residual error interval but, on average, were within 10% residual error interval.

However, R^2 was 0.7 for the computed data sets, while the experimentally measured data was 0.8. This indicated a positive correlation between the computed and experimental beans grain damage during threshing. Since the bean grain damages that resulted from the simulation model were the expected outputs, it can therefore be used for simulation and optimization of common beans thresher. The student t-test was also conducted on the two sets of paired means, resulting in $t_{\text{stat}, 5\%} = 2.55 > t_{\text{critical}} = 1.86$, indicating that there was statistically significant difference between the two data sets. This was true because outliers occurred at high peg peripheral speed for the experimentally measured bean grain damage; otherwise, the trend of output values were almost the same. At a 10% residual error interval, the prediction performance of the damage model based on actual data was 77%.

2.1.3 Effect of peripheral pegs velocity on threshing efficiency

It was also important to determine the threshing efficiency for common bean thresher using computational mathematical model equations and experimental measured data. Threshing efficiency was determined as a fraction of threshed bean grains from the pods to the total sum of threshed and unthreshed bean grains expressed as a percentage. However, the total grain loss considers the sum of the total of damaged grains and threshing losses. Figure 4 shows the experimental and computed threshing efficiency of common beans thresher under different peg peripheral cylinder speeds. Common beans at moisture content less than 20% do not require much impact force for threshing. A little touch impact will break common beans pods, evident from the 100% efficiency results from experimental common beans thresher. At low peg peripheral speed tested between 1.8 and 2.8 ms^{-1} , the threshing efficiency of the measured thresher was a mean of 99%, after which a constant figure of 100% efficiency was maintained. This shows that during the operation of a beans thresher, the problem is not threshing instead, conveyance is the issue because of the long straws that wind on the drum cylinder (Ukatu, 2006).

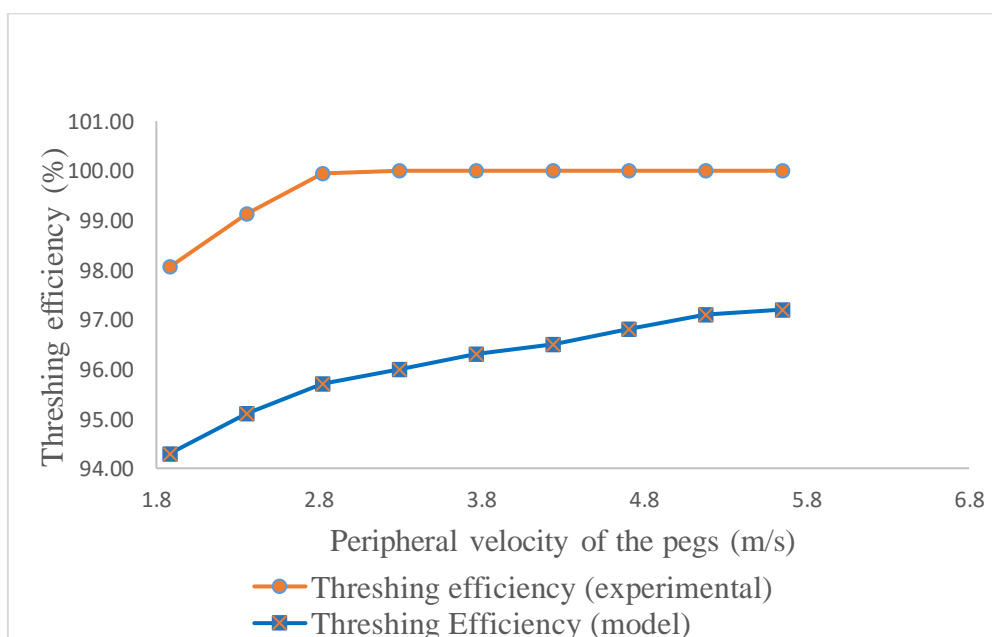


Fig. 4 - Comparison of experimental and computed threshing efficiency of beans thresher for different cylinder peg peripheral speeds

The average computed threshing efficiency was 96%. This is acceptable by many farmers for a thresher in the market (Moussa, 2006). There was an increase in threshing efficiency with an increase in peripheral velocity of the cylinder pegs for both experimental and computed output data. This is justified because threshing efficiency relates to the velocity of the pegs exponentially. R^2 was 0.91 and 0.5 for the computed and measured sets of data, respectively. Again this shows a positive correlation and the trend between the two sets of outputs from the model and experimental methods. Therefore, either of the two can be used for simulating the threshing efficiency of common beans thresher. However, there was a statistically significant difference between the two data sets since t -stat at 5% = 20.9 > t critical = 1.85. This could be explained by the little impact required for threshing dried common beans. The absolute residual error analysis results between the simulated and the mean experimental observed fraction of the damaged grains for the 9 data ranged from -2.8% to -4.5%, with a mean value of 3.5%. This implies some differences between the simulated and actual data on a number of peripheral velocities of the pegs, however, within -5% residual error interval. At 5% absolute residual error, the prediction performance of threshing efficiency based on actual data was 100%.

2.1.4 Effect of pegs velocity on throughput capacity

Processing time is of great essence in agricultural production, especially to get value for money from the produce. This can be significantly reduced by using machinery as opposed to hand working (Ndirika, 2006). Throughput capacity is an important output of a machine that influences the time of production. For common beans thresher, throughput capacity can be defined as the amount of threshed bean grains in an hour. As already mentioned, traditional methods of threshing that involve using sticks and animals are slow and tedious. Therefore, simulation of throughput capacity during design and development of common bean thresher was key for further optimization. Figure 5 shows results of measured and computed throughput capacity of common beans thresher under different speeds of cylinder pegs. The trend from observation of Figure 5 was almost the same for computed and measured data sets.

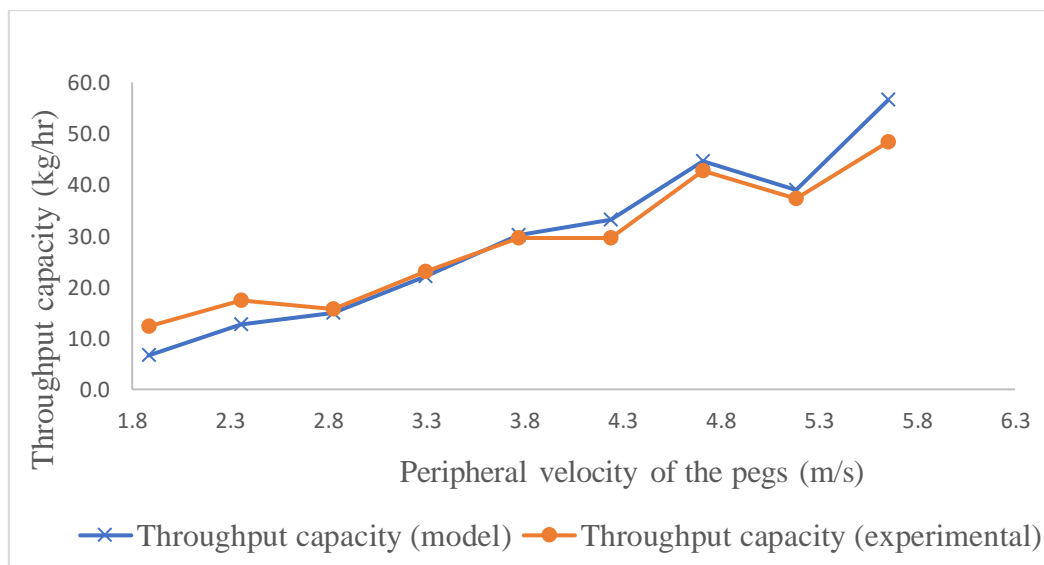


Fig. 5 - Comparison of computed with measured throughput capacity of common beans thresher under different peripheral speed of cylinder pegs

An increase in peripheral velocity of cylinder pegs resulted in increased throughput capacity. At high speed, the threshing process is faster, and the feeding rate is also enhanced. This is backed by the fact that the velocity of pegs, grain-straw ratio, bulk density, feed rate, separation efficiency, and concave configurations affect grain threshers' output capacity (Behera *et al.*, 1990; Enaburekhan, 1994; Ndirika, 1997). This forms a good optimization criterion of maximizing the dependent variable based on independent variables, which can be achieved at low cost using simulation. R^2 was 0.99 for both computed and measured throughput capacity of common beans thresher. Again, this confirms a positive correlation between the simulated throughput capacity using mathematical models and the experimentally measured

output capacity. Therefore, the model can be used for further simulation and optimization of the beans thresher. The student *t*-test was also conducted to check if there was significant difference between the two data sets. The *t*-stat at 5% = 0.29 < *t*-critical = 1.89, an indication that there was no statistically significant difference among the two data set samples. Absolute residual error analysis was conducted, and the results between the simulated and the mean experimental observed fraction of the damaged grains for the 9 data ranged from 2.1% to 16%, with a mean value of 8%. This implies some disparities between the simulated and actual data on a few peripheral velocities of the pegs, which were above 5% residual error interval but on average were within 10% residual error interval. Based on the actual data and 10% absolute residual error interval, the prediction performance of the throughput capacity model was 77%.

2.1.5 Simulating the effect of moisture content on bean grain damage and threshing efficiency

While carrying out experiments to evaluate the performance of common beans thresher, grain damage at high peripheral peg speed was an issue of concern as opposed to threshing efficiency. Common beans threshability is high when the moisture content is low. The aim, therefore, is to minimize the fraction of damaged bean grain possibly to less than 2%. After validating a mathematical predicting equation for a performing common beans thresher, it was essential to simulate the effect of moisture content on performance.

The oven-drying method of moisture determination was used in calculating moisture content by wet basis for common beans. The moisture content was 56.7% and 46.6% for unthreshed common beans and bean grains, respectively, after harvesting from the farm. After sun drying, the moisture content by wet basis reduced to 18.7% and 17.6% for unthreshed common beans and bean grains, respectively, which was ideal for threshing using the developed common beans thresher. Using the same moisture content range, the performance of the bean thresher was simulated. Figure 6 shows the results of simulating the effect of moisture content on threshing efficiency and grain damage.

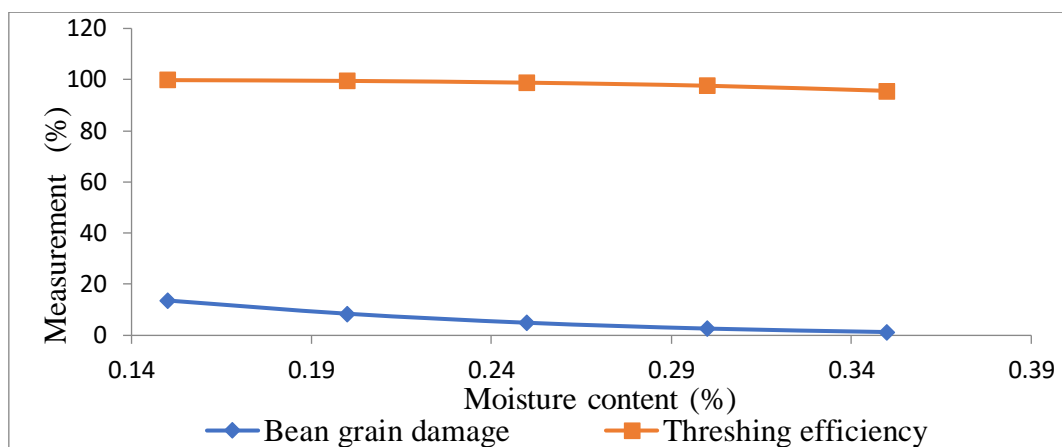


Fig. 6 - Effect of moisture content on threshing efficiency and grain damage of common beans thresher

The efficiency of threshing common beans decreased with an increase in moisture content of unthreshed beans as observed from Figure 6. The results are similar to *Osueke (2011)*, which observed a decrease in threshing efficiency with increased moisture content. During threshing, the bean grains are detached from the pods by a combination of stripping, rubbing, and impact action through the application of tensile, compressive, bending, and twisting forces. However, this is not effective at high moisture content. At a moisture content of 35% similar to that when harvesting, it can be observed that threshing efficiency will be at 95%, leading to high grain losses. Therefore, the recommended moisture content for threshing will be 20% and below.

Increased moisture content resulted in decreasing in damages of common bean grains. The results were similar to *Khazaei (2008)*, who found that increasing moisture content from 5 to 15% (wet basis), the mean values of the percentage of damaged beans decreased by 1.4 times. This could be because of the high threshability that exposes the bean grains to excess impact and rubbing action.

Therefore, optimization criteria will be to achieve high threshing efficiency with the lowest grain damages. Based on Figure 6, the recommended moisture content for threshing common beans will be 23% for low grain damage and high efficiency.

2.1.6. Simulating the effect of effective cylinder diameter on threshing efficiency and grain damage

Based on the cylinder-concave arrangement, an increase in effective diameter decreases the concave clearance. Therefore, concave clearance is inversely proportional to the effective diameter. To this extent, simulation of effective diameter results has a relationship with concave clearance. Figure 7 shows the results of simulating effective cylinder diameter on threshing efficiency and beans grain damage. It was observed that an increase in effective cylinder diameter results in increased threshing efficiency. This can be explained by the increased impact and rubbing action due to the reduced concave clearance leading to increased threshing. Similar results were discussed by *Osueke (2011)* based on published experimental data. He reported that decreasing the concave clearance resulted in increased efficiency. This was because decreasing concave clearance may have increased the chance of a grain being struck by the bar or spike and increased the chance of multiple impacts to the grain before it is passed from the threshing zone. The range of effective cylinder diameter of 0.2 m to 0.3 m was based on the spherical diameter of common beans, which was 0.16 m. The same interval was used during the experimental evaluation of the developed common beans thresher.

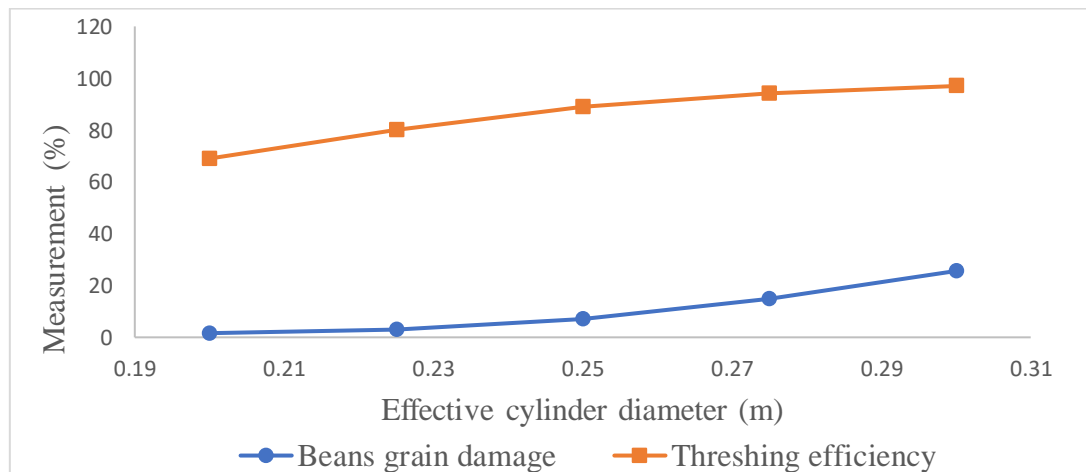


Fig. 7 - Simulation results of effect of effective cylinder diameter on threshing efficiency and bean grains damage.

An increase in effective diameter resulted in an increase in bean grains damage. The explanation for this is that rubbing and impact action was increased with reduced concave clearance leading to increased grain damage. Therefore, the choice of the correct effective diameter is very key in the reduction of grain damage. Optimization criteria are necessary to determine the correct cylinder-concave configuration (low seed damage) for effective germination of seeds and increased market value for the beans. This can be achieved by conducting experiments on the validated model system at low or zero cost.

2.2 Simulating the effect of concave width on threshing efficiency

During design, the determination of the correct and effective concave width is the key. Longer width of the concave calls for more materials, which has cost implications and makes the machine heavier for portability cases. Therefore, it was important to simulate the effect of linear concave width on threshing efficiency, as indicated in Figure 8. The 1 m span of linear concave width was divided into quarters of 0.25 m. The results from Figure 8 show that an increase in linear concave width resulted in increased threshing efficiency. This is justified by the increased exposure time of the unthreshed bean pods to impact, twisting, and rubbing action within the concave area. At a concave width of 0.25 m, the threshing efficiency was 25.4%, resulting in many losses. From the results, linear concave length less than 1 m gave an output threshing efficiency of less than 94.1%. This implies that for the design of a common bean thresher, the recommended linear concave width should be equal to or greater than 1 m.

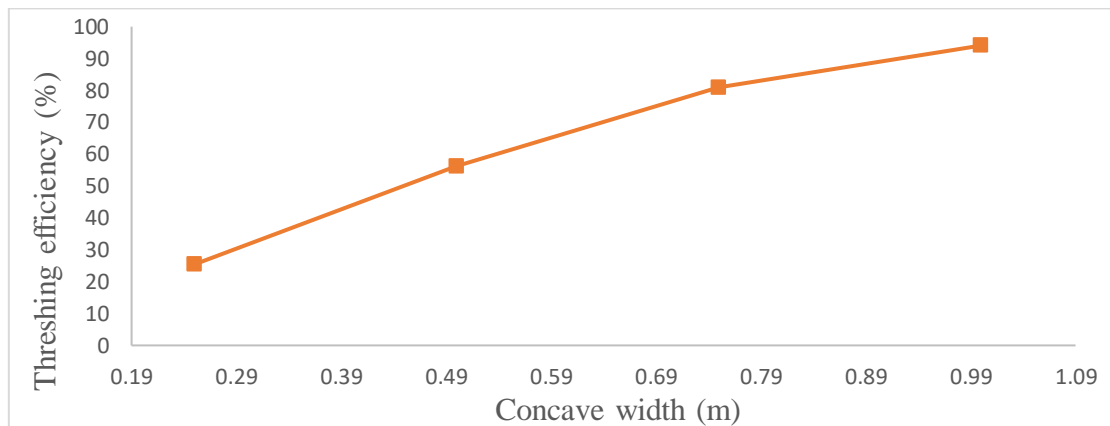


Fig. 8 - Simulation results for the effect of linear concave width on threshing efficiency

CONCLUSIONS

The goal of the study was to develop a common bean thresher by first simulating the design variables to understand the effect of independent and dependent variables on the performance of the thresher. The results then informed the sizing and design based on the correct cylinder-concave configurations, feed rate, peripheral speed of the pegs, moisture content, and bulk density of the unthreshed common beans. This is in relation to the performance of the developed thresher. The mathematical predicting equations for power requirement, bean grain losses, grain damages, efficiency, and throughput capacity were developed and validated using experimental data from the same study. The results showed a positive correlation based on the coefficient of determination for the used simulation models. Furthermore, the difference between the means of the computed and measured experimental outputs was not statistically significant at a 5% level of significance for all the performance models apart from the predicting damage equation. This gives a high confidence level to use the mathematical predicting equations for simulation and optimization of common bean thresher. The results noted that an increase in cylinder peripheral speed of the pegs increased power requirement, bean grain damages, threshing efficiency, and throughput capacity. In addition, the increase in the moisture content of beans resulted in a decrease in threshing efficiency and bean grain damages. The recommended moisture content for threshing common beans was 21% on a wet basis. Also, an increase in effective cylinder diameter caused an increase in threshing efficiency and grain damages. The spherical bean grain size is the determinant for the concave clearance size. Finally, an increase in linear concave width resulted in an increase in threshing efficiency. The recommended minimum width of 1 m can improve the threshing efficiency (94.1%) and thus avoid grain losses.

ACKNOWLEDGEMENT

Special thanks go to Jomo Kenyatta University of Agriculture and Technology that has provided a very conducive environment and opportunity for us to implement this project. We are grateful to the entire School of Biosystem of Environmental Engineering (SOBEE) for their contribution and advice. Finally, we would like to acknowledge the African Development Bank (AfDB) through the Ministry of Education Science and Technology in Kenya (MoEST) and Japan International Cooperation Agency (JICA) through the AFRICA-ai-JAPAN project phase II for providing financial support to the implementation of this research.

REFERENCES

- [1] Behera, B. K., Dash, S. K., & Das, D. K. (1990). Development and testing of a power-operated wheat thresher. *Agricultural Mechanization in Asia, Africa and Latin America (Japan)*, 21(4), 15-21.
- [2] De Groote, H., Marangu, C., & Gitonga, Z. M. (2020). Evolution of agricultural mechanization in Kenya. *An evolving paradigm of agricultural mechanization development: How much can Africa learn from Asia?* Washington DC: Intl Food Policy Rest Inst. <https://doi.org/10.2499/9780896293809>.
- [3] Desta, K., & Mishra, T. N. (1990). Development and performance evaluation of a sorghum thresher. *AMA, Agricultural Mechanization in Asia, Africa and Latin America*, 21(3), 33-37.

- [4] Duke, J. (2012). *Handbook of legumes of world economic importance*. Springer Science & Business Media.
- [5] Dysarz, T. (2018). Application of python scripting techniques for control and automation of HEC-RAS simulations. *Water*, 10(10), 1382.
- [6] Enaburekhan, J. S. O. (1994). Mathematical and optimization modelling of the threshing process in a stationery grain thresher. *Unpublished PhD Thesis. Department of Agricultural Engineering. Ahmadu Bello University, Zaria, Nigeria*, 23.
- [7] Gregory, J. M. (1988). Combine model for grain threshing. *Mathematical and Computer Modelling*, 11, 506-509.
- [8] Hart, W. E., Watson, J. P., & Woodruff, D. L. (2011). Pyomo: modelling and solving mathematical programs in Python. *Mathematical Programming Computation*, 3(3), 219-260.
- [9] Huynh, V. M., Powell, T., & Siddall, J. N. (1982). Threshing and separating process—A mathematical model. *Transactions of the ASAE*, 25(1), 65-73.
- [10] Joshi, N. L. (2006). Harvest and post-harvest practices and losses in arid legumes. *Arid Legumes for Sustainable Agriculture and Trade*, 2(2), 385-388.
- [11] Kiptoo, G. J., Kinyua, M., Kiplagat, O., Wanjala, F. M. E., Kiptoo, J. J., Cheboi, J. J., & Ngurwe, J. K. (2016). Evaluation of common bean (*Phaseolus vulgaris* L.) varieties for resistance to bean stem maggot (*Ophiomyia* spp.) in Kenya. *Journal of Experimental Agriculture International*, 12(3), 1-7.
- [12] Kanali, C. L. (1997). Prediction of axle loads induced by sugarcane transport vehicles using statistical and neural-network models. *Journal of Agricultural Engineering Research*, 68(3), 207-213.
- [13] Kituu, G. M., Shitanda, D., Kanali, C. L., Mailutha, J. T., Njoroje, C. K., Wainaina, J. K., & Silayo, V. K. (2010). Thin layer drying model for simulating the drying of Tilapia fish (*Oreochromis niloticus*) in a solar tunnel dryer. *Journal of Food Engineering*, 98(3), 325-331.
- [14] Law, A. M., Kelton, W. D., & Kelton, W. D. (2000). *Simulation modelling and analysis*. (Vol. 3). New York: McGraw-Hill.
- [15] Mutuku, J. M., Wamonje, F. O., Mukeshimana, G., Njuguna, J., Wamalwa, M., Choi, S. K., & Harvey, J. J. (2018). Metagenomic analysis of plant virus occurrence in common bean (*Phaseolus vulgaris*) in Central Kenya. *Frontiers in Microbiology*, 9, 2939.
- [16] Muna, N. H., Muhammed, U. S., El-Okente, A. M., & Isiaka, M. (2016). Development and Validation of Threshing Efficiency Mathematical and Optimization Model for Spike-Tooth Cereal Threshers. *International Journal of Engineering Research and Development*, 12(11), 50-60.
- [17] Mwangi, J. K., Mutungi, C. M., Midingoyi, S. K. G., Faraj, A. K., & Affognon, H. D. (2017). An assessment of the magnitudes and factors associated with post-harvest losses in off-farm grain stores in Kenya. *Journal of Stored Products Research*, 73, 7-20.
- [18] Moussa, A. J. (2006). The effect of selected mechanical threshing parameters on threshability of some legume crops. *Journal of Agricultural Economics and Social Sciences*, 31(7), 4297-4312.
- [19] Ndirika, V. I. O. (1997). Modelling the performance of selected stationary grain threshers. *Unpublished PhD Thesis, Department of Agricultural Engineering, Ahmadu Bello University, Zaria*.
- [20] Ndirika, V. I. O. (2006). A mathematical model for predicting output capacity of selected stationary spike-tooth grain threshers. *Applied Engineering in Agriculture*, 22(2), 195-200.
- [21] Osueke, C. O. (2011). Simulation and optimization modelling of performance of a cereal thresher. *Int J Eng Technol IJET-IJENS*, 11(3), 143-152.
- [22] Osueke, E. C. (2014). Study of the influence of crop, machine and operating parameters on performance of cereal threshers. *International Journal of Engineering Research and Development*, 7(9), 1-9.
- [23] Ramteke, A. S., & Sirohi, N. P. S. (2003). Studies on Design parameters for linseed crop thresher. *Journal of Agricultural Engineering*, 40(2), 39-45.
- [24] Singh, K. P., Poddar, R. R., Agrawal, K. N., Hota, S., & Singh, M. K. (2015). Development and evaluation of multi millet thresher. *Journal of Applied and Natural Science*, 7(2), 939-948.
- [25] Ukatu, A. C. (2006). A modified threshing unit for soya beans. *Biosystems engineering*, 95(3), 371-377.
- [26] Harrison, H. P. (1969). The Effect of Selected Mechanical Threshing Parameters on Kernel Damage. *Canadian Agricultural Engineering*, 11(2), 83-87.
- [27] Wortmann, C. S. (1998). *Atlas of common bean (Phaseolus vulgaris L.) production in Africa* (No. 297). CIAT.

RESEARCH STATUS AND DEVELOPMENT TREND OF MECHANIZED STRAW RETURNING TECHNOLOGY. A REVIEW

/

秸秆机械化还田技术研究现状与发展趋势综述

Liang Fang^{1,2*}, Wang YuBing¹, Deng WeiHong¹, Yuan Shaoning¹, Wang Zirui¹

¹College of Engineering, Huazhong Agricultural University, Wuhan 430070, China;

²Key Laboratory of Agricultural Equipment in Mid-lower Yangtze River, Ministry of Agriculture and Rural Affairs, Wuhan 430070, China;

Tel: +8618771938723; E-mail: liangfang101@sina.com

DOI: <https://doi.org/10.356.33/inmateh-65-48>

Keywords: straw returning, composite process, evaluating indicator, precision control, development trend

ABSTRACT

As the application of agricultural mechanized production technology becomes more and more extensive, the application of mechanized straw returning technology has become more and more valuable. The mechanized return of straw to the field is a time-saving and labor-saving technology. It is an effective way to achieve sustainable agricultural development and is of great significance to the development and progress of modern agriculture. This article analyzes the current research status of mechanized straw returning to the field, discusses the process structure and characteristics of different mechanized straw returning methods, and focuses on the analysis of the composite technology of straw returning to the field. At the same time, the key problems of straw returning to the field, such as the length of straw not meeting the standard, the shallow depth of straw returning to the field, and the uneven distribution of straw, are put forward and analyzed. By taking the cover and burial rate of straw on the soil surface and the spatial distribution uniformity of straw in the soil as the performance evaluation indexes of straw mechanized field return, each index is elaborated. Finally, two major development trends are proposed: the development of mechanized straw returning to the field from a single process to a composite process, and the effect of straw returning to the field towards uniform mixed burying and precise control.

摘要

随着农业机械化生产技术的应用越来越广泛，秸秆机械化还田技术的应用也愈来愈变得有价值。秸秆机械化还田是一项既省时又省力的技术，是实现农业可持续发展的有效途径，对现代农业的发展进步有着极为重要的意义。文章对当前秸秆机械化还田技术研究现状进行分析，探讨了秸秆不同机械化还田方式工艺结构与特点，重点对秸秆还田的复合工艺方式进行分析。同时，提出了秸秆长度不达标、秸秆还田深度浅以及秸秆分布不均匀等秸秆还田存在的关键问题，并对其展开分析。通过将地表秸秆的覆盖率与埋覆率以及土壤中秸秆的空间分布均匀性作为秸秆机械化还田的性能评价指标，并对其各指标展开阐述。最后提出了秸秆机械化还田由单一工艺向复合工艺发展，秸秆还田效果向均匀混埋和精准调控发展的两大发展趋势。

INTRODUCTION

The general term for the stems and leaves of crops after mature threshing is straw. The crop stalks in China are widely distributed, large in quantity, and diverse in variety. At present, the total amount of crop straw produced in our country each year is nearly one billion tons, accounting for about one-third of the total amount of straw in the world, ranking first in the world, of which corn, rice and wheat straw are mainly used. The total straw of these three major food crops accounted for nearly three-quarters of the total crop straw in the country (Qiao, 2020; Zhao, 2019). With the continuous improvement of the national economy, farmers' harvests are getting better and better, and the output of crop stalks is also increasing (Chang, Bian, 2015). The crop straw is rich in a lot of nutrients, which is a good fertilizer and renewable energy (Xu, 2020). The treatment of crop straw resources has always been an important issue in agricultural production. The existing treatment methods for crop straw resources are mainly picking up and bundling, burning and returning to the field. The way of picking up and bundling greatly increases operation and transportation costs, and incineration will pollute the environment and cause serious ecological problems. Therefore, returning straw to the field has become an effective way to rationally use straw resources (Huang et al., 2021). Returning straw to the field can effectively promote the maintenance of soil nutrients and is an important management method to increase crop yields (Chen et al., 2017).

Returning straw to the field can not only increase the content of soil organic matter and increase soil fertility, but also increase soil porosity, reduce soil bulk density, and improve soil permeability, which has important economic and ecological benefits (Wang *et al.*, 2013; Hu *et al.*, 2012).

RESULTS OF THE RESEARCH

STRAW MECHANIZED RETURNING TO THE FIELD BACKGROUND

Distribution of Crop Straw Resources in our Country

Due to China complex geographic environment, the distribution of crop straw resources also shows obvious regional differences (Zhang, 2019). Looking at the distribution of crop straw resources in our country, it shows a stepped distribution characteristic of "high in the east and low in the west, high in the north and low in the south". China's straw resources are mainly concentrated in the Northeast, North China and the middle and lower reaches of the Yangtze River. Among them, corn straws are mainly distributed in North China and Northeast China. The distribution of rice straw resources appears at two levels: the northeast region with Heilongjiang as the gradation center and the Jiangnan region with Hunan and Jiangxi as the gradation center (including the middle and lower reaches of the Yangtze River, southwest and southeast). Wheat straw resources are mainly concentrated in North China, with Shandong and Henan as the center, with short-term spreading from north to south, and extending to the west along the Hexi Corridor in depth. Except for the straws of the three major food crops, although the straw resources of other crops do not account for much, they also show obvious regional enrichment. More than half of the cotton straw resources are concentrated in Xinjiang. Among them, Shandong, Hebei, Hubei and other places in North China and the middle and lower reaches of the Yangtze River are also rich in cotton. North China is the main enrichment area of peanut straws, most of which are concentrated in the three provinces of Henan, Shandong and Hebei. The middle and lower reaches of the Yangtze River and the southwest are the areas where rape straw is enriched, and Hubei, Hunan and Sichuan are the most concentrated (Cong *et al.*, 2019).

Biological characteristics of main crop straw

Corn straw is composed of roots, stems and leaves, of which the proportion of stems is the largest, and there are differences in different components (Xu., 2019). The potassium content of corn straw is about 2.28%, the nitrogen content is about 0.6%, the phosphorus content is 0.27%, and the organic matter content can reach about 15% (Dai *et al.*, 2019). When the rice is harvested and threshed in the sun (the water content of the rice is not more than 16%), the total weight of the straw and the rice is basically 1:1, and the ratio between them is related to the water content and the height of the stubble at harvest. The rice is firm. There is a great relationship between rate and maturity, and there is no absolute value. Under normal circumstances, the stalks of wheat and rice are relatively thin and soft, and the above-ground parts generally have 5-6 nodes, which are large tortuous and elastic; while the stalks of maize are relatively tall, and the number of above-ground nodes can generally reach 17-18. The internodes are thick, hard, and not easy to break (Li *et al.*, 2019). The stem of wheat stalk is hollow with only the outer skin layer, while corn stalk contains the middle layer, but the middle is the medulla part, which is lighter in texture (Huo *et al.*, 2012). There are structural differences between rice straw and wheat straw. The cross section of rice straw is generally flat, and the cross section of wheat straw is basically elliptical, not standard cylindrical (Guo, 2017). The outer skin of rape stalks is dense and smooth, and has good air permeability. Under normal circumstances, the straw coefficient of rapeseed is 2.87, second only to cotton (3.0) among large-scale cultivated crops in my country, and higher than rice (1.00), wheat (1.17), corn (1.04), peanut (1.14), and beans (1.60) and other crops. Rapeseed has a large amount of straw, high grass-to-grain ratio, thick stalk, high stubble, dense and thick root system, and it is difficult to treat the root stubble (Luo, 2013; Li, 2014; Zhang *et al.*, 2014)

WAYS OF RETURNING STRAW TO FIELD BY MECHANIZATION

Aiming at the mechanized return of straw to the field, at present, the main methods at home and abroad include straw directly smashed and returned to field, rotary tillage of stubble, crushing and returning, use of plowing to return to the field, whole straw burying and returning to field and so on (Chief, 2007). The technological structure and characteristics of different mechanized methods of returning straw to the field are summarized as follows:

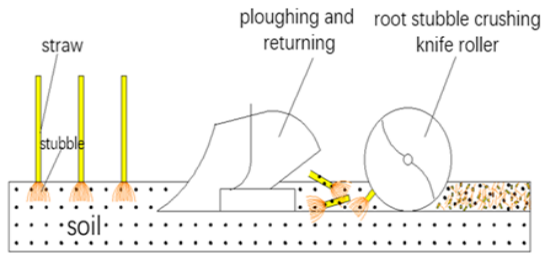
Table 1

Process structure and characteristics of different mechanized return methods of straw

The way	Process schematic	Features	Structure chart
Direct smash			<p>The straw is crushed by a flinger or the straw is picked up and transported by a picker to a crushing roller to complete the crushing, and then thrown directly on the ground. The structure of the whole machine is simple and light. The length of chopped straws is less than 10 cm, but the straws are located on the ground and are piled up by wind. The distribution is uneven and the decomposition is insufficient, which is easy to cause the congestion of the seeding opener in the later stage (Qiu et al., 2015).</p>
Rotary crushed			<p>The root stubble and soil are cut, crushed, mixed and covered with a rotary tiller. It not only completes the return of straw to the field but also realizes soil plowing, the operation efficiency is high, but for the high-stalk and high-density straw such as rice, it is easy to cause the stalk entanglement of the knife shaft, and the problems of seeding, trenching, congestion, and seed beds (Zhang, 2014).</p>
Plowing			<p>The tractor is used to pull the plow to complete the soil buckle and straw burial. When the length of straw is less than the depth of plowing, the burial effect is significant, but when the length of straw is greater than the depth of plowing, the part of the straw that exceeds the depth of plowing stays on the surface of the adjacent soil and can't be buried. The root system is brought to the surface, which affects the construction of subsequent planting beds.</p>

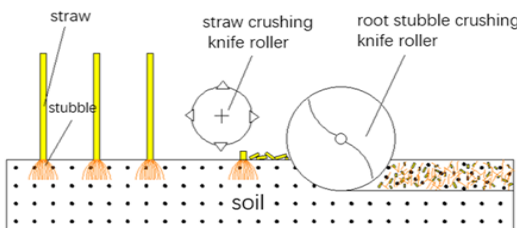
The way	Process schematic	Features	Structure chart
---------	-------------------	----------	-----------------

Plough and rotary tillage compound



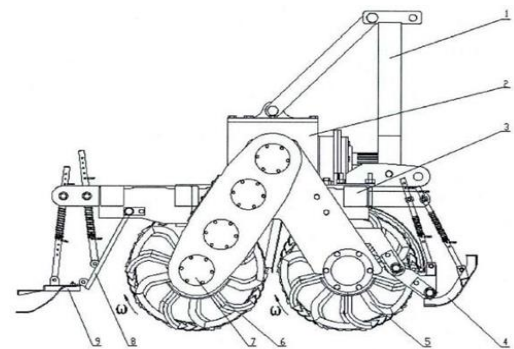
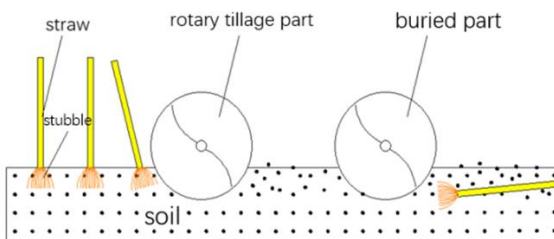
The turning and burying of soil and straw are realized by the plough, and the cutting and crushing of the soil and straw are completed by the rotary tillage tool. The advantages of large ploughing depth (below 20 cm) and good burying effect are brought into play, and the advantages of rotary tillage tools for crushing soil and roots and mixing are used, and the crushing and burying effect is good. The turning and disturbance of the soil by the split plough changes the mechanical properties of the soil and reduces the power consumption of rotary tillage and crushing (Qin et al., 2016; Heinze et al., 2016).

Crushing and rotary tillage compound



The straw is crushed by the scalpel, and the cutting, crushing and burying of the straw stubble and the soil are completed by the rotary tillage tool. Under the combined action of the straw crushing tool and the rotary tillage tool, the straw crushing length is smaller and the burial distribution is more uniform, which helps to improve the straw burial and decomposing effect.

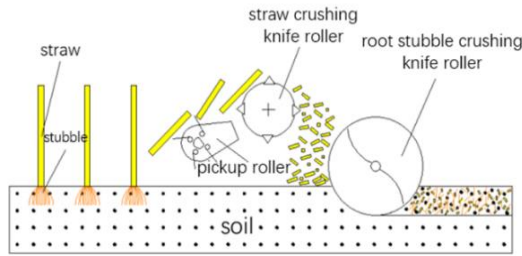
Rotary tillage and mulching



The cutting and smashing of straw stubble and soil are completed by rotary tillage tools, and straw-soil mixing and burying are completed by burying rollers. It is especially suitable for returning high-stubble straws in paddy fields to realize the whole straw burial of rice straw with high burial rate.

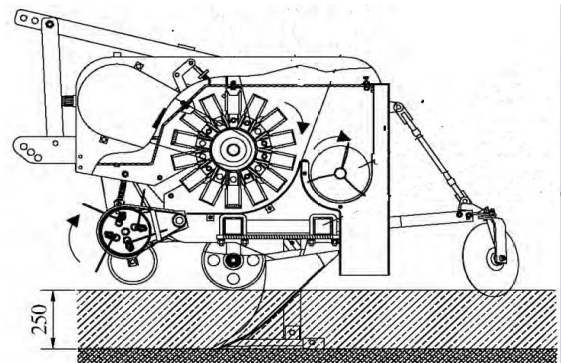
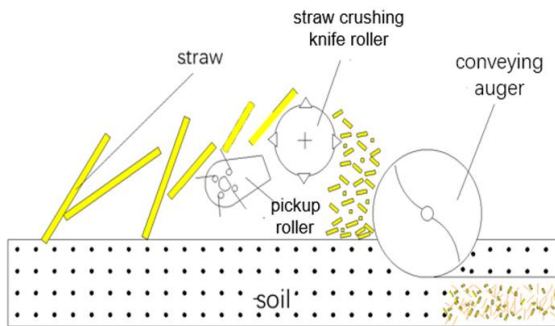
The way	Process schematic	Features	Structure chart
---------	-------------------	----------	-----------------

Picking up, smash, and bury



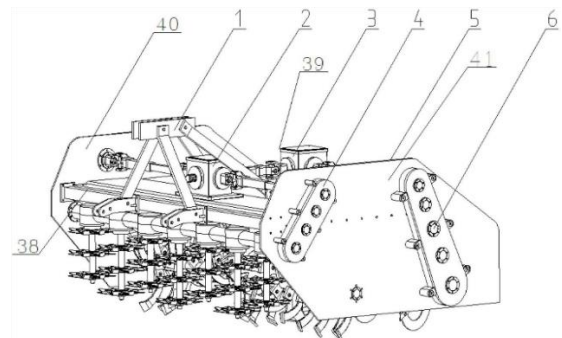
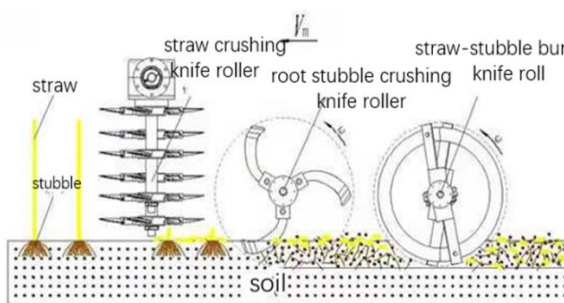
The straw is picked up and transported to the crushing knife roller by a picker, and then crushed and thrown on the ground. Then the soil, stubble cutting, crushing and mixing are completed by a rotary cutter. This method uses a feed crushing knife roller to crush the straw. The length is short and uniform. Under the action of rotary tillage tools, the burial rate is high and the soil mixes evenly, which helps to accelerate the decomposition of straw, especially suitable for straw with large amount of straw and thick stalk.

Pick up and smash the ditch to bury



The surface straw is picked up by the picker and transported to the crushing knife roller to complete the crushing, and the straw is conveyed through the churn to both sides of the compartment ditch deep burial, which solves the blockage of the opener and the seeds entering the soil during the subsequent sowing process. The unreal problem also has the function of "drainage ditch" and "retaining nitrogen".

Straw stubble crushing and burying



The straw is crushed by vertical or horizontal straw crushing knives, the soil and root stubble are cut, crushed and mixed by rotary knives, and the straw-root stubble is mixed and buried in the soil by buried knife rollers. It is especially suitable for rape and other straw with high stubble, high grass to grain ratio and strong stalk. The special mixed burying knife roller improves the burying rate and uniformity of straw, and accelerates the decomposition of straw.

ANALYSIS OF THE KEY PROBLEMS OF MECHANIZED STRAW RETURNING TO THE FIELD

The purpose of returning straw to the field is to bury the decomposed straw, and the speed of decomposing is the key. Different methods of returning straw to the field have different rates of straw decomposing. Returning parameters such as straw crushing length, buried depth and straw distribution uniformity had significant effects on straw decomposition rate.

Straw length is not up to standard

Different crops have different characteristics of straw, but almost all satisfy the rule that the shorter the length of straw, the faster the decomposing rate. Yang Xuying found that rape straw with length less than 10 cm decomposed faster than that with length greater than 10 cm (Yang, 2014). Pang Lidan found that the decomposition rate of 3–5 cm corn straw was higher than that of 5–10 cm corn straw (Pang, 2017). Qian Feng proposed that for small crops such as wheat and rice, the crushing length of less than 15 cm is qualified, while the crushing length of sorghum and corn is less than 10 cm (Qian, 2018). For each crop straw, due to its different characteristics, the most suitable length of straw crushing after returning to the field needs further study. Relevant studies have shown that when the length of straw crushing is too long, it will affect the plowing effect of returning straw to the field, which will not only cause the soil to be overhead, but also lead to residual straw on the ground, which will affect the sowing and rooting of seedlings (Dong, 2019).

Shallow depth of returning straw to field

After the straw is buried and returned to the field, the decomposition of the straw mainly depends on the action of the microorganisms in the soil, and the microorganisms in the soil are mainly concentrated in the 0–10cm soil surface. Hu Hongxiang and others found that the decomposition rate of rice straw returning at 5cm depth was faster than that returning at 10cm depth and surface layer (Hu, 2012). If the straw is buried in the shallow layer of soil after returning to the field, the shallow layer of soil will be too loose, resulting in insufficient mixing of the straw and the soil, and the phenomenon of stacking of the straw, which will affect the quality of sowing. For paddy fields in South China, part of straw in shallow layer will float on the water surface, which seriously affects the quality of transplanting rice. Crop straw itself carries pathogens and pests. After straw returning, pathogens and pests will be buried underground. Straw returning depth is too shallow, which is more conducive to the survival and reproduction of diseases and pests. It will cause the continuous accumulation of diseases and pests in the soil, which is easy to induce diseases in the next crop and greatly affect the crop yield. Straw buried deep into the field can effectively improve the soil's ability to retain water, fertilizer and supply fertilizer, and it can also promote the distribution of roots, which is conducive to the growth of crops (Liu et al., 2021).

Uneven distribution of straw

After the straw is returned to the field, the amount of straw that can be decomposed per unit volume of soil is limited. Improving the uniformity of the straw distribution in the soil will help to further increase the decomposition rate of the straw (Hu et al., 2012). If the straw distribution is uneven, the phenomenon of stacking and clustering appears, the sowing will be uneven and the seed depth is different, which seriously affects the sowing quality. At the same time, the straw after returning to the field will affect the contact between the seed and soil after sowing, which will lead to the loose contact between the seed and soil, and then affect the rooting and germination of the seed. At present, the main performance parameters of the straw returning machine are the returning depth and burial rate. Obviously, this parameter cannot accurately and comprehensively reflect the characteristics of the decomposing rate. To this end, Shi Yong divided a certain volume of soil into units of the same volume, and measured the amount of straw in each unit to establish a straw burial uniformity evaluation system, and used different rice straw lengths (5 cm, 12.5 cm, 20 cm). Experiments show that the length of straw has a significant effect on the uniformity of burial, but the two do not show a simple positive correlation (Shi, 2015; Li, 2020). It can be seen that improving the uniformity of burial is very important to increase the decomposing rate, and the suitable length of straw crushing also needs further study.

PERFORMANCE EVALUATION INDEX OF STRAW MECHANIZED RETURNING TO FIELD

Coverage rate of ground straw

According to the positional relationship between the straw and the soil, the straw return operation can be divided into: straw on the soil surface (the straw is crushed and thrown directly on the ground), and the straw is under the soil (the plow opens the ditch to buckle the surface straw and the soil, and it is buried deep into the field.) And the straw and the soil are evenly mixed (the soil and the crushed straw are relatively evenly mixed by rotary tillage) (Zhou et al., 2019).

The mulch of ground straw can effectively maintain and improve the function of the soil (Akhtar *et al.*, 2019). The state of the surface soil and the distribution state of the straw after returning the straw to the field are the main evaluation indicators for the quality of the straw returning to the field. The coverage rate of surface straw is recognized as an important technical indicator of conservation tillage technology. Coverage refers to the proportion of straw covering the ground in a unit measurement area. At present, there are many calculation methods for the surface straw coverage rate. The traditional method before is to use manual rope measurement, the calculation formula is as follows:

$$\mu = \frac{N_0}{N} \times 100\% \quad (1)$$

Among them: N_0 is the number of nodes with straw under the intersection of the rope and the rope; N is the number of the summary point of the intersection of the rope and the rope.

Although this method is relatively simple to operate, it is not accurate and labor-intensive. Nowadays, people are more inclined to use image processing technology to calculate the surface straw coverage, which is also the more accurate measurement method at present. However, when the number of straws is large, the distribution is uneven, and the overlap is serious, large errors will occur. At the same time, the color of some straws with more serious corrosion will be similar to the soil, which will also cause certain errors. Based on the existing image processing method, Li Jia, Lv Chengxu and others proposed an automatic recognition method of straw coverage combining fast Fourier transform and support vector machine, which can effectively solve the impact of real field complex environment on straw and soil recognition, with small measurement error and high performance (Li *et al.*, 2019). Obviously, after the straw is returned to the field, the surface straw coverage rate cannot accurately reflect the quality of the straw returned to the field, so other indicators need to be evaluated and analyzed.

Burying rate of ground straw

At present, regardless of whether the straw is returned to the field for plowing or rotary tillage, the burial rate is an important indicator to measure the quality of straw returning to the field. After returning the straw to the field, by measuring the quality of the straw per unit area before and after ploughing at the sampling point, and then calculating according to formula (1), the burial rate η of the surface straw after returning the straw to the field can be obtained.

$$\eta = \frac{m_q - m_h}{m_q} \times 100\% \quad (2)$$

In the formula:

m_q is the straw mass per unit area of the sampling point before ploughing, g.

m_h is the straw mass per unit area of the sampling point after ploughing, g (Wang *et al.*, 2010).

The current measurement of the burial rate of straw returning to the field is mainly calculated based on the change in the quality of the straw per unit area before and after the operation, which is also a more accurate measurement method commonly used at present. However, when the straws on the local surface are unevenly distributed and stacked on top of each other, there will be large errors in the measurement of the straw quality per unit area before and after ploughing. Therefore, the method of measuring the straw burial rate needs further research.

Spatial distribution uniformity of straw in soil

At present, there are many studies on the distribution of straw on the ground, but there are few studies on the spatial distribution of straw in the soil. Previous related studies mainly used stratified sampling to determine the mixing ratio of straw in each layer of straw, that is, the mass percentage of straw in the soil per unit volume was used as the evaluation index, without further exploring the true distribution of straw in the soil status. The uniformity of the spatial distribution of straw in the soil is the best reflection of the quality of straw returning to the field. Under normal circumstances, the burial rate is very limited in evaluating the burial uniformity and cannot be accurately reflected. For this reason, Chen Qingchun and Shi Yong *et al.* constructed the spatial distribution uniformity rate of the straw along the depth of the soil, the straw-soil mixing effect, and the surface flatness in the plough width to evaluate the quality of straw returning to the field, and used Pro-Engineering soft to show the space of the straw distribution status (Chen *et al.*, 2015).

The uniformity of straw burial is determined by the spatial distribution characteristics of straw in the soil. Through the study of the distribution law of straw crushing, rotary tillage, burial and mulching, the spatial distribution uniformity of straw in the soil is further explored. Through field experiments, using the method of layered stripping measurement, collecting the three-dimensional coordinates of the two ends of the straw in the soil, the analytical formula of a certain section of straw in the soil can be obtained, and the spatial distribution state of the straw community in the soil can be mathematically analyzed (Fig. 1), furthermore, the spatial distribution characteristics of the straw community such as the position of the straw (indicated by the center point), the range of length and the ratio, the range and ratio of the three-way included angle, and the amount of straw per unit volume are analyzed.

(1) The position of the straw (indicated by the center point)

Assuming that there are n straws in the 1m^3 test field, the measured three-dimensional coordinates of the two ends of a certain section of straw are respectively: $a_1(x_{1a}, y_{1a}, z_{1a})$ and $b_1(x_{1b}, y_{1b}, z_{1b})$, the linear equation of this section of straw in space can be expressed as formula (3).

The coordinates of the midpoint of this section of straw can be calculated as: $c_1\left(\frac{x_{1a}+x_{1b}}{2}, \frac{y_{1a}+y_{1b}}{2}, \frac{z_{1a}+z_{1b}}{2}\right)$, that means the spatial position of the straw, by analogy, the spatial position of the n^{th} straw can be obtained as: $c_n\left(\frac{x_{na}+x_{nb}}{2}, \frac{y_{na}+y_{nb}}{2}, \frac{z_{na}+z_{nb}}{2}\right)$. By measuring the position of all the straws, the distribution status of the straws in the soil space can be roughly reflected.

$$\frac{x - x_{1a}}{x_{1b} - x_{1a}} = \frac{y - y_{1a}}{y_{1b} - y_{1a}} = \frac{z - z_{1a}}{z_{1b} - z_{1a}} \quad (3)$$

(2) The range of length and the ratio

Knowing the three-dimensional coordinates of the two ends of n straws, the length of each straw can be obtained by formula (4), respectively denoted as $l_1, l_2, l_3, l_4 \dots l_n$. Taking the straw length range as 0~5, 5~10, 10~15, 15~20 cm one can calculate the length ratio of each straw length range. The appropriate length of straw is very important for the decomposition of straw in the soil. By measuring the length of each straw and its range ratio, it is helpful to analyze the uniformity of the spatial distribution of straw in the soil.

$$l_n = \sqrt{(x_{na} - x_{nb})^2 + (y_{na} - y_{nb})^2 + (z_{na} - z_{nb})^2} \quad (n = 1, 2, 3, 4 \dots) \quad (4)$$

(3) The range and ratio of the three-way included angle

Measure the angle between each straw and the three coordinate axes of x, y, z , respectively denoted as: $\theta_{x_n}, \theta_{y_n}, \theta_{z_n}$ ($n=1, 2, 3 \dots$). The angles with the three coordinate axes are all on the side of $\leq 90^\circ$. For each coordinate axis direction, the angle range is: $0^\circ \sim 30^\circ, 30^\circ \sim 60^\circ, 60^\circ \sim 90^\circ$, the range and ratio of the angle between the straw and the three coordinate axes of x, y and z can be calculated. By measuring the three-way included angle of the straw, the state of the straw can be further accurately indicated. By analyzing the range and ratio of the three-way included angle of the straw, the approximate direction and inclination state of the straw after the rotary tillage operation can be known.

(4) The amount of straw per unit volume

Divide the test field into 64 square fields of equal volume, and measure the quality of all straws in each field and record it as: $m_1, m_2, m_3, \dots, m_{36}$, by comparing the straw quality of each field, it can clearly show the spatial distribution characteristics of the straw in the soil, and the more the fields are divided, the more obvious the spatial distribution characteristics of the straw. However, when dividing the fields, there will be certain touches on the stalks that are in or across the dividing line, and certain errors will inevitably occur.

According to the analysis characteristics of the straw soil distribution, one or more of the above-mentioned spatial distribution characteristics of the straw in the soil are used to evaluate the uniformity of the straw burial, and the relationship between the length of the straw and its distribution on the ground and the parameters of the crushing tool. The relationship between the medium spatial distribution and rotary tillage cutters and straw thrown length and distribution on the surface, and the relationship between the spatial distribution characteristics of the straw soil and the parameters of the burying components, and the system optimization of the parameters of each component to achieve as much as possible the adjustment of the straw burying distribution characteristics (such as Fig. 2) to improve the uniformity of burial.

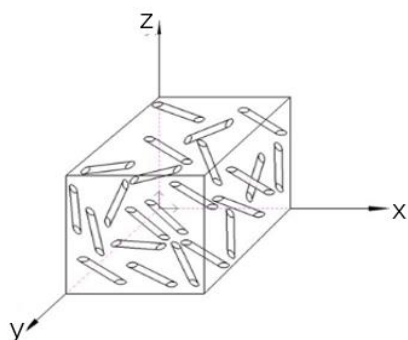


Fig. 1 - Real distribution of straw

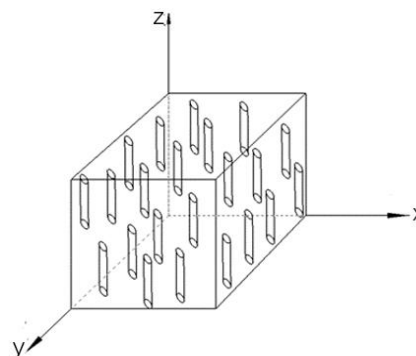


Fig. 2 - Ideal distribution of straw

THE DEVELOPMENT TREND OF MECHANIZED STRAW RETURNING TO THE FIELD

The development of straw returning from a single process to a composite process

Although returning straw to the field can decompose straw, increase soil organic matter, improve soil structure, promote microbial activity and the development of crop roots, and increase crop yields, too high a content of soil straw can also lead to ditching and clogging, improper seed beds, problems such as the increase of germs and the aggravation of crop diseases. How to increase the decomposing rate of straw returned to the field and reduce the impact of straw on the construction of planting and planting beds is the future development direction. Using cutting and crushing, uniform mixing, fixed depth burying, quantitative returning to the field, and adding decomposing agents to speed up the decomposition rate of straw, reducing the impact of straw on the opener and seed bed is an important goal of returning straw to the field. By comparing and analyzing the existing methods of mechanized straw returning to the field, it can be seen that the composite returning technology can integrate the advantages of a single returning technology, which is conducive to achieving the above goals and improving the effect of straw returning to the field. It is the future development direction of the mechanized straw returning technology.

The effect of returning straw to the field is developing towards uniform burial and precise control

The uniformity of straw burial is an important index to evaluate the quality of straw returning to the field. After the straw is mechanized and returned to the field, its spatial distribution in the soil directly determines the uniformity of the straw burial. Related studies have shown that the more uniform the spatial distribution of straw in the soil, the better the mixing effect of straw with the soil, and the higher the rate of straw decomposing in the soil. Reproducing the spatial distribution characteristics of straw in the soil and constructing a comprehensive scientific evaluation method for the quality of straw returning to the field is the key to improving the uniformity of straw returning to the field. In the future development of mechanized straw returning to the field, the realization of uniform mixing of straw and soil and the precise regulation of straw in the soil are the main means to improve the effect of straw returning to the field, and it is also an important direction for future research.

CONCLUSIONS

In the future development of agricultural production, the technology of mechanized straw returning to the field will certainly play a greater role. In the new era of continuous development of society, my country's research in the field of mechanized straw returning to the field requires more technological innovation. It is necessary to further increase the research on the composite multi-functional straw returning machinery, and on the basis of ensuring the safety and reliability of the operation and working efficiency, strive to realize the uniform burial of the straw and the soil, promote the decomposition of the straw, and promote the continuous development of the agricultural economy.

ACKNOWLEDGEMENT

This work was supported by National Natural Science Foundation of China (52175233) and Natural Science Foundation of Hubei Province (2021CFB433).

REFERENCES

- [1] Akhtar Kashif, Wang W.Y, Ren G.X. et al, (2019), Integrated use of straw mulch with nitrogen fertilizer improves soil functionality and soybean production. *Environment international*, 132.
- [2] Chang Y.N., Bian S., (2015), The application and development trend analysis of the mechanization technology of crop straw returning to the field. *Agriculture and Technology*, 2015, 35(12): 48.
- [3] Chen J., Zheng M.J., Pang D.W. et al, (2017), Straw return and appropriate tillage method improve grain yield and nitrogen efficiency of winter wheat. *Journal of Integrative Agriculture*, 16(08):1708-1719.
- [4] Cong H.B., Yao Z.L., Zhao L.X. et al, (2019), Distribution of crop straw resources and its industrial system and utilization path in China [J]. *Journal of Agricultural Engineering*, 35 (22):132-140.
- [5] Chief Editor of China Agricultural Machinery Research Institute. *Agricultural Machinery Design Manual (Part 1) [M]*. Beijing: *China Agricultural Science and Technology Press*, 2007, 5: 294-299.
- [6] Chen Q.C., Shi Y., Ding Q.S. et al, (2015), Comparison of straw incorporation effect with down-cut and up-cut rotary tillage. *Transactions of the Chinese Society of Agricultural Engineering*, 31(09):13-18.
- [7] Dai Z.C., Zhang H.T., Xu D. et al, (2019), The technology of returning corn stalks to the field. *Modern Agriculture*, (4): 24-26.
- [8] Dong J.R., (2019), Problems and countermeasures of Straw mechanization returning to field. *Agricultural Development and Equipment*, (01):28-30.
- [9] Guo J., (2017), Research on working performance of serrated and rotary blades based on straw returning to field machine [D]. *Nanjing Agricultural University*.
- [10] Heinze S., Rauber R., Joergensen R. G., (2016), Influence of moldboard plough and rotary harrow tillage on microbial biomass and nutrient stocks in two long-term experiments on loess derived Luvisols. *Applied Soil Ecology*, 6: 405-412
- [11] Huang W., Wu J.F., Pan X.H. et al, (2021), Effects of long-term straw return on soil organic carbon fractions and enzyme activities in a double-cropped rice paddy in South China. *Journal of Integrative Agriculture*, 20(01):236-247.
- [12] Hu H.X., Cheng Y, Ma Y.H. et al, (2012), Decomposition characteristics of returned rapeseed straw in soil and effects on soil fertility. *Chinese Journal of Eco-Agriculture*, 20(03): 297- 302.
- [13] Huo L.L., Meng H.B., Tian Y.S. et al, (2012), Experimental study on physical property of smashed crop straw. *Transactions of the Chinese Society of Agricultural Engineering*, 28(11): 189-195.
- [14] Hu H.X., (2012), Study on the decomposing characteristics of straw returning to the field at different depths. *Chinese Soil Society. Soil Science Facing the Future (Volume 1)-The Twelfth National Congress of the Chinese Soil Society and the 9th Cross-Strait Soils Proceedings of the Fertilizer Academic Exchange Symposium, Chinese Soil Society*, 2012.
- [15] Hu H.X., Cheng Y., Ma Y.H. et al, (2012), Decomposition characteristics of returned rapeseed straw in soil and effects on soil fertility. *Chinese Journal of Eco-Agriculture*, 20(03): 297- 302.
- [16] Li H., Ban T., Guo Z.F. et al, (2019), Study on the material characteristics and cutting methods of common crop straw. *Agriculture and Technology*, 39(22): 23-26.
- [17] Luo H.F., (2013), Study on material characterization of rape stalk and stalk divider [D]. Changsha, Hunan: *Hunan Agricultural University*.
- [18] Li P., (2014), Experimental study and working mechanism of key parts for 4SY-1.8 rape windrower [D]. Wuhan, Hubei: *Huazhong Agricultural University*.
- [19] Liu N., Li Y.Y., Cong P. et al, (2021), Depth of straw incorporation significantly alters crop yield, soil organic carbon and total nitrogen in the North China Plain. *Soil & Tillage Research*, 205.
- [20] Li K., (2020), *Research and design of the new type of rice straw crusher cutting tools* [D]. Chengdu University.
- [21] Li J., Lv C.X., Yuan Y.W. et al, (2019), Automatic recognition of corn straw coverage based on fast Fourier transform and SVM. *Transactions of the Chinese Society of Agricultural Engineering*, 35(20):194-201.
- [22] Pang L.D., (2017), Decomposition rate of corn straw returning and its effects on soil nutrients [D]. *Northeast Agricultural University*.
- [23] Qiao F.X., (2020), Importance and countermeasures of comprehensive utilization of crop straw. *Modern Agricultural Science and Technology*, (13): 164-166.
- [24] Qiu J., Wu M. L., Guan C.Y. et al, (2015), Design and experiment of chopping device with dynamic fixed knife coaxial for rice straw. *Transactions of the Chinese Society of Agricultural Engineering*, 31(10): 11- 19.

- [25] Qin K., Ding W.M., Fang Z.Z. et al, (2016), Design and experiment of plowing and rotary tillage combined machine. *Transactions of the Chinese Society of Agricultural Engineering*, 32(16):7-16.
- [26] Qian F., (2018), Analysis of the technology of mechanized straw returning to the field [J]. *Think Tank Times*, (50): 144+148.
- [27] Shi Y., (2015), Experimental research on the effect of straw incorporation with rotary tillage [D]. *Nanjing Agricultural University*.
- [28] Wang Y, Lu J.W., Li X.K. et al, (2013), Effects of nitrogen, phosphorus, potassium, and boron fertilizers on winter oilseed rape (*Brassica napus L.*) direct-sown in the Yangtze River Basin [J]. *Acta Agronomica Sinica*, 39(08):1491 -1500.
- [29] Wang Z.S., Xia J.F., Xu Q.C. et al, (2010), Power Consumption Experiment of Rotary Tillage and Stubble-mulch Knife Roller [J]. *Transactions of the Chinese Society of Agricultural Machinery*, 41(12): 44-47.
- [30] Xu H.Y., (2020), Mechanized processing methods and development characteristics of corn stalks. *Use and Maintenance of Agricultural Machinery*, (04):101.
- [31] Xu Z.L., (2019), Research on the abrasion mechanism of extruder screw based on material characteristics of corn stalk [D]. *Liaoning Technical University*, Doi:10.27210/d.cnki.glnju.000076.
- [32] Yang X.Y., (2014), Analysis of the decomposition rate of rape straw decay under three modes [J]. *Southern Agriculture*, 8(22): 40-41.
- [33] Zhao J., (2019), Analysis and countermeasure of comprehensive utilization of crop straw in China [J]. *Agricultural Outlook*, 15(12): 121-124.
- [34] Zhang Y., (2019), Straw returning ecological value estimate, spatial temporal differences and support policies. [D]. *Huazhong Agricultural University*
- [35] Zhang Y., Ding G.D., Cai H.M. et al, (2014), Effects of different planting methods on root system architecture and yield of oilseed rape. *Journal of Huazhong Agricultural University*, 33(4): 25-32.
- [36] Zhang J.M., (2014), Study on mechanism of high stubble burying rotary tiller for wet land [D]. *Huazhong Agricultural University*.
- [37] Zhou H., Li D., Liu Z.Y. et al, (2019), Simulation and Experiment of Spatial Distribution Effect after Straw Incorporation into Soil by Rotary Burial. *Transactions of the Chinese Society of Agricultural Machinery*, 50(09): 69-77.

APPLICATION OF BIG DATA ANALYSIS IN PATH PLANNING OF INTELLIGENT PICKING ROBOT

/

大数据分析在智能采摘机器人路径规划中的应用

Hejun Zhao^{1) 2)} *, Stoyanets Nataliya¹⁾, Guohou Li³⁾

¹⁾ Sumy National Agrarian University, Ukraine.

²⁾ Xinxiang Vocational and Technical College, Xinxiang, Henan, China.

³⁾ Henan Institute of Science and Technology, Henan, China.

*E-mail: ueooao@163.com

Corresponding author: Dr. Hejun Zhao

DOI: <https://doi.org/10.35633/inmateh-65-49>

Keywords: picking robot, path planning, big data analysis

ABSTRACT

In order to solve the problem of autonomous movement of intelligent picking robot, a method for big data analysis is proposed. The data collected by laser ranging sensor, CCD camera and electronic compass are analyzed to determine the current robot position and heading. The robot walking route is preset in the orchard, and the nixie tube ground sign is installed. Because the coordinates of the ground sign are known, the heading angle of the robot can be determined by an electronic compass. The CCD camera captures the sign image, and adopts the methods of image graying, image segmentation, image corrosion and image thinning to extract the digital tube image data on the sign. Fuzzy control method is used to identify digital tube numbers on the ground sign, and CCD camera scans whether there are obstacles in front of the road at the same time. The laser ranging sensor completes two tasks: (1) detecting the sign distance and direction angle of the distance, and calculating the current position and heading angle of the robot through the coordinates of the sign; (2) detect the distance from obstacles, and start the obstacle avoidance system when it is less than 1m. The path planning system of picking robot based on big data analysis relies on a variety of sensors, and has a strong ability to perceive orchard environment, and it has high ability of path planning.

摘要

为了解决智能采摘机器人自主运动问题，一种面向大数据分析的方法被提出。对激光测距传感器、CCD 摄像机和电子罗盘等传感器采集的数据进行分析，确定当前机器人位置与航向。在果园中预先设定机器人行走路线，安装数码管地标牌。因为地标牌坐标已知，所以可用电子罗盘确定机器人航向角。CCD 摄像头拍摄地标牌图像，采用图像灰度化、图像分割、图像腐蚀及图像细化的方法提取表示牌上数码管图像数据。采用模糊控制方法识别地标牌上数码管数字，CCD 摄像头同时扫描行进前方是否有障碍物。激光测距传感器完成两个任务：①检测距离地标牌距离和方向角，通过标识牌坐标计算机器人当前位置与航向角；②检测与障碍物间距离，当小于 1m 时启动避障系统。基于大数据分析的采摘机器人路径规划系统依托多种传感器，对果园环境感知能力强，具有较高的路径规划能力。

INTRODUCTION

Path planning is one of the most important technologies in mobile robot navigation. Path planning means finding an optimal collision-free path from the starting point to the target point in a given environment with obstacles according to some performance indexes (such as shortest distance, shortest time or minimum energy consumption, etc.). For mobile robots, path planning optimization is to solve the problem of platform path optimization under specific working environment and task requirements. The scientific and rational path planning has a very important impact on the working efficiency of mobile robots (Cerone A., 2019). At present, the commonly used path planning optimization methods can be divided into traditional algorithms and intelligent algorithms. Among them, traditional algorithms mainly include artificial potential field method, fuzzy logic algorithm, viewable method, grid method, free space method and so on. Since the path planning problem was put forward in 1970s, these traditional algorithms have played an important role in the field of robot path planning, and obtained many research results.

For example, in practical applications such as marine science, industrial field and military operations, these traditional path planning optimization methods have some defects when dealing with these complex environments (Cheung K. S. et al., 2019). For example, the artificial potential field method is easy to fall into local minima, which has the problem that the target is unreachable, and the viewable method is inefficient and cannot meet the real-time requirements of path planning. Fuzzy control algorithm is difficult to establish fuzzy rule base in complex and changeable environment, and lacks intelligent obstacle avoidance strategy for dynamic obstacles (Cza B. et al., 2021).

In recent years, with the rise of artificial intelligence, more and more intelligent algorithms have been proposed and applied to the path planning optimization of mobile robots to overcome the limitations of traditional path planning algorithms. An important feature of these intelligent algorithms is that their operating mechanism is very similar to the biological group behavior or ecological mechanism in nature. Moreover, the efficiency of these intelligent algorithms is usually higher than that of traditional algorithms (Fan T. et al., 2020). In order to distinguish them from traditional optimization algorithms, these intelligent algorithms are defined as intelligent bionic algorithms. CZA, B. think that fuzzy control is a control mode similar to human thinking ability, which has the reasoning ability and fuzziness of human intelligence. In the path planning of robot, fuzzy reasoning is often used, and the behaviors such as obstacle avoidance, speed regulation and target navigation of robots are generally referred to as robot movement (Chen J. et al., 2005). Garg et al, believe that robots control these behaviors in different ways and choose the optimal traveling plan of robots through a series of decisions (Garg H. et al., 2019). Hasanipناه et al thinks that besides fuzzy control methods, there are many algorithms for path planning, such as A-star algorithm, visibility method, artificial potential field method and ant colony algorithm (Hasanipناه M. et al., 2020). In this system, walking track is preset for robot, landmark sign is made, and digital map with known coordinates of landmark sign is established. The robot adopts CCD camera, laser ranging sensor and electronic compass, and has strong environmental perception ability. Using big data fusion technology, multiple groups of signals are fused to determine the coordinate position and heading of the robot. CCD camera is used to identify road signs and obstacles, and laser ranging sensor is used to detect and identify road signs. The fuzzy control method is used to establish an obstacle avoidance system to judge the distance between the obstacle and the robot. Test results show that the system has high environmental awareness, and has good path planning performance (Hou X., 2020).

MATERIALS AND METHODS

Sensors are the elements of a robot to obtain information, which can be called "eyes" of a mobile robot. Some basic behaviors of robots, such as positioning and navigation, environment modeling and avoiding obstacles, are realized through such eyes. The word data is in plural form as the input signal of the fuzzy controller by the sensor. Position sensing is an important condition for picking robot to work autonomously, and the robot senses its position in the digital map through sensors. This system uses multi-dimensional sensors to determine its own position, and cameras to photograph reference objects for terrain matching. The laser ranging sensor is adopted to detect the distance between itself and the reference object, and determine the head direction by electronic compass. The three groups of detected data are fused to finally determine the robot position (Hu J. et al., 2019).

Robot Terrain Matching

Terrain matching system is used by robots to identify landmarks and indicate the direction of their next progress. Because the growth of fruit trees in apple orchards is similar, and the spacing is not much different, it is difficult to use each apple tree as a marker. According to the preset working track of the robot, eight-segment code numbers are written on white cardboard as position marks. Terrain matching mainly completes two tasks: (1) image processing, eliminating useless information of the image, and keeping only eight-segment digital images; (2) image recognition, determining the image number of eight-segment code (Kumar P. B. et al., 2019). The image processing process includes: (1) image graying; (2) image segmentation; (3) image corrosion; (4) image thinning.

The process of converting a color image into a gray image becomes the gray processing of the image. The color of each pixel in the color image is determined by three components: R, G and B, and each component has 255 values. Such a pixel can have more than 16 million ($255 * 255 * 255$). The gray image is a special color image with the same R, G and B components, and the change range of one pixel is 255.

Therefore, in digital image processing, images of various formats are generally transformed into gray images to reduce the amount of calculation of subsequent images. The description of gray images is the same as that of color images. However, it reflects the distribution and characteristics of the overall and local chromaticity and brightness levels of the whole image. Image segmentation is the technology and process of dividing an image into several specific regions with unique properties and putting forward the target of interest. It is a key step from image processing to image analysis. From a mathematical point of view, image segmentation is the process of dividing digital images into disjoint regions. The process of image segmentation is also a marking process, that is, pixels belonging to the same region are given the same number. The corrosion process of image is similar to the convolution operation of image. Template matrix is required to control the operation results. In the corrosion and expansion of image, this template matrix is called structural element, which is the same as convolution. Structural elements can arbitrarily specify the center point of image, and the volume content of structural elements can be defined according to their own needs. Image thinning generally refers to an operation of image skeletonization of binary images. Thinning is the abbreviation of the process of reducing image lines from multi-pixel width to unit pixel width. Some articles often describe the thinning results as "skeletonization", "middle axis conversion" and "symmetry axis conversion".

Now take the floor sign with the number "3" as an example to design. Because each pixel of each color picture is synthesized by RGB three-channel intensity, the amount of information is too complicated. Therefore, it can effectively reduce the amount of picture information by transforming color pictures into gray pictures by using the gray-scale method. When the image is segmented, the threshold k is calculated, and when the gray level of the picture pixel is greater than k , the point is assigned 255. When the gray level of a pixel is less than k , assign a value of 0 to the pixel to form a picture that is either black or white (as shown in Fig. 1). Etching the binary image, and a 3×3 reference matrix is established with a certain pixel as the center. When all pixels in the 3×3 reference matrix are 255, the value of this point is 255. On the contrary, assign a value of 0 to this point, and get the binary image of the ground sign showing the number "3". Image thinning is to peel off the image under the condition that the image connection is unchanged, and Hilditch thinning algorithm is selected to establish a 3×3 matrix of target pixels. After deleting this point, the number of connected domains remains unchanged, and then the median filtering method is used for noise reduction. Firstly, the 3×3 matrix of the target pixel point and the average gray levels (I_v) of 8 pixels around the point are calculated. When $|I_p - I_v| > 127.5$, I_p is 255. When $|I_p - I_v| < 127.5$, I_p is assigned to 0. The filtered image showing the number "3" sign is obtained (Liu S. *et al.*, 2020).



Fig. 1 - Landmark image processing

By extracting and compressing part of the image containing the nixie tube number, the pixel size of the image is 10×10 resolution. Establish a 10×10 constant matrix, scan the compressed image line by line, and assign a value of 1 to the corresponding constant matrix when the gray level of the pixel is 0; By analogy, the digital image information is extracted into a 10×10 constant matrix. In view of the fact that the signboard is composed of 10 digital tube numbers such as 0~9. The system needs to be able to identify 0~9. In the process of camera shooting, the recognition results will be affected by environmental light sources, weeds and leaves. Therefore, the BP neural network method is used for recognition to enhance the recognition accuracy and fault tolerance. The two most important indexes for establishing neural network are the number of hidden neurons and allowable error. The number of hidden neurons, namely the central value of membership function and the number of rule bases, determines the accuracy and complexity of the network. The allowable error is the error between the output and the expectation, which determines the number of calculation iterations.

The allowable error is the system acceptance value of the difference between the actual output and the expected output, which represents the approximation degree of the expected output of the actual output phase.

When the actual error is less than the allowable error, the neural network operation is finished, and the system outputs the recognition result. When the actual error is greater than the allowable error, the system performs the next iteration calculation until the allowable error is met. The influence of allowable error on the system is shown in Fig. 2. When the allowable error is 0.05, the training time is 920 Ms. With the increase of allowable error, the training time decreases gradually. When the allowable error is 0.05, the recognition accuracy is 87%. With the increase of the number of neurons in the hidden layer, the training time gradually increased and the training speed accelerated. However, the recognition rate increases at first and then decreases. When the number of neurons is 9, the recognition rate reaches the maximum. This is because the number of neurons increases, the complexity of the network increases, and the anti-noise ability decreases, resulting in a decrease in recognition rate (Santos L. C. et al., 2021).

The allowable error is the system acceptance value of the difference between the actual output and the expected output, which represents the approximation degree of the expected output of the actual output phase. When the actual error is less than the allowable error, the neural network operation ends and the system outputs the recognition result. When the actual error is greater than the allowable error, the system performs the next iteration calculation until the allowable error is met. The influence of allowable error on the system is shown in Fig. 3. When the allowable error is 0.05, the training time is 920 ms. With the increase of allowable error, the training time decreases gradually. When the allowable error is 0.05, the recognition accuracy is 87%. At this time, the system recognizes that the number on the sign is "3". And then it gradually decreased. Considering the recognition rate and training time, the allowable error is 0.05. At this time, the system identifies the number on the sign of this place as "3" (Tourajizadeh H. et al., 2020).

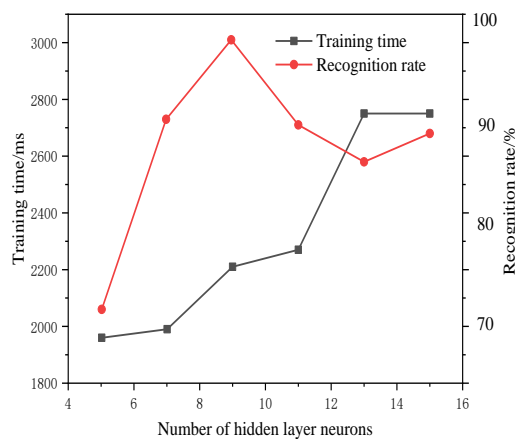


Fig. 2 - Influence of neuron number on neural network

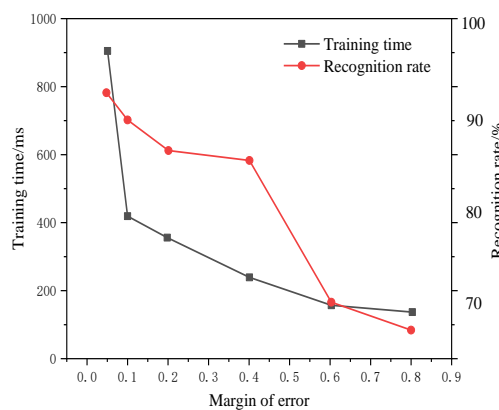


Fig. 3 - Error of allowable error to neural network

Calculation of Absolute Coordinates of Ground Signs

The detection of the coordinates of the ground sign includes two coordinate systems, as shown in Fig. 4. $(x_0, y_0)^T$, P_0 is the geometrical point, in fact after figure 4, $(X_0, Y_0)^T$. (X_0, Y_0) are the absolute Cartesian coordinates in the plane of the reference point of the robot o , which must be specified, and (r, θ) are polar coordinates of the point P , in the local system of the robot, according to fig. 4. (X_p, Y_p) are the absolute Cartesian coordinates of the point P in the absolute reference system and (x_p, y_p) is the coordinates of the point P in the local reference system of the robot. The absolute coordinate system of P_0 is $P_0(x_0, y_0, \theta)^T$, and the coordinate of the target in the local coordinate system of the robot is $P_p(x_p, y_p)^T$. Because the distance of the marker is detected by the left and right radar ranging sensors in the local coordinate system of the robot, the detection data are distance r and azimuth α (between r and ox axis of robot moving axis system). Therefore, the local coordinates are expressed as:

$$\begin{aligned} x_p &= r \cos \alpha \\ y_p &= r \sin \alpha \end{aligned} \tag{1}$$

x_p is projected on x axis as $r \cos \alpha$, and y_p is projected on y axis as $r \sin \alpha$. Since the vector directions of the two are opposite, let the coordinate of P in the decision coordinate system be $P(x_g, y_g)^T$, then the abscissa x_g is:

$$x_g = x_p \cos \theta - y_p \sin \theta + x_0 \tag{2}$$

Y_g can be obtained in the same way.

$$y_g = x_p \sin \theta + y_p \cos \theta + y_0 \tag{3}$$

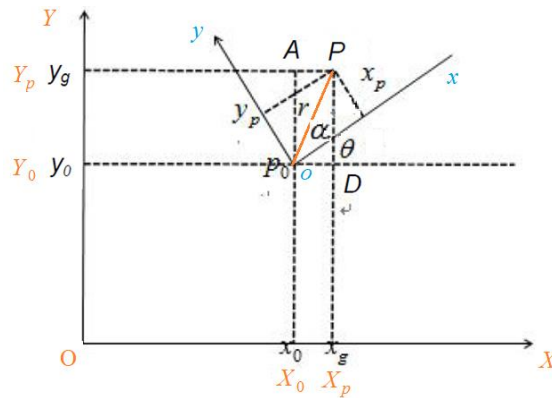


Fig. 4 - Coordinate transformation

Multi-Sensor Data Fusion

Use the electric compass to determine the current direction angle θ of the robot. Use cameras to identify landmarks and signs. The position coordinates (P) are known in the absolute coordinate system. The two laser distance sensors detect the distance r and the included Angle a between the robot and the position P of the ground sign, and the coordinates of the robot relative to the target in the coordinate system can be obtained. At present, it is necessary to calculate the robot's own position coordinates according to the above detection data. Since multiple sensors are used and the laser ranging sensors are divided into left and right ones, it is necessary to fuse multiple sets of detection data: (1) Fusion of the electric compass detection data and the ranging sensor data; (2) The left and right ranging sensors are fused, and finally the current robot position coordinates are deduced (Wan S. et al., 2020).

Derive the position coordinates of the left ranging sensor from landmark coordinates. The relationship between the absolute coordinates of the landmark and the absolute coordinates of the position of the left ranging sensor can be obtained by formula (2) and formula (3), and the absolute position coordinate $P_{OL}(x_{OL}, y_{OL})$ of the left sensor is:

$$\begin{bmatrix} x_{OL} \\ y_{OL} \end{bmatrix} = P_g - \begin{bmatrix} \cos \theta & -\sin \theta \\ \sin \theta & \cos \theta \end{bmatrix} \cdot \begin{bmatrix} x_{pL} \\ y_{pL} \end{bmatrix} \tag{4}$$

Similarly, the absolute position coordinate $P_{OR}(x_{OR},y_{OR})$ of the right sensor can be obtained as follows:

$$\begin{bmatrix} x_{OR} \\ y_{OR} \end{bmatrix} = P_g - \begin{bmatrix} \cos \theta & -\sin \theta \\ \sin \theta & \cos \theta \end{bmatrix} \cdot \begin{bmatrix} x_{pR} \\ y_{pR} \end{bmatrix} \tag{5}$$

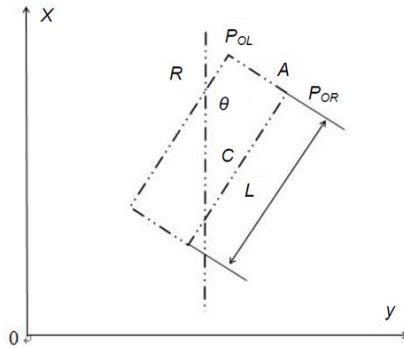


Fig. 5 - Robot coordinate calculation

The absolute coordinate $P_c(x_c,y_c)$ of robot center is shown in fig. 5. In fig. 5, it is necessary to fuse the coordinates of the left and right distance sensors, and calculate the coordinates of point a of the robot according to $P_{OR}(x_{OR},y_{OR})$ and $P_{OL}(x_{OL},y_{OL})$ coordinates, namely:

$$\begin{bmatrix} x_c \\ y_c \end{bmatrix} = \begin{bmatrix} \frac{x_{OR} + x_{OL}}{2} \\ \frac{y_{OR} + y_{OL}}{2} \end{bmatrix} \tag{6}$$

Vectors RA and CR are positive when they are in the same direction as the positive direction of coordinate axis and negative when they are opposite, then $RA=L \sin \theta/2$, and $CR=L \sin \theta/2$, then the absolute coordinates of the robot center P_c are:

$$\begin{bmatrix} x_c \\ y_c \end{bmatrix} = \begin{bmatrix} \frac{x_{OR} + x_{OL}}{2} - \frac{1}{2}L \sin \theta \\ \frac{y_{OR} + y_{OL}}{2} - \frac{1}{2}L \cos \theta \end{bmatrix} \tag{7}$$

RESULTS

Path planning is the whole process in which the robot travels from the starting point to the end according to the instructions of the target digital card. In the process of implementation, two problems are mainly solved, namely obstacle avoidance and target guidance. Finally, the unmanned traveling from the starting point to the end point is realized.

Obstacle Avoidance

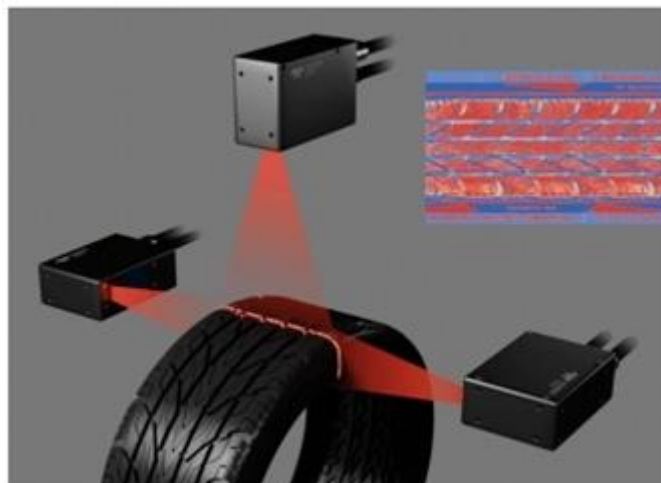


Fig. 6 - Image of 3D laser sensor

The schematic diagram of three-dimensional laser sensor is shown in Figure 6. It is difficult to give an exact concept of mobile robot obstacles in unknown environment. Intuitively, any object that forms a certain obstacle in the moving direction of the robot can become an obstacle. In recent years, the application of vision based obstacle recognition has attracted more and more attention. Obstacle avoidance uses two laser distance sensors as detection elements, and the detection data of the sensors are distance r and azimuth a . The minimum detection distance between the two sensors is r_{min} . When r_{min} is less than 1m, start the obstacle avoidance system. The obstacle avoidance system adopts fuzzy design. The input of the fuzzy system is the azimuth of two distance sensors, and the membership function has five central values, $-\pi/2, -\pi/4, 0, \pi/4, \pi/2$. When the left and right sensors detect obstacles are on the same side in the forward direction, the robot keeps its original direction unchanged. When the left and right sensors detect that the output of the membership function of the included angle of the obstacle is 0, the robot turns $\pi/2$ in the direction of smaller included angle; When that obstacle appear on both sides of the advance direction and are at the maximum and middle positions respectively, the robot turns $\pi/4$ to the maximum position. The obstacle avoidance planning is shown in Table 1 (Zhou Y. et al., 2019).

Table 1

Obstacle avoidance rules					
a_R	a_L				
	LB	LM	C	RM	RB
LB	C	C	RB	LM	C
LM	C	C	RB	C	RM
C	RB	RB	RB	LB	LB
RM	C	C	LB	JM	LM
RB	C	C	LB	LM	C

Target guidance

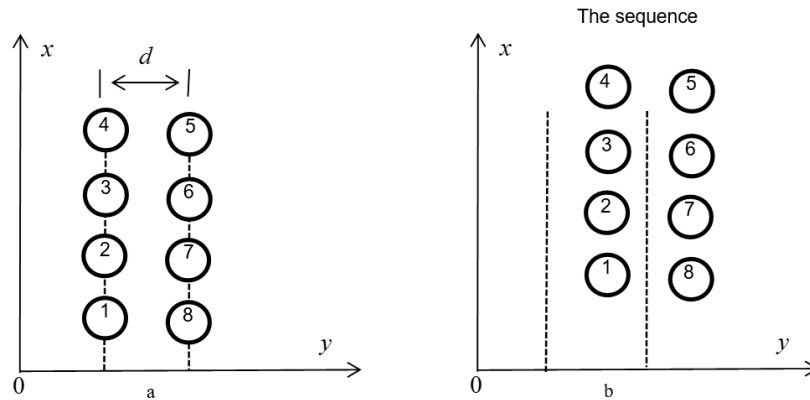


Fig. 7 - Target guidance

The robot is guided by the ground signs. Eight-segment codes such as 1, 2, 3, etc. are arranged on the planned travel route of the robot, and the distance between the two columns of trees is d . Since the signboard is installed on the tree, and the robot recognizes each signboard coordinate in the process of walking, the signboard coordinate shifts to the right by $d/2$ in the digital map system, as shown in fig. 7(a). The boot process is as follows:

- 1) The distance measuring sensor detects the coordinate $p(x,y)$ of the sign position and calculates the coordinate $p_c(x_c,y_c)$ of the robot, and the distance D between them is $D = \sqrt{(x-x_c)^2 + (y-y_c)^2}$.
- 2) When $D > 0.3$ m, the robot advances to the sign; when $D < 0.3$ m, the robot stops and the camera starts looking for the next sign.
- 3) Determine whether the current signboard is the final target: if not, return to step 1); if yes, the robot stops moving, as shown in fig. 7(b).

System Test

The layout of the orchard referred to is similar to the plantation in Figure 8. In this case, it shall be specially arranged into an alley between rows of trees. The system test results are shown in Fig. 8.

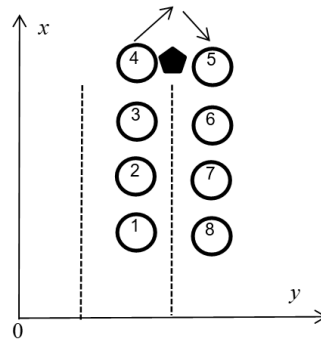


Fig. 8 - System test

Translate the coordinate of the sign to the right by $d/2$ to create a digital map. Starting from the "1" position, the robot first scans the camera to find the digital tube "2" and calculate the distance d . When $D > 0.3$ m, the robot advances to the sign; When $D < 0.3$ m, the robot stops. The camera starts looking for the next sign. When the robot moves to position "4", the robot position sensor scans and finds obstacles. When the distance from the obstacle is less than 1 m, the robot rotates $\pi/4$ counterclockwise and advances, then continues to scan the sign "5" and advances to the landmark 5, until it moves to the sign "8", when the system confirms that it has moved to the final target, and the robot stops moving. This topic is not described in detail. This paper does not develop this topic now, it should be used as the direction or goal of further research and development in the future. The schematic diagram of site acceptance test is shown in Figure 9.



Fig. 9 - Site acceptance test drawing

Since ancient times, mankind has been seeking inspiration for invention and creation from nature. It is found that individual behavior is very simple, but complex tasks can be completed through individual cooperation.

In these intelligent bionic algorithms, most of them are inspired by the foraging behavior of biological groups, such as ant colony algorithm, particle swarm algorithm, artificial fish swarm algorithm, bacterial foraging algorithm, Hybrid Shuffled Frog-Leaping Algorithm and artificial bee colony algorithm. Others are inspired by the behavior of other groups of organisms. The following mainly discusses the research results of some intelligent bionic algorithms inspired by the behavior of biological groups in the field of path planning and optimization of mobile robots. These field tests are done through a very laborious experimental activity. Good experimental results were obtained.

CONCLUSION

In order to realize the automatic walking of picking robot in orchard, big data fusion laser ranging sensor, CCD camera and electronic compass are used to collect data and calculate the current robot position coordinates and heading. When working, the left and right laser sensors mark the position of objects and obstacles. When the left and right laser sensors work, the obstacle position can be marked. When the marking distance is less than 0.3m, the CCD camera starts scanning the next target. When the distance is less than 1m, the obstacle avoidance mechanism is activated. The system uses a variety of sensor data comprehensive analysis, has a strong orchard environment perception ability.

REFERENCES

- [1] Cerone, A. (2019). Model mining: integrating data analytics, modelling and verification. *Journal of Intelligent Information Systems*, Vol. 52, Issue 3, pp. 501-532. United States;
- [2] Chen J, Li L R. (2005) Path planning protocol for collaborative multi-robot systems, 2005 International Symposium on Computational Intelligence in Robotics and Automation. IEEE, pp. 721-726. Finland;
- [3] Cheung K S., Leung W K., & Seto, W. K. (2019). Application of Big Data analysis in gastrointestinal research. *World Journal of Gastroenterology*, Vol. 25, Issue 24, pp. 2990-3008. China;
- [4] Cza B., Pi A., Xi A., Mw, A., Wh C., Gang L. D., (2021). Application of compositional data analysis in geochemical exploration for concealed deposits: a case study of Ashele copper-zinc deposit, Xinjiang, China. *Applied Geochemistry*, Vol. 130, Issue 2, pp. 104997. England;
- [5] Fan T., Liu Z., Ouyang J., Li P. (2020). Preparation of an intelligent oleophobic hydrogel and its application in the replacement of locally damaged oil pipelines. *ACS Applied Materials & Interfaces*, Vol. 12, Issue 46, pp. 52018-52027. United States;
- [6] Garg H., Arora R. (2019). Generalized intuitionistic fuzzy soft power aggregation operator based on t-norm and their application in multicriteria decision-making. *International Journal of Intelligent Systems*, Vol. 34, Issue 2, pp. 215-246. United States;
- [7] Hasanipanah M., Zhang W., Armaghani D. J., Rad, H. N. (2020). The potential application of a new intelligent based approach in predicting the tensile strength of rock. *IEEE Access*, Vol. 8, Issue 99, pp. 57148-57157. United States;
- [8] Hou X. (2020). Haptic teleoperation of a multirotor aerial robot using path planning with human intention estimation. *Intelligent Service Robotics*, Issue 11, pp. 1-14. Germany;
- [9] Hu J., Fang J., Du Y., Liu Z., Ji P. (2019). Application of PLS algorithm in discriminant analysis in multidimensional data mining. *Journal of supercomputing*, Vol. 75, Issue 9, pp. 6004-6020. United States;
- [10] Kumar P. B., Rawat H., Parhi D. R. (2019). Path planning of humanoids based on artificial potential field method in unknown environments. *Expert Systems*, Vol. 36, Issue 2, pp. 1-12. England;
- [11] Liu S., Liu S., Xiao H. (2020). Optimization of structural parameters of jet end in the underwater intelligent pigging robot. *Ocean Engineering*, Vol. 216, Issue 7, pp. 108092. England;
- [12] Santos L. C., Santos A., Santos F. N., (2021), A Case Study on Improving the Software Dependability of a ROS Path Planner for Steep Slope Vineyards. *Robotics*, Vol. 10, Issue 3, pp. 103. United States;
- [13] Tourajzadeh H., Gholami O., (2020), Optimal control and path planning of a 3PRS robot using indirect variation algorithm. *Robotica*, Vol. 38, Issue 5, pp. 903-924. England;
- [14] Wan S., Lu J., Fan P., & Letaief K. B., (2020). Toward big data processing in IoT: path planning and resource management of UAV base stations in mobile-edge computing system. *IEEE Internet of Things Journal*, Vol.7, Issue 7, pp. 5995-6009. United States;
- [15] Zhou Y., Li W., Yi P., & Guo Y. (2019). Behavioral ordered weighted averaging operator and the application in multiattribute decision making. *International Journal of Intelligent Systems*, Vol. 34, Issue 3, pp. 386-399. United States.

DEVELOPMENT AND TESTING OF SOIL IMPURITIES REMOVING APPARATUS FOR POTATO

马铃薯土杂去除装置研制与试验

Hongguang Yang, Huanxiong Xie*, Hai Wei, Jianchun Yan, Huichang Wu, Longlong Ji, Xiaowei Xu¹

Nanjing Institute of Agricultural Mechanization, Ministry of Agriculture and Rural Affairs, Nanjing, 210014/China

Tel: +86-025-84346223; E-mail: 17372778337@163.com

DOI: <https://doi.org/10.356.33/inmateh-65-50>

Keywords: potato, soil impurities, flexible rubber finger conveying mechanism, slender filament rotary brushing mechanism, removal rate, damage rate

ABSTRACT

Aiming at the problem that contain more soil impurities of potato post-harvest, which affects subsequent deep processing, an apparatus for removing soil impurities from potato was developed. The whole structure is mainly composed of frame, feeding port, flexible rubber finger conveying mechanism, slender filament rotary brushing mechanism, discharging port and the like. The research and analysis determined that the main parameters influencing the soil impurities removal performance were the movement speed of conveying mechanism, the movement speed of brushing mechanism and the clearance between conveying mechanism and brushing mechanism (hereinafter referred to as the mechanism clearance). Taking the main influencing parameters as test factors, and the soil impurities removal rate and potato damage rate as indexes, the orthogonal test with three factors and three levels was carried out. The optimal parameter combination was obtained as follows: the movement speed of conveying mechanism was 0.35m/s, the movement speed of brushing mechanism was 0.40m/s, and the mechanism clearance was 55mm. At this time, the average soil impurities removal rate was 87.18%, and the potato average damage rate was 1.95%, which met the requirements of potato cleaning operation.

摘要

针对马铃薯产后含有较多土杂影响后续深加工的问题,设计了一种马铃薯土杂去除装置。该装置主要由机架、入料口、柔性橡胶拨指式输送机构、细长毛回转式刷洗机构和出料口等组成。通过研究分析确定了影响去土杂作业性能的主要参数为输送机构运动速度、刷洗机构运动速度、输送机构与刷洗机构间隙(简称机构间隙)。以主要影响参数为试验因素、去土杂率和马铃薯损伤率为试验指标,开展了三因素三水平正交试验,获取了最优参数组合为输送机构运动速度0.35m/s、刷洗机构运动速度0.4m/s和机构间隙55mm。最优参数下的验证试验结果表明,平均去土杂率为87.18%、马铃薯平均损伤率为1.95%,满足马铃薯去土杂作业要求。

INTRODUCTION

Potato is an important grain and vegetable crop in the world, which is widely planted in many countries. In recent years, under the background that the adjustment of China's grain planting structure and potato staple food strategy, the potato planting area in China has increased. Although China is a big potato producer, its mechanized production level is very low, especially there is a big gap between China and other countries in potato post-harvest mechanized processing, which seriously restricts the whole mechanization process and industrial development of potato. Removing the soil impurities of potato is necessary for primary processing (making whole flour, starch, dried potatoes, etc.), edible processing (making potato chips, French fries, etc.), and deep processing (making adhesives, biodegradable materials, fine chemical raw materials, etc.), which will directly affect the quality of potato processed products (Bai *et al*, 2019).

Because potato tubers grow underground and have irregular shapes, mechanical harvesting operations contain more soil impurities. Although the existing potato harvester has a certain function of soil impurities removal (Hrushetsky *et al*, 2019), it still contains a lot of soil impurities, which needs further removal.

¹ Hongguang Yang, MS.Eng.; Huanxiong Xie*, Prof.; Hai Wei, MS.Eng.; Jianchun Yan, MS.Eng.; Huichang Wu, Prof.; Longlong Ji, MS. Stud. Eng.; Xiaowei Xu, MS. Stud. Eng.

At present, potato cleaning technology is mainly divided into dry-cleaning and wet cleaning according to different operation methods and use requirements. Dry-cleaning technology is mainly used in the primary processing stage of potato (Yang *et al*, 2020). Without water treatment, it can effectively avoid the rot caused by washing and soaking. According to different operation principles, wet cleaning technology is mainly divided into spray brush roller type, drum type and squirrel cage type (Ji *et al*, 2020), which are widely used in potato food processing and deep processing.

At present, the research on potato post-harvest processing apparatus focuses on sorting, grading and damage detection. For example, some scholars developed a kind of potato sorter, which can realize the potato cleaning and sorting operations (Wang *et al*, 2017). Based on the machine vision technology, some scholars studied the grading method of potato (Su *et al*, 2018). Some scholars developed a machine vision system for potato tuber detection based on ultraviolet imaging, and proposed an algorithm for automatically detecting the thresholds between tuber, clod and conveyor belt (Al-Mallahi *et al*, 2010).

In view of the problem that high soil impurities content in potato post-harvest affects the subsequent washing and deep processing, according to the biological characteristics and the impurities characteristics of potato post-harvest, the process of imitating manual potato scrubbing will be adopted, and by means of differential motion principle, the soil impurities will be removed. It is of great significance to design and develop soil impurities removing apparatus suitable for the initial cleaning operation in fields, so as to reduce the operation burden of washing apparatus and further improve the cleaning effect. At the same time, the research of this apparatus will greatly promote the development of potato industry, especially the implementation of potato staple food strategy in China.

MATERIALS AND METHODS

2.1 Whole structure and working principle

2.1.1 Whole structure

According to the characteristics of soil impurities in potato post-harvest and the structural dimensions of potato washing apparatus, the soil impurities removing apparatus was designed as shown in Fig. 1. It is mainly composed of frame, power system, feeding port, flexible rubber finger conveying mechanism, slender filament rotary brushing mechanism, discharging port and walking wheel, etc., which can remove large pieces of soil impurities and residual soil attached to the surface of potato.

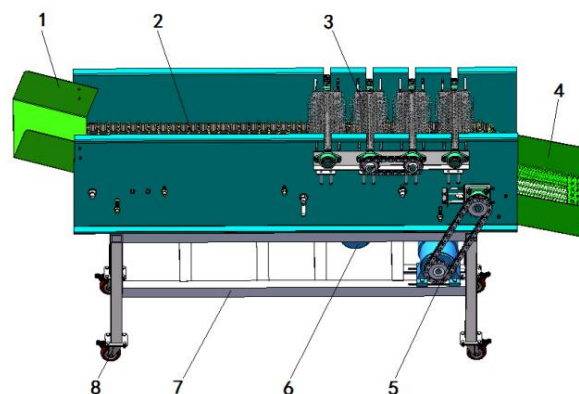


Fig. 1 - Whole structure

1. Feeding port; 2. Flexible rubber finger conveying mechanism; 3. Slender filament rotary brushing mechanism; 4. Discharging port; 5. Driving motor of conveying mechanism; 6. Driving motor of brushing mechanism; 7. Frame; 8. Walking wheel

2.1.2 Working principle

The working process of soil removing apparatus is divided into two stages, the first is to remove large pieces of soil impurities and the second is to remove the residual soil attached to potato surface. The specific working principle is as follows. Firstly, the potatoes to be cleaned enter the flexible rubber finger conveying mechanism through the feeding port, and the cleaning operation of clods, crushed stones and other impurities mixed in potatoes is completed under the action of flexible rubber finger of conveying mechanism. Then the potato continues to move backward to enter the next stage, and under the combination action of conveying mechanism and brushing mechanism, the circumferential rolling brushing operation is realized, and the residual soil attached to potatoes surface is removed. Finally, the cleaned potatoes are output from the discharging port.

2.2 Design analysis of key mechanisms

2.2.1 Design analysis of conveying mechanism

The conveying mechanism is one of the key components of soil impurities removing apparatus, and its structural characteristics have an important influence on the removing effect. The front part of the designed flexible rubber finger conveying mechanism mainly completes the removal of clods, crushed stones and other impurities mixed in potatoes. The rear part cooperates with the slender filament rotary brushing mechanism to complete the removal of residual soil attached to potato surface. As shown in Fig. 2, the conveying mechanism is mainly composed of connecting belt, flexible rubber finger rod, supporting wheel, driving part, tension adjusting part and tightening wheel. The power is provided by driving part motor. And the front and rear connecting positions on the side plates of frame are adjusted by the tension adjusting part.

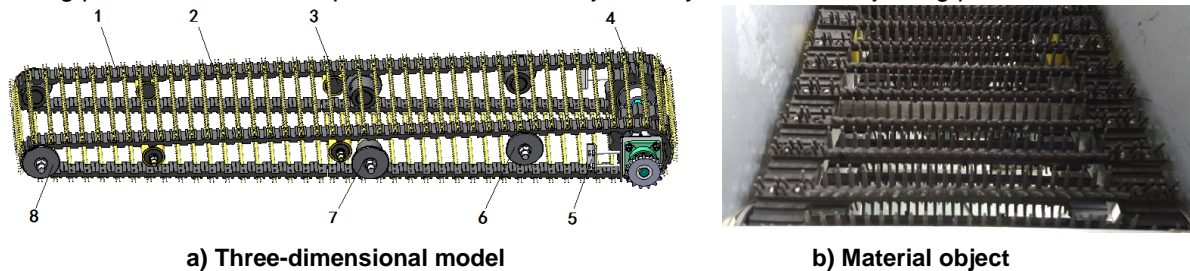


Fig. 2 - Structure of conveying mechanism

1. Connecting belt; 2. Flexible rubber finger rod; 3. Supporting wheel; 4. Driving part; 5. Tension adjusting part; 6. First tightening wheel; 7. Second tightening wheel; 8. Third tightening wheel

In order to cooperate with potato washing apparatus, referring to the structure size of existing potato washing apparatus, the design conveying mechanism has a width of 470mm, on which 90 flexible rubber finger rods are uniformly distributed. Meanwhile, the conveying mechanism is provided with two pairs of supporting wheels for ensuring the upper surface of flexible rubber finger rods to be horizontal, which is beneficial to the conveying of potatoes. And there are three pairs of tightening wheels. The first pair of tightening wheel is arranged close to the driving part and has the same function as the supporting wheel. The second is arranged in the middle of the conveying mechanism, and its function is to adjust the tension degree of flexible rubber finger rods downwards to ensure the smooth conveying of potatoes. The third is arranged in the rear part of conveying mechanism and plays a role of driven wheel. The supporting wheel and the tightening wheel are connected with the side plate of the frame through bolts. Among them, the diameter of supporting wheel is $\Phi 75\text{mm}$ and the diameter of tightening wheel is $\Phi 90\text{mm}$.

Design analysis of rod spacing

The structure of conveying mechanism rods and the spacing between the two rods have great influence on the soil impurities removal rate and potato damage rate, and the selection of spacing and the structural design are particularly important. According to the principle of better supporting potato, the rod spacing of conveying mechanism is 50mm with reference to the potato harvester (Wei et al, 2019; Lv et al, 2015). At the same time, in the process of removing soil impurities, due to the irregular movement of potato in the conveying mechanism, it is easy to cause collision and friction damage under the action of external force (Deng et al, 2019). In order to avoid collision caused by direct contact between potatoes and rods, the rubber fingers are added to play a buffer protection role.

As shown in Fig. 3, according to the width of conveying mechanism and the size of connecting belt, the total length of flexible rubber finger rod is designed to be 466mm, the inner diameter of rod is $\Phi 11\text{mm}$, the material is 55CrSi, the distance between two outer holes of rod is 437mm, and the distance between two holes on one side is 28mm, which is connected with the belt by bolts. In order to reduce the damage of potato on the rod, the rubber skin with a thickness of 3mm is attached to the rod surface, which can play a role in buffering the loss of potato. Meanwhile, two rows of rubber fingers are designed outside the rubber skin, and the effect of removing soil impurities is further improved through the toggle action of the fingers. Among them, the diameter of lower end of rubber finger is $\Phi 6\text{mm}$, the diameter of upper end is $\Phi 4\text{mm}$ and the total length is 20mm. The distance between adjacent fingers in each row is 15mm, and the two rows of fingers are triangular dislocation branches.

In order to facilitate the connection between the flexible rubber finger rod and the belt, the 65mm long part at both ends of the rod is processed into a flat structure with a width of 15mm and a thickness of 9mm. The structure has two holes for bolted connection between the belt and the rod.



Fig. 3 - Flexible rubber finger rod

Design analysis of driving part

The driven part is the power source of conveying mechanism. As shown in Fig. 4, the driven part is mainly composed of mounted bearings, quincunx rubber wheel, transmission sprocket, tension adjusting plate and hexagonal shaft, etc. In order to facilitate the installation and positioning of quincunx rubber wheel, the drive shaft is designed as a hexagonal shaft with $\Phi 36\text{mm}$ inscribed circle. And in order to ensure good meshing between quincunx rubber wheel teeth and rods, increase the wrap angle of rods in conveying mechanism and avoid tooth climbing phenomenon. Referring to the structure types of rubber wheels used in potato harvester, the number of teeth of quincunx rubber wheel is 11, the diameter of graduation circle is $\Phi 180\text{mm}$, and two groups of quincunx rubber wheels are evenly distributed on hexagonal shaft with a spacing of 190 mm.

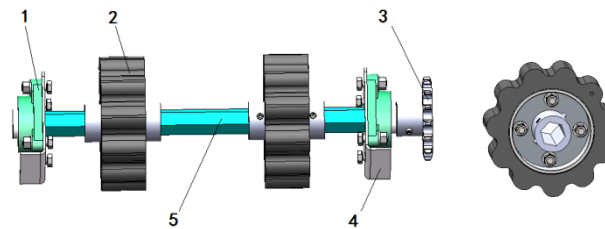


Fig. 4 - Structure of drive part

1. Mounted bearings; 2. Quincunx rubber wheel; 3. Transmission sprocket; 4. Tension adjusting plate; 5. Hexagonal shaft

2.2.2 Design analysis of brushing mechanism

The brushing mechanism is another key component of soil impurities removing apparatus, and its structural characteristics also have an important impact on soil removing effect. As shown in Fig. 5, the designed slender filament rotary brushing mechanism mainly consists of brush roller, brush roller mounting plate, height adjusting part, etc. The power input is realized through the motor and three groups of chain transmission parts. The brushing mechanism can be adjusted up and down along the side plate of frame under the action of height adjusting part, so as to adjust the clearance between the conveying mechanism and the brushing mechanism, and adapt to different size of potatoes and different feeding amounts.

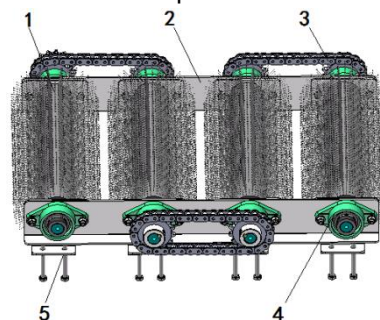


Fig. 5 - Structure of brushing mechanism

1. Brush roller; 2. Brush roller mounting plate; 3. Chain transmission part; 4. Mounted bearings; 5. Height adjusting part

Design analysis of brush roller

On the basis of the actual operation needs, the brushing mechanism is designed to be uniformly distributed at the upper rear position of conveying mechanism, which consists of four groups of brush rollers, and the distance between each group is 220mm. In order to meet different transmission coordination, the four brush rollers are same except for mandrel length. As shown in Fig. 6, the brush roller is mainly composed of mandrel, brush filament attachment and nylon filament. The attachment material of nylon filament is plastic with diameter of $\Phi 100\text{mm}$ and length of 470mm. And considering the irregular shape and size of potato, there are many sprout eyes (where potato tubers germinate) on the surface, and the skin of potato is very thin, which is easily damaged by external force. Therefore, the slender soft nylon filament with a diameter of $\Phi 0.3\text{mm}$ and a length of 50mm is selected to reduce the potato damage in the process of brushing. At the same time, the designed slender soft nylon filament can better clean the soil impurities in the sprout eye.

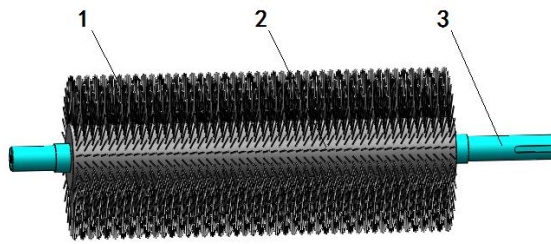


Fig. 6 - Structure of brush roller

1. Nylon filament; 2. Brush filament attachment; 3. Mandrel

Design analysis of mechanism clearance

The clearance between brushing mechanism and conveying mechanism has an important influence on soil removing effect. Excessive clearance leads to the failure of brushing mechanism to contact with potatoes, resulting in the reduction of soil impurities removal rate, while too small clearance will increase its squeezing force on potatoes, which will easily lead to the damage of potato skin. As shown in Fig. 7, for the convenience of measurement, the distance between the tangent line at the bottom of outer circle of brush roller and the upper plane of rubber finger is defined as the clearance, which can be adjusted by the height adjusting part. According to the size of potato in China and the movement characteristics of potato on the conveying mechanism and the brushing mechanism, the mechanism clearance L is preliminarily designed to be 35 to 75 mm.

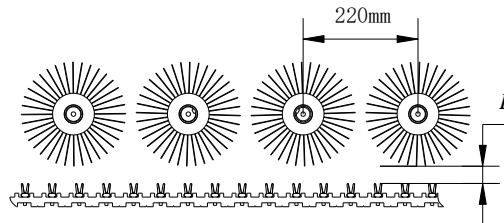


Fig. 7 - Diagram of mechanism clearance

2.2.3 Analysis of potato in conveying and brushing

The main function of conveying and brushing stage is to remove the residual soil attached to potato surface. According to the physical and impurities characteristics of potato, the process of manually brushing potato with a brush is imitated. As shown in Fig. 8, ignoring the deformation and additional force of brush roller and flexible rubber fingers caused by potato support, taking a single potato between the flexible rubber finger rod of conveying mechanism and brush roller of brushing mechanism as an example, at this time, besides its own gravity, the potato is mainly affected by the downward pressure and backward friction of brush roller, and the oblique upward support and friction of flexible rubber finger.

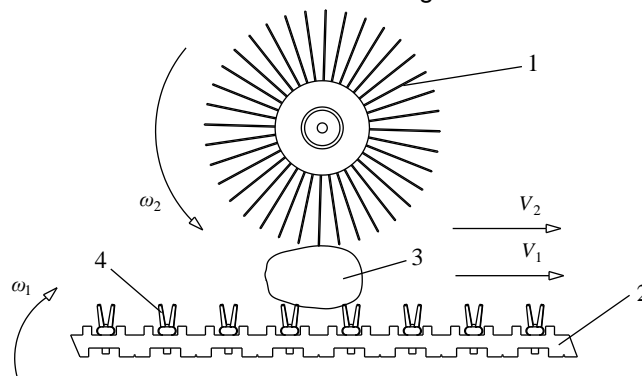


Fig. 8 - Analysis of potato in conveying and brushing

1. Brush roller; 2. Connecting belt; 3. Potato; 4. Flexible rubber finger

The movement speed of conveying mechanism can be expressed as:

$$V_1 = \omega_1 R = \pi D_1 n_1 / 60 \tag{1}$$

where: V_1 is the movement speed of conveying mechanism, m/s;

ω_1 is the angular velocity of conveying mechanism, rad/s;

R is the dividing circle radius of quincunx rubber wheel, mm;

D_1 is the dividing circle diameter of quincunx rubber wheel, mm;

n_1 is the rotating speed of conveying mechanism, r/min.

The movement speed of brushing mechanism can be expressed as:

$$V_2 = \omega_2 r = \pi D_2 n_2 / 60 \quad (2)$$

where: V_2 is the movement speed of brushing mechanism, m/s;

ω_2 is the angular velocity of brushing mechanism, rad/s;

r is the round radius of brush roller, mm;

D_2 is the round diameter of brush roller, mm;

n_2 is the rotating speed of brushing mechanism, r/min.

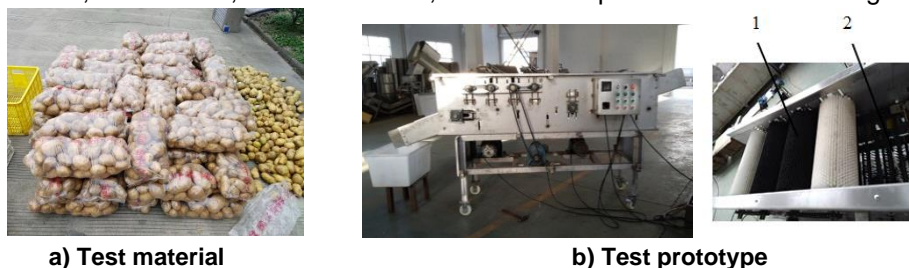
The movement speed of conveying mechanism and the brushing mechanism has an important influence on soil removing effect, and the appropriate speed relationship between them is the key and difficult point of design. In order to ensure that potatoes can be removed with high quality and low loss between the two mechanisms in the operation process, so that the potato surface is in full contact with the brush roller at 360 degrees, the movement speed of conveying mechanism should match the movement speed of brushing mechanism (Chen et al, 2018; Bulgakov et al, 2018).

The soil impurities removal operation mainly removes large pieces of soil impurities and residual soil attached to potato surface. Too fast movement speed will not get a good effect of removing soil impurities, and too slow movement speed will easily cause subsequent potato accumulation and damage. Considering the work efficiency and performance, and on the basis of the preliminary pre-test research, the moving speed range of conveying mechanism and the brushing mechanism is 0.20 to 0.60 m/s, and the specific values need to be determined by subsequent tests.

2.2.4 Prototype testing

Test conditions

The test is carried out in a cooperative company. The test material is Dutch No.15 potato. The average three-dimensional (length×width×height) of potatoes is 86.13mm×61.98mm×47.25mm, the average moisture content is 78.12%, and the average mass is 89.34 g. The test equipment mainly includes soil impurities removing apparatus, tachometer, electronic scale, etc. The test photos are shown in Fig. 9.



a) Test material

b) Test prototype

Fig. 9 - Test material and prototype

1. Brush roller of brushing mechanism; 2. Flexible rubber finger rod of conveying mechanism

Test factors and indicators

Through theoretical analysis and pre-test research, the main influencing factors of soil impurities removal performance are the feeding amount, the movement speed of conveying mechanism, the movement speed of brushing mechanism and the mechanism clearance. In order to improve the effect of removing soil impurities and ensure that the potatoes are fed in a single layer without blockage, the feeding amount of potatoes is finally selected as 3t/h. And the test contents and methods are as follows. Firstly, the parameter ranges of the conveying mechanism, the brushing mechanism and the mechanism clearance are obtained by using single factor test. Then, taking the conveying mechanism, the brushing mechanism and the mechanism clearance as test factors, taking the soil impurities removal rate and the potato damage rate as test indexes, the orthogonal test of three factors and three levels is carried out. The height difference between the conveying mechanism and the brushing mechanism is made to the specified distance by the height adjusting part. The

conveying mechanism and the brushing mechanism can change the movement speed by adjusting the rotating speed of their respective matched driving motors.

During the test, three groups of potato samples are taken at the discharging port at equal time intervals, and the mass of each sample is not less than 50 kg. Defining the soil impurities removal rate of potato is the percentage of the weight of potato cleaned after the removing apparatus operation among the sampled potato. The damage rate of potato is defined as the percentage of mechanical damage potatoes in the sample after the action of the removing apparatus. Among them, after operation of soil impurities removing apparatus, the potato with more than 1.5 cm impurities diameter and less than 3 sides were cleaned. And the potato with more than 1.5 cm long damage skin on its surface or with a single damage skin with an area of more than 200mm², is defined as a damaged potato.

Choosing potatoes surface with new mechanical damage and no removing soil impurities from each sample, and weighing their quality respectively. The soil impurities removal rate (T_c) and potato damage rate (T_s) calculation methods are as follows:

$$T_c = \frac{M - M_1}{M} \quad (3)$$

$$T_s = \frac{M_2}{M} \quad (4)$$

where: M is the weight of potato samples, kg;

M_1 is the weight of potato without removing soil impurities, kg;

M_2 is the weight of potato with new mechanical damage, kg.

RESULTS

Single factor test scheme and results

In Fig.10 is shown the influence of the movement speed of conveying mechanism, the movement speed of brushing mechanism and the mechanism clearance on soil removal performance. Fig. 10a is a graph showing the influence of the movement speed of conveying mechanism on potato damage rate and soil impurities removal rate when the movement speed of brushing mechanism is 0.4m/s and the mechanism clearance is 55 mm. Fig.10b is a graph showing the influence of the movement speed of brushing mechanism on the potato damage rate and soil impurities removal rate when the movement speed of conveying mechanism is 0.4m/s and the mechanism clearance is 55 mm. Fig.10c is a graph showing the influence of the mechanism clearance on potato damage rate and soil impurities removal rate when the moving speed of conveying mechanism and brushing mechanism are 0.4m/s, respectively.

From Fig. 10a, it can be seen that with the increase of the movement speed of conveying mechanism, the potato damage rate and the soil impurities removal rate both show an upward trend. The reason is that when the movement speed of conveying mechanism is high, the potatoes are bounced and turned over continuously, and are strongly impacted and rubbed by the brushing mechanism and the conveying mechanism. At this time, the soil impurities removal effect is good, but the potato damage rate is high. However, when the movement speed of conveying mechanism gradually decreases, the turning movement of potatoes weakens, and potatoes are discharged without being completely brushed in the circumferential direction, which leads to the decrease of soil impurities removal rate. On the whole, when the movement speed of conveying mechanism is in the range of 0.30 to 0.40 m/s, the soil impurities removal rate is higher than 82%, and the potato damage rate is lower than 2%.

From Fig. 10b, it can be seen that with the increase of the movement speed of brushing mechanism, the potato damage rate first decreased and then increased, and the soil impurities removal rate showed an overall upward trend. The reason is that when the movement speed of brushing mechanism is low, the potato touches the brushing mechanism for a long time which causes damage to potatoes. At this time, the soil impurities cleaning ability of the brushing mechanism is weak, resulting in a decrease in the soil impurities removal rate. When the movement speed of brushing mechanism increases gradually, the ability of removing soil impurities increases, but when the speed is too high, it will cause potato damage. On the whole, when the movement speed of brushing mechanism is in the range of 0.30 to 0.50 m/s, the soil impurities removal rate is higher than 83%, and the potato damage rate is generally at a low value.

From Fig.10c, it can be seen that with the increase of the mechanism clearance, the potato damage rate and soil impurities removal rate both showed a downward trend. The reason is that when the mechanism clearance is small, the squeezing and rubbing action between potatoes is enhanced in the conveying mechanism and brushing mechanism. At this time, although the effect of removing soil impurities is good, it is easy to cause potato damage. When the mechanism clearance gradually increases, the potato is weakened by the action of conveying mechanism and brushing mechanism, and the potato damage rate decreases, but at this time, the soil impurities removal rate will also decrease. On the whole, when the mechanism clearance is in the range of 45 to 55mm, the comprehensive effect of soil impurities removal rate and potato damage rate is better.

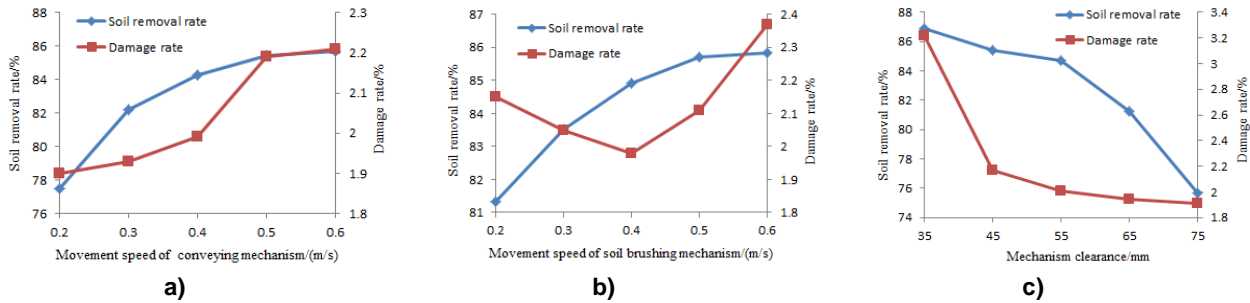


Fig. 10 - Influence of single factor on performance of removal soil impurities

Orthogonal test scheme and results

Through the single factor test analysis, it is obtained that the range of factors with good performance of soil impurities removal is that the movement speed of conveying mechanism is 0.30 to 0.40 m/s, the movement speed of brushing mechanism is 0.30 to 0.50 m/s, and the mechanism clearance is 45 to 55 mm. The orthogonal test of three factors and three levels is designed (Liu *et al*, 2021; Bao *et al*, 2020), and L₉ (3⁴) test table is selected, and each test is repeated 3 times to take the average value as the test result. The factors and levels are shown in Table 1.

Table 1

Factors and levels of orthogonal test

levels	Factors		
	Movement speed of conveying mechanism	Movement speed of brushing mechanism	Mechanism clearance
	[m/s]	[m/s]	[mm]
1	0.30	0.30	45
2	0.35	0.40	50
3	0.40	0.50	55

The test scheme and results are shown in Table 2, and the test factors, such as the movement speed of conveying mechanism, the movement speed of brushing mechanism and the mechanism clearance, are expressed by A, B and C respectively.

Table 2

Test scheme and results

Test No.	Factors				T _c [%]	T _s [%]
	A	B	C	Empty column		
1	1	1	1	1	83.61	2.21
2	1	2	2	2	84.24	2.15
3	1	3	3	3	85.18	2.32
4	2	1	2	3	86.72	2.26
5	2	2	3	1	87.21	1.99
6	2	3	1	2	85.97	2.14
7	3	1	3	2	83.82	2.04
8	3	2	1	3	85.63	2.23
9	3	3	2	1	86.24	2.42

Table 2
(continuation)

Test No.	Factors				T_c [%]	T_s [%]
	A	B	C	Empty column		
K_1	253.03	254.15	255.21		T_c	
K_2	259.90	257.08	257.20			
K_3	255.69	257.39	256.21			
R	6.87	3.24	1.99			
Factor order			A, B, C			
Optimal combination			$A_2 B_3 C_2$			
K_1	6.68	6.51	6.58		T_s	
K_2	6.39	6.37	6.83			
K_3	6.69	6.88	6.35			
R	0.30	0.51	0.48			
Factor order			B, C, A			
Optimal combination			$B_2 C_3 A_2$			

From Table 2, it can be seen that the test factors, such as the movement speed of conveying mechanism, the movement speed of brushing mechanism and the mechanism clearance, have different influences on soil impurities removal rate and potato damage rate. The primary and secondary factors affecting the soil impurities removal rate are $A > B > C$, and the optimal combination is $A_2 B_3 C_2$. The primary and secondary factors affecting the potato damage rate are $B > C > A$, and the optimal combination is $B_2 C_3 A_2$. Among them, the A_2 is an excellent level shared by soil impurities removal rate and potato damage rate, while B_2 and C_3 have great influence on potato damage rate. As raw materials for fresh or starch production, the cleaning requirement of potato is to remove soil impurities and not damage the inside. Therefore, considering comprehensively, the optimal combination is $A_2 B_2 C_3$, that is, the movement speed of conveying mechanism is 0.35m/s, the movement speed of brushing mechanism is 0.40m/s, and the mechanism clearance is 55mm.

Verification test and results

Three repeated verification tests were carried out under the condition that the optimal parameter combination was that the moving speed of conveying mechanism was 0.35 m/s, the moving speed of brushing mechanism was 0.4 m/s and the mechanism clearance was 55 mm. The test results are shown in Table 3. The results showed that the average soil impurities removal rate was 87.18% and the average potato damage rate was 1.95%, which met the requirements of potato cleaning operation.

Table 3

Results of verification test					
Test No.	Sampling quality	Damage quality	Uncleaned quality	soil impurities removal rate	potato damage rate
	[kg]	[kg]	[kg]	[%]	[%]
1	51.20	1.01	6.61	87.09	1.97
2	50.90	0.92	5.75	88.70	1.81
3	52.10	1.08	7.42	85.76	2.07
Average value				87.18	1.95

CONCLUSIONS

1) A potato soil impurities removing apparatus was designed, which used the principle of conveying-brushing combination to remove large pieces of soil impurities and residual soil attached to potato surface.

2) The single factor test was carried out on the influence of movement speed of conveying mechanism, the movement speed of brushing mechanism and the mechanism clearance on test indexes. The range of these factors is that the movement speed of conveying mechanism is 0.30 to 0.40 m/s, the movement speed of brushing mechanism is 0.30 to 0.50 m/s, and the mechanisms clearance is 45 to 55 mm.

3) Through orthogonal test, it is determined that the order of influencing factors on soil removal rate is the movement speed of conveying mechanism, the movement speed of brushing mechanism and the mechanism clearance. The order of influencing factors on damage rate is the movement speed of brushing mechanism, the mechanism clearance and the movement speed of conveying mechanism. The optimized combination is that the movement speed of conveying mechanism is 0.35 m/s, the movement speed of brushing mechanism is 0.40m/s, and the mechanism clearance is 55 mm. The verification test shows that the average soil impurities removal rate is 87.18% and the average potato damage rate is 1.95%, the operation performance meets the potato cleaning requirements.

ACKNOWLEDGEMENT

This research was supported by the Central Public-interest Scientific Institution Basal Research Fund (S202110-02), the National Key Research and Development Programme of China (2018YFD0700102), and the Agricultural Science and Technology Innovation Programme of the Chinese Academy of Agricultural Sciences (CAAS-ASTIP).

REFERENCES

- [1] Al-Mallahi, A., Kataoka, T., Okamoto, H., et al, (2010), Detection of potato tubers using an ultraviolet imaging-based machine vision system. *Biosystems Engineering*, vol. 105, no. 2, pp. 257–265.
- [2] Bulgakov, V., Nikolaenko, S., Arak, M., et al, (2018), Mathematical model of cleaning potatoes on surface of spiral separator. *Agronomy Research*, vol. 16, no. 4, pp. 1590–1606.
- [3] Bai, L., Chen, X., Sun, J., et al, (2019), Development of potato processing industry in China from perspective of industrial integration (产业融合视角下中国马铃薯加工业发展问题研究). *Transactions of the Chinese Society of Agricultural Engineering*, vol. 35, no.8, pp. 316–323.
- [4] Bao, X., Zhao, X., He, J., et al, (2020), Design and performance test of plowing and rotary tillage combined machine. *INMATEH-Agricultural Engineering*, Vol.60, Issue 1, pp.213-222.
- [5] Chen, H., Teng, Yu., Wang, Y., et al, (2018), Design and experiment on single-plant soybean threshing device with differential speed flexible belts (柔性差速带式单株大豆脱粒装置设计与试验). *Transactions of the Chinese Society for Agricultural Machinery*, vol. 49, no. 9, pp. 96–104.
- [6] Deng, W., Wang, C., Xie, S., (2019), Test research on the impact peak force and damage depth of potato. *INMATEH-Agricultural Engineering*, Vol.61, Issue 2, pp.105-114.
- [7] Hrushetsky, S., Yaropud, V., Duganets, V., et al, (2019), Research of constructive and regulatory parameters of the assembly working parts for potato harvesting machines. *INMATEH-Agricultural Engineering*, Vol. 59, Issue 3, pp. 101-110. <https://doi.org/10.35633/inmateh-59-11>
- [8] Ji, L., Xie, H., Yan, J., et al, (2020), Research status and prospect of potato cleaning equipment (马铃薯清洗设备研究现状及展望). *Journal of Chinese Agricultural Mechanization*, vol. 41, no. 4, pp. 98–104.
- [9] Lv, J., Tian, Z., Yang, Y., et al, (2015), Design and experimental analysis of 4U2A type double-row potato digger (4U2A 型双行马铃薯挖掘机的设计与试验). *Transactions of the Chinese Society of Agricultural Engineering*, vol. 31, no.6, pp. 17–24. <https://doi.org/10.3969/j.issn.1002-6819.2015.06.003>
- [10] Liu, F., Lin, Z., Li, D., et al, (2021), Design optimization and performance test of magnetic pickup finger seed metering device. *INMATEH-Agricultural Engineering*, Vol.63, Issue 1, pp.135-142.
- [11] Su, Q., Naoshi, K., Minzan, L., et al, (2018), Potato quality grading based on machine vision and 3d shape analysis. *Computers and Electronics in Agriculture*, vol. 152, pp. 261–268.
- [12] Wang, X., Sun, J., Xu, Y., et al, (2017), Design and experiment of potato cleaning and sorting machine (拨辊推送式马铃薯清洗分选机设计与试验). *Transactions of the Chinese Society for Agricultural Machinery*, vol. 48, no.10, pp. 316–322.
- [13] Wei, Z., Li, H., Su, G., et al, (2019), Development of potato harvester with buffer type potato-impurity separation sieve (缓冲筛式薯杂分离马铃薯收获机研制). *Transactions of the Chinese Society of Agricultural Engineering*, vol. 35, no. 8, pp. 1–11. <https://doi.org/10.11975/j.issn.1002-6819.2019.08.001>
- [14] Yang, H., Xie, H., Yan, J., et al, (2020), Overview of mechanized cleaning technology of post-harvest potato (马铃薯采后机械化清洗技术综述). *Journal of Chinese Agricultural Mechanization*, vol. 41, no. 3, pp. 115–120.

**RESEARCH ON THE UNIFORMITY DEGREE OF SOLID ORGANIC
FERTILIZERS DISTRIBUTION**
/
**CERCETARI PRIVIND GRADUL DE UNIFORMITATE A DISTRIBUTIEI
INGRASAMINTELOR ORGANICE SOLIDE**

Ștefan Vasilica*¹⁾, Zaica Ana¹⁾, Iosif Adrian²⁾

¹⁾ National Institute of Research Development for Machines and Installations Designed for Agriculture and Food Industry – INMA Bucharest/ Romania

²⁾ Herman Oilfield Inspection Service, Ploiești / Romania

E-mail: valistefan.inma@yahoo.com

DOI: <https://doi.org/10.356.33/inmateh-65-51>

Keywords: fertilizer, manure, compost, uniformity, multivariable, function

ABSTRACT

In this paper are presented the results of experimental research conducted in order to improve the uniformity of organic fertilizers distribution (compost and semi-fermented manure) used for soil fertilization, if the administration is done with a machine with a distributor with continuous spiral centrifugal beaters, arranged vertically. The uniformity of organic fertilizers distribution depends on a number of factors such as: the speed and angle of inclination of the distribution device, the distance between the distribution beaters, the humidity and the density of the material, wind speed, the size of the fertilizer particles. The determinations were performed under working conditions and the various parameters were the beaters speed, beaters inclination angle and the feed rate of the distribution device, choosing 3 situations (minimum, average and maximum) for each of them. Based on the obtained results, the multivariable functions of polytropic form was determined, which characterize the degree of uniformity of the spread material, function that can be the basis for the elaboration of constructive solutions to ensure the optimum uniformity of distribution.

REZUMAT

În aceasta lucrare sunt prezentate rezultatele cercetărilor experimentale efectuate în scopul îmbunătățirii uniformității de distribuție a îngrășămintelor organice (compost și gunoi de grajd semifermentat) utilizate pentru fertilizarea solului, în cazul în care administrarea se realizează cu o mașină cu aparat de distribuție cu rotoare centrifugale cu spiră continuă, dispuse în plan vertical. Uniformitatea de distribuție a îngrășămintelor organice depinde de o serie de factori cum ar fi: turația și unghiul de înclinare a aparatului de distribuție, distanța dintre rotoarele distribuitoare, umiditatea și densitatea materialului, viteza vântului, mărimea particulelor de îngrășământ. Determinările au fost efectuate în condiții de lucru reale iar mărimile variabile au fost turația rotoarelor, unghiul de înclinare a acestora și debitul de alimentare a aparatului de distribuție, alegându-se 3 situații (minim, mediu și maxim) pentru fiecare dintre ele. Pe baza rezultatelor obținute s-a determinat funcția multivariabilă de formă politropică care caracterizează gradul de uniformitate a distribuției materialului, funcție ce poate sta la baza elaborării soluțiilor constructive care să asigure uniformitatea de distribuție optimă.

INTRODUCTION

The latest actions implemented by EU regarding climate change and environmental degradation were to adopt the European Green Deal, in order to stop the negative effects. This plan provides strategies to use the resources efficiently by transition to a clean and circular economy and restore biodiversity and cut pollution (European Commission, https://ec.europa.eu/info/strategy/priorities-2019-2024/european-green-deal_en).

The use of manure on a larger scale is part of the measures taken by the European Commission to close the nutrient loop in the agricultural sector. It is intended to allow the wider use of recycled manure and other organic nutrients instead of chemical fertilizers, while taking into account the protection of the environment and ecosystems.

Natural organic fertilizers have been and will remain the main source of improving soil quality through the benefits of their turning into humus. At the same time, their improper distribution causes serious damage to the environment, being an important source of pollution if they are administered excessively and unevenly (Golub et al. 2021). At the same time, if they are administered in small quantities, the effect on the benefits brought to the plants will not be the expected one.

The benefits of applying the organic fertilizer on soil are very important, both for plant growing and for farmer's income too. The results obtained by *Catur, 2011*, reveal that the productivity is higher with organic fertilizer compared to the chemicals, but the productivity decreases during the first two or three years of organic fertilizer application. That's why it is necessary to increase the application of organic fertilizers and understand its importance.

Geng et al, (2019), studied the replacement of chemical fertilizers with organic ones in a two-year study experiment, which was carried out to assess the effects of substituting equal amounts of mineral fertilizer with organic manure on the yield, dry matter (*DM*), and nitrogen (*N*) uptake of spring maize (*Zea mays* L.) and on the mineral *N* (*N_{min}*) distribution in the soil profile. The results have shown the increase by 25% nutrient substitution resulted in the best yield increase.

Another study, realized by *Sengottaian K. et al, (2019)*, analyses the human effort for manure land spreading and proposes an innovative cost-effective manure spreader that consists in a pulverizing drum and blades. The simple manure spreader helps providing support to farmers who are unable to afford heavy machineries for land application.

Landry et al., (2005), analyses two different conveying systems for manure spreader and the influences of the geometry of the hopper above the material flow. The four augers and the scraper conveyor were part of a prototype land applicator.

It is mandatory for the fertilizer spreading equipment to provide the uniform spreading on the entire working surface. Previous research study made by some authors, present the theoretical aspects regarding fertilizers distribution with a vertical beater spreading equipment. It was found that the particle trajectory is influenced by the beater dimensions and rotational speed, inclination angle, material flow rate, wind speed and characteristics of the material such as humidity and density. By testing the vertical beater spreader, it can be determined if the theoretical aspects are confirmed (*Ştefan et al., 2018; 2019; 2019 a; Cârdei et al., 2018*).

Modern fertilizer distribution systems should include monitoring and control systems through which the operator is continuously informed on how the fertilization work is being carried out and can intervene when necessary. These monitoring systems are mainly applied on machines that distribute chemical fertilizers and less or not at all, on those that distribute organic fertilizers (*Petcu et al., 2015; Popa et al., 2009*). Although this equipment have been developed continuously, the uniformity of the distribution over the total spreading width does not fall within the agrotechnical requirements, because in the lateral extremities of the spreading strips, the quantities of distributed material are much smaller than in its centre. It is therefore necessary that the data obtained at a single pass of the machine be processed in order to establish an optimal working width, by the method of overlapping at a next pass.

MATERIALS AND METHODS

The experimental tests were performed at INMA Bucharest and aimed to determine the degree of uniformity of the distribution for two materials (compost and semi-fermented manure) distributed with four vertical helical beaters (Fig. 1).



Fig. 1 - Four beaters spreader

Three distributing beater speed, three beater inclination angle and three material feed flow were chosen, for each material. For the experiments performed in effective working conditions, the forward speed of the machine was kept constant, namely 1 m/s.

The dimensions of the distribution device but also the adjusted sizes were:

- The maximum diameter of the helical coil - 0.345 m;
- The minimum diameter of the helical coil - 0.114 m;
- Helical coil pitch - 0.3 m;
- Total height of the beater - 1.1 m (of which 0.9 m with helical coil);
- Inclination angle of the distributor beater $\alpha = 5^\circ, 10^\circ$ and 15° ;
- Beater speed $n = 360, 440$ and 540 rpm;
- Compost feed flow rate $Q = 6, 15$ and 26 kg/s;
- Semi-fermented manure flow rate $Q = 10, 23$ and 40 kg/s;
- Number of beaters - 4;
- Distance between beaters - 0.5 m.

The machine for solid organic fertilizer spreading with vertical helical beaters used for carrying out the experimental research is intended for fertilizing lowlands with a maximum slope of 6° , for cereal crops, industrial plants, vegetables, etc. During the tests, the machine was fully loaded (Fig. 2) and the fertilizer was distributed on a geotextile material, arranged transversely on the direction of movement of the machine as it can be seen in Fig. 3. The samples were collected in plastic bags, on surfaces of 1 m^2 measured with the help of a square metal frame with a side of 1 m, numbered and weighed.



Fig. 2 – The machine loaded with manure



Fig. 3 - The machine working

The purpose of processing the experimental data was to obtain multivariable regression functions that have a polytrophic and/or polynomial form with which to appreciate the functional and qualitative indicators of the fertilizer machine.

The form of multivariable functions is the following:

$$y = f(x_i, a_0, a_i, a_{ii}, a_{ij}) \quad (1)$$

which expresses the dependence of the function y on the independent variables x_i and on the constants a_0, a_i, a_{ii}, a_{ij} .

It was necessary to perform several steps to determine the constants, as follows

- an adequate program of organizing the experiences was drawn up;
- the values of the constants were determined;
- the significance of the variables was tested;
- the adequacy of the function form was tested.

The structure of the experimental research programs used to determine the y function was as follows:

- the number $n^* = 14$ represents the number of experiments that were performed for distinct values of the independent variables, these being necessary to determine coefficients;
- the number $n_o = 4$ represents the number of identical experiments for the same value of the independent variables, these being necessary to determine the experimental errors;
- the total number of experiments performed $n = n^* + n_o = 18$.

The polytropic regression function, with three independent variables, has the form (Păunescu and David, 1999):

$$y = a_0 \cdot x_1^{a_1} \cdot x_2^{a_2} \cdot x_3^{a_3} \quad (2)$$

where: x_1, x_2, x_3 are the independent variables and y is the dependent variable;

In this case $y = G_{ud}$, $x_1 = n$, $x_2 = \alpha$ and $x_3 = Q$, and a_0, a_1, a_2, a_3 are the constants of the independent variables, Q being the manure feed flow.

Using the calculation algorithm described by Păunescu and David, 1999, a special program was created, which calculates the above mentioned, for both types of multivariable functions.

The degree of uniformity of the distribution was calculated with relation 3, for each proposed variant (Popescu et al., 1983).

$$G_{udj} = \left[1 - \frac{\sqrt{\frac{\sum_{i=1}^j (\sigma_i - \bar{\sigma})^2}{j-1}}}{\bar{\sigma}} \right] \cdot 100 \quad (3)$$

where G_{ud} is the spreading uniformity [%];

σ_i - quantities of material collected from the ground following the experiments [kg],

$\bar{\sigma}$ - collected material arithmetic mean [kg],

j is the total number of samples collected.

RESULTS

The conditions under which the research was carried out were determined in advance.

The *slope of the two lands* where the experiments were carried out was determined with a clinometer, which registered 1° and 2° which falls within the maximum of 6° provided by the national standard. The average *wind speed* was 1.62 m/s, which is in line with the recommendations of the cited standards. *Density* of organic fertilizers: the density of the compost used was $\rho = 510 \text{ kg/m}^3$ obtained as an average of the 5 samples of material taken from the platform and that of the semi-fermented manure was 800 kg/m^3 . The measured *humidity* was 72.33% for compost and 81.73% for semi-fermented manure.

Based on the research conducted, several data were obtained.

Determination of multivariable functions for the degree of distribution uniformity for compost

To determine the coefficients of the multivariable functions needed to calculate the uniformity degree of compost spreading, three independent variables influencing the dependent variable were chosen, as well as their range of variation:

A minimum, a maximum and a medium level were chosen for each independent variable n , α and Q . The experimental test program used to determine the multivariable functions for the degree of compost distribution uniformity is presented in Table 1.

Table 1

The test program of experimental data used to determine the degree of uniformity for compost distribution

Den. no.	Rotational speed, n [rpm]	Beater inclination angle, α [°]	The feed flow rate, Q [kg/s]	Degree of distribution uniformity, G_{ud} , [%]
1	360	5	6	77.67
2	540	5	6	79.16
3	360	15	6	78.43
4	540	15	6	79.78
5	360	5	26	78.21
6	540	5	26	78.99
7	360	15	26	83.70
8	540	15	26	84.30
9	360	10	15	78.99
10	540	10	15	75.50
11	440	15	15	83.11

Table 1
(continuation)

Den. no.	Rotational speed, n [rpm]	Beater inclination angle, α [°]	The feed flow rate, Q [kg/s]	Degree of distribution uniformity, G_{ud} , [%]
12	440	5	15	75.96
13	440	10	26	83.39
14	440	10	6	79.07
15	440	10	15	81.78
16	440	10	15	82.21
17	440	10	15	79.49
18	440	10	15	81.02

The obtained polytrophic regression function with three independent variables, n , α , Q which expresses the uniformity degree of the spreading is:

$$G_{ud} = 68.6706 \cdot n^0 \cdot \alpha^{0.0427} \cdot Q^{0.0221} \tag{4}$$

where G_{ud} is the spreading uniformity [%];

n – beater rotational speed 360 - 540 [rpm];

α – inclination angle of the beaters 5 - 15 [°]

Q – beater feed flow 6 - 26 [kg/s]

It is observed that in the range $n = 360-540$ rpm, the degree of uniformity of the distribution does not depend on the beater rotational speed, the speed coefficient being zero.

For three considered values of the beater inclination angle, the degree of uniformity of the fertilizer distribution, depending on the flow rate, can be expressed as follows:

- for $\alpha = 5^\circ$: $G_{ud} = 68,6706 \cdot 5^{0,0427} \cdot Q^{0,0221}$ (5)

- for $\alpha = 10^\circ$: $G_{ud} = 68,6706 \cdot 10^{0,0427} \cdot Q^{0,0221}$ (6)

- for $\alpha = 15^\circ$: $G_{ud} = 68,6706 \cdot 15^{0,0427} \cdot Q^{0,0221}$ (7)

Deviation of distribution uniformity values calculated with relation 4, compared to the experimental values from table 1, is calculated and a maximum 6.5% is achieved. This shows that the form of the function 4 is precise enough.

Figure 4 shows the distribution uniformity for compost spreading comparing the experimental results and those calculated using the polytrophic regression function obtained previously, for each experiment.

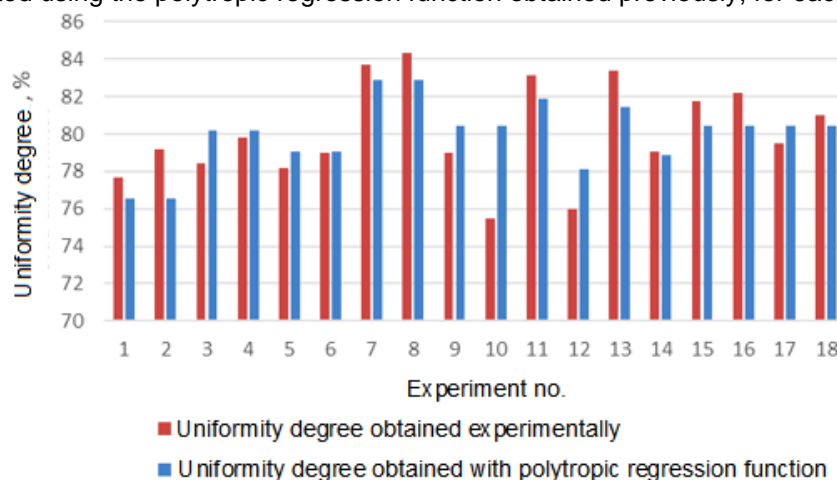


Fig. 4 - The degree of distribution uniformity for compost

Fig. 5 shows graphically the uniformity degree depending on the inclination angle of the beaters and the flow of compost spreading.

From the graph shown in Fig. 5, the degree of uniformity can be determined for any inclination angle of the distributor beaters with values of 5° - 15° and for any flow Q in the range 6 - 26 kg/s.

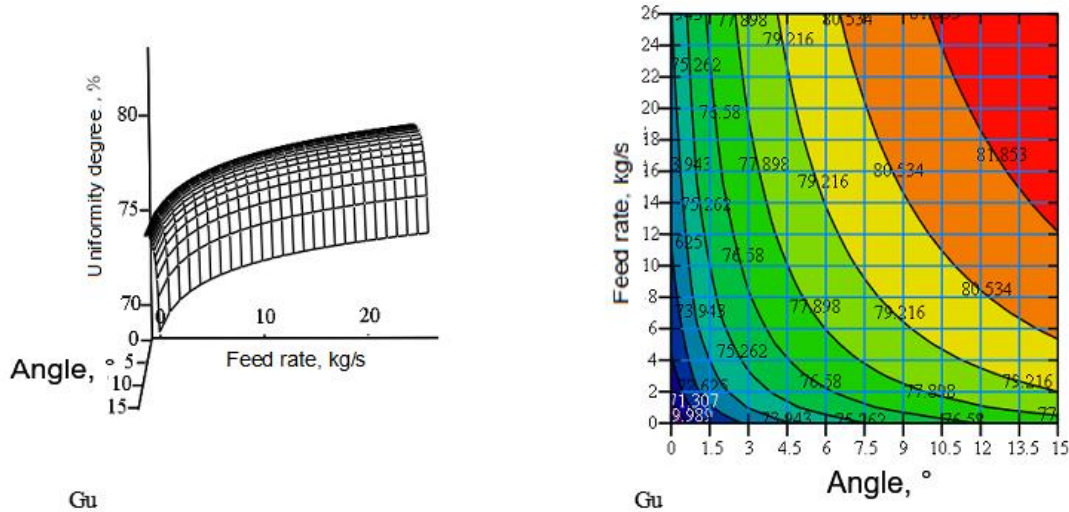


Fig. 5 - Graphical representation of the uniformity degree $G_{ud} = f(\alpha, Q)$ when spreading compost

Fig. 6 shows the variation of the uniformity degree for compost distribution depending on the feed rate for $\alpha = 5^\circ, 10^\circ$ and 15° .

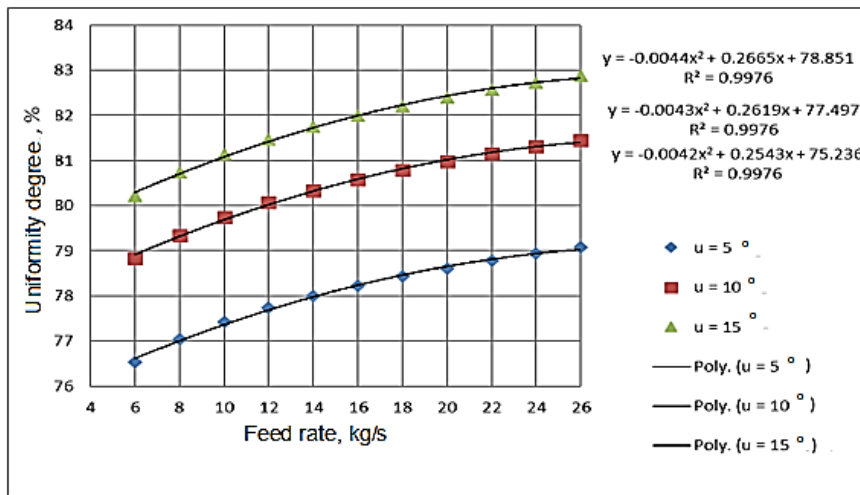


Fig. 6 - Variation of uniformity degree for compost distribution depending on the feed rate for $\alpha = 5^\circ, 10^\circ$ and 15°

From the graph in Fig. 6, it is observed that the degree of uniformity obtained at an inclination of 15° is higher than that obtained at 10° and 5° . For the distributor beaters inclination of 15° , uniformities between 80.21% and 82.97% are obtained. For the inclination of 10° , values between 78.84% and 81.44% are obtained and at the inclination of 5° , values between 76.54 and 79.07% are obtained.

The degree of uniformity in the distribution of compost can be calculated as a function of flow, Q , for the constant angle of inclination of the beaters, with the relations:

- for 15° : $G_{ud} = -0.0044 \cdot Q^2 + 0.2665 \cdot Q + 78.851$ $R^2=0.9976$ (8)

- for 10° : $G_{ud} = -0.0043 \cdot Q^2 + 0.2619 \cdot Q + 77.492$ $R^2=0.9976$ (9)

- for 5° : $G_{ud} = -0.0042 \cdot Q^2 + 0.2543 \cdot Q + 75.236$ $R^2=0.9976$ (10)

It is recommended to incline the beaters of the machine to distribute solid fertilizer at an angle of 15° because it ensures a degree of distribution uniformity of the maximum compost in the range 80.22% - 82.97%.

Determination of multivariable function for the degree of distribution uniformity for semi-fermented manure

For the second type of fertilizer used for tests, the same procedure was applied. In order to determine the coefficients of the multivariable function that calculate the *spreading uniformity degree*, G_{ud} , the following independent variables were considered to be influencing the dependent variable, but also the range of their variation:

- Beater speed: $n = 360; 440; 540$ rpm;
- Beater inclination angle: $\alpha = 5^\circ; 10^\circ; 15^\circ$;
- Feed flow: $Q = 10; 23; 40$ kg/s

For each independent variable n , α and Q , a minimum and a maximum level were chosen, these being located at equal distances from a central level considered as the origin.

The experimental test program, used to determine the multivariable functions for the uniform distribution of semi-fermented waste is presented in Table 2.

Table 2

The test program of experimental data used to determine the degree of uniformity for semi-fermented manure distribution

Den. no.	Speed, n , [rpm]	Beater inclination angle α [°]	The feed flow rate Q [kg/s]	Degree of distribution uniformity G_{ud} [%]
1	360	5	10	80.52
2	540	5	10	80.17
3	360	15	10	83.94
4	540	15	10	82.65
5	360	5	40	88.21
6	540	5	40	84.16
7	360	15	40	82.76
8	540	15	40	82.57
9	360	10	23	83.50
10	540	10	23	76.19
11	440	15	23	83.11
12	440	5	23	82.10
13	440	10	40	83.18
14	440	10	10	83.13
15	440	10	23	83.27
16	440	10	23	81.35
17	440	10	23	80.52
18	440	10	23	80.17

The regression function that approximates the experimental results was found with a Turbo Pascal routine. This function is:

$$G_{ud} = 62.7978 \cdot n^0 \cdot \alpha^{0.0521} \cdot Q^{0.0483} \quad (11)$$

The distribution uniformity of the semi-fermented manure does not depend on the beater speed in the range 360-540 rpm.

Figure 6 shows the experimental values of the uniformity degree of semi-fermented manure distribution, compared to the values calculated using the polytropic regression function obtained previously, for each experimental test.

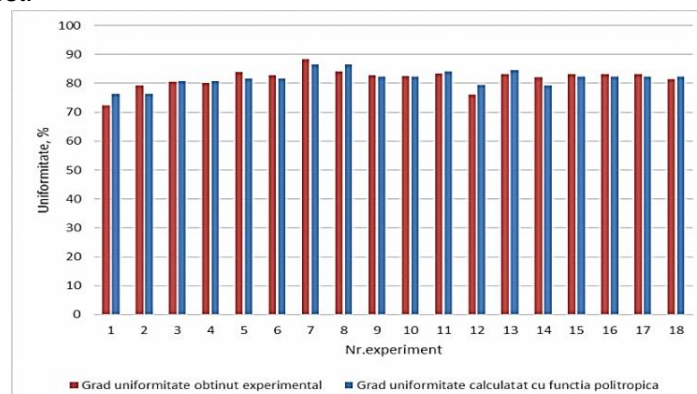


Fig. 6 - Degree of distribution uniformity for experimental and calculated values for semi-fermented manure

The deviation of the calculated values of the uniformity degree for the distribution between the experimental values and calculated ones, is maximum 4.29%, value that shows that the form of the function is quite precise.

Fig. 7 shows graphically the uniformity degree of semi-fermented manure spreading.

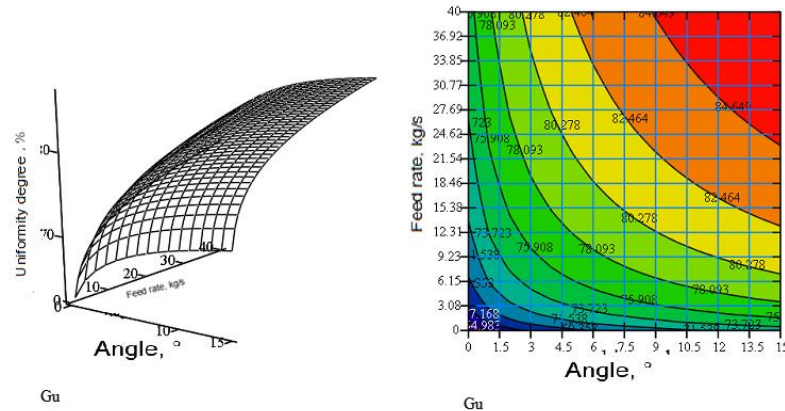


Fig. 7 - Graphical representation of the uniformity degree $G_{ud} = f(\alpha, Q)$ when spreading semi-fermented manure (polytropic function)

Consider the inclination angle of the beaters to be constant and from relation 9 the calculation relations of the uniformity degree as a function of the feed rate Q are obtained:

- for $\alpha = 5^\circ$: $G_{ud} = 62,7978 \cdot 5^{0,0521} \cdot Q^{0,04832}$ (12)

- for $\alpha = 10^\circ$: $G_{ud} = 62,7978 \cdot 10^{0,0521} \cdot Q^{0,04832}$ (13)

- for $\alpha = 15^\circ$: $G_{ud} = 62,7978 \cdot 15^{0,0521} \cdot Q^{0,04832}$ (14)

Fig. 8 shows the variation of the uniformity degree of the semi-fermented manure distribution depending on the feed rate for $\alpha = 5^\circ, 10^\circ$ and 15° .

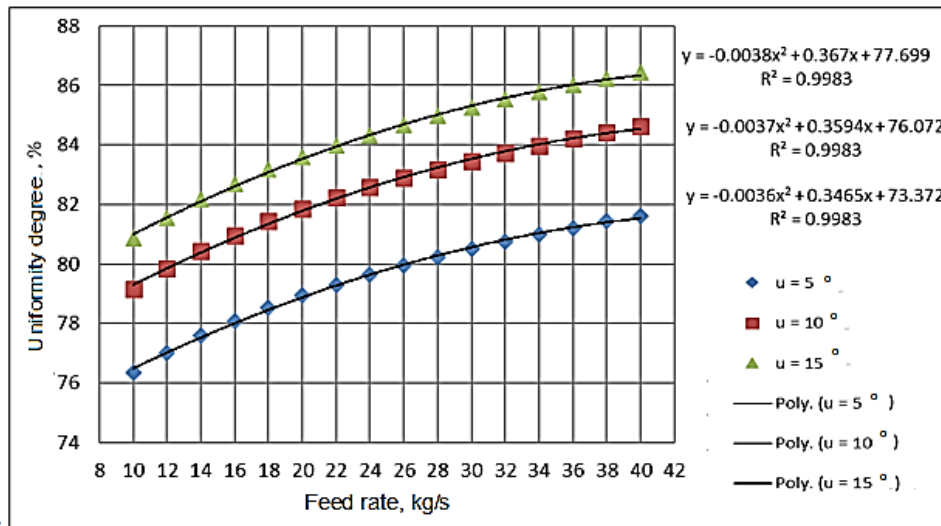


Fig.8 - Variation of the uniformity degree of semi-fermented manure distribution depending on the feed rate for $\alpha = 5, 10$ and 15°

The degree of uniformity in the distribution of semi-fermented manure can be calculated as a function of flow (Q), for the constant angle of inclination of the beaters, with the relations:

- for 15° : $G_{ud} = -0.0038 \cdot Q^2 + 0.3670 \cdot Q + 77.699$ $R^2=0.9983$ (14)

- for 10° : $G_{ud} = -0.0037 \cdot Q^2 + 0.3594 \cdot Q + 76.072$ $R^2=0.9983$ (15)

- for 5° : $G_{ud} = -0.0036 \cdot Q^2 + 0.3465 \cdot Q + 73.372$ $R^2=0.9983$ (16)

It is recommended that the inclination of the beaters of the solid fertilizer spreading machine be 15° because it ensures maximum degree of uniformity ($G_{ud} \in 82.69\% - 86.43\%$).

From the graph in Fig. 8 it is observed that the degree of uniformity obtained at an inclination of 15° is better than that obtained at 10° and 5°. At an inclination of 15°, uniformities between 80.83% and 86.43% are obtained, at an inclination of 10° values between 79.14% and 84.63% are obtained and at an inclination of 5° values between 76.33% and 81.62% are obtained.

CONCLUSIONS

The deviation of the values of the compost distribution uniformity degree, calculated with the polytropic form function, compared to the experimental values is of maximum 6.56%, which shows that the form of the obtained function is quite precise. The degree of uniformity of the compost distribution has the maximum value at the inclination of the beaters of 15° and has the minimum value for the angle of 5°. At the inclination of the distributor beaters of 15° uniformities between 80.22% and 82.97% are obtained, at the inclination of 10° values between 78.84% and 81.45% are obtained and at the inclination of 5° values between 76.54 and 79.07% are obtained.

The deviation of the values of the uniformity degree of semi-fermented manure distribution calculated with the polytropic form function compared to the experimental values is of maximum 4.294% which shows that the form of the function is quite precise. At an inclination of 15° uniformities are obtained between 80.84% and 86.44%, at an inclination of 10° values between 79.15% and 84.63% are obtained and at an inclination of 5° values between 76.34% and 81.63% are obtained.

It is recommended to incline the beaters of the fertilizer spreader to 15°, considering that the research results showed a degree of uniformity between 80.22 ... 82.97%, when distributing the compost and 80.84 ... 86.44%, when distributing semi-fermented manure.

REFERENCES

- [1] Catur, S., (2011). The Benefits of Organic Fertilizer Application: Case Indonesia: Garut and Sragen Regencies. *IRSA 12 Conference*
- [2] Cârdei, P., Ștefan, V., Popa, L., Ciupercă, R., (2019), Statistical models for the working process carried out by the organic fertilizer spreading machine," *INMATEH Agricultural Engineering*, 58(2), 121-128. DOI:<https://doi.org/10.35633/inmateh-58-13>.
- [3] Geng, Y., Cao, G., Wang, L., Wang, S. (2019). Effects of equal chemical fertilizer substitutions with organic manure on yield, dry matter, and nitrogen uptake of spring maize and soil nitrogen distribution. *PLoS ONE* 14(7): e0219512. <https://doi.org/10.1371/journal.pone.0219512>
- [4] Golub, G., Tsyvenkova, N., Holubenko, A., Chuba, V., Tereshchuk, M. (2021). Investigation of substrate mixing process in rotating drum reactor, *INMATEH Agricultural Engineering*, 63(1), 51-60, DOI: <https://doi.org/10.35633/inmateh-63-05>.
- [5] Landry, H., Piron, E., Agnew, J.M., Lague, C., Roberge, M., (2005). Performances of conveying systems for manure spreaders and effects of hopper geometry on output flow, *Applied Engineering in Agriculture*, 21, 159-166.
- [6] Păunescu, I., David, L., (1999). *Basics of experimental research on biotechnical systems (Bazele cercetării experimentale a sistemelor biotehnice)*, Bucharest: Printech Publishing House.
- [7] Petcu, A.S., Popa, L., Ștefan, V., Ciupercă, R., Gârleanu, I.C., Avramescu, A. M., Veringa, D., Zaica, A., Lazar, G. (2015). Theoretical research regarding the working process of the fertilizers managing systems by centrifugation, *Annals of the University of Craiova - Agriculture, Montanology, Cadastre Series*, XLV, 174-184.
- [8] Popa, L., Vlăduț, V., Ștefan, V., (2009), Researches Concerning the Achievement of a Machine for Spreading Low Rates of Chemical Fertilizers, *Bulletin of University of Agricultural Sciences and Veterinary Medicine Cluj-Napoca. Agriculture*, 66 (1).
- [9] Popescu, S., Șandru, A., Cristea, I., Neculăiasa, V., (1983), *Operation of agricultural machinery (Exploatarea utilajelor agricole)*, Bucharest: Didactic and Pedagogical Publishing House.
- [10] Sengottaian K, Mohanrajhu N, Palani S, Jayabalan C, Design of Manure Spreader Machine for agricultural farm field, (2019). *International Journal of Innovative Technology and Exploring Engineering (IJITEE)* ISSN: 2278-3075, Volume-9 Issue-1, DOI: 10.35940/ijitee.A4877.119119
- [11] Ștefan, V., Cârdei, P., Popa, L., David, L., Ciupercă, R., (2019 a), Influence of the manure spreading machines' working parameters on the qualitative performances of the fertilization process, *INMATEH Agricultural Engineering*, 58(2), 115-120. DOI: <https://doi.org/10.35633/inmateh-58-12>.

- [12] Ștefan, V., Cârdei, P., Vlăduț, N.V., Popa, L., Ciupercă, R., Ungureanu, N., (2018), Mathematical model for particle motion applied on a manure spreading apparatus used in environmentally friendly technology, *Environmental Engineering and Management Journal, Gheorghe Asachi Technical University, Iași*, 17, 217-227.
- [13] Ștefan, V., David, L., Popa, L., Ciupercă, R., Zaica, A., Nedelcu, A., Anghelut, A., (2019), Study of the particle motion on a manure fertilizer spreader, *UPB Scientific Bulletin*, 81(4).
- [14] *** European Commission, A European Green Deal, https://ec.europa.eu/info/strategy/priorities-2019-2024/european-green-deal_en.

**RESEARCH ON THE UNIFORMITY DEGREE OF SOLID ORGANIC
FERTILIZERS DISTRIBUTION**
/
**CERCETARI PRIVIND GRADUL DE UNIFORMITATE A DISTRIBUTIEI
INGRASAMINTELOR ORGANICE SOLIDE**

Ștefan Vasilica*¹⁾, Zaica Ana¹⁾, Iosif Adrian²⁾

¹⁾ National Institute of Research Development for Machines and Installations Designed for Agriculture and Food Industry – INMA Bucharest/ Romania

²⁾ Herman Oilfield Inspection Service, Ploiești / Romania

E-mail: valistefan.inma@yahoo.com

DOI: <https://doi.org/10.356.33/inmateh-65-51>

Keywords: fertilizer, manure, compost, uniformity, multivariable, function

ABSTRACT

In this paper are presented the results of experimental research conducted in order to improve the uniformity of organic fertilizers distribution (compost and semi-fermented manure) used for soil fertilization, if the administration is done with a machine with a distributor with continuous spiral centrifugal beaters, arranged vertically. The uniformity of organic fertilizers distribution depends on a number of factors such as: the speed and angle of inclination of the distribution device, the distance between the distribution beaters, the humidity and the density of the material, wind speed, the size of the fertilizer particles. The determinations were performed under working conditions and the various parameters were the beaters speed, beaters inclination angle and the feed rate of the distribution device, choosing 3 situations (minimum, average and maximum) for each of them. Based on the obtained results, the multivariable functions of polytropic form was determined, which characterize the degree of uniformity of the spread material, function that can be the basis for the elaboration of constructive solutions to ensure the optimum uniformity of distribution.

REZUMAT

În aceasta lucrare sunt prezentate rezultatele cercetărilor experimentale efectuate în scopul îmbunătățirii uniformității de distribuție a îngrășămintelor organice (compost și gunoi de grajd semifermentat) utilizate pentru fertilizarea solului, în cazul în care administrarea se realizează cu o mașină cu aparat de distribuție cu rotoare centrifugale cu spiră continuă, dispuse în plan vertical. Uniformitatea de distribuție a îngrășămintelor organice depinde de o serie de factori cum ar fi: turația și unghiul de înclinare a aparatului de distribuție, distanța dintre rotoarele distribuitoare, umiditatea și densitatea materialului, viteza vântului, mărimea particulelor de îngrășământ. Determinările au fost efectuate în condiții de lucru reale iar mărimile variabile au fost turația rotoarelor, unghiul de înclinare a acestora și debitul de alimentare a aparatului de distribuție, alegându-se 3 situații (minim, mediu și maxim) pentru fiecare dintre ele. Pe baza rezultatelor obținute s-a determinat funcția multivariabilă de formă politropică care caracterizează gradul de uniformitate a distribuției materialului, funcție ce poate sta la baza elaborării soluțiilor constructive care să asigure uniformitatea de distribuție optimă.

INTRODUCTION

The latest actions implemented by EU regarding climate change and environmental degradation were to adopt the European Green Deal, in order to stop the negative effects. This plan provides strategies to use the resources efficiently by transition to a clean and circular economy and restore biodiversity and cut pollution (European Commission, https://ec.europa.eu/info/strategy/priorities-2019-2024/european-green-deal_en).

The use of manure on a larger scale is part of the measures taken by the European Commission to close the nutrient loop in the agricultural sector. It is intended to allow the wider use of recycled manure and other organic nutrients instead of chemical fertilizers, while taking into account the protection of the environment and ecosystems.

Natural organic fertilizers have been and will remain the main source of improving soil quality through the benefits of their turning into humus. At the same time, their improper distribution causes serious damage to the environment, being an important source of pollution if they are administered excessively and unevenly (Golub et al. 2021). At the same time, if they are administered in small quantities, the effect on the benefits brought to the plants will not be the expected one.

The benefits of applying the organic fertilizer on soil are very important, both for plant growing and for farmer's income too. The results obtained by *Catur, 2011*, reveal that the productivity is higher with organic fertilizer compared to the chemicals, but the productivity decreases during the first two or three years of organic fertilizer application. That's why it is necessary to increase the application of organic fertilizers and understand its importance.

Geng et al, (2019), studied the replacement of chemical fertilizers with organic ones in a two-year study experiment, which was carried out to assess the effects of substituting equal amounts of mineral fertilizer with organic manure on the yield, dry matter (*DM*), and nitrogen (*N*) uptake of spring maize (*Zea mays* L.) and on the mineral *N* (*N_{min}*) distribution in the soil profile. The results have shown the increase by 25% nutrient substitution resulted in the best yield increase.

Another study, realized by *Sengottaian K. et al, (2019)*, analyses the human effort for manure land spreading and proposes an innovative cost-effective manure spreader that consists in a pulverizing drum and blades. The simple manure spreader helps providing support to farmers who are unable to afford heavy machineries for land application.

Landry et al., (2005), analyses two different conveying systems for manure spreader and the influences of the geometry of the hopper above the material flow. The four augers and the scraper conveyor were part of a prototype land applicator.

It is mandatory for the fertilizer spreading equipment to provide the uniform spreading on the entire working surface. Previous research study made by some authors, present the theoretical aspects regarding fertilizers distribution with a vertical beater spreading equipment. It was found that the particle trajectory is influenced by the beater dimensions and rotational speed, inclination angle, material flow rate, wind speed and characteristics of the material such as humidity and density. By testing the vertical beater spreader, it can be determined if the theoretical aspects are confirmed (*Ştefan et al., 2018; 2019; 2019 a; Cârdei et al., 2018*).

Modern fertilizer distribution systems should include monitoring and control systems through which the operator is continuously informed on how the fertilization work is being carried out and can intervene when necessary. These monitoring systems are mainly applied on machines that distribute chemical fertilizers and less or not at all, on those that distribute organic fertilizers (*Petcu et al., 2015; Popa et al., 2009*). Although this equipment have been developed continuously, the uniformity of the distribution over the total spreading width does not fall within the agrotechnical requirements, because in the lateral extremities of the spreading strips, the quantities of distributed material are much smaller than in its centre. It is therefore necessary that the data obtained at a single pass of the machine be processed in order to establish an optimal working width, by the method of overlapping at a next pass.

MATERIALS AND METHODS

The experimental tests were performed at INMA Bucharest and aimed to determine the degree of uniformity of the distribution for two materials (compost and semi-fermented manure) distributed with four vertical helical beaters (Fig. 1).



Fig. 1 - Four beaters spreader

Three distributing beater speed, three beater inclination angle and three material feed flow were chosen, for each material. For the experiments performed in effective working conditions, the forward speed of the machine was kept constant, namely 1 m/s.

The dimensions of the distribution device but also the adjusted sizes were:

- The maximum diameter of the helical coil - 0.345 m;
- The minimum diameter of the helical coil - 0.114 m;
- Helical coil pitch - 0.3 m;
- Total height of the beater - 1.1 m (of which 0.9 m with helical coil);
- Inclination angle of the distributor beater $\alpha = 5^\circ, 10^\circ$ and 15° ;
- Beater speed $n = 360, 440$ and 540 rpm;
- Compost feed flow rate $Q = 6, 15$ and 26 kg/s;
- Semi-fermented manure flow rate $Q = 10, 23$ and 40 kg/s;
- Number of beaters - 4;
- Distance between beaters - 0.5 m.

The machine for solid organic fertilizer spreading with vertical helical beaters used for carrying out the experimental research is intended for fertilizing lowlands with a maximum slope of 6° , for cereal crops, industrial plants, vegetables, etc. During the tests, the machine was fully loaded (Fig. 2) and the fertilizer was distributed on a geotextile material, arranged transversely on the direction of movement of the machine as it can be seen in Fig. 3. The samples were collected in plastic bags, on surfaces of 1 m^2 measured with the help of a square metal frame with a side of 1 m, numbered and weighed.



Fig. 2 – The machine loaded with manure



Fig. 3 - The machine working

The purpose of processing the experimental data was to obtain multivariable regression functions that have a polytrophic and/or polynomial form with which to appreciate the functional and qualitative indicators of the fertilizer machine.

The form of multivariable functions is the following:

$$y = f(x_i, a_0, a_i, a_{ii}, a_{ij}) \quad (1)$$

which expresses the dependence of the function y on the independent variables x_i and on the constants a_0, a_i, a_{ii}, a_{ij} .

It was necessary to perform several steps to determine the constants, as follows

- an adequate program of organizing the experiences was drawn up;
- the values of the constants were determined;
- the significance of the variables was tested;
- the adequacy of the function form was tested.

The structure of the experimental research programs used to determine the y function was as follows:

- the number $n^* = 14$ represents the number of experiments that were performed for distinct values of the independent variables, these being necessary to determine coefficients;
- the number $n_o = 4$ represents the number of identical experiments for the same value of the independent variables, these being necessary to determine the experimental errors;
- the total number of experiments performed $n = n^* + n_o = 18$.

The polytropic regression function, with three independent variables, has the form (Păunescu and David, 1999):

$$y = a_0 \cdot x_1^{a_1} \cdot x_2^{a_2} \cdot x_3^{a_3} \quad (2)$$

where: x_1, x_2, x_3 are the independent variables and y is the dependent variable;

In this case $y = G_{ud}$, $x_1 = n$, $x_2 = \alpha$ and $x_3 = Q$, and a_0, a_1, a_2, a_3 are the constants of the independent variables, Q being the manure feed flow.

Using the calculation algorithm described by Păunescu and David, 1999, a special program was created, which calculates the above mentioned, for both types of multivariable functions.

The degree of uniformity of the distribution was calculated with relation 3, for each proposed variant (Popescu et al., 1983).

$$G_{udj} = \left[1 - \frac{\sqrt{\frac{\sum_{i=1}^j (\sigma_i - \bar{\sigma})^2}{j-1}}}{\bar{\sigma}} \right] \cdot 100 \quad (3)$$

where G_{ud} is the spreading uniformity [%];

σ_i - quantities of material collected from the ground following the experiments [kg],

$\bar{\sigma}$ - collected material arithmetic mean [kg],

j is the total number of samples collected.

RESULTS

The conditions under which the research was carried out were determined in advance.

The *slope of the two lands* where the experiments were carried out was determined with a clinometer, which registered 1° and 2° which falls within the maximum of 6° provided by the national standard. The average *wind speed* was 1.62 m/s, which is in line with the recommendations of the cited standards. *Density* of organic fertilizers: the density of the compost used was $\rho = 510 \text{ kg/m}^3$ obtained as an average of the 5 samples of material taken from the platform and that of the semi-fermented manure was 800 kg/m^3 . The measured *humidity* was 72.33% for compost and 81.73% for semi-fermented manure.

Based on the research conducted, several data were obtained.

Determination of multivariable functions for the degree of distribution uniformity for compost

To determine the coefficients of the multivariable functions needed to calculate the uniformity degree of compost spreading, three independent variables influencing the dependent variable were chosen, as well as their range of variation:

A minimum, a maximum and a medium level were chosen for each independent variable n , α and Q . The experimental test program used to determine the multivariable functions for the degree of compost distribution uniformity is presented in Table 1.

Table 1

The test program of experimental data used to determine the degree of uniformity for compost distribution

Den. no.	Rotational speed, n [rpm]	Beater inclination angle, α [°]	The feed flow rate, Q [kg/s]	Degree of distribution uniformity, G_{ud} , [%]
1	360	5	6	77.67
2	540	5	6	79.16
3	360	15	6	78.43
4	540	15	6	79.78
5	360	5	26	78.21
6	540	5	26	78.99
7	360	15	26	83.70
8	540	15	26	84.30
9	360	10	15	78.99
10	540	10	15	75.50
11	440	15	15	83.11

Table 1
(continuation)

Den. no.	Rotational speed, n [rpm]	Beater inclination angle, α [°]	The feed flow rate, Q [kg/s]	Degree of distribution uniformity, G_{ud} , [%]
12	440	5	15	75.96
13	440	10	26	83.39
14	440	10	6	79.07
15	440	10	15	81.78
16	440	10	15	82.21
17	440	10	15	79.49
18	440	10	15	81.02

The obtained polytrophic regression function with three independent variables, n , α , Q which expresses the uniformity degree of the spreading is:

$$G_{ud} = 68.6706 \cdot n^0 \cdot \alpha^{0.0427} \cdot Q^{0.0221} \tag{4}$$

where G_{ud} is the spreading uniformity [%];

n – beater rotational speed 360 - 540 [rpm];

α – inclination angle of the beaters 5 - 15 [°]

Q – beater feed flow 6 - 26 [kg/s]

It is observed that in the range $n = 360-540$ rpm, the degree of uniformity of the distribution does not depend on the beater rotational speed, the speed coefficient being zero.

For three considered values of the beater inclination angle, the degree of uniformity of the fertilizer distribution, depending on the flow rate, can be expressed as follows:

- for $\alpha = 5^\circ$: $G_{ud} = 68,6706 \cdot 5^{0,0427} \cdot Q^{0,0221}$ (5)

- for $\alpha = 10^\circ$: $G_{ud} = 68,6706 \cdot 10^{0,0427} \cdot Q^{0,0221}$ (6)

- for $\alpha = 15^\circ$: $G_{ud} = 68,6706 \cdot 15^{0,0427} \cdot Q^{0,0221}$ (7)

Deviation of distribution uniformity values calculated with relation 4, compared to the experimental values from table 1, is calculated and a maximum 6.5% is achieved. This shows that the form of the function 4 is precise enough.

Figure 4 shows the distribution uniformity for compost spreading comparing the experimental results and those calculated using the polytrophic regression function obtained previously, for each experiment.

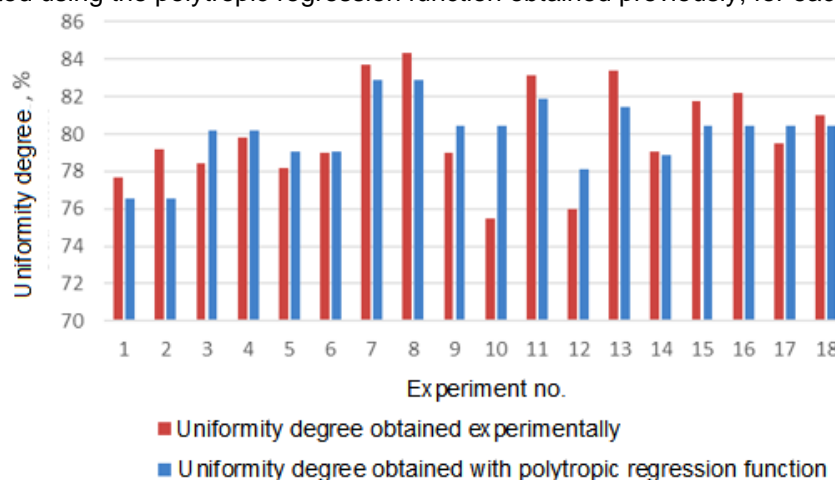


Fig. 4 - The degree of distribution uniformity for compost

Fig. 5 shows graphically the uniformity degree depending on the inclination angle of the beaters and the flow of compost spreading.

From the graph shown in Fig. 5, the degree of uniformity can be determined for any inclination angle of the distributor beaters with values of 5° - 15° and for any flow Q in the range 6 - 26 kg/s.

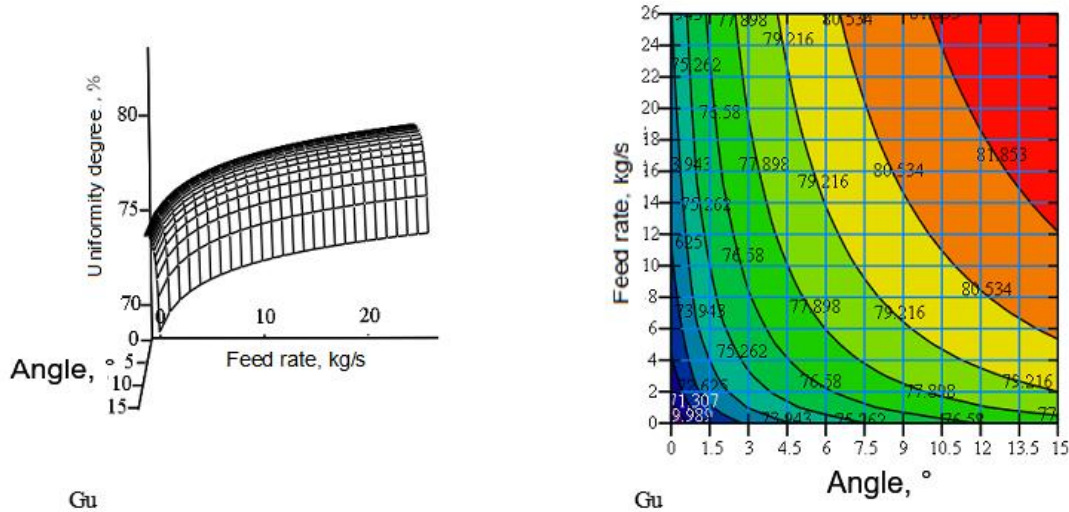


Fig. 5 - Graphical representation of the uniformity degree $G_{ud} = f(\alpha, Q)$ when spreading compost

Fig. 6 shows the variation of the uniformity degree for compost distribution depending on the feed rate for $\alpha = 5^\circ, 10^\circ$ and 15° .

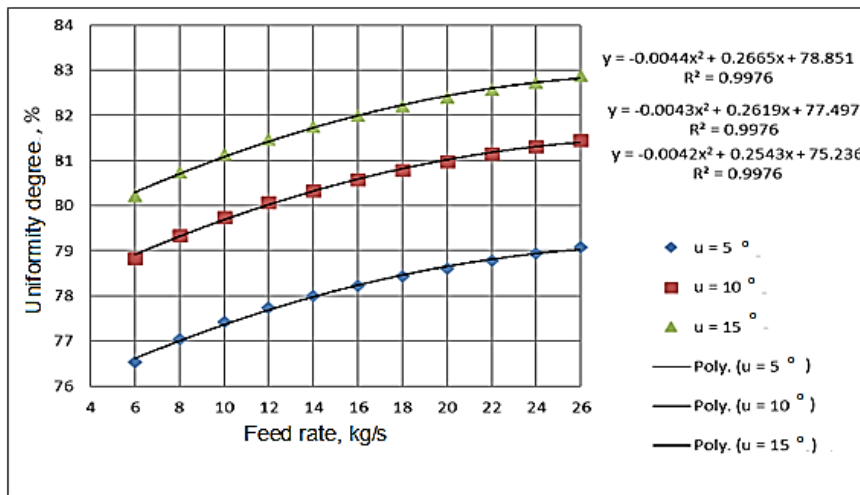


Fig. 6 - Variation of uniformity degree for compost distribution depending on the feed rate for $\alpha = 5^\circ, 10^\circ$ and 15°

From the graph in Fig. 6, it is observed that the degree of uniformity obtained at an inclination of 15° is higher than that obtained at 10° and 5° . For the distributor beaters inclination of 15° , uniformities between 80.21% and 82.97% are obtained. For the inclination of 10° , values between 78.84% and 81.44% are obtained and at the inclination of 5° , values between 76.54 and 79.07% are obtained.

The degree of uniformity in the distribution of compost can be calculated as a function of flow, Q , for the constant angle of inclination of the beaters, with the relations:

- for 15° : $G_{ud} = -0.0044 \cdot Q^2 + 0.2665 \cdot Q + 78.851$ $R^2=0.9976$ (8)

- for 10° : $G_{ud} = -0.0043 \cdot Q^2 + 0.2619 \cdot Q + 77.492$ $R^2=0.9976$ (9)

- for 5° : $G_{ud} = -0.0042 \cdot Q^2 + 0.2543 \cdot Q + 75.236$ $R^2=0.9976$ (10)

It is recommended to incline the beaters of the machine to distribute solid fertilizer at an angle of 15° because it ensures a degree of distribution uniformity of the maximum compost in the range 80.22% - 82.97%.

Determination of multivariable function for the degree of distribution uniformity for semi-fermented manure

For the second type of fertilizer used for tests, the same procedure was applied. In order to determine the coefficients of the multivariable function that calculate the *spreading uniformity degree*, G_{ud} , the following independent variables were considered to be influencing the dependent variable, but also the range of their variation:

- Beater speed: $n = 360; 440; 540$ rpm;
- Beater inclination angle: $\alpha = 5^\circ; 10^\circ; 15^\circ$;
- Feed flow: $Q = 10; 23; 40$ kg/s

For each independent variable n , α and Q , a minimum and a maximum level were chosen, these being located at equal distances from a central level considered as the origin.

The experimental test program, used to determine the multivariable functions for the uniform distribution of semi-fermented waste is presented in Table 2.

Table 2

The test program of experimental data used to determine the degree of uniformity for semi-fermented manure distribution

Den. no.	Speed, n , [rpm]	Beater inclination angle α [°]	The feed flow rate Q [kg/s]	Degree of distribution uniformity G_{ud} [%]
1	360	5	10	80.52
2	540	5	10	80.17
3	360	15	10	83.94
4	540	15	10	82.65
5	360	5	40	88.21
6	540	5	40	84.16
7	360	15	40	82.76
8	540	15	40	82.57
9	360	10	23	83.50
10	540	10	23	76.19
11	440	15	23	83.11
12	440	5	23	82.10
13	440	10	40	83.18
14	440	10	10	83.13
15	440	10	23	83.27
16	440	10	23	81.35
17	440	10	23	80.52
18	440	10	23	80.17

The regression function that approximates the experimental results was found with a Turbo Pascal routine. This function is:

$$G_{ud} = 62.7978 \cdot n^0 \cdot \alpha^{0.0521} \cdot Q^{0.0483} \quad (11)$$

The distribution uniformity of the semi-fermented manure does not depend on the beater speed in the range 360-540 rpm.

Figure 6 shows the experimental values of the uniformity degree of semi-fermented manure distribution, compared to the values calculated using the polytropic regression function obtained previously, for each experimental test.

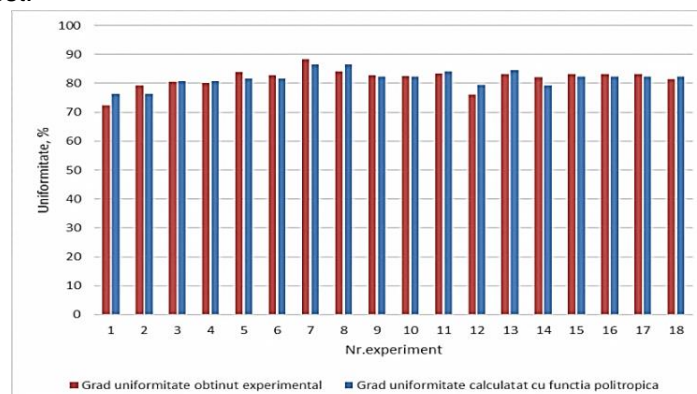


Fig. 6 - Degree of distribution uniformity for experimental and calculated values for semi-fermented manure

The deviation of the calculated values of the uniformity degree for the distribution between the experimental values and calculated ones, is maximum 4.29%, value that shows that the form of the function is quite precise.

Fig. 7 shows graphically the uniformity degree of semi-fermented manure spreading.

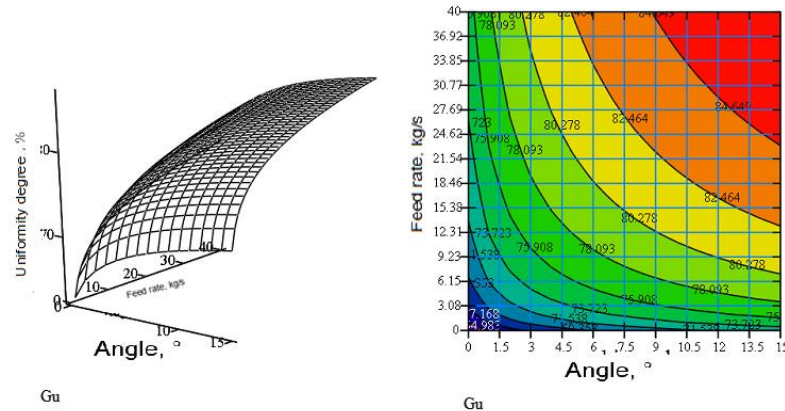


Fig. 7 - Graphical representation of the uniformity degree $G_{ud} = f(\alpha, Q)$ when spreading semi-fermented manure (polytropic function)

Consider the inclination angle of the beaters to be constant and from relation 9 the calculation relations of the uniformity degree as a function of the feed rate Q are obtained:

- for $\alpha = 5^\circ$: $G_{ud} = 62,7978 \cdot 5^{0,0521} \cdot Q^{0,04832}$ (12)

- for $\alpha = 10^\circ$: $G_{ud} = 62,7978 \cdot 10^{0,0521} \cdot Q^{0,04832}$ (13)

- for $\alpha = 15^\circ$: $G_{ud} = 62,7978 \cdot 15^{0,0521} \cdot Q^{0,04832}$ (14)

Fig. 8 shows the variation of the uniformity degree of the semi-fermented manure distribution depending on the feed rate for $\alpha = 5^\circ, 10^\circ$ and 15° .

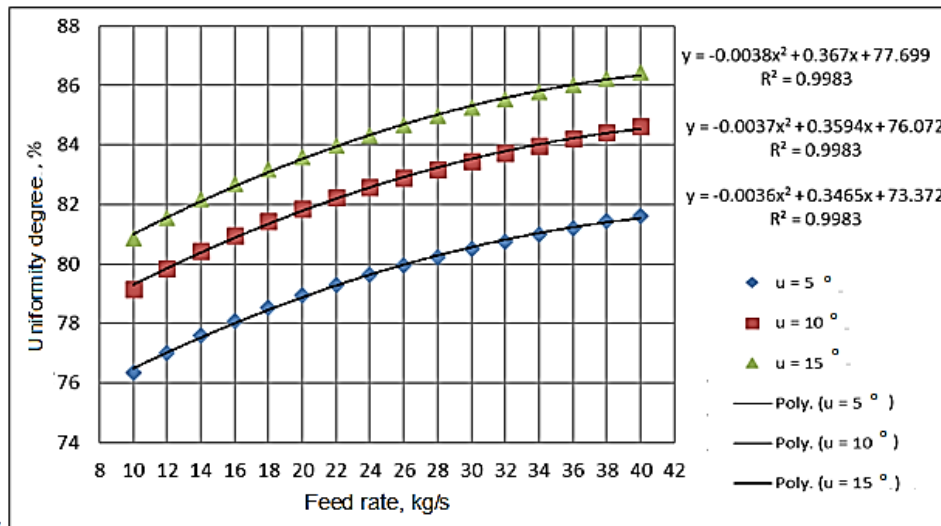


Fig.8 - Variation of the uniformity degree of semi-fermented manure distribution depending on the feed rate for $\alpha = 5, 10$ and 15°

The degree of uniformity in the distribution of semi-fermented manure can be calculated as a function of flow (Q), for the constant angle of inclination of the beaters, with the relations:

- for 15° : $G_{ud} = -0.0038 \cdot Q^2 + 0.3670 \cdot Q + 77.699$ $R^2=0.9983$ (14)

- for 10° : $G_{ud} = -0.0037 \cdot Q^2 + 0.3594 \cdot Q + 76.072$ $R^2=0.9983$ (15)

- for 5° : $G_{ud} = -0.0036 \cdot Q^2 + 0.3465 \cdot Q + 73.372$ $R^2=0.9983$ (16)

It is recommended that the inclination of the beaters of the solid fertilizer spreading machine be 15° because it ensures maximum degree of uniformity ($G_{ud} \in 82.69\% - 86.43\%$).

From the graph in Fig. 8 it is observed that the degree of uniformity obtained at an inclination of 15° is better than that obtained at 10° and 5°. At an inclination of 15°, uniformities between 80.83% and 86.43% are obtained, at an inclination of 10° values between 79.14% and 84.63% are obtained and at an inclination of 5° values between 76.33% and 81.62% are obtained.

CONCLUSIONS

The deviation of the values of the compost distribution uniformity degree, calculated with the polytropic form function, compared to the experimental values is of maximum 6.56%, which shows that the form of the obtained function is quite precise. The degree of uniformity of the compost distribution has the maximum value at the inclination of the beaters of 15° and has the minimum value for the angle of 5°. At the inclination of the distributor beaters of 15° uniformities between 80.22% and 82.97% are obtained, at the inclination of 10° values between 78.84% and 81.45% are obtained and at the inclination of 5° values between 76.54 and 79.07% are obtained.

The deviation of the values of the uniformity degree of semi-fermented manure distribution calculated with the polytropic form function compared to the experimental values is of maximum 4.294% which shows that the form of the function is quite precise. At an inclination of 15° uniformities are obtained between 80.84% and 86.44%, at an inclination of 10° values between 79.15% and 84.63% are obtained and at an inclination of 5° values between 76.34% and 81.63% are obtained.

It is recommended to incline the beaters of the fertilizer spreader to 15°, considering that the research results showed a degree of uniformity between 80.22 ... 82.97%, when distributing the compost and 80.84 ... 86.44%, when distributing semi-fermented manure.

REFERENCES

- [1] Catur, S., (2011). The Benefits of Organic Fertilizer Application: Case Indonesia: Garut and Sragen Regencies. *IRSA 12 Conference*
- [2] Cârdei, P., Ștefan, V., Popa, L., Ciupercă, R., (2019), Statistical models for the working process carried out by the organic fertilizer spreading machine," *INMATEH Agricultural Engineering*, 58(2), 121-128. DOI:<https://doi.org/10.35633/inmateh-58-13>.
- [3] Geng, Y., Cao, G., Wang, L., Wang, S. (2019). Effects of equal chemical fertilizer substitutions with organic manure on yield, dry matter, and nitrogen uptake of spring maize and soil nitrogen distribution. *PLoS ONE* 14(7): e0219512. <https://doi.org/10.1371/journal.pone.0219512>
- [4] Golub, G., Tsyvenkova, N., Holubenko, A., Chuba, V., Tereshchuk, M. (2021). Investigation of substrate mixing process in rotating drum reactor, *INMATEH Agricultural Engineering*, 63(1), 51-60, DOI: <https://doi.org/10.35633/inmateh-63-05>.
- [5] Landry, H., Piron, E., Agnew, J.M., Lague, C., Roberge, M., (2005). Performances of conveying systems for manure spreaders and effects of hopper geometry on output flow, *Applied Engineering in Agriculture*, 21, 159-166.
- [6] Păunescu, I., David, L., (1999). *Basics of experimental research on biotechnical systems (Bazele cercetării experimentale a sistemelor biotehnice)*, Bucharest: Printech Publishing House.
- [7] Petcu, A.S., Popa, L., Ștefan, V., Ciupercă, R., Gârleanu, I.C., Avramescu, A. M., Veringa, D., Zaica, A., Lazar, G. (2015). Theoretical research regarding the working process of the fertilizers managing systems by centrifugation, *Annals of the University of Craiova - Agriculture, Montanology, Cadastre Series*, XLV, 174-184.
- [8] Popa, L., Vlăduț, V., Ștefan, V., (2009), Researches Concerning the Achievement of a Machine for Spreading Low Rates of Chemical Fertilizers, *Bulletin of University of Agricultural Sciences and Veterinary Medicine Cluj-Napoca. Agriculture*, 66 (1).
- [9] Popescu, S., Șandru, A., Cristea, I., Neculăiasa, V., (1983), *Operation of agricultural machinery (Exploatarea utilajelor agricole)*, Bucharest: Didactic and Pedagogical Publishing House.
- [10] Sengottaian K, Mohanrajhu N, Palani S, Jayabalan C, Design of Manure Spreader Machine for agricultural farm field, (2019). *International Journal of Innovative Technology and Exploring Engineering (IJITEE)* ISSN: 2278-3075, Volume-9 Issue-1, DOI: 10.35940/ijitee.A4877.119119
- [11] Ștefan, V., Cârdei, P., Popa, L., David, L., Ciupercă, R., (2019 a), Influence of the manure spreading machines' working parameters on the qualitative performances of the fertilization process, *INMATEH Agricultural Engineering*, 58(2), 115-120. DOI: <https://doi.org/10.35633/inmateh-58-12>.

- [12] Ștefan, V., Cârdei, P., Vlăduț, N.V., Popa, L., Ciupercă, R., Ungureanu, N., (2018), Mathematical model for particle motion applied on a manure spreading apparatus used in environmentally friendly technology, *Environmental Engineering and Management Journal, Gheorghe Asachi Technical University, Iași*, 17, 217-227.
- [13] Ștefan, V., David, L., Popa, L., Ciupercă, R., Zaica, A., Nedelcu, A., Anghelut, A., (2019), Study of the particle motion on a manure fertilizer spreader, *UPB Scientific Bulletin*, 81(4).
- [14] *** European Commission, A European Green Deal, https://ec.europa.eu/info/strategy/priorities-2019-2024/european-green-deal_en.

INTEGRATED NAVIGATION METHOD OF ELECTRIC FORKLIFT BASED ON IMPROVED UKF ALGORITHM

基于改进扩展卡尔曼滤波算法的电动叉车组合导航定位方法

Yibo Li ^{*1)}, Shipeng Zhu¹⁾ ¹

¹⁾ College of Automation, Shenyang Aerospace University, Shenyang / China;

Tel: +86 1764203716; E-mail: Zsp1997629@163.com

Corresponding author: Shipeng Zhu

DOI: <https://doi.org/10.35633/inmateh-65-52>

Keywords: *Integrated navigation, Lidar, IMU, Adaptive, Extended Kalman filtering, Electric forklift*

ABSTRACT

When forklifts are used to move stored crops in a storage environment, the positioning system is severely affected by the presence of multiple stored crops and shelves and other complex factors in the environment. Aiming at the problems of low positioning and navigation accuracy and large accumulated error of forklift system, a Lidar/IMU integrated navigation and positioning method is proposed in this paper, which can improve the positioning accuracy of forklift truck in storage environment. Meanwhile, the improved EKF filtering algorithm is proposed in this paper which can optimize the navigation and positioning system. This method first extracts the environmental information obtained from Lidar scan measurements and the attitude information collected by the IMU. Then the output data from the two sensors are processed with the improved EKF filtering algorithm, which can improve the navigation and positioning accuracy when the forklift is working. The Lidar/IMU integrated navigation and positioning method proposed in this paper is validated by experiments simulating forklifts working in a warehouse environment in the laboratory. Through simulation experiments, it is verified that the improved EKF filtering algorithm in this paper can improve the positioning accuracy of forklift truck, accuracy of forklift movement trajectory, closer to the expected trajectory.

摘要

叉车在仓储环境中搬运储存农作物时，定位系统受环境中多储存农作物以及置物架等复杂因素影响严重。本文针对叉车系统定位导航精度低、累积误差大的问题，提出了一种 Lidar/IMU 相融合的导航定位方法，可以提高叉车在仓储环境下的定位精度。同时改进 EKF 滤波算法，能够优化本文提出的导航定位系统。此方法首先将 Lidar 扫描测量得到的环境信息提取，然后使用改进 EKF 滤波算法处理两个传感器的输出数据，能够提高叉车工作时的导航定位精度。通过在实验室内模拟叉车在仓储环境工作的实验，验证了本文提出的 Lidar/IMU 组合导航定位方法的有效性。又通过仿真实验，验证了本文改进的 EKF 滤波算法，可以提高叉车的定位精度，能够提高叉车移动轨迹的精度，更接近于预期轨迹。

INTRODUCTION

With a large number of intelligent equipment used in the crop storage and transportation industry, warehouse intelligent forklift as a new kind of handling and stacking equipment, the storage protection of agricultural products has been greatly improved (Goran., et al., 2016). In the task of moving agricultural products to warehouses for storage, warehouse forklifts are commonly used in the warehousing industry because of their compact body, flexible movement, light weight and good environmental performance, which can greatly save manpower and time when moving and storing agricultural products (Nguyen., et al., 2020). As the electric forklift adopts new navigation and positioning technology, it makes forklift more convenient and flexible to run in the narrow aisles in the warehouse. The warehouse forklift is specifically transformed on the basis of ordinary forward-moving electric forklift, which is a kind of equipment specially used for small-scale handling and stacking. It retains the original stacking and handling characteristics of the forklift, but adds the function applicable to autonomous navigation, which is very suitable for working in agricultural products storage warehouses with low operational intensity and low stacking height requirements.

¹ Yibo Li, Prof. Ph D; Shipeng Zhu, M.S. Stud

The traditional positioning methods mainly include: odometer projection positioning, magnetic guide positioning, ultrasonic positioning, visual positioning, etc. A method based on robust laser-inertial odometry and map building is proposed to be applied to the positioning system, which can jointly optimize Lidar and INS measurement data. But the data volume of this method is too large and the real-time performance of positioning cannot be guaranteed (Zhao S. *et al.*, 2019). Tightly coupled frame-based Lidar inertial state estimator can be used in low-noise indoor environments, but not in high-noise environments (Neuhaus *et al.*, 2018). Monocular vision methods are proposed for navigation working, but the system takes too long time to process the image information from the camera (Faessler *et al.*, 2015). Since forklifts work in a complex environment with many stacked crops and storage racks, the requirements for getting accurate information about the current environment and their own precise positioning are very high. To solve the problem that electric forklifts can be accurately navigated and positioned indoors, this paper proposes a combined navigation and positioning system based on electric forklifts in complex environments, using the combined navigation technology of Lidar (Light Detection and Ranging) and IMU (Inertial Measurement Unit) to enable forklifts to perform high-precision navigation and positioning work in complex warehouse environments.

In navigation and positioning, the system models all have some degree of nonlinearity. To solve the problem of nonlinear filtering, scholars have focused on the fusion of multiple sensor data to achieve better localisation algorithms. An improved Rao-Blackwellized Particle Filter (RBPF) method combines motion odometer and laser measurement data to obtain an accurate map, which can solve the problem of particle weight degradation, but the structure model is complicated (Wang X. *et al.*, 2020). A Kalman filter based on the minimum error derived under the Gaussian assumption and the minimum mean square error criterion improves the robustness to pulses. But the effect is not ideal for the case of non-Gaussian noise (Benzerrouk. *et al.*, 2020). A Kalman filter based on the inertial navigation error compensation model has higher accuracy than ordinary navigation systems and can monitor the accuracy of error estimation in real time (Zhao X. *et al.*, 2019). An adaptive fading Kalman filter is used as a processing algorithm for target tracking, which improves the filter gain and effectively improves the progress of target tracking, but the ability to adapt to noise is not ideal (Yan C. *et al.*, 2020).

When there is an error in the system or there is external noise, the filtering ability of the EKF algorithm is lower than its normal accuracy, even divergence occurs (Kayacan E. *et al.*, 2019). To solve the problems of low positioning and navigation accuracy and large accumulated error of forklift system, a Lidar /IMU integrated navigation and positioning method is proposed in this paper (Gentil C.L. *et al.*, 2018). Meanwhile, an improved filtering algorithm for Lidar/IMU integrated navigation is proposed based on the fading algorithm. The improved filtering algorithm is obtained by improving from the traditional EKF algorithm (Mouayad S., *et al.*, 2020). Through simulation experiments, it is verified that the improved filtering algorithm can effectively combine the position and attitude observations from Lidar with the position and attitude results from IMU. It can improve the positioning accuracy of the motion trajectory of the forklift system. The combined Lidar/IMU navigation method is proved to be feasible by simulating forklift work in the laboratory. This method is able to obtain higher accuracy and robust positioning results when forklifts work in noisy and complex crop storage environments.

MATERIALS AND METHODS

Integrated navigation solution

The use of Lidar alone for positioning and navigation not only requires a lot of calculation, but also has the problem of slow map construction, and it also causes accumulated errors as the composition time increases. In an indoor environment, the traditional GNSS method fails and cannot be positioned (Wang J., *et al.*, 2017). The introduction of multiple sensors can improve the shortcomings of the traditional positioning system. The IMU has a high update frequency per unit time, and the introduction of IMU can effectively reduce the cumulative positioning error of the Lidar. At the same time, it also avoids accumulated navigation errors caused by long-term use of IMU alone. Therefore, this paper adopts the combined positioning method based on Lidar/IMU to improve the accuracy of the mobile robot's indoor positioning. By the Kalman filter algorithm, different sensor data can be effectively fused to obtain more accurate positioning information. The paper uses an improved EKF algorithm to process sensor data to improve the stability and positioning accuracy of the system. The system block diagram is shown in Fig. 1.

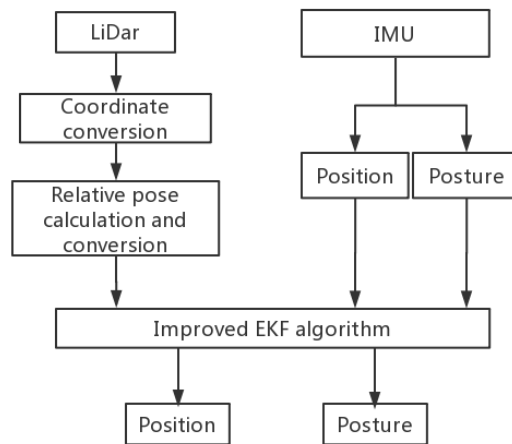


Fig. 1 – Lidar and IMU Combined System Model

Lidar Measurement model

The Lidar scanning environment has a relatively long range and it is suitable for working in a warehouse environment where attitude and position information can be obtained by scanning the environment. Lidar is widely used in the field of SLAM (Simultaneous Localization and Mapping) (Li Xinlei, et al., 2020), and the original data collected are polar points in the local coordinate system. Based on the feedback time from the laser pulse to the received pulse, the angle and distance between the measured object and the sensor are calculated and measured by the Lidar, which continuously updates the IMU data by scanning the indoor environment and processing the extracted information. Lidar measurement model is shown in Fig. 2. The Lidar is placed on the top of the forklift in the electric forklift system designed in this paper, as shown in Fig. 3.

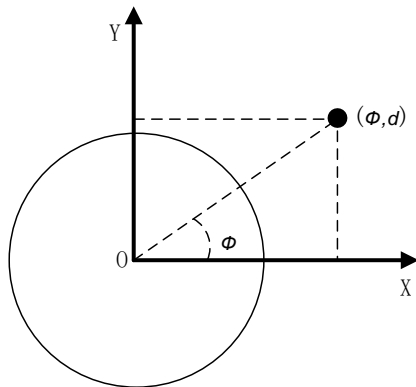


Fig. 2 – Lidar measurement model



Fig. 3 – Forklift equipment with Lidar

The formula commonly used in the conversion of polar coordinates collected by Lidar to direct coordinates is:

$$\left. \begin{aligned} x &= d \cos \phi \\ y &= d \sin \phi \end{aligned} \right\} \quad (1)$$

Lidar, forklift and world coordinate systems are shown in Fig. 4. Lidar scans 360° on forklift to get feature points, and Q is assumed to be a point returned by the laser beam.

For any feature point Q, the vector from the Lidar to point Q is:

$$T_{LQ} = T_{WQ} - (T_{WF} + T_{FL}) \tag{2}$$

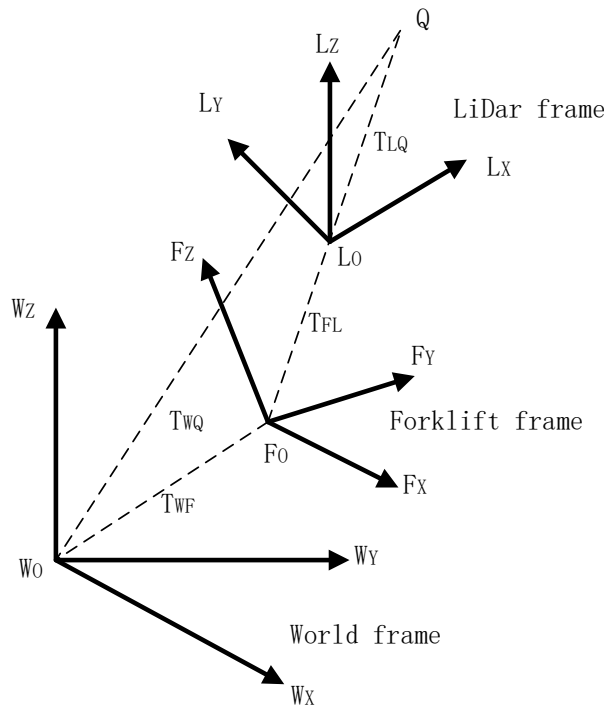


Fig. 4 – Lidar, Forklift and World Coordinate System and feature point Q

When the forklift is moving crops in a storage environment, the Lidar placed on top of the vehicle scans for obstacles with height h . Thus, $T_{WQ}^W(h)$ denotes the vector of height h from T to the feature point Q in the world coordinate system, the vector equation is:

$$T_{WQ}^W(h) = T_{LQ}^W + h e_1 \tag{3}$$

where: h is a scalar, $h \in (0, +\infty)$, vector e_1 parallel and perpendicular to the line, $e_1 = [0, 0, 1]^T$.

For any feature point Q with height h , the equation (2) still holds in all coordinate systems.

In vector equation (2) and in Fig.4, T_{WQ} is a known constant in the world coordinate system. T_{WF} can be calculated in the world coordinate system, T_{FL} is known in the forklift coordinate system and it can be determined by pre-calibration. Define R_F^L as the rotation matrix from the forklift coordinate system to the Lidar coordinate system. So, this yields the vector of feature point Q in the Lidar coordinate system denoted as:

$$T_{LQ}^L = R_F^L (R_W^F (T_{WQ}^W - T_{WF}^W) - T_{FL}^F) \tag{4}$$

Substitute equation (3) into equation (4) to obtain the equation, which is the vector from the Lidar origin to the feature point with height h :

$$T_{LQ}^L = R_F^L (R_W^F (T_{LQ}^W + h e_1 - T_{WF}^W) - T_{FL}^F) \tag{5}$$

Expanding the equation (5), the theoretical coordinates of $T_{LQ}^L(h)$ in the -LZ direction are obtained as:

$$Z(h) = e_1^W T_{LQ}^L(h) = h e_1^W R_F^L R_W^F e_1 + e_1^W R_F^L (R_W^F (T_{WQ}^W - T_{WF}^W) - T_{FL}^F) \tag{6}$$

For single plane Lidar, scan plane $LZ=0$ in the coordinate system.

The Lidar measurement model is obtained as:

$$T_{LQ}^L(h) = R_F^L \left(R_W^F \left(T_{WQ}^W - \frac{e_1^W R_F^L (R_W^F (T_{WQ}^W - T_{WF}^W) - T_{FL}^F)}{e_1^W R_F^L e_1} e_1 - T_{WF}^W \right) - T_{FL}^F \right) \quad (7)$$

Inertial Measurement Unit measurement model

IMU is a motion sensing sensor, different from the environmental sensing sensor Lidar. It measures the angular velocity of the carrier relative to the coordinate axes and the acceleration of the carrier in the carrier coordinate system using 3-axis gyroscope and 3-axis accelerometer. Based on the acceleration and angular velocity of the IMU in 3D space, the system solves for the attitude of the carrier. During the initial operation of the IMU, environmental problems will cause errors, and the error will accumulate as time increases. Error and noise caused by environmental factors should be considered during IMU operation. Due to the existence of deviation, the measured value of IMU will drift over time. This paper adopts the method of IMU and Lidar integration. Assuming that e is the error and n is the noise, the noise is Gaussian white noise and mean value is 0. The schematic diagram of the IMU system is shown in Fig.5.

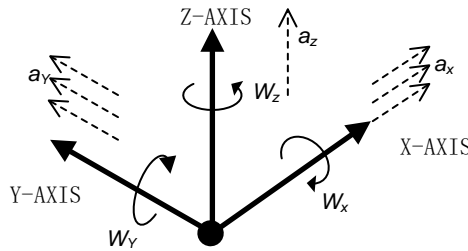


Fig. 5 – Schematic diagram of the IMU system

The data output from the IMU is the information measured by the gyroscope and accelerometer. The speed, position and attitude of the forklift truck can be obtained after these data are calculated. The state C of the forklift can be expressed as:

$$C = [R^T, P^T, v^T, b^T] \quad (8)$$

where R refers to 3×3 rotation matrix, P refers to 1×3 location matrix, v refers to forklift speed, b refers to bias of IMU. b can be expressed as:

$$b = [b^g, b^a] \quad (9)$$

where b^g, b^a refer to bias of gyroscopes and accelerometers.

Based on IMU raw data angular velocity w and acceleration a , measured values \hat{w} and \hat{a} are influenced by the white noise n and the bias b :

$$\hat{w}(t) = w(t) + b^w(t) + n^w(t) \quad (10)$$

$$\hat{a}(t) = R_W^F(t)(a(t) - g) + b^a(t) + n^a(t) \quad (11)$$

where define R_W^F as the rotation matrix from the world coordinate system to the forklift coordinate system, g refers to acceleration of gravity in world coordinates.

Based on the measured values of the IMU, the rotation, position and speed of the forklift at time t are shown in (12)-(14):

$$R(t + \Delta t) = R(t) \exp((\hat{w}(t) - b^w(t) - n^w(t))\Delta t) \quad (12)$$

$$P(t + \Delta t) = P(t) + v(t)\Delta t + \frac{1}{2}gt^2 + \frac{1}{2}R(t)(\hat{a}(t) - b^a(t) - n^a(t))\Delta t^2 \quad (13)$$

$$v(t + \Delta t) = v(t) + g\Delta t + R(t)(\hat{a}(t) - b^a(t) - n^a(t))\Delta t \quad (14)$$

Laser SLAM model

Laser SLAM takes IMU data, odometer data, and Lidar data as input information, and outputs the scanned raster map. Laser SLAM mainly includes five steps, and the process is shown in Fig.6.

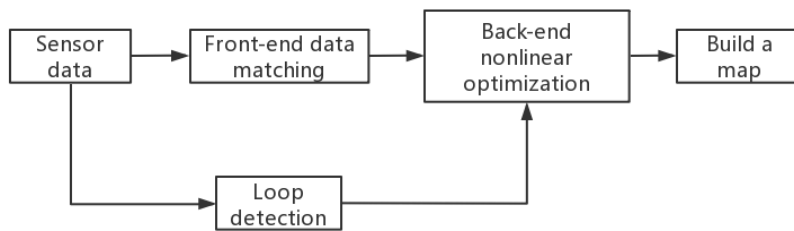


Fig. 6 – The General Flow of Laser SLAM

This map-building method requires information on the coordinate transformation (TF) between the robot base coordinates and the sensor, Lidar information and IMU information. Forklift systems have met the requirements for building maps. After inputting the Lidar data and IMU data, the system will get the a priori bit attitude at the first time. It will determine whether the two sensors' data are valid according to the defined data flow. Then it incorporates the corresponding data of the valid flag bits into the filter for processing. Finally, the posterior pose is obtained and it outputs the map information. The indoor environment map obtained from the forklift system scan is shown in Fig. 7. The Gray areas and black blocks are obstacles.



Fig. 7 – Laser SLAM Scans the Map

Fusion navigation and positioning based on Lidar/IMU

Firstly, solve the Lidar data to obtain position and attitude observations of the forklift. Then, blend the information obtained from Lidar and position, attitude information obtained from IMU data calculated by SINS (Strapdown Inertial Navigation System) algorithm. Finally, the fusion information is used as input to the EKF algorithm. Both Lidar and IMU are independent in terms of acquiring data that can be calibrated against each other based on the results of the solution. So, the positioning accuracy obtained is more reliable. If one of the Lidar and IMU sensors stops collecting due to environmental influences or its own factors, then another sensor can still provide the forklift system with navigation parameters for positioning.

Improved extended Kalman filter algorithm

This paper presents an attitude estimation algorithm based on EKF algorithm, which accords to laser scanning matching pose estimation system and IMU motion estimation system. The method has two main processes: the position and attitude of the forklift truck estimated from the first Lidar scan is used as Lidar's attitude information.

IMU sensor is used to provide the Lidar with a positional position. In order to obtain the attitude estimation information of the Lidar, the scan information of Lidar and the information provided by IMU need to be fused into EKF filter data.

Collect IMU and Lidar data at the current time, then the IMU attitude information is acquired by means of SINS algorithm and derive the Lidar pose at the current moment. There is noise in the forklift system and observation, assuming that its distribution is a conditionally independent Gaussian white noise distribution. The system is not linear and the Gaussian distribution cannot be used directly in a non-linear system. In this paper, an improved EKF filter algorithm is used to solve this problem, specifically it is used in bite-position fusion.

The prediction model uses IMU data. However, if only the angular velocity and acceleration data predicted by the IMU are used to derive velocity and position through integral estimation, the system must be unstable, and additional measurement data must be available to assist with updates. Moreover, in terms of the hardware system, there are insurmountable errors inherent in the system, the data itself produce errors. This hardware level error is also the cause of drift in the system data. Facing such problems, it is necessary to use algorithms to pre-process the data for live correction.

To solve this problem, the improved EKF filter algorithm is chosen for prediction and update in this paper, and the following is a brief procedure:

Estimating the covariance of errors:

$$(P^+)^{-1} = (1 - k) P^{-1} + k C^T R^{-1} C \quad (15)$$

State prediction equations for the Lidar attitude:

$$\hat{x}^+ = P^+ [(1 - k) P^{-1} \hat{x} + k C^T R^{-1} \xi^*]^{-1} \quad (16)$$

Kalman gain solution:

$$K = P C^T \left(\frac{1-k}{k} R + C^T P C \right)^{-1} \quad (17)$$

Update Lidar attitude status:

$$\hat{x}^+ = \hat{x} + K(\xi^* - C\hat{x}) \quad (18)$$

Update error covariance:

$$P^+ = P - (1 - k)^{-1} K C P \quad (19)$$

where: x refers to posture information of Lidar scans, $x = (L_T, \Omega_T, V_T)^T$, $L = (L_x, L_y, L_z)^T$, L refers to location information, Ω refers to Euler angles, $V = (V_x, V_y, V_z)^T$ refers to the instantaneous speed. P refers to covariance of states x , R refers to directional cosine matrix, ξ^* refers to attitude information output by Lidar, k refers to weighting parameters, $k \in (0, 1)$. The size of the k value is proportional to the confidence level of the matching result.

The information data fused by the improved EKF filtering algorithm exhibits greater robustness to process parameter variations and environmental noise disturbances. The improved filter algorithm is able to reduce the influence of historical observations on the system by autonomously adjusting the prior probability density estimates. The combination of attitude information collected by the IMU and position and attitude information from the Lidar scan with the improved EKF filter algorithm can effectively improve the positioning accuracy of the robot movement. The angular velocity after filtering is shown in the Fig. 8.

RESULTS

Experiment and Analysis

The experiment was divided into two parts. Simulation experiments are used to verify the positioning accuracy of the forklift system in an indoor storage environment using the improved EKF filtering algorithm proposed in this paper. Indoor experiments are used to verify the effectiveness of the proposed combined Lidar/IMU navigation and positioning method for forklifts working in a simulated warehouse environment.

Simulation experiments and analysis

The simulation experiments were conducted in the ROS (Robotics Operating System) based on the LINUX system. The electric forklifts model was built in Gazebo Physical Simulation Platform, which can reflect the movement of forklift under different methods in a more realistic way. The physical properties of the forklift are set in detail in the Link tab, which includes data such as shape, size, turning radius, power parameters and crash parameters, etc. The connection diagram position posture and connection relationship are shown in Fig.9. The simulation control model of the forklift is shown in Fig. 10.

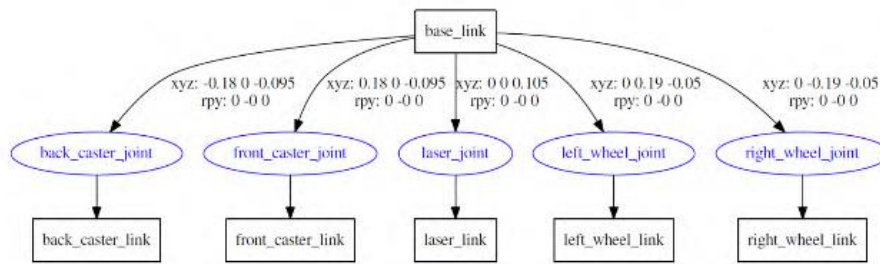


Fig. 9 – Link-joint connection

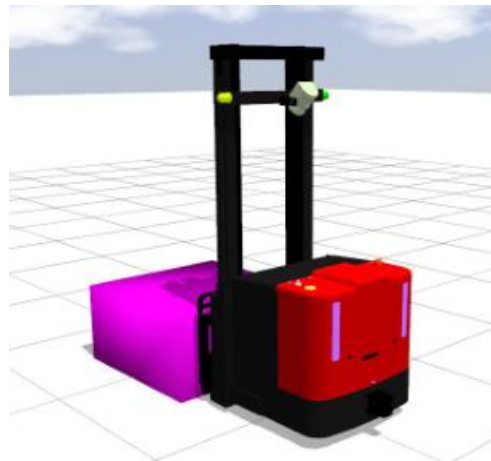


Fig. 10 – Forklift motion control simulation model

The forklift uses a backward approach when loading cargo and a forward approach when operating on the normal path. The forklift uses the same backward approach when unloading cargo. Based on this situation, an expected forklift travel route is planned in the simulation environment at first. Then, let the forklift use Lidar data alone for navigation and positioning, use IMU data alone for navigation and positioning and use the fusion data obtained by Improved EKF filtering algorithm. Placement of the travel paths into the same diagram for comparison is shown in Fig. 11.

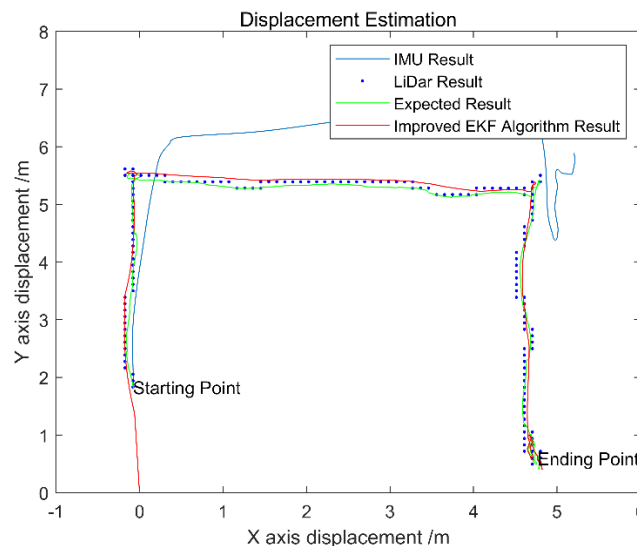


Fig. 11 – Navigation and Positioning Results

If only measurements from the IMU are used over a period of time, it will cause the forklift to move in a different route than expected. Although the path using Lidar data alone matches the expected path, there is no noise factor interfering in the simulation environment which is precisely the most serious problem affecting Lidar. Use traditional and improved filtering algorithms in the simulation environment. The error results of the multiple trials in the simulation environment are shown in Table 1.

Table 1

Statistic Table of Positioning and Velocity Measurement				
State estimation	X-axis position error/m	Y-axis position error/m	X axis speed error/(m/s)	Y axis speed error/(m/s)
Mean	0.018	0.018	0.003	0.003
Mean square error	0.38	0.38	0.06	0.06

Indoor experiments and analysis

To simulate a forklift moving crops in a storage environment, obstacles and shelves are placed in the indoor environment of the laboratory. Let the forklift work in this environment to verify the effectiveness of the combined Lidar/IMU navigation and positioning. The forklift will load the boxes of crops to be transported at *Point 2* and transport them to the racks at *Point 0*. On the way, it will pass the area where the crop is stacked (this area is simulated with some obstacles in the laboratory environment). The forklift system can avoid this area autonomously, avoid obstacles in the forward route and finally reach *Point 0* safely, the actual route is shown in Fig. 12. In Fig. 12 (a), the green line shows the forward path determined by the forklift, and in Fig. 12 (b) (c), the forklift updates the forward path to avoid obstacles.

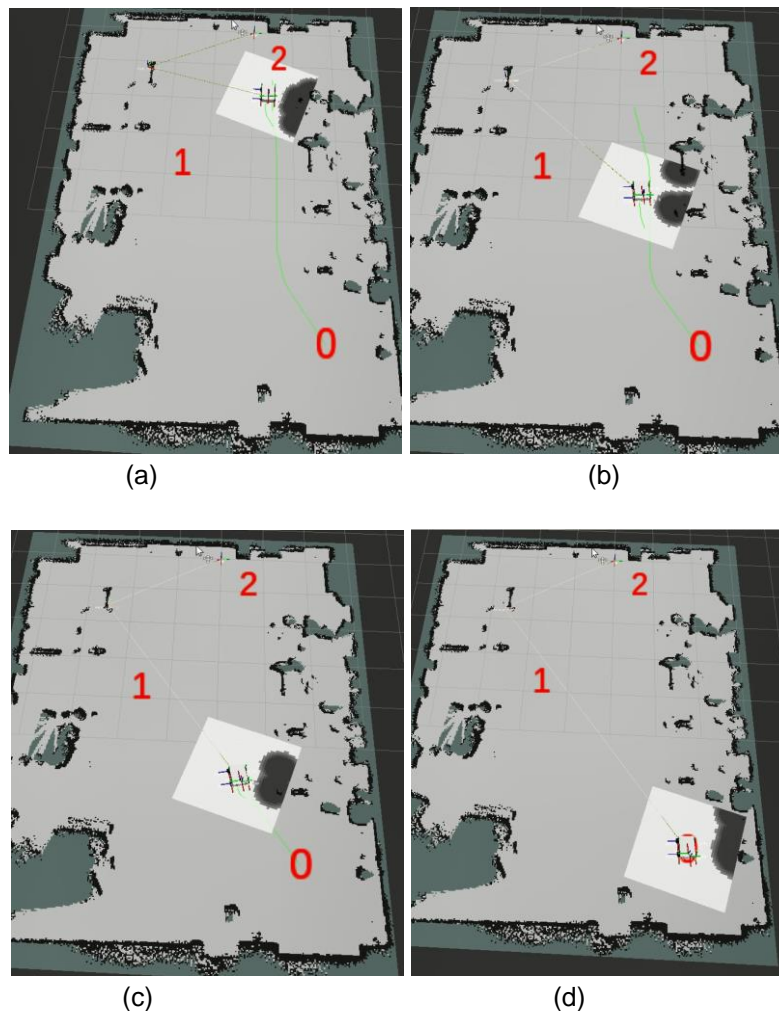


Fig. 12 – Forklift simulation storage experiment

Considering whether the whole system would be affected if the forklift speed was changed, another experience is conducted: let the forklift arrive at the same target area from the same starting point at 50cm/s, 80 cm/s and 1 m/s. The path trajectory is shown in Fig.13. It can be seen that if the speed of the forklift is too fast, although the forklift can also reach the target area, it will rush out of the target area, because it could not reduce the speed in time. The right operating speed can improve the efficiency of the forklift.

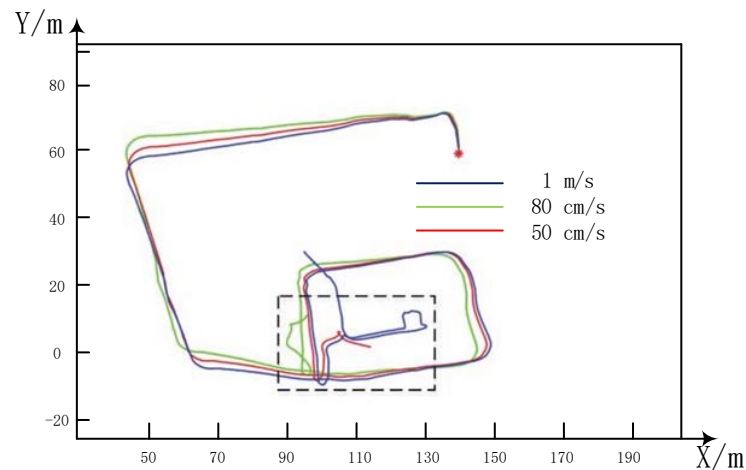


Fig. 13 – Results of running at different speeds

CONCLUSIONS

In order to improve the solution of positioning and navigation accuracy of forklift system in the warehouse environment with complex environment, the article proposes a navigation and positioning method with Lidar/IMU fusion. The system uses Lidar and IMU as posture information collection sensors for forklift. First, the forklift position and attitude information obtained from the Lidar scan is used as an input quantity. Then, the IMU decodes the gyroscope and accelerometer outputs, the forklift speed, position, and attitude information obtained is used as another input quantity. Finally, the data information obtained from Lidar is fused with the data information obtained from IMU by the improved EKF filtering algorithm. This enables accurate position and attitude updates of the forklift system.

The simulation experiment was done in order to demonstrate that the fused IMU data can reduce the trajectory error of Lidar ranging. And the fused Lidar ranging corrects for cumulative IMU errors. The proposed improved EKF filtering algorithm can improve the positioning accuracy of forklifts. Another experimentation of forklifts working in a warehouse environment was conducted in the laboratory. The forklift system can work effectively using the method proposed in this paper. Finally, a comparison experiment of forklifts at different speeds was conducted. The results show that the method proposed in this paper can meet the navigation and positioning needs of forklifts, but if the speed is too high, it will drive out of the target area. It has to work with the right speed.

ACKNOWLEDGEMENT

This work was supported in part by the National Natural Science Foundation of China (Grant no. 52074184), and the name of the work is Interfacial structure control and graphene enhancement mechanism of impinging stream friction stir smart glue welding.

REFERENCES

- [1] Benzerrouk H., Landry R., Nebylov V., Nebylov A., (2020), Robust INS/GPS Coupled Navigation Based on Minimum Error Entropy Kalman Filtering, *2020 27th Saint Petersburg International Conference on Integrated Navigation Systems*, Russia;
- [2] Chunman Yan, Sonlun Wu, (2020), Application of adaptive fading and biased extended Kalman filter in target tracking, *Journal of Sensor Technology*, Vol. 33, Issue 02, pp. 315-320;
- [3] Faessler M., Fontana F., Forster C. et al., (2015), Automatic re-initialization and failure recovery for aggressive flight with a monocular vision-based quadrotor [C], *IEEE*, pp. 1722-1729;
- [4] Gentil C.L., Vidal-Calleja T., (2018), 3D Lidar-IMU calibration based on up-sampled pre-integrated measurements for motion distortion correction, *IEEE*, pp. 2149-2155;
- [5] Goran Vasiljević, Damjan Miklić, Ivica Draganjac, Zdenko Kovačić, (2016), High-accuracy vehicle localization for autonomous warehousing, *Robotics and Computer-Integrated Manufacturing*, IEEE, Vol. 42, pp. 1-16;
- [6] Jian Wang, Chao Liu, Gao Jingxiang, et al., (2017), Research on GNSS/INS Tight Combination Algorithm Based on Robust EKF (基于抗差 EKF 的 GNSS/INS 紧组合算法研究), *Journal of Wuhan University*, Vol. 36, Issue 05, pp. 596-600;

- [7] Kayacan E., Chowdhary G., (2019), Tracking error learning control for precise mobile robot path tracking in outdoor environment, *Journal of Intelligent & Robotic Systems*, vol. 95, issue 3-4, pp. 975-986;
- [8] Mouayad Sahib, Amjad Humaidi, (2020), Multi-objective path planning of an autonomous mobile robot using hybrid PSO-MFB optimization algorithm, *Applied Soft Computing Journal*, Vol. 89. 106076;
- [9] Neuhaus F., Tilman K., Robert K., et al., (2018), MC2SLAM: Real-time inertial Lidar odometry using two-scan motion compensation [C], *Proceedings of 2018 German Conference on Pattern Recognition*, pp.60–72.
- [10] Nguyen, Duy Anh Pham, Truong Thinh Nguyen, Viet Duong, (2020), A better indexing method for closest open location policy in forklift warehouse operation, *Lecture Notes in Electrical Engineering*, Vol. 554, pp. 251-260;
- [11] Xin'ge Wang, Zongqiang Tian, (2020), Research on Laser SLAM Algorithm Based on Improved RBPF (基于改进 RBPF 的激光 SLAM 算法研究), *Journal of Anhui University of Engineering*, Vol. 35, Issue 06, 18-25;
- [12] Xinlei Li., Yanghong Pan., et al., (2020), Fully autonomous mobile robot based on Lidar positioning system (基于激光雷达定位系统的全自主移动机器人), *Science and Technology Innovation*, Vol. 29, 91-92;
- [13] Zhao S., Fang Z., Li H., et al., (2019), A robust laser-inertial odometry and mapping method for large-scale highway environments [C], *Proceedings of 2019 IEEE/RSJ International Conference on Intelligent Robots and Systems*. pp. 1285–1292;
- [14] Zhao X., Kang Y., (2019), Integrated Navigation Error Analysis Based on Kalman Filter of INS Error Compensation, *2019 3rd International Conference on Robotics and Automation Sciences*.

WRITING INSTRUCTIONS

Article Types

Three types of manuscripts may be submitted:

1. **Regular articles:** These should describe new and carefully confirmed findings, and experimental procedures should be given in sufficient detail for others to verify the work. The length of a full paper should be the minimum required to describe and interpret the work clearly (max.10 pages, even number);
2. **Reviews:** Submissions of reviews and perspectives covering topics of current interest are welcome and encouraged (max.12 pages, even number).

Manuscripts should be written in English (American or British usage is accepted, but not a mixture of these) and submitted **electronically** at the following e-mail addresses: ***inmatehjournal@gmail.com***

Please be sure to include your full affiliation and e-mail address (see Sample manuscript)

The authors are responsible for the accuracy of the whole paper and references.

There are allowed 2 papers by each first author.

The text layout should be in single-column format. To avoid unnecessary errors it is strongly advised to use the “spell-check” and “grammar check” functions of your word processor.

Review Process

All manuscripts are reviewed by 2 members of the Scientifically Review Office. Decisions will be made as rapidly as possible and the journal strives to return reviewers' comments to authors in approx.3 weeks.

The editorial board will re-review manuscripts that are accepted pending revision.

NOTE:

Submission of a manuscript implies: that the work described has not been published before (excepting as an abstract or as part of a published lecture or thesis) that it is not under consideration for publication elsewhere.

1. REGULAR ARTICLES

- Manuscripts should be concise, in **1.15 line spacing**, and should have 2 cm all over margins. The font should be **Arial 10 pt.** Ensure that each new paragraph is clearly indicated, using **TAB at 1 cm.**
- Title will be **Arial 12 pt.** and explicit figures will be **Arial 9 pt.**
- Text will be written in English.
- Chapters' titles are written by **Arial 10 pt, Bold, Uppercase** (e.g. **INTRODUCTION, MATERIALS AND METHODS**), between chapters is left a space for 10 pt. At the beginning of each paragraph, TAB of 1 cm.
- The paper body will be written in **Arial 10 pt., Justify alignment.**

TITLE **Arial 12 pt., Uppercase, Bold, Center** (in English language) and **Bold Italic** (in native language).

Should be a brief phrase describing the contents of the paper. Avoid long titles; a running title of no more than 100 characters is encouraged (without spaces).

AUTHORS **ARIAL 9, Bold, Centre alignment**

Under the paper's title, after a space (enter) 9 pt., write **authors' names** and **affiliations (Arial 8 pt.-Regular)**

When the paper has more than one author, their name will be followed by a mark (Arabic numeral) as superscript if their affiliation is different. **Less than 6 authors.**

Corresponding author's name (next row), (**Arial 8 pt.**). Should be added also: phone, fax and e-mail information, for the paper corresponding author (**font: 8 pt., Italic**).

KEYWORDS (**In English**) about 4 to 7 words that will provide indexing references should be listed (**title: Arial 10pt, bold italic, text Arial 10 pt., italic**).

A list of non-standard **Abbreviations** should be added. In general, non-standard abbreviations should be used only when the full term is very long and used often. Each abbreviation should be spelled out and introduced in parentheses the first time it is used in the text. Standard abbreviations (such as ATP and DNA) need not to be defined.

ABSTRACT (**in English and Native language, Arial 10 pt.**), the title **bold**; the text of abstract: **italic**) should be informative and completely self-explanatory, briefly present the topic, state the scope of the experiments, indicate significant data, and point out major findings and conclusions. The Abstract should be max.250 words. Complete sentences, active verbs, and the third person should be used, and the abstract should be written in the past tense. Standard nomenclature should be used and abbreviations should be avoided. No literature should be cited.

INTRODUCTION (**Arial 10 pt.**) should provide a clear statement of the problem, the relevant literature on the subject, and the proposed approach or solution. It should be understandable to colleagues from a broad range of scientific subjects. We should refer to the current stage of researches performed in the field of the paper to be published, by quoting up-to-date specialty studies, preferably published after 2006, excepting certain referential specialty

books/studies, especially papers issued in magazines/journals/conferences/ISI quoted symposia or in other international data bases, which are well known and available.

MATERIALS AND METHODS (*Arial 10 pt.*) should be complete enough to allow experiments to be reproduced. However, only truly new procedures should be described in detail; previously published procedures should be cited, and important modifications of published procedures should be mentioned briefly. Methods in general use need not be described in detail.

RESULTS (*Arial 10 pt.*) should be clearly presented. The results should be written in the past tense when describing findings in the authors' experiments. Results should be explained, but largely, without referring to the literature. Discussion, speculation and detailed interpretation of data should not be included in the Results, but should be put into the Conclusions section.

CONCLUSIONS (*Arial 10 pt.*) The main conclusions drawn from results should be presented in a short Conclusions section. Do not include citations in this section.

Formulae, symbols and abbreviations: Formulae will be typeset in Italics (preferable with the Equation Editor of Microsoft Office 2003) and should be written or marked as such in the manuscript, unless they require a different styling. They should be referred to in the text as Equation (4) or e.g. (4). The formulae should be numbered on the right side, between brackets (*Arial 10 pt.*):

$$P = F \cdot v \quad (1)$$

Terms of the equation and the unit measure should be explained, e.g.

P is the power, [W];

F – force, [N];

v – speed, [m/s]

SI units must be used throughout.

Tables should be self-explanatory without reference to the text. The details of the methods used in the experiments should preferably be described in the legend instead of in the text. The same data should not be presented both in table and graph form or repeated in the text.

Table's title will be typed *Arial 9 pt, Bold, Centered*

In the table, each row will be written Arial 9 pt, single-spaced throughout, including headings and footnotes.

The table should be numbered on the right side, *Arial 10 pt.*

Figures (*Arial 9 pt., Bold, Center*) should be typed in numerical order (Arabic numerals). Graphics should be high resolution (e.g. JPEG). Figure number is followed by what represent the figure or graph e.g.:

Fig.1 – Test stand

Legend: *Arial 8 pt, Italic, Center*, e.g.:

1 - plansifter compartments; 2- break rolls; 3 – semolina machines; 4 – reduction rolls; 5 – flour

ACKNOWLEDGMENTS (*Arial 10 pt.*) of people, grants, funds etc should be brief (*if necessarily*).

REFERENCES (*Arial 10 pt.*)

(*In alphabetical order, in English and in the original publication language*).

Minimum 10 references, last 10 years, minimum 3 references from the last 2 years

It can be used “*References*” tool from the *Word Editor*. **APA Style (American Psychological Association)** <https://apastyle.apa.org/style-grammar-guidelines/references/examples>

All references must be provided in English

Authors are fully responsible for the accuracy of the references.

References should be **alphabetically**, with complete details, as follows:

Examples:

Books: <https://apastyle.apa.org/style-grammar-guidelines/references/examples/book-references>

Jackson, L. M. (2019). *The psychology of prejudice: From attitudes to social action* (2nd ed.). American Psychological Association. <https://doi.org/10.1037/0000168-000>

Kesharwani, P. (2020). *Nanotechnology based approaches for tuberculosis treatment*. Academic Press.

Sapolsky, R. M. (2017). *Behave: The biology of humans at our best and worst*. Penguin Books.

Torino, G. C., Rivera, D. P., Capodilupo, C. M., Nadal, K. L., & Sue, D. W. (2019). *Microaggression theory: Influence and implications*. John Wiley & Sons. <https://doi.org/10.1002/9781119466642>

In text:

- **Paranthesis citations:** (Jackson, 2019; Sapolsky, 2017)
- **Narrative citations:** Jackson (2019) and Sapolsky (2017)

Journal Article:

<https://apastyle.apa.org/style-grammar-guidelines/references/examples/journal-article-references>

Grady, J. S., Her, M., Moreno, G., Perez, C., & Yelinek, J. (2019). Emotions in storybooks: A comparison of storybooks that represent ethnic and racial groups in the United States. *Psychology of Popular Media Culture*, 8(3), 207–217. <https://doi.org/10.1037/ppm0000185>

In text:

- **Paranthesis citation:** (Grady et al., 2019)
- **Narrative citation:** Grady et al. (2019)

Conference or Symposium:

<https://apastyle.apa.org/style-grammar-guidelines/references/examples/conference-proceeding-references>

Duckworth, A. L., Quirk, A., Gallop, R., Hoyle, R. H., Kelly, D. R., & Matthews, M. D. (2019). Cognitive and noncognitive predictors of success. *Proceedings of the National Academy of Sciences, USA*, 116(47), 23499–23504. <https://doi.org/10.1073/pnas.1910510116>

In text:

- **Paranthesis citation:** (Duckworth et al., 2019)
- **Narrative citation:** Duckworth et al. (2019)

Dissertation / Thesis:

<https://apastyle.apa.org/style-grammar-guidelines/references/examples/published-dissertation-references>

Zambrano-Vazquez, L. (2016). *The interaction of state and trait worry on response monitoring in those with worry and obsessive-compulsive symptoms* [Doctoral dissertation, University of Arizona]. UA Campus Repository. <https://repository.arizona.edu/handle/10150/620615>

In text:

- **Paranthesis citations:** (Kabir, 2016; Miranda, 2019; Zambrano-Vazquez, 2016)
- **Narrative citations:** Kabir (2016), Miranda (2019), and Zambrano-Vazquez (2016)

<https://apastyle.apa.org/style-grammar-guidelines/references/examples/unpublished-dissertation-references>

Harris, L. (2014). *Instructional leadership perceptions and practices of elementary school leaders* [Unpublished doctoral dissertation]. University of Virginia.

In text:

- **Paranthesis citation:** (Harris, 2014)
- **Narrative citation:** Harris (2014)

Patents: Names and initials of authors, year (between brackets), patent title (Italic), patent number, country:

Grant, P. (1989). *Device for Elementary Analyses*. Patent. No.123456. USA.

Legal regulations and laws, organizations:

<https://apastyle.apa.org/style-grammar-guidelines/references/examples/iso-standard-references>

International Organization for Standardization. (2018). *Occupational health and safety management systems—Requirements with guidance for use* (ISO Standard No. 45001:2018). <https://www.iso.org/standard/63787.html>

Occupational Safety and Health Administration. (1970). *Occupational safety and health standards: Occupational health and environmental control: Occupational noise exposure* (OSHA Standard No. 1910.95). United States Department of Labor.

<https://www.osha.gov/laws-regs/regulations/standardnumber/1910/1910.95>

In text:

- **Paranthesis citations:** (International Organization for Standardization, 2018; Occupational Safety and Health Administration, 1970)
- **Narrative citations:** International Organization for Standardization (2018) and Occupational Safety and Health Administration (1970)

Web references: The full URL should be given in text as a citation, if no other data are known. If the authors, year, and title of the documents are known and the reference is taken from a website, the URL address has to be mentioned after these data.

Citation in text

Please ensure that every reference cited in the text is also present in the reference list (and vice versa).

Do not cite references in the Abstract and Conclusions !.

Unpublished results, personal communications as well as URL addresses are not recommended in the references list.

Making personal quotations (one, at most) should not be allowed, unless the paper proposed to be published is a sequel of the cited paper. Articles in preparation or articles submitted for publication, unpublished, personal communications etc. should not be included in the references list.

Citations style

Text: All citations in the text may be made directly (or parenthetically) as bellow.

- **single author:** the author's name (without initials, unless there is ambiguity) and the year of publication: "as previously demonstrated (*Brown, 2010*)".
- **two authors:** both authors' names and the year of publication: (*Adam and Brown, 2008; Smith and Hansel, 2006; Stern and Lars, 2009*)
- **three or more authors:** first author's name followed by "et al." and the year of publication: "As has recently been shown (*Werner et al., 2005; Kramer et al., 2000*) have recently shown"

Citations of groups of references should be listed first alphabetically, then chronologically.

Units, Abbreviations, Acronyms

- Units should be metric, generally SI, and expressed in standard abbreviated form.
- Acronyms may be acceptable, but must be defined at first usage.

2. REVIEWS

Summaries, reviews and perspectives covering topics of current interest in the field, are encouraged and accepted for publication. Reviews do not have the requirements for regular articles. However, should include: (*) an introductory chapter, (**) a careful and critical presentation of the relevant aspects of the topic approached and (***) emphasis of the aspects that aren't known and require further research to progress. Reviews should be concise (max. 12 pages).



Edited by: INMA Bucharest

6, Ion Ionescu de la Brad Blvd., sect. 1, Bucharest, ROMANIA

Tel: +4021.269.32.60; Fax: +4021.269.32.73

[https:// inmateh.eu](https://inmateh.eu)

e-mail: inmatehjournal@gmail.com

